

Bedangadas Mohanty
Sanjay Kumar Swain
Ranbir Singh
Varchaswi K. S. Kashyap *Editors*

Proceedings of the XXIV
DAE-BRNS High Energy
Physics Symposium,
Jatni, India

Springer Proceedings in Physics

Volume 277

Indexed by Scopus

The series Springer Proceedings in Physics, founded in 1984, is devoted to timely reports of state-of-the-art developments in physics and related sciences. Typically based on material presented at conferences, workshops and similar scientific meetings, volumes published in this series will constitute a comprehensive up-to-date source of reference on a field or subfield of relevance in contemporary physics. Proposals must include the following:

- name, place and date of the scientific meeting
- a link to the committees (local organization, international advisors etc.)
- scientific description of the meeting
- list of invited/plenary speakers
- an estimate of the planned proceedings book parameters (number of pages/articles, requested number of bulk copies, submission deadline).

Please contact:

For Americas and Europe: Dr. Zachary Evenson; zachary.evenson@springer.com
For Asia, Australia and New Zealand: Dr. Loyola DSilva; loyola.dsilva@springer.com

Bedangadas Mohanty · Sanjay Kumar Swain ·
Ranbir Singh · Varchaswi K. S. Kashyap
Editors

Proceedings of the XXIV
DAE-BRNS High Energy
Physics Symposium, Jatni,
India

Editors

Bedangadas Mohanty
School of Physical Sciences
National Institute of Science Education
and Research
Jatni, India

Homi Bhabha National Institute, Training
School Complex
Mumbai, India

Ranbir Singh
School of Physical Sciences
National Institute of Science Education
and Research
Jatni, India

Homi Bhabha National Institute, Training
School Complex
Mumbai, India

Sanjay Kumar Swain
School of Physical Sciences
National Institute of Science Education
and Research
Jatni, India

Homi Bhabha National Institute, Training
School Complex
Mumbai, India

Varchaswi K. S. Kashyap
School of Physical Sciences
National Institute of Science Education
and Research
Jatni, India

Homi Bhabha National Institute, Training
School Complex
Mumbai, India

ISSN 0930-8989

ISSN 1867-4941 (electronic)

Springer Proceedings in Physics

ISBN 978-981-19-2353-1

ISBN 978-981-19-2354-8 (eBook)

<https://doi.org/10.1007/978-981-19-2354-8>

© The Editor(s) (if applicable) and The Author(s), under exclusive license to Springer Nature Singapore Pte Ltd. 2022

This work is subject to copyright. All rights are solely and exclusively licensed by the Publisher, whether the whole or part of the material is concerned, specifically the rights of translation, reprinting, reuse of illustrations, recitation, broadcasting, reproduction on microfilms or in any other physical way, and transmission or information storage and retrieval, electronic adaptation, computer software, or by similar or dissimilar methodology now known or hereafter developed.

The use of general descriptive names, registered names, trademarks, service marks, etc. in this publication does not imply, even in the absence of a specific statement, that such names are exempt from the relevant protective laws and regulations and therefore free for general use.

The publisher, the authors, and the editors are safe to assume that the advice and information in this book are believed to be true and accurate at the date of publication. Neither the publisher nor the authors or the editors give a warranty, expressed or implied, with respect to the material contained herein or for any errors or omissions that may have been made. The publisher remains neutral with regard to jurisdictional claims in published maps and institutional affiliations.

This Springer imprint is published by the registered company Springer Nature Singapore Pte Ltd. The registered company address is: 152 Beach Road, #21-01/04 Gateway East, Singapore 189721, Singapore

NOC and LOC Members

National Organizing Committee

Aninda Sinha (IISc)
Anshuman Maharana (HRI)
Bhartendu Singh (BHU)
Bipul Bhuyan (IIT-Guwahati)
Diptimoy Ghosh (IISER-Pune)
Hiranmaya Mishra (PRL)
D. Indumathi (IMSc)
James Libby (IIT-M)
Kirti Ranjan (DU)
Lokesh Kumar (PU)
Prafulla Kumar Behera (IIT-M)
Raghunathan Srianand (IUCAA)
Sachindra Naik (PRL)
Sadhana Dash (IIT-B)
B Satyanarayana (TIFR)

Local Organizing Committee

Ajit Srivastava (IOP)
Amaresh K. Jaiswal (NISER)
Arun K. Nayak (IOP)
Bedangadas Mohanty (NISER, Chair)
Chandrasekhar Bhamidipati (IIT-BBS)
Chethan N. Gowdigere (NISER)
Kirtiman Ghosh (IOP)
Manimala Mitra (IOP)

Md. Nasim (IISER-BPR)
Najmul Haque (NISER)
Nishikanta Khandai (NISER)
Pankaj Agrawal (IOP)
Pradip K. Sahu (IOP)
Prolay K. Mal (NISER)
Ranbir Singh (NISER)
Sandeep Chatterjee (IISER-BPR)
Sanjay Swain (NISER, Co-chair)
Sanjib Kumar Agarwalla (IOP)
Sayantani Bhattacharyya (NISER)
Seema Bahniapati (IIT-BBS)
Shamik Banerjee (IOP)
Shesansu S. Pal (UU)
Subhasish Basak (NISER)
Sudhakar Panda (NISER)
Sudhansu Biswal (Ravenshaw University)
Sudipta Mukherjee (IOP)
Swapna Mahapatra (UU)
Tapan Kumar Nayak (NISER)
Tuhin Ghosh (NISER)
Ujjal Kumar Dey (IISER-BPR)
Varchaswi K. S. Kashyap (NISER)
Victor Roy (NISER)
Yogesh K. Srivasatva (NISER)

Preface

The field of High Energy Physics (HEP) is expanding at a great pace with the advent of modern-day particle accelerators like Relativistic Heavy Ion Collider (RHIC) and Large Hadron Collider (LHC) by extending our knowledge of particle physics and the universe. The high energy physics community in India is becoming larger which necessitates scientific congregation in the country. The aim of a conference/symposium is to provide a platform where the researchers gather to discuss and share the scientific knowledge which further helps in growing the field. The **DAE-BRNS High Energy Physics Symposium** is such a premier event that is held every other year in India, supported by the Board of Research in Nuclear Sciences (BRNS), Department of Atomic Energy (DAE), India. The XXIV addition of the symposium was hosted by National Institute of Science Education and Research (NISER), Jatni, Odisha, India, during December 14–18, 2020. Institute of Physics (IoP) Bhubaneswar, Utkal University Bhubaneswar, Ravenshaw University Cuttack, Indian Institute of Technology Bhubaneswar, and IISER Berhampur were co-organizers of the symposium.

The symposium consists of parallel and invited plenary sessions. Since it is impractical to accommodate all the contributions as oral presentations within the timeline of the symposium, a poster session was held to provide an opportunity to young researchers to showcase their research. The deliberations, from both experimental and theoretical perspectives, were held covering a variety of topics from all areas of high energy physics. The broad topics covered in the symposium were Standard and Beyond Standard Model Physics, Relativistic Heavy-ion Physics and QCD, Neutrino Physics, Particle Astrophysics and Cosmology, Formal Theory, Detector development, Future facilities and experiments, and Societal Applications.

For plenary and mini-review talks, suggestions were invited from members of the national and local organizing committees. The speakers were invited based on the recommendations by the committee members according to the topic. A total of 536 contributory abstracts were submitted. After the deadline for abstract submission, the contributory abstracts were sent to NOC and LOC members for review and selection based on the topics. On the recommendations of committee members, contributory abstracts were selected as talks and posters.

There were four special sessions conducted during the symposium. In the inaugural session, Prof. K. Vijay Raghavan, Principal Scientific Adviser to Govt. of India, presented his views on mega and multi-country science projects in high energy physics, and Prof. N. K. Mondal, a Senior Professor in Tata Institute of Fundamental Research, delivered an inspiring talk on “Possibilities, Challenges and Path forward in Building Mega Science high energy physics experiments in India”. Two things came out of the discussion session highlighting “Policy management side to the community” and “Community to policy management and introception”. The summary was circulated to the community. During a special session, Dr. Praveer Asthana from the office of Principal Scientific Advisor, Government of India, announced the Mega Science Vision Exercise—long-range planning by the community. A session was held in the memory of Prof. Pushan Majumadar, a Professor in School of Physical Sciences, Indian Association for the Cultivation of Science, Kolkata, India, who parted us on May 11, 2020—a great loss to the HEP community. He had a significant contribution in the area of lattice gauge theory and was also associated with the National Supercomputing Mission. His collaborators from India and abroad shared their wonderful experiences while working with him. In a special session, a panel discussion was held on exploring pathways for achieving gender parity in the field of high energy physics in India. The panelists and guest speakers from different areas of high energy physics participated and presented their views on gender parity in the field. It was highly encouraging to see increasing female contribution in the field. A session was organized for the award ceremony of IPA Rahul Basu Memorial Award for the best theses. This award is instituted in the memory of late Prof. Rahul Basu, one of the renowned high energy physicists and a key member of the HEP community. The award is coordinated through Indian Physics Association and the nominations for the award are invited from the faculty members working in university or research institutes. Two most outstanding theses across all areas of HEP including theory and experiment during the last 2 years from India are selected for this award. This time, two best theses and three honorable mentions were awarded during this special session in the symposium. The participation of young researchers was highly encouraging and as a token of appreciation, 14 contributions were selected for the award of the best poster in different areas of HEP.

Due to the COVID-19 pandemic situation, the symposium was held in online mode only. All plenary and parallel sessions were conducted through the Zoom platform. Poster sessions were held in virtual rooms using the FRAME platform. Several training sessions were conducted by the volunteers to train the poster presenters. Live streaming of all plenary lectures and special sessions was done using YouTube. All the sessions were recorded on Zoom and/or YouTube to help in future reference and convenience of participants. To keep updated with the symposium program, daily morning and evening bulletins were released throughout the duration of the symposium. More details on the symposium regarding the talks, posters, video recordings, YouTube channel, etc. can be found at the symposium website <https://www.niser.ac.in/daehep2020/>.

The statistics of the symposium manifested a nice comparison of the contributions in theory versus experiment, Institute versus Universities versus Colleges, male versus female, talks versus posters, etc. Out of the total submitted abstracts, theory and experiment covered 53.3% and 46.7%, respectively. We had received contributions from Institutes, Universities as well as graduate Colleges with percentage sharing of 59.3%, 36.2%, and 4.5%, respectively. Female contribution of 29.9% showed a significant increase in the participation of female researchers in the field of high energy physics. The total contributions were divided into 22 invited plenary talks, 24 invited mini-review talks, 204 parallel talks, and 282 poster presentations. In comparison with the last symposium, statistics showed a significant increase in the number of contributions as plenary talks (1.5 times), mini-review talks (2.6 times), parallel talks (1.06 times), and posters (1.9 times). These numbers were highly encouraging for the field of high energy physics in this pandemic situation. Geographically, the contributory abstracts were submitted from almost all parts of India. The abstracts were submitted from 22 out of 28 member states and 4 out of 8 union territories. The international contribution was also significant with 81.8% in plenary talks, 4.2% in mini-review talks, 8.12% in parallel talks, and 9.29% in poster presentations.

The selected contributions were called for the submission as a proceeding of the symposium. The proceedings were peer-reviewed before the final submission.

A general body meeting, open to all the participants, was held to discuss the symposium plan and preparation, and to get feedback from the participants. In this meeting, the proposals were accepted for hosting the next symposium. Indian Institute of Science Education and Research, Mohali, India, will host the DAE-BRNS HEP symposium 2022. We are hoping toward a great symposium in fall 2022, presumably in physical mode.

Jatni, India

Bedangadas Mohanty
Sanjay Kumar Swain
Ranbir Singh
Varchaswi K. S. Kashyap

Acknowledgements

Any event of such an intensity is never easy without the help and support of many people. Firstly, we would like to thank Local Organizing Committee (LOC) and National Organizing Committee (NOC) members for being a part of the symposium and providing continuous support. After receiving more than five hundred contributory abstracts, the challenging job was to review them and converge on selecting oral and poster presentations. We thank the review committees for this immaculate job. The selected contributions were called for the submission as proceedings which were peer-reviewed. We extend our thanks to the reviewers for rigorous reading and giving valuable comments. Our sincere thanks to Springer for publishing the proceedings of the symposium.

We would like to thank the Department of Atomic Energy (DAE) and the Department of Science and Technology (DST), Government of India, for their support. We acknowledge financial support from J. C. Bose National Fellowship of DST, Government of India, awarded to Prof. Bedangadas Mohanty.

We express our special thanks to Prof. K. Vijay Raghavan, Principal Scientific Adviser to Govt. of India, for presenting his view on mega and multi-country science projects, Prof. N. K. Mondal, Senior Professor in Tata Institute of Fundamental Research, for a very nice talk in the inaugural session, Dr. Praveer Asthana from the office of Principal Scientific Advisor, Government of India, for announcing the Mega Science Vision Exercise.

We would like to thank the Director, National Institute of Science Education and Research (NISER), Jatni, Odisha, for providing all the necessary support for the smooth conduct of the symposium. Thanks to the Finance and Store & Purchase section of NISER for their help in the procurement of Zoom licenses and FRAME technical support with time to spare. Thanks to the Institute Works Department, NISER, for continuous help and support. We also extend thanks to Computer Center, NISER, for all the technical support related to the Internet, web page designing, online registration, etc.

It is really difficult to achieve such a milestone without the help of volunteers, and we were fortunate enough to have an energetic and dedicated team of volunteers which comprises Ph.D. students, Masters students, postdocs, and technicians. We

would like to thank NISER Ph.D. students Mr. Sourav Kundu, Mr. Ashutosh Dash, Mr. Vijay Iyer, Mr. Samir Banik, Mr. Debasish Mallick, Mr. Dukhishyam Mallick, Mr. Ashish Pandav, Ms. Mouli Chaudhuri, Ms. Swati Saha, Mr. Prottay Das, Mr. Chandiprasad Kar, Mr. Prafulla Saha, Mr. Alope Kumar Das, Mr. Samapan Bhadury, and Ms. Tribeni Mishra, postdoc Dr. Mohammad Yousuf Jamal, and technician Mr. Subasha Chandra Rout for their untiring efforts and attitude of always being ready to accept challenges.

The help was also extended from outside NISER. We would like to thank Dr. Abhik Jash, postdoc at Weizmann Institute Israel, Dr. Subhasis Samanta, postdoc at Jan-Kochanowski University, Kielce, Poland, Dr. Md RIhan Haque, postdoc at Warsaw University of Technology, Warsaw, Poland, Dr. Chitrasen Jena, Assistant Professor at IISER Tirupati, India, and Mr. Sandeep Dudi, Ph.D. student at Panjab University, Chandigarh, India.

During this pandemic, virtual platforms made it possible to organize such a big scientific event impeccably in online mode. A flawless virtual event is possible with the support of online platforms and a well-trained team. We would like to acknowledge Zoom for conducting the parallel and plenary sessions and recording the lectures. Thanks to YouTube for live streaming the plenary and special sessions and archiving the recordings. We thank FRAME for conducting poster sessions; the support provided by the FRAME team during these sessions is highly appreciated. We have also received nice words from the FRAME team on the development and usage of FRAME rooms in the symposium. The SLACK platform is acknowledged for post-talk discussions. The interactions between speakers and participants on SLACK channels were appreciated. Special thanks to Mr. Vijay Iyer for proposing the idea of conducting poster sessions on FRAME. He was the key person in co-ordinating with the FRAME team and managing training sessions with the help of Ph.D. and Masters students, and postdoc of the EHEP group in NISER.

The event spanned over 5 days including 42 parallel sessions, 7 plenary sessions, and 4 special sessions which posed a challenge to the smooth conduct of the event. We would like to thank all the session chairs for accepting our request and running sessions flawlessly. Thanks to plenary, mini-review, and special session speakers for keeping our request and giving very nice talks followed by fruitful discussions.

The participation of young researchers in the poster sessions was really inspiring and deserved a token of appreciation. Out of 282 posters, 14 were selected for the award of the best poster in different areas of high energy physics. We extend our thanks to the poster judges for taking this job and adjudging the best posters which was really a difficult job.

We also thank all the participants for their overwhelming response—your readiness and willingness to get acquainted with the online platforms was substantial. In the end, we thank again all of you who have helped directly or indirectly in organizing the symposium; it was really a nice experience working with you all throughout this event.

Contents

Part I Standard Model and Beyond Standard Model Physics	
1	Revisiting the Charged Higgs Boson Discovery 3 Agnivo Sarkar, Baradhvaj Coleppa, and Gokul B. Krishna
2	Model Independent Analysis of $B \rightarrow K_1\mu^+\mu^-$ Decay Processes 9 Aishwarya Bhatta
3	Jet Substructure Techniques for a Supersymmetric Scenario with Gravitino LSP 15 Akanksha Bhardwaj
4	Measurement of Cross Section of $pp \rightarrow t\bar{t} + \gamma$ Process in Lepton+Jets Events at $\sqrt{s} = 13$ TeV in LHC Run 2 21 A. K. Das, P. K. Mal, D. Noonan, F. Yumiceva, N. Poudyal, R. Harr, L. Lechner, and R. Schoefbeck
5	Higgs Self-Coupling at the HL-LHC and HE-LHC 27 Amit Adhikary, Shankha Banerjee, Rahool Kumar Barman, Biplob Bhattacharjee, and Saurabh Niyogi
6	Measurement of Strong-Phase Difference Between D^0 and $\bar{D}^0 \rightarrow K_{S/L}^0\pi^+\pi^-$ and the Role of Model-Dependent Inputs at BESIII 33 Anita
7	Light Singlino Dark Matter at the LHC 39 A. Roy and Monoranjan Guchait
8	Jets and Jet Substructure—A Mini Review 43 Arun Thalapillil

9	Two-Loop QCD Amplitudes for Di-pseudo Scalar Production in Gluon Fusion	49
	Arunima Bhattacharya, Maguni Mahakhud, Prakash Mathews, and V. Ravindran	
10	Exploring the Structural Features of Quark Mass Matrices in the Flavor Basis	55
	Aseem Vashisht, Kanwaljeet S. Channey, Gulsheen Ahuja, and Manmohan Gupta	
11	Search for $B^* \rightarrow tW$ with Full Run II Data at CMS	61
	Ashish Sharma	
12	LHC Signals of Triplet Scalars as Dark Matter Portal: Cut-Based Approach and Improvement with Gradient Boosting and Neural Networks	67
	Atri Dey	
13	Gravitational Wave Signatures from First-Order Phase Transitions in an Extended Inert Doublet Dark Matter Model	73
	Avik Paul, Debasish Majumdar, and Biswajit Banerjee	
14	Collider Signatures of Multi-charged Fermions in the Framework of a Radiative Seesaw Model	79
	Avnish	
15	Search for Dark Matter with a Leptoquark and Missing Transverse Energy in the Final State by Using Proton-Proton Collision Data of CMS Detector at LHC at 13 TeV	85
	Bisnupriya Sahu and Bhawna Gomber	
16	Rediscovery of “wrong-sign” D^0 Decays with Belle II	91
	Chanchal Sharma	
17	Recent Measurement on the $B \rightarrow \mu^+ \mu^-$ Properties with CMS Data	97
	Chandiprasad Kar	
18	LHC Bounds on $R_{D^{(*)}}$ Motivated Leptoquark Models	103
	Cyrin Neeraj, Arvind Bhaskar, Tanumoy Mandal, Subhadip Mitra, and Swapnil Raz	
19	Probing Lepton-Number and Baryon-Number Violating Tau Decays at Belle	107
	D. Sahoo, G. B. Mohanty, and K. Trabelsi	
20	aQGC Studies for WZ in the pp Collisions Using EFT Framework at the LHC	113
	Geetanjali Chaudhary	

21 Analysis of Semileptonic Decays of Some b -baryons Within the SM and Beyond 117
 C. P. Haritha and Barilang Mawlong

22 Search for Compressed Mass Spectrum SUSY via Electroweak VBF in Single Lepton Final States Using LHC Run II Data Collected with CMS Detector at $\sqrt{s} = 13$ TeV 121
 Harjot Kaur

23 New Physics Effects in $b \rightarrow sll$ Decays 127
 Ipsita Ray

24 Charged Lepton Flavour Violating Decays as Signatures of A_4 Symmetry 133
 Jai More, Ushak Rahaman, S. Uma Sankar, and Rambabu Korrapati

25 Precision Tests of Electroweak Theory 139
 Kajari Mazumdar

26 Rare Charm Decays at Belle II 145
 Latika Aggarwal

27 Search for LFV in B_s Decays 149
 L. Nayak, S. Nishida, and A. Giri

28 Role of Polarization in Probing Chiral Structure of Heavy Gauge Bosons at an e^+e^- Collider 155
 Lopamudra Sahoo, Sudhansu S. Biswal, Monalisa Patra, and K. Sridhar

29 Study for Vector Boson Production in Association with Heavy-Flavor Jets in Proton-Proton Collisions 161
 M. Meena, S. Bansal, and S. B. Beri

30 Measurement of the Top Quark Mass Using Single Top Events ... 167
 Mintu Kumar

31 Determination of CKM Angle ϕ_3 at Belle and Belle II 173
 Niharika Rout

32 Exploring the Possibility of Right-Angled Unitarity Triangle 177
 Nikhila Awasthi, Gulsheen Ahuja, Monika Randhawa, and Manmohan Gupta

33 Recent Measurements of Higgs Boson Properties in the Diphoton Decay Channel with the CMS Detector 183
 Prafulla Saha

34	Revisiting the Stückelberg Mechanism	187
	Radhika Vinze and Sreerup Raychaudhuri	
35	Search for the New Physics in Bottomonium Decays in Belle and Belle II	193
	Rashmi Dhamija, S. Nishida, and A. Giri	
36	On the Determination of Regions in Multi-scale, Multi-loop Feynman Integrals	199
	B. Ananthanarayan, Abhishek Pal, Sunethra Ramanan, and Ratan Sarkar	
37	A New Distribution for the Charged Particle Multiplicities in DIS at HERA and Hadron-Hadron Collisions at the LHC	203
	Ritu Aggarwal and Manjit Kaur	
38	Probing Doubly and Singly Charged Higgs at pp Collider HE-LHC	209
	Rojalin Padhan, Debottam Das, M. Mitra, and Aruna Kumar Nayak	
39	A Study of the $B^0 \rightarrow K_S^0 \pi^0$ Decay at Belle II	215
	Sagar Hazra	
40	Search for New Physics with Delayed Jets in CMS	221
	Saikat Karmakar	
41	EFT Validity Issues in aQGC Analysis of Same-Sign WW Scattering Process	227
	Sandeep Kaur	
42	Recent Results on Lepton Flavor Universality Test at Belle	231
	Seema Choudhury	
43	Naturally Freezing-In Dark Leptons	237
	Shiuli Chatterjee	
44	Interference Effect in LNV and LNC Meson Decays for Left-Right Symmetric Model	243
	Siddharth P. Maharathy, Rohini M. Godbole, Sanjoy Mandal, M. Mitra, and Nita Sinha	
45	Measurement of Higgs Self-coupling from Non-resonant Higgs Pair Production and Decay to $b\bar{b}\gamma\gamma$ Final State in the CMS Experiment	247
	Soumya Mukherjee	
46	Multiparton Webs Beyond Three Loops	253
	Sourav Pal, Neelima Agarwal, Lorenzo Magnea, and Anurag Tripathi	

47	Search for Lepton Flavor Violation in $\Upsilon(1S)$ Decays	259
	S. Patra, Vishal Bhardwaj, and K. Trabelsi	
48	Indirectly Probing New Physics in Charmless Decays of $B \rightarrow \phi\phi K$	263
	S. Mohanty, A. B. Kaliyar, V. Gaur, and G. B. Mohanty	
49	Flavor Anomalies with Vector Leptoquark	269
	Suchismita Sahoo	
50	Investigating the Parton Shower Model in PYTHIA8 with pp Collision Data at $\sqrt{s} = 13$ TeV	275
	Suman Kumar Kundu, Tanmay Sarkar, and Manas Maity	
51	Search for Supersymmetry with Jets and Missing Transverse Momentum Final States	281
	Tribeni Mishra	
52	Explaining the XENON1T Excess and Dark Matter with Three Scalars	287
	Vandana Sahdev, Suvam Maharana, and Divya Sachdeva	
53	Improving Bounds on Invisible Branching Ratio of the Higgs with Deep Learning	293
	Vishal S. Ngairangbam	
Part II Relativistic Heavy-Ion Collisions and Quantum Chromodynamics		
54	Temperature Fluctuations and Tsallis Statistics in Relativistic Heavy Ion Collisions	299
	Abhisek Saha and Soma Sanyal	
55	Open-Charmed Mesons in Magnetized Asymmetric Strange Hadronic Matter	305
	C. S. Amal Jahan and Amruta Mishra	
56	In-Medium Properties of Heavy Quarkonia	311
	Amruta Mishra	
57	NLL Resummation of Recoil-Sensitive Angularities Using SCET	317
	Ankita Budhraj, Ambar Jain, and Massimiliano Procura	
58	Correspondence Between Israel–Stewart Theory and First-Order Causal and Stable Hydrodynamics for the Boost-Invariant Flow	323
	Arpan Das	
59	ηB Interactions in the Strange Baryonic Matter	329
	Arvind Kumar and Rajesh Kumar	

60	Cumulant Measurement of Net-Kaon Distributions in Au+Au Collisions at $\sqrt{s_{NN}} = 27$ GeV from BES-II Program at RHIC	333
	Ashish Pandav	
61	Far-from-Equilibrium Hydrodynamic Attractor for an Azimuthally Symmetric System	339
	Ashutosh Dash and Victor Roy	
62	Spin Dynamics in Relaxation Time Approximation	343
	Avdhesh Kumar	
63	Simulation Studies of $R_2(\Delta\eta, \Delta\phi)$ and $P_2(\Delta\eta, \Delta\phi)$ Correlation Functions in pp Collisions with the PYTHIA and HERWIG Models	349
	Baidyanath Sahoo, Basanta Kumar Nandi, Prabhat Pujahari, Sumit Basu, and Claude Pruneau	
64	Jet Quenching Parameter in Semi-QGP	353
	Balbeer Singh and Hiranmaya Mishra	
65	Anisotropic Pressure and Quark Number Susceptibility of Strongly Magnetized QCD Medium	359
	Bithika Karmakar, Ritesh Ghosh, Aritra Bandyopadhyay, Najmul Haque, and Munshi G Mustafa	
66	Latest Results on Hadronic Resonance Production with ALICE at the LHC	365
	Dukhishyam Mallick	
67	Multiplicity Dependence Study of Thermodynamic and Transport Properties of the Matter Formed in Ultra-Relativistic Collisions at LHC Using Color String Percolation Model	369
	Dushmanta Sahu, Sushanta Tripathy, R. Sahoo, and Swatantra Kumar Tiwari	
68	Criticality in Statistical Bootstrap Model: Critical Exponents and Transport Properties	375
	Guruprasad Kadam, Hiranmaya Mishra, and Marco Panero	
69	Directed Flow of Identified Hadrons in Au+Au Collisions with the STAR Experiment at RHIC	381
	Kishora Nayak	
70	Constraining the Strength of $U(1)_A$ Symmetry Breaking Using Two-Flavour Non-local NJL Model	385
	Mahammad Sabir Ali, Chowdhury Aminul Islam, and Rishi Sharma	

71	Thermal and Electric Charge Transport in a Weakly Magnetized Hot QCD Medium	391
	Manu Kurian	
72	Study of Heavy Flavour Decay Muons in pp and Pb-Pb Collisions at LHC Energies Using Angantyr Model for Heavy-Ion Collisions in PYTHIA8	397
	Md Samsul Islam, Tinku Sinha, and Pradip Roy	
73	Inclusive Photon Production at Forward Rapidities Using PMD in p–Pb Collisions at $\sqrt{s_{NN}} = 8.16$ TeV with ALICE	403
	Mohammad Asif Bhat	
74	Recent Measurements of (Anti-)Nuclei Production in High Energy Collisions	409
	Natasha Sharma	
75	Recent Results on Jet Quenching and Heavy-Flavors in Heavy-Ion Collisions at the LHC and RHIC	415
	Nihar Ranjan Sahoo	
76	STAR Measurements on Azimuthal Anisotropy of ϕ Mesons in Au+Au Collisions at $\sqrt{s_{NN}} = 27$ and 54.4 GeV	419
	Prabhupada Dixit	
77	A Beyond Mean Field Approach to Yang-Mills Thermodynamics	423
	Pracheta Singha, Rajarshi Ray, Chowdhury Aminul Islam, and Munshi G Mustafa	
78	Understanding Long-Range Near-Side Ridge Correlations in p-p Collisions Using Rope Hadronisation at Energies Available at the CERN Large Hadron Collider	429
	Pritam Chakraborty and Sadhana Dash	
79	Recent Results on Correlations and Fluctuations in Relativistic Heavy-Ion Collisions	433
	Prithwish Tribedy	
80	Kasner Space-Time, Second-Order Hydrodynamics and Gravity Dual	439
	Priyanka Priyadarshini Pruseth and Swapna Mahapatra	
81	Search for the Chiral Magnetic Wave Using the ALICE Detector in Pb-Pb Collisions at $\sqrt{s_{NN}} = 5.02$ TeV	445
	Prottay Das	
82	Causality and Stability in Relativistic Dissipative Non-resistive Magnetohydrodynamics	449
	Rajesh Biswas, Ashutosh Dash, Najmul Haque, and Victor Roy	

83	In Medium Properties of Axion Within a Polyakov Loop Enhanced Nambu-Jona-Lasinio Model	455
	Ranjita K. Mohapatra, Aman Abhishek, Arpan Das, and Hiranmaya Mishra	
84	Deciphering Quark and Gluon Jet Modifications in Heavy-Ion Collisions with γ-Tagged Jets	459
	Rathijit Biswas, Subikash Choudhury, Sidharth K. Prasad, and Supriya Das	
85	Constraining the Chiral Magnetic Effect with Charge-Dependent Azimuthal Correlations in ALICE	463
	Md. Rihan Haque	
86	A Unified Formalism to Study <i>Soft</i> as Well as <i>Hard Part</i> of the Transverse Momentum Spectra	469
	Rohit Gupta and Satyajit Jena	
87	Observation of Light-by-Light Scattering and Search for Axion-Like Particles with CMS Experiment	473
	Ruchi Chudasama	
88	Strangeness- and Rapidity-Dependent Studies in Small Systems with ALICE at the LHC	479
	Sandeep Dudi	
89	Feasibility Studies of J/ψ Measurement with CBM Detector Setup at FAIR SIS100 Energies	483
	Sayak Chatterjee	
90	Structure of Magnetic Field Quantization in Viscosity Expression for Relativistic Fluid	489
	Snigdha Ghosh and Sabyasachi Ghosh	
91	Latest Results on Light Flavour Hadron Production at LHC and RHIC	493
	Sourav Kundu	
92	Quantum Aspects of Anisotropic Conduction in Hadron Resonance Gas	499
	Subhasis Samanta, Jayanta Dey, Sarthak Satapathy, Snigdha Ghosh, and Sabyasachi Ghosh	
93	Topological Studies of Charged Particle Production and Search for Jet Quenching Effects in Small Collision Systems with ALICE	505
	Sushanta Tripathy	

94 Application of Magnetohydrodynamics in High-Energy Heavy-Ion Collisions: Recent Progress 511
 Victor Roy

95 Recent Bottomonium Measurements in pp, p–Pb, and Pb–Pb Collisions at Forward Rapidity with ALICE at the LHC 517
 Wadut Shaikh

Part III Neutrino Physics

96 Probing NSI in Atmospheric Neutrino Experiments Using Oscillation Dip and Valley 525
 Anil Kumar, Amina Khatun, Sanjib Kumar Agarwalla, and Amol Dighe

97 nEXO Searches for Neutrinoless Double Beta Decay of ^{136}Xe 531
 Arun Kumar Soma

98 Effect of Second-Class Currents in $\nu_l(\bar{\nu}_l) - N$ Scattering 535
 A. Fatima, M. Sajjad Athar, and S. K. Singh

99 $\nu_\tau/\bar{\nu}_\tau$ - ^{40}Ar DIS Cross Sections with Perturbative and Nonperturbative Effects 541
 F. Zaidi, V. Ansari, H. Haider, M. Sajjad Athar, and S. K. Singh

100 Coherent Pion Production in Neutrino–Nucleus Interaction 547
 H. Sogarwal and Prashant Shukla

101 Simulation Study of Electron Energy Reconstruction with Thinner Iron Plates in ICAL 553
 Honey Khindri, V. M. Datar, D. Indumathi, S. M. Lakshmi, and M. V. N. Murthy

102 Enhancing the Sensitivities to Standard Unknowns in Neutrino Oscillation Framework Using High-Energy Beams at DUNE 559
 Jogesh Rout, Samiran Roy, Mehedi Masud, Mary Bishai, and Poonam Mehta

103 Hierarchy Sensitivity with Combined Standard and Rock Muons in ICAL at India-Based Neutrino Observatory 565
 R. Kanishka, D. Indumathi, and S. M. Lakshmi

104 Fully Constrained Mass Matrix: Can Symmetries Alone Determine the Flavon Vacuum Alignments? 571
 R. Krishnan

105 Inverse Seesaw Mechanism with A_4 Flavour Symmetry 577
 Maibam Ricky Devi and Kalpana Bora

106	Baryogenesis Through Leptogenesis in a S_4 Flavon Model with TM_1 Mixing for Neutrinos	583
	Mainak Chakraborty, Krishnan Rama, and Ambar Ghosal	
107	The Mitchell Institute Neutrino Experiment at Reactor (MINER)	589
	Mouli Chaudhuri	
108	Probing the CP Phases in 3+1 Scenario at LBL Experiments	595
	Nishat Fiza, Mehedi Masud, and M. Mitra	
109	Leptogenesis in a Multi-Higgs Doublet Model	599
	Pritam Das, Mrinal Kumar Das, and Najimuddin Khan	
110	Implications of Recent Flavour Anomalies on New Physics	605
	Rukmani Mohanta	
111	MiniBooNE Excess with a Light Z' and a Second Higgs Doublet	611
	Samiran Roy, Waleed Abdallah, and Raj Gandhi	
112	Impact of Non-standard Interactions on Violation of Leggett-Garg Inequality in Three-Flavour Neutrino Oscillations	617
	Sheeba Shafaq and Poonam Mehta	
113	Theory of Fast-Flavor Conversion of Supernova Neutrinos	621
	Soumya Bhattacharyya	
Part IV Cosmology and Astroparticle Physics		
114	Tree-Level Leptogenesis Induced by Soft SUSY Breaking in NMSSM Extended by a Right Handed Neutrino Superfield	629
	Abhijit Kumar Saha, Waleed Abdallah, and Abhass Kumar	
115	Probing Ultra-Light Primordial Black Holes as a Dark Matter Candidate	635
	Anupam Ray	
116	Helical Magnetic Fields From Riemann Coupling	639
	Ashu Kushwaha and S. Shankaranarayanan	
117	Low-Scale Leptogenesis From Three-Body Decay	645
	Devabrat Mahanta, Debasish Borah, and Arnab Dasgupta	

118 Latest Results of Cosmic Ray Energy Spectrum and Composition Measurements From GRAPES-3 Experiment 649
 F. Varsi, S. Ahmad, M. Chakraborty, A. Chandra, S. R. Dugad, S. K. Gupta, B. Hariharan, Y. Hayashi, P. Jagadeesan, A. Jain, P. Jain, V. B. Jhansi, S. Kawakami, H. Kojima, S. Mahapatra, P. K. Mohanty, R. Moharana, S. D. Morris, Y. Muraki, P. K. Nayak, A. Oshima, B. Pant, D. Pattanaik, G. Pradhan, P. S. Rakshe, K. Ramesh, B. S. Rao, L. V. Reddy, R. Sahoo, R. Scaria, S. Shibata, K. Tanaka, and M. Zuberi

119 Investigation of Muon Puzzle with GRAPES-3 Experiment 655
 G. S. Pradhan, S. Ahmad, M. Chakraborty, A. Chandra, S. R. Dugad, S. K. Gupta, B. Hariharan, Y. Hayashi, P. Jagadeesan, A. Jain, P. Jain, V. B. Jhansi, S. Kawakami, H. Kojima, S. Mahapatra, P. K. Mohanty, R. Moharana, S. D. Morris, P. K. Nayak, A. Oshima, B. P. Pant, D. Pattanaik, P. S. Rakshe, K. Ramesh, B. S. Rao, L. V. Reddy, R. Sahoo, R. Scaria, S. Shibata, F. Varsi, and M. Zuberi

120 A Detailed Investigation of Thunderstorm Events Recorded in GRAPES-3 Experiment 661
 B. Hariharan, S. Ahmad, M. Chakraborty, A. Chandra, S. R. Dugad, S. K. Gupta, Y. Hayashi, P. Jagadeesan, A. Jain, P. Jain, V. B. Jhansi, S. Kawakami, H. Kojima, S. Mahapatra, P. K. Mohanty, R. Moharana, S. D. Morris, Y. Muraki, P. K. Nayak, A. Oshima, B. Pant, D. Pattanaik, G. Pradhan, P.S. Rakshe, K. Ramesh, B. S. Rao, L. V. Reddy, R. Sahoo, R. Scaria, S. Shibata, K. Tanaka, F. Varsi, and M. Zuberi

121 Cosmological Perturbations in the Interacting Dark Sector: Mapping Fields and Fluids 667
 Joseph P. Johnson and S. Shankaranarayanan

122 Gravitational Wave Echoes from Strange Stars for Various Equations of State 673
 Jyatsnasree Bora and Umananda Dev Goswami

123 Neutrino Emissivity of Dense Quark Matter in Presence of Magnetic Field 679
 Kausik Pal

124 Majorana Dark Matter and Neutrino Mass in a Singlet-Doublet Extension of the Standard Model 685
 Manoranjan Dutta, Subhaditya Bhattacharya, Purusottam Ghosh, and Narendra Sahu

125	Effect of Dark Matter in Compact Realistic Neutron Stars Matter	691
	P. K. Sahu, D. K. Mishra, and S. P. Behera	
126	Signal of Statistical Anisotropy in PLANCK Cosmic Microwave Background Polarization Maps	697
	Pramoda Kumar Samal, Pranati K. Rath, Srikanta Panda, Pavan K. Aluri, and Debesh D. Mishra	
127	Investigation of K/π Ratio with Accelerator and Cosmic Ray Data	703
	R. Scaria, S. Ahmad, M. Chakraborty, A. Chandra, S. R. Dugad, S. K. Gupta, B. Hariharan, Y. Hayashi, P. Jagadeesan, A. Jain, P. Jain, V. B. Jhansi, S. Kawakami, H. Kojima, S. Mahapatra, P. K. Mohanty, R. Moharana, S. D. Morris, P. K. Nayak, A. Oshima, B. P. Pant, D. Pattanaik, G. S. Pradhan, P. S. Rakshe, K. Ramesh, B. S. Rao, L. V. Reddy, R. Sahoo, S. Shibata, F. Varsi, and M. Zuberi	
128	Simulation of Cosmogenic Neutron Backgrounds for a Dark Matter Search Experiment at Jaduguda Underground Science Laboratory	709
	S. Banik, V. K. S. Kashyap, and B. Mohanty	
129	I-Eccentricity-Q Relation as the Universal Relation for Rotating Magnetized White Dwarfs	713
	Somnath Mukhopadhyay, Sujan Kumar Roy, and D. N. Basu	
130	Power Asymmetry in Planck Full-Mission CMB Temperature Maps	719
	Srikanta Panda, Pavan K. Aluri, Pramoda Kumar Samal, and Pranati K. Rath	
131	A Mini Review on Dark Mater: Cosmological Perspective	725
	Subinoy Das	
132	Investigating Ultra Long Short GRBs Using Fermi-GBM Data	731
	Sundar Dhara and R. Moharana	
133	Dark Matter and Leptogenesis in Minimal $U(1)_{B-L}$ Model with Nonminimal Quartic Inflation	737
	Suruj Jyoti Das, Debasish Borah, and Abhijit Kumar Saha	
134	Cosmic Muon Momentum Spectra at Madurai	743
	Suryanarayan Mondal, Apoorva Bhatt, V. M. Datar, G. Majumder, S. Pethuraj, K. C. Ravindran, and B. Satyanarayana	

135 An Estimation of Joint Posterior of CMB Over Large Angular Scales Using Gibbs ILC Method 749
 Vipin Sudevan and Rajib Saha

136 Dense Matter in Strong Magnetic Field: Covariant Density Functional Approach 755
 Vivek Baruah Thapa, Monika Sinha, Jia Jie Li, and Armen Sedrakian

Part V Detectors, Instrumentation, Future Facilities, and Societal Applications

137 Particle Identification in Belle II Silicon Vertex Detector 763
 A. B. Kaliyar

138 Study of Radiation Damage in the CMS Hadron Calorimeter Using Isolated Muons from 2018 Collision Data 769
 Amandeep Kaur

139 Heterogeneous Computing with GPUs for Trigger Decision in CMS Experiment at the LHC 775
 T. S. Aravind

140 Evolution of LHC Computing Grid for Run-III and Beyond with Emphasis on TIFR CMS Tier-II and Indian Contribution 781
 Brij Kishor Jashal, G. Majumder, Kajari Mazumdar, and P. Patel

141 Cosmic Muon Veto for the Mini-ICAL Detector at IICHEP, Madurai 787
 B. Satyanarayana, S. R. Bharathi, Pandi Chinnappan, V. M. Datar, Mamta Jangra, Jim John, S. R. Joshi, K. S. Karthikk, L. Umesh, G. Majumder, N. Panchal, Nagaraj Panyam, S. Pethuraj, Jayakumar Ponraj, K. C. Ravindran, Paul Rubinov, Mahima Sachdeva, M. N. Saraf, Prakash Sharma Kirti, R. R. Shinde, H. Sogarwal, S. S. Upadhya, P. Verma, and E. Yuvaraj

142 Track-Based Muon Alignment of the CMS Detector 793
 Greyson Newton

143 Magnetic Field Simulations and Measurements on Mini-ICAL 799
 Honey, V. M. Datar, S. Ajith, N. Dalal, A. De, G. Majumder, S. Patel, S. Pathak, S. P. Prabhakar, B. Satyanarayana, P. S. Shetty, B. Siva Rama Krishna, T. S. Srinivasan, and S. K. Thakur

144	A Simulation Study of Primary Ionization for Different Gas Mixtures	805
	R. Kanishka, P. K. Rout, S. Mukhopadhyay, N. Majumdar, and S. Sarkar	
145	Development of Front-End Electronics for an SiPM-Based Cherenkov Telescope Camera	809
	K. S. Gothe, S. K. Rao, S. S. Upadhyay, S. Duhan, B. K. Nagesh, N. K. Parmar, M. Ranjan, B. B. Singh, and A. Sarkar	
146	Characterization of Hamamatsu SiPM for Cosmic Muon Veto Detector at IICHEP	815
	Mamta Jangra, M. N. Saraf, V. M. Datar, G. Majumder, Pathaleswar, B. Satyanarayana, and S. S. Upadhyay	
147	Trigger Hardware for CMS Experiment at the LHC	821
	Mandakini Patil, Kushal Bhalerao, and Kajari Mazumdar	
148	Fabrication, Interfacing and Performance of the High Voltage Bias Supply Modules for ICAL RPCs	827
	M. N. Saraf, S. R. Joshi, V. M. Datar, G. Majumder, A. Manna, B. Satyanarayana, R. R. Shinde, and E. Yuvaraj	
149	The Micromegas Detectors for ATLAS New Small Wheel Upgrade	833
	Manisha Lohan	
150	Backend Systems for Mini-ICAL	839
	Nagaraj Panyam, V. M. Datar, Janhavi Deshpande, E. Yuvaraj, G. Majumder, S. Padmini, Mahesh Punna, B. Satyanarayana, Shikha Srivastava, and S. S. Upadhyay	
151	The Single-Channel Data Acquisition (DAQ) Module Developed for Dark Matter Search Experiment Using Superheated Liquid	843
	Niraj Chaddha, Sunita Sahoo, Nilanjan Biswas, Mala Das, and Sarbajit Pal	
152	Improvement of Time and Position Resolutions of RPC Detectors Using Time-Over-Threshold Information	849
	S. Pethuraj, G. Majumder, V. M. Datar, and B. Satyanarayana	
153	A Study of Avalanche and Streamer Simulation in GEM Detector Using Hydrodynamic Approach	855
	P. K. Rout, R. Kanishka, Jaydeep Datta, S. Mukhopadhyay, N. Majumdar, and S. Sarkar	
154	Lepton Identification using the Belle II Silicon-Strip Vertex Detector	859
	Rahul Tiwary	

155 Gain Uniformity of a Quad-GEM Detector 865
 Rupamoy Bhattacharyya, Pradip Kumar Sahu, Sanjib Sahu,
 and Rama Prasad Adak

156 Slow-Pion Relative Tracking Efficiency Studies at Belle II 871
 S. Maity, N. S. Ipsita, and S. Patra

157 Electron Gun Based Magnetic Probe 875
 Srinidhi Bheesette and Marcos Turqueti

**158 Sensitivity of Triple-GEM Detectors for Background
 Radiation in CMS Experiment** 881
 S. Kumar, O. Bouhali, V. Bhatnagar, A. Castaneda,
 S. S. Chauhan, T. Kamon, Y. Kang, and A. K. Viridi

**159 Development of 256-Pixel SiPM-Based Imaging Camera
 and Its Status** 887
 S. S. Upadhyya, A. Chatterjee, V. R. Chitnis, R. L. Deshmukh,
 P. Dorjey, N. Dorji, S. Duhan, K. S. Gothe, A. P. K. Kutty,
 B. K. Nagesh, V. A. Nikam, N. K. Parmar, S. R. Patel,
 M. Ranjan, S. K. Rao, A. Roy, M. N. Saraf, A. Sarkar,
 B. B. Singh, and P. Verma

**160 Large-Mass Single-Electron Resolution Detector for Dark
 Matter and Coherent Neutrino–Nucleus Elastic Interaction
 Searches** 893
 Vijay Iyer

Part VI Formal Theory

**161 A Review on Crossing Symmetric Dispersion Relations
 in QFTs and CFTs** 901
 Ahmadullah Zahed

**162 Compactified Conformal Field Theories in Symplectic
 Manifolds** 905
 G. X. A. Petronilo, S. C. Ulhoa, and A. E. Santana

**163 Parametric Resonance of Complex Scalar Field Under
 Spacetime Oscillations** 913
 Shreyansh S. Dave and Sanatan Digal

**164 Generalized Uncertainty Principle in Bar Detectors
 of Gravitational Waves** 919
 Sukanta Bhattacharyya, Sunandan Gangopadhyay,
 and Anirban Saha

165 Bianchi-I Cosmology in Quantum Gravity 925
 Sunandan Gangopadhyay, Rituparna Mandal, and Amitabha Lahiri

166 Formation of Marginally Trapped Surfaces in Gravitational Collapse	931
Suresh C. Jaryal and Ayan Chatterjee	
Appendix A: Plenary Speakers	935
Appendix B: Special Sessions	941
Appendix C: Best Poster Awardees	945
Appendix D: Symposium Poster	947

Contributors

Abdallah Waleed Harish-Chandra Research Institute, Jhansi, Allahabad, India;
Department of Mathematics, Faculty of Science, Cairo University, Giza, Egypt

Abhishek Aman Theory Division, Physical Research Laboratory, Navrangpura,
Ahmedabad, India

Adhikary Amit Centre for High Energy Physics, Indian Institute of Science,
Bangalore, India

Agarwal Neelima Department of Physics, Chaitanya Bharathi Institute of Tech-
nology, Gandipet, Hyderabad, Telangana, India

Agarwalla Sanjib Kumar Institute of Physics, Bhubaneswar, India;
Homi Bhabha National Institute, Anushaktinagar, Mumbai, India;
The Abdus Salam International Centre for Theoretical Physics, Trieste, Italy

Aggarwal Latika Panjab University, Chandigarh, India

Aggarwal Ritu Savitribai Phule Pune University, Pune, India

Ahmad S. The GRAPES-3 Experiment, Cosmic Ray Laboratory, Raj Bhavan, Ooty,
India;
Aligarh Muslim University, Aligarh, India

Ahuja Gulsheen Department of Physics, Panjab University, Chandigarh, India

Ajith S. Bhabha Atomic Research Centre, Mumbai, India

Ali Mahammad Sabir Department of Theoretical Physics, Tata Institute of Funda-
mental Research, Mumbai, India

Aluri Pavan K. Department of Physics, IIT(BHU), Varanas, Uttar Pradesh, India;
Department of Physics, IIT(BHU), Varanasi, Uttar Pradesh, India

Amal Jahan C. S. Department of Physics, Indian Institute of Technology Delhi,
New Delhi, India

Aminul Islam Chowdhury School of Nuclear Science and Technology, University of Chinese Academy of Sciences, Beijing, China

Ananthanarayan B. Centre for High Energy Physics, Indian Institute of Science, Bangalore, KA, India

Anita Indian Institute of Technology Madras, Chennai, India

Ansari V. Aligarh Muslim University, Aligarh, India

Aravind T. S. Tata Institute of Fundamental Research, Mumbai, India

Avnish Institute of Physics, Bhubaneswar, India;
Training School Complex, Homi Bhabha National Institute, Mumbai, India

Awasthi Nikhila Department of Physics, Panjab University, Chandigarh, India

Bandyopadhyay Aritra Guangdong Provincial Key Laboratory of Nuclear Science, Institute of Quantum Matter, South China Normal University, Guangzhou, China

Banerjee Biswajit Astroparticle Physics and Cosmology Division, Saha Institute of Nuclear Physics, HBNI, Kolkata, India

Banerjee Shankha CERN, Theoretical Physics Department, Geneva 23, Switzerland

Banik S. School of Physical Sciences, National Institute of Science Education and Research, Jatni, India;
Homi Bhabha National Institute, Training School Complex, Mumbai, India

Bansal S. Panjab University, Chandigarh, India

Barman Rahool Kumar Department of Physics, Oklahoma State University, Stillwater, OK, USA

Basu D. N. Variable Energy Cyclotron Centre, Kolkata, India;
Homi Bhabha National Institute, Training School Complex, Mumbai, India

Basu Sumit Department of Physics, Lund University, Lund, Sweden

Behera S. P. Bhabha Atomic Research Centre, Trombay, Mumbai, India

Beri S. B. Panjab University, Chandigarh, India

Bhalerao Kushal Tata Institute of Fundamental Research, Mumbai, India

Bharathi S. R. Tata Institute of Fundamental Research, Mumbai, India

Bhardwaj Akanksha Physical Research Laboratory (PRL), Ahmedabad, Gujarat, India

Bhardwaj Vishal Indian Institute of Science Education and Research Mohali, Punjab, India

Bhaskar Arvind Center for Computational Natural Sciences and Bioinformatics, International Institute of Information Technology, Hyderabad, India

Bhat Mohammad Asif Department of Physics and Centre for Astroparticle Physics and Space Science (CAPSS), Bose Institute, Kolkata, India

Bhatt Apoorva Homi Bhabha National Institute, Mumbai, India

Bhatnagar V. Panjab University, Chandigarh, India

Bhatta Aishwarya University of Hyderabad, Hyderabad, India

Bhattacharya Arunima Saha Institute of Nuclear Physics, A CI of Homi Bhabha National Institute, Kolkata, India

Bhattacharya Subhaditya Department of Physics, Indian Institute of Technology Guwahati, North Guwahati, Assam, India

Bhattacharyya Rupamoy Institute of Physics, HBNI, Sachivalaya Marg, P.O. Sainik School, Bhubaneswar, Odisha, India

Bhattacharyya Soumya Tata Institute of Fundamental Research, Mumbai, India

Bhattacharyya Sukanta Department of Physics, West Bengal State University, Barasat, Kolkata, India

Bhattacharjee Biplob Centre for High Energy Physics, Indian Institute of Science, Bangalore, India

Bheesette Srinidhi Engineering Division, Lawrence Berkeley National Lab, Berkeley, CA, USA

Bishai Mary Brookhaven National Laboratory, Upton, NY, USA

Biswal Sudhansu S. Department of Physics, Ravenshaw University, Cuttack, India

Biswas Nilanjan Astroparticle Physics & Cosmology Division, Saha Institute of Nuclear Physics, Kolkata, India

Biswas Rajesh School of Physical Sciences, National Institute of Science Education and Research, HBNI, Jatni, India

Biswas Rathijit Institute of Modern Physics, Chinese Academy of Sciences, Lanzhou, China;
Department of Physics, Centre for Astroparticle Physics and Space Science, Bose Institute, Kolkata, India

Bora Jyatsnasree Department of Physics, Dibrugarh University, Dibrugarh, Assam, India

Bora Kalpana Department of Physics, Gauhati University, Guwahati, Assam, India

Borah Debasish Department of Physics, Indian Institute of Technology Guwahati, Assam, India

Bouhali O. Texas A & M University, Doha, Qatar

Budhraj Ankita Tata Institute of Fundamental Research, Mumbai, Maharashtra, India

Castaneda A. Universidad de Sonora, Hermosillo, Mexico

Chaddha Niraj Computer & Informatics Group, Variable Energy Cyclotron Centre, Kolkata, India

Chakraborty M. The GRAPES-3 Experiment, Cosmic Ray Laboratory, Raj Bhavan, Ooty, India;
Tata Institute of Fundamental Research, Mumbai, India

Chakraborty Mainak School of Physical Sciences, Indian Association for the Cultivation of Science, Kolkata, India

Chakraborty Pritam Indian Institute of Technology Bombay, Mumbai, India

Chandra A. The GRAPES-3 Experiment, Cosmic Ray Laboratory, Raj Bhavan, Ooty, India;
Aligarh Muslim University, Aligarh, India

Channey Kanwaljeet S. Department of Physics and Astrophysics, University of Delhi, New Delhi, India;
Department of Physics, University Institute of Sciences, Chandigarh University, Ajitgarh, Punjab, India

Chatterjee A. Tata Institute of Fundamental Research, Mumbai, India

Chatterjee Ayan Department of Physics and Astronomical Science, Central University of Himachal Pradesh, Dharamshala, India

Chatterjee Sayak Department of Physics, Bose Institute, Kolkata, India

Chatterjee Shiuli Centre for High Energy Physics, Indian Institute of Science, Bangalore, India

Chaudhary Geetanjali Panjab University, Chandigarh, India

Chaudhuri Mouli School of Physical Sciences, National Institute of Science Education and Research, Jatni, India;
Homi Bhabha National Institute, Training School Complex, Mumbai, India

Chauhan S. S. Panjab University, Chandigarh, India

Chinnappan Pandi Tata Institute of Fundamental Research, Mumbai, India

Chitnis V. R. Tata Institute of Fundamental Research, Mumbai, India

Choudhury Seema Indian Institute of Technology, Hyderabad, India

Choudhury Subikash Key Laboratory of Nuclear Physics and Ion-Beam Application (MOE), Institute of Modern Physics, Fudan University, Shanghai, China

Chudasama Ruchi Tata Institute of Fundamental Research, Mumbai, India

Coleppa Baradhvaj Indian Institute of Technology Gandhinagar, Gandhinagar, Gujarat, India

Dalal N. Bhabha Atomic Research Centre, Mumbai, India

Das A. K. School of Physical Sciences, National Institute of Science Education and Research, Jatni, India;

Homi Bhabha National Institute, Training School Complex, Mumbai, India

Das Arpan Institute of Nuclear Physics Polish Academy of Sciences, Kraków, Poland

Das Debottam Institute of Physics, Bhubaneswar, India;

BARC Training School Complex, Homi Bhabha National Institute, Mumbai, India

Das Mala Astroparticle Physics & Cosmology Division, Saha Institute of Nuclear Physics, Kolkata, India;

Homi Bhabha National Institute, Training School Complex, Anushaktinagar, Mumbai, India

Das Pritam Department of Physics, Tezpur University, Napaam, Assam, India

Das Prottay School of Physical Sciences, National Institute of Science Education and Research, Jatni, India;

Homi Bhabha National Institute, Training School Complex, Mumbai, India

Das Subinoy Indian Institute of Astrophysics, Bangalore, India

Das Supriya Department of Physics, Centre for Astroparticle Physics and Space Science, Bose Institute, Kolkata, India

Das Suruj Jyoti Department of Physics, Indian Institute of Technology Guwahati, Assam, India

Dasgupta Arnab Institute of Convergence Fundamental Studies, Seoul-Tech, Seoul, South Korea

Dash Ashutosh School of Physical Sciences, National Institute of Science Education and Research, Jatni, India;

Homi Bhabha National Institute, Training School Complex, Mumbai, India

Dash Sadhana Indian Institute of Technology Bombay, Mumbai, India

Datar V. M. Department of High Energy Physics, Tata Institute of Fundamental Research, Colaba, Mumbai, India

Datta Jaydeep Applied Nuclear Physics Division, Saha Institute of Nuclear Physics, Salt Lake, Kolkata, India;

Homi Bhabha National Institute, Training School Complex, Anushaktinagar, Mumbai, India

- Dave Shreyansh S.** The Institute of Mathematical Sciences, Chennai, India
- De A.** Homi Bhabha National Institute, Mumbai, India;
Variable Energy Cyclotron Centre, Kolkata, India
- Deshmukh R. L.** Tata Institute of Fundamental Research, Mumbai, India
- Deshpande Janhavi** Electronics Divison, Bhabha Atomic Research Center, Mumbai, India
- Dev Goswami Umananda** Department of Physics, Dibrugarh University, Dibrugarh, Assam, India
- Dey Atri** Regional Centre for Accelerator-based Particle Physics, Harish-Chandra Research Institute, HBNI, Jhansi, Allahabad, India
- Dey Jayanta** Indian Institute of Technology Bhilai, Raipur, Chhattisgarh, India
- Dhamija Rashmi** Indian Institute of Technology Hyderabad, Telangana, India
- Dhara Sundar** Department of Physics, IIT Jodhpur, Jodhpur, Rajasthan, India
- Digal Sanatan** The Institute of Mathematical Sciences, Chennai, India;
Homi Bhabha National Institute, Training School Complex, Mumbai, India
- Dighe Amol** Tata Institute of Fundamental Research, Mumbai, India
- Dixit Prabhupada** Indian Institute of Science Education and Research, Berhampur, India
- Dorjey P.** Tata Institute of Fundamental Research, Mumbai, India
- Dorji N.** Tata Institute of Fundamental Research, Mumbai, India
- Dudi Sandeep** Department of Physics, Panjab University, Chandigarh, India
- Dugad S. R.** The GRAPES-3 Experiment, Cosmic Ray Laboratory, Raj Bhavan, Ooty, India;
Tata Institute of Fundamental Research, Mumbai, India
- Duhan S.** Tata Institute of Fundamental Research, Colaba, Mumbai, India
- Dutta Manoranjan** Department of Physics, Indian Institute of Technology Hyderabad, Kandi, Telangana, India
- Fatima A.** Department of Physics, Aligarh Muslim University, Aligarh, India
- Fiza Nishat** Department of Physical Sciences, IISER Mohali, Mohali, Punjab, India
- Gandhi Raj** Harish-Chandra Research Institute, Jhansi, Allahabad, India
- Gangopadhyay Sunandan** Department of Theoretical Sciences, S.N. Bose National Centre for Basic Sciences, Kolkata, India
- Gaur V.** Virginia Polytechnic Institute and State University, Blacksburg, VA, USA

Ghosal Ambar Saha Institute of Nuclear Physics, Kolkata, India

Ghosh Purusottam Regional Centre for Accelerator-based Particle Physics, Harish-Chandra Research Institute, Jhansi, Allahabad, India

Ghosh Ritesh Theory Division, Saha Institute of Nuclear Physics, Kolkata, India; Homi Bhabha National Institute, Mumbai, Maharashtra, India

Ghosh Sabyasachi Indian Institute of Technology Bhilai, Raipur, Chhattisgarh, India

Ghosh Snigdha Government General Degree College at Kharagpur-II, Paschim Medinipur, West Bengal, India

Giri A. Indian Institute of Technology Hyderabad, Hyderabad, Telangana, India

Godbole Rohini M. Centre for High Energy Physics, Indian Institute of Science, Bengaluru, India

Gomber Bhawna University of Hyderabad, Hyderabad, India

Gothe K. S. Tata Institute of Fundamental Research, Colaba, Mumbai, India

Guchait Monoranjan Department of High Energy Physics, Tata Institute of Fundamental Research, Mumbai, India

Gupta Manmohan Department of Physics, Panjab University, Chandigarh, India

Gupta Rohit Department of Physical Sciences, Indian Institute of Science Education and Research (IISER) Mohali, Manauli, Punjab, India

Gupta S. K. The GRAPES-3 Experiment, Cosmic Ray Laboratory, Raj Bhavan, Ooty, India;
Tata Institute of Fundamental Research, Mumbai, India

Haider H. Aligarh Muslim University, Aligarh, India

Haque Md. Rihan Warsaw University of Technology, Warszawa, Poland

Haque Najmul School of Physical Sciences, National Institute of Science Education and Research, Jatni, India;
Homi Bhabha National Institute, Training School Complex, Mumbai, India

Hariharan B. The GRAPES-3 Experiment, Cosmic Ray Laboratory, Raj Bhavan, Ooty, India;
Tata Institute of Fundamental Research, Mumbai, India

Haritha C. P. School of Physics, University of Hyderabad, Hyderabad, India

Harr R. Wayne State University, Detroit, MI, USA

Hayashi Y. The GRAPES-3 Experiment, Cosmic Ray Laboratory, Raj Bhavan, Ooty, India;
Graduate School of Science, Osaka City University, Osaka, Japan

Hazra Sagar Tata Institute of Fundamental Research, Mumbai, India

Honey Homi Bhabha National Institute, Mumbai, India;
Tata Institute of Fundamental Research, Mumbai, India;
The Institute of Mathematical Sciences, Chennai, India

Indumathi D. Homi Bhabha National Institute, Mumbai, India;
The Institute of Mathematical Sciences, Chennai, India

Ipsita N. S. Indian Institute of Technology, Hyderabad, Telangana, India

Islam Md Samsul High Energy Nuclear and Particle Physics Division, Saha Institute of Nuclear Physics, Kolkata, India

Iyer Vijay School of Physical Sciences, National Institute of Science Education and Research, Jatni, India;
Homi Bhabha National Institute, Training School Complex, Mumbai, India

Jagadeesan P. The GRAPES-3 Experiment, Cosmic Ray Laboratory, Raj Bhavan, Ooty, India;
Tata Institute of Fundamental Research, Mumbai, India

Jain A. The GRAPES-3 Experiment, Cosmic Ray Laboratory, Raj Bhavan, Ooty, India;
Tata Institute of Fundamental Research, Mumbai, India

Jain Ambar Indian Institute of Science Education and Research, Bhopal, Madhya Pradesh, India

Jain P. The GRAPES-3 Experiment, Cosmic Ray Laboratory, Raj Bhavan, Ooty, India;
Indian Institute of Technology Kanpur, Kanpur, India

Jangra Mamta Tata Institute of Fundamental Research, Mumbai, India;
Homi Bhabha National Institute, Mumbai, India

Jaryal Suresh C. Department of Physics and Astronomical Science, Central University of Himachal Pradesh, Dharamshala, India

Jashal Brij Kishor Tata Institute of Fundamental Research, Mumbai, India

Jena Satyajit Department of Physical Sciences, Indian Institute of Science Education and Research (IISER) Mohali, Manauli, Punjab, India

Jhansi V. B. The GRAPES-3 Experiment, Cosmic Ray Laboratory, Raj Bhavan, Ooty, India;
Tata Institute of Fundamental Research, Mumbai, India

John Jim Tata Institute of Fundamental Research, Mumbai, India;
Homi Bhabha National Institute, Mumbai, India

Johnson Joseph P. Department of Physics, Indian Institute of Technology Bombay, Mumbai, India

Joshi S. R. Tata Institute of Fundamental Research, Mumbai, India;
Department of High Energy Physics, Tata Institute of Fundamental Research, Colaba,
Mumbai, India

Kadam Guruprasad School of Physical Sciences, NISER Bhubaneswar,
Bhubaneswar, Odisha, India

Kaliyar A. B. Tata Institute of Fundamental Research, Mumbai, India

Kamon T. Texas A & M University, College Station, TX, USA

Kang Y. University of Seoul, Seoul, South Korea

Kanishka R. Applied Nuclear Physics Division, Saha Institute of Nuclear Physics,
Salt Lake, Kolkata, India;
Homi Bhabha National Institute, Training School Complex, Mumbai, India

Kar Chandiprasad National Institute of Science Education and Research, An OCC
of Homi Bhabha National Institute, Bhubaneswar, India

Karmakar Bithika Theory Division, Saha Institute of Nuclear Physics, Kolkata,
India;
Homi Bhabha National Institute, Mumbai, Maharashtra, India

Karmakar Saikat Tata Institute of Fundamental Research, Mumbai, India

Karthikk K. S. Tata Institute of Fundamental Research, Mumbai, India

Kashyap V. K. S. School of Physical Sciences, National Institute of Science Educa-
tion and Research, Jatni, India;
Homi Bhabha National Institute, Training School Complex, Mumbai, India

Kaur Amandeep Panjab University, Chandigarh, India

Kaur Harjot Panjab University, Chandigarh, India

Kaur Manjit Panjab University, Chandigarh, India

Kaur Sandeep Panjab University, Chandigarh, India

Kawakami S. The GRAPES-3 Experiment, Cosmic Ray Laboratory, Raj Bhavan,
Ooty, India;
Graduate School of Science, Osaka City University, Osaka, Japan

Khan Najimuddin School of Physical Sciences, Indian Association for the Culti-
vation of Science 2A & 2B, Kolkata, India

Khatun Amina Comenius University, Bratislava, Slovakia

Khindri Honey Homi Bhabha National Institute, Mumbai, India;
Tata Institute of Fundamental Research, Mumbai, India;
The Institute of Mathematical Sciences, Chennai, India

Kirti Prakash Sharma Tata Institute of Fundamental Research, Mumbai, India

Kojima H. The GRAPES-3 Experiment, Cosmic Ray Laboratory, Raj Bhavan, Ooty, India;

Faculty of Engineering, Aichi Institute of Technology, Toyota City, Aichi, Japan;
College of Engineering, Chubu University, Kasugai, Aichi, Japan

Korrapati Rambabu Department of Physics, Indian Institute of Technology Bombay, Mumbai, India

Krishna Gokul B. Indian Institute of Technology Gandhinagar, Gandhinagar, Gujarat, India

Krishnan R. Saha Institute of Nuclear Physics, Kolkata, India

Kumar Das Mrinal Department of Physics, Tezpur University, Napaam, Assam, India

Kumar Nayak Aruna Institute of Physics, Bhubaneswar, India;
BARC Training School Complex, Homi Bhabha National Institute, Mumbai, India

Kumar Saha Abhijit School of Physical Sciences, Indian Association for the Cultivation of Science, Kolkata, India

Kumar Sahu Pradip Institute of Physics, HBNI, Sachivalaya Marg, P.O. Sainik School, Bhubaneswar, Odisha, India

Kumar Abhass Physical Research Laboratory, Theoretical Physics Division, Navrangpura, Ahmedabad, India

Kumar Anil Institute of Physics, Bhubaneswar, India;
Homi Bhabha National Institute, Anushaktinagar, Mumbai, India;
Saha Institute of Nuclear Physics, Kolkata, India

Kumar Arvind Department of Physics, Dr. B R Ambedkar National Institute of Technology Jalandhar, Jalandhar, Punjab, India

Kumar Avdhesh School of Physical Sciences, National Institute of Science Education and Research, Jatni, India;

Homi Bhabha National Institute, Training School Complex, Mumbai, India

Kumar Mintu Tata Institute of fundamental research, Mumbai, India

Kumar Rajesh Department of Physics, Dr. B R Ambedkar National Institute of Technology Jalandhar, Jalandhar, Punjab, India

Kumar S. Panjab University, Chandigarh, India

Kundu Sourav European Organization for Nuclear Research (CERN), Geneva, Switzerland;

National Institute of Science Education and Research (NISER), Jatni, India

Kundu Suman Kumar Visva Bharati, Santiniketan, India

Kurian Manu Indian Institute of Technology Gandhinagar, Gandhinagar, Gujarat, India

Kushwaha Ashu Department of Physics, Indian Institute of Technology Bombay, Mumbai, India

Kutty A. P. K. Tata Institute of Fundamental Research, Mumbai, India

Lahiri Amitabha Department of Theoretical Sciences, S.N. Bose National Centre for Basic Sciences, Kolkata, India

Lakshmi S. M. National Centre for Nuclear Research (NCBJ), Warsaw, Poland; National Centre for Nuclear Research, Warsaw, Poland

Lechner L. Institute of High Energy Physics, Vienna, Austria

Li Jia Jie Institute of Modern Physics, Chinese Academy of Sciences, Lanzhou, China; Institute for Theoretical Physics, Goethe University, Frankfurt am Main, Germany

Lohan Manisha IRFU, CEA, Université Paris-Saclay, Gif-sur-Yvette, France

Magnea Lorenzo Dipartimento di Fisica and Arnold-Regge Center, Università di Torino, and INFN, Sezione di Torino, Torino, Italy

Mahakhud Maguni Indian Institute of Science Education and Research Mohali, Manauli, India

Mahanta Devabrat Indian Institute of Technology Guwahati, Assam, India

Mahapatra S. The GRAPES-3 Experiment, Cosmic Ray Laboratory, Raj Bhavan, Ooty, India; Utkal University, Bhubaneswar, India

Mahapatra Swapna Department of Physics, Utkal University, Bhubaneswar, India

Maharana Suvam Department of Physics and Astrophysics, University of Delhi, Delhi, India

Maharathy Siddharth P. Institute of Physics, Bhubaneswar, India

Maity Manas Visva Bharati, Santiniketan, India

Maity S. Indian Institute of Technology, Bhubaneswar, Odisha, India

Majumdar Debasish Astroparticle Physics and Cosmology Division, Saha Institute of Nuclear Physics, HBNI, Kolkata, India

Majumdar N. Applied Nuclear Physics Division, Saha Institute of Nuclear Physics, Salt Lake, Kolkata, India; Homi Bhabha National Institute, Training School Complex, Mumbai, India

Majumder G. Department of High Energy Physics, Tata Institute of Fundamental Research, Colaba, Mumbai, India

Mal P. K. School of Physical Sciences, National Institute of Science Education and Research, Jatni, India;

Homi Bhabha National Institute, Training School Complex, Mumbai, India

Mallick Dukhishyam School of Physical Sciences, National Institute of Science Education and Research, Jatni, India;

Homi Bhabha National Institute, Training School Complex, Mumbai, India

Mandal Rituparna Department of Theoretical Sciences, S.N. Bose National Centre for Basic Sciences, Kolkata, India

Mandal Sanjoy AHEP Group, Institut de Física Corpuscular, CSIC/Universitat de València, Parc Científic de Paterna, Paterna, Valencia, Spain

Mandal Tanumoy Indian Institute of Science Education and Research Thiruvananthapuram, Vithura, KL, India

Manna A. Electronics Division, Bhabha Atomic Research Centre, Trombay, Mumbai, India

Masud Mehedi Homi Bhabha National Institute, Mumbai, India;

Institute of Physics, Bhubaneswar, India;

Center for Theoretical Physics of the Universe, Institute for Basic Science (IBS), Daejeon, South Korea;

Institute of Physics, Odisha, Bhubaneswar, India

Mathews Prakash Saha Institute of Nuclear Physics, A CI of Homi Bhabha National Institute, Kolkata, India

Mawlong Barilang School of Physics, University of Hyderabad, Hyderabad, India

Mazumdar Kajari Tata Institute of Fundamental Research, Mumbai, India

Meena M. Panjab University, Chandigarh, India

Mehta Poonam Jawaharlal Nehru University, New Delhi, India

Mishra Amruta Department of Physics, Indian Institute of Technology Delhi, New Delhi, India

Mishra D. K. Bhabha Atomic Research Centre, Trombay, Mumbai, India

Mishra Debesh D. Hubei University, Wuhan, China

Mishra Hiranmaya Physical Research Laboratory, Ahmedabad, Gujarat, India;

Theory Division, Physical Research Laboratory, Navarangpura, Ahmedabad, India

Mishra Tribeni National Institute of Science Education and Research, An OCC of Homi Bhabha National Institute, Bhubaneswar, India

Mitra M. Institute of Physics, Bhubaneswar, India;

Homi Bhabha National Institute, Training School Complex, Mumbai, India

Mitra Subhadip Center for Computational Natural Sciences and Bioinformatics, International Institute of Information Technology, Hyderabad, India

Mohanta Rukmani School of Physics, University of Hyderabad, Hyderabad, India

Mohanty B. School of Physical Sciences, National Institute of Science Education and Research, Jatni, India;
Homi Bhabha National Institute, Training School Complex, Mumbai, India

Mohanty G. B. Tata Institute of Fundamental Research, Mumbai, India

Mohanty P. K. The GRAPES-3 Experiment, Cosmic Ray Laboratory, Raj Bhavan, Ooty, India;
Tata Institute of Fundamental Research, Mumbai, India

Mohanty S. Utkal University, Bhubaneswar, India;
Tata Institute of Fundamental Research, Mumbai, India

Mohapatra Ranjita K. Theory Division, Physical Research Laboratory, Navrangpura, Ahmedabad, India;
Department of Physics, Banki Autonomous College, Cuttack, India

Moharana R. The GRAPES-3 Experiment, Cosmic Ray Laboratory, Raj Bhavan, Ooty, India;
Indian Institute of Technology Jodhpur, Jodhpur, India;
Tata Institute of Fundamental Research, Mumbai, India

Mondal Suryanarayan Homi Bhabha National Institute, Mumbai, India;
Tata Institute of Fundamental Research, Mumbai, India

More Jai Department of Physics, Indian Institute of Technology Bombay, Mumbai, India

Morris S. D. Tata Institute of Fundamental Research, Mumbai, India;
The GRAPES-3 Experiment, Cosmic Ray Laboratory, Raj Bhavan, Ooty, India

Mukherjee Soumya Tata Institute of Fundamental Research, Mumbai, India

Mukhopadhyay S. Applied Nuclear Physics Division, Saha Institute of Nuclear Physics, Salt Lake, Kolkata, India;
Homi Bhabha National Institute, Training School Complex, Mumbai, India

Mukhopadhyay Somnath National Institute of Technology, Tiruchirappalli, Tamil Nadu, India

Muraki Y. The GRAPES-3 Experiment, Cosmic Ray Laboratory, Ooty, India;
Institute of Space-Earth Environmental Research, Nagoya University, Nagoya, Japan

Murthy M. V. N. Homi Bhabha National Institute, Mumbai, India;
The Institute of Mathematical Sciences, Chennai, India

Mustafa Munshi G Theory Division, Saha Institute of Nuclear Physics, Kolkata, India;

Homi Bhabha National Institute, Mumbai, Maharashtra, India

Nagesh B. K. Tata Institute of Fundamental Research, Colaba, Mumbai, India

Nandi Basanta Kumar Department of Physics, Indian Institute of Technology Bombay, Mumbai, India

Nayak Kishora Key Laboratory of Quark & Lepton Physics (MOE) and Institute of Particle Physics, Central China Normal University, Wuhan, China

Nayak L. Indian Institute of Technology Hyderabad, Hyderabad, Telangana, India

Nayak P. K. The GRAPES-3 Experiment, Cosmic Ray Laboratory, Ooty, India; Tata Institute of Fundamental Research, Mumbai, India

Neeraj Cyrin Center for Computational Natural Sciences and Bioinformatics, International Institute of Information Technology, Hyderabad, India

Newton Greyson Texas A & M University, College Station, Texas, USA

Ngairangbam Vishal S. Physical Research Laboratory (PRL), Ahmedabad, Gujarat, India;

IIT Gandhinagar, Gandhinagar, India

Nikam V. A. Tata Institute of Fundamental Research, Mumbai, India

Nishida S. KEK, Tsukuba, Japan

Niyogi Saurabh Gokhale Memorial Girls' College, Kolkata, India

Noonan D. Florida Tech, Melbourne, FL, USA

Oshima A. The GRAPES-3 Experiment, Cosmic Ray Laboratory, Ooty, India; College of Engineering, Chubu University, Kasugai, Aichi, Japan

Padhan Rojalin Institute of Physics, Bhubaneswar, India;

BARC Training School Complex, Homi Bhabha National Institute, Mumbai, India

Padmini S. Electronics Divison, Bhabha Atomic Research Center, Mumbai, India

Pal Abhishek Department of Physics and Astronomy, Bartol Research Institute, University of Delaware, Newark, USA

Pal Kausik Department of Physics, Serampore College, Serampore, West Bengal, India

Pal Sarbajit Computer & Informatics Group, Variable Energy Cyclotron Centre, Kolkata, India

Pal Sourav Department of Physics, Indian Institute of Technology Hyderabad, Kandi, Sangareddy, Telangana, India

Panchal N. Tata Institute of Fundamental Research, Mumbai, India

Panda Srikanta Department of Physics, Utkal University, Bhubaneswar, Odisha, India

Pandav Ashish School of Physical Sciences, National Institute of Science Education and Research, Jatni, India;
Homi Bhabha National Institute, Training School Complex, Mumbai, India

Panero Marco Department of Physics, University of Turin and INFN, Turin, Italy

Pant B. The GRAPES-3 Experiment, Cosmic Ray Laboratory, Ooty, India;
Indian Institute of Technology Jodhpur, Jodhpur, India

Pant B. P. The GRAPES-3 Experiment, Cosmic Ray Laboratory, Raj Bhavan, Ooty, India;
Indian Institute of Technology Jodhpur, Jodhpur, India

Panyam Nagaraj Tata Institute of Fundamental Research, Mumbai, India

Parmar N. K. Tata Institute of Fundamental Research, Colaba, Mumbai, India

Patel P. Tata Institute of Fundamental Research, Mumbai, India

Patel S. Bhabha Atomic Research Centre, Mumbai, India

Patel S. R. Tata Institute of Fundamental Research, Mumbai, India

Pathak S. Bhabha Atomic Research Centre, Mumbai, India

Pathaleswar Tata Institute of Fundamental Research, Mumbai, India

Patil Mandakini Tata Institute of Fundamental Research, Mumbai, India

Patra Monalisa Jožef Stefan Institute, Ljubljana, Slovenia

Patra S. Indian Institute of Science Education and Research Mohali, Punjab, India

Pattanaik D. The GRAPES-3 Experiment, Cosmic Ray Laboratory, Ooty, India;
Tata Institute of Fundamental Research, Mumbai, India;
Utkal University, Bhubaneswar, India

Paul Avik Astroparticle Physics and Cosmology Division, Saha Institute of Nuclear Physics, HBNI, Kolkata, India

Pethuraj S. Homi Bhabha National Institute, Mumbai, India;
Tata Institute of Fundamental Research, Mumbai, India

Petronilo G. X. A. International Centre of Physics, Universidade de Brasília, Campus Universitário Darcy Ribeiro, DF | CEP, Brasília, Brazil

Ponraj Jayakumar Tata Institute of Fundamental Research, Mumbai, India

Poudyal N. Wayne State University, Detroit, MI, USA

Prabhakar S. P. Bhabha Atomic Research Centre, Mumbai, India

- Pradhan G.** The GRAPES-3 Experiment, Cosmic Ray Laboratory, Ooty, India; Indian Institute of Technology Indore, Indore, India
- Pradhan G. S.** The GRAPES-3 Experiment, Cosmic Ray Laboratory, Raj Bhavan, Ooty, India; Department of Physics, Indian Institute of Technology Indore, Indore, India
- Prasad Adak Rama** Department of Physics, Taki Government College, Taki, West Bengal, India
- Prasad Sidharth K.** Department of Physics, Centre for Astroparticle Physics and Space Science, Bose Institute, Kolkata, India
- Procura Massimiliano** Fakultät für Physik, Universität Wien, Wien, Austria
- Pruneau Claude** Department of Physics and Astronomy, Wayne State University, Detroit, MI, USA
- Pruseth Priyanka Priyadarshini** Department of Physics, Utkal University, Bhubaneswar, India
- Pujahari Prabhat** Department of Physics, Indian Institute of Technology Madras, Chennai, India
- Punna Mahesh** Electronics Divison, Bhabha Atomic Research Center, Mumbai, India
- Rahaman Ushak** Department of Physics, Centre for Astro-Particle Physics (CAPP), University of Johannesburg, Auckland Park, South Africa
- Rakshe P. S.** The GRAPES-3 Experiment, Cosmic Ray Laboratory, Ooty, India; Tata Institute of Fundamental Research, Mumbai, India
- Rama Krishnan** Saha Institute of Nuclear Physics, Kolkata, India
- Ramanan Sunethra** Department of Physics, Indian Institute of Technology Madras, Chennai, TN, India
- Ramesh K.** The GRAPES-3 Experiment, Cosmic Ray Laboratory, Ooty, India; Tata Institute of Fundamental Research, Mumbai, India
- Randhawa Monika** Department of Applied Sciences, UIET, P.U, Chandigarh, India
- Ranjan Sahoo Nihar** Institute of Frontier and Interdisciplinary Science, Shandong University, Qingdao, Shandong, China; Key Laboratory of Particle Physics and Particle Irradiation, Shandong University, Qingdao, Shandong, China
- Ranjan M.** Tata Institute of Fundamental Research, Colaba, Mumbai, India
- Rao B. S.** The GRAPES-3 Experiment, Cosmic Ray Laboratory, Ooty, India; Tata Institute of Fundamental Research, Colaba, Mumbai, India

- Rao S. K.** Tata Institute of Fundamental Research, Colaba, Mumbai, India
- Rath Pranati K.** Department of Physics, Khallikote (Autonomous) College, Berhampur, India
- Ravindran K. C.** Tata Institute of Fundamental Research, Mumbai, India
- Ravindran V.** Saha Institute of Nuclear Physics, A CI of Homi Bhabha National Institute, Kolkata, India
- Ray Anupam** Tata Institute of Fundamental Research, Mumbai, India
- Ray Ipsita** Indian Institute of Technology Guwahati, Guwahati, Assam, Assam, India
- Ray Rajarshi** Center for Astroparticle Physics & Space Science, Bose Institute, Kolkata, India
- Raychaudhuri Sreerup** Department of Theoretical Physics, Tata Institute of Fundamental Research, Mumbai, India
- Raz Swapnil** Center for Computational Natural Sciences and Bioinformatics, International Institute of Information Technology, Hyderabad, India
- Reddy L. V.** The GRAPES-3 Experiment, Cosmic Ray Laboratory, Ooty, India; Tata Institute of Fundamental Research, Mumbai, India
- Ricky Devi Maibam** Department of Physics, Gauhati University, Guwahati, Assam, India
- Rout Jogesh** Jawaharlal Nehru University, New Delhi, India
- Rout Niharika** Indian Institute of Technology Madras, Chennai, India
- Rout P. K.** Applied Nuclear Physics Division, Saha Institute of Nuclear Physics, Salt Lake, Kolkata, India; Homi Bhabha National Institute, Training School Complex, Mumbai, India
- Roy A.** Department of High Energy Physics, Tata Institute of Fundamental Research, Mumbai, India
- Roy Pradip** High Energy Nuclear and Particle Physics Division, Saha Institute of Nuclear Physics, Kolkata, India
- Roy Samiran** Physical Research Laboratory, Ahmedabad, Gujarat, India; Harish-Chandra Research Institute, Allahabad, India; Homi Bhabha National Institute, Mumbai, India
- Roy Sujan Kumar** Variable Energy Cyclotron Centre, Kolkata, India; Homi Bhabha National Institute, Training School Complex, Mumbai, India
- Roy Victor** School of Physical Sciences, National Institute of Science Education and Research, Jatni, India; Homi Bhabha National Institute, Training School Complex, Mumbai, India

Rubinov Paul Fermilab, Batavia, IL, USA

Sachdeva Divya Department of Physics, Indian Institute of Science Education and Research Pune, Pune, India

Sachdeva Mahima Tata Institute of Fundamental Research, Mumbai, India

Saha Abhijit Kumar School of Physical Sciences, Indian Association for the Cultivation of Science, Kolkata, India

Saha Abhisek University of Hyderabad, Hyderabad, India

Saha Anirban Department of Physics, West Bengal State University, Barasat, Kolkata, India

Saha Prafulla National Institute of Science Education and Research, An OCC of Homi Bhabha National Institute, Bhubaneswar, India

Saha Rajib Indian Institute of Science Education and Research, Bhopal, MP, India

Sahdev Vandana Department of Physics and Astrophysics, University of Delhi, Delhi, India

Sahoo Baidyanath Department of Physics, Indian Institute of Technology Bombay, Mumbai, India

Sahoo D. Tata Institute of Fundamental Research, Mumbai, India;
Utkal University, Bhubaneswar, India

Sahoo Lopamudra Department of Physics, Ravenshaw University, Cuttack, India

Sahoo R. The GRAPES-3 Experiment, Cosmic Ray Laboratory, Ooty, India;
Department of Physics, Indian Institute of Technology Indore, Indore, India

Sahoo Suchismita Central University of Karnataka, Gulbarga, Karnataka, India

Sahoo Sunita Astroparticle Physics & Cosmology Division, Saha Institute of Nuclear Physics, Kolkata, India;
Homi Bhabha National Institute, Training School Complex, Anushaktinagar, Mumbai, India

Sahu Bisnupriya University of Hyderabad, Hyderabad, India

Sahu Dushmanta Department of Physics, Indian Institute of Technology Indore, Simrol, Indore, India

Sahu Narendra Department of Physics, Indian Institute of Technology Hyderabad, Kandi, Telangana, India

Sahu P. K. Institute of Physics, HBNI, Sachivalaya Marg, Bhubaneswar, Odisha, India

Sahu Sanjib Institute of Physics, HBNI, Sachivalaya Marg, P.O. Sainik School, Bhubaneswar, Odisha, India

Sajjad Athar M. Department of Physics, Aligarh Muslim University, Aligarh, India

Samal Pramoda Kumar School of Physics, Gangadhar Meher University, Sambalpur, India;
Department of Physics, Utkal University, Bhubaneswar, Odisha, India

Samanta Subhasis Institute of Physics, Jan Kochanowski University, Kielce, Poland

Sankar S. Uma Department of Physics, Indian Institute of Technology Bombay, Mumbai, India

Santana A. E. International Centre of Physics, Universidade de Brasília, Campus Universitário Darcy Ribeiro, Brasília, DF | CEP, Brazil

Sanyal Soma University of Hyderabad, Hyderabad, India

Saraf M. N. Department of High Energy Physics, Tata Institute of Fundamental Research, Colaba, Mumbai, India

Sarkar A. Tata Institute of Fundamental Research, Colaba, Mumbai, India

Sarkar Agnivo Indian Institute of Technology Gandhinagar, Gandhinagar, Gujarat, India

Sarkar Ratan Centre for High Energy Physics, Indian Institute of Science, Bangalore, KA, India

Sarkar S. Applied Nuclear Physics Division, Saha Institute of Nuclear Physics, Salt Lake, Kolkata, India;
Homi Bhabha National Institute, Training School Complex, Mumbai, India

Sarkar Tanmay National Central University (NCU), Taoyuan, Taiwan

Satapathy Sarthak Indian Institute of Technology Bhilai, Raipur, Chhattisgarh, India

Satyanarayana B. Department of High Energy Physics, Tata Institute of Fundamental Research, Colaba, Mumbai, India

Scaria R. The GRAPES-3 Experiment, Cosmic Ray Laboratory, Ooty, India;
Department of Physics, Indian Institute of Technology Indore, Indore, India

Schoefbeck R. Institute of High Energy Physics, Vienna, Austria

Sedrakian Armen Frankfurt Institute for Advanced Studies, Frankfurt am Main, Germany;
Institute of Theoretical Physics, University of Wrocław, Wrocław, Poland

Shafaq Sheeba Jawaharlal Nehru University, New Delhi, India

Shaikh Wadut Saha Institute of Nuclear Physics, Kolkata, India;
Mugberia Gangadhar Mahavidyalaya, Purba Medinipur, India

Shankaranarayanan S. Department of Physics, Indian Institute of Technology Bombay, Mumbai, India

Sharma Ashish IIT madras, Chennai, India

Sharma Chanchal Malaviya National Institute of Technology Jaipur, Jaipur, India

Sharma Natasha Department of Physics, Amity University Punjab, Mohali, India

Sharma Rishi Department of Theoretical Physics, Tata Institute of Fundamental Research, Mumbai, India

Shetty P. S. Bhabha Atomic Research Centre, Mumbai, India

Shibata S. The GRAPES-3 Experiment, Cosmic Ray Laboratory, Ooty, India; College of Engineering, Chubu University, Kasugai, Aichi, Japan

Shinde R. R. Department of High Energy Physics, Tata Institute of Fundamental Research, Colaba, Mumbai, India

Shukla Prashant Nuclear Physics Division, Bhabha Atomic Research Centre, Mumbai, India; Homi Bhabha National Institute, Mumbai, India

Singha Pracheta Center for Astroparticle Physics & Space Science, Bose Institute, Kolkata, India

Singh B. B. Tata Institute of Fundamental Research, Mumbai, India

Singh Balbeer Physical Research Laboratory, Ahmedabad, Gujarat, India

Singh S. K. Department of Physics, Aligarh Muslim University, Aligarh, India

Sinha Monika Indian Institute of Technology Jodhpur, Jodhpur, India

Sinha Nita The Institute of Mathematical Sciences, Chennai, India

Sinha Tinku High Energy Nuclear and Particle Physics Division, Saha Institute of Nuclear Physics, Kolkata, India

Siva Rama Krishna B. Bhabha Atomic Research Centre, Mumbai, India

Sogarwal H. Tata Institute of Fundamental Research, Mumbai, India; Homi Bhabha National Institute, Training School Complex, Mumbai, India

Soma Arun Kumar Drexel University, Philadelphia, PA, USA

Sridhar K. Department of Theoretical Physics, Tata Institute of Fundamental Research, Mumbai, India

Srinivasan T. S. Bhabha Atomic Research Centre, Mumbai, India

Srivastava Shikha Electronics Division, Bhabha Atomic Research Center, Mumbai, India

Sudevan Vipin LeCosPA, National Taiwan University, Taipei, Taiwan

Tanaka K. The GRAPES-3 Experiment, Cosmic Ray Laboratory, Ooty, India; Graduate School of Information Sciences, Hiroshima City University, Hiroshima, Japan

Thakur S. K. Variable Energy Cyclotron Centre, Kolkata, India

Thalapillil Arun Indian Institute of Science Education and Research, Pune, India

Thapa Vivek Baruah Indian Institute of Technology Jodhpur, Jodhpur, India

Tiwari Swatantra Kumar Department of Applied Science and Humanities, Muzaffarpur Institute of Technology, Muzaffarpur, India

Tiwary Rahul Tata Institute of Fundamental Research, Mumbai, India

Trabelsi K. Université Paris-Saclay, CNRS/IN2P3, IJCLab, Orsay, Paris, France

Tribedy Prithwish Brookhaven National Laboratory, New York, NY, USA

Tripathi Anurag Department of Physics, Indian Institute of Technology Hyderabad, Kandi, Sangareddy, Telangana, India

Tripathy Sushanta Department of Physics, Indian Institute of Technology Indore, Simrol, Indore, India;

Instituto de Ciencias Nucleares, UNAM, Mexico City, Mexico;
presently at INFN - sezione di Bologna, Bologna BO, Italy

Turqueti Marcos Electronic Systems, Engineering Division, Lawrence Berkeley National Lab, Berkeley, CA, USA

Ulhoa S. C. Instituto de Física, Universidade de Brasília, Brasília, DF, Brazil;
Canadian Quantum Research Center, Ave Vernon, BC V1T 2L7, Canada

Umesh L. Tata Institute of Fundamental Research, Mumbai, India;
The American College, Madurai, India

Upadhya S. S. Tata Institute of Fundamental Research, Colaba, Mumbai, India

Varsi F. The GRAPES-3 Experiment, Cosmic Ray Laboratory, Raj Bhavan, Ooty, India;
Indian Institute of Technology Kanpur, Kanpur, India

Vashisht Aseem Department of Physics, Panjab University, Chandigarh, India

Verma P. Tata Institute of Fundamental Research, Mumbai, India

Vinze Radhika Department of Physics, University of Mumbai, Mumbai, India

Virdi A. K. Panjab University, Chandigarh, India

Yumiceva F. Florida Tech, Melbourne, FL, USA

Yuvaraj E. Department of High Energy Physics, Tata Institute of Fundamental Research, Colaba, Mumbai, India

Zahed Ahmadullah Indian Institute of Science, Bangalore, India

Zaidi F. Aligarh Muslim University, Aligarh, India

Zuberi M. The GRAPES-3 Experiment, Cosmic Ray Laboratory, Ooty, India;
Tata Institute of Fundamental Research, Mumbai, India

Acronyms

ACORDE	ALICE Cosmic Rays Detector
ALICE	A Large Ion Collider Experiment
AMPT	A Multi-Phase Transport Model
ATLAS	A Toroidal LHC ApparatuS
BES	Beam Energy Scan
BNL	Brookhaven National Laboratory
BSM	Beyond Standard Model
CBM	Compressed Baryonic Matter
CDM	Cold Dark Matter
CDMS	Cryogenic Dark Matter Search
CDMSlite	CDMS Low Ionization Threshold Experiment
CERN	Conseil Européen Pour La Recherche Nucléaire
CE ν NS	Coherent Elastic Neutrino Nucleus Scattering
CF	Correlation Functions
CKM	Cabibo-Kobayashi-Maskawa
CMBR	Cosmic Microwave Background Radiation
CME	Chiral Magnetic Effect
CMS	Compact Muon Solenoid
CMW	Chiral Magnetic Wave
CNM	Cold Nuclear Matter
CNS	Coherent Neutrino Scattering
CP	Charge-Parity
CP	Critical Point
CSE	Chiral Separation Effect
CVE	Chiral Vortical Effect
DIS	Deep Inelastic Scattering
DM	Dark Matter
DPMJet	Dual Parton Model and Jets
DUNE	Deep Underground Neutrino Experiment
EAS	Excessive Air Shower
EIC	Electron Ion Collider
EMCAL	Electro-Magnetic Calorimeter

EoS	Equation of State
EPOS	Energy-sharing Parton Multiple scattering Outshell remnants Screening and shadowing
FAIR	Facility for Anti-proton and Ion Research
FMD	Forward Multiplicity Detector
GEM	Gas Electron Multiplier
GMC	Geiger-Muller Counter
GRAPES-3	Gamma Ray Astronomy PeV EnergieS phase-3
GUT	Grand Unified Theory
HBT	Hanbury Brown and Twiss
HCAL	Hadron Calorimeter
HEP	High Energy Physics
HERA	Hadron Electron Ring Accelerator
HF	Heavy-Flavor
HIC	Heavy-Ion collisions
HIJING	Heavy-Ion Jet INTERaction Generator
HMPID	High Momentum Particle Identification Detector
HRG	Hardon Resonance Gas
HV	High Voltage
HYDJET	Hydrodynamics plus JET
ICAL	Iron Calorimeter
INO	India-based Neutrino Observatory
ITS	Inner Tracking system
iZIP	Interleaved Z-sensitive Ionization Phonon
JUSL	Jaduguda Underground Science Laboratory
LBNE	Long Baseline Neutrino Experiment
LF	Light Flavor
LH	Left-Handed
LHC	Large Hadron Collider
LIPs	Lightly Ionizing Particles
LNC	Lepton Number Conserving
LNV	Lepton Number Violating
LQCD	Lattice QCD
LRSM	Left-Right Symmetric Model
LSS	Large Scale Structure
MBNE	Mini Booster Neutrino Experiment
MHD	MagnetoHydroDynamics
MIP	Minimum Ionizing Particle
MPGD	Micro Pattern Gas Detectors
MPI	Multiple Parton Interactions
MSSM	Minimal Supersymmetric Standard Model
MuCh	Muon Chamber
nEXO	Next Enriched Xenon Observatory
NJL	Nambu-Jona-Lasinio
NMSSM	Next-to-Minimal SUSY Model

NNLO	Next-to-Next-Leading-Order
NOVA	Numi Off-axis neutrino appearance
NTL	Neganov-Trofimov-Luke
OF	Optimal Filter
PDG	Particle Data Group
PHOS	Photon spectrometer
PID	Particle Identification
PMD	Photon Multiplicity Detector
PSD	Power Spectral Density
QCD	Quantum Chromodynamics
QED	Quantum Electrodynamics
QGP	Quark Gluon Plasma
QNS	Quark Number Susceptibilities
QPM	Quasi-Particle Mode
RBE	Relativistic Boltzman Equation
RH	Right-Handed
RHIC	Relativistic Heavy Ion Collider
RPC	Resistive Plate Chamber
RTA	Relaxation Time Approximation
S/N	Signal-To-Noise Ratio
SDD	Silicon Drift Detector
SiPM	Silicon Photomultiplier
SLAC	Stanford Linear Accelerator Center
SM	Standard Mode
SNO	Sudbury Neutrino Observatory
SPD	Silicon Pixel Detector
SPS	Super Proton Synchrotron
sQGP	strongly coupled quark-gluon-plasma
SQUID	Superconducting Quantum Interference Device
SSD	Silicon Strip Detector
STAR	Solenoidal Tracker at RHIC
SUL	Soudan Underground Lab
SuperCDMS	Super Cryogenic Dark Matter Search
SUSY	Supersymmetry
SUSY	Super Symmetric
TES	Transition Edge Sensor
ThGEM	Thick Gas Electron Multiplier
TOF	Time-of-Flight
TPC	Time Projection Chamber
TRD	Transition radiation detector
UrQMD	Ultra Relativistic Quantum Molecular Dynamics
WIMP	Weakly Interacting Massive Particles
ZDC	Zero Degree Calorimeter

Part I
Standard Model and Beyond Standard
Model Physics

Chapter 1

Revisiting the Charged Higgs Boson Discovery



Agnivo Sarkar, Baradhvaj Coleppa, and Gokul B. Krishna

Abstract We describe a model with an extended electroweak gauge symmetry $SU(2) \times SU(2) \times U(1)$ having EWSB facilitated by two scalar doublets ϕ_1, ϕ_2 and a non-linear sigma field Σ . The presence of additional gauge degrees of freedom allows us to identify novel channels and, as a consequence, demarcate both the scenarios in the future LHC experiments. We illustrate this point focusing on the charged Higgs boson phenomenology.

1.1 Introduction

Since the discovery of a Higgs boson at LHC in 2012 [1, 2] both the ATLAS and CMS collaborations have been looking for additional physical scalar states, to determine whether the newly detected scalar state (with $m_h = 125$ GeV) is part of an extended scalar sector than Standard Model (SM). The charged Higgs boson (H^\pm) arises in the particle spectrum of various Beyond Standard Model theories with enlarged scalar sector and detection of this particle in collider experiments would confirm the existence of a new physics signal in the high energy scale. Both ATLAS and CMS have looked for the H^\pm primarily in two channels: (i) where the H^\pm is coupled to the top quark either in production or decay mode or both, (ii) the H^\pm is produced due to the fusion of SM gauge boson W^\pm and Z_μ . In Fig. 1.1, we present the lower bound (obtained from ATLAS measurement) on the H^\pm production cross section for these two mechanisms. Depending on the final state, the combined measurement by ATLAS has been excluded the H^\pm mass-range from 180 GeV to 3 TeV. The CMS collaboration has performed similar searches and the results obtained from their analysis are available in the literature. For the H^\pm boson, the presence or absence of certain tree level couplings furnishes certain insights regarding the representation of the scalar fields which are involved in symmetry breaking [4]. To illustrate this

A. Sarkar (✉) · B. Coleppa · G. B. Krishna
Indian Institute of Technology Gandhinagar, Gandhinagar 382355, Gujarat, India
e-mail: agnivo.sarkar@iitgn.ac.in

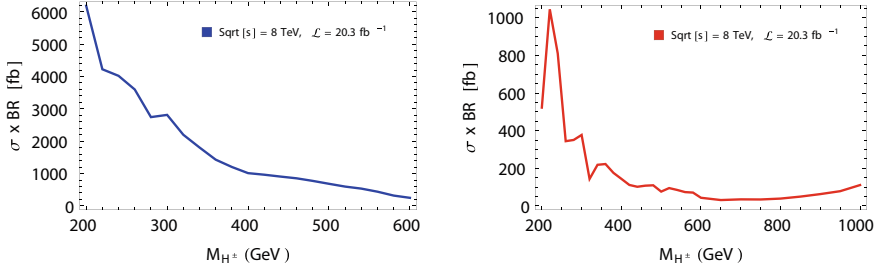


Fig. 1.1 The lower bound on the H^\pm boson production cross-section obtained from ATLAS measurements [3, 5]. The channels that are used for above searches are $\sigma(gb \rightarrow H^\pm t)\mathcal{BR}(H^\pm \rightarrow tb)$ (left) and Vector Boson Fusion (right) process, respectively

point, let us consider the coupling $g_{H^\pm W^\mp Z}$ which in general takes the form: $\mathcal{L} = \xi H^+ W_\mu^- Z_\mu + h.c..$

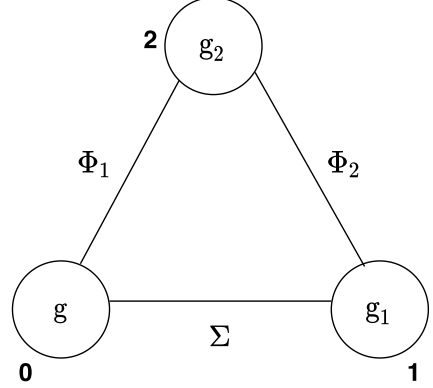
$$\xi^2 = \frac{g^2}{4m_W^2} \left\{ \sum_{T,Y} Y^2 [4T(T+1) - Y^2] |V_{T,Y}|^2 \right\} - \frac{1}{\rho^2}, \quad (1.1)$$

where $\rho = \frac{m_W^2}{m_Z^2 \cos^2 \theta_W}$ and $V_{T,Y}$ defines the VEVs of neutral Higgs fields. For 2HDM, where the EWSB is achieved via two scalar doublets, the above coupling vanishes at tree level. On the other hand, for Georgi-Marchak model, where one introduced additional triplet for symmetry breaking contain a H^\pm which couples to W^\pm and Z boson at tree level but remains fermiophobic. For detail discussion, the reader can consult [6]. It is evident that, depending on model construction the phenomenology associated with various BSM states alter significantly. With that in mind, in this article we propose an alternative avenue of EWSB, where the charged Higgs boson can simultaneously couple to SM gauge bosons and fermions at tree level.

1.2 The Model

In Fig. 1.2, we have sketched out various details of an alternative electroweak symmetry breaking scheme using Moose notation. The gauge structure of the model is a minimal extension of SM with an additional $SU(2)$ group resides at site “1”. The other $SU(2) \otimes U(1)$ gauge group which are similar to the SM gauge group resides at site “0” and site “2”, respectively. The non-linear sigma model field Σ which is charged under both the $SU_0(2)$ and $SU_1(2)$ acquires a vacuum expectation value (vev) and spontaneously breaks the $SU_0(2) \otimes SU_1(2)$ down to diagonal $SU_V(2)$. The Φ_1 and Φ_2 fields which behave like as a doublet under full symmetry group then jointly participate in symmetry breaking and breaks $SU_V(2) \otimes U_2(1)$ down to $U_{EM}(1)$. For simplicity we consider $\langle \Sigma \rangle = \langle \Phi_2 \rangle$ and assume $g_1 \gg g, g_2$ to cal-

Fig. 1.2 A pictorial representation of the model under consideration. The site “0” and site “1” contain a $SU(2)$ gauge group, whereas site “2” contain the $U(1)$ group



culate various model details. In this section we will point out few essential model details which will be required to discuss the charged Higgs boson phenomenology. However, for the interested reader we refer to [7] which gives much more elaborate description.

In Eq. 1.2, we present the general potential for the Φ_1 , Φ_2 , and Σ field which is consistent with full symmetry of the theory.

$$\begin{aligned}
 V(\Phi_1, \Phi_2, \Sigma) = & \lambda_1 \left[\Phi_1^\dagger \Phi_1 - \frac{f^2}{2} \right]^2 + \lambda_2 \left[\Phi_2^\dagger \Phi_2 - \frac{F^2}{2} \right]^2 + \lambda_3 \left[\Phi_1^\dagger \Phi_1 + \Phi_2^\dagger \Phi_2 - \frac{f^2 + F^2}{2} \right]^2 \\
 & + \lambda_4 \left[(\Phi_1^\dagger \Phi_1)(\Phi_2^\dagger \Phi_2) - (\Phi_1^\dagger \Sigma \Phi_2)(\Phi_2^\dagger \Sigma^\dagger \Phi_1) \right] + \lambda_5 \left[\text{Re}(\Phi_1^\dagger \Sigma \Phi_2) - \frac{fF}{2} \right]^2 \\
 & + \lambda_6 \text{Im} \left[\Phi_1^\dagger \Sigma \Phi_2 \right]^2
 \end{aligned} \tag{1.2}$$

Putting the explicit form of the scalar fields and collecting all the quadratic terms arise from the $\Phi_i^\dagger \Phi_j$, we will obtain the mass matrix for the CP-even Higgs states. But for the H^\pm only term which contributes to the mass matrix is λ_4 term in Eq. 1.2. After diagonalizing the mass matrix the physical H^\pm states can be expressed as a linear combination of the charged pions (which are the degrees of freedom of different scalar fields written in gauge basis): $H^\pm = \frac{f}{\sqrt{2}v} \Pi_\Sigma^\pm - \frac{F}{\sqrt{2}v} \Pi_1^\pm + \frac{f}{\sqrt{2}v} \Pi_2^\pm$. From the symmetry breaking one can realize that the model contains two sets of massive gauge bosons W_μ, Z_μ and its heavier counterpart W'_μ, Z'_μ . The H^\pm boson couples to these gauge bosons through the gauge invariant kinetic energy term of the scalar fields and from [7] one can find both couplings $g_{H^\pm W^\pm Z}$ and $g_{H^\pm W'^\pm Z}$ exist at tree level. We will discuss the consequence of these couplings in the H^\pm phenomenology in the next section. The left-handed chiral fermion draws its gauge charges from site 0 and site 1, whereas the right-handed chiral fermion which is singlet under $SU(2)$ resides at site 2. Apart from the chiral fermions there will be vector-like fermions which are charged under $SU_1(2)$. The SM fermions get their masses primarily due to Yukawa like terms $\tilde{\psi}_{L0} \Phi_1 u_{R2}$ and $\tilde{\psi}_{L0} \Phi_1 d_{R2}$. Along with that, a small contribution comes

from the Dirac-like mass term $\bar{\psi}_{L1}\psi_{R1}$. Expanding the fermion sector lagrangian, it can be seen that the coupling between the physical scalar states and the SM fermions mimic the coupling structure of the Type-I 2HDM in the leading order. In fact, the coupling $g_{H^\pm t\bar{b}}$ is proportional to the ratio of VEVs same like the generic 2HDM models.

1.3 The Charged Higgs Phenomenology

In Fig. 1.3, we exhibit the branching ratio of the heavy H^\pm in dominant decay modes for two distinct $\sin\beta$ values while fixing the $\sin\alpha$ at $-\frac{1}{\sqrt{2}}$. As expected for moderate values of $\sin\beta$, $H^\pm \rightarrow t\bar{b}$ channel remains the dominant decay mode for entire range of H^\pm mass. Before discussing the other decay channels, let us point out an interesting prospect of the W'_μ boson, which is applicable for the current model. To satisfy the electroweak precision measurement bounds, we have invoked the concept of ideal fermion delocalization (IFD) for this model. According to IFD, the wave functions of SM fermions overlap with the SM W_μ boson wave function. Now because of the existing relation between W_μ^\pm and W'^\pm_μ , the tree level couplings between heavy gauge boson and SM fermions vanishes. Therefore, the experimental bounds on the W'^\pm_μ mass loosen up because majority of these searches considered fermionic decay modes in their analyses. Hence we can choose, the $M_{W'}$ around 400 GeV for our concurrent discussion.

Coming back to Fig. 1.3, for large value of $\sin\beta$, $H^\pm \rightarrow W'^\pm Z$ decay mode becomes a competing channel. Since W'^\pm does not couple to SM fermions at tree level, the H^\pm can decay via cascade modes, $H^\pm \rightarrow W'^\pm Z \rightarrow W^\pm ZZ$. Due to the presence of multiple gauge bosons in the decay chain, the final state topology of the above channel consists of multiple hard leptons and b-quarks. Due to the moderate value of $g_{H^\pm t\bar{b}}$ coupling, a heavy H^\pm can get produced via the associated production mechanism with a reasonable cross-section. Incorporating both these features,

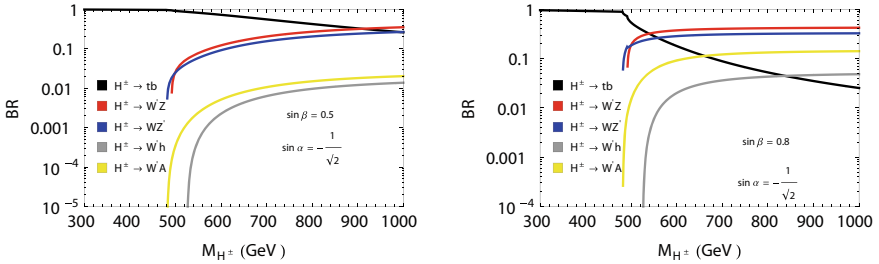


Fig. 1.3 Heavy charged Higgs boson branching ratios for $\sin\beta = 0.5$ (Left) and 0.8 (right)

$g\bar{b} \rightarrow H^+\bar{t} \rightarrow W'^+Z\bar{t}$ can serve as a viable discovery mode in LHC with sufficient luminosity. In that spirit, we undertake a study which will provide a detailed collider analysis for this channel in our future work.

References

1. G. Aad et al. [ATLAS], Phys. Lett. B **716**, 1–29 (2012). <https://doi.org/10.1016/j.physletb.2012.08.020>, [arXiv:1207.7214](https://arxiv.org/abs/1207.7214) [hep-ex]
2. S. Chatrchyan et al. [CMS], Phys. Lett. B **716**, 30–61 (2012). <https://doi.org/10.1016/j.physletb.2012.08.021>, [arXiv:1207.7235](https://arxiv.org/abs/1207.7235) [hep-ex]
3. G. Aad et al. [ATLAS], JHEP **03**, 127 (2016). [https://doi.org/10.1007/JHEP03\(2016\)127](https://doi.org/10.1007/JHEP03(2016)127), [arXiv:1512.03704](https://arxiv.org/abs/1512.03704) [hep-ex]
4. J.A. Grifols, A. Mendez, Phys. Rev. D **22**, 1725 (1980). <https://doi.org/10.1103/PhysRevD.22.1725>
5. G. Aad et al. [ATLAS], Phys. Rev. Lett. **114**(23), 231801 (2015). <https://doi.org/10.1103/PhysRevLett.114.231801>, [arXiv:1503.04233](https://arxiv.org/abs/1503.04233) [hep-ex]
6. J.F. Gunion, H.E. Haber, G.L. Kane, S. Dawson, Front. Phys. **80**, 1–404 (2000). SCIPP-89/13
7. B. Coleppa, A. Sarkar, [arXiv:2011.10926](https://arxiv.org/abs/2011.10926) [hep-ph]

Chapter 2

Model Independent Analysis of $B \rightarrow K_1 \mu^+ \mu^-$ Decay Processes



Aishwarya Bhatta

Abstract Anew, several discrepancies at the level of $(2 - 3)\sigma$ have been noticed in the flavor changing neutral current (FCNC) mediated transitions $b \rightarrow s \ell^+ \ell^-$ decays, which may be examined as the smoking-gun signal of New Physics (NP). Here, we perform a comprehensive analysis of the FCNC decay of B meson to axial vector mesons $K_1(1270)$ and $K_1(1400)$, which are mixtures of the 3P_1 and 1P_1 states K_{1A} and K_{1B} , in a model independent framework. We investigate the semileptonic decays $B \rightarrow K_1(1270)\ell^+\ell^-$ and $B \rightarrow K_1(1400)\ell^+\ell^-$ ($\ell \equiv e, \mu, \tau$). Considering all the possible relevant operators for $b \rightarrow s \ell^+ \ell^-$ transitions, we study their effects on various observables such as branching fractions and lepton polarization asymmetries of these processes, which give relatively strong dependency on the mixing angle θ .

2.1 Introduction and Theoretical Framework

Here we would like to analyze the decay channels $B \rightarrow K_1(1270, 1400)\mu^+\mu^-$

$$\begin{aligned} |K_1(1270)\rangle &= |K_{1A}\rangle \sin \theta + |K_{1B}\rangle \cos \theta, \\ |K_1(1400)\rangle &= |K_{1A}\rangle \cos \theta - |K_{1B}\rangle \sin \theta, \end{aligned} \quad (2.1)$$

where θ is the mixing angle, which is not yet determined precisely. Its value has been estimated to be $-(34 \pm 13)^\circ$ from the decay of $B \rightarrow K_1(1270)\gamma$ and $\tau \rightarrow K_1(1270)\nu_\tau$ [1]. In this context, we would like to investigate these decay processes in a model independent framework, where the possible new physics effects are quantified by introducing additional new operators to the SM effective Hamiltonian. The SM effective Hamiltonian responsible for $b \rightarrow s \ell^+ \ell^-$ transition can be expressed as [2]

A. Bhatta (✉)
University of Hyderabad, Hyderabad 500 046, India
e-mail: aish.bhatta@gmail.com

$$\mathcal{H}_{\text{eff}}^{\text{SM}} = -\frac{\alpha G_F}{\sqrt{2}\pi} V_{tb} V_{ts}^* \left[2 \frac{C_7^{\text{eff}}}{q^2} [\bar{s} \sigma^{\mu\nu} q_\nu (m_s P_L + m_b P_R) b] (\bar{\ell} \gamma_\mu \ell) \right. \\ \left. + C_9^{\text{eff}} (\bar{s} \gamma^\mu P_L b) (\bar{\ell} \gamma_\mu \ell) + C_{10} (\bar{s} \gamma^\mu P_L b) (\bar{\ell} \gamma_\mu \gamma_5 \ell) \right] \quad (2.2)$$

The new physics effective Hamiltonian has the form

$$\mathcal{H}_{\text{eff}}^{\text{SM}} = -\frac{\alpha G_F}{\sqrt{2}\pi} V_{tb} V_{ts}^* \left[C_9^{\text{NP}} (\bar{s} \gamma^\mu P_L b) (\bar{\ell} \gamma_\mu \ell) + C_{10}^{\text{NP}} (\bar{s} \gamma^\mu P_L b) (\bar{\ell} \gamma_\mu \gamma_5 \ell) \right. \\ \left. + C_9^{\text{NP}} (\bar{s} \gamma^\mu P_R b) (\bar{\ell} \gamma_\mu \ell) + C_{10}^{\text{NP}} (\bar{s} \gamma^\mu P_R b) (\bar{\ell} \gamma_\mu \gamma_5 \ell) \right] \quad (2.3)$$

where $C_{9,10}^{\text{NP}}$ and $C_{9,10}'^{\text{NP}}$ are the new Wilson coefficients, and their values can be obtained from the global fit to the observed $b \rightarrow s\mu^+\mu^-$ data. In our analysis, we will consider the impact of two different classes of NP scenarios: in the first case, we will consider the NP structure to be SM-like, with the values of NP coefficients as $(C_9^{\text{NP}}, C_{10}^{\text{NP}}) = (-1.03, 0.08)$, taken from [3] (NP1) and in the second case we will consider the presence of $C_9^{\text{NP}} - C_{10}^{\text{NP}}$ and use the extracted best-fit values of the NP coefficients: $(-1.315, -0.875)$ (NP2).

2.2 Observables

2.2.1 Differential Decay Rate

The differential decay width with respect to the dilepton invariant mass ($q^2 \equiv s$) for the process $\bar{B} \rightarrow \bar{K}_1 \ell^+ \ell^-$ is given as [4]

$$\frac{d\Gamma(\bar{B} \rightarrow \bar{K}_1 \ell^+ \ell^-)}{d\hat{s}} = \frac{G_F^2 \alpha^2 m_B^5 \tau_B}{2^{12} \pi^5} |V_{tb} V_{ts}^*|^2 v \sqrt{\lambda} \Delta(\hat{s}) \quad (2.4)$$

2.2.2 Lepton Polarization Asymmetries

Next, we pay our attention to the single-lepton polarization asymmetry parameters in $B \rightarrow K_1 \ell^+ \ell^-$, defined as [5]

$$P_i = \frac{d\Gamma(\mathbf{s}^\pm = \mathbf{i})/d\hat{s} - d\Gamma(\mathbf{s}^\pm = -\mathbf{i})/d\hat{s}}{d\Gamma(\mathbf{s}^\pm = \mathbf{i})/d\hat{s} + d\Gamma(\mathbf{s}^\pm = -\mathbf{i})/d\hat{s}}, \quad (2.5)$$

where \mathbf{i} denotes the unit vector along longitudinal (L), normal (N) and transverse (T) polarization directions of the lepton and \mathbf{s}^\pm denote the spin direction of ℓ^\pm .

2.3 Results and Discussion

In Fig. 2.1, we first show the q^2 variation of SM differential branching fraction and the longitudinal lepton polarization asymmetry of $B \rightarrow K_1(1270, 1400)\mu^+\mu^-$ process for three different θ values in the left and right panel respectively. From these plots, it should be noted that the observables of $B \rightarrow K_1(1270)\mu^+\mu^-$ process are almost insensitive to mixing angle θ whereas for $B \rightarrow K_1(1400)\mu^+\mu^-$ process, they are strongly dependent on θ , due to the cancellation of the contributions from $B \rightarrow K_{1A}$ and $B \rightarrow K_{1B}$ form factors. As expected, these observables are found to have their minimal values for $\theta = -47^\circ$, which is very close to the maximal mixing. Therefore, the measurement of various observables of $B \rightarrow K_1(1400)\mu^+\mu^-$ process will shed light on the determination of the mixing angle. In Fig. 2.2, in the top panel branching fractions are shown, where the dashed lines are due to the central values of the input parameters whereas the bands are due to the 1σ uncertainties. It can be noticed that for $B \rightarrow K_1(1270)\mu\mu$ process, the branching fractions are lower than the SM values for both types of NP scenarios, whereas for $B \rightarrow K_1(1400)\mu^+\mu^-$, the branching ratio of NP scenario II (NP2) is higher than the SM while for scenario-I (NP1), it is lower than the SM prediction. In the bottom panel the lepton polarization asymmetry is displayed and it is found that the behavior of lepton polarization asymmetry in NP-II scenario is quite different from SM as well as NP-I case. It is also inferred that it receives the dominant contributions for both the decay modes.

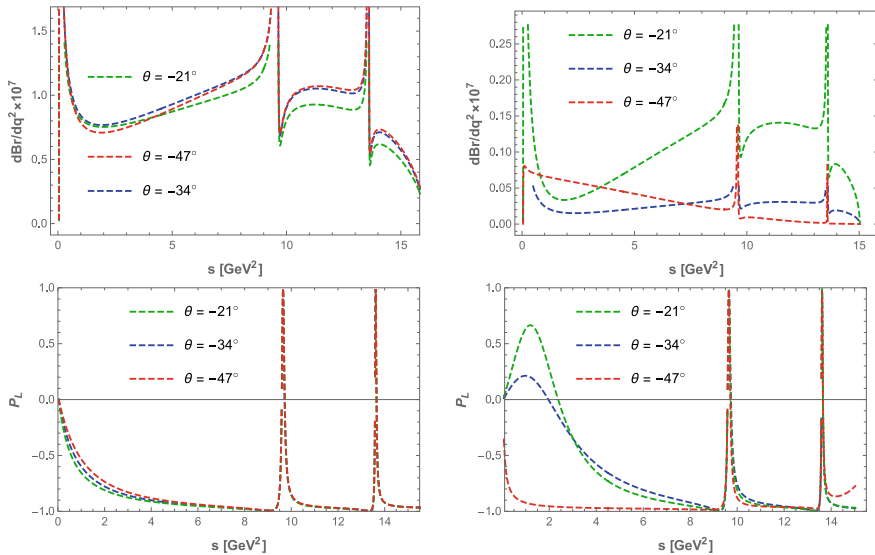


Fig. 2.1 Variation of differential branching ratio and longitudinal polarization fraction with s for different values of the mixing angle θ . The plots in the left panel are for $B \rightarrow K_1(1270)\mu^+\mu^-$ and those in the right panel are for $B \rightarrow K_1(1400)\mu^+\mu^-$ process

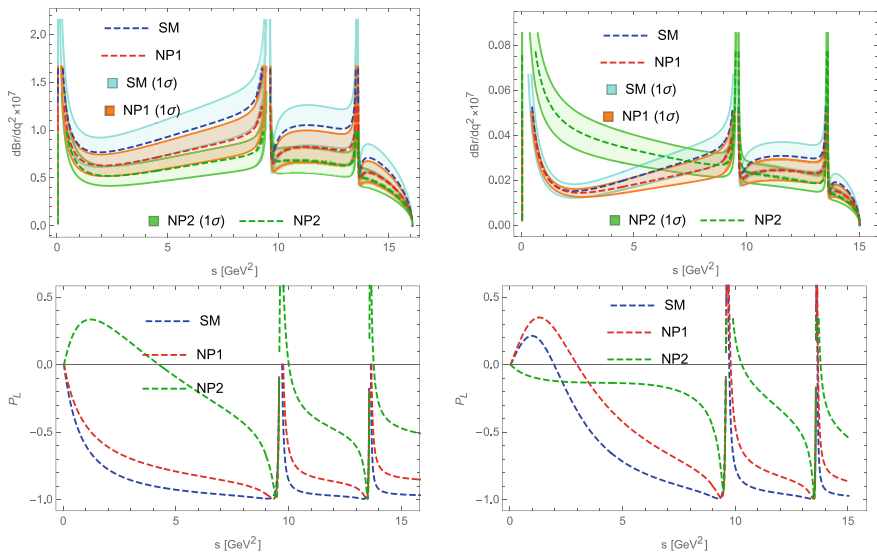


Fig. 2.2 The s variation of the differential branching fraction and longitudinal Lepton polarization asymmetry are shown in the SM as well as the NP scenarios. The plots in left panel correspond to $B \rightarrow K_1(1270)\mu^+\mu^-$ process whereas the right panel plots are for $B \rightarrow K_1(1400)\mu^+\mu^-$ process

2.4 Summary

We found that the observables of $B \rightarrow K_1(1400)\mu^+\mu^-$ processes are quite sensitive to the mixing angle whereas $B \rightarrow K_1(1270)\mu^+\mu^-$ process depends very mildly on it. In NP1, $C_{7,9,10}^{\text{NP}}$ structure is similar to the SM case whose values are extracted from the currently available data on $b \rightarrow s\mu\mu$ anomalies. In NP2, we considered $(C_9^{\text{NP}}, C_9^{\text{NP}})$, i.e., in addition to the standard left-handed quark currents, we have also taken into account the right-handed current. We found various observables deviate significantly from their corresponding SM predictions whereas for NP scenario-I, there are only marginal deviations from SM results. The measurement of these observables would be highly instrumental in exploiting the full potential of $b \rightarrow s\mu\mu$ decays to look for new physics signal and ultimately uncover their true nature.

References

1. H. Hatanaka, K.C. Yang, $B \rightarrow K(1)\gamma$ Decays in the Light-Cone QCD Sum Rules. Phys. Rev. D **77**, 094023 (2008). ([arXiv:0804.3198 [hep-ph]])
2. F. Falahati, A. Zahedidashouri, Forward-backward asymmetries of $\bar{B} \rightarrow \bar{K}_1(1270)\ell^+\ell^-$ and $\bar{B} \rightarrow \bar{K}^*\ell^+\ell^-$ transitions in two Higgs doublet model. Phys. Rev. D **90**, 075002 (2014)
3. A.K. Alok, A. Dighe, S. Gangal, D. Kumar, Continuing search for new physics in $b \rightarrow s\mu^+\mu^-$ decays: two operators at a time. JHEP **06**, 089 (2019). ([arXiv:1903.09617])

4. A. Bhatta, R. Mohanta, Implications of new physics in $B \rightarrow K_1\mu^+\mu^-$ decay processes, [arXiv:2011.05820](https://arxiv.org/abs/2011.05820) [hep-ph]
5. V. Bashiry, Lepton polarization in $B \rightarrow K_1\mu^+\mu^-$ decays. JHEP **06**, 062 (2009). ([arXiv:0902.2578](https://arxiv.org/abs/0902.2578))

Chapter 3

Jet Substructure Techniques for a Supersymmetric Scenario with Gravitino LSP



Akanksha Bhardwaj

Abstract We discuss the search strategy for compressed supersymmetry at multi-TeV scale, in the presence of a light gravitino dark matter. This scenario can get sizable uplift while looking into the associated fat-jets with missing transverse momenta as a signature of the boson produced in the decay process of much heavier next-to-lightest sparticle. Here, we focus on the hadronic decay of the ensuing Higgs and/or Z boson giving rise to at least two fat-jets and \cancel{E}_T in the final state. This channel provides the best discovery prospects with most of the benchmarks discoverable within an integrated luminosity of $\mathcal{L} = 200 \text{ fb}^{-1}$. We will also discuss some kinematic observables which can distinguish between compressed and uncompressed spectra having similar event yields.

3.1 Introduction

In view of the null results at the Run 1 and Run 2 of LHC, compressed SUSY (cSUSY) has gained relevance in its ongoing pursuit. Compressed MSSM sector with the higgsino-like neutralino $\tilde{\chi}_1^0$ as the NLSP along with a light Gravitino \tilde{G} LSP. Gravitino \tilde{G} LSP can be the potential dark matter (DM) candidate. A dominantly higgsino-like $\tilde{\chi}_1^0$ NLSP decays to a Higgs boson or a Z boson along with the \tilde{G} . We focus on the hadronic decay of the ensuing Higgs and/or Z boson giving rise to at least two fat-jets and \cancel{E}_T in the final state. We perform a detailed background study adopting a multivariate analysis using a boosted decision tree to provide a robust investigation to explore the discovery potential for such signal at 14 TeV LHC.

We now discuss the salient features of our benchmark points (BP) as listed in Table 3.1. We construct two sets of them as below. While **BP1-BP6** represent a compressed spectra with narrow mass difference, $\Delta M < 200 \text{ GeV}$, **U1-U2** are for uncompressed spectra having similar yields.

A. Bhardwaj (✉)

Physical Research Laboratory (PRL), Ahmedabad 380009, Gujarat, India
e-mail: akanksha@prl.res.in

© The Author(s), under exclusive license to Springer Nature Singapore Pte Ltd. 2022
B. Mohanty et al. (eds.), *Proceedings of the XXIV DAE-BRNS High Energy Physics Symposium, Jatni, India*, Springer Proceedings in Physics 277,
https://doi.org/10.1007/978-981-19-2354-8_3

Table 3.1 List of benchmark points, corresponding parameters and NLSP branching ratios chosen for our study. The mass parameters are in GeV unless specified otherwise. For all benchmarks, gravitino mass is kept fixed at $m_{\tilde{G}} = 1$ keV

Parameters	BP1	BP2	BP3	BP4	BP5	BP6	U1	U2
M_1	2900	3000	3000	3000	3500	3500	2900	2900
μ	2340	-2442	2505	2600	2812	2910	2390	1000
$\tan \beta$	25	25	5	25	25	25	25	25
A_t	-3200	-3200	-3300	-3200	-3200	-3200	-3200	-3200
m_A	2500	3000	2500	2500	3000	3000	3000	2500
m_h	124.7	124.6	122.1	124.8	124.6	124.6	124.7	124.7
$m_{\tilde{g}}$	2395.1	2494.6	2609.0	2600.9	2999.6	2953.3	3031.7	3031.7
$m_{\tilde{q}_L}$	2399.1	2500.9	2603.5	2667.7	2983.4	2961.7	2402.1	2402.2
$m_{\tilde{q}_R}$	2398.0	2496.7	2599.3	2666.4	2980.0	2960.6	2397.8	2395.7
$m_{\tilde{t}_1}$	2598.5	2612.5	2638.7	2612.5	2893.2	2929.7	2606.4	2587.7
$m_{\tilde{t}_2}$	2787.5	2789.8	2845.9	2800.2	3056.0	3096.5	2784.7	2768.2
$m_{\tilde{b}_1}$	2716.1	2704.9	2734.9	2726.6	2949.2	2985.6	2689.2	2690.5
$m_{\tilde{b}_2}$	2781.3	2790.7	2789.5	2792.3	3010.1	3047.4	2784.7	2722.9
$m_{\tilde{l}_L}$	3338.3	3339.1	3339.6	3339.1	3344.7	3345.1	3338.1	3338.1
$m_{\tilde{l}_R}$	3338.5	3338.8	3338.9	3338.8	3341.3	3341.5	3338.4	3338.5
$m_{\tilde{\chi}_1^0}$	2339.5	2399.9	2498.1	2591.0	2809.9	2905.1	1014.2	2387.3
$m_{\tilde{\chi}_2^0}$	-2348.7	-2408.6	-2510.8	-2603.4	-2817.7	-2914.0	-1018.1	-2397.4
$m_{\tilde{\chi}_1^\pm}$	2342.7	2402.9	2502.2	2595.1	2812.7	2908.2	1015.9	2390.8
$m_{\tilde{\chi}_2^\pm}$	2898.6	2997.3	2997.8	3004.1	3485.6	3486.7	2896.2	2897.8
$m_{\tilde{\chi}_3^0}$	2872.5	2972.0	2971.6	2974.4	3463.0	3462.0	2872.5	2872.6
$m_{\tilde{\chi}_4^0}$	2899.0	2997.7	2998.7	3004.8	3485.9	3487.1	2896.2	2897.8
ΔM	59.6	101.0	110.9	76.7	189.7	56.6	2017.5	644.4
$BR(\tilde{\chi}_1^0 \rightarrow Z\tilde{G})$	0.55	0.55	0.71	0.56	0.55	0.55	0.56	0.55
$BR(\tilde{\chi}_1^0 \rightarrow h\tilde{G})$	0.45	0.45	0.29	0.44	0.45	0.45	0.44	0.45

- **BP1–BP6:** These represent cSUSY spectra where one has comparable branching ratio of the $\tilde{\chi}_1^0 \rightarrow h\tilde{G}$ and $\tilde{\chi}_1^0 \rightarrow Z\tilde{G}$ decay modes. The compression parameter (ΔM) which is defined as the difference between the mass of the heaviest colored sparticle (i.e., gluinos or the first and second generation squarks) and the NLSP, varies in the range $\Delta M \simeq 56 - 190$ GeV while $m_{\tilde{\chi}_1^0} \simeq 2.34 - 2.91$ TeV.
- **U1–U2:** These represent two uncompressed spectra with a lighter NLSP ($m_{\tilde{\chi}_1^0} \simeq 1.01, 2.39$ TeV) with $\Delta M \simeq 2.02, 0.64$ TeV, respectively.

With the above choice, we can have three interesting final states ($\tilde{\chi}_1^0 \tilde{\chi}_1^0 \rightarrow hh\tilde{G}\tilde{G}$, $\tilde{\chi}_1^0 \tilde{\chi}_1^0 \rightarrow ZZ\tilde{G}\tilde{G}$, $\tilde{\chi}_1^0 \tilde{\chi}_1^0 \rightarrow hZ\tilde{G}\tilde{G}$). It is governed by the benchmarks from Table 3.1 that the Higgs and the Z boson will be highly boosted and the total hadronic

activity of the decay of h/Z can be captured in a large radius jet (fat-jet of radius R). We utilize the jet substructure techniques to identify h/Z candidate by looking for the following signal topology

$$pp \rightarrow 2 \text{ CA8 Fat-jets } (J) + \text{ large } \cancel{E}_T,$$

where CA8 represents the jets clustered with Cambridge-Aachen algorithm with $R = 0.8$. The dominant SM background are $Z \rightarrow \nu\bar{\nu} + \text{jets}$, $W \rightarrow l\nu + \text{jets}$, $VV + jets$, Single-top, and $t\bar{t}$ decaying semi-leptonically where the lepton is mistagged. We have generated the cSUSY mass spectrum using `SPheno-v3.3.6`. All the events are generated using `Madgraph5 (v2.6.5)` [1] at leading order (LO) followed by `Pythia (v8)` [2] for showering and hadronization. To incorporate detector effects events are passed through `Delphes-v3.4.1` [3] We use the following observables as input to BDT network for the analysis.

- We use transverse momentum of leading $P_T(J_0)$ and sub-leading fat-jet $P_T(J_1)$. The angular distance difference between two fat-jets $\Delta R(J_0, J_1)$, missing transverse energy \cancel{E}_T , azimuthal angle difference between missing transverse energy and leading/sub-leading fat-jet $\Delta\phi(J_{0,1}, \cancel{E}_T)$, effective mass of the process $M_{eff} = \sum_{vis} |P_T| + |\cancel{E}_T|$ and the mass of leading/subleading fat-jet $M_{J_{0,1}}$
- To reveal the two-prong nature of the fat-jet, we also use the N-subjettiness ratio [4]

$$\tau_N^{(\beta)} = \frac{1}{\mathcal{N}_0} \sum_i p_{i,T} \min \left\{ \Delta R_{i1}^\beta, \Delta R_{i2}^\beta, \dots, \Delta R_{iN}^\beta \right\} \quad (3.1)$$

where, $\mathcal{N}_0 = \sum_i p_{i,T} R_0$ is the normalizing factor, R_0 is the radius parameter of the fat-jet, N is the axis of the subjet assumed within the fat-jet and i runs over the constituents of the fat-jet. We take the thrust parameter $\beta = 2$. We also use 2-prong discriminant energy correlation functions [5]

$$C_2^{(\beta)} = \frac{e_3^{(\beta)}}{(e_2^{(\beta)})^2} \quad (3.2)$$

where, $e_2^{(\beta)} = \sum_{1 \leq i < j \leq N_J} z_i z_j \theta_{ij}^\beta$ and $e_3^{(\beta)} = \sum_{1 \leq i < j < k \leq N_J} z_i z_j z_k \theta_{ij}^\beta \theta_{ik}^\beta \theta_{jk}^\beta$ are 2-point and 3-point energy correlation functions respectively.

Results from BDT analysis considering one sample benchmark point (BP1) are demonstrated in Fig. 3.1. Kolmogorov-Smirnov probability for training and testing sample is shown to confirm that the network is not overtrained. The testing data fit well to the training data and the validation is shown in Fig. 3.1 (left). The BDT is trained for each benchmark point separately. We apply the cut on BDT response and obtain the corresponding number of signal \mathcal{N}_S and background \mathcal{N}_B . The details of BDT analysis are given in [6] (Table 3.2).

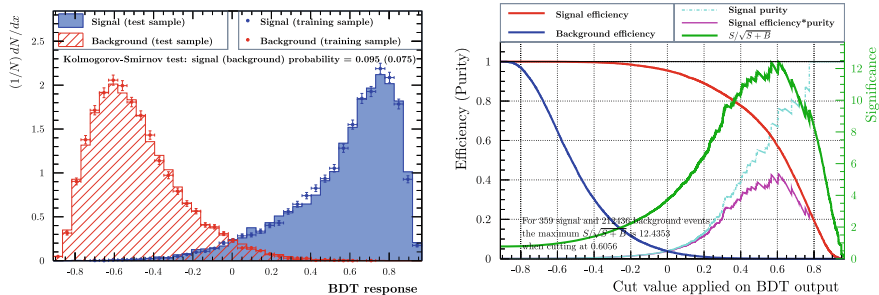


Fig. 3.1 (left) Normalized BDT response distributions for the signal and the background for the benchmark point **BP1**. right Cut efficiencies as functions of BDT cut values. All plots are evaluated for benchmark point **BP1** using integrated luminosity of 200 fb^{-1} at the 14 TeV LHC

Table 3.2 Total number of signal events and background events before and after utilizing the optimum BDT criteria BDT_{opt} for an integrated luminosity of 200 fb^{-1} at the 14 TeV LHC

BPs	\mathcal{N}_S^{bc}	BDT_{opt}	$\mathcal{N}_S(\epsilon_S)$	$\mathcal{N}_B(\epsilon_B \times 10^4)$	$\mathcal{N}_S/\sqrt{\mathcal{N}_S + \mathcal{N}_B}$	$\mathcal{L}_{(5\sigma)}^{req} \text{fb}^{-1}$
BP1	359	0.60	202 (0.56)	63 (2.9)	12.4	32.3
BP2	256	0.67	137 (0.56)	50 (2.3)	10.0	49.7
BP3	346	0.42	183 (0.52)	49 (2.3)	12.0	34.5
BP4	153	0.65	87 (0.56)	15 (0.7)	8.6	67.4
BP5	32	0.61	25 (0.78)	51 (2.4)	2.9	595.4
BP6	74	0.58	37 (0.50)	42 (1.9)	4.2	283.2
U1	266	0.57	149 (0.56)	49 (2.3)	10.6	44.4
U2	352	0.56	216 (0.61)	41 (1.9)	13.5	27.4
\mathcal{N}_{SM}	212436	—	—	—	—	

3.2 Conclusions

With no clear indication of new physics yet at the LHC, compressed mass spectrum gained significant limelight as a possible explanation for the elusive nature in the realization of new physics. We explore compressed SUSY scenario, where both colored and electro-weak new physics sectors are sitting at multi-TeV scale in the presence of a light gravitino. We exploit the characteristics of the jet substructure techniques which can lead to the discovery of the 2 fatjet + MET signal for the. One can exclude masses up to 3.2 TeV at $\mathcal{L} = 3000 \text{ fb}^{-1}$, with a 3.2σ signal significance for $\Delta M \simeq 60 \text{ GeV}$.

References

1. J. Alwall, R. Frederix, S. Frixione, V. Hirschi, F. Maltoni, O. Mattelaer, H.S. Shao, T. Stelzer, P. Torrielli, M. Zaro, The automated computation of tree-level and next-to-leading order differential cross sections, and their matching to parton shower simulations. *JHEP* **07**, 079 (2014)
2. T. Sjostrand, S. Mrenna, P.Z. Skands, PYTHIA 6.4 physics and manual. *JHEP* **05**, 026 (2006)
3. J. de Favereau, C. Delaere, P. Demin, A. Giammanco, V. Lemaître, A. Mertens, M. Selvaggi, DELPHES 3, a modular framework for fast simulation of a generic collider experiment. *JHEP* **02**, 057 (2014)
4. J. Thaler, K. Van Tilburg, Identifying boosted objects with N-subjettiness. *JHEP* **03**, 015 (2011)
5. A.J. Larkoski, I. Mould, D. Neill, Power counting to better jet observables. *JHEP* **12**, 009 (2014)
6. A. Bhardwaj, J. Dutta, P. Konar, B. Mukhopadhyaya, S.K. Rai, Boosted jet techniques for a supersymmetric scenario with gravitino LSP. *JHEP* **10**, 083 (2020)

Chapter 4

Measurement of Cross Section of $pp \rightarrow t\bar{t} + \gamma$ Process in Lepton+Jets Events at $\sqrt{s} = 13$ TeV in LHC Run 2



A. K. Das, P. K. Mal, D. Noonan, F. Yumiceva, N. Poudyal, R. Harr, L. Lechner, and R. Schoefbeck

Abstract Top quark is the heaviest known elementary particle and plays a special role in the dynamics of fundamental interactions. At the LHC the top quarks are predominantly produced through strong interactions. Here, photons can originate in the final state considering initial state and final state radiations and thus involve an additional electroweak vertex [1]. Therefore, studying the top-antitop pair ($t\bar{t}$) production in association with a photon can lead to a thorough scrutiny of the Standard Model (SM) predictions. Any deviation in the measured cross section of this process can lead to beyond standard model (BSM) physics. The results presented here are performed in events containing an well isolated, high p_T lepton (electron and muon), at least four jets from the hadronization of quarks and an isolated photon. The analysis makes use of simultaneous likelihood fits in several control regions to distinguish $t\bar{t} + \gamma$ signal from background.

(R. Schoefbeck for the CMS collaboration)

A. K. Das (✉) · P. K. Mal

School of Physical Sciences, National Institute of Science Education and Research, Jatni 752050, India

e-mail: aloke.das@niser.ac.in

Homi Bhabha National Institute, Training School Complex, Anushaktinagar, Mumbai 400094, India

D. Noonan · F. Yumiceva
Florida Tech, Melbourne, FL, USA

N. Poudyal · R. Harr
Wayne State University, Detroit, MI, USA

L. Lechner · R. Schoefbeck
Institute of High Energy Physics, Vienna, Austria

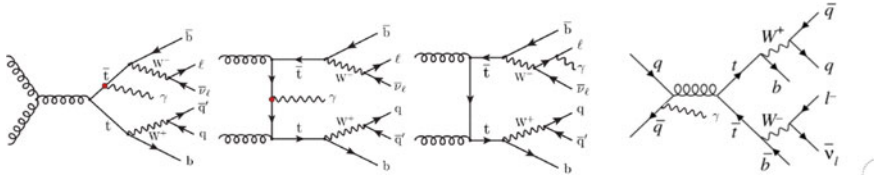


Fig. 4.1 LO Feynman diagram of $t\bar{t}\gamma$ signal process in the semileptonic final state

4.1 Introduction

This analysis uses a data sample recorded by CMS detector during LHC Run II (2016–2018) which corresponds to a total integrated luminosity of 137 fb^{-1} . During LHC Run II, a large statistics of $t\bar{t}$ events have been recorded with the CMS detectors using proton-proton collisions at $\sqrt{s} = 13 \text{ TeV}$. $t\bar{t} + \gamma$ events can get produced either from gluon-gluon fusion or quark-antiquark annihilation. In LHC gluon-gluon fusion (90%) is dominating than the quark-antiquark annihilation (10%). Depending on the decay mode of W boson coming from top, final state can be of three types, all hadronic (45.7%), dileptonic (10.5%), and semileptonic (43.8%). The analysis presented here is focused on semileptonic channel. The objective of the present analysis is to calculate inclusive cross section in the kinematic visible phase space of photon ($p_T(\gamma) \geq 20 \text{ GeV}$, $|\eta| < 1.44$). With help of $t\bar{t}$ acceptance ($A^{t\bar{t}}$) one can extract the fiducial cross section (Fig. 4.1).

$$\sigma_{t\bar{t}\gamma}^{fiducial} = \sigma_{t\bar{t}\gamma}(p_T(\gamma) \geq 20 \text{ GeV}, |\eta| < 1.44) \times A^{t\bar{t}}, \text{ Where } A^{t\bar{t}} = N_{fiducial}^{gen} / N_{\geq \gamma}^{gen}.$$

The CDF Collaboration has measured the $t\bar{t}\gamma$ production cross section using $p\bar{p}$ collisions at $\sqrt{s} = 1.96 \text{ TeV}$ [2], while at the LHC the measurements have been performed in pp collisions at $\sqrt{s} = 7 \text{ TeV}$ by the ATLAS Collaboration [3] and at $\sqrt{s} = 8 \text{ TeV}$ by both the ATLAS Collaboration [4] and CMS Collaboration [5]. In single lepton channel ATLAS Collaboration has also measured $t\bar{t}\gamma$ cross section at $\sqrt{s} = 13 \text{ TeV}$ which is $521 \pm 9 \text{ (stat.)} \pm 41 \text{ (sys.) fb}$ [6] in fiducial kinematic phase space of photon (defined as photon $p_T > 20 \text{ GeV}$ and $|\eta| < 2.37$).

4.2 Dataset and Event Simulation

CMS dataset passing single muon and single electron trigger has been used in this analysis. The $t\bar{t}\gamma$ signal events are generated with MADGRAPH5_aMC@NLO v2.6.5 [7] at leading order (LO) and the cross section is rescaled to next-to-leading-order (NLO). Background processes like single-top (s-channel), Z/W+jets, $W\gamma$, $t\gamma$, $Z\gamma$, WZ , ZZ are generated using MADGRAPH. On the other hand processes like $t\bar{t}$, single-t (t-channel), tW , $W\gamma$, QCD multijets are generated using POWHEG [8]. The event generators are interfaced with PYTHIA [9] to simulate multi-parton interactions, fragmentation, parton shower, and hadronization of partons in the initial and final states, along with the underlying event.

4.3 Analysis Strategy

4.3.1 Event Selection

All events are sorted first with some base line selections. That is, one good primary vertex, passes the triggers and one tight lepton and at least two jets. Then in our signal region we look for events with at least 4 jets, and at least one b-jet, exactly one tight lepton (e/μ), no loose lepton, and one photon. Electrons (muons) must have $p_T > 35(30)$ GeV and $|\eta| < 2.4$ and must not originate from hadron decays. Photons should satisfy the phase space criteria defined in Sect. 4.1 and should be well isolated from lepton. Jets must have $p_T > 30$ and $|\eta| < 2.4$.

4.3.2 Background Estimation

Major background events originate from misidentified electrons as photons, which are mostly from Z+jets events, while Z/W+ γ are important backgrounds. All these backgrounds are estimated using Monte Carlo (MC) events. On the other hand QCD multijet background is minor background in signal region; however it is still needed to be estimated properly as it is not well modeled and becomes more important in other control regions. Hence QCD events are estimated using data-driven techniques. Estimated normalizations for all backgrounds are giving quite good agreement. For QCD multijet normalization, separate fit for each bin of lepton p_T , $|\eta|$ split gives better Data/MC agreement (Fig. 4.2).

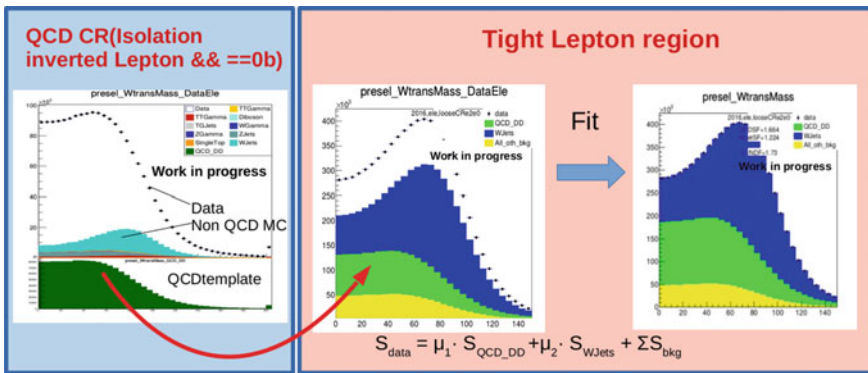


Fig. 4.2 Procedure for QCD multijet estimation: template for QCD background shapes (left); MC, data and QCD distributions before (middle) and after fit (right)

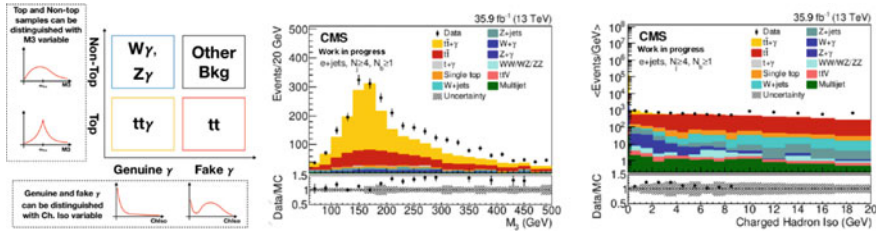


Fig. 4.3 Fitting strategy (left), and variable used in final fit, M_3 (middle) and ChIso (right) distribution in e+jets channel

4.3.3 Signal Process Cross Section Extraction

Finally using a CMS specific software tool, binned likelihood fit is done with two variables simultaneously to extract scale factor(r) on the theory of $t\bar{t}\gamma$ cross section. Where $r = (^{obs} N_{t\bar{t}\gamma} / ^{th} N_{t\bar{t}\gamma})$. Two variables are (i) M_3 which is invariant mass of three jets having highest vector summed p_T and (ii) photon charge hadron isolation (ChIso) is the sum of the transverse momentum of all charged hadrons in a cone of radius 0.4 centered around a photon. M_3 differentiates between $t\bar{t}$ and non- $t\bar{t}$ events and photon charge hadron isolation separates isolated photons from non-prompt photons (see Fig. 4.3). Systematic uncertainties having impact in the $t\bar{t}\gamma$ cross section calculation comes both from experimental and theoretical sources. The leading experimental uncertainties are related to luminosity measurement, pileup events, trigger efficiency, muon efficiency, photon efficiency, btag scale factor, electron efficiency, scale and energy resolution of the jets, etc. On the other hand the leading theoretical uncertainties originate from the Parton distribution function (PDF), initial state radiation (ISR), final state radiation (FSR), color reconnection, etc. are an example of theoretical systematic uncertainties.

4.4 Conclusion

As detailed in the previous sections, this analysis with the full RunII dataset has been established in terms of detailed background estimation and signal extraction. Control regions dominated by different physics processes (e.g., Z+jets) have been studied in detail, and good agreement between the data and SM processes has been observed. However, the final numbers on the inclusive and differential cross sections are in the process of CMS internal review and hence are not quoted here.

References

1. O. Bessidskaia Bylund et al., Probing top quark neutral couplings in the standard model effective field theory at NLO in QCD. *JHEP* **052** (2016)
2. C.D.F. Collaboration, Evidence for $t\bar{t}\gamma$ production and measurement of $\sigma_{t\bar{t}\gamma}/\sigma_{t\bar{t}}$. *Phys. Rev. D* **48**, 031104 (2011)
3. ATLAS Collaboration, Measurement of the $t\bar{t}\gamma$ production cross section in pp collisions at $\sqrt{s} = 7$ TeV. *Phys. Rev. D* **91**, 072007 (2015)
4. ATLAS Collaboration, Measurement of the semileptonic $t\bar{t}\gamma$ production cross section in pp collisions at $\sqrt{s} = 8$ TeV. *JHEP* **10**, 006 (2017)
5. CMS Collaboration, Measurement of the semileptonic $t\bar{t}\gamma$ production cross section in collisions at $\sqrt{s} = 8$ TeV. *JHEP* **10**, 006 (2017)
6. ATLAS Collaboration, Measurements of inclusive and differential fiducial cross-sections of $t\bar{t}\gamma$ production in leptonic final states at $\sqrt{s} = 13$ TeV in ATLAS. *Eur. Phys. J. C* **79**(5), 382 (2019)
7. J. Alwall et al., The automated computation of tree-level and next-to-leading order differential cross sections, and their matching to parton shower simulations. *JHEP* **07**, 079 (2014)
8. S. Frixione, P. Nason, C. Oleari, Matching NLO QCD computations with parton shower simulations: the POWHEG method. *JHEP* **11**, 070 (2007)
9. T. Sjöstrand et al., An introduction to PYTHIA 8.2. *Comput. Phys. Commun.* **191**, 159 (2015)
10. C.M.S. Collaboration, The CMS experiment at the CERN LHC. *JINST* **3**, S08004 (2008)

Chapter 5

Higgs Self-Coupling at the HL-LHC and HE-LHC



Amit Adhikary, Shankha Banerjee, Rahool Kumar Barman,
Biplob Bhattacharjee, and Saurabh Niyogi

Abstract The Higgs boson pair production has been studied in multifarious final states at the HL-LHC and HE-LHC. The optimisation for separating signal from the backgrounds are performed using cut-based and machine learning algorithms like BDT, XGBoost toolkit and DNN. The prospect of observing Higgs pair production is found to be bleak at the HL-LHC. In comparison, the HE-LHC will be sensitive for probing the Higgs boson self-coupling. We further study the consequences of modifying the Higgs boson self-coupling from its SM value.

5.1 Introduction

In the Standard Model (SM), the value of Higgs boson self-coupling is around $\lambda \sim 0.13$, which is obtained by putting the measured Higgs boson mass. But the direct measurement of this coupling is essential to verify the observed Higgs at $m_h = 125$ GeV [1, 2] is the SM Higgs boson, responsible for the electroweak symmetry breaking mechanism. Direct measurement of this coupling at the Large Hadron Collider (LHC) is possible by observing the Higgs boson pair production, which is dominantly produced via gluon fusion mechanism $gg \rightarrow hh$. The Feynman diagrams for this production are shown in Fig. 5.1. There is a negative interference between the triangle and box diagrams, which leads to a very small production rate. This makes the observation of di-Higgs production very challenging.

A. Adhikary (✉) · B. Bhattacharjee
Centre for High Energy Physics, Indian Institute of Science, Bangalore 560012, India
e-mail: amitadhikary@iisc.ac.in

S. Banerjee
CERN, Theoretical Physics Department, CH-1211, Geneva 23, Switzerland

R. K. Barman
Department of Physics, Oklahoma State University, Stillwater, OK 74078, USA

S. Niyogi
Gokhale Memorial Girls' College, Kolkata, India

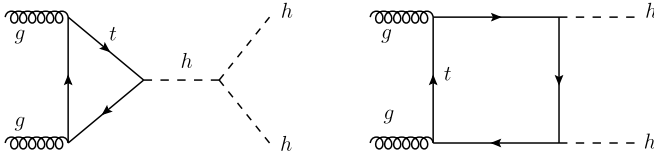


Fig. 5.1 The Feynman diagrams of Higgs pair production in gluon fusion channel, triangle diagram (left plot) and box diagram (right plot)

In this work, we study the strategy for the search of various Higgs pair production final states at the high luminosity LHC (HL-LHC) [3], which is targeted at the centre of mass energy of 14 TeV with 3 ab^{-1} of integrated luminosity and the high energy LHC (HE-LHC) [4] which is expected to operate at $\sqrt{s} = 27 \text{ TeV}$ and provide data corresponding to 15 ab^{-1} of integrated luminosity.

5.2 Analysis

We perform the analysis on various Higgs pair production final states that contain photons or leptons and have appreciable production rates. The di-Higgs signal and background processes are simulated using MG5_aMC@NLO [5], and Pythia [6] is used for showering and hadronisation. For simulating the detector effects, the events are then passed to Delphes-3.4.1 [7]. For the HL-LHC analysis, the tagging efficiency for b-jets is taken to be 70%, the mis-tag efficiency for a light jet and c-jet to be identified as a b-jet is 1% and 30% respectively. The photons in the final state can come from a fake light jet, and its rate is taken as $\sim 0.1\%$. In case of one pronged and three pronged τ 's, the tagging efficiencies are 55% and 50%, respectively. A light jet can be mistagged as a τ tagged jet, which is taken to be 0.35%.

5.2.1 At the High Luminosity LHC

We consider 11 di-Higgs final states, viz. $b\bar{b}\gamma\gamma$, $b\bar{b}\tau_h\tau_h$, $b\bar{b}\tau_h\tau_\ell$, $b\bar{b}\tau_\ell\tau_\ell$, $b\bar{b}WW^*$: $b\bar{b}lj\bar{j} + \cancel{E}_T$, $b\bar{b}l\bar{l} + \cancel{E}_T$; $WW^*\gamma\gamma$: $lj\bar{j}\gamma\gamma + \cancel{E}_T$, $ll\gamma\gamma + \cancel{E}_T$; WW^*WW^* : $2\ell 4j + \cancel{E}_T$, $3\ell 2j + \cancel{E}_T$, $4\ell + \cancel{E}_T$. We do cut-based analysis and multivariate analysis using Boosted Decision Tree (BDT) algorithm in the TMVA framework.

The $b\bar{b}\gamma\gamma$ channel is the most promising search channel, although the production rate is low because of the $h \rightarrow \gamma\gamma$ branching ratio. The dominant background comes from the QCD-QED $b\bar{b}\gamma\gamma$ process. The signal significance after the multivariate analysis is $S/\sqrt{B} = 1.76$, which improves by almost 20% as compared to the cut-based analysis with $S/\sqrt{B} = 1.46$, without any systematic uncertainty. Next, we analyse the $b\bar{b}\tau\tau$ channel. The dominant background in this channel is $t\bar{t}$. We reconstruct the τ pair mass in two kinematic variables, the visible invariant mass $m_{\tau\tau}^{\text{vis}}$ and collinear mass $M_{\tau\tau}$. The BDT analysis on $b\bar{b}\tau_h\tau_h$ with $M_{\tau\tau}$ variable yields

highest signal significance of $S/\sqrt{B} \sim 0.74$, without any systematic uncertainty. The $b\bar{b}WW^*$ channel has a higher signal rate than the previously discussed channels. This channel is dominantly contaminated by the $t\bar{t}$ background. After doing the multivariate analysis, we obtain a signal significance of 0.62 (0% systematics) from the fully leptonic channel. In case of the semi-leptonic channel, we got a reduced $S/\sqrt{B} \sim 0.13$, without any systematic uncertainty. The $\gamma\gamma WW^*$ channel has a clean final state because of the photons, but the overall rate is reduced as the branching ratio of $h \rightarrow \gamma\gamma$ is small. The $t\bar{t}h$, $h \rightarrow \gamma\gamma$ is the dominant background in this channel. After doing the BDT analysis, we got < 5 signal events at the HL-LHC. But this channel has a better S/B ratio, 0.4 and 0.11 from the fully leptonic and semi-leptonic final states, respectively, which could be important to study at higher energy colliders. Lastly, we study a new channel, $hh \rightarrow WW^*WW^*$. The overall rate becomes smaller with more leptons in the final state, whilst the channels lose cleanliness with more jets in the final state. We perform a cut-based analysis and got < 1 signal significance in all the three search final states. We combine all the di-Higgs final states by adding the signal significances in quadrature and we got a combined signal significance of $\sim 2.1\sigma$ without any systematic uncertainty. These results suggest a bleak prospect of direct Higgs pair production observation at the HL-LHC and motivate to go for a higher energy machine, which is discussed in the following section.

We also investigate the ramifications of varying the Higgs boson self-coupling from the SM value, quantified as $\kappa_\lambda = \lambda_{hhh}/\lambda_{SM}$. The BDT analysis on the $b\bar{b}\gamma\gamma$ channel with different κ_λ signal can restrict κ_λ between $[-0.63, 8.07]$. The di-Higgs signal rate is very small and leads to a very small number of events in the final state. Several new physics processes can alter these small number of di-Higgs signals and change the final result. We study these aspects in detail by considering beyond the SM (BSM) processes, giving rise to similar final states described before.

5.2.2 At the High Energy LHC

The Higgs pair production cross section at the HE-LHC increases almost three times the 14 TeV HL-LHC. This motivates us to explore several clean di-Higgs final states which are neglected because of very low production rate. We choose 7 possible Higgs pair final states, viz. $b\bar{b}\gamma\gamma$, $b\bar{b}\tau_h\tau_h$, $b\bar{b}WW^* : b\bar{b}\ell\ell + \cancel{E}_T$; $WW^*\gamma\gamma : \ell\ell\gamma\gamma + \cancel{E}_T$; $b\bar{b}ZZ^* : b\bar{b}(4e/4\mu) + \cancel{E}_T$, $b\bar{b}2e2\mu + \cancel{E}_T$; $b\bar{b}\mu\mu$. We perform three different multivariate analysis using, namely, the BDT algorithm, XGBoost toolkit and Deep Neural Network (DNN).

First, we analyse the most promising $b\bar{b}\gamma\gamma$ channel using the three machine learning techniques. XGBoost performs better than other algorithms with a final signal significance of 12.46. Upon assuming a 5% systematic uncertainty, the signal significance reduces to 5.11. We study the most sensitive $b\bar{b}\tau\tau$ where both of the τ 's decay hadronically. We use the collinear mass approximation technique to reconstruct the di- τ invariant mass. The final signal significance in this final state is 2.77, 4.78 and

4.25 from the analysis using BDT, XGBoost and DNN, respectively. In the case of $b\bar{b}WW^*$ channel, we choose the fully leptonic final state where we use several sophisticated kinematic variables, *viz.* Higgsness, Topness and Mandelstam invariant mass variable, along with the common kinematic variables. The XGBoost technique yields a higher signal significance of ~ 2.75 with zero systematic uncertainty. Similarly, we perform our analysis on the $WW^*\gamma\gamma$ channel by choosing the fully leptonic final state. The signal significance in this channel is 1.64 and 2.05 from the analysis done using the BDT and XGBoost technique, respectively. The $b\bar{b}ZZ^*$ channel is divided in two parts, $b\bar{b}(4e/4\mu)$ and $b\bar{b}e^+e^-\mu^+\mu^-$ final states. We select the Higgs boson mass region, $120 \text{ GeV} < m_{4e/4\mu/2e2\mu} < 130 \text{ GeV}$. The dominant background contribution in this channel comes from the $t\bar{t}h$ production. A combined S/\sqrt{B} of 1.3 is obtained by doing a XGBoost analysis on the two final states. Finally, we investigate the $b\bar{b}\mu\mu$ channel, which has the disadvantage of having very low signal rate as the $h \rightarrow \mu\mu$ branching ratio is small. Another difficulty in this channel is the large background contamination from $t\bar{t}$ and QCD-QED production of $b\bar{b}\mu\mu$ processes. We got a < 1 signal significance in this channel from the BDT and XGBoost analysis.

5.3 Conclusion and Outlook

We have explored the future upgraded LHC's potential in observing the Higgs self-coupling via pair production of Higgs boson. We adopt the standard cut-based and more sophisticated multivariate analysis for signal and background separation. At the HL-LHC, the $b\bar{b}\gamma\gamma$ final state gives a maximum signal significance of 1.76 after doing the BDT analysis. If we combine all the final states, the signal significance reaches up to ~ 2.1 without any systematics. At the HE-LHC, the $b\bar{b}\gamma\gamma$ channel alone yields a discovery prospect with signal significance $> 10\sigma$ ($\sim 5\sigma$) without (with 5%) systematic uncertainty, after doing a multivariate analysis with XGBoost toolkit. The other search channels also have a better prospect at the HE-LHC. We further study the change in the kinematics upon any modification in the Higgs boson self-coupling. Our study suggests that the HE-LHC will be sensitive in the entire considered range $\kappa_\lambda = [-2, 4]$ for the direct production of Higgs boson pair. Here, the κ_λ range is asymmetric because the di-Higgs production rate increases rapidly for negative κ_λ than positive values.

References

1. G. Aad et al., [ATLAS], Observation of a new particle in the search for the Standard Model Higgs boson with the ATLAS detector at the LHC. *Phys. Lett. B* **716**, 1–29 (2012)
2. S. Chatrchyan et al., [CMS], Observation of a New Boson at a Mass of 125 GeV with the CMS Experiment at the LHC. *Phys. Lett. B* **716**, 30–61 (2012)

3. A. Adhikary, S. Banerjee, R.K. Barman, B. Bhattacharjee, S. Niyogi, Revisiting the non-resonant Higgs pair production at the HL-LHC. *JHEP* **07**, 116 (2018)
4. A. Adhikary, R.K. Barman, B. Bhattacharjee, Prospects of non-resonant di-Higgs searches and Higgs boson self-coupling measurement at the HE-LHC using machine learning techniques. *JHEP* **12**, 179 (2020)
5. J. Alwall et al., The automated computation of tree-level and next-to-leading order differential cross sections, and their matching to parton shower simulations. *JHEP* **07**, 079 (2014)
6. T. Sjöstrand et al., An introduction to PYTHIA 8.2. *Comput. Phys. Commun.* **191**, 159–177 (2015)
7. J. de Favereau et al. [DELPHES 3], DELPHES 3, A modular framework for fast simulation of a generic collider experiment. *JHEP* **02**, 057 (2014)

Chapter 6

Measurement of Strong-Phase Difference Between D^0 and $\bar{D}^0 \rightarrow K_{S/L}^0 \pi^+ \pi^-$ and the Role of Model-Dependent Inputs at BESIII



Anita

Abstract The strong-phase difference $\Delta\delta_D$ – between D^0 and \bar{D}^0 decays to a common final state – is a crucial input to the measurement of the weak phase γ of the CKM ($b - d$) unitarity triangle extracted from $B^- \rightarrow DK^-$ decay, where D is a D^0 or \bar{D}^0 meson decaying to the same final state. With the largest quantum-correlated dataset of $D^0\bar{D}^0$ pairs produced at the $\psi(3770)$ resonance, corresponding to an integrated luminosity of 2.93 fb^{-1} , BESIII will reduce the systematic uncertainty on γ coming from $\Delta\delta_D$. Model-independent, as well as model-dependent studies, are required to best constrain the strong-phase difference parameters. This paper reviews the strong-phase measurements reported by BESIII and presents simulation studies of $D^0 \rightarrow K_{S/L}^0 \pi^+ \pi^-$ amplitude models with the BESIII $D^0\bar{D}^0$ dataset.

6.1 Introduction

Precise measurement of the Cabibbo-Kobayashi-Maskawa (CKM) $b - d$ unitarity triangle angles, α , β , and γ (or ϕ_2 , ϕ_1 , and ϕ_3) is of utmost interest in the field of particle physics. These angles are directly linked to the weakly broken \mathcal{CP} symmetry in quark weak interactions as prescribed by the Standard Model (SM) and therefore provide an opportunity to test *new physics* beyond the SM. The angle ϕ_3 is typically measured from the interference between theoretically clean $b \rightarrow c\bar{u}s$ and $b \rightarrow u\bar{c}s$ tree-level transitions [1], which can result in a D^0 and \bar{D}^0 decaying to identical multibody final states.

The strong-phase difference between these D^0 and \bar{D}^0 decays, denoted by $\Delta\delta_D$, is a source of systematic uncertainty in ϕ_3 measurement. Quantum-correlated charm-factory data with negligible background and clean D^0/\bar{D}^0 tagging topology is used

Anita for the BESIII collaboration

Anita (✉)

Indian Institute of Technology Madras, Chennai, India
e-mail: anitalavania@physics.iitm.ac.in

to precisely measure $\Delta\delta_D$. In multibody final states such as $K_{S/L}^0\pi^+\pi^-$, $\Delta\delta_D$ is a function of position in the allowed 2D phase space, also known as the *Dalitz – plot* (DP), parametrized by the squared invariant mass of $K_{S/L}^0\pi^+$ and $K_{S/L}^0\pi^-$, denoted here by m_+^2 and m_-^2 respectively. Therefore, for a model-independent measurement, a binned DP analysis is employed wherein the available phase space is divided into regions or bins of minimum $\Delta\delta_D$ variation. The observables in this analysis are amplitude-weighted average cosines and sines of $\Delta\delta_D$ over each of these bins:

$$c_i^{(\prime)}[s_i^{(\prime)}] = \frac{\int_i |A_D^{(\prime)}(m_+^2, m_-^2)| |A_{\bar{D}}^{(\prime)}(m_-^2, m_+^2)| \cos[\sin]\{\Delta\delta_D^{(\prime)}(m_+^2, m_-^2)\} dm_+^2 dm_-^2}{\sqrt{\int_i |A_D^{(\prime)}(m_+^2, m_-^2)|^2 dm_+^2 dm_-^2 \int_i |A_{\bar{D}}^{(\prime)}(m_-^2, m_+^2)|^2 dm_+^2 dm_-^2}},$$

where A_D and $A_{\bar{D}}$ are the decay amplitudes of D^0 and \bar{D}^0 to $K_S^0\pi^+\pi^-$, respectively, and the primed parameters everywhere in this paper correspond to $K_L^0\pi^+\pi^-$ signal mode, unless stated otherwise.

6.2 Formalism and Analyses

Quantum-correlated $D^0\bar{D}^0$ pairs produced at threshold, decaying to specific *tag* modes are exploited to constrain c_i and s_i . Tags are final states that can indirectly determine the flavor or CP state of the parent D meson of the signal $K_{S/L}^0\pi^+\pi^-$ decay. For example, $K^+\pi^-(K^-\pi^+)$ on the tag-side fixes the signal decay channel as $D^0(\bar{D}^0) \rightarrow K_{S/L}^0\pi^+\pi^-$, up to a small correction for doubly Cabibbo-suppressed decays.

6.2.1 Model-Independent Analysis

The expected yield of the signal $K_{S(L)}^0\pi^+\pi^-$ decay with a tag-side final state of known CP content (\mathcal{F}_{CP}), in the i th bin of DP is given by

$$\langle M_i^{(\prime)} \rangle = h_{CP}^{(\prime)} \left(K_i^{(\prime)} - (2\mathcal{F}_{CP} - 1) 2c_i^{(\prime)} \sqrt{K_i^{(\prime)} K_{-i}^{(\prime)} + K_{-i}^{(\prime)}} \right), \quad (6.1)$$

and the expected yield of a decay channel of type $K_S^0\pi^+\pi^-$ versus $K_{S(L)}^0\pi^+\pi^-$ in the i th bin of tag-side and j th bin of signal-side DP is given by

$$\langle M_{ij}^{(\prime)} \rangle = h_{corr}^{(\prime)} \left[K_i K_{-j}^{(\prime)} + K_{-i} K_j^{(\prime)} - 2\sqrt{K_i K_{-j}^{(\prime)} K_{-i} K_j^{(\prime)}} (c_i c_j^{(\prime)} + s_i s_j^{(\prime)}) \right], \quad (6.2)$$

Table 6.1 Tag modes with respective observed yields [2]

Tag type	Modes	$K_S^0\pi^+\pi^-$ signal	$K_L^0\pi^+\pi^-$ signal
Flavor	$K^+\pi^-, K^+\pi^-\pi^0, K^+\pi^-\pi^+\pi^-, K^+e^-\nu_e$	23457 ± 319	40642 ± 423
CP -even	$K^+K^-, \pi^+\pi^-, K_S^0\pi^0\pi^0, \pi^+\pi^-\pi^0, K_L^0\pi^0$	2528 ± 124	5003 ± 178
CP -odd	$K_S^0\pi^0, K_S^0\eta, K_S^0\eta', K_S^0\omega, K_L^0\pi^0\pi^0$	1725 ± 106	1485 ± 117
Mixed CP	$K_S^0\pi^+\pi^-$	1833 ± 82	3438 ± 72

where $K_{i/j}^{(\prime)}$ is the observed flavor-tagged yield in the i/j th bin of the $K_{S(L)}^0\pi^+\pi^-$ DP. Inclusion of $K_L^0\pi^+\pi^-$ signal mode in addition to $K_S^0\pi^+\pi^-$ provides a more than three-fold increase in the statistics. The tag modes used in this analysis [2] along with the total observed double-tagged yields are summarized in Table 6.1.

6.2.1.1 Fit Procedure and Results

To determine the values of $c_i^{(\prime)}$ and $s_i^{(\prime)}$, a log-likelihood fit is performed and the total likelihood function is given by

$$\begin{aligned}
 -2 \log \mathcal{L} = & -2 \sum_{i=1}^8 \ln P(N_i^{\text{obs}}, \langle N_i^{\text{exp}} \rangle)_{CP, K_S^0\pi\pi} - 2 \sum_{i=1}^8 \ln P(N_i^{\text{obs}}, \langle N_i^{\text{exp}} \rangle)_{CP, K_L^0\pi\pi} \\
 & -2 \sum_{n=1}^{72} \ln P(N_n^{\text{obs}}, \langle N_n^{\text{exp}} \rangle)_{K_S^0\pi\pi, K_S^0\pi\pi} - 2 \sum_{n=1}^{128} \ln P(N_n^{\text{obs}'}, \langle N_n^{\text{exp}} \rangle)_{K_L^0\pi\pi, K_S^0\pi\pi} + \chi^2.
 \end{aligned}$$

where $P(N_i^{\text{obs}}, \langle N_i^{\text{exp}} \rangle)$ are *Poisson* PDFs with observed bin-wise yields N_i^{obs} as variables and the mean expectation $\langle N_i^{\text{exp}} \rangle$ from (6.1) and (6.2). A χ^2 term is introduced, primarily to improve precision on $s_i^{(\prime)}$ values by constraining the measured differences $\{c_i' - c_i, s_i' - s_i\}$ to the predicted differences from an amplitude model $\{\Delta c_i, \Delta s_i\}$ (Sect. 2.2):

$$\chi^2 = \sum_i \left(\frac{c_i' - c_i - \Delta c_i}{\delta \Delta c_i} \right)^2 + \sum_i \left(\frac{s_i' - s_i - \Delta s_i}{\delta \Delta s_i} \right)^2, \quad (6.3)$$

where $\delta \Delta c_i$ and $\delta \Delta s_i$ are the conservative model-dependent uncertainties on the predicted differences.

Figure 6.1 shows the results obtained from this analysis and draws comparisons with previous CLEO results [3] and model-predicted values [4]. Better precision is achieved not only because of the three times larger dataset available at BESIII as

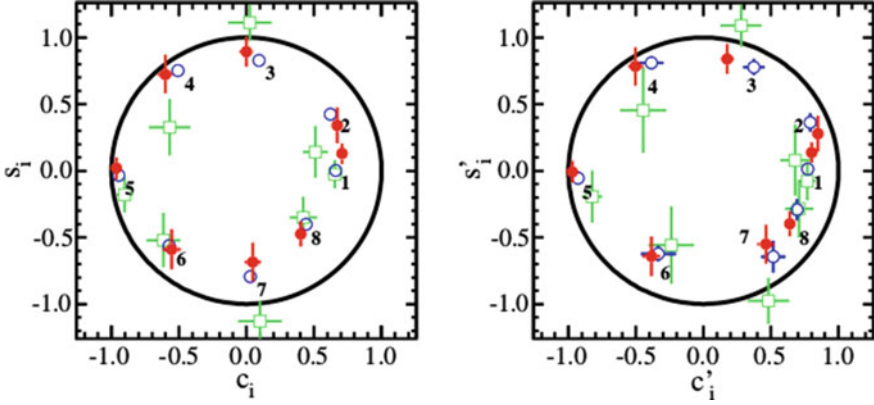


Fig. 6.1 Comparison of model-predicted (blue), CLEO measured (green) $c_i^{(l)}$, $s_i^{(l)}$ values with the results from this analysis (red), for “equal $\Delta\delta_D$ binning” [2]

compared to CLEO but also because of the additional tag modes such as $\pi^+\pi^-\pi^0$, and partial reconstruction techniques used in this analysis [2].

6.2.2 Model-Dependent Analysis

The amplitude of a three-body decay can be described in terms of a series of intermediate two-body resonant decays, often referred to as *isobars*. An amplitude model for the decay $D^0 \rightarrow K_L^0\pi^+\pi^-$, however closely related to the well tested $D^0 \rightarrow K_S^0\pi^+\pi^-$ decay model, exhibits *U – spin symmetry breaking* features resulting from a phase-flip in the amplitude when the decay proceeds through a DCS intermediate state [5]:

$$A(D^0 \rightarrow K_{S(L)}^0\pi^+\pi^-) = A_{\bar{K}^0\pi\pi}^{CF} + (-) A_{K^0\pi\pi}^{DCS} + A_{K_{S(L)}^0\pi\pi}^{CP}. \quad (6.4)$$

As a result, the *CP* amplitudes gain a relative factor of $(1 - 2 \tan^2 \theta_C \times \hat{\rho}_{(D^0 \rightarrow K^0 f_{CP}^k)})$,

$$\frac{A_{K_L^0\pi\pi}^{CP}}{A_{K_S^0\pi\pi}^{CP}} = \frac{1 - \tan^2 \theta_C \hat{\rho}_k}{1 + \tan^2 \theta_C \hat{\rho}_k} = (1 - 2 \tan^2 \theta_C r_k e^{i\delta_k}), \quad (6.5)$$

where θ_C is the Cabibbo angle and we call $\hat{\rho}_k (= r_k e^{i\delta_k})$ the *U – spin* breaking parameter for a *CP*–resonant structure k . The predicted values of Δc_i and Δs_i and the uncertainties on them in (6.3) are obtained from an *assumed* $K_L^0\pi^+\pi^-$ amplitude model where $\hat{\rho}_k$ are assumed to be equal to unity and the uncertainties are randomly generated [2].

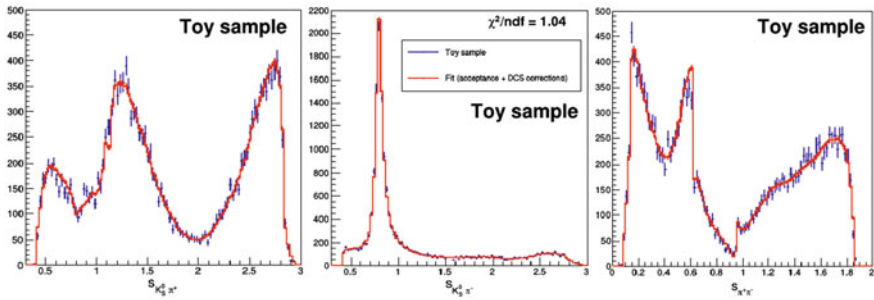


Fig. 6.2 Amplitude fit on a $K_S^0\pi^+\pi^-$ toy sample

Using the $D^0 \rightarrow K_S^0\pi^+\pi^-$ amplitude model described in [4] as the baseline model, we first reproduce the same results with simulated data and subsequently fit a $D^0 \rightarrow K_L^0\pi^+\pi^-$ amplitude model with necessary modifications as suggested in (6.4) and (6.5). Figure 6.2 shows a fit, with a $\chi^2/ndf = 4485.5/4313 = 1.04$, over the projections of the 2D $K_S^0\pi^+\pi^-$ phase space, on a toy data sample consisting of 22000 events, generated from the model described in [4] and fitted back with the same set of resonances.

6.3 Summary

These proceedings present the most precise model-independent strong-phase measurement for the decays $D^0 \rightarrow K_{S/L}^0\pi^+\pi^-$ ensuring lower systematic uncertainty on the measurement of the weak-phase γ by LHCb and BelleII, and propose an independent amplitude model for the statistically dominating mode $D^0 \rightarrow K_L^0\pi^+\pi^-$.

References

1. A. Giri, Y. Grossman, A. Soffer, J. Zupan, Phys. Rev. D **68**, 054018 (2003)
2. M. Ablikim et al., BESIII collaboration. Phys. Rev. D **101**, 112002 (2020)
3. J. Libby et al., CLEO collaboration. Phys. Rev. D **82**, 112006 (2010)
4. I. Adachi et al., BaBar and Belle collaboration. Phys. Rev. D **98**, 112012 (2018)
5. I. Bigi, H. Yamamoto, Phys. Lett. B **349** (1995)

Chapter 7

Light Singlino Dark Matter at the LHC



A. Roy and Monoranjan Guchait

Abstract The light singlino-like neutralino is expected to be a promising candidate for dark matter(DM) in the allowed parameter space of the next-to-minimal supersymmetric standard model(NMSSM). The DM annihilation process takes place via the light Higgs bosons which are natural in this model. Identifying the allowed region of parameter space including various constraints, we present here, the detection prospect of such light DM candidate and Higgs bosons at the LHC. It is found that the range of Higgs bosons and neutralino masses compatible with a low mass DM solution can be discovered at the LHC with the center of mass energy $\sqrt{s} = 14\text{TeV}$ with a reasonable signal significance ($\sim 5\sigma$) corresponding to integrated luminosity options $\mathcal{L} = 300$ and 3000 fb^{-1} .

7.1 Introduction

Light (\sim few GeV) dark matter (DM) particle is still very much allowed even in the presence of stringent constraints on DM particle masses from the direct detection (DD) experiments, in particular, XENON1T [1]. Though the lightest neutralino of minimal supersymmetric standard model(MSSM) offers a popular DM candidate, considering DM as a thermal relic, the relic density condition ($\Omega h^2 = 0.12 \pm 0.001$ [2]) rules out the possibility of having any DM candidate of low mass ($\lesssim 30$ GeV) in MSSM [3]. But it is found that, in the theory of next-to-minimal supersymmetric standard model(NMSSM), the singlino-like neutralino, even with mass \sim few GeV, appears to be a viable dark matter candidate consistent with all experimental limits [4]. The presence of light singlet-like Higgs bosons in this model play important role in achieving the relic density. In this presentation, we briefly revisit the singlino-like neutralino scenario in the NMSSM and report the detection prospect of this light DM and light Higgs bosons. These light Higgs bosons and the singlino-like DM candidate can be indirectly produced at the LHC through

A. Roy (✉) · M. Guchait

Department of High Energy Physics, Tata Institute of Fundamental Research, Mumbai, India
e-mail: arnab.roy@tifr.res.in

production of SM Higgs boson and its subsequent decays. Considering a plausible final state (to be discussed later) detail signal and SM background simulation was performed and signal sensitivity was presented for 300 and 3000 fb⁻¹ luminosity options.

7.2 The NMSSM Model and Dark Matter Relic Density

The NMSSM contains an additional gauge singlet superfield(S) along with two Higgs doublet superfields (H_u and H_d) of MSSM. So the Higgs sector of NMSSM gets enlarged consisting of seven physical Higgs bosons, 3 CP even (H_1, H_2, H_3) and 2 CP odd (A_1, A_2) and 2 charged Higgs (H^\pm) boson states. The Higgs sector and the corresponding masses and composition of physical states are governed by six parameters [5]:

$$\lambda, \kappa, A_\lambda, A_\kappa, \tan \beta, \mu_{\text{eff}}. \quad (7.1)$$

where λ and κ are dimensionless couplings; A_λ, A_κ are related to soft terms and $\mu_{\text{eff}} = \lambda v_s$, where v_s is the vacuum expectation value (VEV) acquired by the S.

On the other hand, the fermionic superpartner (\tilde{S}) of the singlet field mixes with Higgsinos extending the neutralino mass matrix to 5×5 and giving rise to 5 neutralino states. The masses and couplings of neutralinos are sensitive to NMSSM specific parameters, in particular, λ, κ and μ_{eff} , along with M_1 and M_2 [6].

In our proposed solution, DM annihilation takes place via s-channel mediated by light Higgs bosons ($\chi\chi \xrightarrow{H_1/A_1} \bar{f}f$), and the right relic density corresponding to the lower range (~ 20 GeV) of DM masses can be achieved by requiring $\tilde{\chi}_1^0$ and light Higgs boson states singlino and singlet dominated respectively. The significant presence of singlino component in the lightest neutralino helps to evade constraints on DM-nucleon scattering cross-section imposed by several experiments. It turns out that the preferred parameter space favoring our scenario should provide, (a) a light singlino-like LSP, (b) light singlet-like Higgs boson states. To meet these criteria, it has been shown in [4] using the relevant couplings and mass matrices in the neutralino and Higgs sector, that

- light singlino-like LSP requires very small $|\kappa|v_s$, with $\kappa/\lambda \sim 10^{-2}$,
- requirement of light Higgs boson states to be singlet-like leads A_λ to be very large (few TeV), but A_κ not necessarily to be very large, but with a relative sign opposite to κ .

Performing a numerical scan it is observed that for a favored range of parameters, such as $\lambda, \kappa, A_\lambda$ and A_κ , as mentioned above, the BR ($H_{\text{SM}} \rightarrow H_1 H_1 / A_1 A_1$) $\sim 10\%$ or less. Whereas the BR ($H_1 / A_1 \rightarrow \tilde{\chi}_1^0 \tilde{\chi}_1^0$) appears to be quite reasonable, and often turns out to be around $\sim 70\text{--}80\%$ [4].

7.3 Signal and Background

To explore the detection prospect, the DM is considered to be indirectly produced through the production of light singlet-like Higgs bosons via the non-standard decay channel of the SM Higgs boson, $H_{\text{SM}} \rightarrow H_1 H_1 / A_1 A_1$, where $m_{H_{\text{SM}}} > 2m_{H_1/A_1}$. Considering the branching fraction features of this scenario the signal process to our interest appears to be

$$\begin{aligned} gg \rightarrow H_{\text{SM}} + \text{jet} &\rightarrow H_1 H_1 / A_1 A_1 + \text{jet} \\ &\rightarrow b\bar{b} \text{ or } \tau\tau + \tilde{\chi}_1^0 \tilde{\chi}_1^0 + \text{jet} \end{aligned} \quad (7.2)$$

Since the separation between final state visible particles depends mainly on the mass of the light Higgs boson (as $\Delta R(f, \bar{f}) \simeq \frac{m_{H_1/A_1}}{2p_T}$, see [7]), the simulation is performed for the signal setting three ranges of the mass of H_1 or A_1 , as (i) lower mass region: $m_{H_1/A_1} \leq 10$ GeV, (ii) moderate mass region: $10 \text{ GeV} \leq m_{H_1/A_1} \leq 30$ GeV, and (iii) higher mass region: $30 \text{ GeV} \leq m_{H_1/A_1} \leq 60$ GeV.

Instead of tagging individual b-jet or τ -jet, which is challenging in this present scenario, ‘Higgs jet’ is tagged using jet substructure technique [7] to classify signal from the background. Hence, for the moderate and high mass region, the signal events are selected as

$$J_{b\bar{b}} + \cancel{E}_T + \geq 1 \text{ j for } 10 \text{ GeV} \leq m_{J_{b\bar{b}}} \leq 30 \text{ GeV} , \quad (7.3)$$

$$J_{b\bar{b}} + \cancel{E}_T + \geq 1 \text{ j for } 30 \text{ GeV} \leq m_{J_{b\bar{b}}} \leq 60 \text{ GeV} . \quad (7.4)$$

For the low mass region, where the $\tau\tau$ decay of H_1/A_1 is enhanced, leptonic decay of the τ is considered to avoid huge QCD background. In this case, we focus on the following final state,

$$\ell^+ \ell^- + \cancel{E}_T + \geq 1 \text{ jet.} \quad (7.5)$$

Several kinematic variables (e.g., transverse mass between $J_{b\bar{b}}$ and \cancel{E}_T , $m_{J_{b\bar{b}}}$ etc.) are constructed and a detailed cut-based analysis is performed to get the final sensitivities of signal events corresponding to different benchmark points (BP) in the aforementioned three mass regions as shown in Table 7.1, for 300 and 3000 fb^{-1} luminosity options. Remarkably, the significances are more than 5σ for almost all BPs [4].

7.4 Summary

In this study, we explore the scenario with a light DM candidate in the framework of the NMSSM, where the singlino-like lightest neutralino, assumed to be a LSP, is offered as the DM candidate. In this proposed scenario, the DM annihilation takes

Table 7.1 Signal significances of BPs in three ranges of the mass of H_1 or A_1

	Low mass	Moderate mass			High mass	
	BP1	BP2	BP3	BP4	BP5	BP6
$\frac{S}{\sqrt{B}} (\mathcal{L} = 300 \text{ fb}^{-1})$	6	11	14	8	7	3.5
$\frac{S}{\sqrt{B}} (\mathcal{L} = 3000 \text{ fb}^{-1})$	19	35	44	25	22	11

place primarily via resonant process mediated by singlet-like light Higgs bosons which play a role as a portal between the non-SM and the SM sectors. This naive numerical study indicates that the NMSSM parameters of our interest are of the range, $\kappa \sim 10^{-3} - 10^{-2}$, $\lambda \sim 0.1 - 0.3$, $|A_\kappa| \sim 10 - 100 \text{ GeV}$ and $A_\lambda \gtrsim 800 \text{ GeV}$, which are very close to our speculation based on analytical arguments. Interestingly, the DM particles can be indirectly produced from decay of SM Higgs bosons. Performing a detailed simulation of the signal final states and possible backgrounds, we found that, the DM and the light Higgs bosons can be probed at the LHC with a reasonable signal significance $\sim 5\sigma$, at the center of mass energy $\sqrt{s} = 14 \text{ TeV}$ and integrated luminosity options 300 and 3000 fb^{-1} .

References

1. XENON Collaboration, E. Aprile et al., Dark matter search results from a one ton-year exposure of XENON1T. *Phys. Rev. Lett.* **121**(11), 111302 (2018). [arXiv:1805.12562](https://arxiv.org/abs/1805.12562) [astro-ph.CO]
2. Planck Collaboration, N. Aghanim et al., Planck 2018 results. VI. Cosmological parameters. [arXiv:1807.06209](https://arxiv.org/abs/1807.06209) [astro-ph.CO]
3. R.K. Barman, G. Belanger, B. Bhattacharjee, R. Godbole, G. Mendiratta, D. Sengupta, Invisible decay of the Higgs boson in the context of a thermal and nonthermal relic in MSSM. *Phys. Rev. D* **95**(9), 095018 (2017). ([arXiv:1703.03838](https://arxiv.org/abs/1703.03838) [hep-ph])
4. M. Guchait, A. Roy, Light singlino dark matter at the LHC. *Phys. Rev. D* **102**(7), 075023 (2020). ([arXiv:2005.05190](https://arxiv.org/abs/2005.05190) [hep-ph])
5. D.J. Miller, R. Nevzorov, P.M. Zerwas, The Higgs sector of the next-to-minimal supersymmetric standard model. *Nucl. Phys. B* **681**, 3–30 (2004). [arXiv:hep-ph/0304049](https://arxiv.org/abs/hep-ph/0304049) [hep-ph]
6. G. Belanger, F. Boudjema, C. Hugonie, A. Pukhov, A. Semenov, Relic density of dark matter in the NMSSM. *JCAP* **0509**, 001 (2005). ([arXiv:hep-ph/0505142](https://arxiv.org/abs/hep-ph/0505142) [hep-ph])
7. J.M. Butterworth, A.R. Davison, M. Rubin, G.P. Salam, Jet substructure as a new Higgs search channel at the LHC. *Phys. Rev. Lett.* **100**, 242001 (2008). ([arXiv:0802.2470](https://arxiv.org/abs/0802.2470) [hep-ph])

Chapter 8

Jets and Jet Substructure—A Mini Review



Arun Thalapillil

Abstract I briefly review some of the ideas behind jet finding strategies at colliders and extracting substructure information from them. The latter, over the past many years, have enabled us to extract crucial information in particle collisions and in characterizing potentially interesting events. Jet substructure techniques, often in tandem with newer approaches, remain at the forefront of our search for beyond Standard Model phenomena. I present a terse and subjective selection of topics, related to recent progress.

8.1 Introduction

In collider events where QCD interactions are relevant, the final states manifest as hadrons, rather than quarks or gluons, owing to confinement. These hadrons evolving from a particular parton form collimated objects called jets. A way to define and study such objects is therefore crucial.

The first jet algorithm was introduced in the context of e^+e^- collider events with hadrons. An event was said to have two jets if $(1 - \epsilon)$ fraction of the total energy was confined in two cones of half-angle δ [1]. This original definition is an example of a cone algorithm and provides a geometrically intuitive way to think about jets. The jet definitions and algorithms have evolved much since then [2], driven by higher jet multiplicity events whilst also being cognisant of infrared and collinear safety [3]. An example of a high multiplicity event, observed at the LHC, with multiple jets [4] illustrated, is shown in Fig. 8.1.

A class of jet algorithms that has come to prominence today are the sequential jet algorithms. In their iterations, there are two relevant metrics

A. Thalapillil (✉)
Indian Institute of Science Education and Research, Pune, India
e-mail: thalapillil@iiserpune.ac.in

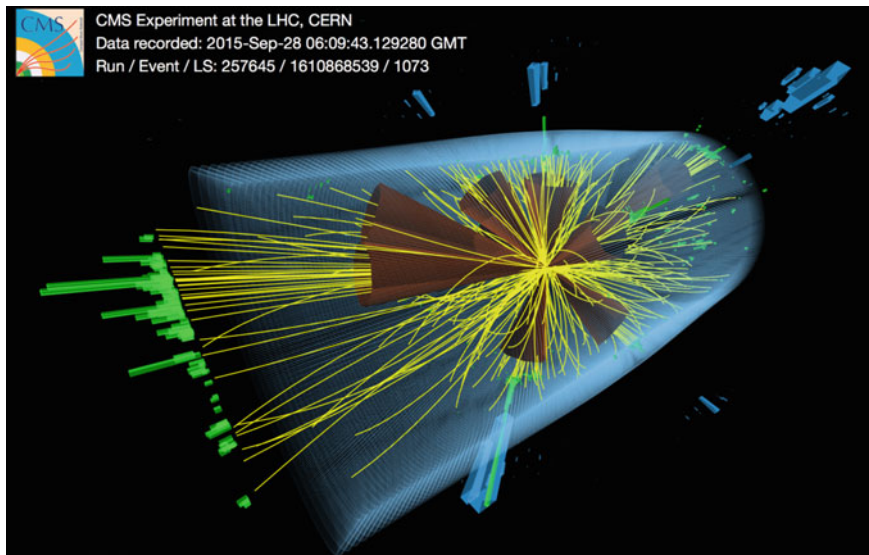


Fig. 8.1 An example of a multi-jet collision event recorded at the LHC by the CMS collaboration [4] (Image source: CMS Collaboration and Mc Cauley, Thomas, CERN)

$$\begin{aligned}\rho_{ij} &= \min\{p_{T,i}^{2k}, p_{T,j}^{2k}\} \frac{\Delta R_{ij}^2}{R^2} \\ \rho_i &= p_{T,i}^{2k}\end{aligned}\tag{8.1}$$

computed for a set of vectors (labeled i, j above) at each step. R acts as a cut-off and k is a parameter. If in a given step of the iteration the minimum is a ρ_{ab} (where a and b denote the specific pair of vectors for which it is the minimum), the two objects are combined, whilst if it is a ρ_a (where again a denotes the specific vector for which it is a minimum) it is declared as a jet and removed from further iterations. This process is then repeated for the new set of objects, and the iteration repeated until all objects have been declared as jets. This way of defining a sequential jet algorithm is sometimes called an inclusive algorithm. Depending on the value of the parameter k , the sequential algorithms go by various names—Cambridge-Aachen ($k = 0$), anti- k_T ($k = -1$) and k_T ($k = 1$) algorithms.

8.2 Jet Shapes and Substructure

Jet shapes try to characterize jets by some intrinsic characteristic they possess, for instance jet-mass. The basic idea may be traced back to attempts to understand the nature of full events by defining event shape variables, for instance, to characterize how broad or pencil-like an event was. To cite a few examples—some of the jet

shapes occasionally employed are jet-mass, jet broadening (denoted by B_H , for a given thrust axis \hat{n} and partitioning particles into hemisphere H)

$$B_H = \frac{1}{\sum_{b \in H} |\mathbf{p}_b|} \sum_{a \in H} |\mathbf{p}_a \times \hat{n}|, \quad (8.2)$$

N -subjettiness [5] (indicated by τ_N , for suitably defined N subjet axes for a jet J)

$$\tau_N = \frac{1}{\sum_{i \in J} p_{T,i} R} \sum_{i \in J} p_{T,i} \min\{\Delta R_{i1}, \Delta R_{i2}, \dots, \Delta R_{iN}\}, \quad (8.3)$$

and jet angularities (labelled A_J^k , for a jet J with k as a parameter) [6, 7]

$$A_J^k = \frac{1}{2E_J} \sum_{a \in J} p_{T,a} e^{(k-1)\eta_a}. \quad (8.4)$$

In above, η_a is the rapidity separation of component a with respect to the jet axis.

These and other associated jet shapes and substructure variables have found extensive applications over the past many years. They have helped enhance signal sensitivities as well as tag interesting objects in hadron collider environments [8].

8.3 New Techniques and Applications

Many of the most recent advancements have come from applications of jet substructure techniques, broadly defined, in tandem with modern machine learning paradigms. The latter has informed and enhanced pile-up mitigation methods and tagging strategies, for instance.

A broad class of strategies have leveraged jet images. The basic idea is to treat calorimetric energy deposits, sometimes with suitable distinction of particle types, as images. These images are then processed by leveraging sophisticated image recognition algorithms. Deep convolutional neural networks are particularly suited for this.

An avenue where the above paradigm has been used very effectively, for instance, is in the discrimination of quark and gluon initiated jets. In a seminal study toward such an application [9] three input “color” channels to the convolutional neural network were taken as the transverse momenta of charged particles, transverse momenta of neutral particles, and charged particle multiplicity. The locality of the energy deposit is maintained by constructing a two-dimensional image (in pseudo-rapidity and azimuthal angle). Remarkably, even without any underlying physics input regarding differences between quark and gluon induced jets, the architecture is found to perform much better than physically motivated discriminants [9].

Another application where a similar paradigm has yielded non-trivial results is in pile-up mitigation. In hadron colliders, since the protons are grouped into bunches,

along with the leading-vertex hard proton collision there is inevitably a multiplicity of soft proton collisions. This constitutes pile-up and it is crucial for it to be removed before constructing jet observables. As the luminosity increases, keeping bunch spacing constant, the pile-up will drastically and becomes more challenging for conventional pile-up subtraction techniques to tackle. Using a three-channel input for the images in a convolutional neural network—with transverse momenta of all neutral particles, transverse momenta of charged particles from pile-up and transverse momenta of leading-vertex charged particles—it has been shown that one may obtain spectacular control over pile-up contributions [10].

Other areas where machine learning assisted approaches have shown efficacy are in identifying electrons relative to jet backgrounds [11], generalizations of N-subjettiness [12] and jet tagging [13].

8.4 Summary

Jet shape and substructure methods, broadly defined, in consort with newer, more sophisticated paradigms coming from deep learning remain a powerful tool in the arsenal of high energy physicists. Apart from new applications, there also exists opportunities to develop new strategies.

References

1. G.F. Sterman, S. Weinberg, Jets from quantum chromodynamics. *Phys. Rev. Lett.* **39**, 1436 (1977). <https://doi.org/10.1103/PhysRevLett.39.1436>
2. G.P. Salam, Recent progress in defining and understanding jets. *Acta Phys. Polon. Supp.* **1**, 455–461 (2008) [hep-ph]
3. R.K. Ellis, W.J. Stirling, B.R. Webber, QCD and collider physics. *Camb. Monogr. Part. Phys. Nucl. Phys. Cosmol.* **8**, 1–435 (1996)
4. CMS Collaboration, T. Mc Cauley, Multi-jet event recorded by the CMS detector (Run 2, 13 TeV) (2015). <https://cds.cern.ch/record/2114784>, CMS Collection
5. J. Thaler, K. Van Tilburg, Identifying boosted objects with n-subjettiness. *JHEP* **03**, 015 (2011). [https://doi.org/10.1007/JHEP03\(2011\)015](https://doi.org/10.1007/JHEP03(2011)015) [hep-ph]
6. C.F. Berger, T. Kucs, G.F. Sterman, Event shape/energy flow correlations. *Phys. Rev. D* **68**, 014012 (2003). <https://doi.org/10.1103/PhysRevD.68.014012> [hep-ph]
7. L.G. Almeida, S.J. Lee, G. Perez, G.F. Sterman, I. Sung, J. Virzi, Substructure of high- p_T Jets at the LHC. *Phys. Rev. D* **79**, 074017 (2009). <https://doi.org/10.1103/PhysRevD.79.074017> [hep-ph]
8. A. Altheimer, A. Arce, L. Asquith, J. Backus Mayes, E. Bergeaas Kuutmann, J. Berger, D. Bjergaard, L. Bryngemark, A. Buckley, J. Butterworth et al., Boosted Objects and Jet Substructure at the LHC. Report of BOOST2012, held at IFIC Valencia, 23rd-27th of July 2012. *Eur. Phys. J. C* **74**(3), 2792 (2014). <https://doi.org/10.1140/epjc/s10052-014-2792-8> [hep-ex]
9. P.T. Komiske, E.M. Metodiev, M.D. Schwartz, Deep learning in color: towards automated quark/gluon jet discrimination. *JHEP* **01**, 110 (2017). [https://doi.org/10.1007/JHEP01\(2017\)110](https://doi.org/10.1007/JHEP01(2017)110) [hep-ph]

10. P.T. Komiske, E.M. Metodiev, B. Nachman, M.D. Schwartz, Pileup Mitigation with Machine Learning (PUMML). *JHEP* **12**, 051 (2017). [https://doi.org/10.1007/JHEP12\(2017\)051](https://doi.org/10.1007/JHEP12(2017)051) [hep-ph]
11. J. Collado, J.N. Howard, T. Faucett, T. Tong, P. Baldi, D. Whiteson, Learning to Identify Electrons [physics.data-an]
12. G. Kasieczka, S. Marzani, G. Soyez, G. Stagnitto, Towards machine learning analytics for jet substructure. *JHEP* **09**, 195 (2020). [https://doi.org/10.1007/JHEP09\(2020\)195](https://doi.org/10.1007/JHEP09(2020)195) [hep-ph]
13. J. Cogan, M. Kagan, E. Strauss, A. Schwartzman, Jet-images: computer vision inspired techniques for jet tagging. *JHEP* **02**, 118 (2015). [https://doi.org/10.1007/JHEP02\(2015\)118](https://doi.org/10.1007/JHEP02(2015)118) [hep-ph]

Chapter 9

Two-Loop QCD Amplitudes for Di-pseudo Scalar Production in Gluon Fusion



Arunima Bhattacharya, Maguni Mahakhud, Prakash Mathews, and V. Ravindran

Abstract We compute the radiative corrections to the four-point amplitude $g + g \rightarrow A + A$ in massless quantum chromodynamics (QCD) up to order α_s^4 in perturbation theory. We used the effective field theory that describes the coupling of pseudo-scalars to gluons and quarks directly in the large top quark mass limit. Due to the CP odd nature of the pseudo-scalar Higgs boson, the computation involves careful treatment of chiral quantities in dimensional regularisation. The ultraviolet finite results are shown to be consistent with the universal infrared structure of QCD amplitudes. The infrared finite part of these amplitudes constitutes the important component of any next-to-next-to-leading order corrections to observables involving pair of pseudo-scalars at the Large Hadron Collider.

9.1 Theoretical Framework

9.1.1 Effective Lagrangian and Kinematics

We work with the effective Lagrangian [1] that describes the interaction of the pseudo-scalar field $\Phi^A(x)$ with the gauge field $G^{a\mu\nu}$ and the fermion ψ :

$$\mathcal{L}_{eff}^A = \Phi^A(x) \left[-\frac{1}{8} C_G O_G(x) - \frac{1}{2} C_J O_J(x) \right]. \quad (9.1)$$

The pseudo-scalar gluonic ($O_G(x)$) and the light quark ($O_J(x)$) operators are defined as

A. Bhattacharya (✉) · P. Mathews · V. Ravindran
Saha Institute of Nuclear Physics, A CI of Homi Bhabha National Institute, 1/AF Saltlake,
Kolkata 700064, India
e-mail: arunima.bhattacharya@saha.ac.in

M. Mahakhud
Indian Institute of Science Education and Research Mohali, Knowledge city, Sector 81, SAS
Nagar, Manauli 140306, India

$$O_G(x) = G^{a\mu\nu} \tilde{G}_{\mu\nu}^a = \epsilon_{\mu\nu\rho\sigma} G^{a\mu\nu} G^{a\rho\sigma}, \quad G^{a\mu\nu} = \partial^\mu G^{a\nu} - \partial^\nu G^{a\mu} + g_s f^{abc} G_b^\mu G_c^\nu, \quad (9.2)$$

where f^{abc} is the SU(3) structure constant and $\epsilon_{\mu\nu\rho\sigma}$ is the Levi-Civita tensor.

The effective Lagrangian is obtained after integrating out the top quark fields in the large top mass limit.

We use the effective Lagrangian (9.1) to obtain amplitudes for the production of pair of pseudo-scalar Higgs bosons A of mass m_A up to two-loop level in perturbative QCD. We restrict ourselves to the dominant gluon fusion subprocess:

$$g(p_1) + g(p_2) \rightarrow A(p_3) + A(p_4), \quad (9.3)$$

where p_1 and p_2 are the momenta of the incoming gluons, $p_{1,2}^2 = 0$, and p_3 and p_4 are the momenta of the outgoing pseudo-scalar Higgs bosons, $p_{3,4}^2 = m_A^2$. The Mandelstam variables for the above process are given by

$$s = (p_1 + p_2)^2, \quad t = (p_1 - p_3)^2, \quad u = (p_2 - p_3)^2, \quad (9.4)$$

which satisfy $s + t + u = 2m_A^2$.

As in the case of di-Higgs production amplitude *via* gluon fusion [2], the di-pseudo scalar production amplitude can also be decomposed in terms of two second-rank Lorentz tensors $\mathcal{T}_i^{\mu\nu}$ ($i = 1, 2$). The second-rank tensors are given by

$$\mathcal{T}_1^{\mu\nu} = g^{\mu\nu} - \frac{p_1^\nu p_2^\mu}{p_1 \cdot p_2}, \quad (9.5)$$

$$\mathcal{T}_2^{\mu\nu} = g^{\mu\nu} + \frac{1}{p_1 \cdot p_2 p_T^2} \left(m_A^2 p_2^\mu p_1^\nu - 2p_1 \cdot p_3 p_2^\mu p_3^\nu - 2p_2 \cdot p_3 p_3^\mu p_1^\nu + 2p_1 \cdot p_2 p_3^\mu p_3^\nu \right), \quad (9.6)$$

with $p_T^2 = (tu - m_A^4)/s$ is the transverse momentum square of the pseudo-scalar Higgs boson expressed in terms of the Mandelstam variables. The scalar functions $\mathcal{M}_{1,2}$ can be obtained from $\mathcal{M}_{ab}^{\mu\nu}$, by using appropriate d -dimensional projectors $P_{i,ab}^{\mu\nu}$ with $i = 1, 2$, respectively, and the projectors are given by

$$P_{1,ab}^{\mu\nu} = \frac{\delta_{ab}}{N^2 - 1} \left(\frac{1}{4} \frac{d-2}{d-3} \mathcal{T}_1^{\mu\nu} - \frac{1}{4} \frac{d-4}{d-3} \mathcal{T}_2^{\mu\nu} \right),$$

$$P_{2,ab}^{\mu\nu} = \frac{\delta_{ab}}{N^2 - 1} \left(-\frac{1}{4} \frac{d-4}{d-3} \mathcal{T}_1^{\mu\nu} + \frac{1}{4} \frac{d-2}{d-3} \mathcal{T}_2^{\mu\nu} \right), \quad (9.7)$$

where N corresponds to the $SU(N)$ colour group.

There are two types of diagrams that contribute to this process. We classify them as type-I and type-II. The form factor type diagrams where a pair of gluons annihilate to a single A , which branches into a pair of A s belong to type-I and type-II, contains t and u channel diagrams where each A is coupled to pair of gluons, or to quarks.

Since type-I is related to form factors of O_G between gluons states and O_J between quark and gluon states, we can readily obtain them from [3–5].

Type-I diagrams are known to order a_s and hence, the results presented here will mainly include the type-II amplitudes. All the corresponding tree level, one-loop and two-loop Feynman diagrams in massless QCD are generated using QGRAF [13] which are converted with the help of in-house codes based on FORM [14]. Several automated computer algebra packages are used like REDUZE2 [6] and LiteRed [7].

9.1.2 UV Renormalisation, Operator Renormalisation and Mixing

In dimensional regularisation with $d = 4 + \epsilon$, the bare strong coupling constant denoted by \hat{a}_s is related to its renormalised coupling by a_s

$$\hat{a}_s S_\epsilon = \left(\frac{\mu^2}{\mu_R^2} \right)^{\epsilon/2} Z_{a_s} a_s, \quad (9.8)$$

with $S_\epsilon = \exp [(\gamma_E - \ln 4\pi)\epsilon/2]$ with $\gamma_E \approx 0.5772\dots$ the Euler-Mascheroni constant and μ is the scale introduced to keep the strong coupling constant dimensionless in $d = 4 + \epsilon$ space-time dimensions. The renormalisation constant Z_{a_s} [10] is given in [5].

Apart from the renormalisation of strong coupling in the massless QCD, the amplitudes require the renormalisation of vertices resulting from the composite operators O_G and O_J of the effective Lagrangian (9.1). The renormalised operators are denoted by $[]$ parenthesis, while the bare quantities are without the parenthesis. The renormalisation constants required are available up to $O(a_s^3)$ [5, 11, 12], which was computed using OPE. Here we compute $g + g \rightarrow A + A$ amplitude to order $O(a_s^4)$ and hence, we need the following renormalised operator $[O_G O_G]$ and $[O_G O_J]$, which is given by

$$\begin{aligned} [O_G O_G] &= Z_{GG}^2 O_G O_G + 2Z_{GG} Z_{GJ} O_G O_J + Z_{GJ}^2 O_J O_J, \\ [O_G O_J] &= Z_{GG} Z_{JJ} O_G O_J + Z_{GJ} Z_{JJ} O_J O_J. \end{aligned} \quad (9.9)$$

Sandwiching $[O_G O_G]$ and $[O_G O_J]$ between gluon states and using (9.9), we obtain up to two loops:

$$\begin{aligned} \mathcal{M}_{GG,g}^{\text{II}} &= Z_{GG}^2 \left(\hat{\mathcal{M}}_{GG,g}^{\text{II}(0)} + \hat{a}_s \hat{\mathcal{M}}_{GG,g}^{\text{II}(1)} + \hat{a}_s^2 \hat{\mathcal{M}}_{GG,g}^{\text{II}(2)} \right) \\ &\quad + 2Z_{GG} Z_{GJ} \left(\hat{a}_s \hat{\mathcal{M}}_{GJ,g}^{\text{II}(1)} + \hat{a}_s^2 \hat{\mathcal{M}}_{GJ,g}^{\text{II}(2)} \right) \\ &\quad + Z_{GJ}^2 \left(\hat{a}_s \hat{\mathcal{M}}_{JJ,g}^{\text{II}(1)} + \hat{a}_s^2 \hat{\mathcal{M}}_{JJ,g}^{\text{II}(2)} \right), \\ \mathcal{M}_{GJ,g}^{\text{II}} &= Z_{GG} Z_{JJ} \left(\hat{a}_s \hat{\mathcal{M}}_{GJ,g}^{\text{II}(1)} + \hat{a}_s^2 \hat{\mathcal{M}}_{GJ,g}^{\text{II}(2)} \right) \end{aligned}$$

$$+Z_{GJ}Z_{JJ}\left(\hat{a}_s\hat{\mathcal{M}}_{JJ,g}^{II(1)}+\hat{a}_s^2\hat{\mathcal{M}}_{JJ,g}^{II(2)}\right), \quad (9.10)$$

$\hat{\mathcal{M}}_{GJ,g}^{II(2)}$, $\hat{\mathcal{M}}_{JJ,g}^{II(1)}$ and $\hat{\mathcal{M}}_{JJ,g}^{II(2)}$ do not contribute in our case as they are of order higher than a_s^4 when combined with their respective Wilson coefficients.

We find that the UV singularities that appear at one-loop and two-loop levels can be taken care of by the coupling constant renormalisation Z_{a_s} and operator renormalisation Z_{ij} . As shown in [12], we find that there are no contact terms as a result of the product of operators at short distances.

9.2 Infrared Factorisation

The UV finite amplitudes that we have computed contain only divergences of infrared origin, which appear as poles in the dimensional regularisation parameter ϵ . The amplitudes beyond leading order show a very rich universal structure in the IR. Following [13], we obtain

$$\begin{aligned} \mathcal{M}_i^{II,(0)} &= \mathcal{M}_i^{II,(0)}, \\ \mathcal{M}_i^{II,(1)} &= 2\mathbf{I}_g^{(1)}(\epsilon)\mathcal{M}_i^{II,(0)} + \mathcal{M}_i^{II,(1),\text{fin}}, \\ \mathcal{M}_i^{II,(2)} &= 4\mathbf{I}_g^{(2)}(\epsilon)\mathcal{M}_i^{II,(0)} + 2\mathbf{I}_g^{(1)}(\epsilon)\mathcal{M}_i^{II,(1)} + \mathcal{M}_i^{B,(2),\text{fin}}, \end{aligned} \quad (9.11)$$

where $\mathbf{I}_g^{(1)}(\epsilon)$, $\mathbf{I}_g^{(2)}(\epsilon)$ are the IR singularity operators.

At one-loop level, it is shown analytically that the IR poles are in agreement with the predictions. For the two-loop case, a fully analytical comparison was possible only for poles ϵ^{-i} with $i = 2 - 4$. The ϵ^{-1} pole term was compared at the numerical level. We found full agreement with the predictions of Catani up to two-loop level for all the IR poles. Having done this, the finite part can be extracted by subtracting the IR poles according to (9.11).

9.3 Conclusion

Here we have presented the two-loop virtual amplitudes that are relevant for studying the production of pair of pseudo-scalar Higgs bosons in the gluon fusion subprocess at the LHC. We have done this computation in the EFT where top quark degrees of freedom is integrated out. For details, see the full article [14].

References

1. K.G. Chetyrkin, B.A. Kniehl, M. Steinhauser, W.A. Bardeen, Nucl. Phys. B **535**, 3 (1998)
2. E.W.N. Glover, J.J. van der Bij, Nucl. Phys. B **309**, 282 (1988)
3. P.A. Baikov, K.G. Chetyrkin, A.V. Smirnov, V.A. Smirnov, M. Steinhauser, Phys. Rev. Lett. **102**, 212002 (2009)
4. T. Gehrmann, E.W.N. Glover, T. Huber, N. Ikizlerli, C. Studerus, JHEP **06**, 094 (2010)
5. T. Ahmed, T. Gehrmann, P. Mathews, N. Rana, V. Ravindran, JHEP **11**, 169 (2015)
6. P. Nogueira, J. Comput. Phys. **105**, 279 (1993)
7. J.A.M. Vermaseren (2000)
8. A. von Manteuffel, C. Studerus (2012)
9. R.N. Lee, J. Phys. Conf. Ser. **523**, 012059 (2014)
10. O.V. Tarasov, A.A. Vladimirov, AYu. Zharkov, Phys. Lett. **93B**, 429 (1980)
11. S.A. Larin, Phys. Lett. B **303**, 113 (1993)
12. M.F. Zoller, JHEP **07**, 040 (2013)
13. S. Catani, Phys. Lett. B **427**, 161 (1998)
14. A. Bhattacharya, M. Mahakhud, P. Mathews, V. Ravindran, JHEP **02**, 121 (2020)

Chapter 10

Exploring the Structural Features of Quark Mass Matrices in the Flavor Basis



Aseem Vashisht, Kanwaljeet S. Channey, Gulsheen Ahuja,
and Manmohan Gupta

Abstract In the present work we have explored the structural features of the quark mass matrices in the flavor basis which is allowed by the weak basis transformations. Our analysis leads to some very interesting results regarding the phases of the quark mass matrices.

10.1 Introduction

Understanding fermion masses and mixings is one of the most important problems of present-day Flavor Physics. In the absence of any viable theory of Flavor Physics, emphasis is mostly on developing phenomenological models [1, 2] of fermion mass matrices which are in agreement with the ever-improving data. In the case of quark sector with three generations, the mass matrices are characterized by complex 3×3 matrices in the up and down sectors, together leading to 36 free parameters. However, without loss of generality, it can be shown that the general mass matrices can be reduced to Hermitian mass matrices with 18 independent parameters [2]. The mass matrices are related to the mixing matrix, referred to as CKM matrix [3–5] characterized by three angles and one CP-violating phase, with six quark masses leading to ten observables.

Weak basis transformations and texture-specific mass matrices have been used to develop viable phenomenological interpretations of the mass matrices [2]. Briefly, weak basis transformations allow one to choose a basis in the standard model, wherein one can have a specific form(s) of the mass matrices in the up and down sectors. In

A. Vashisht (✉) · G. Ahuja · M. Gupta
Department of Physics, Panjab University, Chandigarh 160014, India
e-mail: vashishtaseem@gmail.com

K. S. Channey
Department of Physics and Astrophysics, University of Delhi, New Delhi 110007, India

Department of Physics, University Institute of Sciences, Chandigarh University, Ajitgarh 140413, Punjab, India

particular, without loss of generality, we can have mass matrices to be diagonal in either up or down sector with the other being a completely general Hermitian matrix. The purpose of the present work is to explore in detail the structural features, in particular the phase structure, of the mass matrices in the flavor basis.

10.2 Mass Matrices in the Flavor Basis and Their Analysis

Using weak basis transformations, without loss of generality, the quark mass matrices are defined as follows:

When M_U is general Hermitian and M_D is diagonal

$$M_U = \begin{pmatrix} E_u & |A_u|e^{i\phi_{12}} & |F_u|e^{i\phi_{13}} \\ |A_u|e^{-i\phi_{12}} & D_u & |B_u|e^{i\phi_{23}} \\ |F_u|e^{-i\phi_{13}} & |B_u|e^{-i\phi_{23}} & C_u \end{pmatrix}, \quad M_D = \begin{pmatrix} m_d & 0 & 0 \\ 0 & m_s & 0 \\ 0 & 0 & m_b \end{pmatrix}. \quad (10.1)$$

When M_U is diagonal and M_D is general Hermitian

$$M_U = \begin{pmatrix} m_u & 0 & 0 \\ 0 & m_c & 0 \\ 0 & 0 & m_t \end{pmatrix}, \quad M_D = \begin{pmatrix} E_d & |A_d|e^{i\phi_{12}} & |F_d|e^{i\phi_{13}} \\ |A_d|e^{-i\phi_{12}} & D_d & |B_d|e^{i\phi_{23}} \\ |F_d|e^{-i\phi_{13}} & |B_d|e^{-i\phi_{23}} & C_d \end{pmatrix}. \quad (10.2)$$

As a first step, we briefly discuss the relationship between the quark mass matrices and the mixing matrix. To keep the discussion general, we consider general mass matrices which can always be diagonalized by bi-unitary transformation. For example,

$$V_{U_L}^\dagger M_U V_{U_R} = M_{U_{\text{Diag}}} \equiv \text{Diag}(m_u, m_c, m_t), \quad (10.3)$$

$$V_{D_L}^\dagger M_D V_{D_R} = M_{D_{\text{Diag}}} \equiv \text{Diag}(m_d, m_s, m_b). \quad (10.4)$$

The mismatch of diagonalizations of up and down quark mass matrices leads to the quark mixing matrix V_{CKM} , referred to as the Cabibbo–Kobayashi–Maskawa (CKM) matrix given as

$$V_{CKM} = V_{U_L}^\dagger V_{U_R}. \quad (10.5)$$

The parameterization advocated by the PDG is given as

$$V_{CKM} = \begin{pmatrix} c_{12}c_{13} & s_{12}c_{13} & s_{13}e^{-i\delta} \\ -s_{12}c_{23} - c_{12}s_{23}s_{13}e^{i\delta} & c_{12}c_{23} - s_{12}s_{23}s_{13}e^{i\delta} & s_{23}c_{13} \\ s_{12}s_{23} - c_{12}c_{23}s_{13}e^{i\delta} & -c_{12}s_{23} - s_{12}c_{23}s_{13}e^{i\delta} & c_{23}c_{13} \end{pmatrix}, \quad (10.6)$$

with $c_{ij} = \cos \theta_{ij}$ and $s_{ij} = \sin \theta_{ij}$ for $i, j = 1, 2, 3$. The parameter δ is the CP-violating phase. Before discussing the details of analysis, we present the latest status of the quark masses (at the M_Z scale) and the quark mixing matrix, as per PDG 2020, for example,

$$m_u = 2.16_{-0.26}^{+0.49} \text{ MeV}, \quad m_d = 4.67_{-0.17}^{+0.48} \text{ MeV}, \quad m_s = 93_{-5}^{+11} \text{ MeV}, \quad (10.7)$$

$$m_c = 1.27 \pm 0.02 \text{ GeV}, \quad m_b = 4.13_{-0.02}^{+0.03} \text{ GeV}, \quad m_t = 172.76 \pm 0.30 \text{ GeV}, \quad (10.8)$$

$$V_{CKM} = \begin{pmatrix} 0.97401 \pm 0.00011 & 0.22650 \pm 0.00048 & 0.00361_{-0.00009}^{+0.00011} \\ 0.22636 \pm 0.00048 & 0.97320 \pm 0.00011 & 0.04053_{-0.00061}^{+0.00083} \\ 0.00854_{-0.00016}^{+0.00023} & 0.03978_{-0.00060}^{+0.00082} & 0.999172_{-0.000035}^{+0.00024} \end{pmatrix}. \quad (10.9)$$

Along with these, recent values of some other important parameters of the CKM phenomenology are as follows:

$$\sin 2\beta = 0.699 \pm 0.017, \quad J = (3.0_{-0.09}^{+0.15}) \times 10^{-5}, \quad \delta = (1.196_{-0.043}^{+0.045}). \quad (10.10)$$

10.3 Discussion of Results

To begin with, we would be discussing the results pertaining to the case when M_D is diagonal and M_U is a general 3×3 Hermitian matrix, and the other case wherein M_D is a general, which can be done similarly, however not included here. Using the inputs pertaining to mass ranges given in (10.7) and (10.8) as well as the CKM matrix elements V_{us} , V_{cb} and V_{ub} given in (10.9) as a first step using Monte Carlo simulations we have found the ranges of the elements of the mass matrix M_U , including the phase factors, which are able to reproduce the CKM matrix given in (10.9). This is followed by reproducing details pertaining to the phase structure of the CKM matrix. To this end, we have considered several cases with constraints imposed on the phases ϕ_{12} , ϕ_{23} and ϕ_{13} . This is essentially to explore the possibility of a simplified phase structure which can reproduce the CKM matrix.

10.3.1 For the Case $\phi_{12} = 0$, $\phi_{13} \neq 0$ and $\phi_{23} \neq 0$

Using the constraints, given in (10.7), (10.8) and (10.9), we have first reproduced the CKM matrix and then in Fig. 10.1a, b we have plotted phase-sensitive parameters $\sin 2\beta$ and δ . From Fig. 10.1 it is clear that both can be reproduced easily in this case.

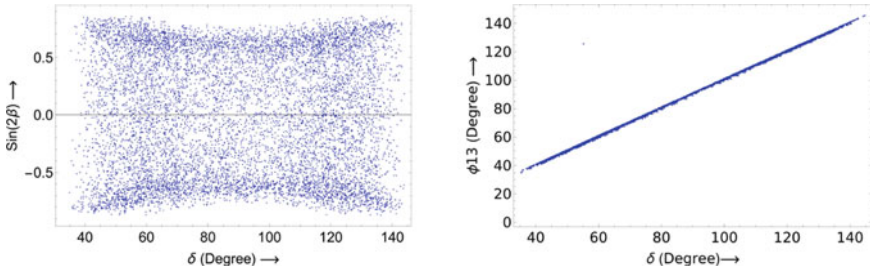


Fig. 10.1 Variation of the CP-violating phase δ with **a** $\sin 2\beta$ and **b** the phase ϕ_{13} for vanishing ϕ_{12}

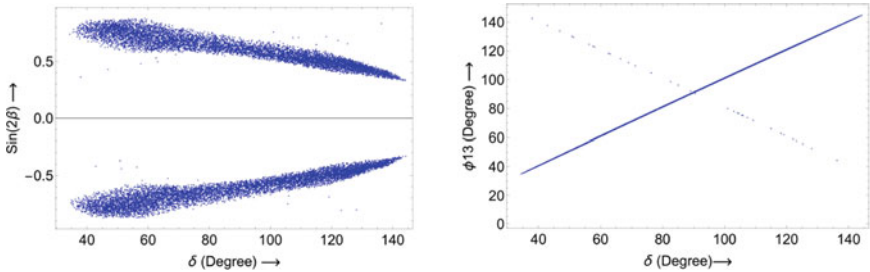


Fig. 10.2 Variation of the CP-violating phase δ with **a** $\sin 2\beta$ and **b** the phase ϕ_{13} for vanishing ϕ_{12} and ϕ_{23}

10.3.2 For the Case $\phi_{12} = 0, \phi_{23} = 0$ and $\phi_{13} \neq 0$

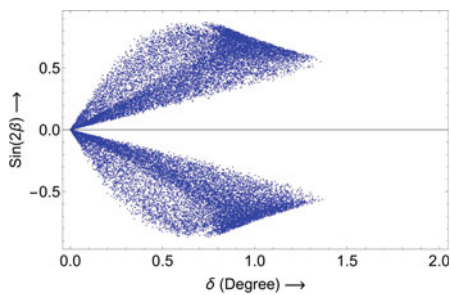
In this case again, first we reproduce the CKM matrix and then attempt to study the phase-sensitive parameters. From Fig. 10.2a, b we find that this case looks to be very much viable.

10.3.3 For the Case $\phi_{13} = 0, \phi_{12} \neq 0$ and $\phi_{23} \neq 0$

Again, in this case, one is able to reproduce the magnitudes of the elements of CKM matrix; however, there are issues in the case of phase-sensitive parameters. For example, in Fig. 10.3 we have plotted $\sin 2\beta$ versus predicted values of δ . From the graph it is clear that to reproduce $\sin 2\beta$, δ has to be restricted to less than 2° , clearly in disagreement with the data.

Apart from the cases considered above, there are other cases; however, their results are similar to the cases considered above, therefore we have not included these in the discussion.

Fig. 10.3 Variation of $\sin 2\beta$ with the CP-violating phase δ for vanishing ϕ_{13}



10.4 Conclusion

In conclusion, we would emphasize that a non-zero ϕ_{13} for the matrix M_U is a prerequisite for reproducing the phase-sensitive parameters. The allowed ranges of ϕ_{13} in different cases are (1) when $\phi_{12} = 0$, $\phi_{13} \neq 0$ and $\phi_{23} \neq 0$, the range is ($39^\circ - 324^\circ$) (2) when $\phi_{12} = 0$, $\phi_{23} = 0$ and $\phi_{13} \neq 0$, the range is ($34^\circ - 323^\circ$) and (3) when $\phi_{23} = 0$, $\phi_{13} \neq 0$ and $\phi_{12} \neq 0$ the range is ($37^\circ - 325^\circ$).

Acknowledgements AV, GA and MG would like to thank the Chairman, Department of Physics, P.U. for providing facilities to work. KSC would like to thank Director, UIS, Chandigarh University for help and support.

References

1. H. Fritzsch, Z.Z. Xing, Prog. Part. Nucl. Phys. **45**, 1 (2000)
2. M. Gupta, G. Ahuja, Int. J. Mod. Phys. A **26** (2011) 2973; Int. Jour. Mod. Phys. A **27** (2012) 1230033
3. N. Cabbibo, Phys. Rev. Lett. **10**, 531 (1963)
4. S.L. Glashow, J. Iliopoulos, L. Maiani, Phys. Rev. D. **2**, 1285 (1970)
5. M. Kobayashi, K. Maskawa, Prog. Theor. Phys. **49**, 652 (1973)

Chapter 11

Search for $B^* \rightarrow tW$ with Full Run II Data at CMS



Ashish Sharma

Abstract A search for a heavy resonance decaying to a top quark and a W boson in the fully hadronic final state is presented. The analysis is performed using proton–proton collisions at a center-of-mass energy of 13 TeV. The search uses data corresponding to an integrated luminosity of 137 fb^{-1} recorded by the CMS experiment at the LHC. The analysis is focused on heavy resonances, where the decay products of each top quark or W boson are expected to be reconstructed as a single, large radius jet with a distinct substructure. An excited quark, b^* , is used as a benchmark model when setting limits on the cross section for a heavy resonance decaying to a top quark and a W boson. The hypotheses of b^* quarks with left-handed, right-handed, and vector-like chirality are excluded at 95% confidence level for masses below 2.61, 2.83, and 3.04 TeV, respectively.

11.1 Introduction

While the standard model (SM) has been extensively verified by experiment, it lacks explanations for dark matter, gravity, and other observed phenomena at the cosmological scales. Many possibilities for physics beyond the standard model have been proposed, including the possibility that quarks are composite. These quarks would have an internal structure that could be excited to produce a state with higher mass [1]. Such a phenomenon is predicted by Randall-Sundrum models and models with a heavy gluon partner [2]. In this paper, we search for a heavy resonance decaying to a top (t) quark and a W boson in the fully hadronic final state using proton–proton collisions at a center-of-mass energy of 13 TeV. The search uses data corresponding to an integrated luminosity of 137 fb^{-1} recorded by the CMS experiment at the

for the CMS Collaboration

A. Sharma (✉)
IIT madras, Chennai 600036, India
e-mail: ashish.sharma@cern.ch

© The Author(s), under exclusive license to Springer Nature Singapore Pte Ltd. 2022
B. Mohanty et al. (eds.), *Proceedings of the XXIV DAE-BRNS High Energy Physics Symposium, Jatni, India*, Springer Proceedings in Physics 277,
https://doi.org/10.1007/978-981-19-2354-8_11

CERN LHC [3] during 2016, 2017, and 2018. We consider as a benchmark model an excited b quark [1], referred to as the b^* quark.

11.2 The CMS Detector

The central feature of the CMS apparatus is a superconducting solenoid of 6 m internal diameter, providing a magnetic field of 3.8 T. A more detailed description of the CMS detector, together with a definition of the coordinate system used and the relevant kinematic variables, can be found in [3]. Events of interest are selected using a two-tiered trigger system, which can be found in [4].

11.3 Data and Simulated Samples

Since the recording of data goes on an annual cycle, data collection and simulation performance can change from year to year. Therefore, we categorize both the data and simulation by year, and statistically combine all three years when deriving a final result. We analyze events from the 2016 data recorded by a trigger that requires the sum of transverse momenta (p_T) of all jets in the event, H_T , to be at least 800 or 900 GeV, or the presence of a jet with p_T greater than 450 GeV. For 2017 and 2018 data, we analyze events recorded by a trigger that requires a minimum H_T of 1050 GeV, or the presence of a jet with p_T greater than 500 GeV or a jet with a p_T greater than 380 GeV with a mass of at least 30 GeV, where jet trimming has been used to reconstruct the jet mass at the trigger level. These higher p_T thresholds in 2017 and 2018 data are due to an increase in the instantaneous luminosity of the LHC between 2016 and 2017. The combination of these triggers is nearly fully efficient in the m_{tW} region of interest, $m_{tW} > 1200$ GeV.

11.4 Event Reconstruction

The physics objects are the jets, clustered using the anti- k_T (AK) jet finding algorithm [5] with the tracks assigned to candidate vertices as inputs. The particle-flow algorithm [6] aims to reconstruct and identify each individual particle in an event, with an optimized combination of information from the various elements of the CMS detector and the associated missing transverse momentum, taken as the negative vector sum of the p_T of those jets. This analysis uses jets which have a radius parameter of $R = 0.8$ to reconstruct the top jet and W jet in an event.

The soft drop algorithm, a generalization of the modified mass drop algorithm, with angular exponent $\beta = 0$ and soft threshold $z = 0.1$, is applied as a grooming technique to all jets in the event to reconstruct the jet mass and identify subjets. We

only consider top jets with a minimum soft drop mass of 50 GeV. Signal-like events require a mass selection between 105 and 220 GeV. The N-subjettiness algorithm [7] defines τ_N variables, which describe the consistency between the jet energy deposits and the number of assumed subjets, N. When compared to jets originating from a gluon or a light quark, a top jet is more consistent with three hard decay products, and the ratio of τ_3 and τ_2 allows top jets to be distinguished from QCD multijet background [8].

Similar to top tagging, the W boson identification algorithm requires a selection based on τ_N and soft drop mass. The W jet is required to have a soft drop mass between 65 and 105 GeV to be consistent with the W boson mass. The N-subjettiness ratio τ_2/τ_1 variable is used to select the characteristic two-prong structure of a hadronic W boson decay since the W jet is more consistent with having two subjets than one. The b^* signal region selection requires $\tau_2/\tau_1 < 0.4$ for 2016 data and simulation and $\tau_2/\tau_1 < 0.45$ for 2017 and 2018 data and simulation. A jet that passes the τ_2/τ_1 and soft drop mass selections is considered “W tagged”.

11.5 Event Selection

To select signal-like events, two jets are required with $p_T > 400$ GeV and $\eta < 2.4$. The jets are required to satisfy $|\Delta\phi| > \pi/2$ in order to select back-to-back dijet events, and have $|\Delta y| < 1.6$ in order to suppress multijet events with high m_{tW} which arise from the scattering of valence quarks. This selection will be referred to as the “preselection”, with a signal event then being selected if one of the two leading jets is identified by the top tagging algorithm and the other is selected with the W tagging algorithm. Initially, we assume that the leading jet is the top jet and the sub-leading jet is the W jet. If the sub-leading jet passes the W boson identification algorithm, the event is selected with the leading jet later checked for passing the top tagging requirements. If the sub-leading jet does not pass the W boson identification algorithm, the algorithm is applied to the leading jet. If the leading jet can be identified as a W jet, the event is selected in this configuration and if not, the event is not selected.

11.6 Background Estimation

For each bin in the two-dimensional (m_t, m_{tW}) distribution, we compare the number of expected events from both the background-only and signal-plus-background hypotheses with the number of observed events in data. Following are the backgrounds considered in this analysis:

- Multijet background
- $t\bar{t}$ and single-top background

The multijet component is estimated via a data-driven estimate, while the $t\bar{t}$ and single-top components are estimated by fitting simulation templates to data.

11.7 Systematic Uncertainties

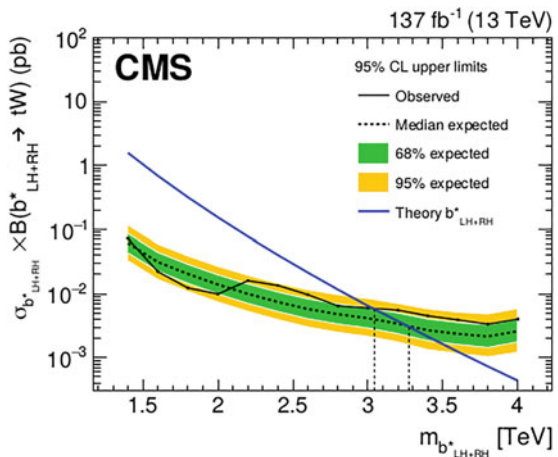
This analysis takes into account several systematic uncertainties which can affect both the shape and normalization of the simulated event samples.

- Normalization uncertainties
- Uncertainties related to jet mass/energy scale
- Uncertainties related to jet mass/energy resolution
- Uncertainties related to pileup reweighting correction
- Uncertainties in the trigger correction, etc.

11.8 Results

We don't observe the resonance, so we obtain 95% CL upper limits on the cross-section times branching ratio for a resonance decaying to a top quark and a W boson, which is shown in Fig. 11.1. The hypotheses of b^* quarks with left-handed, right-handed, and vector-like chirality are excluded at 95% confidence level for masses below 2.6, 2.8, and 3.1 TeV, respectively. These are the most stringent limits on the b^* quark mass to date, significantly extending the previous best limits by almost a factor of two.

Fig. 11.1 The expected (dashed) limits, the observed (dot-solid) limit, and b^* quark theoretical cross section (solid) are shown. The vertical dashed lines indicate the intersection of theory curve with the expected and observed limits. The colored areas around the expected limit show the 68 and 95% confidence intervals



References

1. T.M.P. Tait, C.-P. Yuan, Single top quark production as a window to physics beyond the standard model. *Phys. Rev. D* **63**, 014018 (2000). <https://doi.org/10.1103/PhysRevD.63.014018> [arXiv:hep-ph/0007298](https://arxiv.org/abs/hep-ph/0007298)
2. C. Bini, R. Contino, N. Vignaroli, Heavy-light decay topologies as a new strategy to discover a heavy gluon. *JHEP* **01** (2012). [https://doi.org/10.1007/jhep01\(2012\)157](https://doi.org/10.1007/jhep01(2012)157), [arXiv: 1110.6058](https://arxiv.org/abs/1110.6058)
3. C. Collaboration, The CMS experiment at the CERN LHC. *JINST* **3**, S08004. 361 p (2008). <https://doi.org/10.1088/1748-0221/3/08/S08004>.
4. V. Khachatryan, others, “The CMS trigger system”. *JINST* **12**, 01020 (2017). <https://doi.org/10.1088/1748-0221/12/01/P01020>
5. M. Cacciari, G.P. Salam, G. Soyez, The anti-kT jet clustering algorithm. *JHEP* **04**, 063 (2008). <https://doi.org/10.1088/1126-6708/2008/04/063> [arXiv:0802.1189](https://arxiv.org/abs/0802.1189)
6. A.M. Sirunyan, others, Particle-flow reconstruction and global event description with the CMS detector. *JINST* **12**, 003 (2017). <https://doi.org/10.1088/1748-0221/12/10/P10003>.
7. J. Thaler, K. Van Tilburg, Identifying boosted objects with N-subjettiness. *JHEP* **03**, 015 (2011). [https://doi.org/10.1007/JHEP03\(2011\)015](https://doi.org/10.1007/JHEP03(2011)015) [arXiv:1011.2268](https://arxiv.org/abs/1011.2268)
8. J. Thaler, K. Van Tilburg, Maximizing boosted top identification by minimizing N-subjettiness. *JHEP* **02**, 093 (2012). [https://doi.org/10.1007/JHEP02\(2012\)093](https://doi.org/10.1007/JHEP02(2012)093) [arXiv:1108.2701](https://arxiv.org/abs/1108.2701)

Chapter 12

LHC Signals of Triplet Scalars as Dark Matter Portal: Cut-Based Approach and Improvement with Gradient Boosting and Neural Networks



Atri Dey

Abstract We consider a scenario where an $SU(2)$ triplet scalar also acts as a scalar dark matter portal. We identify regions of the parameter space, where such a triplet coexists with the usual Higgs doublet consistently with all theoretical as well as neutrino, accelerator, and dark matter constraints, and the triplet-dominated neutral state has substantial invisible branching fraction. LHC signals are investigated for such regions, in the final state *same-sign dilepton* + ≥ 2 jets + \cancel{E}_T . While straight-forward detectability at the high-luminosity run is predicted for some benchmark points in a cut-based analysis, there are other benchmarks where one has to resort to gradient boosting/neural network techniques in order to achieve appreciable signal significance.

12.1 Introduction

The recent data on direct search for dark matter (DM), especially from the Xenon1T observation, rather strongly constrain scenarios where the 125 GeV Higgs acts as dark matter portal.

The coupling of, say, a scalar $SU(2)$ singlet DM to the Higgs boson of the standard model (SM) is restricted by such constraints to be $\lesssim 10^{-3}$. Ensuring the DM annihilation rate required for consistency with the observed relic density becomes a big challenge in such a case.

The restriction is considerably relaxed for an extended electroweak symmetry breaking sector. In that case one can have regions in the parameter space where the DM candidate has rather feeble interaction with the SM-like scalar, but sufficient coupling with the heavier neutral scalar H so as to be consistent with both direct search results and the relic density.

A. Dey (✉)

Regional Centre for Accelerator-based Particle Physics, Harish-Chandra Research Institute, HBNI, Chhatnag Road, Jhansi, Allahabad 211 019, India
e-mail: atridey@hri.res.in

© The Author(s), under exclusive license to Springer Nature Singapore Pte Ltd. 2022
B. Mohanty et al. (eds.), *Proceedings of the XXIV DAE-BRNS High Energy Physics Symposium, Jatni, India*, Springer Proceedings in Physics 277,
https://doi.org/10.1007/978-981-19-2354-8_12

67

Here we present the results of a similar investigation in the context of scalar triplet extension of the SM. We consider a scenario where an $SU(2)$ triplet scalar can act as the dominant portal for a scalar(singlet) dark matter particle. We identify regions of the parameter space, where such a triplet coexists with the usual Higgs doublet consistently with all constraints, and the triplet-dominated neutral state has substantial invisible branching fraction. LHC signals are investigated for such regions, in the final state *same-sign dilepton* + ≥ 2 jets + \cancel{E}_T as it also has a rich collider phenomenology, largely due to the presence of a doubly charged scalar that decays to same-sign dileptons pairs. By choosing some benchmark points, detectability at the high-luminosity run is predicted by cut-based analysis as well as some machine learning techniques.

12.2 A Model with a Triplet Scalar and a Scalar Dark Matter

We concentrate on an extension of a Type-II Seesaw scenario containing a $Y = 2$ scalar triplet Δ along with a singlet scalar dark matter candidate χ . χ interacts with Δ and the SM-like higgs doublet Φ via terms in the scalar potential. The Lagrangian of the full scenario is

$$\mathcal{L} = \mathcal{L}_{SM} + \mathcal{L}_{Type-II Seesaw} + \mathcal{L}_{DM} + \mathcal{L}_{Int} \quad (12.1)$$

χ , an $SU(2)_L \times U(1)_Y$ singlet, does not have any vacuum expectation value (VEV). An additional Z_2 symmetry ensures this, under which χ is assumed to be odd but Φ and Δ are even. The most general Higgs potential involving χ , ϕ and Δ can be written as

$$\begin{aligned} \mathcal{V}(\Phi, \Delta, \chi) = & a\Phi^\dagger\Phi + \frac{b}{2}Tr(\Delta^\dagger\Delta) + \frac{1}{2}M_\chi^2\chi^2 + c(\Phi^\dagger\Phi)^2 + \frac{d}{4}(Tr(\Delta^\dagger\Delta))^2 \\ & + \frac{e-h}{2}\Phi^\dagger\Phi Tr(\Delta^\dagger\Delta) + \frac{f}{4}Tr(\Delta^\dagger\Delta^\dagger)Tr(\Delta\Delta) + h\Phi^\dagger\Delta^\dagger\Delta\Phi \\ & + (i\Phi^\dagger\Delta\tilde{\Phi} + h.c) - \lambda_S\chi^4 + \lambda_D\chi^2\Phi^\dagger\Phi + \lambda_T\chi^2Tr(\Delta^\dagger\Delta). \end{aligned} \quad (12.2)$$

where $\tilde{\Phi} \equiv i\tau_2\Phi^*$. After Spontaneous Symmetry Breaking (SSB), one is left with a doubly charge scalar $H^{\pm\pm}$, a singly-charged scalar H^\pm and two neutral scalars h and H , along with a neutral pseudoscalar A . The diagonalization process also yields three mixing angles, where α is the mixing angle between the CP-even parts of Φ and Δ . The Gauge interaction terms are

$$\mathcal{L}_{gauge} = (D_\mu\Phi)^\dagger D^\mu\Phi + \frac{1}{2}Tr((D_\mu\Delta)^\dagger(D^\mu\Delta)) \quad (12.3)$$

with the additional Yukawa terms, $\mathcal{L}_Y^{new} = \sqrt{2}f_{ab}L_a^T Ci\sigma^2\Delta L_b + h.c..$

12.3 Constraints and Allowed Regions of the Parameter Space and Benchmark Selection

So long as there is small mixing between the dark matter particle χ and the scalar triplet and doublet, the main constraints on the scalar sector remain similar as for the Type-II Seesaw model. The constraints we consider here,

- Theoretical constraints, come mainly from the vacuum stability [1], perturbativity (all scalar quartic couplings $\leq 4\pi$) and unitarity [2, 3].
- Phenomenological constraints, coming from the ρ parameter and also electroweak precision measurements constraints, especially those of the oblique parameters S and T .
- The LHC constraint on $m_{H^{\pm\pm}}^2$ can be easily determined from 95% CL of $\sigma(pp \rightarrow H^{++}H^{--}) \times Br(H^{\pm\pm} \rightarrow \ell^\pm\ell^\pm)$, where the same-sign dilepton decay is the dominant channel for the doubly charged scalar.
- The thermal relic density of χ should be consistent with the latest Planck limits at the 95% confidence level.
- The χ -nucleon cross section should be below the upper bound given by XENON1T experiment and should be consistent with indirect detection constraints coming from both isotropic gamma-ray data and the gamma-ray observations from dwarf spheroidal galaxies.
- The total invisible decay of the 125 GeV scalar Higgs h has to be $\leq 19\%$.

We illustrate our results corresponding the case where all neutrino masses are nearly degenerate with the lightest neutrino mass $m_1 \approx 0.1$ eV and $\sin \alpha \sim 1.0$. Considering all constrains our three benchmarks for collider searches in same-sign dilepton channel is (Table 12.1)

Table 12.1 The Benchmark points for same-sign dilepton channel

	BP 1	BP 2	BP 3
m_H in GeV	440.0	628.0	628.0
m_A in GeV	440.0	628.0	628.0
m_{H^\pm} in GeV	520.8	708.0	708.0
$m_{H^{\pm\pm}}$ in GeV	582.8	770.0	770.0
m_χ in GeV	59.3	56.4	56.4
λ_S	0.49	0.0297	0.0297
λ_D	0.00069	0.002125	0.002125
λ_T	11.258	10.51	10.51
ω in GeV	1.348×10^{-4}	4.074×10^{-5}	7.274×10^{-5}

12.4 Collider Analysis (Cut Based and Machine Learning Approaches)

Hence we concentrate on $pp \rightarrow H^{\pm\pm}H^\mp, H^{\pm\pm} \rightarrow \ell^\pm\ell^\pm, H^\pm \rightarrow HW^\pm, H \rightarrow invisible$ channel.

Signal: The signal here is a pair of same-sign leptons (e/μ) + 2 jets + \cancel{E}_T .

Background: The dominant backgrounds for this final state are $t\bar{t}$ semileptonic decay which leads to non-prompt leptons in the final state, W + jets also contributes to the background producing non-prompt leptons, $t\bar{t}W^\pm$ with semileptonic decay of $t\bar{t}$, $W^\pm Z$ with leptonic decay of W^\pm and Z and Charge misidentification.

Based on the preceding observations in Fig. 12.1, we have applied the following cuts as $m_{ll} > 400$ GeV, $M_{cluster} > 700$ GeV, Scalar p_T sum $H_T > 700$ GeV, $M_T > 550$ GeV, $\cancel{E}_T > 300$ GeV and p_T of the leading lepton > 250 GeV and p_T of the sub-leading lepton > 200 GeV on the observables for cut-based analysis. Moreover, we move toward a more sophisticated analysis using packages based on **Gradient boosting (XGBoost) and Artificial neural network (ANN) techniques**. the ROC (Receiver Operating Characteristic) curves are shown in Fig. 12.2.

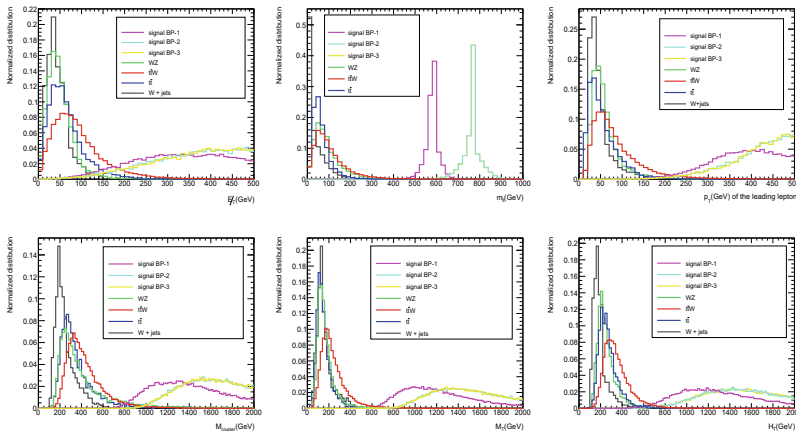


Fig. 12.1 Distribution of different variables for the three signal BPs and backgrounds

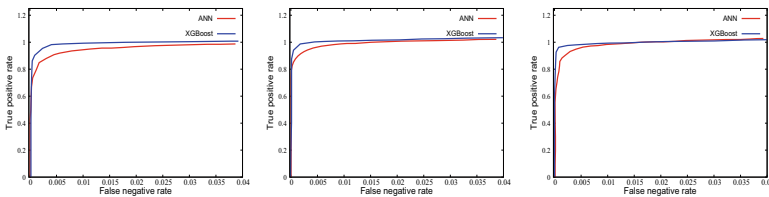


Fig. 12.2 ROC curves of BP 1 (left), BP 2 (middle), and BP 3 (right) with ANN and XGBoost

Table 12.2 Signal significance for the benchmark points at 14 TeV with $\mathcal{L} = 3000 \text{ fb}^{-1}$

BP	\mathcal{S} (Cut-based) (σ)	\mathcal{S} (ANN) (σ)	\mathcal{S} (XGBoost) (σ)
BP 1	3.4	5.9	7.8
BP 2	7.9	8.8	11.0
BP 3	4.6	5.8	7.2

Finally, the projected signal significance \mathcal{S} for the three benchmarks for 14 TeV LHC with 3000 fb^{-1} data are presented in Table 12.2.

We can see that by using machine learning techniques we can improve our significance here. It is quite obvious here because in the case of cut based, rectangular cuts are given by only seeing the distributions wherein XGBoost or ANN machine can be trained by itself by constructing good variables using given variables and putting optimized cut on them.

12.5 Conclusion

We use the fact that theories with extended scalar sectors can provide viable candidates for DM portal. Keeping this in mind, we have explored the scenario where a CP-even scalar from a triplet acts as a dominant portal to the dark sector. We have chosen a few representative benchmark points and calculated the projected signal significance in HL-LHC with cut-based analysis and also applying gradient boosting as well as neural network techniques.

References

1. S. Nie, M. Sher, Phys. Lett. B **449**, 89–92 (1999)
2. D.A. Dicus, V.S. Mathur, Phys. Rev. D **7**, 3111–3114 (1973)
3. B.W. Lee, C. Quigg, H.B. Thacker, Phys. Rev. Lett. **38**, 883–885 (1977)

Chapter 13

Gravitational Wave Signatures from First-Order Phase Transitions in an Extended Inert Doublet Dark Matter Model



Avik Paul, Debasish Majumdar, and Biswajit Banerjee

Abstract We consider a particle dark matter model by extending the Standard Model (SM) of particle physics by an extra Higgs doublet and a real singlet scalar. The added Higgs doublet is attributed to be an inert doublet and the lightest inert particle acts as a viable candidate of dark matter. We consider a finite temperature effective potential to explore the first-order phase transition (FOPT) within the framework of the model. We also discuss the possible production mechanisms of gravitational waves (GWs) from the strong FOPT. Finally, we calculate the intensities and frequencies of such GWs and investigate their detection possibilities at the future space-based detectors such as eLISA, ALIA, BBO, DECIGO, U-DECIGO, and ground-based detector aLIGO.

13.1 Introduction

The gravitational wave (GW) astronomy opens up a new window after the breakthrough discovery of a binary black hole merger event by LIGO [1]. Out of several production mechanisms of GW, first-order phase transition (FOPT) [2] in the early Universe is a prime example. During the FOPT process the Universe tunnels from false to true vacuum state through nucleation of bubbles. The bubbles which are produced at the time of phase transition (PT) encounter collisions with themselves. The colliding bubbles deform the spherical symmetry of the bubbles which leads to the phase transition with eventual emission of GWs. The GWs are produced in the early Universe from FOPT via three mechanisms such as bubble collisions, sound waves in the plasma and magnetohydrodynamic turbulence of bubbles [3]. In the Standard Model (SM) of particle physics the electroweak (EW) PT makes a smooth crossover

A. Paul (✉) · D. Majumdar · B. Banerjee
Astroparticle Physics and Cosmology Division, Saha Institute of Nuclear Physics, HBNI, 1/AF
Bidhannagar, Kolkata 700064, India
e-mail: avik.paul@saha.ac.in

© The Author(s), under exclusive license to Springer Nature Singapore Pte Ltd. 2022
B. Mohanty et al. (eds.), *Proceedings of the XXIV DAE-BRNS High Energy Physics
Symposium, Jaitani, India*, Springer Proceedings in Physics 277,
https://doi.org/10.1007/978-981-19-2354-8_13

transition but not a first-order transition with the observed Higgs mass of 125.09 GeV [4]. However an extension of SM can produce strong first-order phase transitions. Inspired by this motivation, in this work we introduce a particle dark matter (DM) model by extending the Standard Model (SM) with an inert doublet and a singlet scalar [5]. The lightest stable inert particle serves as a viable candidate for DM and we impose a Z_2 symmetry for the stability of the DM. To explore the production mechanism of GWs from FOPT induced by the present DM model, we choose three benchmark points (BPs) from the allowed model parameter space obtained from several theoretical constraints as well as the relic density constraint from PLANCK experiment [6]. We also furnish the observational detection possibilities of such GWs by considering different space-based and ground-based GW interferometers such as BBO, eLISA, ALIA, DECIGO, U-DECIGO, and aLIGO [7].

13.2 Formalism

The Model: As mentioned, we extend the SM by an inert doublet Φ_I with an additional singlet scalar S . The scalar part of the potential for such model can be represented as

$$\begin{aligned}
 V = & m_1^2 \Phi_H^\dagger \Phi_H + m_2^2 \Phi_I^\dagger \Phi_I + \frac{1}{2} m_s^2 S^2 + \lambda_1 (\Phi_H^\dagger \Phi_H)^2 + \lambda_2 (\Phi_I^\dagger \Phi_I)^2 + \lambda_3 (\Phi_H^\dagger \Phi_H) (\Phi_I^\dagger \Phi_I) \\
 & + \lambda_4 (\Phi_I^\dagger \Phi_H) (\Phi_H^\dagger \Phi_I) + \frac{\lambda_5}{2} \left[(\Phi_I^\dagger \Phi_H)^2 + (\Phi_H^\dagger \Phi_I)^2 \right] + \rho_1 (\Phi_H^\dagger \Phi_H) S \\
 & + \rho_1' (\Phi_I^\dagger \Phi_I) S + \rho_2 (\Phi_H^\dagger \Phi_H) S^2 + \rho_2' (\Phi_I^\dagger \Phi_I) S^2 + \frac{\rho_3}{3} S^3 + \frac{\rho_4}{4} S^4,
 \end{aligned} \tag{13.1}$$

where Φ_I is Z_2 odd and the other SM particles Φ_H and S are Z_2 even. After spontaneous symmetry breaking Φ_I does not get any vev while SM Higgs and S get a vev v , v_s , respectively,

$$\phi_H = \begin{pmatrix} 0 \\ \frac{1}{\sqrt{2}}(v+h) \end{pmatrix}, \quad \phi_I = \begin{pmatrix} H^+ \\ \frac{1}{\sqrt{2}}(H_0 + iA_0) \end{pmatrix}, \quad S = v_s + s. \tag{13.2}$$

The mass eigenstates h_1 and h_2 in the diagonal basis are related to the unphysical scalars h and s through the 2×2 unitary matrix U ,

$$\begin{pmatrix} h_1 \\ h_2 \end{pmatrix} = U \begin{pmatrix} h \\ s \end{pmatrix} = \begin{pmatrix} \cos \theta & -\sin \theta \\ \sin \theta & \cos \theta \end{pmatrix} \begin{pmatrix} h \\ s \end{pmatrix}, \tag{13.3}$$

which corresponds to the following relations:

$$h_1 = h \cos \theta - s \sin \theta, \quad h_2 = h \sin \theta + s \cos \theta. \tag{13.4}$$

Here, we attribute h_1 as the SM like Higgs boson with mass 125.09 GeV while H_0 as the DM candidate with the condition $\lambda_5 < 0$.

Finite Temperature Effective Potential: To describe the FOPT properties we add two correction terms namely zero temperature one-loop potential $V_{1-loop}^{T=0}$ and finite temperature potential $V_{1-loop}^{T \neq 0}$ with the tree-level potential (Eq. 13.1). Therefore, the finite temperature effective potential can be written as [8]

$$V_{\text{eff}} = V_{\text{tree-level}} + V_{1-loop}^{T=0} + V_{1-loop}^{T \neq 0}, \quad (13.5)$$

with

$$V_{1-loop}^{T=0} = \pm \frac{1}{64\pi^2} \sum_i n_i m_i^4 \left[\log \frac{m_i^2}{Q^2} - C_i \right], \quad (13.6)$$

and

$$V_{1-loop}^{T \neq 0} = \frac{T^4}{2\pi^2} \sum_i n_i J_{\pm} \left[\frac{m_i^2}{T^2} \right], \quad (13.7)$$

where

$$J_{\pm} \left(\frac{m_i^2}{T^2} \right) = \pm \int_0^{\infty} dy y^2 \log \left(1 \mp \exp \left(-\sqrt{y^2 + \frac{m_i^2}{T^2}} \right) \right). \quad (13.8)$$

GW from FOPT: In this present work, we consider three possible production mechanisms of GWs such as bubble collisions, sound waves in the plasma, and magnetohydrodynamic turbulence of bubbles. Thereby the total GW intensity Ω_{GWh^2} is the sum of the intensities of these three mechanisms and we have [3]

$$\Omega_{\text{GWh}^2} = \Omega_{\text{colh}^2} + \Omega_{\text{Sw}h^2} + \Omega_{\text{turh}^2}. \quad (13.9)$$

The bubble collision contribution of the total GW intensity is given by

$$\Omega_{\text{colh}^2} = 1.67 \times 10^{-5} \left(\frac{\beta}{H} \right)^{-2} \frac{0.11 v_w^3}{0.42 + v_w^2} \left(\frac{\kappa \alpha}{1 + \alpha} \right)^2 \left(\frac{g_*}{100} \right)^{-\frac{1}{3}} \frac{3.8 \left(\frac{f}{f_{\text{col}}} \right)^{2.8}}{1 + 2.8 \left(\frac{f}{f_{\text{col}}} \right)^{3.8}}. \quad (13.10)$$

The sound wave part of the total GW intensity can be written as

$$\Omega_{\text{Sw}h^2} = 2.65 \times 10^{-6} \left(\frac{\beta}{H} \right)^{-1} v_w \left(\frac{\kappa_v \alpha}{1 + \alpha} \right)^2 \left(\frac{g_*}{100} \right)^{-\frac{1}{3}} \left(\frac{f}{f_{\text{sw}}} \right)^3 \left[\frac{7}{4 + 3 \left(\frac{f}{f_{\text{sw}}} \right)^2} \right]^{\frac{7}{2}}. \quad (13.11)$$

The third contribution, i.e., the turbulence part of the total GW intensity has the following form

$$\Omega_{\text{turb}} h^2 = 3.35 \times 10^{-4} \left(\frac{\beta}{H} \right)^{-1} v_w \left(\frac{\epsilon \kappa \nu \alpha}{1 + \alpha} \right)^{\frac{3}{2}} \left(\frac{g_*}{100} \right)^{-\frac{1}{3}} \frac{\left(\frac{f}{f_{\text{turb}}} \right)^3 \left(1 + \frac{f}{f_{\text{turb}}} \right)^{-\frac{11}{3}}}{\left(1 + \frac{8\pi f}{h_*} \right)}. \quad (13.12)$$

The details of the parameters mentioned in Eqs. 13.6–13.12 can be found in [9].

13.3 Calculations and Results

In order to calculate the GW intensities we choose three sets of BPs (Table 13.1). The chosen BPs are consistent with the several theoretical bounds such as vacuum stability, perturbativity, and experimental bounds such as Large Hadron Collider (LHC) bounds, future generation collider bounds [10], PLANCK bound on the DM relic density and direct detection experimental bounds given by XENON-1T, PandaX-II, LUX, and DarkSide-50. Although here we do not elaborate the DM phenomenology part, but it is to be noted that the lightest inert particle H_0 plays the role of DM candidate in the present proposed model. To see the PT dynamics within the framework of our model we include the finite temperature effects with the tree-level potential and for that we use CosmoTransition package [8]. The FOPT parameters, i.e., v_n , T_n , α , β/H corresponding to each of the BPs are presented in Table 13.2 which are the essential parameters for the determination of GW spectrum. Using

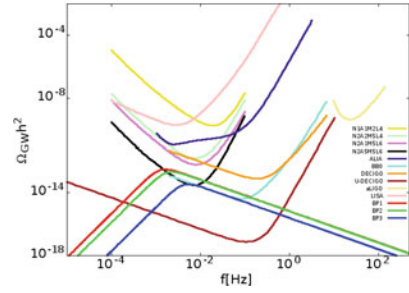
Table 13.1 The chosen three sets of BPs (BP 1–3) from the allowed model parameter space to describe the PT dynamics. (Reproduced from Avik Paul et al., JCAP 10 (2019) 062)

BP	m_{H_0} in GeV	m_{h_2} in GeV	v_s in GeV	$\sin \theta$	ρ_1 in GeV	ρ_3 in GeV	λ_L	λ_s	λ_2	$\Omega_{\text{DM}} h^2$	σ_{SI} cm^2
1	30	100	300	0.01	-3	0.01	0.001	0.0012	0.2	0.1220	9.41×10^{-48}
2	68	150	400	0.06	-7	0.2	0.002	0.033	0.031	0.1208	3.69×10^{-48}
3	76	200	500	0.03	-1	0.1	0.0016	0.0033	0.01	0.1195	3.56×10^{-48}

Table 13.2 The calculated FOPT parameters for the chosen three BPs. (Reproduced from Avik Paul et al., JCAP 10 (2019) 062)

BP	v_n in GeV	T_n in GeV	α	$\frac{\beta}{H}$
1	226.89	119.86	0.24	317.86
2	191.03	132.14	0.25	402.89
3	209.95	158.24	0.19	783.65

Fig. 13.1 Variation of GW intensities with frequencies for the chosen three BPs. (Reproduced from Avik Paul et al., JCAP 10 (2019) 062)



the computed values for the three BPs (Table 13.2) we estimate the GW intensities using the Eqs. 13.9–13.12 and compare the same with the sensitivity curves of future GW observatories such as LISA, eLISA, BBO, ALIA, DECIGO, U-DECIGO, and aLIGO. Figure 13.1 shows that our calculated GW intensities and peak frequencies lie within the detection limits of BBO, U-DECIGO, and eLISA (configuration—N2A5M5L6) detectors.

13.4 Summary and Discussions

In this work, we show that the considered inert doublet with an additional singlet scalar model can explain the production of GWs from the first-order EW phase transition. Within the framework of the model we choose three BPs from the allowed model parameter space to calculate the GW spectrum. Then we compared our calculated GW intensities with the future GW interferometers and found that our estimated signals lie within the detectable range of BBO, U-DECIGO, and eLISA.

References

1. B.P. Abbott et al., LIGO scientific and virgo. Phys. Rev. Lett. **116**, 061102 (2016)
2. E. Witten, Phys. Rev. D **30**, 272 (1984)
3. W. Chao, H.K. Guo, J. Shu, JCAP **09**, 009 (2017)
4. K. Kajantie et al., Phys. Rev. Lett. **77**, 2887 (1996)
5. A. Dutta Banik, D. Majumdar, Eur. Phys. J. C **74**, 3142 (2014)
6. P.A.R. Ade et al., Planck collaboration. Astron. Astrophys. **571**, A16, (2014)
7. C.J. Moore, R.H. Cole, C.P.L. Berry, Class. Quant. Grav. **32**, 015014 (2015)
8. C.L. Wainwright, Comput. Phys. Commun. **183**, 2006 (2012)
9. A. Paul, B. Banerjee, D. Majumdar, JCAP **10**, 062 (2019)
10. S. Profumo et al., Phys. Rev. D **91**, 035018 (2015)

Chapter 14

Collider Signatures of Multi-charged Fermions in the Framework of a Radiative Seesaw Model



Avnish

Abstract The tiny neutrino masses and non-zero mixings are among the most pressing physically observed phenomenons to motivate exploration beyond the framework of the Standard Model (SM). Here, we discuss a part of a collider testable radiative seesaw model explaining the generation of the tiny neutrino masses and mixings. This model's most remarkable feature is that it doesn't demand any Adhoc symmetry to be imposed except the SM symmetry group to avoid tree-level contributions in seesaws. The particle spectrum expanded with isospin doublet and singlet scalars and fermions of the TeV level mass scale to realize the Weinberg operator at 1-loop level results in multi-charged particles. Production, decay, and collider phenomenology of the doubly charged fermions were explored after putting constraints from the neutrino oscillation data and the absolute neutrino mass. The photo-production channel is also considered in addition to the Drell Yan channel for productions.

14.1 Introduction

The SM has been the best phenomenological model to explain the fundamental particles' interaction with great accuracy in the collider experiments. However, the tiny neutrino mass and mixing cast a daunting shadow over its completeness. We have studied a radiative neutrino mass generation model [1–3] and its associated collider phenomenology in the context of the LHC at 13 TeV. The SM particle spectrum enlarged to incorporate new scalars and fermions of the TeV scale to generate neutrino mass at one-loop level [1] with the Weinberg operator. The unique hypercharge assignment of new fields removes the usual requirement to impose Adhoc symmetries over the SM symmetry group. Being of the TeV scale, new particles can be produced and detected through their collider signatures at the LHC. In this proceeding, we are

Avnish (✉)

Institute of Physics, Sachivalaya Marg, Bhubaneswar 751005, India
e-mail: avnish@iopb.res.in

Training School Complex, Homi Bhabha National Institute, Anushaktinagar, Mumbai 400085, India

© The Author(s), under exclusive license to Springer Nature Singapore Pte Ltd. 2022
B. Mohanty et al. (eds.), *Proceedings of the XXIV DAE-BRNS High Energy Physics Symposium, Jatni, India*, Springer Proceedings in Physics 277,
https://doi.org/10.1007/978-981-19-2354-8_14

confining ourselves to the fermion part only. The involvement of Yukawa couplings in neutrino mass generation and the decay of new fermions constrain the parameter space with neutrino oscillation data. In [3], we have also explored the large ionization as well as 4-lepton plus missing energy channels to impose lower exclusion bounds over the mass of the new fermion.

14.2 The Model

The SM particle spectrum has been expanded with new $SU(2)_L$ singlet vector-like fermions (E_{α}^{++} , where $\alpha = 1, 2$ and 3) as well as a singlet scalar (k^{++}) and two doublet scalars ($\Phi_{\frac{3}{2}}$ and $\Phi_{\frac{5}{2}}$) to realize Weinberg operator at the 1-loop level. The gauge quantum numbers of exotic fields are as follows:

$G_{SM} = SU(3)_C \times SU(2)_L \times U(1)_Y$	
Fermions:	$E_{\alpha L(R)}^{++} \sim (1, 1, 2)$
Scalars:	$\Phi_{\frac{3}{2}} = \begin{pmatrix} \phi_{\frac{3}{2}}^{+++} \\ \phi_{\frac{3}{2}}^{++} \end{pmatrix} \sim (1, 2, \frac{3}{2}), \quad \Phi_{\frac{5}{2}} = \begin{pmatrix} \phi_{\frac{5}{2}}^{++++} \\ \phi_{\frac{5}{2}}^{+++} \end{pmatrix} \sim (1, 2, \frac{5}{2})$
	$k^{++} \sim (1, 1, 2)$

Apart from the SM and usual kinetic parts of lagrangian of new scalar/fermion fields, the relevant parts of the Yukawa lagrangian [3] are as follows:

$$\begin{aligned} \mathcal{L}_{\text{Yukawa}} \supset & m_E^{\alpha\beta} \overline{E_{\alpha}^{++}} E_{\beta}^{++} + y_{\frac{3}{2}}^{\alpha\beta} \overline{L_{\alpha L}} \Phi_{\frac{3}{2}} \left(E_{\beta L}^{++} \right)^C + y_{\frac{5}{2}}^{\alpha\beta} \overline{L_{\alpha L}} i\sigma_2 \Phi_{\frac{5}{2}}^* E_{\beta R}^{++} \\ & + y_k^{\alpha\beta} \overline{e_{\alpha R}} k^{--} (e_{\beta R})^C + \text{h.c.}, \end{aligned} \quad (14.1)$$

where C stands for charge conjugation, α and β are the generation indices, $y_{\frac{3}{2}} (y_{\frac{5}{2}})$ and y_k are Yukawa matrices and m_E is the mass matrix for the vector-like doubly charged fermions. Note, $y_{\frac{3}{2}} (y_{\frac{5}{2}})$ contributes to the neutrino mass, while y_k determines the phenomenology at the LHC by allowing the decay of the doubly charged scalars into a pair of SM charged leptons. The renormalizable scalar potential [3] is also expanded with the following phenomenologically important terms:

$$\begin{aligned} V(H, \Phi_{\frac{3}{2}}, \Phi_{\frac{5}{2}}, k^{++}) \supset & \mu \left(H^T i\sigma_2 \Phi_{\frac{3}{2}} \right) k^{--} + \mu' \left(H^\dagger \Phi_{\frac{5}{2}} \right) k^{--} \\ & + \lambda \left(H^T i\sigma_2 \Phi_{\frac{3}{2}} \right) \left(H^T \Phi_{\frac{5}{2}}^* \right) + c.c. \end{aligned} \quad (14.2)$$

The cubic and quartic terms in Eq. 14.2 play an important role in the generation of the neutrino mass and also determine the collider signatures of this model through the mixings among the doubly charged scalars, and the strength of mixing is determined by λ , μ , and μ' . The physical mass eigen-states [3] can be written as

$$H_a^{++} = O_{a1}\phi_{\frac{3}{2}}^{++} + O_{a2}\phi_{\frac{3}{2}}^{++} + O_{a3}k^{++} \tag{14.3}$$

where $a \ni 1, 2, 3$ and O_{ab} is an orthogonal diagonalization matrix.

14.3 Neutrino Masses at 1-loop level

The neutrino masses radiatively generated by the Wienberg operator with Feynman diagrams are depicted in Fig. 14.1. Yukawa couplings $y_{\frac{3}{2}}$ and $y_{\frac{5}{2}}$ violate lepton number conservation in this model [3] and also participate in the generation of Majorana masses of neutrino after the electro-weak symmetry breaking (EWSB). To correlate with neutrino oscillation data, a general parameterization [3] consisting PMNS matrix has been performed, which will reduce to usual Casas-Ibarra parameterization in the limit $y_{\frac{3}{2}} = y_{\frac{5}{2}}$. The parameter space of $(\mu - \lambda)$ has been scanned under the assumptions of $\mu = \mu'$ and $y_{\frac{3}{2}} = y_{\frac{5}{2}}$ to explore the consistent regions with the absolute neutrino mass bound. Only the absolute neutrino mass bound consistent parameters have been employed in further collider exploration.

14.4 Phenomenology of Doubly Charged Fermion

The collider signatures for the doubly charged fermion have been explored in the context of the LHC. For simplicity, only one generation is considered here. We consider only pair production as single production is very suppressed with tiny Yukawa coupling and heavy propagator. The pair production at the hadron colliders mainly occurs via quark- anti-quark initiated s channel Drell Yan processes mediated by a photon (γ) or Z -boson. Being electrically charged, pair production of $E^{\pm\pm}$ can be via photo-fusion (**PF**) ($\gamma\gamma \rightarrow E^{++}E^{--}$) process. The PF is a t/u channel process with a $E^{\pm\pm}$ propagator, hence not suppressed by the parton center-of-mass energy compared to the s -channel DY production. Additionally, being a doubly charged particle, the PF cross-section of $E^{\pm\pm}$ is enhanced by a factor of 2^4 at the Born level. We

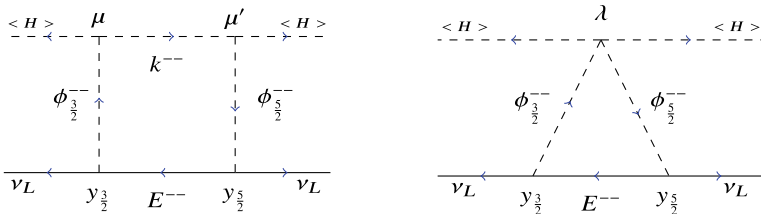


Fig. 14.1 Feynman diagrams generating neutrino masses at 1-loop level [3]

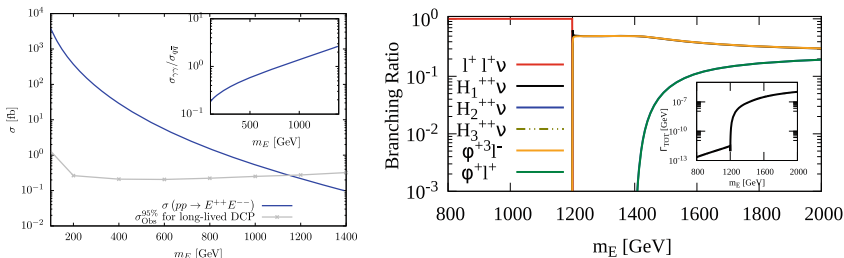


Fig. 14.2 (Left panel) the total ($\sigma_{q\bar{q}} + \sigma_{\gamma\gamma}$) production cross-section of $E^{\pm\pm}$ -pairs is shown with the ATLAS [5] observed 95% CL upper limit (grey line) on the pair production cross-section of long-lived doubly charged particles. Inlet shows the ratio of PF and DY contributions. (Right panel) Branching ratios shown for decay modes of E^{++} and inlet shows the total decay width as a function of mass of $E^{\pm\pm}$ (for more details [3])

have developed a parton-level Monte-Carlo event generator for the numerical evaluation of new particles' production and decay branching ratios. For parton density, the **NNPDF23LO** [4] parton distribution functions are employed with the factorization (μ_F) and renormalization scales being fixed at the subprocess center-of-mass energy.

Discussion on the decay profile of $E^{\pm\pm}$ is vital to determine the collider signatures at the LHC. Decay processes of $E^{\pm\pm}$ take place mainly through Yukawa interactions involving multi-charged scalars and the SM leptons. Being kinematically allowed, $E^{\pm\pm}$ decays via 2 body processes $E^{\pm\pm} \rightarrow \phi^{\pm} l^{\pm}, \phi^{3\pm} l^{\mp}$ and $H_a^{\pm} \nu_l$, where l includes all three generations of the SM leptons. However, on being kinematically forbidden to 2 body decays, $E^{\pm\pm}$ decays through 3 body decay with an off-shell doubly charged scalar to two same-sign leptons and a neutrino, $E^{\pm\pm} \rightarrow H_a^{\pm*} \nu_l \rightarrow l^{\pm} l^{\pm} \nu_l$. The pair production and decay branching ratios of $E^{\pm\pm}$ are shown in Fig. 14.2. At the colliders, $E^{\pm\pm}$ broadly gives two types of signatures depending upon the total decay width (Γ_{TOT}). For large decay width ($\Gamma_{TOT} > 10^{-13}$ GeV), $E^{\pm\pm}$ decays promptly and gives the SM leptons/jets and missing energy as collider signatures. However, for small decay width ($\Gamma_{TOT} < 10^{-16}$ GeV), $E^{\pm\pm}$ is long-lived and gives a very clean and the SM background free of large ionizing tracks at the detector. In the absence of such signatures at the LHC, the ATLAS [5] search has been used to put a bound on the pair production cross-section of $E^{\pm\pm}$ at 95% CL (Fig. 14.2), and it excludes the masses below 1150 GeV. For prompt decay of $E^{\pm\pm}$, we have studied the signature: $pp \rightarrow E^{\pm\pm} E^{\mp\mp} \rightarrow 4\text{-leptons} + \cancel{E}_T$ and new cuts [3] have been proposed. The ATLAS [6] search for 4-lepton plus missing energy has been applied to get a lower exclusion bound of 870 GeV on the mass of $E^{\pm\pm}$.

References

1. F. Bonnet, M. Hirsch, T. Ota, W. Winter, JHEP **07**, 153 (2012)
2. K. Cheung, H. Okada, Phys. Lett. B **774**, 446–450 (2017)

3. Avnish, K. Ghosh. [arXiv:2007.01766](https://arxiv.org/abs/2007.01766)
4. R.D. Ball et al., NNPDF. JHEP **04**, 040 (2015)
5. M. Aaboud et al. [ATLAS], Phys. Rev. D **99**(5), 052003 (2019)
6. M. Aaboud et al. [ATLAS], Phys. Rev. D **98**(3), 032009 (2018)

Chapter 15

Search for Dark Matter with a Leptoquark and Missing Transverse Energy in the Final State by Using Proton-Proton Collision Data of CMS Detector at LHC at 13 TeV



Bisnupriya Sahu and Bhawna Gomber

Abstract Leptoquarks are new bosons predicted by numerous extensions of standard model (SM), having both lepton and baryon number. In the final state for this particular dark matter (DM) search, the selected events should have at least one high transverse momentum p_T muon, one high p_T jet and large missing transverse momentum (MET). A new paradigm “coannihilation codex”, where dark matter particle will either annihilate or produce in conjunction with a coannihilation partner “X”, is used for the this analysis. A pair of scalar leptoquarks are produced, where one decays to a high p_T muon and a jet, and the other decays to dark matter and some undetected SM particles called “X”. The peak in the invariant mass distribution of the leptoquark, where it decays to highest p_T muon and jet, will give the signature of dark matter. The results will be presented using Run2 proton-proton collision data of the cms detector at LHC [1].

15.1 Introduction

The dark matter (DM) is one of a mysterious particle whose existence can be observed by evidences, such as rotational curve of galaxy, bullet clusters, anisotropies measurements in the cosmic microwave backgrounds (CMB) [2]. DM is undetectable through the detectors as they are weakly interacting and their production could be inferred from the observation of events with a sizable imbalance of transverse momentum called missing transverse momentum (MET).

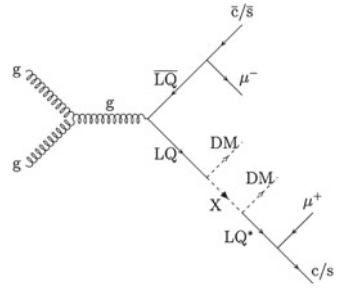
This particular search for DM is performed with a new approach called “Coannihilation codex” paradigm [3]. In this approach, the DM particle will be annihilated

Bhawna Gomber (for the CMS collaboration)

B. Sahu (✉) · B. Gomber
University of Hyderabad, Hyderabad 500049, India
e-mail: bisnupriya.sahu@cern.ch

© The Author(s), under exclusive license to Springer Nature Singapore Pte Ltd. 2022
B. Mohanty et al. (eds.), *Proceedings of the XXIV DAE-BRNS High Energy Physics Symposium, Jatni, India*, Springer Proceedings in Physics 277,
https://doi.org/10.1007/978-981-19-2354-8_15

Fig. 15.1 Feynman Diagram of signal, where “g” is gluon, “LQ” is leptoquark, “DM” is dark matter particle, “X” is new Dirac fermion and superscript “*” is off-shell particles [1]



or produced in conjunction with its coannihilation partner “X”. The equation for DM reaction at the LHC is given by $SM + SM \xrightarrow{M} DM + X$, where “SM” is standard model particles like quarks, gluons, leptons and “M” is mediator which can be a SM particle or a new physics particle. In this particular search “M”, the mediator is a leptoquark (LQ), is produced by pair production, where one LQ decays to a high p_T muon and a high p_T jet and the other decays to DM and X, which further decays to off shell DM and LQ. Fig. 15.1 shows the Feynman diagram of the process for the signal.

15.2 CMS Detector

The Compact Muon Solenoid (CMS) is one of the interesting collision point at the LHC. It is composed of a silicon pixel detector, a tracker, a electromagnetic calorimeter of lead tungstate ($PbWO_4$) crystals, a hadronic calorimeter of brass and plastic scintillator, all are inside a huge magnetic solenoid of 3.8 T magnetic field. A muon chamber of steel is outside of the solenoid detecting only the muon particles. CMS detector has two parts: barrel and endcap, depending on the pseudo-rapidity region $|\eta| < 1.479$ for barrel and $1.479 < |\eta| < 3.0$ for endcap for both electromagnetic and hadronic calorimeter. A detailed description of the CMS detector is in the [4].

15.3 Event Selection

The CMS detector consists of two-level trigger system to select interesting events. The first trigger is a hardware-based trigger, known as Level 1 (L1), The second trigger is software based, called high level trigger (HLT).

The trigger with one muon or a tracker muon $p_T > 50$ GeV is used in this analysis. The selected events will have one high momentum muon, one jet, and MET, at the final state. The muon should pass the tight identification criteria with $p_T > 60$ GeV

and pseudo-rapidity $|\eta| < 2.4$. The jet is required to pass loose jet identification criteria with $p_T > 100$ GeV and $|\eta| < 2.4$. The missing transverse energy (MET) is required to pass through all the MET filters and with the MET > 100 GeV. To discriminate signal from the background, an invariant mass distribution is considered with high p_T muon and a jet along with significant MET from the DM. For signal processes, the peak at the LQ mass, provides a striking signature in the search for signal processes containing DM. The details of event selection is in [1].

15.4 Analysis Strategy

The signal and background processes are generated by using Monte Carlo (MC) generator to validate the analysis, estimate the background, and determine the signal efficiency.

The signal events are generated by using MADGRAPH generator with the condition, that the mass splitting parameter $(\Delta_{X,DM}) \equiv \frac{m_{\chi} - m_{DM}}{m_{DM}} = 0.1$. The leading order (LO) LQ signal samples are generated with the mass of LQ (m_{LQ}) ranging from 800 to 1500 GeV with each steps 100 GeV. Similarly, the LO DM samples are simulated with its mass ranging from 300 to 700 GeV with steps of 50 GeV.

The SM processes such as W+jets, $t\bar{t}$ will be background, when W boson decay leptonically and produce a high p_T muon and a neutrino, which will be added in missing energy. Quantum chromodynamics (QCD) can be a background, if a quark semi-leptonically decays to a muon and a neutrino or if a jet is misidentified as muon with significant MET. The events with Z+jets will become background, when $Z \rightarrow \mu^+ \mu^-$ and one of the lepton could not be reconstructed, leading to MET.

W+jets and Z+jets events are generated using MADGRAPH generator at LO. POWHEG generator is used for the simulation of single top quark and $t\bar{t}$ events. The corrections of data and simulated events for both signal and background samples are made by applying scale factor (SF), where SF is the ratio of efficiency in the data to efficiency in MC.

15.5 Background Estimation

The W+jets background is estimated by applying a correction to normalization in W+jets control sample. The control samples have the W+jets events with 80 % purity and remaining from $t\bar{t}$. The SF is calculated by the ratio of events after the subtraction of non-W+jets events from the data to the events in simulated control region (CR). This is normalized with the same integrated luminosity. The SF for 2016 and 2017 data are calculated to be 1.02 (stat) and 1.11 (stat) with 1% error respectively.

The $t\bar{t}$ background is determined by a normalization of data-to-simulation SF in $t\bar{t}$ enriched control sample. In $t\bar{t}$ control sample, the events with $t\bar{t}$ is with purity 85%, whereas remaining are primarily events of single top quark and W+jets. The

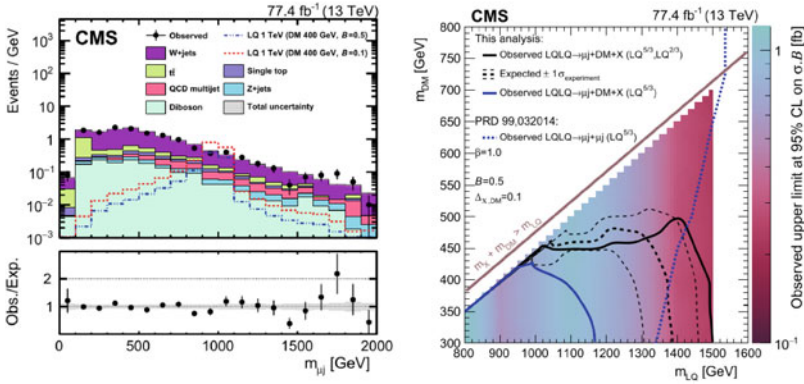


Fig. 15.2 The post fit $m_{\mu j}$ distribution of backgrounds of SM in (left) plot by the combined data of 2016 and 2017. The right plot shows the upper limits are calculated by the product of cross-section of signal and the branching fraction $B = 0.5$ at 95% confidential level (CL) [1]

SF, which is determined by subtracting the non- $t\bar{t}$ background from the data and compare between the data and the $t\bar{t}$ events, is 0.95 (stat) and 1.16 (stat) with 1% error in 2016 and 2017 data set respectively.

QCD background is expected to small and can be estimated by using a jet to muon fake rate (FR), which is the ratio of number of events pass the relative muon isolation < 0.15 to number of events without any isolation. The number of events, in numerator is with purity 25% and denominator with approximately 70% after the subtraction of non-QCD events is used in jet to muon FR.

15.6 Results

The $m_{\mu j}$ distribution in Fig. 15.2 is incorporated with the constraints from maximum likelihood fit. Two signal samples with m_{LQ} 1 TeV and m_{DM} 400 Gev with two different branching fraction $B = 0.5$ and 0.1 are shown. The upper limits are calculated by the product of cross-section of signal and the branching fraction at 95% confidential level (CL). In Fig. 15.2, the decay of LQ to DM and X is allowed under the solid diagonal line. In this particular analysis, the DM masses up to 300 and 500 GeV are excluded for LQ mass $\cong 1500$ and 1400 GeV respectively.

15.7 Summary

Dark matter search is performed with coannihilation process, where the mediator LQ pair is produced with significant MET by combining 2016 and 2017 proton-proton collision data of CMS detector at $\sqrt{s} = 13$ TeV with integrated luminosity 77.4

fb^{-1} . The results are well satisfying the SM predictions within uncertainty. DM masses up to 300 and 500 GeV are excluded for LQ mass \cong 1500 and 1400 GeV, respectively.

Acknowledgements Bhawna Gomber acknowledges the support from SERB, Government of India through Grant number SRG/2019/001046.

References

1. A.M. Sirunyan et al., CMS. Phys. Lett. B **795**, 76–99 (2019)
2. G. Bertone, D. Hooper, J. Silk, Phys. Rept. **405**, 279–390 (2005)
3. M.J. Baker et al., JHEP **12**, 120 (2015)
4. S. Chatrchyan et al., CMS. JINST **3**, S08004 (2008)

Chapter 16

Rediscovery of “wrong-sign” D^0 Decays with Belle II



Chanchal Sharma

Abstract In the standard model, mixing and CP violation in the charm sector are expected to be very small and thus they constitute a sensitive probe for potential new physics contributions. The “wrong-sign” decays $D^0 \rightarrow K^+\pi^-$, $D^0 \rightarrow K^+\pi^-\pi^0$ and $D^0 \rightarrow K^+\pi^-\pi^+\pi^-$ are among the best channels to study charm mixing, as they can be produced through two interfering processes: a direct doubly Cabibbo-suppressed decay of the D^0 meson, or through D^0 - \bar{D}^0 mixing followed by a Cabibbo-favored decay of the \bar{D}^0 meson. In this paper, a preliminary study of these three decays is presented and their signal yields are measured in early Belle II data.

16.1 Introduction

Neutral charm mesons can change their flavor and turn into antimesons, and vice versa, before they decay. This phenomenon is known as flavor oscillation or D^0 - \bar{D}^0 mixing [1]. Among the most sensitive channels to measure charm mixing and search for CP violation in D^0 - \bar{D}^0 oscillations are hadronic D^0 decays to “wrong-sign” (WS) final states, such as $D^0 \rightarrow K^+\pi^-$, $D^0 \rightarrow K^+\pi^-\pi^0$ and $D^0 \rightarrow K^+\pi^-\pi^+\pi^-$. To determine the production flavor, the neutral D mesons are typically restricted to those originating from the flavor-conserving strong-interaction decay $D^{*+} \rightarrow D^0\pi_s^+$. Throughout, the shorthand notations D^{*+} and π_s^+ are used to indicate the $D^*(2010)^+$ meson and the low-momentum pion (slow pion) from the D^{*+} decay, respectively. We denote as WS decays $D^{*+} \rightarrow D^0(\rightarrow K^+\pi^-, K^+\pi^-\pi^0, K^+\pi^-\pi^+\pi^-)\pi_s^+$, where the kaon and the slow pion π_s^+ have the same charge. These decays arise from the direct doubly Cabibbo-suppressed $D^0 \rightarrow K^+\pi^-, K^+\pi^-\pi^0, K^+\pi^-\pi^+\pi^-$ transitions and from the Cabibbo-favored decays $\bar{D}^0 \rightarrow K^+\pi^-, K^+\pi^-\pi^0, K^+\pi^-\pi^+\pi^-$ that follow D^0 - \bar{D}^0 oscillation. On the contrary, “right-sign” (RS) decays $D^{*+} \rightarrow$

Chanchal Sharma (for the Belle II Collaboration)

C. Sharma (✉)

Malaviya National Institute of Technology Jaipur, Jaipur 302017, India
e-mail: 2018rpy9026@mnit.ac.in

$D^0(\rightarrow K^-\pi^+, K^-\pi^+\pi^0, K^-\pi^+\pi^+\pi^-\pi_s^+)$, where the kaon and slow pion have opposite charge, are dominated by a Cabibbo-favored amplitude, thus offering negligible sensitivity to mixing. In the subsequent sections, the analysis of these three WS decays with the early Belle II data is discussed. Belle II [2] is the detector at the electron-positron collider SuperKEKB [3] and is the successor to the Belle experiment.

16.2 Analysis

The analysis uses $D^{*+} \rightarrow D^0\pi_s^+$ candidates reconstructed with early Belle II data corresponding to an integrated luminosity of 37.8 fb^{-1} . In this section, reconstruction and event selection for the decays, $D^0 \rightarrow K^\pm\pi^\mp$, $D^0 \rightarrow K^\pm\pi^\mp\pi^0$ and $D^0 \rightarrow K^\pm\pi^\mp\pi^+\pi^-$ are discussed.

16.2.1 $D^0 \rightarrow K^\pm\pi^\mp$

Candidate $D^0 \rightarrow K^\pm\pi^\mp$ decays are reconstructed using pairs of oppositely charged tracks that are in the Central Drift Chamber (CDC) acceptance ($17^\circ < \theta < 150^\circ$), are consistent with originating from the interaction point ($|dr| < 0.5 \text{ cm}$ and $|dz| < 2 \text{ cm}$), where dr and dz represent the distance of closest approach to the interaction point (IP) in the plane transverse to the beam direction and along the beam direction, respectively. These charged tracks are required to have at least one hit in the Silicon Vertex Detector (SVD), at least 30 hits in the CDC, and are identified as pions or kaons using particle-identification criteria ($\mathcal{L}_\pi/(\mathcal{L}_K + \mathcal{L}_\pi) > 0.3$) or ($\mathcal{L}_K/(\mathcal{L}_K + \mathcal{L}_\pi) > 0.3$), respectively, where \mathcal{L}_K and \mathcal{L}_π are the likelihoods of kaon and pion, respectively. The particle-identification requirements have a combined signal efficiency of $\approx 85\%$ for a doubly-misidentification rate of $\approx 2\%$, as evaluated on RS decays in data. The slow pion candidates satisfy the same criteria, except that they are only required to have one or more hits in the CDC. They are combined with the D^0 candidate to form a $D^{*+} \rightarrow D^0\pi_s^+$ decay. The D^{*+} candidates are fit using `Treefitter` [4] so that the D^{*+} decay vertex is consistent with the beam interaction point. To suppress candidate D^0 decays where the pion candidate is misidentified as a kaon and the kaon candidate is misidentified as a pion, the D^0 mass is computed with the ‘‘swapped’’ mass hypotheses on the final-state particles, which is required to be smaller than $1.85 \text{ GeV}/c^2$ or larger than $1.88 \text{ GeV}/c^2$. Such requirement is estimated to reduce the fraction of doubly misidentified decays in data to about 0.6% of the WS signal yield. Further, to suppress events where the D^0 candidate results from the decay of a beauty meson, the momentum of the D^{*+} in the e^+e^- center-of-mass system is required to exceed $2 \text{ GeV}/c$.

16.2.2 $D^0 \rightarrow K^\pm \pi^\mp \pi^0$

Candidate $D^0 \rightarrow K^\pm \pi^\mp \pi^0$ decays are selected using charged kaon and pion criteria identical to those used in the selection of the two-body modes. In addition, the π^0 candidate is reconstructed from two photons and the π^0 mass is required to be in the range $[0.12, 0.15] \text{ GeV}/c^2$. The `Treefitter` is now used with a mass constraint on the π^0 candidate and the “swapped” D^0 mass is required to be smaller than $1.81 \text{ GeV}/c^2$ or larger than $1.9 \text{ GeV}/c^2$. The fraction of the doubly misidentified decays resulting from the combined use of particle-identification and swapped mass requirements is estimated in data to be about 0.1% of the WS signal. The momentum of the π^0 candidate must be larger than $0.45 \text{ GeV}/c$ and the transverse momentum of the D^0 candidate must be larger than $2.5 \text{ GeV}/c$. All other criteria are the same as those for the two-body modes.

16.2.3 $D^0 \rightarrow K^\pm \pi^\mp \pi^+ \pi^-$

Candidate $D^0 \rightarrow K^\pm \pi^\mp \pi^+ \pi^-$ decays are reconstructed and selected with criteria identical to those used in the two-body modes except that the particle-identification requirement on the pions from the D^0 decay is loosened to $\mathcal{L}_\pi / (\mathcal{L}_K + \mathcal{L}_\pi) > 0.1$. The “swapped” mass requirement applied to both possible combinations of oppositely charged $K\pi$ tracks is smaller than $1.845 \text{ GeV}/c^2$ and larger than $1.88 \text{ GeV}/c^2$. The fraction of the doubly misidentified decays resulting from the combined use of particle-identification and swapped mass requirements is estimated in data to be about 1% of the WS signal. All other criteria are the same as those for the two-body modes.

16.3 Results and Conclusions

The signal yield is determined using an extended unbinned maximum-likelihood fit to Δm , which is defined as the difference between the masses of reconstructed D^{*+} and D^0 candidates, respectively denoted by $m(D^{*+})$ and $m(D^0)$. The Δm distribution is only for the candidates populating the D^0 mass signal region of the respective decays. The fit assumes a signal component parametrized as the sum of one Johnson S_U [5] and two Gaussian distributions. The background component is parameterized as

$$PDF_{bkg}(\Delta m) = (\Delta m - \Delta m_0)^{1/2} + \alpha(\Delta m - \Delta m_0)^{3/2}, \quad (16.1)$$

where Δm_0 is the kinematic threshold and α is a free parameter, which is determined by the fit. The fit is performed first on the RS sample, with all shape parameters

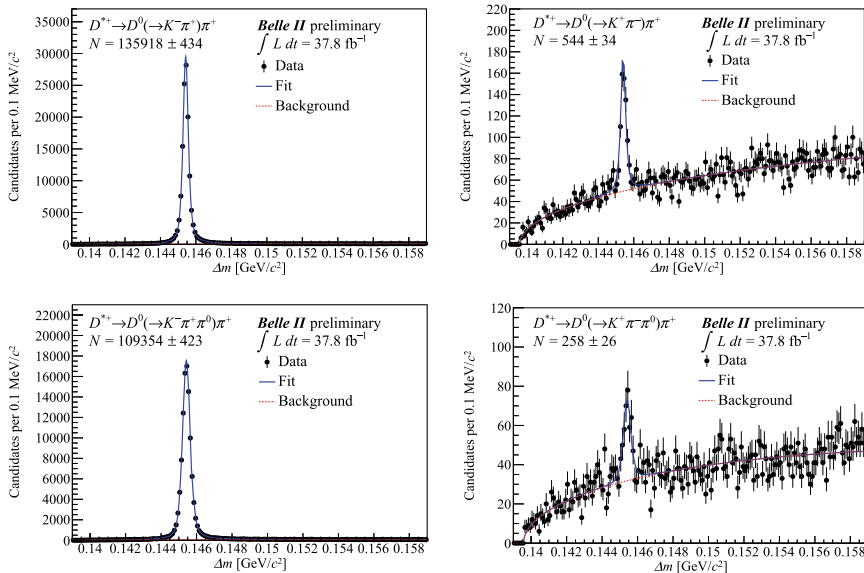
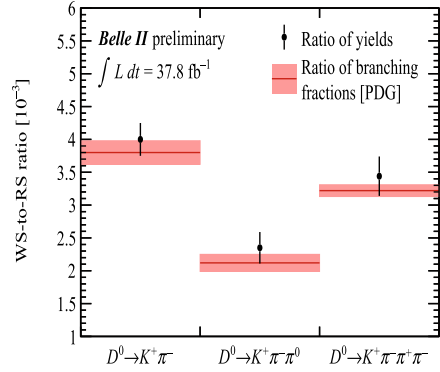


Fig. 16.1 Distribution of Δm for $D^0 \rightarrow K^- \pi^+$ RS (left) and $D^0 \rightarrow K^+ \pi^-$ WS (right) (top) and $D^0 \rightarrow K^- \pi^+ \pi^0$ RS (left) and $D^0 \rightarrow K^+ \pi^- \pi^0$ WS (right) (bottom). In all distributions, the signal candidates are reconstructed in data, with fit projections overlaid

left free. The signal shape parameters are then fixed in the subsequent WS fit to the values obtained from the RS sample.

To measure the signal yield for $D^0 \rightarrow K^\pm \pi^\mp$, we consider the Δm distribution in the signal region of D^0 mass defined as $1.85 \text{ GeV}/c^2 < m(D^0) < 1.88 \text{ GeV}/c^2$. The signal yields for the RS and WS samples are estimated to be 135918 ± 434 and 544 ± 34 , respectively. Here and elsewhere, the quoted uncertainties are statistical only. For $D^0 \rightarrow K^\pm \pi^\mp \pi^0$, the signal region of D^0 mass is defined as $1.84 \text{ GeV}/c^2 < m(D^0) < 1.88 \text{ GeV}/c^2$, while the signal yields for the RS and WS samples are estimated to be 109354 ± 423 and 258 ± 26 , respectively. For $D^0 \rightarrow K^\pm \pi^\mp \pi^+ \pi^-$, the signal region of D^0 mass, defined as $1.855 \text{ GeV}/c^2 < m(D^0) < 1.875 \text{ GeV}/c^2$, and the measured signal yields for the RS and the WS samples are 113254 ± 431 and 389 ± 35 , respectively. These results are shown in Fig. 16.1. It is observed that the RS sample is quite clean, while for the WS sample, there is a significant amount of combinatorial background and background coming from real D^0 combined with random slow pions. Also, the yields per unit of integrated luminosity are in agreement with or larger than the expectations based on previous Belle analysis [6, 7]. Assuming the same efficiencies for WS and RS decays, the ratios of their yields are also measured:

Fig. 16.2 Measured ratios (with statistical-only uncertainties) of wrong-sign (WS) to right-sign (RS) decay yields using data collected by Belle II



$$\frac{N(D^0 \rightarrow K^+ \pi^-)}{N(D^0 \rightarrow K^- \pi^+)} = (4.00 \pm 0.25) \times 10^{-3}, \quad (16.2)$$

$$\frac{N(D^0 \rightarrow K^+ \pi^- \pi^0)}{N(D^0 \rightarrow K^- \pi^+ \pi^0)} = (2.35 \pm 0.24) \times 10^{-3}, \quad (16.3)$$

$$\frac{N(D^0 \rightarrow K^+ \pi^- \pi^+ \pi^-)}{N(D^0 \rightarrow K^- \pi^+ \pi^+ \pi^-)} = (3.43 \pm 0.30) \times 10^{-3}. \quad (16.4)$$

The results are in agreement with the known values [1] as reported in Fig. 16.2. In the future, we may measure the D^0 - \bar{D}^0 mixing and CP violation from these decays at Belle II.

References

1. P.A. Zyla et al. [Particle Data Group] (2020) PTEP **2020**(8), 083C01 (2020)
2. E. Kou, et al. [Belle-II], PTEP **2019**(12), 123C01 (2019) [erratum: PTEP **2020**(2), 029201 (2020)]
3. K. Akai et al., SuperKEKB. Nucl. Instrum. Methods A **907**, 188–199 (2018)
4. J.F. Krohn et al., Belle-II analysis software Group. Nucl. Instrum. Methods A **976**, 164269 (2020)
5. N.L. Johnson, Biometrika **36**, 149–176 (1949)
6. L.M. Zhang et al., Belle. Phys. Rev. Lett. **96**, 151801 (2006)
7. X.C. Tian et al., Belle. Phys. Rev. Lett. **95**, 231801 (2005)

Chapter 17

Recent Measurement on the $B \rightarrow \mu^+ \mu^-$ Properties with CMS Data



Chandiprasad Kar

Abstract Rare decays of beauty mesons are an ideal place to search the effect of New Physics (NP) contributions by measuring decay rates and properties precisely. The decay of B_s^0 and B^0 mesons to two muons are highly suppressed in the Standard Model (SM) because of helicity and CKM suppression. The most recent studies from CMS collaboration and a combination of results from the ATLAS, CMS, and LHCb experiments, using the data collected at LHC between 2011 and 2016 are presented.

17.1 Introduction

The rare B_s^0 and B^0 meson decaying into a pair of muons are the propitious mode to search for an unseen physics effect. These decay modes are particularly interesting for the theoretician and experimentalist because the decay is forbidden at tree level in SM and only proceeds through the electroweak Z-penguin diagram and box diagrams. Additional suppression from CKM matrix element and helicity make the chance of these decay even rare. The critical observable of these decay are branching fraction of $B_s^0 \rightarrow \mu^+ \mu^-$ and $B^0 \rightarrow \mu^+ \mu^-$ and effective lifetime of the B_s^0 meson in $B_s^0 \rightarrow \mu^+ \mu^-$ mode. The combined analysis by CMS and LHCb [1] in the year 2013 led to the discovery of the decay $B_s^0 \rightarrow \mu^+ \mu^-$. The decay of $B^0 \rightarrow \mu^+ \mu^-$ has not been observed yet, but many experiments are performing the search with the latest available data. The effective lifetime is formulated by

$$\tau_{\mu^+ \mu^-} \equiv \frac{\int_0^\infty t \langle \Gamma(B_s^0(t) \rightarrow \mu \mu) \rangle dt}{\int_0^\infty \langle \Gamma(B_s^0(t) \rightarrow \mu \mu) \rangle dt} \equiv \frac{\tau_{B_s^0}}{1 - y_s^2} \left(\frac{1 + 2A_{\Delta\Gamma} y_s + y_s^2}{1 + A_{\Delta\Gamma} y_s} \right) \quad (17.1)$$

Chandiprasad Kar (for the CMS Collaboration)

C. Kar (✉)

National Institute of Science Education and Research, An OCC of Homi Bhabha National Institute, Bhubaneswar 752050, India
e-mail: chandiprasad.kar@gmail.com

where y_s and $A_{\Delta\Gamma}$ are sensitive to NP and defined by $\tau_{B_s^0} \Delta\Gamma_s/2$, and $-\mathcal{R}(\lambda)/(1 + |\lambda|^2)$, with $\lambda = (q/p)(A(\bar{B}_s^0 \rightarrow \mu^+\mu^-)/A(B_s^0 \rightarrow \mu^+\mu^-))$, respectively. The complex coefficient p and q define the mass eigenstates and $A(B_s^0 \rightarrow \mu^+\mu^-)$ ($A(\bar{B}_s^0 \rightarrow \mu^+\mu^-)$) is the B_s^0 (\bar{B}_s^0) decay amplitude. In the SM, only the heavy state decays to $\mu^+\mu^-$, but this condition does not necessarily hold in the case of physics beyond the SM. The SM foresees [2] $\mathcal{B}(B_s^0 \rightarrow \mu^+\mu^-) = (3.57 \pm 0.17) \times 10^{-10}$, $\mathcal{B}(B^0 \rightarrow \mu^+\mu^-) = (1.06 \pm 0.09) \times 10^{-10}$ and $\tau_{\mu^+\mu^-} = 1.615$ ps [3]. Details of the analysis are documented in [4].

17.1.1 Analysis Aspects

The signal decays $B_s^0 \rightarrow \mu^+\mu^-$ and $B^0 \rightarrow \mu^+\mu^-$ are reconstructed by searching for the two opposite charge muons having a common displaced vertex, and the invariant mass should peak around the PDG mass of $M(B_s^0)$ and $M(B^0)$. The backgrounds are separated into three different categories. The major contribution is the combinatorial background, which is coming from the two semi-leptonic B decays or one misidentified hadron and one semi-leptonic B decay. The second background is the rare semi-leptonic background composed of three-body decay, for example, $B \rightarrow K(\pi)\mu\mu$, and the final background is the rare peaking background from the two opposite charge hadrons, where the hadrons from a common B decay are misidentified as muon (e.g., $B \rightarrow \pi\pi, KK$). The peaking and semi-leptonic backgrounds are studied using the Monte-Carlo simulation, whereas combinatorial backgrounds are estimated using sideband data.

To achieve a better muon identification and suppress the larger peaking background from the hadron misidentification in $B^0 \rightarrow \mu^+\mu^-$ signal region, Boosted Decision Tree (BDT) is trained using the tracking and muon-related detector information from different detector subsystems. Further, the combinatorial backgrounds are suppressed by training a separate BDT using the numerous kinematic variables as an input. A few of the most potent variables are isolation variables of muon and B meson, pointing angle between the primary to secondary vertex direction, well reconstructed secondary vertex properties such as impact parameter, and transverse momentum of B meson. The two decay modes $B^+ \rightarrow J/\psi K^+$ as normalization channel and $B_s^0 \rightarrow J/\psi\phi$ as control channel are used to calibrate and validate the procedure. Depending upon the largest significance of the signal and smallest lifetime error, the analysis is performed in fourteen categories to evaluate the branching fraction and in eight categories to measure the effective lifetime.

The branching fractions for $B_{(s)}^0 \rightarrow \mu^+\mu^-$ are calculated using the formula,

$$\mathcal{B}(B_{(s)}^0 \rightarrow \mu^+\mu^-) = \frac{n_{B_{(s)}^0}^{obs} A_{B^+} \epsilon_{B^+}}{n_{B^+}^{obs} A_{B_{(s)}^0} \epsilon_{B_{(s)}^0}} \frac{f_u}{f_{s(d)}} \mathcal{B}(B^+ \rightarrow J/\psi K^+) \quad (17.2)$$

where $n_{B(s)}^{obs}$ and $n_{B^+}^{obs}$ are the number of observed yields of signal and normalization $B^+ \rightarrow J/\psi K^+$ decays, respectively. The product of acceptance times the selection and reconstruction efficiencies ($A_{B^+} \epsilon_{B^+}$ and $A_{B(s)} \epsilon_{B(s)}$) are calculated from the respective simulated samples. The ratio, $\frac{f_u}{f_s}$, accounts for the b-quark fragmentation fraction into B^+ and B_s^0 mesons. The value is $\frac{f_s}{f_u} = 0.252 \pm 0.012(\text{PDG}) \pm 0.015(\text{energy and } p_T \text{ dependence})$ [4].

17.1.2 Results

A 3D extended unbinned maximum likelihood (UML) fit to dimuon invariant mass $m_{\mu\mu}$, the relative mass resolution $\sigma(m_{\mu\mu})/m_{\mu\mu}$, and a dimuon bending configuration (either bending towards or away from each other) is carried out to extract both the branching fraction. The probability density function used to describe the invariant mass distributions is a Crystal Ball function for signal B_s^0 and B^0 where the width is scaled according to $\sigma(m_{\mu\mu})$; a Gaussian plus Crystal Ball function for the peaking background; a non-parametric kernel density estimator model for the semi-leptonic background; a first-order Bernstein polynomial for the combinatorial background. The fitted branching fractions are

$$\begin{aligned} \mathcal{B}(B_s^0 \rightarrow \mu^+ \mu^-) &= [2.9 \pm 0.7(\text{exp}) \pm 0.2(f_s/f_u)] \times 10^{-9} \\ \mathcal{B}(B^0 \rightarrow \mu^+ \mu^-) &= (0.8_{-1.3}^{+1.4}) \times 10^{-10} \end{aligned} \quad (17.3)$$

The observed (expected) significance, derived based on Wilk's theorem, for B_s^0 and B^0 decays are 5.6σ and 0.6σ (6.5σ and 0.8σ), respectively. The fit to dimuon invariant mass distribution along with likelihood contour are shown in Fig. 17.1. The observed results agree within the uncertainties with the SM predictions and the

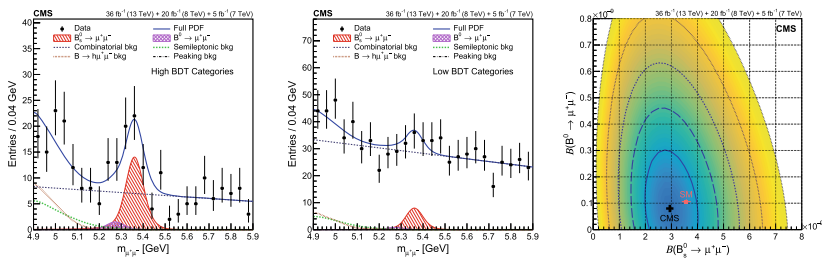


Fig. 17.1 Dimuon invariant mass distributions and the fit projections from the merged high-(low-) range analysis BDT categories for the branching fraction results are shown in the left(middle) plot. The solid blue line is the total fit. The hatched distribution corresponds to the $B_s^0 \rightarrow \mu^+ \mu^-$ and the broken lines represent the different background components. The likelihood contours (right plot) of the branching fraction fit for $\mathcal{B}(B_s^0 \rightarrow \mu^+ \mu^-)$ and $\mathcal{B}(B^0 \rightarrow \mu^+ \mu^-)$, with the SM expectation (red solid cross) and the best fit value (black cross)

previous CMS measurements. Since no excess of $B^0 \rightarrow \mu^+\mu^-$ signal is observed, the one-sided upper limit of branching fraction has been estimated using the CLs method. The result is $\mathcal{B}(B^0 \rightarrow \mu^+\mu^-) < 3.6 \times 10^{-10} (3.1 \times 10^{-10})$ at 95 (90%) confidence level (CL).

The measurement of the effective lifetime of the B_s^0 meson is performed in two independent procedures. A two-dimensional UML fit to the invariant mass and to the decay time is considered as a primary method and a 1D binned likelihood fit approach to the signal only decay time distribution extracted using sPlot technique as the secondary method. The fit model used in the primary method involves per event decay time uncertainty as a conditional parameter in the resolution model. The efficiency as a function of decay time is corrected to the signal shape. The weights used in the sPlot method are derived from the branching fraction fit. The effective lifetime is extracted with a modified exponential function which includes resolution and efficiency effects. A customized algorithm is used to measure the proper asymmetric uncertainties of the effective lifetime. The results are in agreement with each other as well as the SM expectation.

$$\tau_{\mu\mu}(2D \text{ fit}) = 1.70_{-0.44}^{+0.61} \text{ ps, and } \tau_{\mu\mu}(\text{sPlot fit}) = 1.55_{-0.33}^{+0.52} \text{ ps} \quad (17.4)$$

The total uncertainties are dominated by statistical uncertainties compared to the systematic uncertainties.

17.1.3 ATLAS, CMS, and LHCb Combined Analysis Result

A recent combined [5] analysis has been performed using binned two-dimensional likelihood obtained from the fit to dimuon invariant mass distributions from ATLAS, CMS, and LHCb experiments to measure branching fractions and effective lifetime. Each likelihood is fitted with analytic function in $\mathcal{B}(B_s^0 \rightarrow \mu^+\mu^-) - \mathcal{B}(B^0 \rightarrow \mu^+\mu^-)$ plane where both branching fractions are constrained to be positive. Due to the finite dimuon mass resolution between the $B_s^0 \rightarrow \mu^+\mu^-$ and $B^0 \rightarrow \mu^+\mu^-$ mass peak, the correlation between the two observables is accounted with a variable-width Gaussian. Then the sum of three binned log-likelihoods is fitted using a two dimensional variable-width Gaussian. The central value and uncertainties of the branching fractions are evaluated from the maximum. The resulting branching fraction are

$$\begin{aligned} \mathcal{B}(B_s^0 \rightarrow \mu^+\mu^-) &= (2.69_{-0.35}^{+0.37}) \times 10^{-9} \\ \mathcal{B}(B^0 \rightarrow \mu^+\mu^-) &= (0.6 \pm 0.7) \times 10^{-10} \end{aligned} \quad (17.5)$$

There is no substantial excess observed for $B^0 \rightarrow \mu^+\mu^-$ and an upper limit is calculated using the one-dimensional negative log-likelihood. The result is $\mathcal{B}(B^0 \rightarrow \mu^+\mu^-) < 1.6 \times 10^{-10} (1.9 \times 10^{-10})$ at 95 (90%) CL. The results are in agreement with SM at 2.4σ for $B_s^0 \rightarrow \mu^+\mu^-$ and 0.6σ for $B^0 \rightarrow \mu^+\mu^-$. Similarly, the upper

limit for the ratio of the branching fractions is measured to be $\mathcal{R} < 0.052(0.060)$ at 90 (95)% CL. The combined measurement on the effective lifetime is estimated to be $\tau_{\mu\mu} = 1.91^{+0.37}_{-0.35}$ ps [5] using the individual result from CMS and LHCb experiments. The effective lifetime is in agreement with SM predictions and the different experiments.

References

1. V. Khachatryan et al., CMS and LHCb. *Nature* **522**, 68–72 (2015)
2. M. Beneke, C. Bobeth, R. Szafron, *JHEP* **10**, 232 (2019)
3. Y. Amhis et al. [HFLAV], *Eur. Phys. J. C* **77**(12), 895 (2017)
4. A.M. Sirunyan et al., CMS. *JHEP* **04**, 188 (2020)
5. Combination of the ATLAS, CMS and LHCb results on the $B_{(s)}^0 \rightarrow \mu^+ \mu^-$ decays. CMS-PAS-BPH-20-003, LHCb-CONF-2020-002, ATLAS-CONF-2020-049
6. [CMS], CMS-PAS-BPH-20-003

Chapter 18

LHC Bounds on $R_{D^{(*)}}$ Motivated Leptoquark Models



Cyrin Neeraj, Arvind Bhaskar, Tanumoy Mandal, Subhadip Mitra, and Swapnil Raz

Abstract Most of the popular explanations of the observed anomalies in the semileptonic B -meson decays involve TeV scale Leptoquarks (LQs). Among the various possible LQ models, two particular LQs— $S_1(3, 1, 1/3)$ and $U_1(3, 1, 2/3)$ seem to be most promising. Here, we use current LHC data to constrain the $S_1(3, 1, 1/3)$ and $U_1(3, 1, 2/3)$ parameter spaces relevant for the $R_{D^{(*)}}$ observables. We recast the latest ATLAS $\tau\tau$ resonance search data to obtain new exclusion limits. For this purpose, we consider both resonant (pair and single productions) and non-resonant (t -channel LQ exchange) productions of these LQs at the LHC. For the limits, the most dominant contribution comes from the (destructive) interference of the non-resonant production with Standard Model backgrounds. The combined contribution from the pair and inclusive single production processes Mandal et al (JHEP, 07:028, 2015, [1]) is less prominent but non-negligible. The limits we get are independent and competitive to other known bounds. For both the models, we set limits on $R_{D^{(*)}}$ motivated couplings Mandal et al (Phys Rev D 99(5):055028, 2019, [2]), Bhaskar et al (Phys Rev D 104(3):035016, 2021, [3]).

18.1 Introduction

Leptoquarks (LQs) are colored bosons (scalar or vector) that can couple with Standard Model (SM) leptons and quarks. Some of them are well-suited candidates to account for the observed anomalies in the decays of the B -meson. At present, the data for the $R_{D^{(*)}}$ observables, defined as

C. Neeraj (✉) · A. Bhaskar · S. Mitra · S. Raz
Center for Computational Natural Sciences and Bioinformatics, International Institute of
Information Technology, Hyderabad 500 032, India
e-mail: cyrin.neeraj@research.iit.ac.in

T. Mandal
Indian Institute of Science Education and Research Thiruvananthapuram, Vithura
695 551, KL, India

© The Author(s), under exclusive license to Springer Nature Singapore Pte Ltd. 2022
B. Mohanty et al. (eds.), *Proceedings of the XXIV DAE-BRNS High Energy Physics
Symposium, Jatni, India*, Springer Proceedings in Physics 277,
https://doi.org/10.1007/978-981-19-2354-8_18

$$R_{D^{(*)}} = \frac{\mathcal{B}(B \rightarrow D^{(*)} \tau \bar{\nu})}{\mathcal{B}(B \rightarrow D^{(*)} \hat{\ell} \bar{\nu})} \quad (18.1)$$

show a combined excess of $\sim 3.1\sigma$ [4] than the Standard Model predictions. Here we consider two weak-singlet LQs—the scalar $S_1(\mathbf{3}, \mathbf{1}, -1/3)$ and the vector $U_1(\mathbf{3}, \mathbf{1}, 2/3)$. Both are popular candidates for explaining the $R_{D^{(*)}}$ anomalies in the literature.

Our objective in this study is to obtain precise exclusion limits on the parameter spaces of these LQs from LHC data that are complimentary to and independent of other known flavor bounds. We do this by recasting the latest LHC dilepton search results in the $\tau\tau$ channel [5]. We show that LHC is sensitive to the model parameters like the cross generational couplings that are needed to account for $R_{D^{(*)}}$.

18.2 The S_1 and U_1 Models, Relevant Processes

The Lagrangian for S_1 model looks like [2]

$$\mathcal{L} \supset [\lambda_{33}^L \bar{Q}_3^c (i\tau_2) L_3 + \lambda_{23}^L \bar{Q}_2^c (i\tau_2) L_3 + \lambda_{23}^R \bar{c}^c \tau_R] S_1^\dagger + H.c. \quad (18.2)$$

where $Q_\alpha(L_\alpha)$ denotes the α -th generation quark (lepton) doublet, λ_{ab}^X denotes the coupling of S_1 with an a^{th} generation quark and a lepton of generation b with chirality X . For the $R_{D^{(*)}}$ observables, the S_1 is required to couple with $b\nu$ and $c\tau$. This makes the scenario with only λ_{23}^R coupling non-zero inconsequential. Here, for illustration, we choose two minimal scenarios with either $\lambda_{23}^L \neq 0$ or $\lambda_{33}^L \neq 0$. In these scenarios, the one of the desired couplings are generated from the other via CKM mixing of the quarks. For U_1 , the interaction terms are given as [3]

$$\mathcal{L} \supset [\lambda_{23}^L \bar{Q}_2 \gamma_\mu P_L L_3 + \lambda_{33}^L \bar{Q}_3 \gamma_\mu P_L L_3 + \lambda_{33}^R \bar{b} \gamma_\mu \tau_R] U_1^\mu + H.c. \quad (18.3)$$

Here, the essential couplings for the $R_{D^{(*)}}$ observables are $c\nu U_1$ and $b\tau U_1$. We choose similar minimal scenarios (as S_1) to inspect the LHC bounds.

As mentioned above, we recast the latest $\tau\tau$ search data from ATLAS [5]. Here, we illustrate how various processes—both resonant (single production, pair production) and non-resonant (t -channel lepton exchange)—contribute to the $\tau\tau$ final state for S_1 (which puts no additional restriction on the extra jets). The case for U_1 can be argued similarly. When λ_{23}^L is non-zero, pair production of S_1 contributing to $\tau\tau$ final state is

$$pp \rightarrow S_1 S_1 \rightarrow c\tau c\tau \equiv \tau\tau + 2j \quad (18.4)$$

Single productions would also lead to the same final state [1]. The processes that contribute to the $\tau\tau$ final states are

$$pp \rightarrow \left\{ \begin{array}{l} S_1 \tau \rightarrow \tau j \tau \\ S_1 \tau j \rightarrow \tau j \tau j \\ S_1 \tau j j \rightarrow \tau j \tau j j \end{array} \right\} \quad (18.5)$$

These processes are combined using MLM matching to prevent double-counting. The $\tau\tau$ final state can also be produced via non-resonant processes (t -channel exchange of S_1). They interfere destructively with the SM background processes and have significantly higher cross sections than the resonant processes considered, especially for heavier LQs.

Similarly, we find processes contributing to $\tau\tau$ final states for each coupling and combine them systematically to obtain the total contributions from the model. We then recast it with the LHC $\tau\tau$ search data to obtain the latest bounds on each of the model parameters. For details of the recast, see [2, 3].

18.3 Results

In Fig. 18.1, we show the exclusion bounds obtained from the LHC dilepton data along with the $R_{D^{(*)}}$ favorable regions. We have also shown the limits from direct searches (obtained after recast, where necessary). The purple region shows the parameter space excluded with a CL of 95% by the $\tau\tau$ data. In Fig. 18.1b, since the LHC is insensitive to the λ_{33}^L coupling, the bounds on this scenario come only from the pair production searches. In Fig. 18.1a, c, the $R_{D^{(*)}}$ favored regions is completely ruled out by the LHC data. In the case of Fig. 18.1d, there is a minor region which is still allowed by the LHC data and also explains the $R_{D^{(*)}}$ observables.

18.4 Conclusions, Remarks

We see that the LHC is indeed sensitive to model specific parameters and hence, we use that fact to put constraints on the parameter space of the model specific couplings. The results shown above are the most updated and precise limits on the M_{LQ} - λ parameter space of both S_1 , U_1 models for the parameters considered. We find that the non-resonant interferes destructively with the SM and therefore has the most dominant contribution compared to all processes considered here, due to the SM background being large. In the minimal scenarios $R_{D^{(*)}}$, we find that almost most of the favorable regions are under stress by the limits from the LHC data.

The minimal scenarios considered above form only a subset of the possible coupling choices. We have considered scenarios with multiple couplings in [2, 3]. There we demonstrated a generic method to combine contributions from multiple couplings systematically to obtain parameter regions allowed by the dilepton data.

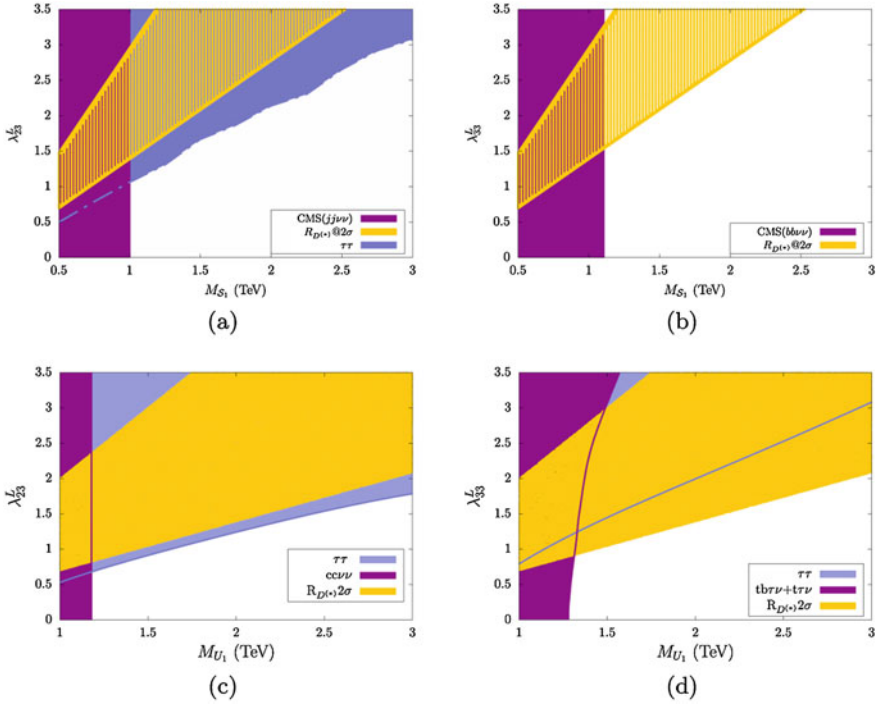


Fig. 18.1 The 2σ exclusion limits from the LHC and the preferred regions by the $R_{D^{(*)}}$ in the M_{LQ} - λ parameter space. The violet regions show the 2σ bounds from the LHC $\tau\tau$ data. The yellow region depicts the $R_{D^{(*)}}$ favored regions. The magenta regions are obtained by recasting the CMS pair production search data [6]. Plots on the top row show the bounds on S_1 parameter space—**a** Only $\lambda_{23}^L \neq 0$, **b** Only $\lambda_{33}^L \neq 0$. Bottom row plots show the bounds on U_1 parameter space—**c** Only $\lambda_{23}^L \neq 0$, **d** Only $\lambda_{33}^L \neq 0$. The magenta region here is obtained by recasting the CMS pair and single production process [7]

Acknowledgements A.B. and S.M. acknowledge support from the Science and Engineering Research Board, India, under grant number ECR/2017/000517. T.M. is supported by the intramural grant from IISER-TVM. C.N. is supported by the DST-Inspire Fellowship.

References

1. T. Mandal, S. Mitra, S. Seth, JHEP **07**, 028 (2015)
2. T. Mandal, S. Mitra, S. Raz, Phys. Rev. D **99**(5), 055028 (2019)
3. A. Bhaskar, D. Das, T. Mandal, S. Mitra, C. Neeraj, Phys. Rev. D **104**(3), 035016 (2021)
4. Y. Amhis et al. [HFLAV], Eur. Phys. J. C **77**(12), 895 (2017)
5. M. Aaboud et al., ATLAS, JHEP **01**, 055 (2018)
6. A.M. Sirunyan et al. [CMS], Phys. Rev. D **98**(3), 032005 (2018)
7. A.M. Sirunyan et al., CMS, Phys. Lett. B **819**, 136446 (2021)

Chapter 19

Probing Lepton-Number and Baryon-Number Violating Tau Decays at Belle



D. Sahoo, G. B. Mohanty, and K. Trabelsi

Abstract The standard model of particle physics accidentally conserves lepton number and baryon number. The Belle experiment at the KEKB asymmetric-energy e^+e^- collider provides an ideal platform to probe lepton number and baryon number violation in the decays of τ leptons. We report the results on a search for lepton number and baryon number violating decays $\tau^- \rightarrow \bar{p}e^+e^-$, pe^-e^- , $\bar{p}e^+\mu^-$, $\bar{p}e^-\mu^+$, $\bar{p}\mu^-\mu^+$, and $p\mu^-\mu^-$ using the data sample collected with the Belle detector.

19.1 Introduction

As lepton number (L) and baryon number (B) are accidental symmetries of the standard model (SM), there is no reason to expect them to be conserved in all possible particle interactions. To explain the matter-antimatter asymmetry observed in nature, the following three conditions formulated by Sakharov [1] must be satisfied.

1. B violation: does not yet have any experimental confirmation.
2. Violation of C (charge conjugation) and CP (combination of C with parity P): both phenomena have been observed.
3. Departure from thermal equilibrium.

Any observation of processes involving L and B violation would be a clear signal of new physics. Such processes are studied in different scenarios of physics beyond the SM like supersymmetry [2], grand unification [3], and models with black holes [4].

K. Trabelsi (for the Belle Collaboration)

D. Sahoo (✉) · G. B. Mohanty
Tata Institute of Fundamental Research, Mumbai, India
e-mail: sahoodev1994@gmail.com

D. Sahoo
Utkal University, Bhubaneswar, India

K. Trabelsi
Université Paris-Saclay, CNRS/IN2P3, IJCLab, Orsay, Paris, France

We report herein the results [5] on a search for six L and B violating decays: $\tau^- \rightarrow \bar{p}e^+e^-, pe^-e^-, \bar{p}e^+\mu^-, \bar{p}e^-\mu^+, \bar{p}\mu^-\mu^+,$ and $p\mu^-\mu^-$ [6] using 921 fb^{-1} of data, equivalent to $(841 \pm 12) \times 10^6 \tau^+\tau^-$ events, recorded with the Belle detector at the KEKB asymmetric-energy e^+e^- collider. Based on 1 fb^{-1} of pp collision data, LHCb [7] has studied the last two channels, setting 90% confidence-level (CL) upper limits on their branching fractions: $\mathcal{B}(\tau^- \rightarrow \bar{p}\mu^-\mu^+) < 3.3 \times 10^{-7}$ and $\mathcal{B}(\tau^- \rightarrow p\mu^-\mu^-) < 4.4 \times 10^{-7}$. Using experimental bounds on proton decay, authors in [8–10] predict a branching fraction in the range of 10^{-30} – 10^{-48} for these kinds of decays.

19.2 KEKB and Belle

Belle detector [11] was placed at an interaction point of the KEKB asymmetric-energy e^+e^- collider [12]. It was a large-solid-angle magnetic spectrometer comprising six subdetectors: silicon vertex detector, central drift chamber, aerogel Cherenkov counter, time-of-flight counter, CsI(Tl) crystal electromagnetic calorimeter, and K_L^0 and muon detector.

19.3 Analysis

We follow an unbiased data hidden analysis technique where the most interesting kinematic region or ‘signal region’ in data is kept hidden until our search strategy is fully developed.

19.3.1 Selection Criteria

At the preliminary level, we try to retain as much $e^+e^- \rightarrow \tau^+\tau^-$ events as possible in the sample while reducing obvious backgrounds by applying suitable selection requirements on different kinematic variables. At the next stage of selection, we apply a dedicated set of criteria to pick up candidate events that are more signal-like.

19.3.2 Reconstruction of τ Candidates

The τ lepton is reconstructed by combining a proton or an antiproton with two charged lepton candidates. To identify the signal, we use two kinematic variables: the reconstructed mass $M_{\text{rec}} \equiv \sqrt{E_{p\ell\ell'}^2 - \mathbf{p}_{p\ell\ell'}^2}$ and the energy difference $\Delta E \equiv E_{p\ell\ell'}^{\text{CM}} -$

$E_{\text{beam}}^{\text{CM}}$, where $E_{p\ell\ell'}$ and $\mathbf{p}_{p\ell\ell'}$ are the sum of energies and momenta, respectively, of the p , ℓ and ℓ' candidates. The beam energy $E_{\text{beam}}^{\text{CM}}$ and $E_{p\ell\ell'}^{\text{CM}}$ are calculated in the center-of-mass (CM) frame.

19.3.3 Sideband Study

We perform a sideband study to identify the sources of background that are dominated by events with a misidentified proton or antiproton, as well as to verify the overall agreement between data and simulation. Since we follow the unbiased data hidden analysis technique, before looking at data in the signal region, we estimate the background contribution in the signal region. For this, we choose a ΔE strip by hiding the signal region to predict the background expected in the signal region as shown in Fig. 19.1. The expected number of background events in the signal region is listed in Table 19.1 for all six channels.

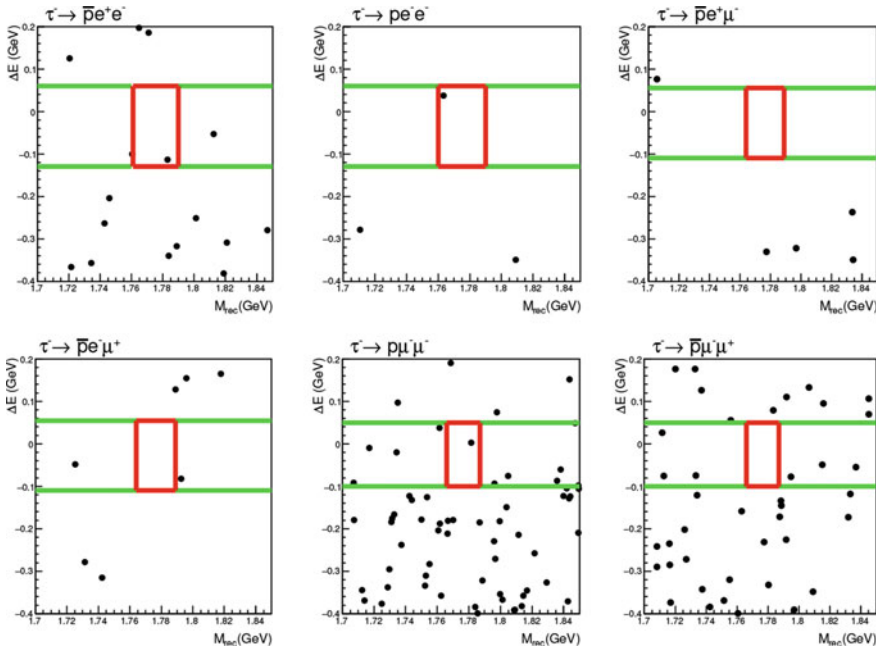


Fig. 19.1 ΔE - M_{rec} distribution where the red box denotes the signal region and the green ΔE strip is used to calculate the expected background in the signal region. Black dots represent the data

Table 19.1 Signal detection efficiency (ϵ), number of expected background events (N_{bkg}), number of observed data events (N_{obs}), 90% CL upper limits on the signal yield and branching fraction for various decay channels

Channel	ϵ (%)	N_{bkg}	N_{obs}	$N_{\text{sig}}^{\text{UL}}$	$\mathcal{B} (\times 10^{-8})$
$\tau^- \rightarrow \bar{p}e^+e^-$	7.8	0.50 ± 0.35	1	3.9	< 3.0
$\tau^- \rightarrow pe^-e^-$	8.0	0.23 ± 0.07	1	4.1	< 3.0
$\tau^- \rightarrow \bar{p}e^+\mu^-$	6.5	0.22 ± 0.06	0	2.2	< 2.0
$\tau^- \rightarrow \bar{p}e^-\mu^+$	6.9	0.40 ± 0.28	0	2.1	< 1.8
$\tau^- \rightarrow p\mu^-\mu^-$	4.6	1.30 ± 0.46	1	3.1	< 4.0
$\tau^- \rightarrow \bar{p}\mu^-\mu^+$	5.0	1.14 ± 0.43	0	1.5	< 1.8

19.3.4 Results

There is one event observed in data in each of the $\tau^- \rightarrow \bar{p}e^+e^-$, pe^-e^- , and $p\mu^-\mu^-$ channels as shown in Fig. 19.1. We find no events in the signal region in the case of $\tau^- \rightarrow \bar{p}e^-\mu^+$, $\bar{p}e^+\mu^-$, and $\bar{p}\mu^-\mu^+$. As the number of events observed in the signal region is consistent with the background prediction, we calculate an upper limit using the Feldman-Cousins method [13]. The 90% CL upper limit on the signal yield ($N_{\text{sig}}^{\text{UL}}$) is obtained with the POLE program [14] based on the number of observed data and expected background events, the uncertainty in background, as well as uncertainties in efficiency and number of τ pairs. We have set 90% CL upper limits on the branching fractions of these tau decays in the range of $(1.8 - 4.0) \times 10^{-8}$. In Table 19.1, we list results for all channels.

19.4 Summary

We report recent Belle results on L and B violating τ decays. In the case of $\tau^- \rightarrow p\mu^-\mu^-$ and $\bar{p}\mu^-\mu^+$, our limits are improved by an order of magnitude compared to LHCb [7]. For the remaining four channels, we set limits for the first time. These results would be useful in the current and future pursuits of baryon number violation.

References

1. A.D. Sakharov, JETP Lett. **5**, 24 (1967)
2. S.P. Martin, (1997). [arXiv:hep-ph/9709356](https://arxiv.org/abs/hep-ph/9709356)
3. H. Georgi, S.L. Glashow, Phys. Rev. Lett. **32**, 438 (1974)
4. J.D. Bekenstein, Phys. Rev. D **5**, 1239 (1972)
5. D. Sahoo et al., Belle collaboration. Phys. Rev. D **102**, 111101(R) (2020)
6. Inclusion of charge-conjugate processes is implied unless explicitly stated otherwise
7. R. Aaij et al., LHCb collaboration. Phys. Lett. B **724**, 36 (2013)

8. W.J. Marciano, Nucl. Phys. B, Proc. Suppl. **40**, 3 (1995)
9. W.-S. Hou, M. Nagashima, A. Soddu, Phys. Rev. D **72**, 095001 (2005)
10. J. Fuentes-Martin, J. Portoles, P. Ruiz-Femenia, JHEP **1501**, 134 (2015)
11. A. Abashian et al., (Belle Collaboration), Nucl. Instrum. Methods Phys. Res., Sec. A **479**, 117 (2002). Also see Section 2 in J. Brodzicka et al., Prog. Theor. Exp. Phys. **2012**, 04D001 (2012)
12. S. Kurokawa, E. Kikutani, Nucl. Instrum. Methods Phys. Res., Sec. A **499**, 1 (2003), and other papers included in this volume; T. Abe et al., Prog. Theor. Exp. Phys. **2013**, 03A001 (2013) and following articles up to 03A011
13. G.J. Feldman, R.D. Cousins, Phys. Rev. D **57**, 3873 (1998)
14. J. Conrad, O. Botner, A. Hallgren, C. Pérez de los Heros, Phys. Rev. D **67**, 012002 (2003); also see <https://github.com/ftegenfe/polepp> (updated version of the POLE program)

Chapter 20

aQGC Studies for WZ in the pp Collisions Using EFT Framework at the LHC



Geetanjali Chaudhary

Abstract Vector boson scattering (VBS) can be idealized as an interaction of gauge bosons radiated from initial state quarks, yielding a final state with two bosons and two jets ($VVjj$) where V can be W or Z bosons. These VBS processes are widely recognized as being the most sensitive to the effects of new physics, which can be described using the effective field theory (EFT) approach. In this paper, we discuss the implementation of the EFT dimension-eight operators in the study of VBS in the $pp \rightarrow WZjj$ channel. As a final state, two jets and three leptons in proton-proton collisions at $\sqrt{s} = 13$ TeV ($pp \rightarrow 2jets + WZ \rightarrow jjll'l'$ where $l = e, \mu$) are observed at the Large Hadron Collider (LHC). The data used are collected by the Compact Muon Solenoid (CMS) detector during Run II from the years 2016–2018 with an integrated luminosity of $137 fb^{-1}$. Results for the searches of the anomalous quartic gauge couplings (aQGC) in the electroweak WZ data sample for the full Run II are presented.

20.1 Introduction

The VBS searches have drawn a great deal of interest in theory and experimental communities in recent years. The study of VBS processes offers an opportunity for investigating the mechanism of electroweak symmetry breaking and looking for the new physics beyond the Standard Model (BSM) in the weak sector. The subject of such studies is typically the $VVVV$ quartic couplings. Without knowledge of the full BSM theory, its low energy effects can be effectively described by a series of operators in an effective field theory (EFT) approach [1], with a mass dimension larger than four to Lagrangian (L) in addition to the dimension-four operators in the SM Lagrangian L_{SM} .

Geetanjali Chaudhary (for the CMS Collaboration)

G. Chaudhary (✉)
Panjab University, Chandigarh 160014, India
e-mail: geetanjali.chaudhary@cern.ch

© The Author(s), under exclusive license to Springer Nature Singapore Pte Ltd. 2022
B. Mohanty et al. (eds.), *Proceedings of the XXIV DAE-BRNS High Energy Physics Symposium, Jaitni, India*, Springer Proceedings in Physics 277,
https://doi.org/10.1007/978-981-19-2354-8_20

$$L = L_{SM} + \sum_i f_i^{(6)} O_i^{(6)} + \sum_i f_i^{(8)} O_i^{(8)} + \dots$$

It is not possible to predict the energy scale Λ at which the potential new physics exists. Dimension-eight operators of the EFT alter the quartic vector boson couplings and induce an increase in the cross-section of the VBS processes that eventually leads to a breach of the unitarity condition at some energy scale. In the range of Wilson coefficients $f_i^{(8)} = C_i/\Lambda^4$ we can currently study at the LHC violation of unitarity occurring well within the maximum attainable range of the VV mass. As a result, the EFT formalism is often not used in a fully consistent manner. Until now, there has been no particular CMS convention to deal with this. Use of the EFT outside of its validity regions in an unphysical range can lead to significantly overestimated limits on BSM effects. This implies that if we are considering the regions where unitarity is not respected, it essentially means we are giving up on the physical interpretation of the Wilson coefficients. We quantify in terms of limits the significance of considering the proper EFT validity range in the analysis.

20.2 Data and Monte Carlo Samples

Multiple Monte Carlo (MC) event generators are used to simulate both signal and background processes for each year. The simulation of the aQGC processes using the MADGRAPH5_aMC@NLO [2] event generator and employing matrix element reweighting to obtain a finely spaced grid of parameters is done for each of the probed anomalous couplings. For all the generated processes, the detector response is simulated using a detailed description of the CMS detector based on the GEANT4 package [3]. For all events, reconstruction is performed using the same algorithms as those used for the data. Additionally, MC samples are created with additional interactions per bunch crossing (pileup). Three sets of simulated events are weighted so that the pileup distributions match the data taking conditions in the various years of data taking. The analysis is carried out with the full Run II dataset, of the proton-proton collision data collected by the CMS detector at the LHC in the years 2016-2018 at center-of-mass energy of 13 TeV. A detailed description of the data and simulated samples used in this analysis is given in [4].

20.3 Analysis Strategy

We select the signal from WZ events with a final state of two leptons from the Z boson, one lepton and a neutrino from the W boson along with VBS-like jets. There are many background processes, such as tri-bosons, ZZ , tZq , non-prompt, QCD WZ , wrong-sign, which can mimic the same final state of three leptons and one neutrino as the signal i.e. electroweak (EWK) WZ . The major background contri-

bution in this analysis is from QCD WZ . In addition to the WZ signal region (SR), four control regions (CRs) are defined to enhance non-prompt lepton, WZb , and ZZ background processes. By inverting some of the signal selection requirements [4] we can select background enriched CRs. A combination of data-driven methods and detailed simulation studies are carried out for estimating the backgrounds. The background processes estimated from the simulation are normalized to the best theoretical cross-section prediction. Kinematic selection cuts are applied along with VBS cuts to get signal events dominance over background events. After applying various kinematic selection [4] the WZ SR is dominated by QCD WZ events. A multivariate analysis (MVA) is performed to enhance WZ EWK production with respect to large WZ QCD production. This gives a good separation between the EWK signal and background. Statistical analysis is done by simultaneously fitting signal yields in WZ signal regions as well as background yields in control regions in order to assess normalization from the data. Statistical uncertainty is dominant in the measurements. We have considered a single dimension-eight operator at a time, assuming the other operators to be zero as in the case of SM. The most sensitive variable for WZ is full diboson transverse mass $m_T(WZ)$ (defined in [4]). Results are presented in terms of the observed and expected limits on the aQGC coefficients using a binned maximum-likelihood fit performed on the $m_T(WZ)$ distribution.

20.4 Correct Usage of EFT: Setting Limits on BSM

Since physics validity of the EFT expansion is restricted up to Λ which is derived from the requirement of unitarity (as a function of Wilson coefficients). Therefore, the lowest unitarity limit that is relevant to a given operator determines the maximum value of Λ . The unitarity limits are calculated using VBFNLO v1.4.0 [5]. In the case of WZ , for most of the dimension-eight operators, the lowest unitarity limits are driven by the $WW \rightarrow ZZ$ process. Therefore, in order to implement the EFT formalism in a correct manner, the kinematic range where the EFT is not valid should be excluded. It involves a high mass tail cut-off at the preselected value of Λ . In the case of a WZ where the full invariant mass is not measured experimentally (unless a technique is worked out to reliably resolve the quadratic ambiguity in the kinematics properties of the missing neutrino), one can apply such a cut-off only on the simulated data. The SM high mass tail is added to the simulation to compensate for the fact that the actual data collected by CMS may have additional input from the region above the Λ cut-off. This technique is known as “clipping” [6]. The region in which BSM physics is interpretable in the EFT framework leads to conservative bounds on the Wilson coefficients. In this analysis, partial “clipping” is used to calculate the limits on the individual dimension-eight operators. To compute the theoretical predictions, simulated samples were clipped at the respective unitarity limits, depending upon the value of each Wilson coefficient. This corresponds to the removal of a maximum of 50% of the simulated WZ events depending on the values of the Wilson coefficient. The CMS data and other SM background samples are left intact in this method.

Table 20.1 Observed and expected 95% CL limits on the coefficients for each single operator while keeping all others as zero using $m_T(WZ)$ as discriminant variable with and without clipping

Operator (TeV^{-4})	Observed limits without clipping	Expected limits without clipping	Observed limits with clipping	Expected limits with clipping
f_{T0}	[-0.62, 0.65]	[-0.82, 0.85]	[-1.65, 1.90]	[-2.0, 2.25]
f_{T1}	[-0.37, 0.41]	[-0.49, 0.55]	[-1.32, 1.54]	[-1.59, 1.81]
f_{T2}	[-1.04, 1.26]	[-1.41, 1.66]	[-2.73, 3.44]	[-4.42, 5.47]
f_{M0}	[-5.80, 5.80]	[-7.60, 7.60]	[-16.2, 16.1]	[-18.9, 18.8]
f_{M1}	[-8.20, 8.30]	[-10.8, 10.9]	[-19.1, 19.6]	[-23.3, 23.8]
f_{M6}	[-11.6, 11.6]	[-15.2, 15.2]	[-33.6, 33.4]	[-39.0, 38.6]
f_{M7}	[-10.4, 10.4]	[-13.8, 13.8]	[-22.2, 22.0]	[-28.2, 28.0]
f_{S0}	[-18.6, 18.8]	[-24.0, 24.3]	[-82.5, 85.4]	[-87.9, 91.1]
f_{S1}	[-30.1, 30.3]	[-38.3, 38.7]	[-107, 109]	[-122, 126]

Table 20.1 shows the observed and expected limits. As can be seen from the table, when considering unitarity, the limits are weaker than the case without considering unitarity by a factor of 4 to 5 depending on the parameter.

Although the unitarity-respecting limits are significantly weaker than those that disregard unitarity, they are more correct if we want the numbers to be interpretable in the EFT framework. This is the first time that “clipping” has been implemented in the CMS data analysis. Analysis of the full “clipping” method using full Run II data is currently underway. Such analysis techniques will serve as a model for future VBS analyses.

Acknowledgements We acknowledge in-depth discussions with Jan Kalinowski and Pawel Kozów of the University of Warsaw on implementing a newly developed clipping method based on EFT used for interpreting the CMS data reported in this work. The speaker acknowledges the Department of Science and Technology (DST) for the fellowship grant.

References

1. C. Degrande et al., *Ann. Phys.* **335**, 21–32 (2013)
2. J. Alwall et al., *JHEP* **09**, 028 (2007)
3. S. Agostinelli et al., *GEANT4. Nucl. Instrum. Methods A* **506**, 250–303 (2003)
4. A.M. Sirunyan et al., *CMS. Phys. Lett. B* **809**, 135710 (2020)
5. K. Arnold et al., *Comput. Phys. Commun.* **180**, 1661–1670 (2009)
6. J. Kalinowski et al., *Eur. Phys. J. C* **78**(5), 403 (2018)

Chapter 21

Analysis of Semileptonic Decays of Some b -baryons Within the SM and Beyond



C. P. Haritha and Barilang Mawlong

Abstract The observation of flavor anomalies in semileptonic B meson decays $\bar{B} \rightarrow D(D^*)l^-\bar{\nu}_l$ and $B_c \rightarrow J/\psi l^-\bar{\nu}_l$ motivates the study of similar decays mediated by $b \rightarrow cl\nu_l$ transitions at the quark level. In this work, we analyze some b -baryon decay modes $\Omega_b \rightarrow \Omega_c \tau^-\bar{\nu}_\tau$ and $\Xi_b \rightarrow \Xi_c \tau^-\bar{\nu}_\tau$, mediated by $b \rightarrow c\tau\nu_\tau$ transitions. We consider a general effective Hamiltonian which includes both standard model and new physics contributions, where new couplings are constrained using the experimental measurements of $R_{D^{(*)}}, R_{J/\psi}$ and $BR(B_c^+ \rightarrow \tau^+\nu_\tau)$. We study the effects of the new parameters on several observables such as the differential branching fraction, ratio of branching fractions, forward-backward asymmetry of the charged lepton and also longitudinal polarization of the charged lepton. Predictions for these observables within the standard model and in various new physics scenarios are presented here.

21.1 Introduction

The limitations of the standard model (SM) of particle physics has led to various new physics (NP) searches via both direct and indirect means. The observation of flavor anomalies in b -hadron decays represents one of the important indirect hints of beyond SM physics. There are a number of measurements of b -decay observables that disagree with the SM predictions. These discrepancies have been seen in b -decays mediated by $b \rightarrow cl^-\bar{\nu}_l$ transitions. Observables such as the ratio of branching ratios R_D and $R_{D^{(*)}}$, defined as $R_{D^{(*)}} = \frac{\mathcal{B}(\bar{B} \rightarrow D^{(*)} \tau^-\bar{\nu}_\tau)}{\mathcal{B}(\bar{B} \rightarrow D^{(*)} l^-\bar{\nu}_l)}$ have been found to violate lepton flavor universality. The present world average values [1] of $R_D^{E_{xpt}} = 0.340 \pm 0.027 \pm 0.013$ and $R_{D^{*}}^{E_{xpt}} = 0.295 \pm 0.011 \pm 0.008$ exceed their SM predictions [2] by 1.4σ and 2.5σ , respectively. LHCb has also measured the ratio $R_{J/\psi}$: $R_{(J/\psi)} = \frac{\mathcal{B}(\bar{B} \rightarrow (J/\psi) \tau^-\bar{\nu}_\tau)}{\mathcal{B}(\bar{B} \rightarrow (J/\psi) l^-\bar{\nu}_l)}$ = $0.71 \pm 0.17 \pm 0.18$ [3], showing about 2σ deviation from the SM prediction [4, 5]. These deviations hint the presence of NP beyond the SM and

C. P. Haritha (✉) · B. Mawlong
School of Physics, University of Hyderabad, Hyderabad 500046, India
e-mail: harithacp2010@gmail.com

motivates the study of similar decays mediated by $b \rightarrow c\tau^-\bar{\nu}_\tau$ transitions. In our work, we study and analyze the b -baryon decays $B_1 \rightarrow B_2\tau^-\bar{\nu}_\tau$ ($B_1 = \Omega_b, \Xi_b; B_2 = \Omega_c, \Xi_c$) following a model-independent approach.

21.2 Theoretical Framework

The most general effective Hamiltonian describing $b \rightarrow cl\nu_l$ transitions considering only left-handed neutrinos is given by [6]

$$\mathcal{H}_{eff} = \frac{4G_F}{\sqrt{2}} V_{cb} \left[(1 + C_{V_L}) O_{V_L} + C_{V_R} O_{V_R} + C_{S_R} O_{S_R} + C_{S_L} O_{S_L} + C_T O_T \right] + h.c., \quad (21.1)$$

where G_F is the Fermi constant, V_{cb} is the CKM matrix element, $O_{V_{L,R}} = (\bar{c}\gamma^\mu b_{L,R})(\bar{l}_L\gamma_\mu\nu_{lL})$, $O_{S_{L,R}} = (\bar{c}b_{L,R})(\bar{l}_R\nu_{lL})$ and $O_T = (\bar{c}\sigma^{\mu\nu}b_L)(\bar{l}_R\sigma_{\mu\nu}\nu_{lL})$ are fermionic operators with corresponding NP Wilson coefficients $C_{V_{L,R}}$, $C_{S_{L,R}}$ and C_T denoting vector, scalar and tensor type NP couplings, respectively. We consider only vector and scalar type of interactions for our analysis with NP couplings assumed to be real.

21.2.1 q^2 -dependent Observables

For the $B_1 \rightarrow B_2 l\bar{\nu}_l$ decay, the differential decay rate including the NP contributions can be written as

$$\frac{d\Gamma}{dq^2} = \frac{G_F^2 |V_{cb}|^2 q^2 |\mathbf{p}_{B_2}|}{192\pi^3 m_{B_1}^2} \left(1 - \frac{m_l^2}{q^2}\right)^2 \left[B_1 + \frac{m_l^2}{2q^2} B_2 + \frac{3}{2} B_3 + \frac{3m_l}{\sqrt{q^2}} B_4 \right], \quad (21.2)$$

where the form of the terms B_1 , B_2 , B_3 and B_4 can be found in [7]. Using (21.2), we can define other interesting q^2 -dependent observables such as differential branching fraction $DBR(q^2)$, ratio of branching fractions $R(q^2)$, forward-backward asymmetry of the charged lepton $A_{FB}^l(q^2)$ and longitudinal polarization of the charged lepton $P_L^\tau(q^2)$. The explicit expressions can be found in [8]. Here, we define $R(q^2)$ as the ratio of differential decay rate with τ in the final state to the differential decay rate with μ in the final state.

Table 21.1 Best-fit values of the NP couplings

NP Coupling	Best-fit value	1σ range
C_{V_L}	0.0714	[0.0460, 0.0961]
C_{V_R}	-0.053	[-0.0648, -0.0417]
C_{S_L}	0.0915	[0.0407, 0.1388]
C_{S_R}	-1.3409	[-1.3846, -1.2938]

21.3 Numerical Analysis and Discussion

Using the observables $R_{D^{(*)}}, R_{J/\psi}$ and $BR(B_c^+ \rightarrow \tau^+ \nu_\tau)$, we constrain the new couplings $C_{V_{L,R}}, C_{S_{L,R}}$ and obtain the allowed NP parameter space by imposing a 1σ constraint coming from the measured values of these observables [1, 3]. In this work, we take the experimental upper limit on $BR(B_c^+ \rightarrow \tau^+ \nu_\tau) < 30\%$ [9]. Considering one new coupling at a time, we find the best-fit values listed in Table 21.1 by performing a χ^2 fitting.

The q^2 -dependency of various observables for the decay modes $\Omega_b \rightarrow \Omega_c \tau^- \bar{\nu}_\tau$ and $\Xi_b \rightarrow \Xi_c \tau^- \bar{\nu}_\tau$ in the presence of different NP couplings are displayed in

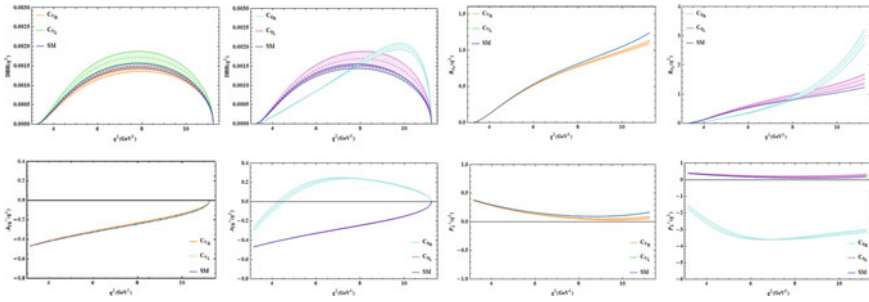


Fig. 21.1 The q^2 -dependency of various observables for the $\Omega_b \rightarrow \Omega_c \tau^- \bar{\nu}_\tau$ decay mode in the presence of vector and scalar NP couplings

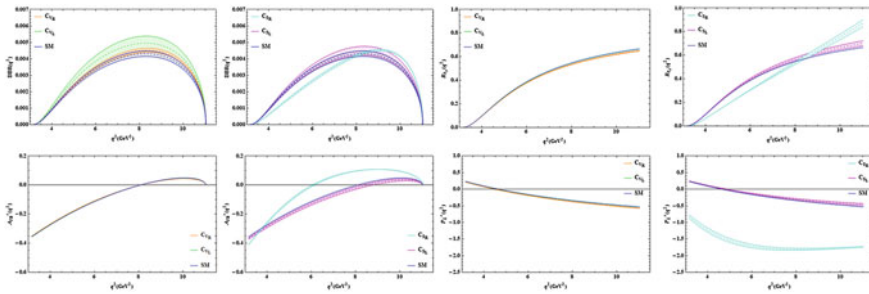


Fig. 21.2 The q^2 -dependency of various observables for the $\Xi_b \rightarrow \Xi_c \tau^- \bar{\nu}_\tau$ decay mode in the presence of vector and scalar NP couplings

Figs. 21.1 and 21.2, respectively. For both the decay modes, we observe a deviation from the SM prediction in case of the C_{V_L} coupling for $DBR(q^2)$ and for all the other observables, the behavior is SM-like as the NP dependency cancels out. For the C_{V_R} coupling, there is deviation from the SM prediction in each observable. The deviation is more pronounced in higher q^2 regions for $R_{\Omega_c}(q^2)$ and $P_L^\tau(q^2)$ for the $\Omega_b \rightarrow \Omega_c \tau^- \bar{\nu}_\tau$ decay mode. In case of the scalar coupling C_{S_L} , the deviation from the SM prediction is more prominent than that of the vector couplings. The effect of C_{S_R} coupling shows a completely different behavior from the SM prediction for each observable. $P_L^\tau(q^2)$ takes negative values in the whole q^2 region for both the decay modes. The forward-backward asymmetry $A_{FB}^l(q^2)$ shows a zero crossing at $q^2 \approx 4.3 \text{ GeV}^2$ for the $\Omega_b \rightarrow \Omega_c \tau^- \bar{\nu}_\tau$ decay mode. For the $\Xi_b \rightarrow \Xi_c \tau^- \bar{\nu}_\tau$ decay mode, the zero crossing of $A_{FB}^l(q^2)$ shifts to a lower q^2 region from the SM prediction.

21.4 Conclusion

In this work, we have analyzed the semileptonic decays $\Omega_b \rightarrow \Omega_c \tau^- \bar{\nu}_\tau$ and $\Xi_b \rightarrow \Xi_c \tau^- \bar{\nu}_\tau$ within the SM and beyond. We find that the observables of interest are sensitive to NP effects and we observe that the deviations from the SM prediction are more conspicuous in the case of scalar NP couplings than that of the vector NP couplings. This observation may be useful to determine the exact nature of the NP contributing to the observed anomalies. The b -baryon decay modes mediated by $b \rightarrow c l \nu_l$ can act as complementary decay channels to b -meson decays with regards to the search for NP.

References

1. Y. S. Amhis et al. [HFLAV], Eur. Phys. J. C **81**(3), 226 (2021)
2. Heavy Flavor Averaging Group Collaboration. <https://hflav-eos.web.cern.ch/hflav-eos/semi/spring19/html/RDsDsstar/RDRDs.html>
3. R. Aaij et al., LHCb. Phys. Rev. Lett. **120**, 121801 (2018)
4. W. Wen-Fei, F. Ying-Ying, X. Zhen-Jun, Chin. Phys. C **37**, 093102 (2013)
5. M.A. Ivanov, J.G. Korner, P. Santorelli, Rev. D **71**, 094006 (2005)
6. C. Murgui, A. Peñuelas, M. Jung, A. Pich, JHEP **09**, 103 (2019)
7. S. Shivashankara, W. Wu, A. Datta, Phys. Rev. D **91**, 115003 (2015)
8. X.Q. Li, Y.D. Yang, X. Zhang, JHEP **02**, 068 (2017)
9. A.G. Akeroyd, C.H. Chen, Phys. Rev. D **96**, 075011 (2017)

Chapter 22

Search for Compressed Mass Spectrum SUSY via Electroweak VBF in Single Lepton Final States Using LHC Run II Data Collected with CMS Detector at $\sqrt{s} = 13$ TeV



Harjot Kaur

Abstract A background estimation methodology for the search of supersymmetric electroweakinos ($\tilde{\chi}_{1\pm}^{\pm}, \tilde{\chi}_{2}^0$) produced in the vector boson fusion (VBF) topology in proton-proton collisions at $\sqrt{s} = 13$ TeV using the full Run II data collected by the Compact Muon Solenoid (CMS) detector at the Large Hadron Collider (LHC) is presented. The benchmark model for this search is the R-parity conserving Minimal Supersymmetric Standard Model (MSSM), focusing on compressed mass spectrum scenarios. The experimental signatures of the signal process involve two forward jets, large missing transverse momentum and one lepton. The dominant standard model background processes are estimated using data-driven techniques. In these proceedings, the background estimation techniques are presented, together with their validation.

22.1 Introduction

The Standard Model (SM) of Particle Physics explains the nature of fundamental particles and interactions between them. In spite of being a successful theory, SM fails to explain matter-antimatter asymmetry, the hierarchy problem, unification of fundamental forces, etc. Supersymmetry (SUSY) is one of the well-motivated theories beyond SM which addresses some of the shortcomings of SM. SUSY is a theoretical symmetry that connects the properties of bosons and fermions. SUSY provides a dark matter (DM) candidate in R-parity conserving models and is able to solve the

Harjot Kaur (for the CMS Collaboration)

H. Kaur (✉)
Panjab University, Chandigarh 160014, India
e-mail: harjot.kaur@cern.ch

© The Author(s), under exclusive license to Springer Nature Singapore Pte Ltd. 2022
B. Mohanty et al. (eds.), *Proceedings of the XXIV DAE-BRNS High Energy Physics Symposium, Jatni, India*, Springer Proceedings in Physics 277,
https://doi.org/10.1007/978-981-19-2354-8_22

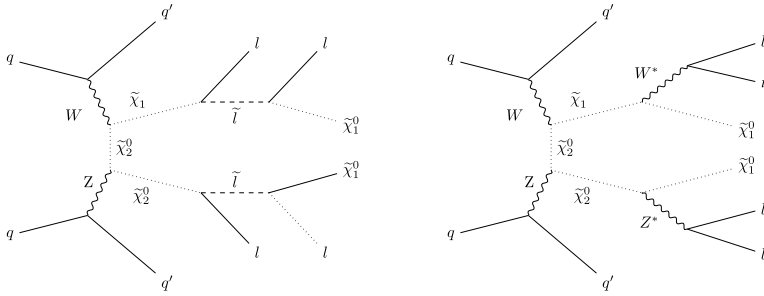


Fig. 22.1 Feynman diagrams for VBF production of chargino-neutralino with decays through sleptons (left) and virtual bosons (right)

gauge hierarchy problem of SM. This is why it is one of the most attractive models among physicists searching for experimental evidence of physics beyond the SM at the LHC. The masses of the strongly produced gluinos (\tilde{g}) and squarks (\tilde{q}) of the first and second generations have been excluded below approximately 2 TeV. The values of the masses of the weakly produced charginos ($\tilde{\chi}_i^\pm$) and neutralinos ($\tilde{\chi}_i^0$) are less constrained at the LHC where these particles have much smaller production cross sections. This electroweak sector of SUSY plays an important role in establishing a connection between SUSY models and the DM. The lightest neutralino, known as the lightest supersymmetric particle (LSP), is the canonical DM candidate in R-parity conserving SUSY models.

In these proceedings, the published results [1] are discussed focusing on SUSY searches with a compressed mass spectrum in the VBF [2] topology and also its underway extension using the pp collision data corresponding to the integrated luminosity of 137 fb^{-1} collected by the CMS [3] detector at $\sqrt{s} = 13 \text{ TeV}$. The final states considered have two jets, large missing transverse momentum and a single lepton. The jets are required to satisfy selection criteria of a VBF-like topology. Figure 22.1 shows the Feynman diagrams for VBF production of chargino-neutralino with decays through sleptons and virtual bosons. The benchmark model for this analysis is the R-parity conserving MSSM, focusing on compressed mass spectrum scenarios.

22.2 SM Background Processes

The SM processes which can mimic the signal process are considered as background processes. The SM background composition depends on the final state of each channel. For the μjj and $e jj$ channels, where μ , e and j denotes muon, electron and jet, respectively, the main backgrounds are from $t\bar{t}$ production and W boson production in association with jets (W +jets). Minor background processes are single top quark, diboson, Z +jets, etc. For the $\tau_h jj$ channel, where τ_h denotes a hadronically decaying tau lepton, the main source of background consists of SM events only containing jets produced via the strong interaction, referred to as quantum chromodynamics (QCD) multijet events, followed by W +jets and $t\bar{t}$ production.

Simulated samples of background events are generated using Monte Carlo (MC) event generators. These are produced with the leading order generators MADGRAPH (MG5), POWHEG and PYTHIA 8.

22.3 Event Selection

Different event selection criteria are applied on the final state particles (μ , e and τ_h). The total set of selections is divided into two parts: central selections and VBF selections. Central selections are composed of lepton selection, identification and requirements of missing transverse energy (MET). The compressed mass spectrum SUSY models considered result in final states with multiple leptons. These also result in visible decay products with low transverse momentum (p_T), making it difficult to reconstruct and identify multiple leptons. Due to this constraint, events with one low p_T lepton are considered. The requirement of high MET (p_T^{miss}) is motivated by the presence of LSP's in the final state of the decay chain of SUSY particles. The transverse mass ($m_T(\mu, p_T^{\text{miss}})$) cut is applied for suppression of the W +jets background. The VBF signal topology is characterized by the presence of two jets in the forward direction, in opposite detector hemispheres, and with large dijet invariant mass. Additionally, the outgoing partons in VBF signal processes must carry relatively large p_T to produce a pair of heavy SUSY particles.

22.4 Background Estimation Strategy

The general methodology used for the estimation of background contributions in the signal region (SR) is similar for all search channels and is based on both simulation and data. Background-enriched control regions (CR) are constructed by applying selections orthogonal to those for the SR. These CRs are used to measure the scale factors (SF) that are then applied to the MC yields to correct for any mismodeling. The idea is that these CRs should have a high purity of the background in consideration and a negligible contribution from signal. The data-to-MC correction factors are evaluated from two CRs. CR1 is used for the central selections and CR2 for the VBF selections. CR2 has to be orthogonal to CR1 and SR. To achieve this, we choose a “variable” that enriches the background process, but at the same time, the inverted requirement on that variable allows to arrive at the SR. We use the following equation to estimate the surviving background yields in the SR:

$$N_{\text{BG}}^{\text{Data}} = N_{\text{BG}}^{\text{MC}}(\text{SR}) \cdot \text{SF}^{\text{CR1}} \cdot \text{SF}^{\text{CR2}} \quad (22.1)$$

where $N_{\text{BG}}^{\text{MC}}(\text{SR})$ is the predicted yield in MC simulation after applying SR selections, SF^{CR1} is the correction factor for the central selections and SF^{CR2} is the correction factor for the VBF requirements obtained from CR2.

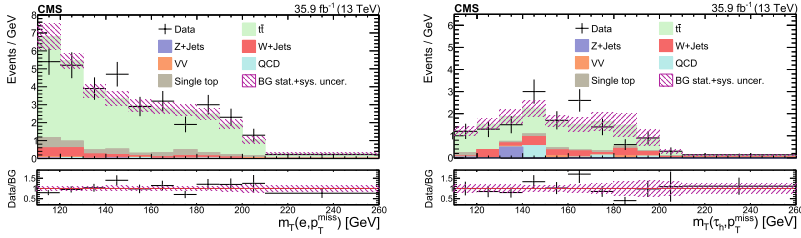


Fig. 22.2 The m_T distributions for the $t\bar{t}$ CR1 for e (left) and τ_h (right) channel [1]

The $t\bar{t}$ CR is obtained with similar selections to the SR, except requiring one jet tagged as a b quark jet. The one b -tagged jet requirement significantly increases the $t\bar{t}$ purity of the control samples while still ensuring that those control samples contain the same kinematics and composition of misidentified leptons as the SR. To obtain a SF for central selections, CR1 is formed by acquiring exactly one b -tagged jet and inverting the VBF selections. Figure 22.2 shows the m_T distributions for the $t\bar{t}$ CR1 for e (left) and τ_h (right) channels for the 2016 data set. CR2 is formed by requiring exactly one b -tagged jet and the VBF selections. This CR2 is used to extract the SF for VBF selections.

The production of W +jets events presents another important source of background for all the search channels. The first W +jets control sample is selected with similar selections to the signal region, except that the VBF requirement is inverted. This control sample (CR1) is used to obtain a correction factor for the central selections. To obtain the SF for the VBF selection, we use the fact that the masses of the Z and W bosons are relatively close. So, we pick two muons to reconstruct the Z mass by requiring two opposite sign muons with $p_T > 30$ GeV/ c , a dimuon mass between 60 and 120 GeV/ c^2 , and all the central cuts. With these selections, we obtain an enriched sample of $Z \rightarrow \mu\mu$. The VBF efficiency measured in $Z(\rightarrow \mu\mu)$ +jets events is used to make conclusions about the VBF efficiency in $W(\rightarrow l\nu)$ +jets events. First, however, we need to validate the correct calibration of the dimuon identification efficiency $\epsilon(\mu\mu)$ in order to ensure that only the VBF efficiency is dominating the level of agreement in CR2. Therefore, before studying CR2, we define a “standard candle” the Z control sample, CR3, with inverted VBF selections. Now, to study the VBF cut efficiencies and VBF shapes, CR2 Z control sample is defined by maintaining the VBF selections. Minor backgrounds are obtained directly from simulation.

22.5 Summary

A methodology is presented for the search of non-colored supersymmetric particles produced in the VBF topology. The VBF topology is a powerful and complementary tool to search for new physics such as compressed mass spectrum SUSY at the LHC. This particular topology reduces SM backgrounds significantly, while keeping large

signal acceptance. The search was performed in single lepton + VBF jets + MET final states using full Run 2 data collected with the CMS detector in proton-proton collisions at $\sqrt{s} = 13$ TeV. This search utilizes events in three different channels depending on the type of leptons: e_{jj} , μ_{jj} , and τ_{hjj} , where τ_h denotes a hadronically decaying τ lepton. The transverse mass distribution and event yields will be utilized to search for the EWKinos with a compressed mass spectrum in the VBF topology.

References

1. A.M. Sirunyan et al., CMS. JHEP **08**, 150 (2019)
2. B. Dutta et al., Phys. Rev. D **91**(5), 055025 (2015)
3. S. Chatrchyan et al., CMS. JINST **3**, S08004 (2008)

Chapter 23

New Physics Effects in $b \rightarrow sll$ Decays



Ipsita Ray

Abstract We perform a data-driven analysis of new physics (NP) effects in exclusive $b \rightarrow s\ell^+\ell^-$ decays in a model-independent effective theory approach with dimension-six operators with the corresponding Wilson coefficients (WC) taken to be complex. We find that a left-handed quark current with vector muon coupling is the only one-operator (\mathcal{O}_9) scenario that can explain the data in both the cases with real and complex WC with a large non-zero imaginary contribution. From the simultaneous application of model selection tools like cross-validation and information-theoretic approach like Akaike Information Criterion (AIC) to find out the operator or sets of operators that can best explain the available data in this channel, we find that \mathcal{O}_9 with complex WC is the only one-operator scenario which survives the test. However, there are a few two and three-operator scenarios (with real or complex WCs) which survive the test, and the operator \mathcal{O}_9 is common among them.

23.1 Introduction

In the last few years, a lot of attention, both experimental and theoretical, has been given to $b \rightarrow s\mu^+\mu^-$ decays. These modes are potentially sensitive to new physics (NP) since the corresponding Standard Model (SM) contributions are loop suppressed. In $B(B_s) \rightarrow K^*(\phi)\mu\mu$ decays, plenty of NP-sensitive observables (viz., CP-averaged, CP-asymmetric and optimized angular observables) have been measured by the ATLAS [1], LHCb [2], Belle and CMS collaborations in different q^2 -bins. A few angular observables have shown deviations from their respective SM predictions, the most interesting one being P'_5 . Very recently, LHCb have updated their results on CP-averaged angular observables with better statistics. The data on P'_5 shows a deviation of $\sim 3\sigma$ [3]. The source of these discrepancies could be the presence of one or more new interactions beyond the SM or due to poorly understood hadronic effects. Furthermore, these decay modes offer theoretically clean observ-

I. Ray (✉)

Indian Institute of Technology Guwahati, 781039 Guwahati, Assam, India
e-mail: ipsitaray02@gmail.com

ables like $R_{K^{(*)}} = \frac{Br(B \rightarrow K^{(*)} \mu^+ \mu^-)}{Br(B \rightarrow K^{(*)} e^+ e^-)}$ and $R_K = \frac{Br(B \rightarrow K \mu^+ \mu^-)}{Br(B \rightarrow K e^+ e^-)}$, which are useful to test lepton-flavor-universality violation (LFUV). In this work, we have considered the contribution of different types of NP interactions (like vector, axial vector, scalar, etc.) with complex Wilson coefficients to explain the data.

23.2 Theory

At the low-energy scale ($\mu \approx m_b$), the effective Hamiltonian for exclusive $b \rightarrow s \mu^+ \mu^-$ decays is written as [4]:

$$\mathcal{H}_{\text{eff}} = -\frac{4G_F}{\sqrt{2}} V_{tb} V_{ts}^* \left[\sum_{i=1\dots 6} C_i \mathcal{O}_i + \sum_{i=7,8,9,10,S,P} (C_i \mathcal{O}_i + C'_i \mathcal{O}'_i) \right] + h.c. \quad (23.1)$$

The relevant WCs in our analysis are the following: C'_7 , ΔC_9 , C'_9 , ΔC_{10} , C'_{10} , $C_S^{(\prime)}$, and $C_P^{(\prime)}$.

The amplitude and the corresponding rate distributions in $B(B_s) \rightarrow K^*(\phi) \mu \mu$ decays are defined using the hadronic form factors computed in full QCD. The SM WCs \tilde{C}_7 , \tilde{C}_9 and \tilde{C}_{10} are taken at next-to-next-to-leading logarithmic (NNLL) approximation, the details of which are provided in [5]. When the final state contains a vector meson, one can construct various helicity/transversity amplitudes like $A_{\perp L,R}$, $A_{\parallel L,R}$, $A_{0L,R}$, etc., which are then used to form angular coefficients relevant in defining the CP-symmetric and asymmetric observables measured by the various experimental collaborations.

23.3 Analysis and Results

In this analysis, we consider measurements of branching fractions, isospin asymmetries, angular observables for various exclusive $b \rightarrow s$ decays and also the ratios R_K and R_{K^*} available from different experimental collaborations as stated earlier amounting to total of 224 observables.

First, we check whether each of the new operators can independently explain the present data. To do so, we perform a frequentist statistical analysis optimizing a χ^2 statistic which is a function of the relevant WCs. With all data, we obtain a poor fit for all the cases. Hence, we drop a few data points in order to get a fit with allowed p -values and note that \mathcal{O}_9 is the only one-operator scenario capable of explaining the present data. Table 23.1 shows the results of the fits corresponding to \mathcal{O}_9 only. In all other one-operator scenarios, the quality of fits is very poor, with the respective p -values ≈ 0 .

As seen from Table 23.1, in all the three fit scenarios, with and without the CP-symmetric observables, a considerable value of $Im(\Delta C_9)$ is allowed. Here, we

Table 23.1 Fit results of the frequentist analysis with all data in one-operator (\mathcal{O}_9) scenarios with real and complex WCs. The cases without the CP-asymmetric observables in $B_s \rightarrow \phi\mu\mu$, and with the CP-asymmetric observables in $B \rightarrow K^*\mu\mu$ are presented separately

Fit scenario: Likelihood dataset 2020			Likelihood dataset 2020: without CP-asymmetric observables in $B_s \rightarrow \phi\mu\mu$		
χ^2_{Min}/DOF	p -value (%)	Confidence intervals	χ^2_{Min}/DOF	p -value (%)	Confidence intervals
206.5/211	57.4	$Re(\Delta C_9) \rightarrow -1.05 \pm 0.11$	198.2/199	50.2	$Re(\Delta C_9) \rightarrow -1.05 \pm 0.11$
202.9/210	62.5	$Re(\Delta C_9) \rightarrow -1.10 \pm 0.11$	194.9/198	54.8	$Re(\Delta C_9) \rightarrow -1.11^{+0.13}_{-0.12}$
		$Im(\Delta C_9) \rightarrow 1.27^{+0.33}_{-0.43}$			$Im(\Delta C_9) \rightarrow -1.36^{+0.44}_{-0.34} \cup [0.84, 1.59]$

Fit scenario: Likelihood dataset 2020 + CP-asymmetric observables in $B \rightarrow K^*\mu\mu$ from

LHCb Likelihood dataset 2016

χ^2_{Min}/DOF	p -value (%)	Confidence intervals
239.8/246	60	$Re(\Delta C_9) \rightarrow -1.06 \pm 0.11$
238.1/245	61.2	$Re(\Delta C_9) \rightarrow -1.09 \pm 0.11, Im(\Delta C_9) \rightarrow -1.11^{+0.62}_{-0.40}$

have found some observables which are responsible for the large imaginary contribution in ΔC_9 which are: $F_L(B^0 \rightarrow K^{*0}\mu^+\mu^-)^{[0.1,0.98]}$, $A_{FB}(B^0 \rightarrow K^{*0}\mu^+\mu^-)^{[2.5,4]}$, $P'_5(B^0 \rightarrow K^{*0}\mu^+\mu^-)^{[0.1,0.98]}$ and $R_{K^+}^{[1,6]}$, respectively.

It is tempting to look for other possible combinations of \mathcal{O}_9 with the potential to explain the present data. In the future, more precise data might prefer more complex multi-operator scenarios or models. However, with the increasing complexity of a model, its predictive capability deteriorates. Thus, model selection needs to take both goodness of the fit and the complexity of the competing models into account. In order to measure model performance and select the best model from a set of potential models we use the mean squared error (MSE) and small-sample-corrected Akaike Information Criterion (AIC_c), results given in Table 23.2. For a detailed discussion, the interested reader is referred to [6] (Fig. 23.1).

23.4 Summary

Following a model-independent effective theory approach with dimension-six operators, we have analyzed the new physics effects in $b \rightarrow s\ell\ell$ decays, based on the data available till date. We have found that \mathcal{O}_9 is the only one-operator scenario with both real and complex WC (with a large non-zero imaginary part), which can provide a plausible explanation of the given data. We have used the method of model selection incorporating both AIC_c and cross-validation to pinpoint the best possible combinations of operators with real and complex WC, which can best explain the

Table 23.2 The selected models for Likelihood 2020 dataset which pass the criterion of $\Delta AIC_c \leq 6$ and $MSE_{X-val} < 1.5$. The parameter uncertainties are obtained from hessian matrix

Model	ΔAIC_c	MSE_{X-Val}	χ^2_{Min}/DOF	p-val (%)	Result
585	0.	0.989	189.05/206	79.6	$Re(\Delta C_9) \rightarrow -1.36 \pm 0.24$, $Im(\Delta C_9) \rightarrow 2.05 \pm 0.36$ $Re(C'_9) \rightarrow 0.57 \pm 0.23$, $Im(C'_9) \rightarrow 0.14 \pm 0.25$ $Re(\Delta C_{10}) \rightarrow 0.51 \pm 0.22$, $Im(\Delta C_{10}) \rightarrow -0.53 \pm 0.46$
18	2.015	0.942	199.41/210	68.9	$Re(\Delta C_9) \rightarrow -1.08 \pm 0.099$, $Re(C'_9) \rightarrow 0.50 \pm 0.18$ $Re(\Delta C_9) \rightarrow -1.4 \pm 0.24$, $Im(\Delta C_9) \rightarrow 1.93 \pm 0.49$ $Re(C'_9) \rightarrow 0.56 \pm 0.23$, $Im(C'_9) \rightarrow 0.31 \pm 0.5$
697	3.506	0.971	188.25/204	77.9	$Re(\Delta C_{10}) \rightarrow 0.52 \pm 0.22$, $Im(\Delta C_{10}) \rightarrow -0.51 \pm 0.41$ $Re(C'_{10}) \rightarrow -0.032 \pm 0.177$, $Im(C'_{10}) \rightarrow 0.75 \pm 0.82$
529	3.791	0.977	197.05/208	69.6	$Re(\Delta C_9) \rightarrow -1.11 \pm 0.11$, $Im(\Delta C_9) \rightarrow -0.12 \pm 0.46$ $Re(C'_9) \rightarrow 0.42 \pm 0.23$, $Im(C'_9) \rightarrow -1.21 \pm 0.41$
641	4.946	1.011	189.69/204	75.6	$Re(C'_7) \rightarrow -0.0075 \pm 0.0136$, $Im(C'_7) \rightarrow -0.015 \pm 0.037$ $Re(\Delta C_9) \rightarrow -1.07 \pm 0.13$, $Im(\Delta C_9) \rightarrow -0.061 \pm 0.296$ $Re(C'_9) \rightarrow 0.61 \pm 0.25$, $Im(C'_9) \rightarrow -1.98 \pm 0.4$ $Re(\Delta C_{10}) \rightarrow 0.59 \pm 0.21$, $Im(\Delta C_{10}) \rightarrow 0.051 \pm 1.254$
530	5.479	0.993	198.74/208	66.6	$Re(\Delta C_9) \rightarrow -1.34 \pm 0.26$, $Im(\Delta C_9) \rightarrow 1.95 \pm 0.44$ $Re(\Delta C_{10}) \rightarrow 0.32 \pm 0.23$, $Im(\Delta C_{10}) \rightarrow -0.56 \pm 0.57$
513	5.492	0.98	202.89/210	62.5	$Re(\Delta C_9) \rightarrow -1.1 \pm 0.11$, $Im(\Delta C_9) \rightarrow 1.27 \pm 0.37$

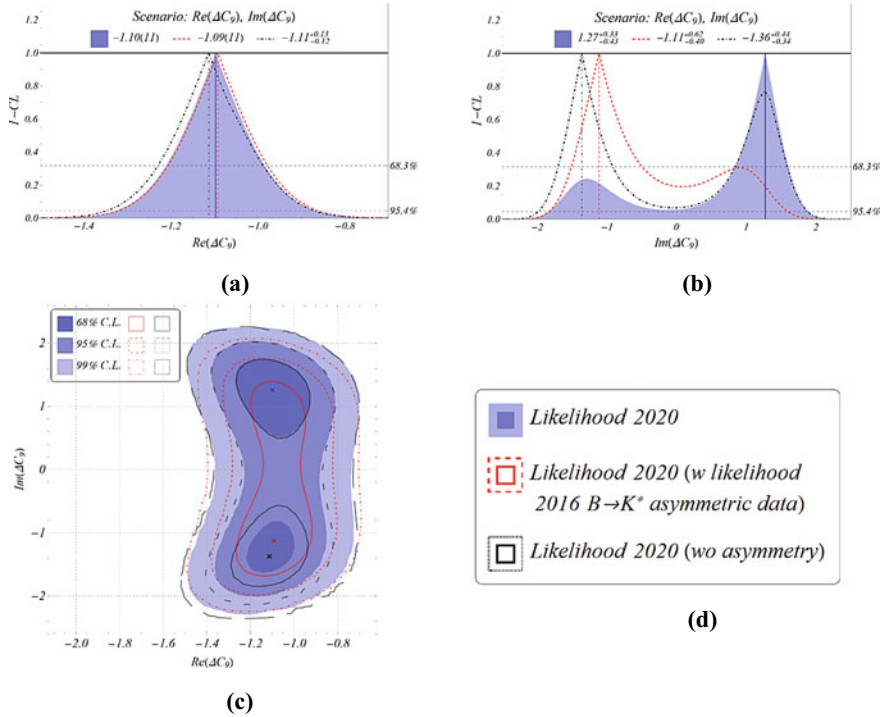


Fig. 23.1 One- and two-parameter profile-likelihoods corresponding to the single operator scenario \mathcal{O}_9 with complex WC in different fit scenarios as discussed in Table 23.1

data. The scenario with \mathcal{O}_9 is the only one-operator scenario which passes the test. However, there are a few two, three, and four-operator scenarios which have passed all the criteria set by the selection methods.

References

1. M. Aaboud et al., ATLAS. JHEP **10**, 047 (2018)
2. R. Aaij et al., LHCb. JHEP **02**, 104 (2016)
3. R. Aaij et al. [LHCb], Phys. Rev. Lett. **125**(1), 011802 (2020)
4. W. Altmannshofer, et al., JHEP **01**, 019 (2009)
5. C. Bobeth, M. Misiak, J. Urban, Nucl. Phys. B **574**, 291–330 (2000)
6. A. Biswas, S. Nandi, S.K. Patra, I. Ray. Nucl. Phys. B **969**, 115479 (2021)

Chapter 24

Charged Lepton Flavour Violating Decays as Signatures of A_4 Symmetry



Jai More, Ushak Rahaman, S. Uma Sankar, and Rambabu Korrapati

Abstract We study the charged lepton flavour violation in a popular neutrino mass model with A_4 discrete symmetry. In this model, the A_4 symmetry of the additional multiple Higgs scalars leads to lepton flavour violating decays. We consider the viable decays of neutral mesons, the top quark and the τ lepton into charged leptons of different flavours at tree level. We discuss the peculiar signatures in these decays, appearing due to the A_4 symmetry, and predict the rates for the most favourable charged lepton flavour violating modes.

24.1 Introduction

In the past few years, there is evidence that neutrino change from one flavour to another when they travel through a distance. The conversion probability is oscillatory leading to the phenomenon of neutrino oscillations. This evidence has come from natural (solar and atmospheric) sources and man-made (reactor and accelerator) sources. Neutrino oscillation experiments lead to the concept of lepton flavour violation. The flavour non-conservation provides a gateway of charged lepton flavour violation (CLFV) in charged lepton sector also. The experimental searches of CLFV decays are of great interest in the past two decades.

All the fermions and bosons of SM get mass through the Higgs mechanism. In SM, there are no neutrino masses as there are no right chiral neutrinos, but the neutrino oscillations clearly indicate that neutrinos do have a tiny mass. So, the neutrino mass mechanism is different from the usual Higgs mechanism. The neutrinos are known to have three flavours and their flavour eigenstates need not have definite mass instead

J. More (✉) · S. U. Sankar · R. Korrapati
Department of Physics, Indian Institute of Technology Bombay, 400076 Mumbai, India
e-mail: jai.more@iitb.ac.in

U. Rahaman
Department of Physics, Centre for Astro-Particle Physics (CAPP), University of Johannesburg,
PO Box 524, 2006 Auckland Park, South Africa

© The Author(s), under exclusive license to Springer Nature Singapore Pte Ltd. 2022
B. Mohanty et al. (eds.), *Proceedings of the XXIV DAE-BRNS High Energy Physics Symposium, Jaitani, India*, Springer Proceedings in Physics 277,
https://doi.org/10.1007/978-981-19-2354-8_24

133

they mix to form three mass eigenstates. These two bases are related by 3×3 matrix called PMNS (Pontecorvo-Maki-Nakagawa-Sakata) matrix and experiments have shown that this matrix is close to tri-bi-maximal (TBM) form [1]. To get a better picture of LFV, we need a theory of neutrino masses, that may provide a link between flavour violation in the neutrino sector and charged lepton sector. Hence, various neutrino mass models have been proposed based on different discrete symmetries [2–5].

The need to understand the neutrino mass mechanism and LFV drives us to go beyond SM physics. This paper is organized as follows: In Sect. 24.2, we give a short description of the He-Keum and Volkas (HKV) model [5]. In Sect. 24.3, we discuss the most promising decays into the charged leptons of different flavours. Finally, in Sect. 24.4, we give our conclusion and remarks.

24.2 About the A_4 Based Model

24.2.1 Features of the HKV Model

The HKV model [5] predicts TBM mixing purely based on symmetry and symmetry breaking and does not require fine-tuning of parameters. The charged fermion content is the same as SM with additional multiple Higgs scalars. The additional Higgs doublets in this model lead to charged lepton flavour violation. Introduction of a small perturbation in the Majorana mass matrix of the heavy right-chiral neutrinos in this model can lead to non-zero $\sin \theta_{13}$ and maximal δ_{CP} violation [6]. The fermions in SM occur in three generations and form a doublet representation under SU(2). The model assumes that the three generations form a triplet representation of A_4 . The HKV model comprises (c.f. Ref. [7]):

- The charged fermions are the same as the SM.
- The three left chiral SU(2) doublets of quarks (Q_{iL}) and leptons (D_{iL}) are also assumed to form triplet representations of A_4 .
- The right chiral SU(2) singlet of charged fermions (f_{iR} , $f \equiv \{u, d, \ell\}$) has non-trivial transformation properties under A_4 .
- The three right-chiral neutrinos (ν_{iR}) form a triplet representation of A_4 but have no gauge quantum numbers.
- The additional three distinct Higgs fields are introduced, viz.: (i) The SU(2) doublets (ϕ_i) which is an A_4 triplet, (ii) The SU(2) doublets (ϕ_0) which is an A_4 singlet and (iii) The SU(2) singlets (χ_i) which is an A_4 triplet.

When different Higgs get vacuum expectation values (VEVs), we obtain neutrino mass matrix leading to mixing matrix in TBM form. We assume that all the members in (i) and (ii) of A_4 triplet have the same VEVs and only the second member in (iii) of A_4 triplet has a non-zero VEV. This vacuum alignment is crucial to obtain the TBM form of PMNS purely from symmetry consideration. The Yukawa Lagrangian is gauge and A_4 invariant and is given by [5, 8]

$$\begin{aligned}
\mathcal{L}_{Yuk} = & - \left[h_{1d} (\bar{Q}_{iL} \phi_i)_{\underline{1}} d_R + h_{2d} (\bar{Q}_{iL} \phi_i)_{\underline{1}'} d_R'' + h_{3d} (\bar{Q}_{iL} \phi_i)_{\underline{1}''} d_R' \right. \\
& + h_{1u} (\bar{Q}_{iL} \phi_i)_{\underline{1}} u_R + h_{2u} (\bar{Q}_{iL} \phi_i)_{\underline{1}'} u_R'' + h_{3u} (\bar{Q}_{iL} \phi_i)_{\underline{1}''} u_R' \\
& + h_{1\ell} (\bar{D}_{iL} \phi_i)_{\underline{1}} \ell_R + h_{2\ell} (\bar{D}_{iL} \phi_i)_{\underline{1}'} \ell_R'' + h_{3\ell} (\bar{D}_{iL} \phi_i)_{\underline{1}''} \ell_R' \\
& \left. + h_0 (\bar{\ell}_{iL} \nu_{iR})_{\underline{1}} \tilde{\phi}_0 \right] + M[\bar{\nu}_R (\nu_R)^c]_{\underline{1}} + h_\chi [\bar{\nu}_R (\nu_R)^c]_{\underline{3}_S} \cdot \chi + h.c.
\end{aligned} \tag{24.1}$$

In this model, the fermion-Higgs couplings are governed by A_4 symmetry. Hence, we explore the signatures of this A_4 symmetry in CLFV decays. The four neutral scalar mix to form four mass eigenstates $\Phi_0^0, \Phi_1^0, \Phi_2^0$ and Φ_3^0 , of which Φ_0^0 is the SM like Higgs, Φ_1^0 has only flavour conserving couplings and Φ_2^0 and Φ_3^0 are flavour violating couplings. Our emphasis is on the flavour violating decays and those are bestowed by Φ_2^0 and Φ_3^0 .

24.3 Lepton Flavour Violating Decays

24.3.1 Neutral Mesons Decays

We focus only on the decays of neutral K, B_d and B_s mesons into charged leptons with flavour violation. Consider the decay process $\bar{q}_i q_j \rightarrow \ell_m^+ \ell_n^-$, with $m \neq n$ mediated by Φ_2^0 and Φ_3^0 at tree level. We can write the generic form of the flavour changing coupling of these heavy neutral scalars as

$$\mathcal{L}_{Yuk} \subset g^{ij} \bar{f}_{iL} f_{jR} \Phi_2^0 + \tilde{g}^{ij} \bar{f}_{iL} f_{jR} \Phi_3^0 + (g^{ji})^* \bar{f}_{iR} f_{jL} (\Phi_2^0)^* + (\tilde{g}^{ji})^* \bar{f}_{iR} f_{jL} (\Phi_3^0)^*, \tag{24.2}$$

where g^{ij} and \tilde{g}^{ij} are defined in Ref. [7].

There are seven meson decays that can be considered for the study of CLFV. But here we discuss four most promising decays as listed below:

- $K^0(\bar{s}d) \rightarrow \mu^+ e^-$; $BR \leq 4.7 \times 10^{-12}$ for $m_\Phi \geq 750 \text{ GeV}$,
- $B_d^0(\bar{b}d) \rightarrow \tau^+ e^-$; $BR = 8 \times 10^{-9}$; (3×10^{-5}) [10],
- $B_s^0(\bar{b}s) \rightarrow \mu^+ e^-$; $BR = 3.5 \times 10^{-11}$; (5.4×10^{-9}) [11],
- $B_s^0(\bar{b}s) \rightarrow \tau^+ \mu^-$; $BR = 8 \times 10^{-9}$; (4.2×10^{-5}) [12].

The neutral meson with a given flavour quantum number can decay into a particular flavour combination of charged lepton pair but not to its conjugate final state. This is purely a signature of A_4 symmetry of Yukawa coupling between fermions and scalar doublets. $K^0 \rightarrow \mu^+ e^-$ has the strongest experimental upper bound which can be obtained from $K_L \rightarrow \mu^+ e^-$. From the $BR(K_L \rightarrow \mu^+ e^-) \leq 4.7 \times 10^{-12}$ [9], we obtain the lower limit on the mass of the Higgs $m_\Phi \geq 750 \text{ GeV}$. The branching ratio of the other three flavour decay is obtained using this lower limit on the Higgs mass.

The respective present experimental upper bounds on these branching ratios are given in the parentheses. The respective present experimental upper bounds on these branching ratios are (3×10^{-5}) [10], (5.4×10^{-9}) [11] and (4.2×10^{-5}) [12].

24.3.2 τ Decays Shows Peculiar Signatures of A_4 Symmetry

Here we discuss, the decay of τ leptons into three charged leptons. We distinguish between two cases:

- # For the decay $\tau^- \rightarrow f_1^- f_1^- f_2^+$, the amplitude due to Φ_2^0 and Φ_3^0 exchange is equal so they add up.
- # However, for the decay $\tau^- \rightarrow f_1^- f_1^+ f_2^-$, the amplitude due to Φ_2^0 and Φ_3^0 exchange is equal and opposite so they give zero contribution.

Here, $f_1, f_2 \equiv \{e, \mu\}$.

24.3.3 Top Decays

We also study top decays mediated by Φ_2^0 and Φ_3^0 as the Yukawa coupling of top quark is large and that would give measurably large branching ratios. The decays of considerably large couplings are:

$$\begin{array}{lll} \star t \rightarrow c\tau^+\mu^- & \star t \rightarrow u\tau^+e^- & \text{BR} \simeq 10^{-9} \text{ for } m_\phi = 750 \text{ GeV.} \\ \star t \rightarrow c\mu^+e^- & \star t \rightarrow u\mu^+\tau^- & \text{BR} \simeq 5 \times 10^{-12} \text{ for } m_\phi = 750 \text{ GeV.} \end{array}$$

However, the experimental upper bound on the branching ratio of the top quark decay to the charged leptons of different flavour is 2×10^{-5} [13].

24.4 Conclusions

This model has the attractive feature:

- ✓ Model predicts the tri-bi-maximal form of the neutrino mixing matrix purely from the symmetry considerations.
- ✓ The Yukawa couplings of the fermions to the multiple Higgs doublets of this model are governed by the A_4 symmetry.
- ✓ The flavour violating decays, mediated by heavy neutral scalars of this model, carry signatures of the A_4 symmetry of the Yukawa couplings.
- ✓ $\text{BR}(K_L \rightarrow \mu^+e^-)$ gives lower bound $m_\phi = 750 \text{ GeV}$, the mass of the heavy neutral scalars.
- ✓ The charged lepton flavour selection is a signature of the A_4 symmetry [14].

References

1. P.F. Harrison, D.H. Perkins, W.G. Scott, Phys. Lett. B **530**, 167 (2002)
2. K.S. Babu, E. Ma, J.W.F. Valle, Phys. Lett. B **552**, 207–213 (2003)
3. E. Ma, G. Rajasekaran, Phys. Rev. D **64**, 113012 (2001)
4. G. Altarelli, F. Feruglio, Nucl. Phys. B **741**, 215–235 (2006)
5. X.G. He, Y.Y. Keum, R.R. Volkas, JHEP **04**, 039 (2006)
6. A. Dev, P. Ramadevi, S.U. Sankar, JHEP **11**, 034 (2015)
7. R. Korrapati, J. More, U. Rahaman, S.U. Sankar, Eur. Phys. J. C **81**(5), 382 (2021)
8. W. Grimus, P.O. Ludl, J. Phys. A **45**, 233001 (2012)
9. D. Ambrose et al., E871. Phys. Rev. Lett. **81**, 5734–5737 (1998)
10. B. Aubert, et al., BaBar. Phys. Rev. D **77**, 091104 (2008)
11. R. Aaij, et al., LHCb. JHEP **03**, 078 (2018)
12. R. Aaij, et al., [LHCb], Phys. Rev. Lett. **123**(21), 211801 (2019)
13. C.A. Gottardo [ATLAS], [arXiv:1809.09048](https://arxiv.org/abs/1809.09048) [hep-ex]
14. Neutral meson can decay only into a particular flavour violating leptonic mode but not into its charge conjugate mode

Chapter 25

Precision Tests of Electroweak Theory



Kajari Mazumdar

Abstract Measurements concerning electroweak interactions continue to play a very important role, from testing the validity of standard model (SM) at high energies, to probing *new physics* with precision measurements. At the LHC, several interesting processes involving multiple heavy SM particles have opened up for the first time, providing crucial understanding of the nature of interactions among them. We only discuss interesting aspects of some of the important precision measurements at the LHC. Assuming *new physics* scale to be very high energy scale, effective field theory analyses at present lead to only moderate constraints on the couplings among various particles.

25.1 Introduction

The LHC machine has been providing collisions for over a decade now, and it is expected to be active for two more. Even if the delivered data volume is only a few percent of the total anticipated, for physics at the electroweak (EW) scale, i.e., $\sqrt{\hat{s}} \sim \mathcal{O}(100)$ GeV, the accumulated data provide excellent statistical precision for a large number of processes. In general, due to the laudable performance of the machine and the experiments combined with matching efforts from the theoretical community, a plethora of very interesting results have been extracted and many more will follow. We define, restrictively here, EW process as the interaction leading to inclusive production of at least one weak boson (W or Z) in the hard scattering.

Precision test comprises of two steps: measurements with the least possible uncertainties and subsequent comparison with theoretical predictions. We consider only a handful of examples in the following. It must be noted that the analyses for precision measurements demand a thorough understanding of many aspects, from the detector performance, to the theoretical issues involved; hence extraction of result requires more time.

K. Mazumdar (✉)
Tata Institute of Fundamental Research, Mumbai, India
e-mail: mazumdar@tifr.res.in

© The Author(s), under exclusive license to Springer Nature Singapore Pte Ltd. 2022
B. Mohanty et al. (eds.), *Proceedings of the XXIV DAE-BRNS High Energy Physics Symposium, Jaiti, India*, Springer Proceedings in Physics 277,
https://doi.org/10.1007/978-981-19-2354-8_25

At the LHC energies, the gluon density is extremely high, which makes higher order processes of W, Z productions (*standard candles*) very significant leading to, quite often, large number of accompanying hard jets. Further, the sea (anti) quarks of the initial proton(s) contribute substantially as well; almost 25% of W^- production is induced by at least one of the second generation (anti)quarks. Thus, high precision measurements by experiments constrain parton density function (PDF), in turn.

During Run 1 (Run 2), the proton-on-proton collisions took place at the centre-of-mass energy (\sqrt{s}) of 7 and 8 (13) TeV. While the integrated luminosity (\mathcal{L}) plays an important role in all the measurements, its uncertainty ($\Delta\mathcal{L}$) is the dominant source of nuisance in precision measurements quite often. While the ATLAS and CMS experiments collected data corresponding to \mathcal{L} about 25 and 140 fb^{-1} during these two runs, considerable amount of efforts has gone into reducing the uncertainties over the years. For CMS experiment, $\Delta\mathcal{L}$ is about 3.4–2.6% (2.5–1.6%) for Run 1 (Run 2).

25.2 Measurement of W-Mass

For the standard model (SM) at tree level only three input parameters are needed to predict everything. We could define mass of W in terms of the electromagnetic fine structure constant (α_{EM}), Fermi constant (G_F) and weak mixing angle ($\sin^2\theta_w$) as $M_W = \sqrt{\frac{\pi\alpha}{\sqrt{2}G_F}} / \sin\theta_w$. However, the measured value is prone to two types of deviations: (i) the higher order corrections and (ii) couplings that could differ from SM. Thus, M_W becomes a precision observable to be measured painstakingly at the experiments.

The physically measured M_W actually receives contributions due to loop diagrams; from top mass, less strongly from Higgs mass, and, potentially, from *wew physics*. This modifies the relation to $M_W^2 \left(1 - \frac{M_W^2}{M_Z^2}\right) = \frac{\pi\alpha}{\sqrt{2}G_F} (1 + \Delta r)$, where Δr accounts for the higher order corrections. Hence accurate measurement of M_W provides a stringent test of EW sector of the SM. Unfortunately, the measurement at the LHC is extremely challenging due to a number of factors. These include need for accurate theoretical modelling (dynamics of boson production, combined with kinematics of decay products) to be matched with excellent understanding of the detector performance. It is to be also noted that the parton content of proton makes the production rate of W^+ to be about 40% higher than that of W^- as well as broader rapidity and softer transverse momentum (p_T) spectra for the later.

The invariant mass m of the decay products is related to M_W via the relativistic Breit-Wigner form $\frac{d\sigma}{dm} \propto \frac{m^2}{(m^2 - M_W)^2 + m^4 \Gamma_W^2 / M_W^2}$. The leptonic decay mode of $W \rightarrow \ell\nu$ is experimentally cleaner, more accurate and has relatively less background. However, the final state cannot be fully reconstructed due to the neutrino escaping detection. Hence the need to deal with the transverse mass $m_T = \sqrt{2p_T^\ell p_T^{\text{miss}}(1 - \cos\Delta\phi)}$. The missing transverse momentum is defined as $\mathbf{p}_T^{\text{miss}} = -(\mathbf{p}_T^\ell + \mathbf{u}_T)$, where \mathbf{u}_T is the

recoil of W in transverse plane. $\Delta\phi$ is the angular separation between the lepton and the direction of $\mathbf{p}_T^{\text{miss}}$ in the azimuthal plane. M_W is determined from fits to two spectra: (i) p_T^ℓ (Jacobian edge at $M_W/2$), and (ii) m_T (M_W as the end point).

Previous to the LHC, the combination of LEP and Tevatron measurements led to an uncertainty of $\Delta M_W = 15$ MeV. In recent times, ATLAS has made a measurement of $M_W = 80.370 \pm 0.019$ GeV [1] leading to the new world average value of $M_W = 80.379 \pm 0.012$ GeV. As mentioned already, the issues include extrapolation of lepton momentum spectrum from Z to W region, consistency of results between different charges and the pseudorapidity spectrum of the charged lepton which validates the production model. Further, compatibility between e and μ channels ensures adequate experimental calibrations. To give some estimate of possible reduction of uncertainty in near future, an uncertainty of $\Delta M_W = 10$ MeV would require at least 2 million W events.

25.3 Drell-Yan Process

Drell-Yan process ($q\bar{q} \rightarrow \gamma/Z^* \rightarrow \ell^+\ell^-$) is the benchmark at hadron colliders with clean signature of two isolated charged leptons, which can be measured with good resolution and negligible contamination. Measurements have been performed at the LHC over a wide range of dilepton invariant mass $m_{\ell\ell}$. With early Run 2 data, CMS has made differential measurement in the range $15 < m_{\ell\ell} < 3000$ GeV with a precision of few % till few hundred GeVs [2]. The event yield in the fiducial region varies over 7 orders of magnitude as shown in Fig. 25.1 (left). The cross-section, derived after unfolding of detector resolution and QED final state radiation effects, is presented in Fig. 25.1 (right) after implementing corrections for acceptance and efficiency. The theoretical prediction obtained from FEWZ is accurate to next-next-to-leading order in QCD and next-to-leading order in EW couplings. Interference of

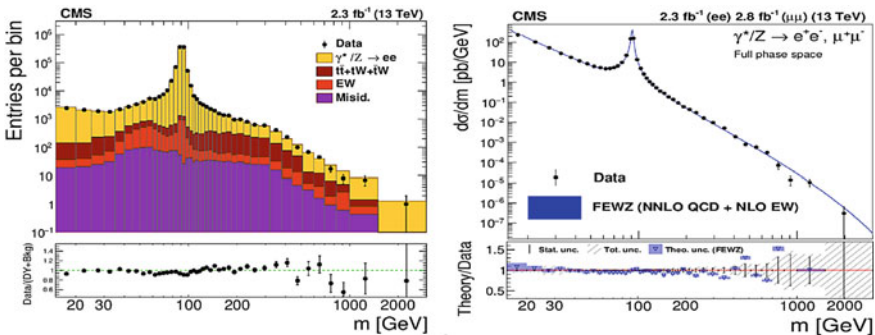


Fig. 25.1 Invariant mass spectrum of Drell-Yan process; (left) event yield in dielectron final state within fiducial region and (right) differential cross-section in combined electron and muon channels

vector and axial-vector currents leads to angular asymmetry for the lepton emission given by $A_{FB} = \frac{\sigma_F - \sigma_B}{\sigma_F + \sigma_B} = \frac{\sigma(\cos\theta^* > 0) - \sigma(\cos\theta^* < 0)}{\sigma(\cos\theta^* > 0) + \sigma(\cos\theta^* < 0)}$. Here θ^* is defined in the Collins-Soper frame and given by $\cos\theta^* = \frac{2(p_1^+ p_2^- - p_1^- p_2^+)}{\sqrt{M^2(M^2 + P_T^2)}} \times \frac{P_z}{|P_z|}$ where M , P_T and P_z refer to the mass, transverse and longitudinal momentum components of the dilepton system and $p_i^\pm = (e_i \pm p_{z,i})/\sqrt{2}$ refers to the individual leptons. It is to be noted that the direction of the incoming quark is determined from the boost and hence the measured asymmetry is partly diluted. Near Z peak A_{FB} is sensitive to $\sin^2\theta_w$, while the sensitivity to PDF lies away from it.

25.4 Transverse Momentum of Z

At the LHC energies, Z (similarly for W or Higgs) typically has substantial amount of longitudinal boost. If produced without any accompanying jets, the transverse momentum (p_T^Z) is negligible and is dictated by the initial state radiation. Theoretically, the description of this region requires resummation technique for soft gluon emission as well as proper parton shower description. For production in association with hard jet(s), the high p_T^Z component is described by fixed-order perturbative calculation which leads to asymptotically diverging cross-section as $p_T^Z \rightarrow 0$. This is illustrated in Fig. 25.2 (left). CMS measurement of associated jet multiplicity using early data of Run2 is presented in Fig. 25.2 (middle), along with theoretical predictions. Measurement of p_T^Z spectrum by combining $Z \rightarrow \nu\bar{\nu}$ and $Z \rightarrow \ell^+\ell^-$ channels provide better precision, specially, at the higher end, which is important for background estimation in search of beyond SM physics. The comparison of CMS data with various theoretical predictions is displayed in Fig. 25.2 (right) [3]. Using $Z + \geq 1$ jet(s) production and utilizing heavy flavour tagging, CMS collaboration has also measured the cross-section for associated production of Z with c and b quarks. To cancel several sources of uncertainties, the ratio of the production cross-sections has been estimated in the fiducial region of $p_T^j > 30$ GeV, $|\eta_j| < 2.4$ and $71 < m_{\ell\ell} < 111$

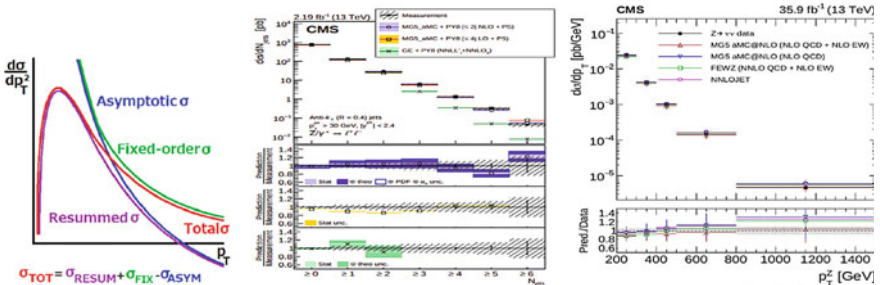


Fig. 25.2 Theoretical modelling of the transverse momentum spectrum of Z and distribution of jet multiplicity when produced in association of Z

GeV. The measured value of $\sigma(Z + c)/\sigma(Z + b) = 1.62 \pm 0.03 \pm 0.15$ matches with perturbative calculations [4].

25.5 Triple and Quartic Gauge Couplings

The SM Lagrangian encompasses self-interaction among the vector fields leading to interactions involving vertices with three (triple gauge coupling, TGC) or four (quartic gauge coupling, QGC) gauge bosons. Analyses have been performed to study inclusive production of multiple bosons. Interactions involving TGCs include $W^+W^- \gamma$, $W^+W^- Z$ productions and their study tests the non-Abelian gauge structure. $W^+W^- \gamma\gamma$, $W^+W^- W^+W^-$, and $W^+W^- ZZ$ productions involving QGCs represent a connection to the scalar sector which can arise as a manifestation of a heavy particle exchange or indicate contact interaction. Hence, anomalous values of QGCs could be the first probe to *new physics*, in the absence of direct observation of heavy, new resonances. In the context of effective field theory, the CP-conserving trilinear operators are constrained from diboson final states while CP-conserving quartic ones can be explored in the study of vector boson scattering and triboson final states. The summary of measurements, involving multiple bosons, by ATLAS collaboration is presented in Fig. 25.3.

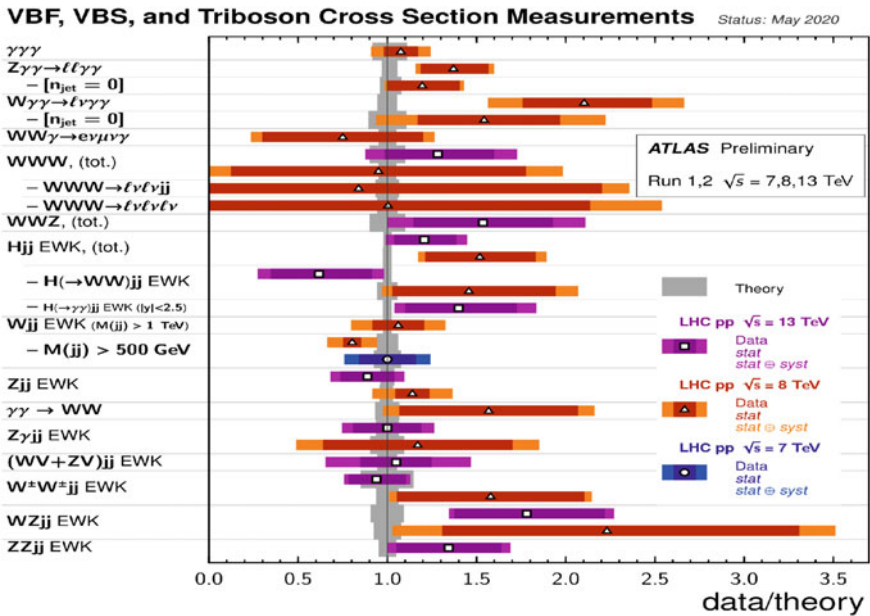


Fig. 25.3 Summary of measurements of vector boson fusion and vector boson scattering

25.6 Conclusion

Precision electroweak measurements at the LHC are crucial for vindication of the standard model at TeV energy scale. Only few measurements performed by ATLAS and CMS collaborations have been discussed here to highlight the rich variety of interesting physics achievable at the LHC.

References

1. M. Aaboud et al., [ATLAS], *Eur. Phys. J. C* **78**(2), 110 (2018) [erratum: *Eur. Phys. J. C* **78**(11), 898 (2018)]
2. A.M. Sirunyan et al., CMS, *JHEP* **12**, 059 (2019)
3. A.M. Sirunyan et al., CMS, *JHEP* **05**, 205 (2021)
4. A.M. Sirunyan et al., [CMS], *Phys. Rev. D* **102**(3), 032007 (2020)

Chapter 26

Rare Charm Decays at Belle II



Latika Aggarwal

Abstract Belle II detector, situated at the SuperKEKB e^+e^- accelerator, will collect 50 times larger data sample than the Belle detector. This will allow more precise measurements and tests of the Standard Model (SM). Flavor Changing Neutral Current (FCNC) processes are forbidden at the tree level in the SM. However, there are several new physics (NP) models that can enhance the branching fractions of the FCNC. $D^0 \rightarrow \gamma\gamma$ is one such decay mode sensitive to the NP searches. We will discuss the prospects for charm rare decays at Belle II, focusing on the $D^0 \rightarrow \gamma\gamma$ decay mode. Further, we will also demonstrate the capability of the Belle II detector by reconstructing the charm mesons from the neutral candidates ($D^0 \rightarrow K_S^0\pi^0$). The study uses the most recently collected data by the Belle II detector corresponding to an integrated luminosity of 34.6 fb^{-1} .

26.1 Introduction

SuperKEKB [1] is an asymmetric e^+e^- collider located at the KEK Laboratory in Tsukuba, Japan. The nominal center-of-mass energy is 10.58 GeV, where the e^+ beam energy is 4 GeV and the e^- beam energy is 7 GeV. The accelerator is designed to deliver a peak instantaneous luminosity $6 \times 10^{35} \text{ cm}^{-2}\text{s}^{-1}$, which is 30 times higher than its predecessor, the KEKB accelerator, and the goal of SuperKEKB is to deliver about 50 ab^{-1} of data to Belle II. It is not just a B -factory but also a charm factory with approximately $5 \times 10^{10} c\bar{c}$ events expected by ~ 2030 . Belle II [2] is a general purpose detector designed to perform precision measurements of the Standard Model (SM) parameters to look for hints of new physics (NP).

A Flavor Changing Neutral Current (FCNC) is one of the processes that constitute an excellent probe to search for NP. FCNCs are forbidden at tree level but proceed

Latika Aggarwal—for the Belle II collaboration.

L. Aggarwal (✉)
Panjab University, Chandigarh, India
e-mail: latikaphy@pu.ac.in

via electroweak loops in the SM. Decays involving $K^0 - \bar{K}^0$, $B_{d(s)}^0 - \bar{B}_{d(s)}^0$ mixing [3] and $b \rightarrow s\gamma$ transitions [4] are extensively studied by previous experiments but the processes involving $c \rightarrow u$ transitions, such as $D^0 \rightarrow \gamma\gamma$, still need further explorations. This is due to the fact that the SM expectations of these processes are very small because of the GIM cancellation [5] of loop-level amplitudes in the SM. The predicted branching ratio of $D^0 \rightarrow \gamma\gamma$ is 3×10^{-11} , if we consider only short distance contributions and this branching ratio gets enhanced to $(3.5_{-2.6}^{+4.0}) \times 10^{-8}$ with the inclusion of long distance contributions [6]. In the minimum supersymmetric SM, decays proceed via exchange of a superpartner of the quark, squark, in the loop and estimated branching ratio of $c \rightarrow u\gamma$ process increases to 6×10^{-6} [7]. Previously $D^0 \rightarrow \gamma\gamma$ studies had been performed by CLEO [8], BESIII [9], BABAR [10] and Belle [11] experiments. $D^0 \rightarrow \gamma\gamma$ decay has not been discovered but the experimental measurements exclude a branching ratio larger than 8.5×10^{-7} at 90% confidence level [11]. New generation detectors such as Belle II and LHCb provide an opportunity to explore these interesting processes. LHCb can perform precise measurements for final states with charged particles but final states with neutrals such as $D^0 \rightarrow \gamma\gamma$ that require good energy resolution and low backgrounds can be better explored with the Belle II detector.

Belle II detector is expected to collect approximately 1 ab^{-1} of data by summer 2022 which will be enough to improve on the existing $D^0 \rightarrow \gamma\gamma$ limit. While Belle II accumulates sufficient statistics to look for the rare decays, it is important that the performance of each sub-detector and particle reconstruction is well established using well-understood processes such as $D^0 \rightarrow K_S^0\pi^0$, $D^0 \rightarrow \pi^+\pi^-$, $D^0 \rightarrow K^-\pi^+$, etc. Here, we present a first look at the $D^0 \rightarrow K_S^0\pi^0$, which is an important control process in the context of the $D^0 \rightarrow \gamma\gamma$ analysis.

26.2 Rediscovery of $D^0 \rightarrow K_S^0\pi^0$ Decay with Belle II Data

Belle II data recorded at the $\Upsilon(4S)$ resonance, corresponding to an integrated luminosity of 34.6 fb^{-1} , are analyzed to look for the $D^0 \rightarrow K_S^0\pi^0$ process. The decay mode of interest $D^0 \rightarrow K_S^0\pi^0$ is reconstructed in the decay chain $D^{*+} \rightarrow D^0(\rightarrow K_S^0\pi^0)\pi^+$. Requiring that the D^0 candidate is consistent with being a decay product of a D^{*+} meson will suppress the background that comes from a random combination of final state particles. An electromagnetic calorimeter (ECL) cluster is treated as a photon (γ) candidate if it is isolated from the extrapolated charged tracks. The photon energy in the laboratory frame, is required to have a minimum value of 30, 120 or 80 MeV depending upon whether it was reconstructed in the barrel, forward endcap or backward endcap of the ECL, respectively. The π^0 candidate is reconstructed from a pair of photons with invariant mass that lies in the range, $121 \text{ MeV}/c^2 < M(\gamma\gamma) < 142 \text{ MeV}/c^2$. Further, the mass of the selected π^0 candidate, $M(\gamma\gamma)$ is the constraint to the nominal π^0 mass, in order to improve the resolution. K_S^0 candidates are reconstructed by using a pair of oppositely charged

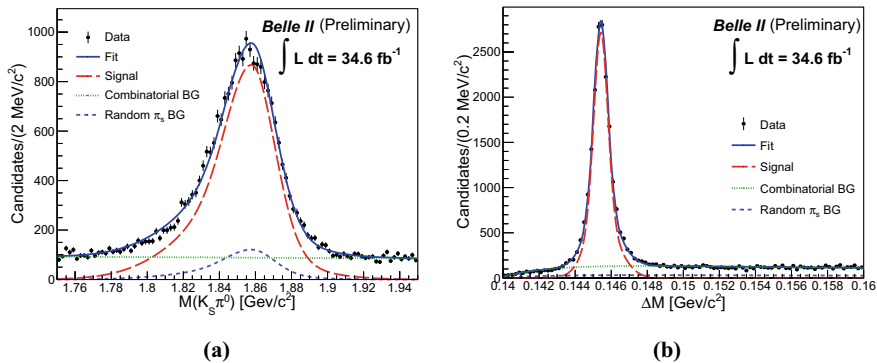


Fig. 26.1 **a** $M(K_S^0\pi^0)$ and **b** ΔM distributions for the Belle II data set, represented with black points with error bars. Solid blue line, red dashed line, green dotted line and purple dashed line represent total fit, signal, combinatorial background and random π_s background, respectively [13]

pion tracks with invariant mass that lies within ± 30 MeV/ c^2 of the nominal K_S^0 mass (497 MeV/ c^2) [12]. Selected K_S^0 and π^0 candidates are combined to reconstruct the D^0 candidate by requiring the invariant mass $M(K_S^0\pi^0)$ lies between 1.75 GeV/ c^2 and 1.95 GeV/ c^2 . Further, this D^0 candidate is combined with low momentum pions known as “slow” pions, π_s^+ , to reconstruct D^{*+} candidates and the mass difference between D^0 and D^{*+} candidates, ΔM , is required to have a value between 0.14 GeV/ c^2 and 0.16 GeV/ c^2 . The center of mass momentum of the D^{*+} candidate, $p^*(D^{*+})$ is required to be > 2.5 GeV/ c , which removes the background of charmed particles coming from the B decays.

Figure 26.1a and b shows the $M(K_S^0\pi^0)$ and ΔM distributions for the selected data candidates. These distributions show a clear peak corresponding to the presence of the $D^{*+} \rightarrow D^0(\rightarrow K_S^0\pi^0)\pi^+$ mode. To extract the $D^0 \rightarrow K_S^0\pi^0$ signal yield, distributions are fitted with signal and background probability distribution functions. A two-dimensional unbinned maximum likelihood fit is performed on $M(K_S^0\pi^0)$ and ΔM observables. For $M(K_S^0\pi^0)$, the signal shape is described by the sum of double Gaussian and bifurcated Gaussian functions. An exponential and a sum of double Gaussian and bifurcated Gaussian functions, with the same parameters as the signal, are used to fit combinatorial and random π_s (peaking) background, respectively. Peaking background is due to the combination of real D^0 candidates and fake π_s candidates. For ΔM , the sum of bifurcated Gaussian and Gaussian functions is used to model the signal and the threshold function is used to fit both combinatorial and random π_s background. The signal yield is measured to be 16800 ± 150 , where the uncertainty is statistical only.

26.3 Summary and Conclusion

FCNCs provide interesting decays to search for NP as SM expectations are very small for these rare processes. With higher statistics, the Belle II experiment will be able to probe these decays for physics beyond the SM. Detector and particle reconstruction performance is validated with a $D^0 \rightarrow K_S^0 \pi^0$ control channel. These studies give confidence in the readiness of the Belle II experiment to explore the rare radiative decay $D^0 \rightarrow \gamma\gamma$ and improve the existing limit.

References

1. K. Akai, K. Furukawa, H. Koiso, SuperKEKB collider. Nucl. Instrum. Meth. A **907**, 188–199 (2018)
2. T. Abe et al., Belle II Technical Design Report, no. KEK-REPORT-2010-1 (2010)
3. M. Dubinin, A. Sukachev, $K^0 \rightarrow \bar{K}^0$, $B^0 \rightarrow \bar{B}^0$ mixings in the MSSM with explicit CP violation in the Higgs sector. Phys. Atom. Nucl. **71**, 374–387 (2008)
4. A. Ishikawa, Radiative B Decays at Belle. [arXiv:1811.03286](https://arxiv.org/abs/1811.03286) [hep-ex]
5. S. Glashow, J. Iliopoulos, L. Maiani, Weak interactions with Lepton-Hadron symmetry. Phys. Rev. D **2**, 1285–1292 (1970)
6. G. Burdman, E. Golowich, J.L. Hewett, S. Pakvasa, Rare charm decays in the standard model and beyond. Phys. Rev. D **66**, 014009 (2002)
7. S. Prelovsek, D. Wyler, $c \rightarrow u\gamma$ in the minimal supersymmetric standard model. Phys. Lett. B **500**, 304–312 (2001)
8. T.E. Coan et al., (CLEO Collaboration), First search for the flavor changing neutral current decay $D^0 \rightarrow \gamma\gamma$. Phys. Rev. Lett. **90**, 101801 (2003)
9. M. Ablikim et al., (BESIII Collaboration), Search for $D^0 \rightarrow \gamma\gamma$ and improved measurement of the branching fraction for $D^0 \rightarrow \pi^0\pi^0$. Phys. Rev. D **91**, 112015 (2015)
10. J.P. Lees et al., (BABAR Collaboration), Search for the decay $D^0 \rightarrow \gamma\gamma$ and measurement of the branching fraction for $D^0 \rightarrow \pi^0\pi^0$. Phys. Rev. D **85**, 091107 (2012)
11. N.K. Nisar et al., (Belle Collaboration), Search for the rare decay $D^0 \rightarrow \gamma\gamma$ at Belle. Phys. Rev. D **93**(5), 051102 (2016)
12. P.A. Zyla et al. (Particle Data Group), Review of particle physics. PTEP **2020**(08), 083C01 (2020)
13. The Belle II Collaboration, Rediscovery of $D^0 \rightarrow K_S \pi^0$ with Belle II detector. <https://docs.belle2.org/record/2050/files/BELLE2-NOTE-PL-2020-022.pdf> BELLE2-NOTE-PL-2020-022

Chapter 27

Search for LFV in B_s Decays



L. Nayak, S. Nishida, and A. Giri

Abstract The flavor changing neutral current process is forbidden at tree level in the Standard Model (SM) and can only proceed via suppressed loop level diagrams. In the recent years, some deviation in the experimental measurements of Lepton Flavor Universality in B decays (i.e., $b \rightarrow s\ell\ell$ and $b \rightarrow c\ell\nu$) from the SM prediction and some theoretical models hint that there are lepton flavor violating interactions. Therefore, observation of the Lepton Flavor Violation (LFV) in B decays would be a clear signal of physics beyond the SM. We report herein the sensitivity study of $B_s \rightarrow \ell\tau$ ($\ell = \mu, e$) at Belle.

27.1 Introduction

The Lepton flavor violating decays (LFV), such as $B_s^0 \rightarrow \ell^\mp \tau^\pm$ ($\ell = \mu, e$), are forbidden at tree level in the SM. These type of reactions are mediated through one-loop diagrams. These processes are highly suppressed in the SM, have negligibly small \mathcal{B} and are very sensitive to new physics(NP). NP can either enhance or suppress the amplitude of the decay or may modify the angular distribution of the final state particles. Signals at the level expected in the SM lie far below current experimental sensitivities. But, many theoretical non-SM models proposed to explain possible experimental tensions observed in other B-meson decays naturally allow for branching fractions that are within current sensitivity. In the SM, the electroweak gauge bosons (Z^0 and W^\pm) have identical couplings to all three lepton flavors. This means that branching fractions of decays involving different lepton families do not depend on lepton flavor but differ only by phase space and helicity-suppressed contributions.

A. Giri—for the Belle collaboration.

L. Nayak (✉) · A. Giri
Indian Institute of Technology Hyderabad, 502285 Hyderabad, Telangana, India
e-mail: lopamudra.nayakcda@gmail.com

S. Nishida
KEK, Tsukuba, Japan

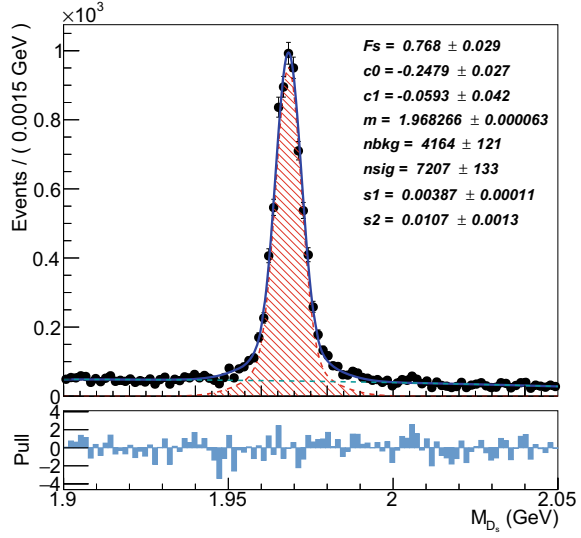
The prediction is known as lepton flavor universality (LFU). Any experimental evidence of lepton flavor non-universality would be a clear sign of physics beyond the SM. Experimental tests of LFU by using $b \rightarrow s\ell^+\ell^-$ and $b \rightarrow c\ell^-\bar{\nu}$ processes observed more than 3σ discrepancies with respect to the SM predictions for the observable R_{K^*} and $R_{D^{(*)}}$. The theoretical models also account for LFV as well as the LFU. So, the observation of LFV processes would be a clear signal of physics beyond the SM. An upper limit $\mathcal{B}(B^0 \rightarrow \mu^\mp\tau^\pm) < 1.2 \times 10^{-5}$ and $(B_s^0 \rightarrow \mu^\mp\tau^\pm) < 3.4 \times 10^{-5}$ at 90% confidence level (CL) has been set by the LHCb collaboration [1]. BaBar also set an upper limit $\mathcal{B}(B^0 \rightarrow \mu^\mp\tau^\pm) < 2.2 \times 10^{-5}$ and $(B^0 \rightarrow e^\mp\tau^\pm) < 2.8 \times 10^{-5}$ at 90% confidence level (CL) [2]. There are currently no experimental results for the $B_s^0 \rightarrow \mu^\mp\tau^\pm$ mode by BaBar. Here, we describe the simulation study of $B_s^0 \rightarrow \ell^\mp\tau^\pm$ decay at Belle.

27.2 Monte Carlo Simulation and Event Selection

The study is performed with the 121 fb^{-1} of data at the $\Upsilon(5S)$ resonance recorded by the Belle detector at the KEKB asymmetric energy e^+e^- collider. These data contain $(14.2 \pm 2.6) \times 10^6 B_s^0 \bar{B}_s^0$ pairs. Our selection is based on, and optimized with an MC simulation study. Ten million signal events are generated using the phase-space for LFV modes with the EvtGen package [3]. The detector simulation is subsequently performed with GEANT3 [4].

Particles in one event are separated into two sides: Signal side and Tag side. We reconstruct $B_s \rightarrow \ell\tau$ by combining a non-tau lepton with another oppositely charged tau lepton on the signal side. We also reconstruct $B_s \rightarrow D_s^+\ell^-\nu_\ell$ by combining D_s meson and a charged lepton in the tag side. Here, ℓ can be either electron or muon. Several decay modes (i.e. $D_s^+ \rightarrow K_S^0 K^+$, $D_s^+ \rightarrow K^+ K^- \pi^+$ etc.) are combined to form a D_s meson. Figure 27.1 shows the distribution of D_s meson. The mass window is selected with an invariant mass within $\pm 10 \text{ MeV}$ of the nominal D_s mass.; $M_{D_s} \in [1.96, 1.98] \text{ GeV}$. The impact parameter criteria for the charged particle tracks are along the z -axis $|dz| < 4 \text{ cm}$ and in the transverse plane $|dr| < 1 \text{ cm}$. Charged kaons are selected based on a ratio $L_{(K/\pi)} = L_K/(L_K + L_\pi)$, where L_K and L_π are the individual likelihood of kaon and pion, respectively. Similarly charged pions are selected based on a ratio $L_{(\pi/K)} = L_\pi/(L_K + L_\pi)$. For our selection, we require $L_{K/\pi}/L_{\pi/K} > 0.4$. Similarly, electrons (muons) are selected with $L_e > 0.1$ ($L_\mu > 0.1$). Background events coming from $e^+e^- \rightarrow q\bar{q}$ process and from B decays are suppressed by using fast boosted decision tree (FBDT) method. The kinematic variable that distinguishes signal from background is $p_{\ell(\mu/e)^*}$.

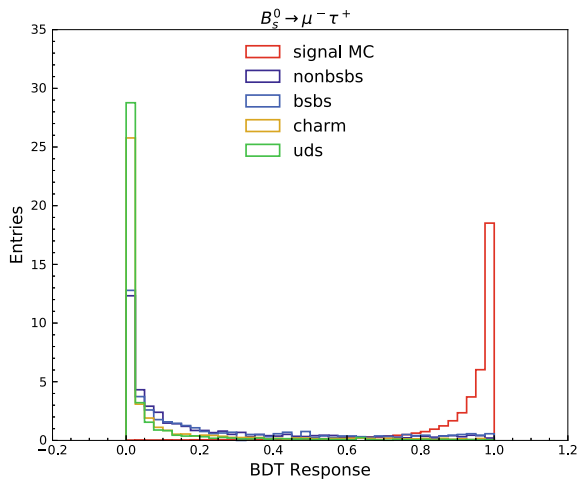
Fig. 27.1 The distribution of D_s for signal MC sample



27.3 Background Rejection

The main sources of background are continuum ($e^+e^- \rightarrow q\bar{q}$) and $B_s\bar{B}_s$ events. We find that some event shape and vertex quality variables can well separate signal from background. After baseline selection, a multivariate classifier based on FastBDT is developed to optimally discriminate signal events from the background contributions by utilizing 28-input variables according to their ranking order using an equal number of signal and background events. The multivariate algorithm is implemented within the basf2 framework. Figure 27.2 shows the FBDT output distribution, where the

Fig. 27.2 FBDT distribution for $B_s \rightarrow \mu\tau$



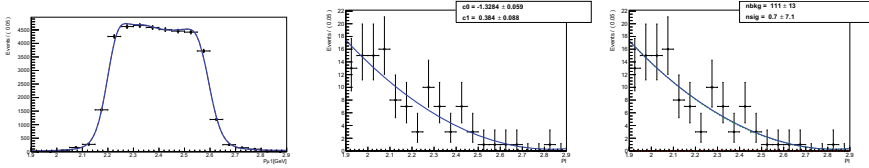


Fig. 27.3 1D fit of $B_s \rightarrow \mu\tau$ for signal (left), background (middle) and combined ML fit (right) in a simulated sample equivalent to the Belle sample. The signal region is defined as $p_{\ell 1} \in [1.9, 2.9]$ GeV

red histogram represents signal MC, green, yellow, blue and deep blue histograms are continuum and $B_s \bar{B}_s$ background, respectively. A cut on the multivariate (FBDT) classifier is then optimized based on the studies of signal and background efficiencies and signal purity. Here, FBDT cut value, chosen to be 0.9 so that it should take as many signal events as possible while suppressing many background events. This criterion reduces 90% of the background. The peaking backgrounds that pass these criteria are mainly coming from $B \rightarrow J/\psi$ because of misidentification and swapping between the leptons or lepton and kaon. These backgrounds are removed by applying invariant mass cut around J/ψ mass region.

27.4 Signal Yield Extraction

We perform a one-dimensional (1D) fit with p_{ℓ} . The signal of p_{ℓ} is modeled with non-parametric one-dimensional Gaussian kernel-estimated PDF and the performed fit are shown in Fig. 27.3:(left) for signal MC. For continuum and the $B_s \bar{B}_s$ MC, the background is fitted with Chebyshev polynomial of order 2 and the performed fit is shown in Fig. 27.3:(middle). The fit results for $B_s^0 \rightarrow \ell^- \tau^+$ are shown in Fig. 27.3.

27.5 Results

The modes that we are studying to search LFV are $B_s^0 \rightarrow \ell^- \tau^+$; ($\ell = \mu, e$). We extracted the signal from these modes by performing 1D extended maximum likelihood fit. The signal enhanced projection plots for $B_s^0 \rightarrow \mu^- \tau^+$ are shown in Fig. 27.3. The upper limit is estimated from $N_{sig}^{(UL)}$, efficiency (ε) of particular mode and num-

ber of $B_s \bar{B}_s$ pairs ($N_{B_s \bar{B}_s}$), which is represented by a formula; $\mathcal{B}^{(UL)} = \frac{N_{sig}^{(UL)}}{N_{B_s \bar{B}_s} \times \varepsilon}$.

Our estimated upper limit for LFV $B_s^0 \rightarrow \mu^- \tau^+$ and $B_s^0 \rightarrow e^- \tau^+$ are $< 1.76 \times 10^{-4}$ and $< 0.58 \times 10^{-4}$, respectively, as tabulated in Table 27.1.

Table 27.1 Upper limit estimation in MC for LFV $B \rightarrow \ell\ell'$ modes

<i>Mode</i>	N_{sig} (MC)	$B(\times 10^{-4})$ (MC)
$B_s \rightarrow \mu\tau$	0.7 ± 7.1	1.76
$B_s \rightarrow e\tau$	-3.72 ± 5.2	0.58

27.6 Summary and Outlook

$B_s \rightarrow \ell\tau$ is a very rare process, which is dominated by a large number of background events. Selected events contain one non-tau lepton and another tau lepton. After baseline selection, a multivariate classifier based on FastBDT is developed to optimally discriminate signal events from the background contributions by utilizing 28-input variables according to their ranking order. A cut on the multivariate (FBDT) classifier is then optimized based on the studies of signal and background efficiencies and signal purity. For the present situation, we have successfully isolated the pure signal events from the background with multivariate analysis method. We will unblind the data to examine the signal and/or put stringent upper limit.

References

1. R. Aaij et al., [LHCb], Phys. Rev. Lett. **123**(21), 211801 (2019)
2. B. Aubert et al., BaBar. Phys. Rev. D **77**, 091104 (2008)
3. D.J. Lange, Nucl. Instrum. Meth. A **462**, 152–155 (2001)
4. R. Brun et al., CERN Report No. **DD/EE**, 84–1 (1984)

Chapter 28

Role of Polarization in Probing Chiral Structure of Heavy Gauge Bosons at an e^+e^- Collider



Lopamudra Sahoo, Sudhansu S. Biswal, Monalisa Patra, and K. Sridhar

Abstract We study the top pair production at the proposed high luminosity e^+e^- linear collider with initial beam polarization. This is done to probe the chiral structure of the heavy gauge boson couplings in the context of warped extra-dimensional models. The polarization of the top will be sensitive to the chiral nature of its coupling to the new resonance; therefore, the top decay channels will be an effective tool in isolating the new physics effects through the study of the different polarization observables. We study in detail the angular distribution of the decay products of the top (antitop) quark and construct various asymmetries to discriminate between the multiple resonances in the various extra-dimensional models. We finally conclude that the top polarization may serve as a window to study the chiral structure of the new physics couplings.

28.1 Introduction

The Standard Model (SM), which basically describes all the fundamental particles of nature and their dynamics, is based on the gauge symmetry $SU(3)_C \times SU(2)_L \times U(1)_Y$. It has become a remarkable successful theory after being tested experimentally. However, the gauge hierarchy and the flavor hierarchy remain unexplained in the SM. The Randall Sundrum Model (RS1) [1] based on warped extra dimension, featuring only one extra dimension, came up with a simple mechanism to address these problems. There are various studies in the literature, which address these problems related to flavor changing neutral current process (FCNC) and elec-

L. Sahoo (✉) · S. S. Biswal
Department of Physics, Ravenshaw University, 753003 Cuttack, India
e-mail: sahoo.lopa25@gmail.com

M. Patra
Jožef Stefan Institute, Jamova 39, P.O. Box 3000, 1001 Ljubljana, Slovenia

K. Sridhar
Department of Theoretical Physics, Tata Institute of Fundamental Research, Homi Bhabha Road, 400 005 Mumbai, India

troweak phase transition (EWPT) based on additional symmetry called custodial isospin symmetry [2–6]. In this case, the electroweak gauge group in the bulk is $SU(2)_L \times SU(2)_R \times U(1)_X$. The detailed summary and overview of this model are discussed in Ref. [7]. Overall the model has three additional neutral gauge bosons A_1, Z_1, Z_X and two charged ones W_L^\pm, W_R^\pm . Being localized in the TeV brane, the couplings of gauge KK modes to light fermions (to top and bottom) are suppressed (enhanced) compared to the SM gauge couplings.

In this paper, we study the process $e^+e^- \rightarrow t\bar{t}$ at the International Linear Collider (ILC) [8] operating at different center of mass energies 500, 800 and 1000 GeV with an integrated luminosity of 500, 800 and 1000 fb^{-1} respectively.

28.2 Results and Discussion

We have performed our calculations, by first generating the Universal Feynrules Output (UFO) model file using FeynRules 2.3 [9] and then implemented the UFO in MadGraph 5 v2.4.2 [10]. The process $e^+e^- \rightarrow t\bar{t}$ receives contribution from the s channel Z and γ -exchange diagrams and also it receives additional contribution due to Z_1, Z_X and A_1 . The theoretical significance S from the total production cross-section can be calculated by the formula

$$S = |\sigma_{NP} - \sigma_{SM}| / \Delta\sigma. \quad (28.1)$$

Here σ_{NP} is the total production cross-section in the presence of the extra gauge bosons from the RS model considered here, whereas σ_{SM} is the SM value. The statistical fluctuation $\Delta\sigma$ in the cross-section, for a given Luminosity \mathcal{L}_{int} and fractional systematic error ϵ , is written as $\Delta\sigma = \sqrt{\sigma_{SM}/\mathcal{L} + \epsilon^2\sigma_{SM}^2}$. We have considered $\epsilon = 0.01$ and $\mathcal{L} = 500 \text{ fb}^{-1}$ for our analysis. The total unpolarized production cross-section for $t\bar{t}$ as a function of center of mass energy and its corresponding significance as a function of m_{KK} is presented in Fig. 28.1. We have done the analysis for the polarized beams with 80% electron beam polarization and 30% positron beam polarization. We

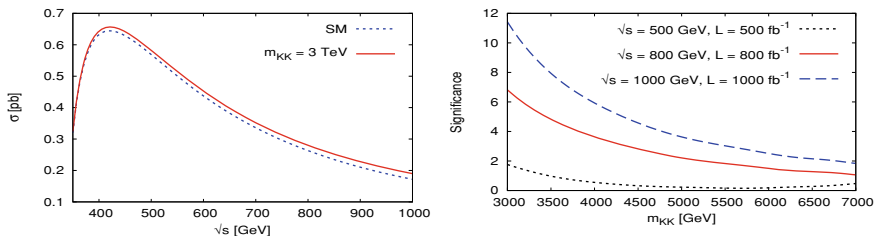


Fig. 28.1 The total production cross-section as a function of center of mass energy (left panel) and its significance as a function of m_{KK} , for different center of mass energies \sqrt{s} , in the ILC (right panel)

conclude that the cross-section with polarized beams may not improve the sensitivity to probe new physics in this case.

The new gauge bosons couple differently to t_L and t_R , therefore the net polarization of the produced top is different from the SM. The top polarization serves as a window to the chiral structure of the new physics couplings. We calculate the theoretical significance S from the asymmetry as:

$$S = |A_{NP} - A_{SM}| / \Delta A.$$

where $\Delta A = \sqrt{\frac{1-A_{SM}^2}{\sigma_{SM}\mathcal{L}} + \frac{\epsilon^2}{2}(1-A_{SM}^2)^2}$

Figure 28.2 shows the variation of top polarization with respect to center of mass energy for $m_{KK} = 3$ TeV. The total effect as well as the individual gauge boson effects are shown. The obtained significance from top polarization is also shown in the right panel of this figure. To understand the behavior of the individual gauge bosons, we next consider the forward-backward asymmetry of the top. The forward-backward asymmetry is defined as

$$A_{fb}(s, \cos \theta_0) = \frac{1}{d\sigma/ds} \left[\int_{\cos \theta_0}^1 d \cos \theta_t - \int_{-1}^{\cos \theta_0} d \cos \theta_t \right] \frac{d\sigma}{ds d \cos \theta_t} \quad (28.2)$$

where θ_0 is the experimental polar-angle cut so as to be away from the beam pipe. We have explicitly checked that A_{fb} is not sensitive to the cut-off angle in this case, therefore for our analysis, we have fixed θ_0 to zero. Next we show the forward-backward asymmetry in Fig. 28.3 for both unpolarized and polarized beams. The top

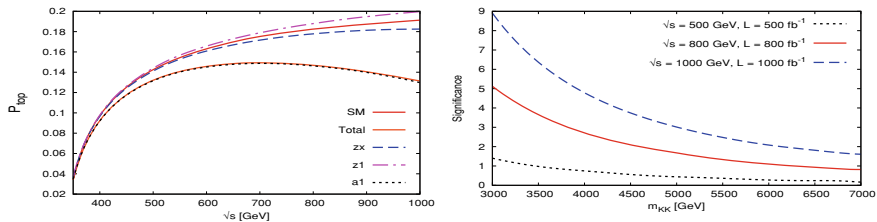


Fig. 28.2 The top polarization as a function of center of mass energy with unpolarized beams (left panel) and its sensitivity as a function of m_{KK} for different center of mass energies (right panel)

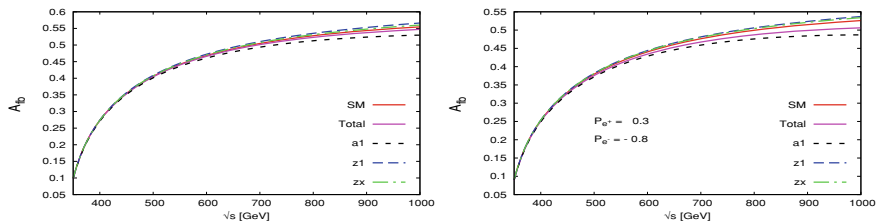


Fig. 28.3 The forward backward asymmetry as a function of \sqrt{s} for a cut-off angle $\cos \theta_0 = 0$ for unpolarized beam (left panel) and polarized beam (right panel)

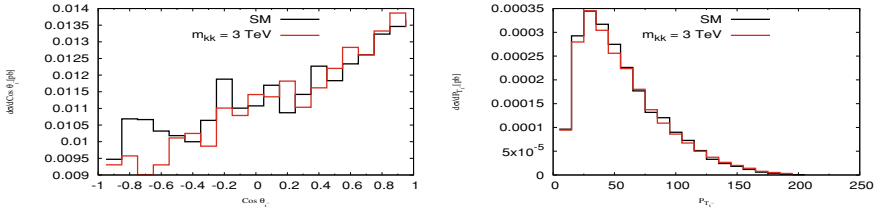


Fig. 28.4 Polar angle distribution (left panel) and P_T distribution (right panel) of the lepton from top decay in $t\bar{t}$ production at $\sqrt{s} = 500$ GeV, with unpolarized beams

polarization can be measured from the angular distribution of the leptons emitted from the decay of the top quark. The polar angle distribution and P_T distribution of decay leptons are shown in Fig. 28.4, where a significant deviation of the new physics signal from the SM is observed.

28.3 Conclusion

To summarize we have analyzed $t\bar{t}$ production at an e^+e^- collider with unpolarized, polarized beams and with the use of polarization of top. In case any new physics is observed for the observables considered here, it will be dominantly due to A_1 only as the effect of Z_1 and Z_x are suppressed. The contribution is mainly from A_1 , which has a dominant vector-like nature, and it leads to a reduction of the forward-backward asymmetry and the polarization of the top from the SM values. However, there will be a significant deviation from the SM, which may be useful to probe the chiral structure of the new physics couplings.

Acknowledgements SSB acknowledges support from the OSHEC, Department of Higher Education, Government of Odisha under OURIIP Grant Number: 1013/69/OSHEC.

References

1. L. Randall, R. Sundrum, Phys. Rev. Lett. **83**, 3370 (1999). [hep-ph/9905221]
2. A.M. Iyer, K. Sridhar, S.K. Vempati, Phys. Rev. D **93**(7), 075008 (2016). [arXiv:1502.06206](#) [hep-ph]
3. J.A. Cabrer, G. von Gersdorff, M. Quiros, JHEP **1105**, 083 (2011). [arXiv:1103.1388](#) [hep-ph]
4. K. Agashe, A. Belyaev, T. Krupovnickas, G. Perez, J. Virzi, Phys. Rev. D **77**, 015003 (2008). [hep-ph/0612015]
5. K. Agashe, S. Gopalakrishna, T. Han, G.Y. Huang, A. Soni, Phys. Rev. D **80**, 075007 (2009). [arXiv:0810.1497](#) [hep-ph]
6. K. Agashe, A. Delgado, M.J. May, R. Sundrum, JHEP **0308**, 050 (2003). [hep-ph/0308036]
7. K. Agashe, H. Davoudiasl, S. Gopalakrishna, T. Han, G.Y. Huang, G. Perez, Z.G. Si, A. Soni, Phys. Rev. D **76**, 115015 (2007). [arXiv:0709.0007](#) [hep-ph]

8. H. Aihara et al., [ILC Collaboration], [arXiv:1901.09829](#) [hep-ex]
9. A. Alloul, N.D. Christensen, C. Degrande, C. Duhr, B. Fuks, *Comput. Phys. Commun.* **185**, 2250–2300 (2013). [arXiv:1310.1921](#) [hep-ph]
10. J. Alwall, M. Herquet, F. Maltoni, O. Mattelaer, T. Stelzer, *JHEP* **06**, 128 (2011). [arXiv:1106.0522](#) [hep-ph]

Chapter 29

Study for Vector Boson Production in Association with Heavy-Flavor Jets in Proton-Proton Collisions



M. Meena, S. Bansal, and S. B. Beri

Abstract The kinematic properties of vector bosons decaying into two opposite-sign same-flavor leptons and heavy-flavor jets that originate from heavy flavor quarks have been studied using proton-proton collisions at the Large Hadron Collider with the CMS experiment at different center of mass energies. Vector boson + heavy flavor jets are originated in p-p collisions from gluon-gluon, quark-quark, and quark-anti-quark interactions. This study is important to test pQCD theory by comparing experimental cross-sections with theoretical predictions and to distinguish signal from the background in many SM processes and BSM searches. The kinematic properties have been compared with the predictions from several Monte Carlo event generators using different parton shower simulations.

29.1 Introduction

The production of a Z boson takes place through electroweak interaction which provides the signature of the event. The Z boson production in association with heavy-flavor (HF) jets provides important information on parton distribution functions (PDF) of the bottom (b) and of the charm (c) quarks. The Z+c jet channel provides the possibility of observing the intrinsic charm quark (IC) component in the nucleon. A good understanding of these processes is also important as they are major backgrounds in many standard model (SM) and beyond standard model (BSM) processes like ZH ($H \rightarrow cc$ or $H \rightarrow bb$) and in supersymmetry models, a top scalar quark (\tilde{t}) could decay into a charm quark and an undetected lightest supersymmetric particle, providing thereby a large p_T imbalance.

In this paper, we will present the recent results on Z vector boson and HF jet production obtained using the CMS experiment [1] at the Large Hadron Collider

S. B. Beri—for the CMS Collaboration.

M. Meena (✉) · S. Bansal · S. B. Beri
Panjab University, Chandigarh, India
e-mail: meena.meena@cern.ch

(LHC). In Sect. 29.2, inclusive and differential cross-section measurements of Z+c jets and differential cross-section ratio measurements of Z+b jets and Z+c jets w.r.t Z + jets and Z+c jets w.r.t Z+b jets ($R(b/j)$, $R(c/j)$, and $R(c/b)$) are presented. In Sect. 29.3, results are summarized.

29.2 Measurement of the Z + HF Jets Cross-Section

The differential and integrated cross-section measurements of Z + HF (b or c) jets are performed using the data collected by the CMS detector at the center of mass energy (\sqrt{s}) of 13 TeV corresponding to an integrated luminosity of 35.9 fb^{-1} in 2016.

The b jets or c jets are those jets that are initiated by b or c quarks with a characteristic lifetime of 1.5 (1.1) ps of the b (c) hadron. The b (c) hadron travels ≈ 1 cm at energy ≈ 10 –100 GeV in the laboratory frame before decaying to several particles and forming a new vertex called the secondary vertex. The invariant mass and impact parameter of the tracks associated with this secondary vertex are the input variables to the b-tagging/c-tagging deep combined secondary vertices algorithm [2]. This algorithm discriminates between signal and background. In Z + HF jets measurements, the secondary vertex mass (M_{SV}) is used to correct simulation by applying the corresponding scale factors for the Z+c jet, Z+b jet, and Z+light jet components. These scale factors are obtained by fitting M_{SV} templates from simulation to the observed data. Figure 29.1a shows the distribution of M_{SV} after applying scale factor and there is good agreement between data and the simulation.

The fiducial phase space for the Z+c jets measurement [3] is defined as: the Z boson candidate is reconstructed by requiring a pair of oppositely charged electrons or muons within the mass range of 71 and 111 GeV and pseudorapidity $|\eta| < 2.4$. In the dilepton and dimuon channel, leading (subleading) leptons are required to have $p_T > 29$ (10) GeV and 26 (10) GeV, respectively. The Z boson candidate is required to be accompanied by at least one c jet selected with the tight operating point of c tagging discriminator with $p_T > 30$ GeV and $|\eta| < 2.4$.

Due to detector resolution and the event selection inefficiency, there can be migrations between bins of reconstructed distributions and it can alter the true distributions. Therefore, bin-by-bin migrations are corrected by the response matrices, which describes the migration probability between the particle- and reconstructed-level quantities of a given observable (Z or jet p_T).

The total fiducial measured cross-section for the Z boson to be 405.4 ± 5.6 (stat) ± 24.3 (exp) ± 3.7 (theo) pb, while MG5_aMC next-to-leading order (NLO) and SHERPA predict 524.9 ± 11.7 (theo) pb and 485.0 pb, respectively. The comparison of the measured differential cross-section with MG5_aMC (leading order (LO), NLO) and SHERPA predictions as a function of c jet p_T is shown in Fig. 29.1b. The prediction MG5_aMC (LO) is describing the measured differential cross-section distribution within 10%, while both MG5_aMC and SHERPA at NLO tend to overestimate the cross-section by 20–30%. Since the prediction of inclusive Z + jets

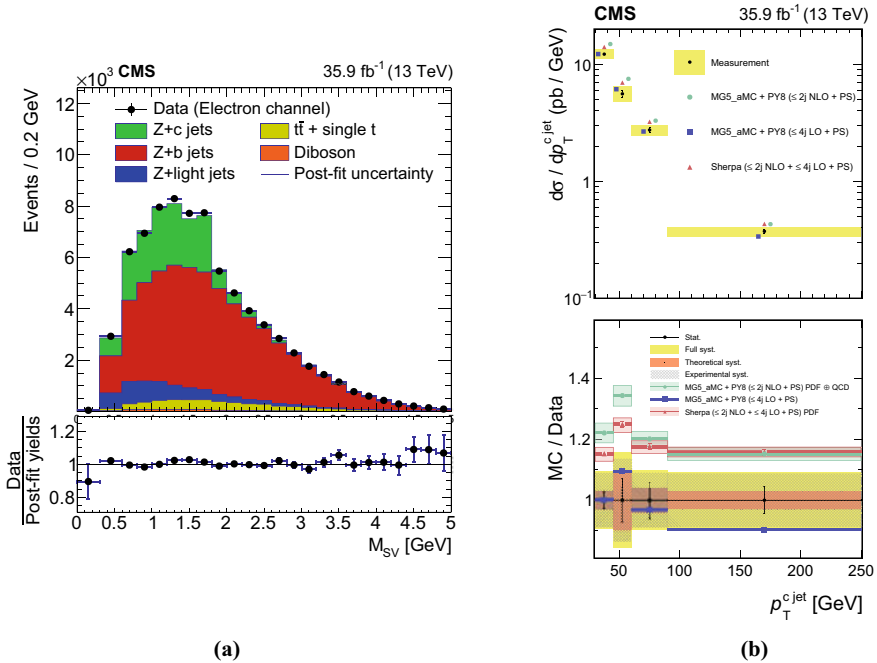


Fig. 29.1 **a** Secondary vertex invariant mass distributions derived from fits using the inclusive Z + HF jets data sample [4] **b** Measured fiducial differential cross-sections for inclusive Z+c jet production as a function of c jet p_T [3]. The yellow band shows total systematic uncertainties. Predictions from MG5_aMC (LO) are shown with statistical uncertainties only. The vertical bars on the data points represent statistical uncertainties

production at NLO order is in better agreement with data than that at LO. This could be an indication that the PDFs overestimate the c quark content and can be useful to improve existing constraints on the c quark content in the proton.

The fiducial volume Z + HF cross-section ratio measurements [4] is defined as: Z boson is selected within the mass range of 71 and 111 GeV requiring leptons (electrons or muons) with $p_T > 25$ GeV and $|\eta| < 2.4$. At least one inclusive jet or b jet or c jet is selecting with $p_T > 30$ GeV and $|\eta| < 2.4$. The measured integrated cross-section ratio values are $R(c/j) = 0.102 \pm 0.002$ (stat) ± 0.009 (syst), $R(b/j) = 0.0633 \pm 0.0004$ (stat) ± 0.0015 (syst), and $R(c/b) = 1.62 \pm 0.03$ (stat) ± 0.15 (syst). The measured integrated cross-section ratio values of $R(c/j)$ and $R(b/j)$ are better described with MG5_aMC (LO), while overestimated by MG5_aMC (NLO), except $R(c/b)$. The MCFM predictions underestimated the $R(c/j)$ and $R(c/b)$, while $R(b/j)$ are overestimated at NLO and LO.

The differential cross-section ratios $R(b/j)$ and $R(c/b)$ are shown in Fig. 29.2a and b, respectively. The MG5_aMC predictions for the cross-section ratios are higher in most of the bins, although still compatible with the data given the large uncertainties. The data are better described with MG5_aMC (LO) compared to MG5_aMC

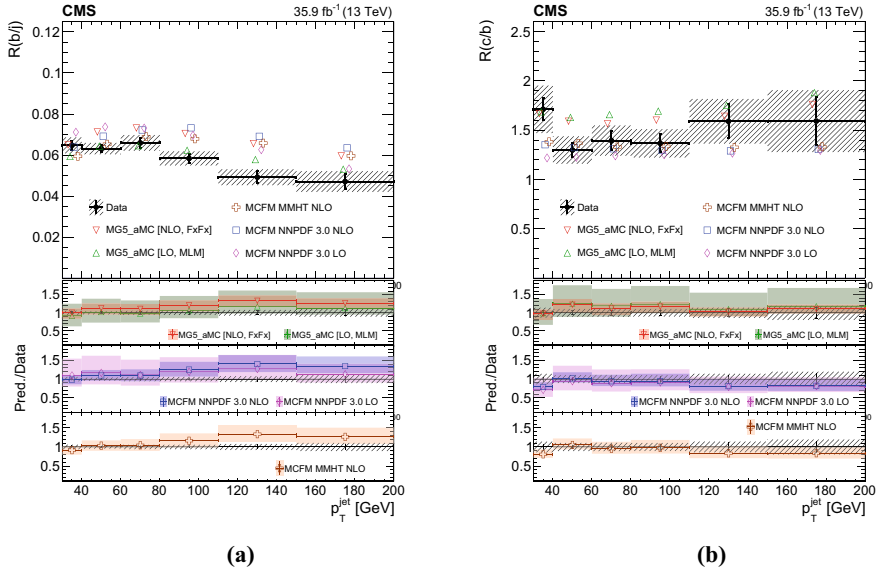


Fig. 29.2 Unfolded, particle-level MG5_aMC, and parton-level MCFM **a** $R(c/j)$ and **b** $R(b/j)$ cross-section ratios versus jet transverse momentum [4]. The vertical error bars for the data points are statistical while the hatched band represents the total uncertainties and their total PDF and scale uncertainties are shown as error bands in the ratio plots

(NLO). The MCFM (NLO) predictions for $R(b/j)$ disagree with the data at high jet p_T for both (MMHT14 and NNPDF3.0) PDFs. For $R(c/b)$, however, all theoretical predictions are consistent with the measured ratios. The difference between the parton- and particle-level jets may affect the MCFM predictions, although the corresponding effects are significantly reduced or vanish in the cross-section ratios. Alternatively, higher order pQCD calculations might be needed to describe the data.

29.3 Summary

The CMS experiment has a rich program on the measurements related to $Z + \text{HF}$ jets. Here, we present recent measurements, by the CMS experiment, using proton-proton collisions data at $\sqrt{s} = 13 \text{ TeV}$. The $Z+c$ jet measured cross-section is overestimated by the NLO prediction of MG5_aMC and SHERPA. The measured cross-section ratios $R(c/j)$, $R(b/j)$, and $R(c/b)$ precision exceed that of the current theoretical predictions. This study can be useful in improving the existing constraints in the simulation of the b quark and c quark PDF as well as tests for the validity of perturbative and non-perturbative QCD predictions.

References

1. S. Chatrchyan et al., [CMS], JINST **3**, S08004 (2008)
2. A.M. Sirunyan et al., [CMS], JINST **13**(05), P05011 (2018)
3. A.M. Sirunyan et al., [CMS], JHEP **04**, 109 (2021)
4. A.M. Sirunyan et al., [CMS], Phys. Rev. D **102**(3), 032007 (2020)

Chapter 30

Measurement of the Top Quark Mass Using Single Top Events



Mintu Kumar

Abstract Single top quark production via t -channel is the most dominant production process at the LHC. This process provides a unique phase space with lower color reconnection probability as compared to $t\bar{t}$. The final state comprises a single top along with a light quark giving rise to at least two jets, one of which arises from the hadronization of b-quark, an isolated energetic lepton (electron or muon), and large missing transverse momentum due to an escaping neutrino from the W boson decay. The measurement is based on proton-proton collision data, equivalent to 35.9 fb^{-1} integrated luminosity, recorded at $\sqrt{s} = 13 \text{ TeV}$ by the CMS [1] experiment during 2016 LHC operations. A multivariate technique based on boosted decision trees is deployed to optimally separate the signal from backgrounds. We obtain the top quark mass by fitting reconstructed top quark distribution using an appropriate combination of parametric shapes.

30.1 Introduction

A precise measurement of the top quark mass is of profound importance, both for theory and experiment, being an important parameter of the standard model (SM). It constitutes a major input to verify the self-consistency of the SM. Among all elementary particles, it is the largest contributor in terms of radiative corrections to the mass of the Higgs boson.

Most of the top-quark mass measurements to date have been obtained with $t\bar{t}$ events at the Large Hadron Collider (LHC) of CERN. The t -channel diagram shown in Fig. 30.1 constitutes the dominant process for single top quark production in pp collisions at the LHC, with a total cross-section of $216.99^{+9.04}_{-7.71} \text{ pb}$ calculated at the next-to-leading order (NLO).

Mintu Kumar—for the CMS Collaboration.

M. Kumar (✉)
Tata Institute of fundamental research, 400005 Mumbai, India
e-mail: mintu.kumar@cern.ch

© The Author(s), under exclusive license to Springer Nature Singapore Pte Ltd. 2022
B. Mohanty et al. (eds.), *Proceedings of the XXIV DAE-BRNS High Energy Physics Symposium, Jatni, India*, Springer Proceedings in Physics 277,
https://doi.org/10.1007/978-981-19-2354-8_30

167

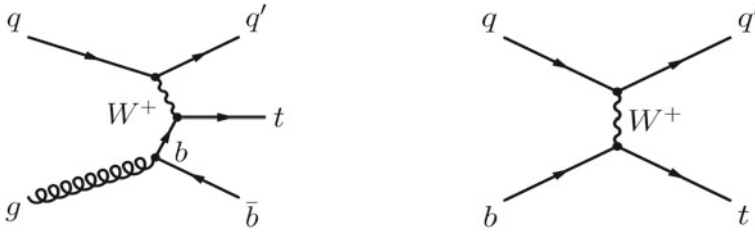


Fig. 30.1 Feynman diagrams of t -channel single top quark production at LO corresponding to four- (left) and five-flavor (right) schemes

30.2 Event Reconstruction

Events are selected in the muon (electron) channel by requiring at least one isolated muon (electron) with $p_T > 26(35)$ GeV and $|\eta| < 2.4(2.1)$. The relative isolation (I_{rel}) for a muon (electron) calculated by summing the transverse energy deposited by photons, charged and neutral hadrons within a cone of size $\Delta R = \sqrt{(\Delta\eta)^2 + (\Delta\phi)^2} < 0.4$ (0.3) around its direction, divided by its p_T must be less than 0.06. We require exactly two jets with $p_T < 40$ GeV and $|\eta| < 4.7$ and out of these one should be b-tagged Jet with $|\eta| < 2.4$.

To suppress the QCD multijet background, the transverse mass of W boson (m_W^T) > 50 GeV is required.

Event categories ($nJmT$) are defined depending on the number of jets (n) and b-tagged jets (m). The 2J1T category is the largest contributor to signal events and 2J0T category is used to validate the estimation of the QCD multijet background contribution in data. The four-momentum of the top quark is reconstructed from the four-momenta of its decay products: the charged lepton, the neutrino, and the b-tagged jet. The transverse momentum of the neutrino, $p_{T,\nu}$, is inferred from \mathbf{p}_T^{miss} . Assuming energy-momentum conservation at the $W \rightarrow \ell\nu$ vertex the longitudinal momentum of the neutrino, $p_{z,\nu}$, can be calculated from the following relation:

$$m_W^2 = \left(E_\ell + \sqrt{(p_T^{miss})^2 + p_{z,\nu}^2} \right)^2 - (\mathbf{p}_{T,\ell} + \mathbf{p}_T^{miss})^2 - (p_{z,\ell} + p_{z,\nu})^2, \quad (30.1)$$

where E_ℓ is the lepton energy and W boson mass $m_W = 80.4$ GeV.

30.3 Estimation of the QCD Multijet Background

QCD multijet production has tiny acceptance in the phase space used in the analysis. A sideband (SB) in data enriched in QCD multijet events is defined by inverting the isolation (identification) criteria for the selected muon (electron). QCD templates are derived by subtracting the total non-QCD contribution in this SB. The QCD

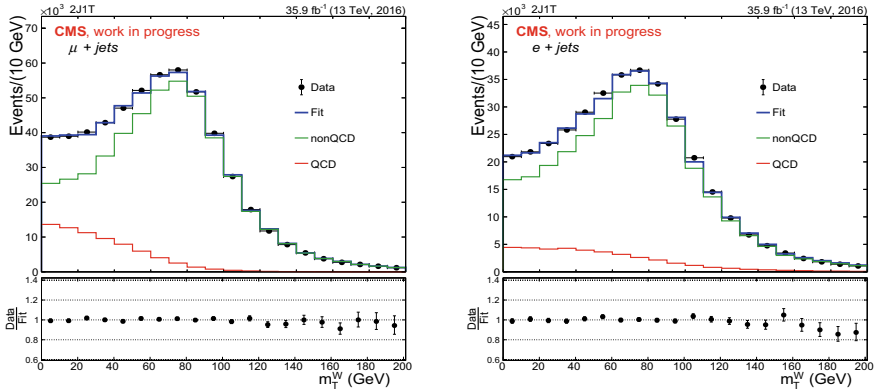


Fig. 30.2 Postfit distributions of m_W^T for the muon (left) and electron (right) final state

contribution in the signal region is then estimated by means of a two-component binned maximum-likelihood fit to the m_W^T distribution as shown in Fig 30.2. The method is first validated in the QCD-dominated category 2J0T.

30.4 Multivariate Analysis (MVA)

A number of kinematic variables are combined into an MVA discriminator to optimally separate t -channel single top quark events from backgrounds. These variables are selected such that they have a significant power to separate the signal and background. Selected variables have a low correction with the reconstructed top quark mass. Two separate boosted decision trees (BDTs) are designed. A criterion on the BDT response > 0.8 is chosen, which results in 64% (58%) signal purity and 20% efficiency for the muon (electron) final state.

30.5 Systematic Uncertainty

The signal and background normalizations are profiled (prof) by including them as nuisance parameters in the fit. All other sources of uncertainty are externalized. Uncertainties are calculated from the difference between the offset-corrected postfit values of m_t corresponding to the nominal and varied templates. The largest shift relative to the nominal result is quoted as the uncertainty. The dominant sources of uncertainties are jet energy scale, parton shower scale, b-quark hadronization model, color reconnection and early resonance decay.

30.6 Fit Strategy and Results

The $y = \ln m_t$ distributions obtained from the muon and electron final states are considered in a maximum likelihood fit, simultaneously. The QCD multijet contribution is subtracted from data before the fit and the remaining distribution is described by a parametric 1D model, $F(y)$ as:

$$F(y; y_0, f_{t\text{-ch}}, f_{\text{Top}}, f_{\text{EWK}}) = f_{t\text{-ch}} \cdot F_{t\text{-ch}}(y; y_0) + f_{\text{Top}} \cdot F_{\text{Top}}(y; y_0) + f_{\text{EWK}} \cdot F_{\text{EWK}}(y)$$

Here $F_{t\text{-ch}}$, F_{Top} and F_{EWK} represent the parametric shapes for the signal, top quark and electroweak backgrounds, respectively. The parameter y_0 of the combined signal and top quark background templates is the parameter of interest.

$F_{t\text{-ch}}$ is modeled with a combination of an asymmetric Gaussian core and a Landau function. F_{Top} is described by a Crystal ball function [2] and F_{EWK} is modeled with a Novosibirsk function [3]. The normalization scale factors are constrained using log-normal priors with 15, 6, and 10% based on their respective cross-section uncertainties. The top quark mass is obtained from the postfit $\ln m_t$ distribution as shown in Fig. 30.3 by taking the exponential of the postfit value of y_0 . The statistical and systematic uncertainty on the measured top quark mass is ≈ 0.29 and < 1 GeV, respectively, from the pseudo experiments.

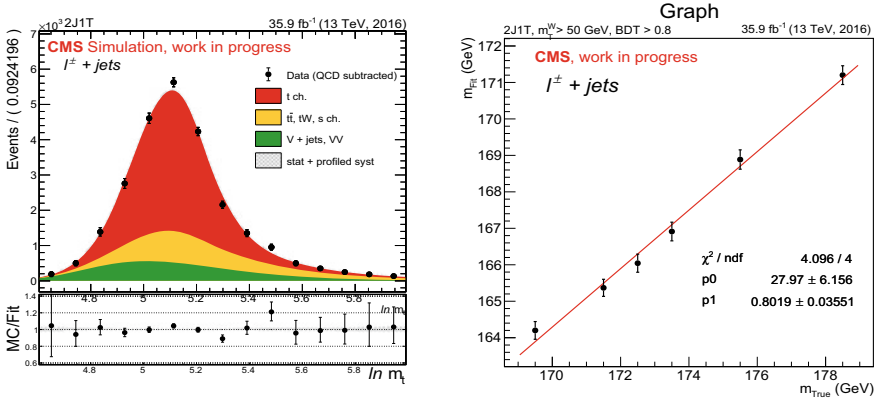


Fig. 30.3 Postfit distribution of $\ln m_t$ (left) and linearity of true and fitted mass (right)

30.7 Summary

We expect to achieve a sub-GeV precision for the first time in this specific channel. This measurement has a relative improvement in precision compared to the previous CMS measurement [4] in an event sample dominated by single top quark production. Final result [5] is aimed to be published in Moriond/EW2021.

References

1. S. Chatrchyan et al., CMS. JINST **3**, S08004 (2008)
2. T. Skwarnicki, Cracow, INP (1986). <http://www-library.desy.de/cgi-bin/showprep.pl?DESY-F31-86-02>
3. H. Ikeda et al., Belle. Nucl. Instrum. Meth. A **441**, 401–426 (2000)
4. A.M. Sirunyan et al. [CMS], Eur. Phys. J. C **77**(5), 354 (2017)
5. CMS Collaboration, Measurement of the top quark mass using events with a single reconstructed top quark in pp collisions at $\sqrt{s} = 13$ TeV. <http://cds.cern.ch/record/2759301>

Chapter 31

Determination of CKM Angle ϕ_3 at Belle and Belle II



Niharika Rout

Abstract We present the measurement of the angle ϕ_3 using a model-independent Dalitz plot analysis of $B^\pm \rightarrow D(K_S^0 \pi^+ \pi^-) K^\pm$ decays, which currently provides the best sensitivity. The method uses, as input, measurements of the strong phase of the $D \rightarrow K_S^0 \pi^+ \pi^-$ amplitude from the BESIII collaboration. This is the first measurement using the combined Belle and Belle II dataset of the order of 1 ab^{-1} . Here, we describe the extraction strategy developed based on the simulation sample.

31.1 Introduction

A more precise determination of the CP -violating parameter ϕ_3 (also called γ) is a highly promising path to a better understanding of the Standard Model (SM) description of CP violation and search for contributions from non-SM physics. It can be extracted via tree-level decays, along with non-perturbative strong interaction parameters, which make the method free of theoretical uncertainties to $\mathcal{O}(10^{-7})$ [1]. The most common channel for ϕ_3 extraction is $B^\pm \rightarrow DK^\pm$, where D indicates a D^0 or \bar{D}^0 meson decaying to the same final state f ; the weak phase ϕ_3 appears in the interference between $b \rightarrow c\bar{u}s$ and $b \rightarrow u\bar{c}s$ transitions. The $b \rightarrow u\bar{c}s$ amplitude (A_{sup}) is suppressed relative to the $b \rightarrow c\bar{u}s$ amplitude (A_{fav}) because of the magnitudes of the CKM matrix elements involved and the requirements of colorless hadrons in the final state. The two amplitudes are related by

$$\frac{A_{\text{sup}}(B^- \rightarrow \bar{D}^0 K^-)}{A_{\text{fav}}(B^- \rightarrow D^0 K^-)} = r_B e^{i(\delta_B - \phi_3)}, \quad (31.1)$$

Niharika Rout—for the Belle and Belle II collaboration.

N. Rout (✉)

Indian Institute of Technology Madras, 600036 Chennai, India
e-mail: niharikarout@physics.iitmadras.ac.in

where r_B is the magnitude of the ratio of amplitudes, and δ_B is the strong-phase difference between the favored and suppressed amplitudes.

31.1.1 BPGGSZ Formalism

The Bondar, Poluektov, Giri, Grossman, Soffer and Zupan (BPGGSZ) method [2–4] uses the phase-space distribution of the products of D decays to multibody self-conjugate final states, such as $K_S^0 h^+ h^-$. In this method, the D Dalitz space is binned to achieve optimal, and model-independent, sensitivity to ϕ_3 . The binning eliminates the model-dependent systematic uncertainty enabling degree-level precision. The signal yield in each bin is given by

$$\Gamma_i^\pm \propto K_i + r_B^2 \bar{K}_i + 2\sqrt{K_i \bar{K}_i} (c_i x_\pm + s_i y_\pm), \quad (31.2)$$

where $(x_\pm, y_\pm) = r_B(\cos(\pm\phi_3 + \delta_B), \sin(\pm\phi_3 + \delta_B))$. Here, K_i is the number of events in the i th bin of a flavour tagged D decay sample. The parameters c_i and s_i are the amplitude-averaged strong-phase difference between \bar{D}^0 and D^0 over the i th bin and can be measured using quantum-correlated pairs of D mesons created at e^+e^- annihilation experiments operating at the threshold of $D\bar{D}$ pair production. The (x_\pm, y_\pm) parameters can be obtained from Eq. 31.2 using the maximum likelihood method. The values of c_i and s_i parameters for $D^0 \rightarrow K_S^0 \pi^+ \pi^-$ decays, as well as the binning scheme to divide the D phase space, used in this analysis are reported in Ref. [5].

31.2 Data Sample and Event Selection

The analysis uses e^-e^+ collision data collected at center-of-mass energy corresponding to $\Upsilon(4S)$ resonance by the Belle [6] and Belle II [7] detectors corresponding to 711 fb^{-1} and 90 fb^{-1} collected by the year 2020, respectively. Studies on Monte Carlo (MC) samples are performed to optimize the selection criteria, determine the signal efficiencies and identify various sources of background.

We reconstruct $B^\pm \rightarrow DK^\pm$ and $B^\pm \rightarrow D\pi^\pm$ decays in which D decays into $K_S^0 \pi^- \pi^+$ final states. Charged particle tracks are selected by requiring $|dr| < 0.2$ cm and $|dz| < 1$ cm, where dr and dz represent the distance of the closest approach to the interaction point (IP) in the plane transverse to the beam direction and in the beam direction, respectively. These tracks are then identified as kaons or pions by the particle identification detectors. We reconstruct the K_S^0 candidates from two oppositely charged pion tracks. The dipion candidate mass is required to be within $\pm 3\sigma$ of the known K_S^0 mass. The $K_S^0 \pi^+ \pi^-$ mass is restricted to match the known D mass, $1.85 < M_{D^0} < 1.88 \text{ GeV}/c^2$, to reduce combinatorial backgrounds. The B -

meson candidates are reconstructed by combining a D candidate with a charged kaon or pion. The kinematic variables used for B reconstruction are the beam-constrained mass (M_{bc}) and the beam-energy difference (ΔE), which are defined as

$$M_{bc} = \sqrt{E_{\text{beam}}^2 - (\sum \vec{p}_i)^2}, \quad \Delta E = \sum E_i - E_{\text{beam}}, \quad (31.3)$$

where E_{beam} is the beam energy in the center-of-mass frame and E_i and \vec{p}_i are the energy and momenta of B daughter particles in the center-of-mass frame. The selection criteria chosen are $-0.13 < \Delta E < 0.18$ GeV and $M_{bc} > 5.27$ GeV/ c^2 . A kinematic constraint is applied so that the B daughters come from a common vertex. In events with more than one candidate, the candidate with the smallest χ^2 value, constructed from the M_{bc} and M_D pulls, is retained.

The main sources of background in our analysis are events coming from the $e^+e^- \rightarrow q\bar{q}$ ($q = u, d, s$ or c) continuum process. These backgrounds are suppressed by utilizing the event topology, which is different from that of $B\bar{B}$ events, with a binary classifier based on boosted decision trees that combine nonlinearly seven inputs into a scalar output discriminator. Continuum events preferentially produce particles collimated into back-to-back jets, whereas the $e^+e^- \rightarrow \Upsilon(4S) \rightarrow B\bar{B}$ are distributed uniformly over the 4π solid angle. The overall selection efficiency is 17.77 and 19.85% for $B^\pm \rightarrow DK^\pm$ at Belle and Belle II, respectively.

31.3 Fit Procedure and (x_\pm, y_\pm) Parameter Extraction

The signal yield in each D phase-space bin is determined from a two-dimensional extended maximum-likelihood fit to ΔE and transformed FBBDT output (C') simultaneously in $B \rightarrow D\pi$ and $B \rightarrow DK$. We use a combined fit with a common likelihood in all 16 bins. Figure 31.1 represents the signal-enhanced fit projections of ΔE and C' of the channel $B^\pm \rightarrow DK^\pm$ in a simulated sample equivalent to the Belle sample. The fit strategy is the same for Belle II.

We have adopted the new strategy, for (x_\pm, y_\pm) parameters extraction, recently used by LHCb [8]. We use the control sample $B \rightarrow D\pi$ to determine the K_i and K_{-i} fractions in the simultaneous fit itself as these events will have the same relative acceptance over phase space as of $B \rightarrow DK$ if a common selection is applied. An alternate parameterization is introduced, to make the fit stable at low r_B value, which utilizes the fact that ϕ_3 is a common parameter, and that the CP violation in $B \rightarrow D\pi$ decays can therefore be described by the addition of a single complex variable [9], which is a function of $x_\pm^{D\pi}, y_\pm^{D\pi}$.

The obtained values of physics parameters of interest x_\pm^{DK}, y_\pm^{DK} in simulation are shown in Table 31.1. As there is no CP violation present in the simulation, the expected values of these parameters are zero. In data, the asymmetry between the signal yields of B^+ and B^- will drive the extraction of hadronic parameters r_B, δ_B and ϕ_3 .

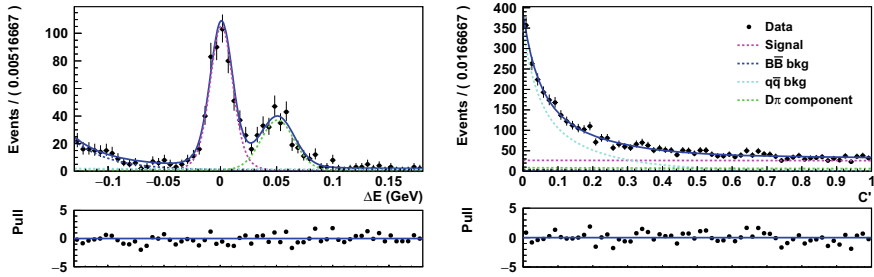


Fig. 31.1 Signal enhanced fit projections of ΔE and C' of the channel $B^\pm \rightarrow DK^\pm$ in a simulated sample equivalent to the Belle sample. The signal region is defined as $|\Delta E| < 0.05$ GeV and $0.65 < C' < 1$

Table 31.1 Results on a simulated sample equivalent to the Belle dataset

Parameter	Value
x_+^{DK}	-0.04 ± 0.04
x_-^{DK}	0.01 ± 0.03
y_+^{DK}	-0.10 ± 0.06
y_-^{DK}	-0.01 ± 0.03

31.4 Summary

The precise measurement of the angle ϕ_3 will give us a SM benchmark to which other measurements of the CKM parameters can be compared to, both within the SM and beyond. Here, we outlined the analysis overview of the decays $B^\pm \rightarrow D(K_S^0 \pi^+ \pi^-) K^\pm$ for ϕ_3 extraction. This is our first attempt to obtain sensitivity from a combined dataset of Belle and Belle II. The signal extraction procedure is established in an MC sample, and we will look at data soon. With the ultimate Belle II data sample of 50 ab^{-1} , a determination of ϕ_3 with a precision of 1° or better is foreseen [7].

References

1. J. Brod, J. Zupan, J. High. Energ. Phys. **051**, 1401 (2014)
2. A. Giri, Yu. Grossman, A. Soffer, J. Zupan, Phys. Rev. D **68**, 054018 (2003)
3. A. Bondar, Proceedings of BINP special analysis meeting on Dalitz analysis, unpublished (2002)
4. A. Poluektov et al., Belle collaboration. Phys. Rev. D **70**, 072003 (2004)
5. M. Ablikim et al., BESIII collaboration. Phys. Rev. D **101**, 112002 (2020)
6. A. Abashian et al., Belle collaboration. Nucl. Instrum. Methods Phys. Res. A **479**, 117 (2002)
7. E. Kou et al., (Belle II collaboration) PTEP **2019**(2), 123C01 (2019)
8. R. Aaij et al., (LHCb collaboration), LHCb-CONF-2020-001. [arXiv:2010.08483](https://arxiv.org/abs/2010.08483)
9. J. Garra Tico et al., Phys. Rev. D **102**, 053003 (2020)

Chapter 32

Exploring the Possibility of Right-Angled Unitarity Triangle



Nikhila Awasthi, Gulsheen Ahuja, Monika Randhawa, and Manmohan Gupta

Abstract Using a unitarity-based analysis, we have explored the possibility of the reference unitarity triangle (UT) to be right-angled. In this context, our analysis shows that the present CKM parameters including CP-violating parameters, such as Jarlskog’s rephasing invariant (J), ϵ_K etc. are in agreement with such a possibility.

32.1 Introduction

The unitarity constraints and the unitary triangle of the Cabibbo-Kobayashi-Maskawa (CKM) [1] have played crucial roles in understanding several crucial features of flavour physics. The CKM matrix is defined as

$$\begin{pmatrix} d' \\ s' \\ b' \end{pmatrix} = \begin{pmatrix} V_{ud} & V_{us} & V_{ub} \\ V_{cd} & V_{cs} & V_{cb} \\ V_{td} & V_{ts} & V_{tb} \end{pmatrix} \begin{pmatrix} d \\ s \\ b \end{pmatrix}, \quad (32.1)$$

where d' , s' and b' are flavour eigenstates and d , s and b are mass eigenstates. The unitarity of the CKM matrix implies

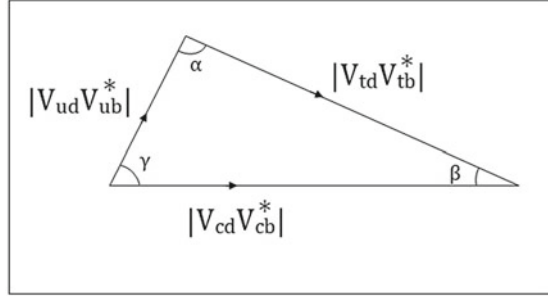
$$\sum_{\alpha=d,s,b} V_{i\alpha} V_{j\alpha}^* = \delta_{ij}, \quad \text{and} \quad \sum_{i=u,c,t} V_{i\alpha} V_{i\beta}^* = \delta_{\alpha\beta}, \quad (32.2)$$

where Latin indices run over the up type quarks (u, c, t) and Greek ones run over the down type quarks (d, s, b). Six of these relations can be represented as triangles in the complex plane. Four of these triangles are highly skewed; one of these involves the CKM matrix elements based on ‘t’ quark, hence not directly observable. Therefore,

N. Awasthi (✉) · G. Ahuja · M. Gupta
Department of Physics, Panjab University, 160014 Chandigarh, India
e-mail: nikhila.awas@gmail.com

M. Randhawa
Department of Applied Sciences, UIET, P.U, 160014 Chandigarh, India

Fig. 32.1 The ‘d,b’ triangle in the complex plane



the most important of these is the ‘db’ triangle or the usually talked about unitarity triangle (UT) (Fig. 32.1).

The CKM matrix can be expressed in terms of three real angles and one non-trivial phase which is responsible for CP violation in the SM. The standard parametrization used by Particle Data Group (PDG) for the representation of the CKM matrix is given by

$$V_{CKM} = \begin{pmatrix} c_{12}c_{13} & s_{12}c_{13} & s_{13}e^{-i\delta} \\ -s_{12}c_{23} - c_{12}s_{23}s_{13}e^{i\delta} & c_{12}c_{23} - s_{12}s_{23}s_{13}e^{i\delta} & s_{23}c_{13} \\ s_{12}s_{23} - c_{12}c_{23}s_{13}e^{i\delta} & -c_{12}s_{23} - s_{12}c_{23}s_{13}e^{i\delta} & c_{23}c_{13} \end{pmatrix}, \quad (32.3)$$

where $s_{ij} \equiv \sin \theta_{ij}$ and $c_{ij} \equiv \cos \theta_{ij}$. The approximations $V_{us} \cong s_{12}$, $V_{ub} \cong s_{13}$ and $V_{cb} \cong s_{23}$ can be readily used, considering the small experimental value of the mixing angle θ_{13} . The angles of the unitarity triangle are expressed as

$$\alpha \equiv \arg \left[-\frac{V_{td}V_{tb}^*}{V_{ud}V_{ub}^*} \right], \quad \beta \equiv \arg \left[-\frac{V_{cd}V_{cb}^*}{V_{td}V_{tb}^*} \right], \quad \gamma \equiv \arg \left[-\frac{V_{ud}V_{ub}^*}{V_{cd}V_{cb}^*} \right]. \quad (32.4)$$

After intense amounts of efforts spanning over several decades, at present the CKM matrix is very precisely determined both from direct and indirect measurements. There have been considerable improvements in the measurements of the angles of the unitarity triangle, e.g., angle β is very precisely known, whereas for the other two there have been marked improvements in the last few years. In the present context, it is perhaps desirable to discuss the recent situation regarding the measurements of the angle α . For example, the world average for α reads $(84.9_{-4.5}^{+5.1})^\circ$ by HFLAV [2] and $(84.5_{-5.2}^{+5.9})^\circ$ by PDG-2018 [3]. CKMfitter [4] and UTfit [5] quote a higher value of α , $(91.6_{-1.1}^{+1.7})^\circ$ and $(90.9 \pm 2.0)^\circ$, respectively. The value of α calculated from $B \rightarrow \rho\rho$ decay as mentioned by PDG is $(90.9_{-5.5}^{+5.6})^\circ$. It is clear from these values that there is a good possibility that the angle α may in fact be 90° [6, 7]. Therefore, using this value of α , we attempt to check its implications for the CKM matrix and other parameters.

32.2 Analysis

Using unitarity of the triangle and the precisely known value of angle β , this value of α has immediate consequence for the angle γ , for example,

$$\gamma = \pi - \alpha - \beta = (67.8 \pm 0.7)^\circ. \quad (32.5)$$

The angle γ is very much related to the CP-violating phase δ , e.g., in the PDG representation, and the two are related as [8]

$$\tan(\delta/2) = \frac{1 \pm \sqrt{1 + \tan^2 \gamma}}{\tan \gamma \left(\frac{c_{12}s_{23}s_{13}}{s_{12}c_{23}} - 1 \right)}. \quad (32.6)$$

It is not difficult to show that for numerical work, γ can be taken to be equal to δ within an error of 0.05%. Before constructing the CKM matrix, we need to find value of V_{ub} , for which there is persisting ambiguity in the literature [2]. To that end we use the relation [8]

$$\tan \beta = \frac{c_{12}s_{12}s_{13} \sin(\alpha + \beta)}{c_{23}s_{23}(s_{12}^2 - c_{12}^2s_{13}^2) + c_{12}s_{12}s_{13}(c_{23}^2 - s_{23}^2) \cos(\alpha + \beta)}, \quad (32.7)$$

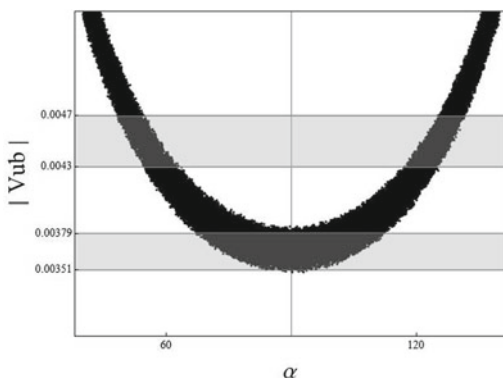
which can be derived using Eq. (32.4). In Fig. 32.2 we have plotted V_{ub} v/s α using input [2, 3]

$$V_{us} = 0.2243 \pm 0.0005, \beta = (22.2 \pm 0.7)^\circ, V_{cb} = (42.2 \pm 0.8) \times 10^{-3}. \quad (32.8)$$

From the figure one can immediately find the value of V_{ub} for $\alpha = 90^\circ$, for example

$$V_{ub} = 0.00348 - 0.00385. \quad (32.9)$$

Fig. 32.2 The variation of $|V_{ub}|$ with respect to α . The vertical line denotes $\alpha = 90^\circ$. The top and bottom shaded regions denote inclusive and exclusive 1σ ranges of $|V_{ub}|$, respectively



Using the input mentioned in Eq. (32.8) and $\alpha = 90^\circ$, we get

$$|V_{ub}| = 0.00367 \pm 0.00013. \quad (32.10)$$

As a next step, we have constructed the CKM matrix, using Eqs. (32.5), (32.8) and (32.10) in Eq. (32.3), which comes out to be

$$V_{CKM} = \begin{pmatrix} 0.97451(11) & 0.2243(5) & 0.00367(13) \\ 0.22415(49) & 0.97364(11) & 0.0422(8) \\ 0.00876(14) & 0.04144(78) & 0.99910(3) \end{pmatrix}. \quad (32.11)$$

This seems to be in excellent agreement with the recent PDG value obtained from global fits [3]. After checking the compatibility of the $\alpha = 90^\circ$ value with the CKM matrix, we would like to find its implications for parameters such as J , ϵ_K , $\left| \frac{\Delta m_d}{\Delta m_s} \right|$, $\left| \frac{V_{cb}}{V_{ub}} \right|$, etc. In the case of J , using the input mentioned above and using the expression

$$J = s_{13}^2 c_{13}^2 c_{12}^2 \frac{\sin \alpha \sin \gamma}{\sin \beta} \quad (32.12)$$

we obtain

$$J = (3.13 \pm 0.14) \times 10^{-5}. \quad (32.13)$$

Similarly, the parameters $|\epsilon_K|$ and $\left| \frac{\Delta m_d}{\Delta m_s} \right|$ can be evaluated to be [3]

$$\begin{aligned} \epsilon_K &= \kappa_\epsilon \frac{e^{i\phi_\epsilon} G_F^2 m_W^2 m_K}{12\sqrt{2}\pi^2 \Delta m_K} F_K^2 \widehat{B}_K [\eta_{tt} S(x_t) \text{Im}[(V_{ts} V_{td}^*)^2] + \\ &\quad 2\eta_{ct} S(x_c, x_t) \text{Im}[V_{cs} V_{cd}^* V_{ts} V_{td}^*] + \eta_{tt} x_c \text{Im}[(V_{cs} V_{cd}^*)^2]], \\ |\epsilon_K| &= 0.00223 \pm 0.00025, \\ \left| \frac{\Delta m_d}{\Delta m_s} \right| &= \frac{1}{\zeta^2} \frac{m_{B_d}}{m_{B_s}} \left| \frac{V_{td}}{V_{ts}} \right|^2 = 0.0297 \pm 0.0009. \end{aligned} \quad (32.14)$$

From these, one can easily conclude that they are very much in agreement with the present experimental limits. In conclusion, we would like to state that the possibility that the UT is a right-angled UT is very much permissible by the present data.

Acknowledgements N.A. would like to acknowledge CSIR, Govt. of India for financial support. N.A., G.A. and M.G. would like to thank the Chairman, Department of Physics, P.U., for providing facilities to work.

References

1. N. Cabibbo, Phys. Rev. Lett. **10**, 531 (1963); M. Kobayashi, T. Maskawa, Prog. Theor. Phys. **49**, 652 (1973)
2. Y. Amhis et al., (Heavy Flavor Averaging Group), Eur. Phys. J. C **77**, 895 (2017). <https://hflav.web.cern.ch/>
3. M. Tanabashi et al., (Particle Data Group), Phys. Rev. D **98**, 030001 (2018)
4. J. Charles et al., (CKMfitter Group). Eur. Phys. J. C **41**, 1 (2005). [hep-ph/0406184], updated results and plots. <http://ckmfitter.in2p3.fr>
5. M. Bona, et al., (UTfit Collaboration), JHEP **0610**, 081 (2006). <https://doi.org/10.1088/1126-6708/2006/10/081> [hep-ph/0606167]
6. Z. Xing, Phys. Lett. B **679**, 111 (2009); Z. Xing, Phys. Rev. D **86**, 113006 (2012)
7. S. Antusch, M. Holthausen, M.A. Schmidt, M. Spinrath, Nucl. Phys. B **877**, 752 (2013)
8. M. Gupta, G. Ahuja, Int. Jour. Mod. Phys. A **27**, 1230033 (2012)

Chapter 33

Recent Measurements of Higgs Boson Properties in the Diphoton Decay Channel with the CMS Detector



Prafulla Saha

Abstract A comprehensive analysis on the $H \rightarrow \gamma\gamma$ signature, including all possible SM Higgs boson production modes using the full Run 2 dataset of 137fb^{-1} recorded by the CMS experiment has been presented here. The present analysis improves the sensitivity by categorising the signal events based on different Higgs production mechanisms: gluon-gluon fusion (GGH), vector boson fusion (VBF), vector boson associated production (VH) and top quark associated production (ttH, tH). Combining all channels, the Higgs boson signal strength is measured to be $1.02_{-0.09}^{+0.11}$ with respect to the corresponding SM predictions.

33.1 Introduction

The Higgs boson has been discovered by the ATLAS and CMS experiments in 2012 during Run1 of LHC operation. However, analyzing a larger volume of LHC dataset collected by the CMS detector from 2016 to 2018 at a higher center of mass energy ($\sqrt{s} = 13\text{ TeV}$) is expected to shed more light on the Higgs boson properties and would improve the corresponding measurement sensitivity. The SM Higgs boson can be produced at the LHC through different production mechanisms such as gluon-gluon fusion (GGH), vector boson fusion (VBF), vector boson associated production (VH) and top quark associated production (ttH, tH). The analysis presented here targets different production modes of the SM Higgs boson in separate categories which are further split into various kinematic regions. Such a strategy enables to perform the fine-grained measurements for individual Higgs production modes in various kinematic regions to enable measurements within the simplified template cross section (STXS) framework [1]. Moreover, this kind of measurement reduces the

Prafulla Saha—for the CMS Collaboration.

P. Saha (✉)

National Institute of Science Education and Research, An OCC of Homi Bhabha National Institute, Bhubaneswar 752050, India
e-mail: prafulla.saha@niser.ac.in

© The Author(s), under exclusive license to Springer Nature Singapore Pte Ltd. 2022
B. Mohanty et al. (eds.), *Proceedings of the XXIV DAE-BRNS High Energy Physics Symposium, Jatni, India*, Springer Proceedings in Physics 277,
https://doi.org/10.1007/978-981-19-2354-8_33

183

theoretical uncertainties that are directly folded into the measurements and provide a common framework for the measurement combining with different decay channels.

In SM, the Higgs boson decaying within two photons has a very small branching ratio of 0.023%. However, in the CMS detector $H \rightarrow \gamma\gamma$ signature can be easily triggered and provides a relatively clean signal having the diphoton invariant mass resolution of $\sim 1-2\%$.

33.2 Analysis Strategy

The analysis is based on the 35.9, 41.5, and 59.4 fb^1 of proton-proton collision data (at $\sqrt{s} = 13$ TeV) recorded with the CMS detector during the 2016, 2017 and 2018, respectively. Simulated signal samples, corresponding to the different Higgs boson production mechanisms, are generated using MADGRAPH5_aMC@NLO (version 2.4.2). The analysis categories are constructed where the narrow signal peak is distinguishable on top of the falling background in diphoton invariant mass distribution. Since the main probe is the photon in the events, the photons are reconstructed with the energy deposits in the electromagnetic calorimeter (ECAL) not associated with the charge particle tracks. Because of the imperfect containment of electromagnetic shower and the energy loss due to the converted photons, a multivariate regression technique is trained on the simulated photon to correct the photon energy. Further, the additional disagreement between the data and MC is corrected simultaneously in bins of $|\eta|$, showershape variable (R_9) and LHC fill. The selection of two photons from the same vertex has a significant impact on the diphoton mass resolution. The event vertex identification algorithm uses a multivariate analysis approach with boosted decision trees (BDT) considering observables related to tracks recoiling against the diphoton system. Finally, the selected vertex is chosen to be within the 1 cm in position along the beam axis (z) and is found to have a negligible impact on the diphoton mass resolution. The vertex identification algorithm is validated with the simulated $Z \rightarrow \mu\mu$ events. Photons in events passing the preselection criteria are further required to satisfy a photon identification criterion based on a BDT trained to separate genuine (“prompt”) photons from jets mimicking a photon signature. This photon identification BDT is trained with simulated sample of γ +jet events, where prompt photons are used as the signal while jets are used as the background.

33.3 Event Categorisation

The analysis is designed to separate different Higgs production modes such as tH, ttH, VH, VBF and ggH. All the analysis categories require two preselected leading photons which satisfy $p_T^{\gamma_1} > m_{\gamma_1\gamma_2}/3$ and $p_T^{\gamma_2} > m_{\gamma_1\gamma_2}/3$, respectively, while the diphoton invariant mass falls in the range of 100–180 GeV. Depending upon the associated particles and their decay modes, additional selections are applied in leptons,

jets, missing transverse energy etc. In the ggH categorisation the events are assigned to an STXS region using a multiclass BDT, which predicts the probability that a diphoton event belongs to a given STXS bin. Furthermore, another BDT training is performed to reject non-Higgs background events entering ggH categorisation. Similarly, VBF, VH Hadronic, VH MET, ZH Leptonic and WH Leptonic categorisation also use BDT based on the respective signal characteristics. The Higgs production associated with single top quark (tHq) and a pair of top quark (ttH) have very similar final-state topologies. Therefore, a dedicated deep neural network (DNN) has been designed to separate tHq and ttH events along with separate BDTs to reject non-Higgs background events in tHq and ttH categories.

33.4 Signal and Background Model

Signal processes are modelled with the MC signal samples passing the dedicated category and the $m_{\gamma\gamma}$ distributions are fitted using a sum of most five Gaussian functions. The background processes are modelled using $m_{\gamma\gamma}$ distribution from data between $m_{\gamma\gamma} < 115$ and $m_{\gamma\gamma} > 135$. A set of functions: exponential functions, Bernstein polynomials, Laurent series and power law functions are used to fit the $m_{\gamma\gamma}$ distribution for the background processes. The discrete profiling method [2] has been used to estimate the systematic uncertainty associated with choosing a particular function for fit. A F-test [3] is performed in the signal model to find the best order of the Gaussian fit to simulated signal events and in the background model for each family of functions to find the order of the polynomial to be used. The signal and the background model are shown in Fig. 33.1.

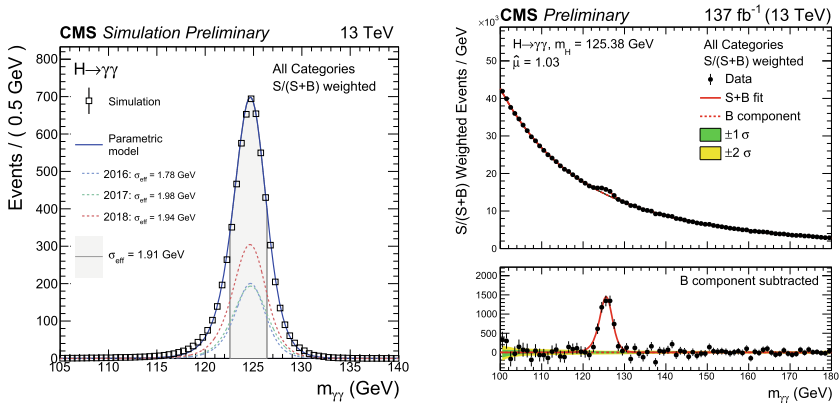


Fig. 33.1 The left side plot is the signal model of all years together plotted with blue line. The grey-shaded area shows the σ eff. value (half the width of the narrowest interval containing 68.3% of the invariant mass distribution). The right side plot is the background model, data points (black) and signal-plus-background model fit for the sum of all categories. The bottom panel shows the residuals after subtraction of this background component

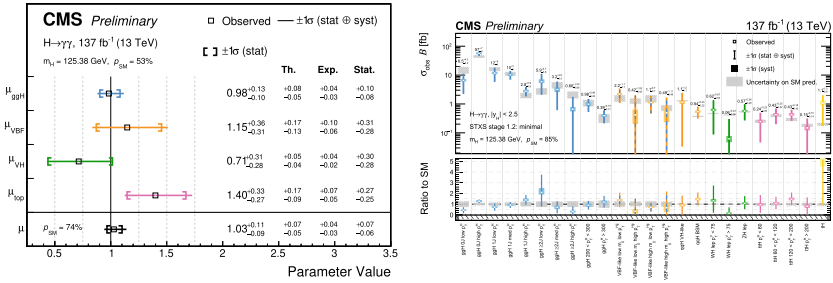


Fig. 33.2 The left plot is the observed results of best-fit signal strength with respective 1σ uncertainty for four Higgs production modes. In the right side plot the observed best-fit cross sections are plotted along with the respective 68% confidence level intervals in different STXS bins

33.5 Results

The signal strength, μ , is defined as the ratio of the observed product of the Higgs boson cross section and diphoton branching fraction to its SM expectation. To extract the results, simultaneous binned maximum likelihood fits are performed to the $m_{\gamma\gamma}$ distributions for all analysis categories, in the mass range $100 < m_{\gamma\gamma} < 180$ GeV. A likelihood function is defined for each analysis category using analytic models to describe the $m_{\gamma\gamma}$ distributions of signal and background events, with nuisance parameters to account for the experimental and theoretical systematic uncertainties. The signal strength of different Higgs boson production mode and the cross section times branching ratio for different STXS bins are shown in Fig. 33.2. Combining all Higgs boson production modes, the Higgs boson signal strength is measured to be $1.02^{+0.11}_{-0.09}$ with respect to the corresponding SM predictions.

References

1. LHC Higgs Cross Section Working Group, Handbook of LHC Higgs cross sections: 4. Deciphering the nature of the Higgs sector. CERN (2016). <https://doi.org/10.23731/CYRM-2017-002>
2. P.D. Dauncey, M. Kenzie, N. Wardle, G.J. Davies, JINST **10**(04), P04015 (2015)
3. R.A. Fisher, On the interpretation of χ^2 from contingency tables, and the calculation of P. J. R. Stat. Soc. **85**, 87 (1922). <https://doi.org/10.2307/2340521>

Chapter 34

Revisiting the Stückelberg Mechanism



Radhika Vinze and Sreerup Raychaudhuri

Abstract The Stückelberg mechanism is a model in which the addition of an extra scalar to a $U(1)$ gauge theory permits the gauge boson to have a mass without breaking the gauge symmetry. It is shown that combining this with a Higgs scalar and a broken symmetry automatically fixes the physical gauge of the model. Extension of this idea to a $U(1)$ -extended Standard Model is used to develop a highly economical model with an extra Z' which is potentially discoverable at colliders.

The fact that electromagnetism originates from a local $U(1)$ gauge theory was discovered by Fock and London in 1927. The gauge boson of such a model is the photon, which is massless because of the gauge symmetry. This $U(1)$ gauge theory, after quantisation, came to be known as *quantum electrodynamics*, or QED. In 1932, however, the neutron was discovered, and with it came Heisenberg's postulation of a strong interaction between nucleons [1]. Yukawa (1935) cast this as a quantum field theory with the exchange of massive scalar particles to reproduce the short-range nature of the nucleon-nucleon potential [2].

In 1937, Stückelberg tried to derive this nucleon-nucleon potential using Yukawa's theory, but ended up with a repulsive, rather than an attractive force. He then tried a vector interchange theory, and it worked! To explain the existence of a vector boson mediator of strong interactions, Stückelberg then postulated another, stronger $U(1)$ gauge theory, with a conserved charge which he called *baryon number*. In order to give mass to these gauge bosons, he added a massive scalar to the theory and invented the ingenious Stückelberg mechanism, by which the gauge boson can acquire mass without breaking the gauge symmetry [3]. The price to pay is that the Stückelberg scalar and the gauge bosons must have the same mass. Though the pions—Yukawa's scalars—were discovered in 1947, there was no sign of these heavy vector mesons at the time. In 1961, however, the rho meson, a vector counterpart of the pion, was

R. Vinze (✉)

Department of Physics, University of Mumbai, Mumbai, India
e-mail: radhika.vinze@physics.mu.ac.in

S. Raychaudhuri

Department of Theoretical Physics, Tata Institute of Fundamental Research, Mumbai, India

discovered. However, its mass is around 770 MeV, whereas the pion mass is only 140 MeV. Clearly, then, it is not possible for the pion to be a Stückelberg scalar to the rho as a gauge boson. By this time, the idea of spontaneous symmetry-breaking was in the air, and thus interest in the Stückelberg model faded after the work of Englert & Brout, Higgs and Guralnik, Hagen and Kibble in 1964 [4]. The correctness of the electroweak symmetry-breaking model was brilliantly proved in 2012 with the discovery of the Higgs boson [5] and has been reinforced with every successive year as the couplings of the Higgs boson turns out to be closer and closer to the Standard Model predictions.

Thus, it would seem that the Stückelberg model lies consigned to the dustbin of ingenious but failed theories and has no part to play in modern particle physics. In recent times, however, a gentle revival of this idea has been witnessed in the literature [6] on theories beyond the Standard Model. Specifically, in models with an extended gauge symmetry—and therefore an extra gauge boson—the Stückelberg mechanism has been invoked to give mass to the extra gauge bosons without breaking the extra gauge symmetries. However, work on these models has been intermittent and does not take all current data into account. This work attempts to fill in this gap by making a systematic and thorough investigation of the above scenario. Our work throws up interesting features of the theory which have not been hitherto stressed in the literature.

As a toy model, we first consider an Abelian gauge theory with a Higgs scalar $\tilde{\phi}(x)$ which breaks the gauge symmetry spontaneously, but which also has an extra Stückelberg scalar $\tilde{\sigma}(x)$. The Lagrangian for this theory is

$$\mathcal{L} = -\frac{1}{4}F_{\mu\nu}F^{\mu\nu} + [D_\mu\tilde{\phi}]^*[D^\mu\tilde{\phi}] + \mu^2\tilde{\phi}^*\tilde{\phi} - \lambda(\tilde{\phi}^*\tilde{\phi})^2 + \mathcal{L}_S \quad (34.1)$$

with

$$\mathcal{L}_S = \frac{1}{2}(M^2 + \lambda_1\tilde{\phi}^*\tilde{\phi})\left(A_\mu + \frac{1}{M}\partial_\mu\tilde{\sigma}\right)^2 - \frac{1}{2}(M^2 + \lambda_2\tilde{\phi}^*\tilde{\phi})\left(\tilde{\sigma} - \frac{1}{M}\partial_\mu A_\mu\right)^2$$

where $D_\mu = \partial_\mu + igA_\mu$ while M is a mass parameter and λ_1, λ_2 are coupling constants. Redefining $\tilde{\phi}(x) = \phi(x) + v/\sqrt{2}$ and $\tilde{\sigma}(x) = \sigma(x)/\sqrt{1 + \lambda_1 v^2/2M^2}$ where, as usual $v^2 = \mu^2/2\lambda$ we get

$$\mathcal{L}_S = \frac{1}{2}M_A^2 A_\mu A^\mu - \frac{1}{2\xi}(\partial_\mu A^\mu)^2 + \frac{1}{2}\partial^\mu\sigma\partial_\mu\sigma - \frac{1}{2}M_\sigma^2\sigma^2 + \dots \quad (34.2)$$

where $M_A^2 = g^2 v^2 + M^2 + \frac{1}{2}\lambda_1 v^2$ and $M_\sigma = M$, setting $\lambda_1 = \lambda_2$ to avoid having bilinear σA_μ terms. Most interestingly

$$\xi^{-1} = 1 + \frac{\lambda_1 v^2}{2M^2} \quad (34.3)$$

i.e. the gauge-fixing parameter is determined by the couplings of the Stückelberg scalar. By choosing M and λ_1 we can go to the unitary gauge, where $M_A = gv$ and $M_\sigma = M$. We must note, however, that this requires $M_\sigma^2 = \frac{1}{2}|\lambda_1|v^2$ which sets a perturbative upper limit on the mass of the Stückelberg scalar. However, since v is not known in an Abelian gauge theory, there is no phenomenological problem. In any case, this is a toy model.

We then consider an extended Standard Model based on an $SU(2)_L \times U(1)_Y \times U(1)_X$ gauge symmetry. Normally, this will have a massive Z boson and a massless photon, like the Standard Model, but also a massless Z' boson. To generate a mass for this Z' boson, an extra Higgs-like scalar has been postulated, which breaks the residual $U(1)_X$ symmetry. However, we find that this can also be achieved by introducing a Stückelberg scalar $\tilde{\sigma}$ into the model. The corresponding Lagrangian (suppressing the fermion sector) has the form

$$\begin{aligned} \mathcal{L} = & (\mathbb{D}^\mu \tilde{\Phi})^\dagger \mathbb{D}_\mu \tilde{\Phi} - \frac{1}{8} \text{Tr}(\mathbb{F}_{\mu\nu} \mathbb{F}^{\mu\nu}) - \frac{1}{4} (B_{\mu\nu} B^{\mu\nu} + C_{\mu\nu} C^{\mu\nu}) + \mu^2 \tilde{\Phi}^* \tilde{\Phi} \\ & - \lambda (\tilde{\Phi}^* \tilde{\Phi})^2 + \mathcal{L}_S \end{aligned} \quad (34.4)$$

with an extra $U(1)_X$ gauge boson C_μ and a covariant derivative is defined as

$$\mathbb{D}_\mu = \partial_\mu + ig\tau_a A_\mu^a + \frac{i}{2}g'_Y Y_\Phi B_\mu + \frac{i}{2}g'_X X_\Phi C_\mu \quad (34.5)$$

The Stückelberg part is

$$\begin{aligned} \mathcal{L}_S = & \frac{1}{2M^2} (M^2 + \lambda_1 \tilde{\Phi}^* \tilde{\Phi}) (\partial_\mu \tilde{\sigma} + M_B B_\mu + M_C C_\mu)^2 \\ & - \frac{1}{2} (M^2 + \lambda_2 \tilde{\Phi}^* \tilde{\Phi}) \left(\tilde{\sigma} - \frac{1}{M_B} \partial_\mu B^\mu - \frac{1}{M_C} \partial_\mu C^\mu \right)^2 \end{aligned} \quad (34.6)$$

where M , M_B , M_C are mass parameters and λ_1 , λ_2 are coupling constants as before. As before, we redefine $\tilde{\Phi} = \Phi + \langle \Phi \rangle$ where $\langle \Phi \rangle^T = \begin{pmatrix} 0 & v/\sqrt{2} \end{pmatrix}$ and set $\lambda_1 = \lambda_2$ to avoid awkward bilinear terms. This also requires us to set $M_B \pm M_C = 0$ as in the Abelian case, and we can obtain a gauge-fixing term

$$\mathcal{L}_{g.f.} = \frac{1}{2\xi} (\partial_\mu \tilde{B}^\mu)^2 \quad (34.7)$$

where we define $\tilde{B}_\mu = \frac{B_\mu + C_\mu}{\sqrt{2}}$ and $\tilde{C}_\mu = \frac{B_\mu - C_\mu}{\sqrt{2}}$ as the physical fields (for unbroken symmetry). Clearly, we get a gauge fixing for the \tilde{B}_μ , but not for the \tilde{C}_μ which can be traced to the residual masslessness of the photon.

We can, moreover, renormalise the Stückelberg scalar as follows

$$\tilde{\sigma} = \sigma \left(1 + \frac{\lambda_1 v^2}{2M^2} \right)^{-\frac{1}{2}} \quad (34.8)$$

to get a canonical kinetic term, and thus obtain for the neutral gauge bosons, a mass matrix

$$\mathbb{M} = \frac{M_W^2}{4} \begin{pmatrix} 2 & -\sqrt{2}a_\Phi & -\sqrt{2}b_\Phi \\ -\sqrt{2}a_\Phi & a_\Phi^2 + 4\mu^2 & a_\Phi b_\Phi \\ -\sqrt{2}b_\Phi & a_\Phi b_\Phi & b_\Phi^2 \end{pmatrix} \quad (34.9)$$

where $a_\Phi = \frac{1}{g} (g'_Y Y_\Phi + g'_X X_\Phi)$, $b_\Phi = \frac{1}{g} (g'_Y Y_\Phi - g'_X X_\Phi)$ and $\mu^2 = Z_\sigma \frac{M_\sigma^2}{M_W^2}$ taking $M_B = M_C$. Diagonalising this mass matrix leads to real, positive gauge boson masses only if $a_\Phi = 0$ and $b_\Phi^2 = 2 \tan^2 \theta_W$. With this choice, we can recover, the Z boson mass, a massless photon, and a Z' boson with mass $M_{Z'} = \sqrt{2} M_W \mu$.

This Z' will evade all mass constraints if the σ is heavy enough. It will also decouple from the scalar sector, but remain coupled to the fermion sector. This may lead to interesting phenomenological considerations [7].

We can similarly consider the case when $M_B = -M_C$. In this case we will get the same mass matrix with $a \leftrightarrow b$ and the same masses of the different gauge bosons. However, the eigenstates will be a little different, and the phenomenological considerations may also be somewhat different.

We have seen therefore that a revival of the Stückelberg mechanism can indeed generate a mass for the Z' boson, generating a model with a very limited number of extra couplings. The reason for this economy is not far to seek because the Stückelberg mechanism keeps the additional $U(1)$ symmetry unbroken. This symmetry then forbids a large number of operators from appearing in the Lagrangian, making the model economic and predictive. We conclude, therefore, that an extra Stückelberg scalar leads to a more predictive theory than an extra Higgs scalar. However, though flavour physics data do hint at the existence of a heavy Z' boson (with very specific couplings), the confirmation of the model must wait for not just the discovery of a heavy Z' vector boson, but also the heavy σ . Till then, of course, the jury is out, and one theoretical model is just as good as another.

Acknowledgements RV would like to thank DST-INSPIRE for their financial support.

References

1. W. Heisenberg, Über den Bau der Atomkerne, Zeits. J. Phys. 77, 1–11 (1932); *ibid.* 78, 156–164 (1932); *ibid.* 80, 587–596 (1933)
2. H. Yukawa, On the interaction of elementary particles. Proc. Phys. Math. Soc. Jpn. 17, 48–57 (1935)
3. E.C.G. Stückelberg, On the existence of heavy electrons. Phys. Rev. 52, 41–42 (1937)
4. F. Englert, R. Brout, Broken symmetry and the mass of gauge Vector Mesons, Phys. Rev. Lett. 13(9), 321–323 (1964); P.W. Higgs, Broken symmetries and the masses of Gauge Bosons. Phys. Rev. Lett. 13(16), 508–509 (1964); G. Guralnik, C.R. Hagen, T.W.B. Kibble, Global conservation laws and massless particles. Phys. Rev. Lett. 13(20), 585–587 (1964)
5. G. Aad et al. (ATLAS Collaboration), Observation of a new particle in the search for the Standard Model Higgs boson with the ATLAS detector at the LHC. Phys. Lett. B 716, 1–29 (2012); S.

- Chachtryan et al (CMS Collaboration), Observation of a new boson at a mass of 125 GeV with the CMS experiment at the LHC. *Phys. Lett. B* **716**, 30–61 (2012)
6. B. Kors, P. Nath, A Stückelberg extension of the standard model. *Phys. Lett. B* **586**, 366–372 (2004); Aspects of the Stückelberg Extension. *JHEP* 0507.069 (2005)
 7. R. Vinze, S. Raychaudhuri, A viable U(1) extended Standard Model with a massive Z' invoking the Stueckelberg mechanism (2021). [arXiv:2107.08840](https://arxiv.org/abs/2107.08840)

Chapter 35

Search for the New Physics in Bottomonium Decays in Belle and Belle II



Rashmi Dhamija, S. Nishida, and A. Giri

Abstract Despite the tremendous success of the Standard Model (SM) of Particle Physics, there are several unexplained phenomena such as neutrino masses and mixing, mass hierarchy problem, etc. The conservation of lepton flavor is one of the accidental symmetries of the SM. Charged lepton flavor violating processes are forbidden in the SM but some new physics models, such as leptoquark model predict these processes that could be observed in a high energy physics experiment. Bottomonium system is a good place to study such processes. Belle experiment is a flavor physics experiment at KEKB asymmetric e^-e^+ collider, at KEK, Japan. It mainly collected the data at the energy of $\Upsilon(4S)$, but it also collected some data at $\Upsilon(nS; n = 1, 2, 3)$, so it is possible to study the decay of $\Upsilon(nS)$. Belle has the world's largest data sample available of $\Upsilon(2S)$. The Belle II experiment is an upgrade version of the Belle experiment which aims to collect 50 ab^{-1} of data. We will present the study of $\Upsilon(2S) \rightarrow 1(l = e, \mu)\tau$ at Belle. We also mention on the future prospects at Belle II.

35.1 Introduction

The conservation of lepton flavor is one of the accidental symmetries of the SM. However, the observation of neutrino oscillation reveals that the lepton flavor is violated in the neutral lepton sector. In the charged lepton sector, lepton flavor violation is heavily suppressed by the order of $\frac{m_\nu^2}{m_W^2}$ within SM. But Beyond Standard Model scenarios can enhance the decay rate of such transitions. So, the observation of charged lepton flavor violation would provide the clear evidence of the new physics.

R. Dhamija (for the Belle and Belle II collaboration)

R. Dhamija (✉) · A. Giri
Indian Institute of Technology Hyderabad, Telangana 502285, India
e-mail: rshmiphysicist@gmail.com

S. Nishida
KEK, Tsukuba 305-0801, Japan

© The Author(s), under exclusive license to Springer Nature Singapore Pte Ltd. 2022
B. Mohanty et al. (eds.), *Proceedings of the XXIV DAE-BRNS High Energy Physics Symposium, Jati, India*, Springer Proceedings in Physics 277,
https://doi.org/10.1007/978-981-19-2354-8_35

BaBar and CLEO has already set upper limits on the branching fraction for $\Upsilon(nS)$ decays [1, 2]. Belle has accumulated the largest data sample for $\Upsilon(2S)$ which corresponds to 158 million $\Upsilon(2S)$ decays.

35.2 Analysis Overview

Our analysis aims to use 25 fb^{-1} data sample taken at the $\Upsilon(2S)$ resonance. The selection is optimized with a monte-carlo (MC) simulation study. A set of 5M signal MC events for $\Upsilon(2S) \rightarrow l^- \tau^+$ where τ^+ decays generically are generated using VLL model by Evtgen [3]. The detector simulation is subsequently performed with GEANT3 [4].

We study the $\Upsilon(2S) \rightarrow l^- \tau^+$ ($l^- = e^-, \mu^-$) decay at Belle. Further, the τ lepton is reconstructed from the leptonic modes where τ can decay to a lepton and a neutrino. Due to the presence of the neutrinos, the $\Upsilon(2S)$ cannot be fully reconstructed. So, we have two leptons which have opposite charges: one is primary lepton ($l_1^- = \mu^-, e^-$) and other is secondary lepton ($l_2^+ = e^+, \mu^+$) from τ . Hence, there can be four combinations for the $l^- \tau^+$ modes with l_1 and l_2 i.e. μ -e, μ - μ , e - μ and e -e modes. For this study, μ -e and e - μ modes are selected to suppress the dimuon and bhabha background events.

35.3 Event Selection

The very minimal criteria on Particle Identification (PID) have been used for this study to identify electrons and muons. The charged tracks are required to originate from the interaction point by applying the selection criteria in the transverse x -y plane and along z -axis, respectively on the impact parameter i.e. $|dr| < 2 \text{ cm}$ and $|dz| < 5 \text{ cm}$.

The signature of the $\Upsilon(2S) \rightarrow l^- \tau^+$ (in the rest frame of the $\Upsilon(2S)$) is the momentum of the primary lepton (P_{l1}^*) in the CMS frame. So, we require the primary lep-

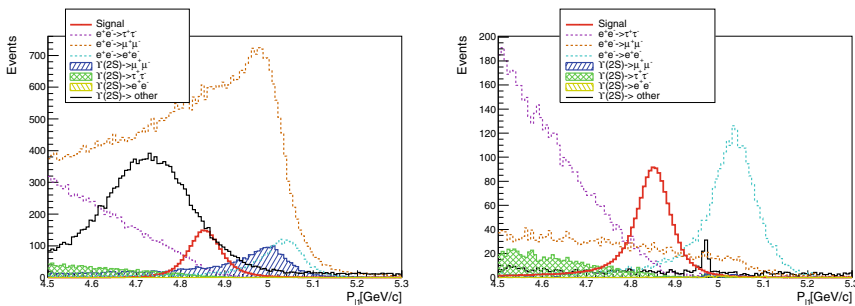


Fig. 35.1 Distribution of P_{l1}^* for μ -e mode (left) and e - μ mode (right)

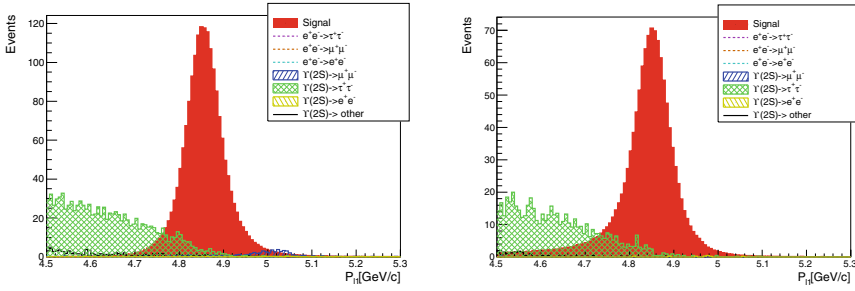


Fig. 35.2 Distribution of the P_{11}^* [GeV/c] after MVA for μ - e mode (left) and e - μ (right)

ton to be the highest momentum lepton. It will be used for the signal extraction. The momentum distribution of the primary lepton for both the modes are shown in Fig. 35.1. The signal region is chosen between $4.7 < P_{11}^* < 5.0$. The 10^{-4} branching fraction is used for the signal.

35.4 Background Rejection

The background samples are prepared from $e^+e^- \rightarrow e^+e^-$, $e^+e^- \rightarrow \mu^+\mu^-$, $e^+e^- \rightarrow \tau^+\tau^-$, and $\Upsilon(2S)$ inclusive sample corresponds to an integrated luminosity of approximately 100 fb^{-1} . The background components are scaled to the integrated luminosity of $\Upsilon(2S)$ resonance.

It is found that the dominant contribution to the background comes from the $e^+e^- \rightarrow \tau^+\tau^-$ and $\Upsilon(2S)$ decays. To suppress the background further, multi-variate analysis (MVA) [5] has been performed for this study. We find that some variables can well separate signal from background. Then, the FBDT algorithm has been used to train the classifier with equal number of signal and background events.

The figure of merit (FOM) [6] has been used to optimize the selection on the BDT response. The FOM is calculated for each BDT output and the value for which the FOM is the highest is chosen. Then, the distribution of the momentum of the primary lepton (P_{11}^*) is seen after applying the optimized FBDT output as shown in the Fig. 35.2. There is 94–95% reduction in the background after MVA while loss in the signal efficiency is about 2–3%.

35.5 Signal Yield Extraction

We perform a 1-D unbinned maximum likelihood (UML) fit on the P_{11}^* as shown in the Fig. 35.3. The sample is fitted with the three components: signal, $\Upsilon(2S) \rightarrow \mu^+\mu^-$ and $\Upsilon(2S) \rightarrow \tau^+\tau^- + \text{other}$, for the μ - e mode and with the two components: signal and $\Upsilon(2S) \rightarrow \tau^+\tau^- + \text{other}$, for the e - μ mode. The signal shape is fixed by modelling

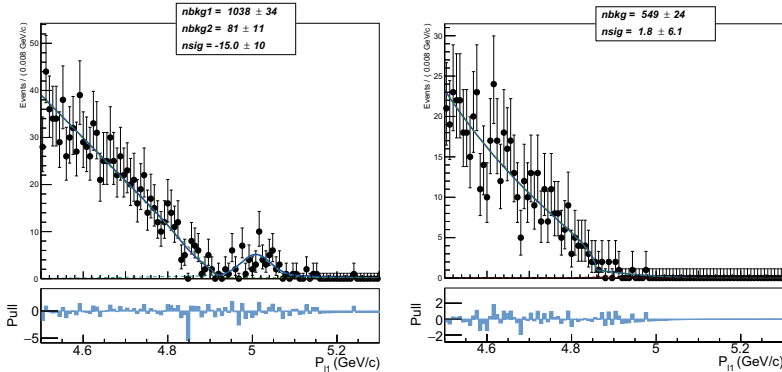


Fig. 35.3 Final Fit of P_{11}^* for μ -e (left) and e - μ mode (right)

with a three Gaussians with a common mean for μ -e mode and with a double-sided Crystal Ball and a Gaussian with a common mean for the e - μ mode. The $\Upsilon(2S) \rightarrow \tau^+\tau^- + \text{other}$ component is modelled with a first order polynomial for the μ -e mode and with Argus function and a Bifurcated Gaussian for the e - μ mode. The $\Upsilon(2S) \rightarrow \mu^+\mu^-$ component is modelled with a Bifurcated Gaussian and a Gaussian with a common mean for the μ -e mode. All the parameters are kept fixed except N_{sig} and N_{bkg} , where, N_{sig} and N_{bkg} are the number of signal and background events, respectively.

35.6 Results

The sensitivity [7] has been measured in the signal region after applying all the conditions by using the formula given below:

$$\mathcal{B}^{\text{UL}} = \frac{N_{\text{sig}}^{\text{UL}}}{\epsilon_{\text{rec}} \times N_{\Upsilon(2S)}} ;$$

where, $N_{\text{sig}}^{\text{UL}}$ and ϵ_{rec} is the upper limit of the signal at 90% confidence level and the reconstructed efficiency. The expected number of signal and background events are 1773.74 ± 2.4 & 336 ± 9.2 for μ -e mode and 1119.0 ± 2.0 & 133.5 ± 5.7 for e - μ mode. The sensitivity is 1.32×10^{-6} for μ -e mode as well as e - μ mode.

35.7 Conclusion

We have successfully separated signal from the background. The rough estimation on the upper limit has been measured which is 1.32×10^{-6} for both the modes.

References

1. BaBar collaboration. *Search for Charged Lepton Flavor Violation in Narrow Upsilon Decays* (2010). [arXiv:1001.1883](https://arxiv.org/abs/1001.1883)
2. CLEO collaboration. *Search for lepton flavor violation in upsilon decays* (2008). PRL.101.201601
3. D.J. Lange et al., Nucl. Instrum. Methods **A462**, 152 (2001)
4. R. Brun et al., *CERN Report No. DD/EE*, 84-1 (1984)
5. CERN-OPEN-2007-007. *TMVA—Toolkit for Multivariate Data Analysis* (2007). [arXiv:0703039](https://arxiv.org/abs/0703039)
6. G. Punzi, *Sensitivity of searches for new signals and its optimization* (2003). [arxiv:0308063v2](https://arxiv.org/abs/0308063v2)
7. Gary J. Feldman et al., A unified approach to the classical statistical analysis of small signals. Phys. Rev. D **57**, 3873 (1998)

Chapter 36

On the Determination of Regions in Multi-scale, Multi-loop Feynman Integrals



B. Ananthanarayan, Abhishek Pal, Sunethra Ramanan, and Ratan Sarkar

Abstract The analytic evaluation of multi-scale Feynman integrals is difficult due to the presence of various scales of the problem. When exact calculation is very difficult or impossible, systematic approximations may help. The strategy of expansion by regions is a useful method for obtaining the asymptotic analysis of multi-scale Feynman integrals. In this talk, we present a novel method for the identification of regions associated with multi-scale Feynman integrals.

36.1 Introduction

The Standard Model which is a quantum field theory based on the gauge groups $SU(3) \otimes SU(2) \otimes U(1)$ describes elementary particle physics very successfully. Each of the gauge group has a coupling constant. The coupling constant of a theory becomes small at very high energy scale, and one can use perturbative analysis in order to obtain prediction for that theory. One writes the physical observable in a power series expansion in the coupling constants. Each term in that perturbative series is described by Feynman integrals derived based on certain rules dictated by the considered theory.

As one calculates higher order terms, Feynman diagrams involve loops. The analytic evaluation of multi-loop Feynman integrals is very challenging. Also, if the scale in the problem increases, the analytic evaluation of the integrals becomes very difficult. One of the useful method to handle this problem is to consider systematic approximations based on the hierarchies of the associated scales of the problem in

B. Ananthanarayan · R. Sarkar (✉)
Centre for High Energy Physics, Indian Institute of Science, Bangalore 560012, KA, India
e-mail: ratansarkar@iisc.ac.in

A. Pal
Department of Physics and Astronomy, Bartol Research Institute, University of Delaware,
Newark 19716, USA

S. Ramanan
Department of Physics, Indian Institute of Technology Madras, Chennai 600036, TN, India

© The Author(s), under exclusive license to Springer Nature Singapore Pte Ltd. 2022
B. Mohanty et al. (eds.), *Proceedings of the XXIV DAE-BRNS High Energy Physics
Symposium, Jatni, India*, Springer Proceedings in Physics 277,
https://doi.org/10.1007/978-981-19-2354-8_36

order to obtain simplification. The Method of Regions (MoR) [1–4] serves as one of the powerful techniques to tackle the analysis of multi-scale Feynman integrals. Within MoR, the whole loop momentum domain is divided into regions, in each of the regions the Feynman integrand is expanded in a Taylor series based on scaling prescription of that region, after the expansion the expanded terms are integrated over whole loop momentum space, and finally the sum of the contributions coming from each of the regions gives the result for the original integral.

It is a non-trivial task to identify all of the regions for a given Feynman diagram. There are implementations [5, 6] which identifies the regions automatically. In this talk, we present an alternative approach ASPIRE [7] which also finds set of regions based on analysis of singularities of Feynman integrals [8] and makes use of Power Geometry [9, 10].

36.2 The Program ASPIRE

The Mathematica program ASPIRE isolated the set of regions for given multi-scale, multi-loop Feynman integrals in given limits. ASPIRE had been developed on the analysis of the sum of the two Symanzik polynomials within the framework of Power Geometry.

The algorithm ASPIRE consists of the following steps:

- For a given Feynman integral in a given limit, find the first and second kind of Symanzik polynomials.
- Consider the Gröbner basis elements of Landau equations which are obtained by equating the second Symanzik polynomials and their derivatives with respect to the alpha parameters to zero.
- Map the Gröbner basis elements to the origin/coordinate axes in order to derive certain linear transformations.
- Find the sum of the Symanzik polynomials with the application of the obtained linear transformations.
- Find the vector exponents of each of terms of each of the obtained polynomials. The set of vector exponents is called the support of the sum.
- Find the convex hull of the obtained supports to obtain the Newton polytopes for each of the polynomials.
- Find the normal vectors for each of the facets of the Newton polytopes.

The set of unique normal vectors¹ gives the set of regions required for the asymptotic expansion of the considered Feynman integral.

¹ According to Bruno's theorem [9, 10], the asymptotic solution for truncated polynomial for each of the facets of Newton polytopes can be obtained from the components of the normal vector of the facets.

36.3 A One Loop Two Point Integral

We consider the following integral:

$$I = \int \frac{d^d k}{(k^2 - m^2)((k - q)^2 - m^2)}. \quad (36.1)$$

Here q is the external momentum, k , the loop momentum and the threshold expansion parameter is defined as $y = m^2 - \frac{q^2}{4}$.

$$\mathcal{U} = x_1 + x_2 \quad (36.2)$$

$$\mathcal{F} = \frac{1}{4}q^2 x_1^2 - \frac{1}{2}q^2 x_1 x_2 + \frac{1}{4}q^2 x_2^2 + y x_1^2 + 2y x_1 x_2 + y x_2^2, \quad (36.3)$$

where x_1 and x_2 are the alpha parameters.

The Gröbner basis elements of Landau equations $\{\mathcal{F}, \frac{\partial \mathcal{F}}{\partial x_1}, \frac{\partial \mathcal{F}}{\partial x_2}\}$ are,

$$\{q^2 y x_2, (x_1 + x_2)y, q^2(x_1 - x_2)\} \quad (36.4)$$

We map the obtained Gröbner basis elements to the origin, x_2 -axis and x_1 -axis via the following transformations:

$$T_1 \equiv \{x_1 \rightarrow x_1, x_2 \rightarrow x_2\} \quad (36.5)$$

$$T_2 \equiv \left\{ x_1 \rightarrow \frac{x_1}{2}, x_2 \rightarrow x_2 + \frac{x_1}{2} \right\} \quad (36.6)$$

$$T_3 \equiv \left\{ x_1 \rightarrow x_1 + \frac{x_2}{2}, x_2 \rightarrow \frac{x_2}{2} \right\} \quad (36.7)$$

We then find the polynomial $\mathcal{G} = \mathcal{U} + \mathcal{F}$ with these transformations. The supports of each of the polynomial are extracted and with those supports we obtain the Newton polytopes. We search for the normal vector for each of the facets of the Newton polytopes. In ASPIRE program, we determine the normal vector corresponding to the facets of the Newton polytope based on following conditions:

1. $\mathbf{r} \cdot \mathbf{v} = c$ and $\mathbf{r}' \cdot \mathbf{v} < c$, where \mathbf{r} belongs to a boundary subset of Newton polytope and \mathbf{r}' does not and \mathbf{v} is the normal vector. We name the surface giving the normal vector depending on this condition “the top facet” and assign a label “ $surf \rightarrow 1$ ” for that surface.
2. $\mathbf{r} \cdot \mathbf{v} = c$ and $\mathbf{r}' \cdot \mathbf{v} > c$. For this condition, we call the surface giving the normal vector “the bottom facet” and label the surface by “ $surf \rightarrow -1$ ”.

The set of unique normal vectors for this examples are given by:

$$\left(\begin{array}{c|c} \textit{Normal} & \textit{Facet : top/bottom}(1/-1) \\ \hline \{0, 0\} & \{-1\} \\ \{-1, -1\} & \{1\} \\ \{-\frac{1}{2}, -1\} & \{-1\} \\ \{-1, -\frac{1}{2}\} & \{-1\} \end{array} \right) \quad (36.8)$$

The bottom facet scalings represent the set of regions. In this example, we isolate the hard region $\{0, 0\}$ and the potential regions $\{-\frac{1}{2}, -1\}$, $\{-1, -\frac{1}{2}\}$. We find complete agreement with the results of [6].

36.4 Conclusion

We have presented the Mathematica program ASPIRE which unveils the set of regions by analysing the singularities and the polynomial $\mathcal{G} = \mathcal{U} + \mathcal{F}$ within the framework Power Geometry. These regions are needed for the asymptotic expansion of multi-scale Feynman integrals in given limit. To this end, within ASPIRE program we consider two kind of facets: bottom and top. The scalings of alpha parameters coming from bottom facets correspond to the regions. In [11], the case of top facets with equal components had been correlated to the maximal cut of the considered Feynman integral in the large mass limit.

In the Lee-Pomeransky representation [12] of Feynman integrals, one considers the analysis of \mathcal{G} polynomial. In [13], the Lee-Pomeransky representation had been advocated “to describe and to prove expansion by regions”. It is useful to evaluate multi-scale Feynman integrals asymptotically using the recipe given in [13].

References

1. M. Beneke, V.A. Smirnov, Nucl. Phys. B **522**, 321–344 (1998)
2. V.A. Smirnov, Springer Tracts Mod. Phys. **177**, 1 (2002)
3. B. Jantzen, JHEP **12**, 076 (2011)
4. T. Becher, A. Broggio, A. Ferroglia, Lect. Notes Phys. **896**, 1 (2015)
5. A. Pak, A. Smirnov, Eur. Phys. J. C **71**, 1626 (2011)
6. B. Jantzen, A.V. Smirnov, V.A. Smirnov, Eur. Phys. J. C **72**, 2139 (2012)
7. B. Ananthanarayan, A. Pal, S. Ramanan, R. Sarkar, Eur. Phys. J. C **79**(1), 57 (2019)
8. L.D. Landau, Nucl. Phys. **13**, 181 (1959)
9. A.D. Bruno, A.B. Batkhin, Resolution of an algebraic singularity by power geometry algorithms. Program. Comput. Softw. **38.2**, 57–72 (2012)
10. A.D. Bruno (ed.), Power geometry in algebraic and differential equations, vol. 57 (Elsevier, 2000)
11. B. Ananthanarayan, A.B. Das, R. Sarkar, Eur. Phys. J. C **80**(12), 1131 (2020)
12. R.N. Lee, A.A. Pomeransky, JHEP **11**, 165 (2013)
13. T.Y. Semenova, A.V. Smirnov, V.A. Smirnov, Eur. Phys. J. C **792**, 136 (2019)

Chapter 37

A New Distribution for the Charged Particle Multiplicities in DIS at HERA and Hadron-Hadron Collisions at the LHC



Ritu Aggarwal and Manjit Kaur

Abstract Charged particle multiplicities produced in the lepton proton collisions at $\sqrt{s} = 300$ GeV recorded using the H1 detector at the HERA accelerator and those from the proton–proton collisions at $\sqrt{s} = 7$ TeV at the LHCb detector at the LHC have been analyzed using Shifted Gompertz distribution. The normalized moments and factorial moments are calculated from the proposed new statistical probability distribution and have been compared to those calculated from the data. The study of the charged particle multiplicities is important to understand the underlying dynamics of hadronisation and charged particle production mechanisms. There are various statistical models which are used to study charged particle multiplicities, the one most commonly and successfully used being the Negative Binomial distribution. The new distribution used in this paper, the Shifted Gompertz distribution, has been used to successfully describe the charged particle multiplicities in the e^+e^- spectra at the ISR energies as well as to the $pp(\bar{p})$ spectra at the highest LHC (Tevatron) energies.

37.1 Introduction

There are many phenomenological models such as Negative Binomial Distribution (NBD) [1, 2], Gamma distribution [3], Tsallis distribution [4], Weibull Distribution (WB) [5], shifted Gompertz distribution (SGD) [6, 7], etc., which are used to describe the charged particle multiplicity distribution and the Koba-Nielsen-Olesen (KNO) scaling violations. In this chapter the charged particle distribution from the

R. Aggarwal (✉)
Savitribai Phule Pune University, Pune, India
e-mail: ritu.aggarwal@gmail.com

M. Kaur
Panjab University, Chandigarh, India

pp collision data at the center of mass system (cms) energy of 7TeV collected using LHCb detector [8] are fitted with SGD, NBD, and WB distributions. The SGD distribution is further used to study the charged particle multiplicity obtained using the H1 detector from ep collisions at the 300 GeV cms energy [9]. The normalized moments, Factorial moments, and the H_q moments are calculated for various fitted distributions are compared with the experimental values.

37.2 Probability Distribution Functions

Shifted Gompertz distribution The probability distribution for a SGD function is given as below

$$P(n|b, \beta) = be^{-bn} e^{-\beta e^{-bn}} [1 + \beta(1 - e^{-bn})], n > 0. \tag{37.1}$$

where b and β are the scale and shape parameters.

Weibull Distribution The probability distribution function for Weibull Distribution is given as

$$P_n(n|\lambda, K) = \begin{cases} \frac{K}{\lambda} \left(\frac{n}{\lambda}\right)^{(K-1)} \exp\left(-\left(\frac{n}{\lambda}\right)^K\right) & n \geq 0 \\ 0 & n < 0 \end{cases} \tag{37.2}$$

with parameters λ and $k > 0$.

Negative Binomial Distribution For the NBD, the probability distribution function is given as

$$P(n| \langle n \rangle, k) = \binom{n+k-1}{k-1} \left(\frac{\langle n \rangle / k}{1 + \langle n \rangle / k}\right)^n (1 + \langle n \rangle / k)^{-k} \tag{37.3}$$

where $\langle n \rangle$ is the expected average and k is the shape parameter.

37.2.1 Moments

The normalized moments (C_q), factorial moments (F_q), K_q moments, and H_q moments are defined for a probability distribution $P(n)$ as below

$$C_q = \frac{\sum_{n=1}^{\infty} n^q P(n)}{(\sum_{n=1}^{\infty} n P(n))^q} \tag{37.4}$$

$$F_q = \frac{\sum_{n=q}^{\infty} n(n-1)\dots(n-q+1)P(n)}{(\sum_{n=1}^{\infty} n P(n))^q} \tag{37.5}$$

$$K_q = F_q - \sum_{m=1}^{q-1} \frac{(q-1)!}{m!(q-m-1)!} K_{q-m} F_m \quad (37.6)$$

$$H_q = K_q / F_q \quad (37.7)$$

37.2.2 Results and Discussion

The experimental charged multiplicity distributions for the minimum bias events and the hard QCD events, collected using the LHCb detector at center of mass energy 7TeV are fitted with the SGD, NB, and WB distributions in five pseudorapidity windows of 0.5 in the range $2.0 < \eta < 4.5$. The different theoretical distributions studied were found to agree well with the data in the small pseudorapidity windows, however in the full range of $2.0 < \eta < 4.5$, the data could only be explained when a two component fit [10] was used

$$P(n)^X = \alpha P(n)_{soft}^X + (1 - \alpha) P(n)_{semi-hard}^X \quad (37.8)$$

where X stands for NBD, SGD, or WB distribution.

Here α is the fraction of soft component and $(1 - \alpha)$ is the semi-hard component of events. The better quality of a two component fit in the full rapidity range is also evident from Fig. 37.1 (bottom row), where H_q moments are shown for the

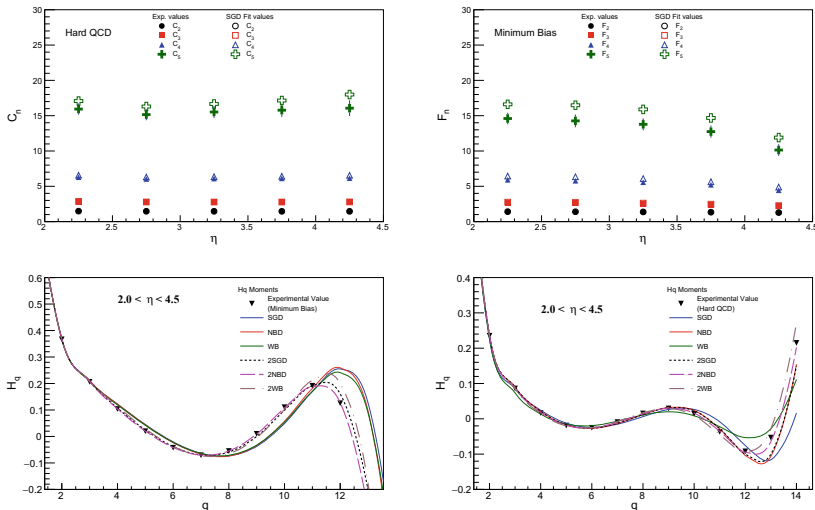


Fig. 37.1 Top row: (left) SGD C_q moments for different η range for the hard QCD events (right) SGD F_q moments for different η range for the minimum bias events. Bottom row: (left) H_q moments for minimum bias events (right) H_q moments for hard QCD events at 7TeV pp collisions from LHCb

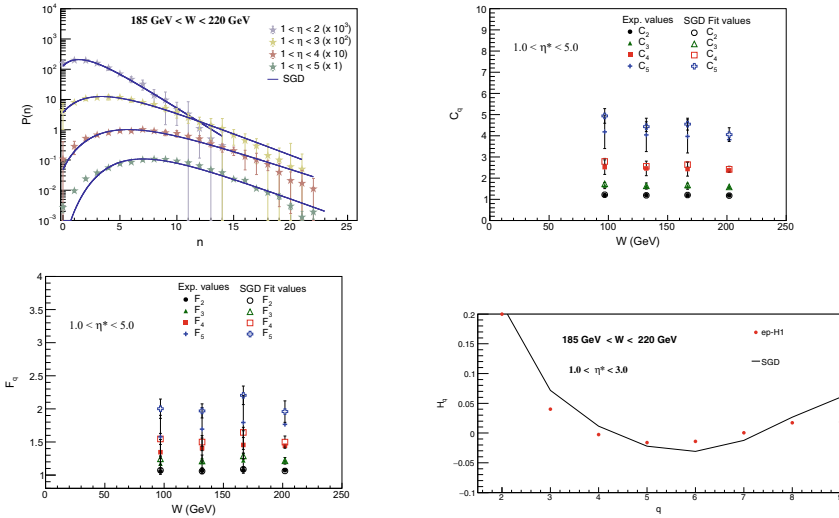


Fig. 37.2 Top row: (left) SGD fit to the ep events in the range $185\text{GeV} < W < 220\text{GeV}$ (right) C_q moments for different W intervals for the pseudorapidity range $1 < \eta^* < 5$. Bottom row: (left) F_q moments for different W intervals for the pseudorapidity range $1 < \eta^* < 5$ (right) H_q moments from SGD fit compared to the experimental value in the pseudorapidity range $1 < \eta^* < 3$

experimental data as compared to all fitted distributions. The C_q moments and F_q moments calculated using fitted distributions are in agreement with the experimental values except for $q = 5$, where it is over-estimated by the fitted distributions, as shown in Fig. 37.1 (top row).

The charged multiplicity distributions from ep collisions measured at the H1 detector with center of mass energy 300 GeV are fitted using the SGD for different η^* (defined as pseudorapidity in the current hemisphere) intervals and in the intervals of W (invariant mass of the hadronic system). The SGD fits are found to explain the data well as shown in Fig. 37.2 (top row). The normalized moments C_q , factorial moments F_q and H_q moments are calculated for the SGD fits and are compared to the experimental values as shown in Fig. 37.2.

Acknowledgements RA acknowledges the support by Department of Science and Technology (DST), India.

References

1. Z. Koba, H.B. Nielsen, P. Olesen, Nucl. Phys. B **40**, 317 (1972)
2. P. Carruthers, C.C. Shih, Phys. Lett. B **127**, 242 (1983)
3. K. Urmosy, G.G. Barnaföldi, T.S. Birò, Phys. Lett. B **701**, 111 (2011)
4. C.E. Agüiar, T. Kodama, Physica A **320**, 271 (2003)
5. S. Dash, B.K. Nandi, P. Sett, Phys. Rev. D **93**, 114022 (2016)

6. A. Singla, M. Kaur, *Adv. High Energy Phys.* **2019**, Article ID 5192193 (2019)
7. R. Aggarwal, M. Kaur, *Adv. High Energy Phys.* **2020**, Article ID 5464682, (2020)
8. R. Aaij, C. Abellan Beteta et al., LHCb Collaboration. *Eur. Phys. J. C* **72**, 1947 (2012)
9. S. Aid et al., H1 collaboration. *Z. Phys. C* **72**, 573–592, 114022 (1996)
10. C. Füglesang, *In Multiparticle Dynamics, Italy* (1989); eds. A. Giovannini, W. Kittel, World Scientific, Singapore, 193 (1997)

Chapter 38

Probing Doubly and Singly Charged Higgs at pp Collider HE-LHC



Rojalin Padhan, Debottam Das, M. Mitra, and Aruna Kumar Nayak

Abstract We analyze the signal sensitivity of multi-lepton final states at the collider that can arise from doubly and singly charged Higgs decay in a type-II seesaw framework. We assume triplet Vacuum Expectation Value (VEV) to be very small and degenerate masses for both the charged Higgs states. The leptonic branching ratio of doubly and singly charged Higgs states have a large dependency on the neutrino oscillation parameters, lightest neutrino mass scale, as well as on neutrino mass hierarchy. We explore this as well as the relation between the leptonic branching ratios of the singly and doubly charged Higgs states in detail. We evaluate the effect of these uncertainties on the production cross-section of multi-lepton signal. Finally, we present a detailed analysis of multi-lepton final states for a future hadron collider HE-LHC, that can plausibly operate with the center of mass energy $\sqrt{s} = 27$ TeV.

38.1 Introduction

The discovery of the Higgs boson at the Large Hadron Collider (LHC) has experimentally proven that fermions and gauge bosons masses in the Standard Model (SM) are generated via Brout–Englert–Higgs (BEH) mechanism. However, one of the key questions that still remains unexplained is the origin of light neutrino masses and mixings, that have been observed in a number of neutrino oscillation experiments [1, 2]. Neutrinos being their own anti-particles, their masses can have a different origin

R. Padhan (✉) · D. Das · A. Kumar Nayak
Institute of Physics, Sachivalaya Marg, Bhubaneswar 751005, India

BARC Training School Complex, Homi Bhabha National Institute, Anushaktinagar, Mumbai 400094, India
e-mail: rojalin.p@iopb.res.in

M. Mitra
Institute of Physics, Bhubaneswar, India

Homi Bhabha National Institute, Training School Complex, Anushaktinagar, Mumbai, India

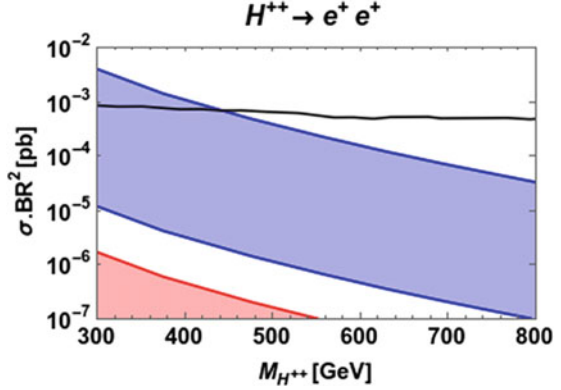
compared to the other SM fermions. The seesaw mechanism is a profound theory, which explains eV-scale Majorana masses of the light neutrinos through lepton number violating (LNV) $d = 5$ operator $LLHH/\Lambda$ [3]. There can be different UV completed theories behind this operator, commonly known as, type-I, -II, and -III seesaw mechanisms. Among the three, type-II seesaw model [4], where a $SU(2)_L$ triplet scalar field with the hypercharge $Y = +2$ is added to the SM, has an extended scalar sector. There are seven physical Higgs states that includes singly charged Higgs (H^\pm) and doubly charged Higgs ($H^{\pm\pm}$), CP even and odd neutral Higgs. The details of the Higgs spectra have been discussed in [5]. The neutral component of the triplet acquires a VEV v_Δ , and generates neutrino masses through the Yukawa interactions.

Depending on the value of v_Δ , $H^{\pm\pm}$ can have distinct decay modes. For degenerate masses of $H^{\pm\pm}$ and H^\pm , dominant decay mode for $v_\Delta \leq 10^{-4}$ GeV is $H^{\pm\pm} \rightarrow l_i^\pm l_j^\pm$ and for $v_\Delta \geq 10^{-4}$ GeV is $H^{\pm\pm} \rightarrow W^\pm W^\pm$. The di-leptonic decays are governed by the neutrino oscillation parameters [6]. The CMS and ATLAS collaboration have searched for the same-sign di-lepton final states with different flavors, and excluded the mass of the doubly charged Higgs ($M_{H^{\pm\pm}}$) below 820 and 870 GeV, respectively, at 95% C.L. [7, 8]. While many searches at the LHC are ongoing to experimentally verify the presence of $H^{\pm\pm}$, in this work we explore the impact of light neutrino mass hierarchy, neutrino oscillation parameters, as well as the lightest neutrino mass scale m_0 on $H^{\pm\pm}$ searches. In our work [11], we present the relation between the branching ratios (BRs) of $H^{\pm\pm}$ and H^\pm decays for both normal and inverted mass hierarchy. We find that among the different leptonic modes, $H^{\pm\pm} \rightarrow e^\pm e^\pm$, and $H^\pm \rightarrow e^\pm \nu$ are the least uncertain for inverted neutrino mass hierarchy (IH), and has the potential to differentiate neutrino mass ordering. We also discuss how the inclusion of uncertainties in the neutrino oscillation parameters affect the theory cross-section, which may, in turn, change the mass limits of doubly charged Higgs in individual channel. As it is well known that for c.m. energy $\sqrt{s} = 13$ (or 14) TeV LHC, production of multi-TeV $H^{\pm\pm}$ will be difficult due to suppressed cross-section. However, by increasing c.m. energy, one can probe heavier $H^{\pm\pm}$. Therefore, we consider pair-production and associated production of $H^{\pm\pm}$ and its subsequent decays into leptonic states, including tau's, and analyze the discovery prospects of doubly charged Higgs at a future hadron collider (HE-LHC), that can operate with c.m. energy $\sqrt{s} = 27$ TeV. We consider both the tri and four-lepton final states, and present a detail analysis taking into account different possible SM background processes. We consider a wide range of doubly charged Higgs mass, and explore the sensitivity reach with the projected luminosity (15 ab^{-1}) of HE-LHC [9].

38.1.1 13 TeV Bound on $M_{H^{\pm\pm}}$

CMS and ATLAS collaboration have already placed constraint on $M_{H^{\pm\pm}}$ by analyzing the leptonic decay channels of $H^{\pm\pm}$ [7, 8]. A degenerate mass spectrum for

Fig. 38.1 Production cross-section of $pp \rightarrow H^{++}H^{--} \rightarrow e^+e^+e^-e^-$ at LHC for $\sqrt{s} = 13$ TeV with including 3σ variation of neutrino oscillation parameters



charged scalars and 100% BR for each leptonic decay mode have been assumed, so the observed limit on $M_{H^{\pm\pm}}$ is valid only for low triplet vev $v_\Delta \leq 10^{-4}$ GeV. CMS collaboration studied both pair and associated production channels of $H^{\pm\pm}$ and subsequent decay of $H^{\pm\pm}$ and H^\pm to different leptonic states. The most stringent constraint $M_{H^{\pm\pm}} > 820$ GeV has been given by assuming $H^{\pm\pm} \rightarrow e^\pm \mu^\pm$ decay. We note that, the maximum possible BR with 3σ variation of neutrino oscillation parameters [10] can never be 100% for a given leptonic mode, rather can be at most 73% (for $H^{\pm\pm} \rightarrow \mu^\pm \tau^\pm$ in NH). For detail discussion; see [11]. Instead of considering $\text{BR}(H^{\pm\pm} \rightarrow l_i^\pm l_j^\pm) = 100\%$, we re-scale the theory cross-section with appropriate branching ratios. This somewhat weakens the individual bounds from different channels. In Fig. 38.1, we show the production cross-section of $pp \rightarrow H^{++}H^{--} \rightarrow e^+e^+e^-e^-$ at LHC for $\sqrt{s} = 13$ TeV. The colored band represents the variation of cross-section due to 3σ uncertainty in neutrino oscillation parameters. For illustration, we show for $m_0 = 0.0008$ eV. The blue (red) band corresponds to IH (NH) neutrino mass spectrum. The black line represents the observed limit from 13 TeV CMS analysis [7]. For IH, we focus on the final states with $e^\pm e^\pm e^\mp e^\mp$, $e^\pm \tau^\pm e^\mp \tau^\mp$ and $e^\pm \mu^\pm e^\mp \mu^\mp$. Due to the absence of any cancelation among the dependent parameters, the first channel is the least uncertain, and hence the bound obtained from this channel will be more precise. We note that, apart from the dependency on neutrino oscillation parameter, the limit from individual channel also depends on the value of lightest neutrino mass m_0 . We tabulate the predicted value of maximum possible branching ratios in Table 38.1, where each entry represents the maximum possible value of $\text{BR}(H^\pm \rightarrow l_i^\pm l_j^\pm)$ for a given value of m_0 . The value within the bracket denotes the best lower limit on $M_{H^{\pm\pm}}$, from each channel. The best limit, $M_{H^{\pm\pm}} \geq 503$ GeV can be obtained from $H^\pm \rightarrow e^\pm \mu^\pm$ assuming IH and $m_0 = 0.007, 0.02$ eV.

Table 38.1 Maximum possible branching ratio for the decay mode $H^{\pm\pm} \rightarrow l_i^{\pm} l_j^{\pm}$. We also show the corresponding lower limit on $M_{H^{\pm\pm}}$ in bracket obtained from the channel $pp \rightarrow H^{++} H^{--} \rightarrow l_i^+ l_j^+ l_i^- l_j^-$ (Here $l_i^+ = e^+/\mu^+/\tau^+$)

Maximum value of BR($H^{\pm\pm} \rightarrow l_i^{\pm} l_j^{\pm}$) ($M_{H^{\pm\pm}}$ [GeV])			
Decay mode	$m_0 = 0.0008$ eV	$m_0 = 0.007$ eV	$m_0 = 0.02$ eV
$e^{\pm} e^{\pm}$ (IH)	0.478 (435)	0.476 (435)	0.454 (424)
$e^{\pm} \mu^{\pm}$ (IH)	0.537 (495)	0.547 (503)	0.552 (503)
$e^{\pm} \tau^{\pm}$ (IH)	0.583 (373)	0.594 (376)	0.594 (376)

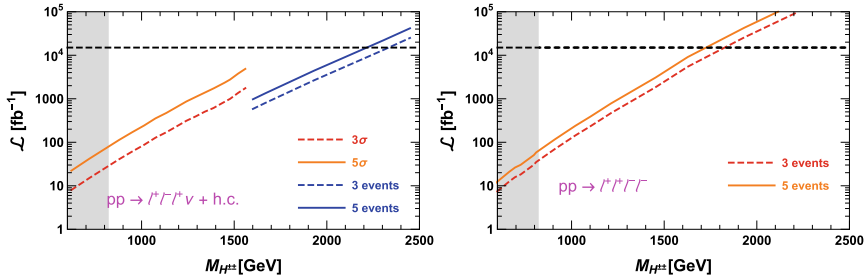


Fig. 38.2 Left: Variation of required luminosity to reach 3σ and 5σ significance, and number of events $N = 3, 5$ versus $M_{H^{\pm\pm}}$ for tri-lepton signal. Right: variation of required luminosity to observe number of events $N = 3, 5$ versus $M_{H^{\pm\pm}}$ for four-lepton signal. The gray shaded band represents the excluded region from CMS search [7]

38.1.2 Multi-lepton Signals from $H^{\pm\pm}$ and H^{\pm} for $\sqrt{s} = 27$ TeV HE-LHC

We consider the set-up for a future pp collider HE-LHC, that can operate with a c.m. energy $\sqrt{s} = 27$ TeV, and carry out a cut- based analysis for the four-lepton ($pp \rightarrow H^{++} H^{--} \rightarrow l_i^+ l_j^+ l_k^- l_l^-$) and tri-lepton ($pp \rightarrow H^{\pm\pm} H^{\mp} \rightarrow l_i^{\pm} l_j^{\pm} l_k^{\mp} \nu$) channels. Distribution of different kinematical variables and details about selection cuts can be found in [11]. Figure 38.2 shows the required luminosity to probe tri-lepton and four-lepton signal for $M_{H^{\pm\pm}}$ in between 820 and 2500 GeV. Higher mass region of $H^{\pm\pm}$ can be probed with more luminosity. We find that sensitivity reach for $H^{\pm\pm}$ in tri-lepton channel is more compared to that in four-lepton channel, as both the pair and associated production of $H^{\pm\pm}$ contribute to the former. $H^{\pm\pm}$ upto mass ~ 2.2 TeV can be probed in tri-lepton channel with 15 ab^{-1} integrated luminosity. In four-lepton channel, five events can be observed for $M_{H^{\pm\pm}} \leq 1.7$ TeV with the same luminosity.

References

1. A.B. McDonald, *Rev. Mod. Phys.* **88**, 030502 (2016)
2. T. Kajita, *Rev. Mod. Phys.* **88**, 030501 (2016)
3. S. Weinberg, *Phys. Rev. Lett.* **43**, 1566–1570 (1979)
4. M. Magg, C. Wetterich, *Phys. Lett. B* **94**, 61–64 (1980)
5. A. Arhrib, R. Benbrik, M. Chabab, G. Moulataka, M.C. Peyranere, L. Rahili, J. Ramadan, *Phys. Rev. D* **84**, 095005 (2011)
6. P. Fileviez Perez, T. Han, G.-y. Huang, T. Li, K. Wang, Neutrino masses and the CERN LHC: testing type II seesaw. *Phys. Rev. D* **78**, 015018 (2008)
7. CMS Collaboration, CMS-PAS-HIG-16-036 (2017)
8. ATLAS Collaboration, M. Aaboud et al., CERN-EP-2017-19. [arXiv:1710.09748](https://arxiv.org/abs/1710.09748)
9. A. Abada et al., *Eur. Phys. J. Special Topics* **228**(5), 1109–1382 (2019)
10. P.F. de Salas, D.V. Forero, C.A. Ternes, M. Tortola, J.W.F. Valle, *Phys. Lett. B* **782**, 633–640 (2018)
11. R. Padhan, D. Das, M. Mitra, A. Kumar Nayak, *Phys. Rev. D* **101**(7), 075050 (2020)

Chapter 39

A Study of the $B^0 \rightarrow K_S^0 \pi^0$ Decay at Belle II



Sagar Hazra

Abstract The decay $B^0 \rightarrow K_S^0 \pi^0$ is dominated by $b \rightarrow s$ loop amplitudes. Such flavor-changing-neutral-current transitions are highly suppressed in the standard model (SM) and provide an indirect route to search for new physics. Especially, the excellent neutral-particle reconstruction capability of Belle II enables a unique measurement of CP violation asymmetry in this channel. We report herein preliminary results based on a simulation sample of the experiment.

39.1 Introduction

Flavor-changing-neutral-current $b \rightarrow s$ transitions are highly suppressed and provide an important route to indirectly search for physics beyond the SM by checking the consistency between measurements and corresponding theory predictions as new particles may enter the quantum loop [1]. Within the SM, CP violation (CPV) arises due to a single irreducible phase in the Cabibbo–Kobayashi–Maskawa (CKM) matrix [2]. At a flavor-factory experiment such as Belle II, neutral B meson pairs are coherently produced in the process $\Upsilon(4S) \rightarrow B^0 \bar{B}^0$. When one of these B mesons decays to a CP eigenstate f_{CP} and the other to a flavor-specific final state f_{tag} , the time-dependent decay rate is given as

$$\mathcal{P}(\Delta t) = \frac{e^{-|\Delta t|/\tau_{B^0}}}{4\tau_{B^0}} [1 + q\{\mathcal{A} \cos(\Delta m_d \Delta t) + \mathcal{S} \sin(\Delta m_d \Delta t)\}], \quad (39.1)$$

where $\Delta t = t_{CP} - t_{\text{tag}}$ is the difference between proper decay time of the decay into f_{CP} and f_{tag} , $q = \pm 1$ is the flavor of f_{tag} being $+1$ (-1) for B^0 (\bar{B}^0) decaying to f_{tag} , Δm_d is the B^0 - \bar{B}^0 mixing frequency, and τ_{B^0} is the B^0 lifetime. The quantity \mathcal{A} is a measure of direct CPV and \mathcal{S} denotes CPV due to interference between decays

Sagar Hazra—for the Belle II Collaboration.

S. Hazra (✉)

Tata Institute of Fundamental Research, Mumbai 400 005, India

e-mail: sagar.hazra@tifr.res.in

© The Author(s), under exclusive license to Springer Nature Singapore Pte Ltd. 2022 215

B. Mohanty et al. (eds.), *Proceedings of the XXIV DAE-BRNS High Energy Physics*

Symposium, Jaitni, India, Springer Proceedings in Physics 277,

https://doi.org/10.1007/978-981-19-2354-8_39

with and without B^0 - \bar{B}^0 mixing. The key challenge in performing a time-dependent CP analysis for $B^0 \rightarrow K_S^0 \pi^0$ arises due to the absence of primary charged final-state particles at the B decay vertex. Instead, we calculate Δt as $(z_{\text{rec}} - z_{\text{tag}})/\beta\gamma c$, where z_{rec} is the z position of the B vertex reconstructed from the intersection of the K_S^0 trajectory with the interaction region, z_{tag} is calculated using the remaining tracks, and $\beta\gamma$ is the Lorentz boost.

The CKM and color suppression of the tree-level $b \rightarrow su\bar{u}$ transition means that the $B^0 \rightarrow K_S^0 \pi^0$ decay is dominated by the top-quark mediated $b \rightarrow s d \bar{d}$ loop diagram, which carries a weak phase $\arg(V_{tb} V_{ts}^*)$. Here V_{ij} are the CKM matrix elements. If subleading contributions are small, $\mathcal{S}_{K_S^0 \pi^0}$ is expected to be equal to $\sin(2\phi_1)$ and $\mathcal{A}_{K_S^0 \pi^0} \approx 0$. Therefore, a precise measurement of the direct CP asymmetry and branching fraction in this decay channel represents an important consistency test of the SM. Further, $B^0 \rightarrow K_S^0 \pi^0$ is a key component in improving the sensitivity of isospin sum-rule [3]. With the data size anticipated at Belle II, we expect to have significantly smaller uncertainties compared to what Belle [4, 5] and BaBar [6, 7] have achieved for these quantities.

39.2 Event Sample and Selection

We use 7×10^5 $B^0 \bar{B}^0$ Monte Carlo (MC) events for the signal study. We also use $e^+e^- \rightarrow q\bar{q}$ ($q = u, d, s, c$), $B^0 \bar{B}^0$ and $B^+ B^-$ MC events, each equivalent to an integrated luminosity of 400 fb^{-1} , to identify backgrounds. These events are simulated with the geometry and background condition for the Belle II detector [8] at SuperKEKB. The detector elements key to reconstruct the $B^0 \rightarrow K_S^0 \pi^0$ decay are the vertexing and tracking system as well as the electromagnetic calorimeter.

A K_S^0 candidate is reconstructed in its $\pi^+ \pi^-$ decay by requiring the dipion mass to lie between 482 and 513 MeV/c^2 , which corresponds to a $\pm 6\sigma$ resolution window around the nominal K_S^0 mass. To reconstruct $\pi^0 \rightarrow \gamma\gamma$ candidates, we apply an energy threshold of 30, 60, and 80 MeV for photons detected in the barrel, backward and forward endcap region, respectively, of the calorimeter. We require the reconstructed π^0 mass to lie between 120 and 145 MeV/c^2 . We also need the magnitude of the cosine of the π^0 helicity angle to be less than 0.98; this helps suppress misreconstructed π^0 candidates.

B -meson candidates are reconstructed by combining K_S^0 and π^0 candidates. For this purpose, we use two kinematic variables, namely the beam-energy-constrained mass (M_{bc}) and the energy difference (ΔE), defined as

$$M_{\text{bc}} = \sqrt{E_{\text{beam}}^2 - \mathbf{p}_B^2}, \quad (39.2)$$

$$\Delta E = E_B - E_{\text{beam}},$$

where E_{beam} is the beam energy, E_B and \mathbf{p}_B are the reconstructed energy and momentum of the B meson, respectively, all calculated in the center-of-mass frame. We

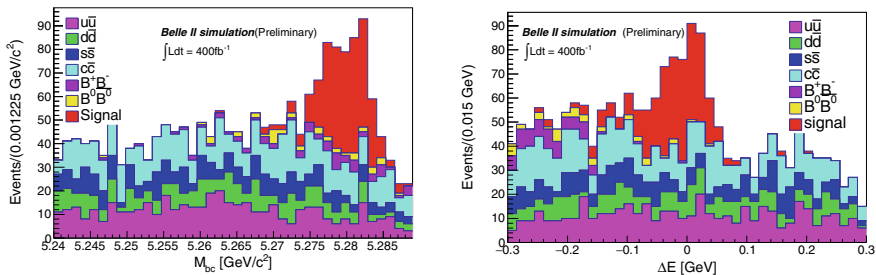


Fig. 39.1 M_{bc} and ΔE distributions obtained after the continuum suppression

retain events satisfying the following criteria: $|\Delta E| < 0.3 \text{ GeV}$ and $5.24 < M_{bc} < 5.29 \text{ GeV}/c^2$. A signal window is defined by applying $\pm 3\sigma$ requirement on these two kinematic variables.

The dominant source of backgrounds comes from $e^+e^- \rightarrow q\bar{q}$ continuum process. This background is suppressed by exploiting the differences in event topology. Continuum events result in final-state particles collimated into two back-to-back jets, whereas the final-state particles from $e^+e^- \rightarrow \Upsilon(4S) \rightarrow B\bar{B}$ are uniformly distributed over the 4π solid angle. We use a boosted decision tree (BDT) [9] classifier to combine event-shape variables and apply a criterion on the BDT output by maximizing the signal significance. The latter is defined as $S/\sqrt{S+B}$, where S (B) is the number of signal (background) events observed in the signal window. Figure 39.1 shows M_{bc} and ΔE distributions obtained after the continuum suppression requirement is applied.

39.3 Signal Yield Extraction

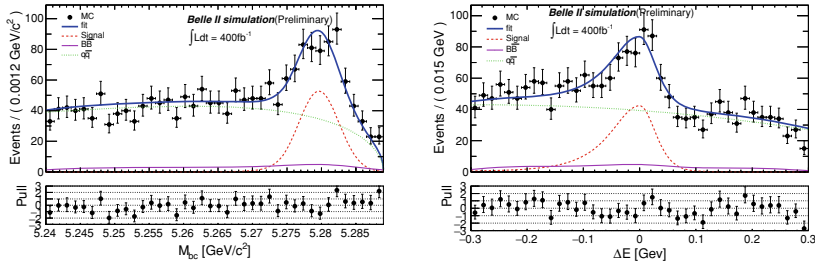
To extract the signal yield, we use an extended unbinned maximum-likelihood fit to the two-dimensional distribution of M_{bc} and ΔE . As the signal M_{bc} is correlated with ΔE , we reduce the correlation by using the modified M_{bc} introduced in [10]. We consider the product of two individual probability density functions (PDFs) to be a good approximation for the total PDF. The extended likelihood function is given as

$$\mathcal{L} = \frac{e^{-\sum_j n_j}}{N!} \prod_i^N \left[\sum_j n_j \mathcal{P}_j^i \right], \quad (39.3)$$

where N is the total number of events, n_j is the yield of event category j , and \mathcal{P}_j^i is the PDF of the same category for event i . Table 39.1 lists various PDFs used to model the M_{bc} and ΔE distributions. We fix the yield and PDF shape of the $B\bar{B}$ background category in the fit.

Table 39.1 List of PDFs used to model M_{bc} and ΔE distributions

Event category	M_{bc}	ΔE
Signal	Crystal Ball [11] + Gaussian	Double-sided Crystal Ball + Gaussian
$B\bar{B}$	Two-dimensional kernel estimation PDF [12]	
$q\bar{q}$	ARGUS [13]	Chebyshev polynomial

**Fig. 39.2** Projections of M_{bc} and ΔE obtained with the maximum-likelihood fit**Table 39.2** Expected and fitted yield for signal and $q\bar{q}$ background obtain from simulation

Category	Expected yield	Fitted yield
Signal	317	316 ± 32
$q\bar{q}$	1519	1499 ± 47

Figure 39.2 shows the M_{bc} and ΔE projections of the fit. In Table 39.2, we compare the fitted yields of signal and $q\bar{q}$ background with their expected values obtain from simulation.

39.4 Summary

The $B^0 \rightarrow K_S^0 \pi^0$ decay constitutes an important channel at Belle II for the precise measurement of time-dependent CP asymmetry and branching fraction, as well as for testing isospin sum-rule. We have deployed a multivariate analysis method to suppress backgrounds and performed an unbinned maximum-likelihood fit to extract the signal yield based on MC samples. We are now developing a time-dependent CPV analysis framework.

References

1. E. Kou et al. (Belle II Collaboration), PTEP **2019**, 123C01 (2019)
2. N. Cabibbo, Phys. Rev. Lett. **10**, 531 (1963); M. Kobayashi, T. Maskawa, Prog. Theor. Phys. **49**, 652 (1973)
3. M. Gronau et al., Phys. Lett. B **627**, 82 (2005)
4. Y. Chao et al. (Belle Collaboration), Phys. Rev. D **69**, 111102 (2004)
5. K.F. Chen et al. (Belle Collaboration), Phys. Rev. D **72**, 012004 (2005)
6. B. Aubert et al. (BaBar Collaboration), Phys. Rev. Lett. **93**, 131805 (2004)
7. B. Aubert et al. (BaBar Collaboration), Phys. Rev. D **71**, 111102 (2005)
8. T. Abe et al. (2010), [arXiv:1011.0352](https://arxiv.org/abs/1011.0352)
9. T. Keck et al. (2016), [arXiv:1609.06119](https://arxiv.org/abs/1609.06119)
10. See Section 7.1.1.2 of A. Bevan et al., Eur. Phys. J. C **74**, 3026 (2014)
11. T. Skwarnicki, Ph.D. Thesis, INP Krakow, DESY-F31-86-02 (1986)
12. K.S. Cranmer, Comput. Phys. Commun. **136**, 198 (2001)
13. H. Albrecht et al. (ARGUS Collaboration), Phys. Lett. B **241**, 278 (1990)

Chapter 40

Search for New Physics with Delayed Jets in CMS



Saikat Karmakar

40.1 Introduction

A large number of models for physics beyond the standard model predict long-lived particles that may be produced at the CERN LHC and decay into final states containing jets with missing transverse momentum, p_T^{miss} . These models include supersymmetry (SUSY) with gauge-mediated SUSY breaking (GMSB) [1], hidden valley models [2], etc. The p_T^{miss} may arise from a stable neutral weakly interacting particle in the final state or from a heavy neutral long-lived particle that decays outside the detector.

A representative GMSB model is used as a benchmark to quantify the sensitivity of the search. In this model, pair-produced long-lived gluinos each decay into a gluon, which forms a jet, and a gravitino, which escapes the detector causing significant p_T^{miss} in the event (Fig. 40.1).

40.2 Object and Event Reconstruction

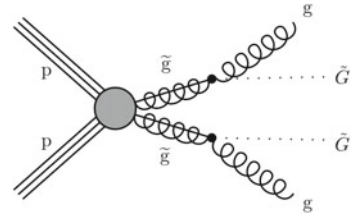
The primary physics objects used in this analysis are jets reconstructed from the energy deposits in the calorimeter towers, clustered using the anti- k_T algorithm with a distance parameter of 0.4.

The jet timing is determined using all ECAL cells that satisfy $\Delta R < 0.4$ between the jet axis and cell position, that exceed an energy threshold of 0.5 GeV and that satisfy reconstruction quality criteria. For each cell within the ECAL detector, the timing offset is defined such that a particle traveling at the speed of light from the center of the collision region to the cell position arrives at time zero. Energy deposits with a recorded time that is either less than -20 ns or greater than 20 ns are

Saikat Karmakar—for the CMS Collaboration.

S. Karmakar (✉)
Tata Institute of Fundamental Research, Mumbai, India
e-mail: saikat.karmakar@tifr.res.in

Fig. 40.1 Diagram showing the GMSB signal model



rejected, to remove events originating from preceding or following bunch collisions, respectively. The time of the jet, t_{jet} , is defined by the median cell time.

The missing transverse momentum vector, \mathbf{p}_T^{miss} , used for this analysis is defined as the projection on the plane perpendicular to the beams of the negative vector sum of calorimeter momenta deposits in an event.

40.3 Data Sets and Simulated Samples

The data sample was collected in 2016, 2017, and 2018 by the CMS detector in pp collisions at a center-of-mass energy of 13 TeV, corresponding to an integrated luminosity of $137 \pm 3.3 \text{ fb}^{-1}$. The trigger required the events to satisfy $p_T^{miss}(\text{trigger}) > 120 \text{ GeV}$.

40.4 Event and Object Selection

The main background contributions are coming from the following sources: ECAL time resolution tails, Electronic noise, Direct ionization in the APD, In-time pileup, Out-of-time pileup, Satellite bunches, Beam halo, Cosmic ray muon hits.

- All jets considered in this analysis must pass the requirements of $p_T > 30 \text{ GeV}$ and $|\eta| < 1.48$.
- The signal region jets must satisfy $t_{jet} > 3 \text{ ns}$ and the ECAL energy deposit $E_{ECAL} > 20 \text{ GeV}$.
- Jets from signal events are expected to have a large number of (N_{ECAL}^{cell}) hit, while jets dominated by direct APD hits or ECAL noise often have a low number of cells hit. A threshold of $N_{ECAL}^{cell} > 25$ is applied.
- In order to reduce the backgrounds coming from noise or beam halo, jets are required to have a hadronic energy fraction $HEF = E_{HCAL}/(E_{HCAL} + E_{ECAL}) > 0.2$. In addition to this, jets must have $E_{HCAL} > 50 \text{ GeV}$.
- Signal jets typically have a small RMS in the time of the constituent cells (t_{jet}^{RMS}) compared to the contributions coming from uncorrelated noise. So a requirement is made on both $t_{jet}^{RMS} < 0.4t_{jet}$ and $t_{jet}^{RMS} < 2.5 \text{ ns}$.

- To suppress the background originating from satellite bunch collisions, and select potential signal jets that do not originate from a primary vertex (PV), a requirement of $PV_{track}^{fraction} < 0.08$ is applied. Where $PV_{track}^{fraction}$ is defined as the ratio of the total p_T of all PV tracks matched to the jet ($\Delta R < 0.5$) to the transverse calorimeter energy of the jet.
- The beam halo background is suppressed using the requirement $E_{ECAL}^{CSC}/E_{ECAL} < 0.8$, where E_{ECAL}^{CSC} ECAL energy that can be associated with CSC hits and E_{ECAL} is the total ECAL energy.

The final selected events must contain at least one jet satisfying the requirements outlined above and $p_T^{miss} > 300$ GeV. The later helps to suppress multijet backgrounds. Finally, events satisfying $\max \Delta \phi_{DT} > \pi/2$ or $\max \Delta \phi_{RPC} > \pi/2$ are rejected to reduce the contribution of cosmic ray muon events.

40.5 Background Estimation

Three dominant backgrounds are estimated independently: **(1) Beam halo, (2) Satellite bunches, and (3) Cosmic ray events**. ABCD method is used to predict the background contributions in the signal region by inverting the cleaning variables targeted for each background.

40.5.1 Beam Halo Bkg Estimation

The beam halo contribution is estimated by measuring the pass/fail ratio of the $E_{ECAL}^{CSC}/E_{ECAL} > 0.8$ requirement for events with $HEF < 0.2$ and applying it to the observed number of events with $HEF > 0.2$. The final prediction for the SR is $0.02_{-0.02}^{+0.06}(stat)_{-0.01}^{+0.05}(syst)$.

40.5.2 Core and Satellite Bunch Background Prediction

The core and satellite bunch background contribution is estimated by measuring the pass/fail ratio of the requirement $PV_{track}^{fraction} < 0.08$ for events with $1 < t_{jet} < 3$ ns and applying it to the observed number of events with $t_{jet} > 3$ ns and $PV_{track}^{fraction} > 0.08$. The final prediction for the core and satellite bunch background is $0.11_{-0.05}^{+0.09}(stat)_{-0.02}^{+0.02}(syst)$.

Table 40.1 Summary of the estimated number of background events

Background source	Events predicted
Beam halo muons	$0.02^{+0.06}_{-0.02}(stat)^{+0.05}_{-0.01}(syst)$
Core and satellite bunch collisions	$0.11^{+0.09}_{-0.05}(stat)^{+.02}_{-0.02}(syst)$
Cosmic ray muons	$1.0^{+1.8}_{-1.0}(stat)^{+1.8}_{-1.0}(syst)$

40.5.3 Cosmic Ray Events

The discriminating variables used for the cosmic background prediction are the t_{jet} of the jet and the larger of $\max(\Delta\phi_{DT})$ and $\max(\Delta\phi_{RPC})$, labeled as $\max(\Delta\phi_{DT/RPC})$. The pass/fail ratio of the $t_{jet}^{RMS} < 2.5$ ns requirement is measured for events with $\max(\Delta\phi_{DT/RPC}) > \pi/2$ and applied to events with $\max(\Delta\phi_{DT/RPC}) < \pi/2$. The final prediction in SR is $1.0^{+1.8}_{-1.0}(stat)^{+1.8}_{-1.0}(syst)$.

The estimated background yields and uncertainties are summarized in Table 40.1. The total background prediction is $1.1^{+2.5}_{-1.1}$.

40.6 Results and Interpretation

Under the signal plus background hypothesis, a modified frequentist approach [3] is used to determine observed upper limits at 95% confidence level (CL) on the cross section σ to produce a pair of gluinos, each decaying with 100% branching fraction to a gluon and a gravitino, as a function of $m_{\tilde{g}}$ and $c\tau_0$. Figure 40.2 (left) shows the

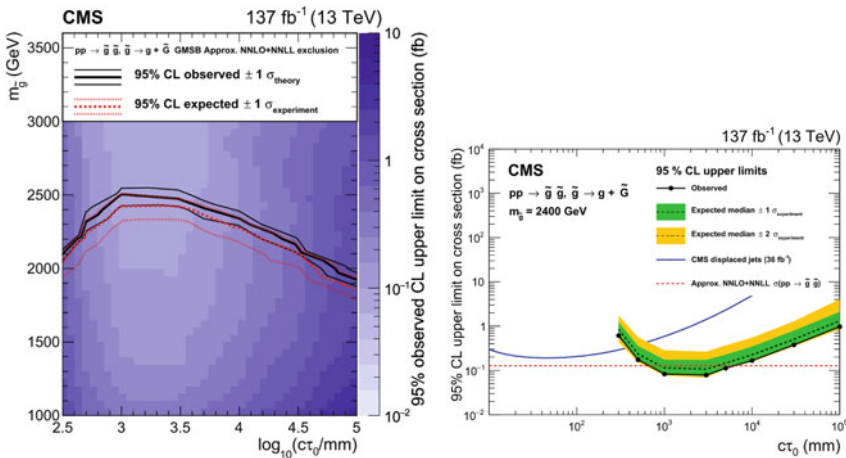


Fig. 40.2 .

observed upper limit on σ as a function of lifetime and gluino mass for the GMSB model. Gluino masses below 2100 GeV are excluded at 95% confidence level for $c\tau_0$ between 0.3 and 30 m. The dependence of the expected and observed upper limit as a function of $c\tau_0$ is shown in Fig. 40.2 (right) for $m_{\tilde{g}} = 2400$ GeV.

40.7 Summary

An inclusive search for long-lived particles has been presented, based on a data sample of proton-proton collisions collected at $\sqrt{s} = 13$ TeV by the CMS experiment, corresponding to an integrated luminosity of 137 fb^{-1} . The results are interpreted using the GMSB signal model and gluino masses up to 2100, 2500, and 1900 GeV are excluded at 95% confidence level for proper decay lengths of 0.3, 1, and 100 m, respectively. The reach for models that predict significant missing transverse momentum in the final state is significantly extended beyond all previous searches for proper decay lengths greater than 0.5 m.

References

1. G.F. Giudice, R. Rattazzi, Phys. Rept. **322**, 419–499 (1999)
2. M.J. Strassler, K.M. Zurek, Phys. Lett. B **651**, 374–379 (2007)
3. ATLAS, CMS Collaborations, Procedure for the LHC Higgs Boson Search Combination in Summer 2011. Technical Report CMS-NOTE-2011-005, ATL-PHYS-PUB-2011-11 (2011), <https://cds.cern.ch/record/1379837>

Chapter 41

EFT Validity Issues in aQGC Analysis of Same-Sign WW Scattering Process



Sandeep Kaur

Abstract Vector Boson Scattering (VBS) processes are regarded as the best laboratory to study the anomalous quartic gauge couplings. Such studies are carried out in the framework of effective field theory (EFT). However, the EFT formalism is often not used in a fully consistent way. In this contribution, we present an analysis of anomalous quartic gauge couplings in WW scattering processes at the LHC in proton-proton collisions at a center-of-mass energy of 13 TeV with the CMS detector. The “Clipping” technique is implemented for data analysis in the EFT language.

41.1 Introduction

The observation of the Higgs boson with a mass of about 125 GeV by the ATLAS and CMS experiments [1, 2] is a triumph of the standard model (SM) that has opened a new era in particle physics. Within the current uncertainties, the newly found particle is consistent with the SM expectations. However, an ultimate test of the Higgs mechanism in Electroweak Symmetry Breaking (EWSB) lies in the vector boson scattering (VBS) process. Extensive VBS measurements are covered by the CMS and ATLAS collaborations [3, 4]. The focus of this report is on the CMS analysis of anomalous quartic gauge couplings in same-sign WW scattering processes in the purely leptonic decay channel ($WW \rightarrow l^\pm \nu l^\pm \nu$ where $l = e, \mu$). Constraints are obtained on the structure of quartic vector boson interactions in the framework of effective field theory (EFT).

A detailed description of the CMS detector, together with a definition of the coordinate system and the relevant kinematic variables, is reported in [5].

Sandeep Kaur—for the CMS Collaboration.

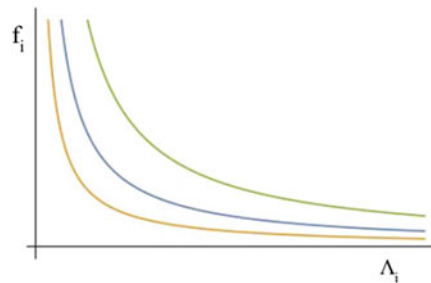
S. Kaur (✉)
Panjab University, Chandigarh 160014, India
e-mail: hundalsandeep1992@gmail.com

41.1.1 Full Clipping Technique

It is well known that EFT amplitudes grow with diboson invariant mass, M_{VV} , and this growth is unphysical above a certain EFT cut-off scale, Λ , which is unknown a priori, except that it cannot be higher than the unitarity limit, $\sqrt{s^U}$ above which the perturbative unitarity condition [$E^2 < \Lambda^2 \leq s^U$], where E is the energy scale of the considered process, is violated. Since Λ is unknown a priori, the limits on the Wilson coefficients, f_i , must be reported as a function of the Λ cut-off choice, and in order to apply the EFT formalism in a physically interpretable and model-independent way, the kinematic region where the EFT is not applicable should be omitted. This theoretically motivating technique to get conservative limits is known as the full clipping technique. It is not specific to dimensionality of the effective operators and involves a high mass cut-off at a preselected value of Λ . The preselected range of the cut-off choices corresponds to the assumption on the scale of the integrated out heavy particles as their masses cannot be smaller than Λ . Since the WW invariant mass is not accessible in the same-sign WW scattering process with leptonic W decays, such a cut-off is possible only for simulated events. To compensate for the fact that the real data may have an additional contribution from the region above Λ , the SM high mass tail must be added to the simulated events. As long as the data are overall consistent with SM predictions, it leads to conservative limits on the Wilson coefficients.

For a given choice of the EFT cut-off scale Λ , unitarity considerations predict an upper bound on f_i . The experimental limits are determined independently of the theoretical bounds, so they may equally well be stronger or weaker than the theoretical bounds; see Fig. 41.1 for a schematic illustration. The blue curve denotes the upper bound on the Wilson coefficient f_i as a function of Λ EFT cut-off. The orange and green curves denote exemplary experimental constraints on f_i , as a function of Λ . Only in the former case, the limits are EFT interpretable. Therefore, it is interesting to compare the limits based on the data and reported as a function of Λ cut-off with the pure theoretical curve $f_i(\Lambda)$ bound; the relation between the curves in different regions of Λ characterizes the strength and physical usefulness of the experimental bounds [6].

Fig. 41.1 Cartoon showing possible relations between the experimental bounds and the pure theoretical ones based on perturbative unitarity condition



41.2 Results

This section presents constraints on the Wilson coefficients f_i for the O_{S0} dimension-8 operator, as functions of the EFT cut-off Λ . For each operator, a region is determined in the Λ cut-off values in which the obtained limits are EFT interpretable. The expected limits on f_i are reported for three observables

$$R_{pt} = (p_T^{l1} * p_T^{l2}) / (p_T^{j1} * p_T^{j2}) \tag{41.1}$$

$$M_{o1} = \sqrt{(|\mathbf{p}_T^{l1}| + |\mathbf{p}_T^{l2}| + |\mathbf{p}_T^{miss}|)^2 - (\mathbf{p}_T^{l1} + \mathbf{p}_T^{l2} + \mathbf{p}_T^{miss})^2} \tag{41.2}$$

$$m_T(VV) = \sqrt{\left(\sum_i E_i\right)^2 - \left(\sum_i p_{z,i}\right)^2} \tag{41.3}$$

and the most sensitive one, which is in general Λ cut-off dependent, is identified. The observed limit for the most sensitive observable is reported; and the expected and the observed limit corresponding to the most sensitive observable is compared with the theoretical limit.

Table 41.1 [7] shows the results for the operators O_{S0} , for a few choices of the EFT cut-off Λ in the range 1–5 TeV. The expected limits are shown in the columns from second to fourth, in $1/\text{TeV}^4$. The most sensitive observable is reported in column five and it is based on the expected limits. Similarly, the observed limit corresponding to the most sensitive observable is shown in the sixth column. The observed limits are to be compared with the theoretical limits calculated with VBFNLO calculator v1.4.0, the latter reported in column seven in $1/\text{TeV}^4$. The visualization of Table 41.1 is shown in Fig. 41.2. It can be seen in Table 41.1 that R_{pt} is the most sensitive observable below the 2.5 TeV region and M_{o1} is the most sensitive observable in region above 2.5 TeV region for the operator O_{S0} . Based on the most sensitive observable, it can

Table 41.1 Expected and observed 95% CL limits in TeV^{-4} on Wilson coefficients of O_{S0} operator as function of cut-off in TeV. The experimental limits corresponding to the most sensitive observable is compared with the theoretical limit

Cut-off	Expected limit			Best sensitivity	Observed limit	Theoretical limit
	R_{pt}	M_{o1}	$(m_T(WW), m_{jj})$			
TeV	TeV^{-4}				TeV^{-4}	
1.0	[-36.4, 41.7]	[-39.5, 42.1]	[-48.2, 51.9]	R_{pt}	[-28.7, 30.9]	[-45, 78.5]
1.5	[-14.9, 16.0]	[-15.5, 16.6]	[-18.7, 19.6]	R_{pt}	[-11.2, 11.6]	[-8.1, 14.2]
2.0	[-8.72, 9.42]	[-8.90, 9.50]	[-10.1, 10.6]	R_{pt}	[-6.48, 6.85]	[-2.54, 4.37]
2.5	[-6.92, 7.45]	[-6.90, 7.38]	[-7.89, 8.33]	M_{o1}	[-4.50, 5.14]	[-1.03, 1.77]
3.0	[-6.03, 6.43]	[-5.93, 6.31]	[-6.81, 7.14]	M_{o1}	[-3.93, 4.41]	[-0.49, 0.85]
3.5	[-5.47, 5.79]	[-5.35, 5.64]	[-6.14, 6.43]	M_{o1}	[-3.58, 3.98]	[-0.27, 0.46]
4.0	[-5.18, 5.46]	[-5.05, 5.31]	[-5.79, 6.03]	M_{o1}	[-3.37, 3.75]	[-0.16, 0.27]

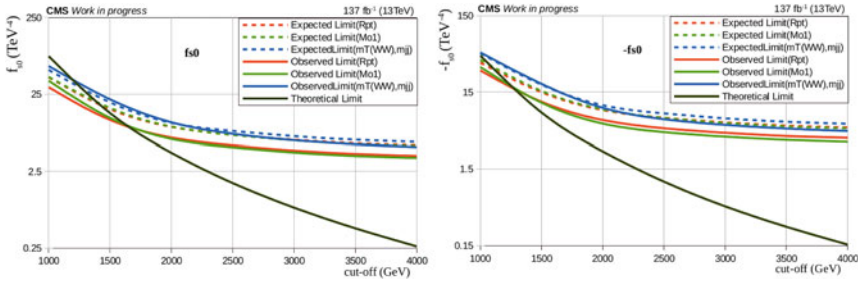


Fig. 4.12 Visualization of expected, observed, and theoretical limits for the \mathcal{O}_{S_0} operator

be seen that the expected and observed limits are EFT interpretable below 1.5 TeV for the operator \mathcal{O}_{S_0} . Along with that, observed limits are also EFT interpretable in the positive region below 2 TeV for this operator.

41.3 Summary

The limits on Wilson coefficients of \mathcal{O}_{S_0} dimension-8 operators are calculated as a function of the EFT cut-off energy scale, taking into consideration the validity of the EFT framework. It is found that for the operator \mathcal{O}_{S_0} , the limits are EFT interpretable below the 1.5 TeV regions and R_{pT} is the most sensitive observable in those regions. Qualitatively, very similar conclusions are observed for the remaining dimension-8 operators. In the HL-LHC context, provided that the results are limited only by the available amount of data, we expect to have EFT interpretable limits in the additional areas.

Acknowledgements We acknowledge in-depth discussions with Jan Kalinowski and Paweł Kozów of the University of Warsaw on implementing the newly developed clipping method based on EFT used for interpreting the CMS data reported in this work. The speaker acknowledges the Council of Scientific and Industrial Research (CSIR) for the fellowship grant.

References

1. G. Aad et al. [ATLAS], Phys. Lett. B **716**, 1–29 (2012)
2. S. Chatrchyan et al. [CMS], Phys. Lett. B **716**, 30–61 (2012)
3. A.M. Sirunyan et al. [CMS], Phys. Lett. B **809**, 135710 (2020)
4. G. Aad et al. [ATLAS], Phys. Rev. Lett. **113**(14), 141803 (2014)
5. S. Chatrchyan et al. [CMS], JINST **3**, S08004 (2008)
6. J. Kalinowski et al., Eur. Phys. J. C **78**(5), 403 (2018)
7. S. Kaur, Ph.D. Thesis in preparation

Chapter 42

Recent Results on Lepton Flavor Universality Test at Belle



Seema Choudhury

Abstract Recent searches for lepton flavor universality (LFU) violation in B decays show a possible hint of new physics, especially in decays mediated by the flavor-changing neutral current $b \rightarrow s\ell\ell$ ($\ell = e$ or μ) transition. We report measurements of LFU violating observable R_K , the ratio of decay branching fractions of $B \rightarrow K\mu\mu$ to $B \rightarrow Kee$. We also measure the differential branching fraction and CP-averaged isospin asymmetry in $B \rightarrow K\ell\ell$ decays. The study is based on the full data sample recorded by the Belle detector at the $\Upsilon(4S)$ resonance, which contains 772×10^6 $B\bar{B}$ events from e^+e^- collisions produced by the KEKB collider.

42.1 Introduction

The $B \rightarrow K\ell\ell$ decay is mediated by the flavor-changing neutral current transition involving the quark transition $b \rightarrow s\ell\ell$. Such decays are suppressed in the standard model (SM) and proceed via electroweak loop and box diagrams. The loop level contributions lead to a small branching fraction (\mathcal{B} , BF), which make them sensitive to new physics [1, 2].

The lepton-flavor-universality ratio is defined as the BF ratio of $B \rightarrow K\mu\mu$ to $B \rightarrow Kee$. According to the SM, this ratio should be approximately 1, as the coupling of leptons to gauge bosons is independent of the flavor. However, recent LHCb [3, 4] results show tantalizing 2.6σ and 2.5σ deviations in R_K for $q^2 \in [1, 6]$ and $[1.1, 6]$ GeV^2/c^4 , where q^2 is the dilepton invariant mass square, with 3 and 5 fb^{-1} data samples, respectively. The previous Belle [5] measurement was performed with 605 fb^{-1} data sample and that for the entire q^2 region.

Another theoretically robust observable is the CP-averaged isospin asymmetry (A_I). According to the SM, the decay rate of charged B mesons should be the same

Seema Choudhury—for the Belle Collaboration.

S. Choudhury (✉)
Indian Institute of Technology, Hyderabad, India
e-mail: choudhuryseema.hep@gmail.com

as that of neutral B mesons. In other words, A_I should be zero. However Belle [5] and BaBar [6] have reported a negative asymmetry, while LHCb [7] results are consistent with SM expectation.

The analysis summarized in this proceedings is performed with the full 711 fb^{-1} data sample of Belle [8]. Especially, we have performed a multidimensional fit to extract maximal information out of the limited data sample of Belle and given results in five different q^2 bins along with the whole q^2 region.

42.2 Event Reconstruction and Background Suppression

The K_S^0 mesons are reconstructed using displaced vertex properties and requiring an invariant mass within 3σ about K_S^0 nominal mass. The charged particles namely K^\pm , μ^\pm , and e^\pm are selected such that they are consistent with originating from the interaction point and required to satisfy some particle ID criteria. The charged kaons are selected using a likelihood ratio $\mathcal{R}_{K/\pi} = \mathcal{L}_K / (\mathcal{L}_K + \mathcal{L}_\pi)$, where \mathcal{L}_K and \mathcal{L}_π are the likelihoods for kaons and pions, respectively. The requirement is $\mathcal{R}_{K/\pi} > 0.6$, which yields an identification efficiency of 92% with 7% pion misidentification rate [9]. The muons and electrons are selected with muon likelihood (\mathcal{R}_μ) and electron likelihood (\mathcal{R}_e) > 0.9 . The muon selection efficiency is 89% with 1.5% pion fake-rate [9]. Similarly, electron selection efficiency and fake-rate are 92% and $< 1\%$ [10], respectively. The charged or neutral kaon candidate is combined with two oppositely charged lepton candidates to form a B^+ or B^0 meson. Two kinematic variables that distinguish signal from background are the beam-energy-constrained mass, $M_{bc} = \sqrt{E_{\text{beam}}^2/c^4 - |p_B|^2/c^4}$, and the energy difference, $\Delta E = E_B - E_{\text{beam}}$. We retain candidate events satisfying $5.2 < M_{bc} < 5.3 \text{ GeV}/c^2$ and $-0.10 < \Delta E < 0.25 \text{ GeV}$.

At this stage of the analysis, we find a significant contamination from continuum ($e^+e^- \rightarrow q\bar{q}$, $q = u, d, s, c$) as well as other B decays. These backgrounds are suppressed by a multivariate analysis technique, namely a neural network (NN). The NN is trained with a number of event-shape, vertex quality, and kinematic variables. The NN output obtained is translated to another variable (\mathcal{O}) using a log function: $\mathcal{O} = \log \frac{\mathcal{O} - \mathcal{O}_{\min}}{\mathcal{O}_{\max} - \mathcal{O}}$. The \mathcal{O}_{\min} is the minimum threshold applied before translating the variable and this causes 4–5% signal efficiency loss with $\sim 75\%$ background rejection. The irreducible backgrounds from J/ψ and $\psi(2S)$ are suppressed by applying appropriate q^2 vetoes. The peaking background coming from misidentification and swapping between the final-state particles, mostly for $B^+ \rightarrow K^+\mu^+\mu^-$, are removed by invariant-mass vetoes. The background from D^0 and J/ψ and are rejected with $M_{K^+\mu^-} \notin [1.85, 1.88] \text{ GeV}/c^2$ and $M_{K^+\mu^-} \notin [3.06, 3.13] \text{ GeV}/c^2$, respectively.

42.3 Fitting

The signal yield is extracted by performing an unbinned extended maximum-likelihood fit in M_{bc} , ΔE , and \mathcal{O}' . The signal component of M_{bc} , ΔE , and \mathcal{O}' is fitted with Gaussian, Gaussian+Crystal Ball [11], and Gaussian+asymmetric Gaussian, respectively. The continuum background for M_{bc} , ΔE , and \mathcal{O}' is fitted with ARGUS [12], Chebyshev polynomial, and Gaussian, respectively. Similarly, the B decay background is fitted with ARGUS, exponential, and Gaussian for M_{bc} , ΔE , and \mathcal{O}' . The signal shape of $B \rightarrow K\ell\ell$ is calibrated with $B \rightarrow J/\psi(\ell\ell)K$ and the continuum background with an 89 fb^{-1} off-resonance data sample, collected 60 MeV below the $\Upsilon(4S)$ peak.

42.4 Results

The maximum-likelihood fit is performed separately for charged and neutral B decays in the muon and electron channels. We find 137 ± 14 , 138 ± 15 , $27.3^{+6.6}_{-5.8}$, and $21.8^{+7.0}_{-6.1}$ signal events for $B^+ \rightarrow K^+\mu^+\mu^-$, $B^+ \rightarrow K^+e^+e^-$, $B^0 \rightarrow K_S^0\mu^+\mu^-$, and $B^0 \rightarrow K_S^0e^+e^-$, respectively. The R_{K^+} , R_{K^0} , and overall R_K are calculated in $q^2 \in [0.1, 4]$, $[4, 8.12]$, $[1, 6]$, $[10.2, 12.8]$, $> 14.18 \text{ GeV}^2/c^4$ along with the whole q^2 region. The results are consistent with SM predictions within uncertainties for different q^2 bins as shown in Fig. 42.1. The isospin asymmetry (A_I) is calculated for $B \rightarrow K\mu^+\mu^-$, $B \rightarrow Ke^+e^-$, and $B \rightarrow K\ell^+\ell^-$. As shown in Fig. 42.2, the results are found to exhibit negative asymmetry for almost all the q^2 bins. The maximum deviation is 2.6σ for $B \rightarrow K\mu\mu$ in $q^2 \in [1, 6] \text{ GeV}^2/c^4$. The differential BF, $d\mathcal{B}/dq^2$, are measured for charged and neutral B decays in the muon and electron channel (Fig. 42.3). The results for $B^+ \rightarrow K^+\mu^+\mu^-$ are consistent with theory predictions while that for the neutral B decay are below the expectations. The $B \rightarrow J/\psi K$ decay is used as a control sample to calibrate the signal shape for $B \rightarrow K\ell\ell$ as well as to check whether the key observables like R_K and A_I are consistent with SM predictions or not. We find 16736 ± 130 , 17010 ± 130 , 4961 ± 71 , and 4710 ± 69 signal events for $B^+ \rightarrow J/\psi(\mu\mu)K^+$, $B^+ \rightarrow J/\psi(ee)K^+$,

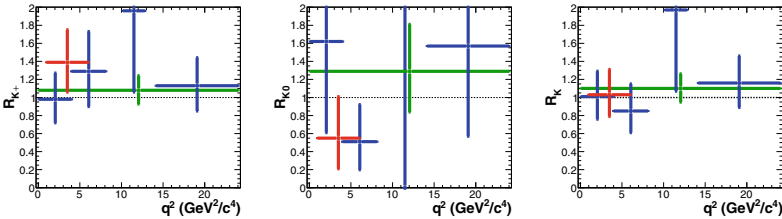


Fig. 42.1 R_{K^+} (left), R_{K^0} (middle), and R_K (right) in the bins of q^2 . The bins shown are $[0.1, 4]$ (blue), $[4, 8.12]$ (blue), $[1, 6]$ (red), $[10.2, 12.8]$ (blue), > 14.18 (blue), and whole q^2 region (green)

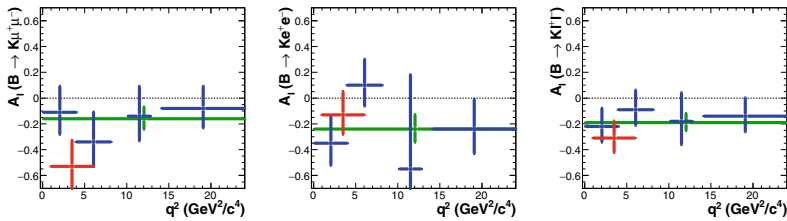
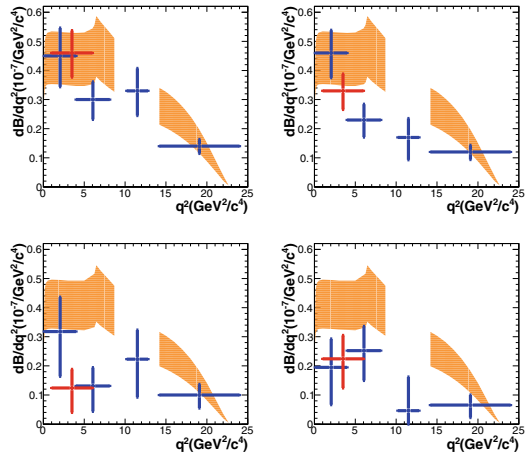


Fig. 42.2 A_1 measurements in bins of q^2 , for decays $B \rightarrow K\mu^+\mu^-$ (left), $B \rightarrow Ke^+e^-$ (middle), and both modes combined (right). The legends are the same as in Fig. 42.1

Fig. 42.3 $d\mathcal{B}/dq^2$ measurements in bins of q^2 , for decays $B^+ \rightarrow K^+\mu^+\mu^-$ (top-left), $B^+ \rightarrow K^+e^+e^-$ (top-right), $B^0 \rightarrow K^0\mu^+\mu^-$ (bottom-left), and $B^0 \rightarrow K^0e^+e^-$ (bottom-right). The legends are the same as in Fig. 42.1. The yellow shaded regions show the predictions from the light-cone sum rule and lattice QCD calculations [13, 14]



$B^0 \rightarrow J/\psi(\mu\mu)K_S^0$, and $B^0 \rightarrow J/\psi(ee)K_S^0$, respectively. The branching fractions $\mathcal{B}(B^+ \rightarrow J/\psi K^+) = (1.032 \pm 0.007 \pm 0.024) \times 10^{-3}$ and $\mathcal{B}(B^0 \rightarrow J/\psi K^0) = (0.902 \pm 0.010 \pm 0.026) \times 10^{-3}$ constitute the most precise measurements to date, the first uncertainty is statistical and second is systematic.

42.5 Systematic Uncertainties

Systematic uncertainties due to muon and electron identification are 0.3% and 0.4%, respectively, and are obtained with an inclusive sample of $J/\psi \rightarrow \ell\ell$. The K^+ and K_S^0 identification systematic uncertainties are 0.8% and 1.6%. The systematic uncertainty due to charged track reconstruction is 0.35% per track. The limited MC statistics results in a systematic of 0.2% while the number of $B\bar{B}$ events has an uncertainty of 1.4%. The systematic due to minimum NN requirement is 0.2–0.3%, obtained using the $B \rightarrow J/\psi K$ sample. The PDF shape systematic is 0.1–0.6% obtained by varying the parameters fixed in the fit within $\pm 1\sigma$. The model-dependent systematic uncertainty (0.3–2.0%) is calculated by replacing the BTOSLLBALL

model [15] with lattice QCD and quark models [16, 17]. The uncertainty due to $\mathcal{B}[\Upsilon(4S) \rightarrow B\bar{B}]$ is 1.2%. The systematic sources like hadron identification, charged track reconstruction, the number of $B\bar{B}$ events, and $\mathcal{B}[\Upsilon(4S) \rightarrow B\bar{B}]$ cancel for R_K , while for the A_I measurement lepton identification and the number of $B\bar{B}$ events cancel.

42.6 Conclusion

The observables R_K , A_I , and $d\mathcal{B}/dq^2$ for $B \rightarrow K\ell\ell$ are measured using the full 711 fb^{-1} data sample of Belle in bins of $q^2 \in [0.1, 4]$, $[4, 8.12]$, $[1, 6]$, $[10.2, 12.8]$, $>14.18 \text{ GeV}^2/c^4$ along with the whole q^2 region. The R_K results are found to be consistent with SM expectations. The A_I show negative asymmetry for almost all q^2 bins. The $d\mathcal{B}/dq^2$ for charged B decays are compatible with theory predictions, while that for neutral B decays are far below the expectations. The branching fractions for $B^+ \rightarrow J/\psi K^+$ and $B^0 \rightarrow J/\psi K^0$ are the most precise measurements to date.

References

1. W. Altmannshofer et al., Phys. Rev. D. **96**, 055008 (2017)
2. B. Capdevila et al., J. High Energy Phys. **01**, 093 (2018)
3. R. Aaij et al. (LHCb Collaboration), Phys. Rev. Lett. **122**, 191801 (2019)
4. R. Aaij et al. (LHCb Collaboration), Phys. Rev. Lett. **113**, 151601 (2014)
5. J.T. Wei et al. (Belle Collaboration), Phys. Rev. Lett. **103**, 171801 (2009)
6. J.P. Lees et al. (BaBar Collaboration), Phys. Rev. D **86**, 032012 (2012)
7. R. Aaij et al. (LHCb Collaboration), J. High Energy Phys. **06**, 133 (2014)
8. S. Choudhury et al. (Belle Collaboration), J. High Energy Phys. **03**, 105 (2021)
9. E. Nakano, Nucl. Instrum. Methods Phys. Res., Sec. A **494**, 402 (2002)
10. K. Hanagaki, H. Kakuno, H. Ikeda, T. Iijima, T. Tsukamoto, Nucl. Instrum. Methods Phys. Res., Sec. A **485**, 490 (2002)
11. T. Skwarnicki, Ph.D. Thesis, Institute for Nuclear Physics, Krakow; DESY Internal Report No. DESY F31-86-02 (1986)
12. H. Albrecht et al. (ARGUS Collaboration), Phys. Lett. B **241**, 278 (1990)
13. C. Bobeth, G. Hiller, D. van Dyk, J. High Energy Phys. **07**, 067 (2011)
14. C. Bobeth, G. Hiller, D. van Dyk, C. Wacker, J. High Energy Phys. **01**, 107 (2012)
15. A. Ali, P. Ball, L.T. Handoko, G. Hiller, Phys. Rev. D **61**, 074024 (2000)
16. D. Melikhov et al., Phys. Lett. B **410**, 290 (1997)
17. P. Colangelo et al., Phys. Rev. D **53**, 3672 (1996)

Chapter 43

Naturally Freezing-In Dark Leptons



Shiuli Chatterjee

Abstract Dark, chiral fermions carrying lepton flavor quantum numbers are natural candidates for freeze-in. Small couplings with the Standard Model fermions of the order of lepton Yukawas arise naturally in the limit of Minimal Flavor Violation. Particles with certain representations under the flavor group are rendered automatically stable when interactions conserve the total lepton number. For masses in the GeV–TeV range, the minimal representation with three flavors leads to signals at future direct detection experiments like LZ and DARWIN. Interestingly, freeze-in with a smaller flavor group such as $SU(2)$ is already being probed by XENON1T. This is based on a talk presented at XXIV DAE-BRNS HEP Symposium.

43.1 Introduction

There is a wide-ranging evidence of Dark Matter (DM) from decades of observations of its gravitational interactions. Furthermore, cosmological observations put stringent constraints on the relic density of DM. While freeze-out of a Weakly Interacting Massive Particle (WIMP) has been popular for long, in recent times, the freeze-in mechanism is being explored as a viable alternative. The negative results from searches for WIMP DM from direct detection experiments give further motivation to understand this mechanism.

The freeze-in production of DM proceeds through very small couplings to Standard Model (SM) particles, such that the DM is never in thermal equilibrium with the SM bath. We motivate this small coupling through the smallness of the dimensionless electron Yukawa that appears naturally in the interactions of a lepton flavored DM in the framework of Minimal Flavor Violation (MFV).

S. Chatterjee (✉)

Centre for High Energy Physics, Indian Institute of Science, Bangalore 560012, India
e-mail: shiulic@iisc.ac.in

© The Author(s), under exclusive license to Springer Nature Singapore Pte Ltd. 2022
B. Mohanty et al. (eds.), *Proceedings of the XXIV DAE-BRNS High Energy Physics Symposium, Jatni, India*, Springer Proceedings in Physics 277,
https://doi.org/10.1007/978-981-19-2354-8_43

237

43.1.1 Minimal Flavor Violation

Interactions of SM lepton sector with the minimal particle content consisting of three flavors each of the $SU(2)_L$ doublets L and the $SU(2)_L$ singlets E , demonstrate a larger symmetry of flavor

$$G_{LF} \equiv SU(3)_L \otimes SU(3)_E, \quad (43.1)$$

where the $SU(3)$'s correspond to the individual rotations of the L and E fields in the generation space, respectively

$$L \sim (3, 1)_{G_{LF}}, \quad E \sim (1, 3)_{G_{LF}}. \quad (43.2)$$

This larger symmetry is violated only by the Yukawa interaction, $L_Y = \bar{L} Y_l E H$. MFV hypothesis requires that the dynamics of flavor violation be completely determined by the structure of this Yukawa matrix, which is treated as a (spurious) field having non-trivial transformation under G_{LF} , $Y_l \sim (3, \bar{3})_{G_{LF}}$, such that the Yukawa term now becomes invariant under G_{LF} . If the dark sector does not add any new flavor structures, then its interactions with SM particles follow the same flavor structures as those of the SM and its interactions are highly restricted.

43.1.2 Flavored DM and Stability

MFV imposes significantly strong constraints on the operators allowed. One can then wonder if such constraints can lead to the stability of DM by disallowing their decay operators. It was shown in [1] that imposing MFV automatically ensures stability of certain representations of DM in the quark sector. However, such stability is not guaranteed by MFV alone in the leptonic sector [2].

We show in [3] that the absence of total lepton number violating interactions leads to the stability of DM with specific flavor representations and lepton giving an analogous stability condition to that in the quark sector, only now including the DM lepton number q_{LN} . We consider a flavored DM χ with lepton number q_{LN} , transforming under G_{LF} as $\chi \sim (n_L, m_L)_L \times (n_E, m_E)_E$, with n_i factors of $\mathbf{3}_i$ and m_i factors of $\bar{\mathbf{3}}_i$. Its stability is given by the condition¹

$$(n_L - m_L + n_E - m_E - q_{LN}) \bmod 3 \neq 0. \quad (43.3)$$

¹ We give a list of stable representations in [3].

43.1.3 Minimal Flavored Model

We make a minimal extension to the SM by adding a chiral, Dirac DM particle that transforms as

$$\chi_L \sim (3, 1)_{G_{LF}}, \quad \chi_R \sim (1, 3)_{G_{LF}}$$

with a lepton number 0 (which can be seen to be stable from (43.3); phenomenology doesn't depend on the specific choice of lepton number). Its interaction with SM is extracted from the lowest dimension effective operators allowed by MFV

$$\begin{aligned} \mathcal{L}_\chi &\supset \bar{\chi}_1 (i\not{\partial} - m_\chi y_e) \chi_1 + \bar{\chi}_2 (i\not{\partial} - m_\chi y_\mu) \chi_2 + \bar{\chi}_3 (i\not{\partial} - m_\chi y_\tau) \chi_3 + \mathcal{L}_\chi^{\text{eff}}, \\ \mathcal{L}_\chi^{\text{eff}} &\equiv \frac{1}{2\Lambda_{MFV}} \underbrace{\left(\bar{\chi}_L \sigma_{\mu\nu} Y_l \chi_R \right) B^{\mu\nu}}_{\text{Magnetic Dipole Moment (MDM)}} + \frac{i}{2\Lambda_{MFV}} \underbrace{\left(\bar{\chi}_L \sigma_{\mu\nu} \gamma_5 Y_l \chi_R \right) B^{\mu\nu}}_{\text{Electric Dipole Moment (EDM)}} \\ &\quad + \frac{1}{\Lambda_{MFV}} \underbrace{\left(\bar{\chi}_L Y_l \chi_R \right) H^\dagger H}_{H\text{-mediated}} \end{aligned}$$

where Λ_{MFV} is the scale of MFV, m_χ is a free parameter of dimension 1. We see that the *chiral* assignment under flavor leads to interactions proportional to the Yukawa matrix. And the lightest particle, χ_1 , has the smallest couplings. The first two terms in $\mathcal{L}_\chi^{\text{eff}}$ are dimension 5 operators and lead to UV freeze-in with sensitivity to the reheating temperature T_{RH} , while the last term gives also a renormalizable term after EWSB, $(vev/\Lambda_{MFV})y_e h \bar{\chi}_1 \chi_1$, giving rise to IR freeze-in that is independent of T_{RH} , albeit still dependent on the scale Λ_{MFV} .

We use micrOMEGAs 5.0 [4] to calculate the freeze-in relic density and show the contours of $\Omega h^2 = 0.12$ in Fig. 43.2a, while taking care that $\Lambda_{MFV} > m_{\chi_3}$ and $T_{RH} < \Lambda_{MFV}$, for the EFT to be valid. The former of these conditions gives the cut-off/edge at large m_{χ_1} . We also restrict for $m_{\chi_2} \gg T_{RH}$ so that the lightest particle χ_1 with the coupling proportional to the electron Yukawa y_e forms the majority of the relic density. This ties up the reheating temperatures to the mass of the DM and gives the cut-off/edge at small values of m_{χ_1} , for each T_{RH} .

We briefly note that the Higgs portal production becomes dominant when $T_{RH} \gtrsim m_h > m_{\chi_1}/2$, while the magnetic dipole moment operator dominates for $m_{\chi_1} > T_{RH}$ or when the Higgs is Boltzmann suppressed ($m_h \gg T_{RH}$); see Fig. 43.1.

Although freeze-in generated dark matter is notoriously difficult to test experimentally, because of the very small couplings with SM particles, in our case, elastic scattering rates through the dipole interactions mediated by photons get enhanced by $1/q^2$ in the low velocity limit. The EDM contribution is seen to give the largest contribution in the non-relativistic limit of small v and E_R and thus is the most constraining.

We show the limits from XENON1T data in Fig. 43.2a (yellow region) which is not yet sensitive to the region of interest, and the projected bounds from DARWIN and LZ which would probe T_{RH} of a few GeV. In Fig. 43.2b, we plot the case for

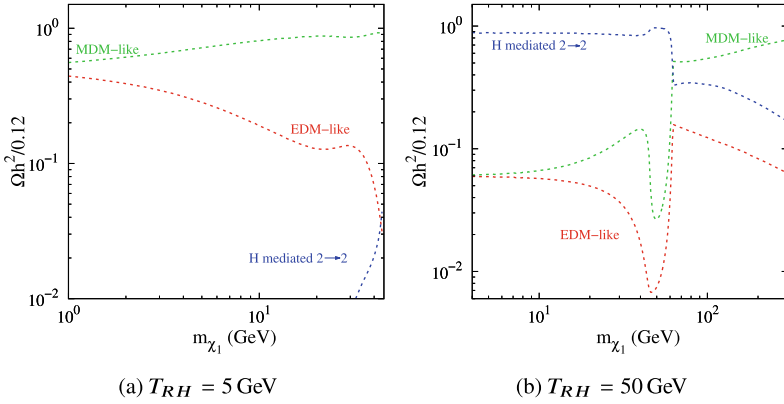


Fig. 43.1 Fractional contribution of annihilation channels to the total relic abundance with Λ_{MFV} chosen to reproduce the observed relic density for each m_{χ_1}

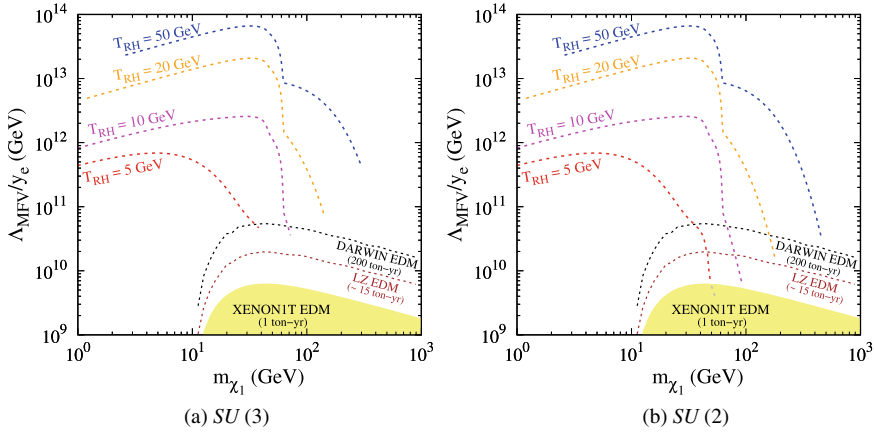


Fig. 43.2 Results from relic density constraints and direct detection experiments

a smaller flavor group $SU(2)$ instead of $SU(3)$ with chiral doublet representations with first two generations of the DM. A region of the parameter space is already ruled out from XENON1T data with LZ and DARWIN projected to probe a much larger region.

For both these cases, a larger T_{RH} mandates smaller coupling, and hence larger Λ_{MFV} . The downward dips are because of a decreasing Λ_{MFV} (increasing effective coupling) required to compensate for the Boltzmann suppression for $m_{\chi_1} > T_{RH}$. We also observe a sharp dip at $m_{\chi_1} \sim m_h/2$ that is explained by the Higgs production going off-shell, requiring larger couplings (smaller Λ_{MFV}) to reproduce the observed relic density.

We thus have freeze-in production of flavored DM that produces the observed relic abundance while also being observable at current and future experiments. Specifi-

cally, detection happens for DM masses greater than T_{RH} where the effective coupling (and hence the elastic scattering rates) increases drastically to compensate for the fact that only the tail of the SM thermal distributions with large momentum can produce such massive DM.

References

1. B. Batell, J. Pradler, M. Spannowsky, *JHEP* **08**, 038 (2011)
2. M.C. Chen, J. Huang, V. Takhistov, *JHEP* **02**, 060 (2016)
3. G. D'Ambrosio, S. Chatterjee, R. Laha, S.K. Vempati, *SciPost Phys.* **11**, 006 (2021)
4. G. Bélanger, F. Boudjema, A. Goudelis, A. Pukhov, B. Zaldivar, *Comput. Phys. Commun.* **231**, 173–186 (2018)

Chapter 44

Interference Effect in LNV and LNC Meson Decays for Left-Right Symmetric Model



Siddharth P. Maharathy, Rohini M. Godbole, Sanjoy Mandal, M. Mitra, and Nita Sinha

Abstract The proceeding delved into the upshot of the interference of lepton number violating (LNV) and lepton number conserving (LNC) three-body meson decays $M_1^+ \rightarrow l_i^+ l_j^\pm \pi^\mp$ in the context of a TeV scale Left-Right Symmetric Model (LRSM) with nearly degenerate right handed (RH) neutrinos. The resonant enhancement is possible in the semi-leptonic LNV and LNC meson decays, considering MeV-to-GeV ranged RH neutrinos. With a single RH neutrino, the new physics LNC and LNV branching ratio (BR) are equal. Depending on the neutrino mixing angles and CP violating phases, we substantiate with our results that the former scenario, equal BRs of LNV and LNC decay channels, can be either enhanced or suppressed, and the ratio of these two rates can differ from unity.

S. P. Maharathy (✉) · M. Mitra
Institute of Physics, Sachivalaya Marg, Bhubaneswar 751005, India
e-mail: siddharth.m@iopb.res.in

R. M. Godbole
Centre for High Energy Physics, Indian Institute of Science, Bengaluru 560012, India
e-mail: rohini@iisc.ac.in

S. Mandal
AHEP Group, Institut de Física Corpuscular, CSIC/Universitat de València, Parc Científic de Paterna, C/Catedrático José Beltrán, 2 E-46980 Paterna, Valencia, Spain
e-mail: smandal@ific.uv.es

M. Mitra
Homi Bhabha National Institute, Training School Complex, Anushaktinagar, Mumbai, India

N. Sinha
The Institute of Mathematical Sciences, C.I.T Campus, Taramani, Chennai 600113, India
e-mail: nita@imsc.res.in

44.1 Introduction

Conclusive experimental evidence of light neutrino masses and mixings clearly indicates the existence of beyond standard model (BSM) physics. Amongst the different BSM models that try to explain the caveats of standard model (SM), LRSM [1] is an interesting one. It explains the smallness of neutrino mass, on top of that, it also sights the parity violation in SM by dealing both the left and right chiral particles on equal footing. The model generates a small neutrino mass considering both Type-I as well as Type-II seesaw mechanism. Existence of Majorana neutrino results in LNV processes, which is the main aspect of the proceeding.

A strong constraint on the RH gauge boson mass $M_{W_R} > 4.8$ TeV has been placed from the boosted RH neutrino search for LRSM considering RH neutrino and gauge boson mass hierarchy of $O(0.1)$ [2, 3]. For very light and heavy neutrino masses, the LNV and tau decays are suppressed to a fault [4], well below the sensitivity reach of any future experiments. An adequate change in the former case is possible if the heavy neutrinos present are in the MeV-to-GeV mass domain, and can be able to produce on-shell in the parent meson decay. Considering a single heavy neutrino, the LNV and LNC meson decay rates, mediated by the RH neutrinos are predicted to be the same, irrespective of the RH neutrino mixing matrix. This scenario changes prominently if more than one degenerate heavy neutrino state contributes to these processes with non-trivial RH neutrino mixing matrix [5]. The corresponding proceeding contains some of the results of our work in [6].

44.2 Formalism

LRSM is a simple extension of SM based on the gauge group $SU(3)_c \otimes SU(2)_L \otimes SU(2)_R \otimes U(1)_{B-L}$. The model contains three RH neutrinos (N_{Ri}) which belongs to three RH lepton doublets, one bi-doublet scalar Φ and two scalar triplets Δ_R and Δ_L [1]. The Majorana nature of the heavy neutrino results in LNV violating meson decays (Fig. 44.1).

For our analysis, we have considered two different ranges of the RH neutrino states: $0.14 \text{ GeV} < M_N < 0.49 \text{ GeV}$ and $0.14 \text{ GeV} < M_N < 5 \text{ GeV}$, relevant for

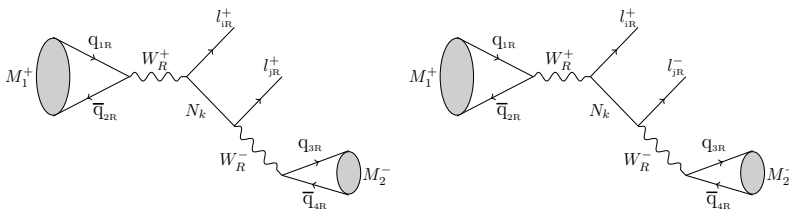


Fig. 44.1 The left and right figures are for LNV and LNC meson decays, mediated by the heavy neutrino, respectively

$K^+ \rightarrow e^+e^\pm\pi^\mp/e^+\mu^\pm\pi^\mp$ and $B^+ \rightarrow e^+e^\pm\pi^\mp/e^+\mu^\pm\pi^\mp$ decays, respectively. The main focus resides on the final states containing electrons and muons. The mass range is considered such that the resonant production of RH neutrino is possible. We consider the scenario where two out of the heavy neutrino states are nearly degenerate, i.e. $M_{N_1} \sim M_{N_2}$ and M_{N_3} is very heavy. To present the effect of interference, we choose the following form of mixing matrix, K_R :

$$K_R = \begin{bmatrix} \cos \theta & -\sin \theta & 0 \\ e^{-i\phi} \sin \theta & e^{-i\phi} \cos \theta & 0 \\ 0 & 0 & 1 \end{bmatrix}, \tag{44.1}$$

Because of this mixing matrix K_R , now the RH neutrino decay width will depend on the mixing angle [6]. With some assumptions, the LNV decay width of RH neutrino has the following simplified dependencies upon mixing angle and phase:

$$\Gamma_{ij}^{\text{LNV}} \propto \begin{cases} (1 - \sin^2 2\theta \sin^2 \phi), & \text{for } i = j \\ (\sin^2 2\theta \sin^2 \phi), & \text{for } i \neq j \end{cases} \tag{44.2}$$

We also considered a full 3×3 mixing matrix and discussed their results in our original work.

44.3 Results and Discussion

The above figure substantiates the angular dependencies on LNV meson decay considering the mixing matrix K_R . The dotted line and solid line correspond to e^+e^+ and $e^+\mu^+$ mode, respectively. For K^+ decay, we have considered $M_N \simeq 0.38$ GeV and $M_{W_R} = 22$ TeV, and for B^+ -meson decay, we have considered $M_N \simeq 2$ GeV and $M_{W_R} = 5$ TeV, respectively. The difference between the two plots are the consequence of the angular dependency on the total decay width of RH neutrino (Γ_N). For the special form of mixing matrix (44.1), the LNC same flavour decay widths are nearly constant, whereas the different flavour decay modes are suppressed to a fault [7] (Fig. 44.2).

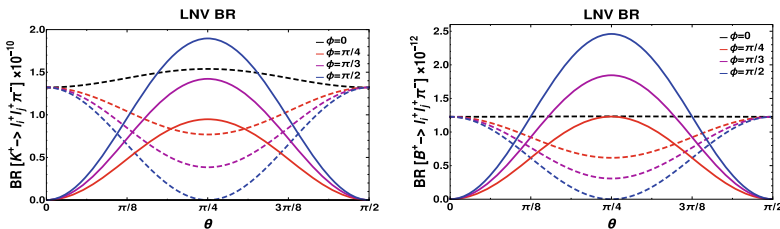


Fig. 44.2 Branching ratio of LNV meson decay to same flavour (e^+, e^+) and different flavor (e^+, μ^+) final state along with a pion (π^+). The plot in the left panel is for kaon (K^+), and the plot in the right panel is for B-meson(B^+) decay, respectively

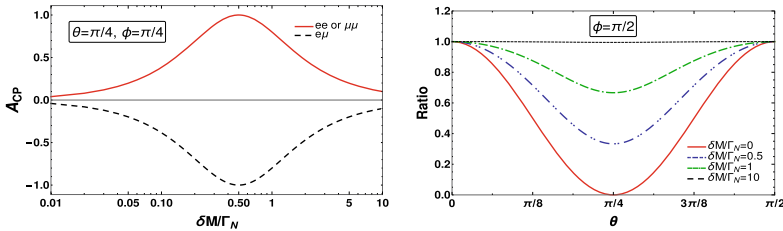


Fig. 44.3 Left: variation of A_{CP} w.r.t. mass splitting of RH neutrinos (δM), Right: variation of ratio of LNV and LNC ee mode w.r.t. mixing angle θ for different values of δM

Using the analytical expressions of LNV and LNC decays calculated in our main paper [6], we have calculated an asymmetry parameter as

$$A_{CP}^{ij} = \frac{\Gamma_{ij}^{\text{LNV},++} - \Gamma_{ij}^{\text{LNV},--}}{\Gamma_{ij}^{\text{LNV},++} + \Gamma_{ij}^{\text{LNV},--}} \quad (44.3)$$

the complementary nature of $A_{CP}^{ee\text{ or } \mu\mu}$ and $A_{CP}^{e\mu}$ w.r.t. $\frac{\delta M}{\Gamma_N}$ can be seen from the left panel of Fig. 44.3. The right plot panel of Fig. 44.3 signifies that for large mass splitting between the RH neutrinos, the interference effect fades away. Thus, for $\delta M \geq \Gamma_N$, the two RH neutrino scenario bears the semblance of the model having one heavy RH neutrino.

44.4 Summary

The proceeding mainly encapsulated some of the important results mentioned in our original paper. We mainly focus on the scenario where two of the RH neutrinos are in MeV-to-GeV mass domain and can be produced resonantly. There can also be interference effect between LNV and LNC semi-leptonic meson decays depending upon the structure of mixing matrix. The oscillatory behaviour shown in Fig. 44.2 is the consequence of the structure of the mixing matrix K_R considered in (44.1). We have discussed the effect of a complete 3×3 mixing matrix also in our work [6].

References

1. J.C. Pati, A. Salam, Phys. Rev. D **10**, 275–289 (1974) [erratum: Phys. Rev. D **11**, 703–703 (1975)]
2. M. Mitra, R. Ruiz, D.J. Scott, M. Spannowsky, Phys. Rev. D **94**(9), 095016 (2016)
3. M. Aaboud et al., ATLAS., Phys. Lett. B **798**, 134942 (2019)
4. S. Mandal, M. Mitra, N. Sinha, Phys. Rev. D **96**(3), 035023 (2017)
5. A. Das, P.S.B. Dev, R.N. Mohapatra, Phys. Rev. D **97**(1), 015018 (2018)
6. J. Gluza, T. Jeliński, Phys. Lett. B **748**, 125–131 (2015)
7. R.M. Godbole, S.P. Maharathy, S. Mandal, M. Mitra, N. Sinha, [arXiv:2008.05467](https://arxiv.org/abs/2008.05467) [hep-ph]

Chapter 45

Measurement of Higgs Self-coupling from Non-resonant Higgs Pair Production and Decay to $b\bar{b}\gamma$ Final State in the CMS Experiment



Soumya Mukherjee

Abstract The trilinear self-coupling of Higgs can directly be accessed at the LHC by inclusive production of Higgs pair. A search for the non-resonant Higgs pair production via gluon-gluon fusion, as well as Vector Boson Fusion processes, has been performed recently by CMS collaboration with the complete LHC Run-2 proton-proton collision data at centre of mass energy of $\sqrt{s} = 13$ TeV, in the most sensitive $2\gamma + 2b$ jets inclusive final state. This article presents the results of the measurement for inclusive Higgs pair production cross section as well as the estimation of relevant coupling parameters.

45.1 Introduction

After the discovery of the Higgs by ATLAS and CMS experiments, one of the important properties which remains to be measured, is the self-coupling leading to self interaction among multiple of Higgs field ϕ . In the standard model (SM), the trilinear coupling λ_{HHH} is same as the quartilinear coupling λ_{HHHH} , denoted by λ . Thus, the shape of the Higgs potential $V(\phi)$ is directly related to this λ and the vacuum expectation value $v = (\sqrt{2}G_F)^{-1/2} \sim 246$ GeV by the relation $V(\phi) = -\mu^2\phi^2 + \lambda\phi^4$. Here G_F is the Fermi coupling constant and $\mu = \sqrt{m_H^2}/2$. Since the mass of the Higgs m_H is now experimentally estimated to be about 125 GeV, $\lambda = \frac{m_H^2}{2v^2} = 0.13$. Hence, by measuring λ , we can either confirm SM or refute it.

In general, λ can be directly accessed via non-resonant Higgs pair (HH) or triplet (HHH) production in experiments. For proton-proton (pp) collision at the LHC at the centre-of-mass energy of $\sqrt{s} = 13$ TeV, the leading production mode of HH is gluon-gluon fusion (ggF) having cross section $31.05_{-1.99}^{+1.41}$ fb at next-to-next-to leading order (N²LO) of QCD coupling while the subleading process is Vector Boson Fusion

Soumya Mukherjee—for the CMS Collaboration.

S. Mukherjee (✉)
Tata Institute of Fundamental Research, Mumbai, India
e-mail: soumya.mukherjee@cern.ch

© The Author(s), under exclusive license to Springer Nature Singapore Pte Ltd. 2022
B. Mohanty et al. (eds.), *Proceedings of the XXIV DAE-BRNS High Energy Physics Symposium, Jatni, India*, Springer Proceedings in Physics 277,
https://doi.org/10.1007/978-981-19-2354-8_45

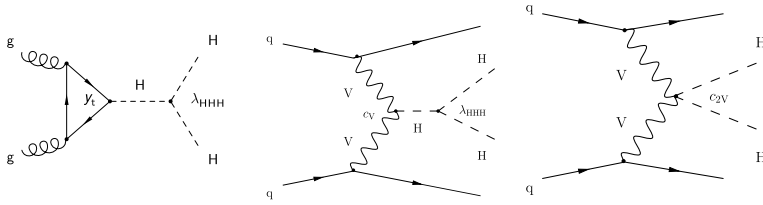


Fig. 45.1 Some of the representative Feynman Diagram of ggF and VBF production

(VBF) with a rate of 1.73 ± 0.036 fb at next-to-next-to-next-to leading order (N^3LO) of electroweak (EW) coupling. Some of the representative Feynman diagrams of ggF and VBF processes are shown in Fig. 45.1. Higgs trilinear coupling λ_{HHH} is involved only in a subset of diagrams. The left diagram only refers to the ggF process; the right most diagram of VBF production gives the direct access to HH production with a pair of vector bosons (C_{2V}) uniquely. Actual measurement is sensitive to the possible effect of *new physics* which can be analyzed in effective field theory formalism assuming the scale of beyond SM physics is very high. The anomalous values of the couplings can be estimated, albeit within moderately wide range, by measuring the cross section of HH production in ggF and VBF modes. The coupling modifier κ is defined as the measured value of coupling parameter with respect to the predicted value from SM. Due to low production cross section, using the data already accumulated, HH production cannot be observed experimentally at the moment; however, an upper limit on inclusive cross section times branching ratio can be set towards testing the Higgs sector of SM.

Several final states of the HH decays were studied by CMS and ATLAS experiments using Run 1 and 2016 Run 2 data delivered by the LHC. Among the various combinations of the decay modes, the best sensitivity for CMS has been found for $b\bar{b}\gamma\gamma$ due to the excellent mass resolution of $H \rightarrow \gamma\gamma$ measured using the electromagnetic calorimeter and relatively less background. Combining with the decay mode of highest branching fraction, i.e., $H \rightarrow b\bar{b}$, the branching fraction of $HH \rightarrow b\bar{b}\gamma\gamma$ is small, about 0.26%. The recent analysis by CMS using full Run 2 data corresponding to integrated luminosity of 137 fb^{-1} targets both ggF and VBF production modes and considers final state of a pair of photons along with a pair of b-jets to achieve the best sensitivity on the coupling modifiers to date. Also, the allowed ranges of the relevant coupling parameters associated with this analysis have been determined in terms of modifiers κ_λ and $\kappa_{V V}$ corresponding to λ and C_{2V} , respectively.

45.2 Data and Simulated Samples

In CMS experiment, data has been collected using a di-photon trigger with asymmetric thresholds for photon transverse momenta (p_T^γ) of 30 and 22 GeV. The HH signal samples for ggF have been generated at NLO accuracy using POWHEG 2.0 for a set of values of coupling parameters. Similarly a set of HH signal for

VBF process with different values of coupling modifiers have been produced using MADGRAPH5_aMC@NLO. The dominant background contributions are due to QCD induced non-resonant irreducible processes producing a pair of prompt photons ($\gamma\gamma$ +jets) and reducible background events from γ +jets, where one jet can be misidentified as a photon. Single Higgs boson production, where the Higgs boson decays to a pair of photons, is considered as a resonant background. These production processes are simulated at NLO in QCD precision using POWHEG 2.0 for ggF and VBF production (ggH and qqH), and MADGRAPH5_aMC@NLO has been used for the production of ttH which is the dominant resonant background at the signal region, vector boson associated production (VH), and production associated with a single top quark (tHq). All simulated samples are interfaced with PYTHIA for parton showering and fragmentation and detector responses are emulated by GEANT4 package.

45.3 Event Selection and Analysis Strategy

Events are selected if they contain at least two photons and two jets clustered by anti- k_T algorithm with distance parameter 0.4 and pairwise maximum score for b jet identification. The photon pair and the b jet pair are required to satisfy the condition of invariant mass of $100 < m_{\gamma\gamma} < 180$ GeV and $70 < m_{jj} < 190$ GeV. For VBF process, two extra forward-backward jets are selected with highest invariant mass (m_{jj}^{VBF}) of the jet pair. Backgrounds are rejected by multivariate analysis (MVA) techniques based on dedicated boosted decision trees. The events are categorized based on their MVA score and the four body invariant mass defined as: $2M_X = m_{\gamma\gamma jj} - (m_{\gamma\gamma} - m_H) - (m_{jj} - m_H)$. The parametric shape of $m_{\gamma\gamma}$ and m_{jj} for signal and resonant background processes have been modelled from simulation and the distributions for non-resonant background is parametrized directly from data in each individual categories simultaneously. Figure 45.2 displays the fitted $m_{\gamma\gamma}$ distribution of ggF

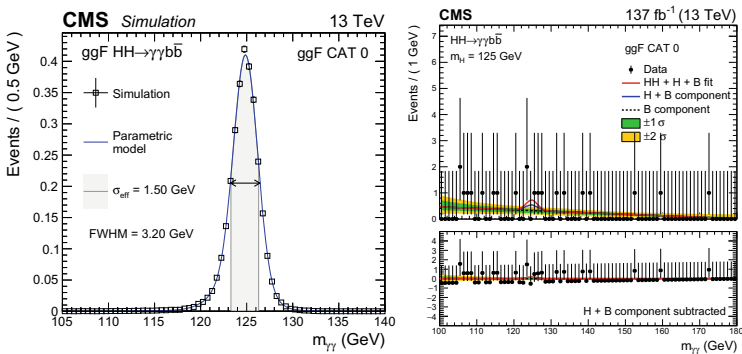


Fig. 45.2 Left: signal modelling of $m_{\gamma\gamma}$ distribution of ggF signal, Right: $m_{\gamma\gamma}$ distribution of the selected events in data (black points) in the most pure category

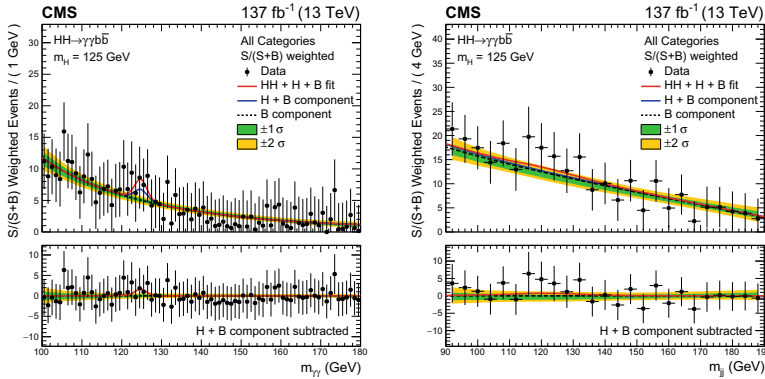


Fig. 45.3 Invariant mass distributions $m_{\gamma\gamma}$ (left) and m_{jj} (right) for the selected events in data (black points) weighted by $S/(S+B)$, where S (B) is the number of signal (background) events

signal on the left and the background modelling on the right for the most pure category. The combined signal and background distributions of $m_{\gamma\gamma}$ and m_{jj} from all categories are shown in Fig. 45.3 left and right, respectively.

45.4 Results

The observed (expected) upper limit on the cross section at 95% confidence level (CL) corresponds to 7.7 (5.2) times the SM prediction of inclusive HH production and 225 (208) times for only the SM VBF HH production. The variation in the excluded cross section as a function of κ_λ and κ_{VV} are shown in Fig. 45.4, where at 95% CL, the observed and expected values κ_λ are constrained in the intervals [3.3, 8.5] and [2.5, 8.2]. These are the most restrictive limits to date. The corresponding ranges for κ_{VV} are [1.3, 3.5] and [-0.9, 3.1].

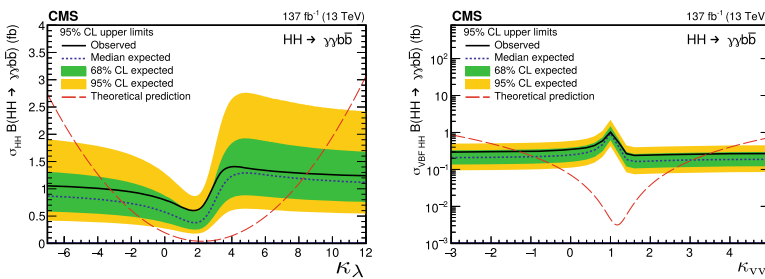


Fig. 45.4 Expected and observed 95% CL upper limits on the HH production cross section times $B(HH \rightarrow b\gamma\gamma)$ as a function of κ_λ and κ_{VV}

Reference

1. A.M. Sirunyan et al. (CMS), JHEP **03**, 257 (2021)

Chapter 46

Multiparton Webs Beyond Three Loops



Sourav Pal, Neelima Agarwal, Lorenzo Magnea, and Anurag Tripathi

Abstract In QCD, the soft function exponentiate in terms of diagrams known as webs. We have defined Cwebs or correlator webs which are useful in the calculation of soft function exponentiation at higher perturbative orders. We review the results of the four-loop Cweb mixing matrices. We also provide a direct construction of a few of the mixing matrices without applying the complicated steps of the replica trick.

46.1 Introduction

In non-abelian gauge theory the studies of infrared singularities have a rich history and have produced remarkable insights in all order results. These singularities get canceled in a well-defined (infrared safe) physical observable but they leave their signatures in the form of large logarithms of the kinematic variables. In the IR limit, the scattering amplitude factorizes into a universal soft function, a collinear jet function, and an infrared finite hard function. Our object of interest, the soft function for a n parton scattering process is defined as

$$\mathcal{S}_n(\beta_i \cdot \beta_j, \alpha_s(\mu^2), \epsilon) \equiv \langle 0 | \prod_{k=1}^n \Phi_{\beta_k}(\infty, 0) | 0 \rangle, \quad (46.1)$$

where $\Phi_{\beta_i}(\infty, 0)$ are semi-infinite Wilson lines along β_i (velocity of the i -th parton), $\alpha_s = g_s^2/4\pi$ and $\epsilon = (4 - d)/2$. As a consequence of factorization, the soft function

S. Pal (✉) · A. Tripathi
Department of Physics, Indian Institute of Technology Hyderabad, Kandi, Sangareddy 502285,
Telangana, India
e-mail: spalexam@gmail.com

N. Agarwal
Department of Physics, Chaitanya Bharathi Institute of Technology, Gandipet, Hyderabad
500075, Telangana, India

L. Magnea
Dipartimento di Fisica and Arnold-Regge Center, Università di Torino, and INFN, Sezione di
Torino, Via Pietro Giuria 1, I-10125 Torino, Italy

obeys renormalization group equation, solving which leads to the exponentiation in terms of soft anomalous dimension Γ_n . The soft function in terms of the soft anomalous dimension is given by

$$\mathcal{S}_n(\beta_i \cdot \beta_j, \alpha_s(\mu^2), \epsilon) = \mathcal{P} \exp \left[-\frac{1}{2} \int_0^{\mu^2} \frac{d\lambda^2}{\lambda^2} \Gamma_n(\beta_i \cdot \beta_j, \alpha_s(\lambda^2), \epsilon) \right]. \quad (46.2)$$

The soft anomalous dimension was computed recently at three loops in [1, 2] and the current frontier is to calculate the soft anomalous dimension at four loops.

The soft function \mathcal{S}_n follows a diagrammatic exponentiation such that

$$\mathcal{S}_n = \exp[\mathcal{W}_n], \quad (46.3)$$

where \mathcal{W}_n are collectively known as webs. Thus, one can directly compute the soft anomalous dimension matrix Γ_n using webs. The diagrammatic exponentiation was first observed in QED, where \mathcal{W}_n contains only connected photon sub-diagrams. In QCD for the general case of n Wilson lines, a *web* is defined as a set of diagrams which are related to one another by the permutation of the gluons on each Wilson line. If $\mathcal{K}(D)$ and $C(D)$ denote the kinematics and color of a diagram D in a web, then the exponent of the soft function is given by

$$\mathcal{S}_n = \exp \left[\sum_{D, D'} \mathcal{K}(D) R(D, D') C(D') \right], \quad (46.4)$$

where R is called the web mixing matrix and

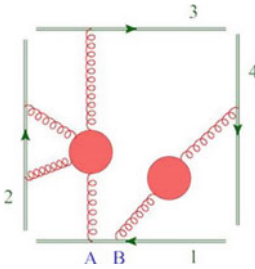
$$\tilde{C}(D) = \sum_{D'} R(D, D') C(D'), \quad (46.5)$$

is called the exponentiated colour factor for a diagram D . The general properties of the web mixing matrices were studied in [3–6] and are given by

1. The web mixing matrices are idempotent, i.e., $R^2 = R$.
2. The row-sum of the matrices are zero.
3. The elements of web mixing matrices obey the column sum rule $\sum_D s(D) R(D, D') = 0$, where $s(D)$ denotes the number of ways that the gluons can be sequentially shrunk to the hard interaction vertex.

46.2 Cwebs at Four Loops

We define a *correlator web*, or a *Cweb* as a set diagrams, built out of connected gluon correlators attached to Wilson lines, and closed under shuffles of the gluon attachments to each Wilson line. As compared to webs, Cwebs have their own perturbative



Diagrams	Sequences	S-factors
C_1	$\{\{BA\}\}$	1
C_2	$\{\{AB\}\}$	1

Fig. 46.1 Diagrams for $W_4^{(1,0,1)}(2, 2, 1, 1)$

expansions and thus useful in the enumeration of webs at higher orders. A Cweb connecting n Wilson lines with c_m number of m -point gluon correlators and with k_l number of attachments on l -th Wilson line is denoted by $W_n^{(c_2, \dots, c_p)}(k_1, \dots, k_n)$. As described in [8], one can generate all the Cwebs at $O(g^{2n})$ from the Cwebs at $O(g^{2n-2})$ by performing the following moves:

1. Add a two-gluon correlator connecting any two Wilson lines.
2. Connect an existing m -point correlator to any Wilson line, turning it into an $(m + 1)$ -point correlator.
3. Connect an existing m -point correlator to an existing n -point correlator, resulting in an $(n + m)$ -point correlator.

Using the above steps, we have generated all the four-loop Cwebs [7, 8]. We have developed an in-house Mathematica code which computes the mixing matrices of all the Cwebs at four loops following the steps of the replica trick algorithm [3].

We show an example of a mixing matrix of a four-loop Cweb $W_4^{(1,0,1)}(2, 2, 1, 1)$ which connects 4 Wilson lines and has one 2-point gluon correlator and a 4-point gluon correlator.

The mixing matrix for this Cweb is given by

$$R = \begin{pmatrix} \frac{1}{2} & -\frac{1}{2} \\ -\frac{1}{2} & \frac{1}{2} \end{pmatrix}. \tag{46.6}$$

This mixing matrix follows all the properties of a general mixing matrix. Using (46.5), one can easily calculate the exponentiated color factors. The mixing matrices for all the four-loop Cwebs connecting 4 and 5 Wilson lines are presented in [8] and for 2 and 3 Wilson lines in [7]. We have checked the correctness of our results by checking the known properties of the mixing matrices: idempotence, zero row-sum rule, and the conjectured column sum rule.

46.3 Direct Construction of Mixing Matrices

In this section, we will describe the construction of the web mixing matrices without applying the replica trick algorithm. All the elements of the possible two-dimensional mixing matrices arising at all perturbative orders are fixed by using the row-sum, column-sum, and the idempotence property. A detail calculation is presented in [7].

The next step is to calculate the three-dimensional mixing matrices using the known properties. The column weight vector of a Cweb with three diagrams is $s = \{1, 0, 1\}$. The diagram which has $s = 0$, cannot be generated from diagrams which have $s = 1$, by the action of the replica ordering operator. Taking this into consideration, the three-dimensional mixing matrix takes the form

$$R = \begin{pmatrix} \frac{1}{2} & 0 & -\frac{1}{2} \\ -\frac{1}{2} & 1 & -\frac{1}{2} \\ -\frac{1}{2} & 0 & \frac{1}{2} \end{pmatrix}. \quad (46.7)$$

This is the only three-dimensional mixing matrix that can appear in any perturbative order. Proceeding further, we find that the mixing matrices for any prime dimension p are unique at all perturbative orders and are given by [7]

$$R = \begin{pmatrix} \frac{1}{2} & 0 & 0 & \dots & 0 & -\frac{1}{2} \\ -\frac{1}{2} & 1 & 0 & \dots & 0 & -\frac{1}{2} \\ & & \dots & & & \\ -\frac{1}{2} & 0 & 0 & \dots & 1 & -\frac{1}{2} \\ -\frac{1}{2} & 0 & 0 & \dots & 0 & \frac{1}{2} \end{pmatrix}. \quad (46.8)$$

We believe that the exponentiation of soft function in terms of Cwebs will make the enumeration of Cwebs at higher orders much simpler as compared to webs. The exponentiated color factors presented in [7, 8] complete the full list of color factors, which will be instrumental in the calculation of the soft anomalous dimension at $O(g^8)$ in the future.

References

1. Ø. Almelid, C. Duhr, E. Gardi, Three-loop corrections to the soft anomalous dimension in multi-leg scattering. *Phys. Rev. Lett.* **117**(17), 172002 (2016). <https://doi.org/10.1103/PhysRevLett.117.172002>. [arXiv:1507.00047](https://arxiv.org/abs/1507.00047) [hep-ph]
2. Ø. Almelid, C. Duhr, E. Gardi, A. McLeod, C.D. White, Bootstrapping the QCD soft anomalous dimension. *JHEP* **09**, 073 (2017). [https://doi.org/10.1007/JHEP09\(2017\)073](https://doi.org/10.1007/JHEP09(2017)073). [arXiv:1706.10162](https://arxiv.org/abs/1706.10162) [hep-ph]
3. E. Gardi, E. Laenen, G. Stavenga, C.D. White, Webs in multiparton scattering using the replica trick. *JHEP* **11**, 155 (2010). [https://doi.org/10.1007/JHEP11\(2010\)155](https://doi.org/10.1007/JHEP11(2010)155). [arXiv:1008.0098](https://arxiv.org/abs/1008.0098) [hep-ph]

4. E. Gardi, C.D. White, General properties of multiparton webs: Proofs from combinatorics. *JHEP* **03**, 079 (2011). [https://doi.org/10.1007/JHEP03\(2011\)079](https://doi.org/10.1007/JHEP03(2011)079). [arXiv:1102.0756](https://arxiv.org/abs/1102.0756) [hep-ph]
5. E. Gardi, J.M. Smillie, C.D. White, On the renormalization of multiparton webs. *JHEP* **09**, 114 (2011). [https://doi.org/10.1007/JHEP09\(2011\)114](https://doi.org/10.1007/JHEP09(2011)114). [arXiv:1108.1357](https://arxiv.org/abs/1108.1357) [hep-ph]
6. M. Dukes, E. Gardi, E. Steingrimsson, C.D. White, Web worlds, web-colouring matrices, and web-mixing matrices. *J. Comb. Theor. A* **120**, 1012–1037 (2013). <https://doi.org/10.1016/j.jcta.2013.02.001>. [arXiv:1301.6576](https://arxiv.org/abs/1301.6576) [math.CO]
7. N. Agarwal, L. Magnea, S. Pal, A. Tripathi, Cwebs beyond three loops in multiparton amplitudes. *JHEP* **03**, 188 (2021). [https://doi.org/10.1007/JHEP03\(2021\)188](https://doi.org/10.1007/JHEP03(2021)188). [arXiv:2102.03598](https://arxiv.org/abs/2102.03598) [hep-ph]
8. N. Agarwal, A. Danish, L. Magnea, S. Pal, A. Tripathi, Multiparton webs beyond three loops. *JHEP* **05**, 128 (2020). [https://doi.org/10.1007/JHEP05\(2020\)128](https://doi.org/10.1007/JHEP05(2020)128). [arXiv:2003.09714](https://arxiv.org/abs/2003.09714) [hep-ph]

Chapter 47

Search for Lepton Flavor Violation in $\Upsilon(1S)$ Decays



S. Patra, Vishal Bhardwaj, and K. Trabelsi

Abstract We present a search for charged lepton flavor violation in $\Upsilon(1S) \rightarrow \ell\ell'$ [$\ell, \ell' = e, \mu, \tau$] decays using the 25 fb^{-1} $\Upsilon(2S)$ collected by the Belle detector. Using the Monte Carlo background, we estimate the upper limits of the branching fractions at 90% confidence level.

47.1 Introduction

Conservation of lepton family is an accidental symmetry in the standard model (SM). Neutrino flavor oscillation which violated the conservation of lepton family number has been observed [1]. Due to the tiny values of light neutrino masses, charged lepton flavor violation (CLFV) is extremely suppressed in SM [2, 3]. However, several new physics models (such as SUSY, leptoquark) inspired by grand unified theory (GUT), enhance the decay rate of the CLFV transitions [4, 5]. Couple of results have already been published on $\Upsilon(nS) \rightarrow \ell\ell'$ decays by the CLEO and BaBar collaborations [6, 7]. But, there are no results available for the $\Upsilon(1S) \rightarrow e\tau/e\mu$ decays. We perform a blind analysis to study the $\Upsilon(1S) \rightarrow \ell\ell'$ decays with the $\Upsilon(1S)$ states produced in $\Upsilon(2S) \rightarrow \pi^+\pi^-\Upsilon(1S)$ decays. Increased charged track multiplicity gives a cleaner sample than direct $\Upsilon(1S) \rightarrow \ell\ell'$ decay. Further, one has better control over the background with two extra pions in the final state.

47.2 Data Sample and Detector

The Belle detector is a large-solid-angle spectrometer, which includes a silicon vertex detector (SVD), a 50-layer central drift chamber (CDC), an array of aerogel thresh-

S. Patra (✉) · V. Bhardwaj
Indian Institute of Science Education and Research Mohali, Punjab, India
e-mail: souravpatra3012@gmail.com

K. Trabelsi
Université Paris-Saclay, CNRS/IN2P3, IJCLab, Orsay, Paris, France

© The Author(s), under exclusive license to Springer Nature Singapore Pte Ltd. 2022
B. Mohanty et al. (eds.), *Proceedings of the XXIV DAE-BRNS High Energy Physics Symposium, Jatni, India*, Springer Proceedings in Physics 277,
https://doi.org/10.1007/978-981-19-2354-8_47

old Cherenkov counters (ACC), time-of-flight scintillation counters (TOF), and an electromagnetic calorimeter (ECL) comprised of 8736 CsI(Tl) crystals located inside a superconducting solenoid coil that provides a 1.5 T magnetic field. An iron flux return located outside the coil is instrumented to detect K_L^0 mesons and identify muons (KLM). We have the world's largest $\Upsilon(2S)$ data (25 fb^{-1}) collected with the Belle detector at KEKB asymmetric-energy e^+e^- collider operating at 10.02 GeV.

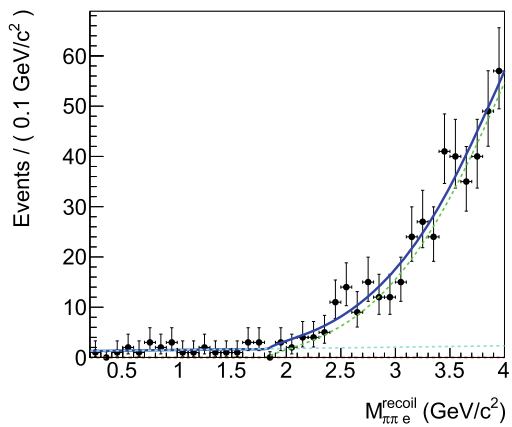
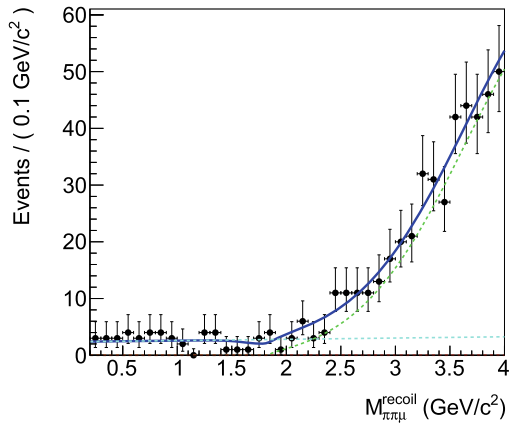
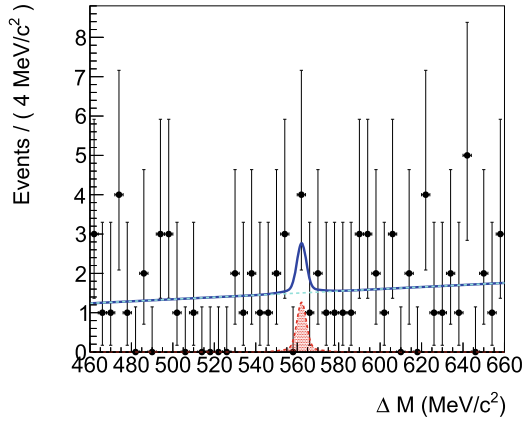
47.3 Event Selection

We reconstruct the $\Upsilon(2S)$ in $\pi^+\pi^-\Upsilon(1S)$ decays, where $\Upsilon(1S)$ has been reconstructed from $e^\pm\mu^\mp$, $\mu^\pm\tau^\mp$ and $e^\pm\tau^\mp$ decays. Further, τ has been reconstructed in $\tau^- \rightarrow e^-\bar{\nu}_e\nu_\tau$, $\tau^- \rightarrow \pi^-\pi^+\pi^-\nu_\tau$ for $\mu\tau$ decays and $\tau^- \rightarrow \mu^-\bar{\nu}_\mu\nu_\tau$, $\tau^- \rightarrow \pi^-\pi^+\pi^-\nu_\tau$ for $e\tau$ decays to avoid potential background from $\Upsilon(1S) \rightarrow ee$ and $\Upsilon(1S) \rightarrow \mu\mu$ decays. For $\Upsilon(1S) \rightarrow e\mu$ study, we select the events with lepton pair invariant mass ($M_{e\mu}$) within 9.09–9.65 GeV/c^2 and $\Upsilon(1S)$ momentum in the lab frame ($|\mathbf{P}_{\Upsilon(1S)}|$) less than 4.4 GeV/c . For $\Upsilon(1S) \rightarrow \mu\tau/e\tau$ decays, to remove huge background coming from other $\Upsilon(2S)$ decays, we use recoil mass of two pions ($M_{\pi\pi}^{\text{recoil}}$), where $M_{\pi\pi}^{\text{recoil}} = \sqrt{(E_{\text{cm}} - E_{\pi\pi})^2 - |\mathbf{P}_{\pi\pi}|^2}$ with E_{cm} , $E_{\pi\pi}$ and $|\mathbf{P}_{\pi\pi}|$ are the total energy of colliding e^+e^- , energy of the two pions and three momentum of the two pions, respectively. We select the events having $M_{\pi\pi}^{\text{recoil}}$ within 9.45–9.466 GeV/c^2 . Further, we select the events with visible momentum of the tau particle greater than 0.3 GeV/c .

47.4 Signal Extraction

For $\Upsilon(1S) \rightarrow e\mu$ decays, we extract the signal yield from an unbinned extended maximum likelihood (UML) fit the ΔM variable, where $\Delta M = M_{\Upsilon(2S)} - M_{\Upsilon(1S)}$. It should peak at the nominal mass difference between $\Upsilon(2S)$ and $\Upsilon(1S)$, 560 MeV/c^2 . The probability density function (PDF) of signal events is modeled with a sum of two Gaussians within 460–660 MeV/c^2 . The expected efficiency for $\Upsilon(1S) \rightarrow e\mu$ mode is 35%. Background PDF is modeled with a first-order Chebyshev polynomial. One could expect 3.0 background events are peaking in the signal region. To extract the signal for $\Upsilon(1S) \rightarrow \mu\tau$ mode, we perform a 1D UML fit to the recoil mass of $\pi\pi\mu$ ($M_{\pi\pi\mu}^{\text{recoil}}$) which should peak at the nominal τ mass (1.78 GeV/c^2). The signal PDFs are modeled with a sum of one Gaussian and one bifurcated Gaussian within 0–4 GeV/c^2 . Considering the branching fraction for corresponding τ decay modes, the expected signal efficiency for $\Upsilon(1S) \rightarrow \mu\tau$ mode 9%. Dominating background comes from $\Upsilon(1S) \rightarrow \tau\tau$ mode which starts from the nominal τ mass value. We model the $\tau\tau$ background PDF using an exponential threshold like likelihood function. Rest of the background flat background is modeled with first-order Chebyshev polynomial. From the combined signal and background fit, no peaking background is expected. Similarly, we extract the $\Upsilon(1S) \rightarrow e\tau$ signal from a UML fit to the recoil mass of

Fig. 47.1 Using MC background, 1D UML fit to ΔM for $\Upsilon(1S) \rightarrow e\mu$ mode (top), to $M_{\pi\pi\mu}^{\text{recoil}}$ for $\Upsilon(1S) \rightarrow \mu\tau$ mode (middle) and to $M_{\pi\pi e}^{\text{recoil}}$ for $\Upsilon(1S) \rightarrow e\tau$ mode (bottom)



$\pi\pi e$ ($M_{\pi\pi e}^{\text{recoil}}$). Expected efficiency of $\Upsilon(1S) \rightarrow e\tau$ signal is 7%. For $\Upsilon(1S) \rightarrow e\tau$ mode, expected peaking background is estimated to be 0. Fits to $\Upsilon(2S)$ generic MC background are shown in the Fig. 47.1.

47.5 Upper Limit Estimation

Before studying the real data, we estimated the upper limit (UL) at 90% confidence level (CL) using the MC backgrounds. We determine the UL using a frequentist method that uses ensembles of pseudo-experiments. The CL is determined from the fraction of samples with a yield larger than the corresponding peaking background. For $\Upsilon(1S) \rightarrow e\mu$ case, that has been considered to be 3.0. That has been considered to be null for $\Upsilon(1S) \rightarrow \mu\tau$ and $\Upsilon(1S) \rightarrow e\tau$. One can estimate the upper limits of branching fractions according to $\mathcal{B} = N_{\text{sig}}^{\text{UL}} / (N_{\Upsilon(2S)} \times \mathcal{B}[\Upsilon(2S) \rightarrow \pi^+\pi^-\Upsilon(1S)] \times \epsilon)$; here, $N_{\text{sig}}^{\text{UL}}$ is the UL of signal yield (@ 90% CL), $N_{\Upsilon(2S)}$ is the number of $\Upsilon(2S)$, ϵ is the reconstruction efficiency and $\mathcal{B}[\Upsilon(2S) \rightarrow \pi^+\pi^-\Upsilon(1S)]$ is the secondary branching fraction taken from PDG [8]. We estimate the $N_{\text{sig}}^{\text{UL}}$ from the above toys. Upper limits on the branching fractions for $\Upsilon(1S) \rightarrow e\mu$, $\Upsilon(1S) \rightarrow \mu\tau$, and $\Upsilon(1S) \rightarrow e\tau$ modes at 90% CL are estimated to be in the order of 10^{-6} .

47.6 Summary

We present a sensitivity test for charged lepton flavor violation in $\Upsilon(1S) \rightarrow \ell\ell'$ decays based on MC simulated events. Preliminary results look promising. The discovery of charged lepton flavor violation would be a clear signal for NP phenomena. Even, in the absence of a significant signal, one can put a constraint on NP parameters.

References

1. Y. Fukuda et al. (Super-Kamiokande Collaboration), Phys. Rev. Lett. **81**, 1562 (1998); Q.R. Ahmad et al. (SNO Collaboration), Phys. Rev. Lett. **89**, 011301 (2002)
2. M. Raidal et al., Eur. Phys. J. C **57**, 13 (2008)
3. A.M. Teixeira, [arXiv:1612.06194](https://arxiv.org/abs/1612.06194) [hep-ph]
4. J.C. Pati, A. Salam, Phys. Rev. D **10**, 275 (1974)
5. H. Georgi, S.L. Glashow, Phys. Rev. Lett. **32**, 438 (1974)
6. W. Love et al., Phys. Rev. Lett. **101**, 201601 (2008)
7. J.P. Lees et al., Phys. Rev. Lett. **104**, 151802 (2010)
8. M. Tanabashi et al. (Particle data group), Phys. Rev. D **98**, 030001 (2018)

Chapter 48

Indirectly Probing New Physics in Charmless Decays of $B \rightarrow \phi\phi K$



S. Mohanty, A. B. Kaliyar, V. Gaur, and G. B. Mohanty

Abstract We present precise measurements of the branching fraction and CP -violation asymmetry in the B meson system, specifically in the charmless decays $B \rightarrow \phi\phi K$, $\phi \rightarrow K^+K^-$. The study is based on the full $\Upsilon(4S)$ data sample of $772 \times 10^6 B\bar{B}$ events collected by the Belle detector at the KEKB asymmetric energy e^+e^- collider. An observation of direct CP violation in $B \rightarrow \phi\phi K$ decays would be a clear sign of physics beyond the standard model. In addition, these decays are sensitive to the possible production of glueball candidates that later decay as $\xi \rightarrow \phi\phi$. Our results obtained with nine times larger statistics and refined analysis techniques significantly improve upon, and supersede, Belle's earlier result.

48.1 Introduction

In 1967, Sakharov proposed three necessary conditions that a baryon-generating interaction must satisfy in order to produce matter and antimatter at different rates. The violation of CP (charge conjugation parity) symmetry is the prominent one among those conditions. The CKM quark-mixing matrix has so far been found to be the only source of CP violation in the standard model (SM). This proceeding focuses on a search for new sources of CP violation in the charmless decays $B \rightarrow \phi\phi K$ with $\phi \rightarrow K^+K^-$ conducted with the data recorded by the Belle experiment.

S. Mohanty, A. B. Kaliyar, V. Gaur, and G. B. Mohanty—for the Belle Collaboration.

S. Mohanty
Utkal University, Bhubaneswar 751004, India

S. Mohanty (✉) · A. B. Kaliyar · G. B. Mohanty
Tata Institute of Fundamental Research, Mumbai 400005, India
e-mail: subhaphy1@gmail.com

V. Gaur
Virginia Polytechnic Institute and State University, Blacksburg, VA 24061, USA

© The Author(s), under exclusive license to Springer Nature Singapore Pte Ltd. 2022
B. Mohanty et al. (eds.), *Proceedings of the XXIV DAE-BRNS High Energy Physics Symposium, Jatni, India*, Springer Proceedings in Physics 277,
https://doi.org/10.1007/978-981-19-2354-8_48

48.2 Belle Detector

The results reported here are based on the full $\Upsilon(4S)$ data sample of $772 \times 10^6 B\bar{B}$ events, collected by the Belle detector [1] at the KEKB asymmetric-energy e^+e^- collider [2]. The detector components relevant for the study are a silicon vertex detector, a central drift chamber, an array of aerogel threshold Cherenkov counters and time-of-flight scintillation counters. All these subdetectors are located inside a 1.5 T axial magnetic field.

48.3 Motivation to Study $B \rightarrow \phi\phi K$ Decays

The $B \rightarrow \phi\phi K$ decays are a classic example of $b \rightarrow s\bar{s}$ transition, where an additional $s\bar{s}$ quark pair is created leading to the final state. The same final state can also originate from the tree-level process $B \rightarrow \eta_c K$, $\eta_c \rightarrow \phi\phi$. The loop and tree amplitudes may interfere if the $\phi\phi$ invariant mass is within the η_c resonance region. On the other hand, potential new physics (NP) contribution to the loop could introduce a nonzero CP violating phase. The author in [3] has suggested that the direct CP asymmetry could be as large as 40% in the presence of NP. Therefore, an observation of large CP violation in $B \rightarrow \phi\phi K$ would be a sign of physics beyond the SM. In addition to being an NP probe, the decay is sensitive to possible production of glueball candidate that later decays as $\xi \rightarrow \phi\phi$ [4]. Based on a 78 fb^{-1} of data sample, Belle reported the first evidence for the decay $B \rightarrow \phi\phi K$. The branching fraction was measured to be $[2.6_{-0.9}^{+1.1}(\text{stat}) \pm 0.3(\text{syst})] \times 10^{-6}$ for a $\phi\phi$ invariant mass below $2.85 \text{ GeV}/c^2$ [5]. The BABAR experiment performed a measurement of this decay using their full dataset of $464 \times 10^6 B\bar{B}$ events [6]. The branching fraction obtained with the same $m_{\phi\phi}$ requirement was $\mathcal{B}(B^+ \rightarrow \phi\phi K^+) = (5.6 \pm 0.5 \pm 0.3) \times 10^{-6}$. BABAR also reported CP asymmetries for charged B decays as $-0.10 \pm 0.08 \pm 0.02$ below the η_c threshold and $+0.09 \pm 0.10 \pm 0.02$ within the η_c region.

48.4 Analysis Strategy

The basic selection requirements are applied to reconstruct a B candidate from two ϕ and one charged or neutral kaon candidate. To identify signal events, we use two kinematic variables, the beam-energy-constrained mass $M_{bc} = \sqrt{E_b^2 - p_B^2}$ and the energy difference $\Delta E = E_B - E_b$, calculated in the center-of-mass frame. Here E_b , E_B , and p_B are the beam energy, reconstructed energy, and momentum of the B candidate, respectively.

The dominant background is from the $e^+e^- \rightarrow q\bar{q}$ ($q = u, d, s, c$) continuum process. A neural network (NN) method is employed to discriminate spherically

distributed $B\bar{B}$ events (signal) from jetlike continuum events (background). We use the transformed variable of NN output (O'_{NN}) in our signal fit.

We have studied dedicated Monte Carlo (MC) samples to assess the potential contamination from $b \rightarrow c$ mediated decays as well as to identify the significant peaking background from $b \rightarrow u, d, s$ transitions. To suppress the latter, we exclude candidates for which the $m_{\phi\phi}$ value is greater than $2.85 \text{ GeV}/c^2$.

The signal yield is obtained with an unbinned extended maximum-likelihood fit to the three variables M_{bc} , ΔE , and O'_{NN} . We define a probability density function (PDF) for each event category, namely signal, $q\bar{q}$, and $B\bar{B}$ backgrounds:

$$\mathcal{P}_j^i \equiv \frac{1}{2}(1 - q_i \mathcal{A}_{CP,j}) \mathcal{P}_j(M_{\text{bc}}^i) \mathcal{P}_j(\Delta E^i) \mathcal{P}_j(O'_{\text{NN}}^i), \quad (48.1)$$

where i denotes the event index, q_i is the charge of the B candidate ($q_i = \pm 1$ for B^\pm), \mathcal{P}_j and $\mathcal{A}_{CP,j}$ are the PDF and CP asymmetry for the event category j , respectively. The latter is defined as

$$\mathcal{A}_{CP} = \frac{N_{B^-} - N_{B^+}}{N_{B^-} + N_{B^+}}, \quad (48.2)$$

where N_{B^+} (N_{B^-}) is the number of B^+ (B^-) events. For neutral B decays, we replace the factor $\frac{1}{2}(1 - q_i \mathcal{A}_{CP,j})$ by 1 in (48.1). The extended likelihood function is

$$\mathcal{L} = \frac{e^{-\sum_j n_j}}{N!} \prod_i \left[\sum_j n_j \mathcal{P}_j^i \right], \quad (48.3)$$

where n_j is the yield of the event category j and N is the total number of candidate events. From the fitted signal yield (n_{sig}), we calculate the branching fraction as

$$\mathcal{B}(B \rightarrow \phi\phi K) = \frac{n_{\text{sig}}}{\varepsilon N_{B\bar{B}} [\mathcal{B}(\phi \rightarrow K^+ K^-)]^2}, \quad (48.4)$$

where ε and $N_{B\bar{B}}$ are the detection efficiency and the number of $B\bar{B}$ events, respectively. In case of $B^0 \rightarrow \phi\phi K^0$, we multiply the denominator by a factor of $\frac{1}{2}$ to account for $K^0 \rightarrow K_S^0$, as well as by the subdecay branching fraction $\mathcal{B}(K_S^0 \rightarrow \pi^+ \pi^-)$ [7].

We apply the 3D fit to $B^+ \rightarrow \phi\phi K^+$ and $B^0 \rightarrow \phi\phi K^0$ candidate events to determine the signal yield (and \mathcal{A}_{CP} in the first case). Figures 48.1 and 48.2 show M_{bc} , ΔE , and O'_{NN} projections of the fits.

The background-subtracted distribution of $m_{\phi\phi}$ obtained for $B^+ \rightarrow \phi\phi K^+$ below the η_c threshold is shown in Fig. 48.3. In particular, we do not find any enhancement near the $2.3 \text{ GeV}/c^2$ region [4] where the glueball candidates are predicted.

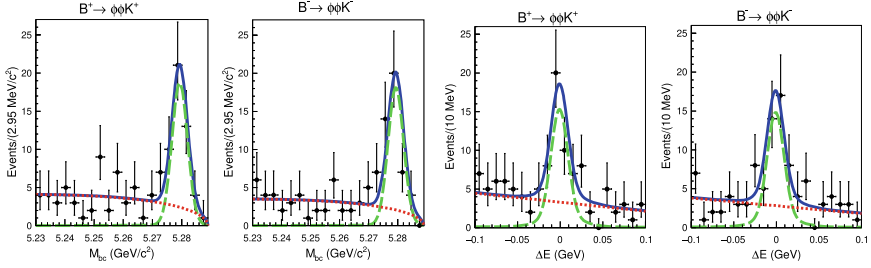


Fig. 48.1 Projections of $B^\pm \rightarrow \phi\phi K^\pm$ candidate events onto (left) M_{bc} and (right) ΔE . Black points with error bars are the data, solid blue curves are the total PDF, dashed green curves are the signal component, and dotted red curves are the combined $q\bar{q}$ and $B\bar{B}$ background components

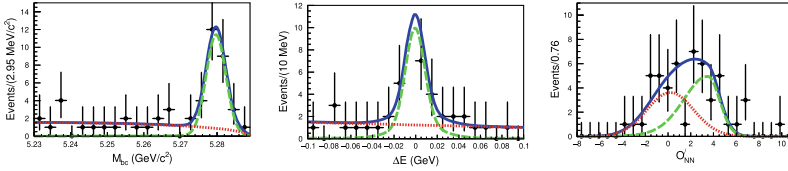


Fig. 48.2 Projections of $B^0 \rightarrow \phi\phi K^0$ candidate events onto (left) M_{bc} , (middle) ΔE , and (right) O_{NN} . The legends of the plots are defined in the same manner as Fig. 48.1

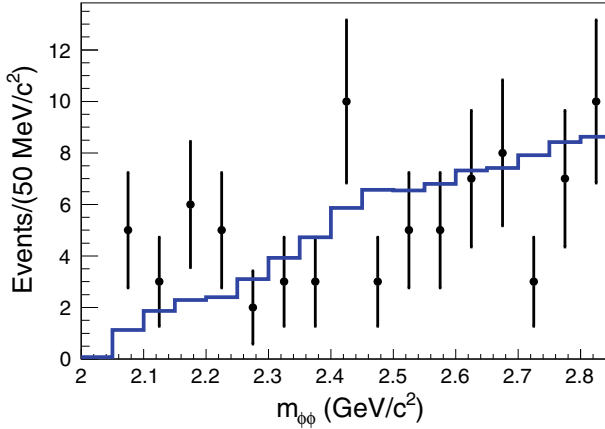


Fig. 48.3 Background-subtracted signal yield as a function of $m_{\phi\phi}$ for $B^\pm \rightarrow \phi\phi K^\pm$. Black points with error bars are the data and solid blue histograms denote the expectation from a phase-space MC sample

48.5 Summary

We have obtained the branching fraction and CP asymmetry for $B^\pm \rightarrow \phi\phi K^\pm$ below the η_c threshold as $(3.24^{+0.51}_{-0.49} \pm 0.25) \times 10^{-6}$ and $-0.02 \pm 0.11 \pm 0.01$, respectively. We also report the CP -violation asymmetry for $B^\pm \rightarrow \phi\phi K^\pm$ in the η_c region

to be $+0.12 \pm 0.12 \pm 0.01$, consistent with no CP violation. The measured branching fraction for $B^0 \rightarrow \phi\phi K^0$ in the charmless region is $(3.07^{+0.90}_{-0.81} \pm 0.24) \times 10^{-6}$. We find no evidence for glueball production in these decays.

References

1. A. Abashian et al. (Belle Collaboration), Nucl. Instrum. Methods Phys. Res. Sect. A **479**, 117 (2002); also see the detector section in J. Brodzicka et al., Prog. Theor. Exp. Phys. 04D001 (2012)
2. S. Kurokawa, E. Kikutani, Nucl. Instrum. Methods Phys. Res., Sect. A **499**, 1 (2003), and other papers included in this Volume; T. Abe et al., Prog. Theor. Exp. Phys. (2013) 03A001 and following articles up to 03A011
3. M. Hazumi, Phys. Lett. B **583**, 285 (2004)
4. C.K. Chua et al., Phys. Lett. B **544**, 139 (2002)
5. H.C. Huang et al. (Belle Collaboration), Phys. Rev. Lett. **91**, 241802 (2003)
6. J.P. Lees et al. (BABAR Collaboration), Phys. Rev. D **84**, 012001 (2011)
7. P.A. Zyla et al. (Particle Data Group), Prog. Theor. Exp. Phys. **2020**, 083C01 (2020)

Chapter 49

Flavor Anomalies with Vector Leptoquark



Suchismita Sahoo

Abstract Driven by the recent experimental hints of lepton-flavor-universality violation in the bottom-quark sector, we consider a simple extension of the Standard Model (SM) with an additional vector leptoquark $V_{LQ}(3, 1, 2/3)$ under the SM gauge group $SU(3)_c \times SU(2)_L \times U(1)_Y$, in order to simultaneously explain the $b \rightarrow s\ell^+\ell^-$ (with $\ell = e, \mu$) and $b \rightarrow cl^-\bar{\nu}_l$ (with $l = e, \mu, \tau$) flavor anomalies. We perform a global fit to all the relevant and up-to-date $b \rightarrow s\ell^+\ell^-$ and $b \rightarrow cl^-\bar{\nu}_l$ data under the assumption that the leptoquark couples predominantly to second- and third-generation SM fermions. We then look over the implications of the allowed parameter space on lepton-flavor-violating B decay modes, such as $B_s \rightarrow l_i^+l_j^-$, $B \rightarrow K^{(*)}l_i^+l_j^-$, $B_s \rightarrow \phi l_i^+l_j^-$, respectively.

49.1 Introduction

In addition to the drawbacks of the Standard Model (SM) such as the answer to the matter–antimatter asymmetry, neutrino mass, and dark matter puzzles, etc., there is a discrepancy of $(2 - 4)\sigma$ [1] in the branching ratios and angular observables of rare semileptonic $b \rightarrow s$ and $b \rightarrow c$ decay modes. Since the above-mentioned anomalies associated with $b \rightarrow s\ell^+\ell^-$ and $b \rightarrow cl^-\bar{\nu}_l$ transitions probe different new physics (NP) scales [2], most of the theoretical studies in the literature have attempted to address either the NC or the CC sector, but not both on the same footing. Only a few specific models, mainly those involving the color-triplet leptoquark boson [3–6] which allows tree-level couplings between quarks and leptons, have been successful in explaining both kinds of flavor anomalies simultaneously. With the aim of understanding the experimental observations linked with both types of processes in a common framework, here we consider a simple extension of the SM by adding a single vector leptoquark (VLQ) V_{LQ} which transforms as $(3, 1, 2/3)$ under the SM gauge group $SU(3)_c \times SU(2)_L \times U(1)_Y$. The observation of lepton flavor universal-

S. Sahoo (✉)

Central University of Karnataka, Gulbarga 585367, Karnataka, India
e-mail: suchismita@cuk.ac.in

ity violation generically implies the existence of lepton-flavor-violating (LFV) decay modes [7]. In this work, we update the discussion on B anomalies with the latest experimental data and we will also investigate the LFV decays of neutral and charged mesons. The organization of this paper is as follows. In Sect. 49.2, we present the effective Hamiltonian and the constraints on the new VLQ couplings. Section 49.3 includes the impact of VLQ on LFV B decay modes followed by conclusion in Sect. 49.4.

49.2 Constraints on New VLQ Parameters

The effective Hamiltonian responsible for the $b \rightarrow c\tau\bar{\nu}_l$ quark-level transitions is given by [8]

$$\mathcal{H}_{\text{eff}}^{\text{CC}} = \frac{4G_F}{\sqrt{2}} V_{cb} \left[\left(\delta_{l\tau} + C_{V_1}^l \right) \mathcal{O}_{V_1}^l + C_{V_2}^l \mathcal{O}_{V_2}^l + C_{S_1}^l \mathcal{O}_{S_1}^l + C_{S_2}^l \mathcal{O}_{S_2}^l + C_T^l \mathcal{O}_T^l \right] \quad (49.1)$$

where G_F is the Fermi constant, V_{cb} is the Cabibbo–Kobayashi–Maskawa (CKM) matrix element, \mathcal{O}_X 's are the effective operators and C_X^l are the Wilson coefficients, with $X = V_{1,2}, S_{1,2}, T$, which are zero in the SM and can arise only in the presence of NP. The effective Hamiltonian mediating the $b \rightarrow s\ell^+\ell^-$ processes can be written as [8, 9]

$$\mathcal{H}_{\text{eff}}^{\text{NC}} = -\frac{4G_F}{\sqrt{2}} V_{tb} V_{ts}^* \left[\sum_{i=1}^6 C_i(\mu) \mathcal{O}_i + \sum_{i=7,9,10,S,P} \left(C_i(\mu) \mathcal{O}_i + C_i'(\mu) \mathcal{O}_i' \right) \right]. \quad (49.2)$$

Here, $V_{tb} V_{ts}^*$ is the product of CKM matrix elements, C_i 's are the Wilson coefficients, and \mathcal{O}_i 's are the dimension-six operators. The interaction Lagrangian of VLQ with the SM fermions is given by [4]

$$\mathcal{L} \supset \lambda_{\alpha\beta}^L \bar{Q}_{L\alpha} \gamma^\mu V_{LQ\mu} L_{L\beta} + \lambda_{\alpha\beta}^R \bar{d}_{R\alpha} \gamma^\mu V_{LQ\mu} l_{R\beta}, \quad (49.3)$$

where Q_L (L_L) is the left-handed quark (lepton) doublet, u_R (d_R) is the right-handed up (down) quark singlet, l_R is the charged lepton singlet, and α, β are the generation indices.

After performing the Fierz transformation, we obtain the new Wilson coefficients for the process $b \rightarrow c\tau\bar{\nu}_l$ as [10]

$$\begin{aligned} C_{V_1}^{\text{LQ}} &= \frac{1}{2\sqrt{2}G_F V_{cb}} \sum_{k=1}^3 V_{k3} \frac{\lambda_{2l}^L \lambda_{k3}^{L*}}{M_{V_{lQ}}^2}, \\ C_{S_1}^{\text{LQ}} &= -\frac{1}{2\sqrt{2}G_F V_{cb}} \sum_{k=1}^3 V_{k3} \frac{2\lambda_{2l}^L \lambda_{k3}^{R*}}{M_{V_{lQ}}^2}, \end{aligned} \quad (49.4)$$

and for the $b \rightarrow s \ell_i^+ \ell_j^-$ processes as [10]

$$\begin{aligned}
 C_9^{\text{LQ}} &= -C_{10}^{\text{LQ}} = \frac{\pi}{\sqrt{2} G_F V_{tb} V_{ts}^* \alpha_{\text{em}}} \sum_{m,n=1}^3 V_{m3} V_{n2} \frac{\lambda_{ni}^L \lambda_{mj}^{L*}}{M_{\text{VLQ}}^2}, \\
 C_9^{\prime\text{LQ}} &= C_{10}^{\prime\text{LQ}} = \frac{\pi}{\sqrt{2} G_F V_{tb} V_{ts}^* \alpha_{\text{em}}} \sum_{m,n=1}^3 V_{m3} V_{n2} \frac{\lambda_{ni}^R \lambda_{mj}^{R*}}{M_{\text{VLQ}}^2}, \\
 -C_P^{\text{LQ}} &= C_S^{\text{LQ}} = \frac{\sqrt{2}\pi}{G_F V_{tb} V_{ts}^* \alpha_{\text{em}}} \sum_{m,n=1}^3 V_{m3} V_{n2} \frac{\lambda_{ni}^L \lambda_{mj}^{R*}}{M_{\text{VLQ}}^2}, \\
 C_P^{\prime\text{LQ}} &= C_S^{\prime\text{LQ}} = \frac{\sqrt{2}\pi}{G_F V_{tb} V_{ts}^* \alpha_{\text{em}}} \sum_{m,n=1}^3 V_{m3} V_{n2} \frac{\lambda_{ni}^R \lambda_{mj}^{L*}}{M_{\text{VLQ}}^2}.
 \end{aligned} \tag{49.5}$$

We consider the LL coupling contributions to both $b \rightarrow sll$ and $b \rightarrow c\tau\bar{\nu}_\tau$ processes, and fit the NP parameters by confronting the SM predictions with the observed data. The expression for χ^2 used in our analysis is given by

$$\chi^2(C_i^{\text{LQ}}) = \sum_i \frac{[\mathcal{O}_i^{\text{th}}(C_i^{\text{LQ}}) - \mathcal{O}_i^{\text{exp}}]^2}{(\Delta\mathcal{O}_i^{\text{exp}})^2 + (\Delta\mathcal{O}_i^{\text{th}})^2}, \tag{49.6}$$

where $\mathcal{O}_i^{\text{th}}(C_i^{\text{LQ}})$ are the theoretical predictions and $\Delta\mathcal{O}_i^{\text{th}}$ contains the 1σ error from theory. Here, $\mathcal{O}_i^{\text{exp}}(\Delta\mathcal{O}_i^{\text{exp}})$, respectively, represent the corresponding experimental central value (1σ uncertainty). Figure 49.1 represents the constraints plot for LL couplings whose $\chi_{\text{min, VLQ+SM/d.o.f}}^2$ value found to be < 1 which implies the VLQ can accommodate the issues in both $b \rightarrow s\tau\tau(\mu\mu)$ and $b \rightarrow c\tau\bar{\nu}_\tau$.

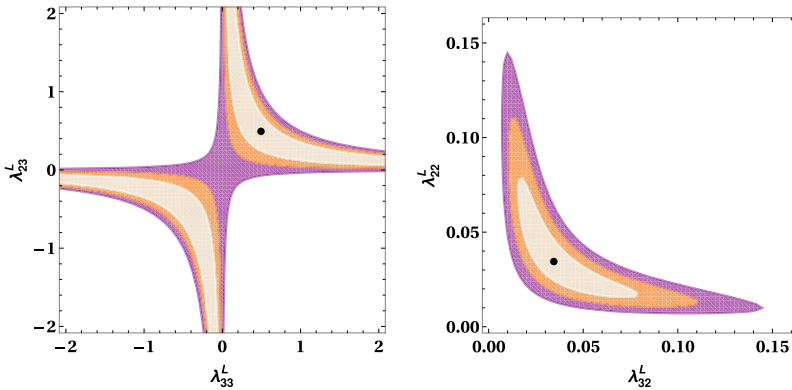


Fig. 49.1 Constraints on new VLQ couplings which include only LL -type operators

Table 49.1 Predicted branching ratios of LFV B decay modes of in the VLQ model

Decay modes	Predicted values	Experimental limit [7]
$B_s \rightarrow \mu^- \tau^+$	2.7×10^{-7}	$< 3.4 \times 10^{-5}$
$B^+ \rightarrow K^+ \mu^- \tau^+$	1.3×10^{-6}	$< 2.8 \times 10^{-5}$
$\bar{B}^0 \rightarrow \bar{K}^0 \mu^- \tau^+$	1.2×10^{-6}	...
$B^+ \rightarrow K^{*+} \mu^- \tau^+$	2.6×10^{-6}	...
$\bar{B}^0 \rightarrow \bar{K}^{*0} \mu^- \tau^+$	2.4×10^{-6}	...
$B_s \rightarrow \phi \mu^- \tau^+$	3.1×10^{-6}	...
$B_s \rightarrow \mu^+ \tau^-$	3.3×10^{-7}	$< 3.4 \times 10^{-5}$
$B^+ \rightarrow K^+ \mu^+ \tau^-$	1.6×10^{-6}	$< 4.5 \times 10^{-5}$
$\bar{B}^0 \rightarrow \bar{K}^0 \mu^+ \tau^-$	1.5×10^{-6}	...
$B^+ \rightarrow K^{*+} \mu^+ \tau^-$	3.1×10^{-6}	...
$\bar{B}^0 \rightarrow \bar{K}^{*0} \mu^+ \tau^-$	2.9×10^{-6}	...
$B_s \rightarrow \phi \mu^+ \tau^-$	3.8×10^{-6}	...

49.3 Impact on Lepton Flavor Violating B Decay Modes

This section will be dedicated to the study of LFV two/three-body decay modes of B meson and τ lepton in the presence of the VLQ, $V_{LQ}(3, 1, 2/3)$. The rare lep-tonic/semileptonic LFV B channels involving $b \rightarrow s l_i^- l_j^+$ quark-level transition, occur at tree level due to the exchange of VLQ. The total effective Hamiltonian for $b \rightarrow s l_i^- l_j^+$ processes in the VLQ model can be written as [5]

$$\mathcal{H}_{\text{eff}}^{\text{VA}} = -\frac{G_F \alpha_{\text{em}}}{\sqrt{2}\pi} V_{tb} V_{ts}^* \left[C_9^{\text{LQ}} (\bar{s} \gamma^\mu P_L b) (\bar{l}_i \gamma_\mu l_j) + C_{10}^{\text{LQ}} (\bar{s} \gamma^\mu P_L b) (\bar{l}_i \gamma_\mu \gamma_5 l_j) \right. \\ \left. + C_9^{\text{LQ}} (\bar{s} \gamma^\mu P_R b) (\bar{l}_i \gamma_\mu l_j) + C_{10}^{\text{LQ}} (\bar{s} \gamma^\mu P_R b) (\bar{l}_i \gamma_\mu \gamma_5 l_j) \right]. \quad (49.7)$$

Now using the best-fit of VLQ coupling from Fig. 49.1 and input parameters from [7], the predicted values of various (semi)leptonic LFV B decay modes are given in Table 49.1, which are found to be well below the current experimental upper bounds.

49.4 Conclusion

We have presented the simultaneous explanation of the $b \rightarrow s$ and $b \rightarrow c$ anomalies in the $(3, 1, 2/3)$ VLQ model. We have performed a global fit to all relevant data and predicted the branching ratios of LFV B decay modes, which are found to be the experimental limit.

References

1. LHCb, R. Aaij et al., Phys. Rev. Lett. **122**, 191801 (2019); C. Bobeth, G. Hiller, G. Piranishvili, JHEP **12**, 040 (2007); LHCb, R. Aaij et al., JHEP **08**, 055 (2017); B. Capdevila, A. Crivellin, S. Descotes, J. Matias, J. Virto, JHEP **01**, 093 (2018); HFLAV, Y.S. Amhis et al., [arXiv:1909.12524](https://arxiv.org/abs/1909.12524)
2. L.D. Luzio, M. Nardecchia, Eur. Phys. J. C **77**, 536 (2017)
3. H. Georgi, S.L. Glashow, Phys. Rev. Lett. **32**, 438 (1974); H. Georgi, AIP Conf. Proc. **23**, 575 (1975); P. Langacker, Phys. Rept. **72**, 185 (1981); J.C. Pati, A. Salam, Phys. Rev. D **8**, 1240 (1973); Phys. Rev. Lett. **31**, 661 (1973); Phys. Rev. D **10**, 275 (1974)
4. P.S.B. Dev, R. Mohanta, S. Patra, S. Sahoo, Phys. Rev. D **102**, 095012 (2020)
5. M. Duraisamy, S. Sahoo, R. Mohanta, Phys. Rev. D **95**, 035022 (2017)
6. I. Dosner, S. Fajfer, A. Greljo, J.F. Kamenik, N. Kosnik, Phys. Rept. **641**, 1 (2016)
7. Particle Data Group, M. Tanabashi et al., Phys. Rev. D **98**, 030001 (2018)
8. M. Tanaka, R. Watanabe, Phys. Rev. D **87**, 034028 (2013)
9. M. Misiak, Nucl. Phys. B **393**, 23 (1993)
10. Y. Sakaki, M. Tanaka, A. Tayduganov, R. Watanabe, Phys. Rev. D **88**, 094012 (2013)

Chapter 50

Investigating the Parton Shower Model in PYTHIA8 with pp Collision Data at $\sqrt{s} = 13$ TeV



Suman Kumar Kundu, Tanmay Sarkar, and Manas Maity

Abstract Understanding the production of quarks and gluons in high-energy collisions and their evolution is a very active area of investigation. Monte Carlo event generator PYTHIA8 uses the parton shower model to simulate such collisions and is optimized using experimental observations. Recent measurements of event-shape variables and differential jet cross sections in pp collisions at $\sqrt{s} = 13$ TeV at the Large Hadron Collider have been used to investigate further the parton shower model as used in PYTHIA8.

50.1 Introduction

Matrix element calculations with fixed-order treatment is not sufficient to understand the production of quarks and gluons, collectively called partons, in high-energy collisions or their evolution into jets of hadrons. Comparison with experimental results demand fully exclusive description of the final states based on the shower evolution and hadronization. Such methods are described through phenomenological models embedded in the shower Monte Carlo (MC) codes.

PYTHIA8 uses leading order (LO) calculations followed by “transverse momentum” (p_{\perp}) ordered parton shower [1] with p_{\perp}^2 as evolution variable for the generation of $2 \rightarrow n$ ($n \geq 2$) final states by taking account initial (ISR) and final (FSR) state shower. Shower evolution for a parton like $a \rightarrow bc$, is based on the standard (LO) DGLAP splitting kernels and the branching probability expressed as

$$d\mathcal{P}_a = \frac{dp_{\perp}^2}{p_{\perp}^2} \sum_{b,c} \frac{\alpha_s(p_{\perp}^2)}{2\pi} P_{a \rightarrow bc}(z) dz \quad (50.1)$$

S. K. Kundu (✉) · M. Maity
Visva Bharati, Santiniketan, India
e-mail: sumankundu.rs@visva-bharati.ac.in

T. Sarkar
National Central University (NCU), Taoyuan, Taiwan

where $P_{a \rightarrow bc}$ is the DGLAP splitting function and p_{\perp}^2 represents the scale of the branching; z represents the sharing of p_{\perp} of a between the two daughters, with b taking a fraction z and c the rest, $1 - z$. Here, the summation goes over all allowed branchings, e.g., $q \rightarrow qg$ and $q \rightarrow q\gamma$, etc. Now, the divergence at $p_{\perp}^2 \rightarrow 0$ is taken care of by introducing a term $\mathcal{P}_a^{\text{no}}(p_{\perp_{\text{max}}}^2, p_{\perp_{\text{evol}}}^2)$ known as *Sudakov form factor* [2]. This Sudakov factor ensures that there will be no emission between scale $p_{\perp_{\text{max}}}^2$ to a given $p_{\perp_{\text{evol}}}^2$.

Considering light cone kinematics, evolution variables $p_{\perp_{\text{evol}}}^2$ for $a \rightarrow bc$ at virtuality scale Q^2 for space-like branching (ISR) and time-like branching (FSR) are given by $(1 - z)Q^2$ and $z(1 - z)Q^2$, respectively. Finally, (50.2) and (50.3) describe the evolutions for ISR and FSR, respectively [1].

$$d\mathcal{P}_b = \frac{dp_{\perp_{\text{evol}}}^2}{p_{\perp_{\text{evol}}}^2} \frac{\alpha_s(p_{\perp_{\text{evol}}}^2)}{2\pi} \frac{x' f_a(x', p_{\perp_{\text{evol}}}^2)}{x f_a(x, p_{\perp_{\text{evol}}}^2)} P_{a \rightarrow bc}(z) dz \mathcal{P}_b^{\text{no}}(x, p_{\perp_{\text{max}}}^2, p_{\perp_{\text{evol}}}^2) \quad (50.2)$$

$$d\mathcal{P}_a = \frac{dp_{\perp_{\text{evol}}}^2}{p_{\perp_{\text{evol}}}^2} \frac{\alpha_s(p_{\perp_{\text{evol}}}^2)}{2\pi} P_{a \rightarrow bc}(z) dz \mathcal{P}_a^{\text{no}}(p_{\perp_{\text{max}}}^2, p_{\perp_{\text{evol}}}^2) \quad (50.3)$$

Currently, both the running re-normalization and factorization shower scales, i.e., the scales at which α_s and the PDFs are evaluated, are chosen to be $p_{\perp_{\text{evol}}}^2$ [3]. The general methodology of PYTHIA8 for ISR, FSR, and MPI is to start from some maximum scale $p_{\perp_{\text{max}}}^2$ and evolve downward in energy towards next branching until the daughter partons reach some cut-off.

50.2 Optimizing the Parton Shower Model of PYTHIA8

CMS and ATLAS have done several tuning of PYTHIA8 around its Monash tune [4] for underlying event (UE), the strong coupling, and MPI-related parameters [5–7]. In this study [8] also, Monash tune is used as default for PYTHIA v8.235 with NNPDF2.3 PDF (LO) set to optimize with four event shapes [9] measurement from CMS. These are—the complement of transverse thrust (τ_{\perp}), total jet mass (ρ_{Tot}), total transverse jet mass ($\rho_{\text{Tot}}^{\text{T}}$), and total jet broadening (B_{T}).

Monash tune overestimates the multijet regions of these event shapes [9]. Hence, we examined ISR and FSR utilizing the provision that PYTHIA8 allows the use of separate values of $\alpha_s(M_Z)$ for showering frameworks used for these. The maximum evolution scale involved in the showering is set to match the scale of the hard process itself. In PYTHIA8, it is set equal to the factorization scale, but allows its modification by multiplicative factors `SpaceShower:PTmaxFudge` for ISR and `TimeShower:PTmaxFudge` for FSR. The latter is seen not to have much effect on the ESVs, it is excluded from the optimization.

For each point in the parameter space, resulting distributions have been compared with data in terms of χ^2/NDF . Then PROFESSOR v2.3.0 [10] along with RIVET v2.6 [11] has been used to optimize the complete set of ESV distributions from

PYTHIA8 [9]. Post-optimization, the new parameter set is checked [8] using other relevant results from the CMS [12] and ATLAS [13].

50.3 Validation of Results

The optimized values of the three parameters are shown in Table 50.1 are used to calculate the ESVs. Agreement with data deteriorates slightly for τ_{\perp} and $\rho_{\text{Tot}}^{\text{T}}$ compared to the good agreement with the Monash tune as shown in Fig. 50.1. But, there

Table 50.1 Optimized result of three parameters of PYTHIA8 is shown along with their default values in the Monash tune and the sampling range

PYTHIA8 parameters set	Monash values	Sampling range	Optimized values
SpaceShower:alphaSvalue	0.1365	0.1092 – 0.1638	$0.11409^{+0.00078}_{-0.00073}$
TimeShower:alphaSvalue	0.1365	0.1092 – 0.1638	$0.15052^{+0.00077}_{-0.00076}$
SpaceShower:P TmaxFudge	1.0	0.6 – 1.4	$0.9323^{+0.0065}_{-0.0064}$

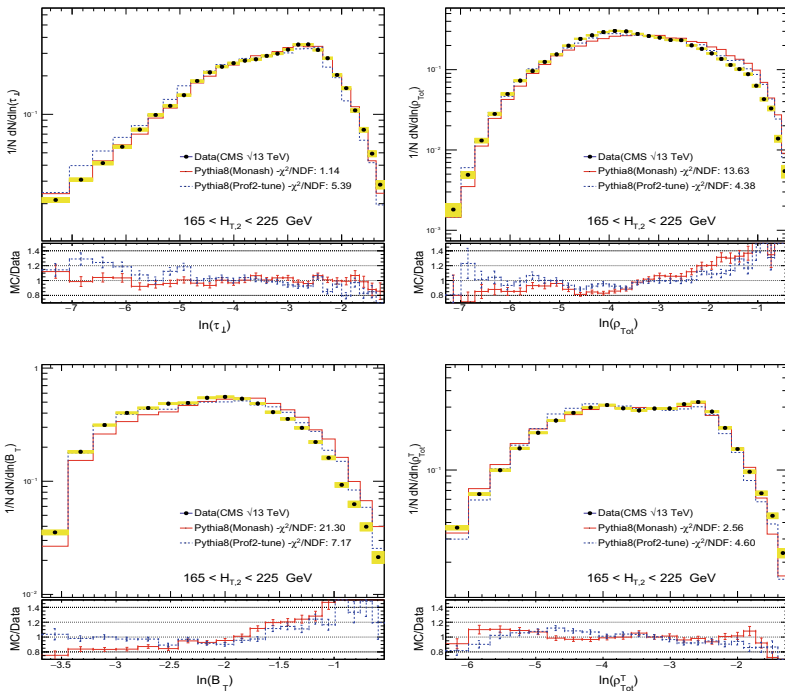


Fig. 50.1 Predictions of the optimized parameter set is compared with CMS data and Monash tune for $H_{T,2}$ range $165 < H_{T,2} < 225$. normalized distributions of the τ_{\perp} (top left), ρ_{Tot} (top right), B_{\perp} (bottom left) and $\rho_{\text{Tot}}^{\text{T}}$ (bottom right)

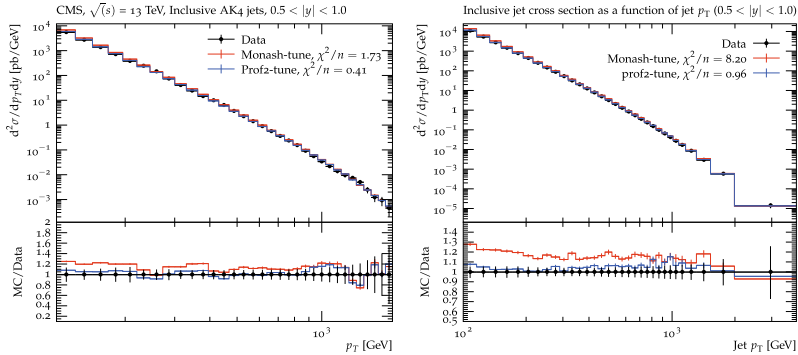


Fig. 50.2 Normalized distributions of differential inclusive cross section for anti- k_T jets ($R = 0.4$) for CMS (left) and ATLAS (right) are compared with the predictions of PYTHIA8 with the optimized parameter set and Monash tune

is significant improvement in agreement with data for ρ_{Tot} and B_T compared to the Monash tune. Since ρ_{Tot} and B_T had a rather poor agreement between data and the Monash tune, overall these new set of parameters give better model for three-dimensional variables.

Inclusive jet cross-sectional measurements being sensitive to PDF of protons and α_s are also compared with those optimized values. CMS [12] and ATLAS [13] studies with the 13 TeV data are considered for this validation. The CMS measurements of inclusive cross sections for anti- k_T jets with $R = 0.4, 0.7$. Figure 50.2 show that the new parameter set improves the agreement between data and the Monash tune of Pythia8. Similar improvement is seen for the ATLAS measurement of anti- k_T jets with $R = 0.4$.

Since PYTHIA8 is widely used, its optimization is important. This study shows that certain aspects of the experimental observations can be better described with these optimized set of parameters.

References

1. T. Sjostrand, P.Z. Skands, Eur. Phys. J. C **39**, 129 (2005)
2. V.V. Sudakov, Sov. Phys. JETP **3**, 65 (1956). [Zh. Eksp. Teor. Fiz. **30**, 87 (1956)]
3. R. Corke, T. Sjostrand, JHEP **03**, 032 (2011)
4. P. Skands, S. Carrazza, J. Rojo, Eur. Phys. J. C **74**, 3024 (2014)
5. V. Khachatryan et al., Eur. Phys. J. C **76**, 155 (2016)
6. A.M. Sirunyan et al., Eur. Phys. J. C **80**(1), 4 (2020)
7. A. Buckley, in *Proceedings of the Sixth International Workshop on Multiple Partonic Interactions at the Large Hadron Collider*. CERN (CERN, Geneva, 2014), p. 29
8. S.K. Kundu, T. Sarkar, M. Maity, Int. J. Mod. Phys. A **34**(33), 1950219 (2019)
9. A.M. Sirunyan et al., JHEP **12**, 117 (2018)
10. A. Buckley, H. Hoeth, H. Lacker, H. Schulz, J.E. von Seggern, Eur. Phys. J. C **65**, 331 (2010)

11. A. Buckley, J. Butterworth, L. Lonnblad, D. Grellscheid, H. Hoeth, J. Monk, H. Schulz, F. Siegert, *Comput. Phys. Commun.* **184**, 2803 (2013)
12. V. Khachatryan et al., *Eur. Phys. J. C* **76**(8), 451 (2016)
13. Measurement of inclusive-jet cross-sections in proton-proton collisions at $\sqrt{s} = 13$ TeV centre-of-mass energy with the ATLAS detector. Technical Report ATLAS-CONF-2016-092, CERN, Geneva (2016)

Chapter 51

Search for Supersymmetry with Jets and Missing Transverse Momentum Final States



Tribeni Mishra

Abstract A search for supersymmetry is performed in the final states containing multiple jets and missing transverse momentum produced in proton–proton collisions using 137 fb^{-1} data collected in 2016–2018 with the CMS detector at the LHC. The analysis is performed in a four-dimensional search region defined in terms of the number of jets, the number of tagged bottom quark jets, the scalar sum of jet transverse momenta, and the magnitude of the vector sum of jet transverse momenta. The observations are consistent with the Standard Model background predictions and no evidence for supersymmetry is obtained. The results are interpreted in the context of simplified models of pair production of gluinos and squarks.

51.1 Introduction

The Standard Model (SM) of particle physics describes the fundamental particles and their interactions with a high level of precision. Although the SM is remarkably successful, it does leave many questions unanswered. Supersymmetry (SUSY) is a favored extension of the SM which provides a suitable and elegant explanation to resolve several problems of SM. It proposes a superpartner for every SM particle which differs in spin by half a unit. Among SUSY processes, gluino and squark pair production has the largest production cross sections, making it a relevant channel for SUSY searches at the Large Hadron Collider (LHC).

If R-parity is conserved, SUSY particles are produced in pairs and decay either directly or via cascades to quarks and neutralinos, $\tilde{\chi}_1^0$. In this paper, the $\tilde{\chi}_1^0$ is assumed to be the lightest SUSY particle (LSP), stable, weakly interacting, leading to true missing transverse momentum (p_T^{miss}) in the events. This paper discusses a search for gluinos and squark–antisquark pair production in a final state with jets from

T. Mishra work for the CMS Collaboration.

T. Mishra (✉)

National Institute of Science Education and Research, An OCC of Homi Bhabha National Institute, Bhubaneswar 752050, India

e-mail: tribeni.mishra@niser.ac.in

© The Author(s), under exclusive license to Springer Nature Singapore Pte Ltd. 2022
B. Mohanty et al. (eds.), *Proceedings of the XXIV DAE-BRNS High Energy Physics Symposium, Jatni, India*, Springer Proceedings in Physics 277,
https://doi.org/10.1007/978-981-19-2354-8_51

281

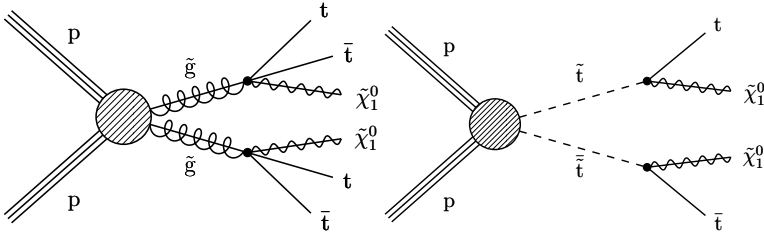


Fig. 51.1 Diagrams displaying the event topologies of gluino pair production (left), each decaying with a 100% branching fraction to a pair of top quarks and the LSP and top squark pair production (right), each decaying with a 100% branching fraction to a top quark and the LSP [2]

hadronization of quarks and large p_T^{miss} from $\tilde{\chi}_1^0$. We use proton–proton collision events at $\sqrt{s} = 13$ TeV collected by the CMS detector [1] in 2016–2018, corresponding to an integrated luminosity of 137 fb^{-1} . The event diagrams for gluinos and top squarks pair production are shown in Fig. 51.1. To make this search sensitive to a wide range of SUSY scenarios, the search region is defined using four key variables: the total number of jets (N_{jet}), the number of b-tagged jets (N_{b-jet}), the scalar sum of jet p_T (H_T), and the magnitude of the negative of the vector sum of p_T of jets (H_T^{miss}).

51.2 SM Backgrounds and Event Selection

Several SM processes can give similar final state, i.e., jets and p_T^{miss} as targeted SUSY topology. The $t\bar{t}$ and W+jets events in which the W boson decays to an undetected or out-of-acceptance lepton and a neutrino, or to a hadronically decaying τ lepton and a neutrino (Fig. 51.2, left) can give rise to significant p_T^{miss} and thus contribute to the background. This background is suppressed by vetoing events with an isolated track or isolated lepton. The Z+jets process where the Z boson decays to a pair of neutrinos, is an irreducible background (Fig. 51.2, middle). Significant p_T^{miss} in QCD

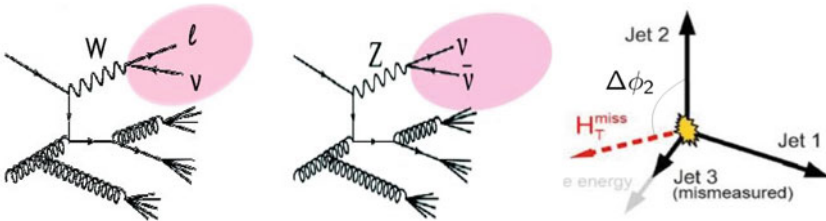


Fig. 51.2 Schematic diagram of SM backgrounds: W+jets (left), Z+jets (in middle), QCD multijet (right)

multijet events can arise from jet mismeasurement, (Fig. 51.2, right), if a jet does not fulfil selection criteria, and from semileptonic decay of b jets. This background is reduced by rejecting events with $\Delta\phi(\text{jet}, H_T^{\text{miss}}) > (0.5, 0.5, 0.3, 0.3)$ for the four highest p_T jets.

To select SUSY like events, we select events with at least two jets each with $p_T > 30$ GeV and $|\eta| < 2.4$, $H_T > 300$ GeV, $H_T^{\text{miss}} > 300$ GeV. The events persisting after the above selections are further divided in bins of N_{jet} , $N_{b\text{-jet}}$, H_T , and H_T^{miss} . The intervals are N_{jet} : 2–3, 4–5, 6–7, 8–9, ≥ 10 ; $N_{b\text{-jet}}$: 0, 1, 2, ≥ 3 , and 10 bins in H_T and H_T^{miss} plane. The total number of search bins is 174.

51.3 Estimation of Backgrounds

The analysis uses a data-driven approach to estimate the backgrounds. The background yield in the signal region is predicted from the corresponding yield in an orthogonal region, called control region. The method is validated using Monte Carlo (MC) samples before using it with data to get the background prediction.

We use γ +jets and $Z(\rightarrow l^+l^-)$ +jets as control sample for the $Z(\rightarrow \nu\bar{\nu})$ +jets background estimation. For search bins with $N_{b\text{-jet}} = 0$, a γ +jets sample is used to derive $Z(\rightarrow \nu\bar{\nu})$ +jets yields and $(H_T, H_T^{\text{miss}}, N_{\text{jet}})$ shape. To evaluate the background for search bins with $N_{b\text{-jet}} \geq 1$, the result from bins with $N_{b\text{-jet}} = 0$ is extended using extrapolation factors from $Z \rightarrow l^+l^-$ data.

A closure test of the estimation procedure is performed by treating simulated $Z(\rightarrow l^+l^-)$ +jets events as data, as shown in Fig. 51.3. Backgrounds from the $t\bar{t}$, W +jets are collectively estimated by extrapolating from the 1-lepton control region and QCD is estimated using the low $\Delta\phi(\text{jet}, H_T^{\text{miss}})$ control region.

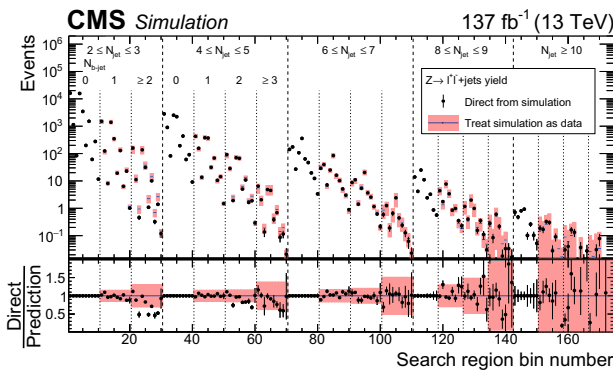


Fig. 51.3 $Z(\rightarrow \nu\bar{\nu})$ +jets background in 174 search bins from the $Z(\rightarrow l^+l^-)$ +jets simulation predicted by background estimation procedure (blue bars) compared with direct $Z(\rightarrow l^+l^-)$ +jets simulation (black points with error bars) [2]

51.4 Results

The total predicted background yields in every bin are compared against observed data in the signal region, as shown in Fig. 51.4. The observed event count agrees with predicted SM backgrounds within uncertainties and no significant excess is found in any of the search bins. Figure 51.5 shows the 95% Confidence Level (CL) upper limits on the production cross section for two signal scenarios, where the gluino mass is probed up to 2180 GeV and the stop mass is probed up to 1190 GeV for nearly massless neutralinos.

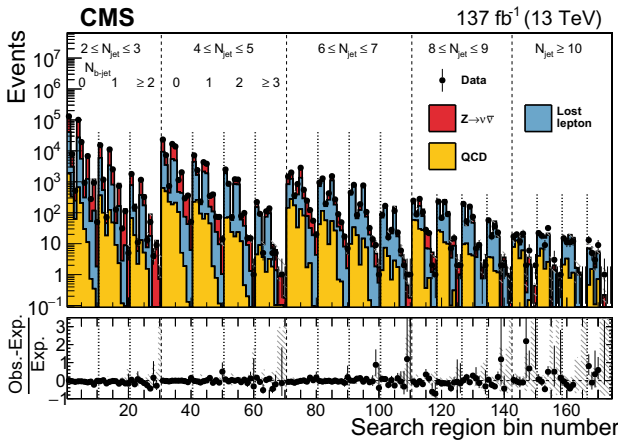


Fig. 51.4 Observed numbers of events and pre-fit SM background predictions in the 174 search bins of the analysis [2]

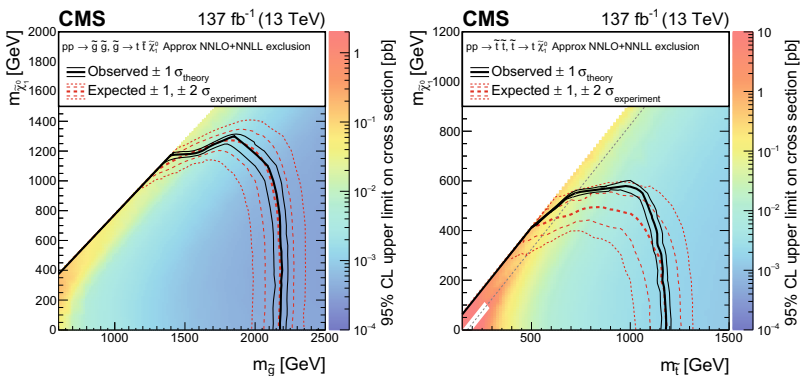


Fig. 51.5 Observed and expected upper limits on the production cross sections at 95% CL for direct gluino pair production (left) where each gluino decays as $\tilde{g} \rightarrow t\bar{t}\tilde{\chi}_1^0$ and top squark-antisquark production (right) in which top (anti)squark decays to a top (anti)quark and $\tilde{\chi}_1^0$ [2]

References

1. S. Chatrchyan et al. (CMS), JINST **3**, S08004 (2008)
2. A.M. Sirunyan et al. (CMS). JHEP **10**, 244 (2019)

Chapter 52

Explaining the XENON1T Excess and Dark Matter with Three Scalars



Vandana Sahdev, Suvam Maharana, and Divya Sachdeva

Abstract We discuss how the recent observation of an excess in the electron recoil events at the XENON1T detector, coupled with the requirement to explain the issue of dark matter relic density and muon anomalous magnetic moment, can be addressed using a scalar sector extension of the standard model.

52.1 Introduction

Despite the immense success of the standard model (SM), the existence of issues like discrepancy in anomalous magnetic moment of leptons, particle nature of dark matter (DM), small non-zero mass of the neutrinos, etc., demand for an extension of the SM. An extension involving only scalar fields is not only economical but also seems more natural. Further, scalar fields are also motivated if theories incorporating supersymmetry and Peccei–Quinn symmetry are to be relevant. Following the reporting of excess in electron recoil events at the XENON1T detector [1], which most likely seemed to be a result of scattering of dark matter of the electron, a plethora of explanations were postulated. As explained in [2], the excess of 2 keV requires DM mass of $\mathcal{O}(100)$ MeV or less. For such low-mass cold dark matter (CDM), elastic scattering would produce recoils of \mathcal{O} (eV) which does not address the excess. In such a situation, two most natural resolutions seem to be the boosted dark matter or inelastic scattering of CDM off the electron. In the following analysis, we show how an extension of SM consisting of only scalar fields not only explains the excess (via inelastic scattering of DM) but also the DM relic density and muon $g-2$ and yet survives all the constraints.

V. Sahdev (✉) · S. Maharana
Department of Physics and Astrophysics, University of Delhi, Delhi 110007, India
e-mail: vandanasahdev20@gmail.com

D. Sachdeva
Department of Physics, Indian Institute of Science Education and Research Pune,
Pune 411008, India

52.2 Model

The model [3] consists of two complex scalars, ϕ and η , and one real scalar ω . The two components of ϕ , viz. ϕ_1 and ϕ_2 , constitute the dark matter and also cause the inelastic scattering off the electron at the XENON1T detector. Scalar ω serves as the mediator for interaction between the dark sector and the SM. The mass splitting between ϕ_1 and ϕ_2 is caused by the quadratic term involving ϕ and given as $\delta_m \simeq \Delta^2/\mu_\phi$ where Δ^2 is the coefficient of the quadratic term and is taken to be real. There are trilinear terms involving ϕ, ϕ^* and ω which engender couplings of the form $g_{ij}\phi_i\phi_j\omega$. For the present work, coefficients of other cubic and quartic terms are assumed small. Further, the $vevs$ of scalars are taken as zero. Focussing on a leptophilic ω , its couplings to electron and muon are generated via the dimension-5 operator $(\omega/\Lambda)H [\tilde{y}_x \bar{L}_x x_R + H.c.]$ [4], where $x = e, \mu$. This leads to effective couplings of ω with e and μ as

$$\mathcal{L}_{\text{Yuk}}^{\text{eff}} \ni \omega [y_\mu \bar{\mu}\mu + y_e \bar{e}e] , \quad y_\ell \equiv \tilde{y}_\ell v/\sqrt{2}\Lambda . \tag{52.1}$$

We further parametrize y_e as $y_e = n_s (m_e/m_\mu) y_\mu$.

Constraints on y_μ and y_e : Coupling y_μ is constrained from the requirement to explain the discrepancy in anomalous magnetic moment of muon, Δa_μ [5] within 2σ and is constrained further from *BABAR* search for dark photons in the 4μ final state [6], reinterpreted for scalar mediator. This is shown in Fig. 52.1 on the left. Coupling y_e is determined from y_μ as $y_e = n_s (\frac{m_e}{m_\mu}) y_\mu$. There are constraints on y_e from beam-dump experiments such as E141 [7], E137 [8, 9] and Orsay linac [10]. *BABAR* search for dark photons via $e^+e^- \rightarrow \gamma A' \rightarrow \gamma l^+l^-$ is also used to constrain y_e further. These are shown in Fig. 52.1 on the right alongwith constraints from low-energy experiment KLOE [11, 12], NA64 [13] and *BABAR* analysis [14] for dark photons.

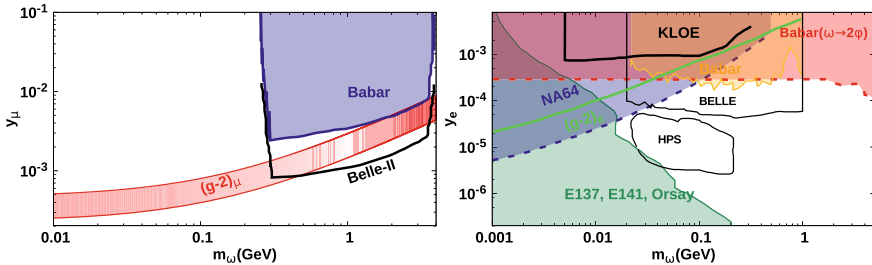


Fig. 52.1 Various constraints on y_μ and y_e . The dotted curves indicate projected sensitivities from HPS [15, 16] and Belle-II [4, 15, 17, 18]

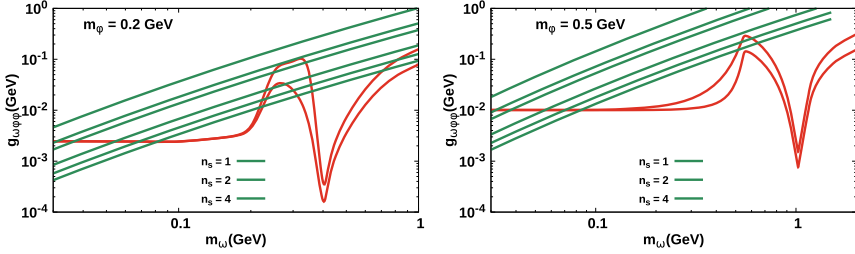


Fig. 5.2 $g_{\omega\phi\phi}$ ($\equiv g_{12}$) values satisfying the XENON1T excess (green) and relic density (red), as a function of m_{ω}

52.3 XENON1T Excess

An excess in the electronic recoil events, prominent between 2–3 keV was observed at the XENON1T detector in June 2020 [1]. Believing the excess to be caused by inelastic scattering of the DM (ϕ) off the electron via the mediator ω , it is explained provided we consider $m_{\phi} \sim \mathcal{O}(100)$ MeV and the splitting (between its two components) $\delta_m \sim 2$ keV. Coupling $g_{12} \equiv g_{\omega\phi\phi}$ as required to explain the excess of 2 keV within 1σ is plotted as a function of the mediator mass m_{ω} , as shown in Fig. 52.2.

52.4 Dark Matter

The smallness of the splitting δ_m ensures that both ϕ_1 and ϕ_2 are DM candidates with almost equal densities. DM pair annihilation occurs via the mediator ω . For very light ϕ_i , only channel $\phi_i\phi_j \rightarrow e^+e^-$ is available, while for heavier ϕ_i , channel $\phi_i\phi_j \rightarrow \omega\omega$ dominates, even though mode $\mu^+\mu^-$ is available. For convenience, we take $g_{11} = g_{22} = g_{12}$. The prompt decay of ω into e^+e^- is in conflict with CMB constraints and is avoided by introduction of the complex scalar η which is charged under an exact Z_3 -symmetry. The most general lagrangian involving η is given as

$$\mathcal{L}_{\eta,\omega} \ni \lambda_{\eta}|\eta|^4 + \mu_{\omega\eta}\omega|\eta|^2 + \lambda'_{\omega\eta}\omega^2|\eta|^2 + (\mu_{\eta}\eta^3 + \lambda_{\omega\eta}\omega\eta^3 + \text{H.c}) \quad (52.2)$$

Then, decay of ω into scalars η occurs via two-body as well as three-body decays. Stability of η is ensured as Z_3 remains unbroken. To ensure that mode $\eta\eta^*$ of ω decay is dominant over the e^+e^- mode, $m_{\eta} \ll m_{\omega}/2$. For $m_{\eta} \sim m_{\omega}/3$, only $\mu_{\omega\eta}$ and one of μ_{η} and $\lambda_{\omega\eta}$ are relevant. In addition, semi-annihilation processes such as $3\eta \rightarrow \eta\eta^*$ (or $\eta + 2\eta^* \rightarrow 2\eta$) would occur and these play a crucial role in determining the relic density for η (with that for the η^* being equal). For $\mu_{\eta} \neq 0$ and $\mu_{\omega\eta} \sim 0.1 m_{\eta}$ (keeping other parameters zero), we get $\Omega_{\eta}h^2 \sim 10^{-4}$ [19]. Similarly, for $\mu_{\eta} = 0$ and $\lambda_{\omega\eta} \sim 0.1 (m_{\eta}/1\text{GeV})$, one obtains $\Omega_{\eta}h^2 \sim 10^{-3}$. Further, the smallness of y_e ensures that the $\eta\eta^* \rightarrow e^+e^-$ cross section is much smaller than that for $3\eta \rightarrow 2\eta$,

despite the latter being a $3 \rightarrow 2$ process. Thus, the η s settle to the tiny relic density much faster than they pump energy into the CMB.

Dependence of DM relic density on g_{12} is plotted as a function of m_ω in Fig. 52.2, for masses $m_\phi = 0.2$ GeV and $m_\phi = 0.5$ GeV. For $m_\omega < m_\phi$, the processes $\phi_i \phi_j \rightarrow \omega\omega$ are dominant. With the cross section having only a mild m_ω -dependence, so does the requisite $g_{\omega\phi\phi}$. Further, with y_μ playing only a subsidiary role, the band collapses to virtually a single curve. For $m_\omega > m_\phi$, this channel is no more allowed and $\phi_i \phi_j \rightarrow \mu^+ \mu^-$ dominates. Consequently, $g_{\omega\phi\phi}$ must increase with m_ϕ to account for the s -channel suppression. Simultaneously, the allowed spread in y_μ becomes relevant. The strong dip around $m_\phi \sim 2m_\omega$ is but a consequence of resonance enhancement.

52.5 Conclusion

From the results obtained here and those in [2, 20], it can be concluded that an explanation of the 2 keV excess at XENON1T demands DM of mass $\sim \mathcal{O}(100)$ MeV and if DM relic density and muon anomalous magnetic moment are to be explained simultaneously, DM of this mass range is constrained severely. Nevertheless, the scalar sector extension of the SM introduced here holds the potential to explain the observed XENON1T excess and address the issues of DM relic density and muon anomalous magnetic moment while surviving various terrestrial and cosmological constraints. To add to it, the model promises testability at collider experiments as well as CMBR observations in near future. For further details, the reader should refer [3].

References

1. E. Aprile et al., [XENON]. Phys. Rev. D **102**(7), 072004 (2020). <https://doi.org/10.1103/PhysRevD.102.072004>. [arXiv:2006.09721](https://arxiv.org/abs/2006.09721) [hep-ex]
2. K. Kannike, M. Raidal, H. Veermäe, A. Strumia, D. Teresi, Phys. Rev. D **102**(9), 095002 (2020). <https://doi.org/10.1103/PhysRevD.102.095002>. [arXiv:2006.10735](https://arxiv.org/abs/2006.10735) [hep-ph]
3. D. Choudhury, S. Maharana, D. Sachdeva, V. Sahdev, Phys. Rev. D **103**(1), 015006 (2021). <https://doi.org/10.1103/PhysRevD.103.015006>. [arXiv:2007.08205](https://arxiv.org/abs/2007.08205) [hep-ph]
4. J. Liu, C.E.M. Wagner, X.P. Wang, JHEP **03**, 008 (2019). [https://doi.org/10.1007/JHEP03\(2019\)008](https://doi.org/10.1007/JHEP03(2019)008). [arXiv:1810.11028](https://arxiv.org/abs/1810.11028) [hep-ph]
5. M. Tanabashi et al., [Particle Data Group]. Phys. Rev. D **98**(3), 030001 (2018). <https://doi.org/10.1103/PhysRevD.98.030001>
6. J.P. Lees et al., [BaBar]. Phys. Rev. D **94**(1), 011102 (2016). <https://doi.org/10.1103/PhysRevD.94.011102>. [arXiv:1606.03501](https://arxiv.org/abs/1606.03501) [hep-ex]
7. E.M. Riordan, M.W. Krasny, K. Lang, P. De Barbaro, A. Bodek, S. Dasu, N. Varelas, X. Wang, R.G. Arnold, D. Benton et al., Phys. Rev. Lett. **59**, 755 (1987). <https://doi.org/10.1103/PhysRevLett.59.755>
8. J.D. Bjorken, S. Ecklund, W.R. Nelson, A. Abashian, C. Church, B. Lu, L.W. Mo, T.A. Nunamaker, P. Rassmann, Phys. Rev. D **38**, 3375 (1988). <https://doi.org/10.1103/PhysRevD.38.3375>

9. B. Batell, R. Essig, Z. Surujon, *Phys. Rev. Lett.* **113**(17), 171802 (2014). <https://doi.org/10.1103/PhysRevLett.113.171802>. [arXiv:1406.2698](https://arxiv.org/abs/1406.2698) [hep-ph]
10. M. Davier, H. Nguyen Ngoc, *Phys. Lett. B* **229**, 150–155 (1989). [https://doi.org/10.1016/0370-2693\(89\)90174-3](https://doi.org/10.1016/0370-2693(89)90174-3)
11. N. Borodatchenkova, D. Choudhury, M. Drees, *Phys. Rev. Lett.* **96**, 141802 (2006). <https://doi.org/10.1103/PhysRevLett.96.141802>. [arXiv:hep-ph/0510147](https://arxiv.org/abs/hep-ph/0510147) [hep-ph]
12. F. Archilli et al., [KLOE-2]. *Phys. Lett. B* **706**, 251–255 (2012). <https://doi.org/10.1016/j.physletb.2011.11.033>. [arXiv:1110.0411](https://arxiv.org/abs/1110.0411) [hep-ex]
13. D. Banerjee et al., [NA64]. *Phys. Rev. D* **97**(7), 072002 (2018). <https://doi.org/10.1103/PhysRevD.97.072002>. [arXiv:1710.00971](https://arxiv.org/abs/1710.00971) [hep-ex]
14. J.P. Lees et al., [BaBar]. *Phys. Rev. Lett.* **119**(13), 131804 (2017). <https://doi.org/10.1103/PhysRevLett.119.131804>. [arXiv:1702.03327](https://arxiv.org/abs/1702.03327) [hep-ex]
15. B. Batell, N. Lange, D. McKeen, M. Pospelov, A. Ritz, *Phys. Rev. D* **95**(7), 075003 (2017). <https://doi.org/10.1103/PhysRevD.95.075003>. [arXiv:1606.04943](https://arxiv.org/abs/1606.04943) [hep-ph]
16. M. Battaglieri, S. Boyarinov, S. Bueltmann, V. Burkert, A. Celentano, G. Charles, W. Cooper, C. Cuevas, N. Dashyan, R. DeVita et al., *Nucl. Instrum. Meth. A* **777**, 91–101 (2015). <https://doi.org/10.1016/j.nima.2014.12.017>. [arXiv:1406.6115](https://arxiv.org/abs/1406.6115) [physics.ins-det]
17. B. Batell, A. Freitas, A. Ismail, D. Mckeen, *Phys. Rev. D* **98**(5), 055026 (2018). <https://doi.org/10.1103/PhysRevD.98.055026>. [arXiv:1712.10022](https://arxiv.org/abs/1712.10022) [hep-ph]
18. T. Abe et al., [Belle-II]. [arXiv:1011.0352](https://arxiv.org/abs/1011.0352) [physics.ins-det]
19. S. Bhattacharya, P. Ghosh, S. Verma, *JCAP* **01**, 040 (2020). <https://doi.org/10.1088/1475-7516/2020/01/040>. [arXiv:1904.07562](https://arxiv.org/abs/1904.07562) [hep-ph]
20. D. Borah, S. Mahapatra, D. Nanda, N. Sahu, *Phys. Lett. B* **811**, 135933 (2020). <https://doi.org/10.1016/j.physletb.2020.135933> ([[arXiv:2007.10754](https://arxiv.org/abs/2007.10754) [hep-ph]].)

Chapter 53

Improving Bounds on Invisible Branching Ratio of the Higgs with Deep Learning



Vishal S. Ngairangbam

Abstract We study the prospect of constraining invisible branching ratio of the Higgs boson in the vector boson fusion channel using deep learning techniques. Taking advantage of the differing QCD radiation patterns between signal and background, we find that modern machine learning techniques have the capability of significantly outperforming traditional analyses.

53.1 Introduction

After discovering the Higgs boson, the focus of the ongoing physics program at the Large Hadron Collider (LHC) is to measure all of its properties precisely to search for any deviations from those predicted by the Standard Model (SM). One such property is the possibility of non-standard coupling of the Higgs boson to so-called dark matter (DM) particles. If such a scenario exists, it should show up in invisible Higgs decay searches, as the DM particle would not interact in the detector, leaving behind a transverse momentum imbalance (Missing Transverse Energy). Although a positive discovery at the LHC may not be enough to vouch for the absolute stability¹ of such particles, it is nevertheless necessary to constrain many diverse scenarios. The current bound on the Higgs boson's invisible branching ratio (0.13) is significantly higher than the one expected in the SM.

Vector boson fusion (VBF) production of the Higgs boson offers a particularly clean yet abundant channel at the LHC. Due to the t-channel color-singlet exchange between two incoming quarks, there is a suppression of hadronic activity between the two final state jets [1]. Inspired by the success of Convolutional Neural Networks

¹It may be possible that the particle may decay to SM particles outside the detector with a long lifetime.

V. S. Ngairangbam (✉)
Physical Research Laboratory (PRL), Ahmedabad 380009, Gujarat, India
e-mail: vishalng@prl.res.in

IIT Gandhinagar, Palaj, Gandhinagar 382355, India

(CNNs) in identifying QCD radiation patterns, we use CNNs to distinguish the differing radiation patterns between the signal and the background [2]. We closely follow a recent experimental analysis of CMS [3] and show that our method provides stricter bounds.

The rest of the paper is organized as follows. We describe the details of the signal and background simulation and the pre-selection cuts in Sect. 53.2. The representation of the data and the preprocessing methods employed are described in Sect. 53.3. The results in the form of expected limits on the invisible branching ratio of the Higgs are presented in Sect. 53.4.

53.2 Simulation Details and Pre-selection Criteria

We consider two signal channels: Gluon fusion production (S_{QCD}) and vector boson fusion (S_{EW}) production of Higgs decaying invisibly. We consider the four major backgrounds: Z_{QCD} : $Z(\nu\bar{\nu}) + jets$, W_{QCD} : $W^\pm(l^\pm\nu) + jets$, Z_{EW} , and W_{EW} , where the last two processes are in the VBF topology. We generated parton level using MadGraph5_aMC@NLO(v2.6.5) [4] at 13 TeV LHC center-of-mass energy, which were showered and hadronized with Pythia (v8.243) [5], and passed through Delphes (v3.4.1) [6] for fast-detector simulation.

The applied pre-selection criteria are summarized as follows:

- **VBF Jet tag:** At least two jets with leading (sub-leading) jet $p_T > 80$ (40) GeV and $|\eta| < 4.7$. At least one of the jets to have $|\eta_{j_i}| < 3$.

$$\eta_{j_1}, \eta_{j_2} < 0 \quad , \quad |\Delta\phi_{jj}| < 1.5 \quad , \quad |\Delta\eta_{jj}| > 1 \quad , \quad m_{jj} > 200 \text{ GeV}$$

- **Lepton-veto:** No electron (muon) with $p_T > 10$ GeV in the central region, $|\eta| < 2.5(2.4)$.
- **Photon-veto:** No photon with $p_T > 15$ GeV in the central region, $|\eta| < 2.5$.
- **τ and b-veto:** no tau-tagged jets in $|\eta| < 2.3$ with $p_T > 18$ GeV, and no b-tagged jets in $|\eta| < 2.5$ with $p_T > 20$ GeV.
- **Missing E_T (MET):** $MET > 200$ GeV (250 GeV for CMS shape analysis).
- **MET jet alignment:** $\min(\Delta\phi(\mathbf{p}_T^{\text{MET}}, \mathbf{p}_T^j)) > 0.5$ for upto four leading jets with $p_T > 30$ GeV with $|\eta| < 4.7$.

After applying these selections, we form the signal and background class by weighting the contribution of each channel with their cross section and baseline selection efficiency.

53.3 Data Representation and Preprocessing

We construct the tower image with the E_T in High Resolution (HR) (0.08×0.08) and Low Resolution (LR) (0.17×0.17). We pad the ϕ axis to take care of its periodicity. After this, we get an image size of 59×45 for LR, and 125×95 for HR. For each event, we rotate along the z-axis such that $\phi_0 = 0$, and reflect such that the leading jet's η is always positive. We choose two instances of $\phi_0 \in \{\phi_{MET}, \phi_{j_1}\}$. After this step, we have four low-level input spaces: \mathcal{P}_{MET}^{LR} , \mathcal{P}_{MET}^{HR} , \mathcal{P}_J^{LR} and \mathcal{P}_J^{HR} .

We also construct two sets of high-level variables. The first one contains information about the event kinematics: $\mathcal{K} \equiv (|\Delta\eta_{jj}|, |\Delta\phi_{jj}|, m_{jj}, MET, \phi_{MET}, \Delta\phi_{MET}^{j_1}$,

Table 53.1 Short description of the different analyses with the expected median upper limit on BR ($h^0 \rightarrow \text{inv}$) at 95% CL for different integrated luminosities

Sl. no	Name	Description	Expected median upper limit on BR($h^0 \rightarrow \text{inv}$)		
			L = 36 fb ⁻¹	L = 140 fb ⁻¹	L = 300 fb ⁻¹
1.	$m_{jj}(\text{MET} > 250 \text{ GeV})$	Reproduced shape analysis of reference [3]	$0.226^{+0.093}_{-0.063}$	$0.165^{+0.082}_{-0.056}$	$0.130^{+0.089}_{-0.027}$
2.	$ \Delta\eta_{jj} (\text{MET} > 250 \text{ GeV})$	$ \Delta\eta_{jj} $ analysis with shape-cuts of reference [3]	$0.200^{+0.080}_{-0.056}$	$0.128^{+0.050}_{-0.036}$	$0.106^{+0.041}_{-0.025}$
3.	$m_{jj}(\text{MET} > 200 \text{ GeV})$	m_{jj} shape analysis with weaker cut	$0.191^{+0.075}_{-0.053}$	$0.116^{+0.071}_{-0.036}$	$0.101^{+0.037}_{-0.045}$
4.	$ \Delta\eta_{jj} (\text{MET} > 200 \text{ GeV})$	$ \Delta\eta_{jj} $ analysis with weaker cut	$0.162^{+0.065}_{-0.045}$	$0.105^{+0.042}_{-0.029}$	$0.087^{+0.034}_{-0.025}$
5.	\mathcal{P}_J^{LR} -CNN	Low-Resolution, $\phi_0 = \phi_{j_1}$	$0.078^{+0.030}_{-0.022}$	$0.051^{+0.020}_{-0.014}$	$0.045^{+0.017}_{-0.013}$
6.	\mathcal{P}_J^{HR} -CNN	High-Resolution, $\phi_0 = \phi_{j_1}$	$0.070^{+0.027}_{-0.020}$	$0.043^{+0.017}_{-0.012}$	$0.035^{+0.013}_{-0.010}$
7.	\mathcal{P}_{MET}^{LR} -CNN	Low-Resolution, $\phi_0 = \phi_{MET}$	$0.092^{+0.037}_{-0.025}$	$0.062^{+0.024}_{-0.017}$	$0.053^{+0.023}_{-0.014}$
8.	\mathcal{P}_{MET}^{HR} -CNN	High-Resolution, $\phi_0 = \phi_{MET}$	$0.086^{+0.035}_{-0.024}$	$0.058^{+0.023}_{-0.016}$	$0.051^{+0.020}_{-0.014}$
9.	\mathcal{K} -ANN	8 kinematic-variables	$0.101^{+0.052}_{-0.022}$	$0.075^{+0.029}_{-0.021}$	$0.063^{+0.027}_{-0.017}$
10.	\mathcal{R} -ANN	16 radiative $H_T^{n_c}$ variables	$0.138^{+0.055}_{-0.039}$	$0.094^{+0.036}_{-0.027}$	$0.079^{+0.032}_{-0.022}$
11.	\mathcal{H} -ANN	Combination of \mathcal{K} and \mathcal{R} variables	$0.094^{+0.038}_{-0.026}$	$0.065^{+0.026}_{-0.018}$	$0.057^{+0.022}_{-0.015}$

$\Delta\phi_{MET}^{j_2}, \Delta\phi_{MET}^{j_1+j_2}$). The second class consists of the scalar sum of E_T in cumulative η bins: $\mathcal{R} \equiv (H_T^{\eta_C} | \eta_C \in \mathcal{E})$, where $H_T^{\eta_C} = \sum_{\eta < |\eta_C|} E_T$, and \mathcal{E} is the set of chosen η_C 's. We vary η_C uniformly in the interval [1, 5] to get 16 $H_T^{\eta_C}$ variable. We also combined these two features spaces and call the corresponding 24-dimensional space as \mathcal{H} .

53.4 Results

We train CNNs for the low-level tower images and densely connected Artificial Neural Networks (ANNs) for the high-level feature spaces. We perform shape-analysis using the m_{jj} and $\Delta\eta_{jj}$ distributions for both the selection cuts used in the deep learning analysis as well as with the harder cut ($MET > 250$ GeV). The expected upper limits on the invisible branching ratios for the different networks and variables for three integrated luminosities are shown in Table 53.1. We see that CNN-based analyses provide the most stringent bounds, while the other ANNs perform better than the single variable shape analyses. We see that the resolution does not make much of a difference to the performance, however, there is a minute difference between the two preprocessing schemes. This can be attributed to the fact that there is better feature regularization for $\phi_{j_i} = 0$.

References

1. S.T.Y. Dokshitzer, V. Khoze, "Proceedings of the international conference," Physics in Collision VI, (Chicago, Illinois) (World Scientific, Singapore, 1986), p. 365
2. V.S. Ngairangbam, A. Bhardwaj, P. Konar, A.K. Nayak, Eur. Phys. J. C **80**(11), 1055 (2020)
3. A.M. Sirunyan et al., CMS. Phys. Lett. B **793**, 520–551 (2019)
4. J. Alwall, R. Frederix, S. Frixione, V. Hirschi, F. Maltoni, O. Mattelaer, H.S. Shao, T. Stelzer, P. Torrielli, M. Zaro, JHEP **07**, 079 (2014)
5. T. Sjöstrand, S. Ask, J.R. Christiansen, R. Corke, N. Desai, P. Ilten, S. Mrenna, S. Prestel, C.O. Rasmussen, P.Z. Skands, Comput. Phys. Commun. **191**, 159–177 (2015)
6. J. de Favereau et al., DELPHES 3. JHEP **02**, 057 (2014)

Part II
Relativistic Heavy-Ion Collisions and
Quantum Chromodynamics

Chapter 54

Temperature Fluctuations and Tsallis Statistics in Relativistic Heavy Ion Collisions



Abhisek Saha and Soma Sanyal

Abstract We study temperature fluctuations in the initial stages of the relativistic heavy ion collision using A Multi-Phase Transport (AMPT) model. We use the non-extensive Tsallis statistics to find the entropic index in the partonic stages of the relativistic heavy ion collisions. We find that the temperature and the entropic index have a linear relationship in the partonic stages of the collision. This is in agreement with the experimental observations in the hadronic phase. A detailed analysis of the dependence of the entropic index on the system parameters is done. Our study indicates that the entropic index can be used to study temperature fluctuations in the initial stages of heavy ion collision system

At extremely high temperatures and pressures, matter undergoes a confinement–deconfinement phase transition and produces strongly interacting matter known as Quark–Gluon plasma (QGP). Heavy ion collision experiments have successfully reproduced this strongly interacting deconfined state of matter and since then it has been a major topic of study over the past few decades. Theoretical models have been developed to describe the heavy ion collision events. The QGP which is in a non-equilibrium state just after the collision does reach equilibrium after subsequent evolution. The AMPT model can describe the whole heavy ion collision event [1]. But in our study, we constrained ourselves to the initial stages of the collision only.

In the initial stages, this plasma is highly unstable and far from equilibrium. We get a lot of fluctuations in terms of initial geometry and number density of the produced particles. We are particularly interested in studying temperature fluctuations. In the case of experiments, the temperature is extracted by fitting the transverse momentum spectra to standard statistical distributions [2]. But this way, we only get the transition temperature. To get the temperature profile, we use the AMPT model. AMPT gives the initial individual particle’s position and momenta. We take the initial position of the particles and coarse-grain them into cells according to the positions. We calculate

A. Saha (✉) · S. Sanyal
University of Hyderabad, Hyderabad 500046, India
e-mail: 17phph12@uohyd.ac.in

© The Author(s), under exclusive license to Springer Nature Singapore Pte Ltd. 2022
B. Mohanty et al. (eds.), *Proceedings of the XXIV DAE-BRNS High Energy Physics Symposium, Jatni, India*, Springer Proceedings in Physics 277,
https://doi.org/10.1007/978-981-19-2354-8_54

299

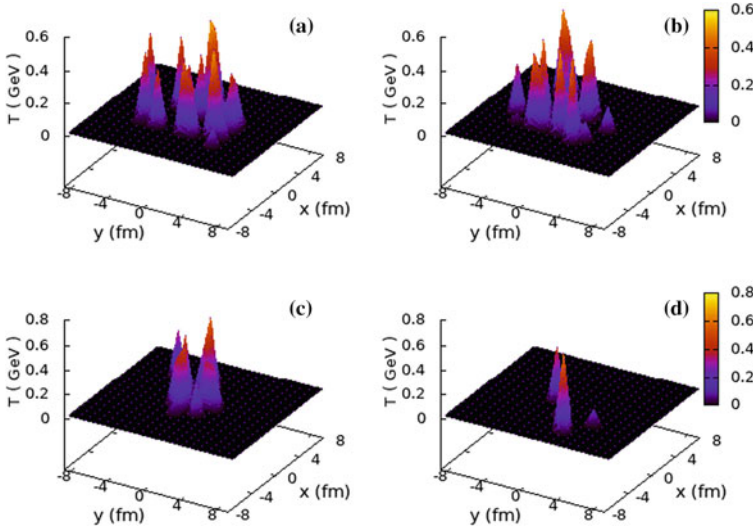


Fig. 54.1 Temperature fluctuations at times **a** 1 fm/c **b** 2 fm/c **c** 3 fm/c **d** 5fm/c at $\sqrt{s} = 200$ GeV

the initial energy density and the temperature is then calculated using [4] $\epsilon(x, y) = 12(4 + 3N_f) \left(\frac{T^4}{\pi^2}\right)$.

Figure 54.1 shows the temperature fluctuations of randomly selected events at different times. By the time, we mean here the proper time at formation of the partons and not the evolution time. This has been observed at a collision energy of 200 GeV. We get more fluctuations in the initial phases and at later times, the number of fluctuations decreases. We did a similar observation on temperature fluctuation as a function of collision energy in the initial stages. We see that the number of fluctuating components remains constant but the average amplitude increases for the higher collision energies. We want to represent this behavior of temperature fluctuation with a parameter. We chose the entropic index (q) to serve this purpose. q is the anisotropy index in the Tsallis distribution, a generalized form of Boltzmann distribution. $q \rightarrow 1$ gives us the equilibrium distribution.

If a system has fluctuating temperature, then the distribution function can be expressed using the non-extensive parameter q . This can also be expressed as an integration over all the fluctuating β states provided the β 's follows χ^2 distribution [3]. This has been illustrated in (54.1).

$$(1 + (q - 1)\beta_0 H)^{-\frac{1}{q-1}} = \int_0^\infty e^{-\beta H} f(\beta) d\beta \tag{54.1}$$

Here, H is the Hamiltonian of the system and the χ^2 distribution is given by

Fig. 54.2 The plot of β for the power spectrum of temperature fluctuations. The value of $(q - 1)$ is obtained by fitting a χ^2 distribution to the plot

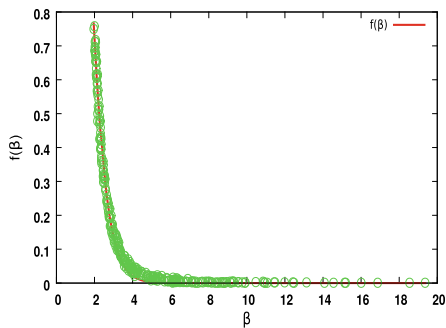
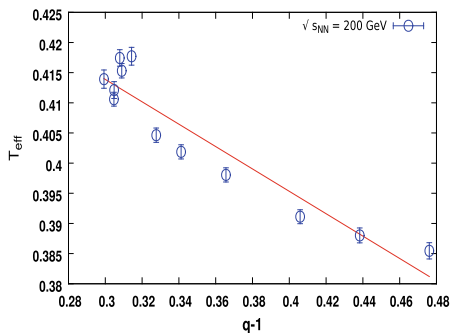


Fig. 54.3 The plot shows the dependence of the effective temperature T_{eff} on the values of q at a collision energy of $\sqrt{s} = 200$ GeV



$$f(\beta) = \frac{1}{\Gamma\left(\frac{1}{(q-1)}\right)} \left(\frac{1}{(q-1)\beta_0}\right)^{\frac{1}{(q-1)}} \beta^{\frac{1}{q-1}-1} \exp\left(\frac{-\beta}{(q-1)\beta_0}\right) \quad (54.2)$$

Here, q is the entropic index and β_0 is the average of the fluctuating β states.

As our system also has temperature fluctuation, we fit the fluctuating β states of our system with the χ^2 distribution given in (54.2). The plot is shown in Fig. 54.2. We obtained a good fit for our temperature fluctuation states. q and β_0 are obtained after suitable fitting. β_0 can be obtained by taking an average over all the fluctuating states, $E(\beta) = \int_0^\infty \beta f(\beta) d\beta$. q can be calculated from the relative variance of the fluctuating temperature states $q - 1 = \frac{E(\beta^2) - E(\beta)^2}{E(\beta)^2}$.

The q value measures how far the system is from equilibrium [3]. q value obtained in this way is higher compared to the q values obtained in the experiments. But in experiments, the q value is obtained by fitting the transverse momentum spectra to the Tsallis distribution [2]. This deals with the final state particle distribution where fluctuations are already diminished due to the presence of various flows. In the initial stage, we expect a lot more fluctuation. Hence, a higher q value is not surprising.

We have obtained q versus T_{eff} plot to check similarities with the experiments which is shown in Fig. 54.3. We get a linear relationship between q and T_{eff} which is also obtained from the Tsallis distribution in experimental observations [5]. We have a range of slopes for Pb–Pb collision to Au–Au collision [5] and p–p collisions which

Fig. 54.4 This plot shows the variation of q for different \sqrt{s} values at different centralities

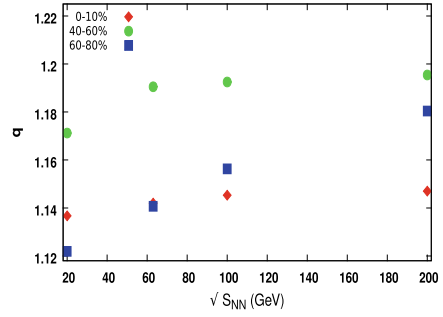
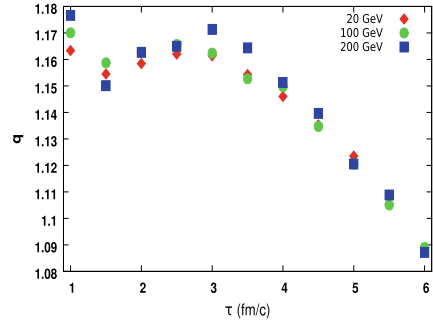


Fig. 54.5 This plot shows the variation of (q) with proper time (τ) at different collision energies (\sqrt{s})



depend on the type of system being used. But effectively, we always find a linear relationship. This emphasizes that the q value can be obtained from the temperature fluctuations.

To study further, we checked the various system parameter dependencies of the q value obtained in this manner. In Fig. 54.4, we have plotted q with respect to collision energies in the range of 20–200 GeV at different centralities. We find that at lower collision energies the Tsallis entropic index is lower. For peripheral collisions (60%–80%), the q values are lower than the q value at central collision (0–10%) below 100 GeV. Above 100 GeV, the opposite is true. This change in trend is also observed in recent studies at collision energies 30–40 GeV [6], whereas we get this around 50–60 GeV.

We have plotted entropic index q with respect to the proper time in Fig. 54.5. Here, time represents the formation time of partons. As we are interested in the initial stage fluctuation, we have only worked with the partons just after their formation. As can be seen from the graph, q increases with the proper time, peaks around 3 fm/c, and then decreases with increasing τ . The increase and subsequent decrease of the q value may be attributed to the increase and decrease in the energy density of the particles in the AMPT model. The interesting thing is, similar behavior has been observed while studying temperature fluctuations where fluctuations are seen to be decreased in later stages.

In the case of the evolution of the system, we expect the equilibrium to be achieved much earlier than the time shown here. Also, in this case, we get lower q values at a higher time which implicates fewer fluctuations. This is also observed in Fig. 54.1, where several fluctuations have been seen to be decreased with time.

To summarize, the temperature fluctuations of an out of equilibrium system are studied using the Tsallis statistics. The β obtained from our simulations is fitted with a χ^2 distribution and then used to obtain the entropic index q .

We have obtained the T_{eff} versus q relation which gives a linear relationship much like the observations from the experiments. We have checked the dependency of the entropic index on the system parameters, e.g., the collision energy and the centrality of collisions. The most encouraging result is the decrease in entropic index with time. This replicates the behavior of temperature fluctuations which also decreases with time. Hence, we can use the entropic index to describe temperature fluctuations in a heavy ion collision system. Also, this can be an effective way of calculating the entropic index in the initial stages of heavy ion collision.

We acknowledge the CMSD at the University of Hyderabad. A. S is supported by DST INSPIRE Fellowship, Grant no: IF170627.

References

1. Z.-W. Lin et al., Phys. Rev. C **72**, 064901 (2005)
2. Rui-Fang Si et al., Advances in High Energy Physics 2018 (2018)
3. Christian Beck. EPL (Europhysics Letters) 57.3 (2002), p. 329
4. Y. Zhang et al., Phys. Rev. C **96**, 044914 (2017)
5. Grzegorz Wilk et al., Phys. Rev. C **79**(5), 054903 (2009)
6. Rajendra Nath Patra et al., (2020). [arXiv:2008.02559](https://arxiv.org/abs/2008.02559)

Chapter 55

Open-Charm Mesons in Magnetized Asymmetric Strange Hadronic Matter



C. S. Amal Jahan and Amruta Mishra

Abstract The in-medium masses of the open-charm mesons such as $D(D^0, D^+)$, $\bar{D}(\bar{D}^0, D^-)$, and $D_s(D_s^+, D_s^-)$ are investigated in strongly magnetized isospin asymmetric strange hadronic matter. A chiral $SU(3)$ Lagrangian model based on a non-linear realization of chiral symmetry and the broken scale invariance of QCD is generalized to chiral $SU(4)$ to derive the interactions of the charmed mesons with the light hadronic sector. The mass modifications of open-charm mesons arise due to their interactions with nucleons, hyperons, and the scalar fields (the non-strange field σ , strange field ζ and, isovector field δ) in the magnetized medium. In the presence of the magnetic field, the number density and scalar density of charged baryons have contributions from Landau energy levels. We have incorporated the effects of strangeness fraction as well as anomalous magnetic moments of baryons in this study.

55.1 Introduction

The properties of strongly interacting matter under the effect of strong magnetic fields have recently received significant interest due to the phenomenological relevance in the relativistic heavy ion collisions. The strength of the magnetic fields in such experiments could be as large as $eB \sim 2m_\pi^2 \sim 6 \times 10^{18}$ Gauss in the Relativistic Heavy Ion Collider (RHIC) at Brookhaven National Laboratory (BNL) and $eB \sim 15m_\pi^2 \sim 10^{19}$ Gauss in the Large Hadron Collider (LHC) at CERN [1, 2]. Since the production of charm quarks takes place at the early stages of the collision, the charm quark systems are sensitive to the magnetic fields [3]. Hence these magnetic fields can modify the properties of open-charm mesons at high baryon densities and/or temperature, resulting from these ultra-relativistic high energy nuclear collisions.

C. S. Amal Jahan (✉) · A. Mishra
Department of Physics, Indian Institute of Technology Delhi, Hauz Khas,
New Delhi 110016, India
e-mail: amaljahan@gmail.com

© The Author(s), under exclusive license to Springer Nature Singapore Pte Ltd. 2022
B. Mohanty et al. (eds.), *Proceedings of the XXIV DAE-BRNS High Energy Physics Symposium, Jatni, India*, Springer Proceedings in Physics 277,
https://doi.org/10.1007/978-981-19-2354-8_55

305

As these experiments involve nuclei that have an excess of neutrons than the number of protons, we have considered an isospin asymmetric hadronic matter in the present investigation.

We shall follow a chiral effective Lagrangian approach based on the symmetries and symmetry breaking pattern of QCD. The spontaneous breaking of chiral symmetry in QCD leads to non-vanishing chiral condensates. The scale invariance of QCD is broken by quantum effects where the non-vanishing contributions from the gluon condensate leads to a non-zero trace for energy–momentum tensor. The chiral condensates and gluon condensates undergo modification in the magnetized medium. As the hadrons interact with these condensates, their in-medium properties are also subjected to modifications in the presence of the magnetic field. In the chiral effective model, the scalar fields (σ , ζ , δ) are associated with the chiral condensates and the dilaton field χ is associated with gluon condensates [4, 5].

55.2 In-Medium Masses of the Open-Charmed Mesons

The Hadronic Lagrangian density in chiral effective model [4, 5] is given as

$$\mathcal{L} = \mathcal{L}_{kin} + \sum_W \mathcal{L}_{BW} + \mathcal{L}_{vec} + \mathcal{L}_0 + \mathcal{L}_{scalebreak} + \mathcal{L}_{SB} + \mathcal{L}_{mag}, \quad (55.1)$$

In this equation, \mathcal{L}_{kin} refers to the kinetic energy term of the hadrons. \mathcal{L}_{BW} is the baryon–meson interaction term, where the index W covers both spin-0 and spin-1 mesons. The baryons we consider in our study are neutrons, protons, Λ , Σ^- , Σ^0 , Σ^+ , Ξ^- , and Ξ^0 . \mathcal{L}_{vec} concerns the dynamical mass generation of the vector mesons. \mathcal{L}_0 contains the meson–meson interaction terms introducing the spontaneous breaking of chiral symmetry and $\mathcal{L}_{scalebreak}$ incorporates the scale invariance breaking of QCD through a logarithmic potential given in terms of scalar dilaton field χ . \mathcal{L}_{SB} corresponds to the explicit chiral symmetry breaking term and \mathcal{L}_{mag} is the contribution by the magnetic field.

We then use mean-field approximation, where fermions are treated as quantum fields and mesons are treated as classical fields. From the mean-field Lagrangian density, the coupled equations of motion for the scalar fields and vector meson fields are obtained in terms of scalar densities and number densities of baryons, respectively. The magnetic field introduce summation over Landau levels in the expressions of number density and scalar density of charged baryons [4, 5]. The equations of motion for scalar fields and vector meson fields are solved as functions of the baryon density at different magnetic fields for isospin asymmetric nuclear matter as well as strange hadronic matter.

The interaction Lagrangian density of the open-charm mesons with the hadronic medium, contains the vectorial Weinberg–Tomozawa term, the scalar-exchange term arising from the explicit symmetry-breaking term, first range term, the d_1 and d_2

range terms [4–6]. From the Fourier transforms of the equations of motion for the corresponding mesons, we obtain their dispersion relation which is given as

$$-\omega^2 + \mathbf{k}^2 + m_j^2 - \Pi_j(\omega, |\mathbf{k}|) = 0 \quad (55.2)$$

Here, the index j denotes the various open-charm mesons D , \bar{D} and D_s and m_j is their corresponding vacuum mass. $\Pi_j(\omega, |\mathbf{k}|)$ denotes the self-energy of the mesons in the medium and it depends on the values of scalar fields, number densities, and scalar densities of the baryons in the magnetized medium. These dispersion relations are solved at various values of magnetic fields and baryon density to obtain the masses of the neutral open-charm mesons ($j = D^0, \bar{D}^0$). In the case of the charged open-charm mesons ($j = D^+, D^-, D_s^+, D_s^-$), they have additional positive mass modification in magnetic fields which, retaining only the lowest Landau level, is given as

$$m_j^{eff} = \sqrt{m_j^{*2} + |eB|} \quad (55.3)$$

where m_j^* are solutions for ω at $|\mathbf{k}| = 0$ of the dispersion relations given by (55.2).

55.3 Results and Discussion

The in-medium masses of the open-charm mesons, plotted as function of ρ_B/ρ_0 (where ρ_B is the baryon density and ρ_0 is the nuclear matter saturation density) in Fig. 55.1, are obtained after solving the corresponding dispersion relations using the values of scalar fields, scalar densities, and number densities of baryons. For a fixed value of magnetic field, when the effects of the anomalous magnetic moment of baryons are taken into account, the magnitude of scalar fields σ , ζ , and χ are observed to drop as baryon density increases, whereas δ tends to saturate at large density. The in-medium masses of open-charm mesons are observed to drop with an increase in baryon density. This is due to the attractive d_1 , d_2 , and scalar meson exchange terms whose magnitude grows with density. The D , \bar{D} and D_s^+ mesons experience a larger mass drop in the magnetized strange hadronic matter compared to the pure nuclear matter, whereas D_s^- exhibits an opposite behavior at low densities. The effects of strangeness fraction are found to be more dominant for the \bar{D} and D_s mesons as compared to the D mesons. In the hyperonic medium, the mass degeneracy of the D_s mesons is observed to be broken, due to the appearance of the Weinberg–Tomozawa interaction term. This mass degeneracy grows with an increase in baryon density and strangeness fraction of the medium.

The presence of the magnetic field modifies the values of the scalar fields and the scalar densities of baryons and hence results in the mass modifications of open-charm mesons. Moreover, through the Landau quantization effect, the charged D^+ ,

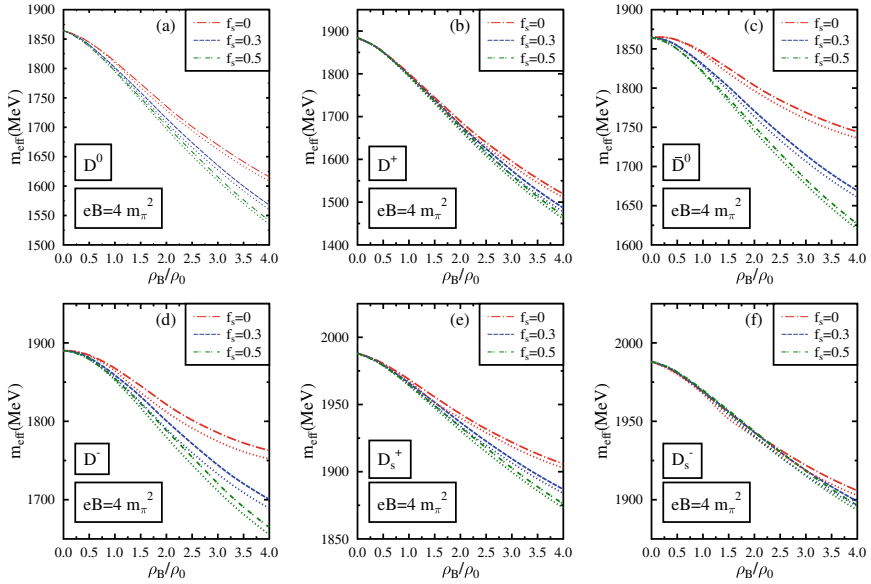


Fig. 55.1 The effective masses of $D(D^0, D^+)$, $\bar{D}(\bar{D}^0, D^-)$, and $D_s(D_s^+, D_s^-)$ mesons in MeV, plotted as function of ρ_B/ρ_0 (where ρ_B is the baryon density and ρ_0 is the nuclear matter saturation density) for nuclear ($f_s = 0$), and hyperonic ($f_s = 0.3, 0.5$) matter situations at magnetic field $eB = 4m_\pi^2$, for isospin asymmetry parameter ($\eta = 0.5$), when the effects of anomalous magnetic moment (AMM) are taken into account (dashed lines), and compared to the case when the effects of AMM are not taken into account (dotted line)

D^- , D_s^+ , and D_s^- mesons have additional positive mass shifts in the presence of the magnetic field. This effect becomes more significant for D_s mesons since their mass modification from baryon density is relatively small as compared to D and \bar{D} mesons. A detailed analysis and discussion of our results are given in [5]. In the present investigation of the study of open-charm mesons, the dominant medium effect is due to the density as compared to the magnetic field which should have observable consequences in the D^+/D^0 , D^-/\bar{D}^0 , and D_s^+/D_s^- ratios in asymmetric heavy ion collisions in Compressed Baryonic Matter (CBM) experiments at FAIR at the future facility of GSI.

Acknowledgements A.J.C.S acknowledges the support towards this work from the Department of Science and Technology, Government of India, via an INSPIRE fellowship (INSPIRE Code IF170745). AM acknowledges financial support from Department of Science and Technology (DST), Government of India (project no.CRG/2018/002226).

References

1. D. Kharzeev, L. McLerran, H. Warringa, The effects of topological charge change in heavy ion collisions: “Event by event P and CP violation”. Nucl. Phys. A **803**, 227–253 (2008). <https://doi.org/10.1016/j.nuclphysa.2008.02.298>
2. V. Skokov, A. Y. Illarionov, V. Toneev, Estimate of the magnetic field strength in heavy-ion collisions. Int. J. Mod. Phys. A **24**, 5925–5932 (2009). <https://doi.org/10.1142/S0217751X09047570>
3. S. Cho, K. Hattori, S.H. Lee, K. Morita, S. Ozaki, QCD sum rules for magnetically induced mixing between η_c and J/ψ . Phys. Rev. Lett. **113**, 172301 (2014). <https://doi.org/10.1103/PhysRevLett.113.172301>
4. P.S. Reddy, C.S. Amal Jahan, N. Dhale, A. Mishra, J. Schaffner-Bielich, D mesons in strongly magnetized asymmetric nuclear matter. Phys. Rev. C **97**, 065208 (2018). <https://doi.org/10.1103/PhysRevC.97.065208>
5. C.S. Amal Jahan, Amruta Mishra, Open-charm mesons and Charmonia in magnetized strange hadronic matter. [arXiv: 2101.08568](https://arxiv.org/abs/2101.08568) to be published in Chin. Phys. C. <https://doi.org/10.1088/1674-1137/ac6b92>
6. D. Pathak, A. Mishra, D_s mesons in asymmetric hot and dense hadronic matter. Adv. High Energy Phys. 697514 (2015). <https://doi.org/10.1155/2015/697514>

Chapter 56

In-Medium Properties of Heavy Quarkonia



Amruta Mishra

Abstract We discuss the in-medium properties of the heavy quarkonium states, specifically, the medium modifications of the masses of the heavy quarkonia and the partial decay widths of charmonium (bottomonium) state to $D\bar{D}$ ($B\bar{B}$). The medium effects considered are due to the density, temperature, isospin asymmetry, strangeness fraction and magnetic field. The partial decay widths of the heavy quarkonium states are studied using a field theoretical model for composite hadrons with quark (and antiquark) constituents, as well as, using a light quark pair model, namely, the 3P_0 model. The in-medium decay widths are computed from the mass modifications of the hidden and open heavy flavour mesons, calculated using a chiral effective model. The density effects are observed to be the dominant medium effects as compared to the effects from the isospin asymmetry, temperature and strangeness fraction of the medium. In the presence of a strong magnetic field, the mixing of the pseudoscalar and the longitudinal component of the vector charmonium states is observed to lead to substantial modifications to the masses of these states, which is observed to lead to an increase in the decay width of $\psi(3770) \rightarrow D\bar{D}$, dominantly to the neutral $D\bar{D}$ pair, at large values of the magnetic fields.

56.1 Introduction

There have been a lot of studies in the recent years on the in-medium properties of the heavy flavour mesons [1] due to their relevance in high-energy heavy ion collision experiments. These have been studied extensively in the literature using the potential models, the QCD sum rule approach, the Quark Meson coupling (QMC) model, the coupled channel approach and a chiral effective model. The estimation of the magnetic fields created in non-central ultra-relativistic heavy ion collision experiments at RHIC and LHC to be huge [2] has also initiated a lot of work on the study of the effects of magnetic fields on the properties of the hadrons. The heavy

A. Mishra (✉)

Department of Physics, Indian Institute of Technology, Delhi 110016, New Delhi, India
e-mail: amruta@physics.iitd.ac.in

© The Author(s), under exclusive license to Springer Nature Singapore Pte Ltd. 2022
B. Mohanty et al. (eds.), *Proceedings of the XXIV DAE-BRNS High Energy Physics Symposium, Jatni, India*, Springer Proceedings in Physics 277,
https://doi.org/10.1007/978-981-19-2354-8_56

311

quarkonium states are nonrelativistic systems comprising of a heavy quark (Q) and heavy antiquark (\bar{Q}), which have been studied quite successfully by solving the Schrödinger equation using the Cornell potential. At finite temperature, for $T > T_c$, the Q - \bar{Q} potential is screened in the presence of quark–gluon plasma (QGP) [3] and the Debye-screened Cornell potential is often used to study the quarkonium state in the thermal partonic medium. As temperature increases, the Debye screening length, $r_D(T)$ decreases and, when $r_D(T)$ becomes smaller than the binding radius, the quarkonium state can no longer stay as a bound state. This leads to a sequential dissociation of the quarkonium states, with the excited states, due to their larger binding radii, dissociating earlier than the ground state. The heavy quarkonium state studied in the presence of a gluon field [4] shows that the mass shift of the quarkonium state is proportional to the medium modification of the scalar gluon condensate. This is the leading order result with the assumption that the Q - \bar{Q} separation is small as compared to the scale of the gluonic fluctuations and the Q and \bar{Q} are bound by colour Coulomb potential. Using the leading order formula, the mass modifications of the charmonium states have been studied [5, 6] using the linear density approximation for the gluon condensate [5], as well as computing the gluon condensate in a chiral effective model from the medium change of a dilaton field, which simulates the gluon condensate in the effective hadronic model [6]. These studies show that the mass shifts for the excited charmonium states are much larger as compared to the mass shift of J/ψ in the hadronic medium. The attractive interaction of J/ψ (η_c) in the nuclear medium has also led to the conjecture of the possibility of J/ψ (η_c) bound in atomic nuclei [7].

We organize the paper as follows. In Sect. 56.2, we discuss the medium modifications of the masses of the hidden and open heavy flavour mesons calculated using a chiral effective model and their effects on the partial decay widths of the heavy quarkonium states to the open heavy flavour mesons. In Sect. 56.3, we summarize the results and discuss possible outlook.

56.2 In-Medium Masses and Decay Widths of the Heavy Quarkonium States

The in-medium masses of the open and hidden heavy flavour mesons are calculated using a chiral effective model. The model is based on a non-linear realization of chiral symmetry and incorporates broken scale invariance of QCD. The mass modifications of the heavy quarkonia in the model arise due to medium modification of a scalar dilaton field, χ , which mimics the gluon condensates of QCD. In the hadronic medium, the masses of the open heavy flavour mesons (D , \bar{D} , B and \bar{B}), arise due to their interactions with the baryons and the scalar mesons (σ , ζ and δ), and, are calculated by solving the dispersion relations for these mesons for $|\mathbf{k}| = \mathbf{0}$. In the mean-field approximation, the medium-dependent values of the scalar fields, σ , ζ , δ and χ are obtained from the solution of the coupled equations of motion of these fields. In the

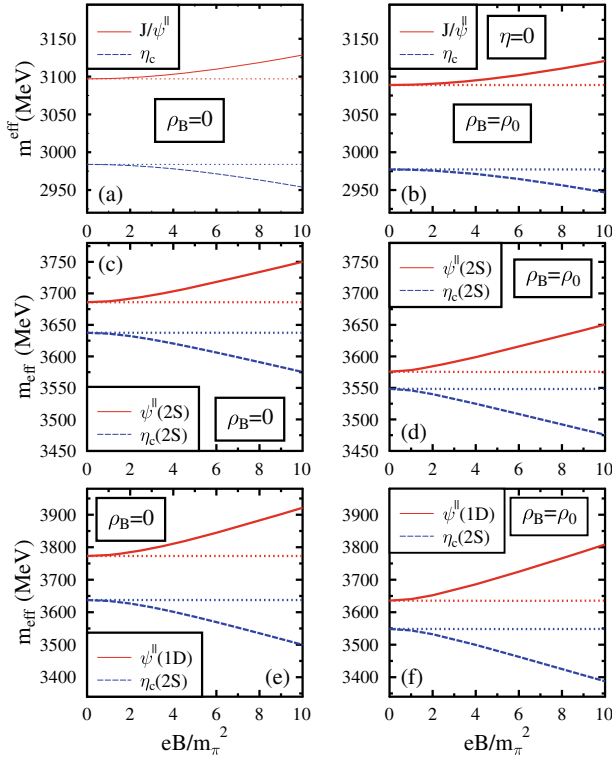


Fig. 56.1 The masses of the pseudoscalar mesons ($\eta_c \equiv \eta_c(1S)$ and $\eta'_c \equiv \eta_c(2S)$) and the longitudinal components of the vector charmonium states (J/ψ , $\psi(2S) \equiv \psi(3686)$, $\psi(1D) \equiv \psi(3770)$) are plotted as functions of eB/m_π^2 for $\rho_B = 0$ and for $\rho_B = \rho_0$ in symmetric ($\eta = 0$) nuclear matter. These are compared to the case of not including the mixing effects (shown as dotted lines)

presence of a magnetic field, the number and scalar densities of the charged baryons have contributions from the Landau levels [8, 9]. This leads to modifications of the values of the scalar fields, and hence of the masses of the heavy flavour mesons in the presence of a magnetic field. The lowest Landau-level contributions are also taken into account for the calculation of the masses of the charged open heavy flavour mesons in the presence of a magnetic field [8, 9]. The in-medium decay widths of the heavy quarkonium states to the open heavy flavour meson pairs are calculated from the mass modifications of these mesons in the medium. Using a light quark pair creation model, namely, the 3P_0 model, the in-medium decay widths of charmonium states to $D\bar{D}$ pairs were computed using the mass modifications of the open-charm mesons in [10]. The model is based on a light quark–antiquark pair ($q\bar{q}$) creation in the 3P_0 state, the light quark (antiquark) combines with the heavy charm antiquark (quark) to produce the $D\bar{D}$ pair. The masses of the charmonium states (Ψ) and open-charm states (D and \bar{D}) as well as the decay widths of $\Psi \rightarrow D\bar{D}$, using the 3P_0 model, have been studied in the isospin asymmetric hot strange hadronic

matter [6] and in magnetized nuclear matter [11]. A field-theoretic model of composite hadrons has also been used to calculate the in-medium decay widths of heavy quarkonia to open heavy flavour meson pairs [12, 13]. The model uses the Dirac Hamiltonian as the light quark–antiquark pair creation, and explicit constructions of the charmonium (bottomonium) state as well as of open-charm (bottom) mesons. The in-medium decay widths depend on the the magnitude of the momentum of the outgoing mesons, $|\mathbf{p}|$, as a polynomial part multiplied by an exponential part in the 3P_0 model as well as in the field-theoretic model of composite hadrons, which is observed to lead to vanishing of the decay width at certain densities [6, 10, 12, 13]. An appreciable difference in the decay widths of heavy quarkonium state to the charged and neutral $D\bar{D}$ ($B\bar{B}$) final states in asymmetric strange hadronic matter is observed arising due to isospin asymmetry of the medium at high densities [6]. The mass of the longitudinal component of the vector (pseudoscalar) meson has appreciable increase (drop) due to the mixing of the pseudoscalar (P) and vector (V) charmonium states in the presence of strong magnetic fields [14–16], as may be seen from Fig. 56.1 [16]. In the presence of strong magnetic fields, there is observed to be significant increase in the decay width of $\psi(3770) \rightarrow D\bar{D}$ [16].

56.3 Summary and Outlook

The in-medium masses of the heavy quarkonium states and the open heavy flavour mesons in the (magnetized) medium are calculated within a chiral effective model, and their effects on the decay widths of the heavy quarkonium state to open heavy flavour meson pairs have been studied. The isospin asymmetry effects were observed to be large at high densities, should have observable consequences in the production of the hidden and open heavy flavour mesons in the asymmetric heavy ion collisions in Compressed baryonic matter (CBM) experiments planned at the future facility at FAIR, GSI. The mass modifications due to PV mixing as well as the (lowest) Landau contribution to the masses of the charged open-charm mesons are observed to lead to an appreciable increase in the decay width of $\psi(3770) \rightarrow D\bar{D}$, dominantly to the neutral $D\bar{D}$ final state, at large magnetic fields. The medium modifications of the masses and decay widths of the heavy quarkonium states should show in the production of the hidden and open heavy flavour mesons in relativistic heavy ion collision experiments.

Acknowledgements The author acknowledges financial support from the Department of Science and Technology (DST), Government of India (project no. CRG/2018/002226).

References

1. A. Hosaka, T. Hyodo, K. Sudoh, Y. Yamaguchi, S. Yasui, *Prog. Part. Nucl. Phys.* **96**, 88 (2017)
2. K. Tuchin, *Adv. High Energy Phys.* **2013**, 490495 (2013)
3. T. Matsui, H. Satz, *Phys. Lett. B* **178**, 416 (1986)
4. M.E. Peskin, *Nucl. Phys. B* **156**, 365 (1979)
5. S. Houng Lee, C. Ming Ko, *Phys. Rev. C* **67**, 038202 (2003)
6. A. Kumar, A. Mishra, *Eur. Phys. A* **47**, 164 (2011)
7. G. Krein, A.W. Thomas, K. Tsushima, *Prog. Part. Nucl. Phys.* **100**, 161 (2018)
8. P. Sushruth Reddy, C.S. Amal Jahan, N. Dhale, A. Mishra, J. Schaffner-Bielich, *Phys. Rev. C* **97**, 065208 (2018)
9. N. Dhale, P. Sushruth Reddy, C.S. Amal Jahan, A. Mishra, *Phys. Rev. C* **98**, 015202 (2018)
10. B. Friman, S.H. Lee, T. Song, *Phys. Lett. B* **548**, 153 (2002)
11. A. Mishra, C.S. Amal Jahan, S. Kesarwani, H. Raval, S. Kumar, J. Meena, *Eur. Phys. J. A* **55**, 99 (2019)
12. A. Mishra, S.P. Misra, W. Greiner, *Int. J. Mod. Phys. E* **24**, 155053 (2015)
13. A. Mishra, S.P. Misra, *Phys. Rev. C* **95**, 065206 (2017)
14. S. Cho, K. Hattori, S.H. Lee, K. Morita, S. Ozaki, *Phys. Rev. Lett.* **113**, 122301 (2014); S. Cho, K. Hattori, S.H. Lee, K. Morita, S. Ozaki, *Phys. Rev. D* **91**, 045025 (2015)
15. J. Alford, M. Strickland, *Phys. Rev. D* **88**, 105017 (2013)
16. A. Mishra, S.P. Misra, *Phys. Rev. C* **102**, 045204 (2020)

Chapter 57

NLL Resummation of Recoil-Sensitive Angularities Using SCET



Ankita Budhraj, Ambar Jain, and Massimiliano Procura

Abstract Jet angularities are a class of event shapes that are designed to measure the energy flow into angular regions of phase space between energetic jets. Angularity description relies on a free parameter b ($b > -1$) such that varying the exponent b changes the sensitivity of the observable to the substructure of the jet. For angularities measured relative to the thrust axis, the observable is sensitive to the recoil of collinear parton due to soft radiation when b is close to 0, while for $b \rightarrow 1$ recoil is power suppressed. Based on the unified framework of SCET_{II}, we discuss the key one-loop results for jet angularity distributions and present the renormalization group structure for $b < 0$ angularities.

57.1 Introduction

Jet observables in QCD often demand perturbative resummations to be under calculational control to provide useful theoretical interpretations, which can be compared with experimental data. In the framework of the Soft Collinear Effective Theory (SCET) [1], the resummation of these large logarithms at the fixed order is generally achieved by solving the renormalization group evolution equations (RGEs). For jet observables described by SCET_I, the resummation is accomplished by the use of standard ultraviolet (UV) RGE as the modes can be separated purely by dimensional regularization, while for problems falling in the domain of SCET_{II}, a new RGE is essential to appropriately resum all the large logarithms. This is achieved by the use of rapidity renormalization group (RRG) flow [2].

A. Budhraj (✉)

Tata Institute of Fundamental Research, Mumbai 400005, Maharashtra, India
e-mail: ankita.budhraj@tifr.res.in

A. Jain

Indian Institute of Science Education and Research, Bhopal 462066, Madhya Pradesh, India

M. Procura

Fakultät für Physik, Universität Wien, Boltzmanngasse 5, 1090 Wien, Austria

© The Author(s), under exclusive license to Springer Nature Singapore Pte Ltd. 2022
B. Mohanty et al. (eds.), *Proceedings of the XXIV DAE-BRNS High Energy Physics Symposium, Jaiti, India*, Springer Proceedings in Physics 277,
https://doi.org/10.1007/978-981-19-2354-8_57

317

In this paper, we focus on a specific class of jet observables known as angularities [3], which are defined as

$$\tau = \frac{1}{Q} \sum_{i \in X} |p_{\perp i}| e^{-b|\eta_i|}, \quad (57.1)$$

where η_i is the rapidity of the i th final-state particle and $p_{\perp i}$ its transverse momentum, with respect to the thrust axis [4] of an $e^+ e^-$ event with hadronic final state.

Angularities are a generalization of the classic jet observables thrust and jet broadening given by the limits $b = 1$ and $b = 0$, respectively. For angularities, the recoil effects of a collinear parton with a soft parton are power suppressed when b is close to the thrust limit (i.e., $b \gtrsim 1$), while as $b \rightarrow 0$, the recoil becomes an $\mathcal{O}(1)$ effect and cannot be ignored. This implies that jet angularities interpolate between recoil-sensitive and recoil-insensitive jet observables thereby providing a novel tool to understand the transition between SCET_I and SCET_{II}-type theories.

In [5], a unified framework was developed to obtain the one-loop angularity cross section for the entire range of b values, taking into account the recoil effects. The differential cross section is obtained following the factorization formula

$$\frac{1}{\sigma_0} \frac{d\sigma}{d\tau_L d\tau_R} = H(Q; \mu) \int d\tau_n d\tau_{\bar{n}} d\tau_n^s d\tau_{\bar{n}}^s \delta(\tau_R - \tau_n - \tau_n^s) \delta(\tau_L - \tau_{\bar{n}} - \tau_{\bar{n}}^s) \int d\mathbf{p}_{\perp}^2 d\mathbf{k}_{\perp}^2 \mathcal{J}(\tau_n, \mathbf{p}_{\perp}^2; \mu, \nu) \mathcal{J}(\tau_{\bar{n}}, \mathbf{k}_{\perp}^2; \mu, \nu) \mathcal{S}(\tau_n^s, \tau_{\bar{n}}^s, \mathbf{p}_{\perp}^2, \mathbf{k}_{\perp}^2; \mu, \nu), \quad (57.2)$$

where $\tau_{L,R}$ denote the angularity of the particles in the left (L) and right (R) hemisphere, respectively. The total angularity is obtained by $\tau = \tau_L + \tau_R$. $H(Q; \mu)$ is the hard function which describes the production of the high-energy parton at the hard scattering, $\mathcal{J}_{n,\bar{n}}$ are the jet functions describing the perturbative evolution of the energetic parton into collimated jets of hadrons and \mathcal{S} is the soft function which describes the distribution of soft hadrons between the jets. Finally, μ and ν are the scales associated with UV and rapidity renormalization, respectively. The quantities τ_n , $\tau_{\bar{n}}$, τ_n^s , and $\tau_{\bar{n}}^s$ return the value of the generalized angularity in the n -collinear, \bar{n} -collinear, and soft sectors.

Using the SCET_{II} framework, it was shown in [5] that the one-loop cross section for generalized angularities contains an extra contribution coming from recoil such that it gives rise to a leading singular contribution for $b = 0$ and reduces to a power suppressed term when $b \gtrsim 1$. For $0 < b < 1$ angularities, there are extra singular corrections which are less dominant than $1/\tau$ or $\ln \tau/\tau$ but more singular than $\ln \tau$. Accordingly, these were referred to as sub-leading singular corrections.

Reference [5] also worked out the first fully analytic result for $b < 0$ angularities at one loop, for which the single-differential cross section, obtained by integrating over the hemisphere angularities, takes the general form

$$\left[\frac{1}{\sigma_0} \frac{d\sigma^{(-)}}{d\tau} \right]_{\tau \neq 0}^{O(\alpha_s)} = \frac{\alpha_s(\mu) C_F}{\pi} \left\{ -\frac{3}{1+b} \frac{1}{\tau} - \frac{4}{(1+b)^2} \frac{\ln \tau}{\tau} - \frac{4}{(1+b)^2} \frac{\ln(1-s)}{\tau} \right\}, \quad (57.3)$$

with, s given by the solution of the equation

$$\frac{s}{(1-s)^{\frac{1}{1+b}}} = \tau^{-\frac{b}{1+b}}. \quad (57.4)$$

Here again, the first two terms in (57.3) are leading singular terms and the third term gives rise to sub-leading singular contributions for $-0.5 < b < 0$, while it reduces to power corrections for $b < -0.5$ angularities. In this article, we will focus on $b < 0$ angularity distributions and study resummed cross-section at the next-to-leading-logarithmic (NLL) order.

57.2 NLL Angularity Distribution for $b < 0$

The bare one-loop soft function for $b < 0$ angularities in the conjugate space is given as

$$\begin{aligned} \tilde{S}_{\text{bare}}^{(1-)}(s_L, s_R, \mathbf{b}_k^2, \mathbf{b}_p^2) &= \frac{\alpha_s(\mu) C_F}{\pi} \frac{1}{(4\pi)^2} \left\{ -\frac{1}{2b\epsilon^2} - \frac{1}{2b\epsilon} \frac{\mathbf{b}_p^2}{4} {}_2F_3\left(1, 1; 2, 2, 2; -\frac{\mathbf{b}_p^2}{4}\right) \right. \\ &\quad - \frac{1}{b\epsilon} \ln\left(s_R e^{\gamma_E} \frac{\mu}{Q}\right) - \frac{1}{b} \ln^2\left(s_R e^{\gamma_E} \frac{\mu}{Q}\right) - \frac{1}{2b} \frac{\mathbf{b}_p^2}{4} {}_3F_4\left(1, 1, 1; 2, 2, 2, 2; -\frac{\mathbf{b}_p^2}{4}\right) \\ &\quad \left. - \frac{1}{b} \frac{\mathbf{b}_p^2}{4} {}_2F_3\left(1, 1; 2, 2, 2; -\frac{\mathbf{b}_p^2}{4}\right) \ln\left(s_R e^{\gamma_E} \frac{\mu}{Q}\right) - \frac{\pi^2}{8b} \right\} + \left\{ \mathbf{b}_k^2 \leftrightarrow \mathbf{b}_p^2 \right\}, \quad (57.5) \end{aligned}$$

where $\mathbf{b}_{p,k}$ are impact parameter conjugate to $\mathbf{u}_{R(L)} \equiv \frac{\mathbf{p}_\perp(\mathbf{k}_\perp)}{Q\tau_{R(L)}}$ and $s_{L,R}$ is Laplace conjugate of $\tau_{L,R}$. From this, the one-loop anomalous dimensions can be obtained as

$$\gamma^{(1-)S} = -\frac{\alpha_s(\mu) C_F}{\pi} \left[\frac{\mathbf{b}_p^2}{4b} {}_2F_3\left(1, 1; 2, 2, 2; -\frac{\mathbf{b}_p^2}{4}\right) + \frac{2}{b} \ln\left(s_R e^{\gamma_E} \frac{\mu}{Q}\right) + \left\{ \mathbf{b}_k^2 \leftrightarrow \mathbf{b}_p^2 \right\} \right]. \quad (57.6)$$

For $b < 0$ angularities, the rapidity regulator cancels amongst the jet and soft sectors independently, giving rise to only a μ -RGE as in standard SCET_I problems. This case is unique due to the fact that the transverse momentum convolutions are still important as recoil cannot be ignored. Moreover, for $b < 0$, the soft hyperbola sits above the jet hyperbola, implying that the soft mode is harder than the jet mode in this case. For notational simplicity, we will still refer to this hard-soft mode as the soft mode.

Using the one-loop anomalous dimensions to solve the μ -RGE, the NLL resummed soft function in the conjugate space can be obtained. The final ingredient we need for obtaining the cross section is the NLL resummed hard function which is the same as that for thrust, broadening or other e^+e^- dijet observables [2]. For the NLL computation, we only need the jet function at the tree level. Substituting all the ingredients, the cross section for $b < 0$ angularities, in the physical space, then takes the form

$$\begin{aligned} \frac{1}{\sigma_0} \frac{d\sigma^{\text{NLL}}}{d\tau_L d\tau_R} &= H^{\text{NLL}} \left[\frac{2}{(1+b)} \frac{e^{\omega_S \gamma_E - \frac{2}{b} K_\Gamma}}{\Gamma(-\omega_S)} \left(\frac{\mu_0}{Q} \right)^{\omega_S} \frac{1}{\tau_R^{1+\omega_S}} \int_0^1 dx \frac{1}{(1-x)^{\frac{b-1}{1+b}}} \frac{1}{x^{3+\omega_S}} \right. \\ &\quad \left. \times \int_0^\infty dz J_0 \left(2\sqrt{z} \frac{(1-x)^{\frac{1}{1+b}}}{x} \right) e^{-\frac{4c_F \ln p}{2b\beta_0} z \tau_R^{\frac{2b}{1+b}}} {}_2F_3 \left(1, 1; 2, 2, 2; -z \tau_R^{\frac{2b}{1+b}} \right) \right] \times \{L \leftrightarrow R\}. \end{aligned} \quad (57.7)$$

where, ω_S and K_Γ are the evolution kernels. For notational simplicity, the dependence of ω_S and K_Γ on the scales μ and μ_0 has been suppressed. These evolution kernels are defined as

$$\begin{aligned} \omega_S(\mu, \mu_0) &= -\frac{2}{b} \int_{\alpha_s(\mu_0)}^{\alpha_s(\mu)} \frac{d\alpha_s}{\beta[\alpha_s]} \Gamma_{\text{cusp}}[\alpha_s], \\ K_\Gamma(\mu, \mu_0) &= \int_{\alpha_s(\mu_0)}^{\alpha_s(\mu)} \frac{d\alpha_s}{\beta[\alpha_s]} \Gamma_{\text{cusp}}[\alpha_s] \int_{\alpha_s(\mu_0)}^{\alpha_s} \frac{d\alpha'_s}{\beta[\alpha'_s]}, \\ \text{and,} \quad p &= \frac{\alpha_s(\mu_0)}{\alpha_s(\mu)}. \end{aligned} \quad (57.8)$$

where Γ_{cusp} is the cusp anomalous dimension and $\beta[\alpha_s]$ is the QCD beta function. At NLL accuracy, we only need Γ_0, Γ_1 coefficients of the cusp anomalous dimension and β_0, β_1 for the beta function coefficients [2]. From the result in (57.8), we find that the leading singular logarithms of τ are appropriately resummed by the $1/\tau^{1+\omega_S}$ factor, while the sub-leading logarithms are contained in the exponentiated hypergeometric function. The exponentiation of this term is important as in the $b \rightarrow 0$ limit, this term generates a leading singular logarithm and hence is appropriately resummed in our formalism.

It is important to point out that the $b \rightarrow 0$ limit of (57.8) is well defined. When μ approaches μ_0 , the integral over μ in the evolution kernels becomes proportional to b . Naively, this implies that $\omega_S \sim \mathcal{O}(1)$ and $K_\Gamma \sim \mathcal{O}(b^2)$ when $b \rightarrow 0$. Similarly, p can be expanded about small- b and it can be shown that $\ln p$ is proportional to b , rendering the cross section finite in the limit $b \rightarrow 0$.

57.3 Conclusion

We have discussed the general framework of SCET_{II} for recoil-sensitive angularities which allows us to obtain one-loop cross section for all values of the exponent b . Using this framework, we have discussed the resummation of $b < 0$ angularities. We have presented the one-loop anomalous dimensions and the NLL cross section for $b < 0$ angularity. We have also discussed how the leading and sub-leading singular contributions get resummed in our framework. A detailed study of our work is under preparation and will be presented in a future publication [6].

References

1. C.W. Bauer, S. Fleming, M.E. Luke, Phys. Rev. **D63**, 014006 (2000); C.W. Bauer, S. Fleming, D. Pirjol, I.W. Stewart, Phys. Rev. **D63**, 114020 (2001); C.W. Bauer, I.W. Stewart, Phys. Lett. **B516**, 134–142 (2001)
2. J.Y. Chiu, A. Jain, D. Neill, I.Z. Rothstein, JHEP **05**, 084 (2012); J.Y. Chiu, A. Jain, D. Neill, I.Z. Rothstein, Phys. Rev. Lett. **108**, 151601 (2012)
3. C.F. Berger, T. Kucs, G.F. Sterman, Phys. Rev. D **68**, 014012 (2003)
4. E. Farhi, Phys. Rev. Lett. **39**, 1587–1588 (1977)
5. A. Budhraj, A. Jain, M. Procura, JHEP **08**, 144 (2019)
6. A. Budhraj, A. Jain, M. Procura, in preparation

Chapter 58

Correspondence Between Israel–Stewart Theory and First-Order Causal and Stable Hydrodynamics for the Boost-Invariant Flow



Arpan Das

Abstract In this proceeding, we discuss a mapping between the well-explored Israel–Stewart (IS) theory of dissipative relativistic hydrodynamics and the recently formulated causal and stable first-order hydrodynamics (FOCS), for Bjorken expanding systems with an ideal gas equation of state. Due to such correspondence, an analytical solution of the new first-order formulation can be determined.

58.1 Introduction

The success of causal and stable Israel–Stewart (IS) theory of relativistic viscous hydrodynamics for modeling the bulk evolution of the thermalized medium produced in heavy-ion collisions triggered a broad interest in general aspects of this theory [1, 2]. Recently, a new formalism of first-order causal and stable hydrodynamic (FOCS) has been put forward by F. S. Bemfica et al. and P. Kovtun by employing the opportunity of a more general choice of the hydrodynamic frames [3–5]. In the FOCS theory, causality and stability have been achieved due to a new set of kinetic coefficients arising from the hydrodynamic gradient expansion and these coefficients also play the role of ultraviolet regulators of the theory. In general, due to the different numbers of the dynamical equations, there may not be any equivalence between the IS and the FOCS theory. Nevertheless, there may exist some special cases where these two frameworks lead to the same dynamical equations. Such cases are interesting and useful as they allow us to transfer the knowledge gained in one theory to the other one. Here, we discuss an exact correspondence between the IS and the FOCS theory for massless particles for the boost-invariant flow with zero baryon density [6].

A. Das (✉)

Institute of Nuclear Physics Polish Academy of Sciences, PL-31-342, Kraków, Poland
e-mail: arpan.das@ifj.edu.pl

© The Author(s), under exclusive license to Springer Nature Singapore Pte Ltd. 2022
B. Mohanty et al. (eds.), *Proceedings of the XXIV DAE-BRNS High Energy Physics Symposium, Jaiti, India*, Springer Proceedings in Physics 277,
https://doi.org/10.1007/978-981-19-2354-8_58

323

58.2 Correspondence Between IS and FOCS Hydrodynamics

For boost-invariant flow (Bjorken flow) with fluid flow vector $u^\mu \equiv (t/\tau, 0, 0, z/\tau)$ the hydrodynamic equations in the IS theory become [7, 8],

$$\frac{d\varepsilon}{d\tau} = -\frac{\varepsilon + p}{\tau} + \frac{\pi}{\tau}, \quad (58.1)$$

$$\tau_R \frac{d\pi}{d\tau} + \pi = \frac{4}{3} \frac{\eta}{\tau} - \left(\frac{4}{3} + \lambda \right) \tau_R \frac{\pi}{\tau}, \quad (58.2)$$

where $\tau = \sqrt{t^2 - z^2}$ is the proper time, ε and p are the energy density and pressure, respectively. π is the rapidity–rapidity component of the shear stress tensor ($\pi^{\mu\nu}$). For massless particles, bulk viscous pressure (Π) does not appear in the IS equations. τ_R is the relaxation time which we consider to be a constant to get the correspondence between the IS and FOCS theory. η is the coefficient of shear viscosity and λ is one of the transport coefficients which appear in the DNMR approach [9]. Assuming the ideal gas equation of state (EoS) $p = \varepsilon/3 = aT^4/3$ (here a is a pure number) and introducing the variable $y = dT/d\tau$, (58.1) and (58.2) can be expressed in the form of the Riccati equation [6, 8],

$$4a\tau_R T^3 \frac{dy}{d\tau} + 12\tau_R a T^2 y^2 + aT^3 y \left[4 + \left(\frac{28}{3} + 4 \left(\frac{4}{3} + \lambda \right) \right) \frac{\tau_R}{\tau} \right] + \frac{4aT^4}{3\tau} + \frac{4}{3} aT^4 \left(\frac{4}{3} + \lambda \right) \frac{\tau_R}{\tau^2} - \frac{4}{3} \frac{\eta}{\tau^2} = 0. \quad (58.3)$$

The variable $y = dT/d\tau$ and (58.3) together are equivalent to the IS theory equations, i.e., (58.1) and (58.2). Within the FOCS approach the boost-invariant hydrodynamic equations get reduced to [5, 6],

$$\frac{d\mathcal{E}}{d\tau} + \frac{\mathcal{E} + \mathcal{P}}{\tau} - \frac{4}{3} \frac{\eta}{\tau^2} = 0, \quad (58.4)$$

where the constitutive relations for \mathcal{E} and \mathcal{P} have the following form [3–6]:

$$\mathcal{E} = \varepsilon + \varepsilon_1^0 T^n \frac{dT}{T d\tau} + \frac{\varepsilon_2^0}{\tau} T^n; \quad \mathcal{P} = p + \pi_1^0 T^n \frac{dT}{T d\tau} + \frac{\pi_2^0}{\tau} T^n, \quad (58.5)$$

where ε_i^0, π_i^0 with $i = 1, 2$ are the regulators in the FOCS theory. The regulators ε_i^0, π_i^0 with $i = 1, 2$ are assumed to be τ -independent. For conformal fluid ε_i^0, π_i^0 are dimensionless which corresponds to $n = 3$ in (58.5) [3–6]. We also consider the case where ε_i^0, π_i^0 have dimension of time which corresponds to $n \neq 3$ in (58.5) [6]. Similar to the IS theory, introducing the variable $y = dT/d\tau$ and using the constitutive relations as given in (58.5), the hydrodynamic equation in the FOCS approach

(58.4) becomes

$$\begin{aligned} \varepsilon_1^0 T^{n-1} \frac{dy}{d\tau} + (n-1) \varepsilon_1^0 T^{n-2} y^2 + \left(4aT^3 + (\varepsilon_1^0 + \pi_1^0 + n\varepsilon_2^0) \frac{T^{n-1}}{\tau} \right) y \\ + \frac{4}{3\tau} aT^4 + \frac{\pi_2^0 T^n}{\tau^2} - \frac{4}{3} \frac{\eta}{\tau^2} = 0. \end{aligned} \quad (58.6)$$

Since the variable $y = dT/d\tau$ is common in IS and FOCS approach, we can get a correspondence between the IS and the FOCS approach by just comparing (58.3) with (58.6). Therefore, comparing terms with $dy/d\tau$ and various powers of y from (58.3) and (58.6), we obtain [6]

$$\varepsilon_1^0 = 4a\tau_R T^{4-n}, \quad (58.7)$$

$$\varepsilon_1^0 = \frac{12}{n-1} a\tau_R T^{4-n}, \quad (58.8)$$

$$\pi_1^0 = \frac{4}{3} a\tau_R (11 + 3\lambda) T^{4-n} - \varepsilon_1^0 - n\varepsilon_2^0, \quad (58.9)$$

$$\pi_2^0 = \frac{4}{9} a\tau_R (4 + 3\lambda) T^{4-n}. \quad (58.10)$$

Equations (58.7) and (58.8) imply that, for conformal fluid ($n = 3$ case), it is impossible to get an exact mapping between FOCS and IS equations. However for $n = 4$, ε_1^0 can be obtain uniquely. But even for $n = 4$ case, ε_2^0 and π_1^0 can not be obtained uniquely using (58.9). To uniquely determine the regulator sector in the FOCS theory, we can use the traceless condition of the energy momentum tensor for massless particles. For the traceless energy-momentum tensor in the FOCS theory, one can easily show that, $\pi_i^0 = \varepsilon_i^0/3$ for $i = 1, 2$ [3–6]. Using the condition $\pi_i^0 = \varepsilon_i^0/3$ along with $n = 4$ in (58.7)–(58.10), we find $\lambda = -1$, and

$$\varepsilon_1^0 = 4a\tau_R; \quad \varepsilon_2^0 = \frac{4}{3} a\tau_R; \quad \pi_1^0 = \frac{4}{3} a\tau_R; \quad \pi_2^0 = \frac{4}{9} a\tau_R. \quad (58.11)$$

Therefore, it is indeed possible to get a one-to-one correspondence between the IS theory and the FOCS theory for the boost-invariant flow with the ideal gas EoS, where the regulator sector in the FOCS theory can be expressed in terms of the constant relaxation time of the IS theory (see (58.11)).

58.3 Analytical Solution for the FOCS Theory

The general analytical solution of the IS equations, i.e., (58.1) and (58.2) for the Bjorken flow has been obtained in [8]. This solution should also hold for the FOCS theory, but with $\lambda = -1$, due to the exact mapping between the IS theory and the

FOCS theory as discussed in the previous section. Therefore, the general solution for the energy density in the FOCS approach as discussed here can be expressed as [6, 8]

$$\varepsilon(\hat{\tau}) = \varepsilon_0 \left(\frac{\hat{\tau}_0}{\hat{\tau}} \right)^{\frac{4}{3} + \frac{\lambda+1}{2}} \exp \left(-\frac{\hat{\tau} - \hat{\tau}_0}{2} \right) \times \left[\frac{M_{-\frac{\lambda+1}{2}, \frac{\sqrt{\lambda^2+4\kappa}}{2}}(\hat{\tau}) + \alpha W_{-\frac{\lambda+1}{2}, \frac{\sqrt{\lambda^2+4\kappa}}{2}}(\hat{\tau})}{M_{-\frac{\lambda+1}{2}, \frac{\sqrt{\lambda^2+4\kappa}}{2}}(\hat{\tau}_0) + \alpha W_{-\frac{\lambda+1}{2}, \frac{\sqrt{\lambda^2+4\kappa}}{2}}(\hat{\tau}_0)} \right] \quad (58.12)$$

where $\lambda = -1$, $\hat{\tau} = \tau/\tau_R$, $\kappa = 16\eta/(9\tau_R T s)$. s is the entropy density, $\hat{\tau}_0$ is the initial time. ε_0 and α are constants and define the initial value problem. $M_{k,\mu}(x)$ and $W_{k,\mu}(x)$ are Whittaker functions [8].

58.4 Discussion and Conclusions

In this proceeding, we have discussed an exact correspondence between the IS theory and the FOCS theory for a baryon-free boost-invariant flow with the ideal gas EoS. Assuming a constant relaxation time in the IS sector, we found an exact mapping between the equations in IS and FOCS theory, where the regulator sector in the FOCS theory can be expressed in terms of the constant relaxation time. Such a correspondence works in the present case for the IS parameter $\lambda = -1$. Note that the parameter λ does not appear in the linearized analysis of the stability and causality in the IS theory [8]. Using 14-moment approximation, it can be shown that $\lambda = 10/21$ [9]. The causality conditions in the FOCS approach in the fully nonlinear regime are known [3–5]. Using the values of ε_i^0 and π_i^0 in term of τ_R as given in (58.11), causality and stability of the FOCS theory can be argued [6]. Therefore, the results indicate that the value of the λ as obtained in the 14-moment approximation can be at odds with the causality in the nonlinear regime. Further investigations in this context are required which may help for a better understanding of the IS and FOCS theories.

Acknowledgements I thank W. Florkowski, J. Noronha, and R. Ryblewski for very fruitful collaboration and numerous illuminating discussions. I also thank R. E. Hout and A. Jaiswal for very useful discussions. This work is supported by the Polish National Science Center Grant No. 2018/30/E/ST2/00432.

References

1. W. Israel, J.M. Stewart, Transient relativistic thermodynamics and kinetic theory. *Annals Phys.* **118**, 341–372 (1979). [https://doi.org/10.1016/0003-4916\(79\)90130-1](https://doi.org/10.1016/0003-4916(79)90130-1)
2. A. Jaiswal, V. Roy, Relativistic hydrodynamics in heavy-ion collisions: general aspects and recent developments. *Adv. High Energy Phys.* **2016**, 9623034 (2016). <https://doi.org/10.1155/2016/9623034>
3. F.S. Bemfica, M.M. Disconzi, J. Noronha, Causality and existence of solutions of relativistic viscous fluid dynamics with gravity. *Phys. Rev. D* **98**, 104064 (2018). <https://doi.org/10.1103/PhysRevD.98.104064>
4. F.S. Bemfica, M.M. Disconzi, J. Noronha, Nonlinear causality of general first-order relativistic viscous hydrodynamics. *Phys. Rev. D* **100**, 104020 (2019). <https://doi.org/10.1103/PhysRevD.100.104020>
5. P. Kovtun, First-order relativistic hydrodynamics is stable. *JHEP* **10**, 034 (2019). [https://doi.org/10.1007/JHEP10\(2019\)034](https://doi.org/10.1007/JHEP10(2019)034)
6. A. Das, W. Florkowski, J. Noronha, R. Ryblewski, Equivalence between first-order causal and stable hydrodynamics and Israel–Stewart theory for boost-invariant systems with a constant relaxation time. *Phys. Lett. B* **806**, 135525 (2020). <https://doi.org/10.1016/j.physletb.2020.135525>
7. J.D. Bjorken, Highly relativistic nucleus-nucleus collisions: the central rapidity region. *Phys. Rev. D* **27**, 140–151 (1983). <https://doi.org/10.1103/PhysRevD.27.140>
8. G.S. Denicol, J. Noronha, Analytical attractor and the divergence of the slow-roll expansion in relativistic hydrodynamics. *Phys. Rev. D* **97**, 056021 (2018). <https://doi.org/10.1103/PhysRevD.97.056021>
9. G.S. Denicol, H. Niemi, E. Molnar, D.H. Rischke, Derivation of transient relativistic fluid dynamics from the Boltzmann equation. *Phys. Rev. D* **85**, 114047 (2012). <https://doi.org/10.1103/PhysRevD.85.114047>

Chapter 59

ηB Interactions in the Strange Baryonic Matter



Arvind Kumar and Rajesh Kumar

Abstract We employ the chiral SU(3) model to study the ηB interactions in the strange baryonic matter. The in-medium scalar and vector densities of baryons are calculated which are later used in the interaction Lagrangian in the chiral model. Along with the strangeness effect, we also include the effect of medium density, ρ_B , and temperature, T . The medium modified mass and optical potential of η meson are calculated from the ηB equations of motion. In this work, the effect of scattering length, $a^{\eta N}$ is also studied. We observe decrement in the in-medium mass of η -meson as a function of density, which may lead to the formation of a bound state between η meson and nuclei.

59.1 Introduction

The impact of the strange asymmetric matter on the in-medium hadron properties is of considerable interest [1]. Specifically, the η -meson has attracted a lot of researchers due to its attractive interactions with nuclear matter [2–4]. In these articles, an appreciable negative mass shift of η -meson is obtained which favors the bound state formation of η -meson with nuclei [2]. In the extension of previous work in nuclear matter [4], in this article, we added the effect of strange matter. In the present work, the impact of strangeness and other medium effects such as temperature and asymmetry are incorporated through the scalar and vector densities of nucleons which are evaluated using the hadronic chiral SU(3) model. Within the model, the above-mentioned densities are solved simultaneously with the scalar (σ , ζ , δ and χ) and the vector fields (ω , ρ and ϕ) [4]. The strange fields ζ and ϕ play an important role in the strange matter to modify the properties of nucleons and baryons. The in-medium scalar densities are further plugged in the ηB equation of motion calculated using the same model. The chiral SU(3) model preserves the basic QCD properties such

A. Kumar (✉) · R. Kumar
Department of Physics, Dr. B R Ambedkar National Institute of Technology Jalandhar,
Jalandhar 144011, Punjab, India
e-mail: kumara@nitj.ac.in

© The Author(s), under exclusive license to Springer Nature Singapore Pte Ltd. 2022
B. Mohanty et al. (eds.), *Proceedings of the XXIV DAE-BRNS High Energy Physics Symposium, Jatni, India*, Springer Proceedings in Physics 277,
https://doi.org/10.1007/978-981-19-2354-8_59

329

as broken scale invariance and non-linear realization of the chiral symmetry [4]. The model has been successfully used in literature to study the in-medium meson properties in the nuclear and strange matter at finite temperature, asymmetry, and magnetic field [1, 4]. In [4] and [2], the ηN equation of motion was derived using the unitary approach of chiral perturbation theory (chPT) with chiral SU(3) model and relativistic mean-field model (RMF), respectively. In the chPT, the next-to-leading order terms in the ηB Lagrangian were incorporated for the improved description of ηB interactions [2, 3].

59.2 Methodology

The eta-baryon equation of motion in the chiral SU(3) model up to second order is given as [4]

$$\begin{aligned} \partial^\mu \partial_\mu \eta + \left(m_\eta^2 - \frac{(\sqrt{2}\sigma' - 4\zeta') m_\pi^2 f_\pi + 8\zeta' m_K^2 f_K}{\sqrt{2} f^2} \right) \eta \\ + \frac{2}{f^2} \left(\frac{d' \rho_B^s}{4} + \frac{d_2 \rho_{A_0}^s}{2} \right) \partial^\mu \partial_\mu \eta - \frac{2}{f^2} \left(\frac{\sqrt{2}\sigma' f_\pi + 4\zeta' (2f_K - f_\pi)}{\sqrt{2}} \right) \partial^\mu \partial_\mu \eta = 0. \end{aligned} \quad (59.1)$$

In the above equation, $f = \sqrt{f_\pi^2 + 2(2f_K - f_\pi)^2}$ and $d' = 3d_1 + d_2$ are the constant parameters with f_K and f_π as decay constant of K and π mesons, respectively. Also, the $\sigma' (= \sigma - \sigma_0)$, $\zeta' (= \zeta - \zeta_0)$ and $\delta' (= \delta - \delta_0)$ denote the deviation of expectation values of fields in medium from expectation value in vacuum [4]. The value of d' parameter is computed from the ηN scattering length $a^{\eta N}$ [4]. Furthermore, the range of η meson–nucleon scattering length $a^{\eta N}$ is taken as 0.91–1.14 fm which is favored by many research articles [2, 4]. Moreover, in (59.1), the symbol $\rho_B^s = \sum_i \rho_i^s$ represents the net scalar density of baryons ($i = p, n, \Sigma^+, \Sigma^0, \Sigma^-, \Xi^-, \Xi^0, \Lambda^0$) which is calculated using the chiral SU(3) model [4]. In the chiral SU(3) model, the scalar density of nucleons have been calculated by solving the coupled equations of motion in the presence of strangeness which is introduced by the definition $f_s = \frac{\sum_i |s_i| \rho_i^v}{\rho_B}$ [4]. The symbols $|s_i|$ and $(\rho_B) \rho_i^v$ denote the number of strange quarks and (total) vector density of baryons, respectively. The explicit expressions of scalar density is shown as

$$\rho_i^s = \gamma_i \int \frac{d^3 k}{(2\pi)^3} \frac{m_i^*}{E_i^*(k)} \left(\frac{1}{1 + \exp[\beta(E_i^*(k) - \mu_i^*)]} + \frac{1}{1 + \exp[\beta(E_i^*(k) + \mu_i^*)]} \right), \quad (59.2)$$

where γ_i denotes the degeneracy factor and $\beta = \frac{1}{kT}$ [4]. Also, μ_i^* and E_i^* represent the effective chemical potential and single particle energy of the baryons, respectively. Similar to strangeness, the effect of isospin asymmetry is included by the definition $\eta = -\frac{\sum_i \tau_{3i} \rho_i^v}{2\rho_B}$ [1]. The symbol τ_3 , denote the 3rd component of isospin quantum number.

The dispersion relation of ηB interactions can be written by doing the Fourier transform of (59.1)

$$-\omega^2 + \mathbf{k}^2 + m_\eta^2 - \Pi^*(\omega, |\mathbf{k}|) = 0, \quad (59.3)$$

where $\Pi^*(\omega, |\mathbf{k}|)$ is the self-energy [4] and the symbol m_η is the vacuum mass of η -meson. The η -meson in the nuclear medium is obtained using the condition, $m_\eta^* = \omega(|\mathbf{k}| = 0)$.

59.3 Results and Discussions

In this section, we discuss the impact of various medium attributes on the in-medium mass of η -meson. In the present work, we have taken $d_2 = 0.28d_1$, which is estimated from the KN interactions [1]. In this reference, the d_1 and d_2 parameters are estimated using the empirical values of KN scattering length in isospin channel $\hat{I} = 0$ and $\hat{I} = 1$. In Fig. 59.1a, we illustrate the in-medium mass of η -meson as a function of baryonic density under different values of strangeness, asymmetry, temperature, and scattering length. We consider $\rho_0 = 0.15 \text{ fm}^{-3}$ for nuclear saturation density [4]. As a function of density, we find that the in-medium mass decreases linearly up to nuclear saturation density and, after that, the decay becomes non-linear. We observe that the in-medium mass decrease with the increase in the strangeness of the medium. The strangeness effect is more appreciable in the high-density regime. Further, if we change the value of I from 0 to 0.5, we find less decrement in the in-medium mass of η -meson. The same effect is observed when we move from low temperature to high temperature. This is because the scalar density of baryons gives less attractive contributions in the asymmetric nuclear matter and high temperature but high contributions for the strange matter. We found that the first range term (fourth term of (59.1)) gives a repulsive effect, whereas mass and d terms (second and third terms of (59.1)) give attractive contributions. In the nuclear matter, the mass shift obtained using the current approach is less than the work done using the combined approach of chiral SU(3) model along with chiral perturbation theory (chPT) [4]. In the chPT, more negative mass shift is observed since the chPT ηN Lagrangian does not contain the first range term [2].

The momentum-dependent optical potential of the η -mesons at $I = 0$ is also evaluated in the present work and is illustrated in Fig. 59.1b. We observe that the magnitude of optical potential decreases with an increase in the momentum \mathbf{k} . Under the influence of different medium parameters, the optical potential shows similar

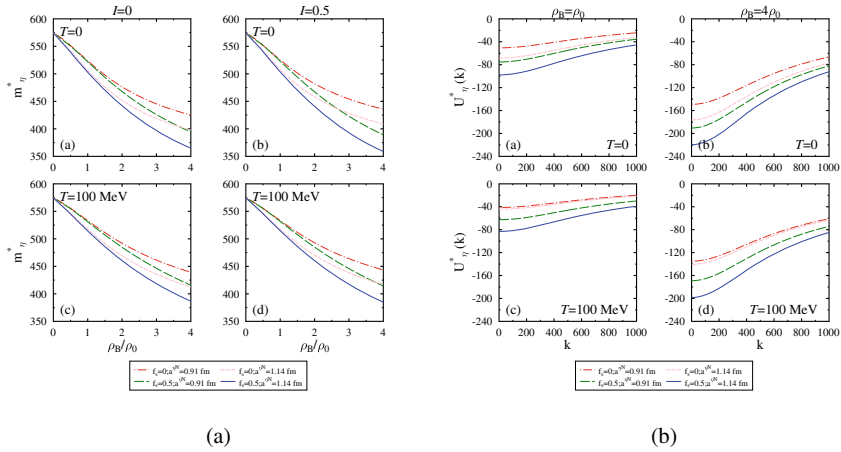


Fig. 59.1 **a** In-medium mass and **b** momentum-dependent optical potential of η -meson evaluated using the chiral SU(3) model

behavior as was observed for the in-medium mass. In the high-momentum region, the higher k values suppress the contribution from in-medium η energy, whereas in the low-momentum regime, the in-medium energy or mass shows dominant behavior.

59.4 Conclusions

We find an appreciable impact of hyperon density on the in-medium mass and optical potential of η -meson at high baryonic density. The increase in the strangeness fraction and $a^{\eta N}$ scattering length leads to a decrease in the in-medium mass. Furthermore, in future studies, the corresponding negative optical potential can be used to study the formation of eta-mesic nuclei and production rate of η -mesons.

Acknowledgements One of the authors, Rajesh Kumar, sincerely acknowledges the support towards this work from the Ministry of Science and Human Resources Development (MHRD), Government of India.

References

1. A. Mishra et al., Eur. Phys. J. A **41**(2), 205–213 (2009)
2. X.H. Zhong et al., Phys. Rev. C **73**, 015205 (2006)
3. Elizabeth Jenkins, Aneesh V. Manohar, Phys. Lett. B **255**(4), 558–562 (1991)
4. Rajesh Kumar, Arvind Kumar, Phys. Rev. C **102**, 065207 (2020)

Chapter 60

Cumulant Measurement of Net-Kaon Distributions in Au+Au Collisions at $\sqrt{s_{NN}} = 27$ GeV from BES-II Program at RHIC



Ashish Pandav

Abstract We report on the measurements of cumulants (C_n) of event-by-event net-kaon distributions up to the fourth order in the most central (0–5%) Au+Au collisions for center-of-mass energy $\sqrt{s_{NN}} = 27$ GeV from the BES-II program at RHIC. Charged kaons are selected at midrapidity $|y| < 0.5$ with transverse momentum range $0.2 < p_T < 1.6$ GeV/c using the STAR detector at RHIC. We find the new measurements at $\sqrt{s_{NN}} = 27$ GeV with high event statistics from BES-II are consistent with those from the BES-I program by RHIC for the same collision energy and centrality. The new results follow the trend of the strong collision energy dependence of cumulants and cumulant ratios up to third order ($C_n, n \leq 3, C_2/C_1, C_3/C_1$) and weak collision energy dependence of C_4 and C_4/C_2 , from the BES-I measurements. The expectation from the UrQMD model calculated in the STAR acceptance is also presented and compared to the measured cumulant ratios.

60.1 Introduction

Studying the QCD phase structure of the strongly interacting matter is one of the primary objectives of relativistic heavy-ion collision experiments. Cumulants of conserved quantities for strong interaction such as net-charge, net-baryon, and net-strangeness numbers are proposed to be sensitive observables for the study of the phase transition between quark–gluon plasma and hadronic matter and search for

Ashish Pandav—for the STAR Collaboration.

A. Pandav (✉)
School of Physical Sciences, National Institute of Science Education and Research,
Jatni 752050, India
e-mail: apandav10@gmail.com

Homi Bhabha National Institute, Training School Complex, Anushaktinagar, Mumbai 400094, India

© The Author(s), under exclusive license to Springer Nature Singapore Pte Ltd. 2022
B. Mohanty et al. (eds.), *Proceedings of the XXIV DAE-BRNS High Energy Physics Symposium, Jatni, India*, Springer Proceedings in Physics 277,
https://doi.org/10.1007/978-981-19-2354-8_60

333

the QCD critical point. The cumulant ratios are related to the thermodynamic number susceptibilities that are calculable in the lattice QCD and various QCD-based models [1–4].

Cumulants up to the fourth order (C_n , $n \leq 4$) of event-by-event distributions of net-charge, net-kaon (proxy for net-strangeness), and net-proton (proxy for net-baryon) were measured by the STAR detector in the phase I of Beam Energy Scan (BES) program at RHIC [5–9]. The cumulant ratios C_4/C_2 of net-proton distribution in the most central (0–5%) gold nuclei collisions exhibit a non-monotonic dependence as a function of beam energy which is qualitatively consistent with expectations from a QCD-based model that includes a critical point [4]. Cumulant ratios are also extensively used in the study of freeze-out dynamics using thermal models which are suggestive of flavor separation during the QCD crossover transition [10].

60.2 Analysis Details

In order to obtain the cumulants of event-by-event net-kaon distributions, charged kaons (K^+ and K^-) are identified at midrapidity $|y| < 0.5$ and within p_T range 0.2–1.6 GeV/c using the Time Projection Chamber (TPC) and Time-of-Flight (TOF) detectors. Event statistics analyzed are about ~ 25 millions in most central (0–5%) collisions. The collision centrality of an event is determined using the charged particle multiplicity within pseudorapidity range $|\eta| < 1$, excluding kaons from the region to prevent any self-correlation. A data-driven method called the Centrality Bin Width Correction (CBWC) is applied in the cumulant measurements for a given centrality, in order to suppress the volume fluctuation effects [11]. First, cumulants at each multiplicity bin of a given centrality are evaluated and corrected for the detector efficiency and acceptance effects with the assumption that the detector response is binomial [12–14], and then the CBWC was applied. Statistical uncertainties on cumulants and their ratios are estimated using a resampling method called the bootstrap [12, 15]. Systematic uncertainties in the measurements are estimated by varying tracking efficiency, track selection, and particle identification criteria.

60.3 Results and Discussions

This section presents new results on cumulants of event-by-event net-kaon distributions up to the fourth order in most central (0–5%) Au+Au collisions at $\sqrt{s_{NN}} = 27$ GeV collected by the STAR detector in the year 2018 from the BES-II program at RHIC. Figure 60.1 shows the event-by-event net-kaon multiplicity distributions for most central (0–5%) collisions. The distribution is uncorrected for the detector efficiency and acceptance effects. Cumulants up to the fourth order are obtained for this distribution, followed by the corrections for finite centrality bin width, the detector efficiency, and acceptance effects. Cumulants (up to the fourth order) of

Fig. 60.1 Event-by-event net-kaon multiplicity distributions in Au+Au collisions at $\sqrt{s_{NN}} = 27$ GeV for 0–5% collision centralities at midrapidity. The distributions are uncorrected for the efficiency and acceptance effects

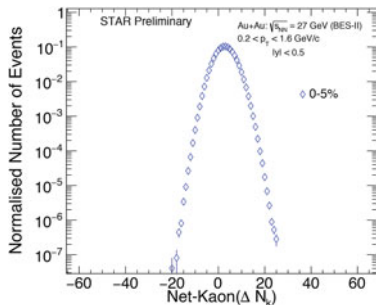
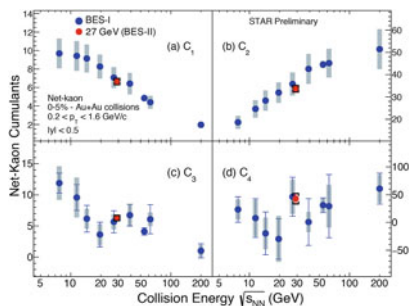


Fig. 60.2 Collision energy dependence of cumulants (C_n , $n \leq 4$) of net-kaon distributions for 0–5% central Au+Au collisions with inclusion of the new measurement at $\sqrt{s_{NN}} = 27$ GeV from BES-II program. The new measurements are slightly shifted in x-axis for better visibility



net-kaon distribution for most central (0–5%) Au+Au collisions as a function of collision energy from BES-I program [6, 16] including the new measurement at $\sqrt{s_{NN}} = 27$ GeV from BES-II (red marker) are shown in Fig. 60.2. The bars and shaded bands on the data points represent the statistical uncertainties and systematic uncertainties, respectively. The precision measurements due to high event statistics at $\sqrt{s_{NN}} = 27$ GeV from BES-II, have significantly reduced the uncertainties as compared to measurements from BES-I program. The new measurements are consistent with previous measurements from BES-I program at $\sqrt{s_{NN}} = 27$ GeV within uncertainties for the same collision centrality. Having measured the cumulants, one can construct the cumulant ratios to eliminate the trivial system volume dependence to facilitate a direct comparison to various theoretical and model predictions. Net-kaon cumulant ratios C_2/C_1 , C_3/C_2 , and C_4/C_2 as a function of collision energy from BES-I program [6, 16] including the new measurement at $\sqrt{s_{NN}} = 27$ GeV from BES-II program (shown in red marker) are shown in Fig. 60.3. It was observed from the previous measurements at BES-I that the ratios C_2/C_1 and C_3/C_2 exhibited a strong dependence on collision energy, whereas C_4/C_2 showed a weak collision energy dependence because of large statistical uncertainties associated with the measurements. The new results at $\sqrt{s_{NN}} = 27$ GeV from BES-II fit into the energy dependence of the cumulant ratios from BES-I measurements. They are consistent with Poisson baseline: which are the expected values of the ratios if both K^+ and K^- follow independent Poisson distribution, and the UrQMD model calculations [17].

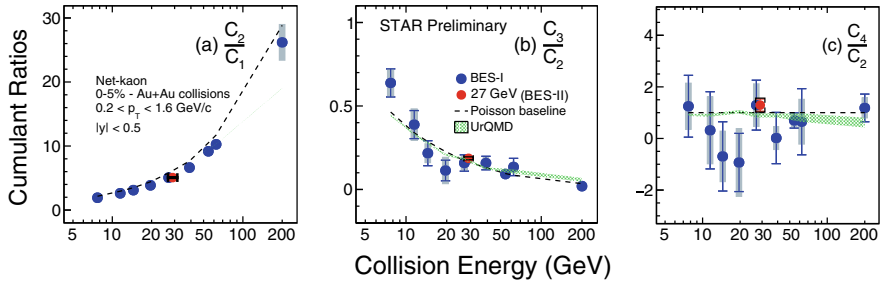


Fig. 60.3 Collision energy dependence of cumulant ratios C_2/C_1 , C_3/C_2 and C_4/C_2 of net-kaon distributions for 0–5% central Au+Au collisions with inclusion of the new measurement at $\sqrt{s_{NN}} = 27$ GeV from BES-II program. The new measurements are slightly shifted in x-axis for better visibility. The UrQMD model expectations shown in green band are taken from the [6]

60.4 Conclusions

We reported the measurements of cumulants of net-kaon distributions and their ratios in most central (0–5%) Au+Au collisions at $\sqrt{s_{NN}} = 27$ GeV from BES-II program at RHIC. The new measurements follow the beam energy dependence established by BES-I energies. They are consistent with the previous measurements from BES-I within uncertainties, for the same collision energy and centrality and also agree with the Poisson baseline and the UrQMD expectations. The new results calculated with ~ 25 million Au+Au collision events show that the statistical uncertainties on cumulants have drastically reduced as compared to BES-I measurements where event statistics were almost one-tenth factor smaller for the same collision energy and centrality. This demonstrates the potential of the precision measurements from the BES-II program at RHIC which will be very crucial in the search for the QCD critical point.

Acknowledgements We acknowledge the support by the Department of Atomic Energy, Govt. of India.

References

1. M.A. Stephanov, Phys. Rev. Lett. **102**, 032301 (2009)
2. R.V. Gavai, S. Gupta, Phys. Lett. B **696**, 459 (2011)
3. S. Gupta, X. Luo, B. Mohanty, H.G. Ritter, N. Xu, Science **332**, 1525 (2011)
4. M.A. Stephanov, Phys. Rev. Lett. **107**, 052301 (2011)
5. L. Adamczyk et al., STAR Collaboration. Phys. Rev. Lett. **113**, 092301 (2014)
6. L. Adamczyk et al., STAR Collaboration. Phys. Lett. B **785**, 551 (2018)
7. L. Adamczyk et al., STAR Collaboration. Phys. Rev. Lett. **112**, 032302 (2014)
8. J. Adam et al., STAR Collaboration. Phys. Rev. Lett. **126**, 092301 (2021)
9. M.S Abdallah et al., STAR Collaboration. [arXiv:2101.12413](https://arxiv.org/abs/2101.12413) [nucl-ex]
10. R. Bellwied et al., Phys. Rev. C **99**(3), 034912 (2019)

11. X. Luo, J. Xu, B. Mohanty, N. Xu, *J. Phys. G* **40**, 105104 (2013)
12. X. Luo, *Phys. Rev. C* **91**, 034907 (2015)
13. T. Nonaka, M. Kitazawa, S. Esumi, *Phys. Rev. C* **95**(6), 064912 (2017)
14. X. Luo, T. Nonaka, *Phys. Rev. C* **99**, 044917 (2017)
15. A. Pandav, D. Mallick, B. Mohanty, *Nucl. Phys. A* **991**, 121608 (2019)
16. A. Pandav, STAR Collaboration. [arXiv:2003.12503](https://arxiv.org/abs/2003.12503) (Proceedings QM 2019)
17. S.A. Bass et al., *Prog. Part. Nucl. Phys.* **41**, 255 (1998)
18. S. Margetis, K. Safarik, O. Villalobos Baillie, *Annu. Rev. Nucl. Part. Sci.* **50**, 299 (2000)

Chapter 61

Far-from-Equilibrium Hydrodynamic Attractor for an Azimuthally Symmetric System



Ashutosh Dash and Victor Roy

Abstract A solution for the Boltzmann equation is obtained for an azimuthally symmetric radially expanding boost-invariant conformal system undergoing Gubser flow. The dynamics of transition is described by the presence of fixed points which describes the evolution of the system far from equilibrium at an early time collisionless free-streaming regime to the hydrodynamic regime at intermediate times and back to free streaming at late times. The attractor solution is found for various orders of moments as an interpolation between these fixed points.

61.1 Introduction

Hydrodynamics is an effective theory for the description of long-wavelength phenomena of fluids, that can be expressed as a small gradient expansion relative to a thermal background. Thus, hydrodynamics is expected to fail for systems that are far from equilibrium where the gradients are expected to be large. The medium produced in pp collisions at LHC and RHIC energies is an example of such a system. However, recent experimental results of high-energy pp collision have shown evidence of collectivity similar to those observed in heavy-ion collisions [1, 2]. The unprecedented success of hydrodynamics to describe collectivity in heavy-ion collisions, as well as small systems, can be attributed to the fact that there exists a stable universal attractor which makes the dynamical equations quickly converge and enter a hydrodynamic regime, at a time scale much smaller than the typical isotropization time scales [3].

Previous works [4–7] have mostly focused on studying the properties of attractors for rapidly expanding 1+1d boost invariant systems undergoing Bjorken flow using relativistic kinetic theory. We went beyond the previous works which considered

A. Dash (✉) · V. Roy
School of Physical Sciences, National Institute of Science Education and Research,
Jatni 752050, India
e-mail: ashutosh.dash@niser.ac.in

Homi Bhabha National Institute, Training School Complex, Anushaktinagar, Mumbai 400094, India

© The Author(s), under exclusive license to Springer Nature Singapore Pte Ltd. 2022
B. Mohanty et al. (eds.), *Proceedings of the XXIV DAE-BRNS High Energy Physics Symposium, Jatni, India*, Springer Proceedings in Physics 277,
https://doi.org/10.1007/978-981-19-2354-8_61

339

(1+1)d longitudinal boost-invariant systems, by considering a system undergoing Gubser flow which has a simultaneous transverse and longitudinal expansion. Using the relativistic Boltzmann equation, we found that, unlike (1+1)d Bjorken flow which has late time thermalization/hydrodynamization, Gubser flow is intrinsically a (3+1)d expanding system with dynamics such that the system goes from early time free-streaming regime to intermediate thermalization/hydrodynamization and back to free streaming in the late time regime.

61.2 Results and Discussion

We have investigated attractor solution for a conformal system undergoing Gubser flow [8]. The Boltzmann equation is solved in the relaxation time approximation (RTA) using a hierarchy of angular moments of the distribution function [9].

$$\begin{aligned} \frac{\partial \mathcal{L}_n}{\partial \rho} &= -\tanh(\rho) (a_n \mathcal{L}_n + b_n \mathcal{L}_{n-1} + c_n \mathcal{L}_{n+1}) - \hat{T}(\rho) \frac{\mathcal{L}_n}{c}, \quad (n \geq 1) \\ \frac{\partial \mathcal{L}_0}{\partial \rho} &= -\tanh(\rho) (a_0 \mathcal{L}_0 + c_0 \mathcal{L}_1), \quad (n = 0) \end{aligned} \quad (61.1)$$

where the coefficients a_n , b_n , and c_n are pure numbers and ρ is the de Sitter time. Here, c is a dimensionless parameter which, in RTA, can be expressed in terms of the shear viscosity (η_s) to entropy density (s) ratio $\bar{\eta}_s \equiv \eta_s/s$ as $c = 5\bar{\eta}_s$.

The n th-order angular moment \mathcal{L}_n of the distribution function is defined as

$$\mathcal{L}_n = \int d\hat{P} (\hat{p}^\rho)^2 P_{2n}(\hat{p}_\eta/\hat{p}^\rho) f(\rho; \hat{p}_\Omega, \hat{p}_\eta), \quad (61.2)$$

where $d\hat{P} = d\hat{p}_\eta d\hat{p}_\theta d\hat{p}_\phi / ((2\pi)^3 \hat{p}^\rho \cosh^2 \rho \sin \theta)$ is the phase space measure and P_{2n} is a Legendre polynomial of order $2n$. Here, $f(\rho; \hat{p}_\Omega, \hat{p}_\eta)$ is the distribution function.

The solution of coupled moments that we get after truncating the infinite set of equations at various orders has been compared to the exact kinetic solution and we found that even for $n < 2$, the solution captures the qualitative details of the exact solution. The dynamics of transition from an early time collisionless free streaming to the hydrodynamic regime at late times is described by the presence of fixed points which correspond to the zeros of $\beta(g_n)$, defined as

$$\frac{\partial g_n}{\partial \ln(\cosh \rho)} = \beta(g_n). \quad (61.3)$$

The quantity g_n is defined as $g_n(\rho) = \frac{\partial \ln \mathcal{L}_n}{\partial \ln(\cosh \rho)}$.

For $\rho > 0$, we find two free-streaming fixed points: $g_n = -2$ (stable fixed point) and $g_n = -3$ (unstable fixed point). For $\rho < 0$, the two fixed points get swapped. The late time behavior in such a system has been attributed to the presence of a different kind of fixed point, called hydrodynamic fixed point. To proceed, we shall assume that all the moments \mathcal{L}_n admit a gradient expansion in powers of $\tanh \rho$ [10]:

$$\mathcal{L}_n(\rho) = \sum_{m=n}^{\infty} (\tanh \rho)^m \gamma_n^{(m)}, \tag{61.4}$$

where $\gamma_n^{(m)}$'s are coefficients of the expansion. The fixed points can be calculated using the definition of $g_n(\rho)$ which yields,

$$g_n(\rho) = \frac{2(n-4)}{3} + n \operatorname{csch}^2(\rho). \tag{61.5}$$

Following [11], we define the ‘‘attractor’’ as the solution of (61.1) that joins smoothly the free-streaming and hydrodynamic fixed points. In Fig. 61.1, the numerical solution of attractor is shown for $n < 3$ in terms of the quantity g_n . We find that both the attractor and solution corresponding to arbitrary initial conditions (thin black lines) approach the hydrodynamic fixed point (shown by the black dotted line, these points are the asymptotic limits of (27) around $\rho \sim -5$. This behavior continues until

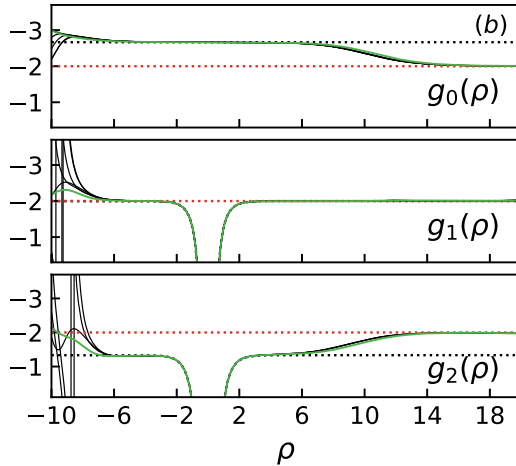


Fig. 61.1 Attractor solutions for \mathcal{L}_n moments (with $n = 0, 1, 2$) in terms of $g_n(\rho)$ truncating (61.1) after 30 terms. Thick green solid line is the ‘‘attractor’’ solution defined as the solution of coupled moments with initial conditions pertaining to stable free-streaming fixed point at $\rho < 0$, while thin black lines correspond to arbitrary initial conditions. Black and red dotted lines correspond to hydrodynamic fixed points and stable fixed point for $\rho > 0$, respectively. For all curves, $\rho_0 = -10$ and $c = 25/(2\pi)$

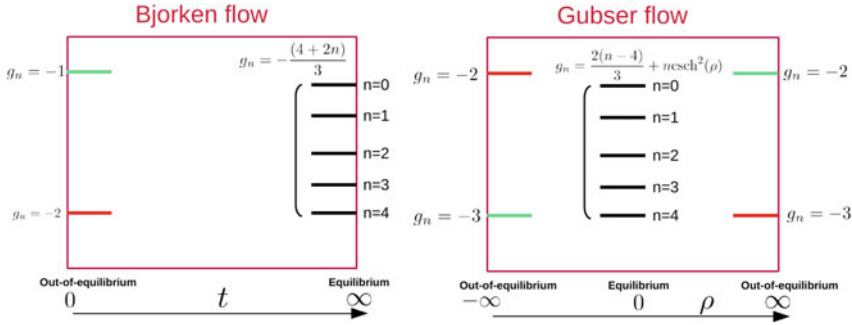


Fig. 61.2 A schematic diagram showing the fixed points for Bjorken (left) and Gubser (right) flow. The colour lines are free-streaming fixed points, whereas the black lines correspond to hydrodynamic fixed points. The green line corresponds to the stable fixed point, while the red line corresponds to the unstable fixed point

$\rho \sim 5$. After that, the system passes from the hydrodynamic fixed point to the stable free-streaming fixed point for $\rho > 0$, which is, of course, $g_n = -2$ (red dotted line).

A comparison between 1+1d Bjorken expansion to the intrinsically 3+1d Gubser expansion is apt here. Unlike Bjorken flow which thermalizes/hydrodynamizes at a late time, Gubser flow goes from FS \rightarrow thermalizes/hydrodynamizes \rightarrow FS as can be seen in Fig. 61.2. This is because the inverse Knudsen number $Kn^{-1} = \tau/\tau_R$ for Bjorken flow in the conformal limit grows with time, in the other hand, $Kn^{-1} = (\hat{\tau}_R |\tanh \rho|)^{-1}$ for Gubser flow increases for $\rho < 0$ and decreases $\rho > 0$ as shown in Fig. 61.2. We hope that these results offer detailed insights into the dynamics of longitudinal/transverse momentum isotropization in relativistic systems undergoing simultaneous transverse and longitudinal expansion.

References

1. V. Khachatryan et al., CMS. Phys. Lett. B **765**, 193–220 (2017). [arXiv:1606.06198](#) [nucl-ex]
2. R.D. Weller, P. Romatschke, Phys. Lett. B **774**, 351–356 (2017). [arXiv:1701.07145](#) [nucl-th]
3. M.P. Heller, R.A. Janik, M. Spaliński, P. Witaszczyk, Phys. Rev. Lett. **113**(26), 261601 (2014). [arXiv:1409.5087](#) [hep-th]
4. M.P. Heller, A. Kurkela, M. Spaliński, V. Svensson, Phys. Rev. D **97**(9), 091503 (2018). [arXiv:1609.04803](#) [nucl-th]
5. I. Aniceto, M. Spaliński, Phys. Rev. D **93**(8), 085008 (2016). [arXiv:1511.06358](#) [hep-th]
6. S. Jaiswal, C. Chattopadhyay, A. Jaiswal, S. Pal, U. Heinz, Phys. Rev. C **100**(3), 034901 (2019). [arXiv:1907.07965](#) [nucl-th]
7. C. Chattopadhyay, U.W. Heinz, Phys. Lett. B **801**, 135158 (2020). [arXiv:1911.07765](#) [nucl-th]
8. A. Dash, V. Roy, Phys. Lett. B **806**, 135481 (2020). [arXiv:2001.10756](#) [nucl-th]
9. J.P. Blaizot, L. Yan, JHEP **11**, 161 (2017). [arXiv:1703.10694](#) [nucl-th]
10. G.S. Denicol, J. Noronha, Phys. Rev. D **99**(11), 116004 (2019). [arXiv:1804.04771](#) [nucl-th]
11. J.P. Blaizot, L. Yan, Phys. Lett. B **780**, 283–286 (2018). [arXiv:1712.03856](#) [nucl-th]

Chapter 62

Spin Dynamics in Relaxation Time Approximation



Avdhesh Kumar

Abstract Using the classical treatment of spin degrees of freedom, we first discuss the formulation of perfect-fluid hydrodynamics with spin. Later, using the classical kinetic equations of massive spin-1/2 particles with the collision term treated in relaxation time approximation (RTA), we present a simple extension of the framework of perfect-fluid hydrodynamics with spin to the case including dissipation and show some results of a complete set of new type of kinetic coefficients that characterize dissipative spin dynamics.

62.1 Introduction

In the non-central heavy ion collisions because of angular momentum conservation the produced particles are expected to be spin polarized. This fact has been indeed confirmed by the STAR [1, 2], ALICE [3] and HADES [4] experiments where spin polarization of various particles (Λ , K^* , ϕ) has been successfully measured. Theoretically, hydrodynamic models turn out to be very useful tool to explain the global polarization of Λ -hyperons [5–8] but fails to describe the another experimental observable i.e. polarization along the beam (z) direction [9]. Hydrodynamic models assumes that the spin polarization at the freezeout is entirely determined by a quantity known as the thermal vorticity tensor, and lacks the dynamical evolution of the spin polarization which should occur with the systems expansion. Initial attempts to include the dynamical evolution of the spin polarization in perfect fluid version of hydrodynamic frameworks has been made in [10–14]. In this contribution we report our recent works [15, 16] where based on the classical treatment of spin degrees of freedom we discuss the formulation of the perfect-fluid hydrodynamics with spin

A. Kumar (✉)

School of Physical Sciences, National Institute of Science Education and Research, Jatni 752050, India

e-mail: avdhesh.kumar@niser.ac.in

Homi Bhabha National Institute, Training School Complex, Anushaktinagar, Mumbai 400094, India

and its extension to the case including dissipation and show explicit results for the new type of kinetic coefficients that characterize dissipative spin dynamics.

62.2 Classical Treatment of Spin Degrees of Freedom and Perfect-Fluid Hydrodynamics with Spin

In the classical treatment of particles with spin-1/2 one expresses the internal angular momentum tensor of particle $s^{\alpha\beta}$ in terms of the particle four momentum p_γ and spin four vector s_δ which are orthogonal to each other $p \cdot s = 0$, as $s^{\alpha\beta} = \frac{1}{m} \epsilon^{\alpha\beta\gamma\delta} p_\gamma s_\delta$. This implies that the spin four vector can be expressed as $s^\alpha = \frac{1}{2m} \epsilon^{\alpha\beta\gamma\delta} p_\beta s_\gamma$. Orthogonality condition of particle four momentum and spin four vector i.e. $p \cdot s = 0$ implies that in the particle rest frame where particle four momentum is given by $p^\mu = (m, 0, 0, 0)$ the spin four vector must be of the form $s^\alpha = (0, s v_*)$ with the normalization $|s v_*| = \mathfrak{s}$ and $-s^2 = |s v_*|^2 = \mathfrak{s}^2 = \frac{1}{2} (\frac{1}{2} + 1)$ being the length of the spin four vector.

Collision invariance of Boltzmann equation suggest for the following classical distribution function $f_s^\pm(x, p, s)$ of particles and antiparticles with spin-1/2 in an extended phase space that apart from the space-time coordinates and momenta also includes the spin four vector.

$$f_{s,\text{eq}}^\pm(x, \mathbf{p}, s) = f_{\text{eq}}^\pm(x, \mathbf{p}) \exp\left(\frac{1}{2} \omega_{\mu\nu} s^{\mu\nu}\right), \quad (62.1)$$

where $f_{\text{eq}}^\pm(x, \mathbf{p}) = \exp[-p^\mu \beta_\mu(x) \pm \xi(x)]$ is the well known Jüttner distribution function. The second rank tensor $\omega_{\alpha\beta}(x)$ is the spin polarization tensor which plays a role of the conjugate variable (spin chemical potential) to the spin angular momentum.

The normal equilibrium phase space-distribution function can be obtained by the normalization, $\int dS f_{s,\text{eq}}^\pm(x, \mathbf{p}v, s) = f_{\text{eq}}^\pm(x, \mathbf{p}v)$, where $dS = (m/\pi \mathfrak{s}) d^4s \delta(s \cdot s + \mathfrak{s}^2) \delta(p \cdot s)$. The hydrodynamic quantities such as conserved charge current N^μ , energy momentum tensor $T^{\mu\nu}$ and spin tensor $S^{\lambda,\mu\nu}$ are connected with the behavior of the microscopic constituents of the system through a phase-space distribution function $f(x, p, s)$. In equilibrium, charge current, energy-momentum tensor and the spin tensor can be determined by the following standard definitions

$$N_{\text{eq}}^\mu = \int dP \int dS p^\mu \left[f_{\text{eq}}^+(x, \mathbf{p}, s) - f_{\text{eq}}^-(x, \mathbf{p}, s) \right], \quad (62.2)$$

$$T_{\text{eq}}^{\mu\nu} = \int dP \int dS p^\mu p^\nu \left[f_{\text{eq}}^+(x, \mathbf{p}, s) + f_{\text{eq}}^-(x, \mathbf{p}, s) \right] \quad (62.3)$$

$$S_{\text{eq}}^{\lambda,\mu\nu} = \int dP \int dS p^\lambda s^{\mu\nu} \left[f_{\text{eq}}^+(x, \mathbf{p}, s) + f_{\text{eq}}^-(x, \mathbf{p}, s) \right] \quad (62.4)$$

In the leading order in ω , the integration on spin and momentum will yield the perfect fluid like form of the expressions for N^μ , $T^{\mu\nu}$ and $S^{\lambda,\mu\nu}$ [15, 16].

62.3 Relaxation Time Approximation of Collision Term and Dissipative Hydrodynamics with Spin

To include the dissipative effects we consider the relaxation time approximation (RTA) of the collision terms. In this case, if effects of mean fields are left out, the distribution function satisfies the following transport equation

$$p^\mu \partial_\mu f^\pm(x, \mathbf{p}, s) = p \cdot u \frac{f_{\text{eq}}^\pm(x, \mathbf{p}, s) - f^\pm(x, \mathbf{p}, s)}{\tau_{\text{eq}}} \quad (62.5)$$

The appropriate moments of the transport equation (62.5), will yield the following conservation laws

$$\partial_\mu N^\mu(x) = 0, \quad \partial_\mu T^{\mu\nu}(x) = 0, \quad \partial_\lambda S^{\lambda,\mu\nu}(x) = 0 \quad (62.6)$$

with $N^\mu = \int dP p^\mu [f^+(x, \mathbf{p}, s) - f^-(x, \mathbf{p}, s)]$, $T^{\mu\nu} = \int dP p^\mu p^\nu [f^+(x, \mathbf{p}, s) + f^-(x, \mathbf{p}, s)]$ and, $S^{\lambda,\mu\nu} = \int dP dS p^\lambda s^{\mu\nu} [f^+(x, \mathbf{p}, s) + f^-(x, \mathbf{p}, s)]$. Note that the necessary conditions for the above conservation laws (62.6), to be valid are $u_\mu \delta N^\mu = 0$, $u_\mu \delta T^{\mu\nu} = 0$ and $u_\lambda \delta S^{\lambda,\mu\nu} = 0$. These equations are known as the Landau matching conditions. Quantities, δN^μ , $\delta T^{\mu\nu}$, and $\delta S^{\lambda,\mu\nu}$ are the dissipative corrections to charge current, energy momentum and spin tensors which are defined in terms off-equilibrium distribution functions as follows

$$\delta N^\mu = \int dP dS p^\mu (\delta f_s^+ - \delta f_s^-) \quad (62.7)$$

$$\delta T^{\mu\nu} = \int dP dS p^\mu p^\nu (\delta f_s^+ + \delta f_s^-) \quad (62.8)$$

$$\delta S^{\lambda,\mu\nu} = \int dP dS p^\lambda s^{\mu\nu} (\delta f_s^+ + \delta f_s^-). \quad (62.9)$$

Using the simple Chapman-Enskog expansion of the single particle distribution as $f^\pm(x, \mathbf{p}, s) = f_{\text{eq}}^\pm(x, \mathbf{p}, s) + \delta f^\pm(x, \mathbf{p}, s) + \dots$ the following expression for the off-equilibrium distribution (up to the first order in space time gradient) can be derived from transport equation (62.5)

$$\delta f^\pm(x, \mathbf{p}, s) = -\frac{\tau_{\text{eq}}}{p \cdot u} p^\mu \partial_\mu f_{\text{eq}}^\pm(x, \mathbf{p}, s). \quad (62.10)$$

Finally, substituting (62.10) in (62.7), (62.8) and (62.9) and carrying out integration on spin and momentum variables, following expressions for the dissipative corrections δN^μ , $\delta T^{\mu\nu}$, and $\delta S^{\lambda,\mu\nu}$ can be obtained in the small polarization limit

$$\delta N^\mu = \tau_{\text{eq}} \beta_n (\nabla^\mu \xi), \quad (62.11)$$

$$\delta T^{\mu\nu} = \tau_{\text{eq}} (-\beta_\Pi \Delta^{\mu\nu} \theta + 2\beta_\pi \sigma^{\mu\nu}), \quad (62.12)$$

$$\delta S^{\lambda,\mu\nu} = \tau_{\text{eq}} \left[B_\Pi^{\lambda,\mu\nu} \theta + B_n^{\kappa\lambda,\mu\nu} (\nabla_\kappa \xi) + B_\pi^{\alpha\kappa\lambda,\mu\nu} \sigma_{\alpha\kappa} + B_\Sigma^{\kappa\beta\alpha\lambda,\mu\nu} (\nabla_\kappa \omega_{\beta\alpha}) \right]. \quad (62.13)$$

In the above expressions $\Delta^{\mu\nu} = g^{\mu\nu} - u^\mu u^\nu$, $\nabla^\mu = \Delta^{\mu\nu} \partial_\nu$. Quantities θ and $\sigma_{\mu\nu}$ are the expansion scalar and the shear flow tensor respectively. The coefficients, β 's are the well known first-order transport coefficients with their expression given in [16]. The tensor coefficients B 's appearing in (62.11), (62.12) and (62.13) are the kinetic coefficients for spin. The general tensor structure of these B -coefficients is given by equilibrium tensor quantities u^μ , $\Delta^{\mu\nu}$ and $\omega^{\mu\nu}$ [16]. It is important to note that in the small polarization limit, the dissipative corrections δN^μ and $\delta T^{\mu\nu}$ as given by (62.11), (62.12) remains same as obtained in the case of spinless system. The dissipative corrections in the spin tensor $\delta S^{\lambda,\mu\nu}$ as given by (62.13) is our main result suggesting that a dissipative corrections in the spin tensor are generated by the thermodynamic forces such as expansion scalar, gradient of chemical potential and temperature ratio, shear-flow tensor, and the gradient of the spin polarization tensor.

62.4 Summary and Conclusions

Using the classical treatment of spin degrees of freedom we have formulated the perfect-fluid hydrodynamics for particles with spin-1/2. Further, using classical kinetic equations for massive particles of spin-1/2, with the relaxation time approximation (RTA) of the collision term we have determined the dissipative effects. Equation (62.13) is our main results indicating that spin dissipation is caused by the various thermodynamic forces, namely, the expansion scalar, gradient of the chemical potential to temperature ratio, shear-flow tensor, and the gradient of a second rank antisymmetric tensor known as the spin polarization tensor. The kinetic coefficients (B 's) associated with the various thermodynamic forces leading to spin dissipation can be very useful to understand physical phenomena associated with the spin dissipation.

Acknowledgements I thank W. Florkowski, R. Ryblewski, A. Jaiswal and S. Bhadury for very fruitful collaboration.

References

1. L. Adamczyk et al., *Nature* **548**, 62 (2017)
2. J. Adam et al., *Phys. Rev. C* **98**, 014910 (2018)
3. S. Acharya et al., *Phys. Rev. Lett.* **125**(1), 012301 (2020)
4. F. Kornas et al., Lambda Polarization in Au+Au collisions at sN N = 2.4 GeV measured with HADES (talk given at the Strange Quark Matter, Bari, Italy, June 11-15, 2019.)
5. F. Becattini, I. Karpenko, M. Lisa, I. Upsal, S. Voloshin, *Phys. Rev. C* **95**(5), 054902 (2017)
6. I. Karpenko, F. Becattini, *Eur. Phys. J. C* **77**(4), 213 (2017)
7. F. Becattini, I. Karpenko, *Phys. Rev. Lett.* **120**(1), 012302 (2018)
8. H. Li, H. Petersen, L.G. Pang, Q. Wang, X.L. Xia, X.N. Wang, *Nucl. Phys. A* **967**, 772 (2017)
9. T. Niida, *Nucl. Phys. A* **982**, 511 (2019)
10. W. Florkowski, B. Friman, A. Jaiswal, E. Speranza, *Phys. Rev. C* **97**(4), 041901 (2018)
11. W. Florkowski, B. Friman, A. Jaiswal, R. Ryblewski, E. Speranza, *Phys. Rev. D* **97**(11), 116017 (2018)
12. W. Florkowski, A. Kumar, R. Ryblewski, *Phys. Rev. C* **98**, 044906 (2018)
13. W. Florkowski, R. Ryblewski, A. Kumar, *Prog. Part. Nucl. Phys.* **108**, 103709 (2019)
14. W. Florkowski, A. Kumar, R. Ryblewski, R. Singh, *Phys. Rev. C* **99**(4), 044910 (2019)
15. S. Bhadury, W. Florkowski, A. Jaiswal, A. Kumar, R. Ryblewski, *Phys. Lett. B* **814**, 136096 (2021)
16. S. Bhadury, W. Florkowski, A. Jaiswal, A. Kumar, R. Ryblewski, *Phys. Rev. D* **103**(1), 014030 (2021)

Chapter 63

Simulation Studies of $R_2(\Delta\eta, \Delta\phi)$ and $P_2(\Delta\eta, \Delta\phi)$ Correlation Functions in pp Collisions with the PYTHIA and HERWIG Models



Baidyanath Sahoo, Basanta Kumar Nandi, Prabhat Pujahari, Sumit Basu, and Claude Pruneau

Abstract We presented a study of charge-independent (CI) and charge-dependent (CD) two-particle differential number correlation functions R_2 and transverse momentum correlation functions P_2 in pp collisions at $\sqrt{s} = 2.76$ TeV with the PYTHIA and HERWIG models. Calculations were presented for unidentified hadrons in three p_T ranges $0.2 < p_T \leq 2.0$ GeV/c, $2.0 < p_T \leq 5.0$ GeV/c, and $5.0 < p_T \leq 30.0$ GeV/c. PYTHIA and HERWIG both qualitatively reproduce the near-side peak and away-side ridge correlation features reported by experiments. At low p_T , both models produce narrower near-side peaks in P_2 correlations than in R_2 as reported by the ALICE collaboration in p–Pb and Pb–Pb collisions. This suggests that the narrower shape of the P_2 near-side peak is largely determined by the p_T dependent angular ordering of hadrons produced in jets. Both PYTHIA and HERWIG predict widths that decrease with increasing p_T . Widths extracted for P_2 correlators are typically significantly narrower than those of the R_2 counterparts [1].

Two- and multi- particle azimuthal correlation functions have confirmed the existence of anisotropic flow and quark scaling (approximate) of flow coefficients in A–A collisions at RHIC and LHC as well as reveals the presence of flow in smaller systems (e.g., pA and high multiplicity pp collisions). Measurements of two particle differential number correlations, R_2 , and transverse momentum correlations, P_2 ,

B. Sahoo (✉) · B. K. Nandi

Department of Physics, Indian Institute of Technology Bombay, Mumbai, India
e-mail: baidya@iitb.ac.in

P. Pujahari

Department of Physics, Indian Institute of Technology Madras, Chennai, India

S. Basu

Department of Physics, Lund University, Lund, Sweden

C. Pruneau

Department of Physics and Astronomy, Wayne State University, Detroit, MI 48201, USA

© The Author(s), under exclusive license to Springer Nature Singapore Pte Ltd. 2022
B. Mohanty et al. (eds.), *Proceedings of the XXIV DAE-BRNS High Energy Physics Symposium, Jatni, India*, Springer Proceedings in Physics 277,
https://doi.org/10.1007/978-981-19-2354-8_63

have provided the collective nature of the azimuthal correlations observed in Pb–Pb collisions [2]. Centrality studies in A–A collisions show that near-side peak of both charge-independent (CI) and charge-dependent (CD) correlations is narrower for P_2 than in R_2 [3]. This correlator P_2 provides a more discriminating probe of the correlation structure of jets and their underlying events than the R_2 . To understand, we performed this study in three p_T ranges $0.2 < p_T \leq 2.0$ GeV/ c , $2.0 < p_T \leq 5.0$ GeV/ c , and $5.0 < p_T \leq 30.0$ GeV/ c , using PYTHIA and HERWIG models for the charged hadrons in pp collisions at $\sqrt{s} = 2.76$ TeV for both CI and CD.

63.1 Correlation Functions Definition

The R_2 and P_2 correlation functions are constructed by using single, $\rho_1(\eta, \phi)$,—and two, $\rho_2(\eta_1, \phi_1, \eta_2, \phi_2)$,—particle densities as a function of the particle pseudorapidity η and azimuthal angle ϕ .

The R_2 is defined as a two-particle cumulant normalized by the product of single particle densities as follows

$$R_2(\eta_1, \phi_1, \eta_2, \phi_2) = \frac{\rho_2(\eta_1, \phi_1, \eta_2, \phi_2)}{\rho_1(\eta_1, \phi_1)\rho_1(\eta_2, \phi_2)} - 1. \quad (63.1)$$

while the P_2 is defined as the ratio of differential correlator $\Delta p_T \Delta p_T$ to the square of the average transverse momentum, p_T , to make it dimensionless like R_2 , as follows

$$P_2(\eta_1, \phi_1, \eta_2, \phi_2) = \frac{\langle \Delta p_T \Delta p_T \rangle(\eta_1, \phi_1, \eta_2, \phi_2)}{\langle p_T \rangle^2} = \frac{1}{\langle p_T \rangle^2} \times \frac{\int_{p_{T,\min}}^{p_{T,\max}} dp_{T,1} dp_{T,2} \rho_2(\mathbf{p}_1, \mathbf{p}_2) \Delta p_{T,1} \Delta p_{T,2}}{\int_{p_{T,\min}}^{p_{T,\max}} dp_{T,1} dp_{T,2} \rho_2(\mathbf{p}_1, \mathbf{p}_2)} \quad (63.2)$$

where $\Delta p_{Ti} = p_{Ti} - \langle p_T \rangle$ and $\langle p_T \rangle$ is the inclusive mean transverse momentum [4]. The $\langle \Delta p_T \Delta p_T \rangle$ correlator is positive leading to positive value of P_2 whenever both particles are coming from higher (or lower) than the $\langle p_T \rangle$, but it is negative when a low- p_T particle ($p_T < \langle p_T \rangle$) is accompanied by a high- p_T particle ($p_T > \langle p_T \rangle$).

In this work, the correlators R_2 and P_2 are convoluted into the differences $\Delta\eta = \eta_1 - \eta_2$ and $\Delta\phi = \phi_1 - \phi_2$ and shifted by $-\pi/2$ for convenience of representation in the figures according to

$$O(\Delta\eta, \Delta\phi) = \frac{1}{\Omega(\Delta\eta)} \int O(\eta_1, \phi_1, \eta_2, \phi_2) \delta(\Delta\phi - \phi_1 + \phi_2) \times d\phi_1 d\phi_2 \delta(\Delta\eta - \eta_1 + \eta_2) d\eta_1 d\eta_2. \quad (63.3)$$

where $\Omega(\Delta\eta)$ represents the width of the acceptance in $\bar{\eta} = (\eta_1 + \eta_2)/2$ at a given value of $\Delta\eta$ [5]. The analysis of the R_2 and P_2 correlation functions is carried

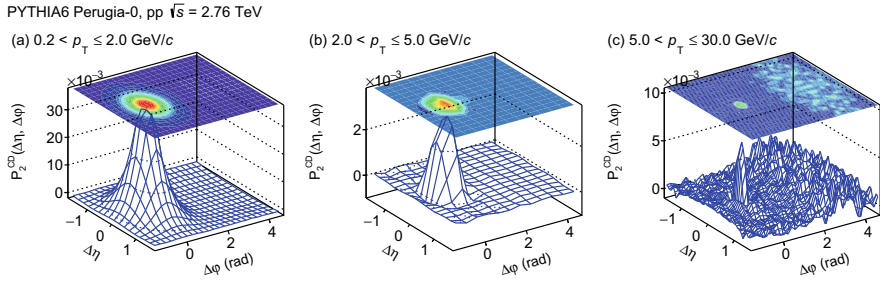


Fig. 63.1 Correlation functions P_2^{CD} of charged hadrons in three p_T ranges **a** $0.2 < p_T \leq 2.0$ GeV/c, **b** $2.0 < p_T \leq 5.0$ GeV/c, and **c** $5.0 < p_T \leq 30.0$ GeV/c, obtained with PYTHIA for pp collisions at $\sqrt{s} = 2.76$ TeV

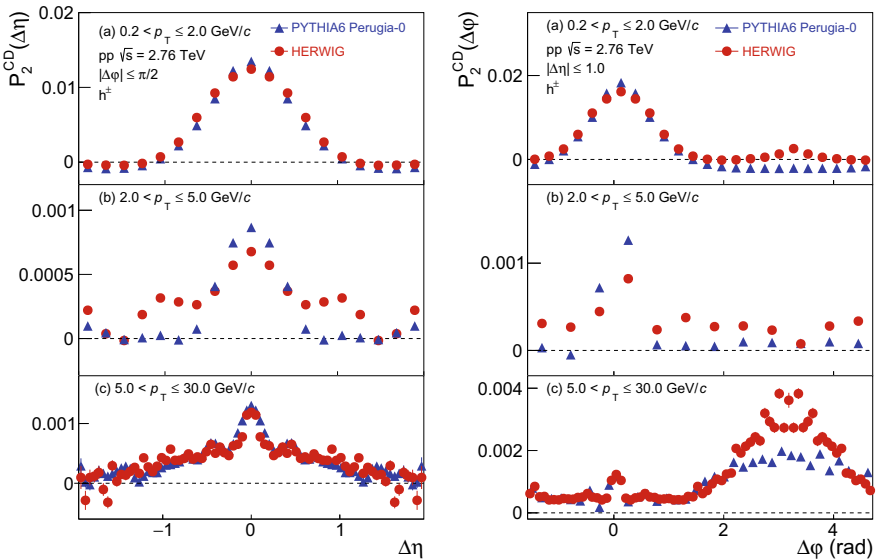


Fig. 63.2 The $\Delta\eta$ (left panel) and $\Delta\phi$ (right panel) projections of P_2^{CD} are calculated as averages of the 2-D correlations in the range $|\Delta\phi| \leq \pi/2$, and $|\Delta\eta| \leq 1.0$ respectively

out for charge combination pairs $(+-)$, $(-+)$, $(++)$, and $(--)$ to yield charge-independent, $O^{\text{CI}} = \frac{1}{2}[O^{+-} + O^{++} + O^{-+} + O^{--}]$, and charge-dependent, $O^{\text{CD}} = \frac{1}{2}[O^{+-} - O^{++} + O^{-+} - O^{--}]$, correlation functions [6].

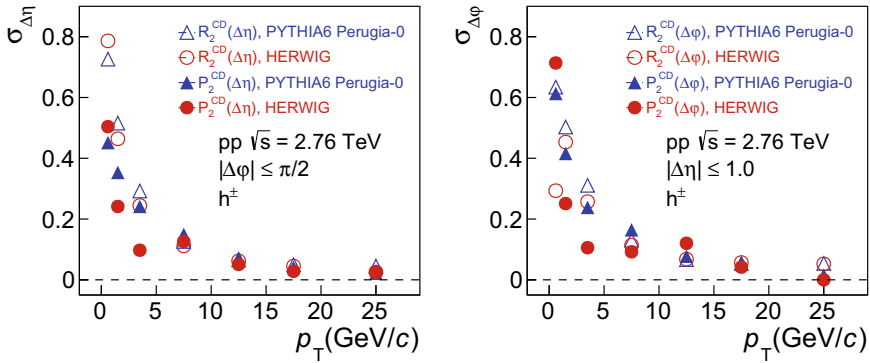


Fig. 63.3 Width of the near-side peak of CD correlation functions along $\Delta\eta$ (left panel), in the range $|\Delta\phi| \leq \pi/2$, and along $\Delta\phi$ (right panel), in the range $|\Delta\eta| \leq 1.0$, as function of p_T

63.2 Results

Figure 63.1 represents the decreasing trend of near-side width of P_2^{CD} using PYTHIA with rising p_T owing to the angular ordering and Schwinger mechanism.

Also, there is a finite away-side CD correlation in the p_T range $5.0 < p_T \leq 30.0$ GeV/c due to quark-quark jets as quarks possess charge. This correlator P_2^{CD} will help to probe the internal structure of jets and the charge production ordering. Comparison of PYTHIA and HERWIG, in Fig 63.2, reveals different behavior of the two models as they use different hadronization model.

To understand the trend, we performed this study in more refined p_T ranges. PYTHIA shows monotonic decrease of the width whereas HERWIG gives a more complicated behavior of the width as a function of p_T in both $\Delta\eta$ and $\Delta\phi$ case as shown in Fig 63.3. We observed that P_2 width is broader than R_2 in some p_T ranges due to the angular ordering, which is reverse in nature as stated [3]. Rigorous study will give a distinction between quark-jets and gluon-jets in future.

References

1. B. Sahoo, B.K. Nandi, P. Pujahari, S. Basu, C. Pruneau, Phys. Rev. C **100**, 024909 (2019)
2. S. Acharya et al., ALICE collaboration. Phys. Rev. Lett. **118**, 162302 (2017)
3. J. Adam et al., (ALICE Collaboration). [arXiv:1805.04422](https://arxiv.org/abs/1805.04422) [nucl-ex]
4. C. Pruneau, S. Gavin, S. Voloshin, Phys. Rev. C **66**, 044904 (2002)
5. M. Sharma, C.A. Pruneau, Phys. Rev. C **79**, 024905 (2009)
6. S. Bass, P. Danielewicz, S. Pratt, Phys. Rev. Lett. **85**, 2689 (2000)

Chapter 64

Jet Quenching Parameter in Semi-QGP



Balbeer Singh and Hiranmaya Mishra

Abstract We study the non-perturbative effects arising from the Polyakov loop effects on the jet quenching parameter within the matrix model of semi-QGP. With the elastic scattering of fast-moving parton and thermal parton, we estimate the suppression factor compared to the one estimated in the pQCD framework.

64.1 Introduction

With the discovery of hot quantum chromodynamics (QCD) matter commonly known as quark-gluon plasma (QGP) at high energy nuclear collision experiments at RHIC and LHC, the current goal is to quantify the non-perturbative effects on the hard probes such as jet quenching. A fast-moving parton (or jet) interacts with the hot and dense medium via multiple elastic/inelastic scatterings with the constituents of the thermal medium and medium induced gluon radiation. As a result of this interaction, the spectra of high transverse momentum (p_T) hadrons shift toward lower p_T , indicating suppression of large p_T hadrons compared to p-p collision. Such mechanism is known as jet quenching and has long been identified as one of the promising phenomenological tools to investigate the properties of the thermal medium created in high energy nuclear collision experiments. Experimentally, various observations such as, centrality dependent dijet asymmetry [1], photon and jet correlations [2], inclusive charged-particle jet production [3], photon-jet transverse momentum correlation [4]. These observations of the jet quenching can be summarized via the partonic transverse diffusion and energy loss mechanisms, which mainly gets contribution from elastic and in-elastic scatterings of the leading parton with the surrounding thermal

B. Singh (✉) · H. Mishra
Physical Research Laboratory, Ahmedabad 380009, Gujarat, India
e-mail: balbeer@prl.res.in

H. Mishra
e-mail: hm@prl.res.in

medium. Perturbative QCD predicts large jet quenching parameter, however, on the other hand, one needs relatively small quenching parameter to explain the observed experimental data for jet quenching.

64.2 Semi-QGP

At high temperature, the density of colored particles like quarks and gluon are large and can be calculated using perturbative QCD. However, at low temperature, colored particles are statistically suppressed and are measured by the small value of Polyakov loop e.g., at chiral cross-over temperature $T_c \sim 156.5 \pm 1.5$ MeV [5] which is way smaller from its asymptotic value, i.e., $\phi = 1$. Because of the suppression of colored particles, the region near chiral cross-over is termed as semi-QGP [6]. Semi QGP is characterized by the Polyakov loop as defined in (64.2). In the mean-field approximation, we take the constant background field as $A_\mu^0 = \frac{1}{g} \delta_{\mu 0} Q^a$ with $Q^a = 2\pi q^a T$. Since A_0 is traceless so sum over Q 's Vanishes, i.e., $\sum_a Q^a = 0$. For an $SU(3)$ group, $Q^a = (-Q^i, -Q^{i-1}, \dots, 0, Q^{i-1}, Q^i)$, where $i = N/2$ if N is even and $(N - 1)/2$ if N is odd. In the temporal direction, the Wilson line is written as

$$P = \mathcal{P} \exp \left(ig \int_0^\beta d\tau A_0(x_0, \mathbf{x}) \right) \tag{64.1}$$

where \mathcal{P} stands for the ordering of imaginary time and τ is imaginary time. Polyakov loop, which is the trace of Wilson line, in the constant background gauge field can be written as

$$\phi = \frac{1}{3} \sum_{a=1}^3 \exp(i2\pi q^a) = \frac{1}{3} (1 + 2 \cos(2\pi q)). \tag{64.2}$$

The generator is given by

$$(t^{ab})_{cd} = \frac{1}{\sqrt{2}} \mathcal{P}_{cd}^{ab}. \tag{64.3}$$

where

$$\mathcal{P}_{cd}^{ab} = \mathcal{P}_{ba;cd} = \mathcal{P}^{ab;dc} = \delta_c^a \delta_d^b - \frac{1}{N} \delta^{ab} \delta_{cd} \tag{64.4}$$

The structure constant of the group in the double line basis is given by

$$f^{ab,cd,ef} = \frac{i}{\sqrt{2}} (\delta^{ad} \delta^{cf} \delta^{eb} - \delta^{af} \delta^{cb} \delta^{ed}). \tag{64.5}$$

The background gauge field acts as an imaginary chemical potential for colored particles so the statistical distribution function of quark/anti-quark and the gluon are [7]

$$f_a(E) = \frac{1}{e^{\beta(E-iQ_a)} + 1}, \quad \tilde{f}_a(E) = \frac{1}{e^{\beta(E+iQ_a)} + 1}, \quad (64.6)$$

$$f_{ab}(E) = \frac{1}{e^{\beta(E-i(Q_a-Q_b))} - 1}, \quad (64.7)$$

where the single and double indices are for quark/antiquark and gluon. Further, the resummed gluon propagator in the presence of a static background gauge field is given as [8]

$$D_{\mu\nu; abcd}(K) = P_{\mu\nu}^L \frac{k^2}{K^2} D_{abcd}^L(K) + P_{\mu\nu}^T D_{abcd}^T(K), \quad (64.8)$$

where $P_{\mu\nu}^T = g_{\mu i} \left(-g^{ij} - \frac{k^i k^j}{K^2} \right) g_{j\nu}$ and $P_{\mu\nu}^L = -g_{\mu\nu} + \frac{k_\mu k_\nu}{K^2} - P_{\mu\nu}^T$ are the longitudinal and the transverse projection operators.

64.3 Suppression Factor for Jet

Assuming that the jet parton is a quark or the jet is initiated by a quark, we compute the matrix element squared for jet parton and thermal parton which will be further be used to estimate quenching parameter. The dominant contribution for the jet-thermal quark scattering arises from the t -channel Coulomb scattering, $q_j^c(p) + q^a(k) \rightarrow q_j^d(p') + q^b(k')$ where q_j denotes a jet and q denotes a thermal quark. Here c, d are the color indices for initial and final state jet. Similarly, a, b are color indices for the initial and final state thermal quark. The corresponding scattering amplitude can be written as.

$$-i\mathcal{M}_{ab,cd} = \frac{g^2}{2} [\bar{u}(k')\gamma^\mu u(k)] \mathcal{P}_{ab}^{ij} D_{\mu\nu}^{ij,kl}(Q) \mathcal{P}_{dc}^{lk} [\bar{u}(p')\gamma^\nu u(p)] \quad (64.9)$$

where $D_{\mu\nu}^{ij,kl}$ is resummed gluon propagator, $Q = k' - k = p - p'$ is exchange gluon four momentum and \mathcal{P}_{ab}^{ij} is the projection operator defined in (64.4). Performing the color sum, the matrix element squared can be simplified to

$$|\mathcal{M}_{ab}^2 = 4g^4 \mathcal{P}_{ab}^{ij} \mathcal{P}_{cd}^{ij} \mathcal{P}_{ba}^{i'j'} \mathcal{P}_{dc}^{j'i'} \left(\frac{|q|^4}{Q^4} D_L^{ij}(Q) D_L^{*i'j'}(Q) [2(p \cdot P^L \cdot k')(p \cdot P^L \cdot k) - (k \cdot k')] \right. \\ \left. \times (p \cdot P^L \cdot p) + D_T^{ij}(Q) D_T^{*i'j'}(Q) [2(p \cdot P^T \cdot k')(k \cdot P^T \cdot p) - (k \cdot k')(p \cdot P^T \cdot p)] \right). \quad (64.10)$$

In the above equation, we have kept terms that give logarithmic contribution. The quenching parameter can be obtained from

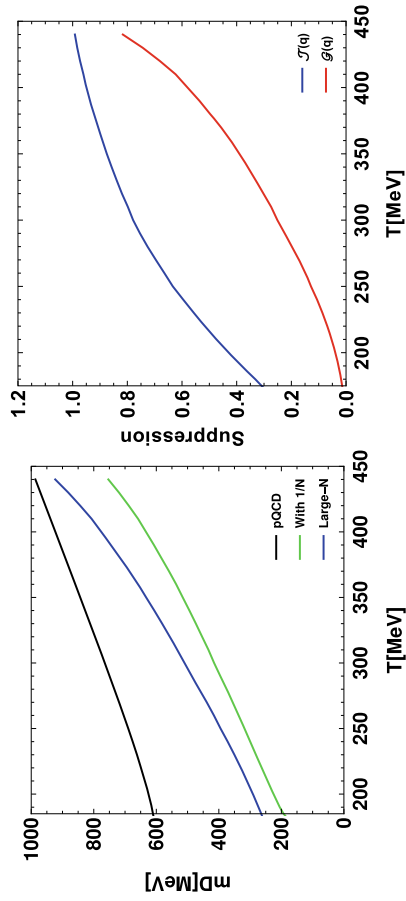


Fig. 64.1 Debye mass as a function of temperature. The black line corresponds to pQCD result and the green and blue lines are within the matrix model (left). Suppression factor for quark jet (blue) and gluon jet (red) obtained within the matrix model

$$\hat{q} = \frac{1}{v} \int d^3q \frac{d\Gamma}{d^3q} \Big|_{q_{\perp}^2} \quad (64.11)$$

where v is velocity of the jet parton and the interaction is given as

$$\begin{aligned} \frac{d\Gamma}{d^3q} &= \frac{1}{4E_p^2(2\pi)^3} \int \frac{d\mathbf{k}}{4E_k E_{k'}} \sum_{a,b} f_{a/ef}(E_k)(1 - f_{b/gh}(E_{k'})) \\ &\times |\mathcal{M}_{ab/efgh}^2(2\pi)\delta(E_k - E_{k'} - \mathbf{v} \cdot \mathbf{q})|. \end{aligned} \quad (64.12)$$

Note that the color of the initial and final thermal partons are summed with the corresponding distribution function. Similarly, the scattering amplitude for the t -channel quark and gluon scattering is

$$\begin{aligned} -i\mathcal{M}_{ef,gh} &= g^2 f^{cd,ef,gh} t_{ab}^{ml} (\bar{u}(P')\gamma^{\delta}u(P))\mathcal{D}_{\sigma\delta;cd,ml}(Q) \\ &\times C^{\mu\nu\sigma}(-Q, -K, K')\epsilon_{\mu}(K)\epsilon_{\nu}^*(K') \end{aligned} \quad (64.13)$$

where ef, gh are color indices for initial and final thermal gluon.

In Fig. 64.1, the Debye mass within the matrix model and perturbative QCD is plotted as a function of temperature. Here, the black solid line is from pQCD and the green and the blue lines are within the matrix model with Polyakov loop expectation value from [9]. Further, the green curve corresponds to including $1/N$ term and the blue one after excluding $1/N$ term of (64.4). It may clearly be seen that the Debye mass is suppressed after including Polyakov loop. In the right panel of the same, the suppression factor, the quark jet ($\mathcal{F}(q)$) and the gluon jet ($\mathcal{G}(q)$) as a function of temperature, is shown. This indicates that at low temperature, the quenching parameter is compared to the one predicted by pQCD. Moreover, the gluon jets are suppressed more compared to the quark one.

References

1. G. Aad et al., ATLAS. Phys. Rev. Lett. **105**, 252303 (2010). [arXiv:1011.6182](#) [hep-ex]
2. S. Chatrchyan et al., [CMS]. Phys. Lett. B **718**, 773–794 (2013). [arXiv:1205.0206](#) [nucl-ex]
3. J. Adam et al., [STAR]. Phys. Rev. C **102**(5), 054913 (2020). [arXiv:2006.00582](#) [nucl-ex]
4. M. Aaboud et al., [ATLAS]. Phys. Lett. B **789**, 167–190 (2019) [arXiv:1809.07280](#) [nucl-ex]
5. A. Bazavov et al., [HotQCD]. Phys. Lett. B **795**, 15–21 (2019). [arXiv:1812.08235](#) [hep-lat]
6. R.D. Pisarski, V.V. Skokov, Phys. Rev. D **94**(3), 034015 (2016). [arXiv:1604.00022](#) [hep-ph]
7. B. Singh, H. Mishra, Phys. Rev. D **101**(5), 054027 (2020). [arXiv:1911.06764](#) [hep-ph]
8. B. Singh, A. Abhishek, S.K. Das, H. Mishra, Phys. Rev. D **100**(11), 114019 (2019). [arXiv:1812.05263](#) [hep-ph]
9. A. Bazavov, N. Brambilla, H.T. Ding, P. Petreczky, H.P. Schadler, A. Vairo, J.H. Weber, Phys. Rev. D **93**(11), 114502 (2016). [arXiv:1603.06637](#) [hep-lat]

Chapter 65

Anisotropic Pressure and Quark Number Susceptibility of Strongly Magnetized QCD Medium



Bithika Karmakar, Ritesh Ghosh, Aritra Bandyopadhyay, Najmul Haque, and Munshi G Mustafa

Abstract In this work, we compute the hard thermal loop pressure of quark-gluon plasma within strong magnetic field approximation at one-loop order. Magnetic field breaks the rotational symmetry of the system. As a result, the pressure of QGP becomes anisotropic and one finds two different pressures along the longitudinal (along the magnetic field direction) and transverse direction. Similarly, the second-order quark number susceptibility, which represents the fluctuation of the net quark number density, also becomes anisotropic. We compute the second-order QNS of deconfined QCD matter in strong field approximation considering the same chemical potential for two quark flavors.

65.1 Introduction

Recent studies have shown that the magnetic field created by the spectator particles at heavy ion collisions can be as high as $eB \sim 10^{18}$ Gauss [1, 2] at the time of collision. The energy of quarks gets quantized in the presence of strong magnetic field. In strong field approximation, only the lowest Landau level of quark energy is considered. The EoS of the system in the presence of strong magnetic field is particularly important as it is used to find the time evolution of the system using

B. Karmakar (✉) · R. Ghosh · M. G. Mustafa
Theory Division, Saha Institute of Nuclear Physics, 1/AF, Bidhannagar, Kolkata 700064, India
e-mail: bithika.karmakar@saha.ac.in

Homi Bhabha National Institute, Anushaktinagar, Mumbai 400094, Maharashtra, India

A. Bandyopadhyay
Guangdong Provincial Key Laboratory of Nuclear Science, Institute of Quantum Matter, South China Normal University, Guangzhou 510006, China

N. Haque
School of Physical Sciences, National Institute of Science Education and Research, Jatni, Khurda 752050, India

Homi Bhabha National Institute, Training School Complex, Anushaktinagar, Mumbai 400094, India

© The Author(s), under exclusive license to Springer Nature Singapore Pte Ltd. 2022 359
B. Mohanty et al. (eds.), *Proceedings of the XXIV DAE-BRNS High Energy Physics Symposium, Jatni, India*, Springer Proceedings in Physics 277,
https://doi.org/10.1007/978-981-19-2354-8_65

various hydrodynamic models. Besides, quark number susceptibility represents the fluctuation of the net quark number density over the average value. Fluctuation of the conserved quantities is used as probe of the hot and dense matter created in heavy ion collisions. Here, we calculate the pressure and second-order diagonal QNS of the strongly magnetized medium using one loop HTL pt. theory within the scale hierarchy $gT < T < \sqrt{|q_f B|}$.

65.2 Formalism

In thermal medium, the presence of the heat bath velocity u^μ breaks the boost symmetry of the system. Moreover, the presence of magnetic field breaks the rotational symmetry of the system. We consider the rest frame of the heat bath velocity $u^\mu = (1, 0, 0, 0)$ and the magnetic field along z direction, i.e., $n_\mu = (0, 0, 0, 1)$.

65.2.1 General Structure of Gluon Effective Propagator

Now, the gluon self-energy $\Pi^{\mu\nu}$ can be expressed in terms of the seven available tensors $P^\mu P^\nu$, $u^\mu u^\nu$, $n^\mu n^\nu$, $P^\mu u^\nu + u^\mu P^\nu$, $P^\mu n^\nu + n^\mu P^\nu$, $u^\mu n^\nu + n^\mu u^\nu$. Using the transversality condition $P^\mu \Pi_{\mu\nu} = 0$, the gluon self-energy can be written [3] in terms of the four constituent tensors $B^{\mu\nu}$, $R^{\mu\nu}$, $Q^{\mu\nu}$ and $N^{\mu\nu}$ which are given in [3].

Using Dyson-Schwinger equation, the general structure of gluon effective propagator can be written as

$$\begin{aligned} \mathcal{D}_{\mu\nu} = & \frac{\xi P_\mu P_\nu}{P^4} + \frac{(P^2 - \gamma)B_{\mu\nu}}{(P^2 - \alpha)(P^2 - \gamma) - \delta^2} + \frac{R_{\mu\nu}}{P^2 - \beta} \\ & + \frac{(P^2 - \alpha)Q_{\mu\nu}}{(P^2 - \alpha)(P^2 - \gamma) - \delta^2} + \frac{\delta N_{\mu\nu}}{(P^2 - \alpha)(P^2 - \gamma) - \delta^2}. \end{aligned} \quad (65.1)$$

65.2.2 General Structure of Quark Effective Propagator

Similarly, the general structure of fermion self-energy in the presence of strong magnetic field can be written as [4]

$$\Sigma(P) = a\not{t} + b\not{t} + c\gamma_5\not{t} + d\gamma_5\not{t}$$

where the form factors in the presence of strong magnetic field are calculated in [4]. The general structure of fermion effective propagator is given as

$$S_{eff}(P) = P_- \frac{\not{L}(P)}{L^2} P_+ + P_+ \frac{\not{R}(P)}{R^2} P_- \quad (65.2)$$

with

$$L^\mu = P^\mu + (a + c)u^\mu + (b + d)n^\mu, \quad (65.3)$$

$$R^\mu = P^\mu + (a - c)u^\mu + (b - d)n^\mu. \quad (65.4)$$

65.3 Anisotropic Pressure and Second-Order QNS of Quark Gluon Plasma in Strongly Magnetized Medium

The pressure of quark gluon plasma in the presence of strong magnetic field becomes anisotropic, i.e., the pressure along the magnetic field (longitudinal) and the pressure perpendicular (transverse) to it become different. In this case, the free energy density in a finite spatial volume V is given by

$$F = \mathcal{F}/V = \epsilon^{\text{total}} - Ts - eB \cdot M, \quad (65.5)$$

where ϵ^{total} and s are the total energy density and entropy density, respectively. The magnetization per unit volume is given by

$$M = -\frac{\partial F}{\partial(eB)}. \quad (65.6)$$

Now, the longitudinal and transverse pressures are given as

$$P_z = -F, \quad P_\perp = -F - eB \cdot M = P_z - eB \cdot M. \quad (65.7)$$

The free energy of quarks and gluons in the presence of strong magnetic field can be calculated using HTL approximation as

$$\begin{aligned} F_q &= -N_c N_f \sum_f \int \ln(\det[S_{eff}^{-1}]) \\ &= -N_c N_f \sum_f \int \ln \left[P_{\parallel}^4 \left(1 + \frac{4a^2 - 4b^2 + 4ap_0 + 4bp_3}{P_{\parallel}^2} \right) \right]. \end{aligned} \quad (65.8)$$

$$F_g = (N_c^2 - 1) \left[\frac{1}{2} \int \ln[\det(D_{\mu\nu}^{-1})] - \int \ln(-P^2) \right].$$

Similarly, the second-order longitudinal and transverse QNS are defined as [5]

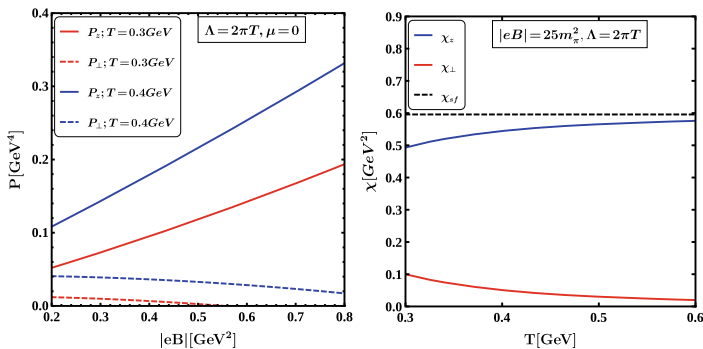


Fig. 65.1 Variation of the longitudinal and transverse pressure at $\mu = 0$ with magnetic field is shown in left panel. Magnetization as a function of temperature at $\mu = 0$ is shown in right panel for $N_f = 3$

$$\chi_z = \left. \frac{\partial^2 P_z}{\partial \mu^2} \right|_{\mu=0}, \quad \chi_\perp = \left. \frac{\partial^2 P_\perp}{\partial \mu^2} \right|_{\mu=0}. \quad (65.9)$$

65.4 Results

In left panel of Fig. 65.1, the longitudinal and transverse pressure of strongly magnetized QGP are shown with the variation of magnetic field strength at $\mu = 0$. It can be seen that the longitudinal and transverse pressure show different natures with magnetic field. The longitudinal pressure increases with the magnetic field whereas the transverse one decreases. This means that the system elongates more along the magnetic field direction and it can even shrink [6] along the transverse direction at very high magnetic field strength.

The variation of second-order diagonal QNS of strongly magnetized QGP is shown with temperature in the right panel of Fig. 65.1. Similar to the anisotropic pressure, the longitudinal and the transverse QNS also shows different nature. At very high temperature, the QNS of the interacting system reaches the ideal value.

65.5 Summary

Using one loop HTL pt theory with strong magnetic field approximation, we found that the QGP pressure becomes anisotropic. Due to the presence of magnetization, the transverse pressure decreases with magnetic field. The transverse pressure can even be negative at very high magnetic field strength indicating the shrinking of the system along the transverse direction. It has been found that the system shows paramagnetic

nature. On the other hand, second-order diagonal QNS has been calculated using the longitudinal and the transverse pressure. We find qualitative match of our results with lattice studies [6]. However, perturbative studies can be improved by considering higher loop order calculations.

References

1. V. Skokov, A.Y. Illarionov, V. Toneev, *Int. J. Mod. Phys. A* **24**, 5925–5932 (2009)
2. D.E. Kharzeev, L.D. McLerran, H.J. Warringa, *Nucl. Phys. A* **803**, 227–253 (2008)
3. B. Karmakar, A. Bandyopadhyay, N. Haque, M.G. Mustafa, *Eur. Phys. J. C* **79**(8), 658 (2019)
4. B. Karmakar, R. Ghosh, A. Bandyopadhyay, N. Haque, M.G. Mustafa, *Phys. Rev. D* **99**(9), 094002 (2019)
5. B. Karmakar, N. Haque, M.G. Mustafa, *Phys. Rev. D* **102**(5), 054004 (2020)
6. G.S. Bali, F. Bruckmann, G. Endrödi, S.D. Katz, A. Schäfer, *JHEP* **08**, 177 (2014)

Chapter 66

Latest Results on Hadronic Resonance Production with ALICE at the LHC



Dukhishyam Mallick

Abstract Hadronic resonances, due to their short lifetimes, are useful to probe the properties of the hadronic phase in ultra-relativistic heavy-ion collisions. They are good candidates to investigate the interplay between re-scattering and regeneration effects on the particle production in the hadronic phase. Measurement of various resonances has different lifetimes, masses, quantum numbers and quark content, which can provide a wealth of information to understand the particle production mechanism, strangeness enhancement, parton energy loss, and the possible onset of collective effects in small systems. We present a comprehensive set of the latest results in the ALICE experiment on $\rho(770)^0$, $K^*(892)^0$, $f_0(980)$, $\phi(1020)$, $\Sigma(1385)^\pm$, $\Lambda(1520)$, and $\Xi(1530)^0$ production in pp, p-Pb, Pb-Pb, and Xe-Xe collisions at various LHC center-of-mass energies. Results include p_T -integrated yields, particle ratios, and nuclear modification factors. The results are also compared with model predictions and measurements at lower energies.

66.1 Introduction

The study of hadronic-resonance production serves as a unique tool to understand the properties of the hadronic medium created in heavy-ion collisions. Due to their short lifetimes ($\sim \text{fm}/c$), resonance yields and particle ratios are expected to be modified due to the interaction of their decay products within the hadronic medium via regeneration and re-scattering processes. Recent measurements in p-p and p-Pb collisions as a function of multiplicity have uncovered various similar features [1, 2] to

Dukhishyam Mallick for the ALICE Collaboration.

D. Mallick (✉)

School of Physical Sciences, National Institute of Science Education and Research, Jatni 752050, India

e-mail: mallick.dukhishyam@cern.ch

Homi Bhabha National Institute, Training School Complex, Anushaktinagar, Mumbai 400094, India

those seen in heavy-ion collisions [3]. For example, the particle ratio of short-lived resonances like K^*/K shows a decreasing trend with increasing charged-particle multiplicity in small systems, similar to what is observed in the heavy-ion collisions [3]. The systematic comparison of measurements related to these resonances may enable us to further investigate the dynamics of the hadronic phase and to study the lifetime of the hadronic phase. The nuclear modification factor for resonances is an observable, which helps in understanding in-medium parton energy loss, distinguishing initial- and final state effects due to cold nuclear matter and the hot dense medium, respectively.

66.2 Analysis Details

A detailed description of the ALICE detector setup and its performance is available at [4, 5]. The sub-detectors relevant for these studies are the Time Projection Chamber (TPC), the Time-of-Flight detector (TOF), the Inner Tracking System (ITS), covering pseudorapidity window of $|\eta| < 0.9$, and the V0A ($2.8 < \eta < 5.1$) and V0C ($-3.7 < \eta < -1.7$) detectors. The ITS and TPC are used for charged-particle tracking and primary vertex reconstruction, whereas particle identification is done by measuring specific energy loss in the detector gas of TPC and the time-of-flight information using TOF. The V0 detectors are used for triggering and estimation of multiplicity/centrality at forward rapidities. The measurements of hadronic resonance production are performed at mid-rapidity ($|y| < 0.5$) in pp, Xe-Xe, and Pb-Pb collisions and at $0 < y_{\text{cms}} < 0.5$ in p-Pb collisions as a function of the charged-particle multiplicity. The invariant-mass method is used to reconstruct resonances from their decay products: $\rho \rightarrow \pi^+\pi^-$ (branching ratio $\sim 100\%$), $K^* \rightarrow K^+\pi^-$ (66.6%), $\phi \rightarrow K^+K^-$ (49.2%), $\Lambda(1520) \rightarrow Kp$ (22.5%) and $\Sigma^{*+}(\Sigma^{*-}) \rightarrow (\Lambda\pi^+)\Lambda\pi^-$ (87%). The combinatorial background has been estimated using event mixing or like-sign method depending on the analysis. For strange and multi-strange hadrons, a set of topological selections are applied. The raw yields are extracted from the signal distribution after the subtraction of the combinatorial background and further corrected for the detector acceptance, tracking efficiency, and branching ratio.

66.3 Results and Discussions

The p_T -integrated yields (dN/dy) and mean transverse momentum ($\langle p_T \rangle$) are determined by integrating or averaging the p_T spectra in the measured range and by using a fit function (Levy-Tsallis or Blast Wave) to extrapolate the yields in the unmeasured p_T region for each multiplicity/centrality class. The yield of K^* scaled by $\langle dN_{\text{ch}}/d\eta \rangle_{|\eta| < 0.5}$ as a function of $\langle dN_{\text{ch}}/d\eta \rangle_{|\eta| < 0.5}$ in pp collisions at $\sqrt{s} = 7$ and 13 TeV, and in p-Pb collisions at $\sqrt{s_{\text{NN}}} = 5.02$ and 8.16 TeV is shown in Fig. 66.1a. The

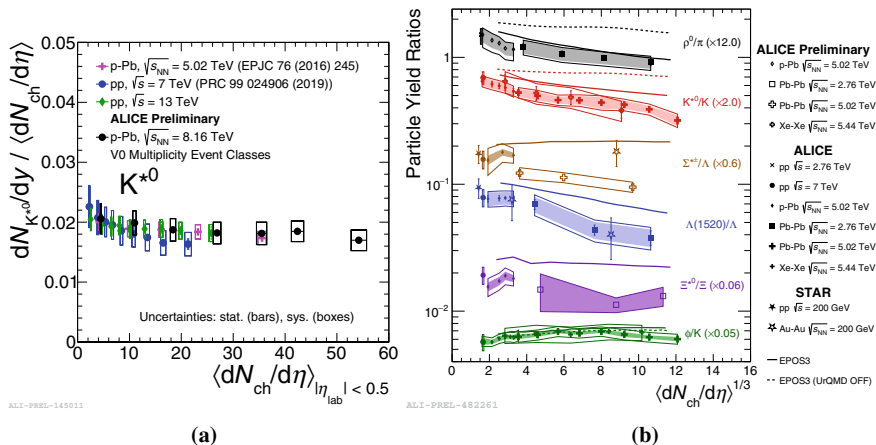
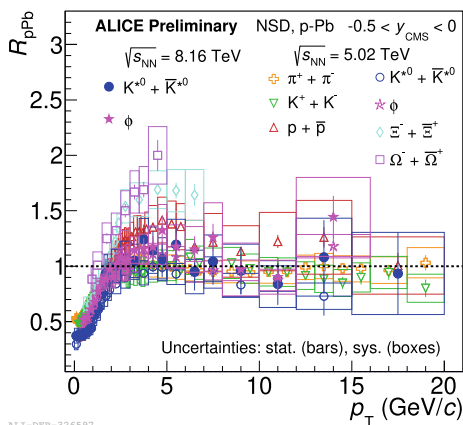


Fig. 66.1 **a** Scaled integrated yield ($dN/dy / \langle dN_{ch}/d\eta \rangle_{|\eta| < 0.5}$) of K^* as a function of charged particle multiplicity ($\langle dN_{ch}/d\eta \rangle_{|\eta| < 0.5}$) in p-Pb collisions at $\sqrt{s_{NN}} = 8.16$ TeV are compared with p-p collisions at $\sqrt{s} = 7, 13$ TeV, and p-Pb collisions at $\sqrt{s_{NN}} = 5.02$ TeV. **b** Summary of p_T -integrated yield ratios of different resonances to their ground state particles (ρ/π , K^*/K , $\Sigma^{*\pm}/\Lambda$, $\Lambda(1520)/\Lambda$, Ξ^{*0}/Ξ and ϕ/K) as a function of $\langle dN_{ch}/d\eta \rangle^{1/3}$ in pp, p-Pb, Xe-Xe and Pb-Pb collisions along with model predictions from EPOS3 (with and without URQMD) and STAR data

Fig. 66.2 Nuclear modification factor of K^* and ϕ as a function of p_T in p-Pb collisions at $\sqrt{s_{NN}} = 5.02$ TeV and 8.16 TeV and Ξ , Ω at $\sqrt{s_{NN}} = 5.02$ TeV are compared with π , K , and p at $\sqrt{s_{NN}} = 5.02$ TeV. The statistical and systematic errors are represented by vertical bars and boxes around the data points



scaled integrated yields are similar and consistent with each other within uncertainties at similar $\langle dN_{ch}/d\eta \rangle_{|\eta| < 0.5}$, irrespective of the colliding systems and energies.

Figure. 66.1b shows the ratio of resonance yields to those of long-lived particles as a function of the cubic root of the average charged-particle multiplicity ($\langle dN_{ch}/d\eta \rangle^{1/3}$) for various resonances in different collision systems and energies measured by the ALICE [3] and STAR [6] collaborations. A decreasing trend with multiplicity in the ratios ρ/π , K^*/K , and $\Lambda(1520)/\Lambda$ is observed when going from peripheral to central collisions, whereas the $\Sigma^{*\pm}/\Lambda$, Ξ^{*0}/Ξ , and ϕ/K ratios are nearly constant across all systems and centrality classes. These results suggest the domi-

nance of re-scattering effects over regeneration in the hadronic phase. The ratios are compared to the EPOS3 with UrQMD [7], which qualitatively describes the measurements. Figure 66.2 shows the comparison of the nuclear modification factor (R_{pPb}) of K^* and ϕ at $\sqrt{s_{NN}} = 5.02$ and 8.16 TeV along with π , K, p and multi-strange baryons (Ξ , Ω) at $\sqrt{s_{NN}} = 5.02$ TeV in p–Pb collisions. No significant energy dependence in R_{pPb} is observed for K^* and ϕ measured at $\sqrt{s_{NN}} = 5.02$ and 8.16 TeV. At intermediate p_T ($2 < p_T < 6$ GeV/c), the R_{pPb} values for baryons seem to exhibit mass dependence, whereas all mesons show similar trend. At $p_T > 8$ GeV/c, results for all light flavour particles are consistent within uncertainties, indicating that no flavor dependence in R_{pPb} is present.

66.4 Conclusions

ALICE has studied several resonances with varying lifetimes (from 1–50 fm/c) in different colliding systems and energies. The p_T -integrated yields are similar for a given multiplicity, irrespective of the colliding systems and energies, which suggests that hadrochemistry is mainly driven by the event multiplicity. A suppression in yield ratios for short-lived resonances in ρ/π , K^*/K , and $\Lambda(1520)/\Lambda$ is observed going from pp and peripheral Pb–Pb to central Pb–Pb and Xe–Xe collisions, which suggests that re-scattering is the dominant process over regeneration in the hadronic phase. However, yield-ratio distributions of long-lived resonances (ϕ/K) remain flat with multiplicity, not significantly affected by re-scattering and regeneration processes. The EPOS3 with UrQMD reproduces these yield ratios qualitatively. No significant energy dependence in R_{pPb} is observed for K^* and ϕ in p–Pb collisions at $\sqrt{s_{NN}} = 5.02$ and 8.16 TeV. The R_{pPb} values demonstrate no species dependence and are consistent with unity within the uncertainties for light flavor hadrons at high- p_T (> 8 GeV/c), which shows the absence of nuclear effects.

References

1. B. Abelev et al., Phys. Lett. B. **726**, 164–177 (2013)
2. S. Chatrchyan et al., Phys. Lett. B. **718**, 795–814 (2013)
3. S. Acharya et al., Phys. Lett. B. **802**, 135225 (2020)
4. K. Aamodt et al., JINST. **3**, S08002 (2008)
5. B. Abelev et al., Int. J. Mod. Phys. A. **29**, 1430044 (2014)
6. M. Aggarwal et al., Phys. Rev. C. **84**, 034909 (2011)
7. T. Pierog, K. Werner, Nucl. Phys. B Proc. Suppl. **196**, 102–105 (2009)

Chapter 67

Multiplicity Dependence Study of Thermodynamic and Transport Properties of the Matter Formed in Ultra-Relativistic Collisions at LHC Using Color String Percolation Model



Dushmanta Sahu, Sushanta Tripathy, R. Sahoo, and Swatantra Kumar Tiwari

Abstract We have estimated various thermodynamic and transport properties of the matter formed in ultra-relativistic collisions using Color String Percolation Model. We observe a threshold of charged particle multiplicity ($\langle dN_{ch}/d\eta \rangle \geq 20$), after which there is a change in the dynamics of the system. From our work, we observe that the matter formed in such collisions is the closest to a perfect fluid found in nature.

67.1 Introduction

It is an interesting domain to study about the behavior of the matter formed in ultra-relativistic collisions. Various thermodynamic and transport properties of the matter will give us valuable insights into the dynamics of high energy collisions [1, 2]. We have used the Color String Percolation Model (CSPM) to estimate various thermodynamic and transport properties of such matter. CSPM [3, 4] is an established model, which assumes that color strings are stretched between the partons of the colliding nuclei. The final state particles are produced by the hadronization of these strings. These strings occupy finite area in the transverse space. As the collision energy and the number of colliding partons increases, the number of strings also grows and they start overlapping, forming clusters in the transverse space. After a

D. Sahu (✉) · S. Tripathy · R. Sahoo
Department of Physics, Indian Institute of Technology Indore, Simrol, Indore 453552, India
e-mail: Dushmanta.Sahu@cern.ch

R. Sahoo
The GRAPES-3 Experiment, Cosmic Ray Laboratory, Ooty, India

S. K. Tiwari
Department of Applied Science and Humanities, Muzaffarpur Institute of Technology,
Muzaffarpur 842003, India

© The Author(s), under exclusive license to Springer Nature Singapore Pte Ltd. 2022
B. Mohanty et al. (eds.), *Proceedings of the XXIV DAE-BRNS High Energy Physics Symposium, Jatni, India*, Springer Proceedings in Physics 277,
https://doi.org/10.1007/978-981-19-2354-8_67

certain critical string density (ξ_c), a macroscopic cluster appears, which corresponds to percolation phase transition.

Isothermal compressibility is defined as the change of the volume of the system with the change in pressure at constant temperature. This gives information about the degree of deviation of the system from a perfect fluid. The shear viscosity to entropy density ratio gives us information about the fluidity of the system. The elliptic flow measurements in the heavy ion collisions at Relativistic Heavy Ion Collider (RHIC) have found a minimum value of η/s , which is closer to the KSS bound value [5]. Similarly, we expect a change in the behavior of bulk viscosity to entropy density ratio near the QCD critical temperature, where the conformal symmetry breaking might be significant. We have taken the charged particle spectra from pp , p -Pb, Xe-Xe and Pb-Pb collisions at the LHC energies [6–12] and extracted the CSPM parameters, such as the color suppression factor, $F(\xi)$, the percolation density parameter, ξ and the initial percolation temperature, T .

67.2 Formulation

In a 2D percolation theory, the dimensionless percolation density parameter is given by [3],

$$\xi = \frac{N_s S_1}{S_N}, \quad (67.1)$$

where N_s is the number of overlapping strings, S_1 is the transverse area of a single string and S_N is the transverse area occupied by the overlapping strings. The color suppression factor is related to ξ by the relation,

$$F(\xi) = \sqrt{\frac{1 - e^{-\xi}}{\xi}}. \quad (67.2)$$

We obtain $F(\xi)$ by fitting the following function to the soft part of the p_T spectra with the p_T range 0.12–1.0 GeV/c of pp , p -Pb, Xe-Xe and Pb–Pb collisions systems of the LHC energies [4],

$$\frac{d^2 N_{ch}}{dp_T^2} = \frac{a}{(p_0 \sqrt{F(\xi)}_{pp, \sqrt{s}=200 \text{ GeV}} / F(\xi)_{pp, pA, AA} + p_T)^\alpha}. \quad (67.3)$$

The initial temperature of the percolation cluster can be defined in terms of $F(\xi)$ as,

$$T(\xi) = \sqrt{\frac{\langle p_T^2 \rangle_1}{2F(\xi)}}. \quad (67.4)$$

By using $T_c = 167.7 \pm 2.8$ MeV [13] and $\xi_c \sim 1.2$, we get $\sqrt{\langle p_T^2 \rangle_1} = 207.2 \pm 3.3$ MeV, from which one can get the single string-squared average momentum, $\langle p_T^2 \rangle_1$. Using this value in (67.4), we can get the initial temperature for different $F(\xi)$ values.

In CSPM, the isothermal compressibility can be given as [1],

$$\kappa_T = \frac{\tau_{\text{pro}} S_N}{\langle m_T \rangle dN_{\text{ch}}/dy}. \quad (67.5)$$

The shear viscosity to entropy density ratio can be expressed as [2],

$$\eta/s = \frac{TL}{5(1 - e^{-\xi})}. \quad (67.6)$$

Similarly, the bulk viscosity to entropy density ratio can be expressed as, [2],

$$\zeta/s = 15 \frac{\eta}{s} \left(\frac{1}{3} - c_s^2 \right)^2. \quad (67.7)$$

67.3 Results and Discussion

In Fig. 67.1, we have plotted the initial percolation temperature as a function of charged particle multiplicity ($\langle dN_{\text{ch}}/d\eta \rangle$). We observe an increasing trend of temperature with an increase in $\langle dN_{\text{ch}}/d\eta \rangle$. For high multiplicity pp collisions, the temperature becomes more than that of the hadronization temperature. This suggests that there could be a possible formation of QGP droplets even in high multiplicity pp collisions. The right panel of fig. 67.1 shows the variation of isothermal compressibility as a function of charged particle multiplicity. We observe that for lower $\langle dN_{\text{ch}}/d\eta \rangle$, the value of κ_T is higher. The value decreases with increase in charged particle multiplicity and almost approaches to zero after $\langle dN_{\text{ch}}/d\eta \rangle \geq 20$. This could suggest that after this threshold charged particle multiplicity, the matter that forms could behave almost like a perfect fluid.

In the left panel of Fig. 67.2, we have plotted the shear viscosity to entropy density ratio as a function of charged particle multiplicity. We observe that at a certain $\langle dN_{\text{ch}}/d\eta \rangle \geq 20$, the η/s becomes minimum and approaches the ADS/CFT value [5]. After this threshold of charged particle multiplicity, the value of η/s starts increasing again. In the right panel, we have plotted the bulk viscosity to entropy density ratio as a function of charged particle multiplicity. We observe that ζ/s value decreases with increases in $\langle dN_{\text{ch}}/d\eta \rangle$ and becomes minimum after $\langle dN_{\text{ch}}/d\eta \rangle \geq 20$. These findings suggest that the medium that forms in high multiplicity collisions behaves almost like a perfect fluid. In both panels of Fig. 67.2, we see that there are separate

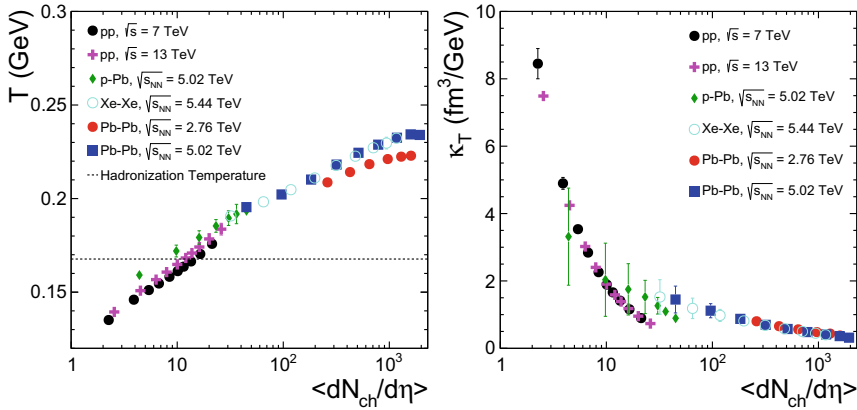


Fig. 67.1 (Color online) Initial temperature and isothermal compressibility as a function of charged particle multiplicity on the left and right panel, respectively. The dotted line represents the reported hadronization temperature [13]

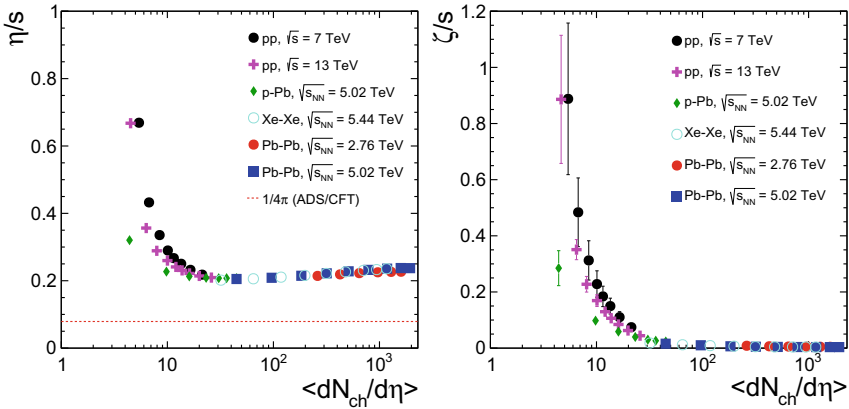


Fig. 67.2 (Color online) Shear viscosity to entropy density ratio and bulk viscosity to entropy density ratio as a function of charged particle multiplicity on the left and right panel, respectively. The dotted line represents the ADS/CFT value [5]

trends for pp collisions at $\sqrt{s} = 7$ and 13 TeV and for p -Pb collisions at $\sqrt{s_{NN}} = 5.02$ TeV. These separate trends however converge together at $\langle dN_{ch}/d\eta \rangle \geq 20$. This suggests that the system and energy dependency of such observables vanishes at the threshold charged particle multiplicity.

67.4 Summary

In this work, we have taken CSPM approach to estimate various thermodynamic and transport properties of matter formed in ultra-relativistic collisions. We observe a threshold of $\langle dN_{ch}/d\eta \rangle \geq 20$, after which there is a change in the dynamics of the system. We also found that the matter formed after this threshold of $\langle dN_{ch}/d\eta \rangle$ could behave almost like a perfect fluid.

References

1. D. Sahu, S. Tripathy, R. Sahoo S.K. Tiwari, [arXiv:2001.01252](https://arxiv.org/abs/2001.01252) [hep-ph]
2. D. Sahu, R. Sahoo, *J. Phys. G* **48**, 125104 (2021)
3. M.A. Braun, J. Dias de Deus, A.S. Hirsch, C. Pajares, R.P. Scharenberg, B.K. Srivastava, *Phys. Rep.* **599**, 1 (2015)
4. A.S. Hirsch, C. Pajares, R.P. Scharenberg, B.K. Srivastava, *Phys. Rev. D* **100**, 114040 (2019)
5. P. Kovtun, D.T. Son, A.O. Starinets, *Phys. Rev. Lett.* **94**, 111601 (2005)
6. S. Acharya et al. [ALICE Collaboration], *Phys. Lett. B* **807**, 135501 (2020)
7. S. Acharya et al., ALICE Collaboration. *Phys. Rev. C* **99**, 024906 (2019)
8. B. Abelev et al., ALICE Collaboration. *Phys. Rev. C* **88**, 044910 (2013)
9. S. Acharya et al., ALICE Collaboration. *Phys. Rev. C* **101**, 044907 (2020)
10. S. Acharya et al., ALICE Collaboration. *Phys. Lett. B* **800**, 135043 (2019)
11. S. Acharya et al., ALICE Collaboration. *Phys. Lett. B* **790**, 35 (2019)
12. S. Acharya et al., ALICE Collaboration. *Eur. Phys. J. C* **79**, 307 (2019)
13. F. Becattini, P. Castorina, A. Milov, H. Satz, *Eur. Phys. J. C* **66**, 377 (2010)

Chapter 68

Criticality in Statistical Bootstrap Model: Critical Exponents and Transport Properties



Guruprasad Kadam, Hiranmaya Mishra, and Marco Panero

Abstract We study shear and bulk viscosity coefficients near the QCD critical point (CP) from hadronic side. We calculate the critical behavior of viscosity coefficients within ambit of statistical bootstrap model. We find that the shear viscosity to entropy density ratio, η/s decreases with an increase in temperature and approach Kovtun-Son-Starinets bound ($1/4\pi$) faster near CP, while the bulk viscosity coefficient is found to rise very rapidly.

68.1 Introduction

Phase diagram of strongly interacting matter has attracted a lot of attention in past couple of decades [1]. A particularly interesting point in the QCD phase diagram is the conjectured critical end point (CEP). CEP is the end point of first-order phase transition line that separates the low temperature (and low baryon density) hadronic phase from high temperature quark-gluon plasma phase. A lot of theoretical investigation has been carried out, and still going on, to locate the CEP and predict possible experimental signatures [2].

Statistical bootstrap model (SBM) [3], describing low energy hadronic phase of QCD, attracted a lot of attention in the particle physics community in the pre-QCD era. The so-called bootstrap condition of SBM requires the density of states of the form $\rho(m) \sim m^a e^{m/T_c}$ [4, 5], where a is a constant. Dual resonance model of strong interactions [6] also supports the similar form of density of states. The constant

G. Kadam (✉)

School of Physical Sciences, NISER Bhubaneswar, P.O. Jatni, Khurda, Bhubaneswar 752050, Odisha, India

e-mail: guruprasadkadam18@gmail.com

H. Mishra

Theory Division, Physical Research Laboratory, Navarangpura 380 009, Ahmedabad, India

M. Panero

Department of Physics, University of Turin and INFN, Turin, Via Pietro Giuria 1, I-10125 Turin, Italy

' a ' plays a very important role in determining the thermodynamics of SBM near the critical temperature T_c . In fact, for the choice $a = -4$, both energy density and entropy density remain finite near T_c , and there must be some sort of phase transition [7].

While the static critical phenomena have been extensively studied theoretically, as it turns out, critical singularities can also occur in the dynamic properties like transport coefficients. In these proceedings, we present our recent work in which we extract the critical exponents [4] and amplitudes of thermodynamic quantities relevant near the critical point within ambit of SBM and then estimate viscosity coefficients near the critical point from hadronic side using critical exponents of SBM.

68.2 Statistical Bootstrap Model: Criticality and Critical Point Exponents

The critical exponents, α , β , γ and ν are defined through following power laws of the form, $W = \mathcal{W}_- |t|^\omega$, where W is thermodynamical quantity of interest, \mathcal{W}_- is the amplitude and ω is the corresponding critical exponent. The amplitudes and critical exponents of QCD matter can be extracted using SBM [4]. Consider an ideal gas of pions and all possible resonance states as non-interacting constituents. The partition function of this system is written as [9]

$$\mathcal{Z}(T, V, z_B) = \sum_N \frac{(V z_B)^N}{N!} \prod_1^N \int \frac{d^3 p_i}{(2\pi)^3} dm_i \rho_i(m_i) e^{-\beta E_i} \quad (68.1)$$

where $z_B = e^{\beta\mu_B}$ is the fugacity and $\beta = 1/T$, $\rho(m)$ is the hadron spectrum included in the HRG model. It can be shown that with the density of states of the form $\rho_h(m) = A m^a e^{bm}$ [3] the partition function reads

$$\ln \mathcal{Z}_h(T, V, z_B) = \frac{AV z_B}{(2\pi\beta)^{3/2}} \int_M^\infty dm m^{a+3/2} e^{-(\beta-b)m} \quad (68.2)$$

Taking appropriate derivatives of the partition function given by (68.2) and in the limit $\beta \rightarrow b$, one can extract the critical exponents and the amplitudes. It turns out that the continuum density of states with $a < -\frac{7}{2}$ render energy density and entropy finite even for point-like hadrons, while all higher order derivatives diverge near T_c . In our analysis of transport coefficients we shall consider the case of $a = -4$.

68.3 Transport Coefficients Near the Critical Point

Approaching critical point, the thermodynamic quantities that would contribute to transport coefficients are: energy density (ϵ), baryon number density (n_B), specific heats (C_V and C_P), isothermal compressibility (k_T), speed of sound (C_s^2) and correlation length (ξ). It can be shown that in the limit $|t| \rightarrow 0$ (i.e $T \rightarrow T_c$ from hadronic side)

$$\begin{aligned} \left(\frac{\eta}{s}\right)_- &= f_\eta \frac{T_c^{3/2} h_c^{1/2} \lambda_c}{s_c} (\mathcal{K}_- \xi_-^{-2} C_-^{-1/2}) \\ &\times (1 + T_c^{-1} \lambda_c^{-2} C_- \mathcal{K}_-^{-1} | -t |^{\gamma-\alpha})^{-\frac{1}{2}} \\ &\times | -t |^{-\gamma+2\nu+\frac{\alpha}{2}} \end{aligned} \quad (68.3)$$

$$\begin{aligned} \left(\frac{\zeta}{s}\right)_- &= f_\zeta \frac{T_c^{3/2} h_c^{1/2} \lambda_c^3}{s_c} (\mathcal{K}_- \xi_- C_-^{-3/2}) \\ &\times (1 + T_c^{-1} \lambda_c^{-2} C_- \mathcal{K}_-^{-1} | -t |^{\gamma-\alpha})^{-\frac{3}{2}} \\ &\times | -t |^{-\gamma-\nu+\frac{3\alpha}{2}} \end{aligned} \quad (68.4)$$

Here, h_c is enthalpy density and s_c is entropy density at T_c , both of which are finite for $a = -4$ in the Hagedorn density of states. $\lambda_c = (\partial P / \partial T)_V$ at $T = T_c$. Parameters f_η and f_ζ can be fixed by imposing a constrain on viscosity coefficients near T_c . In our study, however, we shall treat f_η and f_ζ as free parameters.

68.4 Results and Discussion

Figure 68.1 shows shear and bulk viscosity near the QCD critical point and compared with other models. We take correlation length $\xi_- = 1$ fm and the critical point $(T_c, \mu_c) = (160, 220)$ MeV. For $a = -4$ we can readily read off critical exponents and amplitudes needed to estimate viscosity coefficients near T_c . In Fig. 68.1, a solid blue curve corresponds to shear viscosity to entropy density ratio within ambit of SBM model with the continuum density of states [13]. We note that the critical behavior of statistical bootstrap model leads to linear decrease in η/s . However, the magnitude of η/s estimated within ambit of SBM is in agreement with that of pion gas and hadron gas mixture at low T . Near T_c there is a mild violation of the KSS bound.

Figure 68.1b shows bulk viscosity to entropy density ratio. We note that there is a rapid rise in the bulk viscosity in the statistical bootstrap model. In fact, near T_c , our

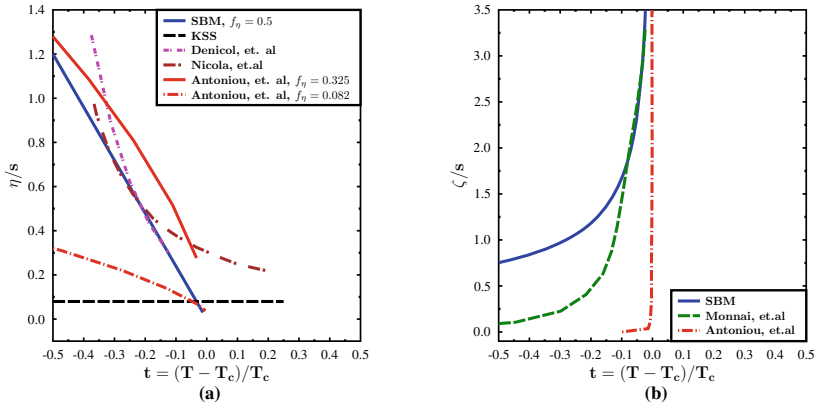


Fig. 68.1 Viscosity coefficients estimated in our model and compared with other works [8, 10–12, 14]. Our results correspond to $f_\eta = 0.5$ and $f_\zeta = 0.85$

results are in remarkable agreement with that of [14] (green dashed curve). In the context of HIC experiments, the large bulk viscosity near the critical point would play a particularly important role in the elliptic flow measurement of the matter produced in the beam energy scan (BES) program at Super Proton Synchrotron (SPS) and the Relativistic Heavy Ion Collider (RHIC).

68.5 Summary and Conclusion

The thermodynamic system with exponentially rising density of states having suitable degeneracy structure shows critical behavior as $T \rightarrow T_c$. We studied the critical behavior of shear and bulk viscosities within ambit of this critical SBM. We found that the ratio η/s estimated within SBM decreases very rapidly near T_c . The magnitude of η/s away from the critical point is found to be in good agreement with that of non-critical model. We also noted a mild violation of KSS bound near T_c . Finally, we found that the ratio ζ/s rises very rapidly near T_c . Further, our results are in remarkable agreement with that of [14] near T_c .

Acknowledgements Guruprasad Kadam is financially supported by the DST-INSPIRE faculty award under Grant Number DST/INSPIRE/04/2017/002293.

References

1. K. Fukushima, T. Hatsuda, Rep. Prog. Phys. **74**, 014001 (2011)
2. B. Mohanty, Nucl. Phys. A **830**, 899C-907C (2009)

3. R. Hagedorn, *Nuovo Cim. Suppl.* **3**, 147–186 (1965)
4. H. Satz, *Phys. Rev. D* **19**, 1912 (1979)
5. J. Noronha-Hostler, J. Noronha, C. Greiner, *Phys. Rev. C* **86**, 024913 (2012)
6. S. Mandelstam, *Phys. Rep.* **13**, 259 (1974)
7. N.G. Antoniou, A.S. Kapoyannis, *Phys. Lett. B* **563**, 165 (2003)
8. N.G. Antoniou, F.K. Diakonou, A.S. Kapoyannis, *Phys. Rev. C* **96**(5), 055207 (2017)
9. E. Beth, G.E. Uhlenbeck, *Physica* **4**, 915 (1937)
10. P. Kovtun, D.T. Son, A.O. Starinets, *Phys. Rev. Lett.* **94**, 111601 (2005)
11. D. Fernandez-Fraile, A. Gomez Nicola, *Eur. Phys. J. C* **62**, 37 (2009)
12. G.S. Denicol, C. Gale, S. Jeon, J. Noronha, *Phys. Rev. C* **88**(6), 064901 (2013). <https://doi.org/10.1103/PhysRevC.88.064901>. [arXiv:1308.1923](https://arxiv.org/abs/1308.1923) [nucl-th]
13. G. Kadam, H. Mishra, M. Panero, *Eur. Phys. J. C* **81**(9), 795 (2021)
14. A. Monnai, S. Mukherjee, Y. Yin, *Phys. Rev. C* **95**(3), 034902 (2017)

Chapter 69

Directed Flow of Identified Hadrons in Au+Au Collisions with the STAR Experiment at RHIC



Kishora Nayak

Abstract Rapidity-odd component of the directed flow (v_1) is considered to be sensitive to the early collision dynamics and the equation of state (EoS) of the QCD matter formed in heavy-ion collisions. Hydrodynamic models predict that the double sign change of v_1 slope at mid-rapidity (dv_1/dy) of net-baryon is a signature of the first-order phase transition. The STAR experiment at RHIC shows that the collision energy dependences of dv_1/dy of net-proton and net- Λ reach a minimum at $\sqrt{s_{NN}} = 14.5$ GeV, implying the possible softening of the EoS. We further explore such observations with new measurements. A comprehensive transverse momentum (p_T)-dependent v_1 measurement of identified light hadrons (π^+ , π^- , K^+ , K^- , p , \bar{p}) enables us to test the constituent quark number scaling and provides a better understanding of the coalescence mechanism of particle production. In this proceeding, new results of p_T and rapidity-dependent v_1 for identified hadrons in Au+Au collisions at $\sqrt{s_{NN}} = 19.6, 27,$ and 54.4 GeV are presented. These results are compared with AMPT model calculations.

69.1 Introduction

The beam energy scan program of the STAR experiment at RHIC aims to understand the QCD phase diagram of strongly interacting matter produced by the ultra-relativistic heavy-ion collisions [1]. The first-order coefficient of Fourier expansion of emitted particles in the momentum space is called directed flow (v_1). The rapidity-odd, $v_1(y) = -v_1(-y)$, component of the directed flow is a sensitive probe of the bulk to study the collective phenomenon in the early stage of the collisions dynamics. A first-order phase transition is predicted by various transport and hydrodynamics models [2, 3]. The model calculations show a sign change in the v_1 -slope (dv_1/dy)

Kishora Nayak—for the STAR collaboration.

K. Nayak (✉)

Key Laboratory of Quark & Lepton Physics (MOE) and Institute of Particle Physics, Central China Normal University, Wuhan 430079, China

e-mail: k.nayak1234@gmail.com

© The Author(s), under exclusive license to Springer Nature Singapore Pte Ltd. 2022
B. Mohanty et al. (eds.), *Proceedings of the XXIV DAE-BRNS High Energy Physics Symposium, Jatni, India*, Springer Proceedings in Physics 277,
https://doi.org/10.1007/978-981-19-2354-8_69

381

as a function of beam energy for baryons. The QCD lattice calculations also predict the first-order phase transition [4].

The number of constituent quark (NCQ) of elliptic flow (v_2) of identified hadrons in BES energies suggests that the flow is developed in the early stage of collisions and also the hadrons are formed via quarks coalescence [5–7]. However, at lower energies hadronic matter dominates. For the first time, a comprehensive p_T -dependent study of identified hadrons-directed flow at different energies is reported here. The rapidity dependence study in BES energies has been published by the STAR collaboration [8].

69.2 Directed Flow of Identified Hadrons

The p_T -dependent v_1 of π^\pm , K^\pm , p and \bar{p} in the rapidity region $0.5 < |y| < 1$ for 10–40% centrality in Au+Au collisions at $\sqrt{s_{NN}} = 27$ GeV along with different tunes of AMPT model calculations is shown in Fig. 69.1. For all the measured hadrons (except proton), the v_1 values are found to be negative (anti-flow) for p_T below 2.5 GeV/c (1.8 GeV/c for proton). The negative v_1 at low p_T region suggests that the produced bulk matter and formed hadrons move opposite to each other [9, 10]. However, one cannot rule out the effect of shadowing in the low p_T region [11]. The AMPT calculations are also compared with the corresponding hadrons. The AMPT-Default configuration qualitatively well describes the hadrons (π^\pm , K^+ , p) formed by quarks (anti-quarks) contributed from both transported and produced quarks [12]. The produced hadrons such as K^- , \bar{p} are formed from the produced quark and anti-quark. These hadrons are qualitatively well described by AMPT-SM with hadronic interaction time, $t_{max} = 0.4$ and 30 fm/c.

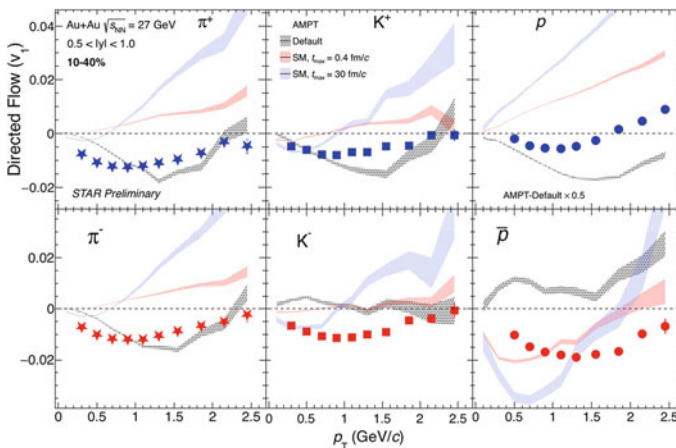


Fig. 69.1 v_1 as a function of p_T for π^\pm , K^\pm , p and \bar{p} in the rapidity region $0.5 < |y| < 1$ for 10–40% centrality Au+Au collisions at $\sqrt{s_{NN}} = 27$ GeV. The black, red and blue shaded bands represents AMPT-Default, AMPT-SM with hadronic interaction time $t_{max} = 0.4$ fm/c and 15 fm/c, respectively [13, 14]

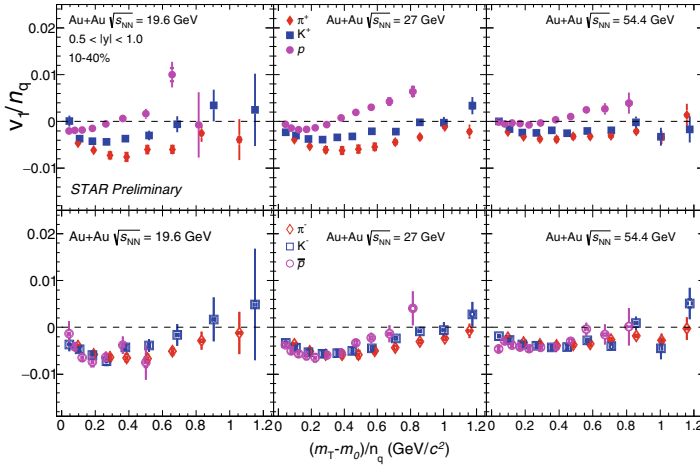


Fig. 69.2 v_1/n_q versus $(m_T - m_0)/n_q$ for π^+ , K^+ , p (upper row) and π^- , K^- , \bar{p} (lower row) in the rapidity $0.5 < |y| < 1$ for 10–40% centrality in Au+Au collisions at $\sqrt{s_{NN}} = 19.6, 27$ and 54.4 GeV in the left, middle and right column, respectively

Figure 69.2 shows the v_1/n_q as a function of $(m_T - m_0)/n_q$ for π^+ , K^+ , p (upper row) and π^- , K^- , \bar{p} (lower row) in the rapidity $0.5 < |y| < 1$ for 10–40% centrality in Au+Au collisions at $\sqrt{s_{NN}} = 19.6$ (left panel), 27 (middle panel) and 54.4 (right panel) GeV. It is observed that NCQ scaling does not hold well for the particles (π^+ , K^+ and p) in all the measured energies. The magnitude of the violation also increases with decrease in energy as the transported quark contribution to the form hadrons increases. However, the NCQ scaling holds better for produced hadrons like K^- and \bar{p} as these are formed via coalescence for quarks and anti-quarks [15].

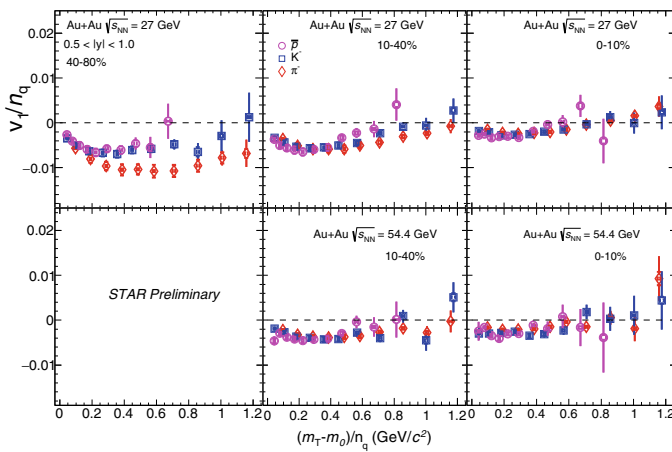


Fig. 69.3 m_T scaling for π^- , K^- , \bar{p} in $0.5 < |y| < 1$ for 40–80% (left), 10–40% (middle) and 0–10% (right) centrality in Au+Au at 27 (upper row) and 54.4 (lower row) GeV

Figure 69.3 shows the centrality dependence of v_1/n_q as a function of $(m_T - m_0)/n_q$ for π^- , K^- , \bar{p} in 40–80% (left), 10–40% (middle) and 0–10% (right) panel in Au+Au collisions at $\sqrt{s_{NN}} = 27$ GeV (upper row) and 54.4 GeV (lower row). The NCQ scaling holds better for produced hadrons such as K^- and \bar{p} in all three centralities in the low- m_T region.

69.3 Conclusion

First, comprehensive measurements of p_T dependence directed flow of identified hadrons (π^\pm , K^\pm , p and \bar{p}) in the rapidity region of $0.5 < |y| < 1.0$ for various collision centralities in Au+Au at $\sqrt{s_{NN}} = 19.6, 27$ and 54.4 GeV are reported. In the low- p_T region, anti-flow is observed in the measured rapidity region $0.5 < |y| < 1$ for all hadrons in these energies. The NCQ scaling is observed for produced hadrons (K^- and \bar{p}) which suggests that coalescence is the dominant mechanism of particle formation for these hadrons. For other hadrons such as π^\pm , K^+ and p , the NCQ scaling is violated as they also receive contribution from transported quarks along with the primary produced quarks. The contribution of transported quarks increases with decrease in energy and hence deviation from the NCQ scaling increases.

Acknowledgements This work is supported in part by the National Natural Science Foundation of China under Grants No. 11890711, National Key Research and Development Program of China under Grant No. 2020YFE0202002 and China Postdoctoral Science Foundation under Grant No. 2019M662681.

References

1. J. Adams et al. (STAR Collaboration), Nucl. Phys. A **757**, 102 (2005)
2. H. Stöcker, Nucl. Phys. A **750**, 121 (2005)
3. C. Zhang et al., Phys. Rev. C **97**, 064913 (2018)
4. Z. Fodor, S.D. Katz, JHEP **0203**, 014 (2002); JHEP **0404**, 050 (2004)
5. L. Adamczyk et al. (STAR Collaboration), Phys. Rev. Lett. **110**, 142301 (2013)
6. L. Adamczyk et al. (STAR Collaboration), Phys. Rev. Lett. **116**, 062301 (2016)
7. S. Shi, Adv. High Energy Phys. 1987432 (2016)
8. L. Adamczyk et al. (STAR Collaboration), Phys. Rev. Lett. **120**, 062301 (2018)
9. E.E. Zabrodin et al., Phys. Rev. C **63**, 034902 (2001)
10. S.A. Voloshin, Phys. Rev. C **55**, R1630(R) (1997)
11. R.J.M. Snellings et al., Phys. Rev. Lett. **84**, 2803–2805 (2000)
12. J.C. Dunlop et al., Phys. Rev. C **84**, 044914 (2011)
13. K. Nayak et al., Phys. Rev. C **100**, 054903 (2019)
14. Zi-Wei. Lin et al., Phys. Rev. C **72**, 064901 (2005)
15. Md. Nasim, S. Singha, Phys. Rev. C **97**, 064917 (2018)

Chapter 70

Constraining the Strength of $U(1)_A$ Symmetry Breaking Using Two-Flavour Non-local NJL Model



Mahammad Sabir Ali, Chowdhury Aminul Islam, and Rishi Sharma

Abstract In the presence of a magnetic field we have done a systematic analysis to constrain the strength of 't Hooft determinant term using LQCD data within a non-local version of two-flavour NJL model. Topological susceptibility, which is related to the axial symmetry breaking, has also been calculated and compared with LQCD results to further validate our calculation.

70.1 Introduction

With the help of the Nambu–Jona-Lasinio (NJL) model one can study the chiral properties of QCD [1]. In many NJL-like models the chiral condensate which breaks the chiral symmetry spontaneously increases with magnetic field (eB) for all temperature (T), termed as magnetic catalysis (MC), whereas the lattice QCD simulation obtained decrease in chiral condensate around the crossover T as eB increases, which is termed as an inverse magnetic catalysis (IMC) [2]. Non-local extensions of the NJL model are very interesting as it captures some aspects of the asymptotic freedom of QCD through the non-local form factor and thus can reproduce the IMC effects automatically [3, 4]. Our main goal is to constrain the strength of the $U(1)_A$ symmetry breaking 't Hooft determinant term, which is usually assumed to be equal to that of the axial $U(1)_A$ symmetric term both in local and non-local versions, and is done in non-local NJL model using lattice QCD results. Along with the phase diagram in $T - eB$ plane to check our model predictions, we also explored the topological susceptibility (χ_t) with the fitted strength of $U(1)_A$ symmetry breaking term and compared it with the available LQCD data.

M. S. Ali (✉) · R. Sharma
Department of Theoretical Physics, Tata Institute of Fundamental Research, Homi Bhabha Road,
Mumbai 400005, India
e-mail: sabir@theory.tifr.res.in

C. Aminul Islam
School of Nuclear Science and Technology, University of Chinese Academy of Sciences, Beijing
100049, China

70.2 Formalism

The most general non-local NJL Lagrangian can be written as [3, 5]

$$\begin{aligned} \mathcal{L}_{\text{NJL}} &= \bar{\psi} (i\partial - m) \psi + \mathcal{L}_1 + \mathcal{L}_2, \quad \text{with} \\ \mathcal{L}_1 &= G_1 \{j_a(x)j_a(x) + j_b(x)j_b(x)\} \quad \text{and} \\ \mathcal{L}_2 &= G_2 \{j_a(x)j_a(x) - j_b(x)j_b(x)\}, \end{aligned}$$

where $j_{a/b}(x)$ are the non-local currents, given by

$$\begin{aligned} j_{a/b}(x) &= \int d^4z \mathcal{G}(z) \bar{\psi} \left(x + \frac{z}{2}\right) \Gamma_{a/b} \psi \left(x - \frac{z}{2}\right) \quad \text{and} \\ \Gamma_a &= (\mathbb{1}, i\gamma_5 \boldsymbol{\tau}) \quad \text{and} \quad \Gamma_b = (i\gamma_5, \boldsymbol{\tau}). \end{aligned}$$

$\mathcal{G}(z)$ is the non-locality form factor. As \mathcal{L}_2 explicitly breaks $U(1)_A$, the symmetry of the Lagrangian (with $m = 0$) is $SU(2)_V \times SU(2)_A \times U(1)_V$. This symmetry only allows the $\langle \bar{\psi} \psi \rangle$ condensate, which depends on $(G_1 + G_2)$. But in the presence of isospin chemical potential (μ_I) and/or eB , the $SU(2)$ symmetry is broken and one can have $\langle \bar{\psi} \tau_3 \psi \rangle$ which has a $(G_1 - G_2)$ dependence. This motivates one to parameterize G_1 and G_2 as $G_1 = (1 - c)G_0/2$ and $G_2 = cG_0/2$, where $c = 1/2$ corresponds to the standard NJL model. The parameters of our model are fitted to obtain physical quantities like pion mass, decay constant etc. in the absence of μ_I or eB .

Due to Lorentz symmetry the Fourier transformation of $\mathcal{G}(z)$, $g(p^2)$ can only depend on p^2 . We have considered $g(p^2)$ to be Gaussian in nature

$$g(p^2) = \exp[-p^2/\Lambda^2].$$

In the presence of eB the non-local currents should transform as [4]

$$j_{a/b}(x) \rightarrow \int d^4z \mathcal{G}(z) \bar{\psi} \left(x + \frac{z}{2}\right) W^\dagger(x + z/2, x) \Gamma_a W(x, x - z/2) \psi \left(x - \frac{z}{2}\right)$$

$$\text{with } W(s, t) = P \exp \left[-iQ \int_s^t dr_\mu A_\mu(r) \right].$$

The bosonized action, after integrating out the fermionic fields, becomes

$$S_{\text{bos}} = -\ln \det(\mathcal{D}) + \int d^4x \left[\frac{\sigma^2(x)}{2G_0} + \frac{\Delta\sigma^2(x)}{2(1 - 2c)G_0} \right].$$

The inverse of fermionic propagator is given by [4]:

$$\mathcal{D}_{\text{MF}}(x, x') = \delta^{(4)}(x - x')(-i\not{\partial} - QBx_1\gamma_2 + m) + \mathcal{G}(x - x') \\ *(\sigma + \tau_3\Delta\sigma) \exp\left[\frac{i}{2}QB(x_2 - x'_2)(x_1 + x'_1)\right].$$

Using Ritus eigenfunctions one obtains the Fourier transform of the above to calculate the action, which is then minimized with respect to meanfields to get the observables. Finite T can be incorporated using Matsubara formalism; the detailed calculation can be found in [6].

The topological term $\frac{\theta g^2}{32\pi^2}\mathcal{F}\tilde{\mathcal{F}}$ breaks the CP symmetry of strong interaction. As the dynamical axion is considered to be a possible solution of strong CP problem, θ can be related to the axion fields, $\theta = a/f_a$. With a chiral rotation of the quark fields by an angle a/f_a one obtains

$$\mathcal{L}_2 = 2G_2 \left\{ e^{i\frac{a}{f_a}} \det\bar{\psi}(1 + \gamma_5)\psi + e^{-i\frac{a}{f_a}} \det\bar{\psi}(1 - \gamma_5)\psi \right\}.$$

With a straightforward generalization to non-local case, one can derive the free energy $\Omega(T, eB, a)$, and the topological susceptibility is given by

$$\left. \frac{d^2\Omega(T, eB, a)}{da^2} \right|_{a=0} = \frac{\chi_t}{f_a^2}.$$

70.3 Results

The parameters of our model are fitted to obtain physical quantities like pion mass, decay constant etc. in absence of μ_I and eB . The numerical values are taken from [7] (referred to as B13 here) as $\langle\bar{\psi}_f\psi_f\rangle^{1/3} = 261(13)(1)$ MeV, $m_\pi = 135$ MeV and $F_\pi = 90(8)(2)$ MeV.

Considering the error in $\langle\bar{\psi}_f\psi_f\rangle^{1/3}$ and F_π , we obtain a range in our model parameters. Figure 70.1 represents the allowed range of our model parameters while obtaining observables of [7]. Increasing F_π results in decreasing Λ , while on the condensate the dependence is opposite.

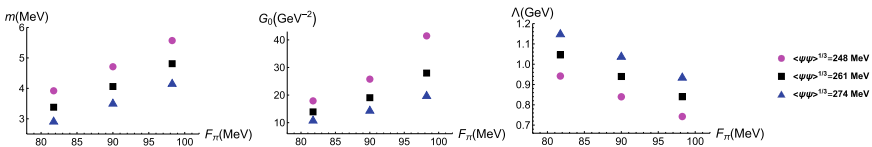


Fig. 70.1 Range of model parameters to access the full allowed range of the condensate, including the errors as given in LQCD [7] (B13)

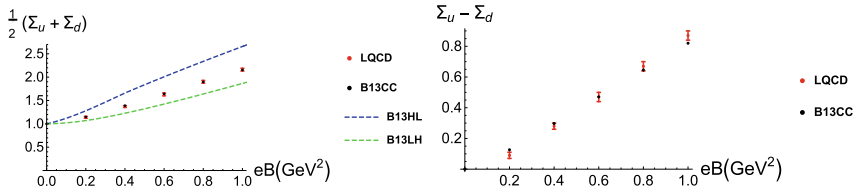


Fig. 70.2 The condensate average (left) and difference (right) as a function of magnetic field at $T = 0$ compared with LQCD [2] data

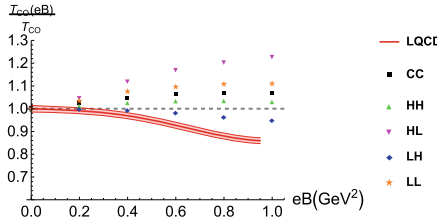


Fig. 70.3 The phase diagram in $T - eB$ plane for the central and all the corner parameter sets compared with LQCD [2]

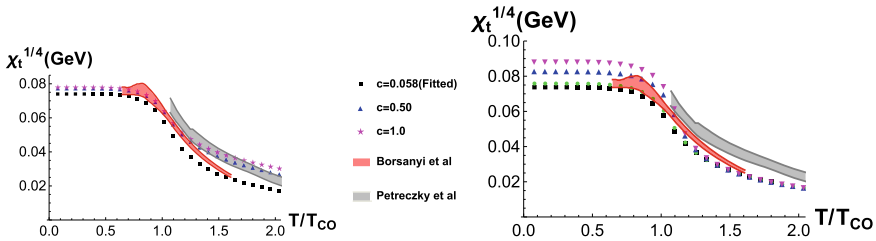


Fig. 70.4 Topological susceptibility as a function of scaled temperature for different c values (left) for the CC parameter set. eB dependence is presented on the right, dot (green), up triangle (blue) and down triangle (magenta) are for $eB=0.2, 0.6$ and 1.0 GeV^2 , respectively. The red and the gray bands represent lattice results from the [8] and [9], respectively

The $T = 0$ and finite eB results are presented in Fig. 70.2 along with the comparison with lattice data [2]. The notations are as follows: C, H and L represent the central, high and low value, respectively, where the first alphabet represents the value of the condensate and the second one represents that of F_π . Using χ^2 fitting we fitted c to obtain the best match of condensate difference (right) with the same obtained in [2]. The fitted c value is 0.06 with $\chi^2/\text{dof} = 1.5$. As the χ^2/dof are small, we can safely assume that at $T = 0$, c does not depend on magnetic field. Finite T behaviour of condensate average and the difference can be found in [6].

Figure 70.3 shows the phase diagram in $T - eB$ plane. One can clearly see that a smaller value of condensate and/or a larger value of F_π produces a stronger IMC effect around the crossover region. To our knowledge this is the first time that the role of F_π on the phase diagram has been explored in an effective model.

Figure 70.4 shows our model prediction for topological susceptibility compared with two different LQCD calculation [8, 9]. Left panel shows $eB = 0$ results for different c values whereas the right one is for different eB . With eB -dependent topological susceptibility from LQCD (which is not available yet) one might expect c to have a non-trivial T and eB dependence.

Acknowledgements CAI would like to thank TIFR and UCAS for the support.

References

1. Y. Nambu, G. Jona-Lasinio, Phys. Rev. **122**, 345 (1961); **124**, 246 (1961)
2. G.S. Bali et al., Phys. Rev. D **86**, 071502
3. D. Gomez Dumm, A. Grunfeld, N. Scoccola, Phys. Rev. D **74**, 054026 (2006)
4. V.P. Pagura et al., Phys. Rev. D **95**, 034013
5. M. Frank, M. Buballa, M. Oertel, Phys. Lett. B **562**, 221–226 (2003)
6. M. Sabir Ali, C. Aminul Islam, R. Sharma, Phys. Rev. D **104**(11), 114026 (2021)
7. B.B. Brandt, A. Juttner, H. Wittig, JHEP **11**, 034 (2013)
8. S. Borsanyi et al., Nature **539**, 69 (2016)
9. P. Petreczky, H.-P. Schadler, S. Sharma, Phys. Lett. B **762**, 498 (2016)

Chapter 71

Thermal and Electric Charge Transport in a Weakly Magnetized Hot QCD Medium



Manu Kurian

Abstract Thermal and electric charge transport in a weakly magnetized quark-gluon plasma has been studied within the framework of an effective kinetic theory. The thermal dissipation in the medium is due to the temperature gradient over the spatial separations of fluid and can be described in terms of thermal conductivity. The Hall-type conductivity associated with thermal dissipation in the medium in the presence of a weak magnetic field has been explored. The induced electric current densities and the associated electrical conductivities in response to an external electric field in a weakly magnetized medium have been estimated. The relative significance of thermal transport and electric charge transport in a weakly magnetized quark-gluon plasma has been studied in terms of Wiedemann-Franz law.

71.1 Introduction

The experimental programs at relativistic heavy-ion collider (RHIC) and Large Hadron Collider (LHC) have provided the opportunity to explore the hot and dense nuclear matter known as quark-gluon plasma (QGP). The detailed analysis of the measured observables of the high-energetic heavy-ion collision experiments from the relativistic hydrodynamical approach involves the dependence on the momentum, electric charge, and thermal transport processes in the QGP medium. The system responses to electromagnetic fields can be quantified in terms of induced current densities and the associated transport coefficients (electrical and Hall conductivities). Similarly, the thermal transport that arises due to the temperature gradient in the QGP medium can be described in terms of thermal conductivity. It is widely believed that an intense magnetic field is produced in the very initial stages of non-central asymmetric collisions at RHIC and LHC. The recent LHC observation on the directed flow v_1 of D/\bar{D}^0 mesons further confirms the existence of such strong magnetic fields in the collision experiments [1]. However, the evolution of the magnetic field

M. Kurian (✉)

Indian Institute of Technology Gandhinagar, Gandhinagar 382355, Gujarat, India
e-mail: manu.kurian@iitgn.ac.in

© The Author(s), under exclusive license to Springer Nature Singapore Pte Ltd. 2022
B. Mohanty et al. (eds.), *Proceedings of the XXIV DAE-BRNS High Energy Physics Symposium, Jatni, India*, Springer Proceedings in Physics 277,
https://doi.org/10.1007/978-981-19-2354-8_71

391

in the QGP depends on the medium properties and is yet to be known. The generated magnetic field may affect the transport properties of the medium. The current focus is on the effective description of the electric charge, thermal transport processes, and their relative significance in a weakly magnetized QGP medium.

71.2 Thermal Dissipation in the Magnetized QGP

Thermal transport describes the relative flow of energy, and the heat current for the k th component particle has the form

$$I_k^i = \Delta T_k^{0i} - h_k \Delta N_k^i, \quad (71.1)$$

where ΔT_k^{0i} and ΔN_k^i denote the non-equilibrium parts of the energy-momentum tensor and particle flow that can be described in terms of thermal driving force $X_i = \frac{\partial_i T}{T} - \frac{\partial_i P}{nh}$ with P as the pressure, n as the number density, and h as the enthalpy of the medium. The transport coefficient, heat conductivity κ , can be defined as $I^i = -\kappa T X^i$. Microscopic description of the heat current is required to obtain the temperature dependence of the thermal conductivity. To that end, the knowledge of the non-equilibrium part of the system is essential. Here, we employ an effective Boltzmann equation based on the effective fugacity quasiparticle model (EQPM) to describe the dynamics of the system and has the following form within the relaxation time approximation (RTA) [2]:

$$\tilde{p}_k^\mu \partial_\mu f_k(x, \tilde{p}_k) + \left(F_k^\mu (u \cdot \tilde{p}_k) + q_{f_k} F^{\mu\nu} \tilde{p}_{k\mu} \right) \partial_\mu^{(p)} f_k = - (u \cdot \tilde{p}_k) \frac{\delta f_k}{\tau_{R_k}}, \quad (71.2)$$

where $F_k^\mu = -\partial_\nu (\delta\omega_k u^\nu u^\mu)$ is the mean field force term and $F^{\mu\nu}$ is the electromagnetic field strength tensor. The near-equilibrium momentum distribution function takes the form $f_k = f_k^0 + \delta f_k$ with $\delta f_k / f_k^0 \ll 1$, where the EQPM equilibrium distribution function for quarks/antiquarks is defined as follows:

$$f_{q/\bar{q}}^0 = \frac{z_q \exp[-\beta(u \cdot p_q \mp \mu)]}{1 + z_q \exp[-\beta(u \cdot p_q \mp \mu)]}. \quad (71.3)$$

It is important to emphasize that the effective fugacity parameter z_k is a temperature-dependent parameter that encodes the hot QCD medium interactions and relates the quasiparticle four-momenta $\tilde{p}_k^\mu = (\omega_k, \mathbf{p}_k)$ and bare particle momenta $p_k^\mu = (\epsilon_k, \mathbf{p}_k)$ as $\tilde{p}_k^\mu = p_k^\mu + \delta\omega_k u^\mu$, where $\delta\omega_k = T^2 \partial_T \ln(z_k)$. We solve the Boltzmann equation to obtain δf_k by choosing the ansatz, $\delta f_k = (\tilde{\mathbf{p}}_k \cdot \Xi) \frac{\partial f_k^0}{\partial \epsilon_k}$, with Ξ related to the temperature gradient and the magnetic field ($\mathbf{b} = \frac{\mathbf{B}}{|\mathbf{B}|}$) as $\Xi = \alpha_1 \mathbf{b} + \alpha_2 \mathbf{X} + \alpha_3 (\mathbf{X} \times \mathbf{b})$. The unknown parameters α_1 , α_2 and α_3 can be estimated by substituting the ansatz in (71.2) and comparing the independent tensor structures on both sides. Hence, the

non-equilibrium distribution takes the form as follows: [3]

$$\delta f_k = \tau_{R_k} \frac{(\omega_k - h_k)}{(1 + \tau_{R_k}^2 \Omega_{c_k}^2)} \left[(\mathbf{v}_k \cdot \mathbf{X}) + \tau_{R_k} \Omega_{c_k} \mathbf{v}_k \cdot (\mathbf{X} \times \mathbf{b}) + \tau_{R_k} \Omega_{c_k}^2 (\mathbf{b} \cdot \mathbf{X}) (\mathbf{v}_k \cdot \mathbf{b}) \right] \frac{\partial f_k^0}{\partial \epsilon_k},$$

where $\Omega_{c_k} = \frac{q_{f_k} |\mathbf{B}|}{\omega_k}$ is the cyclotron frequency. We consider the magnetic field along z -axis and the temperature gradient in the $x - y$ plane. Hence, the heat current in the magnetized medium has the form

$$\mathbf{I} = -\kappa_0 T \mathbf{X} - \kappa_1 T (\mathbf{X} \times \mathbf{b}), \quad (71.4)$$

with κ_0 and κ_1 as the thermal conductivities in the magnetized medium, which respectively take the forms as follows [3]:

$$\begin{aligned} \kappa_0 = & \frac{1}{3T} \sum_k g_k \tau_{R_k} \int d\tilde{P}_k \frac{|\tilde{\mathbf{p}}_k|^2}{\omega_k} \frac{(\omega_k - h_k)^2}{(1 + \tau_{R_k}^2 \Omega_{c_k}^2)} \left(-\frac{\partial f_k^0}{\partial \epsilon_k} \right) \\ & + \frac{1}{3T} \sum_k \delta\omega_k g_k \tau_{R_k} \int d\tilde{P}_k \frac{|\tilde{\mathbf{p}}_k|^2}{\omega_k \epsilon_k} \frac{h_k (\omega_k - h_k)}{(1 + \tau_{R_k}^2 \Omega_{c_k}^2)} \left(-\frac{\partial f_k^0}{\partial \epsilon_k} \right), \end{aligned} \quad (71.5)$$

$$\begin{aligned} \kappa_1 = & \frac{1}{3T} \sum_k g_k \tau_{R_k}^2 \int d\tilde{P}_k \frac{|\tilde{\mathbf{p}}_k|^2}{\omega_k} \frac{(\omega_k - h_k)^2}{(1 + \tau_{R_k}^2 \Omega_{c_k}^2)} \Omega_{c_k} \left(-\frac{\partial f_k^0}{\partial \epsilon_k} \right) \\ & + \frac{1}{3T} \sum_k \delta\omega_k g_k \tau_{R_k}^2 \int d\tilde{P}_k \frac{|\tilde{\mathbf{p}}_k|^2}{\omega_k \epsilon_k} \frac{h_k (\omega_k - h_k)}{(1 + \tau_{R_k}^2 \Omega_{c_k}^2)} \Omega_{c_k} \left(-\frac{\partial f_k^0}{\partial \epsilon_k} \right). \end{aligned} \quad (71.6)$$

The form of heat current in the magnetized QGP form is analogous to that of electric current in the medium. The thermal driving force perturbs the thermal transport, whereas the electric field is the source of perturbation for the charge transport. From (71.4), we have defined two components of the thermal conductivities in the magnetized medium. The analogous coefficients for the charge transport, electrical and Hall conductivities, are described in the next section.

71.3 Electric Charge Transport in Magnetized Medium

The induced electric current due to the external electric field \mathbf{E} in the magnetized medium within the EQPM description takes the following form:

$$\mathbf{j} = \sum_f 2N_c q_{f_q} \int d\tilde{P}_q \mathbf{v}_q (f_q - f_{\bar{q}}) - \sum_f \delta\omega_q 2N_c q_{f_q} \int d\tilde{P}_q \frac{\mathbf{v}_q}{\epsilon_q} (f_q - f_{\bar{q}}). \tag{71.7}$$

From (71.7), the current density vanishes as $\sum_f q_f = 0$ for the equilibrium case. However, δf_k due to the external perturbation \mathbf{E} will depend on q_f and gives rise to finite current densities. Similar to the thermal transport process, we solve the transport equation to obtain δf_k and we have

$$\delta f_k = -q_{f_k} E v_{k,x} \left(\frac{\partial f_k^o}{\partial \epsilon_k} \right) \frac{\tau_{R_k}}{(1 + \tau_{R_k}^2 \Omega_{c_k}^2)} + q_{f_k} E v_{k,y} \left(\frac{\partial f_k^o}{\partial \epsilon_k} \right) \frac{\Omega_{c_k} \tau_{R_k}^2}{(1 + \tau_{R_k}^2 \Omega_{c_k}^2)}. \tag{71.8}$$

Substituting (71.8) in (71.7), we can express the induced current in the QGP in terms of electrical conductivity σ_e and Hall conductivity σ_H as

$$\mathbf{j} = \sigma_e \mathbf{E} + \sigma_H (\mathbf{E} \times \mathbf{b}). \tag{71.9}$$

The forms of electrical and Hall conductivities are discussed in detail in [4, 5]. The relative significance of thermal and electric charge transport processes in the medium can be described in terms of the Wiedemann-Franz law as $\frac{\kappa}{T \times \sigma} = L$, where L is the Lorenz number. For an anisotropic system, L has different components as the electrical and thermal conduction is different in different directions. Here, the temperature dependence of L is depicted in Fig. 71.1 in the directions perpendicular to the direction of the magnetic field. It is seen that the Wiedemann-Franz law is violated in temperature regions not very far from the transition temperature. We have verified the behavior of the Lorenz number in the strong magnetic field regime by incorporating the Landau level dynamics of quarks in the analysis. Perhaps, this violation points toward a more complex behavior of the hot QCD medium near the transition temperature. The results are compared with the observation of [6] where the temperature behavior of L is estimated in the limit of vanishing magnetic field. We have observed that both the equation of state and magnetic field have significant impacts on the thermal and electric charge transport in the medium.

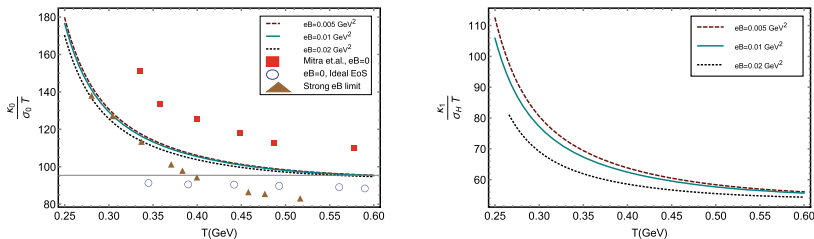


Fig. 71.1 Temperature dependence of Lorenz number within the EQPM at $|eB| = 0.01 \text{ GeV}^2$ and $\mu = 200 \text{ MeV}$ [3]

References

1. S. Acharya et al. [ALICE], Probing the effects of strong electromagnetic fields with charge-dependent directed flow in Pb-Pb collisions at the LHC. *Phys. Rev. Lett.* **125**(2), 022301 (2020)
2. S. Mitra, V. Chandra, Covariant kinetic theory for effective fugacity quasiparticle model and first order transport coefficients for hot QCD matter. *Phys. Rev. D* **97**(3), 034032 (2018)
3. M. Kurian, Thermal transport in a weakly magnetized hot QCD medium. *Phys. Rev. D* **102**(1), 014041 (2020)
4. B. Feng, Electric conductivity and Hall conductivity of the QGP in a magnetic field. *Phys. Rev. D* **96**(3), 036009 (2017)
5. G. K. K, M. Kurian, V. Chandra, Response of a weakly magnetized hot QCD medium to inhomogeneous electric field. [arXiv:2012.07156](https://arxiv.org/abs/2012.07156) [hep-ph]
6. S. Mitra, V. Chandra, Transport coefficients of a hot QCD medium and their relative significance in heavy-ion collisions. *Phys. Rev. D* **96**(9), 094003 (2017)

Chapter 72

Study of Heavy Flavour Decay Muons in pp and Pb-Pb Collisions at LHC Energies Using Angantyr Model for Heavy-Ion Collisions in PYTHIA8



Md Samsul Islam, Tinku Sinha, and Pradip Roy

Abstract The measurement of heavy flavour productions through their semi-leptonic decay channels is being investigated by ALICE (A Large Ion Collider Experiment), one of the main experimental programs at LHC (Large Hadron Collider), CERN. Here we shall present the results of production of muons decaying from heavy flavour hadron using Angantyr model for heavy-ion collisions in PYTHIA8. Angantyr model is an extrapolation of high-energy pp dynamics with PYTHIA8 to the heavy-ion collisions [1]. This PYTHIA8 version of heavy-ion model does not include the assumption of any thermalised medium to be produced in heavy-ion collisions. This model can only serve as a baseline to study the non-collective background in explaining the collective behaviour for the study of heavy-ion collisions. To study the heavy-ion collision in PYTHIA8, the geometric quantities like the number of participating nucleons ($\langle N_{part} \rangle$) and nucleon-nucleon binary collisions ($\langle N_{coll} \rangle$) for a given centrality class have been calculated using Monte Carlo Glauber (MCG) model [2].

72.1 Angantyr Model: A Heavy-Ion Version of PYTHIA8

Angantyr model is an addition to the current hadron-hadron collisions with PYTHIA8 and is intended to study the heavy-ion collisions. This Angantyr model is inspired by the old Fritiof model for pA and AA collisions [3] and is used to estimate the contribution to the final state from each NN collision. This version of PYTHIA8 does not include the mechanism to reproduce the collective effects as well as the earlier PYTHIA8 default version too. The partonic states are hadronised using string fragmentation model, and the general features like charged-particle density distribution as a function of rapidity and transverse momentum are realised by this model with-

M. S. Islam (✉) · T. Sinha · P. Roy
High Energy Nuclear and Particle Physics Division, Saha Institute of Nuclear Physics,
Kolkata 700064, India
e-mail: samsul.islam@saha.ac.in

© The Author(s), under exclusive license to Springer Nature Singapore Pte Ltd. 2022
B. Mohanty et al. (eds.), *Proceedings of the XXIV DAE-BRNS High Energy Physics Symposium, Jatni, India*, Springer Proceedings in Physics 277,
https://doi.org/10.1007/978-981-19-2354-8_72

397

out any flow-like effect. At ultra-relativistic high-energy hadron-hadron collisions, the ingredients like multi-parton interaction (MPI) and colour reconnection (CR) can play important roles to explain the contribution to the underlying event (UE) in the absence of in-medium effect. In this paper, we discuss the production of heavy flavour decay muon (HFM) at forward rapidity $2.5 < y < 4$ in both pp and Pb-Pb collisions using Angantyr model in PYTHIA8.

72.2 Geometric quantities in Heavy Ion from Monte Carlo Glauber (MCG) Model Calculations

The geometric quantities like impact parameter (b), number of participating nucleons (N_{part}), number of binary nucleon-nucleon collisions (N_{coll}), the nuclear overlap function (T_{AA}) etc. are calculated using Monte Carlo Glauber (MCG) model for heavy-ion collisions. Within the framework of MCG, individual nucleons inside a nucleus are distributed event by event and with eikonal approximation, two nuclei are then set to collide each other. Finally, the geometric quantities are calculated by averaging over many events [4]. In relativistic heavy-ion collisions, the centrality of heavy-ion collisions may be calculated by slicing the impact parameter distribution given by the following relation [5]:

$$c_i \simeq \frac{\pi b^2}{\sigma_{AA}}, \quad \text{for } b < \bar{R} \quad (72.1)$$

where c_i is the percentile of the centrality corresponding to an impact parameter(b) value. The σ_{AA} is the nucleus-nucleus cross-section and \bar{R} is the sum of the radii of two colliding nuclei. In PYTHIA8 heavy-ion model, a sharp cut on the number of wounded nucleons (N_{part}) is applied to define a centrality class.

72.3 Results and Discussion

The simulation in pp collisions has been performed using both Angantyr model and default PYTHIA8. In Fig. 72.1, a comparison between the Angantyr model and default PYTHIA8 in pp collisions has been shown for the charged-particle multiplicity distribution (left panel) in mid-rapidity ($|y| < 0.5$) and the production of heavy flavour decay muon (right panel) at forward rapidity ($2.5 < y < 4$) at $\sqrt{s} = 2.76$ TeV. The results for charged particle multiplicity and HFM using the Angantyr model are in good precision agreement with the default PYTHIA8 in the case of pp collisions. A comparison with centrality dependence of the charged-particle multiplicity density at mid-rapidity in Pb-Pb collisions at two LHC energies $\sqrt{s} = 2.76$ TeV (left panel)

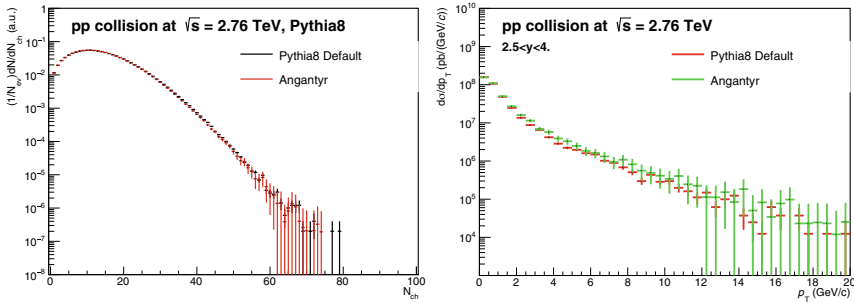


Fig. 72.1 Charged particle multiplicity distribution (left) at mid-rapidity ($|y| < 0.5$) and transverse momentum distributions of HFM (right) at forward rapidity ($2.5 < y < 4$) in pp collisions at $\sqrt{s} = 2.76$ TeV

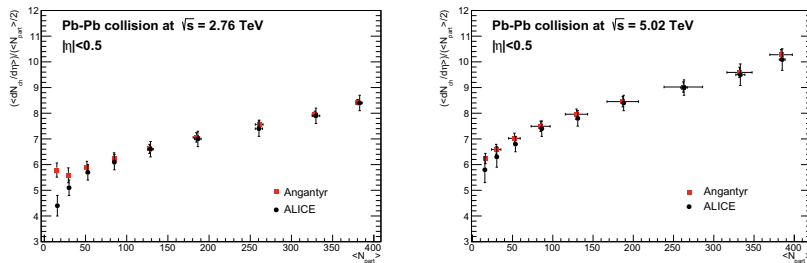


Fig. 72.2 $(dN_{ch}/d\eta)/(\langle N_{part} \rangle / 2)$ dependency on the number of participants for Pb-Pb collisions at $\sqrt{s} = 2.76$ TeV (left panel) and $\sqrt{s} = 5.02$ TeV (right panel), respectively. The same is compared with ALICE results

and 5.02 TeV (right panel) is shown in Fig. 72.2. The results are well in agreement with that measured by ALICE experiment at both the energies $\sqrt{s} = 2.76$ TeV [6] and 5.02 TeV [7], respectively.

In PYTHIA8 [8], PhaseSpace is a base class for all hard process either for $2 \rightarrow 1$ or $2 \rightarrow 2$ or specialised for elastic and diffractive scattering. The cross-section of a process in PYTHIA8 is adjusted only to the allowed phase space corresponding to the applied cuts. For more higher value in the PhaseSpace cut, more number of particles are generated in the final state [9]. The production of heavy flavour decay muon (Fig. 72.3, left panel) at forward rapidity ($2.5 < y < 4$) in pp collisions at $\sqrt{s} = 5.02$ TeV with different PhaseSpace:pTHatMin cuts are measured. Finally those results are compared with that measured by ALICE experiment [10]. A similar comparison with pTHatMin values of 5 GeV/c and 20 GeV/c for most central (0–10%) Pb-Pb collisions at $\sqrt{s} = 5.02$ TeV is done (Fig. 72.3, right panel), which shows there is no significant effect of such cuts applied in Pb-Pb collisions while studying heavy flavour production. However, Fig. 72.3 (left panel) indicates that a PhaseSpace cut at pTHatMin = 5 value describes the ALICE result well in agreement at

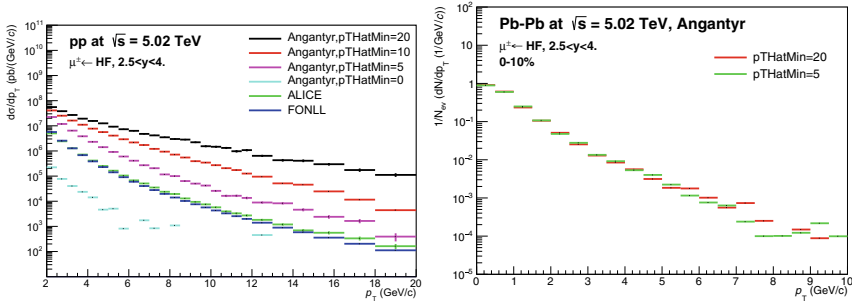


Fig. 7.23 The p_T -differential yield of heavy flavour decay muons at forward rapidity ($2.5 < y < 4$) at $\sqrt{s} = 5.02$ TeV for pp collisions (left panel) and for most central (0–10%) Pb-Pb collisions (right panel). The results are compared for different PhaseSpace:pTHatMin cuts available with PYTHIA8

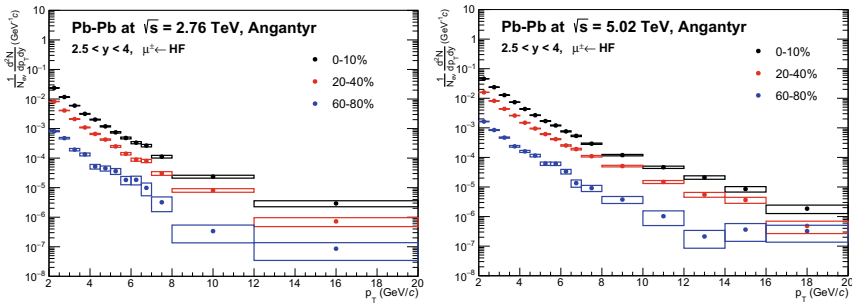


Fig. 7.24 The p_T -differential yield of heavy flavour decay muons (HFM) at $2.5 < y < 4$ for central (0–10%), semi-central (20–40%) and peripheral (60–80%) Pb-Pb collisions at $\sqrt{s} = 2.76$ TeV (left panel) and $\sqrt{s} = 5.02$ TeV (right panel), respectively. The boxes are representing the corresponding statistical errors in the measurement

$\sqrt{s} = 5.02$ TeV in pp collisions. The p_T -distribution of HFM in Pb-Pb collisions at three centrality classes are shown in Fig. 7.2.4 at two energies $\sqrt{s} = 2.76$ TeV (left panel) and $\sqrt{s} = 5.02$ TeV (right panel).

Centrality dependence of the charged-particle multiplicity density at mid-rapidity in Pb-Pb collisions at two LHC energies is compared with that measured by ALICE. It is possible to reproduce HFM production at a given energy with proper PYTHIA8 tuning. One can also check the same for the production of a charged particle in both pp and Pb-Pb systems. It is worthwhile to mention that a detailed study on this PhaseSpace:pTHatMin cut can be done at all experimental energies measured by ALICE and to check if a particular tuning reproduces the HFM production cross-section.

References

1. C. Bierlich, G. Gustafson, L. Lonnblad, H. Shah, The angantyr model for heavy-ion collisions in PYTHIA8. *JHEP* **10**, 134. [https://doi.org/10.1007/JHEP10\(2018\)134](https://doi.org/10.1007/JHEP10(2018)134)
2. C. Loizides, J. Kamin, D. d'Enterria, Improved Monte Carlo Glauber predictions at present and future nuclear colliders. *Phys. Rev. C* **97**, 5 (2018). [arXiv:1710.07098](https://arxiv.org/abs/1710.07098) [nucl-ex]
3. B. Andersson, G. Gustafson, B. Nilsson-Almqvist, A model for low p(t) hadronic reactions, with generalizations to hadron - nucleus and nucleus-nucleus collisions. *Nucl. Phys. B* **281**, 289 (1987) [INSPIRE]. <https://inspirehep.net/literature/227352>
4. C. Loizides, J. Nagle, P. Steinberg, Improved version of the PHOBOS Glauber Monte Carlo. <https://doi.org/10.1016/j.softx.2015.05.001>
5. W. Broniowski, W. Florkowski, *Phys. Rev. C* **65** (2002). Geometric relation between centrality and the impact parameter in relativistic heavy ion collisions, [arXiv:nucl-th/0110020](https://arxiv.org/abs/nucl-th/0110020)
6. K. Aamodt, others, ALICE collaboration, Centrality dependence of the charged-particle multiplicity density at mid-rapidity in Pb-Pb collisions at $\sqrt{s_{NN}} = 2.76$ TeV. <https://doi.org/10.1103/PhysRevLett.106.032301>
7. J. Adam, others, ALICE collaboration, Centrality dependence of the charged-particle multiplicity density at midrapidity in Pb-Pb collisions at $\sqrt{s_{NN}} = 5.02$ TeV. <https://doi.org/10.1103/PhysRevLett.116.222302>
8. Stefan, Ask, et al., An Introduction to PYTHIA 8.2. *Comput. Phys. Commun.* **191**, 159 (2015). <https://doi.org/10.1016/j.cpc.2015.01.024>
9. PYTHIA8 Online manual. <http://home.thep.lu.se/~torbjorn/pythia82html/Welcome.html>
10. ALICE collaboration, Production of muons from heavy-flavour hadron decays in pp collisions at $\sqrt{s} = 5.02$ TeV. *JHEP* **09**, 008 (2019). [https://doi.org/10.1007/JHEP09\(2019\)008](https://doi.org/10.1007/JHEP09(2019)008)

Chapter 73

Inclusive Photon Production at Forward Rapidities Using PMD in p–Pb Collisions at $\sqrt{s_{NN}} = 8.16$ TeV with ALICE



Mohammad Asif Bhat

Abstract We report on the performance studies of two correction methods, namely the efficiency–purity method and the Bayesian unfolding method applied to the pseudorapidity distribution of photons. The pseudorapidity distribution of inclusive photons at forward rapidities in the range $2.3 < \eta < 3.9$ in p–Pb collisions at $\sqrt{s_{NN}} = 8.16$ TeV is obtained with the HIJING Monte Carlo event generator. The simulated data samples were obtained by the GEANT tracking system from the Photon Multiplicity Detector (PMD) in ALICE.

73.1 Introduction

Relativistic heavy-ion collisions are believed to produce a Quark–Gluon Plasma (QGP) [1] which hadronizes dominantly into pions, of which approximately one-third are neutral pions that decay into photons. Therefore, the measurement of photon multiplicity can provide important information about bulk physics from initial scatterings to the final state of QGP medium formation [2]. The measurement of photon multiplicity in p–Pb collisions [3] is very important as it is an intermediate step going from hadronic to heavy-ion collisions.

In this analysis, we generated the pseudorapidity distribution of inclusive photons at forward rapidities ($2.3 < \eta < 3.9$) in p–Pb collisions at $\sqrt{s_{NN}} = 8.16$ TeV using the HIJING [4] Monte Carlo event generator. The photons are detected by the Photon Multiplicity Detector (PMD) [5, 6]. The raw pseudorapidity distribution of inclusive photons was corrected by the following two methods: (i) Efficiency–purity method and (ii) Bayesian unfolding method. We used the minimum bias events, which produce at least one hit in V0A and V0C trigger detectors. The events with the collision

(for the ALICE collaboration).

M. A. Bhat (✉)

Department of Physics and Centre for Astroparticle Physics and Space Science (CAPSS), Bose Institute, EN-80, Sector V, Kolkata 700091, India
e-mail: mohammad.asif.bhat@cern.ch; asifqadir@jcbose.ac.in

© The Author(s), under exclusive license to Springer Nature Singapore Pte Ltd. 2022
B. Mohanty et al. (eds.), *Proceedings of the XXIV DAE-BRNS High Energy Physics Symposium, Jatni, India*, Springer Proceedings in Physics 277,
https://doi.org/10.1007/978-981-19-2354-8_73

403

vertex coordinate along the beam axis z lying between -10 and $+10$ cm from the nominal interaction point are taken for physics analysis.

73.2 Pseudorapidity Distribution of Photons

Photons are identified using two different conditions imposed on all detected clusters on the PMD. These are $\text{ADC} > 6\text{MPV}$, $N_{\text{cell}} > 2$ and $\text{ADC} > 9\text{MPV}$, $N_{\text{cell}} > 2$, where ADC is the sum of the ADC channel numbers of the cells within the cluster, $\text{MPV} = 72$ ADC channels are the most probable value of the pion ADC distribution and N_{cell} is the average number of cells affected by 3 GeV pion from the test beam result [7]. The pseudorapidity distribution of photons obtained using the above-mentioned conditions is shown in the left panel of Fig. 73.1. This distribution is affected by the detector finite resolution, limited detector efficiency and acceptance and secondary contamination such as hadron clusters. Therefore, correction is needed to be applied to get the true distribution. We used two methods for correction as detailed in the following section.

73.3 Correction Methods

73.3.1 Efficiency-Purity Method

Efficiency (ϵ_γ) is defined as the ratio of the number of detected photons to the number of incident photons within the same acceptance coverage

$$\epsilon_\gamma = \frac{N_{\gamma\text{-detected}}}{N_{\gamma\text{-incident}}}, \quad (73.1)$$

where $\gamma\text{-detected}$ are those $\gamma\text{-like}$ clusters whose cluster identity matches with the incident photon identity, and $\gamma\text{-incident}$ are the incident photons produced from HIJING.

Purity (p) is defined as the ratio of the number of detected photons to the number of $\gamma\text{-like}$ clusters within the same acceptance coverage

$$p = \frac{N_{\gamma\text{-detected}}}{N_{\gamma\text{-like}}}, \quad (73.2)$$

where $\gamma\text{-like}$ or $\gamma\text{-measured}$ are those clusters that satisfy the photon-hadron discrimination conditions.

The right panel of Fig. 73.1 shows the efficiency and purity values as a function of pseudorapidity for two different photon-hadron discrimination conditions.

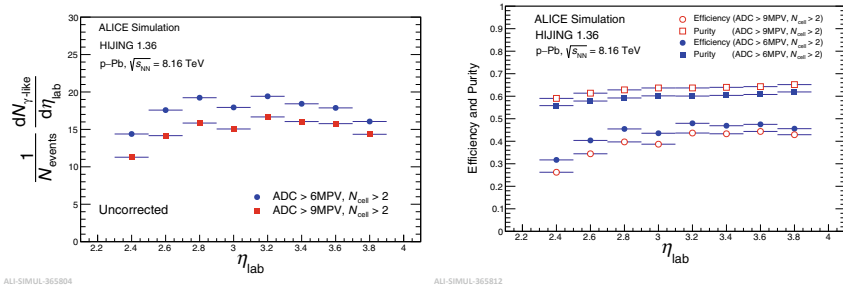


Fig. 73.1 Left: Uncorrected pseudorapidity distribution of photons in p–Pb collisions at $\sqrt{s_{NN}} = 8.16$ TeV using MC event generator HIJING. Right: Efficiency and purity values as a function of pseudorapidity

To obtain the corrected photon distribution, we used the following relation:

$$N_{\gamma\text{-true}} = \frac{P}{\epsilon_{\gamma}} \times N_{\gamma\text{-measured}}. \quad (73.3)$$

73.3.2 Bayesian Unfolding Method

Unfolding is a technique to get the true distribution from the measured distribution. Bayesian unfolding [8] is based on the Bayes' theorem

$$P(A|B) = \frac{P(B|A) \times P(A)}{P(B)}. \quad (73.4)$$

In our notation

$$\bar{A}_{ij} = \frac{A_{ji} f_i}{\sum_k A_{ik} f_k} \quad (73.5)$$

$$f_i = \sum_j \bar{A}_{ij} g_j \quad (73.6)$$

where f_i is the unfolded distribution, \bar{A}_{ij} is the inverse of the response matrix A_{ij} and g_j is the measured distribution. The fluctuation in the error is controlled by the regularization parameters such as the number of iterations and smoothing. The unfolding was carried out in each pseudorapidity bin and for each pseudorapidity bin, we have obtained the response matrix as shown in the left panel of Fig. 73.2, measured (γ -like) distribution and the unfolded distribution for a different set of regularization parameters. The sets of parameters which give the minimum possible fluctuations in the error were selected. The average value of the unfolded distribution

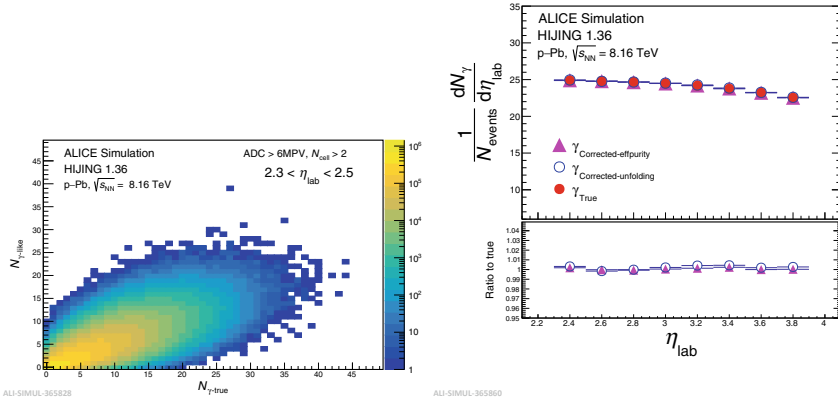


Fig. 73.2 Left: Response matrix for pseudorapidity interval $2.3 < \eta < 2.5$. Right: Efficiency-purity corrected and Bayesian-unfolded pseudorapidity distribution of photons compared with the pseudorapidity distribution of true incident photons from HIJING

divided by the bin width was used to get the pseudorapidity distribution of photons bin by bin.

73.4 Results

The pseudorapidity distribution of photons obtained after applying the two correction methods is compared with the pseudorapidity distribution of true incident photons from HIJING as shown on the right side of Fig. 73.2. The ratios of the true pseudorapidity distribution with the one obtained after applying each of the two correction methods are consistent with unity with an error of 0.5%. This shows that while analyzing the data, any one of the two correction methods can be applied and the difference arising from using the other can be included in the systematic uncertainty.

73.5 Summary

We reported on the corrected pseudorapidity distribution of photons obtained by two correction methods: the efficiency-purity method and the Bayesian unfolding method. The pseudorapidity distributions of photons obtained by these two correction methods are in good agreement with the true incident photon distribution obtained from HIJING.

References

1. K. Aamodt et al., [ALICE]: The ALICE experiment at the CERN LHC. *JINST* **3**, S08002 (2008)
2. W. Ke, X.N. Wang, QGP modification to single inclusive jets in a calibrated transport model. *JHEP* **05**, 041 (2021)
3. A. Adare et al., [PHENIX]: cold-nuclear-matter effects on heavy-quark production at forward and backward rapidity in d+Au collisions at $\sqrt{s_{NN}} = 200$ GeV. *Phys. Rev. Lett.* **112**(no. 25), 252301 (2014)
4. X.N. Wang, M. Gyulassy, HIJING: a Monte Carlo model for multiple jet production in p p, p A and A A collisions. *Phys. Rev. D* **44**, 3501–3516 (1991)
5. G. Dellacasa et al., [ALICE]: ALICE technical design report: photon multiplicity detector (PMD). ALICE technical design report, CERN-LHCC-99-32
6. J. Adams et al., [STAR]: multiplicity and pseudorapidity distributions of photons in Au + Au collisions at $\sqrt{s_{NN}} = 62.4$ GeV. *Phys. Rev. Lett.* **95**, 062301 (2005)
7. B.B. Abelev et al., [ALICE]: inclusive photon production at forward rapidities in proton-proton collisions at $\sqrt{s} = 0.9, 2.76$ and 7 TeV. *Eur. Phys. J. C* **75**(no. 4), 146 (2015)
8. G. D'Agostini, A multidimensional unfolding method based on Bayes' theorem. *Nucl. Instrum. Meth. A* **362**, 487–498 (1995)

Chapter 74

Recent Measurements of (Anti-)Nuclei Production in High Energy Collisions



Natasha Sharma

Abstract The recent measurements of light nuclei and anti-nuclei production by different experiments in high energy collisions are discussed. The comparison of data with the thermal and coalescence models is also discussed to understand their production mechanisms in high energy collisions. The recent measurements of the hyper-triton (${}^3_{\Lambda}\text{H}$) lifetime from the STAR and ALICE experiments are also discussed.

74.1 Introduction

The measurements of light nuclei and anti-nuclei production in high energy collisions have been of great interest. It is known that the Universe started with the Big Bang with a nearly equal abundance of matter and anti-matter. This symmetry got lost in the evolution of the Universe with no visible amounts of anti-matter being present now. The data from the high energy experiments suggest equal abundance of matter and anti-matter in the midrapidity region irrespective of the colliding system. Thus, the study of (anti-)nuclei production in these collisions can shed light on their production mechanism as well as can be related to the early evolution of the Universe after the Big Bang.

The two proposed production mechanisms for the (anti-)nuclei including (anti-)hypernuclei are the coalescence model [1, 2] and the statistical thermal model [3, 4]. The simple coalescence model assumes that (anti-)nuclei are formed if the constituent baryons are close in the coordinate and momentum phase space. Since the binding energy of (anti-)nuclei is small (\sim few MeV), it can break into its constituent (anti-)nucleons and can be regenerated by the final-state coalescence of (anti-)nucleons. The thermal model assumes that the particle yields get fixed at the chemical freeze-out of the system. The particle yields depend on its mass m , the baryon chemical potential (μ_B), and the chemical freeze-out temperature (T_{chem}) by the relation: $dN/dy \propto \exp((\mu_B - m)/T_{\text{chem}})$.

N. Sharma (✉)

Department of Physics, Amity University Punjab, Mohali 140306, India
e-mail: natasha.sharma@cern.ch

The production of light (anti-)nuclei has been studied in the vast energy range in the experiments at Bevalac, AGS, SPS, RHIC, and LHC. In the next section, the recent measurements of (anti-)nuclei production from different experiments covering various observables such as transverse momentum distributions, yields, and ratios are discussed. With the high statistics of data collected by these experiments, it became possible to measure the lifetime of hypertriton more precisely, to constrain the hyperon-nucleon interaction, and to measure mass difference between particle and anti-particle. The comparison of experimental results with different model expectations is also discussed.

74.2 Results and Discussions

The STAR experiment at RHIC and the ALICE experiment at LHC have measured the production of (anti-)deuterons, (anti-)tritons, (anti-) ^3He , (anti-) ^4He , and (anti-) $^3_\Lambda\text{H}$ in the midrapidity region in heavy-ion collisions for energies ranging from $\sqrt{s_{\text{NN}}} = 7.7$ GeV to 5.5 TeV [5–8]. The NA49 experiment at SPS studied the production of d, t, ^3He in central lead-lead (Pb-Pb) collisions as a function of rapidity at various energies $\sqrt{s_{\text{NN}}} = 6.3$ GeV to 17.3 GeV [9]. The ALICE experiment has performed the systematic study of these light (anti-)nuclei by measuring their production as a function of the multiplicity of the produced particles in proton-proton (pp), proton-lead (p-Pb), and lead-lead (Pb-Pb) collisions at LHC energies [10–14]. It is observed that the transverse momentum distribution as a function of p_T becomes flatter with increasing centrality in heavy-ion collisions and increasing multiplicities of produced charged particles in small systems. This observation is consistent with the hydrodynamic model expectations, i.e. supports the presence of light (anti-)nuclei during the expansion of the produced system and in radial flow of the system.

Since the light (anti-)nuclei are weakly bound particles while the kinetic freeze-out temperature (temperature at which inelastic collisions among produced particles stop and spectral shape of the particle gets fixed) of the system is ~ 100 MeV, to understand the production mechanism of these (anti-)nuclei, various observables like coalescence parameter, particle yields, and ratios are studied.

In coalescence mechanism, the spectral distribution of deuterons is related to that of primordial protons via $E_d \frac{d^3 N_d}{d p_d^3} = B_2 \left(E_p \frac{d^3 N_p}{d p_p^3} \right)^2$, assuming that protons and neutrons have the same momentum distribution. B_2 is the coalescence parameter for deuteron with momentum $p_d = 2 p_p$. The left panel of Fig. 74.1 shows the energy dependence of the coalescence parameter B_2 in heavy-ion collisions. The value of B_2 decreases with energy up to $\sqrt{s_{\text{NN}}} = 20$ GeV, which implies that the overall size of the emitting source of nucleons increases with the collision energy. For $\sqrt{s_{\text{NN}}} = 20$ GeV to 62.4 GeV, B_2 saturates which might imply a dramatic change of the equation of state of the medium. From RHIC, top energy to LHC energy B_2 shows slight decrease [15]. In the coalescence picture, this behavior is explained by an increase in

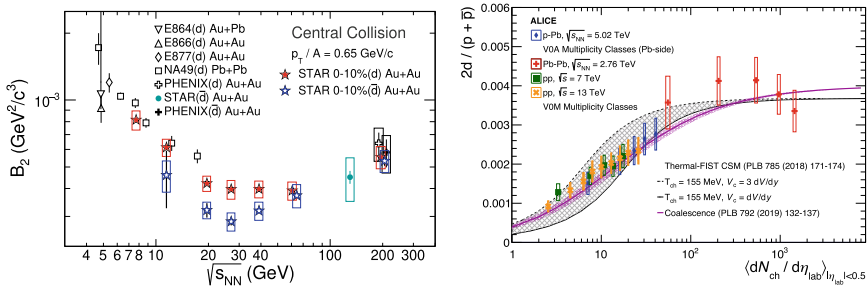


Fig. 74.1 Left: B_2 measured from various experiments as a function of $\sqrt{s_{NN}}$; Right: Deuteron over proton ratio as a function of produced charged particle multiplicities for pp, p-Pb, and Pb-Pb collision systems at LHC energies

the source volume, i.e. the larger the distance between protons and neutrons which are created in the collision, the less likely is that they coalesce.

The right panel of Fig. 74.1 shows the ratio of the p_T integrated yields of deuteron to proton as a function of the charged particle multiplicities in pp, p-Pb, and Pb-Pb collisions at the LHC energies [14]. The symbols represent the experimental data and the lines represent different model predictions. It is observed that the d/p ratio increases monotonically with multiplicity for pp and p-Pb collisions and saturates for Pb-Pb collisions. The solid and dash lines with a gray band show the prediction from the canonical statistical thermal model (CSM) with exact conservation of baryon number (B), charge (Q), and strangeness (S). The model qualitatively reproduces the trend observed in data. This might suggest that the light (anti-)nuclei production in small collision systems could be canonically suppressed. The line with a magenta band represents the full coalescence calculation, taking into account the interplay between system size and width of the wave function of produced (anti-)deuterons. It describes the data consistently better than the canonical statistical thermal model for all system sizes.

The left panel of Fig. 74.2 shows yields of protons, deuterons, and ^3He normalized by the spin degeneracy as a function of the mass number A for inelastic pp, non-single diffractive (NSD) p-Pb, and central Pb-Pb collisions [12]. An exponential decrease with mass number is represented as dotted lines in the figure for all colliding systems. The reduction of the yield for each additional nucleon also known as the penalty factor is obtained as about 1000 for pp, 600 in p-Pb, and 400 in Pb-Pb collisions. Such an exponential decrease of the (anti-)nuclei yield with mass number has also been observed at lower incident energies [9]. This is consistent with the thermal model expectations.

The right panel of Fig. 74.2 shows the experimental measurements of hyper-triton ($^3_\Lambda\text{H}$) lifetime from various experiments [16, 17]. The figure also shows the lifetime of the free Λ from the PDG and recent high precision measurements from the STAR and ALICE experiments. The recent $^3_\Lambda\text{H}$ lifetime measurements from STAR [17] is 3σ below the lifetime of free Λ hyperon. While the recent measurements from

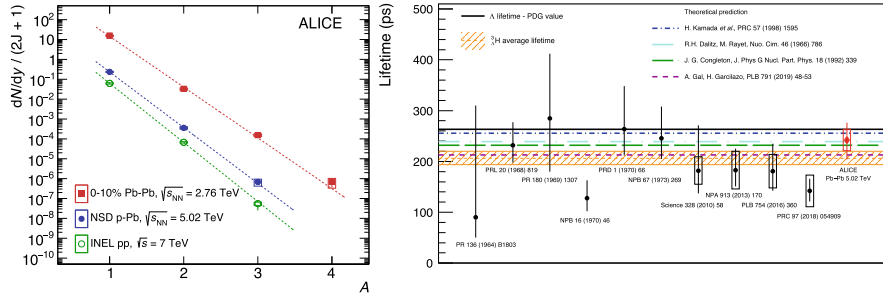


Fig. 74.2 Left: Yields of p, d, and ^3He normalized by the spin degeneracy as a function of mass number A . The dotted lines represent fits with an exponential function; Right: Lifetime measurements of hypertriton from different experiments

ALICE [16] is compatible with world average and free Λ lifetime. More work is needed for precise lifetime measurement in future.

Recently, the ALICE experiment has measured the mass and binding energies of d (\bar{d}), ^3He ($^3\bar{\text{He}}$), and the STAR experiment has measured the same of $^3_\Lambda\text{H}$ ($^3_\Lambda\bar{H}$) [18, 19]. It is found that the mass and binding energies of both nuclei and anti-nuclei are compatible within uncertainties. This confirm the CPT invariance of light nuclei including hypernuclei [18]. The Quantum Chromodynamics (QCD) predicts the existence of exotic bound states of baryons [20]. The thermal and coalescence models explain well the experimentally measured yields of light nuclei and $^3_\Lambda\text{H}$ in Pb-Pb collisions [6, 19]. These models may predict the yields of exotic bound states and hence may provide a baseline to test the existence of these states. Various experiments attempt to search for these weakly decaying bound state of baryons. Recently, ALICE has tried to search for the $\Lambda\Lambda$ and $\bar{\Lambda}\bar{n}$ bound states [20]. No evidence for these bound states is observed. Theoretical explanation is needed to understand the non-observation of these states.

74.3 Summary

The production of light (anti-)(hyper)nuclei has been studied by various experiments. It is observed that at LHC energies, the d/p ratio increases with increasing multiplicity in pp and p-Pb collisions and saturates for Pb-Pb collisions. The coalescence model could explain such a behavior of d/p ratio as the function of produced charged particle multiplicity. However, the canonical statistical thermal model with exact conservation of baryon number, charge, and strangeness qualitatively explains the observed trend at $T_{\text{chem}} = 155$ MeV. The yields of (anti-)nuclei follow an exponential decrease with increasing mass number. This implies that it is difficult to produce heavier (anti-)nuclei. The CPT invariance for nuclei like d , ^3He , and $^3_\Lambda\text{H}$ has been tested and confirmed experimentally. Experiments are trying to measure the $^3_\Lambda\text{H}$ lifetime precisely which can be used to constrain hyperon-nucleon interaction. Searches are ongoing to discover the exotic bound state of baryons.

Acknowledgements This work is supported by DST-SERB Ramanujan Fellowship, grant no. SB/S2/RJN-084/2015. NS thanks Dr. L. Kumar for the discussions.

References

1. S. Butler, C. Pearson, Phys. Rev. **129**, 836–842 (1963)
2. J.I. Kapusta, Phys. Rev. C **21**, 1301–1310 (1980)
3. S. Wheaton, J. Cleymans, Comput. Phys. Commun. **180**, 84–106 (2009)
4. A. Andronic et al., Phys. Lett. B **697**, 203–207 (2011)
5. J. Adam et al., STAR. Phys. Rev. C **99**(6), 064905 (2019)
6. J. Adam et al., ALICE. Phys. Rev. C **93**(2), 024917 (2016)
7. S. Acharya et al., ALICE. Nucl. Phys. A **971**, 1–20 (2018)
8. S. Acharya et al., ALICE. Phys. Rev. C **102**(5), 055203 (2020)
9. T. Anticic et al., NA49. Phys. Rev. C **94**(4), 044906 (2016)
10. S. Acharya et al., ALICE. Phys. Rev. C **97**(2), 024615 (2018)
11. S. Acharya et al., ALICE. Phys. Lett. B **794**, 50–63 (2019)
12. S. Acharya et al., ALICE. Phys. Lett. B **800**, 135043 (2020)
13. S. Acharya et al., ALICE. Phys. Rev. C **101**(4), 044906 (2020)
14. S. Acharya et al., ALICE. Eur. Phys. J. C **80**(9), 889 (2020)
15. N. Sharma, Springer Proc. Phys. **203**, 639–642 (2018)
16. S. Acharya et al., ALICE. Phys. Lett. B **797**, 134905 (2019)
17. L. Adamczyk et al., Phys. Rev. C **97**(5), 054909 (2018)
18. J. Adam et al., ALICE collaboration. Nat. Phys. **11**, 811–814 (2015)
19. J. Adam et al., STAR. Nat. Phys. **16**(4), 409–412 (2020)
20. J. Adam et al., ALICE Collaboration. Phys. Lett. B **752**, 267–277 (2016)

Chapter 75

Recent Results on Jet Quenching and Heavy-Flavors in Heavy-Ion Collisions at the LHC and RHIC



Nihar Ranjan Sahoo

Abstract I discuss the recent development of jet quenching and heavy-flavor measurements to study the properties of Quark-Gluon Plasma—a strongly coupled QCD plasma at finite temperature—produced in heavy-ion collisions at the LHC and RHIC. Future measurements in this direction are also discussed.

Heavy-ion collision experiments provide a suitable laboratory condition to study the properties of the Quark-Gluon Plasma (QGP) using hard probes at the LHC and RHIC. Jet and heavy-flavors are considered as hard probes—produced from high momentum transfer ($Q^2 \gg \Lambda_{QCD}$) processes—in heavy-ion collisions. I discuss succinctly some of the recent influential observations on the saga of jet quenching and heavy-flavors that strengthen our wisdom about the strongly interacting QGP medium at the TeV to GeV collision energy range.

Jet quenching is a consequence of both vacuum and in-medium gluon radiations observed in heavy-ion collisions. Recent measurements on the suppression of inclusive high transverse momentum (p_T) particles and also jet spectra in heavy-ion collisions relative to their vacuum expectations reaffirm the jet quenching phenomenon at the LHC [1–3] and RHIC [4] with higher precision and a wider range of collision energies. Measurements on jet-fragmentation function [5] and jet-radial profile [6] observables reveal that inside a jet the soft particles ($\sim < 2$ GeV/c) are redistributed at wider angles relative to the jet-axis. This is a manifestation of jet-medium interaction in the QGP medium. In this direction, vector boson ($Z/W/\gamma$) coincidence with a recoil jet (V+jet) is considered as a clean probe to study jet quenching in heavy-ion collisions. The advantages of V+jet over inclusive jet and dijet measurements in heavy-ion collisions are discussed in [7–10]. CMS [7] and ATLAS [8] experiments measure the ratio of p_T of recoil jets to γ (and Z [9]) $x_{j\gamma} = p_{T,jet}/p_T^\gamma$ and observe a strong modification of the shape in central Pb+Pb collisions relative to p+p collisions. Similarly, the recoil jets as a function of jet p_T show significant suppression in central

N. Ranjan Sahoo (✉)

Institute of Frontier and Interdisciplinary Science, Shandong University, Qingdao, Shandong 266237, China

e-mail: nihar@sdu.edu.cn

Key Laboratory of Particle Physics and Particle Irradiation, Shandong University, Qingdao, Shandong 266237, China

Pb+Pb collisions whereas almost no suppression in peripheral collisions [7]. STAR experiment, at RHIC, has also reported recently a similar measurement with significant recoil jet suppression at RHIC [11]. Furthermore, to explore quark versus gluon jet energy loss, the ATLAS experiment [12] has reported a comparison between γ +jet and inclusive jet-fragmentation function and found that γ +jet are modified differently than latter. This could be due to a geometrical bias. Besides, at RHIC, the STAR experiment has reported their preliminary results using the semi-inclusive recoil jet technique while comparing γ +jet and π^0 +jet I_{AA} which shows the same level of strong suppression for both the cases within uncertainties [11]. Precision measurement is required that is planned to be explored in the upcoming sPHENIX and STAR heavy-ion high statistics data taking. Besides, jet quenching is commonly measured by yield suppression at fixed p_T (R_{AA} and I_{AA}) [11]. However, to isolate the effect of energy loss alone we convert the suppression to a p_T -shift, $-\Delta p_{T,jet}$, enabling quantitative comparison of jet quenching measurements with different observables, and comparison of jet quenching at RHIC and the LHC. A compilation of $\Delta p_{T,jet}$ from the similar measurement, compared to those of inclusive jets [4] and h+jet at RHIC [15], and h+jet at the LHC [14, 15]. An indication of smaller in-medium energy loss is observed at RHIC than at the LHC. To study the microstructure of the QGP and its strong/weak coupling limit, measurement of the azimuthal angular correlation between trigger particle (like Z, γ , high- p_T hadron, etc.) and recoil jet axis are proposed. Experimental efforts are ongoing both at the LHC [13, 16] and RHIC to study the shape of the azimuthal correlations and recoil jet yields at a large angle relative to the trigger axis.

Heavy-flavors (HF)—quark mass, $m_Q \gg \Lambda_{QCD}$, and the QGP temperature—are produced with a short formation time and their thermalization time comparable with the QGP lifetime. Due to these characteristics, HF observables provide important information about the QGP: thermalization and transport properties of the QGP, and their hadronization mechanism [17, 18]. In experiments, HF hadrons are classified into open (D-meson, Λ_c baryons, etc.) and hidden (quarkonium states $Q\bar{Q}$, e.g., J/ψ , Υ (nS) families, and multi-HF hadrons, like Ξ_{cc}). Inclusive hidden-charm, J/ψ , hadrons measurement shows a strong evidence of color-screening effect in the QGP at high- p_T whereas, at low- p_T , the charm-quark regeneration is dominant at the LHC than RHIC [19–21]. On heavier quarkonium states like Υ (nS), LHC measurement shows the sequential melting of Υ (nS) states depending upon their binding energy and the Debye screening in the medium providing the thermal properties of the QGP [22]. Flow measurement of these HF-hadrons shows a finite v_2 of J/ψ but vanishing v_2 of Υ (1S) state and also infers that different medium effect plays an important role for charmonia and bottomonia [23, 24] states. On the other hand, measurements on nuclear modification factor of open-HF hadrons and their comparison with light-flavor hadrons show an indication of heavy-flavors mass-hierarchy of gluon radiation [25, 26] in the QGP medium [25, 26]. RHIC measurement reports the mass-ordering in v_2 at low p_T of D-meson and light-flavor hadrons [27]. Furthermore, the comparison of D-meson v_2 with different theory predictions gives access to extract the spatial diffusion coefficient (D_s)—to quantify the interaction of heavy-quark with the medium. The value of $2\pi TD_s$ is ~ 2 – 4 at near T_c for charm quark

and that is consistent with lattice calculations. R_{AA} measurements as a function of p_T of light- and heavy-flavors show an indication of heavy-flavors mass-hierarchy of gluon radiation [25, 26]. STAR experiment reports D -meson and its comparison with light-flavor hadrons' v_2 that shows a mass-ordering of D -meson at low p_T [27]; its comparison with different theory predictions gives access to extract the spatial diffusion coefficient (D_s)—to quantify the interaction of heavy-quark with the medium. The value of dimensionless $2\pi TD_s$ is $\sim 2-4$ at near T_c for charm quark and consistent with lattice calculations [17, 18]. In the QCD hadronization sector, recent STAR and ALICE measurements on Λ_c/D^0 show that the coalescence (recombination) hadronization models quantitatively explain the data [28]. Besides, directed flow (v_1) of D -meson as a function of rapidity is also proposed to provide the initial geometry and the magnetic field information during heavy-ion collisions [31, 32] and both at LHC and RHIC such measurements have already been reported [29, 30].

Many efforts from both the experiment and theory sides are nevertheless ongoing to extend our understanding of the properties of the QGP. Forthcoming high luminosity data at the LHC and RHIC can provide sufficient statistics to have precision measurements on jet quenching and heavy-flavor hadron observables to constrain the theory and different model predictions.

Acknowledgements I would like to thank Saskia Mioduszewski, Shanshan Cao, Rongrong Ma, Peter Jacobs, Santosh Das, Sandeep Chatterjee, Subhash Singha, and Md. Nasim for giving feedback during this talk preparation. I would also like to thank the organizer for this invitation. The author is supported by the Fundamental Research Funds of Shandong University and National Natural Science Foundation of China, Grant number: 12050410235.

References

1. S. Acharya et al., ALICE, Phys. Rev. C **101**(3), 034911 (2020). [arXiv:1909.09718](https://arxiv.org/abs/1909.09718) [nucl-ex]
2. M. Aaboud et al., ATLAS. Phys. Lett. B **790**, 108–128 (2019). [arXiv:1805.05635](https://arxiv.org/abs/1805.05635) [nucl-ex]
3. V. Khachatryan et al., CMS. Phys. Rev. C **96**(1), 015202 (2017). [arXiv:1609.05383](https://arxiv.org/abs/1609.05383) [nucl-ex]
4. J. Adam et al., STAR. Phys. Rev. C **102**(5), 054913 (2020). [arXiv:2006.00582](https://arxiv.org/abs/2006.00582) [nucl-ex]
5. M. Aaboud et al., ATLAS. Phys. Rev. C **98**(2), 024908 (2018). [arXiv:1805.05424](https://arxiv.org/abs/1805.05424) [nucl-ex]
6. A.M. Sirunyan et al., CMS. JHEP **05**, 006 (2018). [arXiv:1803.00042](https://arxiv.org/abs/1803.00042) [nucl-ex]
7. A.M. Sirunyan et al., CMS. Phys. Lett. B **785**, 14–39 (2018). [arXiv:1711.09738](https://arxiv.org/abs/1711.09738) [nucl-ex]
8. M. Aaboud et al., ATLAS. Phys. Lett. B **789**, 167–190 (2019). [arXiv:1809.07280](https://arxiv.org/abs/1809.07280) [nucl-ex]
9. A.M. Sirunyan et al., CMS. Phys. Rev. Lett. **119**(8), 082301 (2017). [arXiv:1702.01060](https://arxiv.org/abs/1702.01060) [nucl-ex]
10. L. Adamczyk et al., STAR. Phys. Lett. B **760**, 689–696 (2016). [arXiv:1604.01117](https://arxiv.org/abs/1604.01117) [nucl-ex]
11. N.R. Sahoo, STAR. [arXiv:2008.08789](https://arxiv.org/abs/2008.08789) [nucl-ex]
12. M. Aaboud et al., ATLAS. Phys. Rev. Lett. **123**(4), 042001 (2019). [arXiv:1902.10007](https://arxiv.org/abs/1902.10007) [nucl-ex]
13. S. Chatrchyan et al., CMS. Phys. Lett. B **718**, 773–794 (2013). [arXiv:1205.0206](https://arxiv.org/abs/1205.0206) [nucl-ex]
14. J. Adam et al., ALICE. JHEP **09**, 170 (2015). [https://doi.org/10.1007/JHEP09\(2015\)170](https://doi.org/10.1007/JHEP09(2015)170). [arXiv:1506.03984](https://arxiv.org/abs/1506.03984) [nucl-ex]
15. L. Adamczyk et al., STAR. Phys. Rev. C **96**(2), 024905 (2017). <https://doi.org/10.1103/PhysRevC.96.024905>. [arXiv:1702.01108](https://arxiv.org/abs/1702.01108) [nucl-ex]
16. J. Norman, ALICE. [arXiv:2009.08261](https://arxiv.org/abs/2009.08261) [hep-ex]
17. X. Dong, V. Greco, Prog. Part. Nucl. Phys. **104**, 97–141 (2019). <https://doi.org/10.1016/j.pnpnp.2018.08.001>

18. X. Dong, Y.J. Lee, R. Rapp, *Ann. Rev. Nucl. Part. Sci.* **69**, 417–445 (2019). <https://doi.org/10.1146/annurev-nucl-101918-023806>. [arXiv:1903.07709](https://arxiv.org/abs/1903.07709) [nucl-ex]
19. J. Adam et al., *STAR. Phys. Lett. B* **797**, 134917 (2019). <https://doi.org/10.1016/j.physletb.2019.134917>. [arXiv:1905.13669](https://arxiv.org/abs/1905.13669) [nucl-ex]
20. J. Adam et al., *ALICE. JHEP* **07**, 051 (2015). [https://doi.org/10.1007/JHEP07\(2015\)051](https://doi.org/10.1007/JHEP07(2015)051). [arXiv:1504.07151](https://arxiv.org/abs/1504.07151) [nucl-ex]
21. V. Khachatryan et al., *CMS. Eur. Phys. J. C* **77**(4), 252 (2017). <https://doi.org/10.1140/epjc/s10052-017-4781-1>. [arXiv:1610.00613](https://arxiv.org/abs/1610.00613) [nucl-ex]
22. A.M. Sirunyan et al., *CMS. Phys. Lett. B* **790**, 270–293 (2019). <https://doi.org/10.1016/j.physletb.2019.01.006>. [arXiv:1805.09215](https://arxiv.org/abs/1805.09215) [hep-ex]
23. S. Acharya et al., *ALICE. Phys. Rev. Lett.* **123**(19), 192301 (2019). <https://doi.org/10.1103/PhysRevLett.123.192301>. [arXiv:1907.03169](https://arxiv.org/abs/1907.03169) [nucl-ex]
24. A.M. Sirunyan et al., *CMS. arXiv:2006.07707* [hep-ex]
25. A.M. Sirunyan et al., *CMS. Phys. Rev. Lett.* **123**(2), 022001 (2019). <https://doi.org/10.1103/PhysRevLett.123.022001>. [arXiv:1810.11102](https://arxiv.org/abs/1810.11102) [hep-ex]
26. M. Kelsey, *STAR. Nucl. Phys. A* **1005**, 121806 (2021). [arXiv:2002.09057](https://arxiv.org/abs/2002.09057) [nucl-ex]
27. L. Adamczyk et al., *STAR. Phys. Rev. Lett.* **118**(21), 212301 (2017). <https://doi.org/10.1103/PhysRevLett.118.212301>. [arXiv:1701.06060](https://arxiv.org/abs/1701.06060) [nucl-ex]
28. J. Adam et al., *STAR. Phys. Rev. Lett.* **124**(17), 172301 (2020). <https://doi.org/10.1103/PhysRevLett.124.172301>. [arXiv:1910.14628](https://arxiv.org/abs/1910.14628) [nucl-ex]
29. J. Adam et al., *STAR. Phys. Rev. Lett.* **123**(16), 162301 (2019). <https://doi.org/10.1103/PhysRevLett.123.162301>. [arXiv:1905.02052](https://arxiv.org/abs/1905.02052) [nucl-ex]
30. S. Acharya et al., *ALICE. Phys. Rev. Lett.* **125**(2), 022301 (2020). <https://doi.org/10.1103/PhysRevLett.125.022301>. [arXiv:1910.14406](https://arxiv.org/abs/1910.14406) [nucl-ex]
31. S.K. Das, S. Plumari, S. Chatterjee, J. Alam, F. Scardina, V. Greco, *Phys. Lett. B* **768**, 260–264 (2017). <https://doi.org/10.1016/j.physletb.2017.02.046>. [arXiv:1608.02231](https://arxiv.org/abs/1608.02231) [nucl-th]
32. S. Chatterjee, P. Bożek, *Phys. Rev. Lett.* **120**(19), 192301 (2018). <https://doi.org/10.1103/PhysRevLett.120.192301>. [arXiv:1712.01189](https://arxiv.org/abs/1712.01189) [nucl-th]

Chapter 76

STAR Measurements on Azimuthal Anisotropy of ϕ Mesons in Au+Au Collisions at $\sqrt{s_{NN}} = 27$ and 54.4 GeV



Prabhupada Dixit

Abstract The elliptic flow coefficient (v_2) of ϕ mesons at mid-rapidity as a function of transverse momentum (p_T) is measured for Au+Au collisions at the center of mass energies ($\sqrt{s_{NN}}$) 27 and 54.4 GeV. The v_2 measurement is done using event plane from Time Projection Chamber (TPC, $|\eta| < 1.0$) and Event Plane Detectors (EPD, $2.1 < |\eta| < 5.1$) for 54.4 and 27 GeV, respectively. A high precision test of the number of constituent quark scaling of ϕ meson v_2 (by including measurements for other hadrons) has been shown.

76.1 Introduction

In an extremely hot and dense medium, the matter exists in a new state where quarks and gluons are no longer bound inside the hadrons. This state is called Quark-Gluon Plasma (QGP). To study the various macro-state properties of QGP, azimuthal anisotropy in its expansion is used as one of the well-known observables [1]. Due to the difference in pressure gradient along different axes of the collision system, the expansion of the medium is not isotropic, and this initial spatial anisotropy gives rise to the anisotropy in momentum space. To study different orders of azimuthal anisotropy, Fourier expansion of the azimuthal distribution of particles in momentum space is used [2], which is given by

$$E \frac{d^3 N}{dp^3} = \frac{1}{2\pi} \frac{d^2 N}{p_T dp_T dy} \left[1 + \sum_n 2v_n \cos n(\phi - \psi_R) \right]. \quad (76.1)$$

The coefficient v_n is called n th-order flow coefficient which is given by

$$v_n = \langle \cos n(\phi - \psi_R) \rangle. \quad (76.2)$$

P. Dixit (✉)

Indian Institute of Science Education and Research, Berhampur, India
e-mail: prabhupadad@iiserbpr.ac.in

© The Author(s), under exclusive license to Springer Nature Singapore Pte Ltd. 2022
B. Mohanty et al. (eds.), *Proceedings of the XXIV DAE-BRNS High Energy Physics Symposium, Jatni, India*, Springer Proceedings in Physics 277,
https://doi.org/10.1007/978-981-19-2354-8_76

419

The angled bracket indicates the average over all the particles and all the events. ψ_R is the reaction plane (plane spanned by the impact parameter vector and collision axis) of the collision system. In this proceedings, we have studied the second-order flow coefficient v_2 , known as elliptic flow coefficient. The elliptic flow of ϕ mesons is considered as a good probe for the initial stage of the medium produced in heavy-ion collisions. Due to its small hadronic interaction cross-section and early freeze-out, ϕ -meson v_2 is expected to be less affected by the late-stage hadronic interactions. In this proceedings, elliptic flow of ϕ mesons at mid-rapidity as a function of transverse momentum in Au+Au collision at $\sqrt{s_{NN}} = 27$ and 54.4 GeV is presented. We have used high statistics 27 GeV data from the year 2018 and 54.4 GeV data from the year 2017.

76.2 Data Sets and Methods

The main STAR detectors that we have used in our analysis are the Time Projection Chamber (TPC), the Time Of Flight (TOF) detector and the Event Plane Detectors (EPDs). The TPC and TOF have full azimuthal coverage and have pseudorapidity coverage of $|\eta| < 1.0$. The TPC is used to detect charged particles by measuring their ionization energy loss (dE/dx), and TOF is used to identify charged particles with high p_T . The EPDs have pseudorapidity coverage of $2.1 < |\eta| < 5.1$. These EPDs are used to construct the event plane of the collision.

We first reconstruct ϕ mesons by calculating the invariant mass ($M_{inv} = \sqrt{E_i^2 - p_i^2}$) of its daughter particles K^+ and K^- from the same events. The combinatorial background is calculated by using the event-mixing method. The normalized background distribution is subtracted from the signal + background distribution from the same events to get the signal of ϕ mesons. The signal distribution is then fitted with the Breit-Wigner function to calculate the yield of ϕ mesons.

We have used the second-order event plane from TPC using the η sub-event method for 54.4 GeV and EPD full event plane for 27 GeV to calculate v_2 . The observed v_2 has been corrected by the event plane resolution. The event plane resolution as a function of centrality is shown in Fig. 76.1. More details can be found in [3].

v_2 of ϕ mesons has been calculated by using the invariant mass method [4], in which, v_2 is calculated as a function of the invariant mass of K^+ and K^- as shown in the lower panel of Fig. 76.1 (right) and the distribution is fitted with Eq. (76.3).

$$v_2^{S+B}(M_{inv}) = v_2^S \frac{S}{S+B}(M_{inv}) + v_2^B \frac{B}{S+B}(M_{inv}) \quad (76.3)$$

where v_2^S is v_2 of signal and v_2^B is v_2 of background. S is the yield of the ϕ meson and B accounts for the total background counts. v_2^B can be approximated as a first-order polynomial function of invariant mass, and v_2^S can be obtained as a free parameter of the fit.

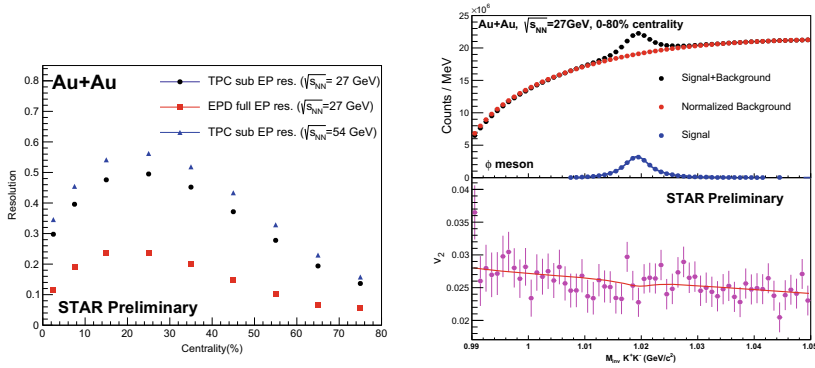


Fig. 76.1 Left panel shows TPC sub-event plane resolutions for $\sqrt{s_{NN}} = 27$ and 54.4 GeV as a function of centrality. EPD full-event plane resolution for $\sqrt{s_{NN}} = 27$ GeV is also shown. In the upper right panel, invariant mass distribution of K^+ and K^- from the same events (signal + background), from the mixed events (normalized background) and the background subtracted signal is shown. In the lower right panel, v_2 using EPD event plane is plotted as a function of the invariant mass of K^+ and K^- . The distribution is fitted with Eq. (76.3)

76.3 Results

The p_T dependence of ϕ meson v_2 has been studied at $\sqrt{s_{NN}} = 27$ GeV using EPD event plane and compared to v_2 using TPC event plane [5] for 0–80% centrality events. TPC and EPDs have different η coverage and have different minimum η gap between reconstructed ϕ mesons and the event plane (0.05 for TPC and 1.1 for EPD) but as shown in Fig. 76.2 (left panel), the v_2 for both the event planes are compatible with each other within statistical uncertainties which indicates that the effect of non-flow is negligible. In the right panel, we have compared the high precision measurement of ϕ meson v_2 at $\sqrt{s_{NN}} = 54.4$ with that at 62.4 GeV [5] and found that they are compatible with each other. One of the main goals of the STAR

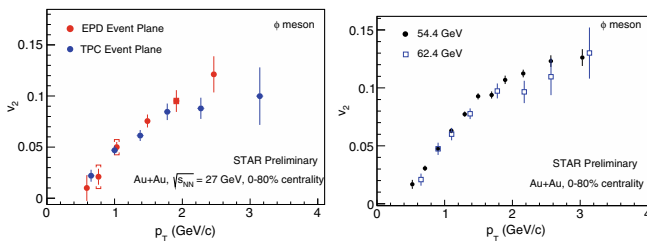


Fig. 76.2 Left panel shows the comparison of v_2 using TPC event plane and EPD event plane at $\sqrt{s_{NN}} = 27$ GeV for centrality 0–80%, and the right panel shows the comparison between v_2 at $\sqrt{s_{NN}} = 54.4$ GeV and 64.4 GeV for centrality 0–80%. Vertical lines represent statistical uncertainties and cap-symbols represent systematic uncertainties. The systematic errors are shown for only v_2 using EPD event plane

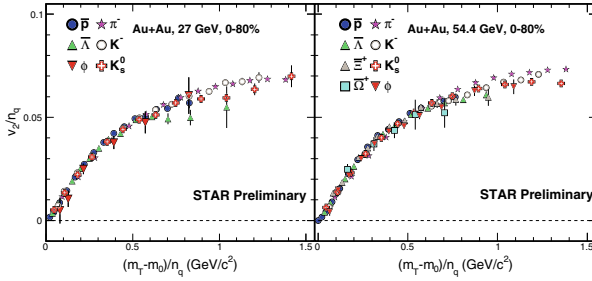


Fig. 76.3 v_2 scaled by the number of constituent quarks as a function of transverse kinetic energy per number of constituent quarks for various charged hadrons are shown at $\sqrt{s_{NN}} = 27$ and 54.4 GeV for 0–80% centrality. Only statistical error bars are shown in Fig. 76.3

experiment is to search for the turn-off signal of QGP which can be studied by the number of constituent quark (NCQ) scaling in v_2 for all hadrons as a function of energy. The number of constituent quark scaling has been studied at $\sqrt{s_{NN}} = 27$ and 54.4 GeV using v_2 of ϕ as well as other identified hadrons [5]. The results are shown in Fig. 76.3. The NCQ scaled v_2 is found to be similar for all the particles under study. This observation can be interpreted as the collectivity being developed at the partonic stage of the evolution of the system in Au+Au collisions at $\sqrt{s_{NN}} = 27$ and 54.4 GeV.

76.4 Summary

The elliptic flow coefficient v_2 of ϕ mesons has been studied for Au+Au collisions at $\sqrt{s_{NN}} = 27$ and 54.4 GeV. v_2 of ϕ meson at $\sqrt{s_{NN}} = 27$ GeV using EPD event plane is found to be in good agreement with v_2 using TPC event plane. The NCQ scaling is observed for all the hadrons at both these energies which indicates the partonic collectivity developed inside the medium during the earlier stage of its evolution.

References

1. H. Sorge, Phys. Rev. Lett. **78**, 2309–2312, 064905 (1997)
2. S. Voloshin, Y. Zhang, Z. Phys. C **70**, 665–672 (1996)
3. A.M. Poskanzer, S.A. Voloshin, Phys. Rev. C **58**, 1671–1678, 064905 (1998)
4. N. Borghini, J.-Y. Ollitrault, Phys. Rev. C **70**, 064905 (2004)
5. L. Adamczyk et al., Phys. Rev. C **88**, 014902 (2013)

Chapter 77

A Beyond Mean Field Approach to Yang-Mills Thermodynamics



Pracheta Singha, Rajarshi Ray, Chowdhury Aminul Islam,
and Munshi G Mustafa

Abstract We propose a beyond mean field approach to evaluate Yang-Mills thermodynamics from the partition function with n-body gluon contribution, in the presence of a uniform background Polyakov field. Using a path integral based formalism, we obtain, unlike the previous mean field studies within this model framework, physically consistent results with good agreement to the lattice data throughout the temperature range.

77.1 Introduction

Thermodynamic quantities are some of the fundamental observables to understand the properties of the strongly interacting medium and the nature of the associated phase transition. For SU(3) pure gauge theory the center symmetry, a global Z(3) symmetry, is spontaneously broken at high temperatures resulting in a first-order phase transition from the confined phase to the plasma phase [1]. The order parameter for this phase transition is the average of Polyakov loop, defined by,

$$L(\mathbf{x}) = \frac{1}{3} \text{Tr} \left(\mathcal{T} \exp \left[i g \int_0^\beta d\tau \mathcal{A}_0(\mathbf{x}, \tau) \right] \right) \quad (77.1)$$

where, $\mathcal{A}_0(\mathbf{x}, \tau)$ is the temporal component of the gluonic field and τ is the Euclidean time.

P. Singha (✉) · R. Ray
Center for Astroparticle Physics & Space Science, Bose Institute, Block-EN, Sector-V, Salt Lake,
Kolkata 700091, India
e-mail: pracheta.singha@jcbose.ac.in

C. Aminul Islam
School of Nuclear Science and Technology, University of Chinese Academy of Sciences, Beijing
100049, China

M. G. Mustafa
Theory Division, Saha Institute of Nuclear Physics, 1/AF, Bidhannagar, Kolkata 700064, India

To study SU(3) pure gauge system, we considered a partition function of thermal gluons in the presence of a background Polyakov field [2, 3], but instead of the mean field approximation, which may lead to the unphysical results [2, 3], we took a beyond mean field approach based on the path integral formalism to achieve a physically consistent model framework with gluonic distribution function. In Sect. (77.2) we describe our formalism followed by results and discussion in Sect. (77.3).

77.2 Formalism

The thermodynamic description of a gluonic quasiparticle system with a background Polyakov field can be formulated using the partition function [2, 3],

$$Z = \int \prod_{\mathbf{x}} d\theta_3(\mathbf{x}) d\theta_8(\mathbf{x}) \text{Det}_{V_{dM}} \exp \left(-2V \int \frac{d^3 p}{(2\pi)^3} \ln \left(1 + \sum_{n=1}^8 a_n e^{-\frac{n|p|}{T}} \right) \right), \quad (77.2)$$

where θ_3 and θ_8 , are two independent parameters that characterize the SU(3) group elements and can be associated with two diagonal generators T_3 and T_8 .

The coefficients a_n for $n = 1 \cdots 8$, are the following,

$$\begin{aligned} a_1 = a_7 = 1 - 9\bar{\Phi}\Phi; \quad a_2 = a_6 = 1 - 27\bar{\Phi}\Phi; \quad a_3 = a_5 = -2 + 27\bar{\Phi}\Phi - 81(\bar{\Phi}\Phi)^2 \\ a_4 = 2[-1 + 9\bar{\Phi}\Phi - 27(\bar{\Phi}^3 + \Phi^3) + 81(\bar{\Phi}\Phi)^2]; \quad a_8 = 1. \end{aligned} \quad (77.3)$$

Here, Φ and $\bar{\Phi}$ are the normalised characters defined as,

$$\Phi = \frac{1}{N_c} \text{Tr} \hat{L}_F; \quad \bar{\Phi} = \frac{1}{N_c} \text{Tr} \hat{L}_F^\dagger, \quad (77.4)$$

with, \hat{L}_F , the Polyakov line in the fundamental representation, given as,

$$\hat{L}_F = \text{diag}(e^{i\theta_3}, e^{i\theta_8}, e^{-i(\theta_3+\theta_8)}). \quad (77.5)$$

$\text{Det}_{V_{dM}}$ is the Vandermonde determinant [2, 3], given by,

$$\text{Det}_{V_{dM}} = 64 \sin^2 \frac{(\theta_3 - \theta_8)}{2} \sin^2 \frac{(2\theta_3 + \theta_8)}{2} \sin^2 \frac{(\theta_3 + 2\theta_8)}{2}. \quad (77.6)$$

Next, to obtain the thermodynamic observables, instead of evaluating the infinite dimensional integration in (77.2), one may use the saddle point approximation. Here, solving the following equations,

$$\frac{\partial \Omega}{\partial \Phi} = 0; \quad \frac{\partial \Omega}{\partial \bar{\Phi}} = 0, \quad (77.7)$$

one can obtain the mean fields Φ_{mf} and $\bar{\Phi}_{mf}$ and all the thermodynamic observables in terms of those fields. However, the thermodynamic quantities evaluated from this $\Omega = \Omega(\Phi_{mf}, \bar{\Phi}_{mf})$ show unphysical behaviour below the transition temperature [2, 3], which we claim to be an artefact of using the mean field approximation. Noting that the thermodynamic potential, in terms of the Polyakov loop, is an oscillating function of θ_3 and θ_8 , we propose a beyond mean field approach to include the significant contribution from the configurations away from the mean field. As the Polyakov loop fields in (77.2) are spatially uniform, we consider the configuration space to consist of $N \rightarrow \infty$ points and defining,

$$z = \int d\theta_3 d\theta_8 \text{Det}_{VdM} \exp \left(-2\delta v \int \frac{d^3 p}{(2\pi)^3} \ln \left(1 + \sum_{n=1}^8 a_n e^{-\frac{n|p|}{T}} \right) \right), \quad (77.8)$$

where δv is a parameter with the dimension of volume, we write (77.2) as,

$$Z = z^N. \quad (77.9)$$

The thermodynamic variables then follow simply from the pressure which is given as,

$$p = \frac{T}{V} \ln[Z] = \frac{T}{N\delta v} N \ln z = \frac{T}{\delta v} \ln z. \quad (77.10)$$

The expectation values of the operators are obtained as,

$$\begin{aligned} \langle O[\Phi, \bar{\Phi}] \rangle = & \frac{1}{z} \int d\theta_3 d\theta_8 \text{Det}_{VdM} O[\Phi, \bar{\Phi}] \\ & \exp \left(-2\delta v \int \frac{d^3 p}{(2\pi)^3} \ln \left(1 + \sum_{n=1}^8 a_n e^{-\frac{n|p|}{T}} \right) \right). \end{aligned} \quad (77.11)$$

77.3 Result and Discussion

Parameters:

We choose $\delta v = (0.5T_d)^{-3}$ where T_d is the deconfinement temperature and the obtained pressure shows physically consistent behaviour through out the complete temperature range. However, to have a quantitative agreement to the lattice simulation we introduce an effective gluon mass of the form,

$$m_g(T)/T = \alpha + \beta / \ln(\gamma T/T_d), \text{ for } T/T_d > 1 \quad (77.12)$$

$$= \zeta (T_d/T)^2, \text{ for } T/T_d < 1, \quad (77.13)$$

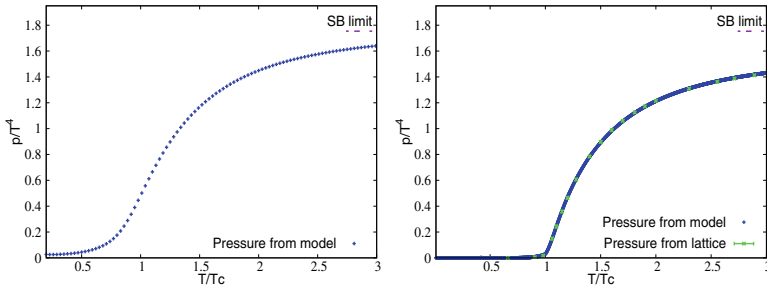


Fig. 77.1 Thermal behaviour of pressure without (left) and with (right) mass parameter. Lattice source [4]

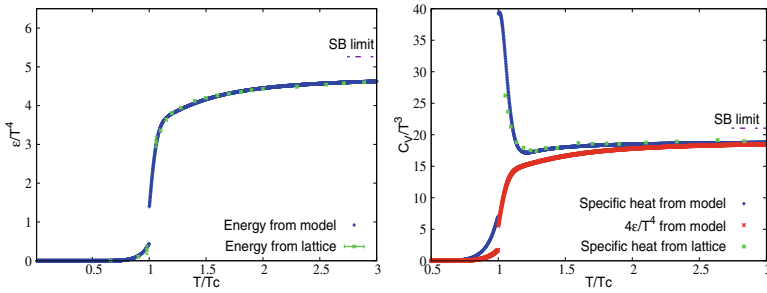


Fig. 77.2 Thermal variation of energy (left) and specific heat (right). Lattice source [4] (left) [5] (right)

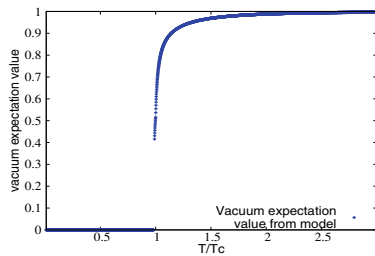


Fig. 77.3 Thermal behaviour of $\langle \Phi \rangle$

where the parameters are fitted to reproduce the lattice result for the pressure of the SU(3) pure gauge system [4] and are given by, $\alpha = 0.564$; $\beta = 0.176657$; $\gamma = 1.08526$ and $\zeta = 2.70066$. In the Fig. 77.1, we show the thermal variation of pressure scaled by T^4 for both without (left) and with (right) the mass term. Other thermodynamic quantities, derived with the mass term, also show a good agreement with the lattice results Fig. 77.2.

In the Fig. 77.3, The thermal behaviour of $\langle \Phi \rangle$, shows a discontinuity at transition point, signaling the first order phase transition.

We thus now have a complete model description for the gluonic medium that can reproduce the symmetry properties and the thermodynamic observables of an SU(3) pure gauge system.

Acknowledgements This work is supported by DST and DAE of the Government of India. CAI would like to thank TIFR and UCAS for the support.

References

1. F. Karsch, Simulating the quark-gluon plasma on the lattice. *Adv. Ser. Direct. High Energy Phys.* **6**, 61–115 (1990)
2. C. Sasaki, K. Redlich, An Effective gluon potential and hybrid approach to Yang-Mills thermodynamics. *Phys. Rev. D* **86**, 014007 (2012)
3. C.A. Islam, R. Abir, M.G. Mustafa, S.K. Ghosh, R. Ray. *J. Phys. G* **41**, 025001 (2014)
4. Leonardo Giusti, Michele Pepe, Equation of state of the SU(3) Yang–Mills theory: a precise determination from a moving frame. *Phys. Lett. B* **769**, 385–390 (2017)
5. G. Boyd, J. Engels, F. Karsch, E. Laermann, C. Legeland, M. Lutgemeier, B. Petersson, Thermodynamics of SU(3) lattice gauge theory. *Nucl. Phys. B* **469**, 419–444 (1996)

Chapter 78

Understanding Long-Range Near-Side Ridge Correlations in p-p Collisions Using Rope Hadronisation at Energies Available at the CERN Large Hadron Collider



Pritam Chakraborty and Sadhana Dash

Abstract The long-range ridge-like structure in the near-side region of the two-particle $\Delta\eta - \Delta\phi$ correlations, estimated by LHC experiments in high multiplicity p-p collisions signals the presence of collectivity which are similar to that observed in p-A (nucleon-nucleus) and A-A collisions. The two-particle correlation in $\Delta\eta - \Delta\phi$ between the charged particles produced in p-p collisions at $\sqrt{s} = 7$ TeV and 13 TeV is studied using Pythia8 event generator which includes the final-state partonic color reconnection effects and the microscopic rope hadronisation model. The rope hadronisation corresponds to the formation of ropes due to overlapping of strings in high multiplicity events followed by string shoving. By enabling the rope hadronisation mechanism (with shoving), a near-side ridge-like structure has been observed for high-multiplicity events which are qualitatively similar to the ridge observed in the data.

78.1 Introduction

The first-ever observation of a ridge-like structure in the near side, long-range region of the two-dimensional $\Delta\eta - \Delta\phi$ distributions of charged particle pairs, produced in high multiplicity p-p collisions at $\sqrt{s} = 7$ TeV and 13 TeV at CMS and ATLAS experiments at LHC [1–3] is similar to the ridge-like features in heavy-ion collisions produced due to the collectivity of the partonic matter [4, 5]. Since the system produced in p-p collisions is very small in size and short-lived, no quark gluon plasma-like (QGP) effect is expected to be seen in hadronic collisions.

P. Chakraborty (✉) · S. Dash
Indian Institute of Technology Bombay, Mumbai 400076, India
e-mail: prchakra@iitb.ac.in

© The Author(s), under exclusive license to Springer Nature Singapore Pte Ltd. 2022
B. Mohanty et al. (eds.), *Proceedings of the XXIV DAE-BRNS High Energy Physics Symposium, Jatni, India*, Springer Proceedings in Physics 277,
https://doi.org/10.1007/978-981-19-2354-8_78

In this work, the two-particle correlation of charged particles in $\Delta\eta - \Delta\phi$ is investigated for p–p collisions at $\sqrt{s} = 7$ TeV and 13 TeV using Pythia8 [6] event generator with three-colour reconnection schemes (MPI mode or CR0, QCD mode or CR1 and gluon-move scheme or CR2) along with the rope hadronisation mechanism (with shoving), without assuming the formation of QGP.

78.2 Analysis Method

A total of 80 and 100 million events were generated using Pythia8.2 for p–p collisions at $\sqrt{s} = 13$ TeV and 7 TeV, respectively, which are classified into different classes of multiplicities depending on the number of particles produced within $|\eta| < 2.4$ and $p_T > 0.4$ GeV/c. This analysis was done for three different multiplicity classes: $0 < N_{trk} < 20$, $80 < N_{trk} < 100$ and $N_{trk} > 100$, where N_{trk} is the number of charged particles within the acceptance of $|\eta| < 0.5$ and the trigger and associated particles for a given multiplicity class are selected from the p_T range: 1.0–3.0 GeV/c. Each trigger particle is then associated with the remaining charged or associated particles to form pairs of particles. The per trigger particle yield of such pairs from the same event is $S(\Delta\eta, \Delta\phi)$ and is expressed as [7]

$$S(\Delta\eta, \Delta\phi) = \frac{1}{N_{trig}} \frac{d^2 N^{same}}{d\Delta\eta d\Delta\phi}. \quad (78.1)$$

where $\Delta\eta$ and $\Delta\phi$ denote the differences in η and ϕ of the formed pair and N_{trig} is the total number of trigger particles. The mixed event pair distribution is constructed by forming pairs of the trigger particles in a given event with the associated particles from different events which are given by [7]

$$B(\Delta\eta, \Delta\phi) = \frac{1}{N_{trig}} \frac{d^2 N^{mix}}{d\Delta\eta d\Delta\phi}. \quad (78.2)$$

The number of events mixed for this analysis was 10. For a given multiplicity class, the $S(\Delta\eta, \Delta\phi)$ and $B(\Delta\eta, \Delta\phi)$ are constructed eventwise. The ratio of $S(\Delta\eta, \Delta\phi)$ and $B(\Delta\eta, \Delta\phi)$ is averaged over all considered events to get the distribution of the corrected associated yield per trigger particle [7]:

$$\frac{1}{N_{trig}} \frac{d^2 N^{pair}}{d\Delta\eta d\Delta\phi} = B(0, 0) \frac{S(\Delta\eta, \Delta\phi)}{B(\Delta\eta, \Delta\phi)} \quad (78.3)$$

Enabling the multi-partonic interactions, three different modes of colour reconnection mechanism (MPI-based(CR0), QCD -based(CR1) and gluon-move(CR2)) were studied with (and without) the rope hadronisation mechanism to observe their effects on two-particle correlations.

78.3 Results

From the two-dimensional (2D) $\Delta\eta - \Delta\phi$ correlation functions for charged particle pairs shown in Fig. 78.1, it is observed that in both high and low multiplicity classes irrespective of the rope hadronisation effect, a correlation peak appears near $\Delta\eta - \Delta\phi = (0,0)$ which primarily originates due to jet fragmentation and a ridge-like structure also appears at the away side ($\Delta\phi \sim \pi$) due to the back-to-back jets which is extended up to higher values of $|\Delta\eta|$. A long-range ridge-like structure extending almost three units in $\Delta\eta$ can also be seen in the near-side ($\Delta\phi \sim 0$) region of the correlation function for high multiplicity class only when the rope hadronisation effect is enabled.

The one-dimensional projections of the 2D correlation functions over $\Delta\phi$ for $|\Delta\eta| > 2.0$ (long range) and $|\Delta\eta| < 1.0$ (short range) for both the energies are given in Fig. 78.2. In long-range region, along with the away-side peak appearing in all multiplicity events due to back-to-back jets, a non-zero associated yield peak is also observed in the near side for high multiplicity events when the rope hadronisation is enabled. In short-range region, the near-side peak and away-side ridge are observed whose strength is higher for CR-1 and CR-2 mode compared to CR-0 mode. The qualitative similarity of the observed ridge-like structure in the near-side region with the ones observed in data supports the idea that the microscopic processes at partonic level can mimic collectivity-like features without assuming the formation of a thermalised medium.

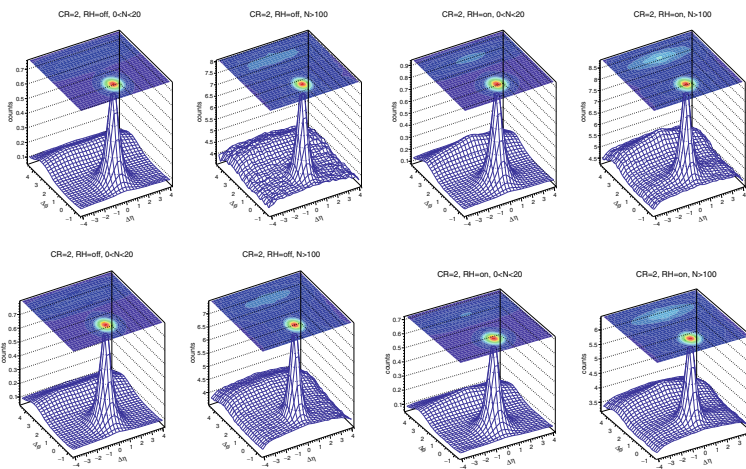


Fig. 78.1 (Colour online) The two-dimensional $\Delta\eta - \Delta\phi$ correlation function of charged particle pairs in p–p collisions at $\sqrt{s} = 7$ TeV (upper row) and 13 TeV (bottom row) for two different multiplicity classes with RH on and off [7]

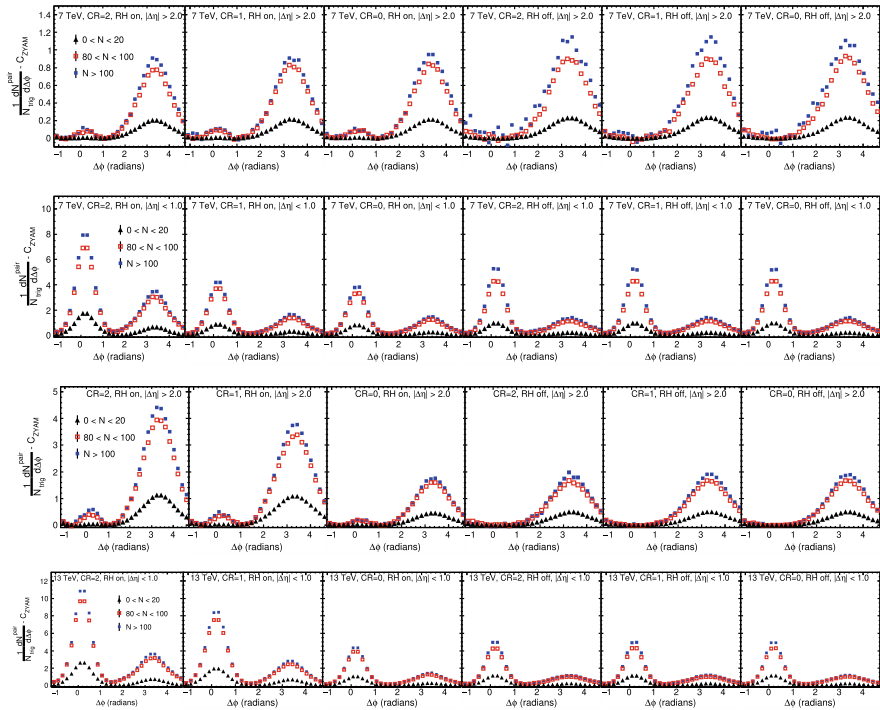


Fig. 78.2 (Colour online) The one-dimensional $\Delta\phi$ projection of two-particle correlation function of charged particles in p–p collisions at $\sqrt{s} = 7$ TeV and 13 TeV for three different multiplicity classes in the long-range region ($\Delta\eta > 2.0$, first and third row) and the short-range region ($\Delta\eta < 1.0$, second and fourth row) [7]

78.4 Summary

In the high multiplicity p–p events, the long-range correlations observed in the near-side region of $\Delta\eta - \Delta\phi$ distribution could be produced due to the formation of ropes for the overlapping of strings followed by string shoving without assuming the formation of a thermalised medium.

References

1. V. Khachatryan et al. (CMS Collaboration), *JHEP* **09**, 091 (2010)
2. V. Khachatryan et al. (CMS Collaboration), *Phys. Rev. Lett.* **116**(17), 172302 (2016)
3. G. Aad et al. (ATLAS Collaboration), *Phys. Rev. Lett.* **116**(17), 172301 (2016)
4. J. Adams et al. (STAR Collaboration), *Phys. Rev. Lett.* **95**, 152301 (2005)
5. S. Chatrchyan et al. (CMS Collaboration), *JHEP* **07**, 076 (2011)
6. T. Sjostrand et al., *Comput. Phys. Commun.* **191**, 159–177 (2015)
7. P. Chakraborty, S. Dash, *Phys. Rev. C* **102**, 055202 (2020)

Chapter 79

Recent Results on Correlations and Fluctuations in Relativistic Heavy-Ion Collisions



Prithwish Tribedy

Abstract In this conference proceedings I attempt to provide a brief overview of the recent measurements on correlations and fluctuations in relativistic heavy-ion collisions. I focus on three topics: collectivity, criticality, and chirality. A significant fraction of the content is based on results from the STAR experiment at RHIC.

79.1 Introduction

The area of correlations and fluctuations has expanded quite a bit in its width and depth over the recent years. I have, therefore, been very selective and decided to focus only on three major topics for this contribution: (1) the interest in our community on the search for collectivity in collisions with decreasing system size: $A+A > p+A > p+p > \gamma+A$ (ultra-peripheral $A+A$), (2) a decade-long quest to locate the conjectured QCD critical point, and (3) developments on the dedicated search for the signatures of chiral and vortical effects in heavy-ion collisions. Experimental search on these topics requires: (i) versatile colliders like relativistic heavy ion collider (RHIC) known for its energy and species maneuver capabilities and (ii) detectors like solenoidal tracker at RHIC (STAR) that has an excellent particle identification capability over a wide acceptance.

79.1.1 *Collectivity in Small and Large Systems*

In a naive way observing collectivity in a system refers to the observation of a specific pattern or behavior that is followed by most of its constituents. Something similar happens in relativistic collisions when a particle is emitted at an angle ϕ , and one finds: (1) there are many accompanied emissions around ϕ and (2) the

P. Tribedy (✉)

Brookhaven National Laboratory, New York, NY 11973, USA

e-mail: ptribedy@bnl.gov

pattern is repeated over a wide acceptance in pseudorapidity (η). The ridge-like structure seen in the 2D ($\Delta\eta - \Delta\phi$) correlation function near zero relative azimuthal angle ($\Delta\phi \sim 0$) over a wide range of relative pseudorapidity ($\Delta\eta > 1$) is a signature of collectivity. Emissions of particles over a small acceptance ($\Delta\eta \leq 1$, $\Delta\phi \leq 1$) due to fragmentation or, e.g., back-to-back emission of pairs of particles due to conservation of momentum ($\Delta\phi \sim \pi$) are not referred to as signatures of collectivity. The observation of collectivity across systems of all sizes, A+A, p+A, and p+p, is no longer a matter of debate. The latest additions to this list are photonuclear processes in ultra-peripheral Pb+Pb collisions [1]. Interestingly, similar processes can be studied at the future electron ion collider. Although signatures of collectivity in small collision systems (p+p and p+Pb) were first observed in the LHC experiments, for a long time the jury was out on what drives such phenomena. It took the small system scan at RHIC that collided p+Au, d+Au, and $^3\text{He}+\text{Au}$ at 200 GeV to settle this long outstanding question in our community [2]. Two competing theoretical approaches were in the game as follows: (1) gluons from projectile (p, d, ^3He) get scattered by the color domains inside the target (Au) and move collectively, as described by the color glass condensate (CGC) framework, (2) formation of a medium that expands hydrodynamically convert the pressure gradient from initial spatial anisotropy to collective motion of particles. In high activity events, while CGC predicts [3]: $v_2(\text{p+Au}) > v_2(\text{d+Au}) > v_2(^3\text{He+Au})$, hydrodynamics predict quite the opposite trend: $v_2(\text{p+Au}) < v_2(\text{d+Au}) \sim v_2(^3\text{He+Au})$. The PHENIX measurements indicated that the data are consistent with the second scenario, thereby decisively establishing the dominant role of hydrodynamic final state effects on the observability of collectivity in small collision systems [2]. However, the data do not rule out the sub-dominant role of CGC-driven correlations.

An outstanding puzzle is that PHENIX results: $v_3(^3\text{He+Au}) > v_3(\text{d+Au}) \sim v_3(\text{p+Au})$ using the combination particles from forward and mid-rapidity supports the formation of triangular shape droplets in $^3\text{He}+\text{Au}$ collisions [2]. The STAR preliminary results $v_3(^3\text{He+Au}) \sim v_3(\text{d+Au}) \sim v_3(\text{p+Au})$ using correlations of two particles, both from mid-rapidity, point to a qualitatively different conclusion that shape independent sub-nucleonic fluctuations drive v_3 [4].

Although v_3 results indicate that the precise role of collision geometry and shape on small collectivity is still not fully understood, the same is not a matter of debate in large collision systems. STAR preliminary measurements on the correlation of v_2 with mean transverse momentum $\langle p_T \rangle$ probes how collision shape and geometry transmute to collective flow in large systems. In U+U collisions, $v_2 - \langle p_T \rangle$ correlations change sign from positive to negative in central events. This is consistent with the prolate shape of the Uranium nucleus that leads to anti-correlation between v_2 and $\langle p_T \rangle$ due to body-body (large v_2 , small $\langle p_T \rangle$) and tip-tip (small v_2 , large $\langle p_T \rangle$) collision configurations [5]. No such sign change is seen for Au+Au (round nuclei) and for $v_3 - \langle p_T \rangle$ (fluctuation-driven) correlations that serve as baselines.

In this symposium, Kishora Nayak and Prabhupada Dixit presented directed (v_1) and elliptic flow measurements from STAR to explore partonic collectivity at lower collision energies. The results indicate particles containing purely produced quarks

obey constituent quark scaling very well, the ones containing transported quarks show deviations for v_1 measurements.

79.1.2 *Search for the QCD Critical Point*

What kind of observables should be designed to search for the signatures of QCD critical point (CP)? This has been a topic of discussion over the last two decades. The fluctuation of the number of nucleons produced in collisions and detected over a limited acceptance is by far considered as the most suitable observable for this purpose. Two possible options are being explored by the STAR collaboration using the data collected during the beam energy scan program (BES) of RHIC: (1) fluctuations in the number of net-protons and (2) fluctuations in the density of neutrons.

For the recent results on the former, I refer the reader to the most recent publication from the STAR collaboration [6]. The compilation of results on kurtosis times variance of net-proton shows a non-monotonic dependence on collision energy with 3.1σ significance in central events. Such a measurement from STAR is a big step toward the search for the QCD CP, the significance of which can be improved in the near future using data from the second phase of RHIC BES program (BES-II) with an upgraded STAR detector. The impact of higher statistics STAR data at 27 GeV collected after the BES-I program on higher moment analysis was discussed by Ashish Pandav at this conference. Additionally, STAR plans to use its fixed target program to increase the lever-arm for scanning the QCD phase diagram along the baryon chemical potential (μ_B) axis.

The novel second observable to explore criticality by studying neutron density fluctuations through light nuclei production was introduced in [7]. Detecting a triton is equivalent to the detection of two neutrons at the same time, whereas the same for deuteron means detecting a single neutron. Therefore, an observable suitably constructed out of yields of triton (N_t), proton (N_p), and deuteron (N_d), such as the ratio $N_t N_p / N_d^2$, measures the variance of neutron density. Preliminary measurements from the STAR collaboration show a significant non-monotonic energy dependence of this quantity [8]. A recent discussion on the connection of such an observation with nucleonic interactions near CP can be found in [9].

79.1.3 *Chirality, Polarization, and Strong Field Effects*

Let's assume the previous sections have convinced ourselves that a medium can be produced in heavy-ion collisions which: (1) expands hydrodynamically, (2) has the fundamental degrees of freedoms as quarks and gluons, and (3) has an abundance of light chiral quarks. On top of that, theoretically, such collisions should also produce strong magnetic and vortical fields. Given these possibilities, we have the necessary impetus to search for many interesting phenomena.

Large angular momentum (\mathbf{L}) produced in collisions can generate vorticity in the local frame of fluid and polarize quarks via spin-orbit coupling. The polarization of quarks can survive hadronization and can be measured: (1) directly for hyperons such as Λ , Ξ , and Ω exploiting their parity violating decays and, (2) partially for vector mesons K^{*0} , ϕ , J/ψ via angular momentum conservation during decays. In $\Lambda \rightarrow p + \pi^-$ decays the direction of the momentum vector of the proton (aligned to Λ spin), in the rest-frame of Λ , was first observed to be correlated with the reaction plane (Ψ_{RP}) by the STAR collaboration. Since Ψ_{RP} is correlated to the direction of \mathbf{L} , this indicated strong vorticity is created in the medium. Recently, STAR collaboration has performed similar measurements for Ξ and Ω [10]. These particles with different masses are produced at different times and can help map the time evolution of the strength of \mathbf{L} . The same cannot be done for vector mesons which allow us to only measure a component of their spin density matrix ρ_{00} . Significant deviations of ρ_{00} from 1/3 observed recently by the ALICE and STAR collaboration for ϕ and K^{*0} particles are qualitatively consistent with expectation of spin polarization along \mathbf{L} [11]. How to reconcile the strength of Λ polarization and spin alignment of ϕ meson is an outstanding question.

The strong color fields produced at the early stages of collisions can lead to an imbalance in the number of left and right-handed quarks. This chirality imbalance amidst the strong electromagnetic field (\mathbf{B}) leads to electric charge separation along the direction of \mathbf{B} . This phenomenon is known as the chiral magnetic effect (CME). The measurement of the separation of a pair of opposite sign charged particles across the reaction plane in isobar collisions (Ru+Ru that has 10–18% higher B-field than Zr+Zr) provides the best chance to make a decisive experimental test of CME. For more discussion on this topic I refer the reader to contributions from Victor Roy and Rihan Haque at this symposium and my overview on behalf of the STAR collaboration [12].

79.2 Epilogue

Correlation measurements are of paramount interest in the community of heavy collisions. Due to various limitations I could only cover three major topics that I find quite interesting in this context. My thanks are due to the organizers for inviting me to present this mini-review and for arranging this nice virtual symposium in challenging times.

References

1. G. Aad et al. (2021, 1)
2. C. Aidala et al., *Nat. Phys.* **15**, 214–220 (2019)
3. M. Mace et al., *Phys. Rev. Lett.* **121**, 052301 (2018) [Erratum: *Phys. Rev. Lett.* **123**, 039901 (2019)]
4. R.A. Lacey, *Nucl. Phys. A.* **1005**, 122041 (2021)
5. G. Giacalone, *Phys. Rev. Lett.* **124**, 202301 (2020)
6. J. Adam et al. (2020, 1)
7. K. Sun et al., *Phys. Lett. B.* **774**, 103–107 (2017)
8. D. Zhang, *Nucl. Phys. A.* **1005**, 121825 (2021)
9. D. DeMartini, E. Shuryak (2020, 10)
10. J. Adam et al. (2020, 12)
11. S. Acharya et al., *Phys. Rev. Lett.* **125**, 012301 (2020)
12. P. Tribedy, *J. Phys. Conf. Ser.* **1602**, 1 (2020)

Chapter 80

Kasner Space-Time, Second-Order Hydrodynamics and Gravity Dual



Priyanka Priyadarshini Pruseth and Swapna Mahapatra

Abstract We consider Kasner space-time describing three-dimensional anisotropic expansion of quark-gluon plasma (QGP) and study the generalization of Bjorken's one-dimensional expansion of the conformal fluid by taking into account second-order relativistic viscous hydrodynamics. We have obtained explicit expressions for the time evolution of the components of energy momentum tensor, energy density, temperature and entropy in terms of Kasner parameters. Using time-dependent AdS/CFT correspondence, we have studied the gravity dual of the anisotropically expanding fluid in the late time approximation.

80.1 Introduction

One of the fundamental questions in the field of high-energy physics is to understand the properties of matter at extreme density and temperature in the first few microseconds after the big bang. Such a state of matter is known as quark-gluon plasma (QGP) state where the quarks and the gluons are in a deconfined state. Hydrodynamics plays an important role after the system undergoes a rapid thermalization and local thermal equilibrium is reached. A lot of progress has been made in understanding the qualitative features of the evolution of QGP in the hydrodynamics regime by using time-dependent AdS/CFT duality. AdS/CFT correspondence [1] has been very useful in understanding the boundary and the bulk theories through the gravity dual description of the strongly coupled QGP.

P. P. Pruseth (✉) · S. Mahapatra
Department of Physics, Utkal University, Bhubaneswar 751004, India
e-mail: I.pkpruseth@gmail.com

© The Author(s), under exclusive license to Springer Nature Singapore Pte Ltd. 2022
B. Mohanty et al. (eds.), *Proceedings of the XXIV DAE-BRNS High Energy Physics Symposium, Jatni, India*, Springer Proceedings in Physics 277,
https://doi.org/10.1007/978-981-19-2354-8_80

80.2 Kasner Space-Time and Second-Order Hydrodynamics

We consider the viscous hydrodynamics including second-order gradient expansion terms and study the anisotropic three-dimensional expansion of the fluid with Kasner space-time as the local rest frame (LRF). This is a generalization of Bjorken’s one-dimensional expansion of the plasma with first-order hydrodynamics [2]. Kasner space-time is given by

$$ds^2 = -(d\tau)^2 + \tau^{2a}(dx_1)^2 + \tau^{2b}(dx_2)^2 + \tau^{2c}(dx_3)^2 \tag{80.1}$$

Here x_1, x_2, x_3 are the co-moving coordinates. a, b, c are constants and are known as Kasner parameters which satisfy the conditions,

$$a + b + c = 1, \quad a^2 + b^2 + c^2 = 1 \tag{80.2}$$

The above Kasner metric is an exact solution of vacuum Einstein’s equation and it describes a homogeneous and anisotropic expansion of the universe. In the relativistic viscous hydrodynamics, the energy momentum tensor is given by

$$T^{\mu\nu} = \epsilon u^\mu u^\nu + P \Delta^{\mu\nu} + \Pi^{\mu\nu} \tag{80.3}$$

where u^μ, ϵ and P are 4-velocity, the energy density and pressure, respectively. $\Pi^{\mu\nu}$ represents the dissipative part. The dissipative part including second-order gradient expansion terms is given by [3, 4],

$$\begin{aligned} \Pi^{\mu\nu} = & -\eta\sigma^{\mu\nu} + \eta\tau_\pi \left[D\sigma^{\mu\nu} + \frac{1}{3}\sigma^{\mu\nu}(\nabla \cdot u) \right] + \kappa [R^{<\mu\nu>} - 2u_\alpha R^{\alpha<\mu\nu>\beta} u_\beta] \\ & + \lambda_1 \sigma^{<\mu}_\lambda \sigma^{\nu>\lambda} + \lambda_2 \sigma^{<\mu}_\lambda \Omega^{\nu>\lambda} + \lambda_3 \Omega^{<\mu}_\lambda \Omega^{\nu>\lambda} \end{aligned} \tag{80.4}$$

where η is the shear viscosity, τ_π is the relaxation time and $\kappa, \lambda_1, \lambda_2, \lambda_3$ are the other second-order transport coefficients. For flat space, κ term vanishes. In the first-order hydrodynamics, only the first term in $\Pi^{\mu\nu}$ involving shear viscosity η is relevant. The bulk viscosity is zero for the conformal fluid. We have obtained the explicit expressions for the components of the energy momentum tensor by including the dissipative part [5]. The equation of state $T^\mu_\mu = 0$ and the conservation law $\nabla_\mu T^{\mu\nu} = 0$ become (using Kasner conditions),

$$P = \frac{\epsilon}{3} \tag{80.5}$$

$$\frac{d\epsilon}{d\tau} + \frac{4\epsilon}{3\tau} = \frac{4\eta}{3\tau^2} + \frac{8\eta\tau_\pi}{9\tau^3} + \frac{2\kappa(-1 + a^3 + b^3 + c^3)}{\tau^3} - \frac{\lambda_1(-7 + 9(a^3 + b^3 + c^3))}{9\tau^3} \tag{80.6}$$

As one can see, the equation of state is independent of the Kasner parameters, but the energy momentum conservation law does depend on the Kasner parameters. From the conformal invariance of the fluid, the proper time dependence of the transport coefficients are given by

$$\eta = \epsilon_0 \eta_0 \left(\frac{\epsilon}{\epsilon_0} \right)^{3/4}, \tau_\pi = \tau_\pi^0 \left(\frac{\epsilon}{\epsilon_0} \right)^{-1/4}, \lambda_1 = \epsilon_0 \lambda_1^0 \left(\frac{\epsilon}{\epsilon_0} \right)^{1/2}, \kappa = \epsilon_0 \kappa_0 \left(\frac{\epsilon}{\epsilon_0} \right)^{1/2} \quad (80.7)$$

where $\epsilon_0, \eta_0, \tau_\pi^0, \lambda_1^0, \kappa_0$ are constants. The solution of the equation for energy density $\epsilon(\tau)$ is obtained as

$$\frac{\epsilon(\tau)}{\epsilon_0} = \tau^{-4/3} - 2\eta_0 \tau^{-2} + \tilde{\epsilon}_0^{(2)} \tau^{-8/3} + \dots \quad (80.8)$$

where $\tilde{\epsilon}_0^{(2)}$ is given by [5],

$$\tilde{\epsilon}_0^{(2)} = \left[\frac{3\eta_0^2}{2} + \frac{\lambda_1^0}{3}(-7 + 9a^3 + 9b^3 + 9c^3) - \frac{2\eta_0 \tau_\pi^0}{3} - \frac{3\kappa_0}{2}(-1 + a^3 + b^3 + c^3) \right] \quad (80.9)$$

For $a = 1, b = 0, c = 0$, the above solution reduces to that of the one-dimensional expansion case (where $\kappa = 0$ in flat space) in second-order hydrodynamics [3]. Using the above solution for the energy density, the components of the energy momentum tensor can be explicitly expressed in terms of energy density [5]. From Stefan-Boltzmann's law, where $\epsilon \propto T^4$, we obtain the proper time dependence of the temperature T as [5],

$$T(\tau) = \epsilon_0^{1/4} \left(\frac{1}{\tau^{1/3}} - \frac{\eta_0}{2\tau} + \frac{3\kappa_0(-1 + a^3 + b^3 + c^3)}{8\tau^{5/3}} + \frac{\lambda_1^0(-7 + 9a^3 + 9b^3 + 9c^3)}{12\tau^{5/3}} - \frac{\eta_0 \tau_\pi^0}{6\tau^{5/3}} + \dots \right) \quad (80.10)$$

Using the thermodynamic relation $dE + PdV = TdS$, the entropy per unit co-moving volume (as a function of proper time τ) is obtained as [5]

$$S(\tau) = \epsilon_0^{3/4} \left\{ 1 - \frac{3\eta_0}{2} \tau^{-2/3} + \frac{3\eta_0^2}{4} \tau^{-4/3} - \frac{9\kappa_0(-1 + a^3 + b^3 + c^3)}{8} \tau^{-4/3} + \frac{\lambda_1^0(-7 + 9a^3 + 9b^3 + 9c^3)}{4} \tau^{-4/3} - \frac{\eta_0 \tau_\pi^0}{2} \tau^{-4/3} + 0(\tau^{-2}) \right\} \quad (80.11)$$

Our expressions for energy density, temperature and entropy as a function of proper time τ in second-order hydrodynamics in Kasner space-time depend on the Kasner parameters a, b and c .

80.3 A Proposal for the Gravity Dual of Anisotropic Expansion

Next, we discuss the gravity dual of the anisotropically expanding fluid in the late time approximation by using Eddington-Finkelstein (EF) coordinates. In analogy with the one-dimensional expansion of the fluid [6], we propose the following parametrization for the dual geometry in the late time regime corresponding to the three-dimensional expansion case with Kasner space-time as the local rest frame of the fluid [5]:

$$ds^2 = -r^2 P d\tau^2 + 2d\tau dr + r^2 \tau^{2a} e^{2Q-2R} \left(1 + \frac{1}{u\tau^{2/3}} \right)^2 dx_1^2 + r^2 \tau^{2b} e^R dx_2^2 + r^2 \tau^{2c} e^R dx_3^2 \tag{80.12}$$

where the variable u is defined as $u = r\tau^{1/3}$ and the late time approximation is taken in an expansion in $\tau^{-2/3}$ keeping u fixed. a, b, c are Kasner parameters and P, Q, R are functions of u and τ . The boundary conditions correspond to $P \rightarrow 1, Q \rightarrow 0$ and $R \rightarrow 0$ as $r \rightarrow \infty$ (where r is the fifth dimension). With these boundary conditions, the quantity inside the square bracket of the 5D bulk metric reduces to the boundary four-dimensional Kasner metric. The parameters P, Q, R are expanded in powers of $\tau^{-2/3}$ as [6]

$$\begin{aligned} P(\tau, u) &= P_0(u) + P_1(u)\tau^{-2/3} + P_2(u)\tau^{-4/3} + \dots \\ Q(\tau, u) &= Q_0(u) + Q_1(u)\tau^{-2/3} + Q_2(u)\tau^{-4/3} + \dots \\ R(\tau, u) &= R_0(u) + R_1(u)\tau^{-2/3} + R_2(u)\tau^{-4/3} + \dots \end{aligned} \tag{80.13}$$

where P_n, Q_n and R_n are obtained by solving the 5D bulk Einstein's equation with a negative cosmological constant, order by order in late time regime with the boundary conditions as mentioned above. The zeroth-order solution (with w as a constant) is given by [5],

$$ds^2 = -r^2 \left(1 - \frac{w^4}{u^4} \right) d\tau^2 + 2d\tau dr + r^2 \tau^{2a} \left(1 + \frac{1}{u\tau^{2/3}} \right)^2 dx_1^2 + r^2 \tau^{2b} dx_2^2 + r^2 \tau^{2c} dx_3^2 \tag{80.14}$$

The corresponding Kretschmann scalar in large τ limit is independent of Kasner parameters and is obtained as [5]

$$R_{KLMN}R^{KLMN} = 8 \left(5 + \frac{9w^8}{u^8} \right) + O(\tau^{-2/3}) \tag{80.15}$$

where the physical singularity is at $u = 0$.

80.4 Summary

We have studied the three-dimensional anisotropic expansion of a conformal fluid by using Kasner space-time using time-dependent AdS/CFT correspondence. We have considered relativistic viscous hydrodynamics to second order in gradient expansion and have obtained the expressions for energy density, temperature, entropy density per unity rapidity and the components of the energy momentum tensor in terms of Kasner parameters and the transport coefficients in the late time regime. We have made a proposal for the five-dimensional dual geometry in the large proper time approximation using Eddington-Finkelstein coordinates in the three-dimensional expansion case with the boundary metric as the 4D Kasner space-time. The zeroth-order metric is found to be an exact solution of the 5D Einstein's equation in the large proper time limit with constraints on the Kasner parameters [5]. We have also computed the corresponding Kretschmann scalar and have shown that the geometry is regular except for the physical singularity at $u = 0$.

References

1. J.M. Maldacena, Adv. Theor. Math. Phys. **2**, 231 (1998) (Int. J. Theor. Phys. **38**, 1113 (1999)) [[hep-th/9711200](#)]
2. S.J. Sin, S. Nakamura, S.P. Kim, JHEP **0612**, 075 (2006) [[hep-th/0610113](#)]
3. R. Baier, P. Romatschke, D.T. Son, A.O. Sterinets, M.A. Stephanov, JHEP **0804**, 100 (2008) [[arXiv:0712.2451](#)] [[hep-th](#)]
4. S. Bhattacharyya, V.E. Hubeny, S. Minwalla, M. Rangamani, JHEP **0802**, 045 (2008) [[arXiv:0712.2456](#)] [[hep-th](#)]
5. P.P. Pruseth, S. Mahapatra [[arXiv:2008.13699](#)] [[hep-th](#)]
6. S. Kinoshita, S. Mukohyama, S. Nakamura, K. Oda, Prog. Theor. Phys. **121**, 121 (2009) [[arXiv:0807.3797](#)] [[hep-th](#)]

Chapter 81

Search for the Chiral Magnetic Wave Using the ALICE Detector in Pb-Pb Collisions at $\sqrt{s_{NN}} = 5.02$ TeV



Prattay Das

Abstract In a non-central heavy-ion collision, a strong magnetic field is created which is theorised to give rise to collective excitation in the hot and dense medium (QGP). As a result of this non-trivial chiral currents, the elliptic flow of produced particles show charge dependence which is called the Chiral Magnetic Wave (CMW). Here, we present systematic studies of charge dependent Fourier coefficients (v_n) of azimuthal distribution of particles for Pb-Pb collisions at $\sqrt{s_{NN}} = 5.02$ TeV. These v_n measurements are performed for charged particles (pions) in the pseudorapidity (η) and transverse momentum (p_T) ranges $|\eta| < 0.8$ and $0.2 < p_T < 1.0$ (0.5) GeV/c. The third-order Fourier coefficient (v_3) shows a similar behaviour with a similar magnitude of the normalised slope as seen for v_2 . The similarity of normalised slopes for v_2 and v_3 in Pb-Pb collisions suggests that the effect of CMW, on the charge dependent splitting of v_2 at LHC energy, is consistent with zero.

81.1 Introduction

In heavy ion collision, a strong magnetic field is created [1] by the moving spectator protons. This magnetic field along with non zero electric and axial charge density leads to vector and axial currents called **Chiral Magnetic Effect (CME)** [2] and **Chiral Separation Effect (CSE)** [3], respectively. The combination of CME and CSE gives rise to a wave termed as **Chiral Magnetic Wave (CMW)** [4].

CMW is theorised [5] to separate the elliptic flow of positive and negative charge particles. The v_2 thus becomes charge dependent and it is given by [6]

Prattay Das—for the ALICE collaboration.

P. Das (✉)

School of Physical Sciences, National Institute of Science Education and Research, Jatni, India
e-mail: prattay.das@niser.ac.in

Homi Bhabha National Institute, Training School Complex, Anushaktinagar, Mumbai 400094, India

$$v_2^\pm = v_2 \mp r_e A_{ch}/2 \quad (81.1)$$

where v_2 on right-hand side of the equation is termed as baseline v_2 , which is expected from hydrodynamic flow alone [7]. r_e is used to parameterise the asymmetry in the distribution of positive and negative hadrons. It is also called as slope which is the CMW observable when v_2 is plotted as function of the net charge asymmetry in an event, A_{ch} given by

$$A_{ch} = \frac{N_+ - N_-}{N_+ + N_-} \quad (81.2)$$

N_+ and N_- are the number of positive and negative charged hadrons in an event, respectively.

The main background in CMW is Local Charge Conservation (LCC) [8] which can describe the charge dependent v_2 data qualitatively. LCC affects all order of Fourier coefficients and so to probe this kind of background, one can do a similar analysis with v_3 . Another prediction of LCC [7] is that slope obtained is proportional to baseline Fourier coefficient, therefore, this observation motivates the use of a **new observable called normalised slope** ($r_{\Delta v_n}^{norm} = r_{\Delta v_n} / \langle v_n \rangle$) as proposed by the CMS collaboration [9].

81.2 Data Set and Analysis Method

Analysis is done using 60 million events in Pb-Pb collisions at $\sqrt{s_{NN}} = 5.02$ TeV. Measurements of Fourier coefficients (v_2 and v_3) are performed for charged particles (pions) in the pseudorapidity (η) and transverse momentum (p_T) ranges $|\eta| < 0.8$ and $0.2 < p_T < 1.0$ (0.5) GeV/c, respectively. The event charge asymmetry (A_{ch}) is estimated with charged particles within $|\eta| < 0.8$ and $0.2 < p_T < 10.0$ GeV/c. The V0 detectors are used for triggering and centrality determination. Fourier coefficients are calculated in 10 uniform A_{ch} bins from -0.1 to 0.1 for all the centralities. v_2 and v_3 are calculated using the Q-cumulant method [10]. In this analysis, two subevents (A and B) have been taken with some pseudorapidity gap to reduce non flow background [11]. The two particle correlation for single event is given by $\langle 2' \rangle^A = \frac{p_n^A \cdot Q_n^{B*}}{m_p^A M_B}$ where p_n^A and Q_n^B are the flow vectors from subevents A and B. m_p^A and M_B are multiplicities of these two subevents. The two particle correlation for all event is given by $\langle\langle 2' \rangle\rangle^A = \frac{\sum_{i=1}^N (w_{(2')})_i \langle 2' \rangle_i}{\sum_{i=1}^N (w_{(2')})_i}$. Then v_n can be calculated by (81.3), where $d_n\{2\} = \langle\langle 2' \rangle\rangle^A$. The flow coefficient is calculated as

$$v_n'\{2\} = \frac{d_n\{2\}}{\sqrt{c_n\{2\}}} \quad (81.3)$$

$c_n\{2\}$ is called the reference flow.

81.3 Results

Left panel of Fig. 81.1 shows v_2 of charged hadrons in $0.2 < p_T < 1.0$ GeV/c and right panel shows the normalised difference of v_2 of charged hadrons both as function of corrected charge asymmetry, A_{ch} . We observe a finite value of $r_{\Delta v_2}^{norm}$.

Figure 81.2 shows $r_{\Delta v_2}^{norm}$ and $r_{\Delta v_3}^{norm}$ for both charged hadrons and pions as function of centrality. To quantify their values, we have fitted both $r_{\Delta v_2}^{norm}$ and $r_{\Delta v_3}^{norm}$ with pol0 function and we observe that $r_{\Delta v_2}^{norm}$ and $r_{\Delta v_3}^{norm}$ are consistent with each other within uncertainties.

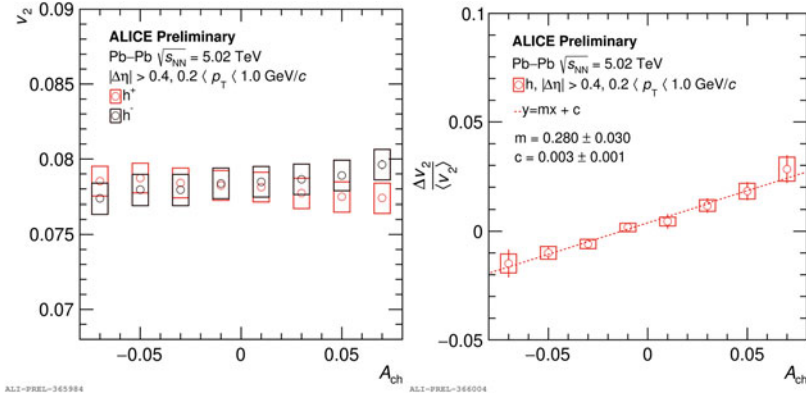


Fig. 81.1 Left panel shows v_2 of h^+ (red marker) and h^- (blue marker) and right panel shows normalised Δv_2 of hadrons as function of charge asymmetry in Pb-Pb 5.02 TeV in centrality 40–50%

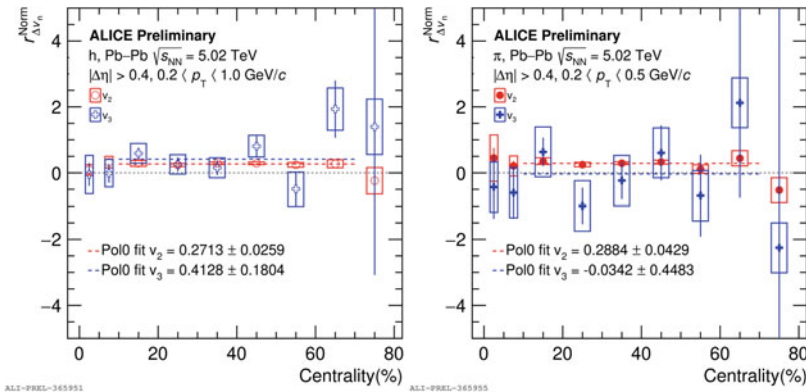


Fig. 81.2 Left panel shows the comparison of $r_{\Delta v_2}^{Norm}$ (red marker) and $r_{\Delta v_3}^{Norm}$ (black marker) for unidentified charged hadrons and right panel shows the same for pions as function of centrality

81.4 Summary

We calculated the normalised v_2 and v_3 slope for charged hadrons (pions) in the pseudorapidity (η) and transverse momentum (p_T) ranges $|\eta| < 0.8$ and $0.2 < p_T < 1.0$ (0.5) GeV/ c in Pb-Pb at $\sqrt{s_{NN}} = 5.02$ TeV. We observed that the normalised slopes of v_2 and v_3 are consistent with each other within large uncertainties, thus presenting a challenge to the presence of chiral magnetic wave phenomena at LHC energies.

References

1. K. Tuchin, Particle production in strong electromagnetic fields in relativistic heavy-ion collisions. *Adv. High Energy Phys.* **2013**, 490495 (2013)
2. D. Kharzeev, Parity violation in hot QCD: why it can happen, and how to look for it. *Phys. Lett. B* **633**(2–3), 260–264 (2006)
3. D.T. Son, A.R. Zhitnitsky, Quantum anomalies in dense matter. *Phys. Rev. D* **70**(7), 074018 (2004)
4. D.E. Kharzeev, H.-U. Yee, Chiral magnetic wave. *Phys. Rev. D* **83**(8), 085007 (2011)
5. Y. Burnier, D.E. Kharzeev, J. Liao, H.-U. Yee, Chiral magnetic wave at finite baryon density and the electric quadrupole moment of the quark-gluon plasma. *Phys. Rev. Lett.* **107**(5), 052303 (2011)
6. X.-L. Zhao, G.-L. Ma, Y.-G. Ma, Novel mechanism for electric quadrupole moment generation in relativistic heavy-ion collisions. *Phys. Lett. B* **792**, 413–418 (2019)
7. W. Li, G. Wang, Chiral magnetic effects in nuclear collisions (2020), [arXiv:2002.10397](https://arxiv.org/abs/2002.10397)
8. A. Bzdak, P. Bozek, *Phys. Lett. B* **726**(1–3), 239–243 (2013)
9. A.M. Sirunyan, et al., Probing the chiral magnetic wave in pPb and PbPb collisions at $\sqrt{s_{NN}} = 5.02$ TeV using charge-dependent azimuthal anisotropies. *Phys. Rev. C* **100**(6), 064908 (2019)
10. A. Bilandzic, R. Snellings, S. Voloshin, Flow analysis with cumulants: direct calculations. *Phys. Rev. C* **83**(4), 044913 (2011)
11. N. Borghini, P.M. Dinh, J.-Y. Ollitrault, Is the analysis of flow at the CERN super proton synchrotron reliable? *Phys. Rev. C* **62**(3), 034902 (2000)

Chapter 82

Causality and Stability in Relativistic Dissipative Non-resistive Magnetohydrodynamics



Rajesh Biswas, Ashutosh Dash, Najmul Haque, and Victor Roy

Abstract We studied the causality and stability of the relativistic dissipative non-resistive magnetohydrodynamics. We perturbed the system around a global equilibrium state and linearized the system of equations to obtain the dispersion relation. The asymptotic causality conditions were found to be independent of the magnitude of the magnetic field and the direction of propagation for all the propagating modes except the shear-Alfvén modes. For the finite number density, the causality criteria remains the same with the modified sound velocity.

82.1 Introduction

In relativistic heavy-ion collisions, an extremely strong transient magnetic field is produced mostly due to the fast-moving spectator protons in the colliding nucleus. The transient magnetic field is particularly large ($\sim 10^{18} - 10^{19}$ Gauss) in the initial stages of heavy-ion collisions [1]. The large magnetic fields give rise to interesting phenomena such as Chiral Magnetic Effect (CME), chiral separation effect (CSE), etc.

On the other hand, it is widely accepted that the Quark-Gluon-Plasma (QGP) produced in high energy heavy-ion collisions after a very short period of pre-equilibrium phase behave as an almost ideal fluid. Relativistic hydrodynamics is the successful theory in describing the space-time evolution of QGP, and due to the coupling with a strong magnetic field, one needs to use the relativistic magnetohydrodynamics (MHD) which is a self-consistent macroscopic framework. The relativistic Navier–Stokes equation shows an acausal and unstable nature [2] and these problems are resolved by Israel and Stewart with the second-order relaxation equations [3].

R. Biswas (✉) · A. Dash · N. Haque · V. Roy

School of Physical Sciences, National Institute of Science Education and Research, Jatni 752050, India

e-mail: rajeshphysics143@gmail.com

A. Dash · N. Haque · V. Roy

Homi Bhabha National Institute, Training School Complex, Anushaktinagar, Mumbai 400094, India

The IS second-order theory of causal dissipative fluid dynamics, although successful, known to allow acausal signal propagation under certain circumstances [4]. So it is very important to study the causality and stability of the relativistic MHD, and in [5], we address the causality bounds for the second-order dissipative non-resistive MHD.

82.2 Formalism

Let us consider a relativistic viscous fluid in the presence of a magnetic field. The total energy-momentum tensor of the fluid and field can be written as [5]

$$T^{\mu\nu} = (\varepsilon + P + \Pi + B^2) u^\mu u^\nu - \left(P + \Pi + \frac{B^2}{2} \right) g^{\mu\nu} - B^2 b^\mu b^\nu + \pi^{\mu\nu}, \quad (82.1)$$

where ε , P are fluid energy density, pressure, u^μ is the fluid four velocity and Π , $\pi^{\mu\nu}$ are bulk viscous pressure and shear viscous tensor, respectively. The unit four vector along the magnetic field given by $b^\mu = \frac{B^\mu}{B} = \frac{1}{2B} \epsilon^{\mu\nu\alpha\beta} u_\nu F_{\alpha\beta}$, where $F^{\mu\nu} = (\partial^\mu A^\nu - \partial^\nu A^\mu)$ is the field strength tensor.

The conservation of energy-momentum and the Maxwell's equations given by

$$\partial_\mu T^{\mu\nu} = 0, \quad (82.2)$$

$$\epsilon^{\mu\nu\alpha\beta} \partial_\beta F_{\nu\alpha} = 0. \quad (82.3)$$

In this work, we consider the causal relativistic second-order IS theory and the relaxation equations for the viscous stress [4]

$$\Pi = \Pi_{\text{NS}} - \tau_\Pi \dot{\Pi}, \quad (82.4)$$

$$\pi^{\mu\nu} = \pi_{\text{NS}}^{\mu\nu} - \tau_\pi \dot{\pi}^{<\mu\nu>}. \quad (82.5)$$

Note that for simplicity, here we neglect other possible second-order terms.

To study the stability and causality of the relativistic viscous magnetohydrodynamics, we perturbed the system around the equilibrium. We consider a perturbation around the static quantities X_0

$$X = X_0 + \delta\tilde{X}, \quad \delta\tilde{X} = \delta X e^{i(\omega t - \mathbf{k}\cdot\mathbf{r})}. \quad (82.6)$$

In the linear regime, one need to linearize the system of equations which can be written in a matrix form

$$A\delta\tilde{X} = 0, \quad (82.7)$$

where $\delta\tilde{X}$ is a column vector made by the independent variables and A is a square matrix made by the coefficient of these variables. The nontrivial solutions of equation (82.7) exist if the $\det(A) = 0$, which leads to the dispersion relation $\omega(k)$. After

obtaining the dispersion relation, it is straightforward to find out whether the modes are causal and stable or not. The condition for the stability of the modes is given by

$$\Im(\omega) > 0. \quad (82.8)$$

For the causality of the modes, we have to ensure the asymptotic causality condition [4]

$$v_L \equiv \lim_{k \rightarrow \infty} \left| \frac{\partial \Re(\omega)}{\partial k} \right| \leq 1, \quad (82.9)$$

here v_L is the asymptotic group velocity of the modes.

82.3 Results and Conclusions

In the ideal MHD limit, we get total six modes: two Alfvén modes and four magneto-sonic modes. The Alfvén wave and the magneto-sonic wave propagates with velocity v_A and v_M , respectively. Note that, “fast” and “slow” magneto-sonic modes are present and for the propagation perpendicular to the magnetic field, the slow magneto-sonic modes becomes zero and the fast magneto-sonic moves with velocity $v_f^2 = v_A^2 + \alpha(1 - v_A^2)$. All six modes shows the stable and causal propagation.

For the MHD with bulk viscosity, we get a total of seven modes: two are the same as Alfvén modes and five corresponds to the different magneto-sonic modes. Here the Alfvén modes are stable and causal but the magneto-sonic modes have some bound on causality.

For MHD with shear viscosity, we get a total of eleven modes: two non-propagating and stable modes with frequency i/τ_π , three are the shear-Alfvén type modes and six are magneto-sonic type modes. Here we find that the asymptotic causality conditions do not depend on the magnitude of the magnetic field and the direction of propagation, but for the shear-Alfvén modes, the causality conditions depend on both the parameters. The asymptotic causality condition for the shear-Alfvén modes is given as [5]

$$\frac{B_0^2 \cos^2 \theta}{(\varepsilon_0 + P_0 + B_0^2)} + \frac{\eta}{\tau_\pi (\varepsilon_0 + P_0 + B_0^2)} \leq 1. \quad (82.10)$$

In Fig. 82.1, θ represents the angle between the wave vector and the magnetic field and y -axis represents $b = \frac{(\varepsilon+P)\tau_\pi}{\eta}$. The red contour is the critical line of causality, denoting $v_L^2 = 1$. The region above the red line is causal, and below the red line corresponds to the acausal. The magnitude of the magnetic field has been fixed to $qB = 10m_\pi^2$ and the other parameters used are $c_s = 1/\sqrt{3}$, $T = 200$ MeV.

For a fluid with non-zero bulk and shear viscosity in a magnetic field, there has a total of twelve modes. The asymptotic group velocity for the Alfvén modes are found

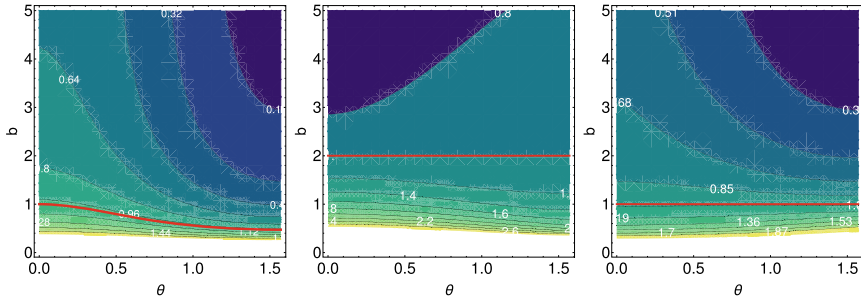


Fig. 82.1 (Color online) Contour plot showing various causal regions, obtained from MHD with shear viscosity case, for Alfven mode (left) and the set of fast (middle) and slow modes (right)

to be the same as shear-Alfvén modes. For slow magneto-sonic modes, causality bound remains independent of the bulk viscous coefficient but it depends on the shear viscosity. On the other hand, for the fast magneto-sonic modes, the causality condition depends on both the bulk and shear viscosity and they are inversely proportional to each other.

82.3.1 Finite Number Density

For finite number density, we define number four-current

$$N^\mu = nu^\mu, \tag{82.11}$$

where n is the number density. The corresponding conservation equation is written as

$$\partial_\mu N^\mu = 0. \tag{82.12}$$

Like in the previous case perturbed the number density around equilibrium and linearized the (82.12). For the fluid with bulk viscosity only, we write the linearized equations (82.2)–(82.4) and (82.12) in a matrix form like (82.7). The determinant of matrix A gives the same dispersion relation except for the change in the sound velocity. Previously, the square of the sound velocity was $c_s^2 = \alpha$, now it changes by

$$c_s^2 = \left(\frac{\partial P}{\partial \varepsilon} \right)_n + \frac{n}{\varepsilon + P} \left(\frac{\partial P}{\partial n} \right)_\varepsilon. \tag{82.13}$$

So, we can conclude that inclusion of the number current, the causality criteria remain the same; it only needs to replace the square of the sound velocity α by the c_s^2 written in (82.13).

Acknowledgements RB and VR acknowledge financial support from the DST Inspire faculty research grant (IFA-16-PH-167), India.

References

1. A. Bzdak, V. Skokov, Phys. Lett. B **710**, 171–174 (2012), [arXiv:1111.1949](#) [hep-ph]
2. W.A. Hiscock, L. Lindblom, Phys. Rev. D **31**, 725–733 (1985)
3. W. Israel, J.M. Stewart, Annals Phys. **118**, 341–372 (1979)
4. S. Pu, T. Koide, D.H. Rischke, Phys. Rev. D **81**, 114039 (2010), [arXiv:0907.3906](#) [hep-ph]
5. R. Biswas, A. Dash, N. Haque, S. Pu, V. Roy, JHEP **10**, 171 (2020), [arXiv:2007.05431](#) [nucl-th]

Chapter 83

In Medium Properties of Axion Within a Polyakov Loop Enhanced Nambu-Jona-Lasinio Model



Ranjita K. Mohapatra, Aman Abhishek, Arpan Das, and Hiranmaya Mishra

Abstract In this proceeding, We estimate different properties of axion like its mass, topological susceptibility and the self-coupling within the framework of Polyakov loop enhanced Nambu-Jona-Lasinio (PNJL) model at finite temperature and quark chemical potential. The Polyakov loop in PNJL model plays an important role near the critical temperature.

83.1 Introduction

The axion was originally predicted to solve the strong CP (charge conjugation and parity) problem in a dynamical way [1–3]. To estimate the response of the axion to a QCD thermal medium one can use QCD inspired effective field theories and phenomenological models, e.g. the chiral perturbation theory and Nambu-Jona-Lasinio (NJL) model [4, 5] etc. One can't use perturbative results around the QCD transition region since QCD is nonperturbative in this region. Because of the limitation of χ PT and perturbative techniques one can use QCD inspired chiral effective models, e.g. Nambu-Jona-Lasinio (NJL) model to investigate the thermal properties of the axion. Since both chiral and deconfinement aspects of QCD are captured within a single framework [6, 7] in the PNJL model, we study different axion properties in PNJL model.

R. K. Mohapatra (✉) · A. Abhishek · H. Mishra
Theory Division, Physical Research Laboratory, Navrangpura, Ahmedabad 380009, India
e-mail: ranjita.iop@gmail.com

R. K. Mohapatra
Department of Physics, Banki Autonomous College, Cuttack 754008, India

A. Das
Institute of Nuclear Physics Polish Academy of Sciences, PL-31-342, Krakow, Poland

© The Author(s), under exclusive license to Springer Nature Singapore Pte Ltd. 2022
B. Mohanty et al. (eds.), *Proceedings of the XXIV DAE-BRNS High Energy Physics Symposium, Jatni, India*, Springer Proceedings in Physics 277,
https://doi.org/10.1007/978-981-19-2354-8_83

83.2 Formalism: Axion Within PNJL Model

In the mean-field approximation the thermodynamic potential (Ω) of the PNJL model at finite temperature (T) and quark chemical potential (μ) can be expressed as [8],

$$\begin{aligned} \Omega(\sigma, \eta, \Phi, \bar{\Phi}, a, T, \mu) = & \Omega_q(\sigma, \eta, a, \Phi, \bar{\Phi}, T, \mu) - g_2(\eta^2 - \sigma^2) \cos\left(\frac{a}{f_a}\right) \\ & + g_1(\eta^2 + \sigma^2) - 2g_2 \sigma \eta \sin\left(\frac{a}{f_a}\right) + \mathcal{U}(\Phi, \bar{\Phi}, T), \end{aligned} \quad (83.1)$$

Here a represents the background axion field and f_a is axion decay constant. In the PNJL model the fermionic contribution to the thermodynamic potential in the grand canonical ensemble is,

$$\begin{aligned} \Omega_q = & -4N_c \int \frac{d^3 p}{(2\pi)^3} E_p - 4T \int \frac{d^3 p}{(2\pi)^3} \left(\log \left[1 + 3\Phi \exp[-\beta(E_p - \mu)] + \right. \right. \\ & \left. \left. 3\bar{\Phi} \exp[-2\beta(E_p - \mu)] + \exp[-3\beta(E_p - \mu)] \right] \right) \\ & + \log \left[1 + 3\bar{\Phi} \exp[-\beta(E_p + \mu)] + 3\Phi \exp[-2\beta(E_p + \mu)] + \exp[-3\beta(E_p + \mu)] \right], \end{aligned} \quad (83.2)$$

The physical values of the condensates σ_0 , η_0 , Φ_0 and $\bar{\Phi}_0$ can be obtained by solving the gap equations,

$$\frac{\partial \Omega}{\partial \sigma} = 0; \quad \frac{\partial \Omega}{\partial \eta} = 0; \quad \frac{\partial \Omega}{\partial \Phi} = 0; \quad \frac{\partial \Omega}{\partial \bar{\Phi}} = 0. \quad (83.3)$$

Note that the physical values of the condensates, σ_0 , η_0 , Φ_0 and $\bar{\Phi}_0$ are functions of a , T and μ . The effective thermodynamic potential for the QCD axion within the framework of PNJL model in a hot and dense medium is then given by,

$$\tilde{\Omega}(a, T, \mu) = \Omega \left[\sigma_0(a, T, \mu), \eta_0(a, T, \mu), \Phi_0(a, T, \mu), \bar{\Phi}_0(a, T, \mu), a, T, \mu \right]. \quad (83.4)$$

Using the axion potential one can obtain the axion mass and the axion self coupling can be obtained as,

$$m_a^2 = \frac{d^2 \tilde{\Omega}}{da^2} \Big|_{a=0} = \frac{\chi}{f_a^2}; \quad \lambda_a = \frac{d^4 \tilde{\Omega}}{da^4} \Big|_{a=0}. \quad (83.5)$$

Here χ is the topological susceptibility. Note that all the physical condensates σ_0 , η_0 , Φ_0 and $\bar{\Phi}_0$ have implicit dependence on the axion field.

83.3 Results and Discussion

In Fig. 83.1, the periodic behavior of the scalar condensate with respect to a/f_a is due to $\cos(a/f_a)$ and $\sin(a/f_a)$ terms present in the thermodynamic potential. σ reaches its maximum value for $a/f_a = (2i + 1)\pi$, for $i=0, 1, 2 \dots$ etc. and attains minimum for $a/f_a = 2i\pi$ at all temperatures. At $T = 0$, η is discontinuous for $a/f_a = (2i + 1)\pi$, for $i=0, 1, 2 \dots$ etc. But η vanishes for $a/f_a = 2i\pi$. At $T = 0$ and $a/f_a = (2i + 1)\pi$ due to spontaneous CP symmetry violation there exists two degenerate vacua which is in agreement with the Dashen-ÄZs phenomena. Note that the magnitude of Φ does not change significantly with a/f_a . This is due to the fact that Φ does not depend upon a/f_a directly, also the Polyakov loop potential is independent of a/f_a .

In the low-temperature range $T \lesssim 100$ MeV there is not much difference between the axion mass for NJL model, PNJL model (Fig. 83.2 left plot). In fact, at zero temperature the axion mass as obtained in the PNJL model is $m_a f_a = 0.00638$ GeV².

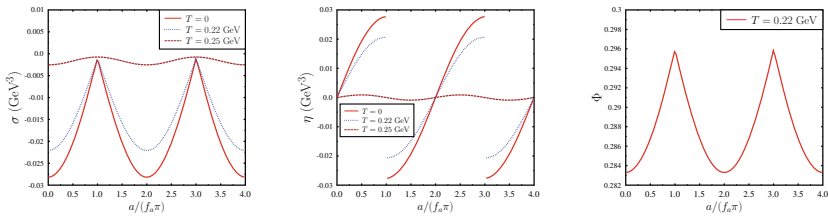


Fig. 83.1 Variation of scalar condensate σ , η and Φ with a/f_a in the PNJL model

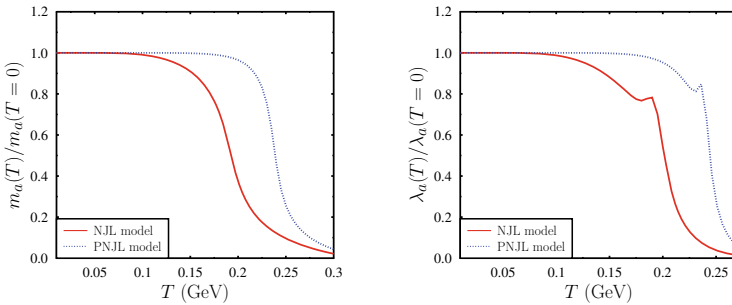


Fig. 83.2 Left plot: Variation of the normalized axion mass $m_a(T)/m_a(T = 0)$ with temperature for PNJL model. $m_a(T = 0)$ is the axion mass in vacuum. Right plot: Variation of the normalized axion self coupling $\lambda_a(T)/\lambda_a(T = 0)$ with temperature for PNJL model. $\lambda_a(T = 0)$ is the axion self coupling in vacuum

Only in the high-temperature range ($T > 100$ MeV) there is a significant difference between the results between NJL and PNJL model. This is because in the high-temperature range the Polyakov loop plays an important role in the PNJL model, where the scalar and the pseudoscalar condensate are affected by the Φ . From this figure, it is clear that the axion mass is sensitive to the chiral transition temperature. In the PNJL model the Polyakov loop affects the chiral transition temperature. In fact chiral transition temperature increases in the PNJL model compared to the NJL model. This increase in the chiral transition temperature is also manifested in the variation of the axion mass with temperature.

Variation of the normalized axion self coupling $\lambda_a(T)/\lambda_a(T = 0)$ with temperature is shown in Fig. 83.2 (right plot). For comparison, we have also given the results for $\lambda_a(T)/\lambda_a(T = 0)$ estimated in the NJL model. At zero temperature the value of the axion self-coupling as estimated in the PNJL model is, $\lambda_a f_a^4 = -(55.64)^4 \text{ MeV}^4$. But for the high-temperature range, the PNJL model results are significantly different from that of NJL model results. As mentioned earlier this is due to the fact that in the PNJL model the Polyakov loop Φ only becomes effective in the high-temperature range $T > 100$ MeV.

83.4 Conclusion

In this article, we have studied the effects of hot and dense QCD medium on the axion properties e.g. its mass and self coupling in PNJL model. The Polyakov loop which takes a nonvanishing value at finite temperature and quark chemical potential plays an important role near the critical temperature in PNJL model. Therefore there is a significant difference in axion properties calculated in NJL and PNJL model. We find that axion properties are correlated with the chiral transition or confinement-deconfinement transition.

Acknowledgements The work of A.D. is supported by the Polish National Science Center Grants No. 2018/30/E/ST2/00432.

References

1. R.D. Peccei, H.R. Quinn, Phys. Rev. Lett. **38**, 1440–1443 (1977)
2. R.D. Peccei, H.R. Quinn, Phys. Rev. D **16**, 1791–1797 (1977)
3. S. Weinberg, Phys. Rev. Lett. **40**, 223–226 (1978)
4. M. Buballa, Phys. Rep. **407**, 205–376 (2005)
5. S.P. Klevansky, Rev. Mod. Phys. **64**, 649 (1992)
6. C. Ratti, S. Roessner, M.A. Thaler, W. Weise, Eur. Phys. J. C **49**, 213–217 (2007)
7. C. Ratti, S. Roessner, W. Weise, Phys. Lett. B **649**, 57–60 (2007)
8. Y. Sakai, H. Kouno, T. Sasaki, M. Yahiro, Phys. Lett. B **705**, 349 (2011)

Chapter 84

Deciphering Quark and Gluon Jet Modifications in Heavy-Ion Collisions with γ -Tagged Jets



Rathijit Biswas, Subikash Choudhury, Sidharth K. Prasad, and Supriya Das

Abstract Heavy-ion collisions at relativistic energies produce a dense deconfined partonic medium known as the Quark-Gluon-Plasma (QGP). A prominent way to characterise QGP is by studying the energy loss of the high momentum particles or jets, a phenomenon referred to as the jet quenching. The mechanisms by which a jet loses its energy while passing through the QGP is perceived to depend on the jet-initiating parton's flavour, and to study the process in detail, one needs to discriminate pure sample of quark and gluon-initiated jets. There have been efforts in this regard and one of the techniques uses jets which are recoiled against prompt photons, known as the γ -tagged jets. In this work, we have used a dynamical jet quenching model, Jet Evolution With Energy Loss (JEWEL) and sample γ +jet events for pp and 0–10% central Pb+Pb collision at 5.02 TeV. We have calculated radial momentum distributions of γ -tagged jets in those samples and compared them with the results from inclusive jets to elucidate the flavour dependence of jet energy loss.

84.1 Introduction

The formation of Quark-Gluon Plasma (QGP) in high energy heavy-ion collisions is often characterised by the energy loss of high- p_T partons or jets that eventually lead to modifications of inclusive jet-yields and intra-jet properties (also known as jet quenching) compared to that in elementary proton-proton (pp) interactions [1]. An important ingredient in the QCD energy loss mechanism is the initial flavour of

R. Biswas (✉)

Institute of Modern Physics, Chinese Academy of Sciences, Lanzhou 730000, China
e-mail: rathijit.academics@gmail.com

R. Biswas · S. K. Prasad · S. Das

Department of Physics, Centre for Astroparticle Physics and Space Science, Bose Institute, Kolkata 700091, India

S. Choudhury

Key Laboratory of Nuclear Physics and Ion-Beam Application (MOE), Institute of Modern Physics, Fudan University, Shanghai 200433, China

the jet-initiating parton. It is argued that quark and gluon-initiated jets are modified differently in the QGP and gluon-initiated jets are expected to be more quenched or modified than that of the jets initiated by quarks. However, till date, such claims could not be verified experimentally mainly because accessing direct information on the flavour of the jet-initiating parton has remained elusive. In this regard, jets recoiled against a high- p_T photon also known as photon-tagged jets provide a mean to achieve a statistically enriched sample of quark-initiated jets. The exact fraction may, however, depend on the kinematics of both jets and photons [2, 3].

84.1.1 Model Setup and Analysis Technique

In this proceeding, we investigate, whether medium modifications of jets depend on the initial flavour of the jet-initiating parton. For this purpose, we use a QCD-inspired Monte Carlo event generator, JEWEL [4] that simulates jet evolution in heavy-ion collisions based on perturbative approach of in-medium scatterings of high- p_T partons resulting in elastic and inelastic energy losses. We generate JEWEL events in its “recoil-on” mode and set default JEWEL parameters ($\tau_i = 0.4$ and $T_i = 590$ MeV) as an input for modelling the underlying background. About a million γ +jet events each are generated for pp and 0–10% centrality class of Pb+Pb collisions at 5.02 TeV. We also generate control samples of γ + quark-jet and γ + gluon-jet as the flavour of jet-initiating parton in these samples are known exactly.

Jets are reconstructed from all final state particles using anti- k_T [5] algorithm for radius $R = 0.3$ and required to have $p_{T,\text{jet}} > 40$ GeV/c and $|\eta_{\text{jet}}| < 1.6$ and, background subtraction is done using a JEWEL-compatible *4MomSub* technique [6]. For isolated photon selection, a generator level photon is considered as a potential isolated photon candidate if the sum of transverse momentum of all the final state particles around the direction of the photon in a cone $\Delta R = \sqrt{\Delta\eta^2 + \Delta\phi^2} = 0.4$ is less than 7–8% of the original photon energy. If another generator level photon is found within the same cone, we reject both of them because such a photon-pair may have originated from a decay of a neutral meson. Isolated photon candidates are also required to satisfy kinematic selection of $p_{T,\gamma} > 60$ GeV/c and $|\eta_\gamma| < 1.44$. To form a photon-tagged jet, isolated photon candidates and jets that have satisfied all selection criteria mentioned above are paired with an addition constraint of $\Delta\phi_{\gamma,\text{jet}} = |\phi^{\text{jet}} - \phi^\gamma| > 7\pi/8$ [7].

84.1.2 Observable Definition and Result

In this section, we present results on the modification of a jet shape observable, namely the radial momentum distribution ($\rho(r)$) for γ -tagged jets in 0–10% central Pb+Pb collision at 5.02 TeV relative to pp interactions in same collision energy. The $\rho(r)$ observable as defined in (84.1) essentially measures the momentum distribution

transverse to the jet-axis.

$$\rho(r) = \frac{1}{\delta r} \frac{\sum_{jets} \sum_{tracks \in [r_a, r_b]} (p_t^{trk})}{\sum_{jets} \sum_{tracks \in [0, r_f]} (p_t^{trk})} \quad (84.1)$$

Here r_a, r_b is the inner and outer radii of an annular disc around the jet-axis and r_f is the full jet radius (R) [8].

Since gluons interact more frequently with the medium because of its higher colour charge than quarks, a naive expectation would be that gluon-initiated jets are wider and more quenched (softer) than that of the jets initiated by quarks which are presumably harder and collimated. From Fig. 84.1, we observe a significant broadening of jets in central Pb+Pb collisions relative to pp interactions. Interestingly, the modifications of γ +jet exactly follow the same trend as that of the γ +q-jet which implies that γ -tagged jets may serve as a good proxy for jets initiated by quarks. However, in contrary to the naive expectation, modifications of γ +g-jets do not exhibit any

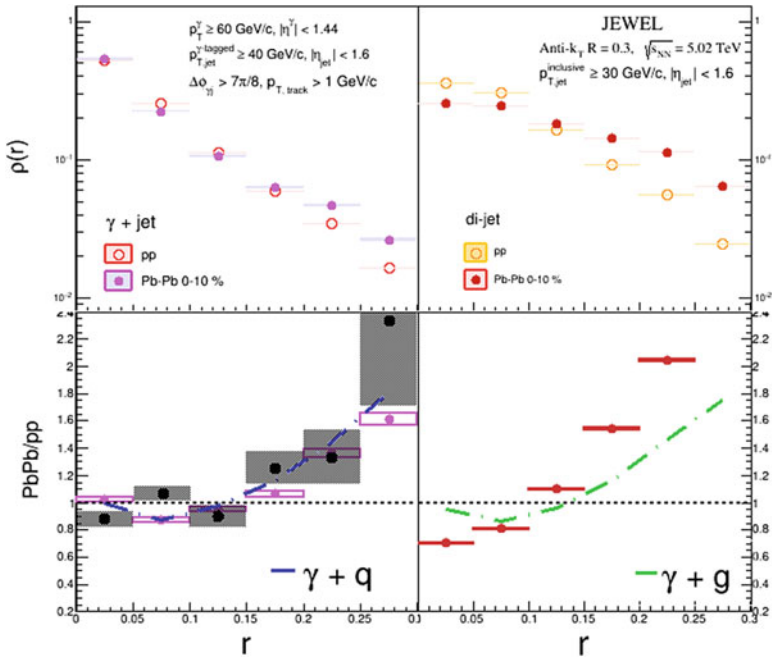


Fig. 84.1 $\rho(r)$ measured for both Pb+Pb and pp collisions in γ -tagged jets (top left) and in di-jets (top right). Ratio of $\rho(r)$ measured in PbPb to that in pp compared to CMS measurement [8] (black solid points with boxes) and compared with measurement in $\gamma+q$ jet sample (bottom left). Ratio of $\rho(r)$ measured in Pb+Pb to that in pp checked with measurement in $\gamma+g$ jet sample (bottom right)

characteristic difference. Further studies are under way to understand this unexpected behaviour of γ +g-jet.

84.1.3 Summary

In summary, we have studied and presented results on the modifications of γ -tagged jets based on QCD-inspired model of jet energy loss, JEWEL that has demonstrated reasonable success in describing modifications of inclusive jets and momentum asymmetry of jets recoiled against isolated-photons. We observe that JEWEL can reasonably reproduce the jet shape modification of γ +jet in data and the characteristic modification of γ -tagged jet matches well with γ +q-jet.

Acknowledgements We acknowledge the computing server facility at CAPSS, Bose Institute which helped us in event generation for this study.

References

1. J.D. Bjorken, Energy Loss of Energetic Partons in Quark-Gluon Plasma: Possible Extinction of High p_T Jets in Hadron-Hadron Collisions, FERMILAB-PUB-82-059-THY (1982)
2. ATLAS Collaboration, Comparison of fragmentation functions for light-quark- and gluon-dominated jets from pp and Pb+Pb collisions in ATLAS. Phys. Rev. Lett. **123**, 042001 (2019)
3. CMS Collaboration, Observation of medium induced modifications of jet fragmentation in PbPb collisions at $\sqrt{s_{NN}} = 5.02$ TeV using isolated-photon-tagged jets. Phys. Rev. Lett. **121**, 242301 (2018)
4. K. Zapp, JEWEL 2.0.0: directions for use. Eur. Phys. J. C **74**, 2762 (2014)
5. M. Cacciari, G.P. Salam, G. Soyez, The anti- K_T jet clustering algorithm. JHEP **0804**, 063 (2008)
6. R.K. Elayavalli, K. Zapp, Medium response in JEWEL and its impact on jetshape observables in heavy ion collisions. JHEP **1707**, 141 (2017)
7. CMS Collaboration, Study of jet quenching with isolated-photon+jet correlations in PbPb and pp collisions at $\sqrt{s_{NN}} = 5.02$ TeV. Phys. Lett. B **785**, 14 (2018)
8. CMS Collaboration: Jet shapes of isolated photon-tagged jets in PbPb and pp collisions at $\sqrt{s_{NN}} = 5.02$ TeV. Phys. Rev. Lett. **122**, 152001 (2019)

Chapter 85

Constraining the Chiral Magnetic Effect with Charge-Dependent Azimuthal Correlations in ALICE



Md. Rihan Haque

Abstract Charge-dependent correlations measured in Pb–Pb collisions at $\sqrt{s_{\text{NN}}} = 2.76$ and 5.02 TeV recorded by ALICE are presented in this article. These correlations are used to probe parity violating processes, namely the Chiral Magnetic Effect (CME), in heavy-ion collisions. The CME-sensitive correlator $\gamma_{1,1} = \langle \cos(\varphi_\alpha + \varphi_\beta - 2\Psi_2) \rangle$ along with the correlator $\gamma_{1,2} = \langle \cos(\varphi_\alpha + 2\varphi_\beta - 3\Psi_3) \rangle$, which is sensitive to background only, are used to estimate the CME fraction (f_{CME}). A blast-wave model coupled to effects from local charge conservation is also used to predict the background for the CME-sensitive $\gamma_{1,1}$ correlator.

85.1 Introduction

The strong magnetic field \mathbf{B} ($\sim 10^{18}$ Gauss) generated by the motion of charged nucleons in heavy-ion collisions can interact with the spins of (anti-)quarks in the quark–gluon plasma (QGP) created in such collisions [1]. This creates a vector current in the medium, resulting in the modulation of the charge distribution in the azimuthal direction, which is called the Chiral Magnetic Effect (CME) [2]. The two-particle correlator $\delta_n = \langle \cos(n\varphi_\alpha - n\varphi_\beta) \rangle$ and the generalized three-particle correlator, namely $\gamma_{m,n} = \langle \cos(m\varphi_\alpha + n\varphi_\beta - (m+n)\Psi_{m+n}) \rangle$, are used to probe CME phenomena in Pb–Pb collisions in ALICE. The correlator $\gamma_{1,2} = \langle \cos(\varphi_\alpha + 2\varphi_\beta - 3\Psi_3) \rangle$ is not sensitive to the CME but includes all backgrounds which are also present in the CME-sensitive $\gamma_{1,1} = \langle \cos(\varphi_\alpha + \varphi_\beta - 2\Psi_2) \rangle$ [3]. The CME contribution in $\gamma_{1,1}$ is estimated using the background-sensitive $\gamma_{1,2}$ correlator [4]. The detailed procedure is discussed in the results section.

Md. Rihan Haque—for the ALICE collaboration.

Md. R. Haque (✉)
Warsaw University of Technology, Warszawa, Poland
e-mail: rihan.haque@pw.edu.pl

85.2 Experiment

The central barrel of the ALICE apparatus consists of a set of detectors located within a longitudinal magnetic field of 0.5 T. The Inner Tracking System (ITS) [5] and the Time Projection Chamber (TPC) [6] are used to reconstruct the charged particles employed in this analysis. The combined pseudorapidity (η) coverage of the ITS and the TPC is $-0.9 < \eta < 0.9$. A set of forward detectors, namely the VOA and V0C [7], were used for triggering, event selection, and determination of the collision centrality. The VOA and the V0C are located on either side of the interaction point and cover the pseudorapidity ranges $2.8 < \eta < 5.1$ and $-3.7 < \eta < -1.7$, respectively. A detailed description of ALICE and its sub-detectors can be found in [5] and their performance in [8].

85.3 Results and Discussion

The left panel of Fig. 85.1 shows the centrality dependence of $\gamma_{1,1}$, $\gamma_{1,-3}$, $\gamma_{1,2}$, and $\gamma_{2,2}$ for different charge combinations, i.e., Opposite-Sign (OS) and Same-Sign (SS) pairs for Pb–Pb collisions at $\sqrt{s_{NN}} = 5.02$ TeV. The right panel of Fig. 85.1 presents the centrality dependence of the charge-dependent differences, i.e., OS–SS. The CME-sensitive correlators $\gamma_{1,1}$ and $\gamma_{1,-3}$ show significant charge-dependent difference that increases from central to peripheral collisions. The $\gamma_{1,2}$ correlator also exhibits a significant charge dependence which increases for more peripheral collisions. However, $\gamma_{1,2}$ probes solely the background scaled by the third order flow harmonic (v_3) [4]. No significant charge dependence is observed for $\gamma_{2,2}$.

A blast-wave (BW) model initialized with parameters obtained by fitting the p_T spectra and v_2 of identified particle in Pb–Pb collisions at $\sqrt{s_{NN}} = 5.02$ TeV is extended to incorporate local charge conservation (LCC) effects [4]. The model is then tuned to reproduce charge-dependent difference of the two-particle correlator, namely $\Delta\delta_1$, as shown in the left panel of Fig. 85.2. The model then predicts the value for $\Delta\gamma_{1,1}$ as shown in the right panel of Fig. 85.2. The BW-LCC model underestimates the measured data points by as much as $\approx 39\%$.

In order to evaluate the CME background, we have used $\gamma_{1,2}$, i.e., correlations relative to the third order symmetry plane (Ψ_3). Since the charge-separation effects resulting from the CME are generated mainly relative to Ψ_2 , $\gamma_{1,2}$ is expected to have negligible contribution from them. Therefore, the charge-dependent part (OS–SS) of $\gamma_{1,2}$ could thus be used as a proxy for the background that consists of local charge conservation modulated by the corresponding flow harmonics, i.e., v_3 . We can approximate the $\gamma_{1,1}$ and $\gamma_{1,2}$ according to [9] as $\gamma_{1,1} \approx \langle \cos[(\varphi_\alpha - \varphi_\beta) + 2(\varphi_\beta - \Psi_2)] \rangle \propto \delta_1 v_2$, and $\gamma_{1,2} \approx \langle \cos[(\varphi_\alpha - \varphi_\beta) + 3(\varphi_\beta - \Psi_3)] \rangle \propto \delta_1 v_3$.

Hence, we can approximate the charge-dependent difference as $\Delta\gamma_{1,1} \approx \kappa_2 v_2 \Delta\delta_1$ and $\Delta\gamma_{1,2} \approx \kappa_3 v_3 \Delta\delta_1$, respectively. Here κ_1 and κ_2 are proportionality constants.

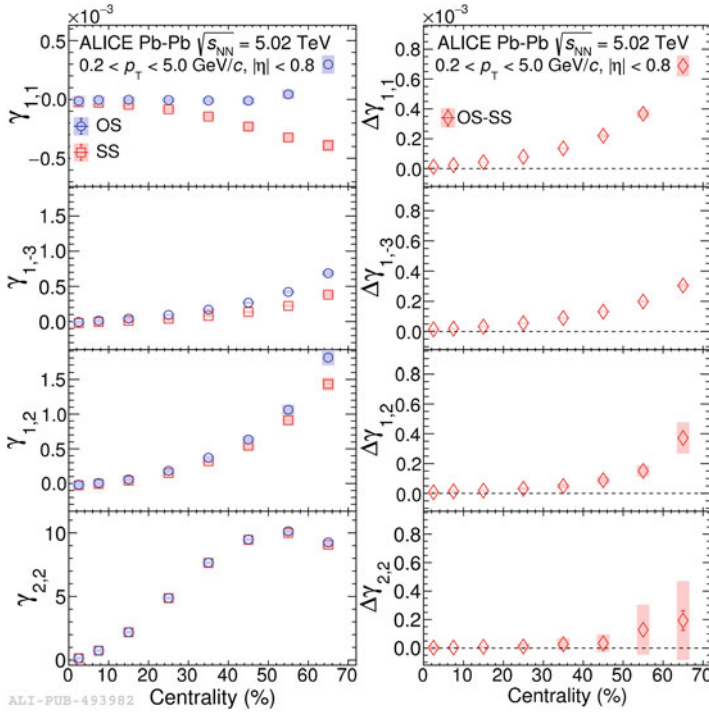


Fig. 85.1 (Left column): The centrality dependence of $\gamma_{1,1}$, $\gamma_{1,-3}$, $\gamma_{1,2}$, and $\gamma_{2,2}$ for pairs of particles of opposite (OS) and same (SS) sign measured in Pb–Pb collisions at $\sqrt{s_{NN}} = 5.02$ TeV [4]. (Right column): The charge-dependent differences $\Delta\gamma_{1,1}$, $\Delta\gamma_{1,-3}$, $\Delta\gamma_{1,2}$, and $\Delta\gamma_{2,2}$ as a function of collision centrality [4]. The statistical and systematic uncertainties are represented by vertical lines and shaded boxes, respectively

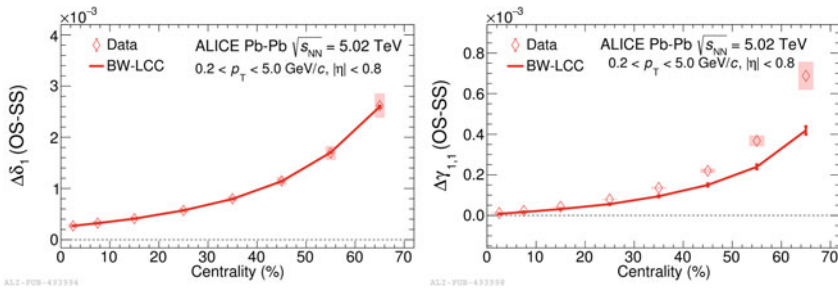


Fig. 85.2 The centrality dependence of $\Delta\delta_1$ (left) and $\Delta\gamma_{1,1}$ (right) measured in Pb–Pb collisions at $\sqrt{s_{NN}} = 5.02$ TeV [4]. The red curves (labeled BW-LCC) present the expectations from the BW-LCC model (see text for details)

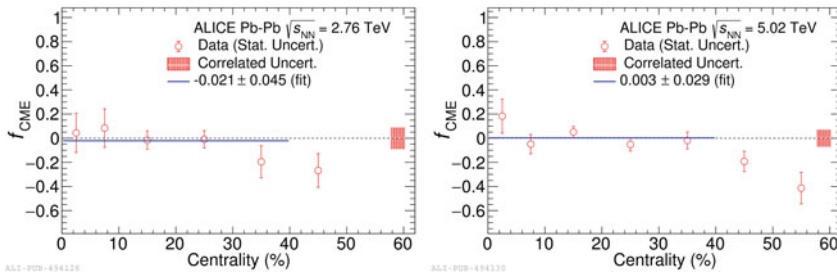


Fig. 85.3 The CME fraction extracted in Pb–Pb collisions at $\sqrt{s_{NN}} = 2.76$ TeV (left) and $\sqrt{s_{NN}} = 5.02$ TeV (right) [4]. The systematic uncertainty is shown as hatched band at zero around the centrality value of 60%. The solid blue lines correspond to fit with a constant function to the data points. See text for details

Then, the background in $\Delta\gamma_{1,1}$ can be expressed as $\Delta\gamma_{1,1}^{\text{Bkg}} \approx \Delta\gamma_{1,2} \times (\kappa_2 v_2) / (\kappa_3 v_3)$. The values of κ_1 and κ_2 depend on kinematic ranges (e.g. detector acceptance, event, and particle selection criteria). The relationship between κ_2 and κ_3 has been studied using Monte Carlo-based models [4] which show $\kappa_2/\kappa_3 \approx 1$. The CME fraction is then defined as $f_{\text{CME}} = 1 - \Delta\gamma_{1,1}^{\text{Bkg}}/\Delta\gamma_{1,1}$. Figure 85.3 presents the centrality dependence of the CME fraction at $\sqrt{s_{NN}} = 2.76$ TeV (left plot) and $\sqrt{s_{NN}} = 5.02$ TeV (right plot). It is seen that for both energies, f_{CME} is compatible with zero up to centrality $\approx 40\%$.

85.4 Summary and Conclusions

The charge-dependent three-particle correlation measured in Pb–Pb collisions, recorded by ALICE at $\sqrt{s_{NN}} = 2.76$ and 5.02 TeV, are presented. The CME-sensitive three-particle correlation relative to the second order symmetry plane, namely $\gamma_{1,1}$, exhibit a significant charge-dependent difference, which increases toward peripheral collisions. The three-particle correlation relative to the third order symmetry plane denoted by $\gamma_{1,2}$, which is mainly sensitive to background correlations, also exhibits a significant charge-dependent difference. The $\gamma_{1,2}$, scaled with the ratio of elliptic to triangular flow (v_2/v_3), is used to measure the background in $\gamma_{1,1}$ and estimate the CME fraction (f_{CME}). The obtained f_{CME} is found to be consistent with zero for Pb–Pb collisions at $\sqrt{s_{NN}} = 2.76$ and 5.02 TeV.

References

1. F. Karsch, E. Laermann, [arXiv:hep-lat/0305025](https://arxiv.org/abs/hep-lat/0305025) (2003)
2. K. Fukushima, D.E. Kharzeev, H.J. Warringa, Phys. Rev. D **78** (2008)
3. S.A. Voloshin, Phys. Rev. C **70**(057901) (2004)

4. S. Acharya et al. (ALICE collaboration), *JHEP* **2020**(160) (2020)
5. K. Aamodt et al. (ALICE collaboration), *JINST* **3**(S08002) (2008)
6. J. Alme et al. (ALICE collaboration), *Nucl. Instrum. Meth.* **A622**(316) (2010)
7. E. Abbas et al. (ALICE collaboration), *JINST* **8**(P10016) (2013)
8. B. Abelev et al. (ALICE collaboration), *Int. J. Mod. Phys.* **A29**(1430044) (2014)
9. A. Bzdak, V. Koch, J. Liao, *Lecture Notes Phys.* **871**(503) (2013)

Chapter 86

A Unified Formalism to Study *Soft* as Well as *Hard* Part of the Transverse Momentum Spectra



Rohit Gupta and Satyajit Jena

Abstract Transverse momentum (p_T) spectra of final state particles produced in high energy heavy-ion collision can be divided into two distinct regions based on the difference in the underlying particle production processes. We have provided a unified formalism to explain both low- and high- p_T regimes of spectra in a consistent manner. The p_T spectra of final state particles produced in heavy-ion collision at LHC energy have been analysed using unified formalism to test its applicability at different energies, and a good agreement with the data is obtained across all energies. Further, the prospect of extracting the elliptic flow coefficient directly from the transverse momentum spectra is explored.

86.1 Introduction

Among the primary goals of heavy-ion collision, experiments are to understand the QCD matter produced under extreme temperature and energy density called Quark–Gluon Plasma (QGP). Experiments at Relativistic Heavy-Ion Collider (RHIC) and Large Hadron Collider (LHC) are trying to explore the QCD phase diagram in a quest to search for the confinement–deconfinement phase transition and the QCD critical point.

Constraints on the detector capabilities and the short time scale of the collision limit the direct search for this new state of strongly interacting quarks and gluons. Hence, we rely on the information carried by the final state particles to study the initial stages of high energy collision. Kinematics observables of the final state particles such as the transverse momenta p_T and pseudorapidity η play a crucial role in understanding the dynamics of particle production. Quantum Chromodynamics (QCD) is

R. Gupta (✉) · S. Jena
Department of Physical Sciences, Indian Institute of Science Education and Research (IISER)
Mohali, Sector 81 SAS Nagar, Manauli PO 140306, Punjab, India
e-mail: ph15049@iisermohali.ac.in

S. Jena
e-mail: sjena@iisermohali.ac.in

© The Author(s), under exclusive license to Springer Nature Singapore Pte Ltd. 2022
B. Mohanty et al. (eds.), *Proceedings of the XXIV DAE-BRNS High Energy Physics Symposium, Jatni, India*, Springer Proceedings in Physics 277,
https://doi.org/10.1007/978-981-19-2354-8_86

the theoretical framework to study the strongly interacting particles; however, the asymptotic freedom in the coupling strength of the theory limits the applicability of the perturbative theory only at higher energy as it breaks at lower energy. Hence, we utilize the statistical thermal models to study the spectra of particles produced in such collision. In the present work, we will discuss a unified formalism developed to study the transverse momentum spectra in the heavy-ion collision.

In Sect. 86.2, we will discuss the theoretical framework that is being used to study the transverse momentum spectra. The unified formalism that we have developed to study the spectra is discussed in Sect. 86.3 followed by the results and conclusion in Sect. 86.4.

86.2 Conventional Approach

Considering a purely thermal source, we can use standard Boltzmann–Gibbs (BG) statistics to explain the energy distribution of the particles. The formula governing the energy distribution in the case of BG statistics will be in the form of a negative exponential of energy. The distribution function for transverse momentum in BG statistics is given as [1]

$$\frac{1}{2\pi p_T} \frac{d^2 N}{dp_T dy} = \frac{g V m_T}{(2\pi)^3} \exp\left(-\frac{m_T}{T}\right) \quad (86.1)$$

It is observed that the BG distribution function deviates heavily from the data indicating that the modification is required in standard BG formalism to explain the spectra. Application of BG statistics is limited to the extensive systems where entropy is additive; however, there exist some strongly correlated non-extensive systems where entropy can be non-additive.

Tsallis statistics [2] is proposed as a generalization to standard BG statistics with an additional parameter taking care of non-extensivity in the system. Tsallis statistics modifies normal exponential into a q -exponential where ‘ q ’ is the non-extensivity parameter. The distribution function for transverse momenta in Tsallis formalism is of the form:

$$\frac{1}{2\pi p_T} \frac{d^2 N}{dp_T dy} = \frac{g V m_T}{(2\pi)^3} \left[1 + (q - 1) \frac{m_T}{T}\right]^{-\frac{q}{q-1}} \quad (86.2)$$

Tsallis distribution function given in (86.2) has been used extensively to explain the spectra in the low p_T region.

Transverse momentum spectra of particles produced in the heavy-ion collision can be divided into two distinct regions depending on the difference in the underlying process of particle production. The low- p_T region consists of particle produced in soft processes, whereas the particles produced in hard-scattering processes populates the high- p_T part of the spectra. The low- p_T part of the spectra is explained using the

Tsallis statistics, whereas pQCD-based power-law form of the function is used for the high- p_T region. We have developed a unified formalism to explain both soft and hard processes in a consistent manner.

86.3 Unified Statistical Framework

A generalized distribution function defined in terms of the first four moments related to mean, sigma, skewness and kurtosis of the distribution has been provided by Karl Pearson [3] in 1895. It is described in terms of a differential equation:

$$\frac{1}{p(x)} \frac{dp(x)}{dx} + \frac{a+x}{b_0 + b_1x + b_2x^2} = 0 \quad (86.3)$$

and under different limits on its parameters a, b_0, b_1, b_2 ; it reduces to Gaussian, Cauchy, gamma, inverse-gamma and other distribution [4]. Solution to differential equation (86.3) is given as

$$p(x) = B \left(1 + \frac{x}{e}\right)^f \left(1 + \frac{x}{g}\right)^h \quad (86.4)$$

This formalism is used to develop a unified framework [5] and the function for transverse momentum in this model is given as

$$\frac{1}{2\pi p_T} \frac{d^2N}{dp_T dy} = B' \left(1 + \frac{p_T}{p_0}\right)^{-n} \left(1 + (q-1) \frac{p_T}{T}\right)^{-\frac{q}{q-1}} \quad (86.5)$$

The backward compatibility to Tsallis statistics and thermodynamical consistency of this unified formalism has been proved in [6].

86.4 Results and Conclusion

We have tested the applicability of unified formalism by analysing transverse momentum spectra of particles produced in heavy-ion collision.

In Fig. 86.1, we have plotted the p_T spectra of charged hadrons produced in 2.76 TeV $PbPb$. Solid lines correspond to the final fit to the unified function obtained using the χ^2 -minimization technique. The best fit value of χ^2/NDF for most central (0–5%) collision data is 25.3451 for Boltzmann fit, 1.99445 for Tsallis fit and 0.10100 for the unified function fit. The centrality-wise data for the χ^2/NDF values for Boltzmann, Tsallis and unified function is provided in Table 1 of the [5], and the values obtained for the unified formalism are lowest suggesting a good agreement with the data.

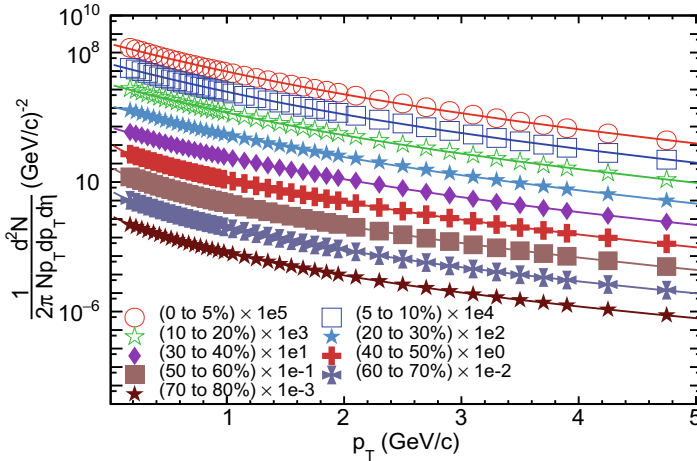


Fig. 86.1 Unified function fit to the charged hadron p_T -spectra produced in $Pb-Pb$ collision at 2.76 TeV [7]. Data points are scaled for better visibility

We extended our analysis to search for the connection of two parameters p_0 and n with the observables in collider experiments. A similarity in the centrality dependence of the second-order flow coefficient v_2 [8] and the unified function parameter $f(= -n)$ is observed, indicating a connection between two quantities. We obtained a linear relation between the two parameters for charged hadrons data at 2.76 TeV as shown in the [5].

In conclusion, a unified formalism has been discussed to study the transverse momentum spectra at different energies and the relation between the fit parameter and the flow coefficient is established.

References

1. E. Schnedermann, J. Sollfrank, U.W. Heinz, Phys. Rev. C **48**, 2462–2475 (1993)
2. C. Tsallis, J. Statist. Phys. **52**, 479 (1988)
3. K. Pearson, Philos. Trans. R. Soc. Lond. A Math. Phys. Eng. Sci. **186**, 343 (1895)
4. J.H. Pollard, *Numerical and Statistical Techniques* (Cambridge University Press, 1979)
5. S. Jena, R. Gupta, Phys. Lett. B **807**, 135551 (2020)
6. R. Gupta, A. Menon, S. Jena, [arXiv:2012.08124](https://arxiv.org/abs/2012.08124) [hep-ph]
7. B. Abelev et al., [ALICE], Phys. Lett. B **720**, 52–62 (2013)
8. K. Aamodt et al., [ALICE Collaboration], Phys. Rev. Lett. **105**, 252302 (2010)

Chapter 87

Observation of Light-by-Light Scattering and Search for Axion-Like Particles with CMS Experiment



Ruchi Chudasama

Abstract Light-by-light (LbL) scattering ($\gamma\gamma \rightarrow \gamma\gamma$) is a fundamental quantum mechanical process which could not be observed until recently due to its tiny cross section. By using huge photon fluxes from lead-on-lead (PbPb) ultraperipheral collisions (UPCs), the process has now been observed by both ATLAS and CMS experiments. LbL process is also a sensitive channel to probe physics beyond the standard model where an intermediate pseudoscalar, axion-like-particle (a) could be produced, i.e., ($\gamma\gamma \rightarrow a \rightarrow \gamma\gamma$). The diphoton invariant mass distribution of LbL process is used to search for such a resonance production. A new exclusion limits on the mass of the pseudoscalar axion-like particles, in the range of 5–90 GeV has been set. This report will discuss highlights of the measurement of LbL scattering by CMS experiment.

87.1 Introduction

Elastic light-by-light scattering is a fundamental quantum mechanical process in the Standard Model (SM). At leading order, the $\gamma\gamma \rightarrow \gamma\gamma$ process proceeds via virtual box-diagram containing SM charged particles (Fig. 87.1 (left)). Due to its tiny cross sections, its first evidence [1, 2] and final observation [3] has not been performed until recently in PbPb ultraperipheral collisions (UPCs) at the LHC, by exploiting the very large fluxes of quasi-real photons emitted by the nuclei accelerated at TeV energies as proposed in [4]. In UPCs, the charged ions interact at impact parameter larger than the sum of their radii via electromagnetic interactions. In the equivalent photon approximation, strong electromagnetic fields can be considered as a flux of virtual photons. The $\gamma\gamma \rightarrow \gamma\gamma$ process at the LHC is also sensitive to physics beyond the SM. Modifications of the LbL rates can occur if new heavy particles, such as magnetic

Ruchi Chudasama—for the CMS Collaboration.

R. Chudasama (✉)
Tata Institute of Fundamental Research, Mumbai, India
e-mail: ruchi.chudasama@cern.ch

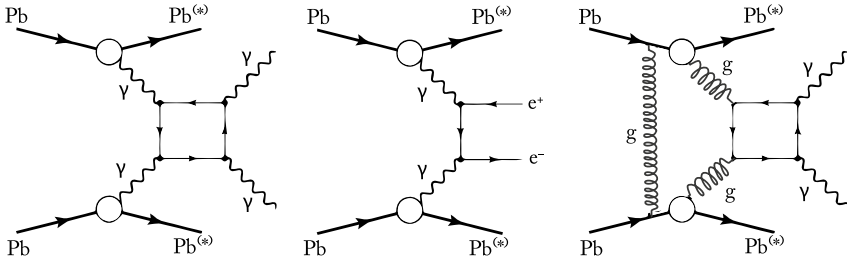


Fig. 87.1 Schematic diagrams of light-by-light scattering ($\gamma\gamma \rightarrow \gamma\gamma$, left), QED dielectron ($\gamma\gamma \rightarrow e^+e^-$, center), and central exclusive diphoton ($gg \rightarrow \gamma\gamma$, right) production in ultra-peripheral PbPb collisions

monopoles, vector-like fermions or other new spin-even particles, such as axion-like particles (ALPs) or gravitons, contribute to the virtual corrections of the box depicted in Fig. 87.1. This report presents an evidence for LbL scattering and exclusion limits on ALPs production [5], using PbPb collision data recorded by the CMS experiment [6] in 2015 at $\sqrt{s_{NN}} = 5.02$ TeV with integrated luminosity of $390 \mu\text{b}^{-1}$ [2].

87.2 Event Selection and Background Estimation

The light-by-light signal was generated with the Madgraph v5 [7] Monte Carlo (MC) event generator. The $\gamma\gamma \rightarrow e^+e^-$ process is a potential background when both electrons are misidentified as photons but is also used for calibration studies in the analysis. The process was modeled with the STARLIGHT [8] generator. The exclusive diphoton final state can also be produced via the strong interaction through a quark loop in the exchange of two gluons in a color-singlet state. This central exclusive production process, $gg \rightarrow \gamma\gamma$, is simulated using SuperChic 2.0 [9] event generator. This process has large theoretical uncertainty for PbPb collisions, therefore the absolute normalization of this MC contribution is determined from a control region in the data. The exclusive diphoton candidates are selected at the trigger level by requiring at least two electromagnetic showers above transverse energy (E_T) greater than 2 GeV and one of the Hadron Forward calorimeter empty. At the offline level, events with exactly two photons with $E_T > 2$ GeV and $|\eta| < 2.4$, and no extra charged-particle and calorimeter activity are selected. The non-exclusive diphoton background is eliminated by requiring events with diphoton acoplanarity $A_\phi < 0.01$ and diphoton transverse momentum $p_T^{\gamma\gamma} < 1$ GeV. In order to have a full control of the QED background in the LbL scattering signal region, the same analysis

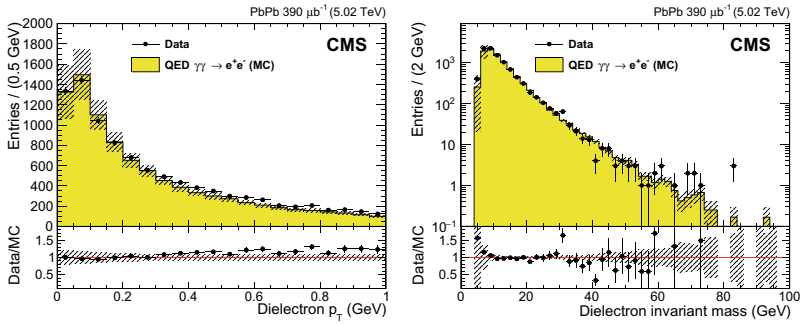


Fig. 87.2 Dielectron p_T and invariant mass distributions compared for data and STARLIGHT MC expectations for the exclusive e^+e^- events [2]

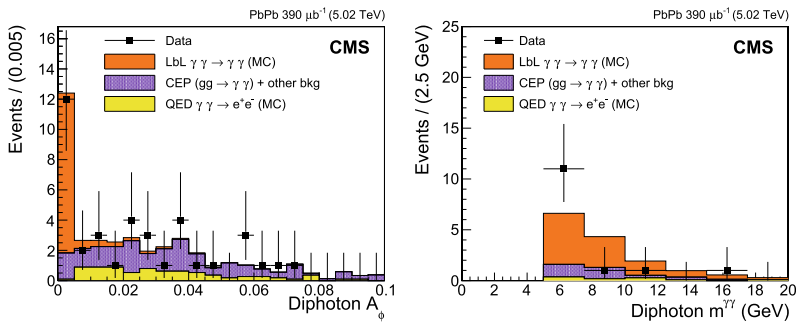


Fig. 87.3 Diphoton acoplanarity and invariant mass distributions for exclusive $\gamma\gamma$ events in data (squares) compared to MC expectations [2]

is carried on exclusive dielectron candidates, applying the same event selection criteria. Figure 87.2 shows the dielectron p_T and invariant mass distribution for events passing the exclusivity criteria. A good agreement is found between data and MC which confirms the quality of the electromagnetic particle reconstruction, and of the exclusive event selection criteria, as well as of the MC predictions.

After applying all LbL event selection criteria, we observe 14 LbL scattering candidates, to be compared with 11.1 ± 1.1 (theo) expected from the LbL scattering signal, 3.0 ± 1.1 (stat) from CEP, and 1.0 ± 0.3 (stat) from QED e^+e^- background events. Figure 87.3 shows the comparison of the measured and simulated diphoton acoplanarity and invariant mass distributions. Both the measured yields and kinematic distributions are in accord with the combination of the LbL signal plus QED

e^+e^- and CEP+other background expectations. The compatibility of the data with the background-only hypothesis has been evaluated from the measured acoplanarity distribution. The significance of the excess at low diphoton acoplanarity is 4.1 standard deviations (4.4 standard deviations expected).

87.3 Results and Discussion

The fiducial cross section for LbL process was obtained by measuring the ratio R of cross sections of the LbL scattering over the QED e^+e^- processes. Measuring the ratio reduced the uncertainties related to trigger and reconstruction efficiencies, and integrated luminosity. The ratio R amounts to $(25.0 \pm 9.6 \text{ (stat)} \pm 5.8 \text{ (syst)}) \times 10^{-6}$. The LbL fiducial cross section is estimated to be $\sigma_{\text{fid}}(\gamma\gamma \rightarrow \gamma\gamma) = 120 \pm 46 \text{ (stat)} \pm 28 \text{ (syst)} \pm 4 \text{ (theo)} \text{ nb}$, which is in good agreement with the theoretical LbL prediction, $\sigma_{\text{fid}}(\gamma\gamma \rightarrow \gamma\gamma) = 138 \pm 14 \text{ nb}$.

The measured invariant mass distribution (Fig. 87.3) is used to search for pseudoscalar ALPs produced in the process $\gamma\gamma \rightarrow a \rightarrow \gamma\gamma$. The LbL, QED, and CEP+other processes are considered as a background in this search. The ALPs samples were generated using the STARLIGHT generator for masses ranging from 5 to 90 GeV. Limits on $\sigma(\gamma\gamma \rightarrow \gamma\gamma)$ cross sections for ALPs are set in the 1500–20 nb range. These cross section limits are used to set exclusion limits in the the $g_{a\gamma}$ versus m_a plane, where $g_{a\gamma} \equiv 1/\Lambda$ is the ALP coupling to photons or also to hypercharge. Figure 87.4 shows the exclusion limits for ALPs coupling to photons only (left) or also to hypercharge (right). For an ALP coupling to the photons only, the exclusion limits are best so far over the $m_a = 5\text{--}50$ GeV. For ALPs coupling to the photons and hypercharge, the results provide new constraints in the region $m_a = 5\text{--}10$ GeV.

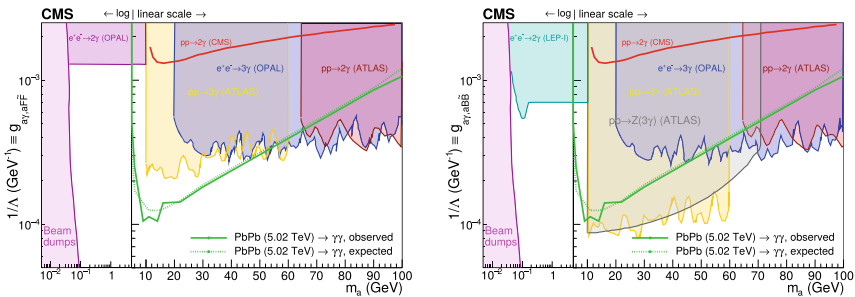


Fig. 87.4 Exclusion limits at 95% confidence level in coupling versus mass plane for **a** ALPs coupling to photons only **b** including also the hypercharge coupling [2]

References

1. ATLAS Collaboration, *Nat. Phys.* **13**(9), 852–858 (2017)
2. C.M.S. Collaboration, *Phys. Lett. B* **797**, 134826 (2019)
3. ATLAS Collaboration, *Phys. Rev. Lett.* **123**(5), 052001 (2019)
4. D. d’Enterria, G.G. da Silveira, *Phys. Rev. Lett.* **111**, 080405 (2013)
5. S. Knapen et al., *Phys. Rev. Lett.* **118**, 171801 (2017)
6. C.M.S. Collaboration, *JINST* **3**, S08004 (2008)
7. J. Alwall et al., *JHEP* **07**, 079 (2014)
8. S.R. Klein, J. Nystrand, *Phys. Rev. Lett.* **92**, 142003 (2004)
9. L.A. Harland-Lang, V.A. Khoze, M.G. Ryskin, *Eur. Phys. J. C* **76**, 9 (2016)

Chapter 88

Strangeness- and Rapidity-Dependent Studies in Small Systems with ALICE at the LHC



Sandeep Dudi

Abstract We report about recent studies of strange hadron production in p–Pb at $\sqrt{s_{NN}} = 5.02, 8.16$ TeV and in pp collisions at $\sqrt{s} = 7, 13$ TeV. The transverse momentum (p_T) integrated yields and particle ratios as a function of charged-particle multiplicity are reported to study the particle production mechanism and the strangeness enhancement. The rapidity asymmetry (Y_{asym}) for ϕ and K^{*0} is measured in p–Pb collisions to explore possible nuclear effects. The Y_{asym} is measured as a function of transverse momentum (p_T) in various multiplicity classes and are compared with EPOS and HIJING model predictions.

88.1 Introduction

The study of hadron production in pp and p–Pb collisions systems can be used as a reference for the interpretation of the heavy-ion results. As resonances are short-lived particles (lifetime $\approx 10^{-23}$ s), they carry the information regarding the dynamic evolution of particle production in heavy-ion collisions [1]. The measurement of strange hadron production in high-energy hadronic interactions provides a way to study the characteristics of quantum chromodynamics (QCD), the theory of strongly interacting matter. The particle production in asymmetric collision system (e.g. p–Pb) is influenced by nuclear effects in the initial state. Partons from the proton side (backward rapidity) are expected to undergo multiple scattering while traversing the Pb nucleus. Pb-side yields (forward rapidity) are likely to be affected by the properties of the nucleus. Previously, a rapidity-dependent study has been done in d–Au collisions at the Relativistic Heavy-Ion Collider (RHIC) for pions and protons

Sandeep Dudi—for the ALICE Collaboration.

S. Dudi (✉)

Department of Physics, Panjab University, Chandigarh, India
e-mail: sandeep.dudi@cern.ch

© The Author(s), under exclusive license to Springer Nature Singapore Pte Ltd. 2022
B. Mohanty et al. (eds.), *Proceedings of the XXIV DAE-BRNS High Energy Physics Symposium, Jaiti, India*, Springer Proceedings in Physics 277,
https://doi.org/10.1007/978-981-19-2354-8_88

479

[2]. The rapidity-dependent study of particle production can be carried out by using a ratio called the rapidity asymmetry (Y_{asym}), defined as

$$Y_{\text{asym}}(p_T) = \frac{Y_F(p_T)}{Y_B(p_T)}, \tag{88.1}$$

where Y_F and Y_B are the spectra measured at forward and backward rapidities, respectively.

The study of Y_{asym} will help to determine the relative contributions of various physics processes to particle production, such as multiple scattering, nuclear shadowing, recombination of thermal partons and parton saturation [2].

We present the measurement of the integrated yields of ϕ mesons and the integrated-yield ratios of p , K_s^0 , Λ , ϕ , Ω and Ξ to pions as a function of charged-particle multiplicity in pp and p–Pb collisions. In addition, the Y_{asym} of ϕ and K^{*0} in p–Pb collisions at $\sqrt{s_{\text{NN}}} = 5.02$ TeV are discussed.

88.2 Results

Figure 88.1 shows multiplicity-scaled integrated yields of the ϕ as a function of the charged-particle multiplicity in pp collisions at $\sqrt{s} = 7$ [3] and 13 TeV and, in p–Pb collisions at $\sqrt{s_{\text{NN}}} = 5.02$ [4] and 8.16 TeV. The multiplicity-scaled integrated yield is constant within uncertainty as a function of $\langle dN_{\text{ch}}/d\eta \rangle$. The integrated yield is independent of collision systems and energy. The right plot of Fig. 88.1 shows

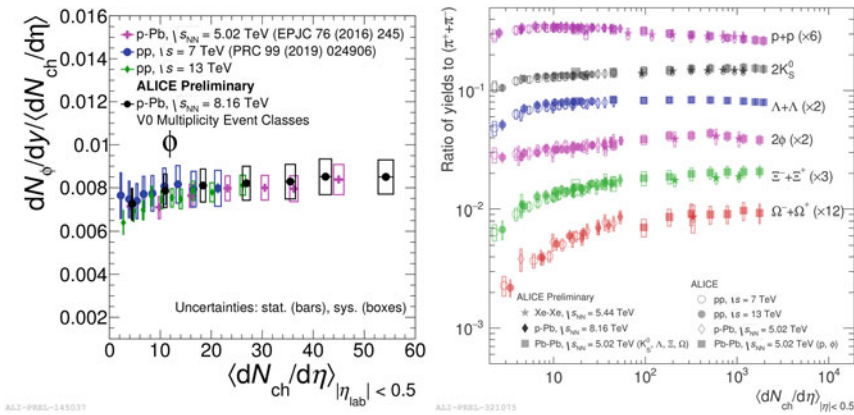


Fig. 88.1 [Left Plot] The multiplicity-scaled integrated yield $\langle dN_\phi/dy \rangle / \langle dN_{\text{ch}}/d\eta \rangle$ for ϕ as a function of $\langle dN_{\text{ch}}/d\eta \rangle$ in pp collisions at $\sqrt{s} = 7$ and 13 TeV and in p–Pb collisions at $\sqrt{s_{\text{NN}}} = 5.02$ and 8.16 TeV. [Right plot] The ratio of yield of hadrons (p , K_s^0 , Λ , ϕ , Ω , Ξ) to pions as a function of $\langle dN_{\text{ch}}/d\eta \rangle$ in pp, p–Pb, Pb–Pb and Xe–Xe collisions

the ratios of the yields of p , K_s^0 , Λ , ϕ , Ξ and Ω to pions as a function of charged-particle multiplicity in various collision systems at different energies. The strange to non-strange particle yield ratio shows a significant enhancement with increasing charged-particle multiplicity in pp and p–Pb collisions [5]. No significant energy dependence is observed. Particles having a higher strangeness content show strong enhancement in the yield ratio as a function of the charged-particle multiplicity. The yield ratios show similar behaviour at high multiplicity in pp and p–Pb collisions as the measurements in Pb–Pb collisions.

The rapidity asymmetry ratios (Y_{asym}) for ϕ and K^{*0} as a function of p_T for various multiplicity classes based on the V0A detector in p–Pb collisions at $\sqrt{s_{\text{NN}}} = 5.02$ TeV are shown in Fig. 88.2. An asymmetry is observed at low p_T , whereas it is consistent with unity within uncertainties at high p_T . The Y_{asym} value are large at high multiplicity, and it decreases as going from high to low multiplicity classes. Y_{asym} for ϕ and K^{*0} shows similar behaviour within uncertainties. Figure 88.3 shows the comparison of ϕ and K^{*0} Y_{asym} in 0–100% multiplicity class with EPOS [6] and HIJING [7] model predictions. Both the models reproduce the data at low p_T , whereas they deviate at high p_T . The HIJING model predictions with and without shadowing parameters show similar behaviour within uncertainties, whereas a large deviation is observed in case of K^{*0} then ϕ at high p_T . The EPOS model calculations with UrQMD [8] ON and OFF also show a similar behaviour within uncertainty. The EPOS model shows less deviation for K^{*0} at high p_T than the HIJING model.

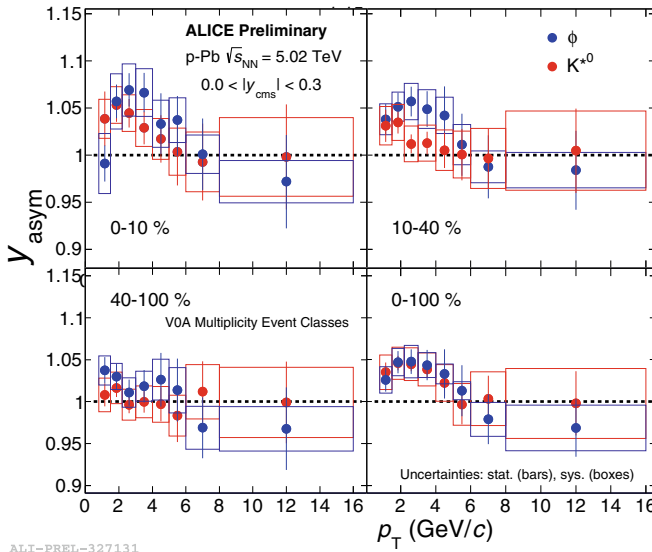


Fig. 88.2 The Y_{asym} of ϕ and K^{*0} as function of p_T for various multiplicity classes in p–Pb collisions at $\sqrt{s_{\text{NN}}} = 5.02$ TeV at mid-rapidity

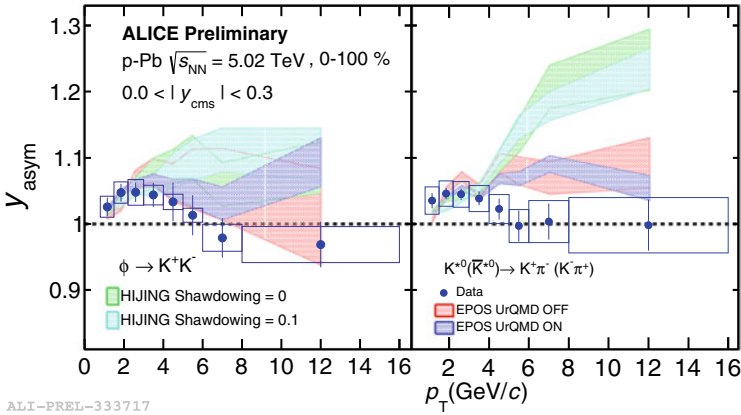


Fig. 88.3 The Y_{asym} of ϕ and K^{*0} with model (EPOS, HIJING) predictions as a function of p_T for 0–100 % multiplicity in p–Pb collisions at $\sqrt{s_{\text{NN}}} = 5.02$ TeV at midrapidity

88.3 Summary

The multiplicity-scaled integrated yield of ϕ as a function of the charged-particle multiplicity is independent of collision system and energies. Strangeness enhancement is observed from strange to non-strange hadron yield ratios to pions in pp and p–Pb collisions. The enhancement is larger for particles having larger strangeness content. High multiplicity pp and p–Pb collisions show similar ratios as those measured in Pb–Pb collisions. A rapidity asymmetry is observed at low p_T in the high multiplicity class. Y_{asym} decreases from high to low multiplicity class and it is consistent with unity at high p_T within uncertainties. EPOS and HIJING models explain the Y_{asym} data at low p_T but show deviation at high p_T . The deviation is more important for HIJING than for EPOS. Y_{asym} is also observed to be species independent.

References

1. B.I. Abelev et al. (STAR Collaboration) Phys. Rev. C **76**, 054903 (2007)
2. A.H. Mueller, Nucl. Phys. B **335**, 115 (1990)
3. S. Acharya et al., ALICE collaboration. Phys. Rev. C **99**, 024906 (2019)
4. J. Adam et al., ALICE collaboration. Eur. Phys. J. C **76**, 245 (2016)
5. J. Adam et al., ALICE collaboration. Nat. Phys. **13**, 535–539 (2016)
6. T. Pierog, I. Karpenko, J.M. Katzy, E. Yatsenko, K. Werner, Phys. Rev. C **92**(3), 034906 (2015)
7. M. Gyulassy, X.-N. Wang, Comput. Phys. Commun. **83**, 307 (1994)
8. M. Bleicher et al., J. Phys. G **25**, 1859–1896 (1999)

Chapter 89

Feasibility Studies of J/ψ Measurement with CBM Detector Setup at FAIR SIS100 Energies



Sayak Chatterjee

Abstract The Facility for Anti-proton and Ion Research (FAIR) at Darmstadt, Germany, enables us with the opportunity to measure J/ψ production in low energy nuclear collisions with unprecedented high interaction rates. In this article, the Monte-Carlo (MC) based studies of the detection of J/ψ mesons via their di-muon decay channel ($J/\psi \rightarrow \mu^+ \mu^-$) and with the realistic detector setup as implemented in GEANT3 for pure central ($b = 0$ fm) 10 A GeV/c Au+Au collision are discussed.

89.1 Introduction

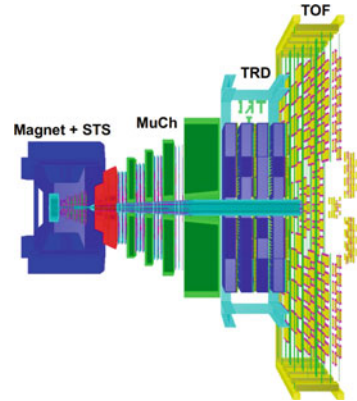
The Compressed Baryonic Matter (CBM) experiment at FAIR [1] is planned to perform pioneering measurements on J/ψ production in relativistic nuclear collisions at moderate beam energies with unprecedented high interaction rates [2], thanks to the foreseen high-intensity heavy-ion beams and the state-of-the-art detectors with high rate handling capability. At FAIR SIS100, heavy-ions will be accelerated up to beam kinetic energies of 11 A GeV, whereas light ions up to 14 A GeV and protons up to 29 GeV [3]. The Muon Chamber (MuCh) [4] at CBM will be used for the identification of muons coming from the decay of low mass vector mesons and J/ψ [5]. In Fig. 89.1, the schematic of the muon detection setup in CBM is shown. The present article reports the feasibility of J/ψ reconstruction in muon channel with the realistic detector setup in 10 A GeV/c Au+Au pure central ($b = 0$ fm) collision system.

Sayak Chatterjee—for the CBM collaboration.

S. Chatterjee (✉)
Department of Physics, Bose Institute, Kolkata, India
e-mail: sayakchatterjee@jcbosc.ac.in

© The Author(s), under exclusive license to Springer Nature Singapore Pte Ltd. 2022
B. Mohanty et al. (eds.), *Proceedings of the XXIV DAE-BRNS High Energy Physics Symposium, Jatni, India*, Springer Proceedings in Physics 277,
https://doi.org/10.1007/978-981-19-2354-8_89

Fig. 89.1 The schematic of the di-muon detection setup at CBM



89.2 Simulation Details

The MuCh sub-system is composed of five absorber layers of variable thicknesses and four detector stations placed in between the absorbers. Each of the detector stations is composed of three detector layers. For the first two stations, Gas Electron Multipliers (GEM) are implemented to account for the large particle densities and in the next two stations, Resistive Plate Chambers (RPC) are implemented, where the particle densities are considerably lower due to hadron absorbers. The thickness of the successive absorbers is 58, 20, 20, 30, and 100 cm. The first absorber is made of 28 cm graphite + 30 cm concrete, and the rest of the absorbers are made of iron. Hits registered in the transition radiation detector (TRD) behind the 100 cm thick iron absorber are used to devise the di-muon trigger logic. The angular coverage of MuCh is 5° – 25° . For physics performance simulation, the hadronic background is calculated with the UrQMD [6] event generator, and the phase-space distribution and decay of $J/\psi \rightarrow \mu^+\mu^-$ is simulated using the PLUTO [7] event generator.

89.3 Results

J/ψ 's are reconstructed using invariant mass spectra of oppositely charged muon track candidates. The muon track candidates are identified by applying a set of single track quality cuts to the reconstructed global tracks. The reconstructed global tracks having associated STS hits ≥ 7 , MuCh hits ≥ 11 , TRD hits ≥ 3 , TOF hits ≥ 1 , $\chi_{\text{Vertex}}^2 \leq 2.2$, $\chi_{\text{STS}}^2 \leq 3.4$, $\chi_{\text{MuCh}}^2 \leq 2.6$ and $\chi_{\text{TRD}}^2 \leq 6.0$ are selected as valid muon track candidate. The contribution of non-muonic tracks is further reduced by applying 2σ cut on the reconstructed TOF mass. The cuts are optimised to get the optimum significance value. Two different approaches have been employed to calculate the pair reconstruction efficiency ($\epsilon_{J/\psi}$) and signal to background (S/B) ratio.

In the first approach, the signal is extracted using the MC Particle ID (MCPID)

tag, and the background is calculated from a pure UrQMD simulated sample following super event (SE) technique, where one muon candidate track is combined with all the other oppositely charged muon candidate tracks to calculate the combinatorial background. The signal entries are scaled properly with the multiplicity (from UrQMD [8]) and branching ratio values. After that, the entries within the 2σ mass range of the signal, fitted with a symmetric Gaussian distribution, are used to estimate the pair reconstruction efficiency and signal to background (S/B) ratio. In the second approach, the invariant mass spectra of oppositely charged muon candidate tracks are fitted with a combined Gaussian (signal) + 2nd degree polynomial (background) function and then the signal is extracted in the 2σ mass range. In this method, no MC information is used for signal extraction and thus would be directly applicable to raw data. Figure 89.2 (left plot) shows the invariant mass spectra fitted using the second approach, and the results of the fitting are summarised in Table 89.1. As evident, the results from different fit procedures show a good agreement. The obtained mass resolution (32 MeV) is small enough to distinguish between J/ψ and ψ' signals, thanks to the low material budget of STS. The laboratory rapidity (y) and transverse momen-

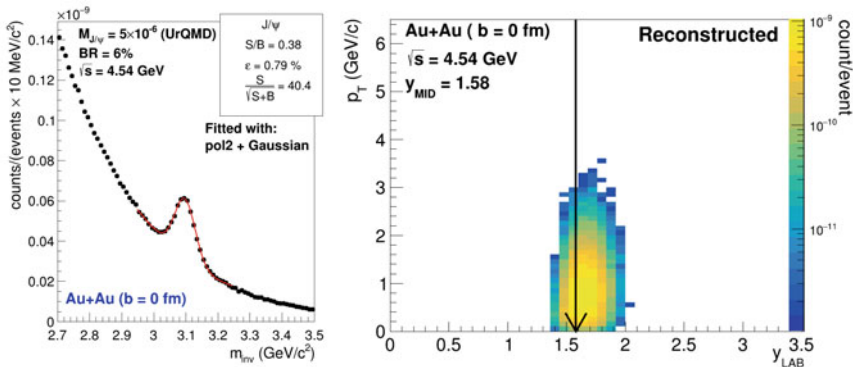


Fig. 89.2 Invariant mass distribution of the reconstructed J/ψ mesons for 10A GeV/c Au+Au pure central collision (left) fitted by Gaussian (signal) and 2nd order polynomial (background). Laboratory rapidity (y) and transverse momentum (p_T) distribution of reconstructed muon pairs (right)

Table 89.1 Reconstruction efficiency and S/B ratio for J/ψ mesons in pure central Au+Au collision at 10A GeV/c from different fitting methods. Method 1 & 2 are based on MC information and full fit respectively

Method (System)	$\epsilon_{J/\psi}$ (%)	S/B	Mass resolution (MeV)	Significance $S/\sqrt{S+B}$
Method 1 (Au+Au)	0.81	0.36	33	39.4
Method 2 (Au+Au)	0.79	0.38	32	40.4

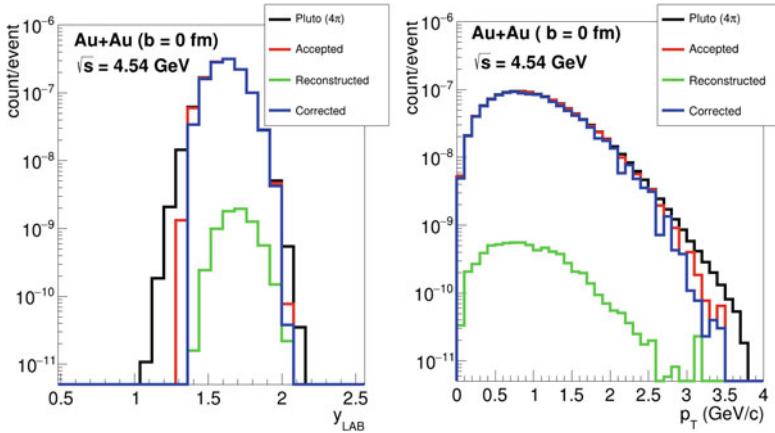


Fig. 89.3 Input, Accepted, reconstructed and corrected rapidity (y_{LAB}) and p_T spectra for pure central 10 A GeV/c Au+Au system

tum (p_T) distribution of the signal muon pairs, at the reconstructed level (selected using MC information), is shown in Fig. 89.2 (right plot), and good mid-rapidity coverage is observed. The efficiency correction to the extracted spectra is also performed without using the MCPID. The accepted tracks are extracted, from the full phase space input signal distribution depending on the acceptance criteria of the simulated MC tracks. Among those accepted MC tracks, only a fraction is reconstructed based on the tracking algorithm and analysis criteria. The ratio of the reconstructed to the accepted tracks gives us the efficiency matrix and then the ratio of the reconstructed matrix to the efficiency matrix, gives us the corrected spectra. In Fig. 89.3, the corrected y and p_T spectra along with the input, accepted and reconstructed spectra is shown for pure central Au+Au collision system. After the efficiency correction, the reconstructed spectra matches well with the accepted spectra.

89.4 Summary and Outlook

The feasibility studies of J/ψ measurement at FAIR SIS100 energies is investigated via di-muon channel detection with realistic CBM detector setup for Au+Au pure central collision at beam momentum of 10 A GeV/c. The measurement of J/ψ is found to be feasible with the predicted meson multiplicity and with the obtained reconstruction efficiency, 2×10^{-7} J/ψ can be detected per event. The efficiency correction is performed and the corrected spectra matches well with the input spectra.

References

1. P. Senger, Nucl. Phys. A **862**, 139 (2011)
2. T. Galatyuk, Nucl. Phys. A **982**, 163 (2019)
3. I. Augustin et al., *Fission and Properties of Neutron-Rich Nuclei* (2008), p. 128 (2008). [arXiv:0804.0177](https://arxiv.org/abs/0804.0177), https://doi.org/10.1142/9789812833433_0016
4. S. Chattopadhyay et al., *Technical Design Report for the CBM: Muon Chambers (MuCh)*, GSI (2015). <https://repository.gsi.de/record/161297>
5. T. Ablyazimov et al., Eur. Phys. J. A **53** (2017)
6. M. Bleicher et al., J. Phys. G **25**, 1859 (1999)
7. I. Fröhlich et al., J. Phys.: Conf. Ser. **219**, 032039 (2010). [arXiv:0905.2568v1](https://arxiv.org/abs/0905.2568v1)
8. J. Steinheimer et al., Phys. Rev. C **95**, 014911 (2017)

Chapter 90

Structure of Magnetic Field Quantization in Viscosity Expression for Relativistic Fluid



Snigdha Ghosh and Sabyasachi Ghosh

Abstract The expressions of the shear and bulk viscous coefficients in the presence of an arbitrary external magnetic field are obtained for general relativistic Bosonic and Fermionic systems at finite temperature employing the one-loop Kubo formalism. This is done by explicitly evaluating the thermo-magnetic spectral functions of the energy momentum tensors using the real time formalism of finite temperature field theory and the Schwinger proper time formalism.

90.1 Introduction

In a non-central or asymmetric heavy ion collision (HIC) experiment at RHIC and LHC, the produced hot and/or dense ‘strongly’ interacting matter is expected to be exposed under a strong magnetic field $B \sim 10^{18}$ Gauss which may also lead to various interesting QCD-linked phenomena [1, 2]. In this work, we attempt to calculate the transport coefficients namely the shear and bulk viscosity for general relativistic systems at finite temperature and background magnetic field using the Kubo framework.

Owing to Kubo relation, the viscous coefficients can be related to the static limit (zero four-momentum limit) of the two point correlation functions of the local energy momentum tensor (EMT) or the in-medium EMT spectral functions. In the present work, we have considered two general relativistic systems of scalar Bosons and Dirac Fermions and have calculated the corresponding thermo-magnetic spectral functions of the EMTs. The evaluation of the spectral function is done using the real time formalism of finite temperature field theory and the Schwinger proper

S. Ghosh (✉)

Government General Degree College Kharagpur-II Madpur, Paschim Medinipur 721149, West Bengal, India

e-mail: snigdha.physics@gmail.com

S. Ghosh

Indian Institute of Technology Bhilai, GEC Campus, Sejbahar, Raipur 492015, Chhattisgarh, India

time formalism. Then we use the covariant tensor basis of [3] to extract the viscous coefficients from the thermo-magnetic spectral functions using the Kubo relations.

90.2 Formalism

In absence of external magnetic field, the shear viscosity (η) and bulk viscosity (ζ) are obtained from the EMT spectral function $\mathcal{S}^{\mu\nu\alpha\beta}$ as [4, 5]

$$\nu = \mathcal{P}_{\mu\nu\alpha\beta}^{(\nu)} \mathcal{S}^{\mu\nu\alpha\beta} \quad ; \quad \nu \in \{\eta, \zeta\} \quad (90.1)$$

where

$$\mathcal{P}_{\mu\nu\alpha\beta}^{(\eta)} = \frac{1}{10} \left(\Delta_{\mu}^{\sigma} \Delta_{\nu}^{\rho} - \frac{1}{3} \Delta^{\sigma\rho} \Delta_{\mu\nu} \right) \left(\Delta_{\sigma\alpha} \Delta_{\rho\beta} - \frac{1}{3} \Delta_{\sigma\rho} \Delta_{\alpha\beta} \right), \quad (90.2)$$

$$\mathcal{P}_{\mu\nu\alpha\beta}^{(\zeta)} = \left(\frac{1}{3} \Delta_{\mu\nu} + \theta u_{\mu} u_{\nu} \right) \left(\frac{1}{3} \Delta_{\alpha\beta} + \theta u_{\alpha} u_{\beta} \right) \quad (90.3)$$

in which u^{μ} is the fluid 4-velocity, $\Delta^{\mu\nu} = (g^{\mu\nu} - u^{\mu} u^{\nu})$, $\theta = \left(\frac{\partial P}{\partial \varepsilon} \right)$, P is the pressure and ε is the energy density of the system. In the local rest frame (LRF) of the medium, $u_{\text{LRF}}^{\mu} = (1, \mathbf{0})$.

On simplifying (90.1), we obtain the viscous coefficients at zero magnetic field as [5]

$$\eta_{\text{Scalar}} = \frac{2}{15T} \int \frac{d^3k}{(2\pi)^3} \frac{\mathbf{k}^4}{\omega_k^2 \Gamma} f(\omega_k) \{1 + f(\omega_k)\}, \quad (90.4)$$

$$\eta_{\text{Dirac}} = \frac{4}{15T} \int \frac{d^3k}{(2\pi)^3} \frac{\mathbf{k}^4}{\omega_k^2 \Gamma} \tilde{f}(\omega_k) \{1 - \tilde{f}(\omega_k)\}, \quad (90.5)$$

$$\zeta_{\text{Scalar}} = \frac{2}{9T} \int \frac{d^3k}{(2\pi)^3} \frac{1}{\omega_k^2 \Gamma} \{m^2 + (3\theta - 1)\omega_k^2\}^2 f(\omega_k) \{1 + f(\omega_k)\}, \quad (90.6)$$

$$\zeta_{\text{Dirac}} = \frac{4}{9T} \int \frac{d^3k}{(2\pi)^3} \frac{1}{\omega_k^2 \Gamma} \{m^2 + (3\theta - 1)\omega_k^2\}^2 \tilde{f}(\omega_k) \{1 - \tilde{f}(\omega_k)\}, \quad (90.7)$$

where $f(\omega)$ and $\tilde{f}(\omega)$ are respectively the Bose-Einstein and Fermi-Dirac distribution functions. It is to be noted that the above expressions of shear and bulk viscosity from Kubo framework are exactly identical to same obtained using the RTA in kinetic theory formalism [6]. The Γ in the above equation is the thermal width or collision rate of the constituent particles, which reciprocally measures the dissipative coefficients, like the shear viscosity and the bulk viscosity.

In presence of magnetic field, one can get five (trace-less) and two (non-zero trace) independent gradient tensors, for which five shear viscosity coefficients η_n

($n = 0, 1, 2, 3, 4$) and two bulk viscosity coefficients $\zeta_{\perp, \parallel}$ will be introduced [3, 7, 8]. In the covariant tensor basis of [3, 8], the connecting relations between viscous coefficients ν and the EMT spectral function are:

$$\nu = -\xi^{(\nu)}\eta_0 + \mathcal{P}_{\mu\nu\alpha\beta}^{(\nu)}\mathcal{S}^{\mu\nu\alpha\beta} \quad ; \nu \in \{\eta_0, \eta_1, \eta_2, \eta_3, \eta_4, \zeta_{\perp}, \zeta_{\parallel}\} \quad (90.8)$$

where $\xi^{(\nu)} = \begin{cases} 4/3 & \text{if } \nu = \eta_1 \\ 1 & \text{if } \nu = \eta_2 \\ 0 & \text{otherwise} \end{cases}$ and $\mathcal{P}_{\mu\nu\alpha\beta}^{(\nu)}$ are given by

$$\mathcal{P}_{\mu\nu\alpha\beta}^{(\eta_0)} = \frac{1}{4} \left(\Xi_{\mu}^{\sigma} \Xi_{\nu}^{\rho} - \frac{1}{2} \Xi^{\sigma\rho} \Xi_{\mu\nu} \right) \left(\Xi_{\sigma\alpha} \Xi_{\rho\beta} - \frac{1}{2} \Xi_{\sigma\rho} \Xi_{\alpha\beta} \right), \quad (90.9)$$

$$\mathcal{P}_{\mu\nu\alpha\beta}^{(\eta_1)} = 2 (b_{\mu} b_{\nu} - \theta u_{\mu} u_{\nu}) \left(\frac{1}{2} \Xi_{\alpha\beta} + (\theta + \phi) u_{\alpha} u_{\beta} \right), \quad (90.10)$$

$$\mathcal{P}_{\mu\nu\alpha\beta}^{(\eta_2)} = -\frac{1}{2} \Xi_{\mu}^{\sigma} b_{\nu} \Xi_{\sigma\alpha} b_{\beta}, \quad (90.11)$$

$$\mathcal{P}_{\mu\nu\alpha\beta}^{(\eta_3)} = -\frac{1}{8} \left(\Xi_{\mu}^{\sigma} \Xi_{\nu}^{\rho} - \frac{1}{2} \Xi^{\sigma\rho} \Xi_{\mu\nu} \right) b_{\sigma}^{\lambda} \left(\Xi_{\lambda\alpha} \Xi_{\rho\beta} - \frac{1}{2} \Xi_{\lambda\rho} \Xi_{\alpha\beta} \right), \quad (90.12)$$

$$\mathcal{P}_{\mu\nu\alpha\beta}^{(\eta_4)} = \frac{1}{2} b_{\rho\sigma} \Xi_{\mu}^{\rho} b_{\nu} \Xi_{\alpha}^{\sigma} b_{\beta}, \quad (90.13)$$

$$\mathcal{P}_{\mu\nu\alpha\beta}^{(\zeta_{\perp})} = \frac{1}{3} (\Delta_{\mu\nu} + (3\theta + 2\phi) u_{\mu} u_{\nu}) \left(\frac{1}{2} \Xi_{\alpha\beta} + (\theta + \phi) u_{\alpha} u_{\beta} \right), \quad (90.14)$$

$$\mathcal{P}_{\mu\nu\alpha\beta}^{(\zeta_{\parallel})} = -\frac{1}{3} (\Delta_{\mu\nu} + (\theta + 2\phi) u_{\mu} u_{\nu}) (b_{\alpha} b_{\beta} - \theta u_{\alpha} u_{\beta}) \quad (90.15)$$

where, $b^{\mu} = \frac{1}{2B} \epsilon^{\mu\nu\alpha\beta} F_{\nu\alpha} u_{\beta}$, $F^{\mu\nu} = (\partial^{\mu} A_{\text{ext}}^{\nu} - \partial^{\nu} A_{\text{ext}}^{\mu})$ is the electromagnetic field strength tensor, $b^{\mu\nu} = \epsilon^{\mu\nu\alpha\beta} b_{\alpha} u_{\beta}$, $\Xi^{\mu\nu} = \Delta^{\mu\nu} + b^{\mu} b^{\nu}$ with the convention of the Levi-Civita tensor $\epsilon^{0123} = 1$. In the LRF, $b_{\text{LRF}}^{\mu} \equiv (0, 0, 0, 1)$. In (90.9)–(90.15), the thermodynamic quantities $\theta = \left(\frac{\partial P}{\partial \varepsilon} \right)_B$ and $\phi = -B \left(\frac{\partial M}{\partial \varepsilon} \right)_B$ where M is the magnetization of the system.

Simplification of (90.8) yields the expressions of viscous coefficients in presence of constant external magnetic field as [5]

$$\begin{aligned} \nu = & -\xi^{(\nu)}\eta_0 + \sum_{l=0}^{\infty} \sum_{n=0}^{\infty} \frac{1}{T} \int_{-\infty}^{\infty} \frac{dk_z}{(2\pi)} \frac{1}{4\omega_{kl}\omega_{kn}} \frac{\Gamma}{(\omega_{kl} - \omega_{kn})^2 + \Gamma^2} \\ & \times \{af_a(\omega_{kl}) + af_a(\omega_{kn}) + 2f_a(\omega_{kl})f_a(\omega_{kn})\} \tilde{\mathcal{N}}_{ln}^{(\nu)}(k_z) \quad (90.16) \end{aligned}$$

where $\omega_{kl} = \sqrt{k_z^2 + (2l + 1 - 2s)eB + m^2}$ is the Landau quantized energy and the complicated expressions of $\tilde{\mathcal{N}}_{ln}^{(\nu)}(k_z)$ can be found in [5].

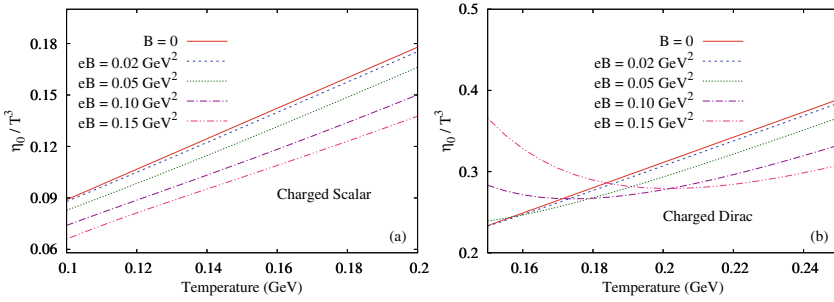


Fig. 90.1 The variation of η_0/T^3 as a function of temperature for different values of magnetic field for massless systems with relaxation time $\tau_c = 1/\Gamma = 1$ fm

90.3 Numerical Results and Conclusion

Figure 90.1 depicts the variation of the dimensionless quantity η_0/T^3 as a function of temperature for different values of magnetic field. For the Bosonic fluid, η_0 decreases with B and increases with T . We can identify the opposite roles played by T and B on the transport coefficients. Physically, we can also comprehend that the temperature is the measurement of randomness, while the magnetic field tries to align the system. So their roles on the system are expected to be opposite in nature. For the Fermionic fluid, similar trend for η_0 is observed at the lower values of magnetic field and high temperature regions. However, a non-monotonic behavior of η_0 at higher values of external magnetic field is also noticed which is probably due to the non-trivial spin structure contained in $\tilde{N}_{ln}(k_z)$ for the Dirac case. The detail discussion is addressed in [5]. As a quick and brief conclusion, we have found a field theoretical expressions with an additional temperature and magnetic field dependent information, which might be zoomed in for strong magnetic field domain.

Acknowledgements Snigdha Ghosh is funded by the Department of Higher Education, Government of West Bengal.

References

1. D.E. Kharzeev, J. Liao, S.A. Voloshin, G. Wang, *Prog. Part. Nucl. Phys.* **88**, 1–28 (2016)
2. J.O. Andersen, W.R. Naylor, A. Tranberg, *Rev. Mod. Phys.* **88**, 025001 (2016)
3. X.G. Huang, A. Sedrakian, D.H. Rischke, *Annals Phys.* **326**, 3075–3094 (2011)
4. S. Ghosh, *Int. J. Mod. Phys. A* **29**, 1450054 (2014)
5. S. Ghosh, S. Ghosh, *Phys. Rev. D* **103**, 096015 (2021)
6. S. Gavin, *Nucl. Phys. A* **435**, 826–843 (1985)
7. E.M. Lifshitz, L.P. Pitaevski, *Physical Kinetics*. Elsevier India (1981). ISBN:978-0-08-057049-5
8. X.G. Huang, M. Huang, D.H. Rischke, A. Sedrakian, *Phys. Rev. D* **81**, 045015 (2010)

Chapter 91

Latest Results on Light Flavour Hadron Production at LHC and RHIC



Sourav Kundu

Abstract The ultimate goal of heavy-ion collisions is to study the properties of the deconfined medium known as the Quark-Gluon-Plasma. Light flavour hadrons allow investigation of the bulk properties of the created medium. The light flavour particle densities at mid-rapidity allow for the study of the hadrochemistry of the event and comparison with the statistical hadronization model provide a crucial understanding of the hadronization and freeze-out temperatures. On the other hand, the shape of the transverse momentum distributions of identified hadrons at low and intermediate transverse momentum, and their evolution with the collision centrality allow constraints to be placed on the collective expansion properties of the fireball. In this review, I will discuss some recent results on light flavour hadron production at LHC and RHIC energies in the context of freeze-out temperatures in heavy-ion collisions, and the collectivity and strangeness enhancement in small collision systems.

91.1 Freeze-Out Temperatures

The hot and dense matter created in heavy-ion collisions expands collectively and cools down with time. At the pseudo-critical temperature quarks and gluons hadronize and a state of hadron gas is created. At chemical freeze-out, chemical composition of the system is fixed; the relative abundance of different kinds of particles does not change after the system reached chemical equilibrium. The chemical freeze-out stage of the system can be successfully described within a framework of a statistical thermal model [1] with system parameters such as chemical freeze-out temperature (T_{ch}) and baryon chemical potential (μ_B). The panel (a) of Fig. 91.1 shows measured light flavour hadron yields along with the non-interacting thermal model prediction in the grand canonical ensemble in 0–10% Pb–Pb collisions at $\sqrt{s_{\text{NN}}} = 2.76$

S. Kundu (✉)

European Organization for Nuclear Research (CERN), Geneva, Switzerland

e-mail: sourav.kundu@cern.ch

National Institute of Science Education and Research (NISER) HBNI, Jatni 752050, India

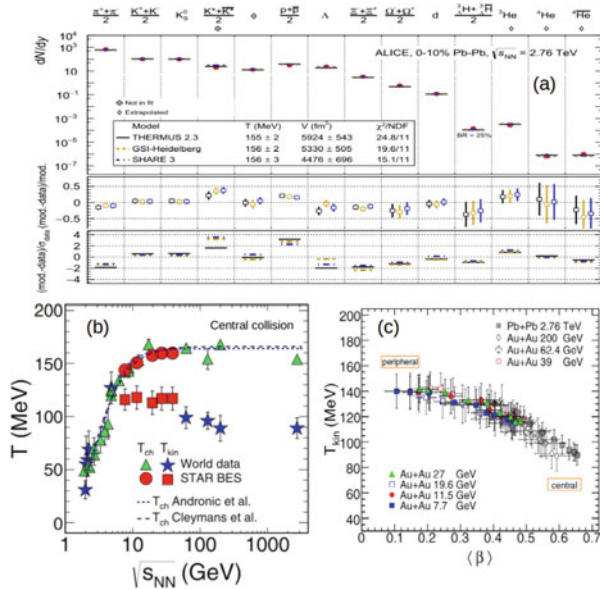


Fig. 91.1 Panel a shows the comparison between experimentally measured particle yields and three different grand canonical thermal model estimations in 0–10% Pb–Pb collisions at $\sqrt{s_{NN}} = 2.76$ TeV [2]. Panel b shows chemical and kinetic freeze-out temperature as a function of collision energy [6]. Panel c shows the correlation between kinetic freeze-out temperature and collective average transverse radial flow velocity [6]

TeV [2]. Most of the hadron yields are described by the thermal model with a good precision. The corresponding T_{ch} value in central Pb–Pb collisions at $\sqrt{s_{NN}} = 2.76$ TeV is ~ 156 MeV which is consistent with the pseudo-critical temperature 156 ± 1.5 MeV, predicted by the lattice QCD calculation [3]. Light nuclei yields are also reproduced quite well by the model although the binding energies of light nuclei are much smaller compared to the obtained T_{ch} . There are several aberrations also present. For example, the yield of short-lived resonances such as $K^*(892)^0$ is overestimated by the thermal model. Deviation of measured $K^*(892)^0$ yield from thermal yield can be understood as a loss of $K^*(892)^0$ signal due to re-scattering [4] of $K^*(892)^0$ decay daughters with other particles in the hadronic phase via elastic interactions. Tension can also be observed between the thermal model and the proton yield. This discrepancy of measured proton yield and thermal model is recently explained by interacting thermal model that includes the pion-nucleon interactions [5].

After the chemical freeze-out, the system further cools down and elastic interactions between hadrons continue till the kinetic freeze-out, where the mean free path of hadrons becomes large compared to the dynamical size of the system. The p_T spectra of the produced particles get fixed at the kinetic freeze-out. The kinetic freeze-out of the system is described by the hydrodynamics-inspired models such as the blast wave model [7] with a common average transverse radial flow velocity $\langle\beta\rangle$ which

reflects the expansion in the transverse direction and kinetic freeze-out temperature T_{kin} . Experimentally, performing a combined fit of pion, kaon and proton p_T spectra to the blast wave model, one can obtain T_{kin} and $\langle\beta\rangle$. The panel (b) of Fig. 91.1 shows extracted T_{ch} and T_{kin} as a function of $\sqrt{s_{\text{NN}}}$ [6]. Difference between the two freeze-out temperatures increases with increasing $\sqrt{s_{\text{NN}}}$, suggesting the system interacts for a longer duration at higher collision energy. On the other hand, extracted $\langle\beta\rangle$ are found to be anti-correlated with T_{kin} and is shown in the panel (c) of Fig. 91.1 for both RHIC and LHC energies [6]. Anti-correlation between $\langle\beta\rangle$ and T_{kin} fall in a universal band and does not show any significant dependency on collision energies and collision systems. In addition, $\langle\beta\rangle$ increases from peripheral to central Pb–Pb collisions indicating more rapid expansion in central heavy-ion collisions.

91.2 Collectivity in Small Collision System

In AA collisions, elliptic and radial flow manifests the hydrodynamical evolution of the produced QGP medium. Observation of elliptic flow [8], an increase of $\langle p_T \rangle$ with increasing multiplicity [9], enhancement in the baryon to meson ratio at intermediate p_T ($2 < p_T < 7$ GeV/c) [9] in pp and p–Pb collisions suggests the possibility of the presence of collective motion in small collision systems. Due to the collective motion of the produced medium, particles get a momentum boost in the transverse direction with respect to the beam direction, leading to the enhancement in the baryon to meson ratio. In the hydrodynamical picture, momentum boost due to the collective motion is expected to increase from low multiplicity to high multiplicity pp collisions and is also expected to enhance for higher mass particles compared to lower mass

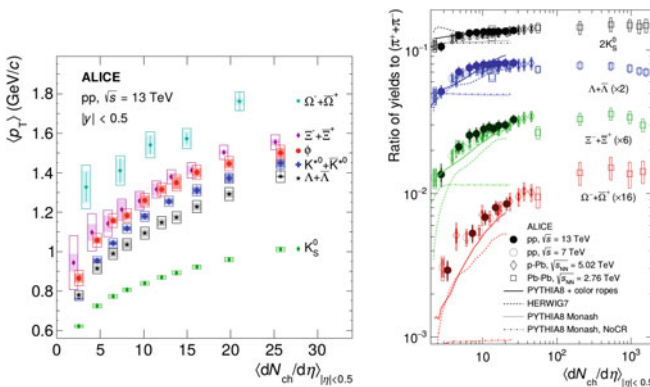


Fig. 91.2 Left panel shows $\langle p_T \rangle$ of light flavour hadrons as a function of charged particle multiplicity in pp collisions at $\sqrt{s} = 13$ TeV [10]. Right panel shows the p_T integrated yield ratio of strange hadrons to charged pion as a function of charged particle multiplicity in pp, p–Pb and Pb–Pb collisions [13]. Statistical, total systematic and multiplicity uncorrelated systematic uncertainties are represented by bars, boxes and shaded boxes

particles. The left panel of Fig. 91.2 shows the $\langle p_T \rangle$ as a function of charged particle multiplicity for various light flavour hadrons with different masses [10]. We observe that the $\langle p_T \rangle$ of light flavour hadron increases with increasing multiplicity and the enhancement of $\langle p_T \rangle$ from low to high multiplicity is more for heavier mass particles compared to lighter mass hadrons. It has been shown in [11] that the collective flow-like behaviour in small systems, similar to those observed in heavy-ion collisions, can also be explained by QCD based MC generator like PYTHIA in presence of colour reconnection (CR). The CR mechanism allows the interaction between strings and creates a flow-like effect. In central AA collisions, a mass ordering of the $\langle p_T \rangle$ values has been observed; particles with similar masses (e.g. K^{*0} , p and ϕ) have similar $\langle p_T \rangle$. This behaviour has been attributed as a consequence of hydrodynamical radial flow. However, this mass ordering breaks down for small collision systems. In pp collisions $\sqrt{s} = 13$ TeV, the $\langle p_T \rangle$ values for K^{*0} are greater than those for the more massive proton and Λ and the $\langle p_T \rangle$ values for ϕ exceed those for Λ and even approach those for Ξ , despite the approximately 30% larger mass of the Ξ compared to ϕ . This suggests that the resonances do not follow the mass ordering of $\langle p_T \rangle$ in small collision systems.

91.3 Strangeness Enhancement in Small Collision System

Enhancement of the strange particle production in heavy-ion collisions is considered as one of the primary signatures of QGP production. However, recent measurements in ALICE collaboration for the first time demonstrates the presence of strangeness enhancement in high multiplicity pp and p-Pb collisions [12, 13]. Right panel of Fig. 91.2 shows ratios of the yield of light flavour strange hadrons to the yield of charged pion in pp, p-Pb, Xe-Xe and Pb-Pb collisions [13]. The ratios are evolved smoothly with charged particle multiplicity across all collision systems at different collision energies. Strange hadron production enhanced with respect to non-strange pion from low multiplicity pp to central Pb-Pb collisions. Enhancement increases with the strangeness content of the particle in all collision systems. PYTHIA8 model with only colour reconnection does not predict any evolution or enhancement of the ratios as a function of multiplicity. However, the enhancement of strange hadron production in small collision system is qualitatively explained by PYTHIA8 with colour rope hadronization [15], which form colour ropes with larger effective string tension. On the other hand, HERWIG7 [14] that includes baryonic ropes also qualitatively explain the enhancement of strange and multi-strange baryons. Baryonic ropes is a reconnection scheme that enhances the probability of partons forming a baryon.

References

1. J. Cleymans et al., *Comp. Phys. Comm.* **180**, 84 (2009)
2. S. Acharya et al., ALICE collaboration. *Nucl. Phys. A* **971**, 1 (2018)
3. A. Bazavov et al., (HotQCD collaboration). *Phys. Lett. B* **795**, 15 (2019)
4. S. Acharya et al., ALICE collaboration. *Phys. Lett. B* **802**, 135225 (2020)
5. A. Andronic et al., *Phys. Lett. B* **792**, 304 (2019)
6. L. Adamczyk et al., STAR collaboration. *Phys. Rev. C* **96**, 044904 (2017)
7. E. Schnedermann et al., *Phys. Rev. C* **48**, 2462 (1993)
8. S. Acharya et al., ALICE collaboration. *Phys. Rev. Lett.* **123**, 142301 (2019)
9. S. Acharya et al., ALICE collaboration. *Phys. Rev. C* **99**, 024906 (2019)
10. S. Acharya et al., ALICE collaboration. *Phys. Lett. B* **807**, 135501 (2020)
11. A. Ortiz Velasquez et al., *Phys. Rev. Lett.*, **111**, 042001 (2013)
12. J. Adam et al., ALICE collaboration. *Nat. Phys.* **13**, 535, 135501 (2017)
13. S. Acharya et al., ALICE collaboration. *Eur. Phys. J. C* **80**, 693, 135501 (2020)
14. J. Bellm et al., *Eur. Phys. J. C* **76**, 196 (2016)
15. C. Bierlich et al., *JHEP* **10**, 134 (2018)

Chapter 92

Quantum Aspects of Anisotropic Conduction in Hadron Resonance Gas



Subhasis Samanta, Jayanta Dey, Sarthak Satapathy, Snigdha Ghosh, and Sabyasachi Ghosh

Abstract We have sketched multi-component structure of conductivity tensor in presence of magnetic field for hadron resonance gas (HRG), where classical to quantum transition zone is explored. A noticeable magnetic field dependent reduced conductivity in the direction of magnetic field is observed beyond the magnetic field $eB \approx m_\pi^2$ in HRG system, which is never expect in classical picture.

92.1 Introduction

A huge magnetic field can be produced in heavy ion collision (HIC) experiments. Owing to this fact, understanding the impact of this strong magnetic field on different transport coefficients of QGP is recently appeared to be an important research topic within the community of heavy ion physics. One can find a long list of [1–8] for microscopic calculations of electrical conductivity in presence of magnetic field, which is our matter of interest in present study. Among the [1–8], [1, 2, 5, 7] have gone through the classical expressions of electrical conductivity, whose multi-component values clearly show the anisotropy in co-ordinate space. However, they have not considered the quantum aspects via Landau quantization. [3, 4, 6, 8] have considered this Landau quantization, where most of them [3, 4, 6] have gone through (one component) lowest Landau level (LLL) approximation, applicable for strong field limit. In this regards, present work has explored the full multi-component structure of conductivity tensors. Their classical estimations for hadron resonance gas (HRG)

S. Samanta (✉)

Institute of Physics, Jan Kochanowski University, 25-406 Kielce, Poland
e-mail: subhasis.samant@gmail.com

J. Dey · S. Satapathy · S. Ghosh

Indian Institute of Technology Bhilai, GEC Campus, Sejbahar,
Raipur 492015, Chhattisgarh, India

S. Ghosh

Government General Degree College at Kharagpur-II Madpur,
Paschim Medinipur 721149, West Bengal, India

model are already done by [2, 7], whose quantum extension is done here, which mainly focus on the possible range of magnetic field for transition from classical to quantum conduction.

92.2 Formalism

In presence of magnetic field $\mathbf{B} = B\hat{z}$ along z -direction and electric field $\mathbf{E} = E_x\hat{x}$ along the x -direction, Ohm's law will get a matrix structure:

$$\begin{pmatrix} J_x \\ J_y \end{pmatrix} = \begin{pmatrix} \sigma_{xx} & \sigma_{xy} \\ \sigma_{yx} & \sigma_{yy} \end{pmatrix} \begin{pmatrix} E_x \\ 0 \end{pmatrix}. \quad (92.1)$$

Along with current density J_x due to non-zero σ_{xx} , we will get additional current density J_y due to Hall component σ_{yx} . In the kinetic theory framework with relaxation time approximation (RTA), we will get microscopic expressions of conductivity components σ_{xx}, σ_{yx} in terms of relaxation time τ_c and inverse of cyclotron frequency $\tau_B = \frac{\omega}{\tilde{e}B}$ with $\omega = \sqrt{\mathbf{k}^2 + m^2}$:

$$\sigma_{xx} = \sum_{B,M} g\tilde{e}^2\beta \int \frac{d^3k}{(2\pi)^3} \tau_c \frac{1}{1 + (\tau_c/\tau_B)^2} \frac{k_x^2}{\omega^2} f_0(1 \mp f_0) \quad (92.2)$$

$$\sigma_{yx} = \sum_{B,M} g\tilde{e}^2\beta \int \frac{d^3k}{(2\pi)^3} \tau_c \frac{\tau_c/\tau_B}{1 + (\tau_c/\tau_B)^2} \frac{k_y^2}{\omega^2} f_0(1 \mp f_0), \quad (92.3)$$

where $g\tilde{e}^2$ is multiplication of spin degeneracy factor g and electric charge \tilde{e} . Here, we will use hadron resonance gas (HRG) model to estimate electrical conductivity tensor of hadron matter in presence of magnetic field. So we have to use carefully different spin degeneracy factor g and electric charge \tilde{e} of different hadrons. e.g. $g = 4$ and $\tilde{e} = 2e$ for Δ^{++} , $g = 2$ and $\tilde{e} = e$ for proton p . The summation in (92.2) will go for all baryons (B) and mesons (M) in HRG model up to 2 GeV mass. Distribution function of B and M are $f_0 = 1/[e^{\beta\omega} \pm 1]$ and corresponding phase-space part $f_0(1 \mp f_0)$.

Longitudinal conductivity along z -axis will remain unaffected by magnetic field because Lorentz force never work along the direction of magnetic field (at least classically). Hence, the classical expression of the longitudinal conductivity will be

$$\sigma_{zz} = \sum_{B,M} g\tilde{e}^2\beta \int \frac{d^3k}{(2\pi)^3} \tau_c \frac{k_z^2}{\omega^2} f_0(1 \mp f_0). \quad (92.4)$$

Table 92.1 Particles energy and degeneracy

Particle species	Spin	ω_l	α_l
Baryon	1/2	$\omega_l = (k_z^2 + m^2 + 2l \tilde{e} B)^{1/2}$	$2 - \delta_{l0}$
Baryon	3/2	$\omega_l = (k_z^2 + m^2 + 2l \tilde{e} B)^{1/2}$	$4 - 2\delta_{l0} - \delta_{l1}$
Meson	0	$\omega_l = (k_z^2 + m^2 + (2l+1) \tilde{e} B)^{1/2}$	1
Meson	1	$\omega_l = (k_z^2 + m^2 + (2l+1) \tilde{e} B)^{1/2}$	$3 - \delta_{l0}$

Now, this scenario will be changed in quantum description via Landau quantizations, where energy ω and phase space $\int d^3k$ will be modified as $\omega \rightarrow \omega_l$ and

$$g \int \frac{d^3k}{(2\pi)^3} \rightarrow \sum_{l=0}^{\infty} \alpha_l \frac{|\tilde{e}|B}{2\pi} \int_{-\infty}^{+\infty} \frac{dk_z}{2\pi}. \quad (92.5)$$

The ω_l 's and α_l 's for different hadrons are given in Table 92.1.

Here, we also assume roughly, $k_x^2 \approx k_y^2 \approx \left(\frac{k_x^2 + k_y^2}{2}\right) = \frac{2|\tilde{e}|B}{2}$ for B and $\frac{(2l+1)\tilde{e}B}{2}$ for M, then conductivity components can be expressed as

$$\begin{aligned} \sigma^{xx} &= \sum_{B,M} \tilde{e}^2 \beta \sum_{l=0}^{\infty} \alpha_l \frac{|\tilde{e}|B}{2\pi} \int_{-\infty}^{+\infty} \frac{dk_z}{2\pi} \frac{l|\tilde{e}|B}{\omega_l^2} \tau_c \frac{1}{1 + (\tau_c/\tau_B)^2} f_0(\omega_l) [1 \mp f_0(\omega_l)] \\ \sigma^{xy} &= \sum_{B,M} \tilde{e}^2 \beta \sum_{l=0}^{\infty} \alpha_l \frac{|\tilde{e}|B}{2\pi} \int_{-\infty}^{+\infty} \frac{dk_z}{2\pi} \frac{l|\tilde{e}|B}{\omega_l^2} \tau_c \frac{\tau_c/\tau_B}{1 + (\tau_c/\tau_B)^2} f_0(\omega_l) [1 \mp f_0(\omega_l)] \\ \sigma^{zz} &= \sum_{B,M} \tilde{e}^2 \beta \sum_{l=0}^{\infty} \alpha_l \frac{|\tilde{e}|B}{2\pi} \int_{-\infty}^{+\infty} \frac{dk_z}{2\pi} \frac{k_z^2}{\omega_l^2} \tau_c f_0(\omega_l) [1 \mp f_0(\omega_l)]. \end{aligned} \quad (92.6)$$

92.3 Results and Conclusion

If we analyze the expression of conductivity tensor, then we will get $\sigma_{xx} = \sigma_{yy} = \sigma_{zz}$ in the limit of $B \rightarrow 0$ but at finite magnetic field ($B \neq 0$), we will get anisotropic property $\sigma_{xx} = \sigma_{yy} < \sigma_{zz}$. It is cyclotron motion of charge particle due to magnetic field, for which σ_{xx} is reduced by a factor $1/[1 + \left(\frac{\tau_c}{\tau_B}\right)^2]$, where τ_c and τ_B are relaxation time and inverse of cyclotron frequency. On the other hand, σ_{zz} remain unchanged as Lorentz force will not work along the direction of magnetic field. For a fixed value of relaxation time $\tau_c = 1$ fm, the τ_B 's of different hadrons collectively

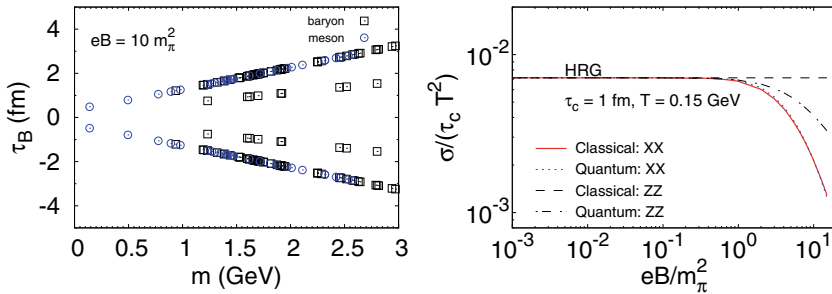


Fig. 92.1 Left panel: Inverse of cyclotron frequency of different hadrons. Right panel: Parallel (xx) and perpendicular (zz) components of electrical conductivity for classical and quantum expressions

make σ_{xx} reduce from its isotropic or field free value. Left panel of Fig. 92.1 shows τ_B vs mass m of different hadrons. One can realize that lower mass and larger charge hadrons have more contribution in anisotropic conduction than higher mass and lower charge hadrons.

Next in the right panel of Fig. 92.1, we have plotted electrical conductivity components for classical and quantum cases, addressed in (92.2, 92.4, and 92.6) respectively. Here, we notice that in low B , classical values of σ_{xx} and σ_{zz} are same, which indicates isotropic properties of medium and at high B , σ_{xx} is becoming lower than σ_{zz} , which represents anisotropic conduction. Now, when we go to quantum estimations of σ_{xx} and σ_{zz} , then we find their deviations from their corresponding classical curves. Though the deviation between classical and quantum curves of σ_{xx} is almost non-distinguishable but same for σ_{zz} is quite noticeable. It is due to Landau quantization, quantum curves are deviated from classical curves. Interestingly, quantum curves of σ_{zz} for baryons and mesons are respectively enhanced and reduced respectively. During their collective sum, mesons are appeared to be dominating due to abundance of mesons in lower mass range. At the end, quantum version of HRG system can face a reduced value of B dependent longitudinal conductivity beyond $eB \approx m_\pi^2$ (for $T = 0.150$ GeV), which cannot be expected in classical picture and to the best of our knowledge, this is first time addressed by present work.

References

1. J. Dey, S. Satapathy, P. Murmu, S. Ghosh, Shear viscosity and electrical conductivity of relativistic fluid in presence of magnetic field: a massless case. [arxiv:1907.11164](https://arxiv.org/abs/1907.11164) [hep-ph]
2. A. Dash, S. Samanta, J. Dey, U. Gangopadhyaya, S. Ghosh, V. Roy, Anisotropic transport properties of Hadron resonance gas in magnetic field. *Phys. Rev. D* **102**, 016016 (2020)
3. K. Hattori, D. Satow, Electrical conductivity of quark-gluon plasma in strong magnetic fields. *Phys. Rev. D* **94**, 114032 (2016)
4. M. Kurian, V. Chandra, Effective description of hot QCD medium in strong magnetic field and longitudinal conductivity. *Phys. Rev. D* **96**(no. 11), 114026 (2017)

5. A. Harutyunyan, A. Sedrakian, Electrical conductivity of a warm neutron star crust in magnetic fields. *Phys. Rev. C* **94**, 025805 (2016)
6. S. Rath, B.K. Patra, Revisit to electrical and thermal conductivities, Lorenz and Knudsen numbers in thermal QCD in a strong magnetic field. *Phys. Rev. D* **100** 016009 (2019); Effect of magnetic field on the charge and thermal transport properties of hot and dense QCD matter. *Eur. Phys. J. C* **80** (2020)
7. A. Das, H. Mishra, R.K. Mohapatra, Electrical conductivity and Hall conductivity of a hot and dense hadron gas in a magnetic field: a relaxation time approach. *Phys. Rev. D* **99**, 094031 (2019)
8. S. Ghosh, A. Bandyopadhyay, R.L.S. Farias, J. Dey, G. Krein, Anisotropic electrical conductivity of magnetized hot quark matter. *Phys. Rev. D* **102**, 114015 (2020)

Chapter 93

Topological Studies of Charged Particle Production and Search for Jet Quenching Effects in Small Collision Systems with ALICE



Sushanta Tripathy

Abstract Results for high multiplicity pp and p–Pb collisions at the LHC have revealed that these small collision systems exhibit features of collectivity. To understand the origin of these unexpected phenomena, the relative transverse activity classifier (R_T) can be exploited as a tool to disentangle soft and hard particle production, by studying the yield of charged particles in different topological regions associated with transverse momentum trigger particles. This allows to study system size dependence of charged particle production of different origins and in particular search for jet-quenching effects. Here, results on the system size and R_T dependence of charged particle production in pp, p–Pb and Pb–Pb collisions at $\sqrt{s_{NN}} = 5.02$ TeV are presented.

93.1 Introduction

Recent measurements by ALICE [1] show a smooth increase of strange to non-strange particle ratios across pp, p–Pb and Pb–Pb collisions as a function of charged-particle multiplicities at the LHC. This universal scaling with particle multiplicity may point towards a common underlying physics mechanism across collision systems. However, no onset of jet quenching effects has been observed so far in the smaller pp and p–Pb systems [2]. To disentangle the phenomena of soft (underlying event) and hard (jet induced) particle production, the relative transverse activity classifier (R_T), an event shape observable, can be exploited as a powerful tool. Here, the production of

(for the ALICE collaboration).

S. Tripathy (✉)

Instituto de Ciencias Nucleares, UNAM, Mexico City, Mexico

presently at INFN - sezione di Bologna, Bologna BO, Italy

e-mail: sushanta.tripathy@cern.ch

light flavour charged hadrons for different classes of R_T in pp, p–Pb and Pb–Pb collisions at $\sqrt{s_{NN}} = 5.02$ TeV are reported. Also, we present a search for jet quenching behaviour in small collision systems.

93.2 Relative Transverse Activity Classifier (R_T)

Using R_T proposed in [3], the final-state particle production can be studied as a function of varying underlying events. To define R_T , the analysed events are required to have a leading trigger particle above a certain p_T . Relative to the leading trigger particle, an event can be classified into three different azimuthal regions. Assuming ϕ_t as the azimuthal angle for the trigger particle and ϕ_a as the azimuthal angle of the associated particles, the regions can be classified as the following:

- Near side: $|\phi_t - \phi_a| < \frac{\pi}{3}$
- Away side: $|\phi_t - \phi_a| > \frac{2\pi}{3}$
- Transverse side: $\frac{\pi}{3} \leq |\phi_t - \phi_a| \leq \frac{2\pi}{3}$

The near side is dominated by the jet activity related to the trigger particle. Since jets are typically produced as pairs back-to-back in azimuthal angle, the away side will contain some of these back-scattered jets. The transverse side is dominated by particle production in the underlying events (UE). Both the near and away side also contain similar UE production as in transverse side. Thus, one can subtract the UE from near and away side by subtracting the yield in transverse side, see Sect. 93.3. The leading- p_T selection of $8 < p_T^{\text{trig}} < 15$ GeV/ c ensures that the number density in the transverse region remains almost independent of leading particle p_T [4] and reduces the impact of possible elliptic flow on the measurements. R_T is defined as [3, 5],

$$R_T = \frac{N_{\text{ch}}^{\text{TS}}}{\langle N_{\text{ch}}^{\text{TS}} \rangle}, \quad (93.1)$$

where $N_{\text{ch}}^{\text{TS}}$ is the charged particle multiplicity in the transverse side. The events with $R_T \rightarrow 0$ are the events expected to be dominated by jet fragmentation.

93.3 Results and Discussion

Figure 93.1 shows $\langle p_T \rangle$ of charged-particles as a function of R_T in the near (left), away (middle), and transverse (right) sides for pp, p–Pb and Pb–Pb collisions. The measurement of charged-particles follows a similar procedure as described in [6]. The near and away side $\langle p_T \rangle$ for pp and p–Pb collisions decreases at low- R_T and it saturates for high- R_T . This behaviour indicates that the contribution from the near and away side jet dominates at low- R_T and the soft particle production starts contributing

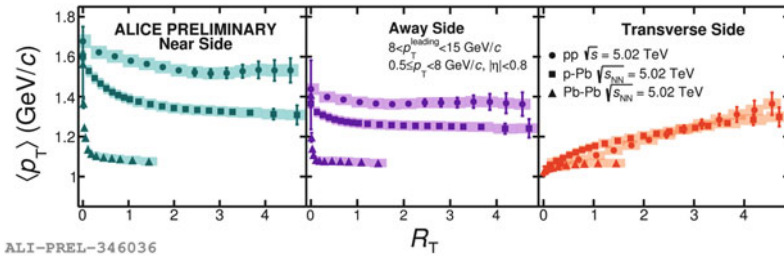


Fig. 93.1 System size dependence of $\langle p_T \rangle$ for charged-particles as a function of R_T in the near (left), away (middle), and transverse (right) sides

in high- R_T region. Another interesting observation to note that the values of $\langle p_T \rangle$ are similar for all systems for $R_T \rightarrow 0$. One would naively expect this behaviour as this region has very little contribution from soft particles i.e. UE. The $\langle p_T \rangle$ for transverse side increases with R_T as the UE increases with increase in R_T . For large R_T , the $\langle p_T \rangle$ approaches to a similar value in all three topological regions for a given system as they are mostly dominated by the UE.

To investigate the presence of jet-quenching effects in small collision systems, $I_{pp,p-Pb,Pb-Pb}$, an observable which is calculated from the yields of different topological regions, is calculated as a function of $\langle N_{ch}^{TS} \rangle$ for different VOM (VOA) multiplicity classes of pp and Pb-Pb (p-Pb) collisions. The $I_{pp,p-Pb,Pb-Pb}$ is a similar quantity (I_{AA}) calculated as in [7]. The $I_{pp,p-Pb,Pb-Pb}$ is expected to be highly sensitive to medium effects. A suppression of this observable in the away side would indicate the presence of jet quenching, while an enhancement in the near side would indicate a bias due to trigger particle selection and/or presence of medium effects. It is defined as the ratio of yield in the near or away region (after subtraction of yield in transverse side) in different collision systems to the yield in the near or away region in minimum bias pp collisions. It can be expressed as

$$I_{pp,p-Pb,Pb-Pb} = \frac{Y_{pp,p-Pb,Pb-Pb} - Y_{TS}^{pp,p-Pb,Pb-Pb}}{Y_{pp \text{ min.bias}} - Y_{TS}^{pp \text{ min.bias}}}. \quad (93.2)$$

Here, Y represents the integrated yield of charged particles in a particular topological region. For these results we have not made a direct selection on N_{ch}^{TS} , as the direct selection on N_{ch}^{TS} biases the near and away side yields [8]. Thus, the events are selected based on the forward rapidity estimator (VOM for pp and Pb-Pb collisions and VOA for p-Pb collisions) and the corresponding N_{ch}^{TS} are calculated for each multiplicity class. Figure 93.2 shows the $I_{pp,p-Pb,Pb-Pb}$ in the range $4 < p_T^a < 6$ GeV/c as a function of $\langle N_{ch}^{TS} \rangle$ in different VOM/VOA multiplicity classes for the near (left) and away (right) side in pp, p-Pb, and Pb-Pb collisions at $\sqrt{s_{NN}} = 5.02$ TeV. Here, p_T^a is the transverse momentum of associated particles with respect to a leading trigger particle. The values of I_{Pb-Pb} for most central and most peripheral

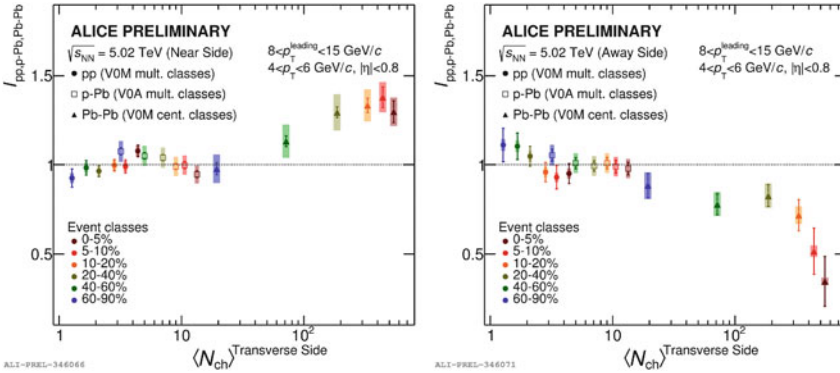


Fig. 93.2 $I_{pp,p-Pb,Pb-Pb}$ as a function of $\langle N_{ch}^{TS} \rangle$ in different VOM/VOA multiplicity classes for the near (left) and away (right) side in pp, p-Pb, and Pb-Pb collisions at $\sqrt{s_{NN}} = 5.02$ TeV

Pb-Pb collisions show similar trends as reported by ALICE in [7] at Pb-Pb collisions at $\sqrt{s_{NN}} = 2.76$ TeV. In small collision systems, no enhancement (suppression) of $I_{pp,p-Pb}$ is observed in near (away) sides for pp or p-Pb collisions within uncertainties. This indicates the absence of jet-quenching effects in small collision systems in the measured $\langle N_{ch}^{TS} \rangle$ ranges.

93.4 Summary

In summary, using R_T one can vary the magnitude of the underlying event contribution and study the final state particle production in different topological regions. The system size dependence of charged-particle production indicates that the contribution from the near and away side jet dominates at low- R_T . For high- R_T , the $\langle p_T \rangle$ approaches a similar value in all three topological regions for a given collision system. In contrast to Pb-Pb collisions, no suppression of $I_{pp,p-Pb}$ is observed in the away side for pp and p-Pb collisions, which indicates the absence of jet-quenching effects for small collision systems or if any, the jet-quenching effects are very small to be detected in the measured $\langle N_{ch}^{TS} \rangle$ ranges.

Acknowledgements S. T. acknowledges the support from CONAcYT under the Grant No. A1-S-22917 and postdoctoral fellowship of DGAPA UNAM.

References

1. J. Adam et al., ALICE collaboration. *Nat. Phys.* **13**, 535 (2017)
2. J.L. Nagle, W.A. Zajc, *Ann. Rev. Nucl. Part Sci.* **68**, 211 (2018)
3. T. Martin, P. Skands, S. Farrington, *Eur. Phys. J. C* **76**, 299 (2016)
4. S. Acharya et al., ALICE collaboration. *JHEP* **04**, 192 (2020)
5. A. Ortiz, L. Valencia Palomo, *Phys. Rev. D* **96**, 114019 (2017)
6. S. Acharya et al., ALICE collaboration. *JHEP* **11**, 013 (2018)
7. K. Aamodt et al., ALICE collaboration. *Phys. Rev. Lett.* **108**, 092301 (2012)
8. G. Bencédi, A. Ortiz, S. Tripathy, *J. Phys. G* **48**, 015007 (2020)

Chapter 94

Application of Magnetohydrodynamics in High-Energy Heavy-Ion Collisions: Recent Progress



Victor Roy

Abstract The strong transient magnetic field produced in the early stages of high-energy heavy-ion collisions provides the opportunity to understand the finite temperature QCD matter under strong fields. One of the main goals of high energy heavy-ion collisions experiments is the detection of Chiral Magnetic Effect (CME), a quantum anomaly-based phenomena of charge separation in hot and dense Quark-Gluon-Plasma (QGP). Relativistic magneto-hydrodynamics is the relevant framework to describe the space-time evolution of the fluid and field. In this mini-review, we discuss the recent progress in relativistic magneto-hydrodynamics and its application in heavy-ion collisions.

94.1 Introduction

Long-range magnetic fields generate fascinating phenomena. For example, the magnetic field plays a vital role in solar dynamics, astrological structure formation. In laboratory experiments, it is used for confining electromagnetic plasma in fusion studies and for controlling beams of nuclei in collider experiments, to name a few. In most of the above examples, the system under consideration can be approximated as a fluid consists of charged particles, and hence the interaction of these systems with the electromagnetic field is described by the magneto-hydrodynamics (MHD) framework, which is solving energy-momentum conservation and Maxwell equations self consistently. In recent years, the magneto-hydrodynamics has found new applications in other branches of physics such as transport near relativistic quantum critical points in graphene [1], Weyl semi-metal etc. [2]. Also, femto-scopic Quark-Gluon-Plasma (QGP) produced in high energy nuclear physics collider experiments

V. Roy (✉)
School of Physical Sciences, National Institute of Science Education and Research,
Jatni 752050, India
e-mail: victor@niser.ac.in

Homi Bhabha National Institute, Training School Complex, Anushaktinagar, Mumbai 400094, India

are expected to be evolved for some time as fluid under intense transient magnetic field, and the corresponding space-time evolution is expected to be governed by the relativistic MHD equations. This is because the first principle lattice QCD studies show that QGP is an electrically conducting fluid with temperature dependent electrical conductivity σ [3] in the temperature range $T \sim (0.5 - 3.0)T_c$. The positively charged nucleus moving with relativistic speed produces a strong transient magnetic field ($\sim 10^{18} G$ for Au+Au $\sqrt{S_{NN}}=200$ GeV collisions) in the overlap zone of the two colliding nuclei. The presence of such an intense magnetic field and the interplay of it with chiral fermions (approximately massless quarks) in the QGP opens up the possibility of experimental observation of quantum anomaly induced phenomenon of Chiral Magnetic Effect(CME) [4]. Unfortunately, we cannot cite many excellent experimental and theoretical articles on CME for space limitation. According to CME, a charged current is produced along the direction of the magnetic field. It is possible to find it experimentally by studying charge-dependent flow harmonics of hadrons. However, the small-signal and large backgrounds have so far inhibited an unambiguous conclusion. It is also essential to have an exact space-time evolution of the magnetic fields to estimate the strength of the CME signal theoretically.

94.1.1 Relativistic Magnetohydrodynamics Formulation

In its simplest form, the relativistic (ideal) magneto-hydrodynamics equations in flat space-time ($g^{\mu\nu} = \text{diag}(1, -1, -1, -1)$) are given by

$$\partial_\nu T^{\mu\nu} = 0, \partial_\mu F^{\mu\nu} = j^\mu, \partial_\mu \mathcal{F}^{\mu\nu} = 0, \quad (94.1)$$

where $T^{\mu\nu} = T_{\text{fluid}}^{\mu\nu} + T_{\text{field}}^{\mu\nu}$, $F^{\alpha\beta} = u^\alpha E^\beta - E^\alpha u^\beta + \epsilon_{\gamma\delta}^{\alpha\beta} u^\gamma B^\delta$, $\mathcal{F}^{\mu\nu} = \frac{1}{2} \epsilon^{\mu\nu\alpha\beta} F_{\alpha\beta}$. The electric and magnetic field four vectors can be defined with respect to an appropriate time-like velocity four vector u^μ as $E^\alpha = F^{\alpha\beta} u_\beta$, $B^\beta = \frac{1}{2} \epsilon^{\alpha\beta\gamma\delta} F_{\gamma\delta} u_\alpha$. The ideal MHD limit is realised in the limit of large electrical conductivity ($\sigma \rightarrow \infty$), more precisely for magnetic Reynolds number $R_m = l\mu\nu\sigma \gg 1$ (here v is the fluid three velocity, l length scale, and μ is magnetic permeability). In the ideal MHD limit the electric field vanishes inside fluid ($E^\mu = 0$). Neglecting viscous dissipation, the energy-momentum tensor for the fluid and the field in this case can be written as: $T_{\text{fluid}}^{\mu\nu} = (\epsilon + p)u^\mu u^\nu - pg^{\mu\nu}$ and $T_{\text{field}}^{\mu\nu} = -F^{\mu\alpha} F_\alpha^k + \frac{1}{4} g^{\mu\nu} F_{\gamma\delta} F^{\gamma\delta} = B^2 u^\mu u^\nu - \frac{1}{2} B^2 g^{\mu\nu} - B^2 b^\mu b^\nu$, where $B^2 = B^\mu B_\mu$ and $b^\mu = \frac{B^\mu}{B}$. In general, inside the fluids with finite conductivity $E^\mu \neq 0$ and to a linear approximation the charged current is given by $j^\mu = \rho u^\mu + \sigma^{\mu\beta} E_\beta$, where ρ is the charge density and $\sigma^{\mu\beta}$ is the conductivity tensor. Up until recently the formulation of causal relativistic viscous MHD (CRVMHD) from the kinetic theory was unavailable. In [5] the first formulation of CRVMHD from the Boltzmann equation was derived using the moment method. The equations for CRVMHD were recently derived using Relaxation Time Approximation (RTA) and Chapman-Enskog expansion for the ideal-MHD case [6].

Unlike the moment method, in RTA approximation, the off-equilibrium distribution function does not truncate to a certain order in momentum. The two formulations give similar results for the evolution of viscous stresses in a magnetic field albeit, with few new terms found in the RTA approximation. For more details, see [6]. Widely used relativistic causal second-order hydrodynamics theory for ordinary fluid due to the Israel-Stewart is causal in a limited way. The causality and stability of ideal-RMHD and recently developed CRVMHD were investigated in [7]. It was found that ideal-MHD and CRVMHD are stable and causal for realistic values of magnetic fields, like the second-order IS theory for zero magnetic fields, with additional non-hydrodynamic modes. As expected, additional modes of sound propagation (Alfvén and Magnetosonic) appeared in the MHD case; accordingly, the mode dependence causality condition was observed. Interested readers may refer to [8] for other recent development of theoretical aspects of RMHD. In this mini-review, we mainly focus on the numerical aspects of RMHD in heavy-ion collisions. It is worthwhile to mention that a few analytic/semi-analytic solutions have also been found recently in the context of heavy-ion collisions, but we will not discuss them here.

94.1.1.1 Application of RMHD in Heavy Ion Collisions

Although the need for an RMHD simulation in the heavy-ion collision was realized almost fifteen years ago [4], it was not until recently applying numerical RMHD in heavy-ion collisions began. In Table 94.1 we give summary of recent progress. In one of the pioneering works, Mohapatra et al. [9] showed that the anisotropy of fluid velocity hence the elliptic flow of charged hadrons, increases in the presence of a magnetic field. After that, Tuchin calculated the anisotropic viscosities from the Boltzmann equation for a QGP in magnetic field [10]. He further showed (with some

Table 94.1 Chronological development of numerical RMHD in heavy ion collisions

Year	Main features and findings	References
2011	Prediction of complex flow pattern and enhancement of v_2	Mohapatra et al. [9]
2012	The viscous correction to the distribution function in a magnetic field and enhancement of elliptic flow	Tuchin [10]
2013	Charged dependence directed flow in non-relativistic MHD	Gursoy et al. [11]
2014	Electromagnetic response of the QGP at RHIC and LHC energies is in a quantum regime	Zakharov [12]
2016	3+1-d hydro+external magnetic field, paramagnetic squeezing small reduction in elliptic flow	Pang et al. [13]
2017	2+1-d reduced MHD, enhanced momentum anisotropy and elliptic flow	Roy et al. [14]
2020	3+1-d ideal-MHD (ECHO-QGP), the initial magnetic field obtained for finite chiral and normal conductivity	Inghirami et al. [15, 16]

assumptions) that the elliptic flow enhances $\sim 30\%$ in the presence of a magnetic field. One of the first numerical estimations of the influence of magnetic fields on anisotropic flow was due to Gursoy et al. [11] where using non-relativistic MHD they showed that the directed flow changes in magnetic fields. One of the first studies of relativistic MHD by Pang et al. [13] showed that the elliptic flow of charged hadrons reduces slightly for a paramagnetic QGP. This phenomenon was named “paramagnetic squeezing.” In collaboration with others, the current author explored the effect of magnetic field on the anisotropic flow observable [14]. Considering QGP as an ideal-MHD system, we showed that there might be a substantial amount of enhancement of charged pion elliptic flow in a magnetic field. Note that the main difference between [13] and [14] is the magnetic nature of QGP. Both [13], and [14] considered a parameterized magnetic field; hence these studies are not self-consistent RMHD. To our best knowledge, there are only a few works using self-consistent numerical simulation of RMHD in heavy-ion collision [12, 15, 16] albeit with some strong assumptions. In [15, 16] an improved version of the ECHO-QGP numerical code was used, and it was found that indeed the elliptic flow of charged pion increases in the presence of the magnetic field.

Notes and Comments.

The numerical RMHD is an essential and useful framework for high-energy heavy-ion collisions. There are quite a few exciting developments in the recent past. Many more things to be done in the future, for example, the interplay of spin and magnetic fields may give rise to the polarisation of vector mesons. A proper framework of causal RMHD with spin is still missing; very recently, this issue was discussed in [17]. The ideal MHD approximation is not appropriate for QGP; developing a resistive RMHD code for heavy-ion collisions is required for a realistic description. Last but not least, the extraction of shear viscosity to entropy density ratio of QGP perhaps needed more careful consideration of taking anisotropic transport coefficients into account.

References

1. J. Crossno, J.K. Shi, K. Wang et al., *Science* **351**, 1058 (2016)
2. A. Lucas, R.A. Davison, S. Sachdev, *Proc. Natl. Acad. Sci.* **113**, 9463 (2016)
3. A. Amato, G. Aarts, C. Allton, P. Giudice, S. Hands, J.I. Skullerud, *Phys. Rev. Lett.* **111**(17), 172001 (2013)
4. D.E. Kharzeev, L.D. McLerran, H.J. Warringa, *Nucl. Phys. A* **803**, 227–253 (2008)
5. G.S. Denicol, X.G. Huang, E. Molnár, G.M. Monteiro, H. Niemi, J. Noronha, D.H. Rischke, Q. Wang, *Phys. Rev. D* **98**(7), 076009 (2018)
6. A.K. Panda, A. Dash, R. Biswas, V. Roy, [arXiv:2011.01606](https://arxiv.org/abs/2011.01606) [nucl-th]
7. R. Biswas, A. Dash, N. Haque, S. Pu, V. Roy, *JHEP* **10**, 171 (2020)
8. J. Hernandez, P. Kovtun, *JHEP* **05**, 001 (2017)
9. R.K. Mohapatra, P.S. Saumia, A.M. Srivastava, *Mod. Phys. Lett. A* **26**, 2477–2486 (2011)
10. K. Tuchin, *J. Phys. G* **39**, 025010 (2012)
11. U. Gursoy, D. Kharzeev, K. Rajagopal, *Phys. Rev. C* **89**(5), 054905 (2014)

12. B.G. Zakharov, *Phys. Lett. B* **737**, 262–266 (2014)
13. L.G. Pang, G. Endrődi, H. Petersen, *Phys. Rev. C* **93**(4), 044919 (2016)
14. V. Roy, S. Pu, L. Rezzolla, D.H. Rischke, *Phys. Rev. C* **96**(5), 054909 (2017)
15. G. Inghirami, L. Del Zanna, A. Beraudo, M.H. Moghaddam, F. Becattini, M. Bleicher, *Eur. Phys. J. C* **76**(12), 659 (2016)
16. G. Inghirami, M. Mace, Y. Hirono, L. Del Zanna, D.E. Kharzeev, M. Bleicher, *Eur. Phys. J. C* **80**(3), 293 (2020)
17. R. Singh, M. Shokri, R. Ryblewski, [arXiv:2103.02592](https://arxiv.org/abs/2103.02592) [hep-ph]

Chapter 95

Recent Bottomonium Measurements in pp, p–Pb, and Pb–Pb Collisions at Forward Rapidity with ALICE at the LHC



Wadut Shaikh

Abstract In ultrarelativistic nucleus–nucleus collisions, a deconfined state of strongly interacting matter is thought to be produced, commonly known as the quark–gluon plasma (QGP). Quarkonia, bound states of a heavy quark and antiquark, are important probes to study the properties of the QGP. At the LHC, bottomonium ($b\bar{b}$) is of particular interest to study the QGP complementarily to the lighter charmonium ($c\bar{c}$) system. In addition to the measurements in nucleus–nucleus collisions, reference measurements in proton–proton and proton–nucleus collisions have been also carried out in order to better understand the bottom quark production and cold nuclear matter effects. ALICE measures the bottomonium production in the dimuon decay channel at forward rapidity ($2.5 < y_{\text{lab}} < 4.0$) with the muon spectrometer. In this contribution, the recent measurements of bottomonium nuclear modification factors and azimuthal anisotropies in Pb–Pb collisions are presented. The bottomonium production in p–Pb and pp collisions is also discussed.

95.1 Introduction

Quarkonia are useful probes to investigate the properties of the deconfined medium created in ultrarelativistic heavy-ion collisions. The modification of the ground charmonium state (J/ψ) production at LHC energies in heavy-ion collisions with respect to the binary-scaled yield in pp collisions has been explained as an interplay of the suppression [1] and the regeneration mechanisms [2, 3]. Bottomonia (Υ) are also expected to be suppressed inside the QGP by the color-screening effect and medium-induced dissociation [4]. For the Υ family, the regeneration effects are expected to be negligible due to the smaller number of b quarks produced in the collisions [5]. In

W. Shaikh (✉)
Saha Institute of Nuclear Physics, Kolkata 700064, India
e-mail: wadut.shaikh@cern.ch

Mugberia Gangadhar Mahavidyalaya, Purba Medinipur 721425, India

© The Author(s), under exclusive license to Springer Nature Singapore Pte Ltd. 2022
B. Mohanty et al. (eds.), *Proceedings of the XXIV DAE-BRNS High Energy Physics Symposium, Jatni, India*, Springer Proceedings in Physics 277,
https://doi.org/10.1007/978-981-19-2354-8_95

517

addition, the regenerated quarkonia are expected to inherit the azimuthal anisotropy that the constituting quarks may have obtained by participating to the collective motion in the QGP. However, the Cold Nuclear Matter (CNM) effects which include shadowing, parton energy loss, and interaction with hadronic degrees of freedom may also lead to a modification of bottomonium production. In order to disentangle the CNM effects from the hot nuclear matter effects, Υ production has been studied in p–Pb collisions, in which the QGP is traditionally not expected to be formed. In pp collisions, the quarkonium production can be described as the creation of a heavy-quark pair ($q\bar{q}$) (perturbative process) followed by its hadronization into a bound state (non-perturbative process). None of the existing models fully describes the quarkonium production in pp collisions and more differential measurements can further constrain the quarkonium production models in elementary hadronic collisions.

95.2 Analysis and Results

The ALICE Collaboration has studied bottomonium production in various collision systems (pp, p–Pb, Pb–Pb) at different center-of-mass energies per nucleon pair $\sqrt{s_{NN}}$ down to zero transverse momentum (p_T) and at forward rapidity ($2.5 < y < 4$) with the Muon spectrometer [6] through the dimuon decay channel.

pp Collisions

The inclusive $\Upsilon(nS)$ production cross sections have been measured for the first time in pp collisions at $\sqrt{s} = 5.02$ TeV at forward rapidity. In Fig. 95.1 (left), the energy dependence of $\Upsilon(nS)$ states is shown and a steady increase of the cross sections is observed with increasing \sqrt{s} . The differential cross sections as function of rapidity and p_T at $\sqrt{s} = 5.02$ TeV have been also measured. In Fig. 95.1 (right), the bottomonium production shows a linear increase with charged-particle multiplicity at forward rapidity.

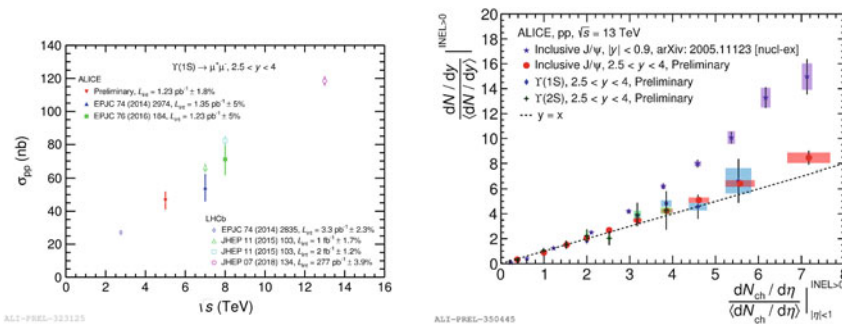


Fig. 95.1 Inclusive $\Upsilon(nS)$ production cross sections as a function of the collision energy in pp collisions of ALICE and LHCb measurements (left). Relative quarkonium yield as a function of the relative charged-particle density in pp collisions at $\sqrt{s} = 13$ TeV (right)

p–Pb Collisions

The CNM effects can be studied in p–Pb collisions via the nuclear modification factor (R_{pA}), defined as

$$R_{pPb} = \frac{\sigma_{pPb}}{A_{Pb} \cdot \sigma_{pp}},$$

where σ_{pPb} and σ_{pp} are the production cross sections in p–Pb and pp collisions, respectively. A_{Pb} is the atomic mass number (208) of the Pb nucleus. The Υ production as function of rapidity, transverse momentum and multiplicity in p–Pb collisions at $\sqrt{s_{NN}} = 8.16$ TeV have been measured by ALICE [7]. The results show a suppression of the $\Upsilon(1S)$ yields, with respect to the ones measured in pp collisions. The R_{pPb} values are similar at forward and backward rapidity with a slightly stronger suppression at low p_T , while in both rapidity intervals there is no evidence for a centrality dependence [7]. Models based on nuclear shadowing, coherent parton energy loss or interactions with comoving particles fairly describe the data at forward rapidity, while they tend to overestimate the R_{pPb} at backward- y_{cms} as shown in Fig. 95.2 (left).

$\Upsilon(2S)$ and $\Upsilon(3S)$ R_{pPb} as a function of y_{cms} are shown in Fig. 95.2 (right). The $\Upsilon(2S)$ measurement also shows a suppression, similar to the one measured for the $\Upsilon(1S)$, in the two investigated rapidity intervals. Finally, a first measurement of the $\Upsilon(3S)$ has been performed, even if the large uncertainties prevent a detailed comparison of its behavior in p–Pb collisions with respect to the other bottomonium states.

Pb–Pb Collisions

The nuclear modification factor for a given centrality class i in A–A collisions can be defined as

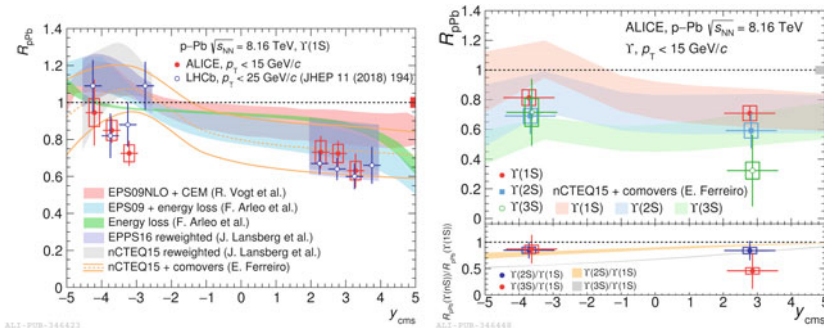


Fig. 95.2 The $\Upsilon(1S)$ R_{pPb} as a function of y_{cms} with different model predictions in p–Pb collisions at $\sqrt{s_{NN}} = 8.16$ TeV (left). $\Upsilon(nS)$ R_{pPb} as a function of y_{cms} with nCTEQ15 shadowing prediction including the comover interaction

$$R_{AA}^i = \frac{d^2 N_i^{AA}/dy dp_T}{\langle T_{AA}^i \rangle d^2 \sigma^{pp}/dy dp_T},$$

where $d^2 N_i^{AA}/dy dp_T$ is the yield in nucleus–nucleus collisions, $\langle T_{AA}^i \rangle$ is the nuclear overlap function, and $d^2 \sigma^{pp}/dy dp_T$ is the production cross section in pp collisions. The measurements of $\Upsilon(1S)$ and $\Upsilon(2S)$ production at forward rapidity have been obtained for Pb–Pb collisions at $\sqrt{s_{NN}} = 5.02$ TeV by combining the 2015 and 2018 datasets [8]. The suppression of $\Upsilon(1S)$ gets stronger for the more central collisions, as shown in Fig. 95.3 (left). The rapidity dependence of $\Upsilon(1S)$ R_{AA} hints at a decrease for the most forward rapidity interval [8]. No significant p_T dependence of R_{AA} is observed [8, 9]. It is worth noting that the nuclear modification factor in p–Pb collision shows a significant p_T dependence in both forward and backward rapidity interval measured by ALICE. The different behavior between p–Pb and Pb–Pb collisions may impose some constraints on theoretical models in near future. A larger suppression of $\Upsilon(2S)$ compared to $\Upsilon(1S)$ is also observed.

The azimuthal anisotropic “elliptic” flow is usually quantified in terms of the second harmonic coefficient (v_2) of the Fourier decomposition of the azimuthal particle distribution. In Fig. 95.3 (right), the v_2 coefficient of $\Upsilon(1S)$ in three centrality intervals is shown, together with that of the J/ψ [10]. The measured $\Upsilon(1S)$ v_2 coefficient is compatible with zero within current uncertainties and this result contrasts with the J/ψ v_2 measurement in Pb–Pb collisions.

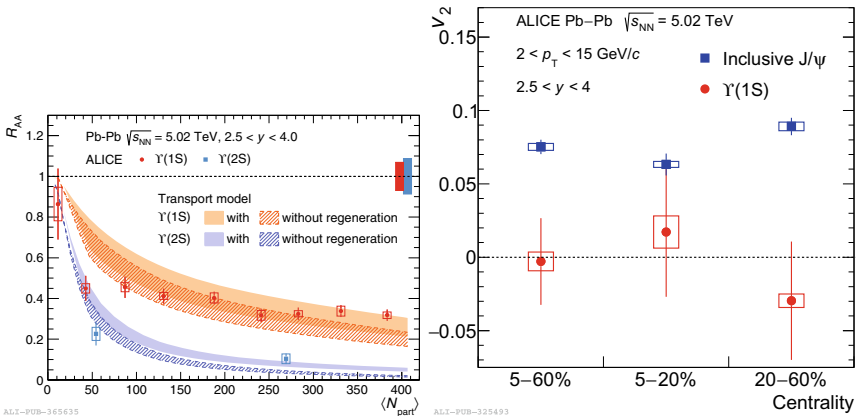


Fig. 95.3 The $\Upsilon(1S)$ R_{AA} in Pb–Pb at $\sqrt{s_{NN}} = 5.02$ (5.44) TeV (left). The $\Upsilon(1S)$ v_2 coefficient integrated over the transverse momentum range $2 < p_T < 15$ GeV/c in three centrality intervals compared to that of inclusive J/ψ at $\sqrt{s_{NN}} = 5.02$ TeV (right)

References

1. T. Matsui, H. Satz, Phys. Lett. B **178**, 416 (1986)
2. P. Braun-Munzinger, J. Stachel, Phys. Lett. B **490**, 196 (2000)
3. R.L. Thews, M. Schroedter, J. Rafelski, Phys. Rev. C **63**, 054905 (2001)
4. A. Rothkopf, Phys. Rept. **858**, 1–117 (2020)
5. L. Grandchamp, S. Lumpkins, D. Sun, H. van Hees, R. Rapp, Phys. Rev. C **73**, 064906 (2006)
6. S. Abramovitch et al., ALICE collaboration. CERN-LHCC-99-22
7. S. Acharya et al., ALICE collaboration. Phys. Lett. B **806**, 135486 (2020)
8. S. Acharya et al., ALICE collaboration. [arXiv:2011.05758](https://arxiv.org/abs/2011.05758) [nucl-ex]
9. S. Acharya et al., ALICE collaboration. Phys. Lett. B **790**, 89 (2019)
10. S. Acharya, et al., ALICE collaboration. Phys. Rev. Lett. **119**(24), 242301 (2017)

Part III
Neutrino Physics

Chapter 96

Probing NSI in Atmospheric Neutrino Experiments Using Oscillation Dip and Valley



Anil Kumar, Amina Khatun, Sanjib Kumar Agarwalla, and Amol Dighe

Abstract We propose a new approach to probe neutral-current non-standard neutrino interaction parameter $\varepsilon_{\mu\tau}$ using the oscillation dip and oscillation valley. Using the simulated ratio of upward-going and downward-going reconstructed muon events at the upcoming ICAL detector, we demonstrate that the presence of non-zero $\varepsilon_{\mu\tau}$ would result in the shift in the dip location as well as the bending of the oscillation valley. Thanks to the charge identification capability of ICAL, the opposite shifts in the locations of oscillation dips as well as the contrast in the curvatures of oscillation valleys for μ^- and μ^+ is used to constrain $|\varepsilon_{\mu\tau}|$ at 90% C.L. to about 2% using 500 kt-yr exposure. Our procedure incorporates statistical fluctuations, uncertainties in oscillation parameters, and systematic errors.

In this talk, we propose a new approach to probe neutral-current Non-Standard Interactions (NSI) [1, 2] parameter $\varepsilon_{\mu\tau}$ during propagation of atmospheric neutrinos. Due to the charge identification capability, the 50 kt Iron Calorimeter (ICAL) detector at the proposed India-based Neutrino observatory [3] would be able to detect atmospheric neutrinos and antineutrinos separately in the multi-GeV range of energy over a wide range of baselines. The oscillation dip and valley features in the ν_μ survival probability can be reconstructed separately for μ^- and μ^+ using the ratio of upward-

A. Kumar (✉) · S. K. Agarwalla
Institute of Physics, Bhubaneswar 751005, India
e-mail: anil.k@iopb.res.in

Homi Bhabha National Institute, Anushaktinagar, Mumbai 400094, India

A. Kumar
Saha Institute of Nuclear Physics, Kolkata 700064, India

A. Khatun
Comenius University, Bratislava 81499, Slovakia

S. K. Agarwalla
The Abdus Salam International Centre for Theoretical Physics, 34151 Trieste, Italy

A. Dighe
Tata Institute of Fundamental Research, Mumbai 400005, India

going (U) and downward-going (D) reconstructed muon events at the ICAL detector as demonstrated in [4].

Using the χ^2 analysis with reconstructed muon momentum, it has been demonstrated that one can obtain a bound of $|\varepsilon_{\mu\tau}| < 0.015$ at 90% C.L. [5] with 500 kt-yr exposure at ICAL. The approach presented in this work is complementary, which uses the observation that, in the presence of non-zero $\varepsilon_{\mu\tau}$, the oscillation dips get shifted in opposite directions for μ^- and μ^+ . In addition, we demonstrate how the contrast in the curvatures of oscillation valleys for μ^- and μ^+ can also be used to constrain $\varepsilon_{\mu\tau}$.

96.1 Shift of the Oscillation Dip Location

We simulate reconstructed muon events at the ICAL detector using NUANCE neutrino event generator, three flavor neutrino oscillations with matter effect considering PREM Profile, and detector properties [4]. Figure 96.1 shows the oscillation dip in the U/D distribution as a function of $\log_{10}(L_{\mu}^{\text{rec}}/E_{\mu}^{\text{rec}})$ for a simulated set of 10-year data using $\sin^2 2\theta_{12} = 0.855$, $\sin^2 \theta_{23} = 0.5$, $\sin^2 2\theta_{13} = 0.0875$, $\Delta m_{32}^2 = 2.46 \times 10^{-3}$ (eV²), $\Delta m_{21}^2 = 7.4 \times 10^{-5}$ (eV²), and $\delta_{\text{CP}} = 0$ with normal ordering (NO, $m_1 < m_2 < m_3$). The solid lines show the mean of 100 simulated sets of 10-year data, and the colored boxes show the statistical fluctuations. The red, black, and blue curves are for $\varepsilon_{\mu\tau}$ of 0.1, 0.0, and -0.1 , respectively. We can observe that the red (blue) curve shifts toward the left (right) for μ^- and toward the right (left) for μ^+ . We propose a new observable $\Delta d = d^- - d^+$ where d^- and d^+ represent the dip locations obtained using dip identification algorithm [4] for μ^- and μ^+ , respectively. The observable Δd depends on the value of $\varepsilon_{\mu\tau}$ but is independent of Δm_{32}^2 [6].

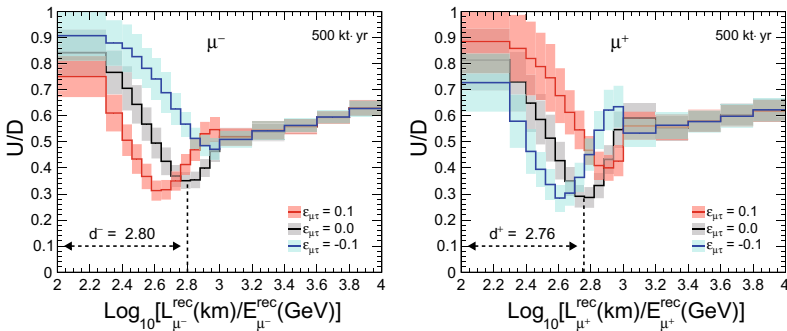


Fig. 96.1 The U/D distributions as a function of $\log_{10}(L_{\mu}^{\text{rec}}/E_{\mu}^{\text{rec}})$ using simulated sets of 10-year data. The red, black, and blue curves correspond to $\varepsilon_{\mu\tau}$ of 0.1, 0.0, and -0.1 , respectively, whereas the colored boxes show statistical fluctuations calculated using 100 simulated sets. Left and right panels correspond to μ^- and μ^+ , respectively. These figures are taken from [6]

96.2 Bending of the Oscillation Valley

In the plane of energy and direction of neutrino, the oscillation dip feature appears as a straight diagonal band in the absence of NSI, and this band is defined as ‘‘oscillation valley’’ [4]. In the presence of non-zero $\varepsilon_{\mu\tau}$, the oscillation valley bends. For the same value of $\varepsilon_{\mu\tau}$, the bending is in opposite directions for neutrino and anti-neutrino. The direction of bending depends on the sign of $\varepsilon_{\mu\tau}$ [6].

Figure 96.2 shows the mean U/D distributions of 100 simulated sets of 10-year data in the plane of $(E_{\mu}^{\text{rec}}, \cos\theta_{\mu}^{\text{rec}})$ with $\varepsilon_{\mu\tau} = 0.1$ for μ^- and μ^+ . The dark blue diagonal band corresponds to the oscillation valley, which is observed to bend in opposite directions for μ^- and μ^+ . The direction of bending will be reversed for $\varepsilon_{\mu\tau} = -0.1$ [6]. We fit the oscillation valley with the function

$$F_{\alpha}(E_{\mu}^{\text{rec}}, \cos\theta_{\mu}^{\text{rec}}) = Z_{\alpha} + N_{\alpha} \cos^2 \left(m_{\alpha} \frac{\cos\theta_{\mu}^{\text{rec}}}{E_{\mu}^{\text{rec}}} + \alpha \cos^2\theta_{\mu}^{\text{rec}} \right), \tag{96.1}$$

where $Z_{\alpha}, N_{\alpha}, m_{\alpha}$, and α are free parameters which will be determined from the fitting of the U/D ratio in the plane of $(E_{\mu}^{\text{rec}}, \cos\theta_{\mu}^{\text{rec}})$ as described in [6]. The parameters m_{α} and α contain information about the alignment and the curvature of oscillation valley. The white lines in Fig. 96.2 show the contours for representative values of the function $F_{\alpha}(E_{\mu}^{\text{rec}}, \cos\theta_{\mu}^{\text{rec}})$, which clearly identify the curvature of the oscillation valley.

96.3 Results

We calibrate $\varepsilon_{\mu\tau}$ with respect to Δd using 1000-year Monte Carlo (MC) as shown in the left panel of Fig. 96.3 by blue points. We use 100 statistically independent

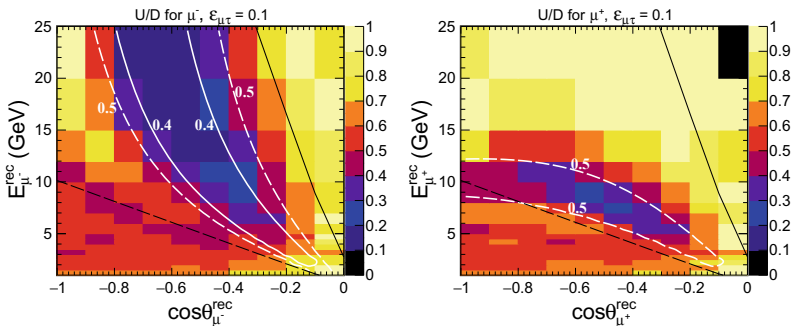


Fig. 96.2 The mean U/D distribution of 100 simulated sets of 10-year data in the plane of $(E_{\mu}^{\text{rec}}, \cos\theta_{\mu}^{\text{rec}})$ of reconstructed muons with $\varepsilon_{\mu\tau} = 0.1$. The white solid and dashed curves represent the fitted function $F_{\alpha}(E_{\mu}^{\text{rec}}, \cos\theta_{\mu}^{\text{rec}})$ with values 0.4 and 0.5, respectively. Left and right panels correspond to μ^- and μ^+ , respectively. These figures are taken from [6]

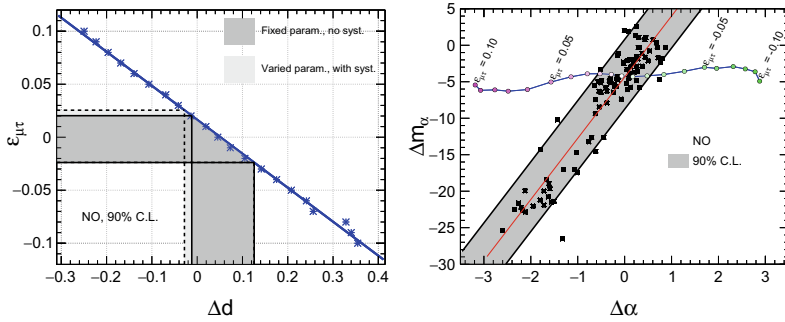


Fig. 96.3 The 90% C.L. bounds on $\varepsilon_{\mu\tau}$ using oscillation dip (left panel) and oscillation valley (right panel). The blue lines show the calibration curve using 1000-year MC, whereas the dark (light) gray band shows the 90% C.L. interval obtained using multiple 10-year simulated datasets without (with) variation over oscillation parameters and systematic errors. These figures are taken from [6]

simulated sets of 10-year data with $\varepsilon_{\mu\tau} = 0$, to determine expected bounds on Δd , and hence on $\varepsilon_{\mu\tau}$. The results with fixed oscillation parameters and without systematic errors, as shown by the dark gray band, give $-0.024 < \varepsilon_{\mu\tau} < 0.020$ at 90% C.L. We further incorporate uncertainties in the neutrino oscillation parameters and systematic errors following the procedure mentioned in [6] to obtain the 90% C.L. bounds on $\varepsilon_{\mu\tau}$ to be $-0.025 < \varepsilon_{\mu\tau} < 0.024$, as shown by the light gray band in Fig. 96.3.

The blue line with colored circles in the right panel of Fig. 96.3 shows the calibration curve using 1000-year MC for $\varepsilon_{\mu\tau}$ in the plane of $(\Delta m_\alpha, \Delta\alpha)$ where $\Delta\alpha = \alpha^- - \alpha^+$ and $\Delta m_\alpha = m_{\alpha^-} - m_{\alpha^+}$. The black points are obtained after fitting multiple 10-year simulated datasets with $\varepsilon_{\mu\tau} = 0$. The calibration curve overlapped by the gray band gives the expected 90% C.L. bound for $\varepsilon_{\mu\tau}$, which is $-0.022 < \varepsilon_{\mu\tau} < 0.021$. Variation in oscillation parameters and systematic uncertainties does not affect these results appreciably.

96.4 Conclusion

We demonstrated that the presence of non-zero NSI parameter $\varepsilon_{\mu\tau}$ results in the shift of the oscillation dip location, and the curvature of the oscillation valley. For a given non-zero value of $\varepsilon_{\mu\tau}$, the oscillation dips have opposite shifts, and the oscillation valleys have opposite curvatures for the reconstructed μ^- and μ^+ events. Thanks to the charge identification capability of ICAL, these features can be used to constrain $|\varepsilon_{\mu\tau}|$ at 90% C.L. to about 2% using 500 kt · yr exposure at ICAL.

Acknowledgements We acknowledge financial support from the DAE, DST (Govt. of India), and INSA.

References

1. L. Wolfenstein, *Phys. Rev. D* **17**, 2369 (1978)
2. Y. Farzan, M. Tortola, *Front. in Phys.* **6**, 10 (2018)
3. S. Ahmed et al., *Pramana* **88**(5), 79 (2017)
4. A. Kumar, A. Khatun, S.K. Agarwalla, A. Dighe, *Eur. Phys. J. C* **81**(2), 190 (2021)
5. S. Choubey, A. Ghosh, T. Ohlsson, D. Tiwari, *JHEP* **12**, 126 (2015)
6. A. Kumar, A. Khatun, S.K. Agarwalla, A. Dighe, *JHEP* **04**, 159 (2021)

Chapter 97

nEXO Searches for Neutrinoless Double Beta Decay of ^{136}Xe



Arun Kumar Soma

Abstract The observation of neutrinoless double beta decay would confirm the Majorana nature of neutrinos. nEXO is a proposed single-phase time projection chamber with 5 tons of liquid xenon (enriched $\sim 90\%$ in ^{136}Xe) to search for neutrinoless double beta decay of ^{136}Xe . At the top of a cylindrical TPC, charge is collected by silica “tiles” patterned with crossed metallic strips. The VUV-sensitive silicon photo-multipliers installed all along the barrel of TPC facilitate the photon detection. The R & D efforts on charge collection and photon detection toward achieving 1% energy resolution ($\frac{\sigma}{E}$) at Q-value along with signal and background discrimination that would help toward reaching target half-life sensitivity of $\sim 10^{28}$ years will be discussed.

97.1 Introduction

The observation neutrino oscillation confirms neutrinos have non-zero mass. Further, the absolute mass of neutrinos, neutrino mass hierarchy, i.e., inverted or normal, nature of neutrinos, i.e., Majorana or Dirac, and CP-transformation properties are still open questions [1]. The observation of neutrinoless double beta decay ($0\nu\beta\beta$) would confirm the Majorana nature of neutrinos.

$0\nu\beta\beta$ is second-order weak interaction that involves simultaneous decay of two neutrons into two protons, two electrons accompanied by energy released ($Q_{\beta\beta}$) and without antineutrinos. The half-life of $0\nu\beta\beta$ in light neutrino exchange model is given by $T_{\frac{1}{2}}^{0\nu} = (G^{0\nu} |M^{0\nu}|^2 \langle m_{\beta\beta} \rangle^2)^{-1} \simeq \left(\frac{0.01 \text{ eV}}{\langle m_{\beta\beta} \rangle} \right)^2 \text{ year}$ [1], where lepton phase space integral $G^{0\nu} \propto Q_{\beta\beta}^5$ is of order $10^{-25}/(\text{y eV}^2)$; effective Majorana mass $m_{\beta\beta} \sim 0.01 \text{ eV}$ and nuclear matrix element ($|M^{0\nu}|^2 \sim 10$).

The characteristic signature of $0\nu\beta\beta$ decay is the peak at $Q_{\beta\beta}$ and measured by observing the kinematics of the two emitted electrons. The $Q_{\beta\beta}$ values are well estab-

A. K. Soma (✉)

Drexel University, Philadelphia, PA 19104, USA
e-mail: arunkumar.soma@drexel.edu

lished and so $0\nu\beta\beta$ signal search can be conducted in the energy window defined by detector resolution around $Q_{\beta\beta}$. The sensitivity of an experiment depends on number of events in the defined energy window, some of which might be due to background. Therefore, the next generation of proposed $0\nu\beta\beta$ detectors [1] is ton scale with excellent energy resolution and is constructed with radio-pure components. The salient features of next generation of enriched xenon observatory (nEXO) experiment toward studies on $0\nu\beta\beta$ decay are presented in Sect. 97.2.

97.2 nEXO

nEXO is a proposed single-phase time projection chamber with 5 tons of liquid xenon (LXe, enriched $\sim 90\%$ in ^{136}Xe) to search for $0\nu\beta\beta$ decay of ^{136}Xe . The nEXO design is based on successful demonstration of predecessor, EXO-200 [2].

The LXe TPC is cylinder with a height of 1.3 m and diameter of 1.2 m. The artistic view of nEXO with LXe TPC, vacuum insulated cryostat filled with HFE-7000 refrigerant fluid and outer detector is shown in Fig. 97.1 (left). The cross-sectional view of TPC with charge collection, photon detection system, high-voltage field cage, and cathode are shown in Fig. 97.1 (right).

The target half-life sensitivity of nEXO is $\sim 10^{28}$ years [3, 4] with 1% energy resolution ($\frac{\sigma}{E}$) at $Q_{\beta\beta}$. The R&D efforts in terms of effective charge collection and photon detection are further discussed.

Charge Collection: The nEXO anode comprises segmented fused silica wafers of dimensions $10\text{ cm} \times 10\text{ cm}$ called “tiles” assembled as an array and is held at ground potential. Each tile contains 60 electrically isolated orthogonal metal strips of 3mm wide made by depositing layers of Au and Ti onto the fused silica wafer surface [5]. A tile mounted on a flange is shown in Fig. 97.2 (left). The prototype tile is operated in a liquid xenon test setup with ^{207}Bi source and a PMT for triggering. An event

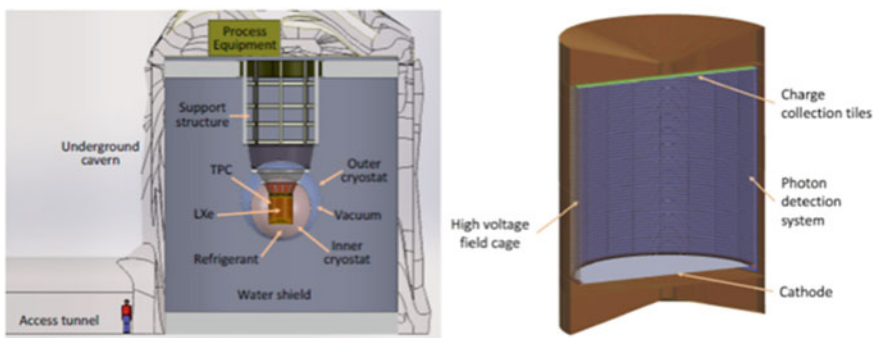


Fig. 97.1 The nEXO detector concept in the SNOLAB cryopit (left) along with cross-sectional view liquid xenon TPC (right)

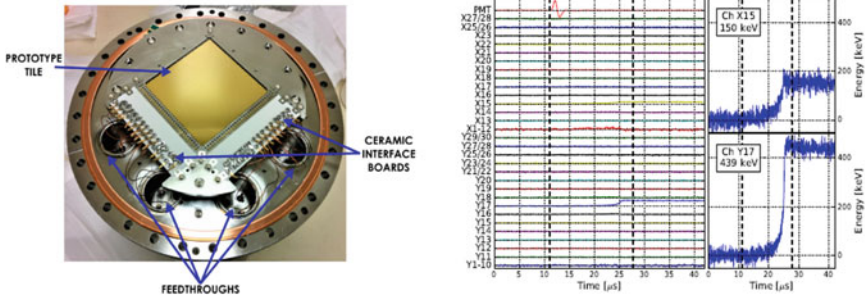


Fig. 97.2 The charge collection tile attached to a flange with X- and Y-signal routed by cables and feedthroughs (left). A sample waveform corresponding to 570 keV of ^{207}Bi is shown (right). The PMT signal provides trigger for data taking and energy deposits seen by channel Y17 and X15

corresponding to 570 keV of ^{207}Bi is shown in Fig.97.2 (right). The charge-only resolution of 5.5% at 570 keV in LXe is achieved [5].

VUV Photon Detection: nEXO plans to use SiPMs as photosensors. The SiPMs are arranged along 4.5 m² barrel of the cylindrical LXe TPC. SiPMs availability as radio-pure components, low operational bias voltage, high gain, low noise, and good single photon peak resolution make them suitable candidates. The target of 1% energy resolution at $Q_{\beta\beta}$ imposes stringent requirement like photon detection efficiency >15% at xenon scintillation wavelength of ~175 nm, dark noise < 50 Hz/mm², and correlated avalanche rate <20% at cryogenic temperatures. This requirement would yield >3% total photon collection efficiency.

The photon collection efficiency is a function of photon detection efficiency and photon transport efficiency. It has already been demonstrated that SiPMs from Fondazione Bruno Kessler (FBK) and Hamamatsu meeting the desired requirements [7–9]. However, the angular dependency of photon detection efficiency and reflectivity of SiPM in LXe were recently measured [6, 10]. It was observed that Hamamatsu SiPMs PDE and reflectivity were decreasing with increase in angle of incidence and are shown in Fig. 97.3.

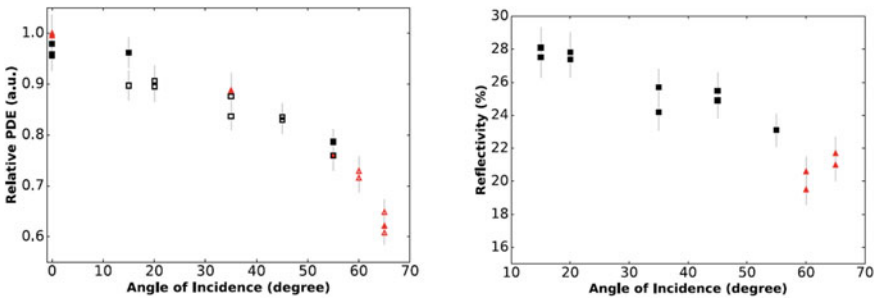


Fig. 97.3 Hamamatsu SiPMs relative PDE and reflectivity as a function of incident angle are shown in the left and right figures, respectively [6]. It can be noticed that photon detection efficiency and reflectivity decrease with the increase of incident angle

97.3 Conclusion

The SiPMs meeting desired R&D goals and successful demonstration of charge tile operation in LXe will help in achieving the nEXO target of 1% energy resolution ($\frac{\sigma}{E}$) at $Q_{\beta\beta}$. The monolithic detector accompanied with selection of radio-pure detector components and analysis techniques toward discrimination of single-site (signal events) and multi-site events (background) will help in achieving ultra-low background levels that would, in turn, help in reaching the nEXO targeted $0\nu\beta\beta$ decay half-life sensitivity $\sim 10^{28}$ years for 5 years of data taking.

References

1. M.J. Dolinski, A.W.P. Poon, W. Rodejohann, Neutrinoless double-beta decay: status and prospects. *Ann. Rev. Nucl. Part. Phys.* **69**, 219 (2019)
2. G. Anton et al., (EXO-200 collaboration): search for neutrinoless double-beta decay with the complete EXO-200 dataset. *Phys. Rev. Lett.* **123**, 161802 (2019)
3. S. Al Kharusi et al., (nEXO collaboration): nEXO pre-conceptual design report, [arXiv:1805.11142](https://arxiv.org/abs/1805.11142) V2 (2018)
4. J.B. Albert et al., (nEXO Collaboration): sensitivity and discovery potential of the proposed nEXO experiment to neutrinoless double- β decay. *Phys. Rev. C* **97**, 065503 (2018)
5. M. Jewell et al., (nEXO collaboration): characterization of an ionization readout tile for nEXO. *JINST* **13**, P01006 (2018)
6. P. Nakarmi et al., (nEXO collaboration): reflectivity and PDE of VUV4 Hamamatsu SiPMs in Liquid Xenon. *JINST* **15**, P01019 (2020)
7. G.Gallina et al., (nEXO collaboration): characterization of the Hamamatsu VUV4 MPPCs for nEXO. *NIM A* **940**, 371 (2019)
8. A. Jamil et al., (nEXO collaboration): VUV-sensitive silicon photomultipliers for Xenon scintillation light detection in nEXO. *IEEE Trans. Nucl. Sci.* **65**, 2823 (2018)
9. I. Ostrovskiy et al., Characterization of silicon photomultipliers for nEXO. *IEEE Trans. Nucl. Sci.* **62**, 1825 (2015)
10. P. Lv et al., (nEXO collaboration): reflectance of silicon photomultipliers at vacuum ultraviolet wavelengths. *IEEE Trans. Nucl. Sci.* **67**, 2501 (2020)

Chapter 98

Effect of Second-Class Currents in $\nu_l(\bar{\nu}_l) - N$ Scattering



A. Fatima, M. Sajjad Athar, and S. K. Singh

Abstract An enhanced value of the axial dipole mass M_A has been discussed in the literature to explain the experimental data on the charged current quasielastic scattering of neutrinos on the nuclear targets by MiniBooNE, K2K, T2K, NOvA, MINOS, MINERvA, etc., collaborations. Recently, we have shown that in the case of $\nu_\mu(\bar{\nu}_\mu)$ induced charged current quasielastic (CCQE) scattering on the free nucleon target, the higher values of cross section can be obtained by taking $M_A = 1.026$ GeV (the world average value) and the presence of the second-class currents. In this work, we have extended our study to include the CCQE $\nu_\tau(\bar{\nu}_\tau)$ interactions on the free nucleon target.

98.1 Introduction

In this paper, we have studied the effect of second-class currents with time reversal invariance in the reaction

$$\begin{aligned}\nu_l(k) + n(p) &\longrightarrow l^-(k') + p(p'), \\ \bar{\nu}_l(k) + p(p) &\longrightarrow l^+(k') + n(p'), \quad \text{where } l = \mu, \tau,\end{aligned}\tag{98.1}$$

where the quantities in the brackets represent the four momenta of the respective particles.

We find the effect of the form factor associated with the second-class current (SCC) to be significant. The effect of lepton mass (m_μ vs. m_τ) on the cross section in CCQE $\nu_l(\bar{\nu}_l) - N$ scattering processes has also been studied.

A. Fatima (✉) · M. Sajjad Athar · S. K. Singh
Department of Physics, Aligarh Muslim University, Aligarh 202002, India
e-mail: atikafatima1706@gmail.com

98.2 Formalism

The transition matrix element for the processes given in (98.1) is written as [1]:

$$\mathcal{M} = \frac{G_F}{\sqrt{2}} \cos \theta_c l^\mu J_\mu, \quad (98.2)$$

where G_F is the Fermi coupling constant and θ_c ($= 13.1^\circ$) is the Cabibbo mixing angle. The leptonic current l^μ is given by

$$l^\mu = \bar{u}(k') \gamma^\mu (1 \pm \gamma_5) u(k), \quad (98.3)$$

where (+)– sign is for (anti)neutrino. The hadronic current J_μ is expressed as

$$J_\mu = \bar{u}(p') \Gamma_\mu u(p) \quad (98.4)$$

with

$$\Gamma_\mu = V_\mu - A_\mu. \quad (98.5)$$

The vector (V_μ) and the axial vector (A_μ) currents are given by [1–3]:

$$\begin{aligned} \langle N'(p') | V_\mu | N(p) \rangle = \bar{u}(p') \left[\gamma_\mu f_1(Q^2) + i \sigma_{\mu\nu} \frac{q^\nu}{M_p + M_n} f_2(Q^2), \right. \\ \left. + \frac{2 q_\mu}{M_p + M_n} f_3(Q^2) \right] u(p) \end{aligned} \quad (98.6)$$

and

$$\begin{aligned} \langle N'(p') | A_\mu | N(p) \rangle = \bar{u}(p') \left[\gamma_\mu \gamma_5 g_1(Q^2) + i \sigma_{\mu\nu} \frac{q^\nu}{M_p + M_n} \gamma_5 g_2(Q^2) \right. \\ \left. + \frac{2 q_\mu}{M_p + M_n} g_3(Q^2) \gamma_5 \right] u(p), \end{aligned} \quad (98.7)$$

where N , N' represents a nucleon n , p , with M_p and M_n being the masses of the proton and the neutron, respectively. $q_\mu (= k_\mu - k'_\mu = p'_\mu - p_\mu)$ is the 4-momentum transfer with $Q^2 = -q^2$, $Q^2 \geq 0$. $f_1(Q^2)$, $f_2(Q^2)$ and $f_3(Q^2)$ are the vector, weak magnetic, and induced scalar form factors and $g_1(Q^2)$, $g_2(Q^2)$, and $g_3(Q^2)$ are the axial vector, induced tensor (or weak electric), and induced pseudoscalar form factors, respectively. According to the classification of G-invariance, the hadronic current associated with the form factors $f_{1,2}(Q^2)$ and $g_{1,3}(Q^2)$ correspond to the first-class currents, while the hadronic current associated with the form factors $f_3(Q^2)$ and $g_2(Q^2)$ correspond to SCC.

We are assuming T invariance which implies that all the vector and axial vector form factors, i.e., $f_{1-3}(Q^2)$ and $g_{1-3}(Q^2)$ are real. The hypothesis that the weak vector currents and its conjugate along with the isovector part of the electromagnetic current form an isotriplet implies that the weak vector form factors $f_1(Q^2)$ and

$f_2(Q^2)$ are related to the isovector electromagnetic form factors of the nucleon, i.e., $f_{1,2}(Q^2) = f_{1,2}^p(Q^2) - f_{1,2}^n(Q^2)$. The hypothesis ensures conservation of vector current (CVC) in the weak sector, which implies $f_3(Q^2) = 0$. The principle of G-invariance implies the second-class current form factors to be zero, i.e., $f_3(Q^2) = 0$ and $g_2(Q^2) = 0$. The hypothesis of PCAC relates the form factor $g_3(Q^2)$ to the form factor $g_1(Q^2)$ through the Goldberger–Treiman (GT) relation. In order to study the effect of SCC, we have taken non-zero values of $g_2(Q^2)$ by parameterizing it to be of the dipole form in analogy with $g_1(Q^2)$, viz.

$$g_{1,2}(Q^2) = \frac{g_{A,2}(0)}{1 + Q^2/M_{A,2}^2}, \quad (98.8)$$

where $g_A = 1.267$ is the axial charge and is determined from the semileptonic nucleon and hyperon decays, M_A is the axial dipole mass, $g_2^R(0)$ is varied in the range -1 to $+1$ and M_2 is taken as $M_2 = M_A$. The detailed discussion of the form factors is given in [1, 2].

98.3 Results and Discussion

In Fig. 98.1, we have presented the results for the total scattering section ($\sigma(E_\nu)$) versus E_ν for $\nu_\mu(\bar{\nu}_\mu)$ and $\nu_\tau(\bar{\nu}_\tau)$ induced processes corresponding to (98.1). These results are presented for $g_2^R(0) = 0, +1$ and -1 , with $M_A = 1.026$ GeV. It may be noticed that for ν_μ induced process the results with $g_2^R(0) = +1$ and -1 are the same and it results in the enhancement of the cross section both for neutrino- as well as antineutrino-induced reactions. While for $\nu_\tau(\bar{\nu}_\tau)$ induced processes, the cross section increases for $g_2^R(0) = +1$ and decreases for $g_2^R(0) = -1$.

In Fig. 98.2, the results are presented for $\sigma(E_\nu)$ versus E_ν at different M_A , as well as by taking different values of $g_2^R(0)$. It may be observed that for ν_μ induced process with $g_2^R(0) = 1$ and $M_A = 1.026$ GeV, the results simulate for $g_2^R(0) = 0$ and $M_A = 1.1$ GeV. In the case of $\bar{\nu}_\mu$ induced process with $g_2^R(0) = 1$ and $M_A = 1.026$ GeV, the results simulate for $g_2^R(0) = 0$ and $M_A = 1.1$ GeV.

In Fig. 98.3, the results are presented for $\nu_\tau/\bar{\nu}_\tau$ induced process for $\sigma(E_\nu)$ versus E_ν at different M_A , as well as by taking different values of $g_2^R(0)$. It may be observed that effect of non-zero value of $g_2^R(0)$ is more pronounced in these processes and the results with $g_2^R(0) = 1$ and $M_A = 1.026$ GeV, simulate the result for $g_2^R(0) = 0$ and $M_A = 1.1$ GeV.

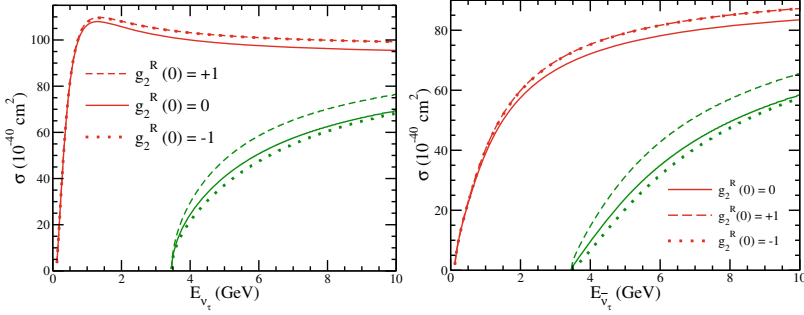


Fig. 98.1 σ as a function of neutrino (left panel) and antineutrino (right panel) energies for the processes $\nu_\mu(\bar{\nu}_\mu) + N \rightarrow \mu^-(\mu^+) + N'$ (red-colored lines) and $\nu_\tau(\bar{\nu}_\tau) + N \rightarrow \tau^-(\tau^+) + N'$ (green-colored lines) by varying the value of $g_2^R(0) = 0$ (solid line), $+1$ (dashed line) and -1 (dotted line) at $M_A = M_2 = 1.026$ GeV

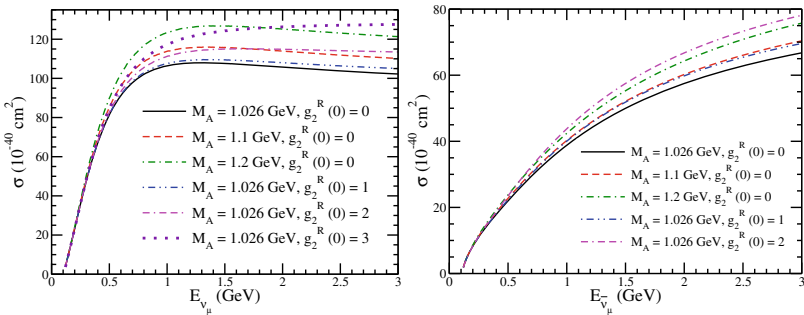


Fig. 98.2 σ versus $E_{\nu_\mu}(\bar{\nu}_\mu)$ for the processes $\nu_\mu + n \rightarrow \mu^- + p$ (left panel) and $\bar{\nu}_\mu + p \rightarrow \mu^+ + n$ (right panel) with different combinations of M_A and $g_2^R(0)$ viz. $M_A = 1.026$ GeV and $g_2^R(0) = 0$ (solid line), $M_A = 1.1$ GeV and $g_2^R(0) = 0$ (dashed line), $M_A = 1.2$ GeV and $g_2^R(0) = 0$ (dashed-dotted line), $M_A = 1.026$ GeV and $g_2^R(0) = 1$ (double-dotted-dashed line), $M_A = 1.026$ GeV and $g_2^R(0) = 2$ (double-dashed-dotted line) and $M_A = 1.026$ GeV and $g_2^R(0) = 3$ (dotted line)

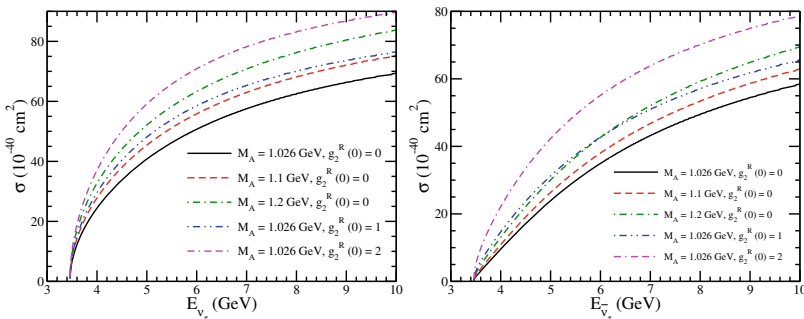


Fig. 98.3 σ versus $E_{\nu_\tau}(\bar{\nu}_\tau)$ for the processes $\nu_\tau + n \rightarrow \tau^- + p$ (left panel) and $\bar{\nu}_\tau + p \rightarrow \tau^+ + n$ (right panel). Lines and points have the same meaning as in Fig. 98.2

98.4 Conclusion

The production cross section for μ^\pm and τ^\pm are sensitive to the second-class current form factor. For the muon production cross section, the results obtained using $g_2^R(0) = +1$ and -1 are approximately the same, and higher than the results obtained with $g_2^R(0) = 0$, but this is not true for tauon production. In the case of tauon production cross section, the results obtained using $g_2^R(0) = +1(-1)$ are higher (lower) than the results obtained with $g_2^R(0) = 0$. This difference (between μ vs. τ production) arises only because of the higher mass of the τ lepton. The presence of second-class currents would reduce the value of M_A for both ν_μ and ν_τ induced reactions.

References

1. A. Fatima, M. Sajjad Athar and S. K. Singh, Phys. Rev. D **102**, 113009 (2020)
2. A. Fatima, M. Sajjad Athar, S.K. Singh, Phys. Rev. D **98**, 033005 (2018)
3. A. Fatima, M. Sajjad Athar, S.K. Singh, Eur. Phys. J. A **54**, 95 (2018)

Chapter 99

$\nu_\tau/\bar{\nu}_\tau$ - ^{40}Ar DIS Cross Sections with Perturbative and Nonperturbative Effects



F. Zaidi, V. Ansari, H. Haider, M. Sajjad Athar, and S. K. Singh

Abstract In this work, we have studied $\nu_\tau/\bar{\nu}_\tau$ - ^{40}Ar deep inelastic scattering cross sections with nuclear medium effects. The results are obtained using the nucleon structure functions by incorporating the perturbative evolution of parton densities at next-to-leading order, as well as nonperturbative effects of the target mass correction and the higher twist following the operator product expansion and the renormalon approach, respectively. Nucleon structure functions are then used to obtain the nuclear structure functions by incorporating the effect of Fermi motion, binding energy, and nucleon correlations. In the nuclear medium, we also take into account the contributions arising due to the mesonic (π and ρ) effect and the (anti)shadowing corrections. The effects of massive charm quark and center-of-mass energy cut have also been studied.

99.1 Introduction

ν_τ interaction studies are required to better determine the third neutrino weak eigenstate to have a precise understanding of neutrino oscillation parameters besides the intrinsic interest to better explore ν_τ physics. ν_τ events have been observed by the NOMAD, OPERA, DONUT, IceCube, and SuperK experiments, and the experiments like HyperK, DsTau, SHiP, T2HK, and DUNE are planned to be performed in future using different nuclear targets, where a significant number of ν_τ events are expected to be observed. In the different theoretical studies for $\nu_\tau/\bar{\nu}_\tau - N$, deep inelastic scattering (DIS) large variations in the cross sections have been observed [1]. There is no theoretical study of the nuclear medium effects for $\nu_\tau/\bar{\nu}_\tau - A$ DIS. We have theoretically studied the $\nu_\tau/\bar{\nu}_\tau$ - ^{40}Ar DIS process in the energy region relevant to the DUNE experiment which is planned to be performed using LArTPC. We have incorporated the nuclear medium effects arising due to Fermi motion, binding energy, and nucleon correlations using the nucleon spectral function [2]. Furthermore, the

F. Zaidi (✉) · V. Ansari · H. Haider · M. Sajjad Athar · S. K. Singh
Aligarh Muslim University, Aligarh, India
e-mail: zaidi.physics@gmail.com

© The Author(s), under exclusive license to Springer Nature Singapore Pte Ltd. 2022
B. Mohanty et al. (eds.), *Proceedings of the XXIV DAE-BRNS High Energy Physics Symposium, Jatni, India*, Springer Proceedings in Physics 277,
https://doi.org/10.1007/978-981-19-2354-8_99

541

effect of meson cloud contribution [3] as well as shadowing corrections [4] also have been taken into account. Moreover, the numerical results are evaluated by taking into account the perturbative evolution of parton densities at next-to-leading order (NLO) [5] and nonperturbative effects of the target mass correction (TMC) following [6] and the higher twist (HT) [7] at the free nucleon level. The results are presented for the differential scattering cross section using the perturbative and nonperturbative effects as well as the effects due to the nuclear medium. We also study the effects of charm mass and the center-of-mass (c.m.) energy cut.

99.2 Formalism

Generally, the expression for the differential scattering cross section for charged current $\nu_\tau/\bar{\nu}_\tau$ induced DIS [5, 6] with the nucleons bound inside a nuclear target ($\nu_\tau/\bar{\nu}_\tau(k) + A(p_A) \rightarrow \tau^-/\tau^+(k') + X(p'_A)$) is written in terms of the dimensionless nuclear structure functions $F_{iA}(x, Q^2)$; ($i = 1 - 5$) as

$$\begin{aligned} \frac{d^2\sigma}{dx dy} = & \frac{G_F^2 M_N E}{\pi \left(1 + \frac{Q^2}{M_W^2}\right)^2} \left\{ \left[y^2 x + \frac{m_\tau^2 y}{2EM_N} \right] F_{1A}(x, Q^2) + \left[\left(1 - \frac{m_\tau^2}{4E^2}\right) - \left(1 + \frac{M_N x}{2E}\right) y \right] \right. \\ & \times F_{2A}(x, Q^2) \pm \left[xy \left(1 - \frac{y}{2}\right) - \frac{m_\tau^2 y}{4EM_N} \right] F_{3A}(x, Q^2) \\ & \left. + \frac{m_\tau^2 (m_\tau^2 + Q^2)}{4E^2 M_N^2 x} F_{4A}(x, Q^2) - \frac{m_\tau^2}{EM_N} F_{5A}(x, Q^2) \right\}, \end{aligned} \quad (99.1)$$

where G_F is the Fermi coupling constant, M_N is the nucleon mass, E is the incoming beam energy, and Q^2 is the 4-momentum transfer squared. The scaling variables x and y lie in the region given by

$$\begin{aligned} \frac{m_\tau^2}{2M_N(E - m_\tau)} \leq x \leq 1 \quad & \text{and} \quad a - b \leq y \leq a + b, \quad \text{with} \\ a = \frac{1 - m_\tau^2 \left(\frac{1}{2M_N E x} + \frac{1}{2E^2} \right)}{2 \left(1 + \frac{M_N x}{2E} \right)} \quad & \text{and} \quad b = \frac{\sqrt{\left(1 - \frac{m_\tau^2}{2M_N E x} \right)^2 - \frac{m_\tau^2}{E^2}}}{2 \left(1 + \frac{M_N x}{2E} \right)}. \end{aligned}$$

All the nuclear structure functions $F_{iA}(x, Q^2)$; ($i = 1 - 5$) are evaluated independently, i.e., without using the Callan–Gross and Albright–Jarlskog relations at the nuclear level. These numerical calculations have been performed in the laboratory frame, where the target nucleus is at rest, i.e., ($p_A = (M_A, 0)$) and the momentum transfer (\mathbf{q}) of the bound nucleons is chosen to be along the Z -axis. For details, please see [1, 8]. The expressions of $F_{iA}(x, Q^2)$; ($i = 1 - 5$) are obtained in terms of the free nucleon structure functions $F_{iN}(x, Q^2)$ ($i = 1 - 5$) and the hole spectral

function S_h which contains complete information about the nuclear dynamics [1, 8] as

$$F_{iA}^N(x_A, Q^2) = 4 \int d^3r \int \frac{d^3p}{(2\pi)^3} \frac{M_N}{E_N(\mathbf{p})} \int_{-\infty}^{\mu} dp^0 S_h(p^0, \mathbf{p}, \rho(r)) \times f_{iN}(x, Q^2).$$

In the above expression, μ is the chemical potential, $\rho(r)$ is the nuclear density and r is the position coordinate of the interaction vertex. $f_{iN}(x, Q^2)$ is the factor corresponding to free nucleon structure functions, for $i = 4, 5$, it is given by

$$\begin{aligned} f_{4N}(x, Q^2) &= A F_{4N}(x_N, Q^2). \\ f_{5N}(x, Q^2) &= A F_{5N}(x_N, Q^2) \times \frac{2x_N}{M_N v_N} \times (a_1 + a_2 + a_3), \end{aligned}$$

where

$$\begin{aligned} a_1 &= \frac{|\mathbf{q}|q_0}{q^2} \left(\frac{|\mathbf{q}| + q_0}{|\mathbf{q}| + 2q^0} \right) \times \left\{ -p_x^2 + \frac{|\mathbf{q}|^2}{Q^2} \frac{M_N v_N}{q_0(p_N^0 - \gamma p_N^z)} \left(\frac{Q^2}{|\mathbf{q}|^2} \left[\frac{|\mathbf{p}_N|^2 - p_N^{z2}}{2} \right] \right. \right. \\ &\quad \left. \left. + (p_N^0 - \gamma p_N^z)^2 \left[1 + \frac{p_N^z Q^2}{q^0 |\mathbf{q}| (p_N^0 - \gamma p_N^z)} \right]^2 \right) \right\} \end{aligned} \quad (99.2)$$

$$a_2 = \left(\frac{q_0}{|\mathbf{q}| + 2q^0} \right) \left(p_N^0 + \frac{q^0}{2x_N} \right)^2 \left(1 + \frac{p_N^z + |\mathbf{q}|/2x_N}{p_N^0 + q^0/2x_N} \right), \quad (99.3)$$

$$a_3 = \left(\frac{p_N^0 q^0}{2x_N} \right) \left(1 + \frac{p_N^z q^0}{p_N^0 (|\mathbf{q}| + 2q^0)} \right).$$

For $f_{1,2,3N}(x, Q^2)$, please see [8]. The free nucleon structure functions are evaluated at NLO by using the MMHT nucleon PDFs parameterization [9] in the four-flavor MSbar scheme treating u , d , s quarks to be massless, and c quark as a massive object. We define

$$F_{iN}^{n_f=4}(x, Q^2) = \underbrace{F_{iN}^{n_f=3}(x, Q^2)}_{\text{massless}} + \underbrace{F_{iN}^{n_f=1}(x, Q^2)}_{\text{massive}}.$$

Moreover, the nucleons bound inside the nucleus may interact among themselves via meson (mainly π and ρ) exchange. The intermediate vector boson interacts with these mesons and plays an important role in obtaining the nuclear structure functions. The contribution of π , i.e., $F_{iA}^\pi(x, Q^2)$ and ρ meson, i.e., $F_{iA}^\rho(x, Q^2)$ is taken following [3]. We have also incorporated the contribution from shadowing and antishadowing effects ($F_{iA}^{sh}(x, Q^2)$) following the works of Kulagin and Petti [4]. Thus, in our theoretical model, the total nuclear structure functions are defined as

$$F_{iA}(x, Q^2) = F_{iA}^N(x, Q^2) + F_{iA}^\pi(x, Q^2) + F_{iA}^\rho(x, Q^2) + F_{iA}^{sh}(x, Q^2).$$

Using the nuclear structure functions, we obtain the differential scattering cross section and the results are presented in the next section.

99.3 Results and Discussion

In Fig. 99.1, the results of the differential scattering cross section $\frac{1}{E} \frac{d^2\sigma}{dx dy}$ versus y are shown for different values of x and $E = 10 \text{ GeV}$ for $\nu_\tau/\bar{\nu}_\tau$ - ^{40}Ar DIS processes. The numerical results obtained with all nuclear medium effects are labeled as ‘Total’ and the results with the contribution only from the spectral function are labeled as ‘SF’.

From Fig. 99.1, it may be noticed that at $E = 10 \text{ GeV}$ the (anti)neutrino cross section is limited to the intermediate and high x region due to the threshold effect. Further, we notice that the inclusion of c.m. energy (W) cut of 1.6 and 2.0 GeV

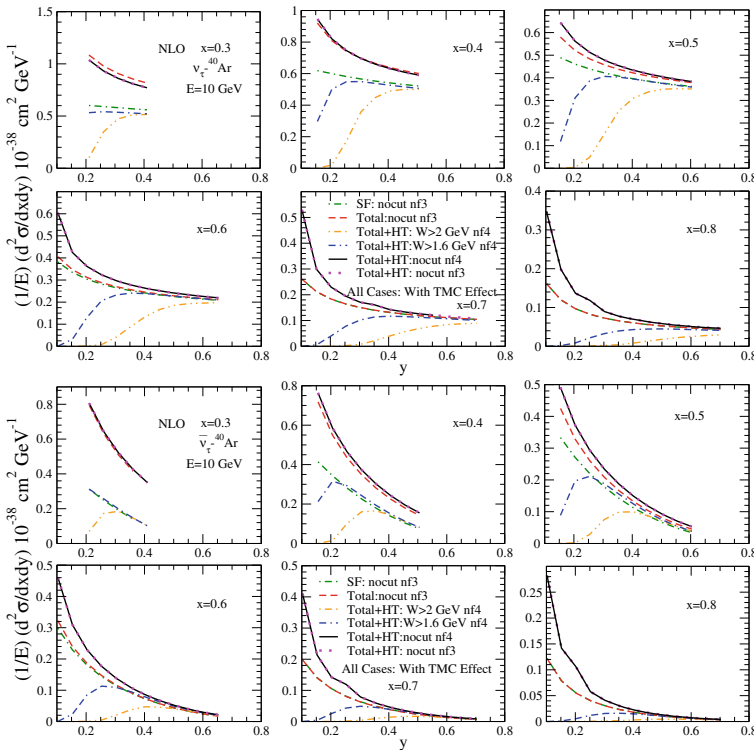


Fig. 99.1 Results for $\frac{1}{E} \frac{d^2\sigma}{dx dy}$ versus y are shown at different x for $E = 10 \text{ GeV}$ in ν_τ - ^{40}Ar (left) and $\bar{\nu}_\tau$ - ^{40}Ar (right) DIS processes

reduces the tauon cross section in the DIS region in comparison to the results obtained without W cut. Moreover, comparing the results obtained with the spectral function only (dashed-dotted line) and the results with the full model (dashed line) for the three massless quarks ($n_f = 3$), we noticed that the mesonic cloud contribution is significant for $0.3 \leq x < 0.6$, while it becomes small for $x \geq 0.6$. In the present kinematic region of x , shadowing effect is found to be negligible. We notice that the HT effect results in an enhancement of the scattering cross section (dotted lines), especially at low y in comparison to the results obtained with TMC effect only (dashed line). We have also noticed that the contribution of the massive charm quark gets suppressed in the nuclear medium. Qualitatively, the behavior of differential scattering cross section and its modifications due to nuclear medium effects are observed to be similar for both ν_τ - ^{40}Ar and $\bar{\nu}_\tau$ - ^{40}Ar induced DIS processes. However, quantitatively, the effects due to nonperturbative corrections, energy dependence, W cut as well as nuclear medium modifications are found to be different in both scatterings.

99.4 Summary and Conclusions

We have observed that the kinematic constrain on the c.m. energy is important in the evaluation of the differential scattering cross sections for high x and low y regions. Our theoretical results would be helpful to interpret the future experimental results from DUNE as well as for the development of a better theoretical understanding.

References

1. V. Ansari et al., Phys. Rev. D **102**, 113007 (2020)
2. P. Fernandez de Cordoba, E. Oset, Phys. Rev. C **46**, 1697 (1992)
3. E. Marco et al., Nucl. Phys. A **611**, 484 (1996)
4. S. A. Kulagin, R. Petti, Nucl. Phys. A **765**, 126 (2006); *ibid* Phys. Rev. D **76**, 094023 (2007)
5. S. Kretzer, M.H. Reno, Phys. Rev. D **66**, 113007 (2002)
6. S. Kretzer, M.H. Reno, Phys. Rev. D **69**, 034002 (2004)
7. M. Dasgupta, B.R. Webber, Phys. Lett. B **382**, 273 (1996)
8. F. Zaidi et al., Phys. Rev. D **101**, 033001 (2020)
9. L.A. Harland-Lang et al., Eur. Phys. J. C **75**, 204 (2015)

Chapter 100

Coherent Pion Production in Neutrino–Nucleus Interaction



H. Sogarwal and Prashant Shukla

Abstract We present a study of coherent pion production in neutrino–nucleus interactions using the formalism based on PCAC theorem which connects the neutrino–nucleus cross section to the pion–nucleus elastic scattering cross section. Pion–nucleus elastic scattering cross section is calculated using Glauber model which uses nuclear densities as inputs. We calculate the differential and integrated cross sections for coherent pion production in neutrino (anti-neutrino)–nucleus scattering for carbon, iron and lead and compare with the measured data and GENIE package. There is excellent agreement between the calculated and measured cross sections with the fixed parameter Glauber model.

100.1 Introduction

The scattering processes of charge (CC) and neutral current (NC) coherent pion production are given as

$$\nu_{\mu} + A \rightarrow \mu^{-} + \pi^{+} + A. \text{ (CC)}$$

$$\nu_{\mu} + A \rightarrow \nu_{\mu} + \pi^{0} + A. \text{ (NC).}$$

The momentum transfer Q between the incoming neutrino and outgoing lepton is given by $Q^2 = -q^2 = \mathbf{q}^2 - \nu^2$. Here, q is the 4-momentum transfer and ν ($= E_{\nu} - E_{\mu}$) is the energy transfer between the incident neutrino and outgoing lepton. For coherent pion production, the squared momentum transfer to the nucleus from the

H. Sogarwal (✉)

Tata Institute of Fundamental Research, Mumbai 400005, India

e-mail: sogarwalhariom@gmail.com

H. Sogarwal · P. Shukla

Homi Bhabha National Institute, Training School Complex, Anushaktinagar, Mumbai, India

P. Shukla

Nuclear Physics Division, Bhabha Atomic Research Centre, Mumbai 400085, India

neutrino–pion system $|t| = |(q - p_\pi)^2|$ remains small. Here, p_π is the 4-momenta of outgoing pion.

The most common theoretical approach for describing coherent pion production is based on Adler's Partially Conserved Axial Current (PCAC) theorem which relates the neutrino-induced coherent pion production to the pion–nucleus elastic scattering [1, 2]. To obtain the elastic pion–nucleus scattering cross section Berger–Sehgal (BS) model [2] is used widely. The work presented in [3] calculates the pion–nucleus elastic scattering cross section using Glauber model in terms of measured nuclear densities and measured pion–nucleon cross sections.

100.2 The Formulation of the Model

The differential cross section for the charge current coherent pion production scattering process [1, 2] is

$$\frac{d\sigma^{CC}}{dQ^2 d\nu dt} = \frac{G_F^2 \cos^2 \theta_C f_\pi^2 uv}{2\pi^2 |\mathbf{q}|} \left[\left(G_A - \frac{1}{2} \frac{Q_m^2}{(Q^2 + m_\pi^2)} \right)^2 + \frac{\nu}{4E_\nu} (Q^2 - Q_m^2) \frac{Q_m^2}{(Q^2 + m_\pi^2)^2} \right] \times \frac{d\sigma(\pi A \rightarrow \pi A)}{dt}. \quad (100.1)$$

Here, G_F ($=1.16639 \times 10^{-5} \text{ GeV}^{-2}$) is the Fermi coupling constant and $\cos \theta_C$ ($=0.9725$). The kinematic factors u and v are given by: $u, v = (E_\nu + E_\mu \pm |\mathbf{q}|)/(2 E_\nu)$. The pion decay constant is f_π ($=0.93 m_\pi$). The axial vector form factor can be defined as $G_A = m_A^2/(Q^2 + m_A^2)$ [2] with the axial vector meson mass m_A ($=1.05 \text{ GeV}/c^2$). $Q_m^2 = m_l^2 \nu/(E_\nu - \nu)$, where m_l is the mass of outgoing lepton. The kinematic limits are given in [3]. The ν integration should be done in the range $\max(\xi \sqrt{Q^2}, \nu_{min}) < \nu < \nu_{max}$. In our calculation, we use $\xi = 1$ and 2 which controls the theoretical lower limit of ν integration.

We use scattering theory to obtain the pion–nucleus differential elastic cross section given as

$$\frac{d\sigma_{el}}{dt} = \frac{\pi}{k^2} |f(t)|^2, \quad (100.2)$$

where $f(t)$ is given by

$$f(t) = \frac{1}{2ik} \sum_{l=0}^{\infty} (2l+1) (S_l - 1) P_l(\cos \theta). \quad (100.3)$$

Here, $t = -4k^2 \sin^2 \theta/2$ and k is the momentum of pion. We use Glauber model to obtain the scattering matrix S_l in terms of pion–nucleus impact parameter b by

$$S_l = \exp \left(i \frac{1}{2} \sigma_{\pi N} (\alpha_{\pi N} + i) AT(b) \right). \tag{100.4}$$

Here, $\sigma_{\pi N}$ is the average total pion–nucleon cross section and $\alpha_{\pi N}$ is fixed to 1.1. The overlap function $T(b)$ is calculated using the nuclear density function.

100.3 Results and Discussions

Figure 100.1(a) shows the total cross section for the CC neutrino–carbon scattering and Figure 100.1(b) shows the same for anti-neutrino obtained using the Glauber model-based present approach. The calculations and GENIE gives a good description of MINER ν A data [4] at low energies while at high energies our calculation is in better agreement with data as compared to GENIE.

Figure 100.2(a) shows the total cross section for the charged current coherent pion production in neutrino–lead interaction. Figure 100.2(b) shows differential cross section as a function of Q^2 (averaged over neutrino flux) compared with MINER ν A data [5]. The calculations give a good description of the data.

Figure 100.3(a) shows the total cross section for the CC coherent pion production in neutrino–iron interaction. Figure 100.2(b) shows differential cross section compared with the data of MINER ν A experiment [5] and GENIE. The GENIE gives a good description of the data at lower energies, while our calculation gives a reasonable description in the whole energy range.

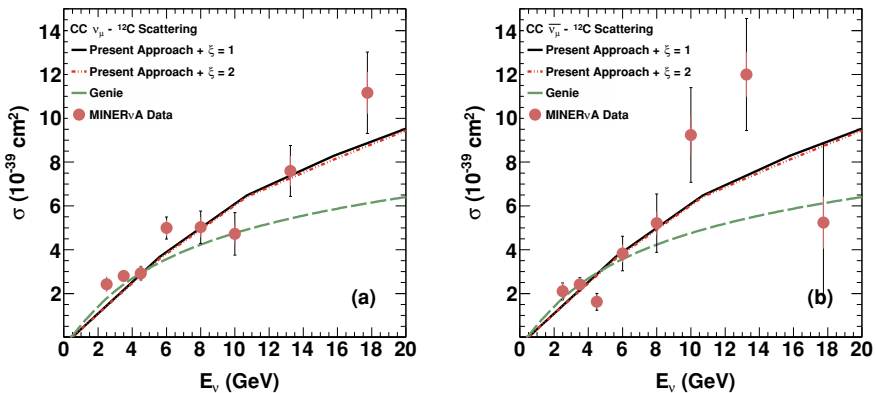


Fig. 100.1 Total cross section σ for the CC coherent pion production in $\nu_{\mu} - {}^{12}\text{C}$ interaction as a function of neutrino energy E_{ν} obtained using our calculations for (a) neutrino and (b) anti-neutrino. The calculations are compared with the MINER ν A data [4] and GENIE

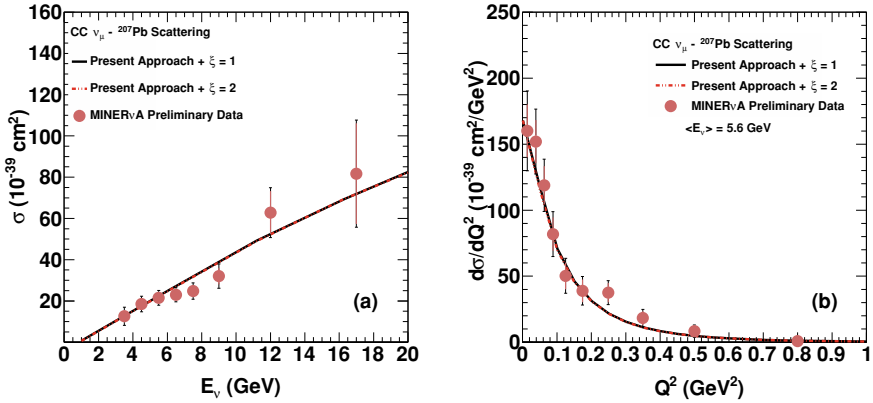


Fig. 100.2 CC coherent pion production in $\nu_\mu - {}^{207}\text{Pb}$ interaction obtained using our calculations (a) Total cross section σ as a function of neutrino energy and (b) Differential cross section as a function of Q^2 (averaged over neutrino flux) along with MINER ν A data [5]

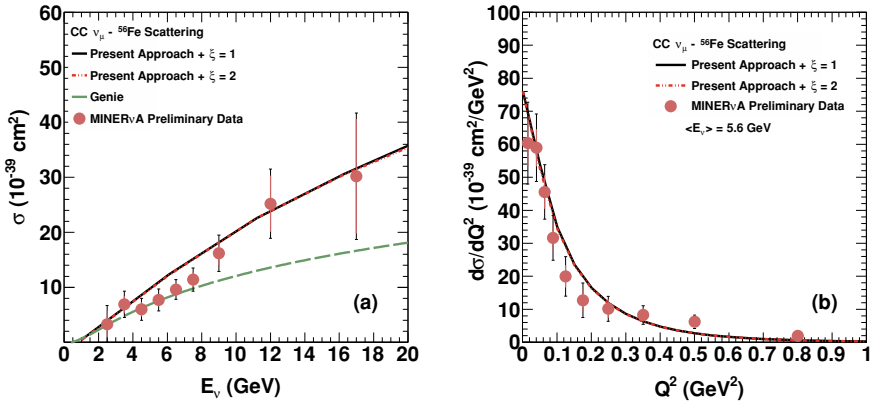


Fig. 100.3 CC coherent pion production in $\nu_\mu - {}^{56}\text{Fe}$ interaction obtained using our calculations. (a) Total cross section σ compared with MINER ν A data [5] and GENIE. (b) Differential cross section compared with the MINER ν A data [5]

100.4 Conclusions

We presented a study of coherent pion production in neutrino–nucleus interactions in the resonance region using the formalism based on PCAC theorem. The pion–nucleus elastic scattering cross section is calculated using Glauber model. We calculate the differential and integrated cross sections coherent pion production in neutrino–nucleus scattering for a range of nuclear targets, carbon, iron and lead. There is excellent agreement between the calculated and measured cross sections with fixed parameter Glauber model for all the nuclear targets.

References

1. B.Z. Kopeliovich, P. Marage, *Int. J. Mod. Phys. A* **8**, 1513 (1993)
2. C. Berger, L.M. Sehgal, *Phys. Rev. D* **79**, 053003 (2009)
3. K. Saraswat, P. Shukla, V. Kumar, V. Singh, *Phys. Rev. C* **93**, 035504 (2016)
4. A. Mislivec et al., MINERvA Collaboration. *Phys. Rev. D* **97**, 032014 (2018)
5. R. Delgado, M. Alejandro, Minerva experiment. FERMILAB-THESIS-2020-10

Chapter 101

Simulation Study of Electron Energy Reconstruction with Thinner Iron Plates in ICAL



Honey Khindri, V. M. Datar, D. Indumathi, S. M. Lakshmi,
and M. V. N. Murthy

Abstract Sub-GeV ν_e and $\bar{\nu}_e$ charged current (CC) events are sensitive to the CP phase δ_{CP} , *irrespective* of the neutrino mass hierarchy. The magnetized iron calorimeter (ICAL) detector at the proposed India-based Neutrino Observatory, INO, is optimized to detect atmospheric ν_μ and $\bar{\nu}_\mu$ via muons in the few GeV energy range. To increase the sensitivity to low-energy electrons in ICAL, a study of electron energy resolution in the sub-GeV range with thinner 1.8 cm Fe plates, rather than the design value of 5.6 cm, is performed and presented. A comparison of RPCs and plastic scintillators as active detectors was also made.

101.1 Introduction

The proposed 50 kton magnetized ICAL detector at INO is optimized for measuring muons in the energy range of $\sim 1\text{--}20$ GeV [1]. The proposed geometry consists of 150 layers of RPCs (the active detectors) inter-leaved in the 40 mm air gap between layers of 56 mm thick iron plates. The muons would be produced through charged current (CC) interactions of atmospheric muon neutrinos (ν_μ and $\bar{\nu}_\mu$) and will help resolve neutrino mass ordering by using the Earth matter effect.

H. Khindri (✉) · D. Indumathi · M. V. N. Murthy
Homi Bhabha National Institute, Mumbai 400094, India
e-mail: honey@tifr.res.in

H. Khindri
Tata Institute of Fundamental Research, Colaba, Mumbai 400005, India

H. Khindri · D. Indumathi · M. V. N. Murthy
The Institute of Mathematical Sciences, Taramani, Chennai 600113, India

V. M. Datar
Department of High Energy Physics, Tata Institute of Fundamental Research, Colaba, Mumbai, India

S. M. Lakshmi
National Centre for Nuclear Research (NCBJ), Warsaw, Poland

The atmospheric neutrino flux also contains ν_e and $\bar{\nu}_e$ and peaks at low energies of about 100 MeV. It was shown in [2] that probing electrons produced from CC scattering of these electron neutrinos can give us sensitivity to δ_{CP} without hierarchy ambiguity. Energy resolution of electrons is a major factor affecting δ_{CP} sensitivity from the low-energy events. In particular, it was shown that sensitivity of about 2σ can be achieved in a narrow range of δ_{CP} in the presence of systematic uncertainties, if the energy resolution is reasonably good, i.e. $\sim \sigma/E = 15\%/\sqrt{E}$, where E is in GeV. Our aim is to check if such an electron energy resolution can be obtained in ICAL with a different geometry. This is done by performing a GEANT-4 based simulation of the ICAL detector with various geometries. Since the radiation length of electrons in Fe is about 1.76 cm in iron [3], we study the electron energy resolution of an ICAL with 18 mm Fe plates and variable air gap. The possibility of using plastic scintillators as an alternative active detector is also studied and compared.

101.2 Comparison Between RPC and Plastic Scintillator as an Active Detector

Geant-4-based simulation studies are done by reducing the thickness of Fe plate from 56 to 18 mm while keeping the air gap between the plates as 45 or 40 mm. In doing so, the number of Fe (RPC) layers changes from 151 (150) to 223 (222) or 250 (249) in order to keep the height of the detector constant at 14.45 m. Studies are done with both scintillator material as well as RPCs as the active detectors. For the study with scintillators, the RPC material in the Geant-code is simply replaced by scintillator material, and the same x - y resolution of 3 cm is assumed.

The distributions of the total hit multiplicity (labelled *orighits_old*) and the number of RPC/scintillator layers containing hits (labelled *nLayer*) of events for various geometries are shown in Fig. 101.1. These variables will be used as the unbiased parameters for further studies. Here, *orighits_old* represents the maximum number of hits in X or Y plane.

To compare RPC and scintillator charge current electron events are generated using Nuance neutrino events generator and used as input to Geant-code. On the left, the hits using 1.8 cm iron plates (222 layers of RPC) are compared with the hits obtained using 1.8 cm iron plates (222 layers of scintillators) in the simulation with 45 mm air gap. The figure on the right compares the number of layers obtained with 1.8 cm iron plates with RPC and scintillator detectors. As can be seen in Fig. 101.1, there is not much difference between RPC and scintillator.

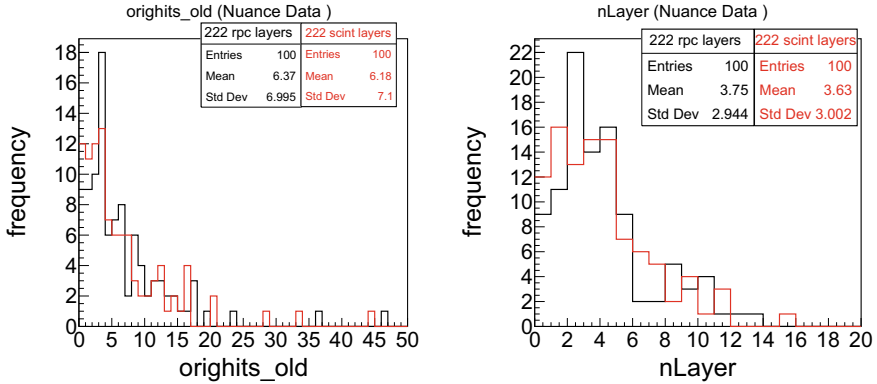
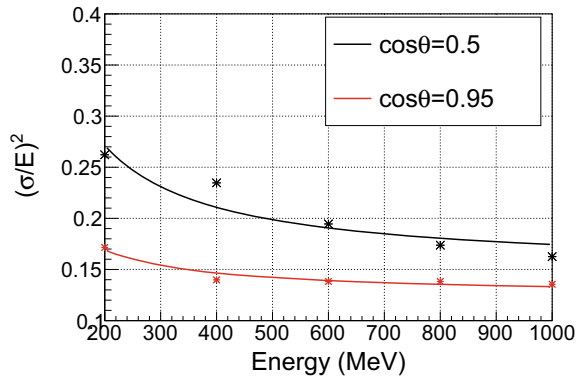


Fig. 101.1 Left: Total hits (*orighits_old*) obtained using 222 RPC layers and 222 scintillator layers with 1.8 cm iron plates, respectively; Right: No. of layers (*nLayer*) for 222 RPC and scintillator layers with 1.8 cm iron

Fig. 101.2 $(\sigma/E)^2$ versus E for electrons with energy from 0.2 to 1.0 GeV for $\cos\theta = 0.5, 0.95$



101.3 σ/E for Electrons with 18 mm Iron Plates

We use the framework used in [4] to estimate the energy response of hadrons and electrons. The energy resolution σ can be expressed in terms of the mean \bar{n} and RMS width Δn of the hits distribution obtained from *orighits_old* for a given electron energy, E :

$$\frac{\sigma}{E} \equiv \frac{\Delta n(E)}{\bar{n}} = \sqrt{\frac{a^2}{E} + b^2}. \tag{101.1}$$

The resolution σ/E is shown in Fig. 101.2 as a function of E .

The values of a and b from the fit tabulated in Table 101.1 show that an electron energy resolution of $\sigma/E = 15\%/\sqrt{E}$ is achievable in the 0.1–1.2 GeV energy range by “thin ICAL”.

Table 101.1 Best fit values of parameters a and b for 2 different values of cos theta

$\cos \theta$	a^2	b^2	a	b
0.5	0.0242	0.15	0.156	0.39
0.95	0.00896	0.1242	0.095	0.35

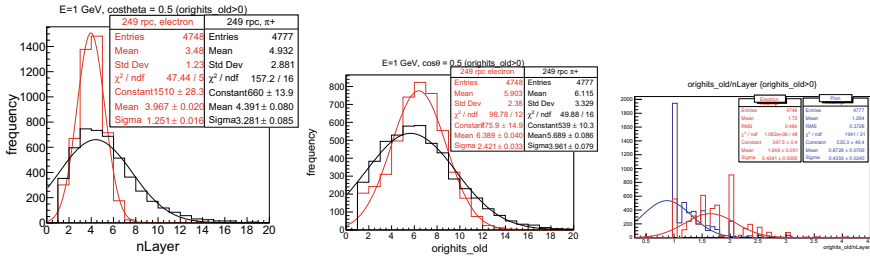


Fig. 101.3 $nLayer$, $orighit_old$ and $nLayer/orighit_old$ for electrons with 1.0 GeV energy, with angle $\cos \theta = 0.5$, in comparison with pions with the same energy and angle

101.4 Comparison of Pions and Electrons

Since both electron and pions produce showers, we need to distinguish true electron events from pion events. In Fig. 101.3 $nLayer$ and $orighits_old$ are plotted for electrons and pions of 1 GeV and $\cos \theta = 0.5$ with 249 iron layers and 40 mm air gap. While both $nLayer$ and $orighits_old$ histograms are narrow for electrons, the pion distribution shows large asymmetric tails since they undergo strong interaction. Hence, reconstruction for electron is expected to be better than pions.

The ratio of $orighits_old$ (S) and $nLayer$ (L) for energy of 1 GeV and $\cos\theta$ 0.5 is also shown Fig. 101.3. The S/L ratio is larger for electrons than pions; hence a cut on this ratio can be used to reject neutral current (NC) background dominated by pions.

101.5 Conclusion and Discussion

With thinner iron plates it is found that a resolution of $15\%/\sqrt{(E)}$ is achievable that will be relevant to study the CP phase using electron neutrino CC events in ICAL. For further studies, detailed analysis for δ_{CP} for “thin ICAL” will be done. Furthermore, other physics goals that can be explored by making such modifications in ICAL will be done.

Acknowledgements We thank Gobinda Majumder for help with the GEANT4 code; we thank members of the INO collaboration for valuable comments.

References

1. S. Ahmed et al., ICAL. *Pramana* **88**(5), 79 (2017)
2. S.M. Lakshmi et al., Hierarchy independent sensitivity to leptonic CP with atmospheric neutrinos. *Phys. Rev. D* **100**, 115027 (2019)
3. P.A. Zyla et al., Particle data group. *PTEP* **2020**(8), 083C01 (2020)
4. S.M. Lakshmi et al., Simulation studies of hadron energy resolution as a function of iron plate thickness at INO-ICAL. *JINST* **9**, T09003 (2014)

Chapter 102

Enhancing the Sensitivities to Standard Unknowns in Neutrino Oscillation Framework Using High-Energy Beams at DUNE



Jogesh Rout, Samiran Roy, Mehedi Masud, Mary Bishai, and Poonam Mehta

Abstract Even though neutrino oscillations have been conclusively established, there are a few unanswered questions pertaining to leptonic Charge Parity violation (CPV), mass hierarchy (MH) and θ_{23} octant degeneracy. Addressing these questions is of paramount importance in the current and future neutrino experiments including the Deep Underground Neutrino Experiment (DUNE) which has a baseline of 1300 km. In the standard mode, DUNE is expected to run with a *low-energy* (LE) tuned beam which peaks around the first oscillation maximum (2–3 GeV) (and then sharply falls off as we go to higher energies). However, the wideband nature of the beam available at long-baseline neutrino facility (LBNF) allows for the flexibility in utilizing beam tunes that are well suited at higher energies as well. In this work, we utilize a beam that provides high statistics at higher energies which is referred to as the *medium-energy* (ME) beam. This opens up the possibility of exploring not only the usual oscillation channels but also the $\nu_\mu \rightarrow \nu_\tau$ oscillation channel which was otherwise not accessible. Our goal is to find an optimal combination of beam tune and runtime (with the total runtime held fixed) distributed in neutrino and antineutrino mode that leads to an improvement in the sensitivities of these parameters at DUNE. In our analysis, we incorporate all the three channels ($\nu_\mu \rightarrow \nu_e$, $\nu_\mu \rightarrow \nu_\mu$, $\nu_\mu \rightarrow \nu_\tau$) and develop an understanding of their relative contributions in sensitivities at the level of $\Delta\chi^2$. Finally, we obtain the preferred combination of runtime using both

J. Rout (✉) · P. Mehta
Jawaharlal Nehru University, New Delhi 110067, India
e-mail: jogesh.rout1@gmail.com

S. Roy
Physical Research Laboratory, Ahmedabad 380009, India
Harish-Chandra Research Institute, Allahabad 211019, India

S. Roy · M. Masud
Homi Bhabha National Institute, Mumbai 400085, India

M. Masud
Institute of Physics, Bhubaneswar 7510059, India

M. Bishai
Brookhaven National Laboratory, P.O. Box 5000, Upton, NY 11973, USA

the beam tunes as well as neutrino and antineutrino modes that lead to enhanced sensitivity to the current unknowns in neutrino oscillation physics, i.e. CPV, MH and θ_{23} octant.

102.1 Introduction

The upcoming Deep Underground Neutrino Experiment (DUNE) [1–3] has the potential to resolve the key questions mentioned above with a very high precision. DUNE is expected to use the standard low-energy (LE) tuned flux (having a peak around 2–3 GeV and sharply falling at energies $E \gtrsim 4$ GeV) with a total runtime of 7 years distributed equally between the ν and $\bar{\nu}$ modes (3.5 years + 3.5 years). Among the viable additional beams that can be used at DUNE, there is a possibility of deploying a medium-energy tune (ME) based on the NuMI focusing system which offers substantial statistics even at energies $E \gtrsim 4$ GeV (albeit at the cost of some loss of statistics around 2–3 GeV). The role of the ME beam at DUNE has been explored in disentangling non-standard neutrino interactions (NSI) from the standard oscillation [4], constraining parameter degeneracies in the presence of NSI [5] and constraining unitarity using the $\nu_\mu \rightarrow \nu_\tau$ channel [6, 7]. To exploit the full potential of DUNE, we make use of this ME beam with a focus to exploit the high statistics it offers at higher energies. Since the neutrinos and antineutrinos encounter different potential due to earth matter effects, the variation of runtime of a long-baseline experiment such as DUNE while running in neutrino (ν) mode versus antineutrino ($\bar{\nu}$) mode could lead to a difference in sensitivities to MH, CPV and octant of θ_{23} . In the present work, we combine LE and ME beam tunes and vary runtime in the ν and $\bar{\nu}$ modes corresponding to each of the beams with the goal to improve the sensitivities of DUNE to MH, CPV and octant of θ_{23} . The present work goes beyond studies existing in the literature in two aspects. Firstly, we use an additional beam tune (ME beam) in conjunction with the standard LE beam (thus utilizing the wideband nature of DUNE to a greater extent) and analyse the variation of runtime for both the fluxes in the ν and $\bar{\nu}$ modes in order to improve the sensitivities. Secondly, since the ME beam we implement in our simulation has been optimized to detect a large number of ν_τ events, we include a $\nu_\mu \rightarrow \nu_\tau$ (as well as $\bar{\nu}_\mu \rightarrow \bar{\nu}_\tau$) appearance channel, in addition to $\nu_\mu \rightarrow \nu_e$ ($\bar{\nu}_\mu \rightarrow \bar{\nu}_e$) and $\nu_\mu \rightarrow \nu_\mu$ ($\bar{\nu}_\mu \rightarrow \bar{\nu}_\mu$) channels, in our analysis to estimate the sensitivities to CPV, MH and octant of θ_{23} .

102.2 Results and Discussion

We keep the total runtime at DUNE fixed at 7 years and numerically calculate χ^2 [8, 9] as a function of true $\delta \in [-\pi, \pi]$ after varying the distribution of runtime among the following four variables:

- Runtime using LE beam and in neutrino mode (\mathcal{R}_{LE})
- Runtime using LE beam and in antineutrino mode ($\overline{\mathcal{R}}_{LE}$)
- Runtime using ME beam and in neutrino mode (\mathcal{R}_{ME})
- Runtime using ME beam and in antineutrino mode ($\overline{\mathcal{R}}_{ME}$).

We present our main results by estimating the optimized runtime combinations of ($\mathcal{R}_{LE}, \overline{\mathcal{R}}_{LE}, \mathcal{R}_{ME}, \overline{\mathcal{R}}_{ME}$) that give the best sensitivities to resolve CPV, MH and octant of θ_{23} . Fig. 102.1 shows our results for the optimal combinations of runtimes and which are reported as ($\mathcal{R}_{LE} + \overline{\mathcal{R}}_{LE} + \mathcal{R}_{ME} + \overline{\mathcal{R}}_{ME}$) for the three different questions addressed in the present work.

CP violation, MH and octant of θ_{23} are the crucial unknowns and current and future long-baseline experiments such as DUNE are planned to address these questions. In the basic configuration, it is assumed that DUNE would have a runtime of 7 years (distributed equally in the ν and $\bar{\nu}$ mode) with the standard LE beam. The LE beam that is often used in DUNE simulations has a peak around 2–3 GeV (the first oscillation maximum for $\nu_{\mu} \rightarrow \nu_e$ transition probability) but very sharply falls off at $E \gtrsim 4$ GeV. Consequently, the number of events beyond 4 GeV rapidly becomes smaller, providing very little statistics. In the present work, we propose to use higher energy, ME beam that has a substantial flux even beyond 4 GeV in addition to the LE beam and ask whether this can offer any improvement to the standard sensitivity reach of DUNE in answering a question pertaining to CPV, MH and octant of θ_{23} . Table 102.1 summarizes the results for estimated optimized combinations with respect to CPV sensitivity, MH sensitivity and sensitivity to the octant of θ_{23} , respectively.

From Fig. 102.1, we find that a runtime combination of (3 + 2.5 + 1 + 0.5) gives the best sensitivity to CP violation if the hierarchy is normal. Also, the sensitivity

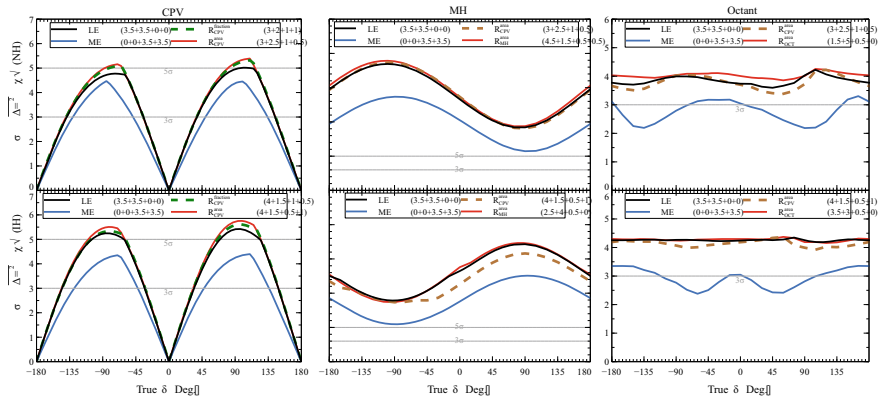


Fig. 102.1 The sensitivity to CPV, MH and θ_{23} octant for the different combinations of runtime and beam tunes is shown in the figure

Table 102.1 Best runtime combinations for sensitivity to CPV, MH and octant of θ_{23} where $R_{\text{CPV}}^{\text{area}}$, $R_{\text{MH}}^{\text{area}}$ and $R_{\text{OCT}}^{\text{area}}$ refer to the combinations with optimized area under respective curves and $R_{\text{CPV}}^{\text{fraction}}$ refers to the combination that resolves CPV above 3σ for the largest fraction of true σ parameter space

Sensitivity to	Optimization combination	NH	IH
		$(\mathcal{R}_{\text{LE}} + \overline{\mathcal{R}}_{\text{LE}} + \mathcal{R}_{\text{ME}} + \overline{\mathcal{R}}_{\text{ME}})$ (in years)	$(\mathcal{R}_{\text{LE}} + \overline{\mathcal{R}}_{\text{LE}} + \mathcal{R}_{\text{ME}} + \overline{\mathcal{R}}_{\text{ME}})$ (in years)
CPV	$R_{\text{CPV}}^{\text{area}}$	3 + 2.5 + 1 + 0.5	4 + 1.5 + 0.5 + 1
	$R_{\text{CPV}}^{\text{fraction}}$	3 + 2 + 1 + 1	4 + 1.5 + 1 + 0.5
MH	$R_{\text{MH}}^{\text{area}}$	4.5 + 1.5 + 0.5 + 0.5	2.5 + 4 + 0.5 + 0
Octant of θ_{23}	$R_{\text{OCT}}^{\text{area}}$ (HO)	1.5 + 5 + 0.5 + 0	3.5 + 3 + 0.5 + 0

can reach beyond 5σ , which was otherwise not possible with the standard DUNE configuration with LE beam alone near $\delta \simeq \pm\pi/2$ (maximal CPV). In addition to resolving CPV, this particular optimized runtime combination also offers high sensitivity to resolve the MH and octant of θ_{23} (see Fig. 102.1). For MH and octant of θ_{23} , the optimized runtime combinations providing the best sensitivities are found to be $(4.5 + 1.5 + 0.5 + 0.5)$ and $(1.5 + 5 + 0.5 + 0)$, respectively (assuming the neutrino mass hierarchy to be normal).

The improvement occurs near-maximal CP violation ($\delta = \pm\pi/2$) for CPV case and, for MH and Octant of θ_{23} cases, the combined beam tunes have similar results to LE beam.

102.3 Conclusion

This study, therefore, underscores the availability of the room for improvement within the DUNE experimental configuration by using a combination of runtime in the ν and $\bar{\nu}$ mode, exploiting two different (LE and ME) beam tunes. This suggested runtime configuration with the two available beam tunes will eventually help DUNE to answer, with more robustness, its main goals pertaining to leptonic CP violation, determination of MH and octant of θ_{23} . For details, see [10].

References

1. R. Acciarri et al., DUNE. [arXiv:1512.06148](https://arxiv.org/abs/1512.06148) [physics.ins-det]
2. B. Abi et al., DUNE. [arXiv:2002.03005](https://arxiv.org/abs/2002.03005) [hep-ex]
3. B. Abi et al., DUNE. *Eur. Phys. J. C* **80**(10), 978 (2020)
4. M. Masud, M. Bishai, P. Mehta, *Sci. Rep.* **9**(1), 352 (2019)
5. M. Masud, S. Roy, P. Mehta, *Phys. Rev. D* **99**(11), 115032 (2019)
6. A. De Gouvêa, K.J. Kelly, G.V. Stenico, P. Pasquini, *Phys. Rev. D* **100**(1), 016004 (2019)
7. A. Ghoshal, A. Giarnetti, D. Meloni, *JHEP* **12**, 126 (2019)
8. P. Huber, M. Lindner, W. Winter, *Comput. Phys. Commun.* **167**, 195 (2005)
9. P. Huber, J. Kopp, M. Lindner, M. Rolinec, W. Winter, *Comput. Phys. Commun.* **177**, 432 (2007)
10. J. Rout, S. Roy, M. Masud, M. Bishai, P. Mehta, *Phys. Rev. D* **102**, 116018 (2020)

Chapter 103

Hierarchy Sensitivity with Combined Standard and Rock Muons in ICAL at India-Based Neutrino Observatory



R. Kanishka, D. Indumathi, and S. M. Lakshmi

Abstract The neutrino mass ordering of the third mass eigen state vis-a-vis the first remains one of the undetermined parameters of neutrino physics. The proposed magnetized iron calorimeter detector (ICAL) at the India-based Neutrino Observatory (INO) has good sensitivity to this mass ordering, which it achieves by its capacity to distinguish neutrino and anti-neutrino-induced events through its charge identification capability. The charged current (CC) interactions of atmospheric muon neutrinos with the ICAL detector will produce muons and hadrons. The atmospheric muon neutrinos can also interact with the rock material surrounding the detector and produce muons and hadrons in corresponding CC interactions with the rock. While the hadrons get absorbed in the rock, some of these muons will reach the detector and get detected as well. We show that the combined sensitivity exceeds the sum of the two sensitivities by comparing the $\Delta\chi^2$ for the two cases. We discuss their significance for INO.

103.1 Introduction

The ICAL at INO experiment [1] aims to study atmospheric neutrinos which interact with the material of ICAL and give events in the detector. These events are called “standard muons” [2]. We focus on muon CC events, so signatures of these events are the muon tracks [3] and muon tracks along with hadron hits [4]. The atmospheric

R. Kanishka (✉)

Applied Nuclear Physics Division, Saha Institute of Nuclear Physics, 1/AF, Bidhannagar, Kolkata 700064, India

e-mail: kanishka.rawat.phy@gmail.com

D. Indumathi

The Institute of Mathematical Sciences, Chennai 600113, India

R. Kanishka · D. Indumathi

Homi Bhabha National Institute, Mumbai 400094, India

S. M. Lakshmi

National Centre for Nuclear Research, 05400 Warsaw, Poland

neutrinos also interact with the rock surrounding the detector and give muons and hadrons. However, these lose energy momentum when they traverse the detector, so the typical signature of these events in ICAL is muon tracks alone, coming in from outside. While such “rock muon” [5] events occur in rock surrounding the detector, the ones reaching from above cannot be distinguished from cosmic-ray muon background, and so we consider only upward-going rock muons.

The present paper is organized as follows: methodology, analysis and results, and conclusions have been discussed in the following sections.

103.2 Methodology

In combining the analysis of standard and rock muons, there are interesting correlations between all the pulls which are the same, and moreover, they are correlated between the two sets of events. Hence if the pulls increase the flux normalization by some amount in the standard muon computation, they increase it by the same amount in the rock muon computation. This means that when we combine the data from these two sources and do a simultaneous analysis, the combined $\Delta\chi^2$ is expected to be better than just the sum of the two when considered separately. The rock muons lose energy in the rock and hence are detected with much lower energy than that at which they were produced in the rock. While the muon is a minimum ionizing particle, there are still uncertainties (not included yet in the analysis) in its energy loss, which can be parameterized as [6]:

$$\frac{dE_\mu}{dx} = -a - bE_\mu.$$

103.3 Analysis and Results

The rock muons can enter from the bottom and four sides (called front, back, left, and right) of the ICAL detector. The rock muons from above (top) are ignored. The rock muons entering from the bottom can be confused with standard muons produced in the bottom iron layer of ICAL since the first detection is at the resistive plate chamber (RPC) [7] above this layer. Hence, we removed this sample from standard muon analysis by considering only 150 layers of iron in ICAL detector. The standard muons produced in the bottom plate are a background to the rock muons. So, we removed those events: from visible hadron energy and an energy cut was applied for no visible hadron energy, i.e., $E_\mu \geq 1$ GeV for rock muons from the bottom part of ICAL as shown in Fig. 103.1. The rock muons entering from the sides can be confused with standard muons which are produced at the edges and also going upwards. The contamination of rock muons in the standard muon sample is very small which was ignored. The contamination of standard muons in the rock sample

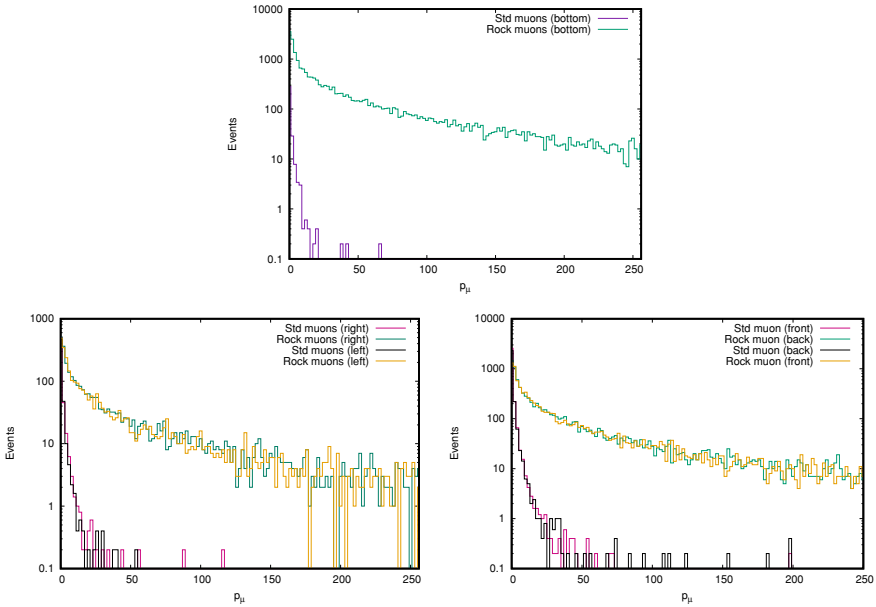


Fig. 103.1 The energy profile shows the contamination of standard muons in rock muons in the bottom part of ICAL (top), standard muons in rock muons in right and left (left) and in front and back (right) part of ICAL detector

can be reduced by putting $E_\mu > 4$ GeV cut for rock muons as shown in Fig. 103.1. We then used a χ^2 analysis and analyzed the data separately and together. We used the usual 11 pulls (5 each for μ^- and μ^+ and one constraint (11th pull)) [8, 9]: normalization, tilt, zenith angle, cross-section, reco-eff, μ^-/μ^+ ratio (constraint). Then we marginalized over θ_{23} , Δm^2 and θ_{13} and other values were fixed at their input values. Lastly, a prior (refer (5.16) of [9]) was included with an error of 1σ on $\sin^2 2\theta_{13}$ [10]. The χ^2 Poisson definition for 10 pulls with 1 constraint has been taken (refer (5.11)–(5.14) of [9]). The input neutrino oscillation parameters were used from [10]. Figure 103.2 shows hierarchy sensitivity for normal ordering. The same cuts on E_μ were used for both plots. The bottom line shows (old) results from standard muon analysis alone [2], the middle line shows sum of $\Delta\chi^2$ from standard and rock muons, and the top line shows the result of the combined analysis which is better than the naive sum.

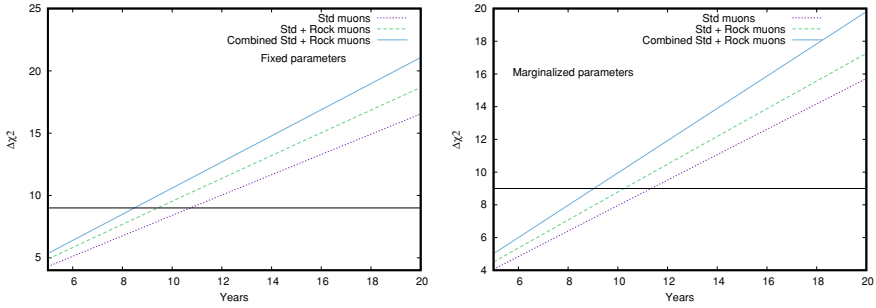


Fig. 103.2 The hierarchy sensitivity for normal ordering for fixed parameters (left) and marginalized parameters (right)

103.4 Conclusion

The proposed magnetized iron calorimeter detector (ICAL) at the India-based Neutrino Observatory (INO) [1] distinguishes neutrino and anti-neutrino through charge identification (cid) and therefore will solve the neutrino mass ordering problem [11]. The combined hierarchy sensitivity with standard and rock muons has been presented here. Both of these muons arise from the charged current (CC) interactions of atmospheric muon neutrinos. The standard muons arise from interactions of atmospheric muon neutrinos with ICAL detector, whereas rock muons arise from the interaction of atmospheric muon neutrinos with the rock material surrounding the detector. The analysis presented here shows that the combined sensitivity is greater than the sum of the two sensitivities.

Acknowledgements The authors thank DAE for funding and INO collaboration for the support.

References

1. A. Kumar et al., Invited review: physics potential of the ICAL detector at the India-based Neutrino Observatory (INO). *Pramana* **88**(5), 79 (2017)
2. L.S. Mohan, D. Indumathi, Pinning down neutrino oscillation parameters in the 2–3 sector with a magnetised atmospheric neutrino detector: a new study. *Eur. Phys. J. C* **77**(54) (2017)
3. A. Chatterjee et al., A simulations study of the muon response of the iron calorimeter detector at the india-based Neutrino Observatory. *JINST* **9**(7), 07001 (2014)
4. M.M. Devi et al., Hadron energy response of the iron calorimeter detector at the India-based Neutrino Observatory. *JINST* **8**(11), 11003 (2013)
5. R. Kanishka, V. Bhatnagar, D. Indumathi, Oscillation Sensitivity with Upward-going muons in ICAL at India-based Neutrino Observatory (INO). *Proc. Sci.* **226**(127) (2015)
6. P.A. Zyla et al., Particle data group. *Prog. Theor. Exp. Phys.* **2020**, 083C01 (2020)
7. B. Satyanarayana, Design and characterisation studies of resistive plate chambers. Ph.D thesis, Department of Physics, IIT Bombay, PHY-PHD-10-701 (2009)
8. M. Maltoni, M.C. Gonzalez-Garcia et al., Atmospheric neutrino oscillations and new physics. *Phys. Rev. D* **70**, 033010 (2004)

9. Kanishka: A study of upward-going muons in ICAL detector at India-based Neutrino Observatory. Ph.D thesis, Department Of Physics, Centre of Advanced Study in Physics, Panjab University, Chandigarh (2015)
10. I. Esteban, M. Gonzalez-Garcia, M. Maltoni et al., The fate of hints: updated global analysis of three-flavor neutrino oscillations. *J. High Energ. Phys.* **2020**, 178 (2020)
11. M. Blennow, T. Schwetz, Identifying the neutrino mass ordering with INO and NO ν A. *JHEP* **08**, 058 (2012)

Chapter 104

Fully Constrained Mass Matrix: Can Symmetries Alone Determine the Flavon Vacuum Alignments?



R. Krishnan

Abstract We introduce a new framework in which the flavour group is obtained as the direct product $G_f = G_r \times G_x$ where the flavons transform under both G_r and G_x while the fermions transform only under G_r . By coupling together several such flavons, we obtain an effective irreducible multiplet that transforms only under G_r . We define the alignments of the elementary flavons in terms of their residual symmetries under $G_r \times G_x$. As a result, we uniquely obtain the alignment of the effective G_r -multiplet as well, even though this multiplet may not possess any residual symmetry under G_r . We call this the framework of the auxiliary group. We argue that models constructed in this framework can lead to interesting predictions in flavour physics, specifically in the case of the fully constrained neutrino mass matrices.

104.1 Introduction

Discrete symmetries implemented using finite groups have been studied extensively [1–3] to construct flavour models in particle physics. In neutrino mixing phenomenology, tribimaximal (tbm) mixing [4] has been a popular template used by model builders. Since the reactor angle was found to be non-zero, several extensions of tbm have been proposed ([5–7] to name a few). One such extension is the triphimaximal mixing [8]

$$U_{T\phi M} = \begin{pmatrix} \sqrt{\frac{2}{3}} \cos \phi & \frac{1}{\sqrt{3}} & \sqrt{\frac{2}{3}} \sin \phi \\ -\frac{\cos \phi}{\sqrt{6}} - \frac{\sin \phi}{\sqrt{2}} & \frac{1}{\sqrt{3}} & \frac{\cos \phi}{\sqrt{2}} - \frac{\sin \phi}{\sqrt{6}} \\ -\frac{\cos \phi}{\sqrt{6}} + \frac{\sin \phi}{\sqrt{2}} & \frac{1}{\sqrt{3}} & -\frac{\cos \phi}{\sqrt{2}} - \frac{\sin \phi}{\sqrt{6}} \end{pmatrix}. \quad (104.1)$$

In [18], a Majorana neutrino mass matrix given by

R. Krishnan (✉)

Saha Institute of Nuclear Physics, 1/AF Bidhannagar, Kolkata 700064, India
e-mail: krishnan.rama@saha.ac.in

$$M_{\text{Maj}} \propto \begin{pmatrix} i + \frac{1-i}{\sqrt{2}} & 0 & 1 - \frac{1}{\sqrt{2}} \\ 0 & 1 & 0 \\ 1 - \frac{1}{\sqrt{2}} & 0 & -i + \frac{1+i}{\sqrt{2}} \end{pmatrix} \tag{104.2}$$

was proposed. It predicted triphimaximal mixing with $\phi = \frac{\pi}{16}$ as well as neutrino mass ratios

$$m_1 : m_2 : m_3 = \sqrt{2} \tan\left(\frac{3\pi}{16}\right) : 1 : \sqrt{2} \tan\left(\frac{5\pi}{16}\right). \tag{104.3}$$

Since this mass matrix does not contain any free parameter, it was called fully constrained.

To construct such a fully constrained mass matrix in general, we would require a flavon transforming as a complex sextet [9] which can span both the diagonal and off-diagonal parts of the mass matrix. $\Sigma(72 \times 3)$ is a group suited for this purpose since the tensor product of two triplets of this group gives rise to a complex sextet:

$$\mathbf{3} \otimes \mathbf{3} = \mathbf{6} \oplus \bar{\mathbf{3}}. \tag{104.4}$$

For a detailed study of this group, the reader may refer [10]. To construct the Majorana mass matrix, we assume that the right-handed neutrinos transform as a triplet under $\Sigma(72 \times 3)$:

$$\nu_R = (\nu_{R1}, \nu_{R2}, \nu_{R3})^T \equiv \bar{\mathbf{3}}. \tag{104.5}$$

We obtain the sextet as

$$\sum_{jk} S_{ijk} \nu_{Rj} \cdot \nu_{Rk} \equiv \bar{\mathbf{6}}_i, \tag{104.6}$$

where $\nu_{Rj} \cdot \nu_{Rk}$ are the Lorentz invariant products and

$$S_{111} = S_{222} = S_{333} = 1, S_{423} = S_{432} = S_{531} = S_{513} = S_{612} = S_{621} = \frac{1}{\sqrt{2}} \tag{104.7}$$

are the Clebsch-Gordan coefficients. We also have a flavon sextet

$$\xi = (\xi_1, \xi_2, \xi_3, \xi_4, \xi_5, \xi_6)^T \equiv \mathbf{6}, \tag{104.8}$$

which couples with (104.6) to obtain the invariant mass term:

$$\sum_{ijk} S_{ijk} \xi_i \nu_{Rj} \cdot \nu_{Rk} = \begin{pmatrix} \nu_{R1} \\ \nu_{R2} \\ \nu_{R3} \end{pmatrix}^T \begin{pmatrix} \xi_1 & \frac{1}{\sqrt{2}}\xi_6 & \frac{1}{\sqrt{2}}\xi_5 \\ \frac{1}{\sqrt{2}}\xi_6 & \xi_2 & \frac{1}{\sqrt{2}}\xi_4 \\ \frac{1}{\sqrt{2}}\xi_5 & \frac{1}{\sqrt{2}}\xi_4 & \xi_3 \end{pmatrix} \cdot \begin{pmatrix} \nu_{R1} \\ \nu_{R2} \\ \nu_{R3} \end{pmatrix}. \tag{104.9}$$

There is a one-to-one correspondence between the components of the complex sextet and the elements of the 3×3 complex symmetric Majorana mass matrix. The vacuum expectation value (vev) of the flavon that corresponds to the mass matrix (104.2) is

$$\langle \xi \rangle \propto \left(i + \frac{1-i}{\sqrt{2}}, 1, -i + \frac{1+i}{\sqrt{2}}, 0, (\sqrt{2}-1), 0 \right)^T. \quad (104.10)$$

We can obtain this vev by minimising the flavon potential [9]. However, this requires fine-tuning of parameters in the potential. To overcome this problem, the framework of the auxiliary group was proposed [11].

104.2 The Framework of the Auxiliary Group

In this framework, we assign more symmetries to flavons compared to fermions, i.e. fermions form only an unfaithful representation of the flavour group. We express the flavour group as a direct product $G_r \times G_x$, where G_r is a finite subgroup of $U(3)$ under which fermions, as well as flavons, transform nontrivially. Groups such as A_4 , S_4 and $\Sigma(72 \times 3)$ which are widely studied in flavour physics constitute G_r . On the other hand, only flavons transform nontrivially under G_x which we call the auxiliary group. Several flavons are coupled together to obtain an effective multiplet that is invariant under G_r so that it can be coupled with the fermions. The purpose of G_x is to provide additional symmetries to the flavons resulting in specific vevs whose alignments are completely determined by their symmetries. With such construction we can avoid fine-tuning of parameters in the flavon potential. For a detailed study of how to vacuum alignments can be obtained independent of fine-tuning, please see [12]. We note that a mechanism similar to what we described here was proposed earlier [13–15] in the context of decoupling the neutrino sector from the charged-lepton sector.

Our objective is to obtain the $\Sigma(72 \times 3)$ -sextet, ξ , (104.8), as an effective multiplet. For this, we construct a group which we call X_{24} [11]. We use two copies of X_{24} which form G_x along with $\Sigma(72 \times 3)$ which forms G_r . Three elementary flavons $\hat{\phi}$, $\check{\phi}$ and Δ are proposed which transform as $\mathbf{3} \times \mathbf{6} \times \mathbf{1}$, $\mathbf{3} \times \mathbf{1} \times \mathbf{6}$ and $\mathbf{1} \times \mathbf{6} \times \mathbf{6}$ under the flavour group $\Sigma(72 \times 3) \times X_{24} \times X_{24}$. The effective triplet is obtained as

$$\xi_i = \sum S_{imn} \hat{\phi}_{\alpha m} \check{\phi}_{\beta n} \Delta_{\alpha\beta}. \quad (104.11)$$

The elementary fields acquire the following vev:

$$\langle \hat{\phi} \rangle = \langle \dot{\phi} \rangle \propto \begin{pmatrix} \tau & 0 & 0 \\ 0 & \omega & 0 \\ 0 & 0 & \bar{\tau} \\ -i & 0 & 0 \\ 0 & \bar{\omega} & 0 \\ 0 & 0 & i \end{pmatrix}, \langle \Delta \rangle \propto \begin{pmatrix} 1 & 0 & 0 & 1 & 0 & 0 \\ 0 & 1 & 0 & 0 & 1 & 0 \\ 0 & 0 & 1 & 0 & 0 & 1 \\ 0 & 0 & 1 & 0 & 0 & 1 \\ 0 & 1 & 0 & 0 & 1 & 0 \\ 1 & 0 & 0 & 1 & 0 & 0 \end{pmatrix}. \quad (104.12)$$

We show that the alignment of this vev is fully determined by its residual symmetries under our flavour group $\Sigma(72 \times 3) \times X_{24} \times X_{24}$. As a result, the vev can be obtained without the need for any fine-tuning of the parameters in the potential. Combining the vev of the elementary fields (104.12) using (104.11), we obtain the vev of the effective multiplet (104.10) as required.

104.3 Summary

We discuss the framework of the auxiliary group where we allow flavons to have a larger set of symmetries than fermions. Effective multiplets of flavons are constructed, which couple with fermions to obtain the mass terms. This framework can help model builders in two ways. It can naturally decouple mass terms of different sectors, a problem commonly encountered in models ([16, 17] to name a few). It can also result in very interesting vevs [9] which are otherwise difficult to model.

Acknowledgements I thank Paul Harrison and Bill Scott for the helpful discussions. I acknowledge the support from the University of Warwick and the hospitality of the Particle Physics Department at the Rutherford Appleton Laboratory. I thank the organisers of DAE-BRNS HEP Symposium 2020 for giving me the opportunity to present this work.

References

1. W. Grimus, *Phys. Part. Nucl.* **42**, 566–576 (2011)
2. S. King, C. Luhn, *Rept. Prog. Phys.* **76**, 056201 (2013)
3. D. Meloni, *Front. Phys.* **5**, 43 (2017)
4. P. Harrison, D. Perkins, W. Scott, *Undefined. Phys. Lett. B.* **530**, 167 (2002)
5. S. Pakvasa, W. Rodejohann, T. Weiler, *Phys. Rev. Lett.* **100**, 111801 (2008)
6. X. He, A. Zee, *Phys. Rev. D.* **84**, 053004 (2011)
7. S. Garg, S. Gupta, *JHEP* **10**, 128 (2013)
8. P. Harrison, W. Scott, *Phys. Lett. B.* **535**, 163–169 (2002)
9. R. Krishnan, P. Harrison, W. Scott, *Eur. Phys. J. C.* **78**, 74 (2018)
10. W. Grimus, P. Ludl, *J. Phys. A.* **43**, 445209 (2010)
11. R. Krishnan, *Phys. Rev. D.* **101**, 075004 (2020)
12. R. Krishnan, *Phys. Rev. D.* **103**, L051701 (2021)
13. K. Babu, S. Gabriel, *Phys. Rev. D.* **82**, 073014 (2010)
14. M. Holthausen, M. Schmidt, *JHEP* **1**, 126 (2012)
15. M. Holthausen, M. Lindner, M. Schmidt, *Phys. Rev. D* **87**, 033006 (2013)

16. R. Krishnan, A. Mukherjee, S. Goswami, *JHEP* **9**, 050 (2020)
17. M. Chakraborty, R. Krishnan, A. Ghosal, *JHEP* **9**, 025 (2020)
18. R. Krishnan, Undefined. *J. Phys. Conf. Ser.* **447**, 012043 (2013)

Chapter 105

Inverse Seesaw Mechanism with A_4 Flavour Symmetry



Maibam Ricky Devi and Kalpana Bora

Abstract We study the low-scale inverse seesaw model [1], within the framework of A_4 flavour symmetry. We also include some other discrete symmetries [2], like Z_4 , Z_5 etc., which are needed to forbid the unwanted terms in the Lagrangian. Next, we obtain the correlation plots among neutrino oscillation parameters and also study neutrinoless double beta decay. The computation is done up to the tolerance level of 10^{-5} , and in the future will apply the results to investigate the charged lepton flavour violating decays too.

105.1 Introduction

Seesaw mechanisms are generally used to obtain the ultra-light mass of the neutrinos, and many seesaw models have been proposed by the researchers—like type I, type II, type III, inverse, linear and hybrid seesaw models. In this work, we study a low-scale model—the inverse seesaw mechanism to investigate about the rich phenomenological aspects of neutrinos such as their masses and mixings, viable flavour structure and neutrinoless double beta decay. Low-scale models become particularly interesting as they are testable at ongoing/future experiments. We have chosen to do so within the framework of A_4 flavour symmetry (so as to explain the observed flavour structure of particles) and some other discrete symmetries, like Z_4 and Z_5 to explain the measured unknown oscillation parameters. These other discrete symmetries are required to forbid the unwanted terms in the Lagrangian. The values of light neutrino oscillation parameters thus obtained can be used later to analyse the

After presenting this work at XXIV DAE-BRNS High Energy Physics, Jatni, 2020, this work was communicated to Modern Physics Letters A and got published on the same on 17th of May, 2022 (<https://doi.org/10.1142/S0217732322500730>).

M. Ricky Devi (✉) · K. Bora
Department of Physics, Gauhati University, Guwahati 781014, Assam, India
e-mail: deviricky@gmail.com

K. Bora
e-mail: kalpana@gauhati.ac.in

© The Author(s), under exclusive license to Springer Nature Singapore Pte Ltd. 2022
B. Mohanty et al. (eds.), *Proceedings of the XXIV DAE-BRNS High Energy Physics Symposium, Jatni, India*, Springer Proceedings in Physics 277,
https://doi.org/10.1007/978-981-19-2354-8_105

favoured Octant degeneracy (lower or upper octant of atmospheric mixing angle), favoured neutrino mass hierarchy (inverted or normal) and charged lepton flavour violation decays as well.

105.2 Seesaw Models

In this section we discuss the inverse seesaw model with A_4 flavour symmetry, where the SM is extended with the additional discrete symmetries like $Z_N, U(1)_X$, to make sure that no unwanted terms appear up to dimension 6 in the model.

105.2.1 The Inverse Seesaw (ISS) Model

The particle content of the ISS model is shown in Table 105.1, and its Lagrangian is constructed using $A_4 \times Z_4 \times Z_5 \times U(1)_X$ symmetry whose neutrino sector is given as

$$\mathcal{L}_Y \supset Y_D \frac{\bar{L} \tilde{H} N \rho^\dagger}{\Lambda} + Y_M N S \rho^\dagger + Y_\mu S S \left[\frac{\rho' \rho''^\dagger (\Phi_s + \eta + \xi + \tau)}{\Lambda^2} \right] + h.c., \quad (105.1)$$

where $\Phi_T, \Phi_S, \eta, \xi, \tau, \rho, \rho', \rho''$ are flavons (that can acquire VEV to break the flavour symmetry), Λ is the cut-off scale of the theory, $N_{i=1,2,3}$ is a $SU(2)_L$ singlet right-handed neutrino and $S_{i=1,2,3}$ (Sterile neutrinos) are three other singlet fermions. We know that the light neutrino mass matrix can be constructed from the parametrised PMNS mixing matrix, U_{PMNS} as

$$m_\nu = U_{PMNS} M_\nu^{\text{diag}} U_{PMNS}^T, \quad (105.2)$$

where $M_\nu^{\text{diag}} = \text{diag}(m_1, m_2, m_3)$ is the diagonal matrix with three light neutrino masses as its eigenvalues.

Table 105.1 Transformation of the fields under $A_4 \times Z_4 \times Z_5 \times U(1)_X$ symmetry for neutrino mass model realising inverse seesaw mechanism

	L	H	e_R	μ_R	τ_R	N	S	Φ_T	Φ_s	η	ξ	τ	ρ	ρ'	ρ''
A_4	3	1	1	1''	1'	3	3	3	3	1	1'	1''	1	1	1
Z_4	1	1	i	i	i	i	1	i	-i	-i	-i	-i	i	i	1
Z_5	1	1	ω	ω	ω	ω^2	1	ω	1	1	1	1	ω^2	1	1
$U(1)_X$	-1	0	-1	-1	-1	-1	1	0	-1	-1	-1	-1	0	-4	-3

This table is a part of the paper already published in MPLA on 17th of May, 2022 (<https://doi.org/10.1142/S0217732322500730>)

105.3 Numerical Analysis

To begin with, we construct the Lagrangian of the model, allowed by the symmetries of the theory, as explained above. We next compare the mass matrices formed from the Lagrangian in (105.1) (in terms of various mass scales and flavon VEVs) with that obtained from global best-fit values of the light neutrino oscillation parameters, from (105.2), and solve for unknown parameters ($m_{lightest}$, δ_{CP} , α , β), using different VEV alignments of the triplet flavon field. The 3σ range of the global best-fit values of light neutrino oscillation parameters is used as inputs. The solutions obtained can be plotted to show correlation among them, and these can be used for studying other phenomenological aspects such as neutrinoless double beta decay, branching ratio (BR) of the $\mu \rightarrow e\gamma$ decay to study lepton flavour violation, etc. We have done this analysis up to the tolerance level of 10^{-5} . These results can be used to constrain our model.

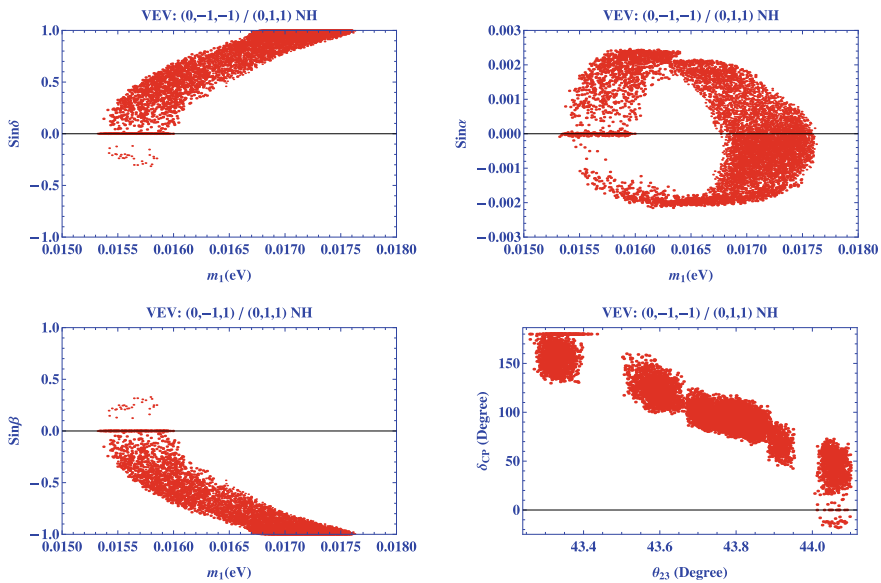


Fig. 105.1 Correlation plots for neutrino oscillation parameters for inverse seesaw model (normal hierarchy) with allowed triplet flavon VEV alignment $(0, -1, -1)/(0, 1, 1)$. These figures are part of the paper already published in MPLA on 17th of May, 2022 (<https://doi.org/10.1142/S0217732322500730>)

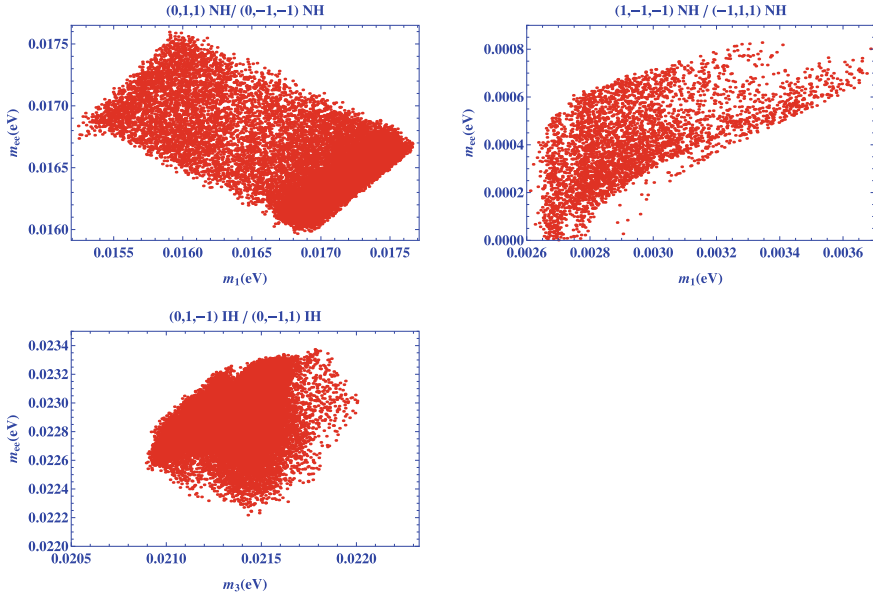


Fig. 105.2 Plots of lightest neutrino mass versus effective neutrino mass of neutrinoless double beta decay for allowed triplet flavon VEV alignments for inverse seesaw model. These figures are part of the paper already published in MPLA on 17th of May, 2022 (<https://doi.org/10.1142/S0217732322500730>)

105.4 Results

A few of the correlation plots among light neutrino oscillation parameters and lightest neutrino mass, and effective neutrino mass obtained in neutrinoless double beta decay are shown in Figs. 105.1 and 105.2, respectively. In Table 105.2, we have shown some results of effective neutrino mass in neutrinoless double beta decay for the three allowed cases. After solving the set of simultaneous equations for the inverse seesaw model, it is found that the range of θ_{23} for VEV $(0, -1, -1)$ NH/ $(0, 1, 1)$ NH, $(1, -1, -1)$ NH/ $(-1, 1, 1)$ NH and $(0, -1, 1)$ IH/ $(0, 1, -1)$ IH are $(43.17, 44.07, \text{LO})$, $(50.06, 50.70, \text{HO})$ and $(43.09, 43.30, \text{LO})$, respectively.

105.5 Discussion and Conclusion

We observe that in our model we have obtained the values of parameters— θ_{23} , lightest neutrino mass, CPV phases and effective mass in neutrinoless double beta decay, within their 3σ ranges. So our model is testable in ongoing/future experiments. For three allowed triplet flavon VEV alignments, we can tell the favoured octant of θ_{23} and mass hierarchy, as discussed in Results. This can also help to study the rich

Table 105.2 Ranges of parameters as obtained in our analysis, for the inverse seesaw mechanism-based neutrino model with triplet flavon VEV $(0, -1, -1)$ NH/ $(0, 1, 1)$ NH, VEV $(-1, 1, 1)$ NH/ $(1, -1, -1)$ NH and VEV $(0, -1, 1)$ IH/ $(0, 1, -1)$ IH

SL. no	Allowed VEV alignments	m_{ee} (eV)
1	CASE A: $(0, -1, -1)$ NH/ $(0, 1, 1)$ NH	$(0.01599, 0.01760)$
2	CASE B: $(1, -1, -1)$ NH/ $(-1, 1, 1)$ NH	$(8.24651 \times 10^{-6}, 0.00094)$
3	CASE C: $(0, -1, 1)$ IH/ $(0, 1, -1)$ IH	$(0.02215, 0.02337)$

These results are part of the paper already published in MPLA on 17th of May, 2022 (<https://doi.org/10.1142/S0217732322500730>)

phenomenology in neutrino physics which is related to octant degeneracy problem in future. Since we do not know about the VEV alignment of flavons, the results obtained in this work can be used to discriminate among them in the future when the octant of atmospheric mixing angle and mass hierarchy are fixed. The simulated data generated here can be extensively used later to study the lepton flavour violation (LFV). We also observe from Fig. 105.2 that the pattern of correlation between the effective light neutrino masses that can be measured in the $0\nu\beta\beta$ experiments depends on the hierarchy of neutrino masses. So, from these results one can also pinpoint the mass hierarchy of neutrinos, and with the mass hierarchy, the favoured VEV alignment of triplet flavon will also change. Due to limitation of space, we are not able to show other results here, so will be presented in detail in a future publication elsewhere.

References

1. R.N. Mohapatra, Phys. Rev. Lett. **56**, 561 (1986); R.N. Mohapatra, J.W.F. Valle, Phys. Rev. D **34**, 1642 (1986); B. Karmakar, A. Sil, Phys. Rev. D **96**(1), 015007 (2017). <https://doi.org/10.1103/PhysRevD.96.015007> arXiv:1610.01909[hep-ph]
2. H. Ishimori, T. Kobayashi, H. Ohki, H. Okada, Y. Shimizu, M. Tanimoto, Lect. Notes Phys. **858**, 1 (2012). <https://doi.org/10.1007/978-3-642-30805-5>

Chapter 106

Baryogenesis Through Leptogenesis in a S_4 Flavon Model with TM_1 Mixing for Neutrinos



Mainak Chakraborty, Krishnan Rama, and Ambar Ghosal

106.1 Introduction

To explain the present neutrino oscillation data and observed baryon asymmetry of the universe simultaneously, we extend the well-known standard model (SM) by adding right-handed (RH) neutrinos and a few scalar fields (known as flavons) which transform nontrivially under the newly imposed discrete symmetries (S_4, C_3, C_6) [1]. CP violation in the leptonic sector has been introduced by the complex vacuum expectation value (VEV) of the flavons. CP violating out of equilibrium decay of heavy Majorana-type RH neutrinos creates lepton asymmetry, part of which is converted to baryon asymmetry [2] by sphaleron process.

106.2 S_4 Symmetry Invariant Lagrangian in the Flavon Model

The part of the invariant Lagrangian [3] responsible for generation of masses of charged leptons and neutrinos is given by

$$\mathcal{L} = \left\{ y_\tau \bar{L} \frac{\phi_C}{\Lambda} \tau_R H + y_\mu \bar{L} \frac{\phi_C^*}{\Lambda} \mu_R H + y_e \bar{L} \frac{(\phi_C^* \phi_C)_3}{\Lambda^2} e_R H \right\} + \left\{ y_{D1} \bar{L} N \frac{\eta_D}{\Lambda} \tilde{H} + y_{D3} (\bar{L} N)_3 \frac{\phi_D}{\Lambda} \tilde{H} \right\} + \left\{ y_{M1} \bar{N}^c N \eta_M + y_{M3} (\bar{N}^c N)_3 \phi_M \right\}. \quad (106.1)$$

M. Chakraborty (✉)
School of Physical Sciences, Indian Association for the Cultivation of Science, Kolkata, India
e-mail: psmc2382@iacs.res.in

K. Rama · A. Ghosal
Saha Institute of Nuclear Physics, HBNI, 1/AF Bidhannagar, Kolkata 700064, India
e-mail: krishnan.rama@saha.ac.in

A. Ghosal
e-mail: ambar.ghosal@saha.ac.in

106.2.1 Mass Matrices and their Diagonalization

The charged lepton mass matrix given by

$$M_C = i\sqrt{3}v \frac{v_C^2}{\Lambda^2} \begin{pmatrix} y_e & 0 & 0 \\ y_e & 0 & 0 \\ y_e & 0 & 0 \end{pmatrix} + v \frac{v_C}{\Lambda} \begin{pmatrix} 0 & y_\mu & y_\tau \\ 0 & \bar{\omega}y_\mu & \omega y_\tau \\ 0 & \omega y_\mu & \bar{\omega}y_\tau \end{pmatrix} \quad (106.2)$$

arises from the first three terms of the Lagrangian (106.1) after the corresponding flavon and SM Higgs fields acquire VEVs. M_C is diagonalized by a bi-unitary transformation as $VM_C \text{diag}(-i, 1, 1) = \text{diag}(m_e, m_\mu, m_\tau)$, where V is the tri-maximal mixing matrix (which is sometimes referred to as the magic matrix). The Dirac neutrino mass matrix (M_D) is obtained by substituting the VEVs of SM Higgs and two flavon fields ($\langle \eta_D \rangle = v_{D1}$, $\langle \phi_D \rangle = v_{D3}(-1, -1, 1)$). The Majorana-type mass matrix (M_M) for the heavy RH neutrinos arises through the substitution of complex VEVs of the flavons $\langle \eta_M \rangle = v_{M1}e^{i\xi_1}$ and $\langle \phi_M \rangle = v_{M3}e^{i\xi_3}(0, 1, 0)$. The smallness of the light neutrino mass is achieved through the Type-I seesaw mechanism which gives the light neutrino mass matrix¹

$$M_{ss} = -M_d M_M^{-1} M_D^T = -\frac{\mathcal{M}_w^2}{\mathcal{M}_f} \begin{pmatrix} d_1 & -f_1 & f_2 \\ -f_1 & d_2 & f_1 \\ f_2 & f_1 & d_1 \end{pmatrix}. \quad (106.3)$$

It is diagonalized through successive rotations by the bi-maximal mixing matrix (U_{BM}) followed by an orthogonal rotation in the 23 block (U_{23}). Considering the contribution of charged lepton diagonalization matrix (V), the total neutrino mixing matrix is given by $U_{PMNS} = V U_{BM} U_{23}$.

106.3 Generation of Baryon Asymmetry Through Leptogenesis

The heavy Majorana-type RH neutrinos can decay to lepton, Higgs pair through their Yukawa couplings. Due to the imbalance in the decay rate of the actual process and its CP conjugate, a net CP asymmetry arises. These CP asymmetry parameters are then used in the set of Boltzmann equation which tracks the evolution of the lepton asymmetry down to the present-day temperature.

¹ d_1, d_2, f_1, f_2 are functions of $\mathcal{M}_w^2/\mathcal{M}_f, k, \Re(z), \Im(z)$ where k, z are dimensionless parameters which are functions of various flavon Yukawa couplings and VEVs.

106.3.1 CP Asymmetry and Solution of Boltzmann Equation

The measure of flavour-dependent CP asymmetry is characterized by

$$\begin{aligned} \varepsilon_i^\alpha &= \frac{\Gamma(N_i \rightarrow l_\alpha^- H^+, \nu_\alpha H^0) - \Gamma(N_i \rightarrow l_\alpha^+ H^-, \nu_\alpha^c H^{0*})}{\sum_\alpha [\Gamma(N_i \rightarrow l_\alpha^- H^+, \nu_\alpha H^0) + \Gamma(N_i \rightarrow l_\alpha^+ H^-, \nu_\alpha^c H^{0*})]} \\ &= G(H', M'_D, x_{ij}), \end{aligned} \quad (106.4)$$

where Γ is the decay width of RH neutrino (N_i). The indices i and α are used to specify the generation of RH neutrinos and lepton flavours, respectively. It is to be noted that the decay widths are calculated in the standard basis.² Here $H' = M'_D{}^\dagger M'_D$, $x_{ij} = M_j^2/M_i^2$. The unflavoured CP asymmetry parameter (ε_i) is obtained by summing over the flavour index α . The Boltzmann equations can be solved in principle to get the final value of the $(B - L)$ asymmetry as $\eta_{B-L}^f = -\sum \varepsilon_i \kappa_i^f$ (assuming no pre-existing asymmetry). An appropriate analytic approximation for the final value of efficiency factor (κ_i^f) corresponding to the lightest RH neutrino (N_1) has been found to be

$$\kappa_1^f(K_1) = \{2/(K_1 z_B(K_1))\} \{1 - \exp(-.5K_1 z_B(K_1))\}. \quad (106.5)$$

$K_i = \Gamma/H(z = 1)$ is known as decay parameter. Taking into account the sphaleronic conversion factor (a_{sph}) and the dilution factor (f), the baryon asymmetry parameter³ is evaluated as $\eta_B = (a_{\text{sph}}/f)\eta_{B-L}^f = -0.96 \times 10^{-2} \sum_i \varepsilon_i \kappa_i^f$.

106.3.2 Flavour Decoherence and Importance of Pure N_2 Contribution

At a temperature ($T > 10^{12}$) GeV (or equivalently ($M_1 > 10^{12}$) GeV) the RH neutrino decay produces lepton doublet ($|l_i\rangle$) states which can be treated as a coherent superposition of the lepton flavour states. In this regime there are no such fast-charged lepton interactions that can break the coherence between the lepton flavours and thus the net asymmetry is produced along $|l_i\rangle$. When the temperature drops below 10^{12} GeV, (but still above 10^9 GeV) the τ -Yukawa interactions become faster than the inverse decay rate. Thus the coherence between the three flavours (in $|l_i\rangle$ state produced due to the decay of N_i) is broken partially and the τ flavour gets projected in a specific direction, whereas the admixture of e and μ is projected in a plane perpendicular to that of τ . Below $T = 10^9$ GeV the lepton flavour decoherence is achieved fully which demands separate treatment for all three flavours. Therefore in

² 'Standard basis' \Rightarrow RH neutrino diagonal basis where $M_D \rightarrow M'_D = V M_D U_{\text{BM}} U_p$.

³ $\eta_B(Y_B) =$ (baryon-antibaryon) number density scaled by photon(entropy) density.

this case we have flavour-dependent efficiency factor ($\kappa_{i\alpha}^f$) which can be obtained from (106.5) simply by the replacement $K_1 \rightarrow K_1^\alpha |A_{\alpha\alpha}|$, where $A_{\alpha\alpha}$ is the asymmetry coupling matrix. Now as an example let us briefly discuss about the computation of asymmetry in the τ -flavoured regime. The asymmetry produced by N_1 and N_2 (assuming N_3 much heavier) along τ direction is given by

$$N_{\Delta_\tau} = -\varepsilon_{1\tau}\kappa_{1\tau}^f - \varepsilon_{2\tau}\kappa_{2\tau}^f \exp\{-(3\pi K_{1\tau})/8\}, \quad (106.6)$$

where the exponential suppression in the RHS of (106.6) denotes the washout of N_2 generated asymmetry by N_1 interaction. But in τ_\perp direction only a fraction (p_{12} = probability of overlap between $|l_2^{\tau_\perp}\rangle$ and $|l_1^{\tau_\perp}\rangle$) of the N_2 generated asymmetry will be washed out by N_1 . Summing over the contributions of N_1 and N_2 we get

$$N_{\Delta_{\tau_\perp}} = -\varepsilon_{1\tau_\perp}\kappa_{1\tau_\perp}^f - p_{12}\varepsilon_{2\tau_\perp}\kappa_{2\tau_\perp}^f \exp\{-(3\pi K_{1\tau_\perp})/8\}. \quad (106.7)$$

If asymmetry is produced in such a direction which is perpendicular to τ_1^\perp , it becomes orthogonal to $|l_1^{\tau_\perp}\rangle$ and thus remains totally unaffected by N_1 washout. So sometimes it is referred to as the ‘pure N_2 contribution’. Due to absence of exponential suppression it contributes significantly to the total asymmetry as

$$N_{\Delta_{\tau_\perp}} = -(1 - p_{12})\varepsilon_{2\tau_\perp}^\perp \kappa_{2\tau_\perp}^f. \quad (106.8)$$

106.4 Numerical Results and Conclusion

The effective neutrino mass matrix M_{ss} can be parameterized by four parameters ($\mathcal{M}_w^2/\mathcal{M}_f$, k , $\Re e(z)$, $\Im m(z)$). A detailed numerical analysis reveals that indeed there exists a common parameter space (shown in Fig. 106.1) satisfying neutrino oscillation data [4] as well as the bound [5] on the baryon asymmetry parameter ($Y_B = (n_B - n_{\bar{B}})/s = (8.55 - 9.37) \times 10^{-11}$). Therefore demanding a positive value of the baryon asymmetry, the existing 3D parameter space has shrunk further which is shown in the right panel of Fig. 106.1. The factor M_f is basically the mass scale of the RH neutrino which actually determines the regime (unflavoured/flavoured) we are working in, whereas \mathcal{M}_w is a completely unknown parameter. It can be constrained by using the bound on the baryon asymmetry parameter. The usefulness of the analytical formulas for efficiency factors (κ) has been justified through its comparison with the result of the actual numerical solution of the Boltzmann equation (Table 106.1). The sizeable contribution to asymmetry from N_2 has also been shown in the same table.

Before concluding let us make a few important remarks to substantiate this study. It has been shown that the light neutrino mass matrix (M_{ss}) is diagonalized by a TM_1 type matrix. The final value of the baryon asymmetry parameter has been calculated by a detailed numerical solution of the coupled Boltzmann equation as well as using some appropriate analytical fits. Near equality of the results obtained through these

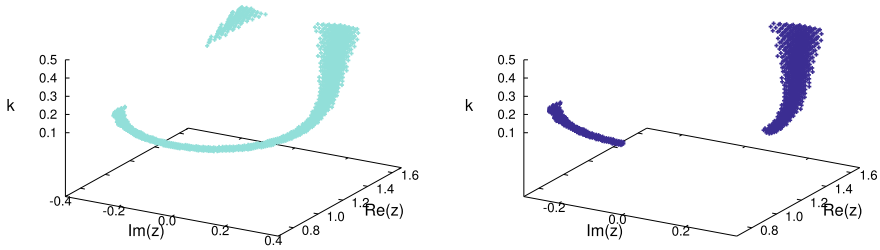


Fig. 106.1 Left: Parameter space allowed by 3σ global fit of oscillation data, right: parameter space constrained further by the condition of positive baryon asymmetry

Table 106.1 $(Y_B)_1, (Y_B)_2$: Results evaluated through numerical solution of Boltzmann equations with and without pure N_2 contribution, respectively, whereas $(Y_B)_{\kappa_1}, (Y_B)_{\kappa_2}$ are their counterparts obtained using analytical formula. $E\% = \left| \frac{(Y_B)_{\kappa_1} - (Y_B)_1}{(Y_B)_1} \right| \times 100$

\mathcal{M}_w (GeV)	M_1 (GeV)	M_2/M_1	$(Y_B)_1$	$(Y_B)_2$	$(Y_B)_{\kappa_1}$	$(Y_B)_{\kappa_2}$	$E\%$
2	1.49×10^{12}	1.90	8.09×10^{-11}	2.76×10^{-11}	8.87×10^{-11}	3.07×10^{-11}	9.6
2.04	1.55×10^{12}	1.90	8.42×10^{-11}	2.87×10^{-11}	9.23×10^{-11}	3.19×10^{-11}	9.61
2.08	1.62×10^{12}	1.90	8.75×10^{-11}	2.99×10^{-11}	9.6×10^{-11}	3.32×10^{-11}	9.71

two processes justifies the use of the analytical formulas to scan the whole of the 3σ parameter space. Substantial contribution of the next to lightest RH neutrino (N_2) towards the total asymmetry (in flavoured regime only) has also been noted.

References

1. T. Brown, S. Pakvasa, H. Sugawara, Y. Yamanaka, Phys. Rev. D **30**, 255 (1984)
2. M. Fukugita, T. Yanagida, Phys. Lett. B **174**, 45–47 (1986)
3. M. Chakraborty, R. Krishnan, A. Ghosal, JHEP **09**, 025 (2020)
4. I. Esteban, M.C. Gonzalez-Garcia, A. Hernandez-Cabezudo, M. Maltoni, T. Schwetz, JHEP **01**, 106 (2019)
5. N. Aghanim et al., Planck. Astron. Astrophys. **596**, A107 (2016)

Chapter 107

The Mitchell Institute Neutrino Experiment at Reactor (MINER)



Mouli Chaudhuri

Abstract The Mitchell Institute Neutrino Experiment at Reactor or MINER at Texas A&M University, USA is a reactor-based neutrino experiment which aims to measure coherent elastic neutrino-nucleus scattering ($CE\nu NS$). MINER uses two types of low-energy threshold novel silicon detectors which allow discrimination of signal from a background on an event-by-event basis while providing baseline resolution of $\sim 1 e^-/h^+$ pair. MINER is presently taking engineering runs with the detectors at a distance of ~ 4.5 m from the reactor core. We discuss in this proceeding the science goals, report the detector performance from the engineering runs, show the proposed experimental setup and provide an outlook for the experiment.

107.1 Introduction

$CE\nu NS$ is a Standard Model (SM) process where a neutrino (ν) interacts with a nucleus as a whole by exchanging a Z boson and scatters off the nucleus creating a nuclear recoil [1]. $CE\nu NS$ requires incident energies of the ν a few MeV which results in a nuclear recoil energy of 1 eV to a few keV depending on the mass of the nucleus [2]. MINER experiment at the Nuclear Science Center (NSC) at Texas A&M University, USA aims to be the first experiment to measure precisely the $CE\nu NS$ cross-section utilizing the large ν flux ($\sim 10^{17}$ ν/s) from the 1 MW reactor with low-enriched (20%) ^{235}U core. MINER will use two types of low-energy threshold, phonon-mediated novel cryogenic silicon detectors; one has single electron sensitivity while the other provides discrimination of signal from a background

(for the MINER collaboration)

M. Chaudhuri (✉)

School of Physical Sciences, National Institute of Science Education and Research, Jatni 752050, India

e-mail: mouli.chaudhuri@niser.ac.in

Homi Bhabha National Institute, Training School Complex, Anushaktinagar, Mumbai 400094, India

on an event-by-event basis. The distance between the core and the detector can be varied from 1 to 10 m to observe short baseline ν oscillation and to better understand the backgrounds [3]. In addition to measuring CE ν NS, MINER will also search for sterile ν by probing for a deficit in the predicted SM rates of CE ν NS at different distances from the core [4] and axion-like-particles (ALPs) directly in the detector by inverse Primakoff process or by measuring excess gamma (γ) flux as ALPs decay to γ s [5].

107.2 Detectors

A reactor ν or a neutron (n) will interact with the nuclei of the detector resulting in a nuclear recoil (NR), whereas a γ or a beta (β) particle will interact with the electron creating electron recoil (ER). Detectors measure phonon energy, where the phonon readout channels at the surface of the detector consist of transition edge sensors which are divided into multiple channels for position reconstruction. MINER plans to use two types of phonon-mediated cryogenic semiconductor detectors made up of silicon:

HV detector: The HV detector has a mass of ~ 100 g with 7.5 cm diameter and 2 cm thickness. It has four phonon channels (A, B, C and D) covering one face of the detector as shown in Fig. 107.1a. It can measure low recoil energies exploiting the Neganov-Trofimov-Luke (NTL) effect [6, 7]. The detector is operated at voltages (up to ~ 250 V), hence named as HV detector. The total phonon energy E_t measured in the detector is given by $E_t = E_R + eVE_Q/\epsilon$, where E_R is recoil energy, e is the electronic charge, V is the applied bias, ϵ is the average energy required to create an electron-hole pair (e^-/h^+) in Si and E_Q is the total charge energy. The second term is responsible for the NTL effect which is proportional to the applied bias. The detector has a baseline resolution of $\sim 1 e^-/h^+$ pair [8].

Hybrid detector: The hybrid detector has a mass of ~ 112 g with a diameter of 2.5 cm at the top and 7.6 cm at the bottom. The detector is typically operated at a

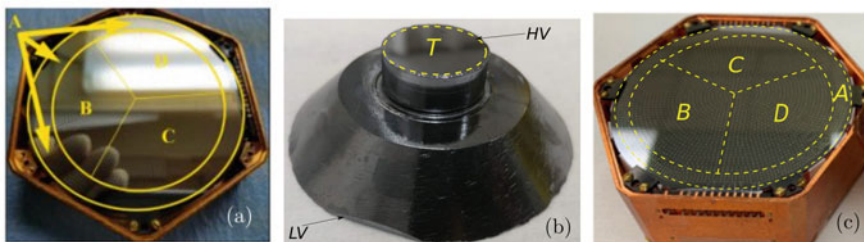


Fig. 107.1 a HV detector showing 4 phonon channels (A, B, C, D) b Hybrid detector showing 1 phonon channel (T) at top and c 4 phonon channels (A, B, C, D) at bottom

bias of ~ 12 V. Due to its geometry, the electric field intensity is higher in the top (called HV region) and lower in the bottom (called LV region). These two regions are separated by a narrow channel which allows charge transport and constrains phonon transport from LV to HV. Since the crystal volume is larger at the bottom, most of the interactions occur in the LV region where recoiling phonons are sensed while the HV region senses NTL phonons due to the movement of charges. The ratio, Y , of the measured phonon energy in HV to the LV region will act as a discriminator of ER and NR in the hybrid detector. Pictures of the hybrid detector with five channels are shown in Fig. 107.1b, c.

Since the HV and hybrid detectors complement each other for low threshold and ER/NR discrimination, they will be deployed in tandem.

107.3 Detector Performance at the NSC

The performance of HV and hybrid detectors were tested using X-ray (^{55}Fe : ~ 6 keV), γ (^{241}Am : ~ 60 keV) and n (^{252}Cf) sources. Data from the detectors was acquired using a digitizer-based DAQ. To obtain information such as pulse amplitude and time, the raw pulses were analysed using the optimal filter (OF) technique. The OF method converts the pulse information in the time domain to the frequency domain to estimate signal characteristics by performing better noise subtraction. By applying cuts on the pulse parameters like rise time, fall time, baseline std. deviation etc., good events were selected. A pulse template was made by averaging all the good pulses. Noise data was acquired with random triggers. Noise traces were averaged to obtain its power spectral density (PSD). The noise PSD, pulse template and the raw data are the input to the OF method. The amplitude of the signal is determined from the best fit of the pulse template to individual pulses. To estimate the baseline resolution (BR, i.e. noise-to-signal ratio) and demonstrate the NTL effect in the HV detector, ^{55}Fe source was used. Data was taken from 0 to 250 V in 50 V intervals. The signals from

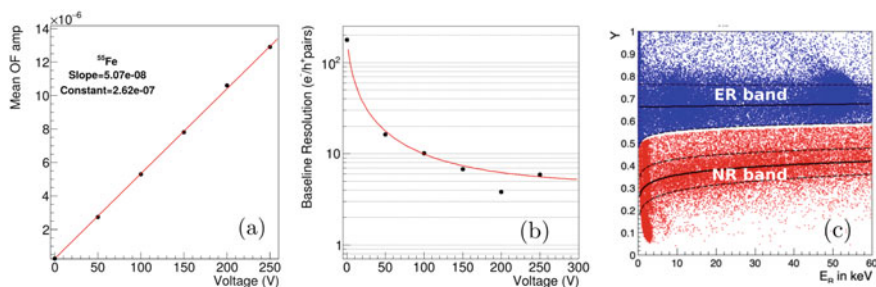
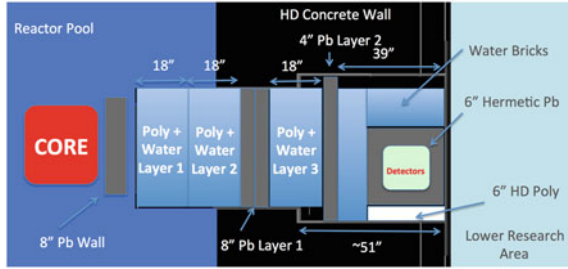


Fig. 107.2 a NTL gain demonstration of different voltages with HV detector using ^{55}Fe source, b BR as a function of voltage in HV detector, c Discriminator, Y vs E_R plot showing the two separate band for ER-NRs in hybrid detector using ^{252}Cf source

Fig. 107.3 Schematic of experimental setup with a preliminary shield design



all the channels were summed up to obtain the total phonon amplitude. The mean OF amplitude for ^{55}Fe as a function of voltage is shown in Fig. 107.2a. It increases as a function of the voltage demonstrating the NTL effect. Figure 107.2b shows the BR as a function of voltage. BR improves with voltage, and the observed lowest BR is $\sim 7 e^-/h^+$ pairs at 150 V. From Fig. 107.2c two separate bands for ERs (blue dots) and NRs (red dots) are clearly visible. To look for ER/NR discrimination γ and n from ^{252}Cf and ^{241}Am were shown simultaneously on the hybrid detector. From Fig. 107.2c two separate bands for ERs (blue dots) and NRs (red dots) are clearly visible.

107.4 Proposed Experimental Setup

For a rare event search experiment like MINER understanding and mitigation of all the possible backgrounds is crucial. Dominant backgrounds in MINER experiment are fast n and γ flux from the reactor core and cosmogenic muons. Figure 107.3 shows the schematic of the MINER experimental setup at NSC. The NSC pool-type reactor is surrounded by high-density concrete (about 3.5 g/cm^3) which acts as a shield to the high flux of n and γ byproducts in the reactor. The experimental setup will consist of several layers of lead, polyethylene and water bricks to shield high-energy γ and fast n . Additional lead and polyethylene are included after the initial shielding to reduce backgrounds from the secondary particles coming from the n capture in the shielding materials. Cosmogenic muons are rejected by an active muon veto setup [3]. Also, the movable core is useful in understanding the backgrounds and to probe short baseline ν oscillation.

107.5 Summary and Outlook

The detector performance presented here is from the recent engineering run of MINER with the detectors placed at a distance of 4.5 m from the reactor core. The hybrid detector provides discrimination between ER and NR events at lower recoil

energies. HV detector shows a BR of $\sim 7 e^-/h^+$ pairs in the reactor environment. This is higher than the reported BR of $\sim 1 e^-/h^+$ pair in a non-reactor environment with a LASER source. Reasons for this are being investigated. MINER plans to take engineering runs with different payloads using both HV and hybrid detectors. Using these two detector technologies MINER plans to detect CE ν NS and search for sterile ν and axion-like particles at NSC.

References

1. D.Z. Freedman, Phys. Rev. D **9**, 1389–1392 (1974)
2. A. Drukier, L. Stodolsky, Phys. Rev. D **30**, 2295 (1984)
3. G. Agnolet et al., MINER. Nucl. Instrum. Meth. A **853**, 53–60 (2017)
4. B. Dutta et al., Phys. Rev. D **94**(9), 093002 (2016)
5. J.B. Dent et al., Phys. Rev. Lett. **124**(21), 211804 (2020)
6. B.S. Neganov, V.N. Trofimov, Otkryt. Izobret. **146**, 215 (1985)
7. P.N. Luke, J. Appl. Phys. **64**, 6858 (1988)
8. V. Iyer et al., Nucl. Instrum. Meth. A **1010**, 165489 (2021)
9. H. Neog et al., [arXiv:2006.13139](https://arxiv.org/abs/2006.13139) [physics.ins-det]

Chapter 108

Probing the CP Phases in 3+1 Scenario at LBL Experiments



Nishat Fiza, Mehedi Masud, and M. Mitra

Abstract Anomalies in a few short-baseline experimental data have indicated towards the existence of a fourth neutrino (essentially sterile) in addition to the $3 + 0$ neutrino oscillation picture. Should sterile neutrino exist in nature and its presence is not taken into consideration properly in the analyses of neutrino data, the interference terms arising due to the additional CP phases in the presence of a sterile neutrino can severely impact the physics searches in long baseline (LBL) neutrino oscillation experiments. In this analysis we have considered one eV-scale sterile neutrino and illustrated the χ^2 correlations of the CP phases among each other and also with the three active-sterile mixing angles.

108.1 Introduction

Various global analyses have been working in the direction to resolve the problems, such as whether there exists CP violation in the neutrino sector, whether the neutrino mass eigenstates are arranged in normal ordering or inverted ordering, and whether the value of θ_{23} lies in higher octant or lower octant. There are, however, a few short-baseline (SBL) anomalies [1, 2] that hint towards the existence of oscillation governed by $\mathcal{O}(\text{eV}^2)$ mass squared difference ($\Delta_{41}^2 = m_4^2 - m_1^2 \sim \text{eV}^2$) that

N. Fiza (✉)

Department of Physical Sciences, IISER Mohali, Knowledge City, SAS Nagar, Mohali 140306, Punjab, India
e-mail: ph15039@iisermohali.ac.in

M. Masud

Center for Theoretical Physics of the Universe, Institute for Basic Science (IBS), Daejeon 34126, South Korea

M. Masud · M. Mitra

Institute of Physics, Sachivalaya Marg, Odisha 751005, Bhubaneswar, India

M. Mitra

Homi Bhabha National Institute, BARC Training School Complex, Anushaktinagar, Mumbai 400094, India

cannot be accommodated by the standard 3+0 scenario. The effort to explain the SBL anomalies (excess of electron-like events at low energy) has led to the models with the possible presence of a sterile, fourth type of neutrino (this scenario is referred to as 3+1 hereafter), which can have small mixing with the three active neutrinos. The effect of sterile neutrino, should it exist with $\Delta_{41}^2 \sim 1 \text{ eV}^2$, is more pronounced around $L/E \sim 500 \text{ km/GeV}$ [3] in case of LBL experiments.

It is noteworthy that the sterile CP phase δ_{34} and its correlation with the other phases have been little addressed in the literature. Recently [4], we have tackled this issue of estimating the capability to reconstruct all three CP phases ($\delta_{13}, \delta_{24}, \delta_{34}$), taking into consideration their χ^2 correlations with each other and also with the active-sterile mixing angles ($\theta_{14}, \theta_{24}, \theta_{34}$). We carry out this exercise in the context of DUNE and illustrate the improvement when combined with T2K, NO ν A (both these currently running experiments are simulated up to their present exposure) and T2HK.

108.2 Results

Using the widely used General Long Baseline Experiment Simulator (GLOBES) [5, 6] and the relevant plugin *snu.c* for implementing sterile neutrinos, we now illustrate how the probabilities for different oscillation channels depend on the three CP phases (δ_{13}, δ_{24} , and δ_{34}) individually at the DUNE baseline of 1300 km. In Fig. 108.1, we plot the bands for $P_{\mu e}, P_{\mu\mu}$, and $P_{\mu\tau}$, in the three panels, respectively. The insets in the second and third panels show magnified versions of the rectangular regions indicated. As expected, the CP phases have a larger impact on appearance channels rather than the disappearance channels. We also observe that with increase in energy the effect of δ_{34} on $P(\nu_\mu \rightarrow \nu_e)$ further reduces.

In Fig. 108.2, we illustrate how efficiently the combination of LBL experiments can reconstruct the three CP phases δ_{13}, δ_{24} , and δ_{34} at 1σ C.L. in the three columns, respectively, given their true value lying anywhere in the whole parameter space of

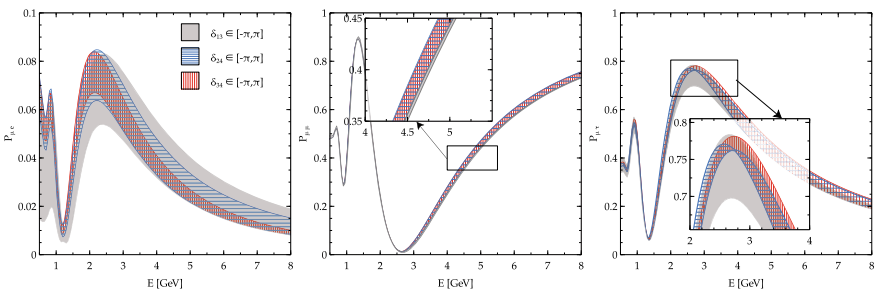


Fig. 108.1 We show the probability bands due to individual variation of the CP phases in the whole range of $[-\pi, \pi]$ at a baseline of 1300 km. The three active-sterile mixing angles were taken as $\theta_{14} = 10^\circ, \theta_{24} = 6^\circ$, and $\theta_{34} = 25^\circ$. The normal hierarchy was assumed for generating this plot

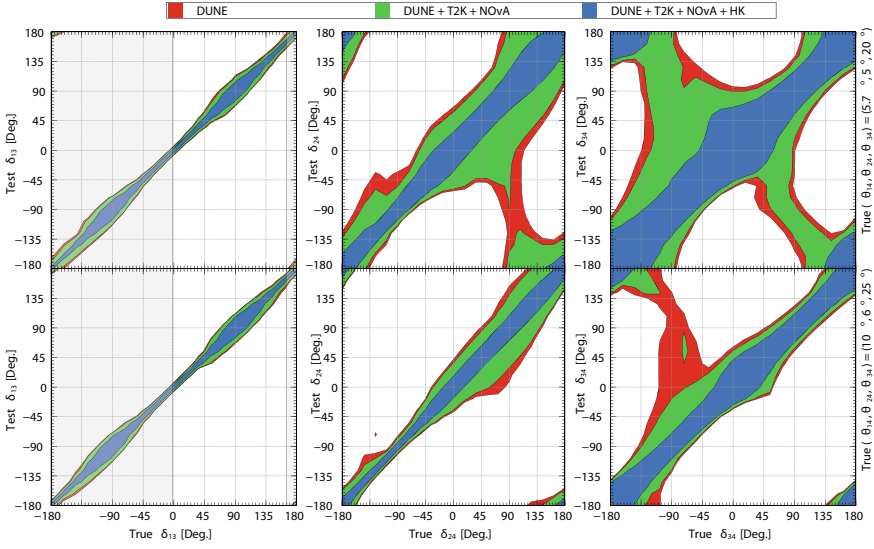


Fig. 108.2 Reconstruction of the CP phases δ_{13} , δ_{24} , and δ_{34} , for all the choices of their true values in $[-\pi, \pi]$. The top (bottom) row corresponds to the choice of the active-sterile mixing angles as true $\theta_{13}, \theta_{24}, \theta_{34} = 5.7^\circ, 5^\circ, 20^\circ$ ($10^\circ, 6^\circ$, and 25°). In the first column the grey-shaded regions depict the 3σ allowed values measured by T2K [7]

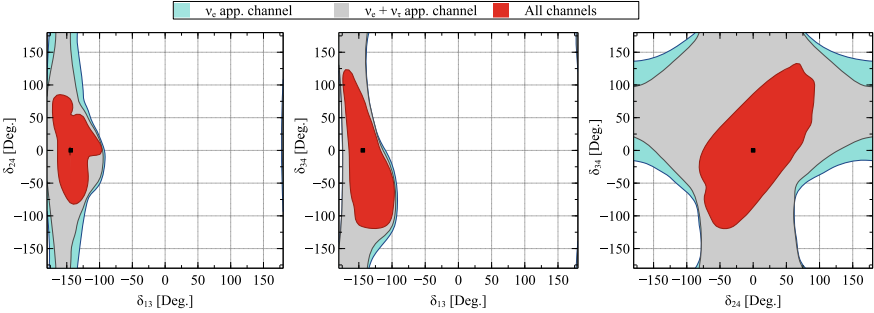


Fig. 108.3 Reconstruction of the CP phases, taken pairwise at a time for three different channels at DUNE at a C.L. of 1σ (2 D.O.F.)

$[-\pi, \pi]$. In addition to the poorly measured 3+0 parameters ($\theta_{23}, \Delta m_{31}^2$) and the active-sterile mixing angles ($\theta_{14}, \theta_{24}, \theta_{34}$), in each panel we have also marginalised over the two other CP phases ($\in [-\pi, \pi]$) not shown along the axes. The top (bottom) row depicts small (large) active-sterile mixing with true $\theta_{14}, \theta_{24}, \theta_{34} = 5.7^\circ, 5^\circ, 20^\circ$ ($\theta_{14}, \theta_{24}, \theta_{34} = 10^\circ, 6^\circ, 25^\circ$). For each true value of the CP phases ($\in [-\pi, \pi]$), the corresponding vertical width of the contours provides an estimate of the precision of reconstructing that true value.

Figure 108.3 illustrates the impact of different appearance and disappearance channels on the reconstruction of the CP phases. We can clearly see the decrease

in uncertainty in the measurement of the CP phases as we keep on adding $\nu_\mu \rightarrow \nu_\tau$ appearance and $\nu_\mu \rightarrow \bar{\nu}_\mu$ disappearance channel to the $\nu_\mu \rightarrow \nu_e$ appearance channel.

108.3 Conclusion

In this paper we have considered the presence of an eV-scale sterile neutrino (the so-called 3 + 1 scenario which might turn out to be a possible resolution of the short baseline neutrino oscillation anomalies) and have analyzed how the present and future long baseline experiments T2K, NOvA, DUNE, and T2HK can potentially probe the additional CP phases. Though $\nu_\mu \rightarrow \nu_e$ oscillation channel contributes the most in probing these parameter spaces, $\nu_\mu \rightarrow \nu_\mu$ and to a lesser extent $\nu_\mu \rightarrow \nu_\tau$ channel also help in exploring the $\delta_{24} - \delta_{34}$ parameter space in particular. We find that δ_{24} and δ_{34} cannot be reconstructed very efficiently by DUNE and also even after adding data from NOvA and T2K. But adding T2HK data removes much of the degeneracies and the uncertainties in reconstruction become much less.

References

1. A. Aguilar-Arevalo et al., [LSND], evidence for neutrino oscillations from the observation of $\bar{\nu}_e$ appearance in a $\bar{\nu}_\mu$ beam. *Phys. Rev. D* **64**, 112007 (2001)
2. A.A. Aguilar-Arevalo et al., [MiniBooNE], unexplained excess of electron-like events from a 1-GeV Neutrino beam. *Phys. Rev. Lett.* **102**, 101802 (2009)
3. R. Gandhi, B. Kayser, M. Masud, S. Prakash, The impact of sterile neutrinos on CP measurements at long baselines. *JHEP* **11**, 039 (2015)
4. N. Fiza, M. Masud, M. Mitra, Exploring the new physics phases in 3+1 scenario in neutrino oscillation experiments, [arXiv:2102.05063](https://arxiv.org/abs/2102.05063) [hep-ph]
5. P. Huber, M. Lindner, W. Winter, Simulation of long-baseline neutrino oscillation experiments with GLOBES (General Long Baseline Experiment Simulator). *Comput. Phys. Commun.* **167**, 195 (2005)
6. P. Huber, J. Kopp, M. Lindner, M. Rolinec, W. Winter, General long baseline experiment simulator, new features in the simulation of neutrino oscillation experiments with GLOBES 3.0. *Comput. Phys. Commun.* **177**, 432–438 (2007)
7. K. Abe et al. [T2K], constraint on the matter–antimatter symmetry-violating phase in neutrino oscillations. *Nature* **580**(7803), 339–344 (2020) [erratum: *Nature* **583**(7814), E16 (2020)]

Chapter 109

Leptogenesis in a Multi-Higgs Doublet Model



Pritam Das, Mrinal Kumar Das, and Najimuddin Khan

Abstract We study a model of neutrino and dark matter within the framework of a minimal extended seesaw. This framework is based on A_4 flavor symmetry along with the discrete Z_4 symmetry to stabilize the dark matter and construct desired mass matrices for neutrino mass. We use a non-trivial Dirac mass matrix with broken $\mu - \tau$ symmetry to generate the leptonic mixing. A non-degenerate mass structure for right-handed neutrinos is considered to verify the observed baryon asymmetry of the universe via the mechanism of thermal leptogenesis.

109.1 Introduction

At the very beginning of the universe, there were equal numbers of matter and corresponding anti-matter. However, in the current scenario, there is an asymmetry in the observed baryon number, and this scenario can be explained by the well-known process, known as baryogenesis or baryon asymmetry of the universe. Numerical definition for baryon asymmetry at current date reads as [1], $Y_{\Delta B} (\equiv \frac{n_B - n_{\bar{B}}}{s}) = (8.75 \pm 0.23) \times 10^{-11}$.

In this work, we have chosen the minimal extended seesaw (MES) framework, where the canonical type-I seesaw is extended with a singlet fermion generation, which can accommodate three active neutrinos and a single generation of sterile neutrino. Here, along with the active and sterile neutrino mass generation, the validity of baryogenesis is checked in the presence of a heavy flavor of sterile neutrino. Within the scalar sector, we have considered two additional Higgs doublets along with the SM Higgs doublet, where one additional Higgs doublet acquires VEV. At the same time, another one remains VEVless due to an additional Z_4 symmetry. The lightest neutral

P. Das (✉) · M. Kumar Das
Department of Physics, Tezpur University, Napaam 784028, Assam, India
e-mail: pritam@tezu.ernet.in

N. Khan
School of Physical Sciences, Indian Association for the Cultivation of Science 2A & 2B, Raja
S.C. Mullick Road, Kolkata 700032, India

Z_4 -odd Higgs doublet does not decay. Hence, it behaves as a potential candidate for dark matter. A dark matter study has been carried out in [2].

109.2 Model Framework

Minimal extended seesaw (MES) is realized in this work to construct active and sterile masses. Under MES framework, the active and sterile masses are realized as follows (Table 109.1):

$$m_\nu \simeq M_D M_R^{-1} M_S^T (M_S M_R^{-1} M_S^T)^{-1} M_S (M_R^{-1})^T M_D^T - M_D M_R^{-1} M_D^T, \tag{109.1}$$

$$m_s \simeq -M_S M_R^{-1} M_S^T. \tag{109.2}$$

It is to be noted that the first term of the (109.1) arises due to the contribution from the sterile mass M_S , which is a vector rather than a square matrix. If M_S were a square matrix, both the terms in (109.1) would cancel each other, and the active neutrino mass would simply be zero. The mass scale of M_S is slightly higher than the M_D scale, which is near to the EW scale, while M_R is around 10^{13} GeV. A new physics scale (Λ) is imposed to achieve this MES structure. A_4 flavon symmetry has been broken in the model by the heavy scale, in order to generate the required neutrino mass, thus making the scale very heavy ($\sim 10^{14}$ GeV).

The leading order invariant Yukawa Lagrangian for the lepton sector is given by

$$\begin{aligned} \mathcal{L} = & \frac{y_2}{\Lambda} (\bar{l} \tilde{\phi}_1 \zeta)_1 \nu_{R1} + \frac{y_2}{\Lambda} (\bar{l} \tilde{\phi}_1 \varphi)_{1'} \nu_{R2} + \frac{y_3}{\Lambda} (\bar{l} \tilde{\phi}_2 \varphi)_1 \nu_{R3} \\ & + \frac{1}{2} \lambda_1 \xi \overline{\nu_{R1}^c} \nu_{R1} + \frac{1}{2} \lambda_2 \xi' \overline{\nu_{R2}^c} \nu_{R2} + \frac{1}{2} \lambda_3 \xi \overline{\nu_{R3}^c} \nu_{R3} + \frac{1}{2} \rho \chi \overline{S^c} \nu_{R1}. \end{aligned} \tag{109.3}$$

$y_{\alpha,i}, \lambda_i$ (for $\alpha = e, \mu, \tau$ and $i = 1, 2, 3$) and ρ representing the Yukawa couplings for respective interactions and all Higgs doublets are transformed as $\tilde{\phi}_i = i \tau_2 \phi_i^*$ (with τ_2 being the second Pauli's spin matrix) to keep the Lagrangian gauge invariant.

Table 109.1 Particle content and their charge assignments under SU(2), A_4 and Z_4 groups. The second block of the particle content ($l, e_R, \mu_R, \tau_R, \phi_1$) represents the left-handed lepton doublet, RH charged fermions and SM Higgs doublets, respectively. ϕ_2 and ϕ_3 (inert) are the additional Higgs doublet. ν_{Ri} ($i = 1, 2, 3$) and S are RH neutrinos and chiral singlet. Rest of the particles ($\zeta, \varphi, \xi, \xi', \chi$) are the additional flavons

Particles	l	e_R	μ_R	τ_R	ϕ_1	ϕ_2	ϕ_3	ζ	φ	ξ	ξ'	ν_{R1}	ν_{R2}	ν_{R3}	S	χ
SU(2)	2	1	1	1	2	2	2	1	1	1	1	1	1	1	1	1
A_4	3	1	$1''$	$1'$	1	1	1	3	3	1	$1'$	1	$1'$	1	$1''$	$1'$
Z_4	1	1	1	1	1	i	-1	1	i	1	-1	1	- i	-1	i	- i

The scalar flavons involved in the Lagrangian acquire VEV along $\langle \zeta \rangle = (v_m, 0, 0)$, $\langle \varphi \rangle = (v_m, v_m, v_m)$, $\langle \xi \rangle = \langle \xi' \rangle = v_m$ and $\langle \chi \rangle = v_\chi$ by breaking the flavor symmetry, while $\langle \phi_i \rangle (i = 1, 2)$ get VEV (v_i) by breaking EWSB at electro-weak scale ($v_3 = 0$ due to additional Z_4 symmetry). We achieve the light neutrino mass matrix as well as the sterile mass using Eqs. (109.1) and (109.2), respectively. Complete matrix structures are shown in Table 109.2.

109.2.1 Neutrino Mass and Mixing Angles

The diagonalize neutrino mass matrix M_ν is achieved as

$$\text{Diag}(m_1, m_2, m_3) = U_{PMNS} M_\nu U_{PMNS}^T, \quad (109.4)$$

where m_i (for $i = 1, 2, 3$) stands for three active neutrino masses. Conventionally, the leptonic mixing matrix for active neutrino is parameterized as

$$U_{PMNS} = \begin{pmatrix} c_{12}c_{13} & s_{12}c_{13} & s_{13}e^{-i\delta} \\ -s_{12}c_{23} - c_{12}s_{23}s_{13}e^{i\delta} & c_{12}c_{23} - s_{12}s_{23}s_{13}e^{i\delta} & s_{23}c_{13} \\ s_{12}s_{23} - c_{12}c_{23}s_{13}e^{i\delta} & -c_{12}s_{23} - s_{12}c_{23}s_{13}e^{i\delta} & c_{23}c_{13} \end{pmatrix} \cdot P. \quad (109.5)$$

The abbreviations used are $c_{ij} = \cos \theta_{ij}$, $s_{ij} = \sin \theta_{ij}$ where θ_{ij} stands for active mixing angles with $i, j = 1, 2, 3$ and P would be a unit matrix $\mathbf{1}$ in the Dirac case but in Majorana case $P = \text{diag}(1, e^{i\alpha}, e^{i(\beta+\delta)})$. The Dirac and Majorana CP-violating phases are simply represented by δ and (α, β) in the U_{PMNS} , respectively. Since we have included one extra generation of neutrino along with the active neutrinos in our model, thus the final neutrino mixing matrix for the active-sterile mixing takes 4×4 form as

$$V \simeq \begin{pmatrix} (1 - \frac{1}{2}RR^\dagger)U_{PMNS} & R \\ -R^\dagger U_{PMNS} & 1 - \frac{1}{2}R^\dagger R \end{pmatrix}. \quad (109.6)$$

Here, $R = M_D M_R^{-1} M_S^T (M_S M_R^{-1} M_S^T)^{-1}$ is a 3×1 matrix governed by the strength of the active-sterile mixing, *i.e.*, the ratio $\frac{\mathcal{O}(M_D)}{\mathcal{O}(M_S)}$. Using MES, the mass matrices obtained for active neutrinos and active-sterile mixing elements are shown in Table 109.2. Respective interaction terms from the Lagrangian 109.3 are parametrized as b, c, d, e, f, g to minimize the complexity.

109.2.2 Baryogenesis via Thermal Leptogenesis

We consider a hierarchical mass pattern for RH neutrinos, among which the lightest will decay to a Higgs doublet and a lepton doublet. This decay would produce sufficient lepton asymmetry to give rise to the observed baryon asymmetry of the

Table 109.2 The light neutrino mass matrices (m_ν), sterile mass (m_S) and active-sterile mixing patterns (R) with corresponding M_D , M_R and M_S matrices for NH and IH mass pattern

Ordering	Structures	$-m_\nu$	m_S	R
NH	$M_R = \begin{pmatrix} d & 0 & 0 \\ 0 & e & 0 \\ 0 & 0 & f \end{pmatrix}$ $M_D = \begin{pmatrix} b & b & c+p \\ 0 & b+p & c \\ p & b & c \end{pmatrix}$ $M_S = (g \ 0 \ 0)$	$\begin{pmatrix} \frac{b^2}{e} + \frac{(c+p)^2}{f} & \frac{b(b+p)}{e} + \frac{c(c+p)}{f} & \frac{b^2}{e} + \frac{c(c+p)}{f} \\ \frac{b(b+p)}{e} + \frac{c(c+p)}{f} & \frac{(b+p)^2}{e} + \frac{c^2}{f} & \frac{b(b+p)}{e} + \frac{c^2}{f} \\ \frac{b^2}{e} + \frac{c(c+p)}{f} & \frac{b(b+p)}{e} + \frac{c^2}{f} & \frac{b^2}{e} + \frac{c^2}{f} \end{pmatrix}$	$\simeq \frac{g^2}{10^4}$	$\simeq \begin{pmatrix} \frac{b}{g} \\ 0 \\ \frac{p}{g} \end{pmatrix}$
IH	$M_R = \begin{pmatrix} d & 0 & 0 \\ 0 & e & 0 \\ 0 & 0 & f \end{pmatrix}$ $M_D = \begin{pmatrix} b & -b & c+p \\ 0 & -b+p & c \\ p & 2b & c \end{pmatrix}$ $M_S = (g \ 0 \ 0)$	$\begin{pmatrix} \frac{b^2}{e} + \frac{(c+p)^2}{f} & \frac{b(b-p)}{e} + \frac{c(c+p)}{f} & \frac{-2b^2}{e} + \frac{c(c+p)}{f} \\ \frac{b(b-p)}{e} + \frac{c(c+p)}{f} & \frac{(b-p)^2}{e} + \frac{c^2}{f} & \frac{-2b(b-p)}{e} + \frac{c^2}{f} \\ -\frac{2b^2}{e} + \frac{c(c+p)}{f} & \frac{-2b(b-p)}{e} + \frac{c^2}{f} & \frac{4b^2}{e} + \frac{c^2}{f} \end{pmatrix}$	$\simeq \frac{g^2}{10^4}$	$\simeq \begin{pmatrix} \frac{b}{g} \\ 0 \\ \frac{p}{g} \end{pmatrix}$

Universe. We have used the parametrization from [1], where the working formula of baryon asymmetry produced is given by

$$Y_B = ck \frac{\epsilon_{11}}{g_*}. \tag{109.7}$$

The quantities involved in this 109.7 can be found in [1, 2].

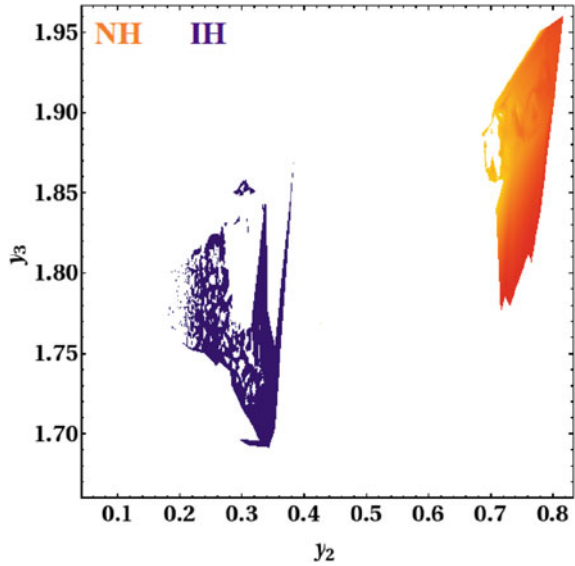
Now, baryon asymmetry of the universe can be calculated from (109.7) followed by the evaluation of lepton asymmetry. The Yukawa matrix is constructed from the solved model parameters b, c and p , which is analogous to the 3×3 Dirac mass matrix.

109.2.3 Neutrino and Baryogenesis

The involvement of the Higgs mass can be visualized through the Yukawa coupling of the Lagrangian, therefore we have incorporated our analysis concerning the Yukawa couplings. To achieve the observed bound on the baryon asymmetry of the universe, the Yukawa coupling matrix must possess non-zero and complex entries.

The Yukawa coupling y_2 corresponds to the SM Higgs ϕ_1 and y_3 corresponds to the second Higgs doublet ϕ_2 (see 109.3). Major constrains on experimental parameters like θ_{13}, m_3 and m_2 are coming from y_2 and y_3 can be visualized from the Fig. 109.1. One can notice here the distinct and separate contour regions arising from normal and inverted mass patterns. This can be explained as follows: Within the MES framework, the lightest neutrino mass is always zero [3], and for NH m_1 is zero and for IH m_3 is

Fig. 109.1 Projection of current BAU value (in 3σ range: $Y_B = 8.75 \pm 0.25 \times 10^{-11}$) in a plane of Yukawa coupling with y_2 along the x -axis and y_3 along the y -axis. Orange region stands for NH while purple region stands for IH mass ordering



zero. Since those mass eigenstates influence the Yukawa couplings, we get separate regions for both the mass patterns. As BAU value is highly sensitive to the experimental results, very narrow regions are observed with y_2 and y_3 , the orange region represents NH, while the purple region represents IH for $y_2 - y_3$ plane, projecting the latest 3σ bound for BAU. We found that y_2 gets constrained between 0.68 and 0.81 in NH while for IH large numbers of points are accumulated between 0.18 and 0.36. Similarly for y_3 , the NH mode is spread around 1.78–1.96 and for IH, its value lies within 1.68–1.86 satisfying the current BAU bound. At the current dimension-5 scenario, the Yukawa coupling within the range of $\mathcal{O}(10^{-2} - 1)$ is acceptable; however, within our study, the large and small values of y_3 violate the experimental range of Δm_{31}^2 . For example, for large $y_3 (\geq 2.0)$, the Δm_{31}^2 value exceeds the current upper bound of 3σ value, whereas for small $y_3 (\leq 1.6)$, the Δm_{31}^2 value goes beneath the lower 3σ bound. These results confirm the successful execution of BAU within the MES framework for both the mass orderings. Large excluded regions in Fig. 109.1 are due to the bounds on light neutrino parameters imposed by the Yukawa matrix involved in the baryogenesis calculation.

109.3 Conclusion

In this minimal extended version of the type-I seesaw, the involvement of the high-scaled VEVs of A_4 singlet flavons ξ and ξ' ensure the $B - L$ breaking within our framework, which motivates us to study baryon asymmetry of the universe within this framework. As the RH masses are considered in a non-degenerate fashion, we

have been successfully able to produce desired lepton asymmetry (with anomalous violation of $B + L$ due to chiral anomaly), which eventually converted to baryon asymmetry by the *sphaleron* process.

In the fermion sector, the involvement of the Higgs doublets is related to the model parameters via the Yukawa couplings. Relations between the constrained Dirac CP-phase and satisfied baryogenesis resulting from two different Yukawa couplings are shown, which are related via two Higgs' VEV.

Acknowledgements The research work of P.D. and M.K.D. is supported by the Department of Science and Technology, Government of India under the project grant EMR/2017/001436.

References

1. S. Davidson, E. Nardi, Y. Nir, Phys. Rept. **466**, 105–177 (2008)
2. P. Das, M.K. Das, N. Khan, JHEP **03**, 018 (2020)
3. P. Das, A. Mukherjee, M.K. Das, Nucl. Phys. B **941**, 755–779 (2019)

Chapter 110

Implications of Recent Flavour Anomalies on New Physics



Rukmani Mohanta

Abstract In recent times, several hints of lepton flavour universality violation have been observed in semileptonic B decays at the level of 2 – 4 standard deviations both in the rare flavour changing neutral current transitions $b \rightarrow s\ell^+\ell^-$ and charged current transitions $b \rightarrow c\ell^-\bar{\nu}_\ell$. These tantalizing signals point towards the possible existence of new physics beyond the standard model. We will discuss these anomalies in detail and show that the new physics contributions arising from the exchange of a vector leptoquark $U_1(3, 1, 2/3)$ would provide simultaneous explanation for these anomalies.

110.1 Introduction

There is no dispute that the standard model (SM) of particle physics is not the ultimate theory of nature, rather a low-energy manifestation of a more fundamental theory. Thus, deciphering the nature of physics beyond the SM is the prime objective of present-day particle physics research. In the absence of the direct observation of any new particles in the colliders, especially at the LHC [1], much attention has been paid to the indirect signals, where considerable discrepancies have been observed between the measurements and their corresponding SM predictions. In this regard, the rare decays of B mesons play a vital role. Recently, several anomalies in the form of lepton flavour universality violations (LFUV) have been observed in the semileptonic B decays mediated through charged-current (CC) $b \rightarrow c\ell^-\bar{\nu}_\ell$ and neutral-current (NC) $b \rightarrow s\ell^+\ell^-$ transitions by various flavour factory experiments BaBar, Belle and LHCb, which may be considered as the smoking-gun signals of new physics (NP).

R. Mohanta (✉)

School of Physics, University of Hyderabad, Hyderabad 500046, India
e-mail: rmsp@uohyd.ac.in

© The Author(s), under exclusive license to Springer Nature Singapore Pte Ltd. 2022
B. Mohanty et al. (eds.), *Proceedings of the XXIV DAE-BRNS High Energy Physics Symposium, Jatni, India*, Springer Proceedings in Physics 277,
https://doi.org/10.1007/978-981-19-2354-8_110

605

110.2 Anomalies in $b \rightarrow s\ell^+\ell^-$ Transitions

The rare decay processes mediated through flavour changing neutral current transitions $b \rightarrow s\ell^+\ell^-$ are loop suppressed in the SM, and hence are highly sensitive to NP. In this sector, there are a plethora of observables which exhibit deviations from their SM predictions at the level of 2 – 4 standard deviations. Amongst them, the main candidates are the LFUV observables R_K and R_{K^*} , defined as

$$R_K = \frac{\mathcal{B}(B^+ \rightarrow K^+\mu^+\mu^-)}{\mathcal{B}(B^+ \rightarrow K^+e^+e^-)}, \quad R_{K^*} = \frac{\mathcal{B}(\bar{B} \rightarrow \bar{K}^*\mu^+\mu^-)}{\mathcal{B}(\bar{B} \rightarrow \bar{K}^*e^+e^-)}. \quad (110.1)$$

In 2014, the measurement of the LFUV ratio $R_K = 0.745_{-0.074}^{+0.090} \pm 0.036$, in the low $q^2 \in [1, 6]$ GeV² region, where q^2 is the dilepton invariant mass squared, by the LHCb experiment [2] attracted huge attention, as it manifested a discrepancy of 2.6σ from its SM prediction, which is expected to be unity, with an uncertainty $\mathcal{O}(10^{-3})$ [3]. The updated LHCb measurement of R_K in the $q^2 \in [1.1, 6]$ GeV² bin by combining the Run 1 data with 2 fb⁻¹ of Run 2 data: $R_K^{\text{LHCb}} = 0.846_{-0.054-0.014}^{+0.060+0.016}$ [4], also exhibits a discrepancy at the level of 2.5σ . The LHCb collaboration has also measured the R_{K^*} ratio in the following two low- q^2 bins [5]:

$$R_{K^*}^{\text{LHCb}} = \begin{cases} 0.660_{-0.070}^{+0.110} \pm 0.024 & q^2 \in [0.045, 1.1] \text{ GeV}^2, \\ 0.685_{-0.069}^{+0.113} \pm 0.047 & q^2 \in [1.1, 6.0] \text{ GeV}^2, \end{cases} \quad (110.2)$$

which also depict 2.2σ and 2.4σ deviations from their SM expectations [6]. These discrepancies are generally attributed to the presence of NP in $b \rightarrow s\mu\mu$ processes [7]. In addition to these LHCb results, the Belle experiment has recently announced a new set of measurements on R_K and R_{K^*} [8, 9] in several other bins, which have large uncertainties, and are consistent with both SM and LHCb results.

On a related note, a combined analysis of the branching fraction of $B_s^0 \rightarrow \mu^+\mu^-$ by ATLAS, CMS and LHCb collaborations $\mathcal{B}(B_s^0 \rightarrow \mu^+\mu^-) = (2.69_{-0.35}^{+0.37}) \times 10^{-9}$ [10] shows 2.4σ deviation from its SM value $\mathcal{B}(B_s^0 \rightarrow \mu^+\mu^-)|^{\text{SM}} = (3.66 \pm 0.14) \times 10^{-9}$ [11].

The effective Hamiltonian responsible for $b \rightarrow s\ell^+\ell^-$ transition can be expressed as

$$\mathcal{H}_{\text{eff}}^{\text{SM}} = -\frac{\alpha G_F}{\sqrt{2}\pi} V_{tb} V_{ts}^* \left[2 \frac{C_7^{\text{eff}}}{q^2} [\bar{s}\sigma^{\mu\nu} q_\nu (m_s P_L + m_b P_R) b] (\bar{\ell}\gamma_\mu \ell) \right. \\ \left. + C_9^{\text{eff}} (\bar{s}\gamma^\mu P_L b) (\bar{\ell}\gamma_\mu \ell) + C_{10} (\bar{s}\gamma^\mu P_L b) (\bar{\ell}\gamma_\mu \gamma_5 \ell) \right], \quad (110.3)$$

where G_F is the Fermi constant, V_{ij} are the CKM matrix elements, C_7^{eff} , C_9^{eff} and C_{10} are the Wilson coefficients, evaluated at the m_b scale. It should be noted that the coefficient C_9^{eff} contains both short-distance contributions from the four-quark operators, away from the charmonium resonance domain, and the long-distance part associated with real $c\bar{c}$ intermediate states.

Considering NP contributions to be present in $b \rightarrow s\mu^+\mu^-$ processes, a global fit to all the anomalies provide the best-fit values for the preferred solutions as: (i) $C_{9\mu}^{\text{NP}} = -1.03$, (ii) $C_{9\mu}^{\text{NP}} = -C_{10\mu}^{\text{NP}} = -0.50$ and (iii) $C_{9\mu}^{\text{NP}} = -C_{9\mu}^{\text{NP}} = -1.02$ [12].

110.3 Anomalies in $b \rightarrow c\ell\nu$ Transitions

In the CC transitions $b \rightarrow c\ell\bar{\nu}_\ell$, sizeable deviations have been observed by three different experiments, BaBar, Belle and LHCb, in the LFUV observables, which are characterized as the ratios of branching fractions

$$R_{D^{(*)}} \equiv \frac{\mathcal{B}(B \rightarrow D^{(*)}\tau\bar{\nu})}{\mathcal{B}(B \rightarrow D^{(*)}\ell\bar{\nu})}, \quad R_{J/\psi} \equiv \frac{\mathcal{B}(B_c \rightarrow J/\psi\tau\bar{\nu})}{\mathcal{B}(B_c \rightarrow J/\psi\mu\bar{\nu})}, \quad (110.4)$$

with $\ell = e$ or μ . These observables are considered to be the clean probes of NP as the hadronic uncertainties inherent in individual branching fraction predictions cancel out to a large extent. The present-world averages of $R_{D^{(*)}}$ measurements performed by the Heavy Flavor Averaging Group (HFLAV) [13]

$$R_D^{\text{exp}} = 0.340 \pm 0.027 \pm 0.013, \quad R_{D^*}^{\text{exp}} = 0.295 \pm 0.011 \pm 0.008, \quad (110.5)$$

have 3.1σ deviations (considering their correlation of -0.38) from the corresponding SM predictions $R_D^{\text{SM}} = 0.299 \pm 0.003$ (1.4σ) and $R_{D^*}^{\text{SM}} = 0.258 \pm 0.005$ (2.5σ) [14]. In the same line, the measured ratio $R_{J/\psi} = 0.71 \pm 0.17 \pm 0.18$ [15] also has 1.7σ deviation from its SM prediction, $R_{J/\psi}^{\text{SM}} = 0.289 \pm 0.010$. Furthermore, a recent measurement of the longitudinal polarization of D^* meson in $B^0 \rightarrow D^{*-}\tau^+\bar{\nu}$ by the Belle Collaboration, $F_L^{D^*} = 0.60 \pm 0.08 \pm 0.04$ [16], also shows deviation from its SM value 0.46 ± 0.04 , by 1.6σ . These deviations primarily hint towards the presence of NP in $b \rightarrow c\tau\bar{\nu}$ decay channels.

The effective Hamiltonian responsible for the CC $b \rightarrow c\tau\bar{\nu}_l$ quark-level transitions is given by

$$\mathcal{H}_{\text{eff}}^{\text{CC}} = \frac{4G_F}{\sqrt{2}} V_{cb} \left[(\delta_{l\tau} + C_{V_L}^l) \mathcal{O}_{V_L}^l + C_{V_R}^l \mathcal{O}_{V_R}^l + C_{S_L}^l \mathcal{O}_{S_L}^l + C_{S_R}^l \mathcal{O}_{S_R}^l + C_T^l \mathcal{O}_T^l \right], \quad (110.6)$$

where C_X^l are the Wilson coefficients, with $X = V_{L,R}, S_{L,R}$ and T , which are zero in the SM and can arise only in the presence of NP. The corresponding dimension-six effective operators are given as

$$\begin{aligned} \mathcal{O}_{V_L}^l &= (\bar{c}_L \gamma^\mu b_L) (\bar{\tau}_L \gamma_\mu \nu_{lL}), & \mathcal{O}_{V_R}^l &= (\bar{c}_R \gamma^\mu b_R) (\bar{\tau}_R \gamma_\mu \nu_{lL}), \\ \mathcal{O}_{S_L}^l &= (\bar{c}_R b_L) (\bar{\tau}_R \nu_{lL}), & \mathcal{O}_{S_R}^l &= (\bar{c}_L b_R) (\bar{\tau}_R \nu_{lL}), \\ \mathcal{O}_T^l &= (\bar{c}_R \sigma^{\mu\nu} b_L) (\bar{\tau}_R \sigma_{\mu\nu} \nu_{lL}), \end{aligned} \quad (110.7)$$

where $f_{L(R)} = P_{L(R)}f$ are the chiral fermion (f) fields with $P_{L(R)} = (1 \mp \gamma_5)/2$ being the projection operators.

Model independent analysis shows that NP contributions having the same Lorentz structure as the SM operator (O_{V_L}) are the most preferred scenario [17]. Though the scalar and pseudoscalar NP structures can also accommodate the observed anomalies, they are constrained by B_c lifetime [17].

110.4 Possible NP Scenarios for Explaining Flavour Anomalies

The observed hints of LFUV have triggered a large number of detailed phenomenological studies aiming to find out the nature of possible NP explanation. As the $b \rightarrow c\ell\bar{\nu}$ CC transitions occur at tree-level, while the NC transitions $b \rightarrow s\ell^+\ell^-$ appear at one-loop level, the anomalies associated with these transitions probe essentially different scales of NP. Thus, the explanation of these intriguing sets of anomalies in a coherent manner using a single framework is rather challenging, e.g., the tree-level contribution with single mediator like W' for $b \rightarrow c\ell\bar{\nu}$ and Z' for $b \rightarrow s\ell\ell$ transitions will not provide the common solution. However, some of the leptoquark (LQ) models with generation-dependent couplings could provide a common explanation for the observed anomalies in both the sectors.

110.4.1 $U_1(3, 1, 2/3)$ Vector LQ: A Possible Explanation to Flavour Anomalies

The vector LQ $U_1(3, 1, 2/3)$ is a colour triplet and $SU(2)_L$ singlet gauge boson with hypercharge $2/3$ encountered in many extensions of the SM. This LQ can explain the anomalies in both $b \rightarrow c\tau\bar{\nu}$ and $b \rightarrow s\mu^+\mu^-$ transitions [18]. The interaction Lagrangian of U_1 LQ with the SM fermions can be written as

$$\mathcal{L}_{LQ}^{U_1} = \lambda_{ij}^L \bar{Q}_{iL} \gamma_\mu L_{jL} U_1^\mu + \lambda_{ij}^R \bar{d}_{iR} \gamma_\mu l_{jR} U_1^\mu + h.c., \quad (110.8)$$

where $\lambda_{ij}^{L,R}$ are the couplings of U_1 to quark and lepton pairs, with i, j being the generation indices. The Lagrangian (110.8) is written in the weak basis of the fermion fields, which after transformation into the mass basis and using the Fierz identities, yields the new Wilson coefficients for the process $b \rightarrow c\tau\bar{\nu}$

$$C_{V_L}^{\text{NP}} = \frac{1}{2\sqrt{2}G_F V_{cb}} \sum_{k=1}^3 V_{k3} \frac{\lambda_{2l}^L \lambda_{k3}^{L*}}{M_{LQ}^2}, \quad C_{S_R}^{\text{NP}} = -\frac{1}{2\sqrt{2}G_F V_{cb}} \sum_{k=1}^3 V_{k3} \frac{2\lambda_{2l}^L \lambda_{k3}^{R*}}{M_{LQ}^2}, \quad (110.9)$$

where M_{LQ} denotes the LQ mass. The model also provides additional contributions to the $b \rightarrow s \ell_i^+ \ell_j^-$ processes in the form of new Wilson coefficients $C_i^{(\prime)NP}$ ($i = 9, 10, S, P$), as

$$\begin{aligned}
 C_9^{NP} &= -C_{10}^{NP} = \frac{\pi}{\sqrt{2}G_F V_{tb} V_{ts}^* \alpha} \sum_{m,n=1}^3 V_{m3} V_{n2}^* \frac{\lambda_{ni}^L \lambda_{mj}^{L*}}{M_{LQ}^2}, \\
 C_9^{NP} &= C_{10}^{NP} = \frac{\pi}{\sqrt{2}G_F V_{tb} V_{ts}^* \alpha} \sum_{m,n=1}^3 V_{m3} V_{n2}^* \frac{\lambda_{ni}^R \lambda_{mj}^{R*}}{M_{LQ}^2}, \\
 -C_P^{NP} &= C_S^{NP} = \frac{\sqrt{2}\pi}{G_F V_{tb} V_{ts}^* \alpha} \sum_{m,n=1}^3 V_{m3} V_{n2}^* \frac{\lambda_{ni}^L \lambda_{mj}^{R*}}{M_{LQ}^2}, \\
 C_P^{NP} &= C_S^{NP} = \frac{\sqrt{2}\pi}{G_F V_{tb} V_{ts}^* \alpha} \sum_{m,n=1}^3 V_{m3} V_{n2}^* \frac{\lambda_{ni}^R \lambda_{mj}^{L*}}{M_{LQ}^2}. \quad (110.10)
 \end{aligned}$$

The values of these NP couplings are constrained for a TeV scale LQ, using various flavour observables and can be found in [18].

110.5 Conclusion

The recently observed flavour anomalies in the CC- and NC-mediated semileptonic B meson decays may be considered as one of the most compelling hints of NP at the TeV scale. The explanation of these intriguing sets of discrepancies using a single framework is a daunting task, as the NP scales involved in the CC and NC sectors are significantly different from each other. There are only a few NP scenarios which can successfully accommodate these anomalies. The SM extension with a TeV scale vector LQ, which transforms as $(\mathbf{3}, \mathbf{1}, 2/3)$ under the SM gauge group is one such NP scenario. An interesting feature of this framework is that both the transitions $b \rightarrow c \tau \bar{\nu}_\tau$ and $b \rightarrow s \ell^- \ell^+$ occur at the tree level through the exchange of the LQ, which thus provides the required NP contributions to simultaneously resolve both these anomalies.

Acknowledgements The author acknowledges the financial supports received from SERB, Govt. of India through grant no. EMR/2017/001448 and Univ. of Hyderabad through IoE project UoH/IoE/RC1/RC1-20-012.

References

1. W. Abdallah et al., SciPost Phys. **9**, 022 (2020)
2. LHCb Collaboration, R. Aaij et al., Phys. Rev. Lett. **113**, 151601 (2014)

3. C. Bobeh, G. Hiller, G. Piranishvili, *JHEP* **0712**, 040 (2007)
4. LHCb Collaboration, R. Aaij et al., *Phys. Rev. Lett.* **122**, 191801 (2019)
5. LHCb Collaboration, R. Aaij et al., *JHEP* **08**, 055 (2017)
6. B. Capdevila, A. Crivellin, S. Descotes-Genon, J. Matias, J. Virto, *JHEP* **01**, 093 (2018)
7. M. Alguero et al., *Euro. Phys. J. C* **79**, 714 (2019)
8. Belle Collaboration, S. Wehle et al., *Phys. Rev. Lett.* **126**, 161801 (2021)
9. Belle Collaboration, S. Choudhury et al., *JHEP* **03**, 105 (2021)
10. The ATLAS, CMS and LHCb Collaborations, Report No. LHCb-CONF-2020-002
11. C. Bobeth, M. Gorbahn, T. Hermann, M. Misiak, E. Stamou, M. Steinhauser, *Phys. Rev. Lett.* **112**, 101801 (2014)
12. M. Alguero et al., *Euro. Phys. J. C* **79**, 714 (2019)
13. Y.S. Amhis et al. (HFLAV) (2019), *Eur. Phys. J. C* **81**, 226 (2021)
14. S. Fajfer, J.F. Kamenik, I. Nisandzic, *Phys. Rev. D* **85**, 094025 (2012)
15. LHCb Collaboration, R. Aaij et al., *Phys. Rev. Lett.* **120**, 121801 (2018)
16. Belle Collaboration, A. Abdesselam et al., [arXiv: 1903.03102](https://arxiv.org/abs/1903.03102)
17. C. Murgui, A. Penuelas, M. Jung, A. Pich, *JHEP* **09**, 103 (2019)
18. S. Fajfer, N. Kosnik, *Phys. Lett. B* **755**, 271 (2016); S. Sahoo, R. Mohanta, A. Giri, *Phys. Rev. D* **95**, 035027 (2017); J. Kumar, D. London, R. Watanabe, *Phys. Rev. D* **99**, 015007 (2019); P.B. Dev, R. Mohanta, S. Patra, S. Sahoo, *Phys. Rev. D* **102**, 095012 (2020)

Chapter 111

MiniBooNE Excess with a Light Z' and a Second Higgs Doublet



Samiran Roy, Waleed Abdallah, and Raj Gandhi

Abstract We show that a new $U(1)$ gauge symmetry embedded in two Higgs doublet model explains the electron-like excess events seen in MiniBooNE (MB) experiment. A light Z' associated with the new $U(1)$ couples to a dark neutrino, baryons, and leptons with a non-universal flavor coupling. A dark singlet scalar, which mixes with the two Higgs doublets, gives mass to Z' . We show that both $U(1)_B$ and $U(1)_{B-3L_\tau}$, which is anomaly-free, provide an equally good phenomenological solution to the excess. We also obtain a very good fit to the excess events both in energy and angular distributions.

111.1 Introduction

The excess of electron-like events over the expected background in MiniBooNE (MB) is 4.8σ [1]. Concurrently, the evidence against this excess being due to eV scale sterile neutrinos mixed with the active ones has solidified to a point where this hypothesis can seriously be called into question. The latest instance of this is the recent result announced by the DANSS experiment [2]. Explanations that invoke new, non-oscillation-based new physics thus acquire significant meaning and importance against this backdrop. The two most natural extensions of the standard model (SM) are the addition of a new $U(1)$ gauge symmetry and enlarging the SM Higgs sector with another Higgs doublet. We show that the combination of two can explain the excess events seen in MB. The new neutral gauge boson Z' , associated with the new $U(1)$ gauge, couples to a dark neutrino (ν_d) which mixes with SM neutrinos. The unique choice of the new gauge group is not our concern as long as it satisfies all the

S. Roy (✉)

Physical Research Laboratory, Ahmedabad 380009, Gujarat, India

e-mail: samiran@prl.res.in

W. Abdallah · R. Gandhi

Harish-Chandra Research Institute, HBNI, Chhatnag Road, Jhansi, Allahabad 211019, India

W. Abdallah

Department of Mathematics, Faculty of Science, Cairo University, Giza 12613, Egypt

© The Author(s), under exclusive license to Springer Nature Singapore Pte Ltd. 2022
B. Mohanty et al. (eds.), *Proceedings of the XXIV DAE-BRNS High Energy Physics Symposium, Jaiti, India*, Springer Proceedings in Physics 277,
https://doi.org/10.1007/978-981-19-2354-8_111

611

constraints. We show that both $U(1)_B$ and $U(1)_{B-3L_\tau}$ provide us an equally good fit to the excess events.

111.2 The Lagrangian of the Model

The extended part of the full Lagrangian (\mathcal{L}_{tot}) is given by

$$\mathcal{L}_{\text{tot}} \supset -\frac{1}{4} Z'_{\mu\nu} Z'^{\mu\nu} + \bar{v}_d \gamma^\mu (i \partial_\mu + g_d Z'_\mu) v_d + \mathcal{L}_q + \mathcal{L}_f - \mathcal{L}_Y^f - V + \mathcal{L}_S^{\text{Kin}} + \mathcal{L}_m, \quad (111.1)$$

where

$$\mathcal{L}_q = \sum_q \frac{1}{3} g_B \bar{q} \gamma^\mu Z'_\mu q, \quad \mathcal{L}_f = \sum_f g_B q_f \bar{f} \gamma^\mu Z'_\mu f, \quad (111.2)$$

$$\mathcal{L}_Y^f = \sqrt{2} \left[(Y_{ij}^u \bar{\Phi}_1 + \bar{Y}_{ij}^u \Phi_2) \bar{Q}_L^i u_R^j + (Y_{ij}^d \bar{\Phi}_1 + \bar{Y}_{ij}^d \Phi_2) \bar{Q}_L^i d_R^j + (Y_{ij}^e \bar{\Phi}_1 + \bar{Y}_{ij}^e \Phi_2) \bar{L}_L^i e_R^j \right]. \quad (111.3)$$

In the above, q corresponds to SM quarks, while f corresponds to leptons (ν_τ , τ for $U(1)_{B-3L_\tau}$). The charge $q_f = 0(-3)$ for $U(1)_B$ ($U(1)_{B-3L_\tau}$).

We write the scalar potential V in the Higgs basis ($\phi_h, \phi_H, \phi_{h'}$) [3] with the usual set of quartic couplings (λ_i) as

$$\begin{aligned} V = & \phi_h^\dagger \phi_h \left(\frac{\lambda_1}{2} \phi_h^\dagger \phi_h + \lambda_3 \phi_H^\dagger \phi_H + \mu_1 \right) + \phi_H^\dagger \phi_H \left(\frac{\lambda_2}{2} \phi_H^\dagger \phi_H + \mu_2 \right) + \lambda_4 (\phi_h^\dagger \phi_H) (\phi_H^\dagger \phi_h) \\ & + \left\{ \left(\frac{\lambda_5}{2} \phi_h^\dagger \phi_H + \lambda_6 \phi_h^\dagger \phi_h + \lambda_7 \phi_H^\dagger \phi_H + \lambda'_5 \phi_{h'}^* \phi_{h'} - \mu_{12} \right) \phi_h^\dagger \phi_H + h.c. \right\} \\ & + \phi_{h'}^* \phi_{h'} (\lambda'_2 \phi_{h'}^* \phi_{h'} + \lambda'_3 \phi_h^\dagger \phi_h + \lambda'_4 \phi_H^\dagger \phi_H + \mu'), \end{aligned} \quad (111.4)$$

where

$$\begin{aligned} \phi_h = \left(\frac{H_1^+}{v + H_1^0 + iG_1^0} \right) & \equiv \cos \beta \Phi_1 + \sin \beta \Phi_2, \quad \phi_H = \left(\frac{H_2^+}{H_2^0 + iA^0} \right) \equiv -\sin \beta \Phi_1 + \cos \beta \Phi_2, \\ \phi_{h'} = \frac{v' + H_3^0 + iG_2^0}{\sqrt{2}} \end{aligned} \quad (111.5)$$

so that $v^2 = v_1^2 + v_2^2 \simeq (246 \text{ GeV})^2$ and $\tan \beta = v_2/v_1$, where $\langle \Phi_i \rangle = v_i/\sqrt{2}$ and $\langle \phi_{h'} \rangle = v'/\sqrt{2}$. The scalar kinetic term ($\mathcal{L}_S^{\text{Kin}}$) can be written as

$$\mathcal{L}_S^{\text{Kin}} = \sum_{\mathcal{H}} (D_\mu^{\mathcal{H}} \phi_{\mathcal{H}})^\dagger D_\mu^{\mathcal{H}} \phi_{\mathcal{H}} \supset \frac{1}{2} g_d^2 (v' + H_3^0)^2 Z'_\mu Z'^\mu, \quad (111.6)$$

where

$$D_\mu^{h'} \phi_{h'} \equiv (\partial_\mu + i g_d Z'_\mu) \phi_{h'}. \quad (111.7)$$

Hence, the $Z'-H_3^0-Z'$ coupling is given by

$$G_{Z'H_3^0} = i \frac{2m_{Z'}^2}{v'}, \tag{111.8}$$

where $m_{Z'}^2 = g_d^2 v'^2$. In the alignment limit ($\lambda_6 \simeq 0 \simeq \lambda_3'$), we obtain one SM-like Higgs (h) and two other CP-even scalars (H and h') which are much lighter in mass compared to h . The H and h' are connected to H_2^0 and H_3^0 via the mixing angle δ . Since ϕ_H do not get any vev, the couplings of H to quarks and leptons can be made arbitrary. This helps us to avoid stringent constraints on light scalar. For more details see [4].

111.2.1 The interaction in MB

The dark neutrino (ν_d) mixes with the standard neutrinos. Hence the interaction term in the mass basis is given by

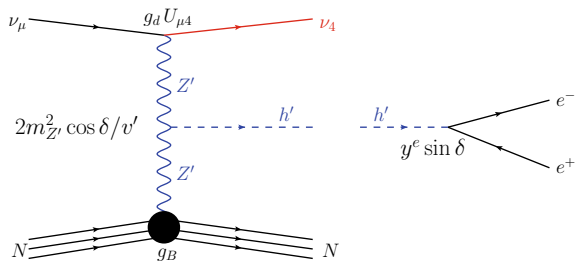
$$\mathcal{L}_{\text{int}} = g_d \bar{\nu}_d \gamma^\mu \nu_d Z'_\mu = g_d \sum_{i,j=1}^4 U_{di}^\dagger U_{dj} \bar{\nu}_i \gamma^\mu Z'_\mu \frac{(1-\gamma_5)}{2} \nu_j. \tag{111.9}$$

Feynman diagram, which produces excess events in MB in our model, is shown in Fig. 111.1. Both incoherent and coherent parts of the cross section will contribute in the production of h' , as shown in Fig. 111.1. Once h' is produced, it decays promptly to a collimated e^+e^- pair. As the invariant mass of the e^+e^- pair is less than 30 MeV, it mimics the single electron-like signal in MB. The total differential cross section for CH_2 target material in MB is given by

$$\left(\frac{d\sigma}{dE_{h'}} \right)_{\text{CH}_2} = \underbrace{14 \times \left(\frac{d\sigma}{dE_{h'}} \right)}_{\text{incoherent}} + \underbrace{144 \times \exp(2b(k' - k)^2) \left(\frac{d\sigma}{dE_{h'}} \right)}_{\text{coherent}}. \tag{111.10}$$

Here $b = 25 \text{ GeV}^{-2}$ for C^{12} [5]. H could also contribute in the MB events but its contribution is very small compared to h' for our benchmark parameters.

Fig. 111.1 Feynman diagram in our model which leads to MB excess events



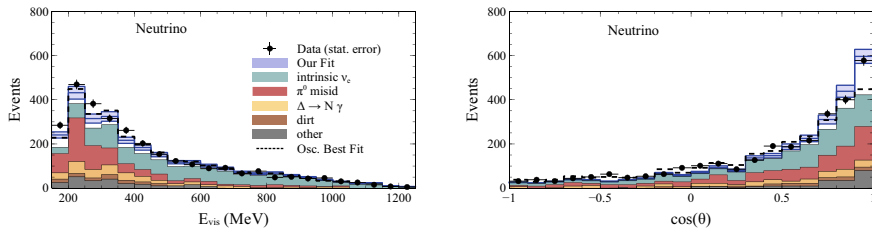


Fig. 111.2 MB electron-like events (backgrounds and signal) correspond to 18.75×10^{20} POT [1]. The blue solid line shows the prediction of our model whereas the blue band corresponds to the variation due to 15% systematic uncertainties. The parameter values used for calculating the events are shown in Table 111.1

Table 111.1 Benchmark parameter values to produce the events in MB

m_{ν_4} (MeV)	$m_{Z'}$ (MeV)	$m_{h'}$ (MeV)	m_H (MeV)	$ U_{\mu 4} ^2$	g_B	g_d	$\sin \delta$	$y_e^{h'} = y^e \sin \delta$
50	800	23	106	2.6×10^{-5}	3×10^{-4}	2.85	0.28	4.5×10^{-5}

111.3 Results

The blue solid line of Fig. 111.2 shows the prediction of our model in each bin with the model parameters as shown in Table 111.1. The left panel plot shows the distribution of neutrino events with the measured visible energy, E_{vis} . For our model, E_{vis} corresponds to the total energy of the collimated e^+e^- pair, i.e., the total energy of $E_{h'}$. The corresponding angular distributions for the emitted light are shown in the right panel. These plots have been generated using fluxes, efficiencies, and all other relevant informations taking from [1, 6] and references therein. We also obtain a very good fit to the observed event excess both in energy and angular distributions.

111.4 Summary

We find that a light Z' associated with $U(1)_B$ or $U(1)_{B-3L_\tau}$, which is anomaly-free, combined with a second Higgs doublet gives a very good fit to the MB excess. The Z' gets its mass from a singlet scalar, and is coupled to a dark neutrino. The Higgs sector consists of three CP-even scalars h (SM-like Higgs), h' and H . Both h' and H are much lighter than h . In MB, $h'(H)$ is produced via $Z'-h'(H)-Z'$ interaction and decays promptly to a collimated e^+e^- pair. Both h' and H contribute to the MB excess, but most of the excess events come from h' for our choice of benchmark parameters.

References

1. A.A. Aguilar-Arevalo et al. [MiniBooNE], Phys. Rev. D **103**(5), 052002 (2021)
2. M. Danilov, [arXiv:2012.10255](https://arxiv.org/abs/2012.10255) [hep-ex]
3. S. Davidson, H.E. Haber, Phys. Rev. D **72**, 035004 (2005). (erratum: Phys. Rev. D **72**, 099902 (2005))
4. W. Abdallah, R. Gandhi, S. Roy, JHEP **12**, 188 (2020)
5. D.Z. Freedman, Phys. Rev. D **9**, 1389 (1974)
6. A.A. Aguilar-Arevalo et al. [MiniBooNE], Phys. Rev. Lett. **121**(22), 221801 (2018)

Chapter 112

Impact of Non-standard Interactions on Violation of Leggett-Garg Inequality in Three-Flavour Neutrino Oscillations



Sheeba Shafaq and Poonam Mehta

Abstract Neutrino oscillations occur due to non-zero masses and mixings and most importantly they are believed to maintain quantum coherence even over astrophysical length scales. Here, we study the quantumness of three-flavour neutrino oscillations by studying the extent of violation of Leggett-Garg inequalities (LGI) if non-standard interactions are taken into account. We report an enhancement in violation of LGI with respect to the standard scenario for a certain choice of NSI parameters.

112.1 Introduction

In their seminal paper, Leggett and Garg [1] derived a class of inequalities which provided a way to test the applicability of quantum mechanics as we go from the microscopic to the macroscopic world by invoking the principle of macroscopic realism. The work was based on our intuition about the macroscopic world which can be defined in terms of the two principles (see [2] for a review): (a) Macroscopic realism (MR) which implies that the performance of a measurement on a macroscopic system reveals a well-defined pre-existing value (b) Non-invasive measurability (NIM) which states that in principle, we can measure this value without disturbing the system. The classical world, in general, respects both of these assumptions. However, in quantum mechanics, both the assumptions are violated as it is based on superposition principle and collapse of wave function under measurement.

If we look at the developments in the neutrino sector, soon after the discovery of the second type of neutrino in the sixties, the idea of neutrino flavour oscillations was proposed by Maki, Nakagawa and Sakata [3] as well as by Gribov and Pontecorvo [4]. The experimental vindication of the idea of neutrino flavour oscillations took several decades. The phenomenon of neutrino flavour oscillation arises from the phase difference acquired by the mass eigenstates due to their time evolution during propagation in vacuum or matter.

S. Shafaq (✉) · P. Mehta
Jawaharlal Nehru University, New Delhi 110067, India
e-mail: sheebakhawaja7@gmail.com

© The Author(s), under exclusive license to Springer Nature Singapore Pte Ltd. 2022
B. Mohanty et al. (eds.), *Proceedings of the XXIV DAE-BRNS High Energy Physics Symposium, Jatni, India*, Springer Proceedings in Physics 277,
https://doi.org/10.1007/978-981-19-2354-8_112

617

The present article weaves together the idea of LGI and neutrino oscillation physics in the presence of non-standard interactions (NSI) to explore the extent and possibility of enhancement of violation of LGI in case of three-flavour oscillations. To the best of our knowledge, NSI-induced effects on violation of LGI in neutrino sector have not been reported so far.

112.2 Leggett-Garg Inequalities in the Context of Neutrino Oscillations

Consider a dichotomic observable Q which can only have values ± 1 , defined over the Hilbert space of a given N -level quantum system. We define a two-time correlation function, C_{ij} , which depends on joint probabilities of various outcomes of successive measurements of the observable Q at t_i and t_j on a state which was prepared at time $t = 0$.

The two-time correlation function can be expressed as

$$C_{ij} = \sum_{Q(t_i)Q(t_j)=\pm 1} Q(t_i)Q(t_j)\mathbb{P}_{Q_i, Q_j}(t_i, t_j) \tag{112.1}$$

where $\mathbb{P}_{Q_i, Q_j}(t_i, t_j)$ is the joint probability of obtaining the results Q_i and Q_j from measurements at times t_i and t_j , respectively. Assuming that the measurements do not violate NIM, macrorealism restricts the following combination of two-time correlation functions

$$K_n = C_{12} + C_{23} + C_{34} + \dots + C_{(n-1)n} - C_{1n} \tag{112.2}$$

Since the observable Q can only have values ± 1 and probability varies between 0 and +1, we get the following inequalities:

$$\begin{aligned} -n \leq K_n \leq (n-2) & \quad 3 \leq n, \text{ odd;} \\ -(n-2) \leq K_n \leq (n-2) & \quad 4 \leq n, \text{ even.} \end{aligned} \tag{112.3}$$

These are Leggett-Garg inequalities in their standard form. The systems that respect the assumptions of NIM and MR will respect these inequalities and will thus lie in the realm of classical physics. The systems that fall out of line with classical physics will not respect these inequalities that can be explained only by quantum mechanics (Fig. 112.1).

In order to explore LGI in the neutrino sector, we consider an electron neutrino on which measurements are made at times t_i . The dichotomic observable Q assumes value +1 when the system to be found in the electron neutrino flavour state $|v_e\rangle$ and -1 if the system is found in the muon neutrino state $|v_\mu\rangle$ or tau neutrino state $|v_\tau\rangle$. For the three-flavour case, which is a three-level quantum system, the correlation

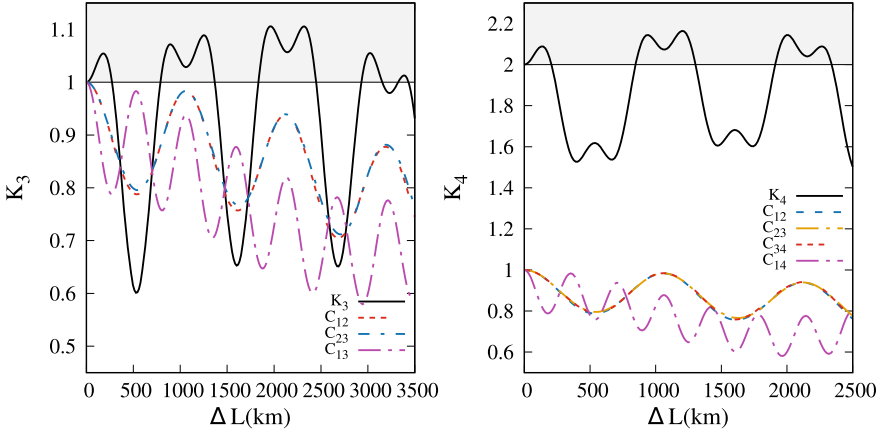


Fig. 112.1 K_3 and K_4 are plotted as a function of ΔL . The contribution of different C'_{ij} 's is depicted in the figure. The grey-shaded region denotes the region where LGI is violated

function is expressed as

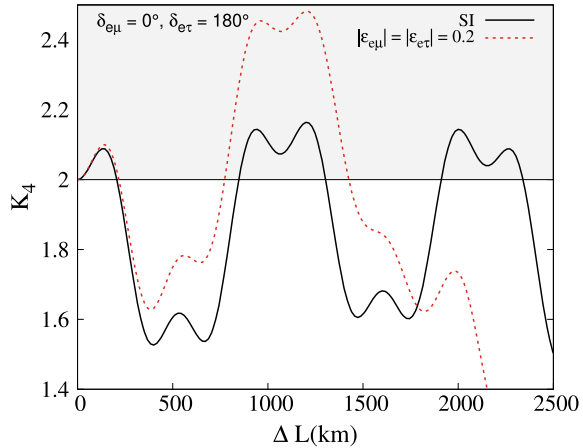
$$\begin{aligned}
 C_{12} = & \mathbb{P}_{\nu_e \nu_e}(t_1, t_2) - \mathbb{P}_{\nu_e \nu_\mu}(t_1, t_2) - \mathbb{P}_{\nu_e \nu_\tau}(t_1, t_2) \\
 & - \mathbb{P}_{\nu_\mu \nu_e}(t_1, t_2) + \mathbb{P}_{\nu_\mu \nu_\mu}(t_1, t_2) + \mathbb{P}_{\nu_\mu \nu_\tau}(t_1, t_2) \\
 & - \mathbb{P}_{\nu_\tau \nu_e}(t_1, t_2) + \mathbb{P}_{\nu_\tau \nu_\mu}(t_1, t_2) + \mathbb{P}_{\nu_\tau \nu_\tau}(t_1, t_2)
 \end{aligned} \tag{112.4}$$

where $\mathbb{P}_{\nu_\alpha \nu_\beta}(t_1, t_2) = P_{\nu_e \rightarrow \nu_\alpha}(t_1) P_{\nu_\alpha \rightarrow \nu_\beta}(t_2)$ is the joint probability of obtaining a neutrino in state α at time t_1 and in state β at time t_2 . In the ultra-relativistic limit, this time difference translates to the spatial difference $(L_i - L_j)$, where L_i and L_j are the fixed distances from the neutrino source where the measurements occur. The detailed expression of the correlation function C_{12} for three-flavour neutrino oscillation is given in [5]. The joint probability shows dependence on L_1 as well as the spatial separation $(L_2 - L_1)$.

112.3 Results and Conclusion

Using the values of the oscillation parameters given in [6], we compute the oscillation probability numerically using the General Long Baseline Experiment Simulator (GLoBES) [7, 8]. The LGI quantities K_3 and K_4 are then obtained using the joint probabilities. The value of the CP-violating phase is taken to be $\delta = 3\pi/2$ and normal ordering is assumed in obtaining the results unless stated otherwise. We assume a fixed value for energy, $E = 1$ GeV and take the initial state to be $|\nu_e\rangle$. In case of K_4 , after inspecting various choices it is found that the maximum value of the correlation function C is attained essentially when all the spatial separations are taken to be the same, i.e. $(L_4 - L_3) = (L_3 - L_2) = (L_2 - L_1) = \Delta L$ and C under this condition

Fig. 112.2 The LGI parameter K_4 is plotted against ΔL for NSI case by taking two dominant NSI parameters non-zero. For the purpose of maximizing the LGI parameter, NSI phases have been appropriately chosen



depends on ΔL and L_1 which has been taken to be 140.15 km [5]. The LGI parameters K_3 and K_4 are plotted as a function of ΔL for three-flavour neutrino oscillation for SI and NSI cases. We notice a significant enhancement in the violation of LGI in the NSI scenario as compared to the SI scenario. For more details, please refer to [9] (Fig. 112.2).

References

1. A.J. Leggett, A. Garg, Quantum mechanics versus macroscopic realism: Is the flux there when nobody looks? *Phys. Rev. Lett.* **54**, 857–860 (1985)
2. C. Emary, N. Lambert, F. Nori, Leggett-Garg Inequalities. 2014 Rep. Prog. Phys. **77**(1), 016001 (2014)
3. Z. Maki, M. Nakagawa, S. Sakata, Remarks on the unified model of elementary particles. *Prog. Theor. Phys.* **28**(5), 870–880 (1962)
4. V.N. Gribov, B. Pontecorvo, Neutrino astronomy and lepton charge. *Phys. Lett. B* **28**, 493 (1969)
5. D. Gangopadhyay, A.S. Roy, Three-flavoured neutrino oscillations and the LeggettGarg inequality. *Eur. Phys. J. C* **77**(4), 260 (2017)
6. P.F. de Salas, D.V. Forero, S. Gariazzo, P. Martínez-Miravé, O. Mena, C.A. Ternes, A. Tórtola, J.W.F. Valle, 2020 Global reassessment of the neutrino oscillation picture. *JHEP* **02**, 071 (2021)
7. P. Huber, M. Lindner, W. Winter, Simulation of long-baseline neutrino oscillation experiments with GLOBES (General Long Baseline Experiment Simulator). *Comput. Phys. Commun.* **167**, 195 (2005)
8. P. Huber, J. Kopp, M. Lindner, M. Rolinec, W. Winter, New features in the simulation of neutrino oscillation experiments with GLOBES 3.0: General Long Baseline Experiment Simulator. *Comput. Phys. Commun.* **177**, 432–438 (2007)
9. S. Shafaq, P. Mehta, Enhanced violation of Leggett-Garg Inequality in three flavour neutrino oscillations via non-standard interactions (2009). (2009.12328)

Chapter 113

Theory of Fast-Flavor Conversion of Supernova Neutrinos



Soumya Bhattacharyya

Abstract A supernova natively emits neutrinos and antineutrinos of all flavors with different luminosities and energy spectra. These neutrinos can undergo neutrino–neutrino forward-scattering inside the dense anisotropic interior of the star and can lead to “fast collective neutrino oscillations”. We present the fast ever theory of “fast flavor conversion” beyond the linear regime to show how the different neutrino flavors are brought closer to each other, or in other words, “flavor depolarizes” due to irreversible decoherence-like processes occurring at a Tera-Hz rate, determined by the large neutrino density. Our theory explains how depolarization happens, when does it happen, what determines the epoch and finally describes a method to calculate the extent of depolarized fluxes. This new result allows detailed implementation of flavor-dependent neutrino transport in supernova simulations and paves the way for supernova neutrino phenomenology.

113.1 Set-Up of the Problem

In the fast oscillation limit, neglecting the vacuum, matter Hamiltonian and considering the fact that neutrino self-interaction term enters the Hamiltonian only through the difference of neutrino angular distributions integrated over energy, defined by the electron lepton number (ELN) distribution or $G_{\mathbf{v}}$, the equation of motion governing flavor evolution of neutrinos in dense environments (e.g., SN) for locally azimuth-symmetric ELNs becomes [1].

$$(\partial_t + v\partial_z)\mathbf{S}_v = \mu_0 \int_{-1}^{+1} dv' G_{v'} (1 - vv') \mathbf{S}_{v'} \times \mathbf{S}_v, \quad (113.1)$$

S. Bhattacharyya (✉)

Tata Institute of Fundamental Research, Homi Bhabha Road, Mumbai 400005, India
e-mail: soumyaquanta@gmail.com

© The Author(s), under exclusive license to Springer Nature Singapore Pte Ltd. 2022
B. Mohanty et al. (eds.), *Proceedings of the XXIV DAE-BRNS High Energy Physics Symposium, Jaiti, India*, Springer Proceedings in Physics 277,
https://doi.org/10.1007/978-981-19-2354-8_113

621

where v is the radial velocity and μ_0 is the collective potential. We work in the flavor basis $\{\hat{e}_1, \hat{e}_2, \hat{e}_3\}$, where the longitudinal component along \hat{e}_3 is denoted by $(\cdot)^\parallel$ and the transverse by $(\cdot)^\perp$. Sans-serif letters denote vectors in flavor space, whose magnitudes are shown in the usual font. We denote spatial averaging as $\langle \dots \rangle$. To solve (113.1) we use initial conditions such that neutrinos and antineutrinos are emitted as electron flavor from all points in space along with periodic boundary condition over space. We choose G_v as piecewise constant that up to zeroth-order mimics the most realistic SN profile which looks like:

$$G_v = \begin{cases} 1, & \text{if } v > 0, \\ A - 1, & \text{if } v < 0. \end{cases} \quad (113.2)$$

113.2 Results

113.2.1 How and When?

Now to understand how and when depolarization happens, it is best understood in terms of time evolution of multipole moment M_n defined as $M_n = \int_{-1}^{+1} dv G_v L_n S_v$ which reduces the spatially averaged EOM to [2, 3]

$$\partial_t \langle M_n \rangle = \frac{\langle M_1 \rangle}{2} \left(\partial_n^2 \langle M_n \rangle + \frac{1}{n} \partial_n \langle M_n \rangle \right). \quad (113.3)$$

Here $\langle M_n \rangle$ denotes the spatially coarse-grained value of $M_n = |M_n|$ and the equation is valid for large n . Equation (113.3) is a diffusion-advection equation where n plays the role of space and $\langle M_1 \rangle$ of the diffusion constant. G_v and initial conditions for S_v are smooth in v so that $\langle M_n \rangle$ are initially small for $n \gg 1$. As time passes, the system *diffuses* from low- n to high- n multipoles. The solution for (113.3) looks like, $\langle M_n \rangle = c_1 \text{Ei}[-n^2/(2\langle M_1 \rangle t)] + c_2$, in terms of the exponential integral $\text{Ei}[x] = \int_{-\infty}^x dy e^y/y$ and c_1, c_2 are constants. This solution, valid for large n , predicts how each $\langle M_n \rangle$, starting at its initial value, grows exponentially, peaks roughly at around $t_n^{\text{peak}} \approx n^2/(2\langle M_1 \rangle)$, and asymptotes to the final value at late times. This solution predicts kinematic decoherence and thus indicates irreversibility in the system owing to which there is a steady-state behavior at late times. On top of that the solution has strong dependence on the effective diffusion coefficient $\langle M_1 \rangle$, for example, lesser (larger) diffusion coefficient results in lesser (larger) kinematic decoherence (see Fig. 113.1).

Naively, the spatial average of (113.1) is $d_t \langle S_v \rangle = \langle H_v \rangle \times \langle S_v \rangle$, which can be visualized as a spin $\langle S_v \rangle$ precessing around the magnetic field $\langle H_v \rangle$. Note that $H_v \approx -(\frac{1}{3}M_0 + vM_1)$ in a frame co-rotating with the M_0 - M_1 plane. Initially, $\langle S_v \rangle$ is along \hat{e}_3 , and it starts tilting away due to the action of the vacuum Hamiltonian. It is

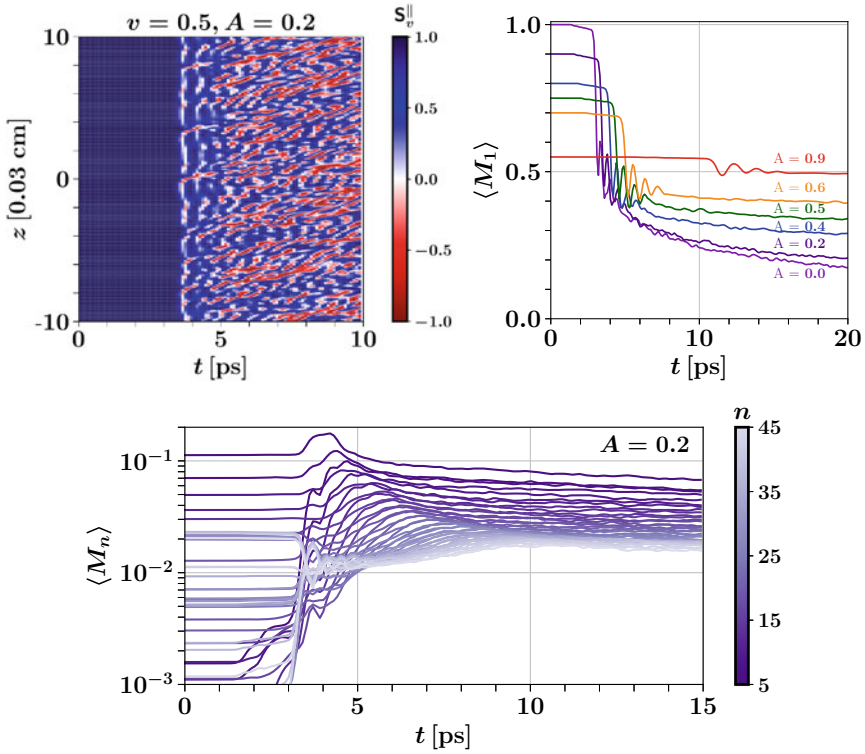


Fig. 113.1 MULTIPOLE DIFFUSION: Evolution of S_v^{\parallel} for $v = 0.5$ and $A = 0.2$ (left) and $\langle M_1 \rangle$ for various ELNs (middle). Evolution of $\langle M_n \rangle$ for large n and $A = 0.2$ (right)

very easy to visualize that $\langle M_1 \rangle$ has the motion of an inverted pendulum so that $\langle M_1 \rangle$ tends to tip over but $\langle M_0 \rangle$ remains conserved. Thus $\langle H_v^{\parallel} \rangle = |\frac{1}{3}A + v\langle M_1^{\parallel} \rangle|$ becomes smaller as well. Eventually, when $\langle H_v^{\perp} \rangle \approx \langle H_v^{\parallel} \rangle$, then $\langle S_v \rangle$ makes a large precession angle and reaches the transverse plane. At this point, S_v at different spatial locations relatively dephase due to transverse relaxation (becomes randomized in space) and thus their coarse-grained transverse component $\langle S_v^{\perp} \rangle$ shrinks irreversibly. Thus the lengths $\langle S_v \rangle$ and $\langle M_1 \rangle$ also become smaller. This transverse relaxation process determining the epoch of depolarization depends on velocity modes as well as lepton asymmetry as can be seen in Fig. 113.2.

113.2.2 Extent of Depolarization

The extent of flavor depolarization can be calculated via a quantity known as depolarization factor or f_v^D defined as, $f_v^D = \frac{1}{2}(1 - \langle S_v^{\parallel} \rangle^{\text{fin}} / \langle S_v^{\parallel} \rangle^{\text{ini}})$. Note by definition,

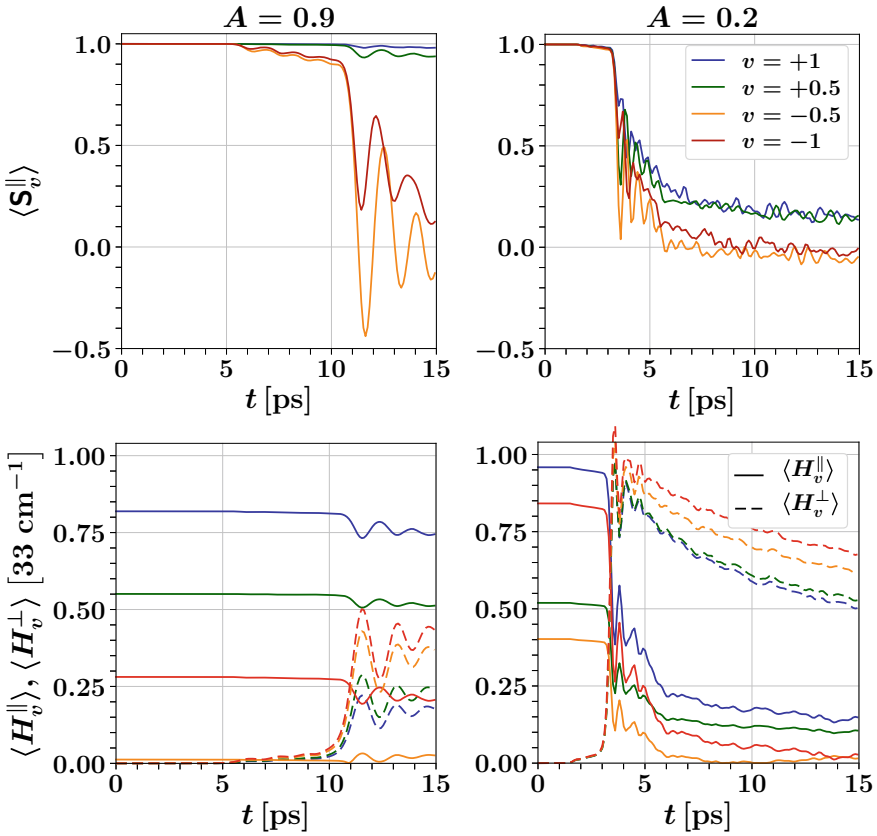


Fig. 113.2 RELAXATION: Evolution of $\langle S_v^{\parallel} \rangle$ for $v = \pm 1, \pm 0.5$ (top panels) for $A = 0.9$ (left) and $A = 0.2$ (right). $\langle H_v^{\parallel} \rangle$ and $\langle H_v^{\perp} \rangle$, in solid and dashed lines, respectively (bottom panels)

$f_v^D = 0$ (or $\frac{1}{2}$) means no (perfect) depolarization. Dropping the higher multipoles as they diffuse away one can truncate the multipole expansion for the Bloch vector up to second order in v as: $G_v \langle S_v^{\parallel} |^{\text{fin}} \rangle = \frac{1}{2} \langle M_0^{\parallel} |^{\text{fin}} \rangle + \frac{3}{2} v \langle M_1^{\parallel} |^{\text{fin}} \rangle + \mathcal{O}(v^2)$. This along with the fact that negative velocity modes are completely depolarized and using the lepton number conservation, one can write f_v^D as a linear function in v as

$$f_v^D \approx \begin{cases} \frac{1}{2} - \frac{A}{4} - \frac{3A}{8} v, & \text{if } v > 0, \\ \frac{1}{2}, & \text{if } v < 0. \end{cases} \quad (113.4)$$

Figure 113.3 shows the numerical as well as analytical results for f_v^D .

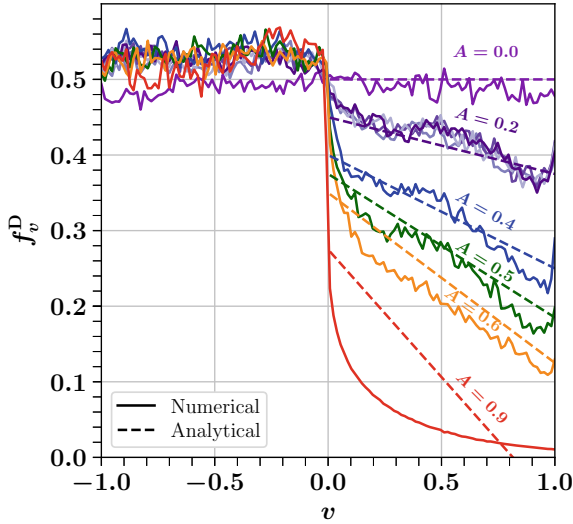


Fig. 113.3 DEPolarization FACTOR: Analytical (dashed) and numerical (solid) results for coarse-grained f_v^D , as a function of the radial velocity, $v = \cos \theta$, for different initial neutrino ELNs labeled by their lepton asymmetry A . For $A = 0.2$, the different purple lines are for different initial seeds

113.3 Conclusion

We showed *how* neutrino flavor differences become smaller due to diffusion to smaller angular scales causing flavor depolarization. Coarse-graining over a small spatial volume can introduce loss of information. We then showed that the epoch of T2 relaxation determines *when* depolarization occurs. Finally, we gave a strategy and a formula for computing the *extent of depolarization*, which is the ultimate outcome for fast collective oscillations.

References

1. S. Chakraborty, R.S. Hansen, I. Izaguirre, G. Raffelt, JCAP **03**, 042 (2016)
2. S. Bhattacharyya, B. Dasgupta, Phys. Rev. Lett. **126**(6), 061302 (2021)
3. G.G. Raffelt, G. Sigl, Phys. Rev. D **75**, 083002 (2007)

Part IV
Cosmology and Astroparticle Physics

Chapter 114

Tree-Level Leptogenesis Induced by Soft SUSY Breaking in NMSSM Extended by a Right Handed Neutrino Superfield



Abhijit Kumar Saha, Waleed Abdallah, and Abhass Kumar

Abstract We analyse soft leptogenesis in NMSSM extended by one right-handed neutrino superfield. Our framework predicts non-zero ε from the right-handed sneutrino decay without the presence of thermal effects that are necessary for MSSM extended by an RH superfield. We provide the required order of magnitudes of the relevant soft supersymmetry parameters to yield sufficient baryon asymmetry of the universe.

114.1 Introduction

In soft leptogenesis mechanism [1, 2], the yield of non-zero lepton asymmetry at the tree-level takes place owing to the mixing between the particle and anti-particle states of the right-handed (RH) singlet sneutrino. The resultant amount of asymmetry crucially depends on the amount of soft supersymmetry (SUSY) breaking terms. Earlier works with a minimal supersymmetric standard model (MSSM) extended by one RH neutrino superfield reveal that a CP asymmetry in the RH sneutrino sector is created upon consideration of thermal masses for the final products. Secondly, we know that one of the major drawbacks of the MSSM is the μ -problem. The next-to-minimal supersymmetric standard model (NMSSM) can solve this problem where a singlet superfield is introduced in addition to the MSSM fields. In the NMSSM setup the scalar partner of the singlet superfield gets non-zero vev and provides an

A. Kumar Saha (✉)

School of Physical Sciences, Indian Association for the Cultivation of Science, 2A and 2B Raja S.C. Mullick Road, Kolkata 700 032, India
e-mail: psaks2484@iacs.res.in

W. Abdallah

Harish-Chandra Research Institute, Chhatnag Road, Jhansi, Allahabad 211 019, India
Faculty of Science, Department of Mathematics, Cairo University, Giza 12613, Egypt

A. Kumar

Physical Research Laboratory, Theoretical Physics Division, Navrangpura, Ahmedabad 380 009, India

© The Author(s), under exclusive license to Springer Nature Singapore Pte Ltd. 2022
B. Mohanty et al. (eds.), *Proceedings of the XXIV DAE-BRNS High Energy Physics Symposium, Jatni, India*, Springer Proceedings in Physics 277,
https://doi.org/10.1007/978-981-19-2354-8_114

629

elegant mechanism to dynamically generate the μ -term of the TeV scale. With this observation, we pose a question of whether we can produce sufficient CP asymmetry without using thermal factors. The work is based on [3].

114.2 The Model

The superpotential for the Z_3 invariant NMSSM is read as

$$W = Y_E^{ij} \hat{H}_d \hat{L}_i \hat{E}_j + Y_D^{ij} \hat{H}_d \hat{Q}_i \hat{D}_j + Y_U^{ij} \hat{H}_u \hat{Q}_i \hat{U}_j + \lambda \hat{S} \hat{H}_u \hat{H}_d + \frac{\kappa}{3} \hat{S}^3 + Y_N^i \hat{N} \hat{H}_u \hat{L}_i + \lambda_N \hat{S} \hat{N} \hat{N}, \quad (114.1)$$

where \hat{H}_u , \hat{H}_d , \hat{L}_i and \hat{Q}_i are the $SU(2)$ doublet Higgs, leptons and quark superfields; \hat{E}_i and \hat{D}_i (\hat{U}_i) represent singlet down (up)-type quark superfields, respectively, and Y 's, λ 's and κ are dimensionless couplings with generation indices ($i, j = 1, 2, 3$). Once the singlet S obtains a vacuum expectation value (vev) $\langle S \rangle$, the μ -term is generated: $\mu_{\text{eff}} = \lambda \langle S \rangle$. The soft SUSY-breaking Lagrangian is written as

$$-\mathcal{L}_{\text{soft}} = -\mathcal{L}_{\text{soft}}^{\text{MSSM}} + \left(A_{\lambda_H} \lambda S H_u H_d + A_\kappa \frac{\kappa}{3} S^3 + A_N^i Y_N^i \tilde{N} H_u \tilde{L}_i + A_\lambda \lambda_N S \tilde{N} \tilde{N} + \text{h.c.} \right) + m_S^2 |S|^2 + M^2 |\tilde{N}|^2, \quad (114.2)$$

where \tilde{L}_i and \tilde{N} are identified as the scalar components of \hat{L}_i and \hat{N} superfields, respectively. When all the three scalars H_u , H_d , S acquire non-zero vevs with relative physical phases, CP symmetry gets spontaneously broken. We express the vev of the singlet S as $\langle S \rangle = v_S e^{i\delta}$. In our case we consider the energy scale of leptogenesis higher than the electroweak (EW) scale, hence spontaneous CP violation takes place only when $\sin \delta \neq 0$.

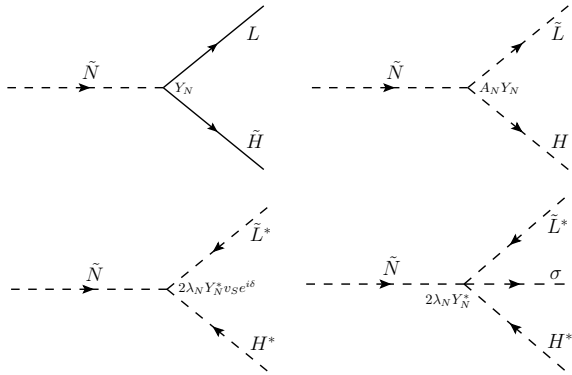
114.3 Estimate of Lepton Asymmetry

The relevant terms of the Lagrangian (including soft SUSY breaking terms) that contribute to lepton asymmetry as derived from the superpotential in (114.1) is given by

$$\mathcal{L}_{\text{int}} = \tilde{N} \left(Y_N \tilde{H} L + 2\lambda_N Y_N^* v_S e^{i\delta} H^* \tilde{L}^* + 2\lambda_N Y_N^* \sigma H^* \tilde{L}^* + A_N Y_N H \tilde{L} \right) + \sigma \left(\lambda_N N N + A_\lambda \lambda_N \tilde{N} \tilde{N} \right) + \text{h.c.}, \quad (114.3)$$

where $\sigma = S - \langle S \rangle$.

Fig. 114.1 Two-body and three-body decay diagrams of a singlet sneutrino, \tilde{N} . The figure is borrowed from [3]



The \mathcal{L}_{int} clearly indicates the presence of a mixing between particle and anti-particle states of the sneutrino and the singlet scalar σ , which is the dynamic part of S . The case is similar to $K_0 - \bar{K}_0$ and $B_0 - \bar{B}_0$ systems. The evolution of these systems in the non-relativistic limit is determined by the Hamiltonian $\mathcal{H} = \mathcal{M} - \frac{i}{2}\Gamma$, where \mathcal{M} is the mass matrix (the mass difference) of the two eigenstates defined by δM . The Γ indicates the decay rate matrix of the corresponding $\tilde{N} - \tilde{N}^*$ system.

The lepton asymmetry from (anti)sneutrino decay has to be calculated at finite time. The decay processes which contribute to lepton asymmetry in the sneutrino system are shown in Fig. 114.1. We ignore three-body tree-level diagrams mediated by \tilde{N} since they are of higher order in soft terms and hence suppressed. The four-point interaction denoting a three-body decay of \tilde{N} is crucial as that makes our case different from the earlier works with MSSM. The time dependence of sneutrino system can be found by solving the Schrodinger-like equation: $\mathcal{H}\psi = i\frac{d\psi}{dt}$, where $\psi = \{\tilde{N}, \tilde{N}^*\}^T$. The CP asymmetry factor ε is defined as the ratio of the difference between the decay rates of \tilde{N} and \tilde{N}^* into final state particles with lepton number +1 and -1 to the sum of all the decay rates, i.e.,

$$\varepsilon = \frac{\sum_f \int_0^\infty dt \left[\Gamma(\tilde{N}(t) \rightarrow f) + \Gamma(\tilde{N}^*(t) \rightarrow f) - \Gamma(\tilde{N}(t) \rightarrow \bar{f}) - \Gamma(\tilde{N}^*(t) \rightarrow \bar{f}) \right]}{\sum_f \int_0^\infty dt \left[\Gamma(\tilde{N}(t) \rightarrow f) + \Gamma(\tilde{N}^*(t) \rightarrow f) + \Gamma(\tilde{N}(t) \rightarrow \bar{f}) + \Gamma(\tilde{N}^*(t) \rightarrow \bar{f}) \right]}, \tag{114.4}$$

where f, \bar{f} are the final states with lepton number +1 and -1, respectively. Note that the $\tilde{N}(t)$ is a superposition of both $\tilde{N}(t=0)$ and $\tilde{N}^*(t=0)$.

We use a few general constraints to reduce the number of free parameters in the model: (i) out of equilibrium condition which is necessary to be in the weak washout regime, (ii) the methodology we follow here requires well separated states denoted by $\Gamma < \Delta M$ and $\Delta\Gamma \ll \Delta M$ and (iii) the upper limit on the lightest SM neutrino mass $m_\nu \lesssim 0.1$ eV. We also consider $M_1 = \sqrt{M^2 + 4\lambda_N v_S^2} \gg M \Rightarrow M_1 \simeq 2\lambda_N v_S$, $M_1 \gg m_\sigma$ and $A_\lambda \simeq \kappa v_S$. With all these constraints and approximation, we reach at

a simpler form of ε at leading order in soft terms which is given by

$$\varepsilon \simeq \frac{1}{2\pi} \left(\frac{\alpha}{2 + \alpha} \right) \times \frac{Y_N^2 \left[A_\lambda \text{Im} A_N + \kappa v_S \{ \cos(3\delta) \text{Im} A_N + \sin(3\delta) \text{Re} A_N \} \right]}{A_\lambda^2 + \kappa^2 v_S^2 + 2A_\lambda \kappa v_S \cos(3\delta)} \tag{114.5}$$

To work out this analytical expression of ε , we choose the soft masses $M, m_S \sim \mathcal{O}(1)$ TeV and v_S to be of $\mathcal{O}(10^7)$ GeV with $\lambda_N \sim \mathcal{O}(1)$. This along with $\kappa \ll \lambda_N$ means both $M, m_\sigma \ll 2\lambda_N v_S \simeq M_1$. An upper limit $Y_N \lesssim \mathcal{O}(10^{-4})$ from the constraints as earlier stated is also derived.

The lepton asymmetry can be converted to baryon asymmetry by non-perturbative sphaleron process. To calculate the amount of baryon asymmetry in the universe, we use the well-known relation $\eta_B = \frac{3}{4} \frac{g_*^0}{g_*} a_{\text{sph}} N_{B-L}^f$, where N_{B-L} is the $B - L$ number density. The N_{B-L} as function temperature can be found by solving the set of coupled Boltzmann equations involving sneutrino number density and B-L number density. In general, $\varepsilon \sim \mathcal{O}(10^{-6})$ is needed to match the observed baryon asymmetry of the universe in the weak washout regime. Equation (114.5) gives few impressions which are: (i) even with real Yukawa parameters non-zero ε can be obtained, (ii) the ε can have definite value even if A_N is real provided $\delta \neq 0$ and (iii) in $\delta \rightarrow \pi$ limit, a resonant enhancement of ε is possible.

We consider two limiting scenarios for numerical estimate of ε . In the first case, δ is near zero. In contrast, the second case is for $\delta \rightarrow \pi$. In the first case sufficient CP asymmetry can be created at leading order in A_N without using thermal phase space factors. On the other hand, we get a resonance behaviour in ε at $A_\lambda \sim \kappa v_S$ in the second case. The latter case is perhaps more acceptable since both the soft SUSY breaking parameters A_N and A_λ could be of the same order (Fig. 114.2).

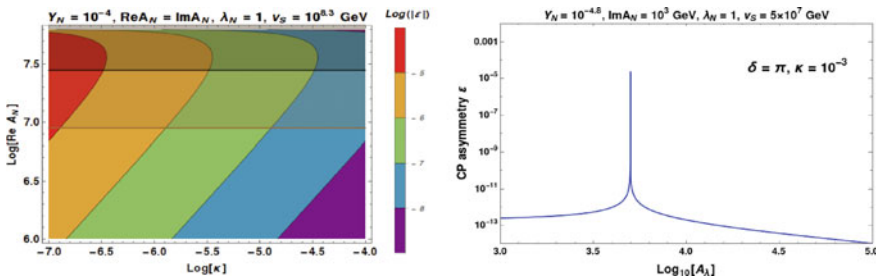


Fig. 114.2 [Left]: Different contours of ε in $\text{Re} A_N - \kappa$ plane have been shown considering A_N complex. The black line indicates the out-of-equilibrium bound, while the horizontal brown solid line marks the leading order approximation in the soft-term A_N ($A_N^2/M_1^2 \simeq 10^{-3}$). [Right]: Variation of ε versus A_λ in the $\delta = \pi$ limit. The resonance in ε occurs when $A_\lambda = \kappa v_S$

114.4 Conclusion

To conclude, we examined the scope of realizing soft leptogenesis in a version of the NMSSM extended by a singlet RH neutrino superfield and found few distinct features compared to the one in MSSM with a RH neutrino superfield. In the present framework where the singlet scalar S takes a complex vev, an asymmetry can be generated even without considering any thermal phase space/mass corrections to the decay products. Both resonant and non-resonant productions of lepton asymmetry can be obtained for different ranges of parameters without using any other complex parameter.

References

1. Y. Grossman, T. Kashti, Y. Nir, E. Roulet, *Phys. Rev. Lett.* **91**, 251801 (2003)
2. G. D'Ambrosio, G.F. Giudice, M. Raidal, *Phys. Lett. B* **575**, 75–84 (2003)
3. W. Abdallah, A. Kumar, A.K. Saha, *JHEP* **04**, 065 (2020)

Chapter 115

Probing Ultra-Light Primordial Black Holes as a Dark Matter Candidate



Anupam Ray

Abstract Dark matter (DM) is omnipresent in our universe. Despite its abundance, the microscopic identity of DM still remains a mystery. Primordial black holes (PBHs), possibly formed via the gravitational collapse of large density perturbations in the early universe, are one of the earliest proposed and viable DM candidates. Recent studies indicate that PBHs can make up a large or even an entire fraction of the DM density for a wide range of masses. Here, we briefly review the observational constraints on PBHs as DM, concentrating on the ultra-light mass window. Ultra-light PBHs emit particles via Hawking radiation and can be probed by observing such Hawking evaporated particles in various spaces as well as ground-based detectors. We also outline how next-generation gamma-ray telescopes can set a stringent exclusion limit on ultra-light PBH DM by probing low-energy photons.

115.1 Introduction

Cosmological observations provide unambiguous evidence of a non-relativistic, collision-less, and weakly interacting non-baryonic matter, commonly known as dark matter (DM), as a dominant component of the universe [1]. Many well-motivated DM candidates have been proposed, and decades of experimental searches have been conducted to hunt for these mysterious DM particles, yet the microscopic identity remains unknown. Primordial black holes (PBHs), possibly formed via the gravitational collapse of large overdensities in the very early universe, are one of the earliest proposed and viable DM candidates [2–4].

PBHs have a wide range of masses depending on their time of formation and can constitute a large or even entire fraction of the present-day DM density in the mass range of $\sim 10^{17}$ – 10^{23} g. The idea of PBHs as DM has recently received a renewed attention with the detection of a BH merger by the LIGO-Virgo collaboration and the subsequent proposals that the BH merger can be primordial in origin [5–7]. Several

A. Ray (✉)

Tata Institute of Fundamental Research, Homi Bhabha Road, Mumbai 400005, India
e-mail: anupam.ray@theory.tifr.res.in

© The Author(s), under exclusive license to Springer Nature Singapore Pte Ltd. 2022
B. Mohanty et al. (eds.), *Proceedings of the XXIV DAE-BRNS High Energy Physics Symposium, Jatni, India*, Springer Proceedings in Physics 277,
https://doi.org/10.1007/978-981-19-2354-8_115

635

techniques have been implemented in order to probe the PBH fraction of DM, and yield a multitude of observational constraints [8–10]. Here, we briefly review the current status of PBHs as DM, mostly concentrating on the ultra-light mass window.

115.2 Ultra-Light PBHs as Dark Matter

PBHs evaporate via Hawking radiation and the evaporation timescale is proportional to the cube of their masses. The lifetime of non-rotating (maximally rotating) PBHs lighter than 5×10^{14} g (7×10^{14} g) is less than the age of our universe; hence, they cannot contribute to the present-day DM density, setting the lower mass limit of ultra-light PBHs as DM [11, 12]. Heavier PBHs, i.e. PBHs with masses between 5×10^{14} g and 2×10^{17} g are typically probed via searching their evaporation products. Non-observation of such Hawking-evaporated neutrinos [13], photons [14–18], and electrons/positrons [13, 19–21] provides the leading exclusions on the PBH fraction of dark matter. Figure 115.1 provides a consolidated view of the existing constraints for the ultra-light evaporating PBHs in the mass range of 10^{15} – 10^{17} g.

Neutrino-derived exclusions: Reference [13] shows that non-observation of $O(10)$ MeV neutrinos in the diffuse supernovae neutrino background (DSNB) searches by

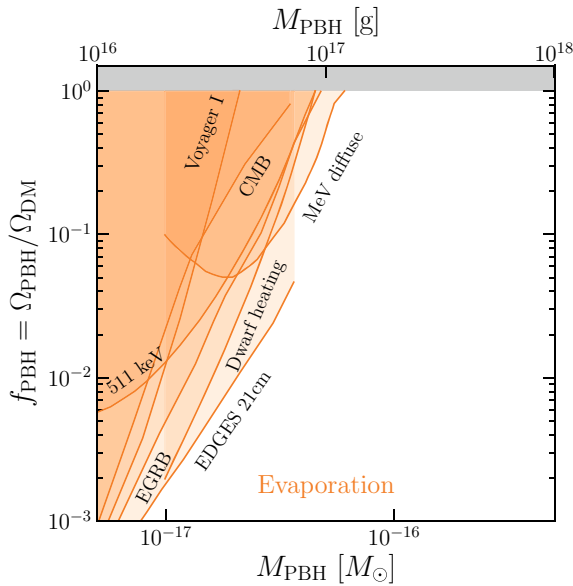


Fig. 115.1 Consolidated upper limit on the fraction of DM composed of ultra-light evaporating PBHs, f_{PBH} , from non-observations of Hawking-radiated particles in various space as well as ground-based detectors. Non-rotating PBHs with a monochromatic mass distribution are considered for this plot, and the figure is adapted from [10]

an underground neutrino observatory Super-Kamiokande sets stringent constraints on ultra-light PBHs as DM. For a monochromatic mass distribution, it excludes non-rotating (maximally rotating) PBHs to form the sole component of DM up to 5×10^{15} g (10^{16} g), and for an extended mass distribution (e.g., log-normal mass distribution with a width of $\sigma = 1.0$), it even excludes up to $\sim 10^{17}$ g.

Photon-derived exclusions: Observations of extra-Galactic gamma-ray background (EGRB) via several space-based telescopes such as COMPTEL, FERMI LAT, SMM exclude monochromatic, non-rotating PBHs to form the sole component of DM up to $\sim 10^{17}$ g [14]. The exclusion limits cover more mass window for rotating PBHs, and allowing maximum rotation can extend the constraints up to 6×10^{17} g for a monochromatic mass distribution [15]. Reference [16] shows that astrophysical modeling of the EGRB sources can significantly improve the photon-derived exclusions. Galactic Center gamma-ray measurements by the space-based telescope INTEGRAL also provide stringent constraints on the PBH fraction of DM [17]. For monochromatic mass distribution, it excludes non-rotating PBHs to form a solitary component of DM up to $\sim 2 \times 10^{17}$ g, and for maximally rotating PBHs, it excludes up to 10^{18} g. Reference [18] obtains a similar result by using the Galactic Center gamma-ray measurements by COMPTEL.

Electron/positron-derived exclusions: Measurement of the e^\pm flux by the spacecraft Voyager 1 significantly constrains the fraction of DM composed of ultra-light PBHs [19]. References [20, 21] show that measurement of the 511 keV gamma-ray line also provide stringent exclusions on ultra-light PBHs as DM. It excludes non-rotating, monochromatic PBHs to form the sole component of DM up to $\sim 10^{17}$ g. However, the positron-derived constraints crucially depend on various astrophysical uncertainties, such as unknown positron propagation distance as well as the choice of DM density profiles, and can vary by almost an order of magnitude due to these uncertainties. Reference [13] extends the positron-derived analysis for PBHs that have rotation, and shows that allowing maximal rotation along with extended mass distributions of the PBHs makes the constraints more stringent, and can even extend them up to $\sim 10^{19}$ g.

Photon-derived projected exclusions: Non-rotating, monochromatic PBHs in the mass range of $\sim 10^{17}$ – 10^{23} g can make up the entirety of the present-day DM density as the existing exclusion limits from Hawking evaporation cease at $\sim 10^{17}$ g, and the existing exclusion limits from optical microlensings start from $\sim 10^{23}$ g. Reference [22] shows that measurement of the low-energy (\sim MeV) photons from the Galactic Center with the imminent telescopes such as AMEGO can probe this entirely unexplored mass window. AMEGO can exclude non-rotating (maximally rotating) monochromatic PBHs as a sole component of DM up to 7×10^{17} g (4×10^{18} g) by assuming no signal is present in the data. Reference [18] also obtains similar results by using a future telescope GECCO.

Summary: Non-rotating monochromatic PBHs with masses $\leq 10^{17}$ g cannot form the solitary component of DM because of the non-observations of Hawking evaporated particles in various spaces as well as ground-based detectors. For PBHs that have

rotation, or which follow extended mass distributions, these exclusion limits probe more mass windows. However, non-rotating monochromatic PBHs in the mass range of $\sim 10^{17}$ – 10^{23} g can form the entirety of the present-day DM density as the exclusion limits in that mass window are invalidated by several recent studies. Measurements of the low-energy photons from the Galactic Center by upcoming soft gamma-ray telescopes such as AMEGO can close this mass window by almost an order of magnitude.

References

1. N. Aghanim et al., Planck. *Astron. Astrophys.* **641**, A6 (2020)
2. Y.B. Zel'dovich, I.D. Novikov, *Astronomicheskii Zhurnal* **43**, 758 (1966)
3. S. Hawking, *Mon. Not. Roy. Astron. Soc.* **152**, 75 (1971)
4. G.F. Chapline, *Nature* **253**(5489), 251–252 (1975)
5. S. Bird et al., *Phys. Rev. Lett.* **116**(20), 201301 (2016)
6. S. Clesse, J. García-Bellido, *Phys. Dark Univ.* **15**, 142–147 (2017)
7. M. Sasaki, T. Suyama, T. Tanaka, S. Yokoyama, *Phys. Rev. Lett.* **117**(6), 061101 (2016)
8. B. Carr, K. Kohri, Y. Sendouda, J. Yokoyama, [arXiv:2002.12778](https://arxiv.org/abs/2002.12778) [astro-ph.CO]
9. B. Carr, F. Kuhnel, *Ann. Rev. Nucl. Part. Sci.* **70**, 355–394 (2020)
10. A.M. Green, B.J. Kavanagh, [arXiv:2007.10722](https://arxiv.org/abs/2007.10722) [astro-ph.CO]
11. D.N. Page, *Phys. Rev. D* **13**, 198–206 (1976)
12. D.N. Page, *Phys. Rev. D* **14**, 3260–3273 (1976). <https://doi.org/10.1103/PhysRevD.14.3260>
13. B. Dasgupta, R. Laha, A. Ray, *Phys. Rev. Lett.* **125**(10), 101101 (2020)
14. B.J. Carr, K. Kohri, Y. Sendouda, J. Yokoyama, *Phys. Rev. D* **81**, 104019 (2010)
15. A. Arbey, J. Auffinger, J. Silk, *Phys. Rev. D* **101**(2), 023010 (2020)
16. G. Ballesteros, J. Coronado-Blázquez, D. Gaggero, *Phys. Lett. B* **808**, 135624 (2020)
17. R. Laha, J.B. Muñoz, T.R. Slatyer, *Phys. Rev. D* **101**(12), 123514 (2020)
18. A. Coogan, L. Morrison, S. Profumo, [arXiv:2010.04797](https://arxiv.org/abs/2010.04797) [astro-ph.CO]
19. M. Boudaud, M. Cirelli, *Phys. Rev. Lett.* **122**(4), 041104 (2019)
20. W. DeRocco, P.W. Graham, *Phys. Rev. Lett.* **123**(25), 251102 (2019)
21. R. Laha, *Phys. Rev. Lett.* **123**(25), 251101 (2019)
22. A. Ray, R. Laha, J.B. Muñoz, R. Caputo, [arXiv:2102.06714](https://arxiv.org/abs/2102.06714) [astro-ph.CO]

Chapter 116

Helical Magnetic Fields From Riemann Coupling



Ashu Kushwaha and S. Shankaranarayanan

Abstract This talk shows that non-minimal coupling to the Riemann tensor generates sufficient primordial helical magnetic fields at all observable scales. The model has three key features: (i) the helical power spectrum has a slight red tilt for slow-roll inflation consistent with bounds from observations and free from back-reaction problem, (ii) the energy density of the helical fields generated is at least one order of magnitude larger than the scalar-field-coupled models, and (iii) unlike the scalar-field-coupled models, the generated helical fields are insensitive to the reheating dynamics. We show that the model generates the magnetic field of strength 0.01 Pico-Gauss over Mpc scale.

116.1 Introduction

Magnetic fields are observed at all scales in the universe; however, there is no compelling model to explain the origin of large-scale magnetic fields. Observations from Faraday rotation and synchrotron radiation show the presence of micro-Gauss strength magnetic fields in the galaxies and the clusters of galaxies [2–4]. While the magnetic field measurements from Faraday rotation and synchrotron radiation provide upper bounds of the magnetic fields, the FERMI measurement of gamma-rays emitted by blazars provides a lower bound of the order of 10^{-15} G in intergalactic voids [5]. However, we do not know from any of these observations whether these magnetic fields are helical or non-helical.

Electromagnetic field has two transverse degrees of freedom, i.e., left and right circular polarisation, which can be associated with the left and right-handed helicity modes. Furthermore, modes having the same evolution (or dispersion relation) lead to non-helical electromagnetic field whereas differently propagating modes with

A. Kushwaha (✉) · S. Shankaranarayanan
Department of Physics, Indian Institute of Technology Bombay, Mumbai 400076, India
e-mail: ashu712@iitb.ac.in

S. Shankaranarayanan
e-mail: shanki@iitb.ac.in

© The Author(s), under exclusive license to Springer Nature Singapore Pte Ltd. 2022
B. Mohanty et al. (eds.), *Proceedings of the XXIV DAE-BRNS High Energy Physics Symposium, Jatni, India*, Springer Proceedings in Physics 277,
https://doi.org/10.1007/978-981-19-2354-8_116

non-zero net helicity imbalance give helical magnetic field. In order to create this helicity imbalance we consider the following scenario: under parity transformation electric and magnetic fields transform as $\mathbf{E} \rightarrow -\mathbf{E}$, $\mathbf{B} \rightarrow \mathbf{B}$, since standard electromagnetic action, $F_{\mu\nu}F^{\mu\nu} = (B^2 - E^2)/2$ is parity invariant, but the Chern-Simon term $F_{\mu\nu}\tilde{F}^{\mu\nu} = -4\mathbf{E} \cdot \mathbf{B}$ is parity non-invariant. Therefore, introducing this term in the action will lead to the different evolution of the modes. There is an interesting quantity related to the $F_{\mu\nu}\tilde{F}^{\mu\nu}$ called magnetic helicity density, which in a given volume is proportional to the difference between the number of left and right-handed photons, and is given by: $\mathcal{H}_M = \frac{1}{V} \int_V d^3x \mathbf{A} \cdot \mathbf{B}$, where \mathbf{A} is electromagnetic vector potential. Helical magnetic fields are very interesting for the following reasons: (1) the decay rate to energy density and coherence length is slow for these fields, which differs from the non-helical, (2) helical magnetic fields leave a very distinct signature as they violate parity symmetry which leads to observable effects, for example, correlations between the anisotropies in the temperature and B-polarisation or the E- and the B-polarisations in the CMB, and (3) if we could measure helical magnetic fields, it would provide evidence of CP violation in the early universe [4].

There are two kinds of magnetogenesis models, i.e., early time and late time model; both of them have problems. Inflation provides a causal mechanism to generate the magnetic fields of large coherence length. The problem with magnetic field generation during inflation is that standard electromagnetic action is conformally flat. Hence, the inflationary mechanism cannot amplify quantum fluctuations of electromagnetic fields. Therefore one needs to break the conformal symmetry of the action. In the literature, models breaking conformal invariance by introducing non-minimal coupling terms in the electromagnetic action are proposed [6] or by the time-dependent coupling with the gauge field [3, 4]. These models produce non-helical magnetic fields. Generation of helical magnetic fields during the early universe requires a parity-violating source.

A more popular scenario of helical field generation is by adding the interaction term $f(\phi)F_{\mu\nu}\tilde{F}^{\mu\nu}$ which is responsible for creating the imbalance between left-handed and right-handed photons [7, 8]. These scalar-field-coupled models suffer from strong coupling and back-reaction problems and sensitivity to the reheating dynamics. In this talk, we discuss our model [1] where the electromagnetic field is coupled to the Riemann curvature.

116.2 Helical Magnetic Field Generation

We consider the following action:

$$S = -\frac{M_{\text{Pl}}^2}{2} \int d^4x \sqrt{-g} R + \int d^4x \sqrt{-g} \left[\frac{1}{2} \partial_\mu \phi \partial^\mu \phi - V(\phi) \right] - \frac{1}{4} \int d^4x \sqrt{-g} F_{\mu\nu} F^{\mu\nu} - \frac{\sigma}{M^2} \int d^4x \sqrt{-g} R_{\rho\sigma}{}^{\alpha\beta} F_{\alpha\beta} \tilde{F}^{\rho\sigma} \quad (116.1)$$

where $R_{\rho\sigma}{}^{\alpha\beta}$ is the Riemann tensor, A_μ is the four-vector potential of the electromagnetic field, $F_{\mu\nu} = \nabla_\mu A_\nu - \nabla_\nu A_\mu$ and $\tilde{F}^{\rho\sigma} = \frac{1}{2}\epsilon^{\mu\nu\rho\sigma}F_{\mu\nu}$ is the dual of $F_{\mu\nu}$. $\epsilon^{\mu\nu\rho\sigma} = \frac{1}{\sqrt{-g}}\eta^{\mu\nu\rho\sigma}$ is fully antisymmetric tensor, $\eta^{\mu\nu\rho\sigma}$ is Levi-Civita symbol whose values are ± 1 and we set $\eta^{0123} = 1 = -\eta_{0123}$.

Note that in (116.1), the first three terms are the standard terms (the Einstein-Hilbert action, scalar field action, and standard electrodynamics, respectively). However, the last term breaks the conformal (and parity) invariance of the action due to the presence of Riemann tensor. We assume that the scalar field (ϕ) dominates the energy density in the early universe (during inflation) and leads to 60 – 70 e-foldings of inflation with $H \simeq 10^{14}\text{GeV}$. M is the energy scale, which sets the scale for the breaking of conformal invariance. We assume that $10^{-3} \leq (H_{\text{inf}}/M) \leq 1$ where $H_{\text{inf}} \sim 10^{14}\text{GeV}$ is the Hubble scale during inflation. It is important to note that due to Riemann coupling, M appears as a time-dependent coupling in the FRW background, i.e., $\frac{1}{M_{\text{eff}}} \sim \frac{1}{M} \frac{a'}{a^2} = \frac{\dot{H}}{M}$. Using $H_0 \approx 10^{-44}\text{GeV}$ and $M \approx 10^{17}\text{GeV}$, we can see that at current epoch $\frac{H_0}{M} \sim 10^{-61}$. Therefore, the Riemann coupling is tiny, and the non-minimal coupling term in the electromagnetic action will have a significant contribution only in the early universe. Our model has the following salient features: First, our model does not require the coupling of the electromagnetic field with the scalar field. Hence, there are no extra degrees of freedom, which will not lead to a strong-coupling problem. Second, the conformal invariance is broken due to the coupling to the Riemann tensor. Since the curvature is significant in the early universe, the coupling term will introduce non-trivial corrections to the electromagnetic action. As mentioned above, the Riemann coupling term will not contribute at late times, and the model is identical to standard electrodynamics. Third, as we show explicitly, our model is free from back-reaction for a range of scale factor during inflation. This is different from other models where a specific form of coupling function is chosen to avoid any back-reaction [7, 8].

116.2.1 Estimating the Strength of the Helical Magnetic Fields

We estimate the total electromagnetic energy density at the horizon exit and to identify whether the modes lead to back-reaction on the metric, we define the quantity, $R = \frac{(\rho_B + \rho_E)|_{\mathcal{H} \sim k_*}}{6H^2 M_{\text{pl}}^2}$, which is the ratio of the total energy density of the fluctuations at horizon exit and background energy density during inflation (Table 116.1).

Since $R \ll 1$ for any $\alpha \leq -\frac{1}{2}$ ($\alpha = -1/2$ corresponds to de-Sitter universe), the model does not have back-reaction.

To estimate the current value of the helical fields, we assume instantaneous reheating, and the fact that universe becomes radiation-dominated after inflation. Due to flux conservation, the magnetic energy density will decay as $1/a^4$, i.e., $\rho_B(0) = \rho_B^{(f)} \left(\frac{a_f}{a_0}\right)^4$, where a_0 is the present-day scale factor, $\rho_B^{(f)}$ and a_f refer to

Table 116.1 The total electromagnetic energy density at the exit of inflation for different values of α , where $\alpha = -1/2 - \epsilon$ is for slow roll inflation and $\rho_{\text{total}} = (\rho_B + \rho_E)|_{\mathcal{H} \sim k_*}$. We have taken $\mathcal{H} \sim \eta_0^{-1} \sim 10^{14}$ GeV, and $M \sim 10^{17}$ GeV

α	ρ_{total} (in GeV^4)	R
$-\frac{1}{2} - \epsilon$	$\sim 10^{64}$	$\sim 10^{-4}$
$-\frac{3}{4}$	$\sim 10^{62}$	$\sim 10^{-6}$
-1	$\sim 10^{61}$	$\sim 10^{-7}$
-3	$\sim 10^{59}$	$\sim 10^{-9}$

the magnetic energy density and the scale factor at the end of inflation, respectively. Using the fact that the relevant modes exited Hubble radius around 30 e-foldings of inflation, with energy density $\rho_B \approx 10^{64} \text{GeV}^4$, the primordial helical fields at Gpc scales is $B_0 \approx 10^{-20} \text{G}$, where we have used $1 \text{G} = 1.95 \times 10^{-20} \text{GeV}^2$. Our model predicts the following primordial helical fields that re-entered the horizon at two different epochs: $B|_{50 \text{ Mpc}} \sim 10^{-18} \text{G}$ ($z \sim 20$) and $B|_1 \text{ Mpc} \sim 10^{-14} \text{G}$ ($z \sim 1000$). Thus, the model generates sufficient primordial helical magnetic fields at all observable scales.

116.3 Conclusion

We have proposed a viable scenario for the generation of helical magnetic fields during inflation. The model does not require coupling to the scalar field and hence does not lead to a strong coupling problem. The power spectrum of the helical fields generated has a slight red tilt (more power on a large scale) for slow-roll inflation, which is different from the scalar-field-coupled models where the power spectrum has a blue tilt, and there is no back-reaction on the metric. The generation of the helical fields is due to the coupling of the electromagnetic fields with the Riemann tensor. Interestingly, our model generates the magnetic field of strength 10^{-18}G and 10^{-14}G over scales $\sim 50 \text{Mpc}$ and $\sim 1 \text{Mpc}$, respectively. Since the model breaks the parity symmetry, it would be interesting to see the effects of the helical modes on the baryon asymmetry during the early universe.

References

1. A. Kushwaha, S. Shankaranarayanan, Helical magnetic fields from riemann coupling. Phys. Rev. D **102**, 103528 (2020)
2. Dario Grasso, Hector R. Rubinstein, Magnetic fields in the early universe. Phys. Rept. **348**, 163–266 (2001)
3. Kandaswamy Subramanian, The origin, evolution and signatures of primordial magnetic fields. Rept. Prog. Phys. **79**(7), 076901 (2016)

4. Ruth Durrer, Andrii Neronov, Cosmological magnetic fields: their generation, evolution and observation. *Astron. Astrophys. Rev.* **21**, 62 (2013)
5. Andrii Neronov, Ievgen Vovk, Evidence for strong extragalactic magnetic fields from fermi observations of tev blazars. *Science* **328**(5974), 73–75 (2010)
6. Michael S. Turner, Lawrence M. Widrow, Inflation produced, large scale magnetic fields. *Phys. Rev. D* **37**, 2743 (1988)
7. R. Durrer, L. Hollenstein, R.K. Jain, Can slow roll inflation induce relevant helical magnetic fields? *JCAP* **1103**, 037 (2011)
8. R. Sharma, K. Subramanian, T.R. Seshadri, Generation of helical magnetic field in a viable scenario of inflationary magnetogenesis. *Phy. Rev. D* **D97**(8), 083503 (2018)

Chapter 117

Low-Scale Leptogenesis From Three-Body Decay



Devabrat Mahanta, Debasish Borah, and Arnab Dasgupta

Abstract We study the possibility of leptogenesis at tree level from a three-body decay along with dark matter and neutrino mass. We propose a first-of-its-kind model where we can have successful leptogenesis from the interference of multiple $1 \rightarrow 3$ diagrams. We show that successful leptogenesis can occur at a scale as low as approximately 500 GeV. Also it can have rich dark matter (DM) phenomenology.

117.1 Introduction

The observed asymmetry between matter and antimatter in the universe, often quantified by $\eta_B = (n_B - n_{\bar{B}})/n_\gamma = 6.1 \times 10^{-10}$ [1, 2], has been a longstanding problem in particle physics and cosmology. Even though the standard model (SM) of particle physics can generate such an asymmetry with an expanding universe, the asymmetry produced within the SM falls way short of the observed asymmetry. Among different beyond the standard model (BSM) proposals, leptogenesis [4] is one of the very interesting ways to generate the observed baryon asymmetry, where a $B - L$ asymmetry is generated by the out of equilibrium, L and CP-violating decays of some heavy fermion which can later be converted into a baryon asymmetry by the electro-weak (EW) sphaleron transitions. Motivated by the baryon asymmetry problem, the existence of non-luminous dark matter and neutrino mass which the SM fails to explain, we consider a minimal extension of the SM which can solve all these puzzles in a unified manner.

D. Mahanta (✉) · D. Borah
Indian Institute of Technology Guwahati, Assam 781039, India
e-mail: devab176121007@iitg.ac.in

A. Dasgupta
Institute of Convergence Fundamental Studies, Seoul-Tech, Seoul 139-743, South Korea

© The Author(s), under exclusive license to Springer Nature Singapore Pte Ltd. 2022
B. Mohanty et al. (eds.), *Proceedings of the XXIV DAE-BRNS High Energy Physics Symposium, Jaitani, India*, Springer Proceedings in Physics 277,
https://doi.org/10.1007/978-981-19-2354-8_117

117.2 The Model

We propose three singlet chiral fermions $N_{1,2}$, ψ and two scalar fields η and S which transform non-trivially under an additional $Z_2 \times Z'_2$ symmetry, as shown in Table 117.1. All the SM fields are even under both the Z_2 symmetries. The relevant Yukawa Lagrangian can be written as

$$\mathcal{L} = -h_{i\alpha} (\bar{l}_L)_i \tilde{\eta} N_\alpha - \frac{1}{2} M_\alpha \bar{N}_\alpha^c N_\alpha - y_\alpha \psi N_\alpha S - \frac{1}{2} m_\psi \bar{\psi}^c \psi. \tag{117.1}$$

117.3 Leptogenesis and Dark Matter

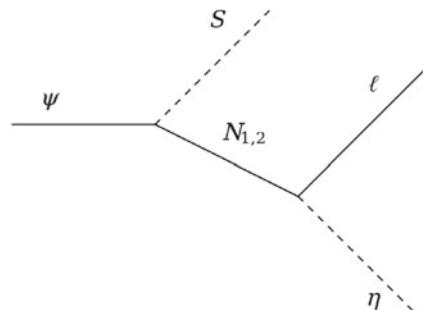
The possibility of generating a CP asymmetry in $2 - 2$ scattering and $1 \rightarrow N$ decay has been studied in detail in [5]. In our model the CP asymmetry arises from interference of the multiple tree diagrams of the three-body decay shown in Fig. 117.1. To prevent the two-body decay of ψ , we restrict our model to the condition $m_\psi < M_{1,2} + m_S$. In addition to this $1 \rightarrow 3$ decay we have the usual $1 \rightarrow 2$ decay of N_1 which can also generate a CP asymmetry. We numerically calculated the new CP asymmetry parameter defined by $\epsilon_\psi = (\Gamma_{\psi \rightarrow Sl\eta} - \Gamma_{\psi \rightarrow S^* \bar{l}\eta^*}) / (\Gamma_{\psi \rightarrow Sl\eta} + \Gamma_{\psi \rightarrow S^* \bar{l}\eta^*})$, the details of which can be found in [6].

It is found that we must have two different propagators for the same $1 \rightarrow 3$ process and at least one of the four couplings should contain some phase to have

Table 117.1 BSM particle content of the model

Particles	$SU(3)_c \times SU(2)_L \times U(1)_Y$	Z_2	Z'_2
$N_{1,2}$	(1, 1, 0)	-1	1
ψ	(1, 1, 0)	-1	-1
η	(1, 2, $\frac{1}{2}$)	-1	1
S	(1,1,0)	1	-1

Fig. 117.1 Three-body decay of singlet fermion ψ



a non-zero CP asymmetry. Apart from the inverse decays of ψ and N_1 , we have few scattering processes which can washout the generated asymmetry. Taking every process into account we write the Boltzmann equations as follows:

$$\begin{aligned} \frac{dn_\psi}{dz} = & -D_\psi(n_\psi - n_\psi^{\text{eq}}) + D_{N_1 \rightarrow \psi S}(n_{N_1} - n_{N_1}^{\text{eq}}) - W_{ID_{N_1 \rightarrow \psi S}} n_\psi \\ & - \frac{s}{H(z)z} [(n_\psi n_\eta - n_\psi^{\text{eq}} n_\eta^{\text{eq}}) \langle \sigma v \rangle_{\psi \eta \rightarrow SI} + [n_\psi n_S - n_\psi^{\text{eq}} n_S^{\text{eq}}] \langle \sigma v \rangle_{\psi S \rightarrow I\eta}], \end{aligned} \quad (117.2)$$

$$\begin{aligned} \frac{dn_{N_1}}{dz} = & -D_{N_1}(n_{N_1} - n_{N_1}^{\text{eq}}) - D_{N_1 \rightarrow \psi S}(n_{N_1} - n_{N_1}^{\text{eq}}) - \frac{s}{H(z)z} [(n_{N_1}^2 - (n_{N_1}^{\text{eq}})^2) \\ & \langle \sigma v \rangle_{N_1 N_1 \rightarrow II} + [n_{N_1} n_{SM} - n_{N_1}^{\text{eq}} n_{SM}^{\text{eq}}] \langle \sigma v \rangle_{\eta l \rightarrow N_1(W^\pm, Z)}], \end{aligned} \quad (117.3)$$

$$\begin{aligned} \frac{dn_{B-L}}{dz} = & -\epsilon_\psi D_\psi(n_\psi - n_\psi^{\text{eq}}) - \epsilon_{N_1} D_{N_1}(n_{N_1} - n_{N_1}^{\text{eq}}) - (W_{N_1} + W_\psi) n_{B-L} \\ & - \frac{s}{H(z)z} [\Gamma_{SI \rightarrow \psi \eta} + \Gamma_{I\eta \rightarrow \psi S} + \Gamma_{II \rightarrow \eta \eta} + \Gamma_{II \rightarrow N_1 N_1} + \Gamma_{I\eta \rightarrow (N_1 W^\pm, Z)} \\ & + \Gamma_{\eta l \rightarrow \eta^* \bar{l}}] n_{B-L}. \end{aligned} \quad (117.4)$$

In our model S and η both are suitable DM candidates because of the unbroken $Z_2 \times Z_2'$ symmetry. In order to cover all the features of annihilations, coannihilations as well as conversions, we use micrOMEGAs to calculate the relic abundance of two-component DM.

117.4 Results and Conclusions

All the processes relevant for leptogenesis depend explicitly on the Yukawas y_i and implicitly on λ_5 through the Yukawas $h_{i\alpha}$ [7]. From Fig. 117.2 one can see that the n_{B-L} increases with the decrease in λ_5 . This is because, with the decrease in λ_5 the Yukawa coupling $h_{i\alpha}$ increases which result in a increase in the asymmetry parameter.

It is important to take note that in Fig. 117.2, the $(n_{B-L})_\psi$ corresponds to the $B - L$ asymmetry generated from the ψ decay while decay while $(n_{B-L})_{N_1}$ corresponds to the $B - L$ asymmetry generated from the usual N_1 decay. We found that the $B - L$ asymmetry generated from the usual N_1 decay is insignificant compared to that generated from the three-body decay of ψ . After analysing the role of certain parameters we performed a numerical scan over the important parameters and showed that successful leptogenesis can occur at a scale as low as 3 TeV for unflavoured case and at scale 2 TeV for flavoured case. After finding the parameter space that can give TeV scale leptogenesis, we calculate the relic abundance of two DM components and

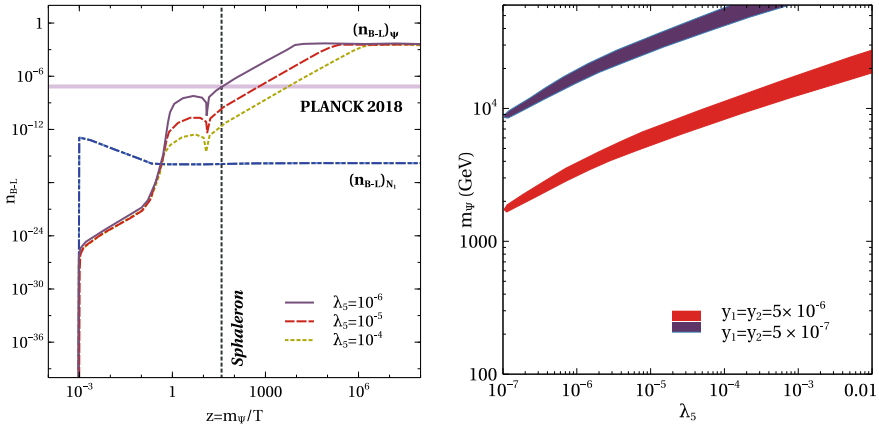


Fig. 117.2 Evolution plot of n_{B-L} (left panel) and the region of parameter space satisfying the observed asymmetry in m_{ψ} - λ_5 plane (right panel). The other parameters are set at the following benchmark values: $M_1 = 5 \times 10^6$ GeV, $M_2 = 10^7$ GeV, $m_{\eta} = 10$ GeV, $m_S = 500$ GeV

showed that the relic abundance can be satisfied within the same parameter space. Such a low-scale model with two-component DM, successful leptogenesis and light neutrino masses should face further scrutiny with future data from collider, neutrino, cosmology as well as rare decay experiments looking for charged lepton flavour violation, neutrinoless double beta decay, etc.

References

1. Particle Data Group Collaboration, M. Tanabashi et al., Review of Particle Physics. Phys. Rev. D **98**(3), 030001 (2018)
2. Planck Collaboration, N. Aghanim et al., Planck 2018 results. VI. Cosmological parameters. [arXiv:1807.06209](https://arxiv.org/abs/1807.06209)
3. Sakharov A.D.: Violation of CP Invariance, C asymmetry, and baryon asymmetry of the universe. Pisma Zh. Eksp. Teor. Fiz. **5**, 32–35 (1967). [Usp. Fiz. Nauk 161, no.5,61(1991)]
4. M. Fukugita, T. Yanagida, Baryogenesis without grand unification. Phys. Lett. B **174**, 45–47 (1986)
5. A. Dasgupta, P. Bhupal Dev, S.K. Kang, Y. Zhang, New mechanism for matter-antimatter asymmetry and connection with dark matter. Phys Rev D **102**(5), 055009 (2020). [arXiv:1911.03013](https://arxiv.org/abs/1911.03013)
6. D. Borah, A. Dasgupta, D. Mahanta, Dark sector assisted low scale leptogenesis from three body decay without loops. [arXiv:2008.10627](https://arxiv.org/abs/2008.10627)
7. T. Hogle, M. Platscher, K. Schmitz, Low-scale leptogenesis in the scotogenic neutrino mass model. Phys. Rev. D **98**(2), 023020 (2018). [arXiv:1804.09660](https://arxiv.org/abs/1804.09660)
8. Masiero, A., Riotto A.: Cosmic Delta B from lepton violating interactions at the electroweak phase transition. Phys. Lett. B **289** 73–80 (1992). [hep-ph/9206212]

Chapter 118

Latest Results of Cosmic Ray Energy Spectrum and Composition Measurements From GRAPES-3 Experiment



F. Varsi, S. Ahmad, M. Chakraborty, A. Chandra, S. R. Dugad, S. K. Gupta, B. Hariharan, Y. Hayashi, P. Jagadeesan, A. Jain, P. Jain, V. B. Jhansi, S. Kawakami, H. Kojima, S. Mahapatra, P. K. Mohanty, R. Moharana, S. D. Morris, Y. Muraki, P. K. Nayak, A. Oshima, B. Pant, D. Pattanaik, G. Pradhan, P. S. Rakshe, K. Ramesh, B. S. Rao, L. V. Reddy, R. Sahoo, R. Scaria, S. Shibata, K. Tanaka, and M. Zuberi

Abstract The open questions in cosmic ray physics like their astrophysical origin, acceleration, and propagation in the interstellar medium can be understood by precise measurements of the nuclear composition, and energy spectrum of the primary cosmic rays at the 'knee' and the region beyond it. The GRAPES-3 experiment located at Ooty in India is designed with a densely packed array of 400 plastic scintillator detectors and a large area muon detector. It measures cosmic rays from several TeV to over 10 PeV that provide a substantial overlap with direct experiments as well

F. Varsi (✉) · S. Ahmad · M. Chakraborty · A. Chandra · S. R. Dugad · S. K. Gupta · B. Hariharan · Y. Hayashi · P. Jagadeesan · A. Jain · P. Jain · V. B. Jhansi · S. Kawakami · H. Kojima · S. Mahapatra · P. K. Mohanty · R. Moharana · S. D. Morris · Y. Muraki · P. K. Nayak · A. Oshima · B. Pant · D. Pattanaik · G. Pradhan · P. S. Rakshe · K. Ramesh · B. S. Rao · L. V. Reddy · R. Sahoo · R. Scaria · S. Shibata · K. Tanaka · M. Zuberi
The GRAPES-3 Experiment, Cosmic Ray Laboratory, Raj Bhavan, Ooty 643001, India
e-mail: fahim@iitk.ac.in

M. Chakraborty · S. R. Dugad · S. K. Gupta · B. Hariharan · P. Jagadeesan · A. Jain · V. B. Jhansi · P. K. Mohanty · R. Moharana · S. D. Morris · P. K. Nayak · D. Pattanaik · P. S. Rakshe · K. Ramesh · B. S. Rao · L. V. Reddy · M. Zuberi
Tata Institute of Fundamental Research, Homi Bhabha Road, Mumbai 400005, India

S. Ahmad · A. Chandra
Aligarh Muslim University, Aligarh 202002, India

Y. Hayashi · S. Kawakami
Graduate School of Science, Osaka City University, Osaka 558-8585, Japan

F. Varsi · P. Jain
Indian Institute of Technology Kanpur, Kanpur 208016, India

H. Kojima · A. Oshima · S. Shibata
College of Engineering, Chubu University, Kasugai, Aichi 487-8501, Japan

as covers the knee region. The muon multiplicity distribution measured by the large area tracking muon detector associated with the array provides precise measurement of the average nuclear composition of primary cosmic rays. Recently, we have attempted to measure the energy spectrum and composition from sub-TeV to over 10 PeV. The details of this study will be discussed.

118.1 The GRAPES-3 Experiment

The **Gamma Rays Astronomy at PeV EnergieS** phase-3 (GRAPES-3) experiment is located at Ooty, South India (11.4° N, 76.7° E and 2200 m a.s.l.). It consists of an array of 400 plastic scintillator detectors (1 m² area each) [1, 2] and a large area (560 m²) muon telescope [3]. The scintillator detectors are arranged in hexagonal geometry with an inter-detector separation of 8 m, to ensure a uniform selection of the extensive air shower (EAS) over the array. Being a highly dense EAS array, the GRAPES-3 experiment is capable of measuring primary cosmic rays (PCRs) from several TeV to over 10 PeV, providing a substantial overlap with direct experiments. The GRAPES-3 muon telescope is sensitive to PCRs composition measurements through muon multiplicity distribution.

118.2 Monte Carlo Simulations and EAS Reconstruction

Proton (H), Helium (He), Nitrogen (N), Aluminium (Al) and Iron (Fe) initiated EAS were produced by using CORSIKA package with QGSJET-II-04 and FLUKA hadronic interaction models. Data were generated in the energy range of 1 TeV to 10 PeV (16 PeV for N, Al and Fe) with a power law of spectral index of -2.5 . The GEANT-4 package was used to simulate the detector response. The relative arrival time of the EAS measured by scintillator detectors in the array was used to reconstruct

S. Mahapatra
Utkal University, Bhubaneswar, India

R. Moharana · B. Pant
Indian Institute of Technology Jodhpur, Jodhpur 342037, India

Y. Muraki · R. Scaria
Institute of Space-Earth Environmental Research, Nagoya University, Nagoya 464-8601, Japan

G. Pradhan
Indian Institute of Technology Indore, Indore 453552, India

R. Sahoo
Department of Physics, Indian Institute of Technology Indore, Simrol, Indore 453552, India

K. Tanaka
Graduate School of Information Sciences, Hiroshima City University, Hiroshima 731-3194, Japan

the arrival direction of EAS by fitting them with a plane front. The shower parameters such as shower size, shower core location and shower age were obtained by fitting a standard lateral distribution function, namely Nishimura-Kamata-Greisen (NKG), to the observed particle densities in the detectors

118.3 Efficiency and Acceptance Calculation

For each primary cosmic ray group, the variation of trigger efficiency (ϵ_T) and reconstruction efficiency (ϵ_R) as a function of energy of primary cosmic rays (E_T) was calculated. Total efficiency (ϵ) was determined by the product of trigger and reconstruction efficiency. Acceptance (A_{acc}) is represented as the product of the effective area and the effective viewing angle. The total efficiency for all primaries is shown in Fig. 118.1a and the total acceptance for GRAPES-3 EAS array is shown in Fig. 118.1b. The trigger efficiency is 90% at 50 TeV, 55 TeV, 60 TeV, 80 TeV and 100 TeV for H, He, N, Al and Fe, respectively. The acceptance for the GRAPES-3 EAS array is $3 \text{ m}^2\text{sr}$ at 1.0 TeV for H and $8 \text{ m}^2\text{sr}$ at 20.0 TeV for Fe. It increases up to $22000 \text{ m}^2\text{sr}$ when trigger efficiency is 100%.

118.4 Energy-Size Relation

The shower size (N_e) is a measure of the energy of PCRs (E_T) and their conversion relation can be derived from simulation. The log-log plot of the N_e and E_T for different primaries is shown in Fig. 118.2a. To get energy-size relation, the plot is fitted with a linear function (the proton is shown Fig. 118.2b). The reconstructed energy (E_R) can be calculated by these relations. The energy bias and resolution are calculated from the median value and standard deviation of the distribution of $\log E_R - \log E_T$. Energy bias and resolution as a function of E_T are shown in Fig. 118.2c, d,

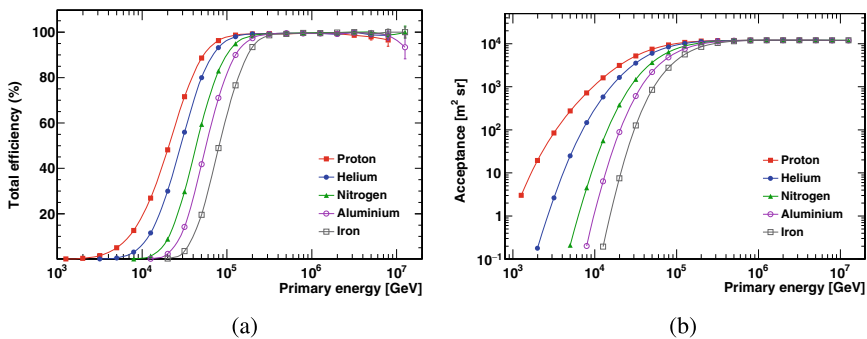


Fig. 118.1 **a** Total efficiency. **b** Total acceptance for GRAPES-3 EAS array, for different primaries

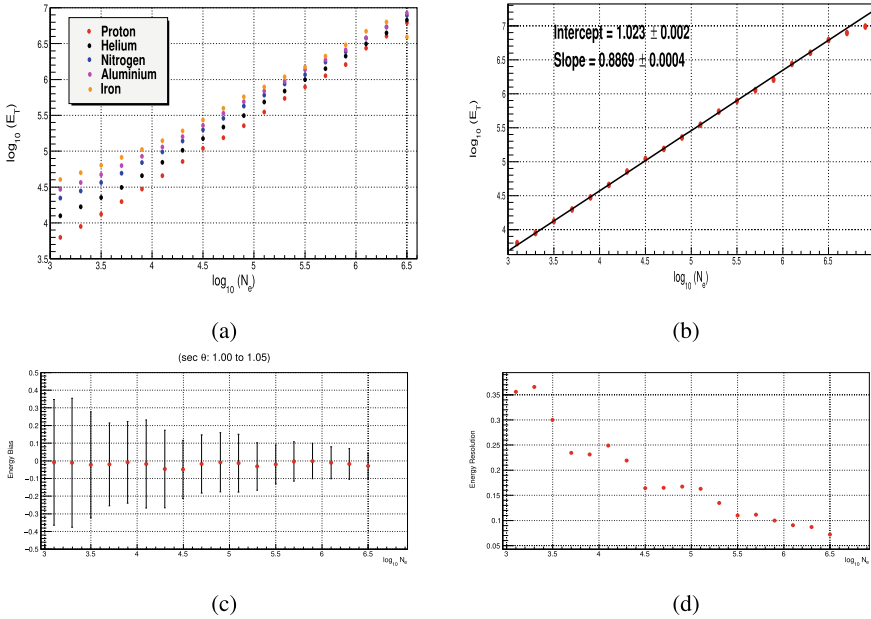


Fig. 118.2 **a** Energy–size relation plot for different elements. **b** Energy–size relation plot for proton, fitted with a linear function, **c**, **d** Energy bias and resolution as a function of E_T for proton and error bar in (c) represents energy resolution

respectively. Error bars in Fig. 118.2c represent the energy resolution. Energy bias is within 5% and energy resolution is 38% at 9 TeV and 8% at 6 PeV for proton.

118.5 Preliminary Cosmic Rays Spectrum

The data for year 2014 is used for the analysis with a live time of 318 days. The number of events recorded during live time is 9.7×10^9 which reduced to 2.3×10^9 after application of quality cuts. The energy for data is reconstructed on an event-by-event basis considering all particles to be proton. The Iterative Bayesian unfolding method is used to obtain the unfolded energy spectrum. In energy range 5–150 TeV, there is a good agreement between unfolding distribution and true distribution. The deviation at higher energy is due to the limiting statistics in simulation to calculate the smearing matrix. Therefore, the unfolding is used from 5 TeV to 150 TeV (termed as low-energy spectrum). But for $E_R > 150$ TeV, the limiting statistics in simulation and good energy resolution motivate us to obtain the spectrum directly from the observed reconstructed energy distribution (termed as high-energy spectrum). The low-energy and high-energy spectrum are shown in Fig. 118.3a, b, respectively. The low-energy spectrum is scaled by $E^{2.5}$ and fitted with broken power laws resulting

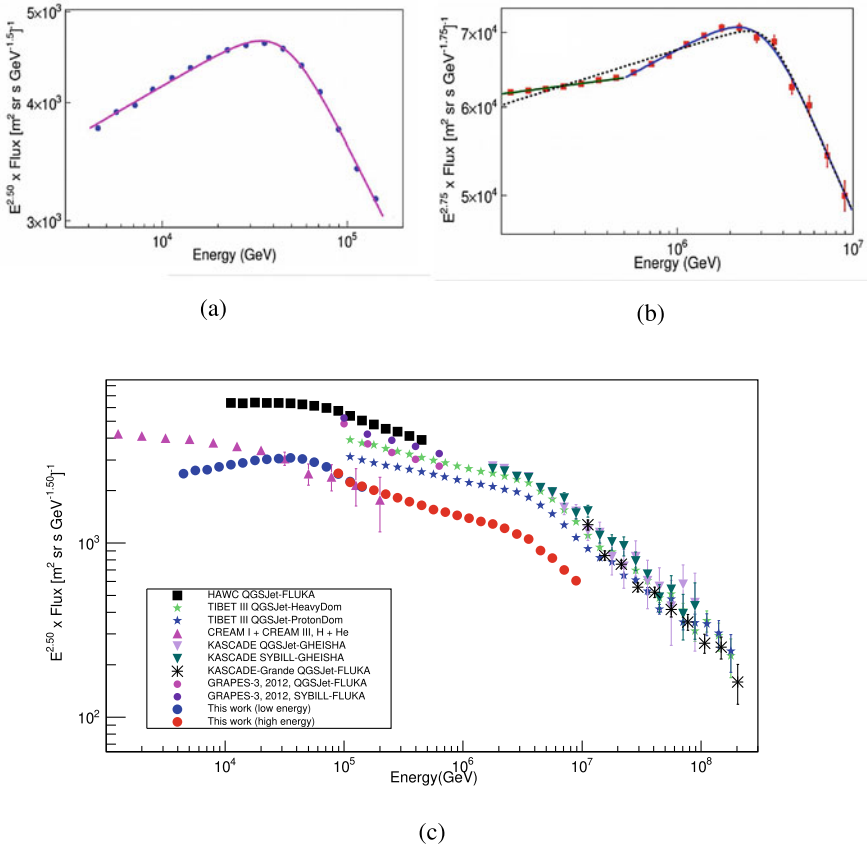


Fig. 118.3 **a** Low energy spectrum scaled with $E^{2.5}$. **b** High energy spectrum scaled with $E^{2.7}$. **c** All particle spectrum obtained by present work compared with other experiments: HAWC [4], TIBET-III [5], CREAM [6], KASCADE [7], KASCADE GRANDE [8], GRAPES-3 [9]

in $\gamma_1^{low} = -2.386 \pm 0.002$ and $\gamma_2^{low} = -2.898 \pm 0.004$ with an energy break E_{br}^{low} at 45.4 ± 0.3 TeV. The high energy spectrum is scaled by $E^{2.75}$ to highlight the fine structure near the knee. First entire range is fitted with a broken power law resulting in $\Gamma_1' = -2.705 \pm 0.004$ and $\Gamma_2' = -3.092 \pm 0.066$ with the knee E_{br}' at 3.3 ± 0.3 PeV. The spectrum is then fitted with a power law in energy range 100 TeV to 500 TeV and a broken power law in the energy range 500 TeV to 10 PeV. The power law fit gives $\Gamma^{high} = -2.729 \pm 0.001$ while the broken power law results in $\gamma_1^{high} = -2.664 \pm 0.007$ and $\gamma_2^{high} = -3.116 \pm 0.064$ with the knee E_{br}^{high} at 3.1 ± 0.3 PeV. Figure 118.3c shows the combined spectrum obtained by GRAPES-3 along with spectrum obtained by other experiments. Since the analysis is done by considering all particles to be proton, the measured absolute flux by GRAPES-3 is smaller as compared to others experiments but has good overlap with direct experiment (CREAM I + CREAM III, H + He) from 50 TeV onward (within error).

References

1. S.K. Gupta et al., Nucl. Instrum. Methods A **540**, 311 (2005)
2. P.K. Mohanty et al., Astropart. Phys. **31**, 24 (2009)
3. Y. Hayashi et al., Nucl. Instrum. Methods A **545**, 643 (2005)
4. R. Alfaro et al., Phys. Rev. D **96**, 122001 (2017)
5. Amenomori et al., Astrophys. J. **678**, 1165Y1179 (2008)
6. Yoon et al., Astrophys. J. **839**(5), 8 (2017)
7. T. Antoni et al., Astropart. Phys. **24**, 1–25, 122001 (2005)
8. W.D. Apel et al., Astropart. Phys. **47**, 54–66, 122001 (2013)
9. H. Tanaka et al., J. Phys. G: Nucl. Part. Phys. **39**, 025201 (2012)

Chapter 119

Investigation of Muon Puzzle with GRAPES-3 Experiment



G. S. Pradhan, S. Ahmad, M. Chakraborty, A. Chandra, S. R. Dugad, S. K. Gupta, B. Hariharan, Y. Hayashi, P. Jagadeesan, A. Jain, P. Jain, V. B. Jhansi, S. Kawakami, H. Kojima, S. Mahapatra, P. K. Mohanty, R. Moharana, S. D. Morris, P. K. Nayak, A. Oshima, B. P. Pant, D. Pattanaik, P. S. Rakshe, K. Ramesh, B. S. Rao, L. V. Reddy, R. Sahoo, R. Scaria, S. Shibata, F. Varsi, and M. Zuberi

Abstract One of the outstanding problems in cosmic ray (CR) physics is the mismatch between simulated and observed muon numbers termed as the muon puzzle. While a theoretical investigation is needed, it is necessary to obtain as much as data possible beyond any ambiguity from various experiments, sensitive in different energy ranges of cosmic ray spectrum. The GRAPES-3 experiment located at Ooty, India is sensitive to the observation of cosmic rays over a wide range of energies from 10^{13} to 10^{16} eV. The large area muon detector of GRAPES-3 provides a sensitive measurement of muon content in the cosmic ray showers. An investigation of muon

G. S. Pradhan (✉) · S. Ahmad · M. Chakraborty · A. Chandra · S. R. Dugad · S. K. Gupta · B. Hariharan · Y. Hayashi · P. Jagadeesan · A. Jain · P. Jain · V. B. Jhansi · S. Kawakami · H. Kojima · S. Mahapatra · P. K. Mohanty · R. Moharana · S. D. Morris · P. K. Nayak · A. Oshima · B. P. Pant · D. Pattanaik · P. S. Rakshe · K. Ramesh · B. S. Rao · L. V. Reddy · R. Sahoo · R. Scaria · S. Shibata · F. Varsi · M. Zuberi
The GRAPES-3 Experiment, Cosmic Ray Laboratory, Raj Bhavan, Ooty 643001, India
e-mail: girijasankarpradhan0@gmail.com

M. Chakraborty · S. R. Dugad · S. K. Gupta · B. Hariharan · P. Jagadeesan · A. Jain · V. B. Jhansi · P. K. Mohanty · R. Moharana · S. D. Morris · P. K. Nayak · D. Pattanaik · P. S. Rakshe · K. Ramesh · B. S. Rao · L. V. Reddy · M. Zuberi
Tata Institute of Fundamental Research, Homi Bhabha Road, Mumbai 400005, India

Y. Hayashi · S. Kawakami
Graduate School of Science, Osaka City University, Osaka 558-8585, Japan

S. Ahmad · A. Chandra
Aligarh Muslim University, Aligarh 202002, India

P. Jain · F. Varsi
Indian Institute of Technology Kanpur, Kanpur 208016, India

S. Mahapatra · D. Pattanaik
Utkal University, Bhubaneswar 751004, India

puzzle based on the Monte Carlo simulation of cosmic ray showers with CORSIKA is discussed.

119.1 Introduction

Cosmic rays are the high-energy charged particles traveling throughout our galaxy and inter-galactic space nearly at the speed of light. An understanding of the nature of cosmic ray sources and processes accelerating the charged particle to ultra-high energies (UHE) ($E \geq 10^{15}$ eV) still eludes us although considerable progress [1] has been made during recent years. Primary cosmic rays (PCRs) consist of the nuclei of hydrogen ($\sim 90\%$), helium ($\sim 9\%$), and a small fraction ($\sim 1\%$) of remaining heavier elements, including carbon, nitrogen, oxygen, aluminum, iron, etc. PCRs have energy in the range $\sim 10^9$ – 10^{20} eV. PCRs, after penetrating into the Earth's atmosphere, interact with the air nuclei and produce secondary particles. These secondary particles further interact with the atmosphere and produce a shower of particles, including photons, electrons, muons, and hadrons at the ground level. Unlike other particles, muons play a vital role in many CR experiments because of two reasons. Firstly, muons can be produced only in the process of weak interaction and electromagnetic interaction. Secondly, muons are very easily detected and identified due to their very high penetrating ability and the possibility to observe them at large distances from the point of generation. The muon excess in cosmic ray data compared to expectation from Monte Carlo simulation observed by cosmic rays as well as accelerator experiments such as ALIPH and DELPHI at CERN have remained a puzzle over one and half decades [2, 3]. A hypothesis to understand this issue is the production of blobs of quark-gluon matter with large angular momentum in nucleus-nucleus interactions [2]. The GRAPES-3, which stands for Gamma Ray Astronomy at PeV Energies phase 3 is a ground-based extensive air shower (EAS) experiment located at Ooty in southern India (11.4° N, 76.7° E, and 2200 m above sea level). It consists of an array of 400 plastic scintillator detectors [4] and a large area tracking muon detector. Tracking muon detector consists of 3712 proportional counters (PRCs) each of length 600 cm and cross-section area of $10\text{ cm} \times 10\text{ cm}$. The scintillator detectors are arranged in a hexagonal geometry with an inter-detector separation of 8 m. This

A. Oshima · S. Shibata

College of Engineering, Chubu University, Kasugai, Aichi 487-8501, Japan

H. Kojima

Faculty of Engineering, Aichi Institute of Technology, Toyota City, Aichi 470-0392, Japan

G. S. Pradhan · R. Sahoo · R. Scaria

Department of Physics, Indian Institute of Technology Indore, Indore 453552, India

R. Moharana · B. P. Pant

Indian Institute of Technology Jodhpur, Jodhpur 342037, India

combination of detectors allows us to record the size and muon multiplicity of EAS. We present initial results from CORSIKA simulations here.

119.2 CORSIKA

In hadronic interaction, EAS simulations are carried out using generators CORSIKA simulation program, which is widely used to simulate air-showers in the Earth's atmosphere [5] for various primaries. It has interfaced with different high energy hadronic interaction models such as EPOS-LHC [6], QGSJET01C [7], QGSJETII-04 [8], SIBYLL [9], VENUS [10], DPMJET [11], and NEXUS [12] and low energy models like GHEISHA [13], FLUKA [14], and UrQMD [15]. We have used the CORSIKA (version 7.69) simulation package using QGSJET-II-04 and FLUKA for high energy and low energy models, respectively. It brings out simulations to study the shower development, including various hadronic and electromagnetic interactions, and decays. 5000 events were simulated with proton and iron nuclei as primaries particles. The data were generated between the energy range 6.3 and 10 TeV.

119.3 Results and Discussions

In Fig. 119.1 we have shown the energy distribution of muons and electrons for proton and iron as primaries with kinetic energies in the range $E_{kin} = 6.3\text{--}10$ TeV. It is evident that the proton primaries produce particles of higher energies in comparison with iron primaries of the same energy. It is because the center of mass energy $\sqrt{s} = \sqrt{2m_p E/A}$ of proton primaries is larger. Here, E , A and m_p are the kinetic

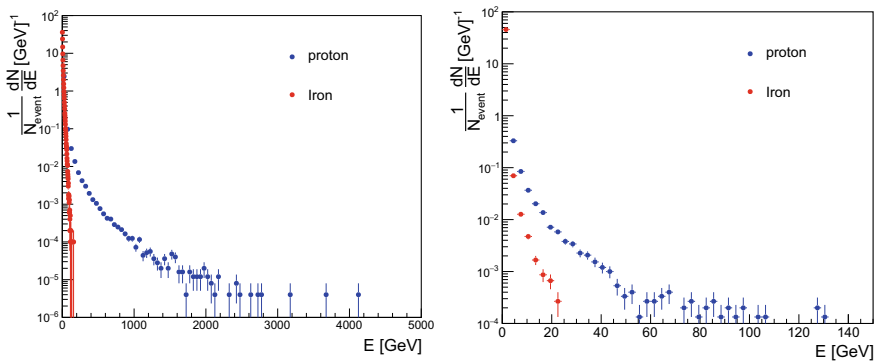


Fig. 119.1 (Color online) Simulated energy distribution of muon (left panel) and electron (right panel) with kinetic energies in the range $E_{kin} = 6.3\text{--}10$ TeV. Blue points are for proton primaries and red points are for iron primaries

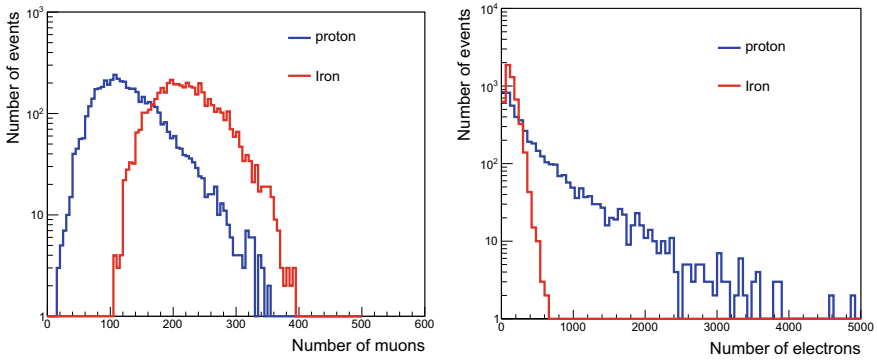


Fig. 119.2 (Color online) Simulated multiplicity distribution of muon (left panel) and electron (right panel) with kinetic energies in the range $E_{kin} = 6.3\text{--}10$ TeV. Blue curve are for proton primaries and red curve are for iron primaries

energy of the projectile, mass number of the projectile and mass of the proton, respectively. In Fig. 119.2 we have shown the multiplicity distribution of muon (left panel) and electron (right panel) for proton and iron as primaries with energies within the range $E_{kin} = 6.3\text{--}10$ TeV. It shows that in case of iron primaries more number of secondary particles are produced than proton primaries as it induces more hadronic interactions due to its higher mass. The muon puzzle refers to an excessive number of muons observed in the measurement than the simulation. However, this is an initial study of various hadronic interaction models with different primaries. Finally, it will be compared with the GRAPES-3 data to resolve the muon puzzle.

119.4 Summary

The muon puzzle gives an opportunity to infer the cosmic ray mass composition unambiguously. One of the possible solutions of muon puzzle is the production of blobs of quark-gluon matter with a large orbital momentum in nucleus–nucleus interactions.

References

1. E.G. Berezhko, L.T. Ksenofontov, J. Exp. Theor. Phys. **89**, 391–403 (1999)
2. A.A. Petrukhin, Nucl. Instrum. Meth. A **742**, 228 (2014)
3. J. Abdallah et al., DELPHI. Astropart. Phys. **28**, 273 (2007)
4. Y. Hayashi et al., GRAPES-3. Nucl. Instrum. Meth. A **545**, 643 (2005)
5. D. Heck et al., FZKA-6019. <http://www-ik.fzk.de/corsika/physicsdescription/corsikaphys.html>

6. T. Pierog et al., Phys. Rev. C **92**(3), 034906 (2015)
7. N. N. Kalmykov et al., Moscow Univ. Phys. **63**, 425 (2008)
8. S. Ostapchenko, Phys. Rev. D **83**, 014018 (2011)
9. E.J. Ahn et al., Phys. Rev. D **80**, 094003 (2009)
10. K. Werner, Phys. Rep. **232**, 87 (1993)
11. J. Ranft, Phys. Rev. D **51**, 64 (1995)
12. H.J. Drescher et al., Phys. Rep. **350**, 93 (2001)
13. H. Fesefeldt, Report PITHA-85/02 (1985)
14. A. Fasso et al., eConf **C0303241**, MOMT005 (2003)
15. S.A. Bass et al., Prog. Part. Nucl. Phys. **41**, 255 (1998)

Chapter 120

A Detailed Investigation of Thunderstorm Events Recorded in GRAPES-3 Experiment



B. Hariharan, S. Ahmad, M. Chakraborty, A. Chandra, S. R. Dugad, S. K. Gupta, Y. Hayashi, P. Jagadeesan, A. Jain, P. Jain, V. B. Jhansi, S. Kawakami, H. Kojima, S. Mahapatra, P. K. Mohanty, R. Moharana, S. D. Morris, Y. Muraki, P. K. Nayak, A. Oshima, B. Pant, D. Pattanaik, G. Pradhan, P.S. Rakshe, K. Ramesh, B. S. Rao, L. V. Reddy, R. Sahoo, R. Scaria, S. Shibata, K. Tanaka, F. Varsi, and M. Zuberi

Abstract The large area tracking muon telescope of the GRAPES-3 experiment reported the measurement of 1.3 GV electric potential developed in one of the massive thunderclouds recorded on 1 December 2014 by using muon imaging technique [1]. The record-breaking Giga-Volt potential is ten times larger than the earlier reported direct measurements by balloon and rocket soundings, which proves ~ 90 years old prediction by C.T.R. Wilson. However, the GRAPES-3 measurements rely on precise estimation of change in angular muon flux caused by the energy change due to acceleration of muons during its propagation through charged layers of thunder-

B. Hariharan (✉) · S. Ahmad · M. Chakraborty · A. Chandra · S. R. Dugad · S. K. Gupta · Y. Hayashi · P. Jagadeesan · A. Jain · P. Jain · V. B. Jhansi · S. Kawakami · H. Kojima · S. Mahapatra · P. K. Mohanty · R. Moharana · S. D. Morris · Y. Muraki · P. K. Nayak · A. Oshima · B. Pant · D. Pattanaik · G. Pradhan · P.S. Rakshe · K. Ramesh · B. S. Rao · L. V. Reddy · R. Sahoo · R. Scaria · S. Shibata · K. Tanaka · F. Varsi · M. Zuberi
The GRAPES-3 Experiment, Cosmic Ray Laboratory, Raj Bhavan, Ooty 643001, India
e-mail: 89hariharan@gmail.com

B. Hariharan · M. Chakraborty · S. R. Dugad · S. K. Gupta · P. Jagadeesan · A. Jain · V. B. Jhansi · P. K. Mohanty · R. Moharana · S. D. Morris · P. K. Nayak · D. Pattanaik · P.S. Rakshe · K. Ramesh · B. S. Rao · L. V. Reddy · M. Zuberi
Tata Institute of Fundamental Research, Homi Bhabha Road, Mumbai 400005, India

S. Ahmad · A. Chandra
Aligarh Muslim University, Aligarh 202002, India

Y. Hayashi · S. Kawakami
Graduate School of Science, Osaka City University, Osaka 558-8585, Japan

P. Jain · F. Varsi
Indian Institute of Technology Kanpur, Kanpur 208016, India

H. Kojima · A. Oshima · S. Shibata
College of Engineering, Chubu University, Kasugai, Aichi 487-8501, Japan

clouds. The electric potential is estimated by detailed modeling of change in muon flux as a function of applied potential using CORSIKA and in-house Monte Carlo simulation tools. A detailed summary on simulation methods and investigation of 184 thunderstorms recorded by the GRAPES-3 during the period from April 2011 to December 2014 will be discussed.

120.1 Introduction

The record-breaking electric potential of 1.3 Giga-Volt (GV) in one of the massive thunderclouds recorded by GRAPES-3 is the first direct experimental evidence proving C.T.R. Wilson's prediction [1]. Unlike the previous methods of measurements based on balloon and rocket soundings, the recent study exploited muon imaging of thunderclouds. This technique is far superior compared to the conventional techniques where the problems of time skew and small sampling area are inevitable and limited by the technologies—thus leads to an underestimation by a factor of ten. Muons being relativistic traverse the entire thundercloud instantaneously. Along with the large sky coverage of GRAPES-3's field of view (FOV of 2.3 sr), it is possible to overcome the above-mentioned problems and have an accurate estimation of thundercloud properties using muon flux variation. However, the interpretation of observed muon flux variation requires a detailed study on Monte Carlo simulations which itself rely on the hadronic interaction models built based on theoretical assumptions and tuned with experimental results.

In this study, a detailed summary of angular distribution of 184 thunderstorm events recorded during April 2011 to December 2014. Though the GRAPES-3 muon telescope (G3MT) is being operated for more than two decades, the electric field measurements required to study the thunderstorm effects are actually available since April 2011. The observed distribution is found to have a significant asymmetry in East–West direction compared to North–South. Further investigations based on Monte Carlo simulations could explain the observed phenomenon found to be due

S. Mahapatra
Utkal University, Bhubaneswar, India

R. Moharana · B. Pant
Indian Institute of Technology Jodhpur, Jodhpur 342037, India

Y. Muraki
Institute of Space–Earth Environmental Research, Nagoya University, Nagoya 464-8601, Japan

G. Pradhan · R. Scaria
Indian Institute of Technology Indore, Indore 453552, India

R. Sahoo
Department of Physics, Indian Institute of Technology Indore, Indore 453552, India

K. Tanaka
Graduate School of Information Sciences, Hiroshima City University, Hiroshima 731-3194, Japan

to asymmetry in muon charge ratio ($\mu_R = \mu^+/\mu^-$) which is due to the effects of geomagnetic field in both inside and outside of Earth's atmosphere.

120.2 GRAPES-3 Muon Telescope

The G3MT is built using proportional counter (PRC) as a basic element. Each PRC is 6 m long mild steel tube with a cross-section of $10 \times 10 \text{ cm}^2$. The wall thickness of the PRC is 2.3 mm. Both ends of the PRC are sealed and filled with P10 gas (a mixture of 90% argon and 10% methane). At the center, a $100 \mu\text{m}$ thick tungsten wire is laid that acts as anode whereas the metal body being cathode. The PRC is supplied with a potential difference of 3000 V DC that works as a detector based on gas ionization principle. The G3MT is organized into sixteen muon modules (3712 PRCs). Each module consists of four layers of PRCs. Each layer consists of a carpet of 58 PRCs. The layers are sandwiched by 15 cm concrete columns. Above the top layer, 2 m thick concrete slabs are placed in the form of inverted pyramidal shape to provide an energy threshold of $\sec(\theta) \text{ GeV}$ up to 45° (sky coverage of 2.3 sr). Such a large absorber ensures the detection of $>1 \text{ GeV}$ muons by filtering out the soft components. The alternate arrangement of layers allows to reconstruct the muons in 169 usable directions for physics studies with an angular resolution of 4° . A detailed account of the G3MT can be found here [2].

120.3 Monte Carlo Simulations

The Monte Carlo simulations are carried out in 61 steps of electric potential ranging from -3 to 3 GV . At each step, a uniform electric field is applied at an altitude of 8–10 km above msl with electric field model implemented inside CORSIKA. The resultant muon intensity is derived in 169 directions using an in-house detector simulation tool. The number of primaries is scaled in such a way that each direction of the G3MT should have at least 10^6 muons for each potential step whereas the background to have statistics ten times of the signal. Figure 120.1 shows the simulated muon intensity variation as the function of applied electric potential in 9-direction configuration for the ease of visualisation. More details about the simulation can be found here [3].

120.4 Distribution of Thunderstorm Events

The large number of thunderstorm events collected during the period from April 2011 to December 2014 are analysed in the 9-directional configuration of the G3MT. From this analysis the angular distribution obtained from 184 events is shown in

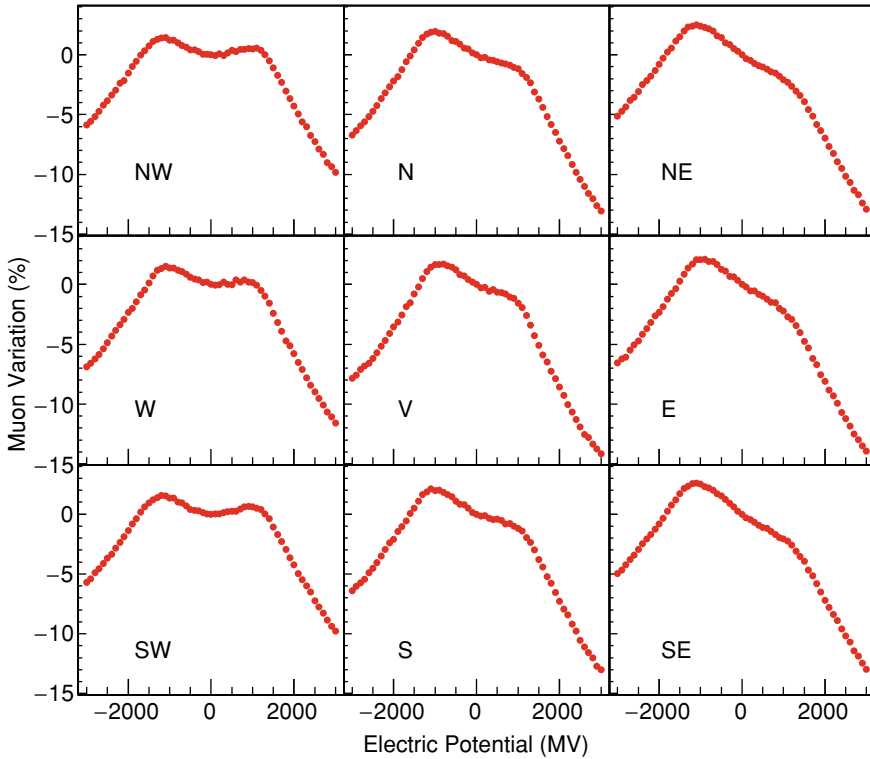


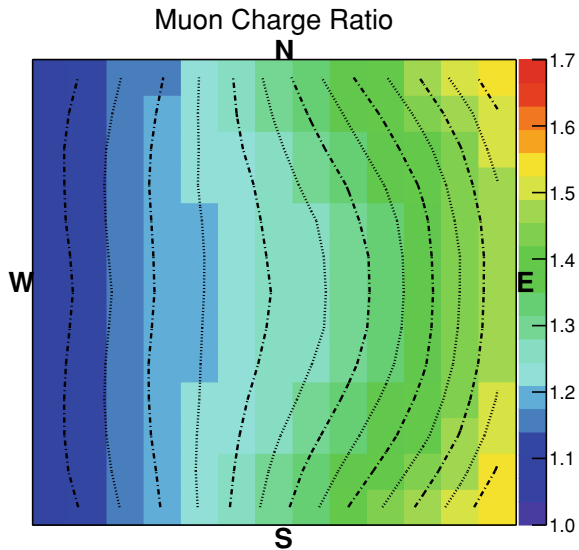
Fig. 120.1 Monte Carlo simulation for GRAPES-3 FOV in 9-direction configuration

Table 120.1. From the distribution a clear symmetry can be observed in North-South orientation compared to a larger asymmetry found in East-West directions. Surprisingly, the percentage of events in the vertical and West directions are the smallest in the entire distribution. These symmetries are found to be caused by the μ_R due to the effects of geomagnetic field. The μ_R obtained from the Monte Carlo simulation is shown in Fig. 120.2. It can be seen that the μ_R in the East direction is greater than one—hence, the μ^+ is decelerated for a positive potential and vice versa. Since the G3MT measures the total muon flux ($\mu^+ + \mu^-$), considering the fact that the thundercloud potential is positive in most cases, majority of the events are found to be in the East (Fig. 120.1). It can be also seen that the μ_R in the West and vertical directions is almost equal to one—hence, the changes in the total muon flux become insignificant.

Table 120.1 Percentage of thunderstorm events in GRAPES-3 FOV. Events in the vertical direction is at the center of the table

NW	N			NE
W	8.1	3.0	29.3	E
	0.5	0.5	3.5	
	8.1	3.0	43.4	
SW	S			SE

Fig. 120.2 Distribution of μ_R for GRAPES-3 FOV in 169-direction configuration



120.5 Conclusions

A study on angular distribution of 184 thunderstorm events recorded by the G3MT during a period of almost four years revealed a clear East-West asymmetry. This is explained by examining the μ_R derived from the detailed Monte Carlo simulations. It is found that the μ_R showed a similar East-West asymmetry due to geomagnetic field. The μ_R plays a key role in impacting the measured muon flux due to the acceleration and deceleration of muons of different polarities. Since, the G3MT records the total muon flux, the observed net change is sensitive to the μ_R of the corresponding direction. This could be also the reason for the detection of smaller number of events in the West and vertical direction due to μ_R being almost equal to one.

References

1. B. Hariharan et al., Phys. Rev. Lett. **122**, 105101 (2019)
2. Y. Hayashi et al., Nucl. Instrum. Methods A **545**, 643 (2005)
3. B. Hariharan et al., *Proceedings of Science PoS (ICRC2017)*, p. 305

Chapter 121

Cosmological Perturbations in the Interacting Dark Sector: Mapping Fields and Fluids



Joseph P. Johnson and S. Shankaranarayanan

Abstract A classical field theory description (which can be obtained from an $f(R, \chi)$) of dark energy–dark matter interaction is considered. Demanding that the interaction strength Q_ν in the dark sector must have a field theory description and a fluid description, a unique form of interaction strength is obtained. It is shown that the one-to-one mapping between the *classical* field theory description and the phenomenological fluid description of dark energy–dark matter interaction exists *only* for this unique form of interaction. Then a novel autonomous system and its stability analysis for the general interacting dark sector is introduced, followed by the background analysis for a specific potential and interaction function.

121.1 Introduction

Dark matter dominates the galaxy mass, and dark energy forms the majority of our Universe’s energy density [2, 3]. However, we have little information about the properties of these two components that dominate the energy content of the Universe today [4]. The only information we have about the two components is that (i) Dark energy contributes negative pressure to the energy budget, and (ii) Dark matter has negligible, possibly zero, pressure. The above properties are based on gravitational interactions. More importantly, we do not know how they interact with each other and Baryons/Photons.

It has been shown that the dark matter–dark energy interaction can reconcile the tensions in the Hubble constant H_0 . In most interacting dark sector models,

Interacting dark sector, based on the work [1]

J. P. Johnson (✉)

Department of Physics, Indian Institute of Technology Bombay, Mumbai 400076, India

e-mail: josephpj@iitb.ac.in

S. Shankaranarayanan

Department of Physics, Indian Institute of Technology Bombay, Mumbai 400076, India

e-mail: shanki@phy.iitb.ac.in

© The Author(s), under exclusive license to Springer Nature Singapore Pte Ltd. 2022
B. Mohanty et al. (eds.), *Proceedings of the XXIV DAE-BRNS High Energy Physics Symposium, Jatni, India*, Springer Proceedings in Physics 277,
https://doi.org/10.1007/978-981-19-2354-8_121

667

phenomenologically, the interaction is proposed between the fluid terms in the dark sector (Cf. Ref. [1]). More specifically, individually, dark matter (DM) and dark energy (DE) do not satisfy the conservation equations; however, the combined sector satisfies the energy conservation equation [5], i.e.,

$$\nabla^\mu T_{\mu\nu}^{(\text{DE,DM})} = Q_\nu^{(\text{DE,DM})}, \quad Q_\nu^{(\text{DE})} + Q_\nu^{(\text{DM})} = 0 \tag{121.1}$$

where Q determines the interaction strength between dark matter and dark energy. Since the gravitational effects on dark matter and dark energy are opposite, even a small interaction can impact the cosmological evolution [6]. Since we have little information about the dark sector, in many of these models, the interaction strength Q_ν is put in by hand. However, it is unclear whether these broad classes of phenomenological models can be obtained from a field theory action.

In this talk, we show that under conformal transformations, $f(R, \chi)$ is equivalent to a model with two coupled scalar fields. The dark energy–dark matter interaction, represented by the coupling between the classical scalar fields, can also be represented by the evolution equations of the dark energy (represented by a scalar field) and dark matter (represented by a fluid). We show that a one-to-one mapping exists between the field theory and fluid description for a unique interaction term.

We define a set of dimensionless variables and construct an autonomous system that completely describes the dark energy–dark matter interaction and background evolution. We analyze the fixed points of the system and show that the system has an accelerated attractor solution. We consider a specific dark energy–dark matter interaction model and study the background evolution. We show that for a range of (both positive and negative) coupling strengths, the dark-energy dominated epoch occurs earlier with an interacting dark sector than in the non-interacting dark sector.

121.2 Dark Sector Interaction: Field and Fluid Description

Consider the following action in Jordan frame:

$$S_J = \int d^4x \sqrt{-\tilde{g}} \left[\frac{1}{2\kappa^2} f(\tilde{R}, \tilde{\chi}) - \frac{1}{2} \tilde{g}^{\mu\nu} \tilde{\nabla}_\mu \tilde{\chi} \tilde{\nabla}_\nu \tilde{\chi} - V(\tilde{\chi}) \right] \tag{121.2}$$

where $f(\tilde{R}, \tilde{\chi})$ is an arbitrary, smooth function of Ricci scalar, and scalar field $\tilde{\chi}$, and $V(\tilde{\chi})$ is the self-interaction potential of the scalar field $\tilde{\chi}$. Under the conformal transformation:

$$g_{\mu\nu} = \Omega^2 \tilde{g}_{\mu\nu}, \quad \text{where} \quad \Omega^2 = F(\tilde{R}, \tilde{\chi}) \equiv \frac{\partial f(\tilde{R}, \tilde{\chi})}{\partial \tilde{R}} \tag{121.3}$$

and a field redefinition, the action in the Einstein frame takes the following form:

$$S = \int d^4x \sqrt{-g} \left(\frac{1}{2\kappa^2} R - \frac{1}{2} g^{\mu\nu} \nabla_\mu \phi \nabla_\nu \phi - U(\phi) - \frac{1}{2} e^{2\alpha(\phi)} g^{\mu\nu} \nabla_\mu \chi \nabla_\nu \chi - e^{4\alpha(\phi)} V(\chi) \right). \quad (121.4)$$

where

$$U = \frac{F\tilde{R} - f}{2\kappa^2 F^2}.$$

and $\alpha(\phi)$ denotes the interaction between dark energy and dark matter.

Defining the dark matter fluid by specifying the four velocity energy density and pressure

$$u_\mu = - \left[-g^{\alpha\beta} \nabla_\alpha \chi \nabla_\beta \chi \right]^{-\frac{1}{2}} \nabla_\mu \chi \quad (121.5)$$

$$p_m = -\frac{1}{2} e^{2\alpha} \left[g^{\mu\nu} \nabla_\mu \chi \nabla_\nu \chi + e^{2\alpha} V(\chi) \right], \quad \rho_m = -\frac{1}{2} e^{2\alpha} \left[g^{\mu\nu} \nabla_\mu \chi \nabla_\nu \chi - e^{2\alpha} V(\chi) \right]. \quad (121.6)$$

Then the interaction function in the field theory and fluid descriptions are given by

$$Q_v^{(F)} = -e^{2\alpha(\phi)} \alpha_{,\phi}(\phi) \nabla_\nu \phi \left[\nabla^\sigma \chi \nabla_\sigma \chi + 4e^{2\alpha(\phi)} V(\chi) \right] = -\alpha_{,\phi}(\phi) \nabla_\nu \phi (\rho_m - 3p_m) \quad (121.7)$$

A one-to-one mapping between the field theory description and fluid description of the interacting dark sector described above exist *only* for this form of interaction function. A classification of interacting dark sector models based on the existence of this mapping can be found in Ref. [1].

121.3 Background Evolution with Dark Energy–Dark Matter Interaction

For the FRW background Universe, the evolution of the dark matter fluid energy density is given by

$$\bar{\rho}_m = \bar{\rho}_{m0} a^{-3(1+\omega_m)} e^{[\alpha(\bar{\phi}) - \alpha_0](1-3\omega_m)}, \quad (121.8)$$

To describe and analyze the complete background evolution, define the following dimensionless variables.

$$x = \sqrt{\frac{C_1}{6}} \frac{\dot{\phi}}{H M_{Pl}}, \quad y = \sqrt{\frac{C_1}{3}} \frac{\sqrt{U}}{H M_{Pl}}, \quad \lambda = -\frac{M_{Pl}}{\sqrt{C_1}} \frac{U_{,\phi}}{U} \\ \Gamma = \frac{U U_{,\phi\phi}}{U_{,\phi}^2}, \quad \alpha = \alpha(\phi), \quad \beta = -\frac{M_{Pl}}{\sqrt{C_1}} \frac{\alpha_{,\phi}}{\alpha}, \quad \gamma = \frac{\alpha \alpha_{,\phi\phi}}{\alpha_{,\phi}^2} \quad (121.9)$$

where H is the Hubble parameter and $M_{Pl} = 1/\sqrt{8\pi G}$

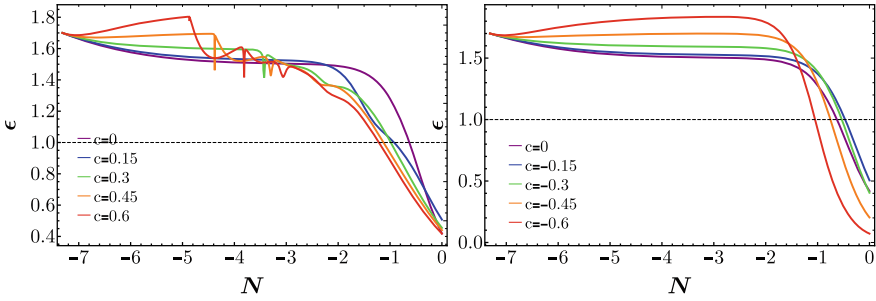


Fig. 121.1 Evolution of slow-roll parameter ϵ as a function of N for different values of interaction strength C ; Left panel: $C \geq 0$, Right panel: $C \leq 0$

Stability analysis of the autonomous system describing the interacting dark sector using these variables shows that the system has a radiation-dominated saddle point, matter-dominated saddle point, and an attractor with the accelerated expansion of the Universe. Hence the model is consistent with the cosmological observations of the background evolution of the Universe.

Next we look at the background evolution for the scalar field potential $U(\phi) \sim 1/\phi$ [7] and a linear interaction function $\alpha(\phi) \sim C\phi$.

As we see in Fig. 121.1, looking at the evolution of the slow-roll parameter $\epsilon \equiv -\dot{H}/H^2$, a range of values of C (positive and negative) lead to the accelerated expansion of the Universe indicated by $\epsilon < 1$. The Universe enters the accelerated phase sooner for larger magnitude interaction strength.

121.4 Conclusion

We have introduced a classical field theory description of the dark energy–dark matter interaction with a one-to-one mapping with the fluid description of the interacting dark sector. This mapping exist *only* for a unique interaction term $Q_v^{(F)}$. We have then defined a set of dimensionless variables to construct an autonomous system that completely describes the background evolution of the Universe with the interacting dark sector. Stability analysis of the system shows that it has a stable attractor solution that describes the accelerated expansion of the Universe. Then for an inverse scalar field potential and a linear interaction function, we show that the model leads to the accelerated expansion of the Universe for a range of values interaction strength. Larger values of interaction strength lead to the earlier onset of the phase of accelerated expansion.

References

1. J.P. Johnson, S. Shankaranarayanan, Cosmological perturbations in the interacting dark sector: mapping fields and fluids. *Phys. Rev. D* **103**, 023510 (2021)
2. A.G. Riess et al., Observational evidence from supernovae for an accelerating universe and a cosmological constant. *Astron. J.* **116**, 1009–1038 (1998)
3. N. Aghanim et al., Planck 2018 results. VI. Cosmological parameters. *Astron. Astrophys.* **641**, A6 (2020)
4. E.J. Copeland, M. Sami, S. Tsujikawa, Dynamics of dark energy. *Int. J. Mod. Phys. D* **15**, 1753–1936 (2006)
5. B. Wang, E. Abdalla, F. Atrio-Barandela, D. Pavon, Dark matter and dark energy interactions: theoretical challenges, cosmological implications and observational signatures. *Rept. Prog. Phys.* **79**(9), 096901 (2016)
6. Yu.L. Bolotin, A. Kostenko, O.A. Lemets, D.A. Yerokhin, Cosmological evolution with interaction between dark energy and dark matter. *Int. J. Mod. Phys. D* **24**(03), 1530007, 09b6901 (2014)
7. A. Pavlov, S. Westmoreland, K. Saaidi, B. Ratra, Nonflat time-variable dark energy cosmology. *Phys. Rev. D* **88**(12), 123513 (2013). [Addendum: *Phys. Rev. D* **88**, 129902 (2013)]

Chapter 122

Gravitational Wave Echoes from Strange Stars for Various Equations of State



Jyatsnasree Bora and Umananda Dev Goswami

Abstract The tentative gravitational wave echo (GWE) at a frequency of about 72 Hz has been recently claimed at 4.2σ significance level in the GW170817 event (Abedi et al. Phys. Rev. D 96:082004, 2017 [1]). GWEs can be used as a tool to study the characteristics of ultra-compact stellar objects. Considering the final ultra-compact, post-merger object as a strange star, the GWE frequency can be calculated. However, GWEs are observed for only those compact stellar structures whose compactness lies between 0.33 and 0.44. Alternatively, GWE can be obtained for those compact stars which feature a photon sphere and compactness not crossing the Buchdahl's limit radius $R_B = 9/4M$. A photon sphere is a surface located at $R = 3M$, R being the radius and M is the total mass of the ultra-compact object. Recently, using the simplest MIT Bag model equation of state (EoS) it has been reported that strange stars can produce GWEs with frequencies of tens of kilohertz (Mannarelli and Tonelli, Phys. Rev. D 97:123010, 2018 [2]). In view of this, for a comparative study, we have calculated the respective echo frequencies associated with strange stars by considering three models of strange star EoSs, viz., MIT bag model, linear and polytropic EoSs (Bora and Goswami, Mon. Not. R. Astron. Soc. 502:1557–1568, 2021 [3]). We found that, not being too stiff, the polytropic EoS cannot emit GWE, whereas the MIT Bag model and the linear EoSs can emit GWEs at a frequency range of about tens of kilohertz. Also, GWE frequency increases with the increase in values of bag constant B and decreases with the increasing values of linear constant b . So a model- dependent nature of GWE frequencies is observed.

122.1 Introduction

The possibilities that compact objects emitting gravitational wave echoes (GWEs) are shown by various authors in the very recent past [2–5]. Among the other compact objects, strange stars (SSs) are able to draw notable attention in the last few years.

J. Bora (✉) · U. Dev Goswami
Department of Physics, Dibrugarh University, Dibrugarh 786004, Assam, India
e-mail: jyatsnasree.borah@gmail.com

© The Author(s), under exclusive license to Springer Nature Singapore Pte Ltd. 2022
B. Mohanty et al. (eds.), *Proceedings of the XXIV DAE-BRNS High Energy Physics Symposium, Jaiti, India*, Springer Proceedings in Physics 277,
https://doi.org/10.1007/978-981-19-2354-8_122

673

The very unique structural and also compositional behaviours of SSs are responsible for the increasing attraction towards such hypothetical stars. It is shown that an SS can be an ultra-compact star having compactness large enough to emit GWE [2, 4]. The echo signal originating from ultra-compact star was first reported in [4]. Considering the final ultra-compact object formed in GW170817 event as an SS, the corresponding echo frequency is reported in [2] using the MIT Bag model EoS. In this GW170817 event the tentative GWE at a frequency of about 72 Hz has been recently claimed with 4.2σ significance level [1]. In this paper we have pointed out the possibilities of GWEs from SSs formed in GW170817 event depicted by various EoSs and re-examined the possibilities of using the MIT Bag model with large values of Bag constants.

After this introductory section, the rest of the paper is organised as follows: In Sect. 122.2 the considered EoSs are described. In Sect. 122.3 we have discussed the echoes emitted by SSs, which is followed by Sect. 122.4 for the result and discussion. In this work we have chosen the natural unit system, in which $c = \hbar = 1$. Also we have assumed $G = 1$ and the metric convention $(-, +, +, +)$ is adopted.

122.2 Equations of State

There is no single EoS which could correctly explain strange quark matters till now. So, in this study we have chosen three EoSs which are found to be quite well in describing the states of such dense matters. The MIT Bag model EoS is the simplest EoS to describe strange matters. In our case we have chosen the stiffer form of this equation as [2]

$$p = \rho - 4B. \quad (122.1)$$

We have taken three feasible values of bag constant B as $(190 \text{ MeV})^4$, $(217 \text{ MeV})^4$ and $(243 \text{ MeV})^4$. The parameter B does not affect the compactness of the stellar configuration [6], so any feasible B value gives star with compactness approximately 0.354 [3]. Another EoS that is used to describe strange matter is linear EoS of the form,

$$p = b(\rho - \rho_s), \quad (122.2)$$

where b and ρ_s are linear constant and the surface energy density, respectively. Here we have chosen $b = 0.910, 0.918$ and 0.926 . These values respect the conditions for emitting GWE frequency and the condition for causality, according to which 0.710 is the minimum and 1.000 is the maximum values of b [3]. Again we can consider SSs as polytropic spheres having polytropic EoS:

$$p = k \rho^\Gamma, \quad (122.3)$$

where k is the polytropic constant, Γ is the polytropic exponent with $\Gamma = 1 + 1/n$, n being the polytropic index. In this work we have chosen $\Gamma = 1.5, 1.67$ and 2 as guess values to describe the structure of SSs.

We have considered SSs as spherically symmetric, isotopic, stable-static configurations and neglected the stellar rotation and possible temperature effects on the EoSs. In such cases, the interior structure of the star can be obtained by solving the equations of Tolman, Oppenheimer and Volkoff (TOV), which are given as

$$\frac{d\chi}{dr} = -\frac{2}{\rho + p} \frac{dp}{dr}, \quad (122.4)$$

$$\frac{dm}{dr} = 4\pi\rho r^2, \quad (122.5)$$

$$\frac{dp}{dr} = -(\rho + p) \left(\frac{m}{r^2} + 4\pi p r \right) \left(1 - \frac{2m}{r} \right)^{-1}, \quad (122.6)$$

where $\rho = \epsilon/c^2$ is the energy density.

122.3 Echoes from Strange Stars

In GW merging events, two massive objects lead to the formation of ultra-compact objects. As mentioned earlier, recently in the GW170817 event the tentative GWE at a frequency of about 72 Hz has been claimed at 4.2σ significance level [1]. The nature of final ultra-compact object of this event is not confirmed yet. It is possible to consider it as an SS. Considering it as an SS the corresponding emitted echoes can be calculated. Now to emit GWE, the ultra-compact star should feature a photon sphere and should have the compactness (M/R) larger than $1/3$ and smaller than $4/9$. The typical echo time can be given as the light crossing time from the centre of the astrophysical object to the photon sphere [2, 4]:

$$\tau_{echo} = \int_0^{3M} \frac{1}{\sqrt{e^{\chi(r)}(1 - 2m(r)/r)}} dr. \quad (122.7)$$

From this equation, the characteristic echo time, the echo frequency can be calculated using the relation $\omega_{echo} = \pi/\tau_{echo}$ and the corresponding repetition frequency of the echo signal can be calculated using the relation $\omega_{repetition} = 1/(2\tau_{echo})$.

122.4 Discussion

In this study we have examined the possibilities of GWE from SSs for different EoSs. From this study it can be concluded that not all SSs can emit GWEs. SSs with MIT Bag model and linear EoS which fulfil the criterion for compactness and possess photon sphere can only emit GWEs. These frequencies are found to be in the

range of about tens of kilohertz. However, SSs with polytropic EoS cannot give the required compact configuration to echo GWs, hence no echo frequency is observed for polytropic SSs. The echo frequency and repetition frequency of GWs have shown a distinctive variation with different values of Bag constant B and linear constant b . It increases with the increase in values of B whereas decreases with the increase in values of b . So a model-dependent nature of GWE frequencies is observed. Again for smaller B value we have obtained larger structures. On the other hand, larger b values are corresponding to larger SS structures. In Table 122.1 and Fig. 122.1 these results are summarised. In the first panel of Fig. 122.1, the comparison of mass-radius relations of stars among all three EoSs is shown. In the second and third plots, mass-radius relationships are shown for MIT Bag model and linear EoS, respectively.

Table 122.1 Mass, radius, compactness and estimated echo times, frequencies and repetition frequencies of the echo signals for SSs predicted by different EoSs

EoSs	Model parameter	Radius R (km)	Mass M (M_0)	Compactness (M/R)	Echo time (ms)	Echo frequency (kHz)	Repetition frequency (kHz)
MIT Bag model	$B = (190 \text{ MeV})^4$	13.766	3.295	0.3540	0.078	39.91	6.35
	$B = (217 \text{ MeV})^4$	10.630	2.544	0.3540	0.060	51.70	8.23
	$B = (243 \text{ MeV})^4$	8.456	2.024	0.3540	0.048	64.98	10.34
Linear EoS	$b = 0.910$	7.535	1.775	0.3484	0.043	72.90	11.60
	$b = 0.918$	7.816	1.844	0.3489	0.044	70.21	11.18
	$b = 0.926$	8.128	1.920	0.3494	0.046	67.42	10.73
Polytropic EoS	$\Gamma = 1.50$	11.200	0.814	0.1081	–	–	–
	$\Gamma = 1.67$	7.980	0.964	0.1790	–	–	–
	$\Gamma = 2.00$	7.500	1.350	0.2600	–	–	–

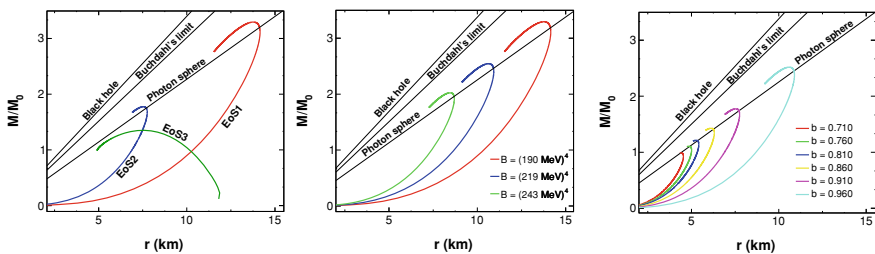


Fig. 122.1 MR curves of stars for all three EoSs (left plot), MIT Bag model with different B values (middle plot) and Linear EoS with different b values (right plot) along with the photon sphere limit, Buchdahl's limit and black hole limit lines. Here EoS1, EoS2 and EoS3 represent the MIT Bag model, Linear EoS and Polytopic EoS respectively

References

1. J. Abedi, H. Dykaar, N. Afshordi, *Phys. Rev. D* **96**(8), 082004 (2017)
2. M. Mannarelli, F. Tonelli, *Phys. Rev. D* **97**(12), 123010 (2018)
3. J. Bora, U.D. Goswami, *Mon. Not. R. Astron. Soc.* **502**(2), 1557–1568 (2021)
4. P. Pani, V. Ferrari, *Class. Quant. Grav.* **35**(15), 15LT01 (2018)
5. A. Urbano, H. Veermäe, *JCAP* **04**, 011 (2019)
6. E. Witten, *Phys. Rev. D* **30**, 272–285 (1984)

Chapter 123

Neutrino Emissivity of Dense Quark Matter in Presence of Magnetic Field



Kausik Pal

Abstract We study the effect of weak and strong magnetic fields on the emissions of neutrinos and antineutrinos involving the direct URCA processes from a normal, degenerate quark phase in the core of a compact star. It has been observed that in presence of weak magnetic field [$O(0.1) \text{ MeV}^2$] the emissivity is slightly suppressed than the field free cases, but under extremely strong magnetic fields [$O(10^4 \sim 10^5) \text{ MeV}^2$] the emissivity enhances very rapidly.

123.1 Introduction

It is known that when a new star is born following a supernova explosion, large amount of neutrinos and antineutrinos are emitted immediately from the core involving the direct or the modified URCA processes, resulting in colder core and a hotter crust, thus a temperature gradient is set up. Then the thermal energy gradually flows inward by heat conduction which alternatively might be viewed as the propagation of the cooling waves from the center toward the surface leading to thermalization. One of the subjects of contemporary research in astrophysics has been the estimation of emissive power of neutron star due to such asymmetric neutrino emission [1–3] in absence or presence of magnetic fields [4, 5]. For example, the magnetic field effect on energy loss in neutron stars through URCA and the modified URCA processes have been estimated in Ref. [4]. It has been shown in [5] that the relativistic emissivity reaches the maximum when the number of hyperons is comparable with the number of protons. It has been argued in [6] that the emissivity of strange stars is strongly dependent on the magnetic field but independent of the electron fraction. The neutrino emission physics has been further explored in [7], where the authors have examined the neutrino emissivity in a strong external magnetic field by considering the nucleon-nucleon scattering via the bremsstrahlung process. Being motivated by series of these

K. Pal (✉)

Department of Physics, Serampore College, Serampore 712201, West Bengal, India
e-mail: kausik.sinp@gmail.com

works, in this proceedings we plan to discuss a comparative study of weak and strong magnetic field effect on neutrino emissivity of dense quark matter with the field free cases.

123.2 Emissivity in Absence and Presence of Magnetic Field

The dominant contribution to the emission of neutrinos is given by the quark analogues of β decay (β) and the electron capture (ec) processes [2]

$$d \rightarrow u + e^- + \bar{\nu}_e \text{ and } u + e^- \rightarrow d + \nu_e. \quad (123.1)$$

The neutrino emissivity is related to the total energy loss due to neutrino emission averaged over the initial quark spins and summed over the final state phase space and spins. It is given by Schäfer and Schwenzer [2]

$$\begin{aligned} \varepsilon = g \int \frac{d^3 p_d}{(2\pi)^3} \frac{1}{2E_d} \int \frac{d^3 p_u}{(2\pi)^3} \frac{1}{2E_u} \int \frac{d^3 p_e}{(2\pi)^3} \frac{1}{2E_e} \int \frac{d^3 p_\nu}{(2\pi)^3} \frac{1}{2E_\nu} \\ E_\nu \{ |M_\beta|^2 (2\pi)^4 \delta^4(P_d - P_u - P_e - P_\nu) n(p_d) [1 - n(p_u)] [1 - n(p_e)] \\ + |M_{ec}|^2 (2\pi)^4 \delta^4(P_u + P_e - P_d - P_\nu) n(p_u) n(p_e) [1 - n(p_d)] \} \end{aligned} \quad (123.2)$$

where g is the spin and color degeneracy and E , n_p , P are the energy, distribution function and four-momentum for the corresponding particle. $|M_{\beta/ec}|^2$ is the squared invariant amplitude averaged over initial d quark spin and summed over final spins of u quark and electron is given by Iwamoto [1], Schäfer and Schwenzer [2], Pal and Dutt-Mazumder [3]

$$|M_{\beta/ec}|^2 = \frac{1}{2} \sum_{\sigma_u, \sigma_d, \sigma_e} |M_{fi}|^2 = 64G^2 \cos^2 \theta_c (P_d \cdot P_\nu) (P_u \cdot P_e) \quad (123.3)$$

Using Eq. (123.3) and performing the integration of Eq. (123.2) following the procedure defined in [1], we have the emissivity in absence of any magnetic field is

$$\varepsilon = \frac{457}{630} G^2 \cos^2 \theta_c \alpha_s \mu_u \mu_d \mu_e T^6 \quad (123.4)$$

where α_s is the strong coupling constant and θ_c is the Cabibbo angle ($\cos^2 \theta_c \simeq 0.948$).

Now, we proceed to calculate the neutrino emissivity in external weak magnetic field which is applied along the positive z axis, i.e., $\mathbf{B} = B\hat{k}$, is not strong enough to force the electrons in the lowest Landau level. The spinors remain unaffected for which the matrix element for the processes given by Eq. (123.3) is unaltered and only modification enters through the phase space factor. In this situation quarks phase space factor remain same and replacing the electron phase space factor [4]

$$\int \frac{d^3 p_e}{(2\pi)^3} \rightarrow \frac{eB}{(2\pi)^2} \sum_{n=0}^{n_{max}} (2 - \delta_{n,0}) \int dp_z \quad (123.5)$$

where n is the Landau level. Using the standard techniques as described by Iwamoto [1] to perform the phase space integrals, finally the neutrino emissivity in presence of weak magnetic field is given by

$$\varepsilon = \frac{457}{1260} G^2 \cos^2 \theta_c \alpha_s \mu_d \mu_u e B T^6 \times \sum_{n=0}^{n_{max}} (2 - \delta_{n,0}) \frac{1}{\sqrt{\mu_e^2 - m_e^2 - 2neB}} \quad (123.6)$$

where $n_{max} = \text{Int}\left(\frac{\mu_e^2 - m_e^2}{2eB}\right)$. The chemical potential of quarks is determined by using the charge neutrality and beta equilibrium conditions [4]. In the limit of vanishing magnetic field ($B = 0$), the sum can be replaced by integral and we recover the usual expression as given by Eq. (123.4).

Now, in presence of high magnetic field modifies the energy of charged particles confining them to low Landau levels. This results in shifting of beta equilibrium and the composition of matter gets significantly modified. It is well known that this quantization effect is important when the field strength is equal to or larger than some critical value $B^{(c)} = \frac{m_l^2 c^3}{q_l \hbar}$ Gauss, where notations have their usual meaning. In the interior of the star particularly in the central region, where the magnetic fields are so strong ($\sim 10^{18}$ G), they must affect most of the physical properties of those strange stellar objects. This is because charged particles populate the Landau levels [7]. The neutrino emissivity in presence of strong field considering the weak processes given by Eq. (123.1), was calculated detail in [6], for brevity we quote the final result.

$$\varepsilon(B) = \frac{3\sqrt{2\pi} G^2 \cos^2 \theta_c e B}{16(2\pi)^6} [\pi^2 \zeta(3) + 15 \zeta(5)] T^5 \int_{-\sqrt{eB}/2}^{\sqrt{eB}/2} dp_{ey} \int_{-\sqrt{2eB/3}/2}^{\sqrt{2eB/3}/2} dp_{uy} \exp\left[-\frac{p_{uy}^2}{eB} - \frac{5(p_{ey} + p_{uy})^2}{2eB} - \frac{p_{ey}^2}{2eB} - \frac{p_{uy}(p_{ey} + p_{uy})}{eB} - \frac{p_{uy} p_{ey}}{eB} + \frac{(p_{ey} + p_{uy}) p_{ey}}{eB}\right]. \quad (123.7)$$

In order to compare the emissivity in presence of strong magnetic field with the field free case, we define the enhancement factor $Y = \frac{\varepsilon(B)}{\varepsilon}$.

123.3 Results and Discussion

In Fig. 123.1, we have shown the weak magnetic field ($\sim 0.1 \text{ MeV}^2$) effect on neutrino emissivity. From the subset of Fig. 123.1, it has been observed that the weak magnetism effects slightly suppresses the emissivity than the unmagnetized case. On the other hand, if the magnetic field of moderate strength ($B > 10^2 \text{ MeV}^2$) is applied, the emissivity enhances. These magnetic field effects can be explained as follows. In Eq. (123.6), we find there exist ‘eB’ in three places. One is linear in ‘eB’ as expected from weak field expansion, one is in the denominator inside the square-root and another is in the denominator of the n_{max} , i.e., maximum number of terms up to which the summation of the Landau level has to be done. Now, if ‘eB’ is small, the linear term as well as each term in the series is small, but the number of terms in the summation is large. These two opposing effects determine the exact behavior of the emissivity. If the field strength increases further above the critical value, all the electrons occupy the Landau ground state which corresponds to $n = 0$ state with electron spins pointing in the direction opposite to the magnetic field. In this situation summation on the Landau level no longer exist and the matrix element should not be unchanged, which can be evaluated using the exact solutions of the Dirac equation [6]. In Fig. 123.2, we have plotted the variation of enhancement factor as function of magnetic field for three different temperatures. It has been observed that in presence of ultra-strong magnetic field, i.e., $B \sim 10^4 \text{ MeV}^2$ or more, the emissivity enhances very rapidly compare to its value in absence of magnetic field. This enhancement may be attributed to the phase space modification and to the change in the dynamical

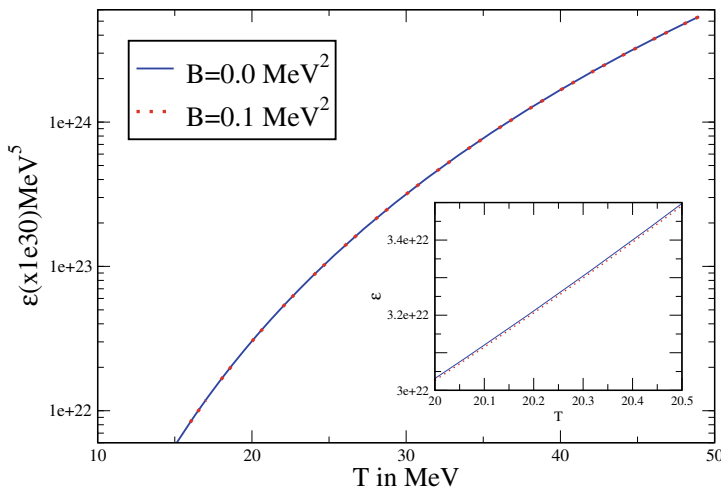


Fig. 123.1 Weak magnetic field effect on neutrino emissivity

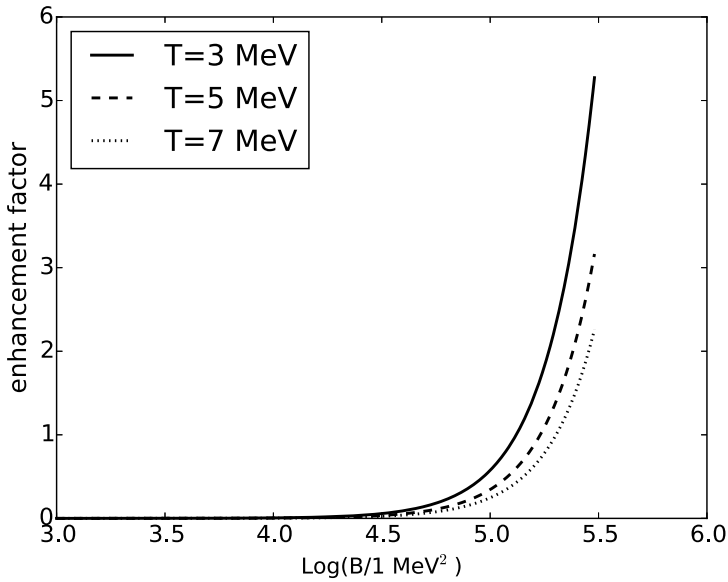


Fig. 123.2 Enhancement factor as function of magnetic field for different temperatures

β -equilibrium conditions. Moreover, the enhancement on the emissivity is higher for the lower temperature. Therefore, the thermal evolution of the neutron stars in the late-time cooling era for $B \geq 10^2 \text{ MeV}^2$ can be dramatically changed [7].

References

1. N. Iwamoto, Ann. Phys. (N.Y.) **141**, 1 (1982)
2. T. Schäfer, K. Schwenzer, Phys. Rev. D **70**, 114037 (2004)
3. K. Pal, A.K. Dutt-Mazumder, Phys. Rev. D **84**, 034004 (2011)
4. A. Goyal, V.K. Gupta, K. Goswami, V. Tuli, Int. J. Mod. Phys. A **16**, 347 (2001)
5. L.B. Leinson, Phys. Lett. B **532**, 267 (2002)
6. X.W. Liu, X.P. Zheng, D.-F. Hou, Astropart. Phys. **24**, 92 (2005)
7. E. Bavarsad, H. Haghighat, R. Mohammadi, Phys. Rev. D **82**, 105015 (2010)

Chapter 124

Majorana Dark Matter and Neutrino Mass in a Singlet-Doublet Extension of the Standard Model



Manoranjan Dutta, Subhaditya Bhattacharya, Purusottam Ghosh,
and Narendra Sahu

Abstract A minimal extension of the Standard Model (SM) by a vector-like fermion doublet and three right-handed (RH) singlet neutrinos is proposed in order to explain dark matter and tiny neutrino mass simultaneously. The DM arises as a mixture of the neutral component of the fermion doublet and one of the RH neutrinos, both assumed to be odd under an imposed \mathcal{Z}_2 symmetry. Being Majorana in nature, the DM escapes from Z -mediated direct search constraints to mark a significant difference from singlet-doublet Dirac DM. The other two \mathcal{Z}_2 even heavy RH neutrinos give rise masses and mixing of light neutrinos via Type-I Seesaw mechanism. Relic density and direct search allowed parameter space for the model is investigated through detailed numerical scan.

124.1 Introduction

Despite compelling evidences from galaxy rotation curves, gravitational lensing, cosmic microwave background (CMB), etc., we are yet to pin down what dark matter (DM) actually is. Among different class of possibilities, Weakly Interacting Massive Particles (WIMPs), where DM acts as a thermal relic from the early universe and can be probed via both direct and collider search experiments is a promising framework. Tiny yet non-zero masses of the neutrinos is another potential mystery, which we simultaneously address in this framework, where the SM has been extended min-

M. Dutta (✉) · N. Sahu

Department of Physics, Indian Institute of Technology Hyderabad, Kandi 502285,
Telangana, India

e-mail: ph18resch11007@iith.ac.in

S. Bhattacharya

Department of Physics, Indian Institute of Technology Guwahati, North Guwahati 781039,
Assam, India

P. Ghosh

Regional Centre for Accelerator-based Particle Physics, Harish-Chandra Research Institute,
HBNI, Chhatnag Road, Jhansi 211019, Allahabad, India

© The Author(s), under exclusive license to Springer Nature Singapore Pte Ltd. 2022
B. Mohanty et al. (eds.), *Proceedings of the XXIV DAE-BRNS High Energy Physics
Symposium, Jaitni, India*, Springer Proceedings in Physics 277,
https://doi.org/10.1007/978-981-19-2354-8_124

685

imally with a vector-like fermion doublet and three right-handed singlet neutrinos (see [1]). Right-handed neutrino having same Z_2 charge as of the vector-like doublet, mixes with the neutral component of the doublet to render a stable Majorana DM after electroweak symmetry breaking (EWSB). The Majorana nature of the DM marks a crucial difference from the singlet-doublet Dirac DM studied earlier [2] in relic density and direct search allowed parameter space. It is worthy to note that only singlet or only doublet fermion DM is phenomenologically constrained significantly.

124.2 The Model for Singlet-Doublet Majorana Dark Matter

In this work, the SM is extended by one vector-like fermion doublet (VLFd) $\Psi^T = (\psi^0, \psi^-)$ (with hypercharge $Y = -1$ where $Q = T_3 + Y/2$) and three heavy right-handed singlet neutrinos (RHN) N_{R_i} ($i = 1, 2, 3$). An additional Z_2 symmetry is imposed under which Ψ and N_{R_1} are odd, while all other fields are even. The Lagrangian of the model is given by

$$\begin{aligned} \mathcal{L} = & \mathcal{L}_{SM} + \bar{\Psi} (i\gamma^\mu D_\mu - M) \Psi + \overline{N_{R_i}} i\gamma^\mu \partial_\mu N_{R_i} - \left(\frac{1}{2} M_{R_i} \overline{N_{R_i}} (N_{R_i})^c + h.c\right) \\ & - \left[\frac{Y_1}{\sqrt{2}} \bar{\Psi} \tilde{H} (N_{R_1} + (N_{R_1})^c) + h.c \right] - \left(Y_{j\alpha} \overline{N_{R_j}} \tilde{H}^\dagger L_\alpha + h.c. \right), \end{aligned} \tag{124.1}$$

where $\tilde{H} = i\tau_2 H^*$ and L denotes SM lepton doublet with indices $j = 2, 3$ and $\alpha = e, \mu, \tau$. N_{R_1} being odd under Z_2 has Yukawa coupling (Y_1) with fermion doublet Ψ and determines the lightest stable component as DM after EWSB. N_{R_2} and N_{R_3} being assumed even under Z_2 , don't couple to Ψ , but couple to the SM lepton doublets ($\sim Y_{j\alpha}$) generating Dirac masses for SM neutrinos after EWSB. The mass terms for the dark sector (after EWSB) can be written as

$$- \mathcal{L}_{mass} = M \overline{\psi_L^0} \psi_R^0 + \frac{1}{2} M_{R_1} \overline{N_{R_1}} (N_{R_1})^c + \frac{m_D}{\sqrt{2}} (\overline{\psi_L^0} N_{R_1} + \overline{\psi_R^0} (N_{R_1})^c) + h.c, \tag{124.2}$$

where $m_D = \frac{Y_1 v}{\sqrt{2}}$, where $v = 246$ GeV. In $((\psi_R^0)^c, \psi_L^0, (N_{R_1})^c)^T$ basis, the mass matrix becomes

$$\mathcal{M} = \begin{pmatrix} 0 & M & \frac{m_D}{\sqrt{2}} \\ M & 0 & \frac{m_D}{\sqrt{2}} \\ \frac{m_D}{\sqrt{2}} & \frac{m_D}{\sqrt{2}} & M_{R_1} \end{pmatrix}. \tag{124.3}$$

The symmetric matrix \mathcal{M} can be diagonalised by $\mathcal{U} \mathcal{M} \mathcal{U}^T = \mathcal{M}_{Diag.}$, where

$$\mathcal{U} = \begin{pmatrix} 1 & 0 & 0 \\ 0 & e^{i\pi/2} & 0 \\ 0 & 0 & 1 \end{pmatrix} \begin{pmatrix} \frac{1}{\sqrt{2}} \cos \theta & \frac{1}{\sqrt{2}} \cos \theta & \sin \theta \\ -\frac{1}{\sqrt{2}} & \frac{1}{\sqrt{2}} & 0 \\ -\frac{1}{\sqrt{2}} \sin \theta & -\frac{1}{\sqrt{2}} \sin \theta & \cos \theta \end{pmatrix}. \tag{124.4}$$

The extra phase matrix is multiplied to make sure all the eigenvalues are positive. The diagonalisation of the mass matrix (Eq. 124.3) requires $\tan 2\theta = \frac{2m_D}{M-M_{R_1}}$. All the three physical states χ_1, χ_2 and χ_3 are therefore of Majorana nature and their mass eigenvalues in the small mixing limit ($\theta \rightarrow 0$) are given by

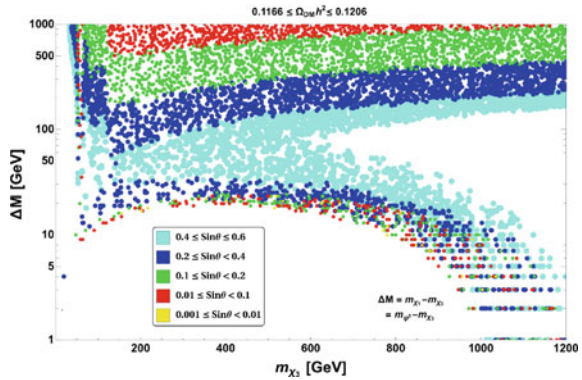
$$m_{\chi_1} \approx M + \frac{m_D^2}{M - M_{R_1}}, m_{\chi_2} = M, m_{\chi_3} \approx M_{R_1} - \frac{m_D^2}{M - M_{R_1}}, \tag{124.5}$$

where we have assumed $m_D \ll M, M_{R_1}$. It is clear that $m_{\chi_1} > m_{\chi_2} > m_{\chi_3}$ and therefore χ_3 becomes the stable DM candidate. The phenomenology of dark sector is therefore governed by the three independent parameters, viz., the DM mass (m_{χ_3}), its mass splitting with the heavier neutral component ($\Delta M = m_{\chi_1} - m_{\chi_3} \approx m_{\chi_2} - m_{\chi_3}$), and the doublet-singlet mixing ($\sin \theta$).

124.3 Relic Abundance and Direct Search Prospects

DM (χ_3) has both gauge interactions (via doublet) and Higgs-portal interactions (via Y_1) with SM, which keeps it in thermal bath in the early universe and thereafter ‘freezes out’ via the number changing processes to provide the correct DM relic density ($\Omega h^2 \simeq 0.1$), provided by PLANCK data [3]. Using MicrOmegas [4], we calculate relic density allowed parameter space of the model, shown in Fig. 124.1, in the $\Delta M - m_{\chi_3}$ plane for different $\sin \theta$ ranges (see figure inset). The region with smaller ΔM has larger co-annihilation contribution like $\chi_3 \chi^\pm \rightarrow SM$, a crucial feature of singlet-doublet frameworks.

Fig. 124.1 DM relic density ($0.1166 \leq \Omega_{DM} h^2 \leq 0.1206$) allowed parameter space in the plane of ΔM vs m_{χ_3} for the singlet-doublet Majorana DM model



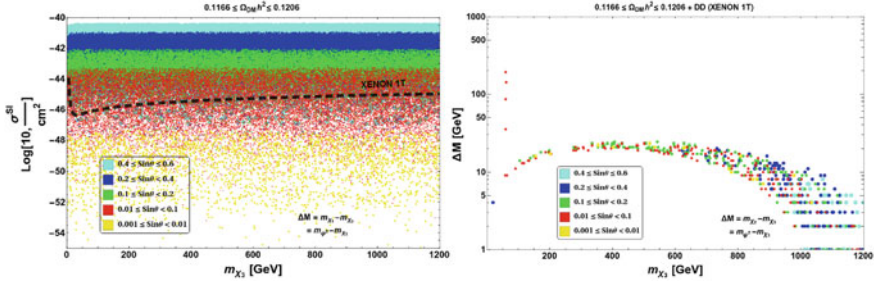


Fig. 124.2 [Left]: Direct detection cross section for the DM (χ_3) confronted with bounds on spin-independent elastic scattering cross section by XENON-1T; [Right]: Correct DM relic density in $\Delta M - m_{\chi_3}$ plane constrained by XENON-1T bound

Direct detection of DM is possible through elastic scattering of the DM with detector nuclei via Higgs-portal interaction (Y_1). Being a Majorana fermion, the DM does not have Z-mediated elastic scattering. In the left panel of Fig. 124.2, we confront the direct detection cross section for the model as a function of DM mass with XENON-1T data (shown by black dashed curve) [5]. The points allowed by both relic and direct search constraints are shown in the right panel of Fig. 124.2, in the $\Delta M - m_{\chi_3}$ plane. We see that direct search constraints limits ΔM (upto 10–15 GeV, excepting resonance region, $m_{\chi_3} \sim m_Z/2$) and mixing $\sin \theta \leq 0.6$ as Higgs-portal coupling $Y_1 = \frac{\sqrt{2}\Delta M \sin 2\theta}{v}$. Somewhat larger mixing with doublet ($\sin \theta \sim 0.6$) as allowed here, crucially distinguishes the model from singlet-doublet Dirac DM case, where $\sin \theta \sim 0.05$ [2] is much smaller due to the presence of Z mediated direct search interaction.

124.4 Non-zero Neutrino Mass

A tiny neutrino mass is generated via Type-I seesaw from parts of Eq. 124.1,

$$-\mathcal{L}_{mass}^{\nu} \supset \left(Y_{j\alpha} \overline{N}_{R_j} \tilde{H}^{\dagger} L_{\alpha} + h.c. \right) + \left(\frac{1}{2} M_{R_j} \overline{N}_{R_j} (N_{R_j})^c + h.c. \right). \quad (124.6)$$

where $\alpha = e, \mu, \tau$ and $j = 2, 3$. In the basis where the heavy Majorana mass matrix that takes part in seesaw is diagonal, i.e., $M_R = \text{Diag}(0, M_{R_2}, M_{R_3})$, the light neutrino mass matrix obtained through Type-I seesaw is given by $m_{\nu} = -m_D M_R^{-1} m_D^T$.

124.5 Conclusion

In an arguably simplest extension of SM with a vector-like doublet (Ψ) and three RHNS (N_{R_i}), one achieves a stable Majorana fermion DM out of doublet-singlet mixing having same Z_2 charge, and correct neutrino mass via Seesaw I mechanism. The relic density and direct search allowed parameter space of the model allows one to search for the model at Large Hadron Collider with leptonic signature accompanied with missing energy or with disappearing charge track and also provides a possible distinction with singlet-doublet Dirac DM through the mixing parameter ($\sin \theta$).

References

1. M. Dutta, S. Bhattacharya, P. Ghosh, N. Sahu, JCAP **03**, 008 (2021)
2. S. Bhattacharya, N. Sahoo, N. Sahu, Phys. Rev. D **96**(3), 035010 (2017); S. Bhattacharya, P. Ghosh, N. Sahu, JHEP **02**, 059 (2019); S. Bhattacharya, N. Sahoo, N. Sahu, Phys. Rev. D **93**(11), 115040 (2016); S. Bhattacharya, P. Ghosh, N. Sahoo, N. Sahu, Front. Phys. **7**, 80 (2019)
3. P.A.R. Ade et al. [Planck], Astron. Astrophys. **571**, A16 (2014)
4. G. Belanger, F. Boudjema, A. Pukhov, A. Semenov, Comput. Phys. Commun. **180**, 747–767 (2009)
5. E. Aprile et al. [XENON], Phys. Rev. Lett. **121**(11), 111302 (2018)

Chapter 125

Effect of Dark Matter in Compact Realistic Neutron Stars Matter



P. K. Sahu, D. K. Mishra, and S. P. Behera

Abstract We study the Fermionic dark matter inside the neutron star, which couples to nucleons through Higgs field via effective Yukawa coupling. The neutron star matter consists of leptons, nucleons and hyperons in the relativistic chiral sigma model. If the dark matter composition is increased then the neutron star gets more compact and hence the size and mass reduce significantly. For example, if there is no dark matter and with dark matter Fermi momenta 0.04 and 0.06 GeV, then the maximum masses and radii of neutron star are 2.2, 1.8 and 1.7 times solar mass and 10, 9.5 and 8.5 km, respectively. The moment of inertia, redshifts of the neutron star are also calculated.

125.1 Introduction

Data from cosmological and astrophysical observation have been suggested that the non-relativistic matter of the Universe is dominated by an unknown type of matter particles and yet to be discovered is known as dark matter (DM). In 1933, Zwicky first introduced the term “missing mass” or dark matter [1], during the analysis of cluster of galaxies. After four decades, Rubin and Ford in 1970 made the case for DM with optical study of M31 [2]. In recent years, though there are many DM candidates, still the origin and nature of DM remains a mystery and is one of the biggest challenges in astrophysics and cosmology [3]. In the present work, we have assumed that the DM matter and normal nuclear matter interact through the gravity. There are many popular models where the DM particle interacts directly with the baryons by exchanging the standard model Higgs bosons [4].

On the other hand, the dense stellar objects such as neutron stars are considered to be very fundamental in nature, as these are governed by the interaction of standard

P. K. Sahu (✉)

Institute of Physics, HBNI, Sachivalaya Marg, Bhubaneswar 751005, Odisha, India
e-mail: pradip@iopb.res.in

D. K. Mishra · S. P. Behera

Bhabha Atomic Research Centre, Trombay 400085, Mumbai, India

model particles from macro to micro size ranging from very low to high densities regions. The best object is known in nature as the neutron stars, which links to quantum hydrodynamics to quantum chromo dynamics. These are mainly characterised with their gross structures such as maximum mass and radius. The maximum mass and radius are mainly dominated by the composition of the standard model particles at the core of the neutron stars. Recently, the maximum mass are predicted to be in the range of $1.97 \pm 0.04 M_\odot$ [5].

In this work, the nuclear equation of state (EoS) of baryons is calculated based on the framework of relativistic chiral sigma mean-field theory, then the interaction between DM and baryons is considered through the realistic values for the Yukawa coupling constants.

125.2 The Relativistic Chiral Sigma Model

The $SU(2)$ chiral sigma Lagrangian can be written as [6, 7]

$$\begin{aligned} \mathcal{L}_{had} = & \frac{1}{2}(\partial_\mu \pi \cdot \partial^\mu \pi + \partial_\mu \sigma \partial^\mu \sigma) - \frac{1}{4}F_{\mu\nu}F_{\mu\nu} + \frac{1}{2}g_{N\omega}^2 x^2 \omega_\mu \omega^\mu \\ & - \frac{\lambda}{4}(x^2 - x_o^2)^2 - \frac{\lambda b}{6m^2}(x^2 - x_o^2)^3 - \frac{\lambda c}{8m^4}(x^2 - x_o^2)^4 \\ & - \sum_i g_{i\sigma} \bar{\psi}_i (\sigma + i\gamma_5 \tau \cdot \pi) \psi_i + \bar{\psi}_i (i\gamma_\mu \partial^\mu - g_{i\omega} \gamma_\mu \omega^\mu) \psi_i \quad (125.1) \end{aligned}$$

Here $F_{\mu\nu} \equiv \partial_\mu \omega_\nu - \partial_\nu \omega_\mu$ and $x^2 = \pi^2 + \sigma^2$. In the Lagrangian, ψ_i is for nucleons, Λ , Σ^- and Ξ hyperons (denoted by subscript i), π is the pseudoscalar-isovector pion field and σ is the scalar field. Here, we have considered the modified non-linear chiral-sigma model STO-5 [7]. The masses of the nucleon, the scalar meson and the vector meson are respectively given by $m = g_\sigma x_o$, $m_\sigma = \sqrt{2\lambda}x_o$, and $m_\omega = g_\omega x_o$. Here x_o is the vacuum expectation value of the σ field, $\lambda = (m_\sigma^2 - m_\pi^2)/(2f_\pi^2)$, with m_π is the pion mass and f_π the pion decay coupling constant, and $g_{N\omega} = g_\omega$ and $g_{N\sigma} = g_\sigma$ are the coupling constants for the vector and scalar fields, respectively.

By adopting mean-field approximation, the equation of motion for fields is obtained and the EoS is evaluated for high density nuclear matter. We have ignored the explicit role of π mesons in the mean field treatment.

The equation of motion for the scalar field in terms of effective nucleon mass is $(1 - R^2) - \frac{b}{m^2 c_\omega} (1 - R^2)^2 + \frac{c}{m^4 c_\omega^2} (1 - R^2)^3 + \frac{2c_\sigma c_\omega n_F^2}{m^2 R^4} - \sum_i \frac{c_\sigma \gamma}{\pi^2} \int_0^{k_F} \frac{k^2 dk}{\sqrt{k^2 + m^{*2}}} = 0$, where $m^* \equiv Rm$ is the effective mass of the nucleon, $c_\sigma \equiv g_\sigma^2/m_\sigma^2$ and $c_\omega \equiv g_\omega^2/m_\omega^2$ are scalar and vector coupling constants, respectively, and b and c are constant parameters of the higher-order self-interaction of the scalar field. The constant unknown parameters are determined in the similar method as given in Ref. [7]. The equation of motion for the iso-scalar vector field is given by $\omega_0 = \frac{g_\omega x^2 \gamma}{(2\pi)^3} \int_0^{k_F} d^3k$. The quantity k_F is the Fermi momentum and γ is the baryon spin degeneracy factor.

The effect of Fermionic DM trapped inside the neutron star on the nuclear EoS is considered. The DM particle χ , the Higgs boson h with mass $M_h = 125$ GeV, a DM-Higgs Yukawa coupling $y = 0.07$, and a nucleon-Higgs Yukawa coupling $f m_N/v$, with $v = 246$ GeV is the Higgs vacuum expectation value and f parameterizes the Higgs-nucleon coupling ($f = 0.3$) [8]. Therefore, the system is described by the Lagrangian density as

$$\mathcal{L} = \mathcal{L}_{had} + \bar{\chi}(i\gamma_\mu\partial^\mu - M + yh)\chi + \frac{1}{2}\partial_\mu h\partial^\mu h - V(h) + \frac{f m_N}{v}\bar{\psi}h\psi, \quad (125.2)$$

where $V(h)$ is the Higgs potential containing the Higgs mass term as well its self-interactions $V(h) = \frac{1}{2}M_h^2 h^2 - \lambda v h^3 - \frac{1}{4}\lambda h^4$, M and y are free parameters. The supersymmetric lightest neutralino χ is considered as fermionic DM, mass $M = 200$ GeV, while for the DM-Higgs coupling we use the expression as given in Ref. [8]. Finally, we assume that inside the neutron star, the DM average number density is ~ 500 times smaller than the average nuclear number density [8]. Using the mean-field approximation, the effective masses $m_i^* = -g_\sigma\sigma_0 - fh_0$ and $M_\chi^* = M - yh_0$ for baryons and DM fermionic particles, respectively, where the constant value of the Higgs boson, $h_0 = f n_s(m_i^*)/M_h^2 + y n_s(M_\chi^*)/M_h^2$, neglecting the Higgs self-interactions. Therefore, the total pressure and energy density of the system are given by $p = \sum_i p_{FG}(m_i^*, \mu^i) + p_{FG}(M_\chi^*) - T1 + T2 - T3 + T4 - \frac{M_h^2 h_0^2}{2}$, $\epsilon = \sum_i \epsilon_{FG}(m_i^*, \mu^i) + \epsilon_{FG}(M_\chi^*) + T1 - T2 + T3 + T4 + \frac{M_h^2 h_0^2}{2}$. Where, $T1 = \frac{m^2(1-R^2)^2}{8c_\sigma}$, $T2 = \frac{b(1-R^2)^3}{12c_\omega c_\sigma}$, $T3 = \frac{c(1-R^2)^4}{16m^2 c_\omega^2 c_\sigma}$, $T4 = \frac{c_\omega n_B^2}{2R^2}$. The EoS can be obtained after the system of coupled algebraic equations for σ_0, h_0 are solved numerically.

125.3 Results and Discussion

After the inclusion of hyperons and leptons, the total EoS can be calculated for a given composition of the baryon components. Since neutron star matter consists of hyperons, nucleons and leptons, we have introduced the ρ mesons and the parameter has been calculated following the Refs. [9, 10]. This allows the determination of the chemical potentials of all species from the equations of chemical equilibrium: $\mu_n = \mu_p + \mu_e$, $\mu_e = \mu_\mu$, $2\mu_n = \mu_p + \mu_\Sigma$, $\mu_n = \mu_\Lambda$. Also, we set the neutrino chemical potentials equal to zero. The above equations must be supplemented with two other conditions, i.e., charge neutrality and baryon number conservation. These are $n_p = n_e + n_\mu + n_\Sigma$, $n_B = n_n + n_p + n_\Sigma + n_\Lambda$. Using all these conditions and including all species of particles, we finally determined the EoS of neutron star matter.

The mass-radius diagram has been obtained for non-rotating neutron stars by integrating the TOV equations [9, 10] numerically, $m'(r) = 4\pi r^2 \epsilon(r)$ and $p'(r) = -(\epsilon(r) + p(r)) \frac{m(r) + 4\pi p(r)r^3}{r^2(1-2m(r)/r)}$, where r is the radial distance, and the prime denotes differentiation with respect to r . These equations are solved using boundary con-

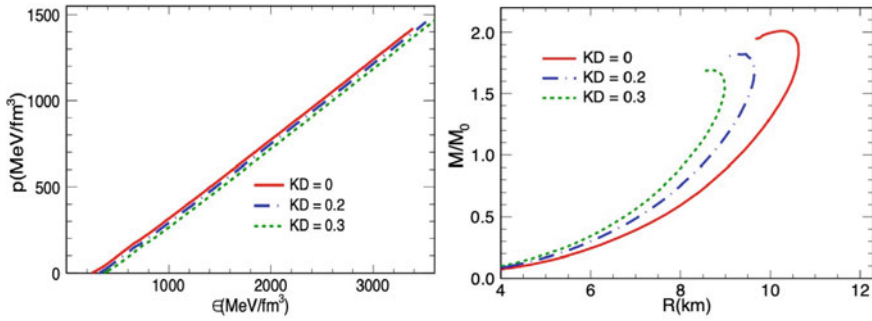


Fig. 125.1 Left panel is shown EoS (ϵ versus p) of the system neutron star matter -DM for $KD=0$, without Dark Matter (solid curve), $KD=0.2 \text{ fm}^{-1}$, ($n_D = n_B/500$, dashed curve) and $KD=0.3 \text{ fm}^{-1}$, ($n_D = n_B/150$, dotted curve). Right panel is shown radius versus neutron star mass

ditions as given in Refs. [6, 9, 10] to find M and R . The left panel in Fig. 125.1, shows pressure versus energy density, for two different values of the DM wave number $k_F^\chi = KD = 0.2 \text{ fm}^{-1}$ (dashed curve) and $k_F^\chi = KD = 0.3 \text{ fm}^{-1}$ (dotted curve). The EoS without DM (solid curve) is also shown for comparison. We see that DM softens the EoS, and therefore one can expect a lower maximum neutron star mass in the mass-radius diagram compared to the purely hadronic case without DM. In, right panel in Fig. 125.1 shows the radius R of the star (in km) as a function of the star mass M_\odot . As already anticipated, the admixed DM-neutron star can support a lower maximum star mass. In the case of pure neutron star, the maximum star mass is found to be $M_{max}^{KD=0} = 2.2M_\odot$ [5], redshift $\phi = 0.5$ [11], moment of inertia $I = 2.1 \times 10^{45} \text{ g/cm}^2$, while in the case of admixed DM-neutron star ($KD = 0.2$ and $KD = 0.3$), it is found to be $M_{max}^{DM} = 1.8$ and $1.7M_\odot$ [5], $\phi = 0.5$ and 0.5 and $I = 1.6 \times 10^{45} \text{ g/cm}^2$ and $1.2 \times 10^{45} \text{ g/cm}^2$, respectively. Furthermore, for a given neutron star mass a compact object made of both hadronic matter and DM is considerably smaller than a compact object made of neutron star matter only.

125.4 Conclusion

In the present work, we have studied the dark matter effect on realistic chiral sigma EoS for baryon matter in neutron stars. We have assumed that the DM particle is a fermion, and interact with the standard model (SM) particles through the SM model Higgs boson. We have applied the relativistic mean-field theory and evaluated the EoS for the system numerically. We have displayed the EoS and the mass-to-radius relation with and without DM. The maximum star mass for all cases has been reported.

References

1. F. Zwicky, *Helv. Phys. Acta* **6**, (1933) 110; *Gen. Relativ. Gravit.* **41**, 207 (2009)
2. V. C. Rubin, Jr. W. K. Ford, *Astrophys. J.* **159**, 379 (1970)
3. M. Taoso et al., *J. Cosmol. Astropart. Phys.* 022 (2008); C. Munoz, *Int. J. Mod. Phys. A* **19**, 3093 (2004)
4. S. Andreas et al., *J. Cosmol. Astropart. Phys.* 034 (2008)
5. P. Demorest et al., *Nature* **467**, 1081 (2010); J. Antoniadis et al., *Science* **340**, 448 (2013)
6. P. K. Sahu et al., *Astrophys. J.* **416**, 267 (1993)
7. P. K. Sahu et al., *Phys. Rev. C* **81**, 014002 (2010); P. K. Sahu, A. Ohnishi, *Prog. Theor. Phys.* **104**, 1163 (2000); P. K. Sahu et al., *Nucl. Phys.* **A733**, 169 (2004)
8. G. Panotopoulos, I. Lopes, *Phys. Rev. D* **96**, 083004 (2017)
9. P. K. Sahu, *Phys. Rev. C* **62**, 045801 (2000); P. K. Sahu, A. Ohnishi, *Nucl. Phys.* **A691**, 439 (2001)
10. G. F. Burgio et al., *Phys. Rev. C* **66**, 025802 (2002)
11. J. M. Lattimer, *Universe* **5**(7), 159 (2019)

Chapter 126

Signal of Statistical Anisotropy in PLANCK Cosmic Microwave Background Polarization Maps



**Pramoda Kumar Samal, Pranati K. Rath, Srikanta Panda, Pavan K. Aluri,
and Debesh D. Mishra**

Abstract We apply our symmetry-based Power tensor technique to test statistical isotropy in PLANCK polarization maps, viz., COMMANDER and NILC. Our preliminary analysis detects many statistically anisotropic multipoles in foreground cleaned full sky maps over a wide range of angular scales $l = 40 - 150$. We also study the effect of residual foregrounds that may still be present in the Galactic plane using the polarization masks. We further probed the data for any coherent alignments across multipoles in several bins from the chosen multipole range.

126.1 Introduction

The standard cosmological model is based on the postulate that the Universe is homogeneous and isotropic on large distance scales. However, there exist many observations which suggest that this postulate is violated. The existence of a preferred axis observed from various data, particularly those of polarization of radio waves, optical polarization from quasars, and low multipoles in CMB $l = 1, 2, 3$, point toward Virgo and is supported by many observations [1–6]. This phenomenon

P. K. Samal (✉)

School of Physics, Gangadhar Meher University, Sambalpur, India

e-mail: pkksamal@gmuniversity.ac.in

P. K. Samal · S. Panda

Department of Physics, Utkal University, Bhubaneswar, India

P. K. Rath

Department of Physics, Khallikote (Autonomous) College, Berhampur, India

P. K. Aluri

Department of Physics, IIT(BHU), Varanas, Uttar Pradesh, India

D. D. Mishra

Hubei University, Wuhan, China

has been called Virgo alignment puzzle. Besides the Virgo alignment, there also exist statistically significant signals of anisotropy in CMB temperature data, viz., hemispherical power asymmetry [7], parity asymmetry [8, 9], and a region of significant temperature decrement known as cold spot [10]. Here we probe statistical anisotropy, if any, in the PLANCK CMB polarization data using our symmetry-based method [6].

The basic maps for the case of polarization are available in terms of the Stokes parameters Q and U . These are coordinate dependent variables and it is convenient to work with the coordinate independent E and B modes. For this purpose one first expands the spin ± 2 fields ($Q \pm iU$) in terms of spin-2 spherical harmonics ${}_{\pm 2}Y_{lm}(\hat{n})$, i.e., $(Q + iU)(\hat{n}) = \sum_{lm} a_{2,lm} {}_2Y_{lm}(\hat{n})$ and $(Q - iU)(\hat{n}) = \sum_{lm} a_{-2,lm} {}_{-2}Y_{lm}(\hat{n})$. For real Q and U , the expansion coefficients obey $a_{-2,lm}^* = a_{2,l-m}$. The spin-0 E and B are now given by

$$E(\hat{n}) = \sum_{l,m} a_{lm}^E Y_{lm}(\hat{n}), \quad B(\hat{n}) = \sum_{l,m} a_{lm}^B Y_{lm}(\hat{n}), \quad (126.1)$$

where $a_{lm}^E = \frac{1}{2}(a_{2,lm} + a_{-2,lm})$ and $a_{lm}^B = \frac{1}{2i}(a_{2,lm} - a_{-2,lm})$. Here, we restrict our attention to the $E(\hat{n})$ field (i.e., a_{lm}^E coefficients), to study statistical isotropy of PLANCK polarization maps.

126.2 Method

The angular orientation of each mode is given by a unique orthonormal frame $e_k^\alpha(l)$ and rotationally invariant singular values $\Lambda_\alpha(k)$ of the Power tensor, $A(l)$, defined as $A_{ij} = \frac{1}{l(l+1)(2l+1)} \sum_{m,m'} a_{lm}^* (J_i J_j)_{mm'} a_{lm'}$. Here $k = 1, 2, 3$ denote the components of the frame vector $e_k^\alpha(l)$ and $\alpha = 1, 2, 3$ stands for the singular value index. In terms of these quantities, the Power tensor matrix for each multipole ' l ' can be expressed as $A_{ij}(l) = \sum_\alpha e_i^\alpha (\Lambda^\alpha)^2 e_j^{\alpha*}$. We refer to the eigenvector corresponding to the largest eigenvalue of the Power tensor as *principal eigenvector* (PEV), and is taken to be the statistical anisotropy axis of that multipole. The preferred direction represented by a PEV of any multipole is quantified by parametrizing the dispersion of eigenvalues using *Power entropy* that is defined as

$$S_p(l) = - \sum_\alpha \lambda^\alpha \log(\lambda^\alpha) \quad (126.2)$$

where $\lambda^\alpha = (\Lambda^\alpha)^2 / \sum_\beta (\Lambda^\beta)^2$. In the ideal case of statistical isotropy, where all the three eigenvalues are degenerate and equal to $C_l/3$, we have maximum Power entropy, $S_p \rightarrow \log(3)$. In the case of a *pure state*, one of the eigenvalues contains the total power and other two vanishes, $S_p \rightarrow 0$. So for our observational data, $0 \leq S_p \leq \log(3)$. Hence low Power entropy in data, compared to consistently

generated concordance model simulations, is a measure of violation of statistical isotropy in the data. Now, a common alignment vector using PEVs for a range of multipoles can be calculated using what is called an *Alignment entropy*, defined by $S_X = -Tr(\rho_X \log(\rho_X))$, where $\rho_X = X/Tr(X)$ is the normalized 3×3 matrix ‘ X ’ that is referred to as *Alignment tensor*. It is given by $X_{ij} = \sum_{l_{min}}^{l_{max}} e^i(l)e^j(l)$, where $e(l)$ is the PEV of a multipole, l . $Tr(X)$ denotes trace of X . An unusually low value of S_X compared to $\log(3)$ confirms violation of statistical isotropy over a wider multipole range. We note that the Power entropy and the Alignment entropy are independent of each other. The significance of statistical anisotropy is determined by a P -value, which is defined as the probability that a random realization may yield a statistic smaller than that seen in data. The effective probability for a collection of PEVs with respective P -values less than a reference probability ‘ \mathbb{P} ’ is estimated by cumulative binomial probabilities $f(k \geq k_* | n, \mathbb{P}) = \sum_{k=k_*}^n f(k | n, \mathbb{P})$, where $f(k | n, \mathbb{P}) = \frac{\mathbb{P}^k (1-\mathbb{P})^{n-k} n!}{(n-k)! k!}$.

126.3 Results

First, we analyze the full sky PLANCK E-mode polarization maps for COMMANDER and NILC. COMMANDER map is produced by Planck software code COMMANDER implementing Bayesian parametric component separation pipeline and Needlet Internal Linear Combination (NILC) is obtained by applying the Internal Linear Combination technique in needlet space. Later we use the data maps applying the common UPB77 mask and the component separation specific polarization mask for COMMANDER (PMCMR) and polarization mask for NILC (PMNILC) and constructing the full sky CMB data IQU maps by filling the masked region with a random CMB realization added with half-ring half-difference (HRHD) noise proxy maps. The full sky E-mode polarization map is extracted from these filled data maps. The statistical significance is computed using 4000 isotropic random CMB E -mode polarization maps that are appropriately filtered and added with the HRHD noise proxy of the respective data (Figs. 126.1 and 126.2).

126.4 Conclusion

The numbers of anomalous multipoles that indicate violation of statistical isotropy at the level of 2σ in the full sky COMMANDER and NILC polarization maps are found to be 9 and 21, respectively. However, when this same range $l = 40 - 150$ is analyzed using filled sky maps constructed using the common UPB77 polarization mask and component specific polarization masks, the number of anomalous modes has reduced to nearly half. Thus, we may say that the Galactic residuals indeed have an effect on our test of statistical isotropy of various multipoles. It is interesting to note that the number of anomalous multipoles with P -value ≤ 0.05 is more in NILC map

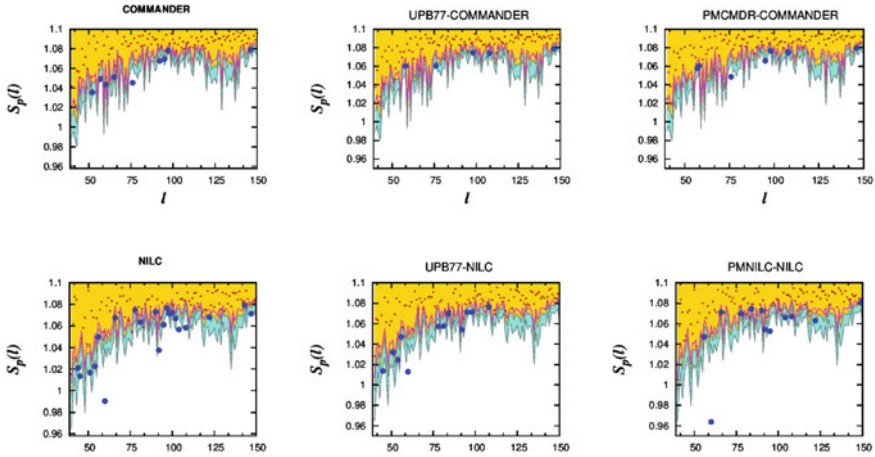


Fig. 126.1 Upper panel shows the Power entropy (S_p) values from full sky COMMANDER and the filled full sky COMMANDER corresponds to the use of UPB77 common polarization mask and the component separation specific PMCMR mask. Lower panel shows the same (S_p) values for NILC. The data S_p values are shown as small red and big blue dots, where the big blue points highlight those multipoles whose Power entropy has a P-value less than 5%. The magenta line, gold, and cyan bands represent 90, 95, and 99% confidence contours estimated from 4000 simulations

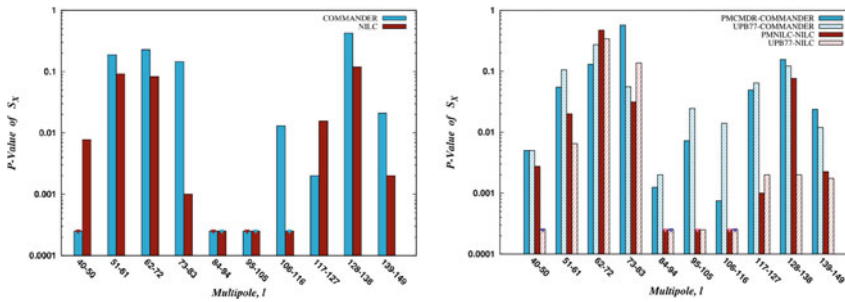


Fig. 126.2 Left panel shows the P-values of Alignment entropy, S_x , corresponding to various multipole bins for fullsky COMMANDER and NILC. The two bars at each multipole bin as indicated correspond to the significance of Alignment entropy. The data statistic is computed as average of the same quantity extracted from 100 such random fillings of the data, which is then used to compute significance. The right panel shows the same but for the filled sky CMB polarization maps by filling the masked using a random CMB realization and HRHD noise proxy

than in the COMMANDER map. We find tentative evidence for collective alignment in some of the multipole blocks. However, we also found that the direction of these common alignment axes lies closer to the Galactic plane in both full sky and filled sky cases. In these alignment tests as well, we find that more number of multipole bins are anomalous in NILC map compared to COMMANDER CMB E-map.

References

1. P. Birch, Is the Universe rotating? *Nature* **298**, 451–454 (1982)
2. D. Hutsemekers, Evidence for very large-scale coherent orientations of quasar polarization vectors. *Astron. Astrophys.* **332**, 410–428 (1998)
3. C.J. Copi, D. Huterer, G.D. Starkman, Multipole vectors: a new representation of the CMB sky and evidence for statistical anisotropy or non-Gaussianity at $2 \leq l \leq 8$. *Phys. Rev. D* **70**, 043515 (2004)
4. A. de Oliveira-Costa, M. Tegmark, M. Zaldarriaga, A. Hamilton, Significance of the largest scale CMB fluctuations in WMAP. *Phys. Rev. D* **69**, 063516 (2004)
5. J.P. Ralston, P. Jain, The virgo alignment puzzle in propagation of radiation on cosmological scales. *Int. J. Mod. Phys. D* **13**, 1857 (2004)
6. P.K. Samal, R. Saha, P. Jain, J.P. Ralston, Testing isotropy of cosmic microwave background radiation. *MNRAS* **385**, 1718 (2008)
7. H.K. Eriksen, F.K. Hansen, A.J. Banday, K.M. Gorski, P.B. Lilje, Asymmetries in the CMB anisotropy field. *Astrophys. J.* **605**, 14 (2004)
8. K. Land, J. Magueijo, The axis of evil revisited. *Phys. Rev. D* **378**, 153 (2005)
9. J. Kim, P. Naselsky, Lack of angular correlation and odd-parity preference in cosmic microwave background data. *ApJ* **739**, 79 (2011)
10. M. Cruz, E. Martinez-Gonzalez, P. Vielva, J.M. Diego, M. Hobson, N. Turok, The CMB cold spot: texture, cluster or void? *MNRAS*, **390**, 913 (2008)

Chapter 127

Investigation of K/π Ratio with Accelerator and Cosmic Ray Data



R. Scaria, S. Ahmad, M. Chakraborty, A. Chandra, S. R. Dugad, S. K. Gupta, B. Hariharan, Y. Hayashi, P. Jagadeesan, A. Jain, P. Jain, V. B. Jhansi, S. Kawakami, H. Kojima, S. Mahapatra, P. K. Mohanty, R. Moharana, S. D. Morris, P. K. Nayak, A. Oshima, B. P. Pant, D. Pattanaik, G. S. Pradhan, P. S. Rakshe, K. Ramesh, B. S. Rao, L. V. Reddy, R. Sahoo, S. Shibata, F. Varsi, and M. Zuberi

Abstract We look at K/π ratio as an indicator for strangeness enhancement and compare cosmic data with the collider data. We use CORSIKA to generate data on Extensive Air Showers (EAS) and compare the K/π ratio with accelerator results. Experimentally observed cosmic K/π values are also compared with results from hadronic and symmetric and asymmetric nucleus-nucleus collisions. Since Cosmic Rays (CRs) consist mostly of protons and the atmosphere is rich mainly in nitrogen and oxygen we expect more proton-nucleus type collisions to occur and such a scenario agrees well with the experimental values.

R. Scaria (✉) · S. Ahmad · M. Chakraborty · A. Chandra · S. R. Dugad · S. K. Gupta · B. Hariharan · Y. Hayashi · P. Jagadeesan · A. Jain · P. Jain · V. B. Jhansi · S. Kawakami · H. Kojima · S. Mahapatra · P. K. Mohanty · R. Moharana · S. D. Morris · P. K. Nayak · A. Oshima · B. P. Pant · D. Pattanaik · G. S. Pradhan · P. S. Rakshe · K. Ramesh · B. S. Rao · L. V. Reddy · R. Sahoo · S. Shibata · F. Varsi · M. Zuberi
The GRAPES -3 Experiment, Cosmic Ray Laboratory, Ooty 643001, India
e-mail: ronaldscaria.rony@gmail.com

M. Chakraborty · S. R. Dugad · S. K. Gupta · B. Hariharan · P. Jagadeesan · A. Jain · V. B. Jhansi · P. K. Mohanty · R. Moharana · S. D. Morris · P. K. Nayak · D. Pattanaik · P. S. Rakshe · K. Ramesh · B. S. Rao · L. V. Reddy · M. Zuberi
Tata Institute of Fundamental Research, Mumbai 400005, India

Y. Hayashi · S. Kawakami
Graduate School of Science, Osaka City University, Osaka 558-8585, Japan

S. Ahmad · A. Chandra
Aligarh Muslim University, Aligarh 202002, India

P. Jain · F. Varsi
Indian Institute of Technology Kanpur, Kanpur 208016, India

A. Oshima · S. Shibata
College of Engineering, Chubu University, Aichi 487-8501, Japan

H. Kojima
Faculty of Engineering, Aichi Institute of Technology, Aichi 470-0392, Japan

© The Author(s), under exclusive license to Springer Nature Singapore Pte Ltd. 2022
B. Mohanty et al. (eds.), *Proceedings of the XXIV DAE-BRNS High Energy Physics Symposium, Jatni, India*, Springer Proceedings in Physics 277,
https://doi.org/10.1007/978-981-19-2354-8_127

127.1 Introduction

Cosmic Rays (CRs) cover a very wide energy spectrum of over 12 orders of magnitude from 10^8 to 10^{20} GeV. These extremely large projectile energies would mean that CRs interact with the nuclei in the atmosphere at center of mass energies ($\sqrt{s_{NN}}$) much higher than those attained by accelerators [1]. Accelerators have seen evidences of the formation of a thermally equilibrated deconfined state of partons called Quark-Gluon Plasma (QGP). QGP formation in CR interactions in the atmosphere has been proposed as a solution to the muon puzzle problem in CR physics [2]. One of the well-accepted signatures for QGP is strangeness enhancement [3] which is reflected in the kaon to pion (K/π) ratio. CR interactions are usually studied by using large-scale Monte Carlo (MC) simulations. CORSIKA [4] is one such simulation model used to study Extensive Air Showers (EAS). We use CORSIKA to simulate CR interactions in the stratosphere which we compare with various experiments and with results from accelerators.

127.2 Introduction to CORSIKA

CORSIKA is a MC simulation package used to model the development of EAS. It can be used with various high energy hadronic interaction models like DPMJET [5], EPOS LHC [6], NEXUS [7], QGSJET [8], QGSJET-II [9], SIBYLL 2.3d [10] and VENUS [11] and low energy event generators like GHEISHA [12], FLUKA [13], and UrQMD [14]. The primary cosmic rays (PCRs) in CORSIKA can have energies up to 10^{20} eV. The particles produced are tracked in the atmosphere until they decay. At the detector level the properties like momentum, position and time of the secondary particles are recorded.

127.3 Cosmic Ray K/π Ratio

The pions and kaons produced as a result of CR interactions in the atmosphere decay very fast into muons. Various underground experiments like the MINOS far detector [15], ICECUBE [16], Soudan mine scintillation detector [17], etc. measured the seasonal variation of muons from which the K/π ratio was calculated. K/π ratios

S. Mahapatra · D. Pattanaik
Utkal University, Bhubaneswar 751004, India

R. Scaria · G. S. Pradhan · R. Sahoo
Department of Physics, Indian Institute of Technology Indore, Indore 453552, India

R. Moharana · B. P. Pant
Indian Institute of Technology Jodhpur, Jodhpur 342037, India

from various heavy-ion and hadron-hadron collisions have also been published from accelerator experiments [18–20].

We have used the CORSIKA 7.7400 version with SYBILL and QGSJET-II as the high energy models and GHEISHA as the low energy model. 10000 events each were simulated for different primary energies differing by an order of magnitude and covering a wide range of available energies in CORSIKA. The detector level was chosen to be at 10km above the sea level as the beginning of stratosphere. We have used the FIXHEI option in CORSIKA to limit ourselves to the initial interactions as pions and kaons decay quickly. The particle information collected at the detector level was used to calculate the K/π ratio.

127.4 Results and Discussions

As we were interested in the initial interactions of CRs in the atmosphere we chose the interaction level to be 25 m away from the detector level and extracted the K/π ratio. These values were then compared with values from accelerators and with underground muon detection experiments (Fig. 127.1). The values were in good agreement with the trend shown by accelerator experiments and was in agreement with the values from CR detectors giving indications that the interactions happening in CR interactions in the atmosphere is similar to the one happening in accelerator experiments. We then tried to see how a change of the high energy model would affect the results. The results (Fig. 127.2a) showed a decrease when we used the QGSJET II model at the higher energy side of the spectrum. This may be attributed to the changes in the interaction strengths in the two models. We also chose to explore the K/π values for four different distances (25, 100, 200, 500 m) from the interaction point to see variation with height. The highest K/π values were obtained for minimum distance from the interaction level (Fig. 127.2b). This can be attributed to the fast decay of mesons while they traverse the atmosphere.

127.5 Summary

In this work we have estimated the K/π ratio for initial interactions of CRs in the atmosphere using the CORSIKA event generator package. We observed an increase in strangeness with an increase in energy which is also observed in accelerator experiments. A detailed study of K/π ratio with other observables would help reveal scenario of QGP formation possibility in CR showers.

RS was supported by Council of Scientific and Industrial Research (CSIR), India. GSP was supported by DST-INSPIRE program of Govt. of India.

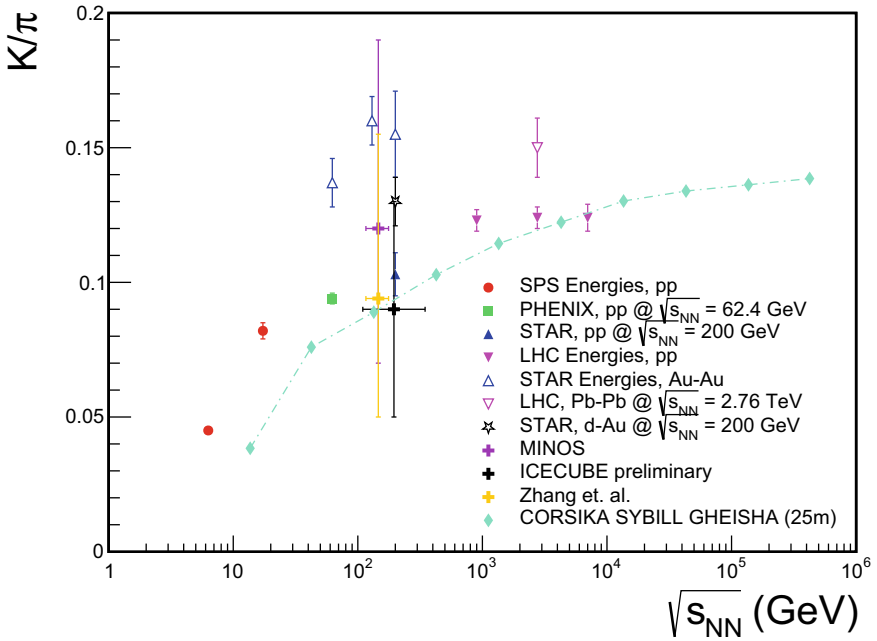


Fig. 127.1 Results from CORSIKA with SYBILL as the high energy option and detector level being 25 m away from interaction point is compared with most central heavy ion results and pp results from accelerators. Results from MINOS, ICECUBE, and Soudan scintillation mine are also shown for comparison

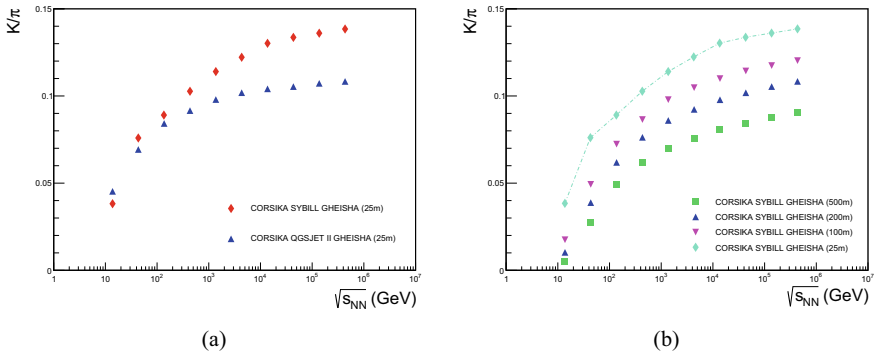


Fig. 127.2 Comparison between SYBILL and QGSJET II as high energy model is shown in (a). The effect of increasing distance from the interaction level to detector level is shown in (b)

References

1. T.K. Gaisser, R. Engel, E. Resconi, *Cosmic Rays and Particle Physics*, 2nd edn. Cambridge University Press (2016)
2. A.A. Petrukhin, Nucl. Instrum. Meth. A **742**, 228 (2014)
3. J. Rafelski, B. Müller, Phys. Rev. Lett. **48**, 1066 (1982)
4. D. Heck, J. Knapp, J.N. Capdevielle, G. Schatz, T. Thouw, FZKA-6019 (1998)
5. S. Roesler, R. Engel, J. Ranft, hep-ph/0012252, SLAC-PUB-8740 (2000)
6. T. Pierog, K. Werner, Nucl. Phys. B Proc. Suppl. **196** (2009)
7. H.J. Drescher, M. Hladik, S. Ostapchenko, T. Pierog, K. Werner, Phys. Rept. **350**, 93 (2001)
8. N.N. Kalmykov, S.S. Ostapchenko, Yad. Fiz. **56**, 105 (1993)
9. S.S. Ostapchenko, Phys. Rev. D **83**, 014018 (2011)
10. R. Engel et al., [arXiv: 1912.03300](https://arxiv.org/abs/1912.03300) [astro-ph] (2019)
11. K. Werner, Phys. Rep. **232**, 87 (1993)
12. H. Fesefeldt, Report PITHA-85/02 (1985)
13. A. Ferrari, P.R. Sala, A. Fasso', J. Ranft, Report CERN-2005-10 (2005)
14. S.A. Bass et al., Prog. Part. Nucl. Phys. **41**, 225 (1998)
15. P. Adamson et al., MINOS. Phys. Rev. D **81**, 012001 (2010)
16. P. Desiati, T. Kuwabara, T.K. Gaisser, S. Tilav, D. Rocco [ICECUBE], *32nd International Cosmic Ray Conference* (2011)
17. C. Zhang, D.M. Mei, Eur. Phys. J. C **79**, 825 (2019)
18. S. Bhattacharyya et al., Adv. High Energy Phys. **2018**, 6307205 (2018)
19. B.I. Abelev et al., STAR. Phys. Rev. C **79**, 034909 (2009)
20. B. Abelev et al., ALICE. Phys. Rev. Lett. **109**, 252301 (2012)

Chapter 128

Simulation of Cosmogenic Neutron Backgrounds for a Dark Matter Search Experiment at Jaduguda Underground Science Laboratory



S. Banik, V. K. S. Kashyap, and B. Mohanty

Abstract The first phase of Dark matter search at India-based Neutrino Observatory (DINO) is proposed to be set up at the Jaduguda Underground Science Laboratory (JUSL). It will be a direct-detection experiment where neutrons, as they can easily mimic dark matter signals, will be an important background. These neutrons are of radiogenic and cosmogenic origin. We present an estimate for the cosmogenic neutron backgrounds produced from the interaction of cosmic muons with rock-overburden at the JUSL site using a GEANT4 based simulation. The muon and muon-induced neutron flux at the JUSL are found to be $4.45(\pm 0.24) \times 10^{-7} \text{ cm}^{-2} \text{ s}^{-1}$ and $0.93(\pm 0.05) \times 10^{-8} \text{ cm}^{-2} \text{ s}^{-1}$, respectively. The estimated flux values compare well with experiments at similar underground depths.

128.1 Introduction

The finding from Planck collaboration suggests that Dark Matter (DM) constitutes $\sim 27\%$ mass-energy content of the universe [1]. However, the DM particles are yet to be observed in an experiment. The interaction rate of dark matter with detector materials is very low. Consequently, the detection of dark matter candidates from the experimentally measured data, which will largely be constituted of backgrounds, is very challenging. The reduction and estimation of backgrounds are therefore highly desirable in a DM search experiment; the experiments are usually located in deep underground laboratories with detectors surrounded by layers of shieldings. Neutrons in DM search pose an irreducible background as they can easily mimic DM signals. These neutrons could be produced from the interaction of cosmic-ray parti-

S. Banik (✉) · V. K. S. Kashyap · B. Mohanty
School of Physical Sciences, National Institute of Science Education and Research, Jatani
752050, India
e-mail: samir.banik@niser.ac.in

Homi Bhabha National Institute, Training School Complex, Anushaktinagar, Mumbai 400094, India

© The Author(s), under exclusive license to Springer Nature Singapore Pte Ltd. 2022
B. Mohanty et al. (eds.), *Proceedings of the XXIV DAE-BRNS High Energy Physics Symposium, Jatni, India*, Springer Proceedings in Physics 277,
https://doi.org/10.1007/978-981-19-2354-8_128

cles with the earth-overburden (cosmogenic neutrons) or from the radioactivity of the overburden (radiogenic neutrons) itself.¹ It is crucial to quantify the flux of neutrons that would reach the experimental cavern to understand the feasibility of performing a dark matter search experiment in an underground laboratory.

A direct-detection DM search experiment is proposed to be set up at a future facility of the India-based Neutrino Observatory (INO) in the Bodi West Hills of the Theni district of Tamil Nadu, India. The experiment is referred to as the Dark Matter Search at INO or the DINO. The first phase of DINO will be at a small underground laboratory (approximately $5\text{ m} \times 5\text{ m} \times 2.2\text{ m}$), named as Jaduguda Underground Science Laboratory (JUSL), which is at a depth of 555 m ($\sim 1600\text{ m}$ water equivalent (m.w.e) vertical rock-overburden) in an existing mine of Uranium Corporation of India Limited (UCIL), Jharkhand, India. The study reported in this proceeding presents an estimation of the cosmogenic neutron background at the JUSL site using a GEANT4-based simulation [2]. Section 128.2 discusses the methodology followed to estimate the background, and Sect. 128.3 the results obtained from the simulation followed by a conclusion.

128.2 Methodology

Estimating the cosmogenic neutron flux requires two major inputs to the simulation: (a) the Jaduguda hill profile, and (b) muon energy and angular distributions. The hill profile comprising the information of latitude, longitude, and elevation of the Jaduguda area is obtained using Google Earth Pro [3]. Figure 128.1a shows the elevation map of the area around JUSL. Energy and angular distribution of muons at the hill-surface level is generated using Gaisser's formula [4] which is given by

$$\frac{d^2 N_\mu}{dE_\mu d\Omega} \approx \frac{0.14 E_\mu^{-2.7}}{\text{cm}^2 \text{ s sr GeV}} \times \left[\frac{1}{1 + \frac{1.1 E_\mu \cos \theta_z}{\epsilon_\pi}} + \frac{\eta}{1 + \frac{1.1 E_\mu \cos \theta_z}{\epsilon_K}} \right], \quad (128.1)$$

where θ_z is the zenith angle, E_μ is the energy of the muon, $d\Omega$ is the solid angle, $\epsilon_\pi = 115\text{ GeV}$, $\epsilon_K = 850\text{ GeV}$ and $\eta = 0.054$.

With start-point positions obtained from hill profile and energy and direction information from Gaisser's formula, one can in principle simulate muon trajectories and the produced particles from muon interactions with the rock. However, simulation of all possible trajectories originating from the hill-surface, where most of them are not expected to reach the cavern, is time-consuming and computationally expensive. The following simulation strategy is developed using the muon lateral-displacements and maximum traveled distances in the rock to counter this difficulty. Muon lateral

¹ Neutrons, via both radiogenic and cosmogenic processes, could also be produced in shielding materials used in DM search experiments. These neutrons are not considered in the proceeding.

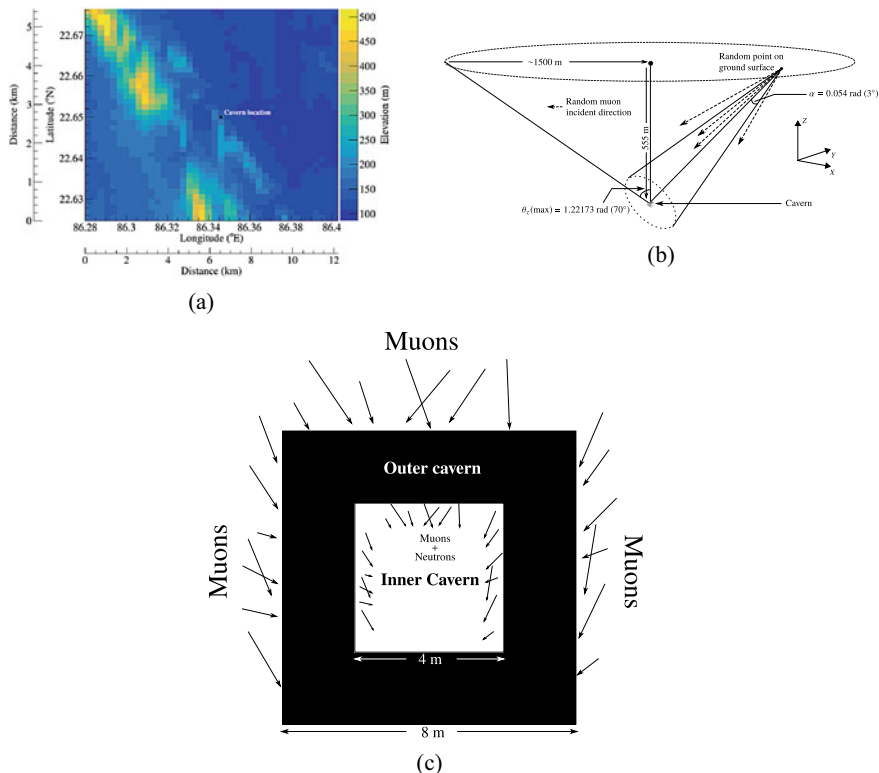
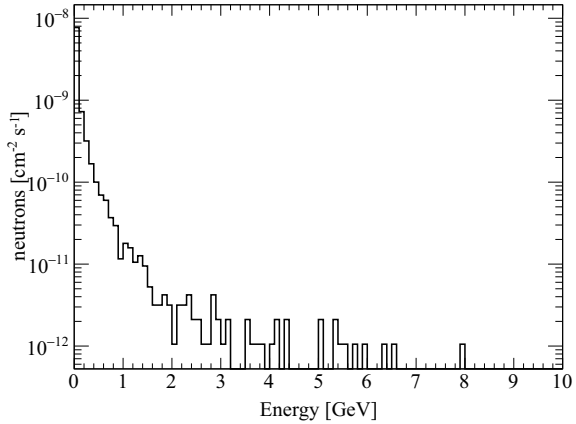


Fig. 128.1 **a** Elevation map of the area around JUSL (12.2 km × 5.45 km). **b** Schematic describing the methodology of calculating muon flux at the cavern. **c** Geometry used in the simulation

displacement calculated at different energy of the particle is found to be as high as 30m; muons with incident directions within a cone having an axis as the line connecting the point of incidence to the center of the cavern and radius 30 m are simulated. A schematic diagram of this is shown in Fig. 128.1a. Also, from the calculation of maximum distance traveled by muons at different energies, it is found that the muons are required to have at least 300 GeV energy to reach the cavern; muons above this energy are therefore only considered in the simulation. It is noted from the simulation that the neutrons which are produced beyond a rock-thickness of 2 m do not contribute significantly to the neutron flux at the cavern and are not tracked in the simulation. Figure 128.1c shows the schematic diagram of the geometry used in the simulation; the neutrons produced in the black shaded region (labeled as “Outer cavern”) of the figure mostly contribute to the neutron flux inside the cavern.

Fig. 128.2 Distribution of muon-induced neutrons at the JUSL cavern



128.3 Results and Conclusion

The flux of muons at the JUSL cavern, as obtained from the simulation, is $4.45(\pm 0.24) \times 10^{-7} \text{ cm}^{-2} \text{ s}^{-1}$. And the cosmogenic neutron flux at the cavern is found to be $0.93(\pm 0.05) \times 10^{-8} \text{ cm}^{-2} \text{ s}^{-1}$ with no energy threshold. If neutrons above 1 MeV are considered, the flux turns out to be $7.25(\pm 0.40) \times 10^{-9} \text{ cm}^{-2} \text{ s}^{-1}$. The uncertainty includes both statistical and systematic uncertainty. The systematic uncertainty, which is around 5.5%, is due to the variation of the rock density. The energy dependence of the neutron flux reaching the cavern is shown in Fig. 128.2; neutrons produced in the rock-overburden are seen to have energies up to 10s of GeVs.

The estimated values of muon and muon-induced neutron fluxes are comparable with the same calculated at a similar depth, in the WIPP salt mine [5] which has a rock-overburden of $\sim 1580 \text{ m.w.e}$. The muon flux and the muon-induced neutron flux at the WIPP salt mine are $4.77 \times 10^{-7} \text{ cm}^{-2} \text{ s}^{-1}$ and $1.6 \times 10^{-8} \text{ cm}^{-2} \text{ s}^{-1}$, respectively. The flux values are close to the same estimated in this work.

References

1. P.A.R. Ade et al., *A&A* **594**, A13 (2016)
2. S. Agostinelli et al., *Nucl. Inst. Meth. Phys. Res. Sect. A* **506**(3), 250 (2003)
3. <https://www.google.com/intl/enin/earth/versions/#earth-pro>
4. M. Tanabashi, K. Hagiwara, K. Hikasa et al., *Phys. Rev. D* **98**, 030001 (2018)
5. E.I. Esch et al., *Nucl. Inst. Meth. Phys. Res. Sect. A* **538**(1), 516 (2005)

Chapter 129

I-Eccentricity-Q Relation as the Universal Relation for Rotating Magnetized White Dwarfs



Somnath Mukhopadhyay, Sujan Kumar Roy, and D. N. Basu

Abstract Within the formulation of Newtonian physics, equilibrium configurations of strongly magnetized white dwarfs with the magnetized Feynman-Metropolis-Teller (FMT) Equation of State (EoS) have been studied. We have obtained the equations of equilibrium using Hartle formalism to calculate different physical quantities of uniformly rotating white dwarfs. The relationship between moment of inertia (I), rotational love number (λ) and spin induced quadrupole moment (Q), for magnetized white dwarfs has been investigated. Furthermore, it has been found that, the relationship between moment of inertia (I), eccentricity and Q, i.e., I-eccentricity-Q relation is more universal in comparison to I-Love-Q relationship.

129.1 Equilibrium Equations Using Hartle Formalism

Under the condition of slow rotation [1], the gravitational potential $\Phi(r, \theta)$ of the rotating star satisfies the Poisson equation, i.e.,

$$\nabla^2 \Phi(r, \theta) = 4\pi G \rho(r, \theta), \quad (129.1)$$

where, G is the universal gravitational constant and the mass density of the star is, $\rho(r, \theta)$. Equilibrium equation of a star, rotating with angular velocity Ω , is,

$$\int \frac{dp(r, \theta)}{\rho(r, \theta)} + \Phi(r, \theta) = \frac{1}{2} \Omega^2 r^2 \sin^2 \theta + Constant. \quad (129.2)$$

S. Mukhopadhyay (✉)

National Institute of Technology, Tiruchirappalli 620015, Tamil Nadu, India
e-mail: somnath@nitt.edu

S. K. Roy · D. N. Basu

Variable Energy Cyclotron Centre, 1/AF Bidhan Nagar, Kolkata 700064, India

Homi Bhabha National Institute, Training School Complex, Anushaktinagar, Mumbai 400085, India

The Hartle coordinate for the rotating deformed star is introduced as follows:

$$r = R + \xi; \quad \Theta = \theta, \tag{129.3}$$

where a point in the non-rotating star is represented by R, Θ and r, θ represents the same point in the rotating configuration. As the rotating star has axial and reflection symmetries the equations would be ϕ independent and therefore, the perturbation term or the deformation ξ can contain only Ω^2 terms [1, 2]. Hence,

$$r(R, \Theta) = R + \xi(R, \Theta) + O(\Omega^4); \quad \Theta = \theta, \tag{129.4}$$

where $\xi(R, \Theta) \sim \Omega^2$ and for the Hartle formalism to be valid, $\frac{\xi(R, \Theta)}{R} \ll 1$.

Therefore, the Equation of State(EoS) for the rotating star can be represented as follows [1, 2],

$$\begin{aligned} \rho(r, \theta) &= \rho(R, \Theta) = \rho(R) = \rho^{(0)}(R), \\ p(\rho) &= p(R, \Theta) = p(R) = p^{(0)}(R), \end{aligned} \tag{129.5}$$

where $\rho^{(0)}(R)$ and $p^{(0)}(R)$ represent the quantities in the non-rotating configuration.

The deformation ξ and the potential Φ can be decomposed as

$$\begin{aligned} \xi(R, \Theta) &= \sum_l \xi_l(R) P_l(\cos \Theta), \\ \Phi(R, \Theta) &= \Phi^{(0)}(R) + \Phi^{(2)}(R, \Theta) + O(\Omega^4), \\ \Phi^{(2)}(R, \Theta) &= \sum_l \Phi_l^{(2)}(R) P_l(\cos \Theta). \end{aligned} \tag{129.6}$$

Using this decomposition Eqs. 129.1 and 129.2 are simplified to get

$$\frac{dp^{(0)}(R)}{dR} = -\rho^{(0)}(R) \frac{GM^{(0)}(R)}{R^2} \quad \& \quad \frac{dM^{(0)}(R)}{dR} = 4\pi R^2 \rho^{(0)}(R), \tag{129.7}$$

$$-\frac{dp_0^*(R)}{dR} + \frac{2}{3}\Omega^2 R = \frac{GM^{(2)}(R)}{R^2} \quad \& \quad \frac{dM^{(2)}(R)}{dR} = 4\pi R^2 \rho^{(0)}(R) \frac{d\rho^{(0)}}{dp^{(0)}} p_0^*(R) \tag{129.8}$$

with, $p_0^*(R) = \xi_0(R) \frac{d\Phi^{(0)}(R)}{dR}$. Radii at pole and equator r_p, r_e are defined as

$$r_p = r(a, 0) = a + \xi_0(a) + \xi_2(a) \quad \& \quad r_e = r(a, \pi/2) = a + \xi_0(a) - \xi_2(a)/2, \tag{129.9}$$

and the eccentricity of the rotating star is given by, $e = \sqrt{1 - \left(\frac{r_p}{r_e}\right)^2}$. Further, we write the total mass M_{tot} and the total moment of inertia I_{tot} as

$$M_{tot} = \int_0^a 4\pi R^2 \rho^{(0)}(R) dR + \int_0^a 4\pi R^2 \rho^{(0)}(R) \frac{d\rho^{(0)}}{d\rho^{(0)}} p_0^{(*)}(R) dR. \quad (129.10)$$

$$I_{tot}(R) = \int_V \rho^{(0)}(R) R^4 \sin^3 \Theta dR d\Theta d\phi + \int_V \rho^{(0)}(R) R^4 \sin^3 \Theta \left(\frac{4\xi(R, \Theta)}{R} + \frac{d\xi(R, \Theta)}{dR} \right) dR d\Theta d\phi. \quad (129.11)$$

The potential of the rotating spheroid, $\Phi(R, \Theta)$, for $R > a$ can be written as follows:

$$\Phi(R, \Theta) = -G \frac{M_{tot}}{R} + \frac{K_1}{R^3} P_2(\cos \Theta). \quad (129.12)$$

The denominator of the $P_2(\cos \Theta)$ coefficient depends on R^3 and therefore, the numerator corresponds to the quadrupole moment, as follows:

$$Q = \frac{K_1}{G}. \quad (129.13)$$

The ellipticity $\epsilon(R)$ is defined as [3],

$$\epsilon(R) = \frac{r_e(R) - r_p(R)}{R}. \quad (129.14)$$

This quantity satisfies the following equation [3],

$$R \frac{d\eta_2(R)}{dR} + 6D(R)[\eta_2(R) + 1] + \eta_2(R)[\eta_2(R) - 1] = 6, \quad (129.15)$$

where $D(R) = \rho(R)/\rho_m(R)$ with $\rho_m(R) = 3M^{(0)}(R)/4\pi R^3$ being the average density of the star and the new variable $\eta_2(R)$ is defined as

$$\eta_2(R) = \frac{R}{\epsilon(R)} \frac{d\epsilon(R)}{dR}. \quad (129.16)$$

Finally, the rotational love number λ is defined by the relation,

$$\lambda = \frac{2}{3G} a^5 k_2, \quad (129.17)$$

where, k_2 is called the rotational apsidal constant and is defined as, $k_2 = \frac{[3-\eta_2(a)]}{2[2+\eta_2(a)]}$.

The EoS has been adopted from Ref. [4] i.e., the extended Feynman-Metropolis-Teller (FMT) treatment for white dwarf matter under density dependent magnetic field [5]. Figure 129.1 shows the mass-radius relationship for white dwarfs of different compositions. On the other hand, upper panel of Fig. 129.2 shows the I-Love-Q relationship, whereas, the I-eccentricity-Q relationship has been shown in the lower

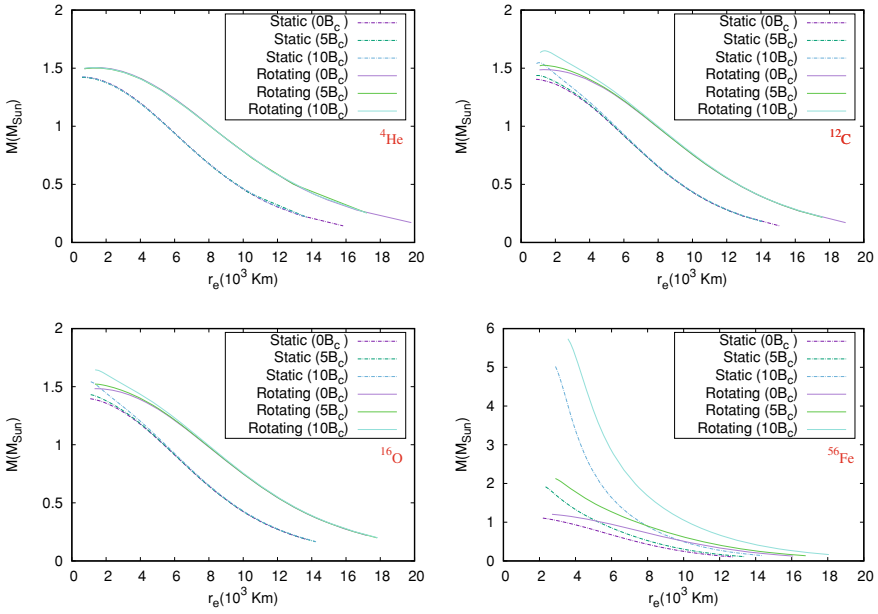


Fig. 129.1 Mass-Radius relationship of white dwarfs of different composition and different central magnetic fields in terms of the critical magnetic field $B_c = \frac{m_e^2 c^3}{e \hbar}$

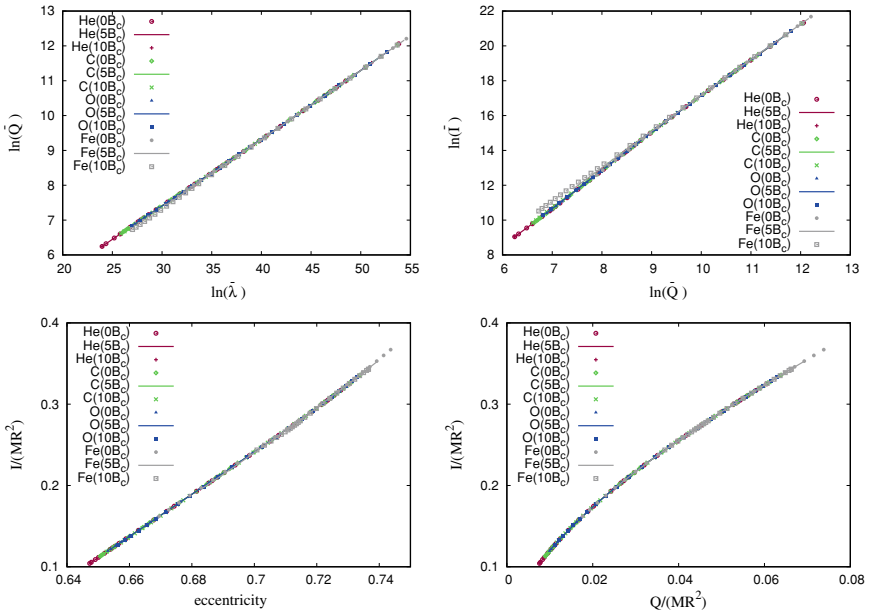


Fig. 129.2 Universal relations of magnetized white dwarfs of different composition and different central magnetic fields in terms of the critical magnetic field $B_c = \frac{m_e^2 c^3}{e \hbar}$

panel. In Fig. 129.2, $\bar{I} = \frac{c^4}{G^2} \frac{I}{M^3}$, $\bar{\lambda} = \frac{c^{10}}{G^4} \frac{\lambda}{M^3}$, $\bar{Q} = \frac{c^2 Q}{I^{(0)} \Omega^2} M^{(0)}$ are all dimensionless quantities where, $M^{(0)}$, $I^{(0)}$ are mass and moment of inertia of the non-rotating star, respectively, and for rotating configuration M , I are the corresponding quantities. We conclude from Fig. 129.2 that the I-Eccentricity-Q relations show a better fit than the I-Love-Q relations. We also see that Iron-56 white dwarfs deviate the most and hence break the universal relations substantially than white dwarfs of other compositions.

References

1. J.B. Hartle, *Astrophys. J.* **150**, 1005 (1967)
2. K. Boshkayev, H. Quevdo, B. Zhami, *Mon. Not. R. Astron. Soc.* **464**, 4349 (2017)
3. S. Chandrasekhar, *Ellipsoidal Figures of Equilibrium* (Yale University Press, New Haven, 1969)
4. S.K. Roy, S. Mukhopadhyay, J. Lahiri, D.N. Basu, *Phy. Rev. D* **100**, 063008 (2019)
5. D. Bandyopadhyay, S. Chakrabarty, S. Pal, *Phys. Rev. Lett.* **79**, 2176 (1997)

Chapter 130

Power Asymmetry in Planck Full-Mission CMB Temperature Maps



Srikanta Panda, Pavan K. Aluri, Pramoda Kumar Samal,
and Pranati K. Rath

Abstract In the cosmological standard model, CMB is expected to show no symmetry preferences. Here we probe the presence of any parity preferences, particularly those of (a)symmetry in power (C_l) between even and odd multipole of CMB angular power spectrum from the Planck 2015 full-mission CMB data from ESA's Planck probe. Further we also assess any specific preference for mirror parity asymmetry as well, by comparing the power contained in $l + m = \text{even}$ or odd mode combinations. In this work we found the odd parity preferences in Planck full-mission data and it is maximally anomalous within the multipole range $\approx [2, 29]$.

130.1 Introduction

Cosmological principle is one of the foundational assumptions of modern cosmology, which states that the Universe is homogeneous and isotropic over a large distance scale. Multiple studies in both WMAP and Planck CMB data indicated instances of isotropy violation [1, 2]. Here we study the anomalous odd power excess in CMB angular power spectrum which corresponds to an inversion parity preference in the data [3–6]. As conventional, the CMB temperature fluctuation is expanded in terms of spherical harmonics as $\Delta T(\hat{n}) = \sum_{l=2}^{\infty} \sum_{m=-l}^{+l} a_{lm} Y_{lm}(\hat{n})$, where, a_{lm} are the coefficients in the spherical harmonic basis, $Y_{lm}(\hat{n})$. Under inversion, i.e., $\hat{n} \rightarrow -\hat{n}$, the spherical harmonic coefficients transform as $a_{lm} \rightarrow (-1)^l a_{lm}$. Correspondingly

S. Panda (✉) · P. K. Samal
Department of Physics, Utkal University, Bhubaneswar, Odisha, India
e-mail: srikantal06@gmail.com

P. K. Aluri
Department of Physics, IIT(BHU), Varanasi 221005, Uttar Pradesh, India

P. K. Samal
School of Physics, Gangadhar Meher University, Sambalpur, India

P. K. Rath
Department of Physics, Khallikote (Autonomous) College, Berhampur, India

the maps $T^\pm(\hat{n}) = \frac{T(\hat{n}) \pm T(-\hat{n})}{2}$, contain only the even/odd modes, respectively. Thus the mean power proportional to $\sum_l C_l$ in some chosen multipole range can be decomposed as $\sum_l C_l = C_l^+ + C_l^-$, where $C_l = \sum_m |a_{lm}|^2 / (2l + 1)$ ($\forall m = -l$ to $+l$) is the angular power spectrum of CMB anisotropies, and C_l^\pm is the power in even/odd multipoles respectively.

It can be shown that the point parity asymmetry is related to antipodal correlations of CMB sky [7]. The two-point correlation function is defined as $C(\theta) = \sum_l \frac{2l+1}{4\pi} C_l P_l(\cos \theta)$, where $C(\theta) = \langle \Delta T(\hat{n}) \Delta T(\hat{n}') \rangle$ and $\hat{n} \cdot \hat{n}' = \cos \theta$. Taking $\theta = \pi$ corresponding to correlation between antipodal points we get, $C(\pi) = \sum_l \frac{2l+1}{4\pi} C_l P_l(\cos \pi) = \sum_l (-1)^l \frac{2l+1}{4\pi} C_l = C_l^+ - C_l^-$, where $C_l = \sum_l \frac{2l+1}{4\pi} C_l$ and C_l^\pm is the corresponding power in even/odd only multipoles up to some chosen maximum multipole and $P_l(x)$ are the usual Legendre polynomials.

130.2 Point Parity Statistics and Mirror Parity Statistics

The power in even multipoles as compared to odd multipoles is probed by computing the mean power in even and odd multipoles separately [4, 6] upto a chosen multipole range (l_{max}) as

$$P^\pm = \sum_{l=2}^{l_{max}} \frac{[1 \pm (-1)^l]}{2} \mathcal{D}_l. \tag{130.1}$$

Here $\mathcal{D}_l = l(l + 1)C_l/2\pi$, and P^\pm represents the mean power in even or odd only multipoles upto a chosen multipole ‘ l_{max} ’. Also we take $l_{max} \geq 3$. A statistic is then defined by taking their ratio as $P(l_{max}) = P^+ / P^-$.

We also use the statistic which is defined as the average ratio of the power in adjacent even over odd multipoles up to a chosen maximum multipole [6]. It is given by

$$Q(l_{odd}) = \frac{2}{l_{odd} - 1} \sum_{l=3}^{l_{odd}} \frac{\mathcal{D}_{l-1}}{\mathcal{D}_l}, \tag{130.2}$$

where l_{odd} is the maximum odd multipole upto which the statistic is computed, which will ensure that there are equal numbers of even and odd multipoles in the multipole range used to compute the statistic. Evidently the summation is taken over only the odd multipoles and the multipole range involved in this computation is $2 \leq l \leq l_{odd}$.

The mirror (a)symmetry was studied in Refs. [8–10] and summarized as below:

$$\begin{aligned} E_l &= \frac{\langle |a_{lm}^2| \rangle_{l+m=even}}{C_l^{th}}, & O_l &= \frac{\langle |a_{lm}^2| \rangle_{l+m=odd}}{C_l^{th}}, \\ R_l &= \frac{\langle |a_{lm}^2| \rangle_{l+m=even}}{\langle |a_{lm}^2| \rangle_{l+m=odd}}, & D_l &= \frac{\langle |a_{lm}^2| \rangle_{l+m=even} - \langle |a_{lm}^2| \rangle_{l+m=odd}}{C_l^{th}}, \end{aligned} \tag{130.3}$$

where $\langle |a_{lm}^2| \rangle_{l+m=even/odd}$ denotes the mean power in even or odd spherical harmonic coefficients for the combination $l + m = \text{even/odd}$, respectively. The E_l and O_l statistics separately probe excess/deficit of power in even/odd $l + m$ modes in a particular ‘ l ’ in the data with respect to expected power in standard concordance model. R_l and D_l probe the ratio of and difference between power in even mirror parity modes compared to odd mirror parity modes, respectively. This is how we can study the power distribution between even and odd mirror parity modes.

130.3 Results

For this study, we use the CMB SMICA (*Spectral Matching Independent Component Analysis*) map from Planck 2015 public release, which is available at an $N_{side} = 2048$. Here we use two masks, viz., the UT78 common analysis mask and the SMICA mask to omit foreground residuals. To study the mirror parity (a)symmetry, we use *inpainting* method. The a_{lm} ’s are thus extracted from the inpainted/pseudo-full-sky SMICA CMB map, and tested for even/odd/no mirror parity preference in the data. The significance of our parity and Mirror statistics is estimated by comparing the data estimated values (both cleaned map as provided and the two inpainted SMICA maps) with 1000 mock CMB maps added with appropriate noise (Fig. 130.1).

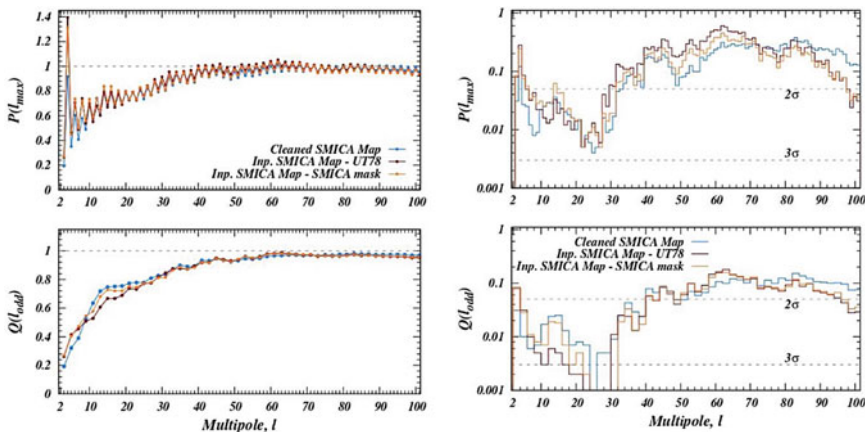


Fig. 130.1 The even–odd multipole power asymmetry in the SMICA temperature map in the multipole range $l = [2, 101]$. The asymmetry is computed using both the $P(l_{max})$ (left top panel) and $Q(l_{odd})$ (left bottom panel) statistics. Similarly p-values estimates of parity asymmetry in data as quantifies by the statistics $P(l_{max})$ and $Q(l_{odd})$ shown in right top and bottom panel. Each panel has three data curved corresponding to the cleaned SMICA map as provided by the Planck collaboration (blue), inpainted SMICA map after masking with UT78 mask (maroon), and inpainted SMICA CMB map after masking with component separation specific mask (orange)

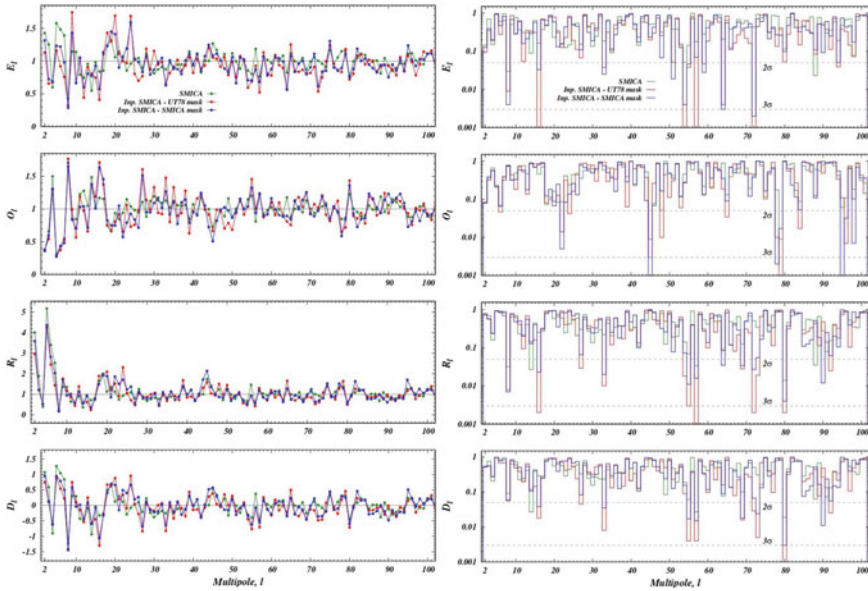


Fig. 130.2 This shows the value of mirror parity statistics \mathcal{E}_l , \mathcal{O}_l , \mathcal{R}_l and \mathcal{D}_l computed from the data on the *left panel*. The horizontal solid gray line in each panel is the theoretically expected value for the statistics at each multipole. The *Right panel* shows the p-value estimates of \mathcal{E}_l , \mathcal{O}_l , \mathcal{R}_l and \mathcal{D}_l for each harmonic mode, l . The color code is similar as given in Fig. 130.1

130.4 Conclusions

Using Planck full-mission second release SMICA CMB map, we analyze the anomalous power excess in odd over even multipoles and preferences of mirror parity in the data (Fig. 130.2). The data is expected to be unbiased with any odd over even point/mirror parity preferences. In our result an odd parity preference i.e., more power in odd multipoles compared to even multipole is found to persist in Planck full-mission data. Both the statistics, defined in equation 1 and 2, become maximally anomalous for the multipole range $\approx [2, 29]$ which matches with Refs. [4, 5], using WMAP data. we also observed no significant even or odd mirror parity preferences in the data at most multipoles l . Thus with respect to the Galactic plane, the SMICA map from Planck PR2 doesn't display a statistically significant mirror parity asymmetry.

References

1. C.L. Bennett et al., ApJS **192**, 17 (2011)
2. Planck Collaboration: P.A.R. Ade et.al., Planck 2015 results. XVI. A & A **594**, A16 (2016)
3. K. Land, J. Magueijo, Phys. Rev D **72**, 101302 (2005)
4. J. Kim, P. Naselsky, ApJL **714**, L265 (2010)

5. A. Gruppuso et al., MNRAS **411**, 1445 (2011)
6. P.K. Aluri, P. Jain, MNRAS **419**, 3378 (2012)
7. P. Naselsky, W. Zhao, J. Kim, S. Chen, ApJ **749**, 31 (2012)
8. A. de Oliveira-Costa, M. Tegmark, M. Zaldarriaga, A. Hamilton, Phys. Rev. D **69**, 063516 (2004)
9. F. Finelli, A. Gruppuso, F. Paci, A.A. Starobinsky, JCAP **07**, 049 (2012)
10. A. Ben-David, E.D. Kovetz, N. Itzhaki, ApJ **748**, 39 (2012)

Chapter 131

A Mini Review on Dark Mater: Cosmological Perspective



Subinoy Das

Abstract In this mini review, we discuss the status of dark matter search from cosmological perspective. The non-detection of cold weakly interacting massive particle (WIMP) has expanded the dark matter research to look beyond thermal canonical WIMP. Here we discuss how cosmology can put few model independent bounds on properties of dark matter—like its mass, formation epoch, and possible decay rate. We also discuss how present and near future cosmological experiments can guide the dark matter search and model building in the coming years. With the increasing sensitivity, cosmological observations are already putting competitive bounds on particle physics parameters of dark matter models and near future cosmology experiments can detect smoking gun signal of non-WIMP dark matter models which has a different prediction for cosmological structure formation in the universe.

131.1 Introduction

The existence dark matter (DM) as 85% of the total matter budget of the universe at present epoch is confirmed only through its gravitational interaction. But the gravitational footprints of DM are everywhere as it is observed in different length scales as well as from different epochs of the universe. From observations like galaxy rotation curve, weak lensing in galaxy clusters and from cosmic microwave background experiments, we now know for sure that dark matter needs to be present in all different length scales like in individual galaxy, as well as in cluster and super cluster of galaxies. Not only that, even in very early universe during CMB epoch, it was present globally spanning the entire horizon and played a crucial role to generate the CMB sky temperature anisotropy which we observe today.

S. Das (✉)

Indian Institute of Astrophysics, Bangalore 560034, India
e-mail: subinoy@iiap.res.in

© The Author(s), under exclusive license to Springer Nature Singapore Pte Ltd. 2022
B. Mohanty et al. (eds.), *Proceedings of the XXIV DAE-BRNS High Energy Physics Symposium, Jaitani, India*, Springer Proceedings in Physics 277,
https://doi.org/10.1007/978-981-19-2354-8_131

725

131.1.1 Search for DM and Status of WIMP

One needs to know the particle nature of DM, and its possible self-interaction or interactions with visible sector other than gravity to understand this mysterious component which not only stabilizes galaxies but was also one of the key ingredients to form the galaxies in the universe. As interaction of DM particle is unknown—one needs to guess the dark matter interaction nature and then design experiments to detect it. One such guess is that dark matter is WIMP (weakly interacting massive particle) which was in thermal equilibrium with standard model particles in very early universe. At this early time heavy DM and lighter standard model particles were smacking into each other and were in happy thermal equilibrium meaning both annihilations of DM into SM particles and reverse production of DM from standard model particles were efficient. As the Universe cools down, SM particles would not have enough momentum to create back heavy DM—as a result DM annihilation became more efficient than its reverse production and its co-moving number density started to fall off exponentially. This generally happens when DM particles become non-relativistic. If this process would have continued, our universe will end up with no dark matter and galaxy would not be formed! But due to Hubble expansion—as space expanded more and more, DM number density diluted and it acted as a brake to DM annihilation. Finally, at some redshift, the expansion rate took over the annihilation rate where DM particle almost cannot find each other to annihilate due to dilution of number density. From this point onward, the co-moving number density of WIMP is constant and known as freeze-out density. This freeze-out density has one to one mapping with WIMP annihilation cross section—meaning given a cross section one can easily calculate the relic density of DM today. The relic density observed from cosmology when mapped back to WIMP cross section, it dramatically matches with weak scale cross section with a weakly interacting particle mass around few hundred GeV. These range of mass and as well as interaction strength are naturally present in many supersymmetric theories which tries to solve a completely different problem of particle physics called Hierarchy problem which explain the mass of Higgs boson. But once community came to know that same theory can naturally give DM candidate, it created a lot of attention and this coincidence known as “WIMP miracle” has driven dark matter search for last two decades.

131.1.2 Challenges with Canonical WIMP

Despite intensive experimental searches in recent decades, the nature of dark matter (DM) remains a mystery. Combined with a cosmological constant (Λ), the simple hypothesis of a cold, collisionless dark matter (CDM) particle that interacts extremely weakly with Standard Model (SM) particles is consistent with all cosmological observations to date, on scales ranging from individual galaxies to galaxy clusters, to the cosmological horizon as probed by large-scale structure and cosmic microwave

background (CMB) measurements. However, particle physics experiments have not detected canonical weakly interacting massive particle (WIMP) CDM, and several astrophysical anomalies have been claimed to provide evidence for physics beyond the CDM paradigm. On top, canonical WIMP predicts an expected value of scattering cross section per nucleon for direct underground searches-like XENON, CDMS, LUX experiments. These experiments have already published their search results by putting stringent limits on DM cross section as they have not detected canonical WIMP in spite of having required sensitivity. Assuming some standard galactic physics and DM velocity distribution in Milky Way, this number turns out to be $\sigma \simeq 10^{-39} \text{ cm}^2$ per nucleon. From XENON results, this has been ruled out by at least 5 orders of magnitude. The lower bound from XENON is around 10^{-45} cm^2 . This non-detection has created two avenues in recent years: people has started looking beyond WIMP and especially for complete new physical origin of DM in universe. The other route has been to modify the simple WIMP mechanism and look for more complicated interactions which can still keep WIMP alive in the context of direct searches. Many a cases, this route had to let go of the WIMP miracle too for model building purpose. But never the less, it is still a very active field of research for model building perspective. Now onwards, I will discuss the other non-WIMP scenarios which are drawing a lot of attention in DM community in recent times!

131.2 Looking for New Lamp Post and Cosmological Guidelines

Once we start to look beyond WIMP from both theoretical as well as experimental perspective, it is important to remind us the model independent constraints which cosmology already puts on dark matter properties.

131.2.1 *Epoch of Formation of Dark Matter*

Cosmology puts constraints on the epoch of dark matter formation for a class of non-WIMP (Weakly Interacting Massive Particle) dark matter candidates. These models allow Cold Dark Matter (CDM) to be formed between the epoch of Big Bang Nucleosynthesis (BBN) and the matter radiation equality. One can show that for such models the matter power spectra might get strong suppression even on scales that could be probed by linear perturbation theory at low redshifts. Unlike the case of Warm Dark Matter (WDM), where the mass of the dark matter particle controls the suppression scale, in Late Forming Dark Matter (LFDm) scenario, it is the redshift of the dark matter formation which determines the form of the matter power spectra. One can use the Sloan Digital Sky Survey (SDSS) galaxy clustering data and the linear matter power spectrum reconstructed from the Lyman- α data to find the latest

epoch of the dark matter formation in our universe. If all the observed dark matter is late forming, the work finds lower bounds on the redshift of dark matter formation $z_f > 1.08 \times 10^5$ at 99.73% C.L from the SDSS data and $z_f > 9 \times 10^5$, at the same C.L, from the Lyman- α data [1].

One can use a forward model of the Milky Way (MW) satellite galaxy population to address same the question: How late can dark matter form? This reports a stringent constraint [2] on DM formation epoch $z_f > 5.5 \times 10^6$ at 95% confidence based on the abundance of known MW satellite galaxies. This limit marginalizes over uncertainties in the connection between dwarf galaxies and dark matter halos and improves upon galaxy clustering and Lyman- α forest constraints by nearly an order of magnitude. They show that this limit can also be interpreted as a lower bound on z_f for LFDM. Thus, dark matter created by a transition from dark radiation must form no later than **one week after the big bang**.

131.2.2 Smoking Gun Signature of Non-WIMP DM in 21 cm Experiments

131.2.2.1 Fuzzy DM

The well-know Fuzzy DM also starts to behave as DM late in universe as in early time, the ultra light axion field was behaving like cosmological constant due to Hubble friction. Once the universe cools down, Hubble friction drops and the axion field starts to become dynamical and finally due to its coherent oscillation around a local minima of the potential, it behaves like a cold DM.

131.2.2.2 Self Interacting DM

An intriguing possibility is that the dark matter particle interacts with a dark radiation component. If the non-gravitational interactions of the dark matter and dark radiation species with Standard Model particles are highly suppressed, then astrophysics and cosmology could be our only windows into probing the dynamics of such a dark sector. It is well known that such dark sectors would lead to suppression of small-scale structure, and signatures of such dark sectors on the re-ionization history of our universe can be crucial to detect them [3].

131.2.2.3 Signature in 21 cm Brightness Power Spectra

Cosmological signatures of LFDM or Fuzzy DM or even self-interacting DM show up in very interesting way in future 21 cm brightness power spectra measurements. LFDM models suppresses power in matter power spectra but one gets higher power

in 21 cm brightness spectra [4]. Thus future experiments like SKA will first detect or rule out these alternative models of DM where one gets cut off in matter power spectra.

References

1. A. Sarkar, S. Das, S.K. Sethi, JCAP **03**, 004 (2015)
2. S. Das, E.O. Nadler, Phys. Rev. D **103**(4), 043517 (2021)
3. S. Das, R. Mondal, V. Rentala, S. Suresh, JCAP **08**, 045 (2018)
4. A. Sarkar, R. Mondal, S. Das, S.K. Sethi, S. Bharadwaj, D.J.E. Marsh, JCAP **04**, 012 (2016)

Chapter 132

Investigating Ultra Long Short GRBs Using Fermi-GBM Data



Sundar Dhara and R. Moharana

Abstract GRBs are mainly classified into two groups based on T_{90} values. In past, many authors are claimed for existence of an intermediate class of GRBs which T_{90} in between SGRBs and LGRBs. This paper aims to investigate possible presence of another class of GRBs, named ulSGRBs, the intermediate one. Motivation is the detections of first GW associated SGRBs, GW17081/GRB170817A as a result of NS-NS merger with $T_{90} \sim 2.73$ s. The presence of ulSGRBs can be established by searching for statistical significant populations around the T_{90} values of 1–3 s in the durations distributions plot of GRBs using FERMIGBRST Catalog.

132.1 Introduction

Gamma-ray bursts (GRBs) are one of the luminous ($E_{\gamma, \text{iso}} \sim 10^{48} - 10^{54}$ erg), short time (lasting from few seconds to few hours) explosions of the universe. These astrophysical objects produce electromagnetic radiations from optical to very high energy gamma-rays ($> \text{GeV}$), even ultra high energy particles like cosmic rays, neutrinos are also expected to be produced in these sources. GRBs have been detected by BATSE, Fermi GLAST, Swift. It is quite a challenging task to reveal the origin of each GRB. GRBs are classified according to their duration of producing gamma-ray, T_{90} (The duration in seconds, during which 90% of the burst fluence was accumulated) values. GRBs with $T_{90} < 2$ s are called as short gamma-ray burst (SGRBs) and its source of origin are NS-NS or NS-black hole (BH) merger. With $T_{90} > 2$ s are called long gamma-ray bursts (LGRBs) and mainly originated from collapse of supermassive

S. Dhara (✉)

Department of Physics, IIT Jodhpur, NH 65, Jodhpur, Rajasthan 342037, India
e-mail: dhara.2@iitj.ac.in

R. Moharana

The GRAPES -3 Experiment, Cosmic Ray Laboratory, Ooty, India

Indian Institute of Technology Jodhpur, Jodhpur, India

Tata Institute of Fundamental Research, Mumbai, India

star into a Black Hole. However many authors have tried to explain the existence of an intermediate class of GRBs [1]. But the physical existence of the intermediate class is, however still not confidently proven. We are analyzing the number of large data of Fermi-GBM (~ 3000) events and expect to get better statistics in finding the new class.

132.2 Analysis of GRB170817A

On August 17, 2017, GW170817 and GRB170817A assigned as first-ever discovery of the NS-NS merger detected both as a gravitational wave (GW) and a SGRB. In this section, we will present data analysis of this Fermi-GBM time tagged event (TTE) data available at the Fermi Science Support Center, released publicly in the form of catalog publications and hosted by the HEASARC, using the **RMFIT v4.3.2** and **GT-Burst** software. For spectral analysis, we use mainly these three common spectral models [2], power-law (PL), Comptonized model (COMP) and Black-Body (BB) taken to fit the data. I present the result of the standardized spectral analysis for GRB170817A (see Table 132.1). This same spectral analysis has been done earlier (see [3]).

After the following standardized analysis we compute, the luminosity, luminosity distance and temperature of the progenitor are, $L \sim 1.2 \times 10^{40}$ Js, $D_L \sim 39.2$ Mpc, $T \sim 12.75 \times 10^7$ K, respectively [4]. This analysis suggest GRB170817A has different properties, it can be considered as an intermediate class of GRB [5].

132.3 Investigations of Ultra Long Short GRBs (ulSGRBs)

For investigations of ulSGRBs, we consider Fermi-GBM Burst (FERMIGBRST) Catalog. FERMIGBRST cataloge presently has total 2990 numbers of GRBs. As the duration distribution plot, we plotted $\log T_{90}$ against no. of GRBs (N) for two cases, firstly for the entire 2990 datasets and secondly for 0–3 s time interval.

132.3.1 Method and Model Comparisons

We have used the Maximum Likelihood Estimations (MLE) method [6] to obtain the fitting curve and estimate the parameters. According to the MLE method, we selected the Gaussian distributions function and defined the loglikelihood function, which is used to be maximized over the parameters by varying the free parameters. For the model comparison, here we take Chi-Square Test (χ^2), Akaike Information Criterion (AIC) and Bayesian Information Criterion (BIC). The model with the lower values of χ^2 , AIC and BIC will be in favor.

Table 132.1 The table of the spectral fit parameters for the GBM data spectral analysis

Time range (s)	Model	Epeak (keV)	Index (α)	KT (keV)	c-stat/dof	Photonflux \times ph/(s.cm ²)	Energyflux $\times 10^{-7}$ erg/(s.cm ²)
0.832: 1.984	COMP	47.01 \pm 6.48	-	-	618.85/485	0.89 \pm 0.20	5.43 \pm 1.1
	PL	-	-1.81 \pm 0.24	-	630.53/480	0.92 \pm 0.22	9.07 \pm 3.6
	BB	-	-	12.33 \pm 1.80	619.37/486	0.95 \pm 0.19	5.53 \pm 1.1
-0.320: 0.256	COMP	202.1 \pm 61.6	-0.63 \pm 0.35	-	590.24/483	2.6 \pm 0.33	3.7 \pm 0.73
	PL	-	-1.5 \pm 0.1	-	603.11/484	2.85 \pm 0.33	4.7 \pm 0.56
	BB	-	-	36.84 \pm 3.71	603.62/484	1.7 \pm 0.19	2.71 \pm 0.34
-0.192: 0.064	COMP	185.3 \pm 39.7	0.31 \pm 0.7	-	536.65/483	2.8 \pm 0.47	4.95 \pm 0.95
	PL	-	-1.4 \pm 0.1	-	564.64/484	3.4 \pm 0.51	6.1 \pm 0.85
	BB	-	-	40.87 \pm 4.65	538.50/484	2.4 \pm 0.3	4.3 \pm 0.62

132.3.2 Analysis and Results

We apply all the techniques whatever we discuss above to the fourth FERMIGBRST catalog [7], for parameters estimations using the *least-square* method which is implemented in module of python library **LMFIT** [8]. Now we present our result of Fermi-GBM data analysis for two different cases.

132.3.2.1 Log-Normal Fits of the Duration Distribution for Full Range Dataset

FERMIGBRST catalog there are 2990 GRBs, we plotted the durations distributions for full range dataset. Then we fitted the following dataset for two ($k = 2$) and three ($k = 3$) component model which as shown in Fig. 132.1a and b, respectively. Since a single Gaussian model is not a good fit, so we take the $k = 2$ as the null hypothesis for model comparisons.

From Table 132.2, we find that χ^2 , reduced chi-square (χ^2/DOF) and AIC implies that $k = 3$ is a better fit over $k = 2$ and $\Delta\text{AIC} = 5.7 (>5)$, which corresponds to strong evidence for the third component [9] (Table 132.3).

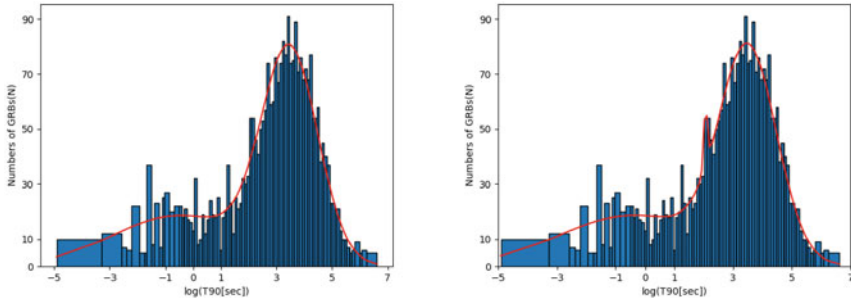


Fig. 132.1 Gaussian curve fits for the full range duration distribution plots for **a** 2-component ($k = 2$) model (Left) and **b** 3-component ($k = 3$) model (Right)

Table 132.2 The table of the fitted parameters for the two components ($k = 2$) and three components ($k = 3$) Gaussian curve fit of the duration distribution

k	Amp (A)	Mean (μ)	Sigma (σ)	Chisq (χ^2)	χ^2/dof	AIC	BIC	ΔAIC	ΔBIC
2	18.531	-0.484 ± 0.52	2.41 ± 0.89	4128.15	49.14	356.32	371.32	5.717	-1.78
	75.90	3.47 ± 0.041	-1.01 ± 0.06						
3	18.61	-0.38 ± 0.53	2.54 ± 0.86	3624.26	44.7	350.603	373.1		
	22.5	2.06 ± 0.022	0.062 ± 0.035						
	75.4	3.50 ± 0.036	0.97 ± 0.06						

Table 132.3 Parameters for the single ($k = 1$) and two ($k = 2$) log-normal fit for 0–3 s dataset

k	Amp (A)	Mean (μ)	Sigma (σ)	Chisq (χ^2)	χ^2/dof	AIC	BIC	ΔAIC	ΔBIC
1	19.214	-0.53 ± 0.48	2.4 ± 0.86	1663.1	55.5	135.36	140.0	-1.26	-5
2	19.482	-1.012 ± 0.28	1.38 ± 0.43	1416.48	52.46	136.1	145.0		
	9.81	0.8 ± 0.13	0.25 ± 0.194						

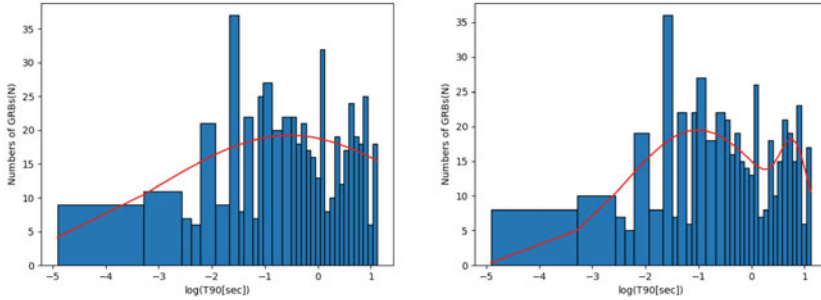


Fig. 132.2 Fits of distribution plots for **a** 1-component ($k = 1$) model (Left) and **b** 2-component ($k = 2$) model (Right) for 0–3 s dataset

132.3.2.2 Log-Normal Fits of the Duration Distribution for 0–3 S Dataset

Again we analysis, for 568 GRBs datasets available from FERMIGBRST catalogue in between 0 and 3 s time durations. Similarly, we fitted this dataset for $k = 1$ and $k = 2$ which as shown in Fig. 132.2a and b, respectively.

We find that χ^2 and reduced chi-square on favor two components ($k = 2$), whereas ΔAIC and ΔBIC favor one component ($k = 1$). We concluded that 2-component fit will better fit with the mentioned dataset (by the observation).

132.4 Summary and Perspectives

We analyzed the FERMIGBRST catalog for two cases, for full range dataset we got the three components fitting and for time interval 0–3 s, got two components Gaussian fitted distributions where midpoint at 0.67 ± 0.45 . From Sects. 132.2 and 132.3, we conclude that these intermediate type GRBs, ulSGRBs may exist in the time interval between 1 and 3 s with origin NS–NS merger(e.g., GRB170817A) [5].

However, the physical existences of the ulSGRBs is still questionable. In future, we will verify in more details and with strong statistical analysis, to verify the evidence that the NS–NS merger is really formed a new class of GRBs, ulSGRBs and their different properties with their spectral analysis.

References

1. S. Mukherjee et al., *Astrophys. J.* **508**(1), 314 (1998)
2. H.-F. Yu et al., *Astron. Astrophys.* **588**, A135 (2016)
3. A. Goldstein et al., *Astrophys. J. Lett.D* **848**(2), L14 (2017)
4. S. Dhara., *To study SGRBs & investigation Ultra Long Short GRBs using Fermi-GBM Data* (Master's dissertation, IIT Jodhpur, India, 2020)
5. I. Horvath et al., GRB 170817A/GW170817 is not a short gamma-ray burst, most likely an intermediate one. [arXiv:1710.11509](https://arxiv.org/abs/1710.11509) (2017)
6. I. Horváth, B.G. Tóth, *Astrophys. Space Sci.* **361**(5), 155 (2016)
7. A. von Kienlin et al., [arXiv:2002.11460](https://arxiv.org/abs/2002.11460) (2020)
8. M. Newville et al., *Astrophysics Source Code Library* (2016): ascl-1606
9. A.R. Liddle, Information criteria for astrophysical model selection. *Mon. Not. R. Astron. Soc. Lett.* **377**(1), L74–L78 (2007)

Chapter 133

Dark Matter and Leptogenesis in Minimal $U(1)_{B-L}$ Model with Nonminimal Quartic Inflation



Suruj Jyoti Das, Debasish Borah, and Abhijit Kumar Saha

Abstract We investigate the production mechanisms for dark matter and lepton asymmetry of the Universe after inflation in minimal $U(1)_{B-L}$ model. The singlet scalar having a non-minimal coupling to gravity serves the role of inflaton. We identify the lightest right-handed neutrino as DM candidate. We present a detail renormalization group evolution (RGE) improved study from inflationary energy scale to EW scale and find out that WIMP like thermal DM is overabundant in general. As an alternative, a scenario of non-thermal yield of dark matter relic is discussed. We also figure out that the model favors non-thermal leptogenesis over the thermal one due to low reheating temperature at the end of inflation.

133.1 Introduction

The incompleteness of the Standard Model (SM) of particle physics in predicting the origin of few cosmological observations and postulates such as inflation, dark matter, and baryogenesis favors beyond standard model (BSM) theory. In this work, we study a minimal extension of the SM, by a gauged $B - L$ symmetry with three right-handed neutrinos (RHN) required to cancel the gauge anomalies and a singlet scalar to spontaneously break the additional gauge symmetry, apart from generating RHN masses. We aim to address the production processes of dark matter and lepton (baryon) asymmetry in this minimal framework with the relevant parameters fixed from the criteria of achieving successful inflation, obeying the experimental bounds. The work is based on [1].

S. J. Das (✉) · D. Borah
Department of Physics, Indian Institute of Technology Guwahati, Assam 781039, India
e-mail: suruj@iitg.ac.in

A. K. Saha
School of Physical Sciences, Indian Association for the Cultivation of Science,
2A and 2B Raja S. C. Mullick Road, Kolkata 700032, India

© The Author(s), under exclusive license to Springer Nature Singapore Pte Ltd. 2022
B. Mohanty et al. (eds.), *Proceedings of the XXIV DAE-BRNS High Energy Physics
Symposium, Jaiti, India*, Springer Proceedings in Physics 277,
https://doi.org/10.1007/978-981-19-2354-8_133

737

133.2 The Model

We work in a $U(1)_{B-L}$ model with SM particle content, three RH neutrinos (N) and a SM gauge singlet scalar field (Φ). The Φ and N fields are assigned with 2 and -1 units of $U(1)_{B-L}$ charges. This simple choice leads to gauge anomalies cancellation in a trivial manner. The gauge invariant Lagrangian of the model is

$$\mathcal{L} = \mathcal{L}_{\text{SM}} - \frac{1}{4} B'_{\alpha\beta} B'^{\alpha\beta} + \mathcal{L}_{\text{scalar}} + \mathcal{L}_{\text{fermion}} \quad (133.1)$$

where $B'^{\alpha\beta} = \partial^\alpha Z_{BL}^\beta - \partial^\beta Z_{BL}^\alpha$ is the kinetic term of $B-L$ gauge boson (Z_{BL}) and

$$\begin{aligned} \mathcal{L}_{\text{fermion}} = & i \sum_{\kappa=1}^3 \overline{N_{R_\kappa}} \not{D} N_{R_\kappa} - \sum_{j=2}^3 \sum_{\alpha=e,\mu,\tau} Y_D^{j\alpha} \overline{l_L^\alpha} \tilde{H} N_R^j \\ & - \sum_{i=2}^3 \sum_{j=2}^3 Y_{N_{ij}} \Phi \overline{N_{R_i}^C} N_{R_j} - Y_{N_1} \Phi \overline{N_{R_1}^C} N_{R_1} + h.c. \end{aligned} \quad (133.2)$$

Due to the presence of Z_2 symmetry, N_{R_1} has no mixing with $N_{R_{2,3}}$ and also does not interact with SM leptons. Hence it qualifies as a stable DM candidate. The right-handed neutrinos and Z_{BL} get masses after the $U(1)_{B-L}$ symmetry breaking. The presence of heavy RHNs can also yield correct light neutrino mass via type I seesaw mechanism.

133.3 Inflation

We identify the inflaton as the real part ϕ of the complex scalar field Φ [2]. The action for ϕ in Jordan frame is of the form

$$S_J = \int d^4x \sqrt{-g} \left[-\frac{M_P^2}{2} R + \frac{1}{2} (D_\mu \phi)^\dagger (D^\mu \phi) - \frac{\lambda_2}{4} \phi^4 - \frac{\xi}{2} \phi^2 R \right]. \quad (133.3)$$

We follow the standard prescription to bring the inflaton action into Einstein frame ($V_E(\phi) = \frac{1}{4} \lambda_2 \phi^4 \left(1 + \frac{\xi \phi^2}{M_P^2}\right)$) and calculate the slow roll parameters and other observables. We work with renormalization group (RG) improved potential and in that case, λ_2 is function of energy scale in V_E . The RGE equation for λ_2 in the limit $g_{BL}^4, Y_N^4 \gg \lambda_2^2$ can be written as

$$\beta_{\lambda_2} \simeq 96g_{BL}^4 - 82Y_N^4 = \Delta. \quad (133.4)$$

Since the λ_2 is expected to be very small to match the observed value of scalar perturbation spectrum, we need to ensure $\beta_{\lambda_2} \sim 0$ to protect the stability of inflaton potential. In the opposite case $g_{BL}^4, Y_N^4 \ll \lambda_2^2$, the scenario merges with the usual non-minimal quartic inflation with λ_2 very tiny.

In the left panel of Fig. 133.1, we show the parameter space in the $g_{BL} - \xi$ plane, which gives correct predictions for inflationary observables : scalar spectral index n_s and tensor-to-scalar ratio r , for the case $g_{BL}^4, Y_N^4 \gg \lambda_2^2$. The other case we do not show here and can be found in existing literatures. The reheating temperature can be determined using the perturbative theory, where the reheating temperature can be written as $T_R \sim 0.5\sqrt{\Gamma_{H_2} M_P}$, where Γ_{H_2} is the total decay width of inflaton. Note that H_1, H_2 are the scalar mass eigenstates. The case with $g_{BL}^4, Y_N^4 \gg \lambda_2^2$ is disfavored as we will shortly see and hence estimate of the reheating temperature is not shown. For the opposite case, in Fig. 133.1 (right), we exhibit the contours of different values of T_R in $g_{BL} - \lambda_2$ plane.

133.4 Dark Matter and Leptogenesis

For the first case, i.e., $g_{BL}^4, Y_N^4 \gg \lambda_2^2$, DM is able to stay in thermal equilibrium with the SM particles in the early universe and thus falls into the WIMP category. The DM can annihilate into different final states in the thermal bath through processes mediated by scalars and the $U(1)_{B-L}$ gauge boson. It can be seen that all the DM relic satisfied points are disfavored from inflationary constraints (see top left of Fig. 133.2). of relic abundance for WIMP. In the second case ($g_{BL}^4, Y_N^4 \ll \lambda_2^2$), the DM-SM couplings are tiny and hence DM may never reach thermal equilibrium with the standard bath. Indeed a consistent non-thermal production of DM from H_2 and Z_{BL} decays can be realized as evident from Fig. 133.2 (top right). In case $M_{H_2} > T_R$ where both the H_2 and Z_{BL} remain out of equilibrium the production of Z_{BL} and N_1 will not be possible like before. One way out is to remove the Z_2 symmetry and turn on Yukawa couplings of DM with ordinary leptons which are present in thermal bath. In that case DM production occurs mostly from tree level decay of W^\pm boson.

Next, we discuss non-thermal leptogenesis in our model, which is closely connected to inflation as well as reheat temperature. Thermal vanilla leptogenesis is not possible in our setup as the predicted values of reheat temperature (for $g_{BL}^4, Y_N^4 \ll \lambda_2^2$) discussed earlier (see Fig. 133.1) falls below the Davidson-Ibarra limit. The right-handed neutrinos produced from inflaton decay turns non-relativistic and decay to SM leptons and Higgs instantaneously. The comoving lepton asymmetry can then be calculated as

$$\frac{n_L}{s} = \epsilon_A^2 \text{Br}_2 \frac{3T_R}{2M_{H_2}} + \epsilon_A^3 \text{Br}_3 \frac{3T_R}{2M_{H_2}}, \quad (133.5)$$

where ϵ_A^i are the CP asymmetry generated by N_i decays and Br_i represents the branching ratio of the inflaton decay to N_i . In bottom of Fig. 133.2, we show the

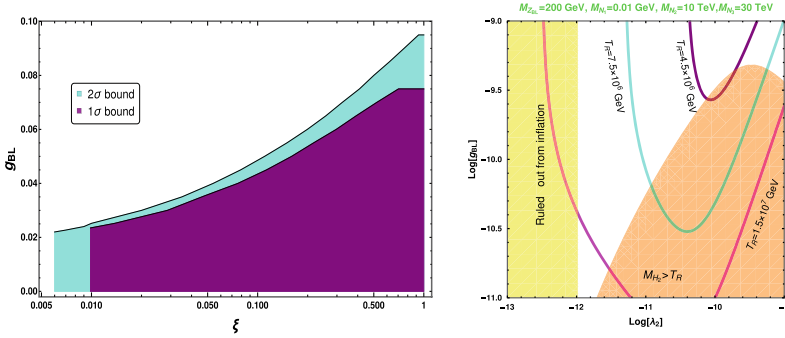


Fig. 133.1 Left: Allowed parameter space from inflation in $g_{BL} - \xi$ plane by Planck 2018 1σ and 2σ bounds. Right: Contours of T_R in $g_{BL} - \lambda_2$ plane. The yellow region is ruled out from inflation and in the orange region mass of the inflaton is larger than the reheating temperature

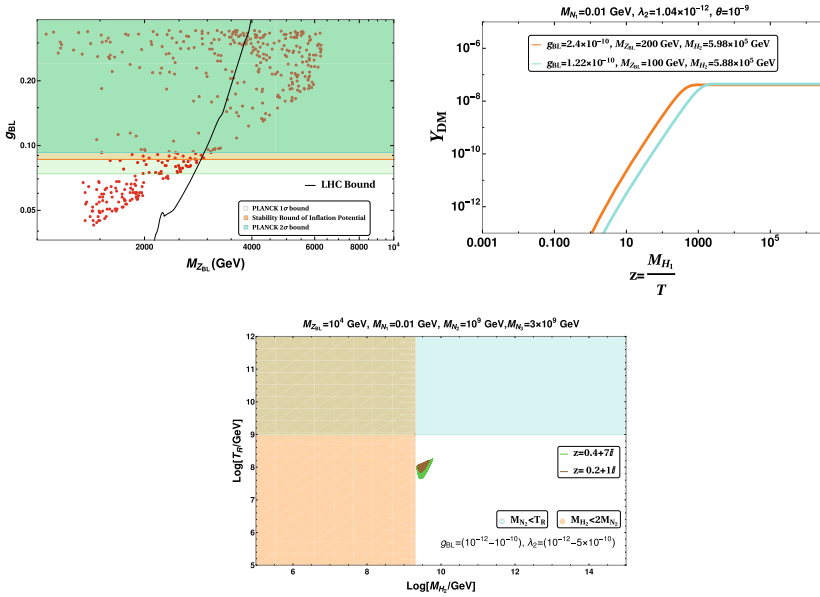


Fig. 133.2 Top left: Parameter space satisfying DM relic abundance in $g_{BL} - M_{Z_{BL}}$ plane by considering $\lambda_2 = 4.35 \times 10^{-10}$ and $\lambda_3 \sim 10^{-6}$ at inflationary energy scale. The shaded regions are disallowed. Top right: Evolution of comoving number densities for DM for two different sets of $(g_{BL}, M_{Z_{BL}})$ that satisfies the correct relic. Bottom: Region allowed by the observed baryon asymmetry in $M_{H_2} - T_R$ plane by varying g_{BL} , λ_2 and angle γ (angle of rotation in 23 plane for Casas Ibarra parametrization [3]), considering $M_{N_2} = 10^9$ GeV

allowed region in $M_{H_2} - T_R$ plane, which satisfies the bound on the comoving baryon asymmetry.

In conclusion, we have analyzed the possibility of simultaneous realization of inflation, dark matter and lepton asymmetry in a very popular gauged $B - L$ exten-

sion of the standard model. We first restrict the model parameters to satisfy the inflationary bounds and reach at an important conclusion that the WIMP dark matter becomes over abundant and thus disfavored. One can opt for FIMP case, however given the small order of reheating temperature, non-thermal leptogenesis turns out to be a natural choice. The breaking of $U(1)_{B-L}$ can also lead to the formation of cosmic strings with interesting phenomenology which we leave for future studies.

References

1. D. Borah, S. Jyoti Das, A.K. Saha, Eur. Phys. J. C **81**(2), 169 (2021)
2. N. Okada, M.U. Rehman, Q. Shafi, Phys. Lett. B **701**, 520–525 (2011)
3. J.A. Casas, A. Ibarra, Nucl. Phys. B **618**, 171–204 (2001)

Chapter 134

Cosmic Muon Momentum Spectra at Madurai



Suryanarayan Mondal, Apoorva Bhatt, V. M. Datar, G. Majumder, S. Pethuraj, K. C. Ravindran, and B. Satyanarayana

Abstract A magnetised mini Iron Calormeter (mini-ICAL) with 10 layers of $2\text{ m} \times 2\text{ m}$ RPCs interspersed with 11 layers of 5.6cm thick soft-iron has been built to study the performance of INO electronics in magnetic field as well as to achieve confidence on other engineering aspects of the ICAL detector and magnet. This detector is operational at IICHEP, Madurai, and is collecting data, triggered by muons produced in the cosmic ray showers at the top of the atmosphere due to the interactions of high energetic cosmic rays with the atmosphere. A magnetic field of $\sim 1.4\text{ T}$ is obtained in the iron by applying 900A of current through the copper coils. The trajectories of the charged particles are fitted to extract the momentum of the muons traversed through the detector. This paper will compare the measured momentum spectra with the Monte-Carlo prediction and the reconstructed spectra is unfolded to eliminate the detector's effects in order to obtain the true momentum spectra of cosmic muons at Madurai.

134.1 Introduction

The study of atmospheric muon charge ratio ($R_\mu = N_{\mu^+}/N_{\mu^-}$) is important to the measurement of the neutrino flux precisely, alongside the relevant information in the composition of the primary cosmic rays and the different mechanisms of matter particle interactions.

The cosmic ray muons are the most abundant charged particles available at the surface of the earth. As the primary cosmic rays are dominated by the proton, air

S. Mondal (✉) · A. Bhatt · S. Pethuraj
Homi Bhabha National Institute, Anushaktinagar, Mumbai, India
e-mail: suryamondal@gmail.com

S. Mondal · S. Pethuraj · K. C. Ravindran · B. Satyanarayana
Tata Institute of Fundamental Research, Homi Bhabha Road, Mumbai, India

V. M. Datar · G. Majumder
Department of High Energy Physics, Tata Institute of Fundamental Research, Colaba, Mumbai, India

molecule contains proton and neutron, the production of the positively charged kaons/pions/muons are more favoured. Hence the muon charge ratio reflects the excess of π^+ over π^- and K^+ over K^- during the formation of the cosmic ray shower in the forward region. In the TeV range however, the associated production of K^+ ($p + air \rightarrow K^+ + \Lambda + \dots$), which has no analogue for K^- , largely favours K^+ production over K^- , making the K^+/K^- ratio greater than π^+/π^- ratio [1].

134.2 Detector Setup of Mini-ICAL

The present setup, named mini-ICAL, is a magnetised iron calorimeter weighing at 85 Tonn. The mini-ICAL detector consists of 11 layers of iron of size $4\text{ m} \times 4\text{ m} \times 5.6\text{ cm}$ with the inter-layer gap of 4.5 cm. This makes the dimensions of this prototype detector are $4\text{ m} \times 4\text{ m} \times 1.06\text{ m}$. The detector setup is shown in Fig. 134.1. This iron layer has low carbon content which makes it strong enough mechanically to support its own weight, but also allows it to have high permeability with knee point at around $\sim 1.5\text{ T}$ when the copper coil is supplied with high DC current (upto 900 A).

Ten glass RPCs of dimensions $174\text{ cm} \times 183.5\text{ cm}$ are used as the active detector and are placed in the central region of the detector in between iron layers. A mixture of gases with the compositions of R134a (95.2%), iso- C_4H_{10} (4.2%) and SF_6 (0.3%) is flown in the RPCs. The RPCs are operated in avalanche mode with 10 kV of electric field applied between glass plates.

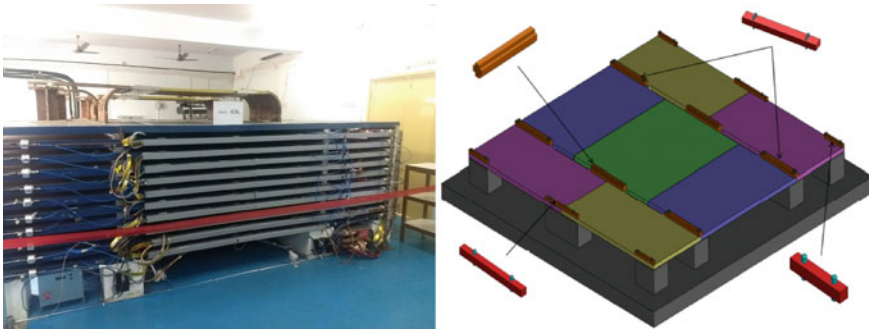


Fig. 134.1 (Left) The mini-ICAL Detector Setup (right) and the different sections of one layer of iron and the stainless-steel spacers

134.3 Monte-Carlo Simulation

The Monte-Carlo Simulation for this study has been executed in two parts. The Extensive Air Shower (EAS) has been simulated by the CORSIKA simulation package (v7.6300) [2]. The information of daughter particles generated by the EAS at the earth's surface level has been extracted and used in the detector simulation. In this study, for simulating the behaviour of hadrons for higher energy range, the SIBYLL hadron physics has been adopted and for the low energy range, the FLUKA model has been used. The magnetic rigidity cutoff has been implemented according to the location of the detector.

The detector simulation has been executed with the help of the GEANT4 toolkit [3]. In the detector simulation; the momentum value and the direction of the muons are randomly generated from the CORSIKA spectra. The detector's parameters are calculated using (efficiency, noise, strip multiplicity and resolution) which are calculated using the cosmic ray data without magnetic field in the detector.

134.4 Momentum Reconstruction and Result

As almost no significant bending is observed in the Y-side of the track, the clusters on the Y-side associated with the tracks are found and grouped using the method of Hough Transformation [4]. This method allows to avoid the noise hits in the detectors. As the magnetic field is mainly in the Y-direction, maximum bending of track is observed on the X-side. The clusters on the X-side are then fitted with a circle. Using the radius (r in meter) of the fitted circle, the transverse momentum (p_t in GeV) of the particle can be roughly estimated by $p_t = 0.3Br$ where, B is the average magnetic field in Tesla. The information of the fitted straight line on the Y-side and the circle on the X-side are further used to calculate the direction (zenith and azimuth) of the incidence particle. The particle is then propagated in the detector medium using the fourth order Runge-Kutta Nystrom [5]. The best fit momentum is then found using the method of Grid-Search. In the GEANT4 simulation, the generated vs reconstructed momentum (or the Response plot) is shown in Fig. 134.2.

The Iterative Bayesian Unfolding method is then used for unfolding the data in order to eliminate the detector's effects. The number of iteration required for the unfolding is obtained in the following. The momentum resolution for this method is calculated from the simulation which is shown in Fig. 134.3a. A response matrix is constructed with generated vs smeared momentum where the smearing values are taken from the calculated resolutions (shown in Fig. 134.3b). Another set of smeared momentum is filled in a 1D histogram which is then unfolded using the response matrix described above. At iteration 4, the unfolded distribution is matching the closest with the generated distribution shown in Fig. 134.3c. The following is shown only for μ^+ , but it showed the same result for μ^- also.

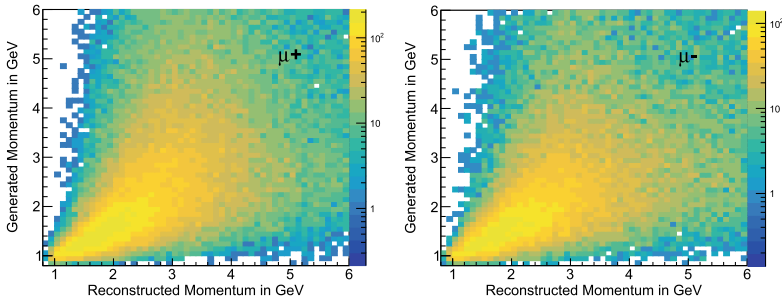


Fig. 134.2 Generated vs Reconstructed momentum for (left) μ^+ and (right) μ^-

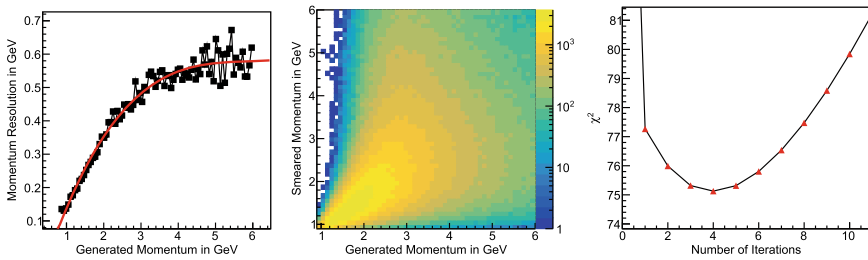


Fig. 134.3 **a** Momentum resolution from simulation, **b** Generated response matrix and **c** χ^2 vs iteration in Bayesian method

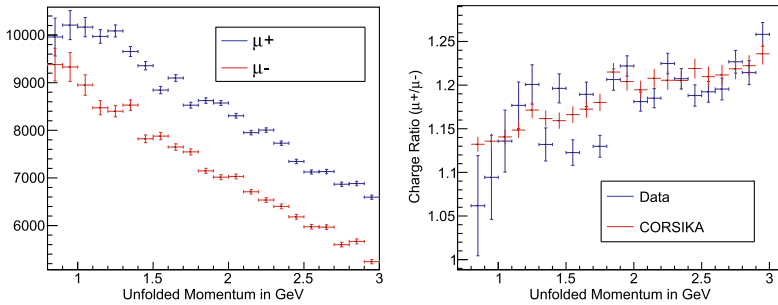


Fig. 134.4 **a** Unfolded momentum spectra and **b** Muon Charge ratio

Then the reconstructed momentum from data is then unfolded using response matrix generated from GEANT4 Simulation which is shown in Fig. 134.4a. The Ratio of the number of μ^+ to μ^- is compared with CORSIKA output (shown in Fig. 134.4b).

134.5 Discussion

Momentum beyond 3 GeV is not unfolded as the momentum resolution saturates beyond this energy. A new detector setup with 20 layers of RPC and 8 times larger in volume, INO Engineering Module is going to be built in few years at IICHEP Madurai. With more number of RPC layers, the momentum should be reconstructed up-to 12 GeV.

References

1. P. Adamson et al., MINOS. *Phys. Rev. D* **76**, 052003 (2007)
2. D. Heck et al., CORSIKA: A Monte Carlo code to simulate extensive air showers (1998)
3. S. Agostinelli et al., GEANT4. *Nucl. Instrum. Meth. A* **506**, 250–303 (2003)
4. R.O. Duda, P.E. Hart, *Commun. ACM* **15**(1), 11–15 (1972)
5. E. Lund, L. Bugge, I. Gavrilenko, A. Strandlie, *JINST* **4**, P04001 (2009)

Chapter 135

An Estimation of Joint Posterior of CMB Over Large Angular Scales Using Gibbs ILC Method



Vipin Sudevan and Rajib Saha

Abstract We present a detailed study of the Gibbs ILC method which provides a novel way to estimate the joint posterior density of Cosmic Microwave Background (CMB) signal (\mathbf{S}) and its theoretical angular power spectrum (C_ℓ) given the observed data in a model-independent manner. In order to generate samples from the joint CMB posterior density, we employ the internal-linear-combination (ILC) technique incorporated with prior information of the theoretical CMB covariance matrix augmented by the Gibbs sampling technique. We implement the method on low-resolution CMB maps simulated at WMAP and Planck frequency channels, assuming that the detector noise is negligible at large angular scales of the sky. We estimate a best-fit CMB cleaned map and its theoretical angular power spectrum (hereafter APS) along with the respective confidence intervals.

135.1 Introduction

One of the important methods to minimize the foregrounds is by applying the blind component separation method called Internal Linear Combination method (ILC) [1–3]. The unique property of this method is that it purely relies on the assumption that the CMB photons follow a blackbody distribution along every direction of the sky so that its temperature fluctuations are independent of frequency in thermodynamic units. In the ILC method, foreground minimization is achieved by linearly superposing all the available foreground contaminated observed CMB maps with appropriate weight factors. These weights can be computed analytically by minimizing the variance of the cleaned map. In Ref. [4], the authors developed a new method, the global ILC method, where the weights are estimated by minimizing a theoretical CMB covariance weighted variance, rather than the usual variance.

V. Sudevan (✉)

LeCosPA, National Taiwan University, Taipei 10617, Taiwan
e-mail: vipinsudevan1988@gmail.com

R. Saha

Indian Institute of Science Education and Research, Bhopal 462066, MP, India

This method outperforms the usual ILC at large angular scales of the sky since the new weights could effectively minimize the contributions from chance-correlations between CMB and foregrounds at large angular scales. The authors [5, 6] developed a Gibbs ILC method to estimate the CMB posterior density and corresponding theoretical CMB APS given the observed data over the large angular scales of the sky in a model-independent manner.

135.2 Formalism

In the Gibbs ILC method, to estimate the joint CMB posterior density, $P(\mathbf{S}, C_\ell | \mathbf{D})$, we draw samples of \mathbf{S} and C_ℓ using the Gibbs sampling technique. Here, \mathbf{S} , C_ℓ , and \mathbf{D} represent the true CMB signal, the theoretical CMB APS, and the observed CMB data, respectively. At the beginning of some iteration ($i + 1$), a cleaned CMB signal \mathbf{S}^{i+1} and a theoretical CMB APS C_ℓ^{i+1} are sampled from their respective conditional densities $P_1(\mathbf{S} | \mathbf{D}, C_\ell)$ and $P_2(C_\ell | \mathbf{D}, \mathbf{S})$ as follows:

$$\mathbf{S}^{i+1} \leftarrow P_1(\mathbf{S} | \mathbf{D}, C_\ell^i), \quad (135.1)$$

$$C_\ell^{i+1} \leftarrow P_2(C_\ell | \mathbf{D}, \mathbf{S}^i). \quad (135.2)$$

Using the pair of samples, \mathbf{S}^{i+1} and C_ℓ^{i+1} generated at the end of ($i + 1$)th iteration, we repeat the two sampling steps (Eqs. 135.1 and 135.2) for a large number of iterations till convergence is achieved. Ignoring some samples generated during the initial (burn-in) phase, all other samples appear as if they are sampled from the joint posterior density $P(\mathbf{S}, C_\ell | \mathbf{D})$.

In order to estimate $P(\mathbf{S}, C_\ell | \mathbf{D})$ in a model-independent manner, instead of sampling \mathbf{S} , we minimize the foregrounds present in the observed CMB data using the global ILC algorithm at each Gibbs step. Using the global ILC method, provided there are n number of observed CMB maps \mathbf{d}_i , an estimate $\hat{\mathbf{S}}$ of the underlying true \mathbf{S} is obtained as

$$\hat{\mathbf{S}} = \sum_{i=1}^n w_i \mathbf{d}_i, \quad (135.3)$$

where w_i is the weight corresponding to the i^{th} frequency channel. These weights follow a constraint that they sum to unity, i.e., $\sum_{i=1}^n w_i = 1$, and are estimated by minimizing the theoretical CMB covariance weighted variance $\sigma^2 = \mathbf{S}^T \mathbf{C}^\dagger \mathbf{S}$. Here, \mathbf{C} is the theoretical CMB covariance matrix and † denotes the Moore-Penrose generalized inverse.

In order to draw the samples of C_ℓ given \mathbf{S} and \mathbf{D} , we first define a variable $z = \hat{C}_\ell(2\ell + 1)/C_\ell$, where \hat{C}_ℓ is estimated from the cleaned CMB map, and obtain the conditional density $P_2(C_\ell | \mathbf{D}, \mathbf{S})$ as $P_2(C_\ell | \hat{C}_\ell) \propto z^{-(2\ell-1)/2-1} \exp\left[-\frac{z}{2}\right]$. To sample

a theoretical CMB APS, we draw z from the χ^2 distribution of $2\ell - 1$ degrees of freedom, as follows:

$$C_\ell = \hat{C}_\ell(2\ell + 1)/z. \tag{135.4}$$

135.3 Monte Carlo Simulations

In order to evaluate the performance of our Gibbs ILC method, we generate 1000 sets of input maps at 12 different WMAP (all channels) and Planck (7 channels from 30–353 GHz) frequencies at a pixel resolution defined by HEALPix [7] parameter $N_{side} = 16$ smoothed by a Gaussian beam of $\text{FWHM} = 9^\circ$ following the same procedure as described in [3, 5]. We use CMB theoretical APS consistent with the Planck-2018 [8] results for generating random CMB realizations used in the input maps.

Each simulation consists of 10 chains each with 10000 Gibbs iterations. After rejecting the initial 50 samples corresponding to the burn-in phase from each chain, we have overall 99500 samples of the cleaned CMB map and theoretical CMB APS to estimate the normalized densities, the best-fit CMB map, best-fit CMB theoretical APS, and their respective error estimates.

The posterior density of theoretical CMB APS estimated following [5] is a discrete estimation of the underlying APS. Using the Blackwell-Rao estimator [9], we estimate the likelihood of our APS. We show the likelihood function for some multipoles in Fig. 135.1. At low multipoles, the likelihood distribution is highly asymmetric with a long tail and becomes more symmetric as we go to higher multipoles.

Using 99500 samples of the cleaned map from each simulation, we estimate the standard deviation map. In the left panel of Fig. 135.2, we show the mean of all the 1000 standard deviation maps, and in the right panel the corresponding standard deviation. We see clearly that the Gibbs ILC method is able to clean the foregrounds effectively and the reconstruction bias along the Galactic plane is $< 5\mu\text{K}$.

We show the mean of the best-fit estimate of underlying CMB theoretical APS from all 1000 Monte Carlo simulations in the top panel of Fig. 135.3 along with the Planck-2018 theoretical APS. In the bottom panel, we show the mean difference between all 1000 input APS and best-fit APS.

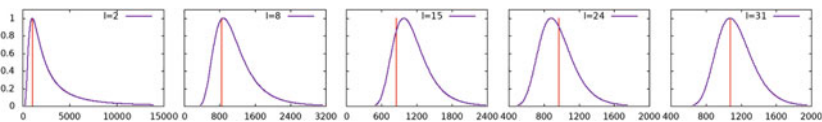


Fig. 135.1 We show the Blackwell-Rao estimates of the likelihood functions for some multipoles. The horizontal axis is plotted as $\ell(\ell + 1)C_\ell/2\pi$ in the unit of μK^2 . The vertical lines correspond to the positions of the CMB theoretical APS used to generate the random realization of the input CMB map used in this work

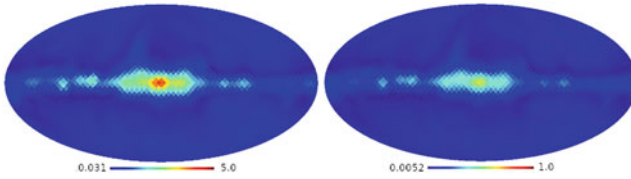


Fig. 135.2 In the left panel, we show the mean of all the 1000 standard deviation maps obtained from the 1000 simulations. The maximum standard deviation value is within $5 \mu\text{K}$. In the right panel, we show the standard deviation of all the 1000 standard deviation maps. Both the maps are expressed in μK^2 thermodynamic units

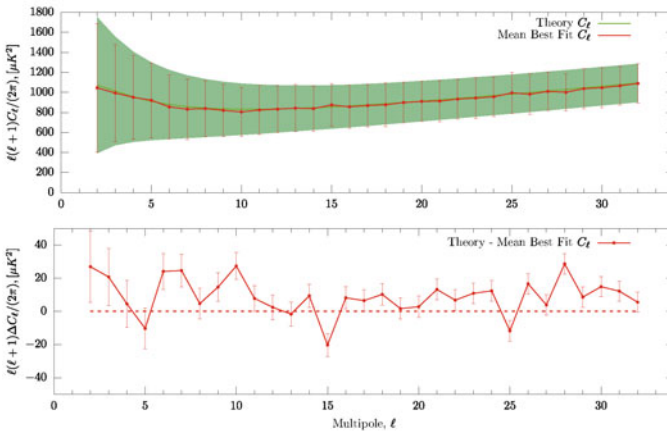


Fig. 135.3 In the top panel, we plot the mean input APS, best-fit APS, and corresponding standard deviation for 1000 simulations. The mean of 1000 differences APS and associated errors are shown in the bottom panel figure. We find that the mean input and the mean best-fit APS agree very well from the top panel figure

135.4 Conclusion

In this article, we discussed a new method, the Gibbs ILC method, to estimate the CMB posterior density over the large angular scales of the sky using the realistic sky simulations at WMAP and Planck channels by using a global ILC method [4] and Gibbs sampling [5] as the basic tools. From 1000 Monte Carlo simulations, we find that our method minimizes foregrounds effectively and the error while reconstructing a best-fit cleaned CMB map is quite low ($<5\mu\text{K}$). Our best-fit CMB signal and its theoretical APS along with the appropriate confidence intervals can be directly incorporated into the cosmological parameter estimation pipeline. A unique feature of the Gibbs ILC method is that it extends the model-independent nature of CMB reconstruction using the ILC method to the estimation of joint posterior density at large angular scales.

References

1. M. Tegmark, G. Efstathiou, *Mon. Not. R. Astron. Soc.* **281**, 1297 (1996)
2. R. Saha, *APJ* **739**, L56 (2011)
3. V. Sudevan et al., *APJ* **842**, 62 (2017)
4. M. Sudevan, R. Saha, *APJ* **867**, 74 (2018)
5. M. Sudevan, R. Saha, *APJ* **897**, 30 (2020)
6. M. Sudevan, R. Saha, *APJ* **902**, 69 (2020)
7. K.M. Górski et al., *APJ* **622**, 759 (2005)
8. N. Aghanim [Planck] et al., *Astron. Astrophys.* **641**, A6 (2020)
9. U. Purkayastha et al., [arxiv:2004.08521](https://arxiv.org/abs/2004.08521) (2020)

Chapter 136

Dense Matter in Strong Magnetic Field: Covariant Density Functional Approach



Vivek Baruah Thapa, Monika Sinha, Jia Jie Li, and Armen Sedrakian

Abstract The existence of compact stars with high mass ($> 2M_{\odot}$) raises the possibility of the appearance of heavy baryons at high-density regimes. With this possibility, we study the effect of a strong magnetic field on the matter composed of baryon-octet and Δ -resonances under strong magnetic fields. The functionals in the hyperonic sector are constrained by the Λ , Ξ^- hypernuclei data from terrestrial experiments. Δ -resonance sector is constrained by studies of their scattering off nuclei and heavy-ion collisions. The main effect of the magnetic field is shown to be the oscillations of various matter properties, viz., particle populations and Dirac effective mass with density resulting from the occupation of the Landau level by charged fermions in strong magnetic fields.

136.1 Introduction

Neutron stars (NSs), the end products of massive stars produced in supernova explosions, are among the most fascinating objects of the universe because matter inside them is expected to be in exotic states, which are not yet possible to produce in terrestrial laboratories. NSs are not only extreme in density (several orders of nuclear

V. B. Thapa (✉) · M. Sinha
Indian Institute of Technology Jodhpur, Jodhpur 342037, India
e-mail: thapa.1@iitj.ac.in

J. J. Li
Institute of Modern Physics, Chinese Academy of Sciences, Lanzhou 730000, China
Institute for Theoretical Physics, Goethe University, Max-von-Laue-Straße, 1,
60438 Frankfurt am Main, Germany

A. Sedrakian
Frankfurt Institute for Advanced Studies, Ruth-Moufang-Straße, 1, 60438 Frankfurt am Main,
Germany

Institute of Theoretical Physics, University of Wrocław, pl. M. Borna 9,
50-204 Wrocław, Poland

saturation density, n_0) but may also possess extreme surface magnetic fields in the range of 10^{14} – 10^{15} G, in which case they are termed as *magnetars* [1]. The strong magnetic field affects the equation of state (EoS) and the static properties of NS, as well as their dynamics such as magneto-thermal evolution and rotational dynamics [2, 3]. The observations of massive NSs [4] ($M_{NS} > 2 M_\odot$) suggest that their central densities are high enough for the emergence of hyperons at about 2 – $3 n_0$ as well as Δ -resonances [5–7] within the matter density range 1 – $2 n_0$. Here, we summarize our recent work on the properties of Δ -resonances admixed hypernuclear matter in intense magnetic fields within the density-dependent covariant density functional (DD-CDF) model [8].

136.2 Formalism and Results

We consider matter composed of the baryon octet ($b \equiv N, \Lambda, \Xi, \Sigma$), Δ -isobars, and leptons ($l \equiv e^-, \mu^-$) interacting via $\sigma, \omega, \rho, \sigma^*, \phi$ -mesons. The total Lagrangian density of the fermionic matter in the presence of magnetic field is given by Thapa et al. [8]

$$\begin{aligned} \mathcal{L} = & \sum_b \bar{\psi}_b (i\gamma_\mu D^\mu - m_b + g_{\sigma b}\sigma + g_{\sigma^* b}\sigma^* - g_{\omega b}\gamma_\mu\omega^\mu - g_{\phi b}\gamma_\mu\phi^\mu - g_{\rho b}\gamma_\mu\tau_b \cdot \rho^\mu) \psi_b \\ & + \sum_\Delta \bar{\psi}_\Delta (i\gamma_\mu D^\mu - m_\Delta + g_{\sigma\Delta}\sigma - g_{\omega\Delta}\gamma_\mu\omega^\mu - g_{\rho\Delta}\gamma_\mu\tau_\Delta \cdot \rho^\mu) \psi_\Delta^v \\ & + \frac{1}{2}(\partial_\mu\sigma\partial^\mu\sigma - m_\sigma^2\sigma^2) + \frac{1}{2}(\partial_\mu\sigma^*\partial^\mu\sigma^* - m_{\sigma^*}^2\sigma^{*2}) - \frac{1}{4}\omega_{\mu\nu}\omega^{\mu\nu} + \frac{1}{2}m_\omega^2\omega_\mu\omega^\mu \\ & - \frac{1}{4}\phi_{\mu\nu}\phi^{\mu\nu} + \frac{1}{2}m_\phi^2\phi_\mu\phi^\mu - \frac{1}{4}\rho_{\mu\nu} \cdot \rho^{\mu\nu} + \frac{1}{2}m_\rho^2\rho_\mu \cdot \rho^\mu \\ & + \sum_{l=e,\mu} \bar{\psi}_l (i\gamma_\mu D^\mu - m_l) \psi_l - \frac{1}{16\pi} F_{\mu\nu} F^{\mu\nu} \end{aligned} \quad (136.1)$$

where the symbols have their usual meanings. The degeneracy factors for the particles with different spins are, for spin-1/2 particles [9]: first landau level: 1; other levels: 2; for spin-3/2 particles [10]: first landau level: 2; second level: 3; other levels: 4. The energy density is given by

$$\varepsilon_m = \sum_{B=b,\Delta} \varepsilon_B + \sum_l \varepsilon_l + \frac{1}{2}m_\sigma^2\sigma^2 + \frac{1}{2}m_{\sigma^*}^2\sigma^{*2} + \frac{1}{2}m_\omega^2\omega_0^2 + \frac{1}{2}m_\rho^2\rho_{03}^2 + \frac{1}{2}m_\phi^2\phi_0^2. \quad (136.2)$$

The matter pressure is then obtained via the Gibbs-Duhem relation as

$$p_m = \sum_b \mu_b n_b + \sum_\Delta \mu_\Delta n_\Delta + \sum_l \mu_l n_l - \varepsilon_m. \quad (136.3)$$

We implement the density-dependent DDME2 [11] parameterization to evaluate the coupling parameters and consider three types of composition: purely nucleonic (labeled N), baryon-octet (NY), and baryon-octet and resonances ($NY\Delta$). For the hyperonic sector, the density-dependent vector coupling constants are determined from SU(6) symmetry. The scalar meson-hyperon couplings are calculated by considering the optical potentials of Λ, Σ, Ξ in symmetric nuclear matter. Due to the lack of experimental information in the Δ -resonances sector, the Δ baryon-meson

couplings are chosen close to nucleon-meson ones. For details, see Ref. [8]. Two approaches are adopted to model the magnetic field profile in the NS interior, viz., *exponential* [12] and *universal* [13].

Figure 136.1 shows the EoSs and the mass-radius (M - R) relations for the different matter compositions without magnetic field. The EoSs satisfy the astrophysical constraints. When including the magnetic field, we assume that the central magnetic field (B_c) for both profiles is 2.9×10^{18} G. The surface magnetic fields for the *exponential* and *universal* profiles are found to be $\sim 10^{15}$ G and $\sim 6 \times 10^{17}$ G, respectively. Figure 136.2 depicts the magnetic field effects on the EoSs for the $NY\Delta$ matter composition in case of *exponential* as well as *universal* profile. The fluctuations in the pressure normalized to its zero-field value [$P(B)/P(0)$] are observed more prominently (**even though marginal**) near the surface with *universal* profile due to the high magnetic fields. Toward the center of the star, the fluctuation trends are quite similar for both the profiles. Figure 136.3, right panel, shows the ratio of fractions of different species as a function of normalized baryon number density for $NY\Delta$ -composition. The oscillating nature of fractions arises due to successive occupation of Landau levels for charged species. The effect of the field is not substantial in the low-density regime for exponential field profile as the field strength in this case is small near the surface. In the case of the universal profile, the low-density regime shows strong oscillations due to small reduction of the magnetic field with density. The variations of the effective mass of a baryon (nucleon) in the presence of a magnetic field are shown in Fig. 136.3, right panel. The amplitudes of oscillations are higher in the case of the universal profile due to the computed higher surface magnetic field. With the emergence of Ξ^- close to $5n_0$, a 4% reduction of effective nucleon mass is observed for both profiles.

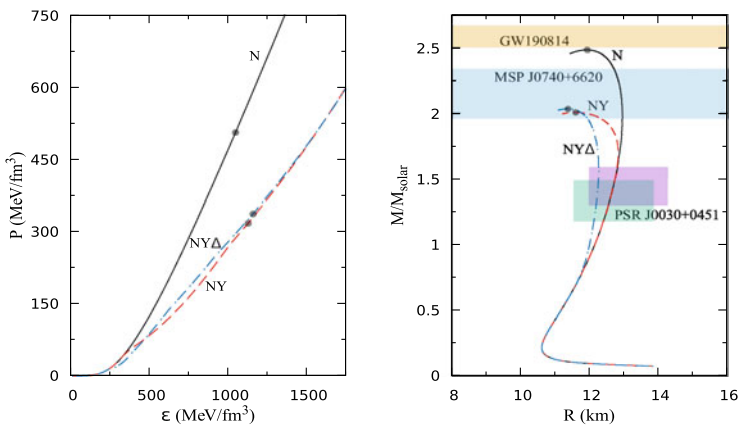


Fig. 136.1 The EoS (left panel) and mass-radius relations (right panel) for NS with different compositions in the static and non-magnetized limit. The black dots label the maximum mass NS for each EoSs

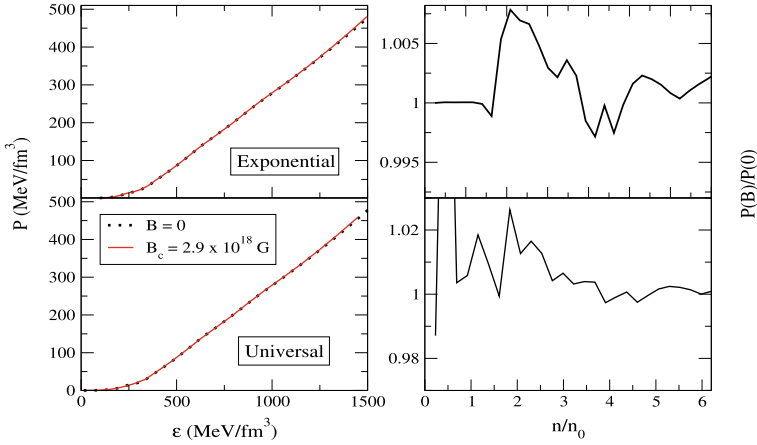
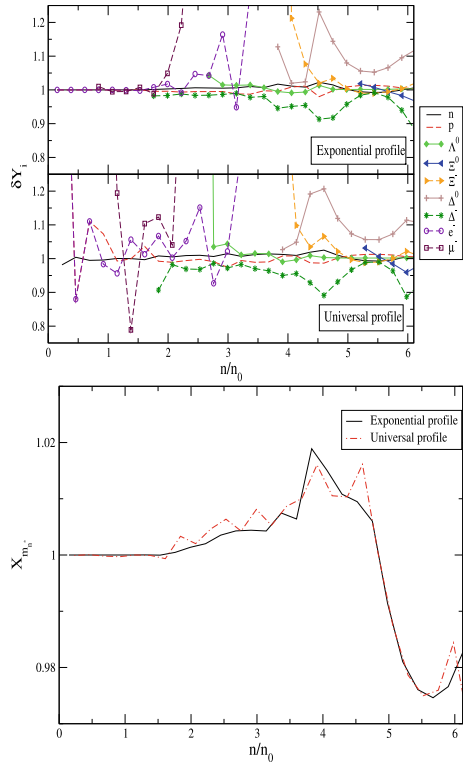


Fig. 136.2 EoS (left panel) and the pressure ratio of $B \neq 0$ and $B = 0$ matter (right panel) for $NY\Delta$ -composition. Upper panel: *exponential*; lower panel: *universal* profile

Fig. 136.3 Left panel: The quantity $\delta Y_i = n_i(B)/n_i(0)$ as a function of the baryon number density normalized to n_0 with $NY\Delta$ composition for *exponential* (upper panel), *universal* (lower panel) profile. Right panel: The quantity $X_{m_n^*} = m_{N^*}^*(B)/m_{N^*}^*(0)$ as a function of baryon number density n in units of n_0 with $NY\Delta$ composition



To summarize, we find that the EoSs which include strong magnetic fields **are slightly stiffened compared to non-magnetized cases. The resulting M - R relations are consistent with the recent maximum mass and mass-radius inferences from the millisecond pulsars J0740+ 6620 and PSR J0030+ 0451.** The observed oscillations in the effective nucleon mass may introduce oscillations in other physical properties of matter such as thermal conductivity and specific heat.

References

1. A.K. Harding, D. Lai, Rep. Prog. Phys. **69**(9), 2631–2708 (2006)
2. M. Sinha, A. Sedrakian, Phys. Rev. C **91**, 035805 (2015)
3. A. Sedrakian, X.-G. Huang, M. Sinha, J.W. Clark, J. Phys. **861**, 012025 (2017)
4. H.T. Cromartie et al., Nat. Astron. **4**, 72–76 (2020)
5. A. Drago, A. Lavagno, G. Pagliara, D. Pigato, Phys. Rev. C **90**, 065809 (2014)
6. B.-J. Cai, F.J. Fattoyev, B.-A. Li, W.G. Newton, Phys. Rev. C **92**, 015802 (2015)
7. J.J. Li, A. Sedrakian, F. Weber, Phys. Lett. B **783**, 234 (2018)
8. V.B. Thapa, M. Sinha, J.J. Li, A. Sedrakian, Particles **3**, 660 (2020)
9. M. Sinha, B. Mukhopadhyay, A. Sedrakian, Nucl. Phys. A **898**, 43–58 (2013)
10. M.G. de Paoli et al., J. Phys. G: Nuc. Part Phys. **40**(5), 055007 (2013)
11. G.A. Lalazissis, T. Nikšić, D. Vretenar, P. Ring, Phys. Rev. C **71**, 024312 (2005)
12. D. Bandyopadhyay, S. Chakrabarty, S. Pal, Phys. Rev. Lett. **79**, 2176–2179 (1997)
13. D. Chatterjee, J. Novak, M. Oertel, Phys. Rev. C **99**, 055811 (2019)

Part V
Detectors, Instrumentation, Future
Facilities, and Societal Applications

Chapter 137

Particle Identification in Belle II Silicon Vertex Detector



A. B. Kaliyar

Abstract We report a particle identification (PID) method developed for charged pions, kaons, and protons using specific ionization information in the silicon-strip vertex detector (SVD) of Belle II with $D^{*+} \rightarrow D^0[\rightarrow K^-\pi^+]\pi^+$ and $\Lambda \rightarrow p\pi^-$ decay samples. The study is based on e^+e^- collision data recorded at the $\Upsilon(4S)$ resonance by the Belle II detector. The introduction of additional information from the SVD is found to improve the overall PID performance in the low-momentum region.

137.1 Introduction

Identification of charged particles such as pions, kaons, and protons is important to the physics program of the Belle II experiment [1]. Belle II has an excellent particle identification (PID) system comprising three main subdetectors, the central drift chamber (CDC), time-of-propagation counter, and aerogel ring-imaging Cherenkov counter. Low-momentum charged particles having a transverse momentum $p_T < 65 \text{ MeV}/c$ are unable to reach the CDC, owing to their highly curved trajectories. Our goal is to exploit specific ionization (dE/dx) [2] by these low-momentum particles in the silicon-strip vertex detector (SVD) toward identifying them. Even if the particles have a p_T greater than $65 \text{ MeV}/c$ and are thus able to reach the CDC, the dE/dx values measured in the SVD can provide complementary information to that obtained from the main PID subdetectors [3].

The study is based on e^+e^- collision data recorded at the $\Upsilon(4S)$ resonance by the Belle II detector. We use relatively clean samples of $D^{*+} \rightarrow D^0(K^-\pi^+)\pi^+$ and $\Lambda \rightarrow p\pi^-$ decays to first obtain the SVD dE/dx calibration for pions, kaons, and protons. Later, we check the impact of dE/dx information on overall PID performance

A. B. Kaliyar (For the Belle II collaboration).

A. B. Kaliyar (✉)
Tata Institute of Fundamental Research, Mumbai 400005, India
e-mail: basithkaliyar@gmail.com

using the same decay channels. To assess the impact of SVD dE/dx information on the overall PID performance, we plot the identification efficiency and fake rate as a function of momentum applying a requirement on the binary PID likelihood $\mathcal{L}(i/j) > 0.5$. The efficiency ϵ_i is defined as the ratio of the number of charged particle tracks identified with PID requirement under the particle hypothesis i and the number of charged particle tracks identified kinematically under the hypothesis i . The fake rate ($f_{j \rightarrow i}$) is the ratio of the number of charged particle tracks identified with PID requirement under the hypothesis i and the number of charged particle tracks identified kinematically under the hypothesis j .

137.2 SVD dE/dx Calibration

The $D^{*+} \rightarrow D^0(\rightarrow K^-\pi^+)\pi^+$ decay is used to calibrate the pion and kaon PIDs based on dE/dx information in SVD. We require the charged particle tracks to have a transverse (longitudinal) impact parameter less than 0.5 cm (2.0 cm). These tracks must have at least one SVD hit and a track-fit χ^2 probability value greater than 10^{-5} . To further purify the sample, we require the reconstructed D^0 mass to lie between 1.85 and 1.88 GeV/c^2 , corresponding to a $\pm 3\sigma$ window around the nominal D^0 mass. The reconstructed D^* mass must be within 1.95 and 2.05 GeV/c^2 . We apply a loose criterion on kaon and pion PID likelihoods, calculated without SVD information, to remove low-momentum secondary pions and kaons produced due to hadronic interaction in the detector material. We model the signal and background shape in the D^*-D^0 mass difference (Δm) by a sum of two Gaussian functions with a common mean and a threshold function, respectively. The $sPlot$ [4] technique is used to subtract the residual background contributions.

The $\Lambda \rightarrow p\pi$ decay is used to calibrate the proton PID based on dE/dx information in SVD. We require the reconstructed $p\pi$ invariant mass of Λ candidates to be in the range [1.10, 1.13] GeV/c^2 , and they are further subjected to a vertex fit. To remove the random combination of two tracks, the distance between the interaction point and the vertex of the Λ candidates is required to be greater than 1.0 cm and the vertex-fit χ^2 probability must be greater than 10^{-3} . We also require at least one SVD hit for both daughter tracks. We suppress the contamination of charged pions coming from the K_s^0 decay by rejecting events that have the $M_{\pi^+\pi^-}$ value in the range [488, 508] MeV/c^2 , corresponding to a $\pm 3\sigma$ window around the nominal K_s^0 mass. Similarly, events with electrons from converted photons are suppressed by excluding $M_{e^+e^-} < 50 \text{ MeV}/c^2$. We impose an additional requirement of at least one CDC hit and a loose criterion on the proton PID calculated without SVD information to remove low-momentum secondary pions produced due to hadronic interaction with the detector material. We model the signal shape in $M_{p\pi}$ with the sum of a Gaussian and two asymmetric Gaussian functions of a common mean and the background shape with a second-order Chebyshev polynomial. Again, the $sPlot$ [4] technique is used to subtract the residual background contributions. The fitted distributions of Δm from the D^* sample and $M_{p\pi}$ from the Λ sample are shown in Fig. 137.1.

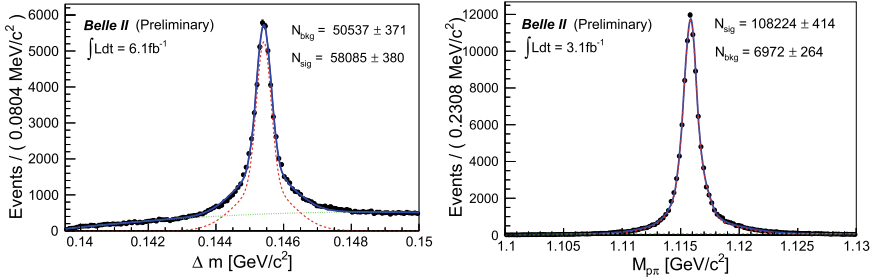


Fig. 137.1 Fitted distributions of Δm from the D^* sample (left) and of $M_{p\pi}$ from the Λ sample (right)

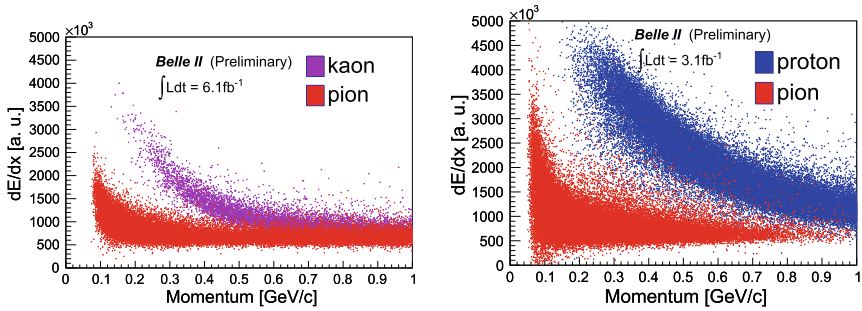


Fig. 137.2 Scatter plot of dE/dx values of pions and kaons as a function of their momentum for the D^* sample (left) and dE/dx values of protons and pions as a function of their momentum from the Λ sample (right)

As shown in Fig. 137.2, the two-dimensional distributions of dE/dx versus momentum shows a clear separation between different particles in the low-momentum region. The $\pi - \text{K}$ and $\text{K} - \text{p}$ separation are found to be $1-5 \sigma$ (width of the dE/dx distribution) below 1 GeV/c. These background subtracted two-dimensional histograms are used as probability density functions for various particle hypotheses and uploaded to the calibration database.

137.3 PID Performance

To assess the impact of the SVD dE/dx information on the overall PID, we use a separate set of data samples processed including the PID information from SVD. We study the efficiency and fake rate as a function of momentum by varying the PID likelihood $\mathcal{L}(i/j)$. The PID likelihood criterion is varied from 0 to 1 in order to produce these plots. The efficiency versus fake rate distributions shown in Fig. 137.3 confirm the improvement in PID performance by adding the SVD dE/dx information.

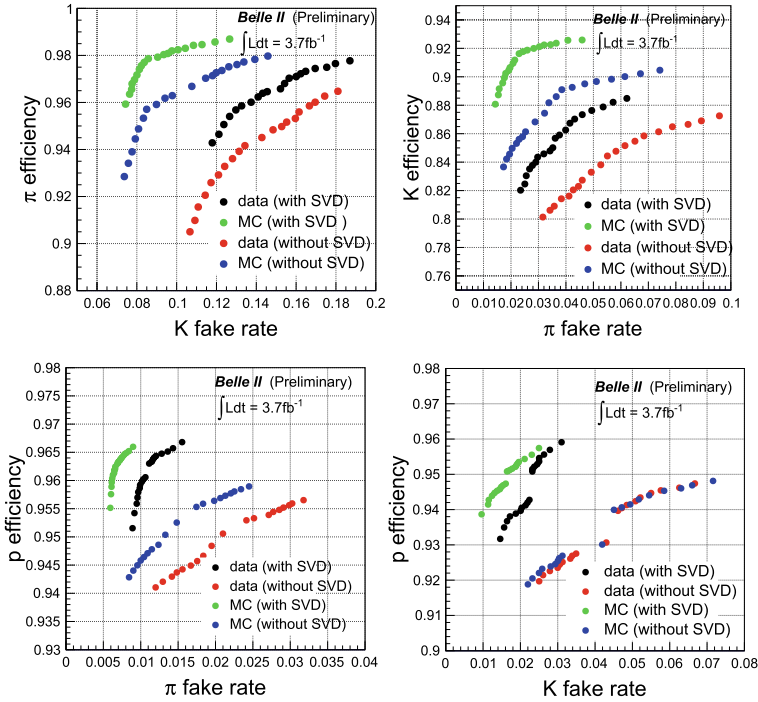


Fig. 137.3 Efficiency versus fake rate distributions with and without SVD for $p < 1 \text{ GeV}/c$

The data-MC difference in performance arises due to imperfect simulation of the cluster energy distribution for which the work is underway. Nonetheless, our study confirms that for a given fake rate the addition of dE/dx information improves the efficiency in the low-momentum region.

137.4 Conclusion

We have developed a PID method for charged pions, kaons, and protons using energy loss information in Belle II SVD with $D^{*+} \rightarrow D^0(\rightarrow K^-\pi^+)\pi^+$ and $\Lambda \rightarrow p\pi^-$ decay samples. The study tells that adding the SVD information improves the overall PID performance in the low-momentum region.

References

1. E. Kou et al., Prog. Theor. Exp. Phys. **2019**, 123C01 (2019)
2. W. R. Leo, *Techniques for Nuclear and Particle Physics Experiments*. (Springer, 1994)
3. T. Abe et al., Belle II Technical Design Report (2010). [arXiv:1011.0352](https://arxiv.org/abs/1011.0352) [physics.ins-det]
4. M. Pivk, F.R. Le Diberder, Nucl. Instrum. Methods Phys. Res. Sect. A **555**, 356 (2005)

Chapter 138

Study of Radiation Damage in the CMS Hadron Calorimeter Using Isolated Muons from 2018 Collision Data



Amandeep Kaur

Abstract Isolated muons from proton-proton collision data, collected by the CMS detector at the LHC, are used to study radiation damage of different towers of the CMS hadron calorimeter. All the channels of the barrel and the endcap calorimeters in 2018 are read using hybrid photo diodes and Silicon photomultipliers, respectively. The data indicate that the barrel towers at larger pseudorapidity ($|\eta|$) show larger degradation in performance at the end of the run period. For endcap towers, the high level of pileup at the highest $|\eta|$ makes it difficult to determine the peak position of the charge distribution and is difficult to make any measurement. To make a measurement in the forward region of the detector, low pileup data collected by the CMS detector in 2018 are analyzed. The peak positions of the most affected towers are estimated with much better precision in these data. It is observed that several low luminosity runs distributed over the year can monitor the level of radiation damage in these most affected towers.

138.1 Introduction

The Hadron Calorimeter (HCAL) [1] of the Compact Muon Solenoid (CMS) [2] experiment at the Large Hadron Collider (LHC) utilizes plastic scintillator with wavelength shifting fiber for its barrel (HB) and endcap (HE) components. The HB is read out using Hybrid Photo Diodes (HPD) and Silicon Photomultipliers (SiPM) were used to read out HE towers during 2018 data taking as shown in Fig. 138.1. Consequently, a smaller number of layers are grouped into a tower in the HB and the number of depth segments increase substantially for HE than in the previous running. The segmentation along $|\eta|$ (58 segments with η index, $i\eta$, running between -29 and $+29$) or ϕ (36 or 72 segments depending on $i\eta$) remains unchanged over years.

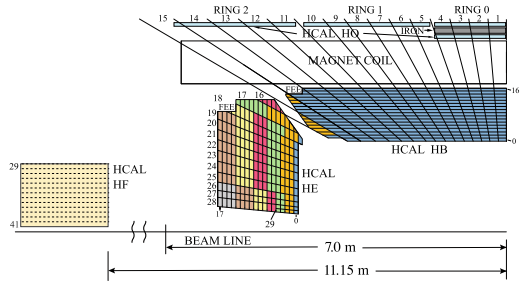
A. Kaur (For the CMS Collaboration).

A. Kaur (✉)
Panjab University, Chandigarh 160014, India
e-mail: amandeep.kaur@cern.ch

© The Author(s), under exclusive license to Springer Nature Singapore Pte Ltd. 2022
B. Mohanty et al. (eds.), *Proceedings of the XXIV DAE-BRNS High Energy Physics Symposium, Jatni, India*, Springer Proceedings in Physics 277,
https://doi.org/10.1007/978-981-19-2354-8_138

769

Fig. 138.1 Layout of the barrel and endcap hadron calorimeter showing the segmentation along $|\eta|$ and depth for the scenario of 2018



The level of radiation damage in the plastic scintillators is monitored in situ using different methods. Both HB and HE have a built-in laser monitoring system where ultraviolet light can reach a subset of scintillator tiles using a triggerable laser, a system of neutral density filters, and a quartz fiber light distribution system. This laser calibration is done regularly, and the results are used in correcting the calorimeter response. However, the laser calibration is restricted to a limited number of scintillator tiles, and these results need a certain amount of modeling to extend for all HB/HE channels. Radiation damage effect in the scintillators is also monitored in situ using energy depositions due to hadrons from the collision data [3]. Muons from collision data can also be used to study the loss of signal in the HB and HE due to the radiation damage effect. Muons, being the minimum ionizing particles (MIPs), do not interact much with the calorimeter materials. Due to its less interactive or showering nature in the HCAL, it is easy to compare the responses in the HCAL due to muons after different values of delivered luminosity.

138.2 Data and Methodology

Studies have been performed using 2018 proton-proton collision data collected by the CMS detector corresponding to a total integrated luminosity of $\sim 66.5 \text{ fb}^{-1}$. The entire data set is divided into 20 parts each spanning over $\sim 3.0 \text{ fb}^{-1}$ integrated luminosity, referred to as luminosity block.

There are in addition two special short runs at low luminosity for some dedicated studies and are used for HE studies detailed here. However, these low luminosity runs happened within a short interval. The integrated luminosity between the two periods is only 1.1 fb^{-1} . Muons used for radiation damage studies are required to be isolated from other charged and neutral particles such that the energy measured in the HCAL tower is expected to be entirely due to the muon. To ensure this, muons are selected with the following additional criteria:

- the muon track propagated to the surface of the Electromagnetic Calorimeter (ECAL) to HCAL has to cross one HCAL tower (having the same $i\eta$ or $i\phi$);

- energy in the HCAL tower hit is the highest within a 3×3 matrix surrounding that tower and is measured as “signal” in that 1×1 cell. For the radiation damage study, the gain or response correction due to radiation damage is removed from the measured energy to get uncorrected energy or raw charge measurement and is then fitted with Gaussian convoluted Landau functions to get the Most Probable Value (MPV) of measured charge.

138.3 Results

Most of the towers in the HB have a single depth with the exception of towers at $i\eta = \pm 15$ and ± 16 . For a comparison of all the $i\eta$ towers, the charges in the two depths of these 4 towers are combined. On the other hand, the radiation level is higher in the front of the calorimeter. So the towers at depth = 1 are also separately looked into for $i\eta = \pm 15$ and ± 16 .

Figure 138.2 (left) shows charge distribution for $i\eta + 15$ for a particular $i\phi$ value. The distributions are fitted using the Gaussian convoluted Landau function within acceptable χ^2 per degree of freedom. MPVs obtained from these fits for each $i\phi$ are plotted as a function of $i\phi$ as shown in Fig. 138.2 (middle). Figure 138.2 (right) shows distributions of MPV values obtained from 72 independent fits corresponding to different $i\phi$'s for $i\eta = 15$ (combined depth). Similar methodology is used for all $|i\eta|$ values for HB.

Figure 138.3 shows MPV values of the charge distribution for combined depth (depth 1+2) as a function of delivered luminosity for $i\eta = 15$. Figure 138.3 (right) shows slopes from the fits to the exponential function of the most probable charge distribution as a function of delivered luminosity as a function of $i\eta$. The measurements are consistent for $\pm z$ sides. The plot on the right indicates that the slopes increase with $|i\eta|$ suggesting larger radiation damage there.

However, this study becomes crucial with increasing $|i\eta|$ due to pileup which is larger for towers with higher $|i\eta|$ as shown in Fig. 138.4 for $i\eta = 26$, depth 1. The

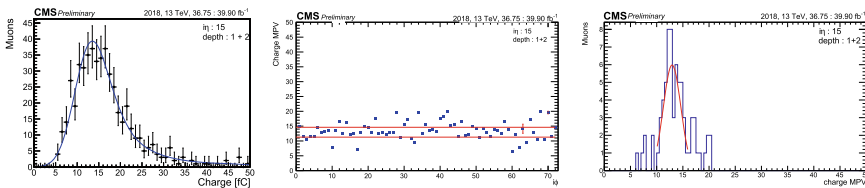


Fig. 138.2 Charge distributions for $i\eta + 15$ fitted with Gaussian convoluted Landau function (left), MPV values obtained from fitting charge distributions to Gaussian convoluted Landau functions (middle), and distributions of MPV values obtained from 72 independent fits corresponding to different $i\phi$'s (right) for $i\eta + 15$

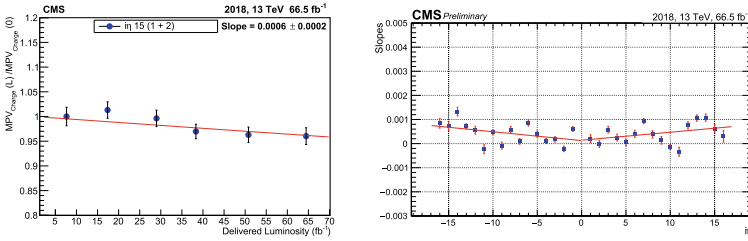


Fig. 138.3 MPV values of the charge distribution as a function of delivered luminosity for $i\eta + 15$ (left), and slopes from the fits to the exponential function of the most probable charge distribution as a function of delivered luminosity as a function of $i\eta$ (right)

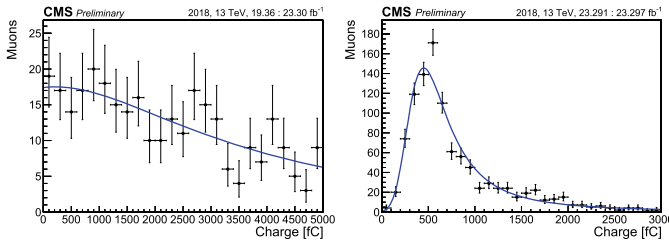


Fig. 138.4 Charge distributions for muons in the HCAL towers corresponding to $i\eta = 26$, depth = 1 from normal pp collision runs (left); from low luminosity runs (right)

distributions are more forward peaked with large uncertainties in the MPV values. To study high $|i\eta|$ regions, low luminosity data is looked as shown in Fig. 138.4 (right). The peak positions of the most affected towers are estimated with much better precision in the low luminosity data than in the regular data. However, the integrated luminosity between the two periods is only 1.1 fb^{-1} , and the scintillators are not expected to undergo measurable radiation damage from these measurements. It may be desirable to have several low luminosity runs in the future distributed over the year to monitor better the level of radiation damage in the most affected towers.

138.4 Conclusion

The single muon data of the 2018 run period of CMS are examined to look into the deterioration of the performance of the HB towers with increasing delivered luminosity. The data show that the deterioration is marginal at smaller $|i\eta|$ values ($\sim 2\%$ for $|i\eta| = 2$), and it increases at larger $|i\eta|$ values ($\sim 10\%$ for $|i\eta| = 16$). The scintillators at the highest $|i\eta|$ and smallest depths do suffer the largest damage due to radiation. However, higher pileup running does not allow measuring the peak position of the charge distribution due to muons with sufficient accuracy in those channels. Small statistics low luminosity runs (corresponding to integrated luminosity in the

range 10 pb^{-1} which is equivalent to 5 hrs run) with a single muon trigger can measure the peak values with precision better than a few percent. It is worthwhile to consider several short low luminosity runs at the beginning or at the end of each run period to study the effect due to radiation damage.

References

1. CMS Technical Design Report for the Phase 1 Upgrade of the Hadron Calorimeter, CERN-LHCC-2012-015, CMS-TDR-010, Sept 27, 2012
2. C.M.S. Collaboration, The CMS experiment at the CERN LHC. JINST **3**, S08004 (2008)
3. C.M.S. Collaboration, Measurements with silicon photomultipliers of dose-rate effects in the radiation damage of plastic scintillator tiles in the CMS hadron endcap calorimeter. JINST **15**, P06009 (2020)

Chapter 139

Heterogeneous Computing with GPUs for Trigger Decision in CMS Experiment at the LHC



T. S. Aravind

Abstract Using current technology, the Compact Muon Solenoid (CMS) experiment at the Large Hadron Collider (LHC) can record only 10^3 events per second out of 10^9 events occurring when protons collide at the interaction point. This huge rejection is achieved in real time by diligent selection implemented in a 2-level *trigger* conditioning, Level 1 (L1) and High-Level Trigger (HLT). For the high luminosity LHC operation, the computing for trigger will be based on heterogeneous resources including substantial usage of GPUs. For the integration of GPUs into the existing computing eco-system, a general framework for heterogeneous computing is being developed. This article describes the scheme of utilising fully reconstructed charged particle tracks for online event reconstruction using the faster and scalable new architecture.

139.1 Introduction

CMS is one of the two general-purpose experiments at the LHC [1] which uses cutting-edge technology to explore the forefront of particle physics.

For RUN 2 operation during 2015–2018, the instantaneous luminosity for proton-on-proton (pp) collisions at the centre-of-mass energy of 13 TeV had crossed the nominal value of $10^{34}/\text{cm}^2/\text{s}$ by a factor of about 2. With an inelastic pp cross section of about 70 mb, in a single bunch crossing every 25 ns, multiple interactions get recorded as a single *event*; this is referred to as event *pile-up* (PU). During 2018, the average number of PU was measured to be about 32 [2]. A single highly inelastic pp interaction at the LHC can produce about 150–200 charged particles (mostly pions) from the combined effect of the hard scattering and the underlying events.

T. S. Aravind (For the CMS collaboration).

T. S. Aravind (✉)
Tata Institute of Fundamental Research, Mumbai 400005, India
e-mail: aravind.s@tifr.res.in

© The Author(s), under exclusive license to Springer Nature Singapore Pte Ltd. 2022
B. Mohanty et al. (eds.), *Proceedings of the XXIV DAE-BRNS High Energy Physics Symposium, Jatni, India*, Springer Proceedings in Physics 277,
https://doi.org/10.1007/978-981-19-2354-8_139

775

With higher instantaneous luminosity, average PU increases and thus higher is the detector readout occupancy, which is challenging for the experiment.

Due to technological constraints, not all the pp collisions can be recorded *permanently* to the disc. *Trigger* in real time selects potentially the most *interesting* events to be stored to disc for further analysis [3]. For CMS, this is achieved in a phased manner, via Level 1 (L 1) and High Level Trigger (HLT). The event acceptance rate for offline analysis is only about 1 in 10^5 . It is obvious that the salient features of all the events must be critically and quickly studied before the *Trigger* decision to accept/reject an event is made. L 1 utilises custom-made hardware to scrutinise the information from various subsystems like Calorimeters and Muon spectrometers separately. The HLT operation takes place in a CPU farm and using information from all subsystems, a fast and complete event reconstruction is performed. With the increasing instantaneous luminosity anticipated in coming years, CMS is now moving towards a heterogeneous computing farm for HLT that uses GPUs as well.

139.2 Detector and Data Acquisition

The innermost detector of CMS is the silicon-based tracking subsystem (*Tracker*) consisting of pixel and strip detectors going radially outward. It is followed by an electromagnetic calorimeter (ECAL) and a hadron calorimeter (HCAL) which measure the energy. The Tracker, with about 135 million readout channels in total, records the passage of all charged particles, emanating from the interaction point, as hits. A solenoidal magnetic field of 3.4 T along the axis encompasses these subdetectors while the outermost subsystem is the muon spectrometer embedded in the return yoke of the magnet.

The high spatial granularity and low dead-time of the silicon detector allow for robust tracking of charged particles lying within a pseudorapidity region of $|\eta| \leq 2.5$, and the whole ϕ range near the interaction point. The layout is represented in Fig. 139.1. The four barrels at 2.9, 6.8, 10.9 and 16 cm along with 3 pairs of endcap

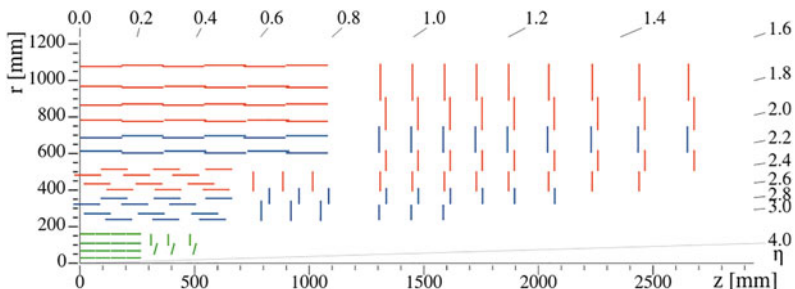


Fig. 139.1 Layout of CMS Tracker. Green: Pixel system; Blue: double-sided Strip system with stereo module; Red: single-sided Si Strip module

discs form the Pixel system, covering the above fiducial region. The Strip tracker that extends from 20 to 116 cm has 10 barrels. The single point resolution of hits varies from 15–20 μm in Pixel and 200–500 μm in the Strip tracker component.

The fine granularity of the silicon detector and large track density close to the interaction point render the CMS tracker a complex system for reconstruction. Consistent assignment of hits in Pixel detector to the trajectory of its parent is a computationally intensive process due to the huge combinatorics involved.

139.3 Heterogeneous Computing for HLT

For the future high luminosity operation of LHC (HL-LHC), the instantaneous luminosity is expected to be $5 - 7.5 \times 10^{34}/\text{cm}^2/\text{s}$ resulting in the average PU of about 140–200. This will create more than 10^4 charged particles per event within the tracking volume. Potentially, this may lead to a reconstruction bottleneck, due to large combinatorics, which should be tackled diligently to achieve the best possible performance of the experiment. Towards this goal, CMS experiment plans to utilise heterogeneous computing platforms, graphics processing unit (GPU) and field programmable gate array (FPGA) being some of them.

The heterogeneity in the reconstruction has been already integrated into the reconstruction framework. The interface optimises the memory management in GPUs. Its asynchronous execution model allows for the framework to launch modules in the external platform while allowing the CPU to process other jobs.

The local reconstruction modules in individual subsystems of ECAL, HCAL and Pixel have already been ported to the GPU framework [4] and are ready for use during RUN-3. The pixel reconstruction in GPUs scales better with the track count. Hence, complete pixel reconstruction of all the tracks for each event passing the L 1 trigger is possible. This provides a significant advantage for the reconstruction of events at the HLT.

139.4 Track Reconstruction

Until now, the complexity of track reconstruction has been handled at the higher level trigger by running the track reconstruction in the whole Tracker *only when it was necessary*, to reduce average latency. Instead, a computationally cheaper *regional reconstruction*, in a specific region of interest in Tracker volume, was carried out for obtaining tracks. However, in future, the CMS experiment plans to execute a GPU-based complete pixel reconstruction of tracks for each event passing L 1 trigger. With the new complete reconstruction in the inner tracker module, many of the old regional track reconstruction schemes have become redundant. To remove this redundancy, a new module was developed recently that selects the tracks from the globally reconstructed track collection (in GPU) within a region of interest.

139.4.1 Replacing the Local Reconstruction in CMS Tracker

In the *Iterative Tracking* scheme [5], the regional reconstruction happens in the initial iterations. It is seeded generally by the primary trigger from L 1. The seeds define a *region of interest* (ROI) which includes the geometric boundaries of the region, the cutoff for the minimum value for the transverse momentum (p_T^{\min}) of the tracks and bounds on the track origin. We use these ROI parameters to select the tracks from the GPU reconstructed pixel tracks.

139.4.2 Performance

The use of the new module has reduced the number of fake tracks since the regional selection is done on the reconstructed tracks rather than candidate sets of hits from the tracker. This removes a huge number of low p_T tracks below (p_T^{\min}) of the ROI that gets reconstructed if we were to use the selected candidate tracker hits.

The timing measurement was done for reconstruction schemes before and after removing the regional reconstruction in the tracker for possible modules used in HLT. The main results, extracted by studying Monte Carlo samples of 2 benchmark processes at the centre-of-mass energy of 13 TeV (reasonably less crowded $pp \rightarrow Z/\gamma^* \rightarrow \mu^+\mu^- + X$ and extremely busy $pp \rightarrow t\bar{t} + X$ productions), are presented in Table 139.1 to underline the gain in latency due to recent developments.

139.5 Conclusion

For the future operation of the LHC at very high instantaneous luminosity, CMS experiment plans to implement the latest technological developments to maximise the physics reach. Towards this goal, the use of GPU systems provides considerable gain in track reconstruction for passage of charged particles in the silicon tracking system. A new scheme utilising these fully reconstructed tracks has been developed and the salient features are described above. There is a significant improvement in the consumed time over the existing scheme of partial reconstruction of tracks within a limited region of interest. This scheme will be used for the selection of interesting physics events at the trigger level for the next operation of the LHC.

Table 139.1 .

Process	Time taken for regional reconstruction (ms)	Time taken for track selection (ms)
$pp \rightarrow Z/\gamma^* \rightarrow \mu^+\mu^- + X$	1.23	0.044
$pp \rightarrow t\bar{t} + X$	1.89	0.068

References

1. S. Chatrchyan et al., CMS. JINST **3**, S08004 (2008). <https://doi.org/10.1088/1748-0221/3/08/S08004>
2. CMS luminosity measurement for the 2018 data-taking period at $\sqrt{s} = 13$ TeV, CMS-PAS-LUM-18-002
3. M. Tosi [CMS], The CMS trigger in Run 2, PoS EPS-HEP2017, 523 (2017) <https://doi.org/10.22323/1.314.0523>
4. A. Bocci, D. Dagenhart, V. Innocente, C. Jones, M. Kortelainen, F. Pantaleo, M. Rovere, EPJ Web Conf. **245**, 05009 (2020). <https://doi.org/10.1051/epjconf/202024505009>
5. S. Chatrchyan et al. [CMS], Description and performance of track and primary-vertex reconstruction with the CMS tracker, JINST **9**(10), P10009 (2014). <https://doi.org/10.1088/1748-0221/9/10/P10009>

Chapter 140

Evolution of LHC Computing Grid for Run-III and Beyond with Emphasis on TIFR CMS Tier-II and Indian Contribution



Brij Kishor Jashal, G. Majumder, Kajari Mazumdar, and P. Patel

Abstract Worldwide LHC Computing Grid (WLCG) has seen continuous evolution since its inception. As the LHC experiments prepare for future operations marked by higher production rate of data volume, the need for agile computing resources has also increased many folds. The community has been preparing for these challenges and over the years has been making important upgrades in almost all the aspects of the Grid such as networking, submission infrastructure, storage technologies and information system, to name a few. As one of the Tier-II sites for CMS experiments, TIFR has been part of this technological evolution and upgrades. Taking lead in many areas, we have been contributing to development, testing and deployment in tandem with grid requirements. We highlight key updates undertaken at the India-CMS Grid computing center under the aegis of WLCG.

140.1 WLCG

The Worldwide LHC Computing Grid (WLCG), since its inception, has been a driver of innovations in the field of distributed computing, storage technologies, worldwide research and education network infrastructures, middleware software stack as well as the user services for big data analysis. The services and infrastructure built under the aegis of WLCG have served not only the LHC community but also other large-scale data-intensive sciences. As LHC prepares for Run3 (slated to start in 2022) as well as for high luminosity operation in future, WLCG and its entities have also undertaken upgrades at all the levels such as hardware, networks, middleware and applications level. India-CMS TIFR grid computing center at TIFR has been an important part of the WLCG, taking part in the research and development activities in addition to

B. K. Jashal (✉) · K. Mazumdar · P. Patel
Tata Institute of Fundamental Research, Mumbai 400005, India
e-mail: brij@cern.ch

G. Majumder
Department of High Energy Physics, Tata Institute of Fundamental Research, Colaba, Mumbai, India

© The Author(s), under exclusive license to Springer Nature Singapore Pte Ltd. 2022
B. Mohanty et al. (eds.), *Proceedings of the XXIV DAE-BRNS High Energy Physics Symposium, Jaitni, India*, Springer Proceedings in Physics 277,
https://doi.org/10.1007/978-981-19-2354-8_140

781

regular services for the smooth operation of the facility. Some of them are briefly mentioned here

- WLCG Data organization, Management and Access infrastructure evolution and upgrades have been organized under the project WLCG DOMA [1]. Community-developed software such as DPM, D-Cache, HDFS and EOS and the respective storage elements have been upgraded to support WebDAV, HTTPs in addition to the legacy GridFTP and Xrootd endpoints.
- Reducing data duplication and efficient data placement enable reducing network load. This requires efficient and intelligent caching mechanisms integrated into the data management and transfer systems. The Storage upgrades at TIFR and other sites within WLCG allow the implementation of these https-based smart data caching solutions.
- CMS as well as other experiments under WLCG like ATLAS, ALICE and LHCb have commissioned Dynamic resource sites with capabilities of providing opportunistic resources by integrating major public cloud infrastructures as well as computing resources from High Performance Computing (HPC) centers. Some of the examples within CMS are the Fermi HEP cloud [2], the dynamic resources site at TIFR [3], the NERSC supercomputing center [4] and many more.

140.2 India-CMS Grid Computing Center

India-CMS Grid computing center hosted by TIFR, Mumbai, is a national center of computing for high energy physics serving members of the Indian as well as global CMS community. This is a national contribution to CMS international collaboration. It consists of two CMS commissioned sites, named T2_IN_TIFR and T3_IN_TIFRCloud which provide resources to global CMS users. In addition, there is a dedicated local T3 site exclusively for India-CMS users for performing data analyses.

140.2.1 T2_IN_TIFR

T2_IN_TIFR is the only Tier-II computing center from India serving CMS VO. The capacity of storage, computing and networking has grown steadily since its inception. In 2020, the center provided 2500 hyper-threading (HT)-enabled cores with 3 Petabyte of storage with international connectivity of 10Gbps via National Knowledge Network (NKN). In 2021, this capacity has been increased to 11,000 cores and 11 Petabytes of storage with a full 10G end-to-end core network. In synchronization with WLCG and CMS-specific developments, the software infrastructure is continuously upgraded. T2 storage is based on the Disk Pool Manager (DPM) software solution and has been upgraded to the latest version to provide support for

WebDAVS and HTTPS protocols. The site will continue to support legacy access protocols, but these are being phased out. Additionally, the site has enabled the real-time space availability using a dedicated space reporting and management system. The site pledges are maintained using WLCG Computing Resource Information Catalogue (CRIC). A Rucio endpoint was commissioned for the data transfers among the sites within CMS collaboration. The compute CE is based on HTCondor-CE and the batch system at the backend has been upgraded to the latest version of HTCondor.

140.2.2 T3_IN_TIFRCloud

With the advent of cloud computing technology, CMS worked toward developing capabilities to interface WLCG with major cloud service providers' infrastructures. T3_IN_TIFRCloud was commissioned as a Dynamic resource site to provide opportunistic resources for CMS from India (see Fig. 140.1). This work required developing software tools and infrastructure for interfacing GRID with cloud services.

Azure Grid ASCII Helper Protocol (Azure-GAHP) [5, 6]

Development of Azure-GAHP (Grid ASCII Helper Protocol) enabled invoking Azure API from within HTCondor software for calling Azure services to spin up VMs as per the given load and defined rules. It facilitated the construction of multi-tier systems. A first-tier client can easily send ASCII commands via a socket (securely via an SSH or SSL tunnel) to a second tier running a GAHP server, allowing grid or cloud services to be consolidated at the second or third tier with minimal effort. This

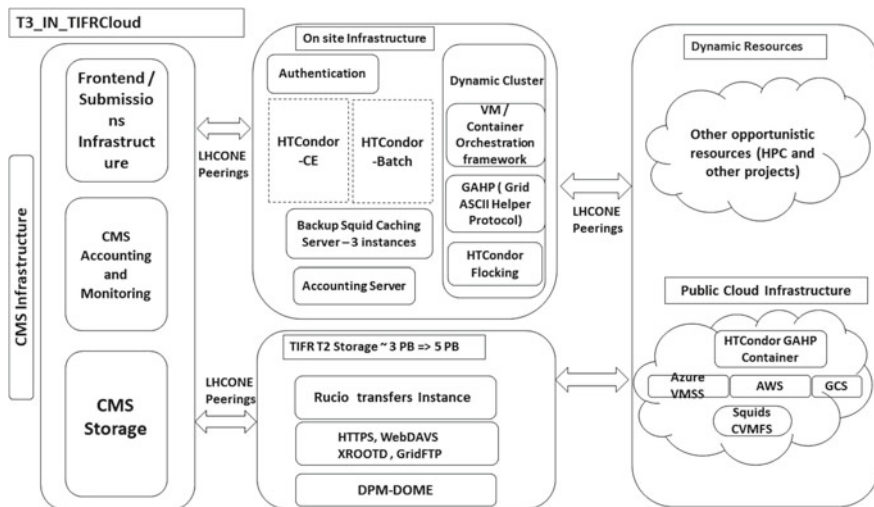


Fig. 140.1 A Schematic of T3_IN_TIFRCloud integrating GRID and public cloud

software is available as the standard Condor released under an open-source license. The site endpoint was deployed at TIFR which consisted of interfacing services, HTCondor-CE and squid proxy servers serving CMS software. Input and output data sources were T2_IN_TIFR storage. The worker nodes were based at Azure data-centers in India and were dynamically added to the HTCondor pool as per the load. The features of Azure-GAHP allowed writing fine-grained rules and conditions for invoking virtual machines from Azure based on a number of factors, such as the number of jobs in the waiting, the priority of the user and jobs and the type of jobs. In this exercise, we commissioned a fully functional Dynamic resource site with static components of the site based at TIFR and the worker nodes were dynamically added from Azure. We developed the required tools, commissioned a new CMS site and demonstrated interfacing WLCG Grid with Microsoft Azure, a public cloud infrastructure. The capacity of the site was dynamically expanded from zero cores to 10,000 cores within a few minutes, and these cores were released back after the successful completion of the jobs [3]. A total of 1 billion jobs were executed on the site during the month of commissioning and testing. This work was executed in collaboration with Microsoft India and supported with Azure credits via a research grant from Microsoft.

140.2.3 T3 for India-CMS Users

CMS members from all the participating Indian institutes rely on the computing resources from India-CMS grid computing center of TIFR. Dedicated T3 at TIFR has evolved over the years and has been upgraded to meet users' needs. Some of the new user services are

- Multiple user interface login machines with a dedicated local HTCondor batch system configured with utilities and software for data access and analysis.
- Dedicated T2 and T3 storage.
- JupyterHub notebook interface supporting C++ and Python kernels with Kubernetes cluster backend.
- Gitlab interface hosted at the `indiacms.res.in` domain.
- Platform for hybrid architecture and parallel computing with professional GPUs.

140.3 Summary

As part of the WLCG, India-CMS Grid computing center has made direct contributions to the advancement of physics by providing critical computing services to the collaboration. In the last decade, the computing facility, hardware, software and networking components have been continuously upgraded. The capacity of the center for Run-III has been expanded and new hardware have significantly increased the

storage and computing capacity. The software infrastructure has been upgraded to provide the next generation of services and the center is ready for Run-III operations.

Acknowledgements We acknowledge the financial support by Department of Atomic Energy and Department of Science and Technology. We also acknowledge the support received from CMS offline and computing, EGI, WLCG, NKN India, Microsoft India and HTCondor teams for their respective contributions to this work and collaboration.

References

1. WLCG-DOMA Twiki. <https://twiki.cern.ch/twiki/bin/view/LCG/MaterialAndPresentations>
2. Fermilab HEP Cloud. <https://computing.fnal.gov/hep-cloud/>
3. Brij Kishor Jashal: European HTCondor week 2017. <https://indico.cern.ch/event/611296/contributions/2608186/attachments/1471802/2277821/HTcondor-week-2017-Final-Brij.pdf>
4. LHCC-WLCG Status June 2021. <https://indico.cern.ch/event/877841/contributions/3698886/attachments/2049764/3435375/LHCC-WLCGStatus-Jun-2020.pdf>
5. Azure GAHP. <https://techcommunity.microsoft.com/t5/azure-global/azure-gahp-server-for-htcondor/ba-p/306278>
6. HTCondor GAHP. <https://research.cs.wisc.edu/htcondor/gahp/>

Chapter 141

Cosmic Muon Veto for the Mini-ICAL Detector at IICHEP, Madurai



B. Satyanarayana, S. R. Bharathi, Pandi Chinnappan, V. M. Datar, Mamta Jangra, Jim John, S. R. Joshi, K. S. Karthikk, L. Umesh, G. Majumder, N. Panchal, Nagaraj Panyam, S. Pethuraj, Jayakumar Ponraj, K. C. Ravindran, Paul Rubinov, Mahima Sachdeva, M. N. Saraf, Prakash Sharma Kirti, R. R. Shinde, H. Sogarwal, S. S. Upadhya, P. Verma, and E. Yuvaraj

Abstract A 51-kiloton magnetised Iron Calorimeter (ICAL) detector, using Resistive Plate Chambers (RPCs) as active detector elements, aims to study atmospheric neutrinos. A prototype—1/600 of the weight of ICAL, called mini-ICAL, was installed in the INO transit campus at Madurai. A modest proof-of-principle cosmic muon veto detector of about $1\text{m} \times 1\text{m} \times 0.3\text{m}$ dimensions was set up a few years ago, using scintillator paddles. The measured cosmic muon veto efficiency of $\sim 99.98\%$ and simulation studies of muon induced background events in the ICAL detector surrounded by an efficient veto detector were promising. This led to the idea of constructing a bigger cosmic muon veto around the mini-ICAL detector. Details of the design and construction of the detector including the electronics, trigger and DAQ systems planned will be briefly presented.

B. Satyanarayana (✉) · S. R. Bharathi · P. Chinnappan · M. Jangra · J. John · S. R. Joshi · K. S. Karthikk · L. Umesh · N. Panchal · N. Panyam · S. Pethuraj · J. Ponraj · K. C. Ravindran · M. Sachdeva · P. S. Kirti · R. R. Shinde · H. Sogarwal · S. S. Upadhya · P. Verma · E. Yuvaraj
Tata Institute of Fundamental Research, Mumbai 400005, India
e-mail: bsn@tifr.res.in

V. M. Datar · G. Majumder · M. N. Saraf
Department of High Energy Physics, Tata Institute of Fundamental Research, Colaba, Mumbai, India

M. Jangra · J. John · S. Pethuraj
Homi Bhabha National Institute, Mumbai 400094, India

L. Umesh
The American College, Madurai 625002, India

P. Rubinov
Fermilab, Batavia, IL 60510-5011, USA

H. Sogarwal
Homi Bhabha National Institute, Training School Complex, Anushaktinagar, Mumbai, India

© The Author(s), under exclusive license to Springer Nature Singapore Pte Ltd. 2022
B. Mohanty et al. (eds.), *Proceedings of the XXIV DAE-BRNS High Energy Physics Symposium, Jatni, India*, Springer Proceedings in Physics 277,
https://doi.org/10.1007/978-981-19-2354-8_141

141.1 Introduction

A 51-kiloton magnetised Iron Calorimeter (ICAL) detector, using Resistive Plate Chambers (RPCs) as active detector elements, aims to study atmospheric neutrinos. It will be the flagship experiment at the India-based Neutrino Observatory (INO) which will be housed in a cavern at the end of a 2km tunnel in a mountain near Pottipuram (Tamil Nadu) [1]. A prototype—1/600 of the weight of ICAL, called mini-ICAL, was installed in the INO transit campus at Madurai, to gain experience in the construction of a large-scale electromagnet, to study the detector performance and to test the ICAL electronics in the presence of a fringe magnetic field. This $4\text{m} \times 4\text{m} \times 1.1\text{m}$ detector, with 11-iron layers and 20 RPCs in the central region, is in operation for over 2 years and collecting cosmic muon data. A modest proof-of-principle cosmic muon veto detector of about $1\text{m} \times 1\text{m} \times 0.3\text{m}$ dimensions was set up a few years ago, using scintillator paddles [2]. The measured cosmic muon veto efficiency of $\sim 99.98\%$ and simulation studies of muon-induced background events in the ICAL detector surrounded by an efficient veto detector [3] were promising. This led to the idea of constructing a bigger cosmic muon veto around the mini-ICAL detector.

141.2 Design of Veto Detector

The veto walls around four sides and top of the mini-ICAL will be built using three staggered (by 15 mm) layers of extruded scintillator strips (donated by Fermilab) [4]. Strips of 4400–4700 mm in length, 50 mm wide and 10 or 20 mm thick will be used to construct the veto shield that aims at 99.99% efficiency to tag cosmic muons. Double clad WLS fibres $\sim 1.4\text{mm}$ in diameter (from Kuraray) are inserted into two extruded fibre holes along the length of the strip and separated by 25 mm to collect the light signal. Hamamatsu SiPM's of $2\text{mm} \times 2\text{mm}$ active area collects the light on both sides of the fibres. About 750 strips, about 7 km of fibre and 3000 SiPM's are going to be deployed. All the five veto walls/stations are designed to be movable from their designed positions, providing service access to the mini-ICAL inside (see Fig. 141.1).

141.3 Veto Detector Requirements

The main requirements of the veto detector are the measurement of charge, position and relative arrival time of the SiPM signals on trigger from mini-ICAL trigger. Event marker is used to collate the veto detector event data with that of the mini-ICAL data.

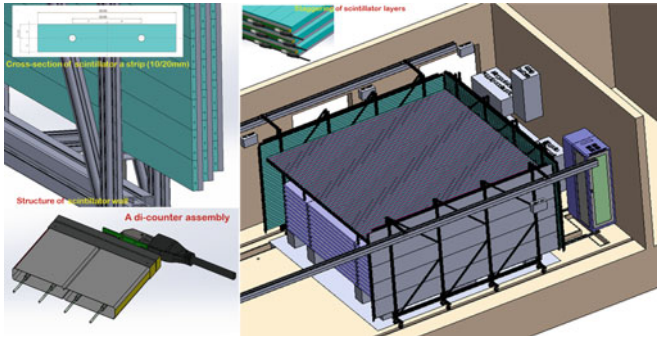


Fig. 141.1 A collage of schematic drawings showing the overall structure of the cosmic muon detector around the mini-ICAL, staggering of scintillator layers, a view of the support structure for the side veto walls and the di-counter readout

For the charge measurement, a dynamic range of 100 pC with a least count of 20 fC and a single photo-electron charge of about 100 fC are specified. A least count of 100 ps is sufficient for the time measurement. Closed-loop gain/biasing control for every SiPM or Di-Counter as well in situ calibration using LED pulser or noise signals are essential for stable and reliable detector operation.

Extensive characterisation and calibration studies were carried out on the main elements of the cosmic muon detector—namely the extruded scintillator strips, fibre and SiPMs. The studies were carried out using LED pulser, ^{22}Na radioactive source as well as cosmic ray muons. Using these studies, we obtained a single PE avalanche charge: 0.242 pC. The typical PE yields obtained for 10/20 mm thick scintillators are 34/57, while the typical signals for cosmic ray muon are 8.33pC (10 mm) and 13.82 pC (20 mm). Using time of flight measurement across the length of the scintillator strip, a position resolution of 9.18 ± 2.27 cm was obtained across the scintillator strip.

141.4 Detector Readout

The veto walls are assembled using pre-fabricated di-counters, which are essentially two extruded scintillator strips glued sideways. One end of the four fibres from each of the di-counter is readout by one SiPM assembly as shown in Fig. 141.2. The fibres are passed through the fibre guide block which is mounted on the di-counter face using sleeves and sleeve pins. A neoprene gasket cushions the fibres to terminate properly on the active windows of the SiPMs which are placed in the SiPM mounting block. The SiPMs are actually individually mounted on tiny SIMPM carrier “mouse bite”

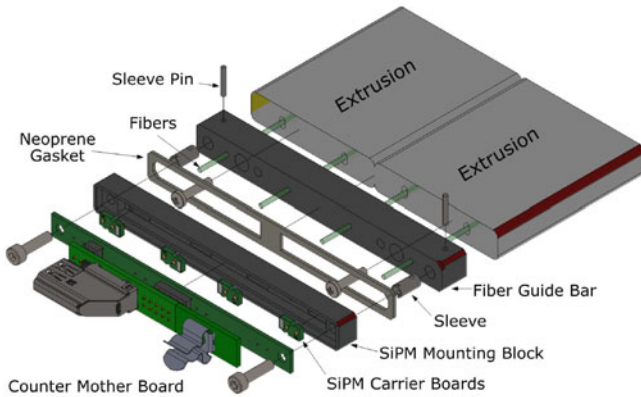


Fig. 141.2 An exploded view of various components of the di-counter detector readout. Two such readout modules are used for readout of either end of a di-counter

boards, which themselves are locked in fixed slots in the SiPM mounting block. Finally, the counter motherboard that houses the SiPM bias voltage services, the ambient parameter sensors, calibration LED source and other services is mated to the SiPM mounting block using plastic screws. The SiPM signals, power supplies, the LED drive voltage, etc. are carried between the detector readout assembly and backend electronics via an HDMI connector mounted on the counter motherboard.

141.5 Electronics and DAQ System

Initially, coincidence of ORed signals from two out of three layers from either side of a station will be used to generate a trigger signal from that station. Trigger signals from five stations are combined to form the final cosmic ray muon veto trigger signal. On veto trigger, the DAQ system will gather the charge produced, arrival time and position of muon tracks in the scintillator strips. But the data collected is transferred to the backend only if the main trigger from the mini-ICAL detector is also received in time, or else the data is discarded. Extensive configuration, control and calibration of the detector elements are also planned. An overall scheme of the electronics and DAQ system is shown in Fig. 141.3.

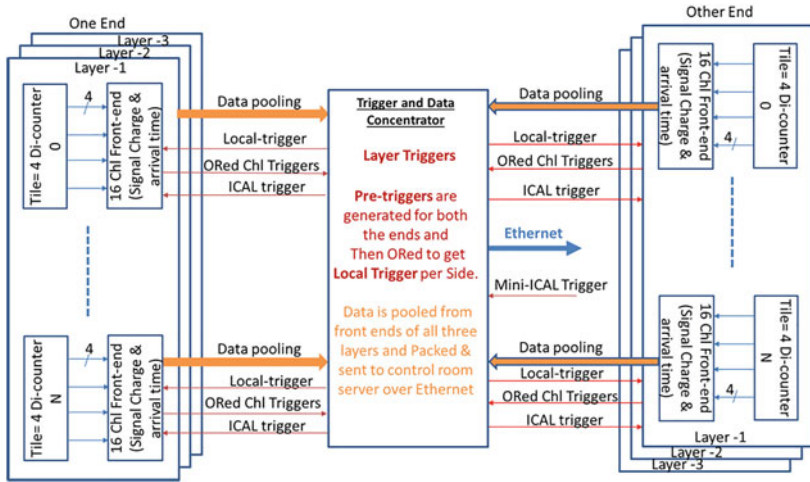


Fig. 141.3 Schematic of the electronics and data acquisition system for the cosmic muon detector. Two identical segments are designed to read data from either side of the veto walls. A central system takes care of final trigger generation and data transfer to the backend

References

1. A. Kumar et al. [ICAL], *Pramana* **88**(5), 79 (2017)
2. N. Panchal et al., *JINST* **12**(11), T11002 (2017)
3. N. Panchal et al., *JINST* **14**(02), P02032 (2019)
4. L. Bartoszek et al. [Mu2e], [[arXiv:1501.05241](https://arxiv.org/abs/1501.05241)] [physics.ins-det]

Chapter 142

Track-Based Muon Alignment of the CMS Detector



Greyson Newton

Abstract The alignment of the CMS muon system is vital to maintaining reliable muon data. Misaligned muon detectors negatively impact the accuracy of recorded muon positions, which in turn affects the momentum resolution and sensitivity of the final physics analyses. To measure the misalignment of muon detectors, recorded muon tracks are used in a multidimensional fit on the misalignment degrees of freedom. The performance of this track-based alignment algorithm is measured by using muons in Z boson decays and evaluating the alignment's accuracy in reconstructing the mass peak. Chamber alignment accuracies on the order of 100 μm are achieved and alignment performance is presented using Run 2 data.

142.1 Introduction

The highly redundant CMS muon system is designed to trigger the CMS readout system, measure detected muon momenta and charge, then finally reconstruct muon tracks. An aligned muon system is critical to stable trigger performance as it allows for certifiably valid muon data to be used in a wide variety of physics analyses at CMS. The CMS muon system consists of four types of gaseous ionization chambers: Drift Tube Chambers (DTs), Cathode Strip Chambers (CSCs), Resistive Plate Chambers (RPCs), and Gas Electron Multipliers (GEMs) as shown in Fig. 142.1.

DTs and CSCs measure an accurate position and momenta of muons while RPCs are primarily designed to provide information on muon trigger timing. GEMs are currently being installed during Long Shutdown 2 (LS2) and will be functional

G. Newton (For the CMS Collaboration).

G. Newton (✉)

Texas A&M University, 578 University Drive, College Station, Texas 77843, USA
e-mail: greynewt@tamu.edu

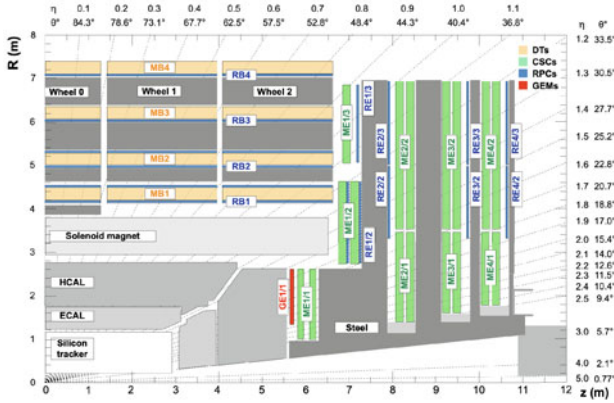


Fig. 142.1 CMS Run 3 muon system chamber arrangement including GEMs

for Run 3. Only DTs, CSCs, and now GEMs are considered for the track-based muon alignment procedure. A detailed description of the CMS detector can be found here [1].

142.2 Track-Based Muon Alignment (TBMA) [2]

High-quality muon tracks are needed to start the TBMA process. Muons with a transverse momentum between $30 < p_T < 200$ GeV are selected to avoid muon scattering. To ensure the muon originated from the interaction point and has enough tracker data, the muon track must have at least ten inner tracker hits, a normalized $\chi^2 < 10$ (measures error in track reconstruction), and be matched with two or more muon stations. Finally, fiducial cuts are placed around muon chamber boundaries to clarify which chambers the muon track passed through.

Muon data that passes the above selection criteria is then run through a series of reference target algorithms that calculate all misalignments present in each degree of freedom (DOF) of individual chambers. First, the data is used in the multidimensional objective function given below.

$$L_{global} = \sum_l \sum_k L_{kl}(x_{kl}^0, \sigma_k \mid x_{kl}) \tag{142.1}$$

where σ_k is a nuisance parameter, x_{kl} and x_{kl}^0 are the measured and expected local track parameters for each residual type (k) in each muon track (l). A residual is defined as $\Delta_{kl} = (x_{kl} - x_{kl}^0)$ which is related to the track misalignment parameters ($\mathbf{p} = \delta x, \delta y, \delta z, \delta\phi_x, \delta\phi_y, \delta\phi_z$), through a coefficient matrix, M as described by Eqs. 142.2 and 142.3.

$$\Delta = M\mathbf{p} \tag{142.2}$$

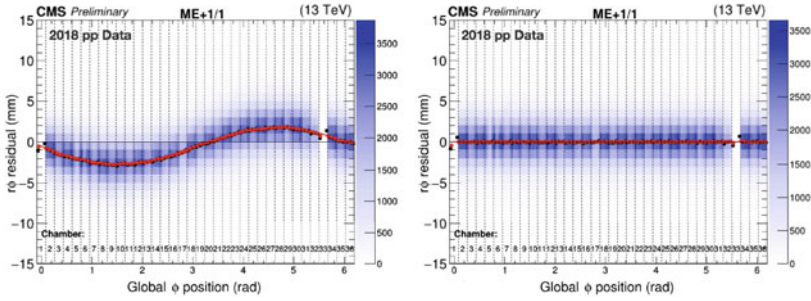


Fig. 142.2 $R\phi$ residual as a function of global ϕ for the first ring on the first disk of the positive endcap. These plots illustrate TBMA eliminating misalignment in CSCs. The residual means (red), medians (black), and distributions (blue heat map) are shown before alignment (left) and after alignment (right)

The residual correlation for DT chambers takes the form of Eq. 142.3.

$$\begin{pmatrix} \Delta x \\ \Delta y \\ \Delta \frac{dx}{dz} \\ \Delta \frac{dy}{dz} \end{pmatrix} = \begin{pmatrix} 1 & 0 & -\frac{dx}{dz} & -y \frac{dx}{dz} & x \frac{dx}{dz} & -y \\ 0 & 1 & -\frac{dy}{dz} & -y \frac{dy}{dz} & x \frac{dy}{dz} & x \\ 0 & 0 & 0 & -\frac{dx}{dz} & 1 + \left(\frac{dx}{dz}\right)^2 & -\frac{dy}{dz} \\ 0 & 0 & 0 & -1 - \left(\frac{dy}{dz}\right)^2 & \frac{dy}{dz} \frac{dx}{dz} & \frac{dx}{dz} \end{pmatrix} \begin{pmatrix} \delta x \\ \delta y \\ \delta z \\ \delta\phi_x \\ \delta\phi_y \\ \delta\phi_z \end{pmatrix} \quad (142.3)$$

The minimizer algorithm, MINUIT [3], calculates optimal alignment variables in every DOF by minimizing chamber residuals and misalignment parameters ($\mathbf{p} = \delta x, \delta y, \delta z, \delta\phi_x, \delta\phi_y, \delta\phi_z$). The same algorithms are used on CSCs; only the CSC correlation matrix reflects the radial geometry of the CSCs. In this geometry, R and ϕ are used to indicate CSC positions relative to the local disk geometry of the endcap. Figure 142.2 displays CSC misalignments before and after the TBMA procedure.

142.3 Past Performance and Future Readiness

Alignment performance is evaluated through a physics validation process that uses an array of methods to verify TBMA performance. These methods commonly include studying differences in dimuon track reconstruction. One method studies the variance in dimuon mass as reconstructed using only muon system information (standalone muon track, STA) versus reconstructing the pair with both the tracker and the muon system information (global muon track, GLB). The STA muon track scales misalignments, making invariant dimuon mass distributions a robust metric for alignment validity (Fig. 142.3).

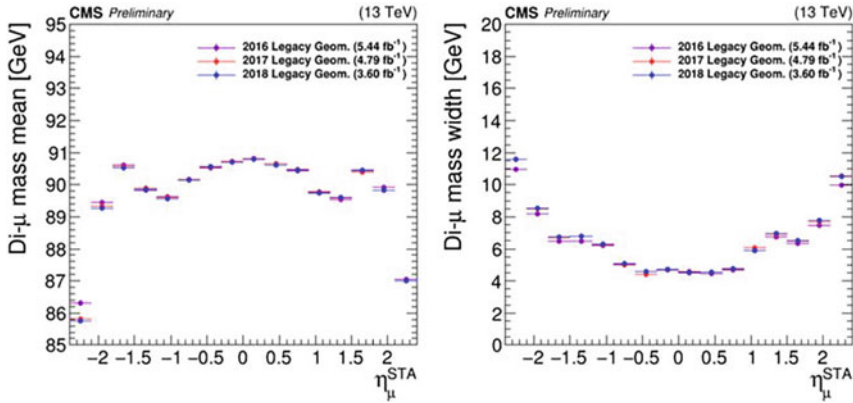


Fig. 142.3 Run 2 dimuon (GLB + STA) data captured from $Z \rightarrow \mu^+ \mu^-$ events and recorded using different alignment geometry scenarios shown in the legends. Left: Dimuon mass mean as a function of the standalone muon track pseudorapidity (η_{μ}^{STA}). Right: Dimuon mass width as a function of η_{μ}^{STA} [4]

The GEM subsystem is an important addition to the overall muon system in Run 3 as it enhances the CSC trigger system's ability to handle a much higher particle rate. TBMA has developed new code to update alignment for GEMs. It has been successfully tested using commissioning, simulation, and cosmic ray muons and will be operational for the coming data-taking period.

142.4 Summary

Performance of track-based muon alignment has been reported and the value of the results of TBMA has been emphasized using Run 2 collision data. The TBMA procedure is used to align the CMS muon system. To do this, high-quality muon tracks are selected to calculate chamber-level residuals which get fed into a multidimensional minimizing function that outputs aligned positions for DT and CSC chambers. Muon data then gets reconstructed within the new aligned chamber geometry. Residual calculation and muon reconstruction are repeated until convergence. Due to excellent muon reconstruction and clever validation techniques, TBMA provides reliable and accurate muon track data for use in CMS-wide particle physics studies. The direct effect TBMA has on the validity of muon track data allows for widespread stability in particle analysis conducted at CMS, therefore aiding CMS's ability to discover new physics as a whole.

References

1. CMS Collaboration, The CMS experiment at the CERN LHC. JINST **3**, S08004 (2008). <https://doi.org/10.1088/1748-0221/3/08/S08004>
2. CMS Collaboration, Alignment of the CMS muon system with cosmic-ray and beam-halo muons. JINST **5**, T03020 (2010). <https://doi.org/10.1088/1748-0221/5/03/t03020>
3. F. James, M. Roos, Minuit—a system for function minimization and analysis of the parameter errors and correlations. Comput. Phys. Commun. **10**, 343 (1975). [https://doi.org/10.1016/0010-4655\(75\)90039-9](https://doi.org/10.1016/0010-4655(75)90039-9)
4. CMS Collaboration, Performance of the CMS muon detector and muon reconstruction with proton-proton collisions at $\sqrt{s} = 13$ TeV. JINST **13**, P06015 (2018). <https://doi.org/10.1088/1748-0221/13/06/P06015>

Chapter 143

Magnetic Field Simulations and Measurements on Mini-ICAL



Honey, V. M. Datar, S. Ajith, N. Dalal, A. De, G. Majumder, S. Patel, S. Pathak, S. P. Prabhakar, B. Satyanarayana, P. S. Shetty, B. Siva Rama Krishna, T. S. Srinivasan, and S. K. Thakur

Abstract The magnetic field B in the ICAL detector (max 1.5 T) at INO is necessary for the electric charge identification and momentum reconstruction of muons resulting from ν_μ and $\bar{\nu}_\mu$ interactions with iron. One of the goals of the 85-ton mini-ICAL detector is to compare measurements of the magnetic field with 3-D finite element electromagnetic simulations and, if necessary, refine the latter. The static 3-D simulation was done using MagNet 7.7 software for 3- and 11-layered models of mini-ICAL for various coil currents. The B-field measurements were done using 150 Hall sensors mounted on PCB strips which were inserted in the 3–4 mm gaps in layers 1, 6, and 11. In addition, 5 sets of coils were wound at suitable locations around the plates in the same layers, and the magnetic flux during ramp up or ramp down of the coil current is measured. A comparison of this data vis-a-vis the simulation will be presented.

Honey (✉) · A. De
Homi Bhabha National Institute, Mumbai 400094, India
e-mail: honey@tifr.res.in

Honey · B. Satyanarayana
Tata Institute of Fundamental Research, Mumbai 400005, India

V. M. Datar · G. Majumder
Department of High Energy Physics, Tata Institute of Fundamental Research, Colaba, Mumbai, India

S. Ajith · N. Dalal · S. Patel · S. Pathak · S. P. Prabhakar · P. S. Shetty · B. Siva Rama Krishna · T. S. Srinivasan
Bhabha Atomic Research Centre, Mumbai 400085, India

Honey
The Institute of Mathematical Sciences, Chennai 600113, India

A. De · S. K. Thakur
Variable Energy Cyclotron Centre, Kolkata 700064, India

143.1 Introduction

The proposed 50 kton magnetized Iron Calorimeter (ICAL) detector will have a maximum magnetic field of 1.5 T and will be the largest electromagnet in the world. The magnetic field in ICAL will help identify the charge of the muons produced in atmospheric muon neutrino interactions with iron as well as in reconstructing their momenta [1, 2]. The 85-ton mini-ICAL detector, commissioned at the transit INO campus at Madurai in 2018, is a prototype version of the ICAL detector. One of the main goals of the mini-ICAL detector is to compare measurements of the magnetic field with 3-D finite element electromagnetic simulations and, if necessary, refine the latter in view of measurements.

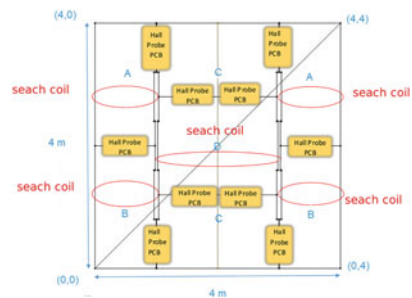
143.1.1 Mini-ICAL Geometry

Mini-ICAL consists of 11 soft iron layers and 10 layers of RPCs that are being used as active detectors (Fig. 143.1). There are 2 sets of copper coils using a hollow OFHC copper conductor (30 mm × 30 mm cross section with 17 mm bore) passing through 80 mm wide slots, each with 18 turns to produce the magnetic field. These current-carrying coils are cooled by low conductivity chilled water.

Fig. 143.1 Mini-ICAL detector



Fig. 143.2 Mini-ICAL (top view)



Each iron layer has 7 plates of 4 types A, B, C, and D (Fig. 143.2). Layer 1 (bottom), 6 (middle), and 11 (top) have a provision of measuring magnetic field using Hall probe sensors (in 3–4 mm gaps between plates) and search coils. The other layers have air gaps of up to 2 mm.

143.1.2 Hall Probes and Search Coils

The Hall probes (2 mm × 2 mm × 15 nos.) are mounted on PCB strips and have a readout with 10 gauss resolution while the 5 search coils consist of double turn teflon coated wires of cross-sectional area 0.25 mm² and a readout resolution of 650 Maxwell turns. Their placement can be seen in Fig. 143.2 (Figs. 143.3 and 143.4).

143.2 Experimental Data Analysis

The magnetic field is measured in layer 11 of mini-ICAL using Hall probes and search coils for currents between 0 to 900 amps with 2-point calibration of Hall probe sensors for $B = 0$ and 0.3T. The current (I) is ramped up and down between 0 and 900 amps and repeated by reversing the current. The maximum current is decreased to near zero to demagnetize mini-ICAL. Figure 143.5 shows the B-I curve with one of the search coils.

Figure 143.6 shows a comparison of Hall probe and search coil measurements for layer 11 in a central zone with an agreement within 5% of each other. Since the search coil measures the magnetic flux over the entire cross section of the plate, and hence an average field strength, the readings from the Hall probes (PCBs 7–10) are also averaged. Below the knee point, the search coil shows a slightly larger value than that of Hall probes whereas beyond the knee point, the trend is reversed.



Fig. 143.3 Hall probe PCBs

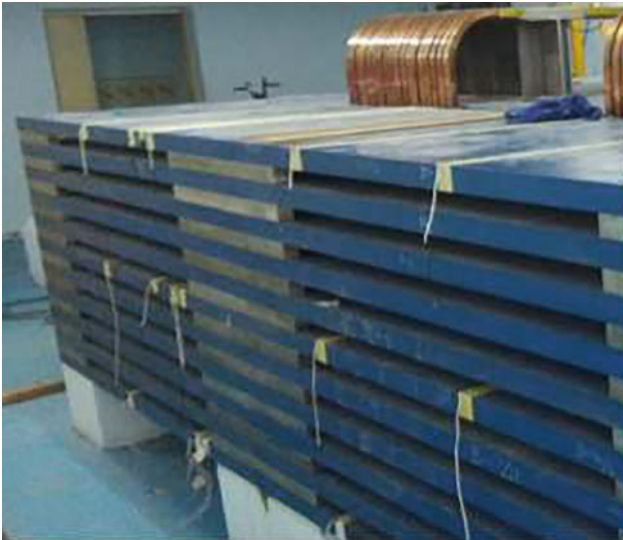


Fig. 143.4 Search coils

Fig. 143.5 B-I plot from data of search coil-1

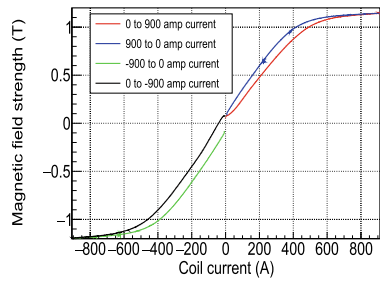
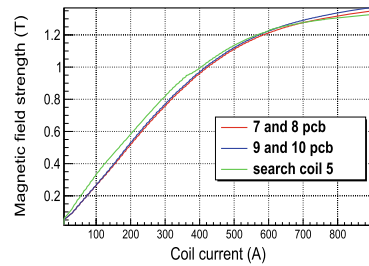


Fig. 143.6 Comparison of B-I curve of Hall probe and search coil



143.3 Magnetic Field Simulation

Magnetic field simulations were performed using MagNet 7.7 software for 3 and 11-layered models at currents between 600 and 900 amps. A 1-layer model of mini-ICAL was also simulated using COMSOL MultiPhysics software to cross check the corre-

Fig. 143.7 Input B-H curve used for simulations

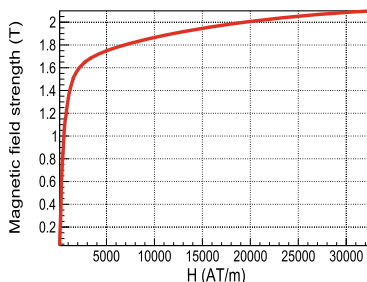


Fig. 143.8 Fraction $|B| \geq 1$ for 11 and 3 layer model (observed variation $<5\%$)

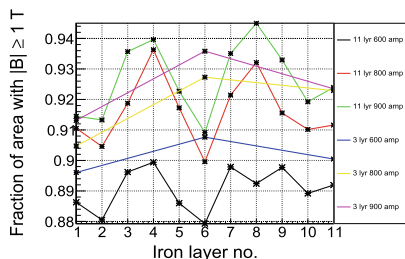


Fig. 143.9 B-field along the diagonal line for 11 layers using 11-layered model for current 900 amps

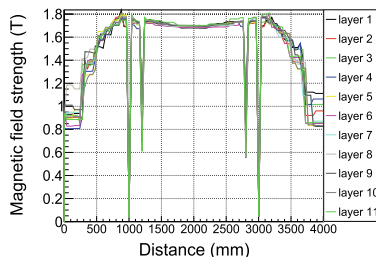
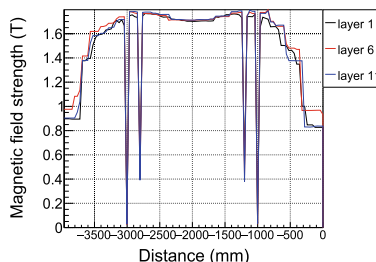


Fig. 143.10 B-field along the diagonal line for 3 layers using 3-layered model for 800 amps



sponding simulation using the MagNet 7.7 software. While the 11-layered model uses the actual geometry, the 3-layered model simulations are faster with smaller memory usage allowing a much smaller mesh size and more accurate B-field simulation near the gaps. B-field values are extracted from both the simulations with bin size of 50 mm along x-axis (Figs. 143.8, 143.9, 143.10). It may be seen that the B-field variation in the D-plate is less as compared to that in the edge plates. The fraction of area of layer 11 with $B > 1$ T (using the B-H curve in Fig. 143.7 as input) for 3 and 11-layer simulations is shown in Fig. 143.8 and they agree with each other within 5%.

143.4 Conclusion and Future Plans

The fractional area of iron plates with magnetic field $B \geq 1$ T for different values of current for both the models shows agreement within 5%. In both 3 and 11-layered models, field strength in the D-plate show 3% variation in B-field for the different layers. The outer plates show a larger variation of 20–30% for the different layers in the 11-layered model and 10% variation in the 3-layered model. This is probably due to the fact that these regions are in lower range of fields. A sudden decrease in the simulated B-field values in the air gaps will be addressed in further studies. In future, Hall probe PCBs will be calibrated for many points up to 1.5 T rather than a 2-point calibration. Simulations will be done with measured values of air gaps (assembly tolerance) that are varying from 2 to 3 mm and with smaller (< 3 mm) mesh size in the air gaps. Finally, we also would like to study the result of variation of B-field on the reconstructed muon momenta in ICAL GEANT4 simulations.

References

1. A. Kumar et al., *Pramana* **88**, 79 (2017)
2. S.P. Behera et al., *IEEE Trans. Mag.* **51**, 7300409 (2014)

Chapter 144

A Simulation Study of Primary Ionization for Different Gas Mixtures



R. Kanishka, P. K. Rout, S. Mukhopadhyay, N. Majumdar, and S. Sarkar

Abstract We present the simulation studies of primary ionization using an alpha source in different gas mixtures. The geant4 toolkit is used to estimate the nature of the primary ionization produced in the entire detector volume with Ar- and Ne-based gas mixtures. The response of alpha source in these gas mixtures is found to be different due to the different properties of these gas mixtures.

144.1 Introduction

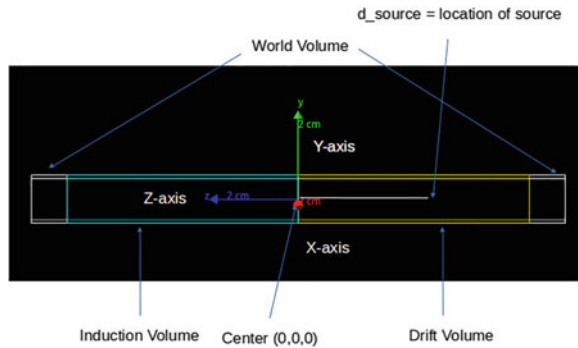
The gaseous ionization detectors [1] have been used in many particle physics experiments like CMS [2, 3], INO [4], LHCb [5], and in the upgraded ALICE TPC [6]. The motivation behind the work presented here is to study primary ionization in different gas mixtures with an alpha source. Primary ionization initiates the transport and amplification of electrons and ions within the detector. As a result, it is very important to understand the process in detail so that it is possible to interpret and predict the response of any gaseous ionization detector. In high rate experiments, radiation hardness, aging resistance, and stability against discharges are the main criteria for the long-term operation of the detectors.

In the paper [7], the primary ionization in Gas Electron Multiplier [8] has been studied and on the basis of that the discharge probability has been measured using geant4 [9] simulation. Ar-CO₂ (90–10) and Ne-CO₂ (90–10) gas mixtures were used for comparison. A mixed alpha source of ²³⁹Pu (5.2 MeV), ²⁴¹Am (5.5 MeV), and ²⁴⁴Cm (5.8 MeV) were used and the energy deposition by them was used to calculate the number of ionized electrons. The discharge probability of Ar-CO₂ (90–10) is greater than Ne-CO₂ (90–10) because the range of alpha particles is shorter in Ar-

R. Kanishka (✉) · P. K. Rout · S. Mukhopadhyay · N. Majumdar · S. Sarkar
Applied Nuclear Physics Division, Saha Institute of Nuclear Physics, 1/AF, Bidhannagar, Salt Lake, Kolkata 700064, India
e-mail: kanishka.rawat.phy@gmail.com

Homi Bhabha National Institute, Training School Complex, Anushaktinagar 400094, Mumbai, India

Fig. 144.1 The geant4 display of the volume considered for the simulation



CO₂. Moreover, the primary ionization is higher in Ar–CO₂ mixture. Using a similar concept, we did a similar analysis for primary ionization studies.

The present paper is organized as follows: numerical model, results, and conclusions are discussed in the next sections.

144.2 Numerical Model

We used geant4 [9] in order to simulate the process of primary ionization in different gas mixtures due to an alpha source. The drift and induction volume was taken to be 7.5 cm (both). The gas mixture used were Ar–CO₂ (90–10) and Ne–CO₂ (90–10). A step size of 10 μm was used. The G4EmLivermorePhysics physics list and alpha particles of energy = 5.5 MeV were used. The number of events processed was 10000. Figure 144.1 shows the geant4 display of the simulated volume.

144.3 Results

Figure 144.2 shows the co-ordinates of primary electrons when alpha source was kept at (0, 0, 0) and the gas mixtures used were Ar–CO₂ (90–10) and Ne–CO₂ (90–10). The x and y co-ordinate exhibits Gaussian distribution and shows higher ionization in Ar–CO₂. The z co-ordinate shows the range (distance traveled by particle from its source) in the gas mixtures. The explanation of this plot is more clear from the Bragg curve which is the energy loss rate, or linear energy transfer as a function of the distance through a stopping medium. A peak occurs due to an increase in the interaction cross section as the charged particle's energy decreases. The energy lost by charged particles is inversely proportional to the square of their velocity which explains the occurrence of the peak just before the particle comes to a complete stop. Figure 144.3 shows the Bragg curve of primary electrons when alpha source was kept

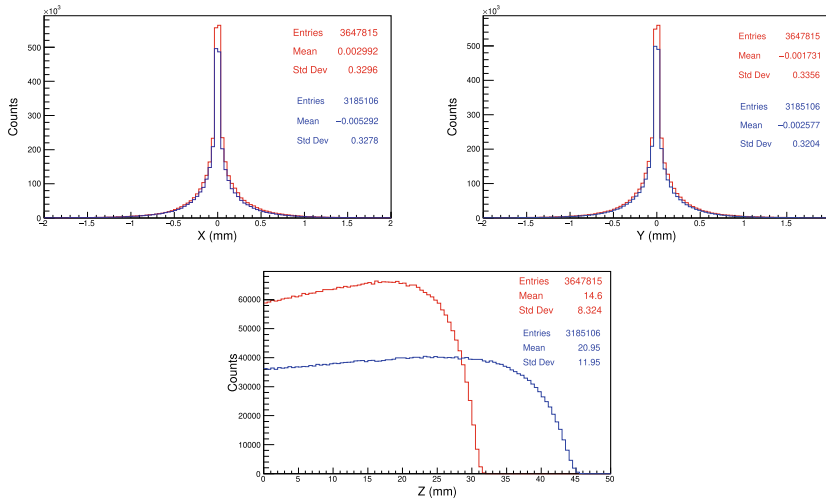
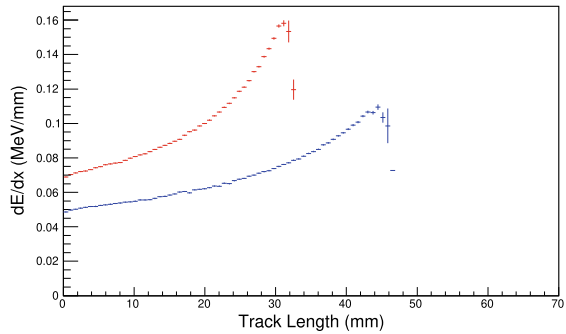


Fig. 144.2 The co-ordinates (x, y, z) of primary electrons with alpha source at (0, 0, 0), the gas mixtures used were Ar-CO₂ (90-10) (red) and Ne-CO₂ (90-10) (blue). The plots show that the primary ionization in Ar-CO₂ (90-10) is higher than Ne-CO₂ (90-10) gas mixture

Fig. 144.3 The Bragg curve of primary electrons when alpha particles kept at (0, 0, 0), the gas mixtures used were Ar-CO₂ (90-10) (red) and Ne-CO₂ (90-10) (blue)



at (0,0,0), the gas mixtures used were Ar-CO₂ (90-10) and Ne-CO₂ (90-10). The range of the alpha particles in Ar-CO₂ (90-10) and Ne-CO₂ (90-10) gas mixtures are 3.3 cm and 4.6 cm, respectively, which is comparable to the range of alpha particles in air = 3.84 cm [10]. The Bragg curve shows that the primary ionization in Ar-CO₂ (90-10) is higher than Ne-CO₂ (90-10) gas mixture as mentioned in Sect. 144.1. The Bragg curve shows the spread of the primaries is almost constant along the path but most of the energy deposition occurs at the peak. If the drift volume of a detector contains this peak, the primary charge density may attain large values and lead to discharges.

144.4 Conclusion

A simulation of primary ionization with different gas mixtures (Ar–CO₂ (90–10) and Ne–CO₂ (90–10) using alpha source has been carried out. The Bragg curve shows that the primary ionization is higher in Ar–CO₂ (90–10) than Ne–CO₂ (90–10). The range of alpha particles in Ar–CO₂ (90–10) is shorter than Ne–CO₂ (90–10). The more number of primaries is expected to give higher discharge probabilities in Ar–CO₂ mixture which is also reported in [7]. These studies are very important for all the gas detectors as it forms the basis of simulation of the detector response. The determination of Bragg curve leads to the deep understanding of the charge density studies. Also, such kind of studies will help to understand the discharge formation which is part of our ongoing studies.

Acknowledgements We would like to thank the computing facilities provided by SINP. We also acknowledge DAE for funding. We also acknowledge RD51 collaboration and members.

References

1. F.L. Michael, *Gas Ionization Detectors, Handbook of Radioactivity Analysis*, 4th edn. (Academic, 2020), pp. 245–305. <https://doi.org/10.1016/B978-0-12-814397-1.00002-9>
2. A. Colaleo, A. Safonov, A. Sharma, M. Tytgat, CMS Technical Design Report for the Muon Endcap GEM Upgrade, CERN-LHCC-2015-012, CMS-TDR-013 (2015)
3. D. Abbaneo et al., Characterization of GEM detectors for application in the CMS Muon detection system, in *2010 IEEE Nuclear Science Symposium, Medical Imaging Conference, and 17th Room Temperature Semiconductor Detectors Workshop, RD51-NOTE-2010-005* (2010), pp. 1416–1422. <https://doi.org/10.1109/NSSMIC.2010.5874006>
4. B. Satyanarayana, Design and Characterisation Studies of Resistive Plate Chambers, Ph.D. thesis, Department of Physics, IIT Bombay, PHY-PHD-10-701 (2009)
5. G. Bencivenni et al., A triple GEM detector with pad readout for high rate charged particle triggering. *NIMA* **488**, 493 (2002)
6. B. Ketzer, A time projection chamber for high-rate experiments: towards an upgrade of the ALICE TPC. *NIMA* **732**, 237 (2013)
7. P. Gasik et al., Charge density as a driving factor of discharge formation in GEM-based detectors. *NIM A* **870**, 116 (2017)
8. F. Sauli, GEM: a new concept for electron amplification in gas detectors. *NIM A* **386**, 531 (1997)
9. S. Agostinelli et al., Geant4—a simulation toolkit. *NIM A* **506**(3), 250 (2003)
10. A.K. Solomon, Experimental nucleonics, in ed. by E. Bleuler, G.J. Goldsmith (Rinehart, New York, 1952), p. 117. <https://doi.org/10.1126/science.117.3030.87-a>

Chapter 145

Development of Front-End Electronics for an SiPM-Based Cherenkov Telescope Camera



K. S. Gothe, S. K. Rao, S. S. Upadhya, S. Duhan, B. K. Nagesh, N. K. Parmar, M. Ranjan, B. B. Singh, and A. Sarkar

Abstract A prototype 64-pixel camera for a 4 m class Imaging Atmospheric Cherenkov Telescope is in its final stage of development. The camera is based on 4×4 array of SiPMs as a pixel sensor and would be mounted on the focal plane of the telescope. Eventually, the camera would be expanded to 256 pixels. The front-end electronics of the camera has an array of pixel sensors, bias supply to provide operating voltage to the sensors, preamplifiers to boost signal-to-noise ratio of the pixel signals, and low voltage dc supplies to power the preamplifiers. Stringent design goals and constraints have led to a customized design of the front-end electronics. The paper describes the design features of the front-end electronics along with its performance evaluation.

145.1 Introduction

A 256-pixel camera with a pixel size of 0.3° based on SiPMs as photosensors is being developed for a 4 m class vertex element of TACTIC telescope at Mt Abu, Rajasthan, India. The telescope is designed to detect the celestial VHE gamma rays using Imaging Atmospheric Cherenkov Technique (IACT). It works by capturing the images of the Cherenkov light flashes of a few ns duration generated by extensive air showers initiated by gamma rays and cosmic rays from celestial sources. These images are recorded by using the pixelated camera placed at the focal plane of the telescope [1]. Eventually, the telescope and the camera we are developing would be set up in Hanle (Ladakh, India). A 4×4 array of SiPMs, S13361-3050AS04 from Hamamatsu is chosen as a pixel photosensor for the camera. Each of the 16 SiPMs in the pixel also referred to as sub-pixels in this article has an area of $3 \times 3 \text{ mm}^2$ with individual cathode and anode. The front-end electronics of the camera is

K. S. Gothe (✉) · S. K. Rao · S. S. Upadhya · S. Duhan · B. K. Nagesh · N. K. Parmar · M. Ranjan · B. B. Singh · A. Sarkar
Tata Institute of Fundamental Research, Dr. Homi Bhabha road, Colaba 40005, Mumbai, India
e-mail: kiran@tifr.res.in

divided into 16 identical modules called Pixel Cluster Module (PCM) [2] with each PCM catering to 16 pixels. It consists of a Sensor Mount Board (SMB), four 4-pixel preamplifier boards, two 8-pixel bias supply cards, and a low voltage supply card. SMB holds 16 pixel sensors in the form of a 4x4 array with a pitch size of 22 mm. The SiPM gain is a function of the applied bias voltage above its breakdown voltage called overvoltage. The bias supply cards have to ensure constant overvoltage to all the pixel sensors to achieve uniform response. Four numbers of 4-channel preamplifier boards are directly plugged onto the SMB through four low pitch high density connectors to maintain a good level of signal integrity. The 16 sub-pixel signals from a pixel sensor are to be processed by each of the 4 channels in a preamplifier board to form a corresponding pixel signal. These signals are further amplified in back-end electronics before trigger generation and the signal readout.

145.2 Design Goals and Constraints

There are three primary goals for the front-end design of the camera: a wide dynamic range of 1–1500 photoelectrons (pe) per pixel, a signal-to-noise ratio (SNR) for single pe higher than 5 for in-situ pixel gain calibration, and extending camera operation under moonlit conditions, where background from night sky could be orders of magnitude higher than dark nights, as far as possible. These goals are to be achieved following some stringent constraints on PCB size, power, noise due to the factors like 16×16 array structure of pixels sensors with the pitch size of 22 mm, large number of sub-pixels to be dealt with, long decay time of SiPM pulses (80 ns), large night sky background, and large detector capacitance (320 pF per sub-pixel). As for the bias supply, the design has to address an issue arising due to temperature dependence of the breakdown voltage of SiPM. Besides, applied bias voltage itself changes with load due to series resistance. Both these factors result into change in the overvoltage and the bias supply has to compensate for these changes by correcting the applied voltage to ensure constant overvoltage and thus constant gain.

145.3 Design of the Analog Processing Chain and SiPM Bias Supply

The preamplifier circuit topology was chosen to have 4 main features. Firstly, every 2 adjacent sub-pixels are combined before the input of the preamplifier itself just by shorting their anodes. Secondly, 8 sub-pixel pair signals from a pixel are separately processed before they are shaped and summed. Also, to facilitate the single pe gain calibration more accurately, sub-pixel pair enable/disable feature is incorporated in the design. Lastly, the long tail portion of the Sub-pixel pair signals is shortened before summing them to give a FWHM of around 20 ns. The topology consists of

four different stages in cascade. The first stage of the circuit takes in 8 sub-pixel pairs signals with ac coupling and converts them into voltage pulses using Trans-Impedance Amplifier (TIA) realized using grounded-base transistor circuit [3]. TIA output voltage pulse is then buffered for impedance matching and shortened using shaping circuit. Pulse shortening is achieved using pole-zero cancellation technique and it brings down integrated noise and thus improves signal over noise. The shaper outputs from all 8 channels are then added using a summing amplifier. Components in these circuits were carefully chosen with considerations to the factors like low power, low noise and high bandwidth. To achieve accurate in-situ calibration of the single pe gain of the analog processing chain, 7 out of 8 sub-pixel processing chain outputs are disabled eliminating noise contribution from the disabled processing chains. A pixel signal from the preamplifier is again amplified using dual gain stages in parallel viz. low and high gain, in the back-end electronics before sending them for digitization. This feature helps to achieve the required dynamic range without going for expensive high-resolution ADC. Two 8-pixel Bias supply cards provide bias voltages to 16 pixel sensors in a PCM. The card is designed using DC-DC convertor HV80 from AiT instruments and Xmega series microcontroller. It is capable of giving up to 80 V dc at 4 mA with a minimum step size of 5 mV. Each card can monitor the temperature around 8 pixel sensors as well as the steady-state load current drawn by the pixel sensors and apply correct bias voltages to maintain the SiPM gain uniformity. A host single-board computer can access and control all the bias cards in the camera using customized SPI port and daisy chaining.

145.4 Performance

The performance of preamplifier was evaluated using a set-up consisting of a PCM in a black box, low gain and high gain amplifiers embedded in the back-end electronics, a pulsed laser system with programmable intensity and a VME based digitizer. Figure 145.1 (left) shows a representative pulse height spectrum for a pixel showing

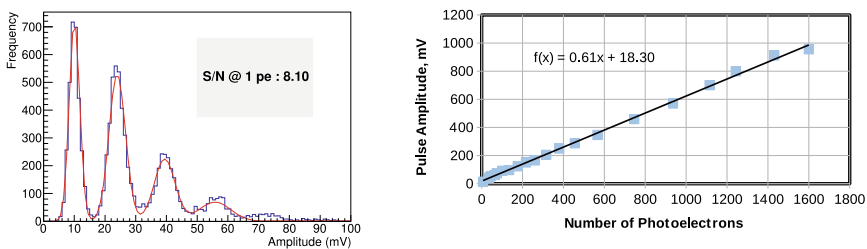


Fig. 145.1 Left: Observed (blue) and fitted (red) pulse height spectrum of a high gain output for pixel 16 exposed to low intensity light pulses with single sub-pixel pair enabled. Right: Observed (blue dots) and fitted (dashed line) amplitude of the low gain output pulses versus number of photoelectrons for pixel 13

clear separation between peaks due to pedestal, 1 pe, 2 pe, etc. Here the sensor was illuminated with a low intensity pulsed laser light and only one of the eight sub-pixel pairs was enabled. Figure 145.1 (right) shows a good linearity of the low gain output pulse amplitude up to 1600 pe with 3% non-linearity for a representative pixel. The data was obtained by varying the intensity of the pulsed laser light and recording the pulse height. The intensity was converted into equivalent number of photoelectrons based on calibration done in a separate exercise. An optical measurement module (C11205 from Hamamatsu) was used for this exercise as a standard light detector system with good linearity. The temperature compensation by the Bias Supply was tested in an exercise wherein the pulses at the low gain output for a pixel were recorded at different temperatures. The tests results showed a remarkable reduction in gain variation from 97% (without temperature compensation) to 3% (with temperature compensation) over the temperature range -20° to $+30^{\circ}$.

145.5 Conclusion

In spite of stiff goals and stringent constraints, we have achieved the required specifications (Table 145.1) for the prototype camera front-end by adopting a novel circuit topology and also by carefully selecting the circuit components with low noise, low power, and high bandwidth.

Table 145.1 Front-end design parameters

Parameter	Achieved specification
Size of the preamplifier PCB	$70 \times 110 \text{ mm}^2$
Signal width (FWHM)	20 ns
DC supply voltages for the preamplifiers	$\pm 3.3 \text{ V}$
Preamplifier output signal amplitude per pe with 50Ω load at overvoltage of 3 V	0.6 mV
SNR at single pe at overvoltage of 3 V	6.35 (Average)
Dynamic range with 3% non-linearity	1–1600
Gain variation over temperature range -20° to $+30^{\circ}$	3%
Power consumption per pixel	0.75 W

References

1. T.C. Weekes et al., Observation of TeV gamma rays from the crab Nebula using the atmospheric Cherenkov imaging technique. *Astrophys. J.* **342**, 379–395 (1989)
2. S.S Upadhyya et al., Development of 256-pixel SiPM based imaging camera and its status, in *This Proceedings*
3. H. Anderhub et al., Design and operation of FACT—the first G-APD Cherenkov telescope. *J. Instrum.* **8**, P06008 (2013)

Chapter 146

Characterization of Hamamatsu SiPM for Cosmic Muon Veto Detector at IICHEP



Mamta Jangra, M. N. Saraf, V. M. Datar, G. Majumder, Pathaleswar,
B. Satyanarayana, and S. S. Upadhya

Abstract As a part of R&D for the veto system of mini-Iron CALorimeter (ICAL), SiPMs were characterized by various techniques available. First of all, standalone SiPM characterization was done using SP5601 CAEN ultrafast LED driver with external trigger inside a small black box. Photoelectron peaks due to different numbers of electrons are clearly visible, which were then used to calculate the gain of the SiPM. Correlated noise like afterpulse and crosstalk were also studied using noise triggers, where a few photoelectron peaks were observed. This can also be used to calculate the gain of SiPM from the spacing between different peaks. Finally, a radioactive source ^{22}Na was also used to cross-check the gain. This paper will present the results of these characterization techniques of SiPM and summarize the results obtained using them.

146.1 Introduction

Cosmic ray muons constitute an important background in rare event searches. For example, the muon flux on the earth's surface is $\sim 200\text{m}^{-2}\text{s}^{-1}$. This reduces by a factor of $\sim 10^6$ at an underground location with 1 km rock cover in all directions. At a depth of ~ 100 m this suppression factor is about 10^2 . In order to achieve a rejection factor 10^6 at this shallow depth, an active cosmic muon veto detector enclosing the detector (on the top and 4 sides) with an efficiency of $>99.99\%$ is required. Mini-ICAL comprises an 85-ton magnet built using 11 layers of 56 mm thick soft iron plates and 10 layers of $2\text{m} \times 2\text{m}$ glass Resistive Plate Chambers (RPCs), and is

M. Jangra (✉)
Homi Bhabha National Institute, Mumbai 400094, India
e-mail: mamta.jangra@tifr.res.in

M. Jangra · Pathaleswar · B. Satyanarayana · S. S. Upadhya
Tata Institute of Fundamental Research, Mumbai 400005, India

M. N. Saraf · V. M. Datar · G. Majumder
Department of High Energy Physics, Tata Institute of Fundamental Research, Colaba, Mumbai, India

currently operating at IICHEP Madurai. The plan is to cover the $4\text{ m} \times 4\text{ m} \times 1.1\text{ m}$ mini-ICAL with a cosmic muon veto (CMV) detector and to estimate its efficiency to veto cosmic muons. The CMV detector will have four layers of extruded scintillators of size $(460\text{ cm} \times 5\text{ cm} \times 2\text{ cm})$ on top and three layers of $(460\text{ cm} \times 5\text{ cm} \times 1\text{ cm})$ on three sides of the mini-ICAL. The photon signal will be collected through wavelength shifting (WLS) fibres embedded in the extruded scintillators and readout will be taken on both sides using $2\text{ mm} \times 2\text{ mm}$ Silicon PhotoMultipliers (SiPMs). This paper describes the characterization of SiPMs which is one of the main components of CMV set-up.

146.2 Experimental Setup

An extruded scintillator strip of $(60\text{ cm} \times 5\text{ cm} \times 2\text{ cm})$ is used for characterization. The extruded scintillator strip contains two holes throughout the length into which 60 cm long WLS fibres of diameter 1.4 mm is embedded. A fibre guide bar made of acrylic is glued on both sides to mount the Counter Mother Board (CMB). Since each extruded scintillator strip contains two WLS fibres, there will be a total four SiPMs for readout as shown in Fig. 146.1.

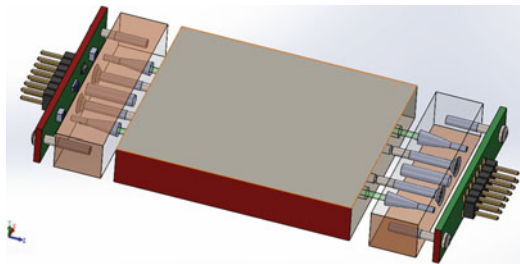
Power supply to SiPMs on CMB is given using Keithley source meter ($105\text{ }\mu\text{A}$ maximum current limit, $0\text{--}90\text{ V}$). Each SiPM has a common supply voltage of 54 V . The output signal is collected by connecting coaxial cables to oscilloscope.

146.3 LED Calibration

The SP5601 LED system is used for SiPM characterization. External pulser on LED driver is used to trigger the oscilloscope. The integrated charge is calculated using the equation:

$$Q = \frac{1}{R} \int_{t_0}^{t_1} V(t) dt \quad (146.1)$$

Fig. 146.1 Scintillator counter schematic



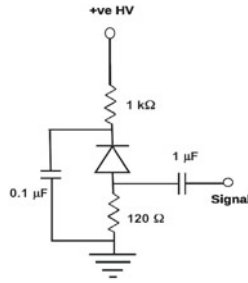


Fig. 146.2 SiPM circuit diagram

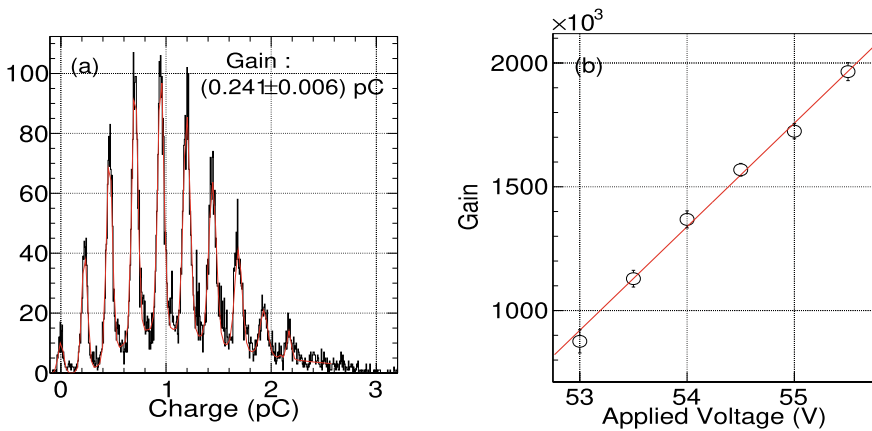


Fig. 146.3 Photoelectron peaks at **a** $V_{ov} = 3 V$, and **b** Gain of SiPM as a function of applied voltage

where $R = 120 \Omega$ as shown in Fig. 146.2. Collected charge is fitted with a function:

$$F(x) = \text{Landau}(x) + \sum_{n=0}^{N-1} R_n \times e^{-\frac{(x - n\mu)^2}{2\sigma^2}} \quad (146.2)$$

where N is the number of photoelectron (p.e.) peaks, R_n is the peak height, μ is the gain of SiPM and σ is the gaussian width of p.e. peak. Several p.e. peaks can be seen clearly as shown in Fig. 146.3a. Average gap between consecutive peaks is calculated from the fit and the gain is quantified as shown in Fig. 146.3b.

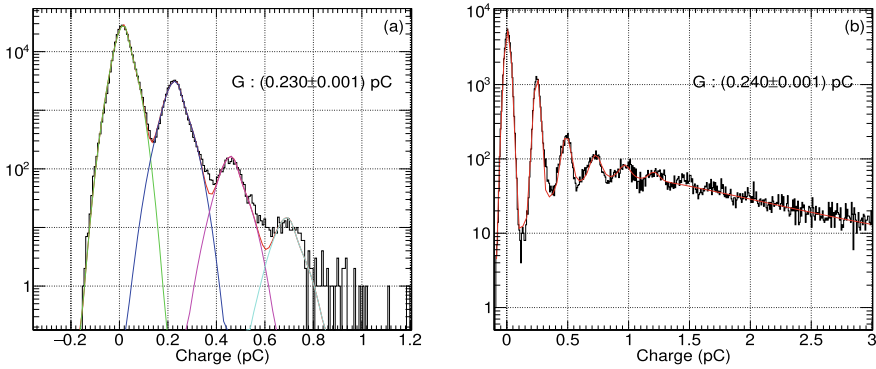


Fig. 146.4 Photoelectron peaks at $V_{Ov} = 3$ V from **a** noise data as well as from **b** radioactive source data for one of the SiPM

146.4 Calibration Using Noise Data and Radioactive Source Data

As compared to LED calibration, the accuracy of calibration from noise data is poorer. Random trigger is used for data collection. One SiPM is used to trigger the system and data from remaining three is used for calibration of SiPM. The radioactive source ^{22}Na was placed on top of the extruded scintillator for testing and characterizing the SiPMs. The trigger is generated using the same technique as that of noise data.

The charge distribution with p.e. peaks is shown in Fig. 146.4a, b, for noise data and radioactive source data, respectively. Gain is measured by calculating the average gap between the consecutive peaks in the spectra for both the cases.

146.5 Dark Rate and Correlated Noise

One of the known methods to quantify the primary noise and correlated noise associated with SiPM is to study the waveforms from SiPM in a dark room at controlled temperature [1, 2]. Using the same technique, primary dark rate is calculated as shown in Table 146.1 for one of the SiPM. Afterpulse and delayed crosstalk counts are clearly separated from primary noise counts in the amplitude versus time difference (difference between peak time of two consecutive peaks) plot as shown in Fig. 146.5. Their rates have been calculated by taking difference between measured and extrapolated values from time difference distribution as shown in Fig. 146.6.

Table 146.1 Dark noise rate as a function of number of photoelectron at $V_{ov} = 3 V$

Threshold (N_{pe})	Noise rate (kHz)
0.5	151.380 ± 1.738
1.5	6.000 ± 0.346
2.5	0.460 ± 0.095
3.5	0.100 ± 0.044

Fig. 146.5 Amplitude versus time difference distribution at $V_{ov} = 3 V$

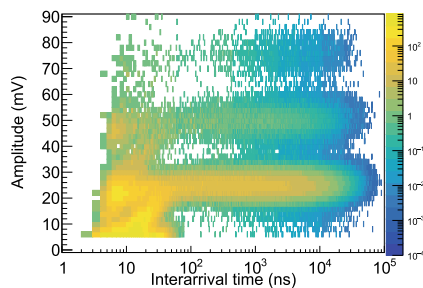
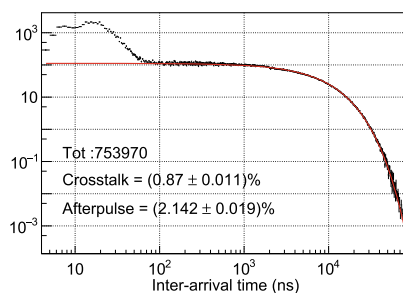


Fig. 146.6 Correlated noise in log-log scale at $V_{ov} = 3 V$



146.6 Conclusion

Apart from LED calibration, two alternate procedures have been established to calibrate the gain of the SiPM. Calibration by all three methods are in agreement with each other. Correlated noise is observed to be (3–4)% of the total noise which is well in agreement with specifications.

References

1. C. Piemonte, A. Gola, Overview on the main parameters and technology of modern Silicon Photomultipliers. Nuclear Inst. Methods Phys. Res. A **926**, 2–15 (2019)
2. R. Klanner, Characterisation of SiPMs. Nuclear Inst. Methods Phys. Res. A **926**, 36–56 (2019)

Chapter 147

Trigger Hardware for CMS Experiment at the LHC



Mandakini Patil, Kushal Bhalerao, and Kajari Mazumdar

Abstract From 2027 onward, the Large Hadron Collider (LHC) machine is expected to deliver proton-on-proton collisions with extremely high instantaneous luminosity, at the level of 5 to $7.5 \times 10^{34} \text{ cm}^{-2}\text{s}^{-1}$. This HL-LHC avatar will boost the scientific capability, but will also pose major technical challenges, including trigger for the experiments which selects collision events in real time. The trigger and data acquisition system of CMS experiment will continue to follow a 2-level strategy while increasing the primary hardware maximum rate at level of about 750 kHz with a latency of $12.5 \mu\text{s}$. The custom-made hardware design for primary level trigger is based on the advanced telecommunications architecture as well as state-of-the-art FPGAs connected via serial optical links running at speeds of up to 25 Gbps . Several types of prototype mezzanine electronic boards, incorporating system-on-chip, to be used in various subsystems of CMS experiment have been fabricated in Indian Industries. The functionality, challenges in fabrication of these boards, and the testing methodology using in-house setup in the lab is discussed briefly.

147.1 Introduction

The Compact Muon Solenoid (CMS) is one of the four experiments at the Large Hadron Collider (LHC). When the LHC is colliding protons, though CMS detects hundreds of millions of collisions every second, only a handful are selected in real time for elaborate physics studies. The job of the CMS Trigger is to select finally only a small fraction of events, considered the most interesting, while discarding the rest. The primary level of this 2-tier operation, known as the Level 1 (or L1) Trigger, selects a maximum of a hundred thousand events each second for more detailed study as the next level, known as the High-Level Trigger. The L1 receives detector data at the full 40 MHz collision rate, performs a fast reconstruction of each event, and determines which event to read out from the detector, sending a signal to

M. Patil (✉) · K. Bhalerao · K. Mazumdar
Tata Institute of Fundamental Research, Mumbai 400005, India
e-mail: manda@tifr.res.in

© The Author(s), under exclusive license to Springer Nature Singapore Pte Ltd. 2022
B. Mohanty et al. (eds.), *Proceedings of the XXIV DAE-BRNS High Energy Physics Symposium, Jatni, India*, Springer Proceedings in Physics 277,
https://doi.org/10.1007/978-981-19-2354-8_147

821

the front-end buffers when this occurs. The L1 Trigger is split into separate systems which reconstruct particles within one sub-detector, and feed into a final system which combines that information and makes the trigger decision.

147.2 Level 1 Trigger Upgrade

From 2027 onward, the Large Hadron Collider (LHC) machine is expected to deliver proton-on-proton collisions with extremely high instantaneous luminosity, at the level of 5 to $7.5 \times 10^{34} \text{ cm}^{-2}\text{s}^{-1}$, defined as HL-LHC operation. The increases in instantaneous luminosity imply that the L1 Trigger would select at least 6 times as many events as it currently does, in order to maintain the same number of useful collisions ultimately stored for detailed analysis. The current detector will be unable to handle this challenge of HL-LHC. Hence, over the next few years, CMS experiment will upgrade most of its readout electronics, data acquisition system as well as L1 Trigger hardware, along with some of the sub-detector systems, the transition being termed as Phase-2 upgrade. The upgraded trigger system will improve the discrimination of interesting physics collisions in real time and operate within the predefined data acquisition rate.

The key technologies and challenges that are being addressed in the current R & D phase are the use of Ultrascale class field programmable gate arrays (FPGAs), the Multi-Gigabit Transceiver (MGT) links designed beyond 10 Gbps line rates (i.e., 16 and 25 Gbps), the Advanced Telecommunications Computing Architecture (ATCA) form factor, the Next Generation Intelligent Platform Management Interface (IPMI), as well as embedded Linux solutions and the System-level integration, maintenance, and operations. The R & D phase has produced an Advanced Processor demonstrator (APd) board, which is the evolving back-end ATCA blade with control daughter boards based on ATCA technology, with emphasis on trigger applications.

147.3 Mezzanine Control Cards for ATCA Blades

The APd card has several mezzanine peripheral boards installed on it, for various supplementary functions. TIFR took the responsibility of fabricating some of these boards in the Indian Industries. Three different types of boards based on proto-type designs are already produced and tested in TIFR. These are now used along with APd boards with the quality certified by the collaborating institutes (Universities of Wisconsin and Florida, USA). The quality control (QC) of these mezzanine boards was carried out in-house. More specifically TIFR has built units of the Ethernet Switch Module (ESM) and Intelligent Platform Management Controller (IPMC) cards, and Embedded Linux Mezzanine (ELM) boards, all targeted for the ATCA blades. The main ATCA blade is evolving from the APd1 (advanced Processor demo) to AP (Advanced Processor) final card and has an Ultra scale FPGA VU9P which

caters to high link speeds. The QC of the ESM and IPMC boards are done entirely in standalone test setups in TIFR lab. The development of complete test suite for ELM cards is underway.

147.3.1 Intelligent Platform Management Controller (IPMC)

This is a versatile, open source and self-contained daughter card for the main trigger board. This uses ZYNQ system-on-chip (SoC) which has a single core 32-bit ARM Cortex-A9 processor running at 666.6 MHz and having 34.4 k LUTs (Look Up Tables), 68.8 k FF Artix-7 FPGA core. The memory chips on the board are 256 Mbytes DDR3, 64 MB QSPI Flash, and 256 Kb EEPROM. Platform management refers to monitoring hardware, its control for debugging, and logging of various states of the system like voltage, current, temperature of the APd board. IPMC negotiates with the crate for power and the connectivity, controls the power, as well as monitors the condition of the board via sensor. It also provides lower level configuration support (e.g., boot control). These boards are tested in a standalone test stand with the test board made locally. The Intelligent Platform Management Controller (IPMC) mezzanine, shown in Fig. 147.1, is intended to be the next generation of blade controllers that communicate with ATCA Shelf Managers. It is part of the PICMG 3.x specification and each blade needs to have one such controllers. They are responsible for doing blade-related health checks (e.g., temperature, voltages) and to act in case of problems, such as over-temperature or over-voltage.

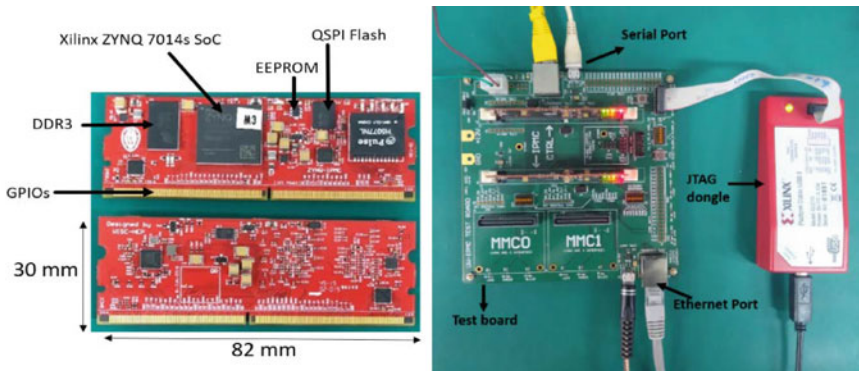


Fig. 147.1 IPMC boards and test setup at TIFR

147.3.2 Ethernet Switch Module (ESM)

This is a compact 6-port 1Gbps Ethernet Switch Module (35 mm × 40 mm) targeted for ATCA blades where ethernet connectivity is required. It connects the on-board endpoints such as the Linux and IPMC to the crate switch in an ATCA hub slot via backplane connection (1000 BASE-T is standard). The prototype cards were fabricated in Bengaluru. We have developed in-house standalone test board and tested all 6 ports of each board. All six 1000 M (1 Gbps) ports were checked for connectivity and 1GBps data transfer (Fig. 147.2).

In the bring up tests for ESM, the on-board EEPROM is loaded with a binary file which provides an interactive console. This console can be accessed with UART having baud rate 115200. This console provides the status of the ports as shown in Fig. 147.3.

In addition to the loopback tests, we also carried out speed rate test of data transfer using tool named iperf. The results are shown in Fig. 147.4.

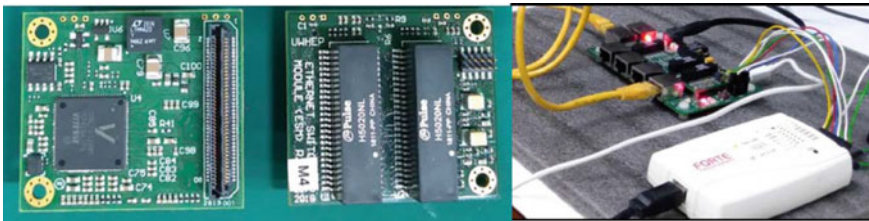


Fig. 147.2 Ethernet switch module and test setup

```

uPort iPort cPort MIIM Bus MIIM Addr PHY/Serdes CRC uPatch Link Status
-----
1 0 0 0 0x00 FERRET_7512 No uPatch Up - 1GFDX FC(D)
2 1 1 0 0x01 FERRET_7512 No uPatch Up - 1GFDX FC(D)
3 2 2 0 0x02 FERRET_7512 No uPatch Up - 1GFDX FC(D)
4 3 3 0 0x03 FERRET_7512 No uPatch Up - 1GFDX FC(D)
5 4 7 2 0xff - Not PHY Up - 1GFDX FC(D)
6 5 10 2 0xff - Not PHY Up - 1GFDX FC(D)
  
```

Fig. 147.3 Console interface showing port status of ESM

```

[ ID] Interval Transfer Bandwidth Retr
[ 4] 0.00-10.00 sec 1.09 GBytes 936 Mbits/sec 0
[ 4] 0.00-10.00 sec 1.09 GBytes 934 Mbits/sec
iperf Done.
  
```

Fig. 147.4 Iperf tests

147.3.3 Embedded Linux Mezzanine (ELM)

This card also installed on the main APd-based ATCA blade provides higher level configuration support (booting FPGAs, configuring memories, clocks, optics, etc.). It acts as primary network-connected TCP endpoint on the board during online operation. The main purpose of ELM is to serve an on-board control interface for ATCA modules. Once booted, the ELM Linux system provides configuration and operational support for the platform. This includes initialization of FPGAs (bit files loading and register/memory initialization) and configuration of support devices such as Firefly optical modules, clock switches, and jitter-cleaner/synthesizers. Our aim is to develop test firmware to automate the bring-up tests. The task is to check various on-board interfaces. Till date we have successfully tested DDR4 interface and UART interface. Firmware for I2C and Ethernet devices is under process. Since the SoC on ELM is Xilinx's ZYNQ Ultrascale+ architecture based, we are using Xilinx's Vivado, SDK, and Petalinux tools.

147.4 Conclusion

Several types of mezzanine daughter electronic boards meant for hardware-based trigger of CMS experiment have been fabricated in Indian industries. They are tested at TIFR in standalone setup. Subsequently, they have displayed excellent performance when tested in the ATCA blades. The chosen ATCA architectures, their testability, integration, and the advantages over existing solutions were understood while we tested these at TIFR.

References

1. J. Mendez et al., Design of an advanced TCA board management controller (IPMC). JINST **12**, C03010 (2017)
2. The Phase-2 Upgrade of the CMS endcap calorimeter: CMS-TDR-019 (2018)
3. J. Mendez et al., CERN-IPMC solution for advanced TCA blades. PoS(TWEPP-17) (313), 053 (2018)
4. PICMG, Advanced TCA Base Specification 3.0, Revision 3.0

Chapter 148

Fabrication, Interfacing and Performance of the High Voltage Bias Supply Modules for ICAL RPCs



M. N. Saraf, S. R. Joshi, V. M. Datar, G. Majumder, A. Manna,
B. Satyanarayana, R. R. Shinde, and E. Yuvaraj

Abstract The Iron-CALorimeter detector of the India-based Neutrino Observatory is designed to use 28,800 single gap Resistive Plate Chambers (RPCs) of $2\text{ m} \times 2\text{ m}$ size as its active detector elements [1]. Each RPC requires a variable High Voltage (HV) bias supply of up to 12 kV for generation of the operating electric field in the RPC's gas medium. Considering the large number of supplies needed for the ICAL detector, an indigenously designed, programmable $\pm 6\text{ kV}$ HV supply module, capable of providing $2\ \mu\text{A}$ current per channel, has been developed [2]. After initial prototyping and thorough testing of the module, a limited number of modules were fabricated and installed in the RPCs of the mini-ICAL detector, which is operational at IICHEP, Madurai [4]. The modules were interfaced using the SPI interface with the digital front-end (RPCDAQ) [3], which is part of the data acquisition electronics of the mini-ICAL detector. The RPCDAQ sends commands to the HV module to control and monitor the voltage, current and ramp rate. The RPCDAQ has an Ethernet link to the back-end servers and uses TCP/IP for control and data communication. A PyQt4-based software was developed to control and monitor the HV module remotely via the RPCDAQ. This software can control HV of multiple RPCs simultaneously. The software can also display and log the periodic monitoring data of the HV modules, like measured output voltage, current, etc. In this paper, we will discuss the fabrication, interfacing and performance of the HV bias supply in the mini-ICAL detector.

M. N. Saraf (✉) · S. R. Joshi · V. M. Datar · G. Majumder · B. Satyanarayana · R. R. Shinde · E. Yuvaraj
Department of High Energy Physics, Tata Institute of Fundamental Research,
Homi Bhabha Road, Navy Nagar, Colaba, Mumbai 400005, India
e-mail: mandar@tifr.res.in

A. Manna
Electronics Division, Bhabha Atomic Research Centre, Trombay, Mumbai 400085, India

© The Author(s), under exclusive license to Springer Nature Singapore Pte Ltd. 2022
B. Mohanty et al. (eds.), *Proceedings of the XXIV DAE-BRNS High Energy Physics Symposium, Jaitni, India*, Springer Proceedings in Physics 277,
https://doi.org/10.1007/978-981-19-2354-8_148

148.1 Introduction

The ICAL detector will study atmospheric neutrino oscillation parameters and mass ordering by tracking charged particles in the magnetised ICAL detector, produced during neutrino interactions [1]. For this purpose, the ICAL will deploy 28,800 single-gap RPCs as active detector elements. The operation of an RPC requires a high voltage bias going up to 12 kV. This requirement of large number of bias supplies motivated the design of an indigenous HV bias supply. To eliminate the cost and space usage of bulky HV connectors and cables, it was decided to place the HV module in a corner of the RPC tray with the RPC.

148.2 HV Supply Construction

The RPC bias supply is built as a bipolar $\pm 6\text{kV}$ supply, so as to minimise the insulation requirement at the RPCs’ surfaces and the HV cabling. The HV generation is done using low noise HV DC-DC converters, which are based on a current fed resonant Royer circuit, so as to minimise harmonic generation, as shown in the simplified block diagram in Fig. 148.1. The HV module is constructed in a triangular shape so as to fit in a corner inside the RPC tray along with the RPC detector as seen in Fig. 148.2.

The salient features of the module are as follows: (a) O/P voltage adjustable in the range from $\pm 100\text{V}$ to $\pm 6\text{kV}$. Setting resolution 2V, accuracy 1% of F.S. (b) O/P ripple and noise: less than 100 mV(p-p). (c) Load current read back: 0–2000 nA (accuracy $\pm 1\%$ of F.S.), measuring resolution 1 nA. (d) HV Ramp rate settable: 0.5–

Fig. 148.1 HV generation schematic

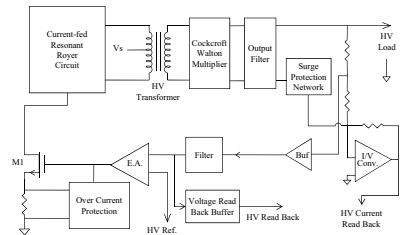
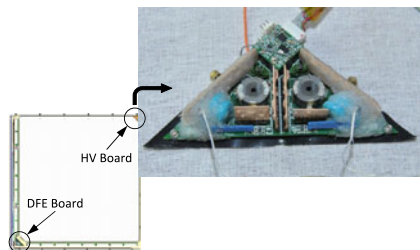


Fig. 148.2 HV placement



200 V/s in 9 steps. (e) Remote voltage programmability through SPI / RS-232 link. (f) HV on/off control, and read back facility for HV o/p voltage and load current.

148.3 Interfacing the HV Module to ICAL DAQ (RPC-DAQ)

The HV module is programmed to receive operating commands from an external controller through an SPI (Serial Parallel Interface) port. The HV supply is configured as a slave in this mode. The SPI interface provides commands for complete control and monitoring of the HV module's two HV channels.

148.4 RPC Performance Vis-á-vis Commercial Module

In order to study the performance of the indigenously made HV Module, a few RPCs in the mini-ICAL [4] (namely, layer-2, 3 and 4 front-side) were powered by the INO-HV module. Remaining RPCs were operated with a CAEN-HV module. To compare the behaviour of the INO-HV module with the existing CAEN module, the INO-HV from the layer-4 front-side RPC was replaced with CAEN-HV module. Detector parameters such as count rate, strip occupancy, strip multiplicity and pixel-wise efficiency estimated using different HV modules (same RPC) are discussed in this section. To estimate the unbiased detector parameters from layer-4, the events were recorded based on hardware trigger from coincidence of onefold signals from layers 6, 7, 8 and 9 (X- or Y-plane, both front- and back-side are in trigger).

148.4.1 Strip-Wise Count Rate

The strips have an average count rate of around 50–250 Hz and are considered healthy. From Fig. 148.3, it can be seen that the strip numbers X55, X56 and Y58 are noisy when RPC is operated with CAEN-HV module. These strips are nearer to the HV connection in RPC. Thus, these strips are rejected offline for further analysis. In the case of INO-HV, these strips have normal count rates. The overall noise rate seems comparable.

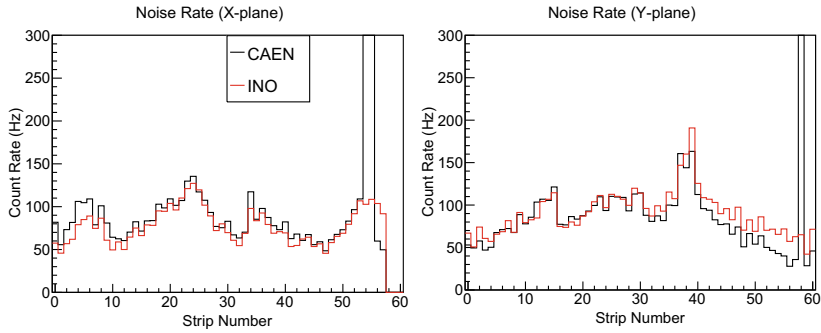


Fig. 148.3 Noise rate distribution for X- and Y-plane of RPC

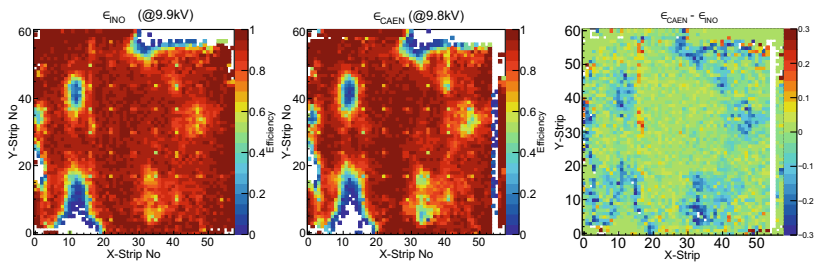


Fig. 148.4 Pixel-wise efficiency of X-plane of RPC (layer-4 with INO HV at 9.9kV and CAEN at 9.8kV)

148.4.2 Pixel-Wise Efficiency of RPC

The pixel efficiency is the ratio of number of events observed in a pixel (where the observed position is within the 3 cm of the fit position) to the number of events passed through (calculated using fit parameters estimated using other layers) in that pixel. Figure 148.4 shows the pixel-wise efficiency of X-plane (Y-plane) using CAEN-HV and INO-HV along with the difference in efficiencies between the two HV modules. The difference in efficiencies between CAEN and INO is more or less about zero, other than the regions where the RPC gain is much less. In the regions around the less efficiency zones, the efficiency estimated using INO-HV is less than CAEN-HV.

148.5 Status and Summary

The indigenously designed high voltage module has been successfully built and tested. A small number of modules have been deployed at the mini-ICAL detector. The performance of the HV module has been tested and compared against a commer-

cial HV supply of the make CAEN. The performance of the RPCs has been found to be comparable when biased with the INO-HV module and the CAEN-HV module, respectively.

References

1. A. Kumar, A..M. Vinod Kumar, A.. Jash et al., Invited review: Physics potential of the ICAL detector at the India-based Neutrino Observatory (INO). *Pramana—J. Phys.* 79–88 (2017) <https://arxiv.org/abs/1505.07380>
2. A. Manna et al., Development of a ± 6 kV Bias Supply for ICAL Detectors of INO, in *XXII DAE High Energy Physics Symposium*. ed. by M. Naimuddin (Springer Proceedings in Physics, Springer, Cham). <https://doi.org/10.1007/978-3-319-73171-1206>
3. M..N.. Saraf et al., Soft-core processor based data acquisition module for ICAL RPCs with network interface, in *XXI DAE-BRNS High Energy Physics Symposium*, vol. 174, (Springer Proceedings in Physics, Springer, Cham, 2016). <https://doi.org/10.1007/978-3-319-25619-186>
4. G. Majumder et al., Design, construction and performance of magnetised mini-ICAL detector module, in *Part of Proceedings, 39th International Conference on High Energy Physics (ICHEP2018)*. (2019). <https://doi.org/10.22323/1.340.0360>

Chapter 149

The Micromegas Detectors for ATLAS New Small Wheel Upgrade



Manisha Lohan

Abstract The upgrade of the Large Hadron Collider (LHC) to the High Luminosity LHC (HL-LHC) is required to probe the physics beyond Standard Model. After the ongoing long shutdown (LS2) and eventually after LS3 in 2026, the accelerator luminosity will be increased up to 7 times as compared to designed luminosity value, thus reaching $7 \times 10^{34} \text{ cm}^{-2}\text{s}^{-1}$. To meet the requirements of HL-LHC era, the muon system of ATLAS detector needs to be upgraded. Therefore, the existing forward inner part of ATLAS muon spectrometer, the small wheel comprised of Cathode Strip Chambers (CSC), monitored Drift Tubes (MDT) chambers, and Thin Gap Chambers (TGC) will be replaced by the New Small Wheel (NSW). The NSW will be constituted by MicroMegas gaseous detectors (from the MPGD family) and small-strip Thin Gap Chambers (sTGC). Micromegas detectors will be used mainly for tracking and sTGC detectors mainly for triggering purpose. But each type of detector is able to participate in both systems. Micromegas are ionization-based gaseous detectors made up of parallel plates, having a thin amplification region separated from the conversion region via a thin metallic mesh. For each of the two NSW, 4 Micromegas detectors will be installed in each of the 16 sectors. Four types of Micromegas termed as SM1, SM2, LM1, and LM2 will be installed, each detector with an individual area between 2 and 3 m². At CERN, integration of these detectors is in progress. In this talk, the construction of Micromegas detectors, the methodology to obtain the required and challenging results as well as obtained results will be presented. Specific measurement devices have been developed in the last few years to determine the mechanical metrology quality of Micromegas chambers, also presented here. The validation results using cosmic muons will also be shown.

Manisha Lohan for the ATLAS Muon Collaboration.

M. Lohan (✉)

IRFU, CEA, Université Paris-Saclay, 91191 Gif-sur-Yvette, France
e-mail: manisha1.lohan@gmail.com

© The Author(s), under exclusive license to Springer Nature Singapore Pte Ltd. 2022
B. Mohanty et al. (eds.), *Proceedings of the XXIV DAE-BRNS High Energy Physics Symposium, Jaitni, India*, Springer Proceedings in Physics 277,
https://doi.org/10.1007/978-981-19-2354-8_149

833

149.1 Introduction

The ATLAS detector [1] nowadays is ongoing through Phase-1 upgrade to fulfill the requirements of HL-LHC [2] era; main projects of ongoing upgrade phase are electronics and trigger upgrade of liquid argon calorimeter, innermost muon endcap stations upgrade, i.e., replacement of present Small Wheel by New Small Wheel (NSW) [3], trigger, and data acquisition, etc. NSW is one of the largest projects of this upgrade phase at LHC. Each NSW is made up of 16 sectors, 8 small, and 8 large sectors. Each sector consists of 4 detector wedges: 2 sTGC wedges and 2 Micromegas wedges. These four detector wedges are integrated with the help of central spacer frame, made up of aluminum. Each sTGC wedge contains three sTGC detectors and each Micromegas wedge contains two Micromegas detectors. For each NSW, total four types of Micromegas detectors are used, named as SM1, SM2 for small sectors and LM1, LM2 for large sectors as shown in Fig. 149.1. Micromegas production is shared between various sites from France, Italy, Germany, Greek, and Russia. IRFU Saclay, France is responsible for LM1 production. Details of various aspects of LM1 type Micromegas production are described here.

149.2 Panel Construction

Panel construction is carried out using granite table [4], shown in Fig. 149.2. First of all, first side PCBs are placed adjacent to each other. Then planarity measurements are carried out, to confirm that there are no bumps having deviation outside the acceptable range. If planarity measurements are found to be good, then glue is applied and first half side is extracted using an extraction tool. After that, second side PCBs are placed in the same way; there will be one extra step—positioning of reference parts which helps in the panel positioning at the time of module assembly. Then glue is applied and already extracted half panel is placed on it. It gets dried within one day.

Fig. 149.1 Layout of new small wheel

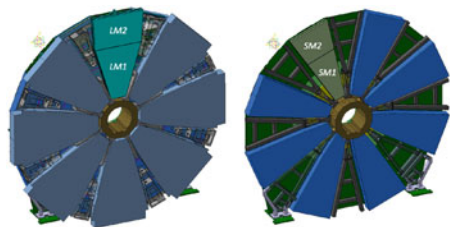
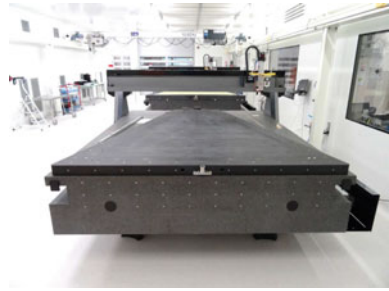


Fig. 149.2 Granite table used for panel construction

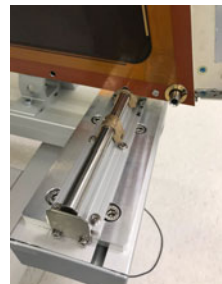


149.3 Module Assembly and Preliminary Testing

Module assembly is done using a specific assembly station, having reference tracks at the feet to position panels as shown in Fig. 149.3. Each LM1 module is made up of 5 composite panels: 3 drift panels and 2 readout panels. Initially, each gap formed by drift and readout panel is closed without O-ring, and HV behavior is checked in air by ramping voltage up to 850 V. If dark current is less than 50 nA and spark rate is less than 6, then that gap is considered ok, otherwise gap is opened, followed by visual inspection and testing until this criterion is qualified. Once this criterion is qualified then gap is closed with O-ring. After closing all 4 gaps in this way, final closing is done. Then module is shifted to granite slab for planarity and positioning measurements. Once these measurements are finished, module is moved outside the clean room for further testing.

Module gas tightness test is done using Argon, up to an overpressure of 3.2 millibar. Module is closed at both the ends and a change in overpressure is recorded. If there are huge leaks, sniffer is used to detect leak point. If leak rate is less than 0.6 millibar/hour then it is ok otherwise module is dismantled to repair/replace leaky panels.

Fig. 149.3 Reference tracks at the feet of assembly station



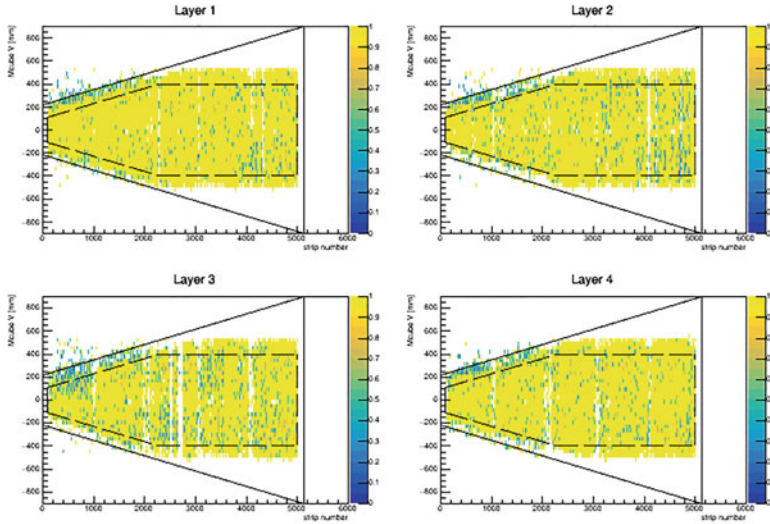


Fig. 149.4 Efficiency map of one of the LM1 module

149.4 Module Validation Using Cosmic Muons

LM1 modules validation is done using cosmic muons. Small micromegas having area $1\text{m}^2 \times 1\text{m}^2$ are used for triggering purpose. Due to size constraints of trigger micromegas, data for LM1 module is collected in three steps—PCB (4, 5), PCB (2, 3), PCB 1. Average efficiency of LM1 is 95%, efficiency map of one of the module is shown in Fig. 149.4. Gases used for operation were Argon and CO_2 till now. Currently NSW collaboration is looking for a new gas mixture, how much Isobutane can be added to obtain long-term stability.

149.5 Summary

After a long and dedicated R&D program, production is progressing well. Challenging specifications and requirements for module production are achieved within acceptable range. Due to some HV instability, the NSW collaboration is currently testing a new gas mixture for aging. Module production for NSW A has been finished at all production sites, soon will finish production for NSW C. Integration activities are progressing well at CERN.

References

1. ATLAS Collaboration, The ATLAS experiment at the CERN Large Hadron Collider, JINST 3 (2008) S08003
2. G. Apollinari et al., High-luminosity large hadron collider (hl-lhc) preliminary design report. CERN-2015-005
3. T. Kawamoto et al., New Small Wheel Technical Design Report. ATLAS-TDR-20-2013
4. Microplan SAS France. <https://www.microplan-group.com/fr/>

Chapter 150

Backend Systems for Mini-ICAL



Nagaraj Panyam, V. M. Datar, Janhavi Deshpande, E. Yuvaraj, G. Majumder, S. Padmini, Mahesh Punna, B. Satyanarayana, Shikha Srivastava, and S. S. Upadhy

Abstract The India-based Neutrino Observatory (INO) is a multi-institutional mega science project supported by DAE and DST, with the aim of experimental neutrino physics besides other topics. INO proposes a large magnetized Iron Calorimeter (ICAL) comprising of about 50KT of magnetized iron and 28800 RPCs as active elements. The mini-ICAL is a scaled-down prototype of the proposed ICAL, and it comprises of 20 RPCs with ~ 85 T of magnetized iron as an absorber. All the proposed design schemes for the ICAL are implemented in the mini-ICAL, which is currently operating and producing physics data, located in the transit campus at Madurai. “Backend systems” refers to the set of servers and applications that receive, record, visualize and act upon various kinds of data that are pushed/pulled from the Frontend of the detector. “Frontend” refers to the set of all devices that generate data—these include the RPCs that generate physics data, devices/gauges that generate various time-series data and also various active devices that put out informational log lines. The RPCs and the Backend systems are connected up in the form of a Local Area Network (LAN) using standard Ethernet hardware and IP protocols. Some software applications are custom designed and some are instances of free and open-source software (FOSS).

150.1 Introduction

Just as for any large and expensive science project, the DAQ systems for INO’s ICAL were designed to include all necessary aspects—for the backend systems,

N. Panyam (✉) · E. Yuvaraj · B. Satyanarayana · S. S. Upadhy
Tata Institute of Fundamental Research, Mumbai, India
e-mail: pn@tifr.res.in

V. M. Datar · G. Majumder
Department of High Energy Physics, Tata Institute of Fundamental Research, Colaba, Mumbai, India

J. Deshpande · S. Padmini · M. Punna · S. Srivastava
Electronics Divison, Bhabha Atomic Research Center, Mumbai, India

© The Author(s), under exclusive license to Springer Nature Singapore Pte Ltd. 2022
B. Mohanty et al. (eds.), *Proceedings of the XXIV DAE-BRNS High Energy Physics Symposium, Jatni, India*, Springer Proceedings in Physics 277,
https://doi.org/10.1007/978-981-19-2354-8_150

these aspects are ease of deployment, longevity/obsolescence, cost, non-proprietary nature, global standards, scalability and reliability. All hardware that makes the LAN and the Backend are available off-the-shelf. The following sections will describe that the schemes that we have adopted are implemented for the backend systems and for the mini-ICAL do include all of these and have been successfully tested in the currently operating mini-ICAL, as will be described in the sections that follow.

For the few applications that were to be necessarily custom made, we have built those on standard platform compilers and are simple to maintain over time and OS/compiler upgrades.

150.2 Connectivity Scheme Between RPCs and the Backend

RPCs form the frontend of the ICAL, and there are approximately 29000 in case of ICAL and 20 in case of mini-ICAL. Each RPC hosts its own onboard DAQ module [1] and the DAQ module includes a Wiznet chip with an assigned IP number. The Ethernet patch cord connects the RPCs to an Ethernet switch that forms the “entry point” to the Backend. The various servers that run the DAQ programs connect to the Ethernet switch and this in brief is the LAN scheme, as is depicted in the figure. Thus, the RPCs are independent hosts on the LAN, as are other Internet-enabled non-physics frontend devices such as various sensors that log and monitor critical parameters and ambient conditions.

All the RPCs and servers are on a private network and firewalled from external access. There is nil to negligible network congestion because the basic data rates in terms of packets per second (Pps), at any point on the LAN, are less than 10% of the rated maximum Pps. The all-important Global Trigger (GT) that is generated by the Trigger subsystem is also sent out in the form of a UDP packet on a dedicated Ethernet that is free of any other traffic. The GT rate for mini-ICAL is 400Hz.

The FEDAQ on each RPC can take all required commands from the servers at the backend. These commands are implemented using UDP, both unicast and multicast. For data, the RPCs initiate TCP connections to designated ports on the backend servers and keep the sockets open for the duration of the run. Buffers of data that are acquired by the onboard FEDAQ are pushed at intervals into the backend sockets. Even though the protocol is TCP, the data payload at any time is kept less than MTU size (1500 Bytes). Physics data is first pushed, by all RPCs, to the server called “Data Concentrator” which then pushes data to the Event Builder.

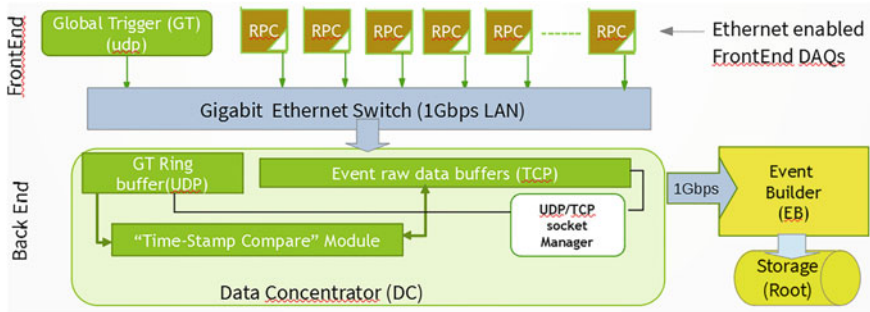


Fig. 150.1 Mini-ICAL's LAN scheme and backend servers

150.2.1 Backend Servers—Data Concentrator

The “DC” is a Linux-based application that is designed for lock-free multi-threaded, multi-socket asynchronous I/O (see Fig. 150.1). It receives physics data from RPCs over TCP and it also receives Global Trigger from the Trigger system over UDP. The basic job of the DC is to use a cyclic buffer and wait for sufficient time (a large fraction of a second, in case of mini-ICAL) for data from RPCs to arrive, do a time-stamp comparison of physics data and Global Trigger and thus give a trigger number identity to the RPC data. The data is then pushed asynchronously to the Event Builder, which is a dedicated server. For the mini-ICAL, the DC runs on a server using just 4 of CPU cores. Scalability is achieved by one or more of multiple actions, namely calling in more CPU cores, adding another Ethernet port to the server and by deploying completely another DC.

150.2.2 Backend Servers—The Event Builder

The EB is a MSWindows[®]-based application that receives data from the DC over TCP sockets. Its functions are to build ROOT format event data from the raw RPC data. EB also provides for live visualization of events and for various other historical data quality plots. Internally, the EB makes use of non-blocking communication patterns for data acquisition, and lockless concurrent data structures for event collation to achieve better throughput. For the mini-ICAL, the EB runs on a single 12-core server that has a large directly attached storage.

150.2.3 Run Console and DQM Consoles

The Run console is a Python program that controls all the RPCs over Ethernet and starts and stops run data acquisition. It will be the single human interface to all the

backend servers and applications that function for data acquisition, ensuring that the critical parameters and services are in place before and during the run [2].

Data Quality Monitors are various plots that are generated from online (in memory) and near online data. These will be displayed on multiple display units in the backend control room. Eventually, these will be made available over secured Internet on remote handheld devices.

150.3 Monitoring

The health of the detector and the quality of physics data are dependent on a large number of critical parameters and ambient conditions. For example, the mini-ICAL has 40 voltage and 40 current settings, 20 temperature readings apart from various other signal rates, host availability pings, various gauges, temperature, pressure, humidity, etc. For monitoring and reporting all meter and gauge readings, we have decided to use Nagios Core which is a widely used FOSS for monitoring and reporting an arbitrarily large number of parameters. The plugins for any parameter are a software code of a few lines in any language; therefore, there will be no need for an expert to deploy it or upscale it. A well-planned instance of Nagios Core can monitor a few thousands of parameters, keep track and raise warnings or critical alerts and also execute pieces of code for automatic back-off from a critical situation.

Monitoring also requires well laid out plots for a visual by the human operator. We have deployed Graphana, which is also a widely used FOSS, for logging and interactive visualization display of numerous plots and charts. Graphana is a feature rich in its rendering of graphs and panels and dashboards, providing the human operator with an easy-to-grasp GUI.

150.4 Conclusions

Using the mini-ICAL as the platform, we have demonstrated the network schemes and the backend systems' designs that we had for the ICAL. We are confident that systems will scale up to the requirements of the upcoming ICAL-engineering module, as also to the ICAL itself.

References

1. M.N. Saraf et al., Springer Proc. Phys. **174**, 565–570 (2016)
2. P. Nagaraj et al., Springer Proc. Phys. **203**, 863–865 (2018)

Chapter 151

The Single-Channel Data Acquisition (DAQ) Module Developed for Dark Matter Search Experiment Using Superheated Liquid



Niraj Chaddha, Sunita Sahoo, Nilanjan Biswas, Mala Das, and Sarbajit Pal

Abstract A single-channel data acquisition (DAQ) module is developed for the dark matter search experiment using a superheated emulsion detector. This paper describes the basic design of the instrument, containing analog signal conditioning and data acquisition using ARM-7-based System-On-Chip. This module detects the production of acoustic emission by superheated liquid due to bubble nucleation using a piezoelectric sensor. Testing of the DAQ module as a prototype of the actual experimental setup is also described with the results.

151.1 Introduction

The Dark Matter (DM), mainly the Weakly Interacting Massive Particles (WIMPs), is expected to interact with the detector material via the elastic WIMP-nucleus scattering and thereby producing the recoil nuclei. These recoil nuclei deposit the energy to the superheated emulsion detector (SED), and if it satisfies the bubble formation condition, the bubble nucleation starts with the formation of critical-sized vapor bubbles by the emission of shock wave that is detected by the acoustic sensors [1]. The properties of the emitted signals like produced amplitude, frequency, and lasting time depend majorly on the type of incident radiation on the detector and its energy

N. Chaddha (✉) · S. Pal

Computer & Informatics Group, Variable Energy Cyclotron Centre, Kolkata 700064, India
e-mail: nchaddha@vecc.gov.in

S. Sahoo · N. Biswas · M. Das

Astroparticle Physics & Cosmology Division, Saha Institute of Nuclear Physics,
Kolkata 700064, India

S. Sahoo · M. Das

Homi Bhabha National Institute, Training School Complex, Anushaktinagar,
Mumbai 400094, India

© The Author(s), under exclusive license to Springer Nature Singapore Pte Ltd. 2022
B. Mohanty et al. (eds.), *Proceedings of the XXIV DAE-BRNS High Energy Physics Symposium, Jaitni, India*, Springer Proceedings in Physics 277,
https://doi.org/10.1007/978-981-19-2354-8_151

level [2]. The threshold energy of the SED can be controlled by the proper choice of temperature and pressure of a superheated liquid and makes it useful in DM search experiment as a particle detector with a better rejection of backgrounds [3, 4].

Though the basic idea of detection remains the same, the advancement of technologies has provided better tools to design the instrumentation for Data Acquisition (DAQ) for these detectors [5, 6]. The availability of a range of wide bandwidth sensors and fast front-end electronics has enhanced the detection resolution by many folds. The implemented circuit module was designed with the same scaling of technology by using high-bandwidth amplifiers to achieve at-top response at desired signal frequencies and a high-performance controller for reliable data collection and optimum dead time. The developed circuit will be used for the DM search experiment at Jaduguda Underground Science Lab, Jaduguda, India.

151.2 Data Acquisition System

The first stage of the system contains a high-gain amplifier and a two-stage bandpass filter. An ARM-7-based Programmable System-On-Chip (PSOC) acquires the data using a built-in ADC (Analog-to-Digital converter) and transfers it to a computer using a serial interface and a GUI (Graphical user interface). The block diagram of the DAQ system is shown in Fig. 151.1.

151.2.1 Hardware

It has been observed during earlier experiments with SED [5] that the gain requirement of the DAQ system is in order of 2000–4000 whereas the maximum signal

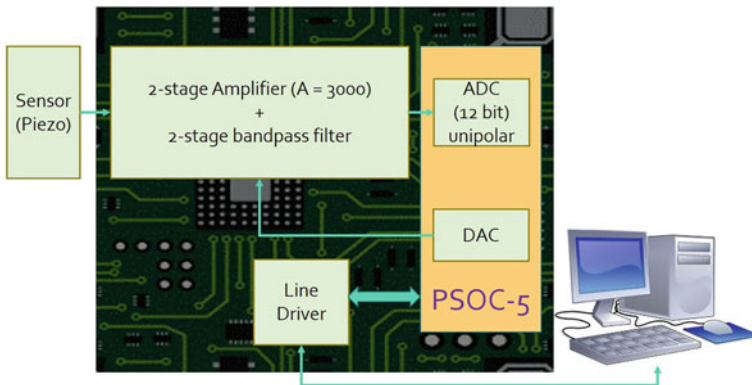


Fig. 151.1 Block diagram of the DAQ system

frequency is 80 kHz. The sampling rate was kept 5 times higher than that, i.e. 400 kS/s. The gain requirement was divided into two stages of trans-impedance amplifiers where the gain of the individual stage was nearly 34.7 dB. The selected op-amp for the first stage is LMP7721 that has a gain-bandwidth product of 17 MHz whereas the slope falls to around 400 kHz at the intended gain. The performance of the second stage op-amp (OPA320) is similar to the first stage. The bandpass filter with cut-off frequencies of 150 Hz to 80 kHz is an integral part of the amplifier section.

The output of this analog part was shifted by +1 V DC to convert the bipolar signal of a maximum amplitude ± 1 V to a unipolar signal of 0–2 V. A Successive Approximation Register-type ADC, with a resolution of 12-bit, was used for acquiring signals. This ADC uses an internal voltage reference having stability (in terms of temperature drift) of 30 ppm/°C. The data acquisition and communication are controlled by PSOC (Programmable System-On-Chip) which runs at a clock frequency of 90 MHz. The UART (Universal Asynchronous Receiver/Transmitter) of this controller is connected to an RS232 line driver for serial interface with PC.

151.2.2 Acquisition Logic and Firmware

The acoustic signals from SED, on average, last for 10–20 ms. The total acquisition time was kept as 25 ms by collecting 10000 samples in a circular buffer at a 400 kS/s rate. The acquisition time consists of 1200 pre-triggered and 8800 post-triggered samples, equivalent to 3 ms and 22 ms intervals.

151.3 Experiment and Results

The circuit module was housed in a metallic box, and adequate shielding and grounding were provided to eliminate external noise (Fig. 151.2). The SED was fabricated

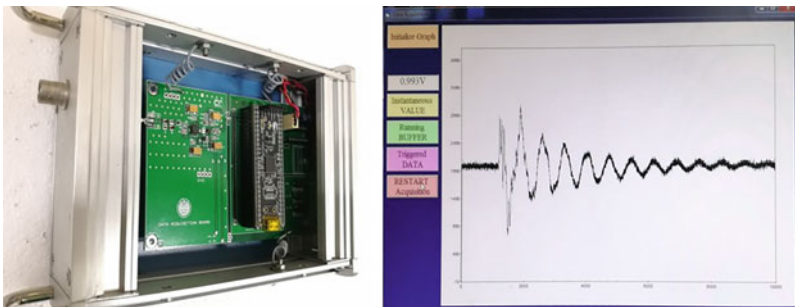
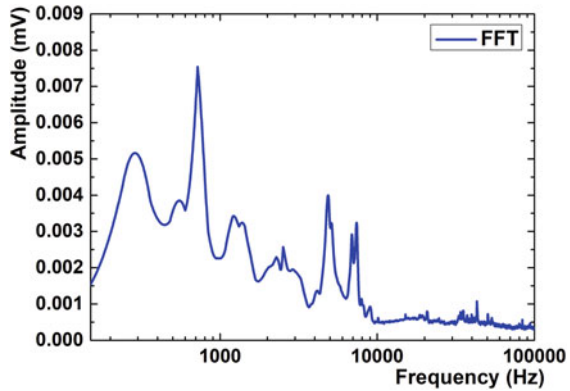


Fig. 151.2 The developed DAQ module and graphical user interface for experiment

Fig. 151.3 FFT of signal in SED



in our laboratory, and R-134a ($C_2H_2F_4$, b.p. $-26.3\text{ }^\circ\text{C}$) is used as the superheated liquid for this experiment. The liquid was transferred at the vapor pressure of about 6.5 bar at room temperature ($\sim 25\text{ }^\circ\text{C}$) and then gradually reduced to the atmospheric pressure to maintain the superheated state. The detector is operated at room temperature ($25\text{ }^\circ\text{C} \pm 1\text{ }^\circ\text{C}$, approx). The acoustic signal is sensed by a piezoelectric sensor. A linear power supply with a specification of $\pm 1\text{ mVp-p}$ ripple voltage was used to power the DAQ module

During the experiment, we found that multiple signals are saturating the amplifier output. The gain of the amplifier was optimized for further experiments. The emitted power was evaluated for the background events which are in the range of about 5–890 Volt². A power-spectra (FFT) graph is constructed with the help of around 100 numbers of collected signals, and the frequency lies in the range of 150–100 kHz, as shown in Fig. 151.3.

151.4 Conclusion

The single-channel DAQ system is performing well with the piezo sensor and SED. The basic methodology of the main experiment, having a higher number of sensors, was verified. Dead time between two events is optimized according to the memory limitations.

References

1. F. Seitz, *Phys. Fluids* **1**(1), 2 (1958)
2. M. Das, S. Seth, S. Saha, S. Bhattacharya, P. Bhattacharjee, *Nucl. Instr. Meth. Phys. A* **622**(1), 196 (2010)

3. F. Aubin, M. Auger, M. Genest, G. Giroux, R. Gornea, R. Faust, C. Leroy, L. Lessard, J. Martin, T. Morlat et al., *New J. Phys.* **10**(10), 103017 (2008)
4. F. d'Errico, *Nucl. Instr. Meth. Phys. B* **184**(1–2), 229 (2001)
5. R. Gornea, J..P. Martin, C. Mercier, N. Starinski, in *EEE Nuclear Science Symposium conference Record*, vol. 1 (IEEE, 2007), pp. 115–119
6. T. Girard, J. Puibasset, M. Felizardo, A. Fernandes, A. Ramos, J. Marques, S. Collaboration et al., *J. Phys.:* Conf. Ser. **375**, 012017–01202, 103017 (2012). IOP Publishing

Chapter 152

Improvement of Time and Position Resolutions of RPC Detectors Using Time-Over-Threshold Information



S. Pethuraj, G. Majumder, V. M. Datar, and B. Satyanarayana

Abstract The INO-ICAL [1] is a proposed underground particle physics experiment to study the neutrino oscillation parameters. RPC detector has been chosen as the sensitive detector element for ICAL due to its position resolution, time resolution and large area coverage at a very low cost. Improving time and position resolution will enhance the sensitivity of the detector by offering excellent directionality and momentum resolution. A small prototype module called mini-ICAL is built to study the detector performance, engineering challenges in the construction of large-scale magnet and magnetic field measurement system and to test the ICAL electronics in presence of the magnetic field. RPC signals are amplified using charge-sensitive NINO front-end boards. The pulse width of the signals is recorded as it crosses the discriminator threshold (called Time over Threshold, ToT) along with strip hit and timing information. The acquired ToT information is used to correct the time information and position for multistrip signals. The paper will discuss the implementation of ToT correction and the resultant improvement in timing and position resolution.

152.1 Experimental Setup

As a part of R & D, a miniaturised version of ICAL called mini-ICAL is made of 11 layers of $4\text{ m} \times 4\text{ m} \times 0.056\text{ m}$ iron plates with an inter-layer gap of 45 mm. The RPC [2] detectors are placed in the inter-layer gap to track the charged particle that passes through the mini-ICAL. RPC detector is made of two 3 mm glass plates with

S. Pethuraj (✉)
Homi Bhabha National Institute, Mumbai, India
e-mail: spethuraj135@gmail.com

S. Pethuraj · B. Satyanarayana
Tata Institute of Fundamental Research, Mumbai, India

G. Majumder · V. M. Datar
Department of High Energy Physics, Tata Institute of Fundamental Research, Colaba, Mumbai, India

a gap of 2 mm. Both sides of the chamber are coated with a thin layer of graphite to establish the High Voltage. The specific gas mixture is made of $C_2H_2F_4$ (95.2%), iso- C_4H_{10} (4.5%) and SF_6 (0.3%) circulated using indigenously built closed-loop gas system. The passage of muon through the gas gap ionises and creates avalanche growth inside the gap and induces the tiny signal on the pickup strips. The pickup panels are made of copper strips with a width of 2.8 cm pasted on the honey-comb panel with an inter-strip gap of 0.2 cm and the other side of the panels is a thin aluminium foil. Either sides of the chamber are covered using a pickup panel orthogonal to each other to read two coordinates (X, Y) of muon position. The induced signals are amplified and discriminated by an 8-channel NINO ASIC [3] chip. The output of NINO is fed to an FPGA-based RPC data acquisition system.

152.2 Time-Over-Threshold (ToT) Information

Cosmic muons events recorded using mini-ICAL (with Magnetic Field OFF) are used to study the performance of the RPC detectors. These performance studies include such as monitoring the detector health in various ambient conditions, position-dependent efficiency of the large-area RPC detectors made in collaboration with the Indian industry and the sensitivity of the detector to sense the position and time of arrival of cosmic muons. The existing offline corrections to improve the time resolution are discussed in [4]. With these existing corrections, the time resolution is found to be better than 1 ns for several RPCs of $1\text{ m} \times 1\text{ m}$ area. Along with the existing techniques, the new algorithm is developed to improve the time and position resolution of the RPCs using Time-Over-Threshold (ToT) information.

152.2.1 Time Correction Using ToT

The time correction based on ToT is straightforward in an ideal condition that when there is no reflection of the signal. If there is a reflection from the readout strips, the ToT is also modified. The reflection happens if there is a mismatch in the impedance of the pickup panel and the termination resistor. The pulse reflection from the pickup panel is shown in Fig. 152.1. To check the dependency of the pulse width with respect to the position along the pickup strip, the distribution of pulse width from X-plane versus muon extrapolated position in Y-plane is shown in Fig. 152.2a. The distribution shows four distinct bands in both X- and Y-plane. The first band is the expected band that corresponds to the signal reaching the pre-amplifier. The other bands are coming from the multiple reflections of the signal due to the impedance mismatch with the termination resistor.

The methods tried for corrections are as follows. **Method 1** : The average time shift for each bin in the Fig. 152.2a calculated from the observed data. The calculated values are shown in Fig. 152.2b. **Method 2** : Instead of using the corrections values from each bin, a functional form of the time shift is estimated based on the pulse

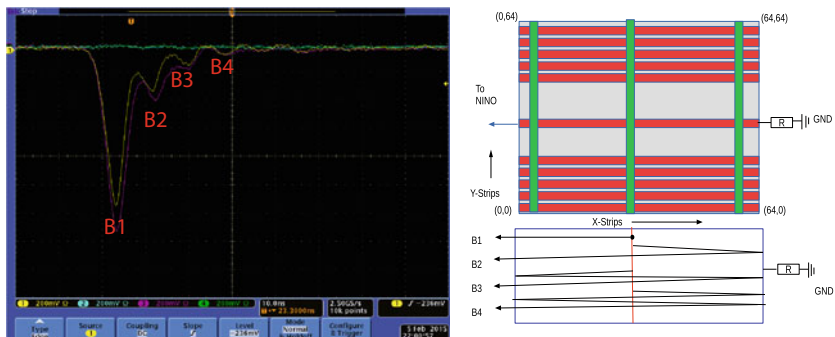


Fig. 152.1 The schematic of RPC pulse in pickup strip and RPC pulse with multiple reflection

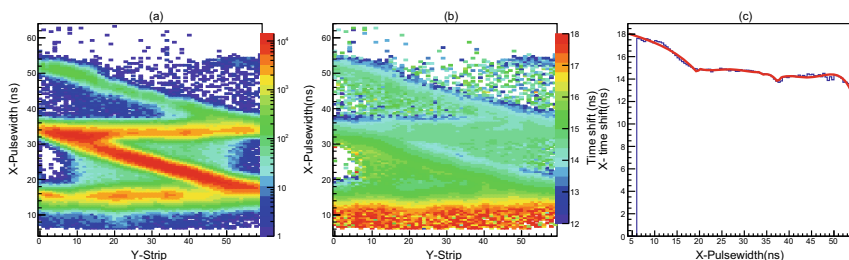


Fig. 152.2 **a** The distribution of Y-strip versus X-Pulse width. **b** The time shift calculated in each bin of (a). **c** The overall time shift (shifted by 15 ns) for all the strips as a function of pulse width in X-plane along with the fit function

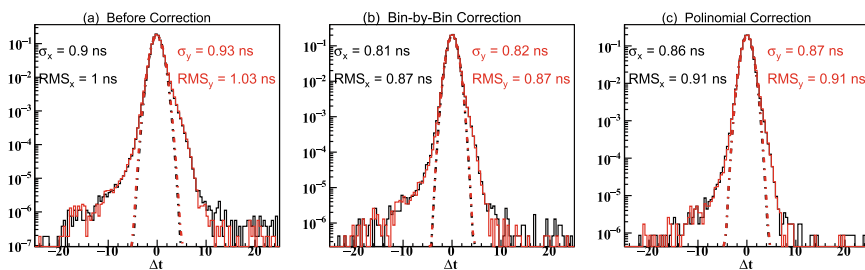


Fig. 152.3 **a**, **b** and **c** are the time residue distribution for Layer-3 before pulse width corrections, after correction with method 1 and method 2, respectively

width. The time shift as a function of pulse width is fitted by the polynomial function as shown in Fig. 152.2c. The distribution of time residues before and after pulse width corrections is shown in Fig. 152.3a, b (Method 1) and c (Method 2), respectively. The fitted σ of time residues with method 2 is a little poorer than method 1 due to a little mismatch in the fit function with the original distribution.

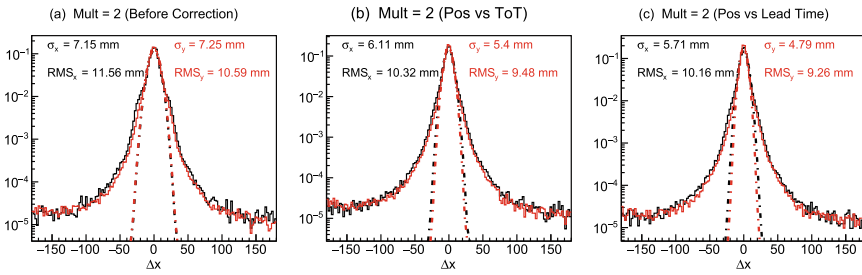


Fig. 152.4 a, b and c are the position residue plot for Layer-2 before pulse width corrections, after correction using ToT and lead time, respectively

152.2.2 Position Correction

Along with the improvement in the timing information, the possibility of improving position information is also explored. The muon position with a strip multiplicity of more than one can be corrected using the leading time of the signal or pulse width information. As the muon passes through the middle of two strips, the charge shared between the strips depends on the position muon passes through. The position correction is calculated again using two techniques; (i) **Lead time**: The difference in lead time between nearby two strips (for multiplicity two) versus the muon position is fitted by the straight line and later used for the event-by-event correction and **ToT**: Similar to lead time, but the ratio of pulse width between the nearby strips versus muon position is fitted by a straight line. The position residue distribution for Layer-2 before the correction (Shown in Fig. 152.4a) and the residue distribution after correction using ToT and lead time is shown in Fig. 152.4b and c, respectively.

152.3 Conclusion

The pulse width information recorded from mini-ICAL is used to improve the time resolution of the large-area single-gap RPCs, and it is observed that there is reasonable improvement in the time resolution. Along with time data, the muon position was also corrected using lead time and ToT information for strip multiplicity of more than one. The improvement in the position resolution is observed. The observed improvement in position and timing information will help in improving the physics parameters such as muon momentum resolution at ICAL and un-down ambiguity.

References

1. I.C.A.L. Collaboration, Physics potential of the ICAL detector at the India-based Neutrino Observatory (INO). *Pramana J. Phys.* **88**, 79 (2017)
2. R. Santonica, R. Cardarelli, Development of resistive plate counters. *Nucl. Instrum. Methods* **187**, 377–380 (1981)
3. F. Anghinolfi et al., NINO: an ultra-fast and low-power front-end amplifier/discriminator ASIC designed for the multigap resistive plate chamber. *Nucl. Instrum. Methods A* **533**, 183–187 (2004)
4. A.D. Bhatt et al., *Improvement of Time Resolution in Large Area Single Gap Resistive Plate Chambers*, vol. 844. NIMA, pp. 53–61 (2017)

Chapter 153

A Study of Avalanche and Streamer Simulation in GEM Detector Using Hydrodynamic Approach



P. K. Rout, R. Kanishka, Jaydeep Datta, S. Mukhopadhyay, N. Majumdar, and S. Sarkar

Abstract In this work, avalanche and streamer operation of GEM-based detectors have been studied using a hydrodynamic model of electron and ion transport. A two-dimensional axisymmetric geometry of GEM has been utilized to perform the simulation. The results obtained include electric field, electron avalanche and streamer formation in a single GEM detector using the Argon-Carbon dioxide gas mixtures in volume proportions of 70–30.

153.1 Introduction

The Gaseous Electron Multiplier (GEM) [1] is a popular Micro-Pattern Gaseous Detector (MPGD) and has been successfully operated in many high particle flux experiments such as LHCb [2] at CERN for its high rate handling capability and radiation hardness. These detectors have shown good gain, fast response and excellent spatial and time resolution in high rate experiments. The gas amplification process in presence of a high electric field and the space charge build-up in the detector volume plays a crucial role in the stable operation of the detector. The effect of space charge is a well-known issue in GEM-based detectors in the high rate experiments. The growth of electron avalanche is affected in the presence of space charges and can lead to the formation of streamers. Such electrical discharges can lead to permanent damage to the detector and make it unsuitable for further experimental activities. In the present work, a numerical simulation study based on a hydrodynamic approach has been attempted to study the transition from avalanche to streamer mode of operation for a single GEM detector.

P. K. Rout (✉) · R. Kanishka · J. Datta · S. Mukhopadhyay · N. Majumdar · S. Sarkar
Applied Nuclear Physics Division, Saha Institute of Nuclear Physics, Sector 1, AF Block, Bidhan Nagar, Salt Lake, Kolkata 700064, India

Homi Bhabha National Institute, Training School Complex, Anushaktinagar, Mumbai 400094, India
e-mail: prasantrout7@gmail.com

© The Author(s), under exclusive license to Springer Nature Singapore Pte Ltd. 2022
B. Mohanty et al. (eds.), *Proceedings of the XXIV DAE-BRNS High Energy Physics Symposium, Jatni, India*, Springer Proceedings in Physics 277,
https://doi.org/10.1007/978-981-19-2354-8_153

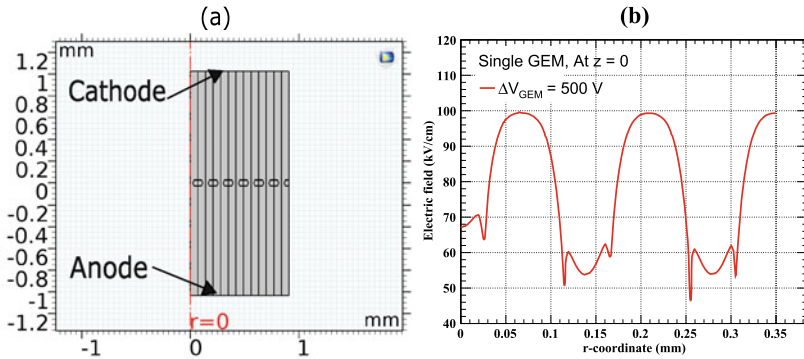


Fig. 153.1 **a** 2D axisymmetric geometry of single GEM. **b** Total electric field along r-direction at $z = 0$ for a single GEM structure

153.2 Numerical Simulation

The present simulation framework is built using the commercial finite element package, COMSOL Multiphysics [3]. The simplified hydrodynamic model by Fonte [4] and Resnati [5] for simulation of charges in GEM detectors has been adopted and improved in the present study. It utilizes the primary ionization information from HEED [6] and the electron transport parameters from MAGBOLTZ [7]. A two-dimensional axisymmetric geometry of a single GEM as shown in Fig. 153.1a has been considered in the simulation. It consists of 1 mm drift gap, 1 mm induction gap and standard biconical holes of inner diameter $50 \mu\text{m}$ and outer diameter $70 \mu\text{m}$. From Fig. 153.1a, it may be noted that $r = 0$ corresponds to the symmetry axis. The electrons and ions are treated as diluted charged species, and their growth in the gas volume follows the drift-diffusion equations as described comprehensively in [8].

153.3 Results

In this work, Fe^{55} radiation source has been simulated which emits 5.9 keV photons in the 2D axisymmetric gas volume. The average number of primaries produced by a 5.9 keV photon has been obtained from HEED and is represented by a seed cluster in the drift gap of the GEM device. The seed cluster is represented by a three-dimensional Gaussian distribution along r- and z-directions as described in [8]. The number of electrons and ions have been obtained by taking the volume integral of the charged fluid in the simulation volume. The evolution of electrons and ions in avalanche and streamer mode operations has been presented for a single GEM structure using Argon- CO_2 gas mixture in volume proportions of 70–30.

153.3.1 Electric Field

The transportation of charged fluid and amplification occurs by the application of an electric field in the gas volume. The charged fluid diffuses and follows the electric field lines in the gas volume. The electric field has been calculated in the detector geometry using the Finite Element Solver(FEM) of COMSOL. Figure 153.1b shows the total electric field along r-direction at $z = 0$. It may be noted that the electric field in different holes is not the same.

153.3.2 Avalanche and Streamer Formation

Townsend avalanche has been observed in the 2D axisymmetric gas volume when the growth of initial charged fluid occurs in the presence of an applied electric field. In the avalanche formation, the electron fluid grows in gas volume until it reaches the anode and drifts through it. The positive ions being heavy move slowly towards the cathode. Figure 153.2a shows the evolution of electrons and ions in an avalanche formation in the gas volume at applied voltage, $\Delta V_{\text{GEM}} = 500$ V for a single GEM configuration. The growth of charged fluid leaves a high density of ions inside the GEM hole, which move slowly along the dielectric surface. This movement of ionic charged fluid distorts the electric field significantly inside the GEM holes. The streamer begins when the field due to the space charge becomes similar to the applied electric field [9]. The increase in field strength causes the electronic and ionic fluid to move towards the GEM cathode from the GEM anode forming a positive streamer in the gas volume. Figure 153.2b shows the evolution of electrons and ions during a streamer formation in a single GEM with an applied voltage $\Delta V_{\text{GEM}} = 570$ V. As seen from the figure, the number of electrons and ions grow sufficiently high $\sim 10^6$ in the streamer

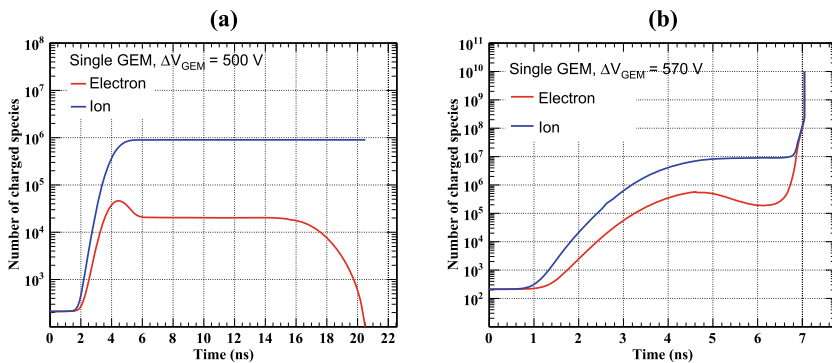


Fig. 153.2 **a** Evolution of electrons and ions in an avalanche formation in the gas volume at applied voltage, $\Delta V_{\text{GEM}} = 500$ V for single GEM. **b** Evolution of electrons and ions in streamer formation in the gas volume at applied voltage, $\Delta V_{\text{GEM}} = 570$ V for single GEM

formation and is in agreement with various hydrodynamic simulated results recently [8, 10] and reported experimentally by [11, 12].

153.4 Conclusion

We have presented the avalanche and streamer formation in a 2D axisymmetric hydrodynamic model of a single GEM detector. Positive streamers due to ionic space charges have been observed from GEM anode to GEM cathode. The critical charge limit needed to form a streamer discharge has been found to be $\sim 5 \times 10^6$ and follows closely with other numerical and experimental observations [10–12]. It may be concluded from the above studies that the fluid model approach explains the avalanche and streamer development in GEM-based detectors reasonably well and can be extended to study other performance parameters of such devices.

Acknowledgements This work has been performed in the framework of RD51 collaboration. The authors wish to acknowledge the members of the RD51 collaboration for their help and suggestions. The authors like to acknowledge the necessary computing infrastructural help and support from SINP. The authors also like to thank the respective funding agencies, DAE and INO collaboration.

References

1. F. Sauli, GEM: A new concept for electron amplification in gas detectors. Nucl. Instrum. Meth. A **386**, 531 (1997)
2. *LHCb Muon System Technical Design Report*, CERN LHCC 2001-010, LHCb TDR 4, (2001)
3. Comsol MultiPhysics, <https://www.comsol.co.in/>
4. P. Fonte, *Calculation of streamer development in MPGDs in an axisymmetric hydrodynamic model*, 5th RD51 Collaboration Meeting, 24–27 May 2010, Freiburg, Germany
5. F. Resnati, Modelling of dynamic and transient behaviours of gaseous detectors, RD-51 Open Lectures - 12/12/17 - CERN. <https://indico.cern.ch/event/676702/contributions/2769934/attachments/1574005/2484807/kjskjb.pdf>
6. I. Smirnov, Heed, <https://heed.web.cern.ch/heed/>
7. S.F. Biagi, Monte Carlo simulation of electron drift and diffusion in counting gases under the influence of electric and magnetic fields. Nucl. Instrum. Meth. A **421**, 234 (1999)
8. P.K. Rout, J. Datta, P. Roy, P. Bhattacharya, S. Mukhopadhyay, N. Majumdar, S. Sarkar, *Fast simulation of avalanche and streamer in GEM detector using hydrodynamic approach*. JINST, **16**, P02018 (2021)
9. Yu. P. Raizer, *Gas Discharge Physics*, Springer, (1997)
10. D.S. Bhattacharya et al., A three-dimensional numerical model of discharge and its application in Micromegas. JINST **15**, P01022 (2020)
11. P. Gasik et al., Nucl. Instrum. Meth. A **870**, 116–122 (2017)
12. H. Raether, *Electron Avalanches and Breakdown in Gases* (Butterworth, London, 1964)

Chapter 154

Lepton Identification using the Belle II Silicon-Strip Vertex Detector



Rahul Tiwary

Abstract We improve the identification performance of low-momentum leptons, especially electrons, using the specific ionization information from the silicon-strip vertex detector (SVD) of the Belle II experiment.

154.1 Introduction

Particle identification (PID) serves a crucial role in any flavor physics experiment. At Belle II [1], we use information from various subdetectors to identify a track as a lepton [2]. The PID algorithm heavily relies on the information provided by the electromagnetic calorimeter (ECL) to identify electrons and the K_L^0 and muon detector (KLM) to identify muons. The performance deteriorates for low-momentum leptons that fail to reach the respective subdetectors and are instead reconstructed in the tracking system comprising the SVD and central drift chamber (CDC). We aim to improve the identification performance of such leptons using the specific ionization information from the SVD and CDC; at very low momentum, only the SVD counts.

Our study will aid physics studies involving low-momentum leptons such as semileptonic decays of B mesons: $B \rightarrow K^{(*)} \ell \ell$, $B \rightarrow K^{(*)} \tau \tau$ and $B \rightarrow X_c \tau \nu$ and lepton-flavor-violating tau decays: $\tau \rightarrow e \ell \ell$ and $\tau \rightarrow \mu \ell \ell$, where ℓ is e or μ . Figure 154.1 shows generator-level distributions of the transverse momentum (p_T) for electrons from two such decays, where a good number of electrons are found to have a p_T below the threshold to reach the ECL.

Rahul Tiwary for the Belle II Collaboration

R. Tiwary (✉)

Tata Institute of Fundamental Research, Mumbai 400005, India
e-mail: rahul.tiwary@tifr.res.in

© The Author(s), under exclusive license to Springer Nature Singapore Pte Ltd. 2022
B. Mohanty et al. (eds.), *Proceedings of the XXIV DAE-BRNS High Energy Physics Symposium, Jatni, India*, Springer Proceedings in Physics 277,
https://doi.org/10.1007/978-981-19-2354-8_154

859

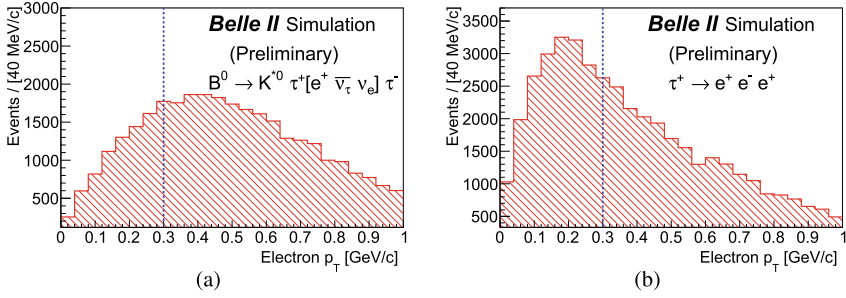


Fig. 154.1 Generator-level distributions of p_T for low-momentum electrons coming from **a** $B \rightarrow K^* \tau \tau$ and **b** $\tau \rightarrow e e e$ decays. The dashed vertical lines indicate the p_T threshold required to reach the ECL

154.2 Electron Identification Using SVD

154.2.1 Event Selection

The study is performed using Monte Carlo (MC) simulated data for e^+e^- collisions recorded near the $\Upsilon(4S)$ resonance with the Belle II detector. We use electrons originating from photon conversions ($\gamma \rightarrow e^+e^-$) that occur within the material of the two inner tracking systems, including the SVD. Electrons are reconstructed as primary particles using track-level information from the detector. A converted photon candidate is reconstructed by combining two oppositely charged tracks. We apply various kinematic and vertex criteria to suppress background. We use the $s\mathcal{P}$ lot [3] technique to subtract the residual background. The $s\mathcal{P}$ lot extracted two-dimensional distribution of specific ionization (dE/dx) versus momentum which is used as the SVD information to the total PID for electron tracks.

154.2.2 PID Performance

The total PID likelihood is constructed by combining the information from all sub-detector components under different particle hypotheses. It can be written as

$$\mathcal{L} = \prod_{\text{det}} \mathcal{L}_{\text{det}},$$

where the product is over the individual likelihoods of each subdetector. The SVD contribution to the total likelihood is obtained as in Ref. [4], with the likelihood for a particle mass hypothesis j defined as

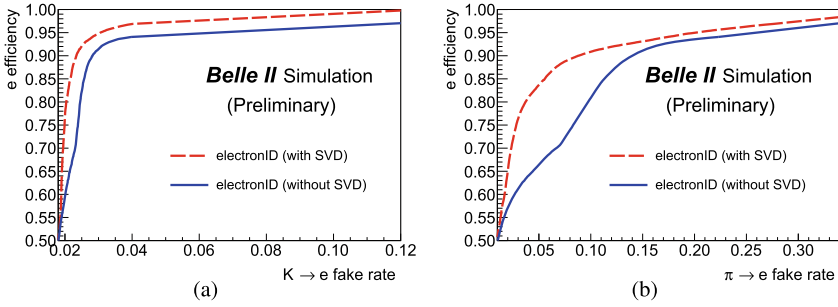


Fig. 154.2 Electron efficiency versus **a** $K \rightarrow e$ and **b** $\pi \rightarrow e$ fake rate for different criteria on the total PID variable

$$\mathcal{L}_j(dE/dx, p) = \prod_i \mathcal{P}_j[(dE/dx)_i, p],$$

where $j = e, \pi, K$ and i runs over all dE/dx values assigned to a track.

We compare the performance of the total PID evaluated with and without the SVD information. To calculate the electron identification efficiency, we use the $\gamma \rightarrow e^+e^-$ sample, while for calculating the rate of a pion (kaon) to be misidentified as an electron, we use the $D^{*+} \rightarrow D^0[\rightarrow K^-\pi^+]\pi^+$ sample. The latter is also used for hadron identification studies [5]. The pion (kaon) to electron misidentification rate is also called the $\pi \rightarrow e$ ($K \rightarrow e$) fake rate. We define

$$i \text{ efficiency} = \frac{\text{No. of tracks identified with PID under the hypothesis } i}{\text{No. of tracks kinematically identified under the hypothesis } i},$$

$$j \rightarrow i \text{ fake rate} = \frac{\text{No. of tracks identified with PID under the hypothesis } i}{\text{No. of tracks kinematically identified under the hypothesis } j}.$$

Figure 154.2 shows the improvement in electron ID performance [6] with the introduction of SVD information. For this study, we consider tracks within the detector fiducial region that have a momentum less than 1 GeV/c. We find the electron efficiency to increase from around 80% to 90% for a fixed 10% $\pi \rightarrow e$ fake rate in MC simulation. Similarly, for a fixed 4% $K \rightarrow e$ fake rate in MC simulation, the electron efficiency increases from around 94% to 97%.

154.3 Muon Identification Using SVD

The performance of the SVD to separate dE/dx distributions of muons and pions is studied using simulated charged tracks. We generate 2×10^6 muon and pion tracks and let them pass through the detector simulation. Figure 154.3a shows the distribution of dE/dx versus momentum for these tracks. We obtain the dE/dx distribution

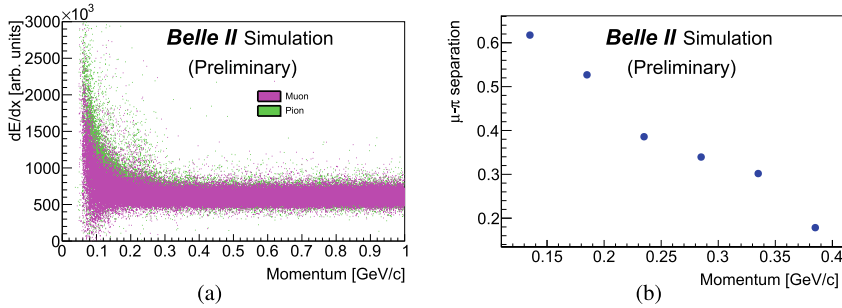


Fig. 154.3 dE/dx versus momentum distributions for muons and pions (a), and the μ - π separation versus momentum (b)

for muons and pions in momentum bins of 50 MeV/c. The distributions are fitted with a Gaussian function to obtain their mean (m) and width (w) values. We then look at the distribution of μ - π separation, defined as

$$\frac{|m_\mu - m_\pi|}{\sqrt{w_\mu^2 + w_\pi^2}},$$

versus momentum as shown in Fig. 154.3b. We observe that muon and pion tracks are not so well separated in the SVD owing to their small mass difference (around 30 MeV/c²). There is a maximum separation of around 0.6 standard deviations between the two hypotheses. This means we can use the same dE/dx versus momentum distribution as the SVD information to the total PID likelihood for both muons and pions. The dE/dx versus momentum distribution for pions is obtained using low-momentum pions coming from the $D^{*+} \rightarrow D^0[\rightarrow K^-\pi^+]\pi^+$ channel, which is an experimentally clean sample with high statistics. Hence, we have decided to use the dE/dx versus momentum distribution of pions as the common SVD input to the total PID likelihood for both muon and pion tracks.

154.4 Summary

We have presented a study on how to improve the PID performance of leptons using information from the SVD of the Belle II experiment. The inclusion of SVD information in the total PID results in a significant improvement of the electron identification performance. The study based on simulated muon and pion tracks shows that low-momentum muons and pions cannot be well separated with the SVD due to their small mass difference. We have, therefore, decided to use the dE/dx versus momentum distribution of pions as the common input from SVD to the total PID likelihood.

References

1. T. Abe et al., [arXiv:1011.0352](https://arxiv.org/abs/1011.0352) (2010)
2. E. Kou et al., *PTEP* **2019**, 123C01 (2019)
3. M. Pivk, F.R. Le Diberder, *Nucl. Instrum. Meth. A* **555**, 356 (2005)
4. C. Pulvermacher, Diploma thesis, KIT, Germany (2012), <https://publish.etp.kit.edu/record/20770>
5. S. Hazra, A.B. Kaliyar, G.B. Mohanty, Belle II Note# TE-2020-019 (2020), <https://docs.belle2.org/record/1974/files/BELLE2-NOTE-TE-2020-019.pdf>
6. Belle II Collaboration, Belle II Note# PL-2020-027 (2020), <https://docs.belle2.org/record/2062/files/BELLE2-NOTE-PL-2020-027.pdf>

Chapter 155

Gain Uniformity of a Quad-GEM Detector



Rupamoy Bhattacharyya, Pradip Kumar Sahu, Sanjib Sahu,
and Rama Prasad Adak

Abstract The Gas Electron Multiplier (GEM) detector is being used in many high-energy physics experiments and will be used in future experiments. The uniformity of a prototype quad-GEM detector in terms of gain is investigated. The active surface area ($10 \times 10 \text{ cm}^2$) of the detector is divided into 8×8 zones, and each zone is irradiated with radioactive Fe^{55} X-ray source. The gain of the detector for a typical voltage distribution across the cathode and anode is calculated from the measured anode current using a pre-mixed gas mixture of Ar:CO₂ in the ratio of 70:30 at a gas flow rate of 24 SCCM. The results are presented in this article.

155.1 Introduction

Gas Electron Multiplier (GEM) technology [1]-based detectors have been used in many experiments (such as PHENIX and ALICE [2, 3]) and will be used in many future experiments (e.g., CBM [4]). GEM foils are the primary building blocks of GEM detectors. A standard GEM foil is made up of Kapton foil of thickness 50 μm , which is sandwiched between two copper planes of thickness 5 μm . Four such foils are placed one over another to make a quad-GEM detector. The drift gap, three transfer gaps, and the induction gap of the prototype quad-GEM detector are fixed at 3 mm, 2 mm, 2 mm, and 2 mm, respectively [5]. There are a large number of bi-conical holes of diameter 70 μm on the GEM foil at a pitch of 140 μm . Holes are etched on the foil in a hexagonal array to cover the maximum area with the minimum number of holes. Now, as the distance between the copper plates of a GEM foil is 50 μm , so a relatively small voltage difference is sufficient to create a high electric field inside the holes (e.g., 360 V voltage difference across the GEM foil can create

R. Bhattacharyya (✉) · P. Kumar Sahu · S. Sahu
Institute of Physics, HBNI, Sachivalaya Marg, P.O. Sainik School, Bhubaneswar 751005,
Odisha, India
e-mail: rupamoy.b@iopb.res.in

R. Prasad Adak
Department of Physics, Taki Government College, Taki 743429, West Bengal, India

© The Author(s), under exclusive license to Springer Nature Singapore Pte Ltd. 2022
B. Mohanty et al. (eds.), *Proceedings of the XXIV DAE-BRNS High Energy Physics Symposium, Jatni, India*, Springer Proceedings in Physics 277,
https://doi.org/10.1007/978-981-19-2354-8_155

72 kV/cm electric field). In the presence of gas, incoming ionizing particles create electron-ion pairs in the drift region. The number of electrons gets multiplied when they transfer through the holes of each GEM foil. Finally, the electron reaches the anode plane, which is kept 2 mm below the last GEM foil, and the anode current is measured. Now gain of the detector is defined as the ratio of the charge collected at the output (i.e., in the readout anode plane) to the charge produced at the input region (i.e., in the drift region). The gain is estimated using the following relation:

$$G = \frac{I}{Rne}, \quad (155.1)$$

where I is the anode current; R is the present count rate of X-ray photons in the detector from the Fe^{55} source; n is the number of primary electrons created inside the drift region for each incoming ionizing particle. For each 5.9 keV X-ray photon in Ar:CO₂ gas mixture at a ratio of 70:30, the value of n is 212 and e is the electronic charge.

155.2 Experimental Procedure

A quad-GEM detector fabricated at IoP, Bhubaneswar, is used in this experiment [5]. The detector is biased by a four-channel HV power supply (CAEN, Model No. N1470) to provide voltage differences across the different gaps of the quad-GEM detector. Initially, the gas chamber is flushed using nitrogen gas of purity 99.999%, and thereafter, a pre-mixed gas mixture of Ar:CO₂ is used at a ratio of 70:30. After biasing the detector, a constant flow rate of 24 SCCM is maintained for at least 8 h in order to properly condition the detector. A temperature- and pressure-measuring module is built in-house, and the same is used to store the temperature and pressure with time. The ambient pressure and temperature are constant throughout the entire experiment. A constant voltage difference (ΔV) of 360 V is maintained across the four GEM foils. The active surface area of the detector ($10 \times 10 \text{ cm}^2$) is divided into 8 rows and 8 columns (64 zones) of area $1.25 \times 1.25 \text{ cm}^2$. Each zone is irradiated with a radioactive Fe^{55} X-ray source. It should be mentioned here that by using a 3 mm thick Aluminum-Copper plate as a collimator, the irradiation area at the top of the drift foil is reduced to 2.14 cm^2 . So, during each exposure, $\leq 9.3\%$ area of each adjacent four zones is also exposed, wherever applicable. The anode current (I) from the Lemo output of the summed up board of readout anode is measured by a Keithley picoammeter [6, 7]. Figure 155.1 (left panel (top) and middle panel) shows the experimental set-up for measuring anode current. The count rate (R) is measured from the discriminated signal (Fig. 155.1: Left panel, bottom) using a scalar built in-house [8], and in the present experimental condition, it is found to be $\approx 8 \text{ kHz}$.

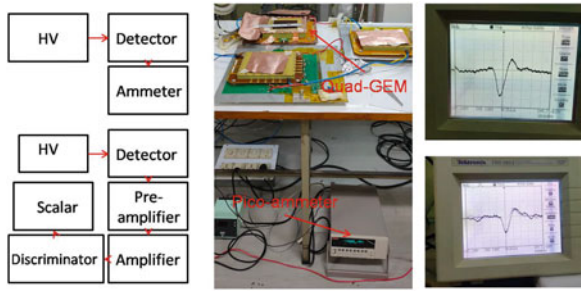


Fig. 155.1 Left panel: Schematic representation of the experimental set-up for measuring the anode current (top) and count rate (R) of the detector for Fe^{55} X-ray source (bottom). Middle panel: Laboratory set-up for estimating gain uniformity of a prototype quad-GEM detector. Right panel: bipolar signals on the oscilloscope for Cosmic ray (top) and Fe^{55} X-ray (bottom)

155.3 Results and Discussion

First, a typical cosmic ray and Fe^{55} X-ray signal from the quad-GEM detector (Fig. 155.1 right panel) is observed on an oscilloscope (Tektronix, model no. TDS 1012) using charge-sensitive pre-amplifier (Ortec, model no. 142 AH) and spectroscopic amplifier (CAEN, model no. N962). Then the absolute gain of each Fe^{55} exposed zone of the detector (Fig. 155.2: left panel) is estimated from the measured anode current using Eq. (155.1). While estimating the absolute gain, to minimize the effect of the pressure difference between the gas inlet and outlet, the anode current is measured for each zone reversing the gas flow direction (Fig. 155.2: right panel) as well. The average anode current is estimated for each zone in the two aforesaid conditions over 64 different zones of the detector, and the 2D distribution of average absolute gain is shown in Fig. 155.3 (right panel). The distribution of relative gain is also presented in Fig. 155.4. It may be mentioned here that the presence of pressure

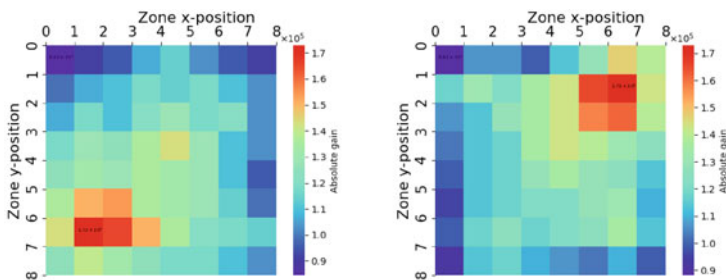


Fig. 155.2 Left panel: 2D distribution of the absolute gain over 64 number of different zones of the detector when gas flows from bottom-left to top-right (left panel) and from top-right to bottom-left (right panel) respectively. From these two figures together, it is evident that no spuriously noisy or dead region is presented in the detector

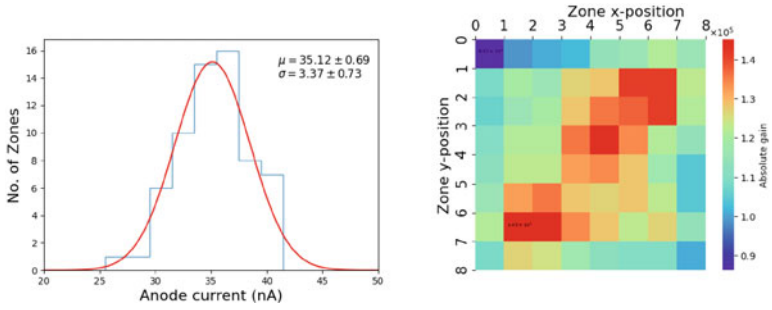


Fig. 155.3 Left panel: 1D distribution of the average anode current over different zones of the detector using Fe⁵⁵ X-ray source. The typical value of anode current without source is ≈ 1.5 nA during the experiment. Right panel: 2D distribution of the average absolute gain of the detector over the 64 zones of the detector

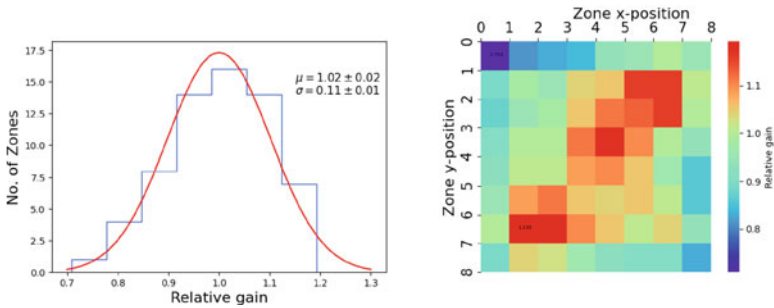


Fig. 155.4 Left panel: 1D distribution of the relative gain of the detector normalized by average absolute gain of the detector. Right panel: 2D distribution of the relative gain of the detector normalized by average absolute gain over the 64 zones of the detector

gradient in some regions could result in fluctuation in gain across the detector. The in-homogeneity of the gap dimensions between the foils (if any) may be another source of spread of gain.

155.4 Conclusion

The uniformity of gain is studied for a quad-GEM detector which was fabricated at IoP, Bhubaneswar [5]. The value of the relative gain has a spread of 10.7% over the 64 zones of the active area of the detector in the present experimental condition.

References

1. F. Sauli, in *NIM A* 386.2 (1997), pp. 531–534
2. B. Azmoun et al., in *IEEE Symposium CRNSc*, vol. 1. (2004), pp. 480–484
3. P. Gasik, *J. Instrum.* **9**(04) C04035–C04035 (2014)
4. R.P. Adak et al., *J. Instrum.* **11**(10), T10001–T10001 (2016)
5. S. Swain et al., *J. Instrum.* **12**(07), T07002–T07002 (2017)
6. R.P. Adak et al., *NIM A* **846**, 29–35 (2017)
7. R.N. Patra et al., *NIM A* **862**, 25–30 (2017)
8. S. Sahu et al., [arXiv:1608.00563v1](https://arxiv.org/abs/1608.00563v1) (2016)

Chapter 156

Slow-Pion Relative Tracking Efficiency Studies at Belle II



S. Maity, N. S. Ipsita, and S. Patra

Abstract We study $B^0 \rightarrow D^{*-}\pi^+$ and $B^0 \rightarrow D^{*-}\rho^+$ decay modes to calculate the slow-pion relative tracking efficiency, where the D^{*-} further goes to \overline{D}^0 and π^- . Owing to its limited phase space, the pion from D^* decay is traditionally referred to as the slow pion due to a small mass difference between the D^* and \overline{D}^0 . We report herein a measurement of efficiency in the momentum region of 50–320 MeV/c using $B^0 \rightarrow D^{*-}\pi^+$ and $B^0 \rightarrow D^{*-}\rho^+$ decay modes in simulated data.

156.1 Introduction

Track finding efficiency provides a vital input as a source of systematic uncertainties in studies involving charged particles. Especially, the track finding efficiency of slow pions emitted from D^* decays plays a key role in $R(D^*)$ measurements [1]. Our aim is to measure the relative tracking efficiency in the low-momentum region and related systematic uncertainty using $B^0 \rightarrow D^{*-}\pi^+$ and $D^{*-}\rho^+$ decays.¹

We study samples of $B^0 \rightarrow D^{*-}\pi^+$ and $B^0 \rightarrow D^{*-}\rho^+$ decays with D^{*-} further decaying to $\overline{D}^0\pi^-$ and ρ^+ to $\pi^+\pi^0$. Here, the \overline{D}^0 decays into the following three final states: $K^+\pi^-$, $K_S^0\pi^+\pi^-$, and $K^+\pi^-\pi^+\pi^-$. We aim to measure the track finding efficiency of the charged pion from the D^* decay in the low-momentum range,

¹Charge conjugate processes are included unless stated otherwise.

S. Maity, N. S. Ipsita, and S. Patra—for the Belle II Collaboration.

S. Maity (✉)

Indian Institute of Technology, Bhubaneswar, Odisha 752050, India
e-mail: sm46@iitbbs.ac.in

N. S. Ipsita

Indian Institute of Technology, Hyderabad, Telangana, India

S. Patra

Indian Institute of Science Education and Research Mohali, Sahibzada Ajit Singh Nagar, Punjab, India

referred to as the slow pion (π_s). In particular, we obtain the reconstruction efficiency in the following four bins of π_s momentum: 0.05–0.12, 0.12–0.16, 0.16–0.20, and 0.20–0.32 GeV/ c . First, we measure slow-pion momentum spectra in data and MC, by doing a fit to ΔE (or M_{bc}) within each momentum bin. Then we take the ratio of the two spectra, which equals the ratio of the efficiencies up to a free normalization factor. Finally, we normalize the ratio to 1 in the highest momentum bin. Hence, this is a relative measurement of the efficiency ratio between data and MC. We keep the binning scheme the same for both the modes so that we can combine them for a more precise estimate.

156.2 Event Sample and Selection

The analysis uses MC event samples equivalent to 57.9 fb⁻¹ of e^+e^- collision data collected by the Belle II detector [2] at the SuperKEKB collider [3].

Charged particles are selected by applying the criteria $|dr| < 1$ cm and $|dz| < 3$ cm to reduce contamination from beam-background tracks that do not originate from the e^+e^- collision point. Here, dr and dz are the distance of the closest approach in the transverse and longitudinal directions, respectively. We reconstruct K_S^0 from two oppositely charged particles assumed to be pions and select the candidates whose invariant mass lies between 450 and 550 MeV/ c^2 . The charged particles are identified as pions or kaons based on the information from the particle identification system. We apply a D -mass window, $|M_{D^0} - m_{D^0}| < 40$ MeV/ c^2 to suppress combinatorial background, where m_{D^0} is the nominal D^0 mass [4]. Further, we constrain the D^* momentum in the center-of-mass frame to be less than 2.5 GeV/ c to enrich the sample in charm mesons from B decays. We introduce a variable $\Delta M = M_{D^{*-}} - M_{D^0}$, where $M_{D^{*-}}$ is the mass of the D^* meson, and require it to lie between 0.143 and 0.147 GeV/ c^2 to further suppress combinatorial background.

We use the beam-energy-constrained mass (M_{bc}) and energy difference (ΔE) to extract the signal yield. They are defined as $M_{bc} = \sqrt{E_{\text{beam}}^2 - (\sum \mathbf{p}_i)^2}$, $\Delta E = \sum E_i - E_{\text{beam}}$, where E_{beam} is the beam energy and E_i and \mathbf{p}_i are the energy and momentum, respectively, of the i th decay product of the B meson in the center-of-mass frame. We require M_{bc} to be within 5.20 to 5.29 GeV/ c^2 and ΔE within -0.2 to 0.2 GeV. A fit is performed in order to ensure that all B^0 decay products originate from a common vertex. We calculate efficiencies by independently fitting M_{bc} and ΔE distributions to check whether the obtained values are consistent or not.

The main background in our analysis is from the $e^+e^- \rightarrow q\bar{q}$ ($q = u, d, s$ or c) continuum events. This background is suppressed by applying a requirement on the ratio of the second to zeroth Fox-Wolfram moment [5], with this topological variable being significantly different between $q\bar{q}$ and $B\bar{B}$ events.

Among the other backgrounds coming from $B\bar{B}$ events, they are mostly semileptonic B decays and are taken care of by a dedicated background PDF for $B^0 \rightarrow D^{*-}\pi^+$.

156.3 Fit Procedure and Result

We fit M_{bc} and ΔE to extract the signal yield after applying all the selection criteria mentioned above. We fit these two variables in each bin of π_s momentum as mentioned in Sect. 156.1. The signal shape in M_{bc} is modeled with a Gaussian function whereas for ΔE a sum of two Gaussian functions with a common mean is used. To model the background component, we use an ARGUS function for M_{bc} and a sum of an exponential function and a first-order Chebyshev polynomial for ΔE . The ARGUS endpoint is fixed to the threshold value of $5.29 \text{ GeV}/c^2$. The fitted distributions of M_{bc} and ΔE obtained using $B^0 \rightarrow D^{*-}\pi^+$ are shown in Fig. 156.1. Similarly, Fig. 156.2 shows the fit of M_{bc} distribution performed to extract the signal yield in the $B^0 \rightarrow D^{*-}\rho^+$ decay. We see a tiny peaking contribution in the M_{bc} mostly coming from its nonresonant final states. We model this peaking component based on the signal MC study. We do not use the ΔE fit here as the background contribution is relatively higher and difficult to model. While fitting M_{bc} , we require ΔE to lie within -0.04 and 0.04 GeV . During the ΔE fit, we require M_{bc} to lie within 5.27 and $5.29 \text{ GeV}/c^2$. The obtained yields (Y_{MC}) and efficiencies (ε_{MC}) are listed in Tables 156.1 and 156.2 for $B^0 \rightarrow D^{*-}\pi^+$ and $B^0 \rightarrow D^{*-}\rho^+$ modes,

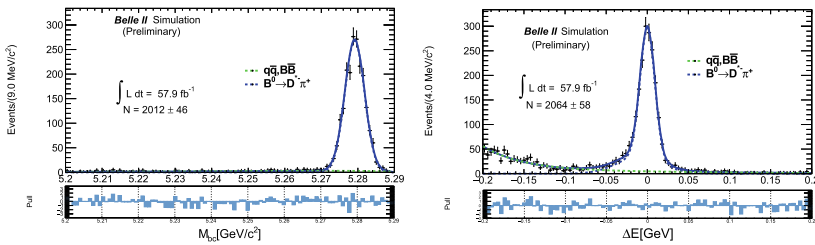


Fig. 156.1 Fitted distributions of M_{bc} and ΔE using the $B^0 \rightarrow D^{*-}\pi^+$ decay in simulated data. Blue curves denote the signal component and green curves represent the background. Black points with error bars are combined simulated data events

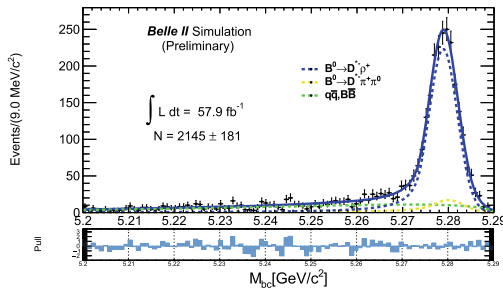


Fig. 156.2 Fitted distribution of M_{bc} obtained using the $B^0 \rightarrow D^{*-}\rho^+$ in simulated data. The blue curve is the signal, the yellow curve is the peaking background coming from the nonresonant $B^0 \rightarrow D^{*-}\pi^+\pi^0$ mode, and the green curve denotes the continuum background. Black points with error bars are combined simulated data events

Table 156.1 Slow-pion efficiency obtained from simulated data in bins of slow-pion momentum (p) for M_{bc} and ΔE using the $B^0 \rightarrow D^{*-}\pi^+$ decay

p (GeV/ c)	Y_{MC}		ε_{MC}	
	M_{bc}	ΔE	M_{bc}	ΔE
0.05–0.12	309 ± 18	309 ± 18	0.15 ± 0.01	0.14 ± 0.01
0.12–0.16	551 ± 24	570 ± 25	0.27 ± 0.01	0.28 ± 0.01
0.16–0.20	422 ± 21	437 ± 22	0.21 ± 0.01	0.21 ± 0.01
0.20–0.32	727 ± 28	747 ± 28	0.36 ± 0.02	0.36 ± 0.02

Table 156.2 Slow-pion efficiency obtained from simulated data in bins of slow-pion momentum for M_{bc} using the $B^0 \rightarrow D^{*-}\rho^+$ decay

p (GeV/ c)	Y_{MC}	ε_{MC}
0.05–0.12	292 ± 17	0.14 ± 0.01
0.12–0.16	538 ± 23	0.26 ± 0.01
0.16–0.20	528 ± 45	0.26 ± 0.02
0.20–0.32	709 ± 53	0.34 ± 0.02

respectively. The efficiencies are calculated by dividing the yield in each bin by the total yield. We measure efficiencies ranging from 15 to 36% that are consistent with both one-dimensional approaches for $B^0 \rightarrow D^{*-}\pi^+$ decay.

Looking ahead, we will follow the same procedure in data to calculate the yields in each bin of π_s momentum. We will then calculate the ratio between these yields in each bin by scaling the highest momentum bin to 1.

156.4 Summary and Future Prospects

We have developed an analysis strategy to calculate the slow-pion relative tracking efficiencies using simulated data for $B^0 \rightarrow D^{*-}\pi^+$ and $B^0 \rightarrow D^{*-}\rho^+$ decays. We obtain efficiencies ranging from 15 to 36%, which are consistent between both the modes. We plan to repeat the study for data in the near future before calculating the data-MC efficiency ratios. Finally, we will combine both the modes to obtain a more precise value.

References

1. G. Caria et al., Belle Collaboration, Phys. Rev. Lett. **124**, 161803 (2020)
2. T. Abe et al., [arXiv:1011.0352](https://arxiv.org/abs/1011.0352) (2010)
3. Y. Ohnishi et al., PTEP **2013**, 03A011 (2013)
4. P.A. Zyla et al. (Particle Data Group), PTEP **2020**, 083C01 (2020)
5. G.C. Fox et al., Phys. Rev. Lett. **41**, 1581 (1978)

Chapter 157

Electron Gun Based Magnetic Probe



Srinidhi Bheesette and Marcos Turqueti

Abstract Accurate magnetic field measurements are fundamental to the construction, testing, and certification of magnetic systems. In high-accuracy systems like undulators for light sources, the measurement technique and implementation may involve a considerable effort. This paper introduces a novel technology for measuring localized magnetic fields for such systems.

157.1 Introduction

Undulators present at the Advanced Light Source (ALS) at LBNL require several magnetic measurements at different stages during their construction.

Existing devices like Hall probes, Nuclear Magnetic Resonance (NMR), and Single Stretched Wires (SSW) have their limitations like D.C. offset, non-linearity, temperature drift, sensor aging, unsuitable for field gradient measurements and for local magnetic field measurements, and the planar Hall effect.

157.2 eProbe

In this novel idea, the magnetic probe electron gun fires a low-energy electron beam into an imaging sensor, which is mounted perpendicularly to the electron stream and located at the opposite end of the mCRT tube (Fig. 157.1). Electrostatic deflecting plates continually manipulate the electric field, thus, projecting a pattern onto the imaging sensor. When the probe is immersed in a magnetic field, the projected pattern

S. Bheesette (✉)

Engineering Division, Lawrence Berkeley National Lab, Berkeley, CA, USA

e-mail: SBheesette@lbl.gov

M. Turqueti

Electronic Systems, Engineering Division, Lawrence Berkeley National Lab,
Berkeley, CA, USA

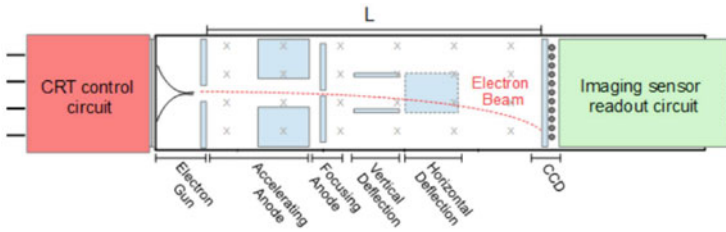


Fig. 157.1 A schematic diagram of mCRT, showing different components of the magnetic probe. Whereas x denotes the incident magnetic field, the electron beam is represented by $-e$

changes shifts and changes shape, and from that, it is possible to precisely derive the strength and geometry of the magnetic field. Several patterns can be projected according to the desired application of the probe. The tolerance of the electronics of eProbe to the magnetic field it is placed in is very high. It takes several Teslas to significantly affect the camera.

157.3 Modeling of the eProbe Assembly in GEANT

In order to understand the behavior and optimize the parameters of the eProbe, the assembly was modeled in GEANT [1], a toolkit for simulating the passage of particles through matter. The sensor [2] consisted of a 0.25 mm thick silicon layer with an active area of 1296 by 976 pixels, each of size 1.9 μm . This mesh-like arrangement helped us to record the energy deposited by the particles in each pixel. The source used in the simulation is an electron source of energy 400 eV with a Gaussian spread of 5 eV dispersion with a diameter of 100 μm .

157.4 Beam Profile

The charge deposited on the CMOS sensor is recorded using the simulation tool. The spot formed on the sensor would not only give the information of the number of particles deposited, the average, and the total energy deposited but also the beam profile. This beam profile information will help us visualize the beam's Gaussian spread and adjust it accordingly (Figs. 157.2 and 157.3).

The position of the beam spot changes when a magnetic field is applied in the x - and y -directions. The centroid of this beam spot would be used to calculate the deviation from the center reference (absence of magnetic field).

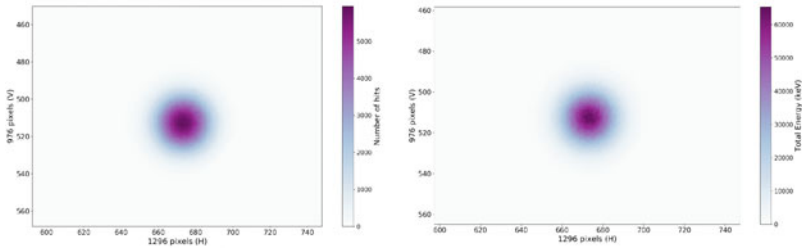


Fig. 157.2 **a** The number of hits per pixel, and **b** the total energy deposited per pixel as a pixel map. The Gaussian spread beam spot is located at the center of the sensor due to the absence of both the magnetic field and the accelerating field

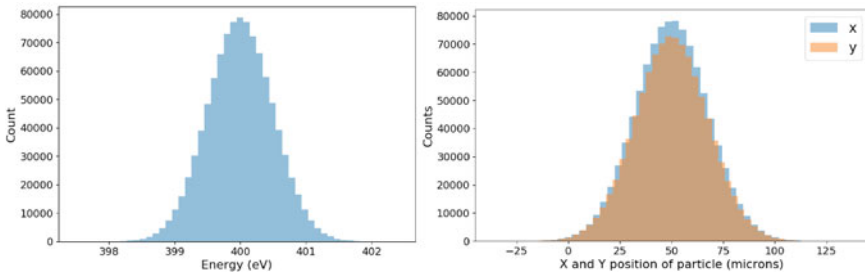


Fig. 157.3 **a** The energy profile of the beam showing particles of 400eV with a 5eV smear, **b** the spatial spread of the Gaussian beam in the x- and y-axis. The standard deviation in the x- and the y-direction was set to 0.35 times the mean

157.5 Validation of Measurements

Real-time field measurements were carried out with an eProbe prototype designed at LBNL. Simulations were not identical to the test conditions for practical reasons, including unknown precise beam profile characteristics of the prototype (Fig. 157.4).

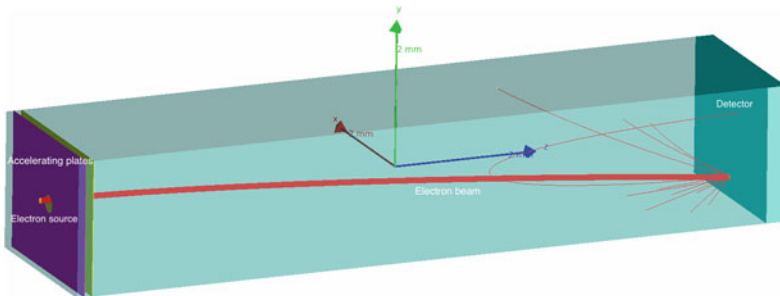


Fig. 157.4 For measurements, the detector was placed at a distance of 10mm from the source. The two accelerating plates (0.01 mm apart) of a thickness (0.01 mm) are placed 0.1 mm from the electron source. The bending of the beam and scattering observed at the image sensor are due to the presence of the magnetic field

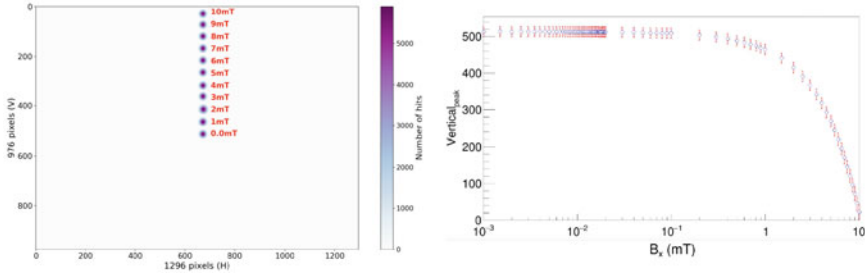


Fig. 157.5 Simulations results run in the above case at 400V acceleration potential show **a** beam projection on the sensor at varied magnetic fields, and **b** the beam centroid versus the magnetic field.

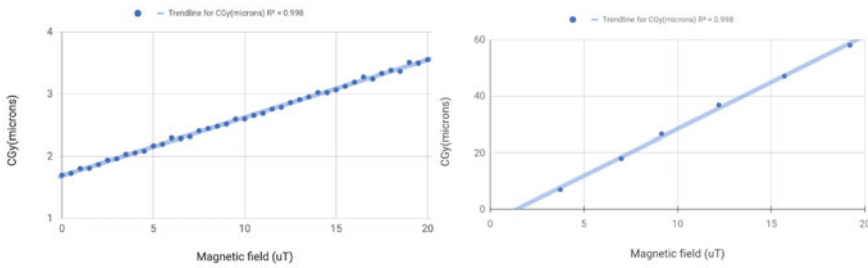


Fig. 157.6 The vertical centroid (CGy) calculated with the k-means clustering algorithm from **a** simulations validated with **b** measurements. The acceleration potential was set to 399.4V. The pixel is square of size 2.2 μm . The magnetic field was created by a calibrated Helmholtz Coil

The beam spot and the change in the vertical deviation at the various magnetic field show the dynamic range of the magnetic field that can be achieved using this orientation.

The centroid deviation (in units of μm) calculated from the simulation and measurement data was plotted with respect to the low magnetic fields (in order of microTesla), as shown in Fig. 157.5. It is seen that the linear trends in both cases agree with a good correlation. However, some data points are seen to be off the linear trend-line due to the k-mean clustering algorithm behavior, which also considers since hits away from the cluster. This produces inaccuracy in the centroid calculations (Fig. 157.6).

157.6 Conclusion

Our studies indicate that an eProbe could be successfully simulated with various magnetic and electric fields using the GEANT simulation tool. We were also able to optimize the measurement range of the eProbe by varying the distance of the source

and the location of the accelerating plates. Previously existing measurements were compared with the similar model simulated in GEANT, and the results were consistent with those obtained from the actual measurements. The simulation results will allow us to develop different eProbe orientations by optimizing different parameters (distance, thickness, and the position of the accelerating plate).

References

1. G.E.A.N.T. Collaboration, S. Agostinelli, GEANT4 - a simulation toolkit. Nucl. Instrum. Meth. A **506**(25) (2003)
2. O.N. Semiconductor, MT9M114 Evaluation Board-User's manual. <https://www.onsemi.com/pub/Collateral/EVBUM2524-D>

Chapter 158

Sensitivity of Triple-GEM Detectors for Background Radiation in CMS Experiment



S. Kumar, O. Bouhali, V. Bhatnagar, A. Castaneda, S. S. Chauhan, T. Kamon, Y. Kang, and A. K. Virdi

Abstract The collider experiments of the modern era produce an extreme environment of radiation fields. It becomes quite challenging to operate the detectors in such an environment as the high-radiation background complicates the particle identification. Particles produced in proton–proton (pp) collisions interact with the beam pipe, shielding and the other detector supporting materials to produce charged hadrons and neutrons along with photons, electrons and positrons. These particles interact with the surrounding material acting as a common background radiation field for the CMS detector. CMS has installed new muon detectors based on Gas Electron Multiplier (GEM) technology at the endcap station 1 ($1.55 < |\eta| < 2.18$), called GE1/1. In this study, an estimation of the GE1/1 detector response to background radiation is presented using the FLUKA and GEANT4 frameworks.

S. Kumar, O. Bouhali, V. Bhatnagar, A. Castaneda, S. S. Chauhan, T. Kamon, Y. Kang, A. K. Virdi—for the CMS Collaboration.

O. Bouhali
Texas A&M University, Doha, Qatar

S. Kumar (✉) · V. Bhatnagar · S. S. Chauhan · A. K. Virdi
Panjab University, Chandigarh, India
e-mail: s.kumar@cern.ch

A. Castaneda
Universidad de Sonora, Hermosillo, Mexico

T. Kamon
Texas A&M University, College Station, TX, USA

Y. Kang
University of Seoul, Seoul, South Korea

158.1 Introduction

The sensitivity to new physics is expected to increase with a series of upgrades of the Large Hadron Collider (LHC) to the so-called High Luminosity-LHC (HL-LHC) [1]. The Compact Muon Solenoid (CMS) experiment [2] must follow the LHC evolution and perform detector upgrades to fully exploit the collisions at higher energy and higher luminosity. The goal of the CMS upgrade is to improve the physics performance of the detector subsystems and optimize the particle reconstruction for LHC luminosity up to $5 - 7 \times 10^{34} \text{ cm}^{-2} \text{ s}^{-1}$. The rise in collision rate due to higher luminosity will increase the background rate in the forward region of the CMS muon endcaps. This background radiation field is mainly composed of low energy neutrons, photons (γ), electrons/positrons (e^\pm) and charged hadrons, namely, kaons (K^\pm), pions (π^\pm) and protons (p) [3]. These background particles can cause damage to detector elements and front-end electronics [4], additionally, they can induce spurious signals that degrade detector performance. This work is related to the first GE1/1 endcap station. The background rate is predicted using FLUKA [5] and GEANT4 [6] simulations.

158.2 Motivation

With the aim of gaining operation experience and demonstrating the integration of the GE1/1 system into the trigger, five superchambers (a combination of two single trapezoidal-shape triple-GEM detector) were installed as an exercise at the positions shown in Fig. 158.1. This exercise is known as GE1/1 Slice Test [7].

Superchambers 27, 28, 29, 30 ($\Delta\phi = 40^\circ$) in Slot-1 are dedicated to muon rate, while superchamber 1 ($\Delta\phi = 10^\circ$) in Slot-2 is to test electronics and a new high-voltage system. The triple-GEM [9] detector of a superchamber facing towards the interaction point of pp collisions is called “layer-1”, while the one facing outwards is called “layer-2” and comes in two flavors; “Long” and “Short”. The background

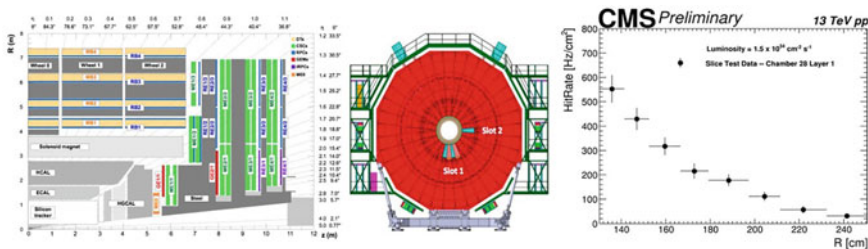


Fig. 158.1 GE1/1 (red) is the position of installation of Slice Test detectors (left). Second from left in slot-1 of light pink colour is chamber 28 (middle). Background hit-rate data from GE1/1 Slice Test for chamber 28 layer 2 [8] (right)

rate for chamber 28 layer-2 is analyzed and a function of perpendicular distance R from beam-line using the zero-bias data is shown in Fig. 158.1. The motivation is to predict the experiential data within some uncertainty so that we can estimate the background rates in Run-3 and for future upgrades.

158.3 Method

For the calculation of the background rate in the GE1/1, the following method is used:

$$\text{Hit-Rate} = \sum_{part} \text{Flux} (part, E, \theta, R) \otimes \text{Sensitivity} (part, E, \theta),$$

where “ $part$ ” is the type of particle (neutron, γ , e^\pm and charged hadrons), E is the energy of the incident particle and θ is the angle with respect to the axis perpendicular to the detector surface. The GE1/1 response to background particles is termed “Sensitivity”. Sensitivity is defined as the probability of a particle to deposit energies greater than a defined threshold in the sensitive volume, producing primary ionized electrons.

The flux is multiplied by an average sensitivity obtained convoluting the sensitivity at a given energy and incident angle with the normalized fraction of particles at that energy and incident angle. The integration of this convolution over a given energy range gives the average sensitivity shown in Fig. 158.2.

158.4 Simulation

As mentioned in the previous section, the flux entering the GE1/1 detector and the average sensitivity of the GE1/1 detector are required for the hit rate calculation. The flux and sensitivity are estimated using FLUKA and GEANT4, respectively.

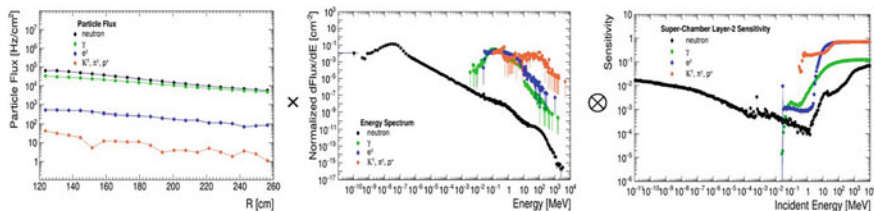


Fig. 158.2 Particle-flux (left) normalized energy distribution (middle) and sensitivity distribution (right) for different particles

158.4.1 FLUKA Simulation

FLUKA v2011-3.0 simulation including the effect of magnetic field in the CMS, Run-2 geometry version 3.31.4.2 is used to estimate the flux and differential energy spectrum of all the particles.

158.4.2 GEANT4 Simulation

The physics processes and decay chains are modeled using GEANT4 v10.6 and the recommended physics list for standard HEP processes (FTFP_BERT_HP). The simulation setup consists of a source plane, of the same size as the drift board of the GEM detector, for primary particle generation at a distance of 3 mm from the surface of the detector on both sides. Energy range used for different particles are 10^{-3} – 10^4 MeV for neutrons, 10^{-3} – 10^4 MeV for γ 's, 10^{-2} – 10^4 MeV for e^\pm and 10^{-1} – 10^4 MeV for charged hadrons (K^\pm , π^\pm , p).

158.4.3 A Single Triple-GEM Detector

A simplified single triple-GEM detector geometry is simulated for the general response. The sensitivity of the GEM detector is studied as a function of the energy and the angular distribution of each particle.

158.4.4 Superchamber

To compare the prediction with experimental data, a superchamber geometry has been simulated to obtain the right plot in Fig. 158.2 for chamber 28 layer-2. This geometry includes all the components, i.e. pull-outs, readout electronics and cooling system as explained in [10].

Table 158.1 shows the average sensitivity of background particles is not same for Layer-1 and Layer-2. It depends on the particle and the interacting material, i.e. for neutron, the average sensitivity for Layer-1 is less as compared to Layer-2 because of the combined effect of the cooling material (Cu) of both the layers.

Table 158.1 Average Sensitivity for each type of particle for the layer-1 and layer-2 of the super-chamber configuration used in CMS data taking in 2018

Particle	Average sensitivity of layer-1 (%)	Average sensitivity of layer-2 (%)
Neutron	0.63 ± 0.01 (stat.)	0.75 ± 0.01 (stat.)
γ	0.29 ± 0.01 (stat.)	0.20 ± 0.01 (stat.)
e^\pm	1.18 ± 0.03 (stat.)	0.31 ± 0.01 (stat.)
Charged Hadrons (K^\pm, π^\pm, p)	27.0 ± 1.3 (stat.)	25.1 ± 1.2 (stat.)

158.5 Conclusion

A comparison of data and simulation was used to validate the FLUKA+GEANT4 model presented in this study. For example, the simulation agrees with the hit rate 600 Hz/cm^2 at $1.5 \times 10^{34} \text{ cm}^{-2} \text{ s}^{-1}$ for $i_\eta = 8$ [10] from the GE1/1 Slice Test within its uncertainties. This model helps us to improve the background hit rate estimation in Run-3 and at HL-LHC.

References

1. C.M.S. Collaboration, The phase-2 upgrade of the CMS muon detectors. CERN-LHCC-2017-012 (2017) CMS-TDR-016 (2017)
2. C.M.S. Collaboration, The CMS experiment at the CERN LHC. JINST **3**, S08004 (2008)
3. M. Huhtinen, The radiation environment at the CMS experiment at the LHC. Master Thesis, (1996)
4. Y. Musienko et al., Radiation damage studies of silicon photomultipliers for the CMS HCAL phase I upgrade. Nucl. Instrum. Methods A **787**, 319–322 (2015)
5. A. Ferrari, R.P. Sala, A. Fasso, J. Ranft, FLUKA: a multi-particle transport code (Program version 2005), CERN-2005-010; INFN-TC-2005-11; SLAC-R-773
6. GEANT4 Collaboration, GEANT4 a simulation toolkit. Nucl. Instrum. Methods A **506**, 250–303 (2003)
7. M. Abbas et al., Detector control system for the GE1/1 slice test. JINST **15**, P05023 (2020)
8. CMS Collaboration, Environmental background hit rate on GE1/1 in the 2018 slice test. CERN-CMS-DP-2020-053, <http://cds.cern.ch/record/2749429> (2020)
9. F. Sauli, Principles of operation of multiwire proportional and drift chambers. SCERN-77-09 (1977)
10. CMS Technical design report for the muon endcap GEM upgrade. CERN-LHCC-2015-012 (2015), [CMS-TDR-013]

Chapter 159

Development of 256-Pixel SiPM-Based Imaging Camera and Its Status



S. S. Upadhyya, A. Chatterjee, V. R. Chitnis, R. L. Deshmukh, P. Dorjey, N. Dorji, S. Duhan, K. S. Gothe, A. P. K. Kutty, B. K. Nagesh, V. A. Nikam, N. K. Parmar, S. R. Patel, M. Ranjan, S. K. Rao, A. Roy, M. N. Saraf, A. Sarkar, B. B. Singh, and P. Verma

Abstract A 256-pixel imaging Camera based on SiPM is being developed for a 4m class Cherenkov telescope would be the first of its kind in India that uses SiPM as a pixel sensor in place of photomultipliers. It would be tested on the vertex element of the TACTIC telescopes at Mt Abu, Rajasthan, and the final proposal is to deploy the telescope at high-altitude site of Hanle, Ladak. The Imaging camera covers a field of view of $5^\circ \times 5^\circ$ with a pixel resolution of 0.3° for the TACTIC telescope. A modular approach is adopted for the camera design, considering quick development, easy maintenance and scalability. A prototype 64-pixel version of the proposed camera is being developed. Various features of the camera will be presented along with the lab evaluation results of the prototype.

159.1 Introduction

The gamma-ray or cosmic-ray particle entering Earth's atmosphere, will interact with atmospheric molecules and produce a cascade of secondary particles called Extensive Air Shower (EAS), in the direction of incident. These secondary particles during propagation in the atmosphere produce a flash of faint bluish light (Cherenkov radiation) lasting for a few nano-seconds, retaining the direction of origin. The Cherenkov shower is used as a probe to detect gamma rays coming from the celestial sources. A large size parabolic reflector is used to collect and focus this faint shower of photons onto an Imaging camera placed at the focal plane and is called Imaging Atmospheric

S. S. Upadhyya (✉) · A. Chatterjee · V. R. Chitnis · R. L. Deshmukh · P. Dorjey · N. Dorji · S. Duhan · K. S. Gothe · A. P. K. Kutty · B. K. Nagesh · V. A. Nikam · N. K. Parmar · S. R. Patel · M. Ranjan · S. K. Rao · A. Sarkar · B. B. Singh · P. Verma
Tata Institute of Fundamental Research, Dr. Homi Bhabha road, Colaba, Mumbai 40005, India
e-mail: upadhyatifr@gmail.com

A. Roy · M. N. Saraf
Department of High Energy Physics, Tata Institute of Fundamental Research, Mumbai, India

© The Author(s), under exclusive license to Springer Nature Singapore Pte Ltd. 2022
B. Mohanty et al. (eds.), *Proceedings of the XXIV DAE-BRNS High Energy Physics Symposium, Jatni, India*, Springer Proceedings in Physics 277,
https://doi.org/10.1007/978-981-19-2354-8_159

887

Cherenkov Technique (IACT) [1]. The image parameters are used to measure the flux of detected gamma rays and their temporal properties. The camera is designed using 4×4 array of SiPMs [2] as basic pixel sensor. A 256-pixel Imaging camera based on a large-size pixel Sensor (S13361 from Hamamatsu), is planned to be tested on a 4m class Cherenkov telescope at TACTIC [3] site at Mount Abu and the final proposal is to deploy at high-altitude HAGAR site in Ladak, along with the telescope. The challenges faced in the camera design are capturing the image of Cherenkov photons arriving within a time spread of few nanoseconds in the presence of a huge night sky background light, high dark noise rate, gain stability of photo sensors in the temperature range from -20°C to $+25^\circ\text{C}$, the requirement of in-situ single photoelectron gain calibration and pixel pulse profile recording on each event, etc.

159.2 Imaging Camera

159.2.1 Camera Electronics

A modular approach as shown in Fig. 159.1a, is adopted for the camera design. A Pixel Cluster Module (PCM) houses a cluster of 16-pixel sensors along with Light Concentrator (LC) in front, preamplifier cards and sensor bias cards. Sixteen such PCMs make up the front end of the camera. The two bias cards control and monitor the bias parameters for all the 16-pixel sensors. The sensors are maintained at constant gains independent of ambient temperature variation by tuning their bias voltages in closed-loop control. All the 16 PCMs in the camera are daisy-chained for bias control and monitoring under Bias Server program running in Raspberry-Pi which in turn is connected over Ethernet to the Control room for supervisory commands and data transfer. Each channel in a preamplifier card processes, shapes and adds pulses from eight elements in a pixel sensor called sub-pixels pairs to form a pixel signal. The back-end electronics crate houses 16 Cluster Digitizer Modules

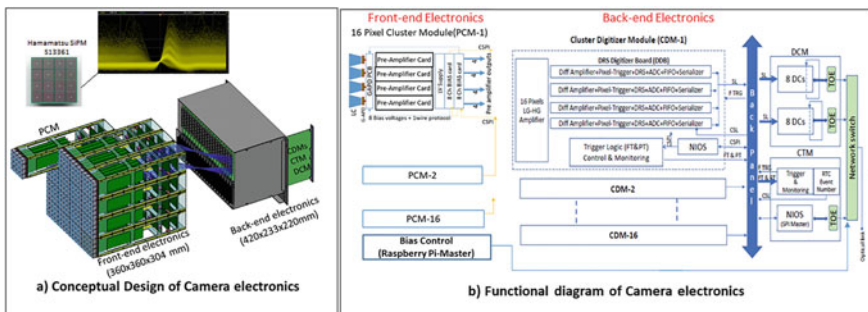


Fig. 159.1 The design concept of SiPM imaging camera

(CDM). A CDM generates pre-triggers based on the neighbouring pixels crossing a set threshold. These pre-triggers are processed in Control and Trigger Module (CTM) to generate a final trigger. On a final trigger, all the CDMs digitize pixel pulse profile sampled @ 1 Giga Samples Per Second (GSPS) and store the event data of camera in the segmented packets in parallel. Each CDM houses 4 mezzanine digitizer boards called DRS Digitizer Boards (DDB) which are designed using Analog chip Domino Ring Sampler (DRS) [4]. Data packets with a common event marker are pushed to a Data Concentrator Module (DCM) over 16 fast serial links. The CTM controls and monitors the camera’s back-end under supervisory commands from the servers in the control room over an Ethernet link. Figure 159.1b represents a functional block diagram of the camera.

159.2.2 Software Scheme

The entire Camera operation and data acquisition are manoeuvred with the help of a stack of firmware plus software programs. At the lowest level of the stack is the firmware associated with the camera components for local control with the flexibility achieved through the supervisory remote commands from the back-end software in the control room PCs. Figure 159.2 depicts the overall scheme and the front-end GUI for user interface. The Camera software is developed using C code running in processors like Atmel Microcontrollers and NIOS soft processors in FPGA. The Camera Bias Server(CBS) running in the camera and also the back-end software hosted by control room PCs are developed using Qt. The communication between the software programs in the camera and those in the control room is based on client-server technology and make use of standard protocols like TCP/IP, UDP, etc.

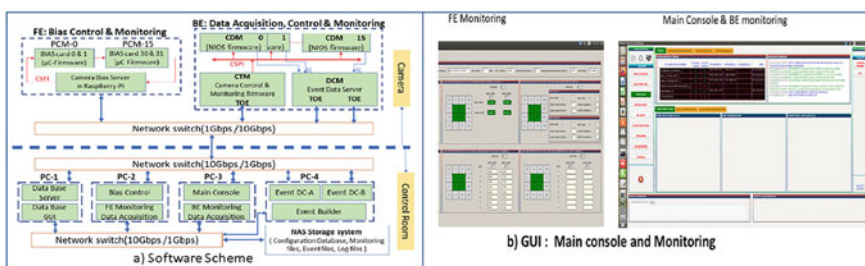


Fig. 159.2 Software scheme and GUI

159.2.2.1 Camera Software

Besides the firmware, there are three pieces of servers hosted by the camera viz. CBS, Camera Control and Monitoring Server (CCMS) and Event Data Server (EDS). These programs communicate over a local network and in addition, talk to the back-end software programs over a single high-speed optical downlink.

159.2.2.2 Control Room Software

At the uppermost level of the stack are the set of back-end software programs running in the control room PCs and include Data Base Server (DBS), Bias Control and Monitoring Software (BCMS), Event Builder (EB) and the Main Console (MC). They communicate with the servers hosted by the camera for the overall operation, control, monitoring and event data acquiring.

159.2.3 Calibrations

It is very essential to operate all the pixel sensors at uniform fixed gain and maintain them throughout the observation. The gain of SiPM is sensitive to over-voltage and breakdown voltage is sensitive to ambient temperature. So, each of SiPM needs to be calibrated for these dependent parameters. DRS analog sampler has systematic cell dc offset and hence each DDB needs to be calibrated for offline offset correction to raw sample data.

159.3 Camera Prototype

The 64 pixels Camera prototype hardware is ready. Presently, the integration of the front end and back end is being evaluated independently in the lab. Front-end houses four PCMs controlled by a Raspberry-Pi camera server and back-end houses four CDMs, one CTM and one DCM. Left panel in the Fig. 159.3 indicates the camera components.

159.4 Performance Evaluation

Light concentrators with an efficiency of around 75% are picked for the LC assembly of 16 pixels. The clearly separated single photoelectron spectrum for a pixel is shown in Fig. 159.3d and, can be used for in-situ calibration and monitoring. Approximately 60 SiPMs are characterized and, distribution of breakdown voltage

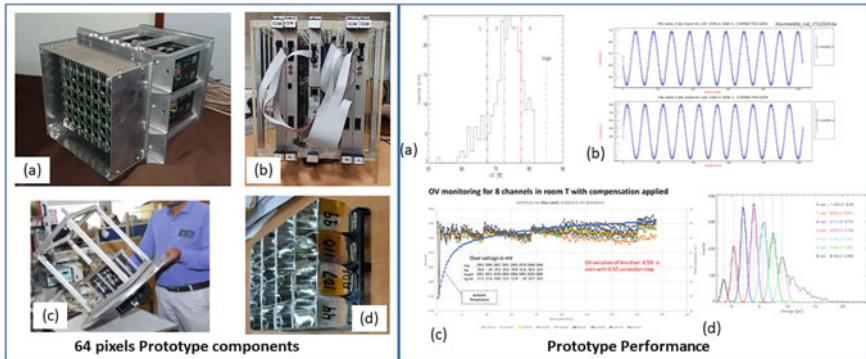


Fig. 159.3 Performance of camera components

and its temperature coefficients is quite significant. So, each SiPM needs to be controlled independently in a closed loop. Fig. 159.3 indicates typical stable condition of the over-voltage within 0.5% for 8 SiPMs under room temperature variation. The 10MHz sinewave reconstruction after offset correction indicates the performance of back-end digitizers (DDBs) in the CDMs.

159.5 Conclusion

The hardware and mechanical housing for a 64-pixel camera prototype are ready for evaluation. Software for front end is ready and software for the back-end control and monitoring is under progress. The event data recording path is ready and is under test for integration stability and reliability. In a short time, we will be deploying 64-pixel prototype camera in a Cherenkov telescope at Mount Abu.

References

1. T.C. Weekes et al., *Ap. J.* **342**, 379 (1989)
2. https://www.hamamatsu.com/eu/en/product/optical-sensors/mppc/mppc_mppc-array/
3. S.R. Kaul et al., *Nucl. Instrum. Methods A* **496**, 400 (2003)
4. <https://www.psi.ch/en/drs>

Chapter 160

Large-Mass Single-Electron Resolution Detector for Dark Matter and Coherent Neutrino–Nucleus Elastic Interaction Searches



Vijay Iyer

Abstract In this proceeding, the development and characterization of a novel 100 g phonon-mediated silicon detector for low-mass dark matter search are presented. The detector is designed to reduce the noise from leakage charges by using a contact-free approach between its metal electrode and silicon crystal on one side. The detector achieved a baseline energy resolution of $\sim 1 e^-/h^+$ pair. The leakage current is on the order of 10^{-16} A which is an improvement of order on previous detectors with a similar design [1]. By exploiting the Neganov–Trofimov–Luke effect [2], the detector is capable of a linear signal gain up to 240 V before exhibiting signs of breakdown. This is a large improvement over the 70 V breakdown threshold reported in previous such detectors [1]. The large mass, improved signal-to-noise (S/N), and single-electron sensitivity of this detector makes it ideal for use in direct low-mass dark matter searches and $CE\nu NS$ [3] measurements.

160.1 Requirements of Building a Low-mass Dark Matter Search Detector

Direct dark matter (DM) searches seek detection via signals from elastic neutral-current scattering of DM particles (coming from a DM halo in the Milky Way galaxy) by the nuclei in a material. As results from direct-search dark matter experiments increasingly return null results in the traditional WIMP mass range, the search for low-mass dark matter (≤ 1 GeV) candidates is gaining momentum [4]. For smaller DM masses, the ratio of the DM mass (M_{DM}) to the target nucleus mass, reduces

Vijay Iyer—for the MINER Collaboration.

V. Iyer (✉)
School of Physical Sciences, National Institute of Science Education and Research,
Jatni 752050, India
e-mail: vijayiyer@niser.ac.in

Homi Bhabha National Institute, Training School Complex, Anushaktinagar, Mumbai 400094, India

the expected recoil energy (E_{th}) from DM interactions as $E_{th} \propto M_{DM}^2$ [5]. Additionally, the weak scale rate expected from DM interactions necessitates detectors with relatively large masses (\sim kg scale) and very low thresholds (\sim eV scale). The main requirement for building a low-mass dark matter search detector is sensitive to very low (eV scale) nuclear recoils with a good detector resolution. To reach low recoil energy measurements, phonon-mediated detectors [6] have exploited the Neganov–Trofimov–Luke [2] effect which increases the phonon amplification linearly with voltage up to a threshold voltage. This threshold voltage is limited by the leakage current of the detector. Previous studies have shown that the early onset of carrier leakage is predominantly due to the electrode–semiconductor interface [1]. In terms of detector resolution, all significant advancements towards developing a single-electron resolution detector have been limited to a very small mass of \sim 1 g [7]. Scaling up the detector mass while maintaining the same single-electron resolution is required to improve the sensitivity reach for low-mass dark matter searches.

160.2 Silicon High-Voltage Detector Design

An Si detector of 100 g with 7.5 cm diameter, and 2 cm thickness was fabricated. The phonon readout consisted of transition-edge sensors (TES) that uniformly cover one face of the detector. The sensors are grouped into four channels as shown in Fig. 160.1a to allow position reconstruction. Each channel is independently read out using a superconducting quantum interference device (SQUID)-based front-end amplifiers. To reduce carrier leakage through the metal–Si interface, the bias voltage is applied through a vacuum gap of \sim 0.5 mm on the other face of the detector as shown in Fig. 160.1b. The predecessors to this detector prototype had an amorphous-Si (a-Si) layer on the phonon readout side to mitigate the problem of a dead-layer [8]. This

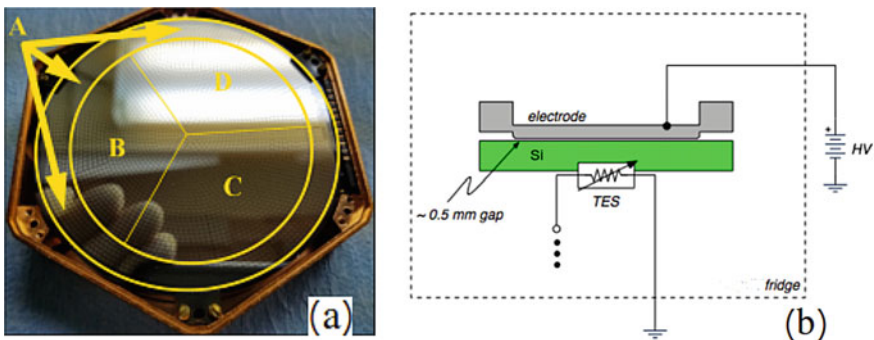


Fig. 160.1 **a** The detector in its Copper housing showing the phonon readout side of the detector with the four phonon channels (A, B, C, and D) **b** a schematic of the detector geometry

layer is absent in this detector owing to the large electric fields within the detector and the reduced thickness compared to its predecessors that make its advantage negligible. Eliminating the a-Si layer improves the athermal phonon absorption efficiency by the phonon sensors resulting in an enhanced S/N which is critical for single-electron resolution detectors.

160.3 Analysis and Results

The experiment was set up in a test facility at Texas A & M. The detector was cooled to a temperature of ~ 10 mK using a 400 μ W BlueFors LD400 dilution refrigerator. A laser emitting 1.9 eV (640 nm) photons was collimated on channel B as a source of signals. The laser pulse energy is calibrated against the ^{55}Fe photons using all four channels of the detector at 0 V bias, and its value is found to be $\sim 1150 \pm 50$ eV. Laser data and randomly triggered noise data were taken from 0 V to 320 V at intervals of 20 V. The amplitudes of the laser signals are extracted using the optimal filter method [2]. We obtain the mean of the amplitude distribution for the laser data set at each voltage. The phonon signal amplification increases linearly with voltage due to the NTL effect as expected from Eq. 160.1 and observed in Fig. 160.2a up to 240 V. In Eq. 160.1 E_R is the recoil energy, E_{NTL} is the energy from NTL gain, q is the electronic charge, V is the bias voltage and ϵ is the average energy required to create an e^-/h^+ pair in Si

$$E_{tot} = E_R + E_{NTL} = E_R + \frac{qE_R}{\epsilon}V. \quad (160.1)$$

Assuming the bandgap energy in Si to be 1.12 eV, the noise amplitude distribution can be converted to e^-/h^+ pair units using the calibration factor $1150/(1.12 \cdot S_n)$, where S_n is the mean of the distribution of the OF amplitudes and n runs from 0 to 320 V in steps of 20 V as shown in Fig. 160.2a. The noise distributions in e^-/h^+ pair units for each voltage are fitted to Gaussians. The sigma of each Gaussian is taken to be the baseline resolution (BR) of the detector at that voltage. Figure 160.2b shows BR as a function of voltage. To obtain the S/N ratio and relate the observed behavior of the BR as a function of the voltage, the functional forms for the noise (N) and signal (S) are taken as shown in Eq. 160.2.

$$N = \sqrt{N_0^2 + (Vb)^2}, \quad S = S_0 + S_0qVG/\epsilon, \quad (160.2)$$

where N_0 is the noise at 0 V, b is the noise associated with the leakage current, S_0 is the mean laser amplitude at 0 V, q is the charge of an electron, and G is a dimensionless quantity to include the effect of the vacuum gap.

The observed behavior of S/N with HV can be divided into three regions and explained as follows. In region (i) the S/N improves linearly with voltage as the

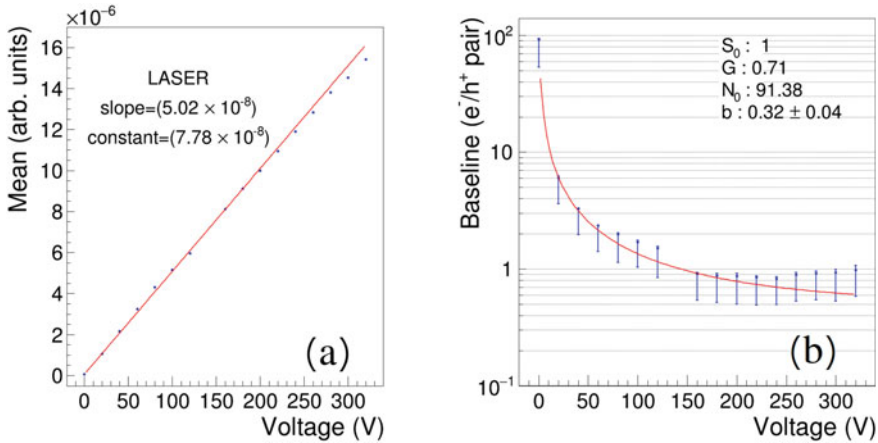


Fig. 160.2 **a** The linear amplification of the signal with HV **b** S/N behavior of the detector with HV. The fit parameters are also shown

dominant noise is the voltage-independent thermal noise associated with the electronics. In region (ii), the dominant noise is associated with the stochastic leakage current and thus both noise and the signal increase linearly with voltage making the S/N independent of bias voltage. In region (iii), the leakage current increases with the bias voltage causing the S/N to decrease with it. Figure 160.2b shows the S/N fit using all the available BR data points even though the fit does not represent the third region. The lowest BR of obtained is $0.83_{-0.34}^{+0.03} e^-/h^+$ pairs at 240 V bias. The systematics are dominated by our assumption about the 1.9 eV photon quantum yield. Lower quantum yield will result in a better BR. The leakage current can be estimated to be on the order of 10^{-16} A if we assume a BR of $\sim 1 e^-/h^+$ pair, a flat shot-noise in the frequency domain, and the phonon pulses to have a bandwidth of ~ 3 kHz.

160.4 Summary and Outlook

Single-electron sensitivity was achieved for a silicon detector of mass 100 g. The contact-free design architecture and absence of an a-Si layer helped raise the detector breakdown threshold to 240 V from 70 V. This novel detector is an ideal candidate for low-mass dark matter search experiments and is already in use at the MINER experiment [9] to measure $CE\nu NS$ from reactor neutrinos.

Acknowledgements We acknowledge the contribution of the key cryogenic infrastructure (Bluefors LD400) provided by NISER, India. We would also like to acknowledge the support of DAE through the project Research in Basic Sciences—Dark Matter.

References

1. N. Mirabolfathi et al., Nucl. Instrum. Methods A **855**, 88–91 (2017)
2. R. Agnese et al., SuperCDMS. Phys. Rev. D **99**(6), 062001 (2019)
3. D.Z. Freedman, Phys. Rev. D **9**, 1389–1392 (1974)
4. N.A. Graf, M.E. Peskin, J.L. Rosner, SLAC-econf-C130729.2
5. J.D. Lewin, P.F. Smith, Astropart. Phys. **6**, 87–112 (1996)
6. K.D. Irwin et al., Rev. Sci. Instrum. **66**, 5322 (1995)
7. R. Agnese et al., SuperCDMS. Phys. Rev. Lett. **121**(5), 051301 (2018)
8. D.S. Akerib et al., CDMS. Phys. Rev. D **82**, 122004 (2010)
9. G. Agnolet et al., MINER. Nucl. Instrum. Methods A **853**, 53–60 (2017)

Part VI
Formal Theory

Chapter 161

A Review on Crossing Symmetric Dispersion Relations in QFTs and CFTs



Ahmadullah Zahed

Abstract In this article, we review the crossing symmetric dispersion relations in QFTs and CFT Mellin amplitudes following [1, 2]. We discuss various applications of the crossing symmetric dispersion relation in both contexts.

161.1 Introduction

Dispersion relations are one of the most elegant non-perturbative ways of representing the scattering amplitudes. Since $2\text{--}2$ scattering amplitudes are functions of two independent Mandelstam invariants, in most of the context, usually, one of the Mandelstam invariants is kept fixed; usually, t is fixed, and a dispersion relation in s variable is written. In the context of the fixed- t dispersion relation, crossing symmetry is not manifest. Nevertheless, in perturbation theory, it is known that crossing symmetry is manifest in each order of perturbation. Can there be a way to write a dispersion relation that has inbuilt crossing symmetry to start with? In 1972, this question was answered in [3].

161.2 Crossing Symmetric Dispersion Relation

In order to write down a crossing symmetric dispersion relation, we parametrize s , t as a function of crossing symmetric variables z , a . We write dispersion relations in variable z for fixed a . In [3], it was shown that such parametrizations exist

$$s_k = a - \frac{a(z - z_k)^3}{z^3 - 1}, \quad k = 1, 2, 3, \quad (161.1)$$

A. Zahed (✉)

Indian Institute of Science, C.V. Raman Avenue, Bangalore 560012, India
e-mail: ahmadullah@iisc.ac.in

where z_k are cube roots of unity. We have adopted the notation $s_1 = s - \frac{\mu}{3}$, $s_2 = t - \frac{\mu}{3}$, $s_3 = u - \frac{\mu}{3} = \frac{2\mu}{3} - s - t = -s_1 - s_2$, with $s + t + u = \mu$, $\mu = 4m^2$. We want a dispersion relation, which will be crossing symmetric as well as Regge bounded in all three channels. The answer is give by (see [1, 3] for derivations)

$$\mathcal{M}(s_1, s_2) = \alpha_0 + \frac{1}{\pi} \int_{\frac{2\mu}{3}}^{\infty} \frac{ds'_1}{s'_1} \mathcal{A}(s'_1; s_2^{(+)}(s'_1, a)) H(s'_1; s_1, s_2, s_3), \tag{161.2}$$

where $H(s'_1; s_1, s_2, s_3) = [s_1 (s'_1 - s_1)^{-1} + s_2 (s'_1 - s_2)^{-1} + s_3 (s'_1 - s_3)^{-1}]$ is the crossing symmetric kernel and $\mathcal{A}(s_1; s_2)$ is s -channel discontinuity with $s_2^{(+)}(s'_1, a) = -\frac{s'_1}{2} \left[1 - \left(\frac{s'_1 + 3a}{s'_1 - a} \right)^{1/2} \right]$. The α_0 is the subtraction constant. It is given by $\alpha_0 = \mathcal{M}(s_1 = 0, s_2 = 0)$. The above dispersion relations is completely crossing symmetric in s_1, s_2, s_3 variables.

A completely crossing symmetric amplitude can be represented by an expansion

$$\mathcal{M}(s_1, s_2) = \sum_{p=0, q=0}^{\infty} \mathcal{W}_{p,q} x^p y^q, \tag{161.3}$$

with $x = -(s_1 s_2 + s_2 s_3 + s_3 s_1)$, $y = -s_1 s_2 s_3$. Also, $a = y/x$.

161.3 Applications in QFTs

Now from the partial wave expansion of $\mathcal{A}(s_1, s_2)$, we can write down an inversion formula for $\mathcal{W}_{p,q}$. For a complete derivation, see [1]

$$\mathcal{W}_{n-m, m} = \int_{\frac{2\mu}{3}}^{\infty} \frac{ds_1}{s_1} \Phi(s_1) \sum_{\ell=0}^{\infty} (2\ell + 2\alpha) a_{\ell}(s_1) \mathcal{B}_{n,m}^{(\ell)}(s_1), \tag{161.4}$$

with $\Phi(s_1) = \Psi(\alpha) \frac{\sqrt{s_1 + \frac{\mu}{3}}}{(s_1 - \frac{2\mu}{3})^{\alpha}}$ and $\Psi(\alpha)$ is some real positive number. The $\mathcal{B}_{n,m}^{(\ell)}(s_1)$ are known functions, they are some combinations of derivative of Gegenbauer polynomials.

161.3.1 Positivity Constraints

In an EFT, we can change the lower limit of the above integral from $\frac{2\mu}{3}$ to $\frac{2\mu}{3} + \delta_0$ where δ_0 serves as EFT scale, we call them $\mathcal{W}_{p,q}^{(\delta_0)}$ and they satisfy the following inequality [1]:

$$\sum_{r=0}^m \chi_n^{(r,m)}(\mu, \delta = \delta_0) \mathcal{W}_{n-r,r}^{(\delta_0)} \geq 0, \quad (161.5)$$

where $\chi_n^{(r,m)}$ are known [1] (with $\chi_n^{(m,m)}(\delta) = 1$). For example,

$$\chi_n^{(0,1)}(\mu, \delta) = \frac{6n+3}{6\delta+4\mu}, \quad \chi_n^{(0,2)}(\mu, \delta) = \frac{9(2n(n+2)+3)}{4(3\delta+2\mu)^2}, \quad \chi_n^{(1,2)}(\mu, \delta) = \frac{6n+3}{6\delta+4\mu}. \quad (161.6)$$

161.3.2 Null Constraints and Bounds on Cross Section

In order to have positive powers of x, y in the amplitude, we must have

$$\mathcal{W}_{n-m,m} = 0 \text{ for } m > n, \quad (161.7)$$

which puts non-trivial constraints on partial wave coefficients, $a_\ell(s_1)$. These are dubbed as null constraints or locality constraints. Using these constraints on $a_\ell(s_1)$, we can put a bound on the cross section (numerical Froissart like bound, but valid for all energies)

$$\frac{s-4}{16\pi} \times \sigma(s) = \bar{\sigma} = \sum_{\ell=0}^{L_{\max}} (2\ell+1) a_\ell(s). \quad (161.8)$$

161.4 Applications in CFTs

Critical exponents are objects of interest. One of the ways to calculate the critical exponents is by conformal bootstrap. Fully crossing symmetric bootstrap seems to be the most elegant and promising way to do that. These methods were first proposed by Polyakov [6]. In Mellin space formalism of conformal bootstrap, the crossing symmetric approach further developed in [4, 5]. This approach currently lacks a non-perturbative derivation for $d \geq 2$. Crossing symmetric dispersion relation provides a rigorous derivation [2].

161.4.1 Crossing Symmetric Block Expansion

Mellin amplitude is defined as

$$\mathcal{G}(u, v) = \int_{-i\infty}^{i\infty} \frac{ds}{2\pi i} \frac{dt}{2\pi i} u^s v^t \Gamma^2(\Delta_\phi - t) \Gamma^2(\Delta_\phi - u) \Gamma^2(\Delta_\phi - s) \mathcal{M}(s, t), \tag{161.9}$$

with $u = 2\Delta_\phi - s - t$. Here, $\mathcal{G}(u, v)$ is the position space conformal correlator and $\mathcal{M}(s, t)$ is Mellin amplitude. Since s-channel discontinuity are just delta functions, we can write a crossing symmetric block expansion of the amplitude (Polyakov blocks, see [2])

$$\begin{aligned} \mathcal{M}(s, t) = & \alpha_0 + \sum_{\Delta, \ell} \sum_{k=0}^{\infty} C_{\Delta, \ell} \mathcal{N}_{\Delta, \ell} \mathcal{Q}_{\ell, k}^{(\Delta)}(a) \\ & \times \left[\frac{1}{\frac{\Delta-\ell}{2} + k - s} + \frac{1}{\frac{\Delta-\ell}{2} + k - t} + \frac{1}{\frac{\Delta-\ell}{2} + k - u} - \frac{3}{\frac{\Delta-\ell}{2} + k - \frac{2\Delta_\phi}{3}} \right], \end{aligned} \tag{161.10}$$

with $\mathcal{Q}_{\ell, k}^{(\Delta)}(a) = P_{d, \ell} \left(\frac{d-\ell}{2} + k - \frac{2\Delta_\phi}{3}, s_2^{(+)} \left(\frac{d-\ell}{2} + k - \frac{2\Delta_\phi}{3}, a \right) \right)$ and $\mathcal{N}_{d, \ell}$ is some normalization, $C_{d, \ell}$ is OPE coefficients square. From the above expansion, one can remove the non-local terms [2], which directly maps to the null constraints (161.7) and we get Witten diagram expansion for Mellin amplitude as proposed in [4]. For complete derivation, see [2]. These null constraints also enable one to relate the Polyakov conditions in crossing symmetric dispersion relation to the fixed t dispersion relationship [7, 8]. For comparison, see [2].

References

1. A. Sinha, A. Zahed, Phys. Rev. Lett. **126**(18), 181601 (2021)
2. R. Gopakumar, A. Sinha, A. Zahed, [arXiv:2101.09017](https://arxiv.org/abs/2101.09017) [hep-th]
3. G. Auberson, N.N. Khuri, Phys. Rev. D **6**, 2953–2966 (1972)
4. R. Gopakumar, A. Sinha, JHEP **12**, 040 (2018)
5. R. Gopakumar, A. Kaviraj, K. Sen, A. Sinha, JHEP **05**, 027 (2017)
6. A.M. Polyakov, Zh. Eksp. Teor. Fiz. **66**, 23–42 (1974)
7. J. Penedones, J.A. Silva, A. Zhiboedov, JHEP **08**, 031 (2020)
8. D. Carmi, J. Penedones, J.A. Silva, A. Zhiboedov, [arXiv:2009.13506](https://arxiv.org/abs/2009.13506) [hep-th]

Chapter 162

Compactified Conformal Field Theories in Symplectic Manifolds



G. X. A. Petronilo, S. C. Ulhoa, and A. E. Santana

Abstract In this work, we study a scalar torus representation of a conformal theory formulated in the light cone of the $(5 + 1)$ -de Sitter space, where the local manifold is a flat symplectic space. This context is a generalization of (covariant) Galilean theory in which one space dimension is in a torus (S^1). Our main goal is to derive the equation of motion such that the solutions are directly associated to the Wigner function.

The light cone of a $(4+1)$ -de Sitter space is a geometric manifold where linear transformations are a $(3+1)$ -Galilei group [1–8]. In this realm, the mass–shell condition is written in a covariant form $p^2 - 2mE = p^\mu p_\mu = 0$, and $p^\mu = g^{\mu\nu} p_\nu$, where $g^{\mu\nu}$ is the five-dimensional metric of the Galilean space given by $g^{ij} = 1$ for $i, j = 1, 2, 3$ and $g^{45} = g^{54} = -1$, with all the other entries being zero. Then using the Dirac correspondence principle, a unitary scalar representation provides the Schrödinger equation written in a covariant form, i.e., $\partial^\mu \partial_\mu \psi(x) = 2im\partial_t \psi + \nabla^2 \psi = 0$.

Galilean covariance has attracted attention in different (theoretical and applied) directions [9–14], but an aspect that are mostly missing in the literature is the study of galilean covariance in quantum phase space with little studies on the subject [15–18]. One of the objective of the present work is to expand the study of quantum phase space in the Galilean manifold. We will approach quantum phase space using the formalism of a symplectic Hilbert space, first introduced by Oliveira et al. [19], in

G. X. A. Petronilo (✉)

International Centre of Physics, Universidade de Brasília, Campus Universitário Darcy Ribeiro,
DF | CEP 70910-900 Brasília, Brazil
e-mail: gustavo.petronilo@aluno.unb.br

S. C. Ulhoa

Instituto de Física, Universidade de Brasília, 70910-900 Brasília, DF, Brazil

Canadian Quantum Research Center, 204-3002 32 Ave Vernon, BC V1T 2L7, Canada

A. E. Santana

International Centre of Physics, Universidade de Brasília, Campus Universitário Darcy Ribeiro,
Brasília, DF | CEP 70910-900, Brazil

which the wave function, called quasi-amplitude of probability, $\psi(q, p)$ is associated with the Wigner function formalism via the identity $\psi(q, p) \star \psi(q, p)^\dagger$, where $a_W(q, p) \star b_W(q, p) = a_W(q, p) e^{\frac{i\hbar}{2} \left(\frac{\overleftarrow{\partial}}{\partial q} \frac{\overrightarrow{\partial}}{\partial p} - \frac{\overleftarrow{\partial}}{\partial p} \frac{\overrightarrow{\partial}}{\partial q} \right)} b_W(q, p)$, is the Moyal (or star) product. An operator $a_W(q, p) \star$ is an star-mapping acting in phase space functions $b_W(q, p)$. Using Hermitian star operators $a_W(q, p) \star$, unitary representations of symmetry groups are derived in a symplectic manifold. With these unitary representations, Galilei and Lorentz group have been studied and non-relativistic, and relativistic equations were obtained [19–21]. Using this unitary representation, in the present work a toroidal representation of a conformal theory is formulated in the light cone of the (5 + 1)-de Sitter space, where the local manifold is a flat symplectic space. Considering the scalar representation, the equation of motion is derived, such from the solutions, quasi-amplitude of probability, and the Wigner function are obtained and analyzed.

Initially, in order to fix the notation, we review some aspects of the (4+1)-de Sitter space, the linear transformations give rise to a Lie algebra defined by the following commutation rule:

$$\begin{aligned}
 [M_{\mu\nu}, M_{\rho\sigma}] &= -i(g_{\nu\rho}M_{\mu\sigma} - g_{\mu\rho}M_{\nu\sigma} + g_{\mu\sigma}M_{\nu\rho} - g_{\mu\sigma}M_{\nu\rho}), \\
 [P_\mu, M_{\rho\sigma}] &= -i(g_{\mu\rho}P_\sigma - g_{\mu\sigma}P_\rho), \\
 [B_\mu, M_{\rho\sigma}] &= i(g_{\mu\rho}B_\sigma - g_{\mu\sigma}B_\rho), \\
 [P_\mu, D] &= iP_\mu, \\
 [D, B_\mu] &= iB_\mu, \\
 [P_\mu, B_\nu] &= -2i(g_{\mu\nu}D - M_{\mu\nu}).
 \end{aligned}
 \tag{162.1}$$

This is the conformal-Lie algebra in five dimensions which transforms the metric $g^{\mu\nu}$ as

$$g_c^{\mu\nu}(x) = \sigma(x)g_{\mu\nu}(x), \quad g_c^{\mu\nu}(x) = \frac{1}{\sigma(x)}g^{\mu\nu}(x).
 \tag{162.2}$$

One of its subalgebras is the Schrödinger–Lie algebra with p_5 in the role of the mass, m . And the Casimir invariants of this subalgebra are $I_1 = p^\mu p_\mu$, $I_2 = p_5$, $I_3 = W_{5\mu}W_5^\mu$.

Using the Casimir invariants I_1 and I_2 and applying in Ψ ,

$$\begin{aligned}
 \widehat{P}_\mu \widehat{P}^\mu \Psi &= 0 \\
 \widehat{P}_5 \Psi &= -m\Psi
 \end{aligned}$$

From this, we obtain

$$\left(p^2 - ip \cdot \nabla - \frac{1}{4} \nabla^2 \right) \Psi = 2 \left(p_4 - \frac{i}{2} \partial_t \right) \left(p_5 - \frac{i}{2} \partial_s \right) \Psi,$$

with $\widehat{P}^\mu = p^\mu \star = p^\mu - \frac{i}{2} \frac{\partial}{\partial q_\mu}$. A solution for this equation is

$$\Psi = e^{-2i[(p_5+m)q_5+(p_4+E)t]} \Phi(q, p).$$

Thus,

$$\frac{1}{2m} \left(p^2 - i \mathbf{p} \cdot \nabla - \frac{1}{4} \nabla^2 \right) \Phi = E \Phi. \quad (162.3)$$

This is the Schrödinger equation in the Symplectic Hilbert space.

These results are then generalized for (5+1)-de Sitter manifold with the following metric:

$$g_{MN} = \begin{pmatrix} 1 & 0 & 0 & 0 & 0 & 0 \\ 0 & 1 & 0 & 0 & 0 & 0 \\ 0 & 0 & 1 & 0 & 0 & 0 \\ 0 & 0 & 0 & 0 & -1 & 0 \\ 0 & 0 & 0 & -1 & 0 & 0 \\ 0 & 0 & 0 & 0 & 0 & 1 \end{pmatrix}, \quad (162.4)$$

The flat metric is consistent with a six-dimensional de Sitter space having the product $\mathcal{G} \otimes S^1$, where \mathcal{G} is the Galilean flat space and S^1 is a 1-torus of radius R . The Lie algebra of the linear transformation generators is of the form given above in the (4+1)-manifold with the indices now specified by M, N , such that for a 6-vector is $x_M = (x_\mu, y)$, with $\mu = 1, \dots, 5$. The equation of motion of a scalar field, φ , in configuration space has the form

$$\partial^M \partial_M \varphi = 0. \quad (162.5)$$

These results are reflecting local properties. In a global perspective, the sixth component is taking in torus- S^1 , i.e., $y \in [0, 2\pi R]$. Then, the equation of motion reads

$$\partial^\mu \partial_\mu \varphi + \partial_y^2 \varphi = 0. \quad (162.6)$$

Since $\varphi(x, y) = \varphi(x, y + 2\pi R)$, so we can write a normalized solution as

$$\varphi(x, y) = \frac{1}{\sqrt{2\pi R}} \sum_n \varphi_n(x) e^{iny/R}. \quad (162.7)$$

Substituting solution (162.7) into Eq. (162.6), we get

$$\partial^\mu \partial_\mu \varphi_n(x) + \frac{n^2}{R^2} \varphi_n(x) = 0. \quad (162.8)$$

or

$$\left(i\partial_t + \frac{1}{2m}\nabla^2\right)\varphi_n(x) + \frac{n^2}{2mR^2}\varphi_n(x) = 0. \tag{162.9}$$

Therefore φ_n is a five-dimensional scalar field in the light cone of de Sitter space, and $\frac{n^2}{2mR^2}$ is a shift in the Energy E . The ground state φ_0 has no energy shift, after it, the shift will increase with n .

For phase space, we have

$$\widehat{P}^M \widehat{P}_M \varphi(q, p) = 0, \tag{162.10}$$

and letting $q_M = (q_\mu, q_6)$ with $q_6 \in [0, 2\pi]$, Eq. (162.10) becomes

$$\widehat{P}^\mu \widehat{P}_\mu \varphi + \widehat{P}_6^2 \varphi = 0. \tag{162.11}$$

As in the case of configuration space $\varphi(q_\mu, q_6, p_M) = \varphi(q_\mu, q_6 + 2\pi R, p_M)$, so

$$\widehat{P}_6 \varphi = \left(p_6 - \frac{i}{2}\partial_6\right)\varphi = \frac{n}{R}\varphi. \tag{162.12}$$

Therefore, the general solution is written as

$$\varphi(q, p) = \sum_n \varphi_n(q_\mu, p_\mu) e^{-2i(p_6 - n/R)q_6}, \tag{162.13}$$

this give a constrain in p_6

$$\begin{aligned} 4\pi R p_6 &= 2n\pi \\ p_6 &= \frac{n}{2R}. \end{aligned}$$

A consistent solution of the equation for a particle confined in $q \in [0, L]$ is

$$\varphi_n = A\sqrt{\delta(p)} \frac{\sin\left(2q\left(\sqrt{2mE_n} + p\right)\right)}{4(\sqrt{2mE_n} + p)}, \tag{162.14}$$

where $\delta(p)$ is the Dirac delta, $n_1 = 1, 2, 3, \dots$, $n_2 = 0, 1, 2, \dots$, and

$$E_{n_1, n_2} = \frac{1}{2m} \left(\frac{\pi^2 n_1^2}{L^2} + \frac{n_2^2 (1 - R^2)}{R^2} \right),$$

and $0 \leq p \leq \sqrt{\frac{\pi n_1}{L^2} - n_2}$. Note that when $n_2 = 0$ we get the usual energy of the particle in a box.

The Wigner function is then

$$f_{W_{n_1, n_2}} = \varphi_{n_1, n_2} \star \varphi_{n_1, n_2}^\dagger = A^2 \sin^2 \left(2q \left(\sqrt{\frac{\pi^2 n_1^2}{L^2} + \frac{n_2^2 (1 - R^2)}{R^2}} \right) + p \right) \delta(p). \tag{162.15}$$

The Wigner function for some values of n_1 and n_2 are plotted bellow, for convenience we set $m = L = 1$ and $R = 2$ (Figs. 162.1, 162.2, 162.3 and 162.4).

Fig. 162.1 Wigner Function for $n_1 = 1$ and $n_2 = 0$

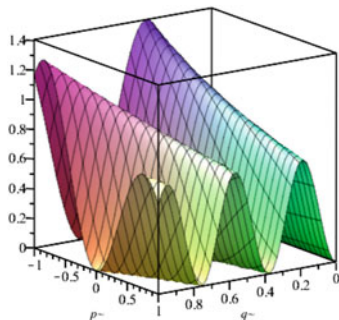


Fig. 162.2 Wigner Function for $n_1 = 1$ and $n_2 = 1$

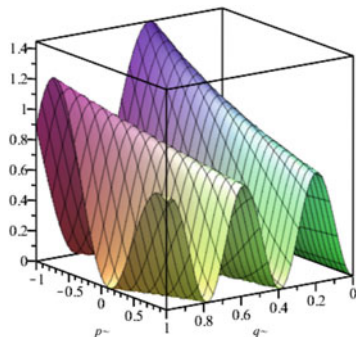


Fig. 162.3 Wigner Function for $n_1 = 2$ and $n_2 = 2$

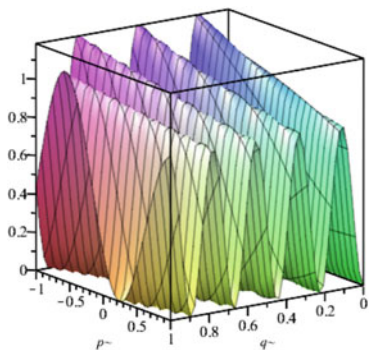
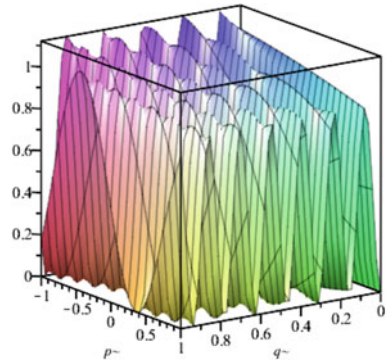


Fig. 162.4 Wigner Function
for $n_1 = 3$ and $n_2 = 3$



In short, in this work, we have used the symplectic Galilean covariance formalism to study a solution for the nonrelativistic compactified scalar field. We showed that these results are consistent with the usual solution in (3+1)-dimensions when $n_2 = 0$. The compactification of the extra dimension creates a constrain in the extra momentum. The Wigner function of the system has been then calculated explicitly. The spin 1/2 representation and a more detailed analysis of the Wigner function will be presented elsewhere. (This work was partially supported by CAPES and CNPq of Brazil.)

References

1. G. Pinski, Undefined. *J. Math. Phys.* **9**, 1927–1930 (1968)
2. G. Burdet, C. Duval, M. Perrin, Undefined. *J. Math. Phys.* **24**, 1752–1760 (1983)
3. E. Kapuscik, Undefined. (Institute of Nuclear Physics, 1985)
4. Y. Takahashi, Undefined. *Fortschr. Phys./Prog. Phys.* **36**, 83–96 (1988)
5. M. Humi, Undefined. *J. Math. Phys.* **28**, 2807–2811 (1987)
6. A. Balachandran, H. Gomm, R. Sorkin, Undefined. *Nucl. Phys. B* **281**, 573–612 (1987)
7. M. Omote, S. Kamefuchi, Y. Takahashi, Y. Ohnuki, Undefined. *Fortschr. Phys./Prog. Phys.* **37**, 933–950 (1989)
8. H. Künzle, C. Duval, Undefined. *Semantical Aspects of Spacetime Theories* (1994), pp. 113–129
9. D. Kutach, Undefined. *Int. Stud. Philos. Sci.* **24**, 15–29 (2010)
10. N. Banerjee, S. Dutta, A. Jain, Undefined. *Phys. Rev. D* **93**, 105020 (2016)
11. M. Cariglia, Undefined. *Phys. Rev. D* **98**, 084057 (2018)
12. K. Morand, Undefined. *J. Math. Phys.* **61**, 082502 (2020)
13. M. Montigny, E. Santos, Undefined. *Int. J. Modern. Phys. A* **35**, 2050086 (2020)
14. F. Ciaglia, F. Di Cosmo, A. Ibort, G. Marmo, L. Schiavone, Undefined. *Modern Phys. Lett. A* **35**, 2050214 (2020)
15. M. Fernandes, A. Santana, J. Vianna, Undefined. *J. Phys. A: Math. Gen.* **36**, 3841 (2003)
16. J. Vianna, M. Fernandes, A. Santana, Undefined. *Found. Phys.* **35**, 109–129 (2005)
17. G. Melo, M. Montigny, E. Santos, Undefined. *Int. J. Theor. Phys.* **51**, 2524–2539 (2012)
18. G.X.A. Petronilo, S.C. Ulhoa, K.V.S. Araújo, R.A.S. Paiva, R.G.G. Amorim, A.E. Santana, *Int. J. Mod. Phys. A* **35**(25), 2050148 (2020)

19. M. Oliveira, M. Fernandes, F. Khanna, A. Santana, J. Vianna, Undefined. *Ann. Phys.* **312**, 492–510 (2004)
20. R. Amorim, S. Ulhoa, E. Silva, Undefined. *Braz. J. Phys.* **45**, 664–672 (2015)
21. R. Amorim, F. Khanna, A. Malbouisson, J. Malbouisson, A. Santana, Undefined. *Int. J. Modern Phys. A* 1950037 (2019)

Chapter 163

Parametric Resonance of Complex Scalar Field Under Spacetime Oscillations



Shreyansh S. Dave and Sanatan Digoal

Abstract In this proceeding, we study time evolution of a complex scalar field, in symmetry broken phase, in presence of oscillating spacetime metric background. We show that spacetime oscillations lead to parametric resonance of the field. This generates excitations in the field for a wide range of frequency of spacetime oscillations which ultimately lead to the formation of topological vortices. The lowest frequency cut-off to induce this phenomenon is set by system size due to finite size effects.

163.1 Introduction

There are various systems ranging from condensed matter to the early Universe where topological defects can exist and form under various conditions [1]. They exist when the order parameter space or vacuum manifold of the system has a non-trivial topology [2]. Formation of topological defects during symmetry breaking phase transitions is studied by Kibble–Zurek mechanism [1, 3]. Nucleation of superfluid vortex lattice in rotating vessel, flux-tube lattice in presence of magnetic field in type-II superconductor, etc. are other methods of formation of topological defects [4].

The phenomenon of parametric resonance of field, in symmetry broken phase, can also produce topological defects [5–7]. This has been studied for periodically oscillating temperature of heat bath, which generates excitations in the field leading to the formation of topological defects [5, 6]. In ref. [7], we have shown that spacetime oscillations can also induce such phenomenon for a wide range of frequencies. At frequencies lesser than the mass of field mainly transverse excitation of the field arises, while at higher frequencies longitudinal excitation also gets generated

S. S. Dave (✉) · S. Digoal
The Institute of Mathematical Sciences, Chennai 600113, India
e-mail: shreyanshsd@imsc.res.in

S. Digoal
Homi Bhabha National Institute, Training School Complex, Anushaktinagar,
Mumbai 400085, India

dominantly. In this case, the lowest frequency cut-off to generate field excitation is set by system size due to finite size effects. In this proceeding, we present some of the results of our work in ref. [7].

163.2 Equation of Motion

For simplicity, we take the *inverse* spacetime metric as $g^{\mu\nu} \equiv \text{diag}(-1, 1 - h, 1 + h, 1)$, where $h = \varepsilon \sin(\omega(t-z))$ and $\varepsilon < 1$; (t, x, y, z) are spacetime coordinates. The action of a complex scalar field on this spacetime manifold is given by [7]

$$S = \int d^4x \sqrt{-g} \left[-\frac{1}{2} g^{\mu\nu} \partial_\mu \Phi^* \partial_\nu \Phi - V(\Phi^* \Phi) \right], \quad (163.1)$$

where $g = \det(g_{\mu\nu}) = -(1 - h^2)^{-1}$, $\Phi = \phi_1 + i\phi_2$, $\Phi^* = \phi_1 - i\phi_2$; ϕ_1 , and ϕ_2 are real scalar fields. We consider symmetry breaking effective potential as

$$V(\Phi^* \Phi) = \frac{\lambda}{4} \left(\Phi^* \Phi - \Phi_0^2 \right)^2, \quad (163.2)$$

where the mass of longitudinal mode of field is $m_\Phi = \Phi_0 \sqrt{2\lambda}$. The equations of motion for (ϕ_1, ϕ_2) fields are [7]

$$\square \phi_i - \frac{dV}{d\phi_i} = 0; \quad \square \phi_i = \frac{1}{\sqrt{-g}} \partial_\mu \left(\sqrt{-g} g^{\mu\nu} \partial_\nu \phi_i \right); \quad i = 1, 2. \quad (163.3)$$

For the simplicity of solving it numerically, (i) we assume that there is no variation of the field Φ along z -direction and (ii) we look at the solution of the field only in the $z = 0$ plane. With these simplifications, the above equations in the expanded form become [7]

$$-\frac{1}{2} \frac{\varepsilon^2 \omega \sin(2\omega t)}{f(t)f(-t)} \frac{\partial \phi_i}{\partial t} - \frac{\partial^2 \phi_i}{\partial t^2} + f(t) \frac{\partial^2 \phi_i}{\partial x^2} + f(-t) \frac{\partial^2 \phi_i}{\partial y^2} - \lambda \phi_i (\phi_1^2 + \phi_2^2 - \Phi_0^2) = 0, \quad (163.4)$$

where $f(t) = 1 - \varepsilon \sin(\omega t)$. These equations clearly indicate that spacetime oscillations can affect field evolution iff the initial field configuration has some fluctuations, which can naturally be present due to thermal and/or quantum fluctuations. The momentum of field modes of initial field configuration get coupled with spacetime oscillations and by following resonance conditions undergo parametric resonant growths [7]. It can be shown that when $\omega < m_\Phi$, mainly transverse excitation of the field arise, while when $\omega > m_\Phi$, along with transverse excitation, longitudinal excitation also get generated dominantly [7].

163.3 Simulation Details and Results

In our simulations, we consider only transverse fluctuations in the initial field configuration. We evolve the field by solving Eq. 163.4 with the use of second-order Leapfrog method and periodic boundary conditions along spatial directions. We use lattice spacing $\Delta x = \Delta y = 0.01 \Lambda$ and time spacing $\Delta t = 0.005 \Lambda$.

In Fig. 163.1, we have shown how the field gets excitations under spacetime oscillations in physical space (left) and in field space (right) at four different times of field evolution; Left: $t = 0, 1.35, 1.7,$ and 1.8Λ , Right: $t = 0.05, 1.05, 1.35,$ and 1.8Λ . The parameters of simulations are $\epsilon = 0.4, \omega = 100 \Lambda^{-1}, \Phi_0 = 10 \Lambda^{-1},$ and $\lambda = 40,$ which imply that for these parameters $\omega > m_\phi$ allowing the dominant generation of longitudinal component of the field along with transverse component. Left plots clearly show that the spacetime oscillations generate a specific field mode at the intermediate stage of the evolution. With further evolution, other field modes also get generated which ultimately lead to the formation of topological vortices in the system. Right plots show that both components of the field, transverse and longitudinal, have been generated during the field evolution.

The generation of longitudinal excitation in this case makes the profile of the formed vortices highly distorted. In Fig. 163.2, we have taken $\omega = 20 \Lambda^{-1},$ for which $\omega < m_\phi$ allowing the generation of mainly transverse excitation. This leads to the formation of well-separated vortices. This has been depicted in physical space (left) and in field space (right) at time $t = 18.5 \Lambda.$

To understand the response of field to frequency $\omega,$ we determine the time of formation of first vortex–antivortex pair in system and denote it by $t_{vortex}.$ A more useful quantity to analyze this response is $t_{vortex} \omega / 2\pi,$ a dimensionless number, which counts the number of cycle (NoC) of spacetime oscillations up to $t_{vortex}.$ In Fig. 163.3 (left), we plot NoC versus $\omega.$ This clearly shows that for sufficiently large $\omega,$ NoC is almost independent from $\omega.$ However, at low $\omega,$ it starts deviating from such a constant value and diverges at very low $\omega.$ This is an indication of finite size effects. In Fig. 163.3 (right), we study the effects of using periodic and fixed boundary

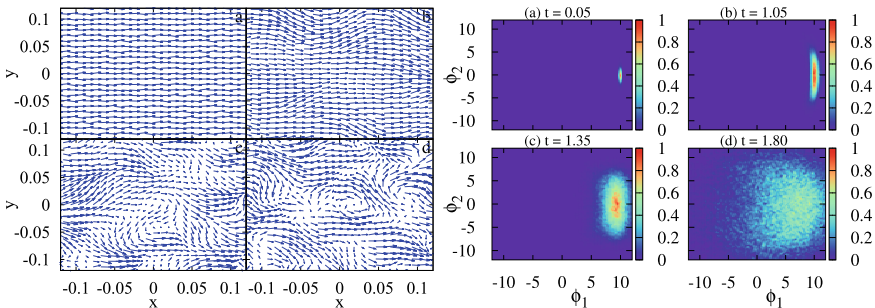


Fig. 163.1 Field configurations in physical space (left) and field distributions in field space (right) at different times of field evolution for $\omega > m_\phi.$ Figures are from ref. [7]

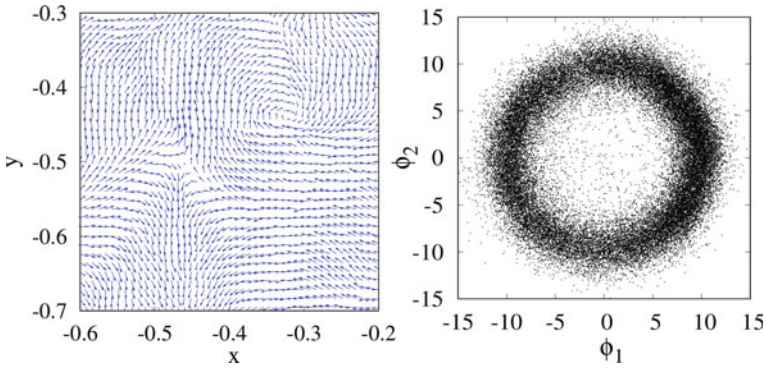


Fig. 163.2 Figures show formation of well-separated vortices (left) and generation of mainly transverse excitation in field space (right) for $\omega < m_\phi$. Figures are from ref. [7]

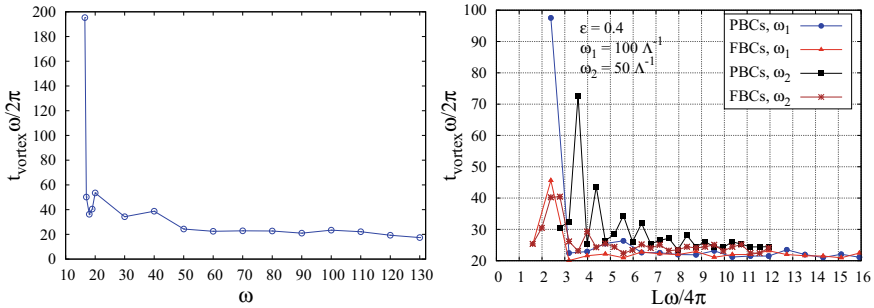


Fig. 163.3 Figures show response of t_{vortex} to frequency ω , choice of boundary conditions, and system size L . Figures are from ref. [7]

conditions (PBCs and FBCs), system size L , and ω on NoC. For each curve, we have taken a fixed value of ω ($\omega_1 = 50\Lambda^{-1}$ and $\omega_2 = 100\Lambda^{-1}$), and $\varepsilon = 0.4$, while we vary L . For sufficiently large values of $L\omega/4\pi$, NoC is independent from $L\omega/4\pi$ and takes roughly a constant value. On the other hand, for low $L\omega/4\pi$, it starts increasing and diverse when $L\omega/4\pi \sim 1$. For PBCs, these deviations are stronger than FBCs. Thus, the lowest frequency cut-off to induce this phenomenon is given by $\omega_L \sim 4\pi/L$.

References

1. W.H. Zurek, Phys. Rept. **276**, 177–221 (1996)
2. N.D. Mermin, Rev. Mod. Phys. **51**, 591–648 (1979)
3. T.W.B. Kibble, J. Phys. A **9**, 1387–1398 (1976)

4. D.R. Tilley, J. Tilley, *Superfluidity and Superconductivity*, 3rd edn. (Institute of Physics Publishing, 2005)
5. S. Digal, R. Ray, S. Sengupta, A.M. Srivastava, *Phys. Rev. Lett.* **84**, 826–829 (2000)
6. R. Ray, S. Sengupta, *Phys. Rev. D* **65**, 063521 (2002)
7. S.S. Dave, S. Digal, *Phys. Rev. D* **103**, 116007 (2021)

Chapter 164

Generalized Uncertainty Principle in Bar Detectors of Gravitational Waves



Sukanta Bhattacharyya, Sunandan Gangopadhyay, and Anirban Saha

Abstract At present, the gravitational waves detectors achieve the sensitivity to detect the length variation (δL), $\mathcal{O} \approx 10^{-17} - 10^{-21}$ m. Recently, a more stringent upperbound on the dimensionless parameter β_0 , bearing the effect of generalized uncertainty principle, has been given which corresponds to the intermediate length scale $l_{im} = \sqrt{\beta_0} l_{pl} \sim 10^{-23}$ m. Hence, it becomes quite obvious to search for the generalized uncertainty principle by observing the response of the vibrations of phonon modes in such resonant detectors in the near future. Therefore, we calculate the resonant frequencies and transition rates induced by the incoming gravitational waves on these detectors in the generalized uncertainty principle framework. This presentation is based on the work published in [1].

The existence of an observer independent minimum length ($l_{pl} \approx 10^{-33}$ cm), proposed by various quantum theories of gravity, demands a modification of the Heisenberg uncertainty principle (HUP) to the generalized uncertainty principle (GUP). Near the Planck energy scale, the Heisenberg uncertainty principle $\Delta x \sim \hbar/\Delta p$ is expected to get modified by gravitational effects. The above observation along with various thought experiments leads to the following simplest form of the GUP [2, 3]

$$\Delta q_i \Delta p_i \geq \frac{\hbar}{2} [1 + \beta(\Delta p^2 + \langle p \rangle^2) + 2\beta(\Delta p_i^2 + \langle p_i \rangle^2)]; \quad i = 1, 2, 3, \quad (164.1)$$

where $p^2 = \sum_{j=1}^3 p_j p_j$ and q_j, p_j are the position and its conjugate momenta. Naturally a lot of effort has been put to find an upper bound of the GUP parameter β as it plays a crucial role for realizing the effects of GUP [4]. Again the testing of the GUP is extremely challenging and therefore initiates the proposal of a realistic

S. Bhattacharyya (✉) · A. Saha
Department of Physics, West Bengal State University, Barasat, Kolkata 700126, India
e-mail: sukanta706@gmail.com

S. Gangopadhyay
Department of Theoretical Sciences, S.N. Bose National Centre for Basic Sciences, JD Block,
Sector III, Salt Lake, Kolkata 700106, India

© The Author(s), under exclusive license to Springer Nature Singapore Pte Ltd. 2022
B. Mohanty et al. (eds.), *Proceedings of the XXIV DAE-BRNS High Energy Physics Symposium, Jatni, India*, Springer Proceedings in Physics 277,
https://doi.org/10.1007/978-981-19-2354-8_164

919

experimental setup to test the GUP. On the other hand, present-day bar detectors [5] are capable of detecting the fractional variations ΔL of the bar length L down to $\frac{\Delta L}{L} \sim 10^{-19}$, with $L \sim 1$ m, which may be sensitive enough to allow us to probe the effects of quantum gravity. Motivated by the above discussion, in this presentation, we shall look at the quantum mechanical effects of the gravitational wave (GW) resonant bar detectors in the GUP framework. Physically these detectors can be described by a quantum mechanical forced GW-HO system. Hence, we construct the quantum mechanical description of the GW-HO interaction in presence of the GUP. To carry this out, we first write down the Hamiltonian of the GW-HO system as

$$H = \frac{1}{2m} (p_j + m\Gamma^j{}_{0k}q^k)^2 + \frac{1}{2}m\varpi^2q_j^2. \quad (164.2)$$

Following the standard prescription of quantum mechanics, we lift the phase-space variables (q^j, p_j) to operators (\hat{q}^j, \hat{p}_j) in the GUP framework. These can be defined up to first order in β as

$$\hat{q}_i = q_{0i}, \quad \hat{p}_i = p_{0i}(1 + \beta p_0^2). \quad (164.3)$$

Here we shall consider the resonant bar detectors as a 1-D¹ system [6]. Now in terms of the standard definition of the raising and lowering operators (a, a^\dagger) , the Hamiltonian in Eq. 164.2 up to first order in β can be recast as $H = H_0 + H_1 + H_2$, where

$$H_0 = \hbar\omega \left(a^\dagger a + \frac{1}{2} \right),$$

$$H_1 = \frac{\beta}{m} \left(\frac{\hbar m \omega}{2} \right)^2 [aaaa - aaaa^\dagger - aaa^\dagger a + aaa^\dagger a^\dagger - aa^\dagger aa + aa^\dagger aa^\dagger + aa^\dagger a^\dagger a - aa^\dagger a^\dagger a^\dagger - a^\dagger aaa + a^\dagger aaa^\dagger + a^\dagger aa^\dagger a - a^\dagger aa^\dagger a^\dagger + a^\dagger a^\dagger aa - a^\dagger a^\dagger aa^\dagger - a^\dagger a^\dagger a^\dagger a + a^\dagger a^\dagger a^\dagger a^\dagger],$$

$$H_2 = i\hbar\dot{h}_{11} \left[-\frac{1}{2} (aa - a^\dagger a^\dagger) + \frac{\beta\hbar m \omega}{4} (aaaa - aaa^\dagger a - aa^\dagger aa + aa^\dagger a^\dagger a - a^\dagger aaa^\dagger + a^\dagger aa^\dagger a^\dagger + a^\dagger a^\dagger aa^\dagger - a^\dagger a^\dagger a^\dagger a^\dagger) \right]. \quad (164.4)$$

Here H_0 stands for the Hamiltonian of ordinary HO while H_1 and H_2 are the time-independent and time-dependent parts of the Hamiltonian, respectively. Now we proceed to calculate the perturbed eigenstates and energies due to time-independent Hamiltonian H_1 . Using time-independent perturbation theory, the perturbed eigenstates and their corresponding energies read

¹ A typical bar is a cylinder of length $L = 3$ m and radius $R = 30$ cm, and therefore one can treat its vibrations as one dimensional.

$$|n\rangle^\beta = |n\rangle + \Delta \left[\frac{(2n+3)\sqrt{(n+1)(n+2)}}{4} |n+2\rangle - \frac{(2n-1)\sqrt{n(n-1)}}{4} |n-2\rangle \right. \\ \left. + \frac{\sqrt{n(n-1)(n-2)(n-3)}}{16} |n-4\rangle - \frac{\sqrt{(n+1)(n+2)(n+3)(n+4)}}{16} |n+4\rangle \right]$$

and

$$E_n^{(\beta)} = \left(n + \frac{1}{2} \right) \hbar\omega \left[1 + \frac{3(2n^2 + 2n + 1)}{2(2n + 1)} \Delta \right]. \quad (164.5)$$

Here $\Delta = \beta \hbar m \omega$ is the dimensionless parameter involving the GUP parameter. Now the time-dependent part of the Hamiltonian, that is, H_2 gives the probability amplitude of transition to be

$$C_{0^\beta \rightarrow 2^\beta} = A \int_{-\infty}^{t \rightarrow +\infty} dt' \dot{h}_{11} e^{i(2+9\Delta)\omega t'} \\ C_{0^\beta \rightarrow 4^\beta} = B \int_{-\infty}^{t \rightarrow +\infty} dt' \dot{h}_{11} e^{i(4+30\Delta)\omega t'}, \quad (164.6)$$

where $A = \left(\frac{1}{\sqrt{2}} + \frac{9}{4\sqrt{2}} \Delta \right)$ and $B = -3\sqrt{6}\Delta$ are dimensionless constants. Equation 164.6 is one of the main results [1]. From the transition amplitudes, the presence of the GUP can be checked by measuring the corresponding transition probabilities $P_{i \rightarrow f} = |C_{i \rightarrow f}|^2$. We now look at some GW templates. In this presentation, we explore the effects of GUP in GWs detection technique using two types of GW templates generated from different astronomical events. First, we consider the periodic GW with linear polarization. This has the form

$$h_{jk}(t) = 2f_0 \cos \Omega t (\varepsilon_{\times} \sigma_{jk}^1 + \varepsilon_{+} \sigma_{jk}^3), \quad (164.7)$$

where the amplitude varies sinusoidally with a single frequency Ω . The transition rates in this case are

$$\lim_{T \rightarrow \infty} \frac{1}{T} P_{0^\beta \rightarrow 2^\beta} = (2\pi f_0 \Omega A \epsilon_{+})^2 \times [\delta(\omega(2+9\Delta) - \Omega)] \quad (164.8)$$

$$\lim_{T \rightarrow \infty} \frac{1}{T} P_{0^\beta \rightarrow 4^\beta} = (2\pi f_0 \Omega B \epsilon_{+})^2 \times [\delta(\omega(4+30\Delta) - \Omega)]. \quad (164.9)$$

With the above results in place, we now make an estimate of the GUP parameter β_0 . The inequality $9\Delta\omega < 2\omega$ gives $\beta_0 < 1.4 \times 10^{28}$, $\beta = \beta_0 / (M_{pl}c)^2$. This upper bound on the GUP parameter is stronger than the one obtained in [7]. Interestingly, we find that the correction to the resonant frequency 2ω due to the GUP is $9\Delta\omega / (2\pi) \approx$

1.3 kHz. Hence, this simple calculation shows that the GUP modes can ring up in order to be detected by the resonant bar detectors.

We shall next take approximated models of the astrophysical phenomenon like bursts which emits aperiodic GWs waveform with modulated Gaussian function as the second GW template. This has the form

$$h_{jk}(t) = 2f_0g(t) (\varepsilon_{\times}\sigma_{jk}^1 + \varepsilon_{+}\sigma_{jk}^3); \quad g(t) = e^{-t^2/\tau_g^2} \sin \Omega_0 t. \quad (164.10)$$

The transition probabilities for this case are

$$P_{0\beta \rightarrow 2\beta} \approx e^{-(2\omega+9\omega\Delta-\Omega_0)^2\tau_g^2/2} \times \{f_0\epsilon_+ A\sqrt{\pi}\tau_g(2\omega+9\omega\Delta)\}^2$$

$$P_{0\beta \rightarrow 4\beta} \approx e^{-(4\omega+30\omega\Delta-\Omega_0)^2\tau_g^2/2} \times \{f_0\epsilon_+ B\sqrt{\pi}\tau_g(4\omega+30\omega\Delta)\}^2. \quad (164.11)$$

Now we proceed to conclude our presentation by summarizing the results. We make the following observations from the exact forms of the transition rates. The resonant frequencies $\Omega = \omega(2 + 9\Delta)$ and $\Omega = \omega(4 + 30\Delta)$ get modified by the GUP parameter β . This observation is quite similar with that obtained in the noncommutative framework [8, 9]. In the presence of the GUP, we find that there are more than one transitions possible from the ground state to the excited states with different amplitudes. We get both the linear and the quadratic terms in the dimensionless GUP parameter Δ in the expressions of the transition amplitudes. The linear dependence in Δ is easier to detect. We have also done this analysis for the circularly polarized GWs which show that they are also good candidates to probe the presence of the GUP in the resonant detectors [1]. In this presentation, we have shown an upper bound estimation of the GUP parameter $\beta_0 < 10^{28}$. This is a much stronger bound than that obtained in [7] which is $\beta_0 < 10^{33}$. The observations made here reveal that resonant detectors may allow in the near future to detect the existence of an underlying generalized uncertainty principle. Moreover, in the recent literature [10], a connection between the generalized uncertainty principle and the spatial noncommutative structure of space has been shown. Our analysis also indicates a similarity between the findings in these two frameworks.

References

1. S. Bhattacharyya, S. Gangopadhyay, A. Saha, *Class. Quant. Grav.* **37**(19), 195006 (2020)
2. A. Kempf, G. Mangano, R.B. Mann, *Phys. Rev. D* **52**, 1108 (1995)
3. R. Mandal S. Bhattacharyya, S. Gangopadhyay, *Gen. Rel. Grav.* **50**(11), 143 (2018)
4. M. Bawaj, et al., *Nat. Commun.* **6**, 7503 (2015); P.A. Bushev et al., *Phys. Rev. D* **100**, 066020 (2019)
5. A. Giazotto, Status of gravitational wave detection, in *General Relativity and John Archibald Wheeler, Ciufolini and R.A. Matzner*. Astrophysics and Space Science Library, vol. 367. (Springer, Berlin, 2010)
6. M. Maggiore, *Gravitational Wave*, vol. I. Theory and Experiments (Oxford University Press, Oxford, 2008)

7. F. Marin, F. Marino, et al., *Nat. Phys.* **9**, 71 (2013); F. Marin, F. Marino, *New J. Phys.* **16**, 085012 (2014)
8. S. Bhattacharyya, S. Gangopadhyay, A. Saha, *Class. Quantum Grav.* **36**, 055006 (2019)
9. S. Gangopadhyay, S. Bhattacharyya, A. Saha, *Ukr. J. Phys.* **64**(11), 1029 (2019)
10. S. Gangopadhyay, S. Bhattacharyya, *Phys. Rev. D* **99**, 104010 (2019)
11. S. Das, E.C. Vagenas, *Phys. Rev. Lett.* **101**, 221301 (2008)
12. A. Saha, S. Gangopadhyay, *Class. Quant. Grav.* **33**, 205006 (2016)

Chapter 165

Bianchi-I Cosmology in Quantum Gravity



Sunandan Gangopadhyay, Rituparna Mandal, and Amitabha Lahiri

Abstract The exact renormalization group flow equations for gravity lead to quantum corrections of Newton's constant and cosmological constant. Using this, we investigate the Bianchi-I cosmological model at late times. In particular, we obtain the scale factors in different directions and observe that they eventually evolve into Friedmann–Lemaître–Robertson–Walker (FLRW) universe for radiation. However, for stiff matter, the universe shows a Kasner-like behaviour. The presentation is based on our work published in [9].

165.1 Introduction

In the last couple of decades, exact renormalization group (RG) equations [1] have become a powerful tool for nonperturbative investigation of both renormalizable and effective quantum field theories. The framework for exact RG of Euclidean quantum gravity [2, 3] has opened up the possibility of investigating cosmological models [4] in a systematic manner. An essential ingredient of this framework is the effective average action $\Gamma_k[g_{\mu\nu}]$ [5–8] describing all gravitational phenomena, including the effect of all loops, at a momentum scale k . Assuming that there is an ultraviolet fixed point much higher than k , all quantum fluctuations with momenta $p^2 > k^2$ are included, while the momenta $p^2 < k^2$ are suppressed by an infrared regulator. The form of this effective average action is

$$\Gamma_k[g, \bar{g}] = (16\pi G(k))^{-1} \int d^d x \sqrt{\bar{g}} \{-R(g) + 2\Lambda(k)\} + S_{gf}[g, \bar{g}], \quad (165.1)$$

S. Gangopadhyay (✉) · R. Mandal · A. Lahiri
Department of Theoretical Sciences, S.N. Bose National Centre for Basic Sciences, Block JD,
Sector III, Salt Lake, Kolkata 700106, India
e-mail: sunandan.gangopadhyay@bose.res.in; sunandan.gangopadhyay@gmail.com

where $\bar{g}_{\mu\nu}$ is a background metric and $S_{gf}[g, \bar{g}]$ is a classical background gauge fixing term. The scale-dependent Newton’s constant $G(k)$ and the cosmological constant $\Lambda(k)$ can be obtained from the RG Eq. [9]

$$G(k) = G_0 [1 - \omega G_0 k^2 + \omega_1 G_0^2 k^4 + \mathcal{O}(G_0^3 k^6)] \tag{165.2}$$

$$\Lambda(k) = \Lambda_0 + G_0 k^4 [v + v_1 G_0 k^2 + \mathcal{O}(G_0^2 k^4)]. \tag{165.3}$$

165.2 Bianchi-I Universe with Running G and Λ

We now proceed to investigate the Bianchi type-I cosmology which reads

$$ds^2 = -dt^2 + a^2(t)dx^2 + b^2(t)dy^2 + c^2(t)dz^2. \tag{165.4}$$

The improved Einstein field equations with time-varying Newton’s gravitational constant and cosmological constant read

$$R_{\mu\nu} - \frac{1}{2}Rg_{\mu\nu} = -8\pi G(t)T_{\mu\nu} + \Lambda(t)g_{\mu\nu} \tag{165.5}$$

with $T_{\mu\nu} = (p + \rho)v_\mu v_\nu + pg_{\mu\nu}$ being the energy–momentum tensor of a perfect fluid. The covariant conservation of the energy–momentum tensor yields the consistency equation $8\pi\rho\dot{G} + \dot{\Lambda} = 0$.

One possibility is to relate the scale k to t as $k \sim t^{-1}$ in an FLRW universe [4]. For a Bianchi-I universe, one needs to include higher order terms in t^{-1} . We have taken $k = \frac{\xi}{t} + \frac{\sigma}{t^2} + \frac{\delta}{t^3}$.

Then we can write from Eqs. (165.2), (165.3)

$$G(t) = G_0 \left[1 - \frac{\tilde{\omega}G_0}{t^2} \left(1 + \frac{2\tilde{\sigma}}{t} + \frac{2\tilde{\delta}}{t^2} + \frac{\tilde{\sigma}^2}{t^2} \right) + \frac{\tilde{\omega}_1 G_0^2}{t^4} + \mathcal{O}\left(\frac{t_{Pl}^6}{t^6}\right) \right], \tag{165.6}$$

$$\Lambda(t) = \Lambda_0 + \frac{G_0}{t^4} \left[\tilde{v} \left(1 + \frac{4\tilde{\sigma}}{t} + \frac{4\tilde{\delta}}{t^2} + \frac{6\tilde{\sigma}^2}{t^2} \right) + \frac{\tilde{v}_1 G_0}{t^2} + \mathcal{O}\left(\frac{t_{Pl}^4}{t^4}\right) \right], \tag{165.7}$$

where we have defined $\tilde{\omega} \equiv \omega\xi^2$, $\tilde{\omega}_1 \equiv \omega_1\xi^4$, $\tilde{v} \equiv v\xi^4$, $\tilde{v}_1 \equiv v_1\xi^6$, $\tilde{\sigma} \equiv \frac{\sigma}{\xi}$, $\tilde{\delta} \equiv \frac{\delta}{\xi}$ and $t_{Pl} = \sqrt{G_0}$ is the Planck time in natural units.

For an equation of state $p(t) = \Omega\rho(t)$, the conservation of energy–momentum together with the consistency equation fixes the energy density ρ and the average scale factor $\mathcal{R} = \sqrt[3]{abc}$ to be

$$\rho(t) = \frac{1}{4\pi} \left(\frac{\tilde{v}}{\tilde{\omega}} \right) \frac{1}{G_0 t^2} \left\{ 1 + \frac{2\tilde{\sigma}}{t} + \frac{2\tilde{\delta}}{t^2} + \frac{\tilde{\sigma}^2}{t^2} + \left(\frac{2\tilde{\omega}_1}{\tilde{\omega}} + \frac{3\tilde{v}_1}{2\tilde{v}} \right) \frac{G_0}{t^2} + \mathcal{O} \left(\frac{t_{Pl}^4}{t^4} \right) \right\}, \tag{165.8}$$

$$\mathcal{R}(t) = \left[\frac{\mathcal{M}G_0}{2} \left(\frac{\tilde{\omega}}{\tilde{v}} \right) \right]^{\frac{1}{(3+3\Omega)}} t^{\frac{2}{(3+3\Omega)}} \left\{ 1 - \frac{1}{(3+3\Omega)} \left(\frac{2\tilde{\sigma}}{t} + \frac{2\tilde{\delta}}{t^2} - \frac{(3\Omega+5)\tilde{\sigma}^2}{(3+3\Omega)t^2} + \left(\frac{2\tilde{\omega}_1}{\tilde{\omega}} + \frac{3\tilde{v}_1}{2\tilde{v}} \right) \frac{G_0}{t^2} \right) + \mathcal{O} \left(\frac{t_{Pl}^4}{t^4} \right) \right\}. \tag{165.9}$$

We now discuss two special cases of cosmic matter separately, namely, radiation ($\Omega = \frac{1}{3}$) and stiff fluid ($\Omega = 1$).

For $\Omega = 1/3$, the directional Hubble parameters read

$$\begin{aligned} \frac{\dot{a}}{a} &= H(t) + \frac{l(2+\beta)\alpha}{3} H_1(t), \\ \frac{\dot{b}}{b} &= H(t) + \frac{l(\beta-1)\alpha}{3} H_1(t), \\ \frac{\dot{c}}{c} &= H(t) - \frac{l(1+2\beta)\alpha}{3} H_1(t), \end{aligned} \tag{165.10}$$

where $\alpha = \left[\frac{\mathcal{M}G_0}{2} \left(\frac{\tilde{\omega}}{\tilde{v}} \right) \right]^{-\frac{1}{1+\Omega}}$ and β, l are constants of integration. Here the ‘‘average Hubble parameter’’ $H(t) = \dot{\mathcal{R}}/\mathcal{R}$ includes isotropic quantum corrections,

$$H(t) = \frac{1}{2t} \left[1 + \frac{\tilde{\sigma}}{t} + \left(2\tilde{\delta} - \tilde{\sigma}^2 + \left(\frac{2\tilde{\omega}_1}{\tilde{\omega}} + \frac{3\tilde{v}_1}{2\tilde{v}} \right) G_0 \right) \frac{1}{t^2} + \mathcal{O} \left(\frac{t_{Pl}^3}{t^3} \right) \right]. \tag{165.11}$$

The function $H_1(t)$ also includes quantum corrections but it will become irrelevant as we shall see now. Keeping terms up to $\mathcal{O} \left(\frac{t_{Pl}}{t} \right)^4$ in the tt -component of Einstein equation and comparing inverse powers of t , we find $\Lambda_0 = 0, \frac{\tilde{\omega}}{\tilde{v}} = 8/3$ and $4 \left(\frac{\tilde{v}}{\tilde{\omega}} \right) \tilde{\sigma} = 3\tilde{\sigma}/2 - l^2\alpha^2 (\beta^2 + \beta + 1)/3$, leading to

$$l^2\alpha^2 (\beta^2 + \beta + 1) = 0. \tag{165.12}$$

If $l \neq 0$, we must have $\beta^2 + \beta + 1 = 0$ which implies that the two roots of β are complex. Since the scale factors must be real, it follows that $l = 0$. Hence, we observe that all the directional Hubble parameters must be equal, that is, the universe must be FLRW in the presence of radiation. Thus, we conclude that the scale factors of anisotropic Bianchi-I metric flow to the isotropic FLRW cosmology due to RG flow of the Newton’s gravitational constant and the cosmological constant.

For $\Omega = 1$, which corresponds to stiff matter, the directional Hubble parameters have the same form as in Eq. (165.10). The expression for the (isotropic) average Hubble parameter reads

$$\frac{\dot{\mathcal{R}}}{\mathcal{R}} = \frac{1}{3t} \left[1 + \frac{\tilde{\sigma}}{t} + \left(2\tilde{\delta} - \tilde{\sigma}^2 + \left(\frac{2\tilde{\omega}_1}{\tilde{\omega}} + \frac{3\tilde{v}_1}{2\tilde{v}} \right) G_0 \right) \frac{1}{t^2} + \mathcal{O} \left(\frac{t_{Pl}^3}{t^3} \right) \right]. \tag{165.13}$$

Proceeding as before, we find $\Lambda_0 = 0$ and

$$2 \left(\frac{\tilde{v}}{\tilde{\omega}} \right) = \frac{1}{3} (1 - \alpha^2 l^2 (\beta^2 + \beta + 1)). \tag{165.14}$$

Writing l in terms of the constant β , we get

$$l = \frac{1}{\alpha} \frac{\sqrt{1 - 6 \left(\frac{\tilde{v}}{\tilde{\omega}} \right)}}{\sqrt{(\beta^2 + \beta + 1)}}. \tag{165.15}$$

From the reality of the directional Hubble parameters, we get the following condition from the above equation:

$$1 - 6 \left(\frac{\tilde{v}}{\tilde{\omega}} \right) \geq 0 \quad \Rightarrow \quad \xi^2 \leq \frac{1}{6} \frac{\omega}{\nu}. \tag{165.16}$$

When Eq. (165.16) is an equality, we see from Eq. (165.14) that $l^2(\beta^2 + \beta + 1) = 0$, which implies that $l = 0$ since β must be real. Therefore, in that case, we again have an FLRW universe.

When Eq. (165.16) is not an equality, that is, $l \neq 0$, we consider the directional Hubble parameters for large β . This is a Kasner-type universe, which means that there are expanding and contracting directions.

165.3 Conclusions

The presentation is based on the study of the Bianchi-I cosmological model at late times taking quantum gravitational effects into account [9]. We used the RG improved cosmological equations following from the scale dependence of Newton’s constant and the cosmological constant. For radiation, the scale factors take the same form and expand at the same rate in all directions. For stiff matter, there are solutions which do not flow to the FLRW universe and show a Kasner-like behaviour. The observation of the quantum-gravity-induced time dependence of the Hubble parameter or scale dependence of G , Λ would determine the validity of this approach.

References

1. J. Berges, N. Tetradis, C. Wetterich, Non-perturbative renormalization flow in quantum field theory and statistical physics. *Phys. Rep.* **363**, 223–386 (2002)
2. M. Reuter, Nonperturbative evolution equation for quantum gravity. *Phys. Rev. D* **57**(10), 971 (1998)
3. M. Reuter, F. Saueressig, Quantum gravity and the functional renormalization group: the road towards asymptotic safety. Cambridge monographs on mathematical physics. <https://doi.org/10.1017/9781316227596>
4. A. Bonanno, M. Reuter, Cosmology of the Planck era from a renormalization group for quantum gravity. *Phys. Rev. D* **65**, 043508 (2002)
5. M. Niedermaier, M. Reuter, The asymptotic safety scenario in quantum gravity. *Living Rev. Rel.* **9**, 5 (2006)
6. A. Codello, R. Percacci, C. Rahmede, Investigating the ultraviolet properties of gravity with a wilsonian renormalization group equation. *Ann. Phys.* **324**, 414–469 (2009)
7. M. Reuter, F. Saueressig, Renormalization group flow of quantum gravity in the Einstein-Hilbert truncation. *Phys. Rev. D* **65**, 065016 (2002)
8. K. Falls, D.F. Litim, K. Nikolakopoulos, C. Rahmede, Further evidence for asymptotic safety of quantum gravity. *Phys. Rev. D* **93**(10), 104022 (2016)
9. R. Mandal, S. Gangopadhyay, A. Lahiri, Cosmology of Bianchi type-I metric using renormalization group approach for quantum gravity. *Class. Quant. Grav.* **37**, 065012 (2020)

Chapter 166

Formation of Marginally Trapped Surfaces in Gravitational Collapse



Suresh C. Jaryal and Ayan Chatterjee

Abstract Using a combination of analytical and numerical techniques, we study the formation and time evolution of collapsing shells, spherically symmetric marginally trapped tubes, as well as the event horizon. Depending on the mass function, density, and the velocity profile, there can be situations where these marginally trapped surfaces becomes space-like, time-like, or null.

166.1 Introduction

The quest of finding the final outcome of a gravitational collapse is central in gravitational theory and relativistic astrophysics. This quest is of great importance in understanding the formation of central singularity, horizons, and cosmic censorship conjecture [1–5]. According to the cosmic censorship conjecture, the gravitational collapse of matter cloud results in the formation of central spacetime singularity [1, 2, 5]. This central singularity is stated to be followed by horizon, and hence it remains closed from a faraway observer. The general description of these horizon is the EH formalism which requires the global development of the spacetime. However, it is not always possible to have access to the global evolution of spacetime. The alternative formalism to the global EH formalism is the local notions of the horizons known as trapped surfaces [5–9]. In these trapped surfaces, the expansion of null rays orthogonal to closed 2-surfaces is negative. Depending upon the sign of θ_l , to be less, equal, or greater than zero, represents the 2-sphere as trapped, marginally trapped, or untrapped sphere, respectively. The notion of the trapping horizon (TH) has important application in BH physics. The dynamical (DH) and isolated horizons (IH) are the useful formalism to describe the evolution of the EH [10–15].

The most important formalism to study the formation and evolution of BH through different phases is the formulation of marginally trapped tubes (MTT) as it does

S. C. Jaryal (✉) · A. Chatterjee
Department of Physics and Astronomical Science, Central University of Himachal Pradesh,
Dharamshala 176206, India
e-mail: suresh.fifthd@gmail.com

not have any specific signature. For example, when MTT is null or space-like, an IH or DH, it represents BH horizon at equilibrium or a growing BH, respectively. The formation and evolution of the MTTs for gravitational collapse of dust-like, LTB matter cloud have been studied in [16–20] In this manuscript, in order to have better understanding of collapsing phenomena, we have extended this formalism of studying the formation and evolution of MTTs for more generic matter clouds. The details of this work can be found in [20].

This work is supported by the DST-MATRICES scheme of government of India through MTR/2019/000916 and by the DAE-BRNS Project No. 58/14/25/2019-BRNS.

166.2 Spherically Symmetric Collapse Formalism

We consider a general spherically symmetric matter cloud having line element

$$ds^2 = -e^{2\alpha(r,t)} dt^2 + e^{2\beta(r,t)} dr^2 + R(r, t)^2 d\theta^2 + R(r, t)^2 \sin^2 \theta d\phi^2. \tag{166.1}$$

The energy–momentum tensor for general anisotropic fluid is

$$T_{\mu\nu} = (p_\theta + \rho)u_\mu u_\nu + p_\theta g_{\mu\nu} + (p_r - p_\theta)X_\mu X_\nu - 2\eta\sigma_{\mu\nu} - \zeta\Theta P_{\mu\nu}, \tag{166.2}$$

where $\eta \geq 0; \zeta \geq 0$ are the coefficients of shear and bulk viscosity. u^μ & X^μ are unit time-like and space-like vectors, respectively, satisfying $u_\mu u^\mu = -X_\mu X^\mu = -1$ and $u_\mu X^\mu = 0$. Also, $\sigma_{\mu\nu}, \Theta$ & $P_{\mu\nu}$ are shear, expansion, and projection tensor fluids. ρ, p_r & p_θ are the energy density, radial, and tangential pressures, respectively. The set of non-vanishing components of the Einstein equations are

$$\rho = \frac{F'}{R^2 R'}; \quad p_r = -\frac{\dot{F}}{R^2 \dot{R}} + \frac{4}{3}\eta\sigma + \zeta\Theta, \tag{166.3}$$

$$\Phi' = \frac{2(\Theta - \sigma)'}{3\sigma} \frac{p_\theta - p_r + 2\eta\sigma}{\rho + p_r - \frac{4}{3}\eta\sigma - \zeta\Theta} - \frac{p_r' - \frac{4}{3}\eta\sigma' - \zeta\Theta'}{\rho + p_r - \frac{4}{3}\eta\sigma - \zeta\Theta}, \tag{166.4}$$

$$2\dot{R}' = R' \frac{\dot{G}}{G} + \dot{R} \frac{H'}{H} \quad \Leftrightarrow \quad \frac{\dot{G}}{G} = -\frac{2\dot{R}\Phi'}{R'}, \tag{166.5}$$

$$F = R(1 - G + H), \tag{166.6}$$

where $H = e^{-2\Phi(r,t)} \dot{R}^2; G = e^{-2\psi(r,t)} R'^2$. Also F, R & A represents the Misner–Sharp mass function, radius, and area of the 2-sphere, respectively. The dynamics of the marginally trapped surfaces depends upon the sign of the expansion parameter C , at $R = F$, defined by

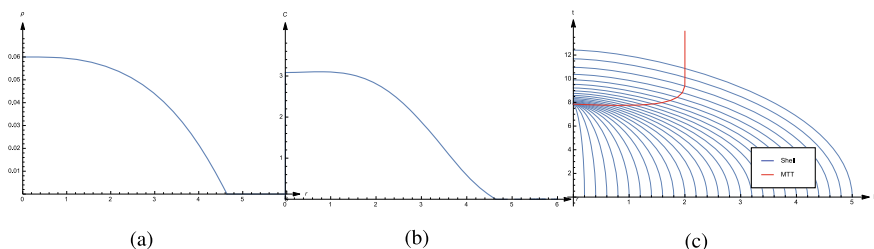


Fig. 166.1 Figure a and b shows the plots of the density ρ and expansion parameter C with respect to r . Figure c shows the plot of collapsing shells (labeled by r) and formation of the MTTs at $R = F$

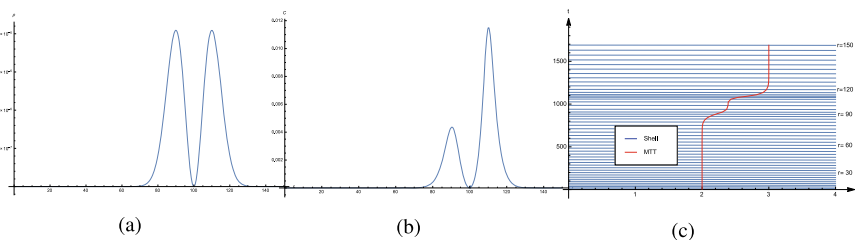


Fig. 166.2 Figure a and b shows the plots of the density ρ and expansion parameter C with respect to r . Figure c shows the plot of collapsing shells (labeled by r) and formation of the MTTs at $R = F$

$$C = \frac{\xi_l \Theta_{(l)}}{\xi_n \Theta_{(l)}} = \frac{\rho + p_\theta - (4/3)\eta\sigma - \zeta\Theta + (p_\theta - p_r)}{(4\pi/\mathbf{A}) - (1/2) [\rho - \{p_\theta - (4/3)\eta\sigma - \zeta\Theta + (p_\theta - p_r)\}]} \tag{166.7}$$

Now, to study the formation and evolution of MTTs, we have considered collapsing matter cloud having forms:

1. $\rho(r) = \frac{3m_0}{5000} (100 - r^3) \text{HeavysideTheta} [100 - r^3]$
2. $\rho(r) = \frac{8(m_0/r_0^3)[(r/r_0) - \zeta]^2}{[2\zeta + (3+2\zeta^2)\sqrt{\pi}e^{\zeta^2} \{1 + \text{erf}(\zeta)\}]} \exp[(2r/r_0)\zeta - (r/r_0)^2]$,

where m_0 is the total mass of the shell and r_0 is the width of each shell (Figs. 166.1 and 166.2).

166.3 Discussion of the Results

Our main focus was to identify and locate spherical MTTs for generic matter field. In order to trace the formation and evolution of MTTs and the EH, we study equations of collapsing cloud in t - R -coordinate. For the matter-density cloud, Fig. 166.1a, it can be seen from Fig. 166.1b that, as the matter shells start to fall, the expansion parameter C grows and remains positive (signature of MTT is space-like) throughout the collapse and as the last matter shell falls it becomes null. This behavior can also be confirmed

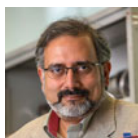
from the t-R plot in Fig. 166.1c, with falling of the matter shells, MTTs first start to grow and then at the end state when all the matter has fallen and density becomes zero, MTT becomes null. Similar behavior holds for the second density profile also. The spacetime curvature is $\simeq R^{-6}$, and hence blows up at spacetime singularity at $R = 0$, where GR itself breaks down. This study is limited to the spherically symmetric collapse but the results obtained here may be extended to build a general framework to study MTTs in both spherical and non-spherical gravitational collapse.

References

1. S.W. Hawking, G.R. Ellis, *The Large Scale Structure of Spacetime* (Cambridge University Press, Cambridge, 1975)
2. M. Robert, Wald, *General Relativity* (University of Chicago Press, 1984)
3. L.D. Landau, E.M. Lifshitz, *The Classical Theory of Fields* (Pergamon Press, New York, 1975)
4. P.S. Joshi, *Gravitational Collapse and Spacetime Singularities* (Cambridge University Press, Cambridge, England, 2007)
5. R. Penrose, Phys. Rev. Lett. **14**, 57 (1965); Gen. Relativ. Gravit. **34**, 1141 (2002)
6. A. Ashtekar, B. Krishnan, Living Rev. Relativ. **7**, 10 (2004)
7. I. Booth, Can. J. Phys. **83**, 1073 (2005)
8. S.A. Hayward, Phys. Rev. D **49**, 6467 (1994)
9. A. Chatterjee, B. Chatterjee, A. Ghosh, Phys. Rev. D **87**, 084051 (2013)
10. A. Ashtekar, C. Beetle, O. Dreyer, S. Fairhurst, B. Krishnan, J. Lewandowski, J. Wisniewski, Phys. Rev. Lett. **85**, 3564 (2000)
11. A. Ashtekar, S. Fairhurst, B. Krishnan, Phys. Rev. D **62**, 104025 (2000)
12. A. Ashtekar, B. Krishnan, Phys. Rev. Lett. **89**, 261101 (2002)
13. A. Ashtekar, B. Krishnan, Phys. Rev. D **68**, 104030 (2003)
14. A. Chatterjee, A. Ghosh, Phys. Rev. D **91**, 064054 (2015)
15. A. Chatterjee, A. Ghosh, Phys. Rev. D **92**, 044003 (2015)
16. A. Ashtekar, G.J. Galloway, Adv. Theor. Math. Phys. **9**, 1 (2005)
17. I. Booth, L. Brits, J.A. Gonzalez, C. Van Den Broeck, Class. Quantum Gravity **23**, 413 (2006)
18. A.M. Sherif, R. Goswami, S.D. Maharaj, Class. Quantum Gravity **36**, 215001 (2019)
19. A.M. Sherif, R. Goswami, S.D. Maharaj, Int. J. Geom. Methods Mod. Phys. **17**, 2050097 (2020)
20. A. Chatterjee, A. Ghosh, S. Jaryal, Phys. Rev. D **102**(6), 064048 (2020)

Appendix A

Plenary Speakers



Science and Status of the Electron Ion Collider

Abhay Deshpande

Department of Physics & Astronomy, Stony Brook University, Stony Brook, NY 11794-3800



Positive Geometry and Quantum Field Theory

Alok Laddha

Chennai Mathematical Institute, Siruseri, Chennai 603103, India



Recent Results from the LHC Heavy-Ion Programme

Andrea Dainese

INFN-Sezione di Padova, via Marzolo 8, 35131 Padova, Italy



MARS: From the Higgs Boson to Molecular Radiology

Anthony P H Butler

^a *MARS Bioimaging Ltd, Christchurch, New Zealand*

^b *School of Chemical and Physical Sciences, University of Canterbury, New Zealand*

^c *Department of Radiology, University of Otago, New Zealand*

^d *PH Department, CERN, Geneva, Switzerland*



Circuit Complexity and (Some of) Its Application

Arpan Bhattacharrya

Indian Institute of Technology, Gandhinagar, Gujarat 382355, India



Beyond Standard Model Theory

Christophe Grojean

^a *Deutsches Elektronen-Synchrotron (DESY), 22607 Hamburg, Germany*

^b *Institut für Physik, Humboldt-Universität zu Berlin, 12489 Berlin, Germany*



Bulk Entanglement Entropy/Quantum Quenches

Gautam Mandal

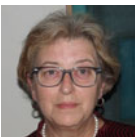
Department of Theoretical Physics, Tata Institute of Fundamental Research, Mumbai 400005, India



2020: Highlights from ATLAS and CMS

Greg Landsberg

Brown University, Dept. of Physics, 182 Hope St, Providence, RI 02912, USA



Future Collider Projects—The European Perspective

Halina Abramowicz

The Raymond and Beverly Sackler School of Physics and Astronomy, Tel Aviv University, 69978 Tel Aviv, Israel



Recent Developments in Silicon and Diamond Detectors—Future of Silicon Trackers at CERN’s LHC and Beyond

Heinz Pernegger

CERN Experimental Physics Department, Espl. des Particules 1, Geneve, Switzerland



Latest Results From Heavy-Ion Collisions at RHIC

Helen Caines

Physics Dept., Yale University, New Haven, CT 06511, USA



Experimental Status of Neutrino Physics

Hirohisa A Tanaka

SLAC, MS 94, Stanford University, 2575 Sand Hill Road, Menlo Park, CA 94025, USA



Measurements of Neutron Stars and The Dense Matter EOS

James Lattimer

Department of Physics and Astronomy, Stony Brook University, Stony Brook, NY 11794-3800, USA



Xenon TPCs for Rare Searches

Juan J Gomez Cadenas

^aDonostia International Physics Center (DIPC), San Sebastián/Donostia, Spain

^bIkerbasque, Basque Foundation for Science, Bilbao, Spain



Theoretical Status of Neutrino Physics

Kaladi S Babu

Department of Physics, Oklahoma State University, Stillwater, OK, 74078, USA



The First Image of a Black Hole

Luciano Rezzolla

Institut für Theoretische Physik, Goethe-Universität Frankfurt, Max-von-Laue-Straße 1, D-60438 Frankfurt am Main, Germany



Indirect Dark Matter Searches: Status and Challenges

Pasquale D Serpico

LAPTh, Univ. Grenoble Alpes, USMB, CNRS, F-74000 Annecy, France



The Square Kilometre Array: A Physics Machine for the 21st Century

Philip Diamond

BCA, Alan Turing Building, School of Physics and Astronomy, The University of Manchester, Oxford Road, Manchester M13 9PL, UK



Future Prospects of Neutrino Physics

Sandhya Choubey

^aDepartment of Physics, School of Engineering Sciences, KTH Royal Institute of Technology, AlbaNova University Center, Roslagstullsbacken 21, SE-106 91 Stockholm, Sweden

^aThe Oskar Klein Centre, AlbaNova University Center, Roslagstullsbacken 21, SE-106 91 Stockholm, Sweden

Recent Theoretical Developments on QCD Matter at Finite Temperature and Density

Sayantana Sharma

The Institute of Mathematical Sciences, HBNI, Chennai 600113



The Next-Generation Event Horizon Telescope: New Approaches to Black Hole Imaging

Sheperd S Doeleman

Center for Astrophysics | Harvard & Smithsonian, 60 Garden Street, Cambridge, MA 02138, USA



Status of Flavour Physics

Valerie Gibson

Cavendish Laboratory, University of Cambridge, Cambridge, United Kingdom

Appendix B

Special Sessions



Pushan Majumdar Memorial Session

N D Hari Dass

Visiting Professor, TIFR-TCIS, Hyderabad-500075, India



Sourendu Gupta

Department of Theoretical Physics, Tata Institute of Fundamental Research, Homi Bhabha Road, Mumbai 400005, India



Christian B Lang

Institute of Physics, University of Graz, Austria



Panel Discussion on Gender Parity

Ajit Srivastava

Institute of Physics, Sachivalaya Marg, Bhubaneswar-751005, India



Anju Bhasin

Physics Department, University of Jammu, Jammu, India



Bindu Bambah

*School of Physics, University of Hyderabad, Gachibowli, Hyderabad, Andhra Pradesh, India
500 046*



Preeti Kharb

*National Centre for Radio Astrophysics, Tata Institute of Fundamental Research, Postbag 3,
Ganeshkhind, Pune 411007, India*



Rohini Godbole

Centre for High Energy Physics, Indian Institute of Science, Bangalore, India



Rahul Basu Memorial PhD Award

Entropy Production and Thermal Fluctuations in Higher Order Dissipative Hydrodynamics

Chandroday Chattopadhyay

Tata Institute of Fundamental Research, Mumbai, India



New Aspects of Supernova Neutrino Flavor Conversions: In the Standard Model and Beyond

Manibrata Sen

Tata Institute of Fundamental Research, Mumbai, India



Jets as Probes for Precision Measurements and Candles for Physics Beyond Standard Model

Suman Chatterjee

Tata Institute of Fundamental Research, Mumbai, India



Measurement of the CKM Angle ϕ_3 from $B^\pm \rightarrow D(K_S^0 \pi^+ \pi^- \pi^0) K^\pm$ Decays and Future Prospects

Resmi P K

Indian Institute of Technology Madras, Chennai, India



Study of the Anomalous Gauge Boson Self Couplings and The Role of Spin 1 Polarizations

Rafiqul Rahaman

Indian Institute of Science Education and Research Kolkata, Kolkata, India

Appendix C

Best Poster Awardees

- 1. Measurement of Inclusive Photon Multiplicity at Forward Rapidity in p–Pb Collisions at $\sqrt{s_{NN}} = 5.02$ TeV with ALICE**
Abhi Modak
Bose Institute, Kolkata, India
- 2. Study of Long-Range Force of $L_\mu - L_\tau$ Symmetry @ INO**
Amina Khatun
Institute of Physics, Sachivalaya Marg, Sainik School Post, Bhubaneswar 751005, India, and Comenius University, Mlynská dolina F1, SK842 48 Bratislava, Slovakia
- 3. Relativistic Non-resistive Viscous Magnetohydrodynamics From Kinetic Theory: A Relaxation Time Approach**
Ankit Kumar Panda
School of Physical Sciences, National Institute of Science Education and Research, HBNI, 752050, Jatni, India
- 4. Enhancing Scalar Productions with Leptoquarks at the LHC**
Bibhabasu De
Institute of Physics, Sachivalaya Marg, Bhubaneswar 751 005, India, and Homi Bhabha National Institute, Training School Complex, Anushaktinagar, Mumbai 400 085, India
- 5. Prototype TPC for the Measurement of Cosmic Muon Flux**
Jim John
Homi Bhabha National Institute, Anushaktinagar, Mumbai, India, and Tata Institute of Fundamental Research, Dr. Homi Bhabha Road, Mumbai, India
- 6. Search for the Rare Decay $B_s \rightarrow \rho^0 \pi^0$ at $\Upsilon(5S)$ Resonance Using Belle Detector**
Jyotirmoi Borah
Indian Institute of Technology Guwahati, Assam, India
- 7. Role of Higher Dimensional Operators in Anomaly-free U(1) Extension**
Kuldeep Deka
Dept of Physics & Astrophysics, University of Delhi
- 8. Sensitivity to 1–2 Oscillation Parameters with GeV Neutrinos and Their Effects on δ_{CP} Measurement**
Lakshmi S Mohan
National Centre for Nuclear Research, Warsaw, Poland
- 9. Effective Interactions of Heavy Quark-Philic Dark Matter**
Lalit Kumar Saini
Dept of Physics & Astrophysics, University of Delhi

10. **Comparison of Muon Flux at Madurai Obtained with Different Phenomenological Models**
Pethuraj Sankaranarayan
Homi Bhabha National Institute, Anushaktinagar, Mumbai, India, and Tata Institute of Fundamental Research, Dr. Homi Bhabha Road, Mumbai, India
11. **Hierarchy Problem and Dimension-6 Effective Operators**
Poulami Mondal
Department of Physics, University of Calcutta, 92 Acharya Prafulla Chandra Road, Kolkata 700009, India
12. **QGP Vorticity and Particle Spin Polarization**
Rajeev Singh
Institute of Nuclear Physics Polish Academy of Sciences, PL 31-342 Kraków, Poland
13. **Study on RPC Charge Dispersion as a Function of Surface Resistivity**
Shamsul Haque Thoker
Department of Physics, University of Kashmir, Srinagar-190006, India
14. **Hybrid Hydrodynamics Attractor and the Quark-Gluon Plasma**
Sukrut Mondkar
Indian Institute of Technology Madras, Chennai, India


Appendix D

Symposium Poster

XXIV DAE-BRNS HIGH ENERGY PHYSICS SYMPOSIUM 2020

December 14 -18

National Institute of Science Education and Research (NISER)
Jatni Odisha 752050




TOPICS

- Standard model physics
- Beyond standard model physics
- Relativistic heavy-ion physics & QCD
- Neutrino physics
- Particle astrophysics & cosmology
- Detector development, future facilities and experiments
- Formal theory
- Societal applications: Medical physics, imaging etc.

<https://www.niser.ac.in/daehep2020>

VIRTUAL CONFERENCE

LOCAL ORGANIZING COMMITTEE	NATIONAL ORGANIZING COMMITTEE	
<p>Ajit Sinhasaria (ICP)</p> <p>Animesh K. Jaiswal (NSER)</p> <p>Arun K. Nayak (ICP)</p> <p>Bodhanpalla Mohanty (NSER)</p> <p>Chandrasekhar Bhambhaniya (IT-IBBS)</p> <p>Chetan N. Gowdigager (NSER)</p> <p>Faizima Ghosh (ICP)</p> <p>Manojita Patra (ICP)</p> <p>PM Nazam (ISER-BPR)</p> <p>Nagendra Nayak (NISER)</p> <p>Nishikanta Khanda (NSER)</p> <p>Pankaj Agrawal (ICP)</p> <p>Pradyip K. Sahu (ICP)</p> <p>Pradyip K. Mishra (NSER)</p> <p>Ranbir Singh (NSER)</p> <p>Sandeep Chatterjee (ISER-BPR)</p> <p>Santosh Swain (NSER)</p> <p>Sarbajit Kumar Agardwala (ICP)</p> <p>Sayantani Bhattacharyya (NSER)</p> <p>Seema Bahuguna (IT-IBBS)</p> <p>Shanku Kumar (ICP)</p> <p>Shivanis S. Patil (IISER)</p> <p>Subhasish Basak (NSER)</p> <p>Sudhakar Panda (NSER)</p> <p>Surbhanu Bhandi (Bansanubhai University)</p> <p>Sudipta Mukherjee (ICP)</p> <p>Susanta Mukherjee (IISER)</p> <p>Tapan Kumar Nayak (NSER)</p> <p>Tapan Ghosh (NSER)</p> <p>Ujjal Kumar Dey (ISER-BPR)</p> <p>Vandana K. S. Kashyap (NSER)</p> <p>Vijay Roy (NSER)</p> <p>Yogesh K. Srivastava (NSER)</p>	<p>Ananda Sinha (ISER)</p> <p>Anuragman Moharana (IISER)</p> <p>Bhramendu Singh (IISER)</p> <p>Buddhi Bhuyan (IT-Guwahati)</p> <p>Diprimy Ghosh (ISER-Pune)</p> <p>Hemanta Mishra (IISER)</p> <p>D. Indumathi (IISER)</p> <p>James Libby (IT-IBBS)</p> <p>Kirti Ranjan (IISER)</p> <p>Lalith Kumar (IISER)</p> <p>Prabhu Kumar Bhatia (IT-IBBS)</p> <p>Raghunathan Srinand (IISER)</p> <p>Sushanta Nath (IISER)</p> <p>Saikat Dasgupta (IT-IBBS)</p> <p>S. Sanyal (IISER)</p>	<div style="text-align: center;">  </div> <p style="margin: 5px 0;">IMPORTANT DATES</p> <p>Abstract submission: August 16 - September 30, 2020</p> <p>Registration (FREE): August 16 - November 15, 2020</p> <p style="margin: 5px 0;">CONTACT</p> <p>daebrnshep2020@gmail.com</p> <p>School of Physical Sciences National Institute of Science Education and Research PO-Bhubaneswar-Padanpur, via-Jatni, Khurda, Odisha 752050</p>